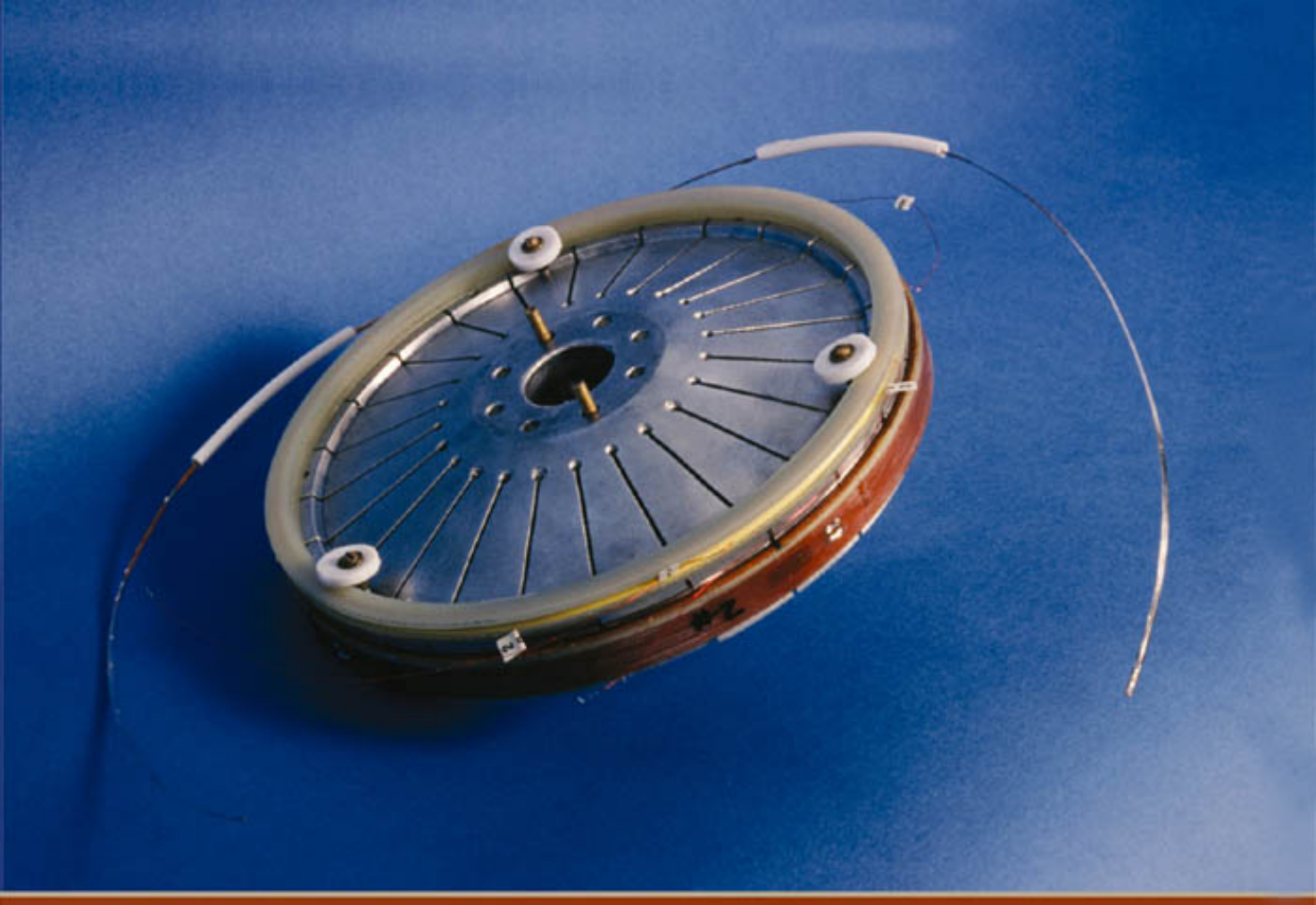

EXPERIMENTAL TECHNIQUES FOR LOW-TEMPERATURE MEASUREMENTS

CRYOSTAT DESIGN, MATERIAL PROPERTIES, AND SUPERCONDUCTOR CRITICAL-CURRENT TESTING

Jack W. Ekin

Experimental Techniques for Low-Temperature Measurements

Cryostat Design, Material Properties, and Superconductor Critical-Current Testing

This page intentionally left blank

Experimental Techniques for Low-Temperature Measurements

Cryostat Design, Material Properties, and Superconductor Critical-Current Testing

Jack W. Ekin

National Institute of Standards and Technology, Boulder, CO, USA

OXFORD
UNIVERSITY PRESS

OXFORD
UNIVERSITY PRESS
Great Clarendon Street, Oxford OX2 6DP
Oxford University Press is a department of the University of Oxford.
It furthers the University's objective of excellence in research, scholarship,
and education by publishing worldwide in

Oxford New York

Auckland Cape Town Dar es Salaam Hong Kong Karachi
Kuala Lumpur Madrid Melbourne Mexico City Nairobi
New Delhi Shanghai Taipei Toronto

With offices in

Argentina Austria Brazil Chile Czech Republic France Greece
Guatemala Hungary Italy Japan Poland Portugal Singapore
South Korea Switzerland Thailand Turkey Ukraine Vietnam

Oxford is a registered trade mark of Oxford University Press
in the UK and in certain other countries

Published in the United States
by Oxford University Press Inc., New York

First published 2006

British Library Cataloguing in Publication Data
Data available

Library of Congress Cataloging in Publication Data
Data available

Typeset by Newgen Imaging Systems (P) Ltd., Chennai, India
Printed in Great Britain
on acid-free paper by
Antony Rowe Ltd., Chippenham.

ISBN 0–19–857054–6 978–0–19–857054–7

10 9 8 7 6 5 4 3 2 1

For my dear family: Sharon, Lindy, and Lisa;

and in memory of my close colleague and friend, Steve Bray.

This page intentionally left blank

Preface

Der Teufel liegt im Detail

When I started low-temperature experimental work in graduate school and wanted to know "how to do it," I was struck by the abbreviated "experimental detail section" of most publications that simply stated the sample was mounted in the test apparatus, leads were attached, and the measurement made. But try to "simply" do that. The details are everything. Somehow the vital bits of experimental know-how do not get into print, the specifics of how to do it yourself. This book starts to answer some of the detailed questions about the design and construction of cryogenic probes in general, and superconductor measurements in particular. Simply put, these are the things I wish I had been told when I began.

This text is not about how to perform the vast array of cryogenic measurements; that is an extensive topic covered in many specialized references. Rather, it is about *design* techniques *common* to most measurement cryostats; the appendixes provide materials-property data for carrying out that design.

The mantra for this book is that it be *useful*. Topics include, for example, thermal techniques for designing a cryogenic apparatus that works (instead of one whose temperature is impossible to control), selecting appropriate materials (that do not thermally contract and rip the rig apart, or embrittle and snap), making high-quality electrical contacts to a superconductor (that avoid thermal runaway), and making a critical-current measurement that is believable (and does not vaporize your sample).

No one book can do it all; to really learn, we have to get into the lab and try it out. A wise man once said that the only way to become an expert is to make all the mistakes; it is my hope that this book will shorten that learning curve. In this spirit, I occasionally share a few of my own mistakes, because I think a lot can be learned from what does *not* work.

Audience: The main text is written for specialists, but it also includes introductory material. Thus, it would be useful for a wide range of experimentalists—graduate students, industry measurement engineers, materials scientists, and experienced researchers. In short, the book is intended for anyone interested in techniques for designing and operating effective low-temperature (1–300 K) measurement systems, with special emphasis on superconductor critical-current measurements in the last few chapters.

Data-handbook: The extensive appendix is a data handbook of material properties and cryostat design. It was written for specialists in the field of cryogenic measurements who want to save time by having much of the information for designing a new measurement probe collected in one place. These tables have been compiled from information supplied by colleagues and from over fifty years of literature. Appendix contents are listed on the inside back cover and include:

- Electrical, thermal, magnetic, thermoelectric, expansion, specific heat, mechanical, and vacuum properties of cryostat materials.

- Data on cryogenic liquids.
- Thermometer properties and standard calibration tables.
- Properties of construction parts and materials: pipes, tubing, bolts, wire, brazing compounds, solders, fluxes, and sticky stuff.
- Suppliers of hard-to-find parts and materials.

Up front, I want to emphasize that this is not a review of the literature. It is a compendium of information that I have freely edited and reduced to the bare bones. On most subjects, I have also taken the license to express my opinion of what I like, along with the ideas of trusted associates. When I start learning a new area, I do not want to know all the possibilities in great detail; rather, I would like a road map based on the subjective thoughts of someone who has been there, so that I can get started. On the other hand, I do want complete, easy-to-find reference tables and figures so that I can return to other possibilities after I have had some experience. The book has been written with this approach in mind. So, for example, a comprehensive table of cryogenic thermometer properties is given in Appendix A5.2, but in the main text (Chapter 5) I recommend which thermometer I would typically use in practical situations. This represents only my opinion, and no doubt others may have different ideas as to what is best. But at least it is a place to start. And the other possible choices are there, tabulated in the appendix for later reference.

Cryogenic measurements are basically a matter of: (1) designing and building a measurement apparatus, (2) mounting samples, and (3) making measurements and analyzing the data. The three main parts to this book are organized along these simple guidelines.

I hope this step-by-step integrated approach, the examples, and the collection of appendix data on technical materials will take some of the devil out of the details.

J.W.E.

Sydney, Australia
Boulder, CO

Contents

This page intentionally left blank

Symbols and abbreviations

a	strain-sensitivity parameter
a^+	tensile intrinsic-strain values of a
a^-	compressive intrinsic-strain values of a
a_1, a_2	accommodation coefficients
a_1, a_2	extended-strain-range fitting parameters for B_{c2}^* (Chapter 10)
A	cross-sectional area
A_c	contact area
A_i, A_o	areas of inner and outer cylindrical surfaces
A_{cross}	cross-sectional area
A_{min}	minimum cross-sectional area
A_{surf}	surface area of a solid
B, B'	magnetic field or magnetic induction in free space
B_c	critical B
B_{c2}	upper critical B
B_{c2}^*	effective upper critical B
B_{irr}	irreversibility B
Bi	Biot number
b	reduced magnetic field
C	conductance
C_e	contribution to specific heat from conduction electrons
C_V	specific heat at constant volume
C_p	specific heat at constant pressure
d	distance or thickness
D	diameter
D_i, D_o	inner and outer diameter
D_t	thermal diffusivity
$\boldsymbol{E}$	factor between 0 and 1 depending on surface emissivity (Chapter 2)
E	Young's modulus
E_c	electric-field criterion level
E_F	Fermi energy
e	electron's charge
F	force
F_{cr}	critical load for buckling
F_L	Lorentz force
F_y	load at which a part will yield
$f(b)$	general pinning-force function
G	gain
$g(\varepsilon), g(\varepsilon_0)$	strain-scaling-law prefactor
g_1, g_2	extended-strain-range fitting parameters for $g(\varepsilon_0)$
H^*	scaling field
H_0	decoupling magnetic field
H_{c1}	lower critical field
H_{c2}	upper critical field
H_{c2}^*	effective upper critical field
H_{irr}	irreversibility field
h	convective heat-transfer coefficient
$h(T), h(t)$	temperature-scaling-law prefactor
I	current
I_c	critical current
$I_c^{\text{el field}}$	critical current determined by electric-field criterion
I_c^{offset}	critical current determined by offset criterion
I_{drive}	coil drive current
I_m	moment of inertia
J	current density
J_c	critical-current density
J_e	engineering critical-current density
J_n	nonstabilizer critical-current density
K	permeation constant of a material
K	scaling prefactor function
K_{1c}	fracture toughness
K_p	plate constant
k_B	Boltzmann's constant
l	mean free path
L	length
L_a	length between turning axes of sample grips
L_s	sample length
L_N	Lorentz number
m	mass
n	index of nonlinearity
$\dot{n}$	gas molar flow rate
N_A	Avogadro constant
p	parameter characterizing shape of low-field pinning force
P	pressure
P_b	proportional band

P_i	pressure inside a vacuum vessel
P_o	pressure outside a vacuum vessel
P_{ult}	ultimate pressure inside a vacuum vessel
$\dot{q}$	rate of heat flow
$\dot{q}_{cond}$	rate of heat transfer by conduction
$\dot{q}_{conv}$	rate of heat transfer by convection
$\dot{q}_{Joule}$	Joule heating rate
Q	gas volume flow rate
R	gas constant
R_c	contact resistance
R_s	sheet resistance
R_f	reflectivity
R	resistance
q	parameter characterizing shape of high-field pinning force
r	radius
s	strain scaling exponent
S_{pump}	pump speed
S	thermometer sensitivity
T	temperature
T_c	critical temperature
T_c^*	effective critical temperature
t	time
t	reduced temperature (Chapter 10)
U	internal energy
V	voltage
V_c	voltage criterion
ν	viscosity
$\overline{\nu}$	average velocity
v	exponent characterizing the temperature dependence of the effective upper critical magnetic field (Chapter 10)
W	total load
w	exponent characterizing the relationship between the effective critical temperature and upper critical magnetic field (Chapter 10)
x_{min}	minimum required current-transfer length

Greek

α	temperature coefficient of linear expansion
$\overline{\alpha}$	average α
β	transformation parameter [equal to $B_{c2}^*(t_2,\varepsilon_2)/B_{c2}^*(t_1,\varepsilon_1)$]
γ	Grüneisen parameter
δ	mass density
ε	surface emissivity (Chapter 2)
ε	strain
ε_0	intrinsic strain
ε_{bend}	bending strain (maximum)
ε_{irr}	irreversible damage strain limit
ε_m	strain where critical current is maximum
ε_y	strain at yield
η	temperature scaling exponent (Chapter 10)
θ	angle
θ_D	Debye temperature
λ	thermal conductivity
$\overline{\lambda}$	mean thermal conductivity
λ_e	thermal conductivity by electrons
λ_p	thermal conductivity by phonons
λ_r	radiation wavelength
μ_0	magnetic constant
ν	Poisson's ratio
ξ	effective spreading distance
ρ	electrical resistivity
ρ_c	specific contact resistivity
ρ_i	ideal resistivity
ρ_{res}	residual resistivity
σ	stress
σ_{hoop}	hoop stress
σ_{ult}	ultimate strength
σ_y	yield strength
σ_e	electrical conductivity
φ	magnetic flux
φ_0	magnetic flux quantum
χ	volume susceptibility
χ/ρ	mass susceptibility

Abbreviations

ABCs	mnemonic for aluminum, brass, copper, stainless steel (order of thermal contraction)
AISI	American Iron and Steel Institute
AWG	American Wire Gauge
b.c.c.	body-centered cubic
Bi-2212	$Bi_2Sr_2CaCu_2O_{8+x}$
Bi-2223	$(Bi, Pb)_2Sr_2Ca_2Cu_3O_{10-x}$
BSCCO	bismuth-based superconductor
EDM	electrical discharge machining
ELI	extra low interstitials
ETP	electrolytic tough pitch
f.c.c.	face-centered cubic

h.c.p.	hexagonal close packed
HTS	high-T_c superconductors
HV	high vacuum
ISO	International Standards Organization
ITS-90	The International Temperature Scale of 1990
KF	Klein Flange
MLI	multilayer insulation
MRI	magnetic-resonance imaging
NMR	nuclear magnetic resonance
OFHC	oxygen-free high conductivity [copper]
PCTFE	Polychlorotrifluoroethylene
PET	Polyethylene terepthalate, Mylar™
PID	proportional-integral-derivative
PMMA	Polymethyl methacrylate, Plexiglas™
PRT	platinum resistance thermometer
PTFE	polytetrafluoroethylene, a type of Teflon™
rf	radio frequency
rms	root-mean square
RRR	residual resistivity ratio
RT	room temperature
scfh	standard cubic feet per hour
SI	The international system of units (Système International d'Unités)
SQUID	superconducting quantum interference device
SS	stainless steel
SSL	strain scaling law
STP	standard pressure and temperature
TIG	tungsten–inert gas [welding]
TFE	Teflon
TSL	temperature scaling law
UHV	ultrahigh vacuum
UNS	Unified Numbering System
USL	unified strain-and-temperature-scaling law
WWH	Werthamer, Helfand, and Hohenberg (1966)
YBCO	yttrium–barium–copper oxide ($YBa_2Cu_3O_7$)

Acknowledgments

Technical information and expertise

With gratitude, I acknowledge many friends, collegues, and students, from whom I have learned much over the years, including my research associates at Cornell University, especially Bruce Maxfield and Niel Ashcroft, who introduced me to the fascinating world of low-temperature measurements and physics; my associates at Rutgers University, especially Bernie Serin, Bill McLean, and Peter Lindenfeld who gave me my first love for superconductivity; and my colleagues at the National Institute of Standards and Technology (NIST), particularly Peter Bradley, Tom Bruno, Najib Cheggour, Alan Clark, Fred Fickett, Ron Goldfarb, Loren Goodrich, Erich Grossman, Jerry Hust, Hassel Ledbetter, Eric Marquardt, John Martinis, Dave McColskey, Mark McLinden, John Moreland, Ron Ono, Dave Pappas, Ray Radebaugh, Dave Read, Dave Rudman, Steve Russek, Tom Siewert, Tom Silva, Larry Sparks, Danko Van Der Laan, and Yizi Xu.

Special appreciation is given to the following colleagues for help in compiling, measuring, and recalculating data for the appendix tables: Norm Bergren, Peter Kirkpatrick, Eric Lemmon, Robert McDonough, and, especially, Andrew Adare and Cam Clickner.

Writing of the text

The project was the result of an interesting series of events that came together to make it possible:

Guy White, for his initial invitation to conceive and plan the text, as well as valuable input from Chris Andrikidis, Lori Besley, Kathy Foley, Karl Muller, Ian Pollock, Grahame Slogget, and the staff at the National Measurements Laboratory in Sydney.

Harold Weinstock, for his invitation to lecture on this subject at the NATO Advanced Study Institute on Applications of Superconductivity (Norway, 1997) and the wonderful support and feedback of the graduate students attending that series, which provided the motivation for the text.

Bob Simmons and Liza Carlson, for encouraging me to create the time needed to write the book.

Dave Sutter of the US Department of Energy (DoE) High Energy Physics program, for the seminal grant that provided the opportunity to write the manuscript; and Jim Daley of the DoE Energy Systems for adding to that support.

Kirk Jensen and Sonke Adlung, Oxford University Press editors, for their heartfelt encouragement and patience in seeing the text through the administration, writing, and publication process.

In addition I would like to thank:

Steve Bray, for his insightful suggestions, technical expertise, generous help with the operations of my group, and personal encouragement during much of the writing of this text.

Najib Cheggour, for his technical editing, helpful comments, and extensive contributions to the operations of my project group.

Bill Anderson, Alan Cookson, Jud French, Dennis Friday, Dick Harris, and Bob Kamper for their administrative support, and, especially, Ron Goldfarb, Fred Fickett, and Al Clark, who provided the long-term encouragement and support needed to complete this work.

John Cumalat, Dan Dessau, Chuck Rogers, Allen Hermann, John Price, and the faculty of the Department of Physics at the University of Colorado for hosting my stay as a Visiting Fellow during part of the writing.

Dennis Dickerson for his careful drawing and redrawing of the figures.

Andrew Adare and Cam Clickner for helping to compile many of the appendix tables.

Cindy Kotary and Ruth Corwin for typing several of the tables.

My dear reviewers, who contributed mightily to the writing of this text (see below).

Reviewers of the text

It is with profound gratitude that I acknowledge the contributions of the wonderful team of technical reviewers of this text. Their heartfelt input and kind feedback have contributed greatly to transforming my initial rough thoughts into a genuinely useful text:

Bruce Brandt has studied magnetic thin films at Pomona College, superconducting films and foils at the University of Rochester, neurons in culture at the Salk Institute, and cryogenic thermometry in high magnetic fields at the Francis Bitter National Magnet Laboratory and National High Magnetic Field Laboratory (NHMFL). He is presently Director of the DC High Field Facilities at the NHMFL.

Mark Colclough: Following "a youth misspent mainly in the theatre," Mark Colclough began his research career in magnetic ordering at millikelvin temperatures. After promotions to 4.2 K and 77 K, he managed the SQUID program at Conductus in the early 1990s, before taking up a UK advanced fellowship in superconducting devices. He is presently a faculty member at the University of Birmingham, UK.

Adam Gromko received a Ph.D. degree specializing in experimental condensed-matter physics under Prof. Daniel Dessau of the University of Colorado while reviewing this book. Adam's research interests include the electronic structure of correlated electron materials, with emphasis on high-temperature superconductors.

Karsten Guth received a diploma in physics at the University of Göttingen in Germany. While reviewing this book, he was working on his Ph.D. thesis under Prof. Herbert Freyhardt at the Materials Science Institute in Göttingen. His Ph.D. thesis work focused on the fabrication and characterization of high-T_c superconducting thin-film bicrystals. In particular, he studied current distributions and transport properties of grain boundaries with magneto-optical imaging.

Mike Janocko received B.S. and M.S. degrees from Carnegie-Mellon University, and worked for the past four decades at Northrop Grumman (formerly Westinghouse) in the field of both large-scale and small-scale applications of superconductors. Projects included superconducting generators, helium calorimeter measurements, high-field superconducting magnets, pulsed energy storage, Josephson junction development, superconducting microwave filters, resonators, and delay line packages.

Hisayasu Kobayashi's research at Nihon University focused originally on instabilities in superconductors and subsequently on stabilization studies with superfluid helium. Presently, he is Vice Director of the Institute of Quantum Science, Nihon University, Japan.

Szuya Liao received B.S. and M.S. degrees in physics from Taiwan. During the reviewing period she pursued a Ph.D. degree in materials science under Prof. David C. Larbalestier at the University of Wisconsin—Madison. Her Ph.D. thesis work focused on the fabrication of high-T_c superconducting thin-film bicrystals and the properties of high-T_c superconducting grain boundaries.

John Pfotenhauer started his cryogenics research at the University of Oregon in 1980 studying convective heat transfer in liquid helium. Since 1984 he has been investigating the use of cryogenics for superconducting applications at the University of Wisconsin—Madison, characterizing transient heat transfer in superfluid helium, optimizing high-T_c superconducting current leads, and developing pulse tube refrigerators and other cryocoolers. He is currently Associate Professor in the departments of Mechanical Engineering and Engineering Physics at the University of Wisconsin—Madison.

Reviewers of selected sections and chapters

It has been a delight working with the following people at NIST who made many insightful suggestions for improving the technical content and clarity of individual sections: Mike Abrecht, Andrew Adare, Steve Bray, Najib Cheggour, Al Clark, Loren Goodrich, John Martinis, Ray Radebaugh, David Rudman, Steve Russek, Danko van der Laan, and, especially, David Smith and Ron Goldfarb for their editorial comments on the entire manuscript.

Also, I very much appreciate helpful suggestions and comments from the greater research community, including Hassane Darhmaoui (Alakhawayn University, Morocco), René Flükiger (University of Geneva), Herbert Freyhardt (University of Göttingen), Wilfried Goldacker (Forschungszentrum Karlsruhe), Dick Gummer (Precision Cryogenics), Damian Hampshire (Durham University), Ed Harley (American Superconductor), Bill Hollander (High Precision Devices), Scott Holmes and Scott Courts (Lakeshore Cryogenics), Randall Kirschman (Mountain View, CA), David Larbalestier (University of Wisconsin), Ken Marken (Oxford Superconductor), Denis Markiewicz (National High Magnetic Field Laboratory (NHMFL), Florida State University), Joe Minervini (MIT Plasma Fusion Center), Tim Murphy (NHMFL), Kozo Osamura (Kyoto University), Larry Rubin (Massachusetts Institute of Technology), Joel Schultz (MIT Plasma Fusion Center), Justin Schwartz (Florida State University), Kyoji Tachikawa (Tokai University), Ulf Trociewitz (National High Field Magnetic Field Laboratory), and Zuyu Zhao (Janis Research).

Deep appreciation is also extended to many friends, family, and colleagues not mentioned, who have consistently encouraged me in this project.

The helium beneath my wings: Special credit is given to my wife, Sharon. She was there at the beginning of graduate school, is still there, and has survived more than thirty-five years of cryogenic testing. Her encouragement and support have been the principal force sustaining the writing of this text.

About the author

Jack Ekin is a research physicist at the National Institute of Standards and Technology in Boulder, CO, where his contributions have spanned a wide range of topics in low-temperature physics, including studies of fundamental conduction processes in normal metals, electromechanical properties of both high- and low-T_c superconductors, and interface conduction in thin films and nanostructures. His discoveries include the first quantitative understanding of Umklapp processes in normal metals, the formulation of the strain and unified scaling laws used to engineer superconducting magnets, the analytic treatment of current-transfer effects in multifilamentary superconductors, and the offset criterion for defining critical current. His early work with high-T_c superconductors led to the first four patents for making practical electrical contacts to these oxide materials. At present, he is engaged in extensive collaborations to measure and understand the physics of strain effects on grain boundaries in high-T_c superconductors.

After completing a B.S. degree at the University of Michigan, Dr. Ekin conducted his early graduate work in physics at the University of Heidelberg as a Fulbright Scholar, and then received M.S. and Ph.D. degrees from Cornell University. Currently, he holds an appointment as Lecturer at the University of Colorado. Outside of his research interests, he serves as a professional fine-art photographer, collaborating with numerous open-space organizations. He is a member of the Institute of Electrical and Electronics Engineers and a Fellow of the American Physical Society. He has published over 150 cryogenic research articles, textbook chapters, and patents, and has lectured and consulted internationally in the field of low-temperature measurements.

Contact Information

Enlarged figure drawings, table updates, and further information are available at www.ResearchMeasurements.com. Comments, suggestions, or inquiries can be sent to Dr. Jack Ekin at JackEkin@ResearchMeasurements.com.

Disclaimer

Trade names, products, and companies named here are cited only in the interest of scientific description, and do not constitute or imply endorsement by NIST or by the US government. Other products may be found to serve just as well.

Part I

Cryostat Design and Materials Selection

This page intentionally left blank

1 Introduction to Measurement Cryostats and Cooling Methods

Everything should be made as simple as possible, but not simpler.

– Albert Einstein

1.1 Introduction

No single multitask measurement apparatus exists that is adequate for many different types of measurements over a wide temperature range. Once, I tried to design one—it turned into a "camel" (a camel has been defined as a "horse put together by a committee"). Measurement cryostats can range anywhere from a simple stainless-steel tube (or even a wooden stick) for dipping a sample in liquid helium, to complex systems with multiple vacuum jackets, internal variable temperature control, and radiation windows. In general, the *simpler* the cryostat for any given job, the better; however, always keep in mind that sometimes a little extra complexity makes a cryostat more flexible for a wider range of measurements.

The design and construction process for measurement apparatus is unlike that used for commercial manufacturing. It would probably make most good production engineers shake their heads in disbelief. Measurement requirements change all the time and so the rigs, which evolve, are usually one-of-a-kind affairs. There is just not enough time or return on investment to perform a full-fledged production-line engineering design. So, a lot of it ends up being "seat-of-the-pants" design. In the true experimental spirit, we sometimes have to make an educated guess and simply try it out. Usually a lot of designs will work, and often it just does not matter which you use. But it is essential to do *some* design, especially heat-transfer calculations, "as simple as possible, but not simpler." The process is a compromise. (Generally, we physicists need to do more engineering than we usually do. We waste too much time fixing stuff that could have been designed better in the first place.)

Also, there is no substitute for selecting construction materials appropriate to the task. Once a rig is built, it is usually an onerous task to replace the main structural supports with a material having a lower susceptibility, better strength, or different thermal-contraction coefficient. So, some up-front thinking about material properties can preclude a lot of problems down the road. The text includes an extensive appendix of tabulated heat-transfer data, materials-selection data, and construction information needed for cryostat design. I have also made some effort to supply the *reference sources* for each material's data, so you can go back to the sources for more information.

This book is about the design process and construction techniques that are *common* to most measurement apparatus; it is not an exhaustive handbook of highly specialized cryostat designs, which we learn mostly from others in our field of specialization and their instrumentation

literature. The emphasis is on those aspects of cryostat design and construction that are nearly universal—the challenge of cooling samples and accurately controlling their temperature throughout the cryogenic range under a wide variety of current, magnetic-field, and mechanical conditions. Additional reading on related subjects is given in the *Further reading* section at the end of each chapter.

1.1.1 ORGANIZATION OF THE BOOK

Contents of this book proceed from *general to specific*. The first six chapters (Part I) present experimental techniques that apply generally to *cryostat design* and *materials selection*. The next two chapters (Part II) focus on mounting and making electrical connections to samples for *transport* measurements. The last two chapters (Part III) narrow the focus still further and apply the information in the early chapters to one specific transport measurement, *critical current*, perhaps the most widely measured property of superconductors.

Throughout this book, concepts are illustrated with figures directly in the chapters, backed up by detailed tables of data in the *appendix*. (The data tables are collected in the appendix for easy look-up later). Appendixes 1 through 10 parallel Chapters 1 through 10 and represent the information I have always wanted assembled in one place when designing a new test rig. In some sense, the appendixes represent a *formalized lab wall*; that is, an assemblage of material that in many cases I have literally taken off the walls of our laboratories, since they were hanging there for good reason (usually).

Part I: Cryostat design and materials selection

Chapter 1 is mainly an *example* chapter, presented at the beginning so you can picture where we are headed. Here, we give an overview of useful types of measurement cryostats for the temperature range from 300 K to about 1 K. We also introduce cooling options and the properties of the most common cryogenic liquids and their powerful cooling capability.

Chapters 2 through 5 focus on practical cryogenic *techniques*. The order of presentation is that of the four steps I usually follow to design and build a measurement rig, or to attach a sample to the cold stage of a cryocooler. First, heat-transfer calculation is the single most important factor in cryostat design (Chapter 2). This is followed by materials selection and construction (Chapter 3), wiring (Chapter 4), and thermometer installation (Chapter 5).

Along the way, a few suggestions are included on how to make a cryostat work. The ultimate success of a rig results more from attitude than technique; it reminds me of a saying on a sign in a factory where a friend worked, and I have never forgotten it: "Cut to fit, bend to shape, paint to cover." It simply implies that in the end you have to take time and be creative to "make it work," to do all the adjusting, fitting, and retooling it takes to get good data. It also means running reality checks to justify confidence in the rig's data, as amplified at the end of this section.

Chapter 6 and the accompanying appendix tables describe *material properties* at cryogenic temperatures. Whereas Chapter 3 presents *guidelines* for choosing construction materials, Chapter 6 looks at the *physics* of material properties at low temperatures, giving detailed

graphs of properties and tables of data (*thermal, electrical, magnetic*, and *mechanical* handbook values).

Part II: Electrical transport measurements—sample holders and contacts

Chapters 7 and 8 focus on *transport* measurements of both bulk- and thin-film samples. These measurements are given special emphasis because of the challenge of *sample mounting* and *connections* when electrical current needs to be introduced into the test sample. The details of sample holders and contacts are the Achilles heel of such measurements as Hall coefficients, critical current, or thermoelectric coefficients. Poor sample-holder design and contact techniques have led to more "unusual" effects and scuttled more transport measurements than any other factor I know.

Part III: Critical-current measurements and data analysis

Finally, in Chapters 9 and 10, we look specifically at superconductor critical-current measurements, which serve to illustrate in a practical way the application of Parts I and II. Although we focus in detail on the measurement of critical current, many of the topics in Chapters 9 and 10 have application to a wide variety of other cryogenic measurements. This measurement provides a rich example of problem solving, including procedures for initial equipment checkout, troubleshooting, automatic data acquisition, reality checks, and detailed data analysis.

So, that is the organization of the book—general cryostat design and construction techniques in the first half, followed by a focus on transport measurements and critical-current testing in the second half. The material *within each chapter* is also organized to proceed from general topics in the first part of each chapter to more specialized techniques in the last part.

In approaching this, or any other book, it is sometimes useful to skip less relevant subjects and look at the parts that best suit your specific requirements at the moment, noting the other material and coming back to read it in detail later when it is needed. To guide you to pertinent sections of the text, I have included in this introductory chapter a *checklist* of questions (Sec. 1.3.1) intended to lead you quickly to information about your specific apparatus. A detailed index and table of contents for both the main text and appendixes are provided for quick navigation. (The latter is also located on the inside of the back cover for quick reference.)

1.1.2 THE LAST STEP

Since it is usually not emphasized in textbooks, let me underscore at the outset the main difference between a good measurement apparatus and anathema. The last step in the cryostat design and construction process is running experimental *reality checks* on a new test rig. No book and no one else can do that for us; it is a matter of personal integrity.

Sometimes it is so tempting to rush to publish a new effect from a new rig, just to be first (but ignoring some flaw in the apparatus or measurement technique). Too often, the "new effect" has to be dealt with, wastes everybody's time and money, and contributes to "literature pollution." It is our responsibility to *check the apparatus by use of (standard) test samples with known*

properties. Any new apparatus should yield not only approximately the right results, but *exactly* the right results. It is incumbent on us to trace down every little foible, jump in value, hysteresis, and so on, before it hurts us in a more difficult situation.

My experience is that theoreticians usually take published experimental data at face value and, given enough time and desire, they can find models to explain experimental artifacts. We know our apparatus and experimental procedure like no one else. So it pays to think about simple alternative explanations, especially for "unusual" data.

A reputation is a fragile thing. The more unusual the results, the greater the caution needed. As Carl Sagan often said, "Extraordinary claims require extraordinary evidence."

1.1.3 EXTRA ITEMS

Experimental tips: From time to time, I have included a few specific suggestions that do not exactly fit the main flow of text, but are, nevertheless, helpful items appropriate to the subject matter. These are separated from the main text by a light box and flagged by a little pointer (→).

Two *addenda* are included at the end of Chapter 1:

- *Safety (Sec. 1.6.1)*: This list is a genuine sharing of a few cryogenic situations where we have gotten into trouble. You might as well know up front what does *not* work. "Those who cannot learn from history are doomed to repeat it" (George Santayana).
- *Transferring cryogenic liquids (Sec. 1.6.2)*: This essential skill is nontrivial; it usually takes many mistakes to become proficient. There is no substitute for having someone knowledgeable *watch* you as you initially learn, but these tips may shorten the learning curve.

Equations: Where there are many equations, a box has been drawn around some of them to distinguish the more important relations and, especially in Chapter 10, to indicate sets of interconnected equations.

Definitions: Often when starting in a new field, it is helpful to decode a few of the terms we throw around all too glibly. A listing of common terms and ubiquitous acronyms is given in the first appendix (Appendix A1.1).

In this vein, let me mention that I have used the word "cryostat" throughout this book to describe the apparatus or insert that holds samples for measurements. More generally, the term cryostat can also refer to the insert *plus* the vacuum-insulated container, or "dewar," that holds cryogenic liquids. However, dewars are not the focus of the book, because efficient, well-designed dewars are available commercially. Other more colloquial terms I have used to describe the measurement cryostat are: "probe, rig, jig, ..."

1.2 **Cryogenic liquids**

This is *not* a textbook on commercial cryogenic refrigerators (cryocoolers) and liquefaction techniques. (Suggestions for more in-depth reading on these subjects are given in Sec. 1.7.1.) Rather, the focus is on designing and building measurement apparatus for *use* with cryogenic

liquids and cryocoolers. That said, a basic understanding of cryogenic liquids (cryogens) is absolutely essential for the rest of the book.

Therefore, we begin with a brief introduction to these amazing fluids. This is basic introductory cryogenic information, so please feel free to skip the material if you are already familiar with it. Much of the essential information on cryogenic liquids is summarized for convenience in Appendixes A1.5 and A1.6 at the end of the book. Updated vapor pressure vs. temperature data based on the International Temperature Scale (ITS-90) are presented separately in Appendix A5.1 under the heading of temperature measurements.

So let us dive right into these fluids. Essentially, there are two methods of cooling a test sample for cryogenic measurements:

1. The first one is the classic technique of directly *immersing* the sample in a cryogenic liquid (or cryogen). This is the most powerful cooling technique and is the method of choice whenever sample heating may be an issue, such as at high current densities. It also allows for easy, efficient cooling of samples of any shape, whether they are films, wires, small crystals, or completely irregularly shaped. However, this method does require learning to handle cryogenic liquids.
2. The second method is to attach the sample to the cold head of a *cryocooler*. This technique minimizes handling and transferring cryogenic fluids. However, it is usually restricted to lower cooling powers and lower transport currents through the sample, and it requires some care in sample mounting to provide adequate cooling.

We focus first on the immersion technique since the properties of cryogens are critical to both methods. (The various types of commercially available cryogenic refrigerators are summarized in Sec. 1.4.)

Figure 1.1 shows the basic scheme for immersion measurements. A test sample is attached to the end of a probe and lowered beneath the surface of a pool of cryogenic liquid contained

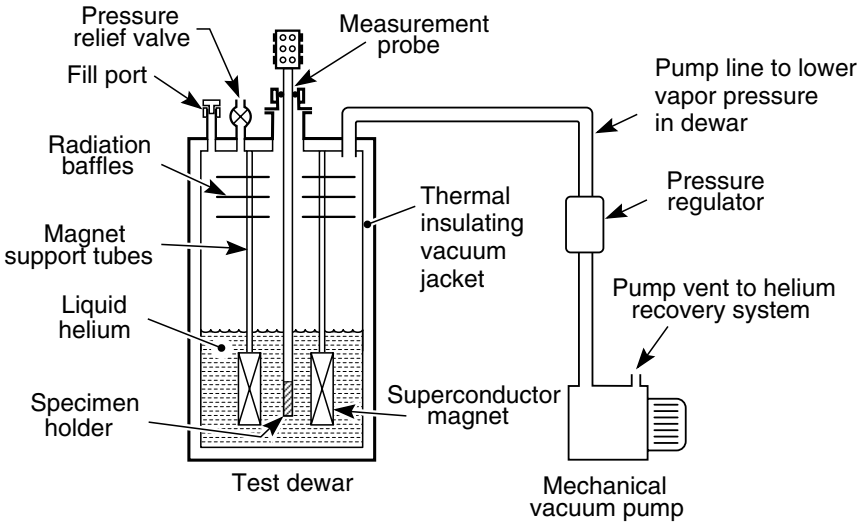

Fig. 1.1 Schematic of an immersion measurement probe in a cryogenic liquid with a vacuum pump for lowering the boiling temperature of the cryogen bath.

in a vacuum-jacketed dewar. The cryogenic liquid boils at a fixed temperature at atmospheric pressure and is very effective at cooling the sample to the cryogen's boiling temperature and holding the sample temperature constant at that value, usually to within a few millikelvins.

The temperature of the sample can be readily lowered below the atmospheric boiling temperature by partially *evacuating* the gas space in the dewar above the cryogenic liquid. This reduces the boiling temperature of the entire bath of cryogenic liquid. Conversely, the sample temperature can be raised by sealing off the dewar vent (with a pressure regulator), which causes the evaporating liquid to *pressurize* the dewar. This increases the equilibrium boiling temperature of the cryogen. (Detailed vapor pressure vs. temperature tables are given for the common cryogenic fluids in Appendix A5.1.)

When pressurizing, it is generally best not to go much above about 2 atm (~200 kPa) because of the risk of blowing up the dewar—and never pressurize glass dewars. The rise in temperature is also limited by the critical temperature and pressure of the cryogen (which are tabulated for common cryogens in Appendix A1.5). However, except for ^{4}He (critical temperature 5.195 K, critical pressure 2.245 atm) and ^{3}He (critical temperature 3.324 K, critical pressure 1.145 atm), the dewar pressure strength is usually the practical factor limiting the temperature rise.

Figure 1.2 shows the temperature ranges that can be covered by common liquid cryogens with this evacuation-and-pressurization technique. The lower temperature limit is given by the *triple point* (solidification temperature) and the upper limit by the boiling temperature at about 2 atm of pressure. Table 1.1 lists the triple points and the boiling temperatures at atmospheric pressure for common cryogens.

The most common cryogenic liquid coolants are liquid *helium* (^{4}He) and liquid *nitrogen* (N_2). The lighter isotope of helium, ^{3}He, is very expensive (more than 10,000 times the cost of ^{4}He).

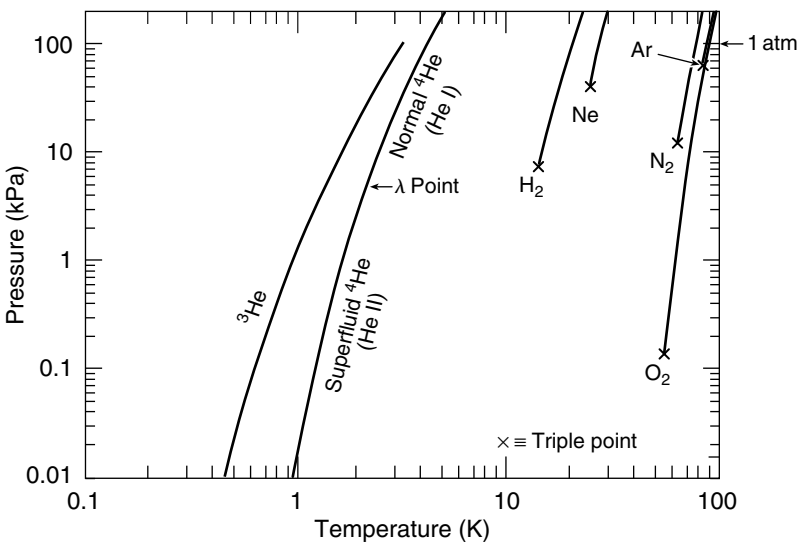

Fig. 1.2 Temperature ranges for measurements in cryogenic liquids obtained by vacuum pumping the vapor space over the liquid or by pressurizing the dewar up to about 2 atm of pressure (normal atmospheric pressure = 101.325 kPa). These data are tabulated in Appendix A5.1. General physical properties of these cryogenic liquids are given in Appendix A1.5, A1.6a, and A1.6b.

Table 1.1 **Boiling temperatures and triple points (solidification temperature) of common cryogenic liquids.**

Cryogenic Liquid	Boiling Temperature (ITS-90) 1 atm (101.325 kPa, 760 mm Hg) [K]	Triple Point	
		Temperature (ITS-90) [K]	(Pressure) [kPa]
^{3}He[a]	3.1905	—	
^{4}He[b]	4.230	2.1768[c]	(4.856)
Hydrogen (para)[d,e]	20.268	13.80	(7.04)
Neon[f]	27.100	24.557	(43.464)
Nitrogen[d,g]	77.355	63.151	(12.52)
Liquid air[h]	78.903	59.75[i]	(5.26)
Argon[d,j]	87.302	83.806	(68.89)
Oxygen[d,k]	90.196	54.359	(0.146)

Data evaluated by Lemmon (2003) from equation-of-state fits to data referenced below.

[a] 1962 temperature scale

[b] McCarty and Arp (1990).

[c] Superfluid-transition temperature (lambda point) for ^{4}He.

[d] Younglove (1982).

[e] Hydrogen can exist in two different molecular forms: higher-energy orthohydrogen (nuclear spins aligned) and lower-energy parahydrogen (nuclear spins opposed). The equilibrium ratio is determined by temperature: at room temperature and above, hydrogen consists of about 25% para and 75% ortho (so-called "normal" hydrogen); but at the atmospheric boiling temperature of liquid hydrogen (20.27 K) and below, the equilibrium shifts almost completely to parahydrogen (99.79% para and 0.21% ortho at 20.27 K).

[f] Katti et al. (1986).

[g] Span et al. (2000).

[h] Lemmon et al. (2000).

[i] Solidification point for liquid air.

[j] Tegeler et al. (1999).

[k] Schmidt and Wagner (1985).

However, as evident from Fig. 1.2, ^{3}He is very useful because it is one of the few simple means of cooling test samples below 1 K. To reach higher temperatures, liquid *neon* or liquid *hydrogen* is also available in some laboratories, but these cryogens are less commonly used as coolants. The reason is that neon is fairly expensive (about 10 times the cost of ^{4}He) and therefore needs to be collected and recycled. Hydrogen, on the other hand, is explosive when mixed with air [for hydrogen concentrations from 4.1% to 75% at standard temperature and pressure (STP)], and therefore needs to be carefully vented outdoors or collected. Liquid *oxygen* is also rarely used because it is dangerous as a combustion agent (see Sec. 1.6.1). Oxygen is also difficult to use with magnetic-field measurements because of its very strong *para*magnetism (Appendix A1.5; see also the practical tip at the end of Sec. 1.4.2).

1.2.1 PUMPING AND PRESSURIZING TECHNIQUES FOR CHANGING THE BATH TEMPERATURE

The temperature of the cryogenic fluid is controlled by maintaining a constant pressure in the vapor space, usually with a *pressure regulator* or *manostat* located in the vacuum line between the pump and dewar (shown schematically on the right side of Fig. 1.1). With this

pressure-regulation technique, the entire bath temperature can be kept constant and uniform, provided some precaution is used. The problem is that only the temperature at the *surface* of the boiling liquid is controlled by the pressure regulator. Vertical *temperature stratification* can exist in the column of liquid within a dewar, with the warmer liquid at the top of the column and the colder liquid at the bottom.

Usually temperature stratification is not a problem if we are pumping the liquid to lower temperature. Pumping produces bubbles throughout the volume of the bath, which keeps the liquid stirred and uniform in temperature. On the other hand, if the dewar is pressurized to raise the temperature, the cold liquid sits at the bottom of the dewar and severe temperature stratification occurs. To ensure temperature uniformity in the case of raising temperature, we need to break up the temperature stratification by placing a resistive heater in the *bottom* of the cryogen bath.

First we consider the more popular technique of pumping the cryogenic bath to lower its temperature, after which we will briefly describe the more tricky process of pressurizing the dewar to raise the bath temperature.

Pumping

Usually cryogenic baths are lowered in temperature rather than raised, because of safety and temperature uniformity. Lowering the temperature of the bath is also usually much faster than raising the temperature. The rate at which temperature can be decreased is set by the vacuum pumping speed.

How much pumping speed is needed and how big must the vacuum pump be? In principle, the amount of liquid that must be evaporated depends on the total heat capacity of the system (bath, measurement apparatus, and dewar), but from a practical standpoint, the main source of heat capacity at cryogenic temperatures is that of the liquid cryogen itself. For example, a gram of liquid helium at 4.2 K has a heat capacity of about 5.3 J/K (from Appendix A1.5) compared with only about 10^{-4} J/K for a gram of copper(!) (Appendix A6.2). Thus, we can usually neglect the heat capacity of the apparatus and dewar.

With this assumption, Fig. 1.3 shows the amount of liquid helium that has to be pumped away to lower the temperature of such a bath from 4.2 K to the indicated temperature. The data of Fig. 1.3 were calculated with the assumption of adiabatic conditions, which is usually a good assumption for liquid helium. Depending on the amount of heat leak into the dewar and the time for pumping, the actual amount of liquid helium remaining can be less than that shown. This is especially true at temperatures below 2.177 K where liquid helium becomes *superfluid* (described below). In this case, extra pumping is required to compensate for superfluid-helium *creep* (also described below), with the net result that only about 50% of the original helium remains after pumping from 4.2 K to the vicinity of 1.5 K.

The required pumping speed of the vacuum pump to reach and maintain a given temperature is determined by the target temperature and the heat leak into the bath. (Heat transfer is the subject of the next chapter.) The following example illustrates the determination of pumping speed for the case of liquid helium, but the same calculation can be carried out for any of the cryogens shown in Fig. 1.2.

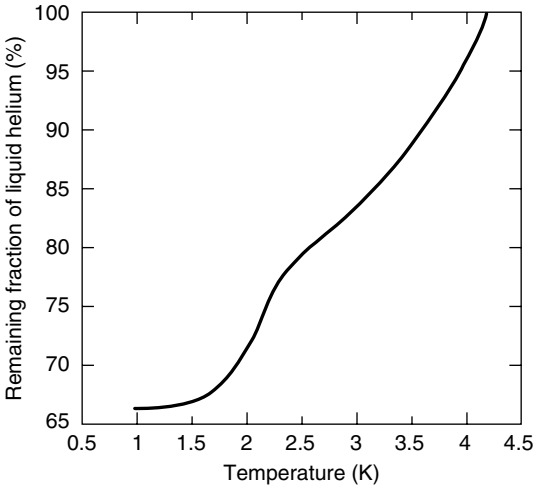

Fig. 1.3 Amount of liquid helium remaining after pumping the bath down to various temperatures (based on data from Pfotenhauer 2002).

Example—Minimum pumping speed: Suppose we wish to maintain a temperature of 1.4 K in a liquid helium bath where the total heat leak at this temperature is 0.1 W. What must the pumping speed of the vacuum pump be to handle this heat load?

The latent heat of vaporization (cooling power) of ^{4}He at 4.2 K is 20.8 J/g (from Appendix A1.5). Since the molecular weight of helium is 4.0026, this corresponds to about (20.8 J/g) × (4.0026 g/mol) = 83 J/mol [the latent heat of vaporization of ^{4}He does not change much over the temperature range 4.2–1.4 K and actually averages about 92 J/mol (Van Sciver 1986)]. Therefore, to maintain 1.4 K with a heat influx of 0.1 W requires helium to be evaporated at the rate $\dot{n}$ of approximately

$$\dot{n} = 0.1\ \text{W}/83\ \text{J/mol} = 1.2 \times 10^{-3}\ \text{mol/s}. \tag{1.1}$$

The vapor pressure P of ^{4}He corresponding to 1.4 K is about 0.3 kPa, from Appendix A5.1. So, to maintain this pressure, the pumping speed must accommodate this molar evaporation rate *at this low pressure*.

If the vacuum pump is at room temperature (295 K), then the volume pumping speed $\dot{V}$ can be determined from the time derivative of the gas law

$$\begin{aligned}\dot{V} = \dot{n}RT/P &= (1.2 \times 10^{-3}\ \text{mol/s})\ (8.314\ \text{Pa m}^3\ \text{mol}^{-1}\ \text{K}^{-1})\ (295\ \text{K})/(300\ \text{Pa}) \\ &\approx 10^{-2}\ \text{m}^3/\text{s} = 10\ \text{L/s} = 36\ \text{m}^3/\text{h},\end{aligned} \tag{1.2}$$

where R is the gas constant and T is the gas temperature in the pump. This pumping speed is typical of that needed in cryogenic laboratories. Of course, the greater the heat leak into the helium bath (assumed to be 0.1 W in this case), the greater the requirements on pumping speed. Pumping speeds for other heat-leak rates, target temperatures, and cryogenic fluids can be evaluated with Eqs (1.1) and (1.2).

Pumping speeds in this range can be obtained by using a rotary mechanical vacuum pump. (When specifying the pump, take into account the decreased volumetric efficiency associated with pumping helium rather than air; the supplier can help with this. The pump should also be adequately cooled to handle this volume of gas.) For increased pumping capacity, especially at lower pressures, a Roots blower can be added before the mechanical pump. (See Further reading for more information on types of pumps.)

Environmentally, it helps to locate the vacuum pump outside the main laboratory room, to minimize noise, vibration, and oil exhaust (which can be copious, especially when beginning to evacuate a dewar). Depending on the target temperature, the connecting vacuum lines also need to be fairly big in diameter (described quantitatively in Sec. 3.7.5).

Pressurizing

The process of pressurizing a dewar to raise the cryogen temperature is a bit more problematic than that of pumping to lower it. As mentioned in the introduction, it is generally best not to pressurize much above 2 atm (~200 kPa) because of the risk of dewar explosion. For safety, use at least two pressure relief valves (for redundancy) set at a pressure the dewar can handle. In maintaining this system pressure, keep in mind that stoppers can pop and O-ring seals start to slip as the pressure is increased.

The cryogen temperature is raised with a heater placed in the bottom of the dewar. The rate at which the dewar temperature is raised is determined mainly by the surface area of the heater. A small heater area will produce a lot of bubbles and waste liquid cryogen, so the surface area of the heater is usually increased by thermally attaching several resistors to a good thermally conducting metal sheet, such as copper. (Usually metal-film resistors are used because their resistance does not change with temperature, unlike carbon resistors, for example.)

To heat the bath, set the manostat pressure slightly *above* the target value and energize the heater. The dewar pressure will come up much more quickly than the temperature at the bottom of the bath. Patience is required to wait for the bottom temperature to rise to the target value. For example, it takes 10–20 min of heating at 15–20 W (with a heater area of many tens of square centimeters) to raise the temperature of ~30 L of liquid helium from 4.2–5 K. Much longer is needed for liquid-nitrogen baths. You can know that the liquid temperature has reached equilibrium by making sure there is a reasonable flow rate through the manostat when the bath temperature is slowly lowered to the target value. Always approach the final pressure by overshooting and then pumping down to it to perform this gas-flow-rate test to check for temperature stratification. When pressurizing it is best to measure the actual temperature at the sample and near the bottom of the dewar with cryogenic thermometers (Chapter 5). (See also the description of hydrostatic pressure-head corrections given in the introduction to Appendix A5.1.)

Pressurization takes patience and some care, but it is a very effective technique of expanding the usable range of a cryogenic fluid. Sometimes it is the only viable technique of measuring high-current-density samples at slightly elevated temperatures.

1.2.2 SUPERFLUID HELIUM

Liquid ^{4}He has some special properties when it is cooled. If the pressure is reduced enough, eventually the temperature of ^{4}He reaches the so-called lambda point (2.177 K) where normal liquid ^{4}He (also called He I) transforms into *superfluid* helium (He II). (The *lambda-point* name stems from the shape of the specific heat curve near this transition, which looks like the Greek letter λ.) It takes extra vacuum-pumping time to lower the temperature through this phase transition because of the very high thermal conductivity of superfluid helium and the

increase in its specific heat at the transition temperature. Figure 1.4 shows the dramatic transition from boiling to no boiling as the bath temperature is pumped through the lambda point.

There is no worry about temperature stratification with superfluid liquid helium. In fact, superfluid He II has an extremely high effective thermal conductivity—about 5 to 7 orders of magnitude higher than that of normal He I (!) and 1 to 3 orders of magnitude higher than that of commercially pure copper. {The thermal conductivity of superfluid He II actually depends on the heat flux it is carrying. At a heat flux of 1 W/cm^2, for example, He II has an effective thermal conductivity of about 100 kW/(m·K), which decreases to about 1 kW/(m·K) at a higher heat flux of 10 W/cm^2 (Van Sciver 1986). Either way, this is a tremendous thermal conductivity when compared with that of He I [less than 20 mW/(m·K)] or, for example, common copper wire [about 0.3 kW/(m·K) at these temperatures].} Thus, He II baths are usually uniform to within a few millikelvins and maintain this temperature uniformity in either a falling or *rising* temperature mode.

However, superfluid helium is weird stuff; a superfluid film a few atoms thick spontaneously *creeps* up the walls of the apparatus and dewar until it warms to normal-helium temperatures, or it can flow over cold walls to a lower part of the dewar, as shown in Fig. 1.5. (For more information on superfluid helium, see Further reading at the end of the chapter.) The important point for our purposes is that this superfluid creep increases the gas flow rate through the vacuum pump and lowers the ultimate cooling power of the system. Dewar designs have been developed for efficiently reaching and maintaining temperatures below 2.177 K, such as the "saturated-liquid container" refrigerator described in Sec. 1.5.3.

Thus, liquid cryogens, especially helium and nitrogen, are the working materials that enable most cryogenic measurements to be made over the temperature range 300–1 K, either by direct immersion (limited to the ranges shown in Fig. 1.2) or indirectly by providing a refrigeration medium for the variable-temperature cryostats and cryocoolers described in the

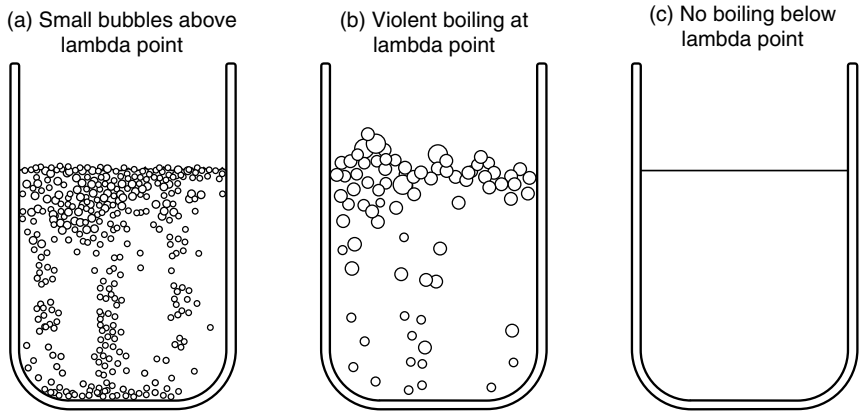

Fig. 1.4 Abrupt change in boiling behavior of liquid helium at the superfluid lambda-point transition (2.177 K). As normal He I is cooled by evaporation with a vacuum pump, it boils with small bubbles while in its normal state (a). As its temperature passes through the lambda point, liquid helium suddenly and briefly boils violently, schematically illustrated by (b), and then suddenly stops boiling completely (c). No boiling occurs below the transition point, even though the superfluid continues to be pumped, evaporated, and cooled.

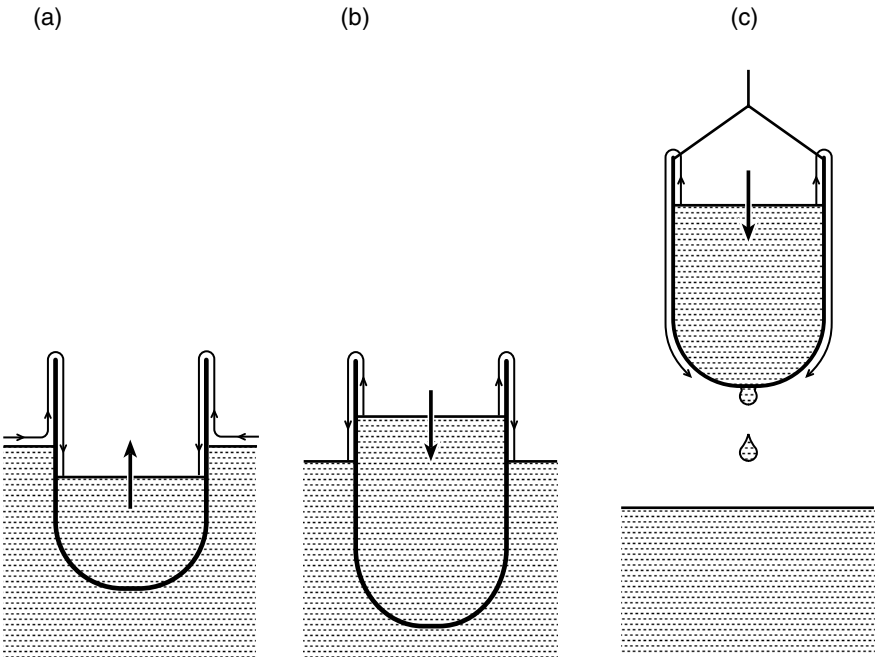

Fig. 1.5 Superfluid film creep. Similar to the behavior of a siphon, a film of superfluid He II will creep up and over the sides of a container to either (a) fill a vessel or (b) empty a vessel, until the level in the vessel matches that in the liquid-helium reservoir. (c) Here, a glass vessel is partially filled with superfluid He II, and is suspended by threads above a reservoir of superfluid helium. Amazingly, superfluid-helium film will creep up and over the vessel wall, then collect at the bottom as a drop that drips into the reservoir (totally unlike a siphon). This process will continue spontaneously until the vessel is empty.

following sections. Further information and data are available in the excellent textbooks on cryogenic engineering referenced in the Further reading section at the end of this chapter. As mentioned at the outset, much of these data are summarized and updated in Appendixes A1.5, A1.6, and A5.1 for convenient reference.

1.3 Introduction to measurement cryostats

We now turn to the main focus of this text, the design of measurement cryostats for use with cryogenic liquids and commercially available refrigerators. In contrast to commercial cryogenic engineering, *research measurement cryostats* usually require a design that can be carried out only by the experimentalist, and so, in practice, it is difficult to buy such an apparatus "off the shelf." We need to provide customized sample support, thermal anchoring, and effective electrical connections to our particular test samples, whether we use immersion cryostats or cryocoolers.

So, where do we start the design process? Invariably, the place to begin is with the *temperature range* of interest. For example, to obtain engineering data for applications, the main objective of the apparatus is usually to test materials at a *fixed* operating temperature. In this case, a simple direct immersion cryostat may well do the job by using a cryogenic bath for cooling, as described in the previous section. For general materials science studies, on the other hand, the objective usually is to carry out measurements over as wide a range of temperatures as possible to provide useful handbook data. In this case, a more complex *variable-temperature* cryostat is needed. (Examples of both types of cryostats are illustrated in Sec. 1.4.)

A second design factor (which can become primary in many circumstances) is to decide on the *electric-current range* needed. In high-current sample testing (such as applies to most bulk superconductors), currents of several hundred to several thousand amperes are common, whereas for low-current measurements (such as thin-film samples), currents rarely exceed several hundred milliamperes. The two cryostats look very different, the first with large vapor-cooled leads and built to handle large forces, the second light and delicate with small current leads and miniature connectors.

A third factor is *magnetic field*. If high fields are needed, real estate can become a problem. The whole apparatus usually has to be made very compact to fit in the small space of a high-field magnet. Also, electrical leads need to be twisted tightly (to minimize electromagnetic noise); and thermometers are required that are insensitive to magnetic fields. A high magnetic field also introduces the challenge of selecting nonferromagnetic materials (to reduce magnetic forces). For magnetic measurements involving very sensitive SQUID (*s*uperconducting *q*uantum *i*nterference *d*evice) magnetometers, materials selection becomes even more challenging, requiring extremely low magnetic susceptibility.

A fourth factor is *mechanical* or geometric design. For example, in optical or radiation measurements, the requirement for a beam of light or neutrons to access the sample may dominate the design. In orientational measurements, the mechanical design of a manipulator to rotate the sample can become the central problem. In high-current measurements, magnetic forces acting on a single superconductor strand carrying 500 A can typically approach 50 N/cm or more. (That is like hanging a bowling ball from every centimeter of a delicate superconductor; this force must be supported and not allowed to damage the sample, let alone destroy the measurement apparatus.)

1.3.1 CHECKLIST/GUIDE TO THE MOST RELEVANT SECTIONS OF THIS BOOK, DEPENDING ON CRYOSTAT TYPE

The following checklist of initial design questions is organized into subsections paralleling each of the four principal design factors listed above (temperature, current, magnetic field, and mechanical properties). This checklist is intended to highlight specific design challenges for *your* particular type of cryostat, as well as serve as a self-directed, self-tailored *guide* to the rest of the book. After each question, I have listed some of the most important design principles for each type of cryostat and sections of the book where they are described. This checklist is intended as a resource to build your own roadmap to the text, one that focuses more specifically on material relevant to your needs.

Temperature

This is usually the most important parameter to pin down initially:

1. Can the measurement be carried out at the *fixed* boiling temperature of a common cryogenic liquid, such as 4.2 K (helium), 27 K (neon), 77 K (nitrogen), or 90 K (oxygen)?

   For example, this is the case with many critical-current measurements (Chapters 9 and 10). In this situation, a direct immersion *cryostat or a simple storage-dewar* dipper probe *might work well (Sec. 1.4.2). The sample is submerged in a liquid cryogen that has a huge cooling capacity, and therefore excellent sample cooling and temperature uniformity*.

2. Is a *small range* of temperature sufficient (such as 1.7–5 K, or 63–80 K)?

   Such a range can be obtained by pumping on a cryogenic liquid and thus a direct immersion cryostat might still work well, if the dewar holding the cryogenic liquid is equipped with an evacuation port and a vacuum pump (Fig. 1.1). As mentioned already, the advantage of this cooling method is the high rate of heat transfer to the cryogenic liquid, which ensures superb temperature control.

3. Or, will temperature need to be varied over a *wide range*, say, from 1–20 K or 1–100 K to cover the low-T_c and high-T_c superconductor ranges, respectively? (T_c is the superconductor critical temperature.) If so, then how constant must the temperature be held and for how long?

   If a slow temperature drift can be tolerated, as with resistance vs. temperature measurements, a dipper probe with vertical height adjustment might be just the ticket (illustrated in Sec. 1.4.2). For measurements of heat capacity, thermal conductivity, or thermoelectric power, on the other hand, long temperature holding times and well-controlled heat-flow environments are needed; then a vacuum-insulated sample chamber will be necessary with solid conductive cooling, such as that shown in Sec. 2.9.3, or one of the commercial refrigerators described in Secs 1.4.3–1.4.6. For this case, the principal design parameters are: heat transfer (Chapter 2, especially Sec. 2.6 and example case 3 in Sec. 2.9), vacuum electrical lead-throughs (Sec. 4.7), and temperature measurement and control (Chapter 5).

4. Will many samples need to be measured in an experimental run?

   If there are more than a few samples, it is best to design some form of sample loading scheme that minimizes the heat capacity of the repetitively cooled *cryostat parts and maximizes their thermal diffusivity (Sec. 6.1.4). A lightweight, top-loading apparatus, such as the dipper probe illustrated in Sec. 1.4.2 can be extremely efficient in measuring many samples with little turnaround time and loss of cryogen.*

Transport current

5. Does the measurement require a transport current through the sample (as opposed to *contactless* measurements such as susceptibility, magnetization, or optical properties)?

   If so, the main design factors will be all the baggage associated with getting current into and out of the sample. See chapters on wiring and connections (Chapter 4), sample holders (Chapter 7), and sample contacts (Chapter 8).

6. Is the sample transport current *high* ($\gtrsim$ 1 A) as with critical-current measurements for bulk superconductors, or *low* ($\lesssim$ 1 A) as with measurements of Hall coefficients and transport properties of thin films and small samples)?

   If the transport current is high, *sample cooling can be critical and usually achieved by immersion in a cryogenic liquid (Sec. 2.5). Efficient current leads (Sec. 4.9) are also essential for the success of such measurements, as well as the mechanical design of the cryostat, which sometimes must handle very large electromagnetic (Lorentz) forces (Sec. 7.3.5).*

   If the sample current is low, *then it may be possible to use a commercial cryocooler, where the sample is cooled by thermal conduction to a refrigerated plate or with exchange gas (Sec. 1.4). Principal design techniques for this case are heat transfer across interfaces (Sec. 2.6), vacuum lead-throughs (Sec. 4.7), and temperature measurement and control (Chapter 5).*

7. Will repeated mounting and demounting possibly damage a rare sample and contacts, or is extra space needed for sample mounting, such as room for soldering high-current connections?

   In either case, it may make sense to have a removable *sample holder for mounting the sample outside the cryostat. The sample can then be easily and repeatedly inserted into the cryostat (Secs 7.3.2 and 7.4.3).*

8. Does the sample need to be rotated while making a transport measurement, such as in the measurement of critical current vs. magnetic-field angle?

   Then it may be necessary to design special flexible current connections to the sample (Sec. 4.10) and incorporate some clever mechanics (Sec. 9.4.2).

Magnetic field

9. Will the measurement be carried out in zero magnetic field or in only low fields ($\lesssim$ 0.2 T)?

   Life is much simpler than at high fields; we do not have to put a lot of effort into making the apparatus compact so it will fit in the small bore of a high field magnet. Furthermore, if transport currents are small, a commercial liquid-flow cryostat or cryocooler of modest cooling power can be used. (Secs 1.4.3 to 1.4.6).

10. Will measurements be carried out, on the other hand, in high magnetic fields ($\gtrsim$ 1 T)?

    If so, a key factor will be selection of cryostat materials that are nonferromagnetic, because they will be subjected to very high magnetic forces. Avoid iron, nickel, and sometimes stainless steels (Sec. 6.5.2). (The least magnetic stainless steels, the AISI 300 series such as 304, 310, and 316, are metastable and can partially transform to a ferromagnetic phase during cooling when under high applied stress or residual stress from machining; welded stainless-steel joints are also a problem; silver-soldering is better.) Magnetic properties of cryostat materials are given in Sec. 6.5 and Appendix A6.8.

11. Will sensitive magnetic measurements be made, such as susceptibility or magnetization?

    In addition to selecting nonferromagnetic cryostat materials, they must also have a very low *magnetic* susceptibility *(Appendixes A6.8a and A6.8b) so as not to mask the magnetic signal of the test specimen.*

Mechanical properties

12. Is the test sample brittle, and does it require a stress-free sample mount?

    If so, it is important to design the sample holder *to minimize differential thermal-contraction forces that can build up between the sample and the sample holder (Secs 7.3.2 and 7.4.2, as well as Appendixes A7.4 to A7.6); it may also require the use of flexible current leads to provide stress-free sample cooling (Sec. 4.10).*

13. Do mechanical loads need to be applied to the sample, such as in low-temperature mechanical-property measurements?

    Then an important design balance is required between the mechanical strength of the cryostat support structure and heat transfer into the low-temperature region of the cryostat. This trade-off is illustrated by the buckling calculation in Sec. 3.5.2.

14. Will mechanical measurements be made at high magnetic fields ($\gtrsim 1$ T)?

    Similar to the case for magnetic measurements, particular attention must then be paid to constructing the movable *cryostat parts from materials that will not experience significant magnetic forces (this usually eliminates stainless steels and requires the use of very low susceptibility materials such as titanium, aluminum alloys, and phosphor bronze). For this case, the magnetic susceptibility of the cryostat construction materials is a principal design parameter (Sec. 6.5 and Appendixes A6.8a and b).*

1.4 Examples of measurement cryostats and cooling methods—low transport current ($\lesssim$1 A)

1.4.1 INTRODUCTION

Before jumping into the subtopics of cryostat thermal design, construction, and wiring in succeeding chapters, we first introduce in this and the next section several examples of generic measurement cryostat systems. These are intended to illustrate the techniques available for cooling and controlling sample temperature in the range from 1–300 K.

As noted above, the principal methods of cooling include either direct *immersion cryostats* or commercial *cryogenic refrigerators* (liquid-flow cryostats and cryocoolers). Each type of system has its advantages and disadvantages:

Immersion cryostats: The great advantage of these systems is their tremendous cooling power and their ability to handle high as well as low sample current. They are also free of vibration, quiet, and inexpensive. But they require the availability of cryogenic liquids and experience with handling, storing, and transferring cryogenic fluids between containers (Sec. 1.6.2).

Liquid-flow cryostats: These systems are easy to set up, inexpensive, free of vibration, and wonderful for variable-temperature operation. However, they are restricted to low-power and low-current experiments, and they require the availability of cryogenic liquids.

Cryocoolers: Because cryocoolers are closed-refrigeration systems, they are the cryostat of choice for extreme convenience; you just flip a switch and voilà—low temperature (and, of course, there is the detail of keeping them maintained, as well as designing an efficient thermal

anchoring scheme for your sample). Cryocoolers are the *only* choice when a source of cryogenic fluids is not readily available. However, they are usually restricted to low cooling power and low testing currents, prone to vibrations, and subject to high initial expense (but still much cheaper than setting up a liquefaction system if cryogen fluids are not commercially available).

The cryostat and cooling-method examples given below are separated into *low*- and *high*-current sections because of the vast difference between the two types of apparatus. This section (Sec. 1.4) gives examples of cryostats for *low* (or zero) transport current, and includes all three types of cooling methods listed above. On the other hand, the next section (Sec. 1.5) gives examples of cryostats for *high*-current measurements that require greater cooling power; these are usually the immersion type.

1.4.2 DIPPER PROBES

The *dipper probe* is the simplest type of cryostat. It is also the most common, useful, and versatile. A huge advantage of the dipper probe is that often it can be easily inserted into a *storage dewar* without the hassle of transferring cryogenic fluid into a separate vessel.

The sample is mounted on a copper block at the end of a low-thermal-conductivity tube (such as stainless steel) and cooled by lowering it into a cryogenic-liquid storage dewar. Figure 1.6 shows a basic dipper probe; Fig. 1.7 shows a detail of the sample holder at the end of the probe.

Usually, the sample is simply *immersed* in the cryogenic liquid, as shown in Fig. 1.1. However, the sample holder can also be *raised* above the surface of the liquid to obtain an extended range of temperature operation, as shown in Fig. 1.6. By varying the height of the probe above the liquid surface, the sample-holder temperature can be varied because of the temperature stratification that occurs naturally in the vapor space above the liquid.

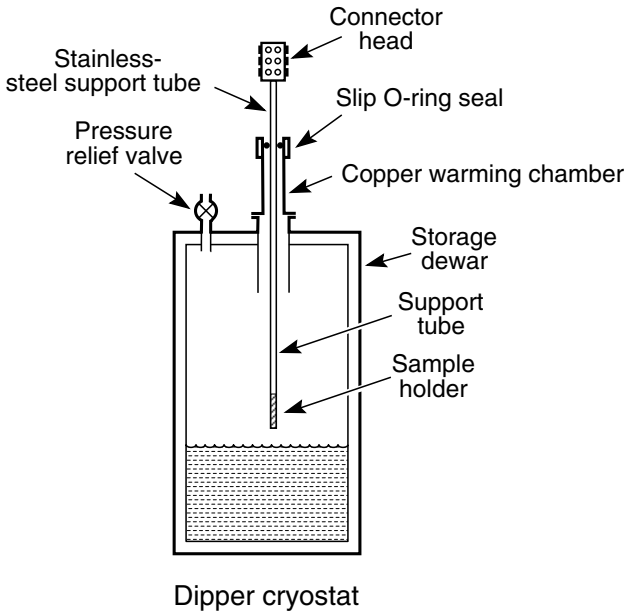

Fig. 1.6 Variable-temperature dipper probe for low-current measurements.

Operation of the dipper probe in the immersion mode is relatively easy, but the variable-temperature mode takes some skill and patience. The temperature gradient in the vapor above the liquid is not constant, and to sweep temperature at a reasonably controlled rate requires constant adjustment of the probe height. The easiest technique is to set the temperature drift rate in crude steps and use a data logging system to record data as the temperature drifts. Automatic data-logging systems are ideally suited to this type of probe; their program architecture is described in detail in Sec. 9.3.3.

For this variable-temperature mode to work well, we need a sample holder (Fig. 1.7) with adequate *thermal mass* to provide temperature stability. Additionally, the sample holder should be made of a material with high *thermal conductivity*, such as copper, so the entire sample-holder volume will come to thermal equilibrium fairly quickly and provide a uniform temperature profile along the sample. Unless you enjoy waiting, keep the mass of *insulating* materials in the rig small. That is, avoid large solid pieces of phenolic, glass, fiberglass–epoxy composites (like G-10), and so on. Such materials have a low *thermal diffusivity* (high mass and low thermal conductivity) and take "forever" to thermally equilibrate. The thermal design of such a variable-temperature dipper probe is treated as an example in case 2 of Sec. 2.9.

Mechanically, it is a good idea to design the dipper probe so it is reasonably robust. If ice builds up in the neck of the storage dewar, sometimes the rig has to be twisted or otherwise forced to break it loose. It is frustrating to have to fully warm a storage dewar to free the probe

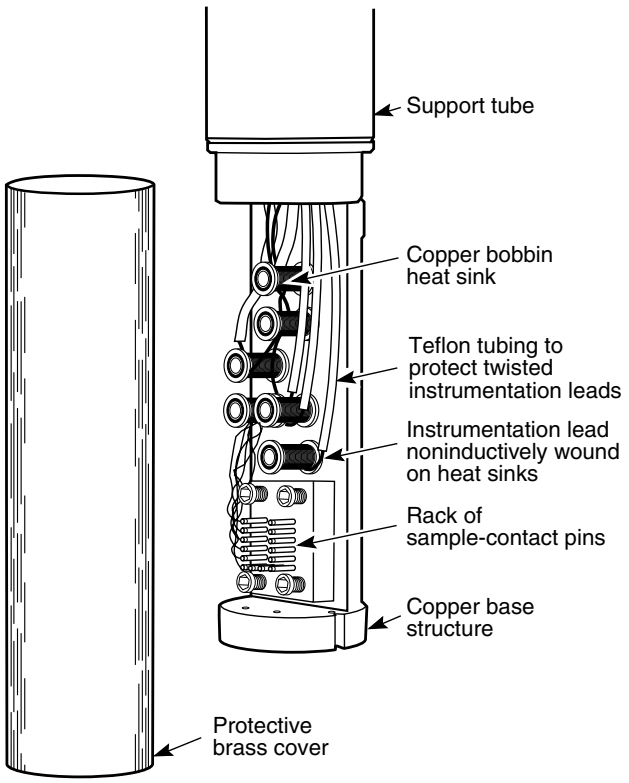

Fig. 1.7 Sample-holder section of a low-current dipper probe, showing copper base structure and sample holder for temperature stability, and copper-bobbin heat-sinking arrangement for the instrumentation leads (based on a design by Russek 1990).

or, even worse, recover part of the apparatus that breaks off. Construction tips on materials selection, sizing parts, and joining techniques are given in Chapter 3.

Electrically, leads need in order to be heat-sunk to the sample holder before attachment to the sample and thermometer in order to intercept heat conduction along the leads from room temperature. This ensures that the sample, thermometer, and holder are all at the same temperature. For larger-diameter rigs (≳2 cm diameter), heat sinks can be provided by copper bobbins screwed to the copper base structure, as shown in Fig. 1.7. The electrical leads are usually "non-inductively" wound onto the bobbins, as explained in tips for wiring in Sec. 4.4. The *length* of wire needed for wrapping to provide adequate heat-sinking is given in Appendix A4.5.

For rigs of smaller diameter, where there is not enough room for copper bobbins, the leads can be heat-sunk by winding them around the body of the copper base structure itself, as shown in Fig. 1.8. This design is a great way to fit a measurement probe into a small-diameter

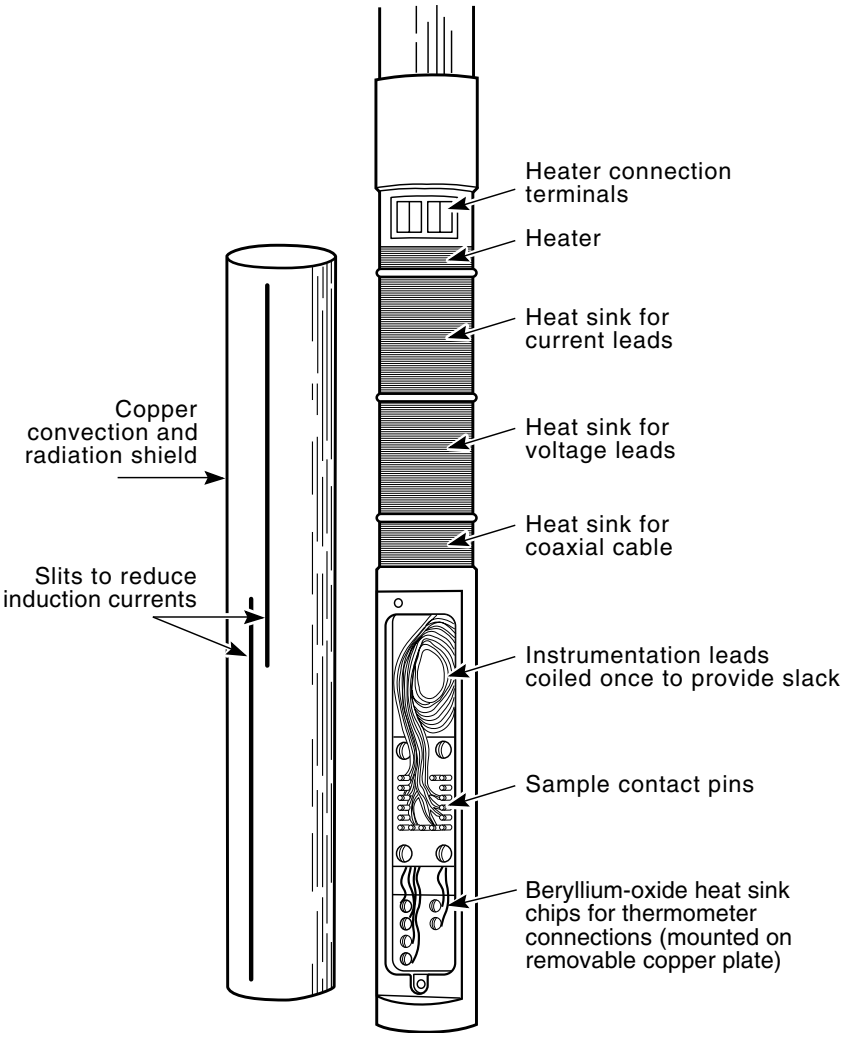

Fig. 1.8 Illustration of a small-diameter dipper probe for testing within the confined space of a high-field magnet (based on a design by Anlage 1988).

space, such as the small bore of a high-field magnet, or a small dewar inside a larger dewar. (The latter "nested" dewar arrangement is often used to obtain a variable-temperature inner-dewar space without having to change the temperature of the outer-dewar space, which might contain a large superconducting magnet, for example.) The only caveat when choosing this smaller heat-sink arrangement is that if there is an insulation failure in the commingled winding pack, the entire rig has to be rewired. It has happened to me more than once; a lot of hassle can be avoided by wiring the rig using wire with *tough insulation* (Sec. 4.3).

When possible, it also pays to design the sample holder with additional *space* and *spare leads* (as many as possible). This creates the flexibility to use the probe in new experiments that may require extra leads or more space. The extra leads also provide redundancy in case there is an electrical or insulation failure in several of the leads.

For *temperature measurement*, a cryogenic thermometer is attached to the copper base structure. For the larger-diameter probe shown in Fig. 1.7, the thermometer is attached to the back of the copper platform shown in Fig. 1.7, just under the position of the sample. For the smaller-diameter probe shown in Fig. 1.8, there is not enough room to do this and so the thermometer is slipped into a close-fitting hole drilled in the bottom of the copper sample support rod. This is illustrated in more detail in Sec. 4.4 (Figs 4.2 and 4.3).

A protective *cover* is usually slipped over the sample holder section of the probe, as shown in Figs 1.7 and 1.8. The cover provides mechanical protection and shields the sample from electromagnetic radiation. It also provides temperature stability against thermal radiation, convection currents (when operated in a gaseous atmosphere), and bubbles (when operated in a liquid cryogen). In really crude dipper probes, even a paper cup is a simple but surprisingly effective shield to deflect cryogen bubbles away from the sample.

➔ *Warming chamber:* As a practical footnote to this section on dipper probes, we take special note of the warming chamber used with these probes, labeled "copper warming chamber" at the top of Fig. 1.6. When samples are changed, this chamber provides a dry gas environment into which the sample holder can be raised, so it can be warmed to room temperature without condensing water onto moisture-sensitive samples. It also provides a convenient way to adjust the height of the sample in the dewar by slipping the support tube of the dipper probe through an O-ring vacuum coupling at the top of the chamber. Figure 1.9 shows the details of the warming chamber. The O-ring clamp is loosened, the support tube height adjusted, and the O-ring retightened to hold the apparatus in the new position.

The warming chamber should be made long enough to accommodate the length of sample holder section (the hatched section at the bottom of the support tube in Fig. 1.6). To shorten the warming time to a few minutes, a hot-air hair dryer can be used to heat the copper tube (but do not use a hair dryer with liquid hydrogen or liquid oxygen!). It helps to replace the rubber O-ring in the vacuum coupling atop the warming chamber with an O-ring made of Teflon™ so it does not freeze when the cold support tube is slipped through it. A convenient way to attach this warming chamber to the top of a commercial dewar is to use a quick-coupling connector, such as a clamped rubber-gasket flange (e.g. a Ladish™ flange; suppliers are listed in Appendix A1.7 under the heading Vacuum accessories).

Please be careful when rapidly warming any dewar. Cryogenic liquids trapped in restricted spaces can rapidly vaporize and cause an overpressure hazard. Prudent design techniques to avoid this problem are noted at the beginning of the discussion on safety in Sec. 1.6.1.

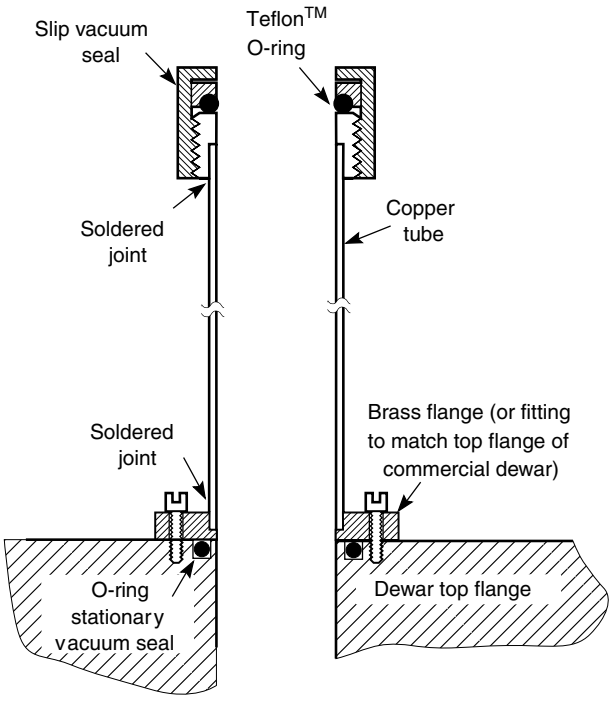

Fig. 1.9 Warming chamber, into which the sample holder of Fig. 1.6 can be withdrawn at the end of a test to prevent condensation of water on the cold sample surface.

➔ *Magnetic snowballs:* The slip vacuum seal at the top of the warming chamber also provides an important secondary function when changing samples in liquid-helium experiments by preventing air from *liquefying* on the cold surface of the probe when it is raised out of the dewar. Otherwise, the liquid air usually drips into the dewar and the consequences are often not good. For example, the liquid air can fall into the close-fitting "tail" of an insert dewar, freeze in place, and block the opening so the probe cannot be reinserted.

Sometimes the effects are far more insidious. As I was writing this book, we had a bizarre situation occur during a magnetic-field experiment. Our apparatus worked wonderfully, in *zero* magnetic field. But once we energized the magnet, our high-sensitivity strain measurement apparatus acted completely crazy. It cost us several weeks of time trying to figure this out.

After many failed attempts to fix the problem (substituting cables, rewiring parts of the apparatus, checking magnetic Lorentz forces on the strain gauge, testing for magnetic effects on the room temperature instrumentation), we finally realized that frozen particles of liquid air had gradually accumulated in the dewar over several weeks of continuous use. That is, each time we pulled the probe out of the dewar to change samples, liquid air formed on the cold surfaces and a little bit dripped momentarily into the mouth of the dewar (because we had no warming chamber).

When the liquid air dripped into the liquid helium, it solidified into little snowflakes, rich in oxygen. Sounds innocent enough. However, solid oxygen has a tremendous *paramagnetic susceptibility* ($10{,}200 \times 10^{-6}$ cm^3/mol, or about 10^4 times larger than the

diamagnetic susceptibility of other cryogens; see Appendix A1.5). These flakes drifted to the bottom of the dewar. Then, when we energized the magnet (and the effect occurred at only 1 T), the magnet sucked the oxygenated snow into the highest-field region of the magnet bore and formed a nice "magnetic snowball", of course right where we carefully located the sample and our highly sensitive strain extensometer. The snowball interfered with the mechanical motion of the extensometer, turning its output into something that looked like a Rorschach inkblot test.

So the moral of the story is *do not let liquid air drip off your probe into liquid-helium dewars* as you extract the probe to change samples. Instead, equip cryostats with a slip-vacuum fitting like the warming chamber in Fig. 1.9. Or, for more complicated rigs that do not lend themselves to this slip-vacuum-fitting approach, wrap a cloth around the probe at the mouth of the dewar, and pull the probe through this crude "cloth seal." The cloth prevents air from entering the dewar and catches liquid air from dripping into the dewar as it forms and drips off the parts of the probe outside the dewar. As a general practice, it is also a good idea to warm up the dewar and apparatus every several weeks to let frozen air evaporate.

In the same vein, watch out for *liquid-nitrogen* dewars that have been left open and *exposed to air*. The cold liquid nitrogen will condense oxygen into it (nitrogen boils at 77 K, whereas oxygen condenses at 90.2 K). Oxygen-contaminated liquid nitrogen can also give rise to some pretty weird magnetic effects. The contaminated liquid becomes paramagnetic, and the magnetic force acting on the liquid can be so strong it will levitate liquid nitrogen into the highest-field regions of a smaller-diameter test dewar (Sample and Rubin 1978). Liquid oxygen condensed into the dewar also represents a combustion hazard (see Sec. 1.6.1 and the recommended book on safety by Edeskuty and Stewart 1996).

1.4.3 LIQUID-FLOW CRYOSTATS

When sample temperature needs to be varied over an *extended range* (say, 4–300 K) with careful control, cryostats of a type other than the versatile dipper probe are usually used. These are the liquid-flow, cryocooler, and gas-flow cryostats. Perhaps the most basic of these is the liquid-flow cryostat. This type of apparatus is available commercially (suppliers are listed in Appendix A1.7 under the heading Complete cryogenic systems). However, this cryostat and the others described in Sec. 1.4 are usually suitable for low-current operation only.

As illustrated in Fig. 1.10, the test sample in a liquid-flow cryostat is thermally mounted on a copper cold plate inside an evacuated container that is surrounded by thermal radiation shields. The cold plate is cooled by continuously transferring a liquid cryogen (usually helium or nitrogen) from a supply dewar down to the cold plate and then venting the gas. The temperature of the cold head is set near the desired temperature by adjusting the *flow rate* of cryogen from the storage dewar, so that the cold head is slightly below the desired temperature. Final temperature control is then obtained by a resistive heater attached to the copper cold head, which is powered by an automatic temperature controller using feedback from a thermometer attached to the cold head. Temperature can be controlled typically to within about ± 2 mK. Temperature can be swept, but, for efficient operation, the transfer flow valve at the top of the storage dewar needs to be electrically controlled.

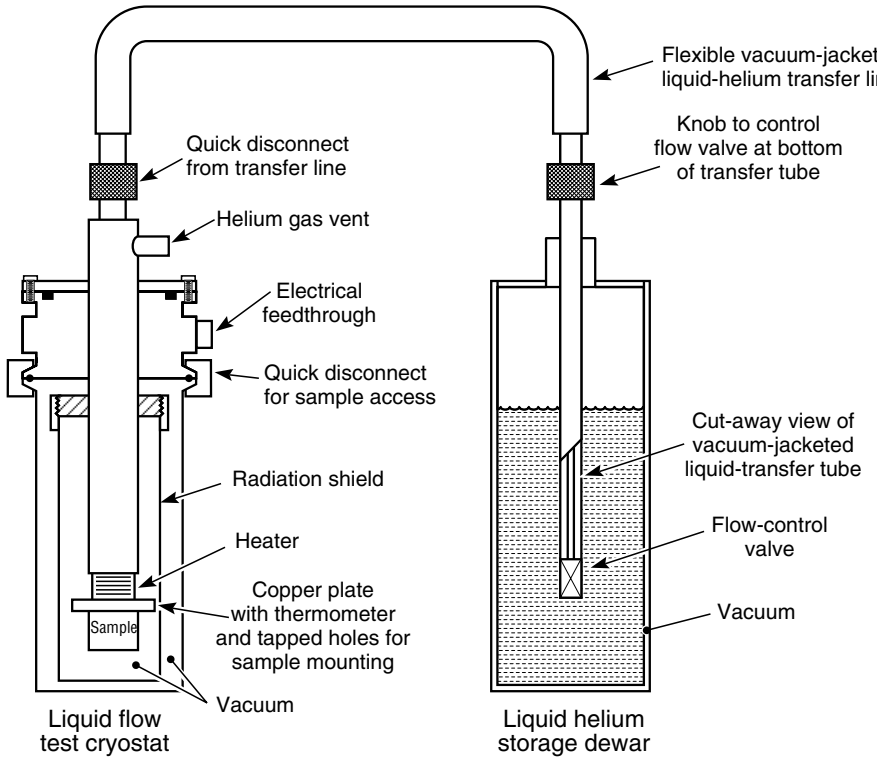

Fig. 1.10 Variable-temperature cryostat based on continuous transfer of liquid cryogen from a storage dewar to a cold copper plate on which the test sample is mounted. Typically, the sample is situated inside an evacuated can, which is surrounded by a thermal radiation shield (figure modeled after one from the catalogue of Cryo Industries 2002).

Since the sample is cooled *conductively* by mounting it onto the cold plate, usually in a vacuum, the main design concern is to make sure that all thermal *joints* between the sample and cold stage have a high thermal conductance. This usually means using solder joints or pressure contacts. *Solder* joints are usually the best. When *pressure* contacts need to be used, heat conductance across the interface can be enhanced considerably with grease, indium foil, or gold plating (corresponding to low-, moderate-, and high-force joints, respectively; see Sec. 2.6 and especially Sec. 2.6.4). Although not shown until later, we call attention to Fig. 2.7, which can be especially useful in determining thermal conductance across joints for mounting samples on refrigerator cold stages.

The chief advantage of the flow cryostat is that it serves as a good, general-purpose, wide-temperature-range workhorse cryostat that is relatively quick to set up. However, it must be tethered to a storage dewar, which requires adequate lab space and permanent use of a dewar.

1.4.4 CRYOCOOLERS

The main distinction of cryocoolers is that refrigeration is provided by a *closed-loop* system, which eliminates the cost of continually supplying liquid helium. Figure 1.11 shows

one of the most common types of cryocoolers—a two-stage Gifford–McMahon (G–M) refrigerator. The first-stage temperature is usually in the range of 40–80 K and serves as a thermal anchor for a radiation shield that surrounds the second-stage cold head, which usually achieves a temperature of about 10 K. G–M cryocoolers can reach 4 K by using a more costly regenerator material in the second stage (see, for example, Ackermann 1997). Cooling power of commercial 4 K G–M refrigerators is usually in the range 0.5–2 W, with 1 W being typical.

Many of the same sample-mounting considerations already outlined for liquid-flow cold-plate cryostats apply equally well to samples mounted (in vacuum) on the cold stages of cryocoolers. Again, Sec. 2.6 and Fig. 2.7 are quite useful.

The rubbing seals in the refrigerator have a one- to three-year life of continuous operation, the valves about three years, and the compressor about five years.

The chief advantage of crycoolers is their convenience. Disadvantages include restriction to lower sample currents and a relatively long time needed to cycle samples in and out. Also, G–M cryocoolers introduce a significant vibration (100 μm amplitude and 1*g* acceleration) at the cold head, which can generate unacceptable noise for some measurements.

1.4.5 PULSE-TUBE CRYOCOOLER

A more recent type of closed-loop cryocooler is the pulse-tube cryocooler, which is new enough that it deserves a little more in-depth description. It offers several significant advantages over other designs. Pulse-tube cryocoolers have a vibration at the cold stage that is about two orders of

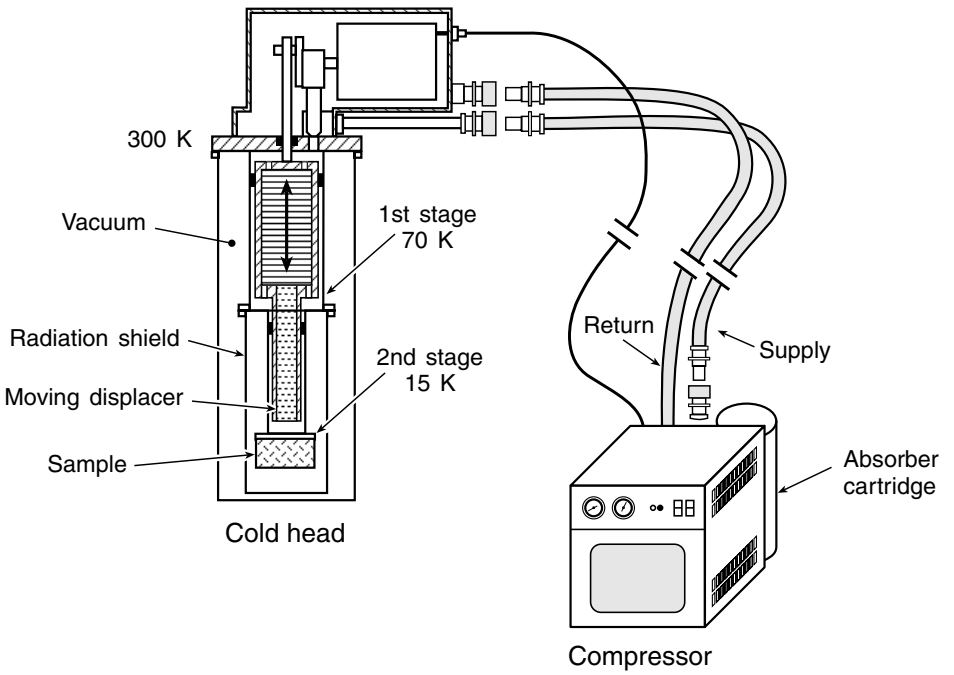

Fig. 1.11 Sample mounted on cooling stage of a commercial Gifford–McMahon (G–M) cryocooler (cold head shown enlarged relative to compressor). (Adapted from Radebaugh 2003a.)

magnitude smaller than that of G–M cryocoolers. They are also among the most reliable cryocoolers, since they have no moving parts at the cold end. Furthermore, they are the most efficient of all cryocoolers for temperatures between 60 K and 120 K. Temperatures down to 2 K can be achieved by using two stages, the first in the 40–80 K range and the second reaching 2 K.

Techniques for mounting samples to the cold stage of a pulse-tube cryocooler are similar to those mentioned just above in Sec. 1.4.3 for continuous liquid-flow refrigerators.

Figure 1.12 shows the principle of operation of the orifice pulse-tube refrigerator. Ignore for the moment the secondary orifice (it is a device that enhances efficiency and is discussed below). The basic refrigeration cycle starts when the *piston* moves down to compress room-temperature helium gas, causing it to flow through a *regenerator* (heat exchanger), past the *cold stage* (T_{cold} in Fig. 1.12), and into the *pulse tube*. The heated, compressed gas in the pulse tube then flows back up, toward room temperature. As gas exits the pulse tube, it is cooled to ambient temperature by a heat exchanger at its warm end (T_{hot}). The gas then flows through a flow restriction provided by an *inertance tube* (which in some cases is replaced by a primary orifice, not shown), and, finally, into a room-temperature *reservoir*. Gas flow out of the pulse tube stops when the pressure in the pulse tube equals the average pressure in the reservoir. The piston then moves up and expands the gas in the pulse tube *adiabatically*, causing it to cool. This cold, low-pressure gas is forced toward the cold end of the pulse tube by the reverse flow of gas from the reservoir. As the cooled gas flows back through the lower heat exchanger, it absorbs heat from the cold stage. The refrigeration cycle ends when gas stops flowing because pressure in the pulse tube increases to the average pressure in the reservoir. The entire cycle is then repeated.

The pulse tube itself is very simple in concept—just an open tube. The basic function of the tube is to *insulate* the processes at each of its ends. Thus, it needs to be large enough that the gas

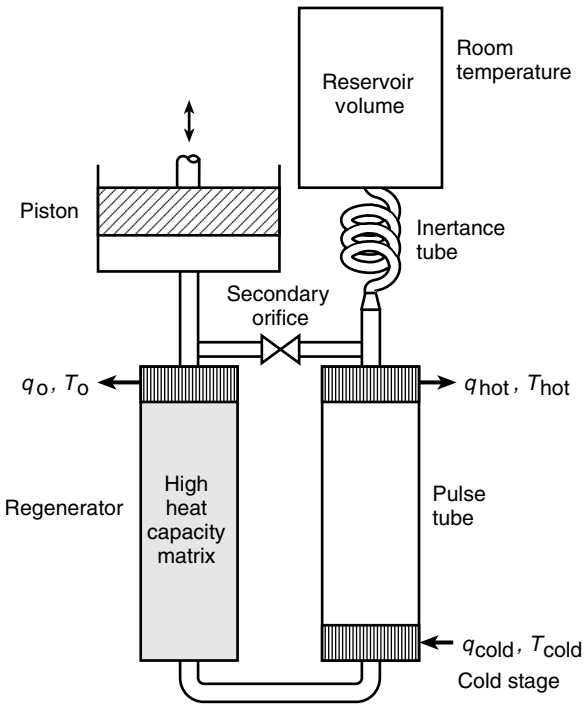

Fig. 1.12 Operation of a pulse-tube cryocooler (q is the heat flow and T is the temperature).

flowing from the warm end travels only part way through the tube before flow is reversed. Similarly, cold gas flow from the cold end never reaches the warm end. The gas in the middle of the tube never actually leaves the pulse tube, serving to form a temperature gradient that insulates the two ends. For the gas in the pulse tube to be an effective insulator, turbulence in the tube has to be minimized. Flow straightening at the two ends is thus crucial to the process. Again, the unique feature of the pulse-tube cryocooler is that there are no moving parts at the cold end and no needle valves that can become plugged.

The function of the *regenerator* is to act as a heat exchanger to precool the incoming high-pressure gas before it reaches the cold end of the cryocooler. The heat of the hot gas flowing into the regenerator is stored for a half cycle in the regenerator matrix material, which has a high heat capacity. The stored heat is then picked up by the cold gas flowing in the opposite direction in the second half of the cycle. The regenerator matrix has a very high surface area for enhancing heat transfer, achieved through the use of stacked fine-mesh screen or packed spheres. At equilibrium, one end of the regenerator is at room temperature, while the other end is at the cold-stage temperature.

Several improvements to this basic concept have been introduced recently, designed to enhance the efficiency and reliability of the pulse-tube cryocooler. Two advances *shift the phase* between the flow and pressure, thereby optimizing the refrigeration cycle at higher operating frequencies where regenerator losses are excessive. The first advance is the introduction of a *secondary orifice* that allows a small fraction (about 10%) of the gas to flow directly between the piston compressor and the warm end of the pulse tube, thus bypassing the regenerator. The second advance is the long narrow inertance tube inserted between the warm end of the pulse tube and the reservoir (which replaces the primary orifice in earlier pulse-tube designs). Pulse-tube systems with just about every combination of these two phase-shifting devices are available. The operating conditions (particularly the size and frequency of the system) determine the best configuration. For example, the inertance tube does not work very well at low frequencies (a few hertz), in which case it is better to use a primary orifice to limit the flow. However, inertance tubes are very effective in large, high-frequency systems.

Further information on basic pulse-tube operation is given in an early paper by Swift (1988), and good summaries of recent advances are given in review articles by Radebaugh (2002, 2003b).

1.4.6 GAS-FLOW CRYOSTATS

Helium-gas-flow cryostats are available commercially and typically cover the temperature range from 1.5–300 K. This type of variable-temperature cryostat differs from the three preceding types in that the sample is not mounted on a cold plate in a vacuum, but rather cooled by cold gas flowing over its surface and the surface of the sample holder. Thus, thermal anchoring is not as much of a prime requirement, and samples with a complex geometry are easier to measure. The system also responds very quickly when the temperature needs to be changed. However, temperature stability is about ± 15 mK, not quite as good as that of the liquid-flow cryostat (± 2 mK).

The operating principle is quite simple in concept, as illustrated in Fig. 1.13. The sample probe is thermally isolated from the surrounding liquid-helium bath by a vacuum-insulated insert dewar. Liquid helium from the surrounding bath is introduced into the insert dewar through a needle valve located at the bottom of the insert, controlled typically from a mechanical linkage to room temperature. The liquid helium then passes through a gas heater, where it is vaporized as it enters the insert dewar. The temperature of the flowing gas is set by controlling both the mechanical flow-rate valve and the electric power to the gas heater.

In using this type of system, particular care must be given to the small capillary that introduces cryogen into the gas heat exchanger. It is prone to becoming blocked if precautions are not taken during cooling to keep it free of liquid air or nitrogen, which would freeze on cooling to liquid-helium temperature. (Procedures to keep sensitive parts free of ice are described, for example, in the technical tip at the end of Sec. 1.5.1.)

Temperature control is best accomplished by an automatic temperature controller (Sec. 5.4.3) attached to the gas heater. This is used in combination with a feedback thermometer attached to the gas heater or, better yet, to the sample holder. At the expense of complexity, finer temperature control can be achieved by use of a second controller and a resistive heater attached directly to the sample holder.

At temperatures below about 20 K, the heat capacity of most materials is very low and the time required to obtain thermal equilibrium is short (usually a few seconds), which makes controllers necessary to eliminate short-term drift. At higher temperatures, on the other hand, equilibrium time is much longer, because the heat capacity of most materials rises very rapidly as the temperature cubed (Sec. 6.1). In this higher-temperature regime, long time constants are required, and an automatic controller is essential to minimize the tedium of controlling temperature manually.

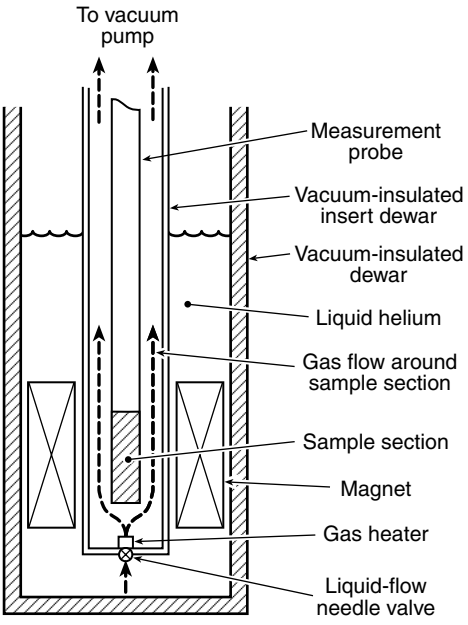

Fig. 1.13 Schematic diagram of a variable-temperature cryostat based on continuous flow of cold helium gas over the test sample.

1.5 Examples of measurement cryostats and cooling methods—high transport current ($\gtrsim$ 1 A)

For high-current measurements, the cooling power usually needed is too great for gas-flow cooling or for mounting the test sample on the cold stage of a cryocooler. There are exceptions, but most of the time, high-current testing calls for direct immersion in a cryogenic fluid. In comparison to low-current rigs, these cryostats can become grandiose affairs, employing large vapor-cooled current leads and sample holders that can handle magnetic forces reaching hundreds of newtons.

1.5.1 IMMERSION TEST APPARATUS

In high-current ($\gtrsim$ 1 A) measurements, cooling of the sample and contact are paramount. At its nominal atmospheric boiling temperature of 4.2 K, liquid helium can handle up to 10^4 W/m^2 of heating at the sample surface without letting the sample temperature rise more than about 0.5 K. Beyond this heat flux, "film boiling" introduces a thermal insulating *gas* layer around the sample, and the sample temperature rises dramatically (Sec. 2.5.1). This is a relatively high heat flux, and so for temperatures in the 1–4.2 K range, liquid helium is a great heat sink.

How long will liquid helium handle high heat loads before boiling away? A good design rule is:

> one watt per liter per hour.

That is, 1 W of heat input into liquid helium will boil away about 1 L of liquid in about 1 h (more precisely, it is 1.377 L/h, from Appendix A1.6a). So, liquid helium not only thermally contacts test samples well, but it has a tremendous cooling power at low temperatures. One liter is able to absorb over 2500 J at 4.2 K. Compare this with a kilogram of copper, for example, which can absorb less than 0.1 J at 4.2 K before rising 1 K in temperature. Liquid nitrogen, on the other hand, at its much higher boiling temperature of 77 K, can handle about 10^5 W/m^2 before its cooling capacity drops because of the onset of film boiling. It takes over 44 W to boil away 1 L of liquid nitrogen in 1 h. So, even greater heat loads can be handled in testing high-current samples in liquid nitrogen than in liquid helium. (Relative boiling rates of many other common cryogens can be determined from the latent heat of vaporization tabulated in Appendix A1.5.)

From a thermal standpoint, an immersion cryostat is a relatively simple cryostat to design; it is an insert probe with current leads holding the sample in the bath, as illustrated in Fig. 1.14. We do not even need a thermometer; sample temperature is measured from the vapor pressure above the liquefied gas (described at the beginning of Sec. 1.2). Heat flow down the *instrument* leads is generally not much of a problem because the leads pass through the cryogenic liquid on the way to the sample. The main concern is evaporating a lot of expensive cryogenic liquid from heat flow down the *high-current* leads. This can be considerable when the cryostat has to handle hundreds to tens of thousands of amperes (single-strand and large-cable superconductor tests, respectively). Current leads are the heart of high-current immersion cryostat design. Techniques for minimizing heat flow down these leads are described in Sec. 4.9.2 and Sec. 4.9.3 (by using vapor-cooled leads or high-T_c superconductor leads).

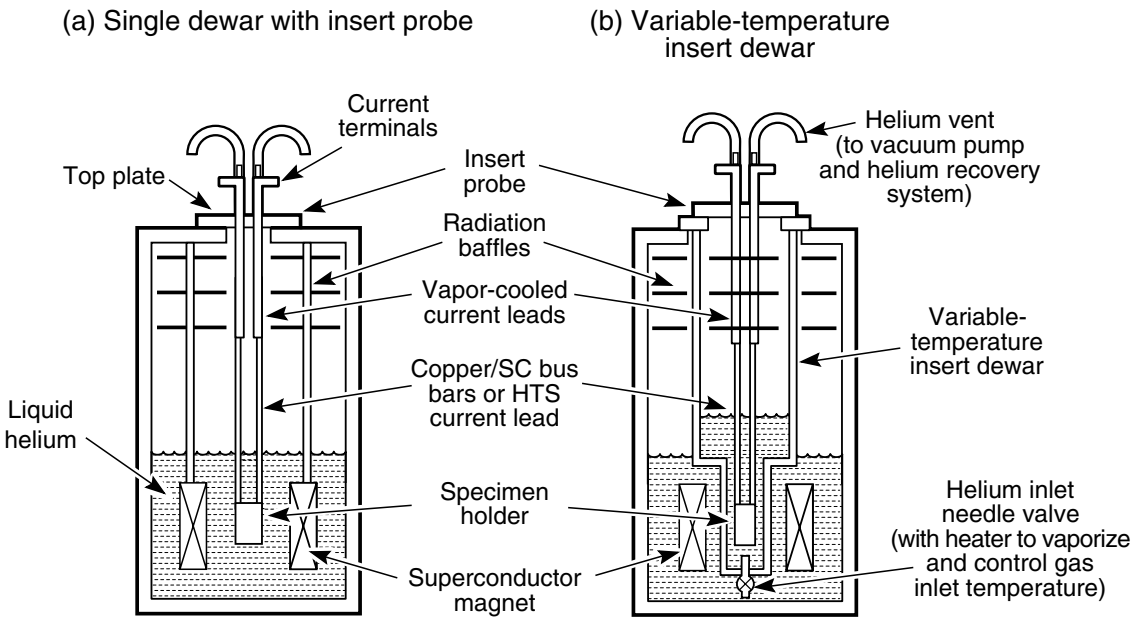

Fig. 1.14 Dewar arrangements for high-current testing: (a) single dewar for cooling both sample and superconducting magnet; (b) separate insert dewar that can be pumped to vary the temperature of just the sample bath.

When measurements are carried out in a superconducting magnet, the same cryogenic liquid can serve the dual purpose of cooling the sample as well as the magnet, as illustrated in Fig. 1.14(a). When the sample needs to be at a temperature different from that of the background magnet, the test sample has to be isolated from the magnet in its own separate insert dewar, as shown in Fig. 1.14(b).

Notice that in the examples of direct immersion apparatus shown in Figs 1.1 and 1.14, the insert probe can be removed from the dewar for changing specimens while leaving the background superconducting magnet at low temperatures. Occasionally, a sample is so big that it cannot be extracted through a top-loading cryostat port. Then the entire magnet-and-sample combination must be warmed in order to change the sample. Occasionally, this cannot be avoided, but it costs a lot of cryogenic liquid, time, and money.

➔ To avoid boiling off any more liquid helium than necessary when changing samples with a top-loading arrangement, it considerably helps with massive probes to *precool* the probe by first dipping it into liquid *nitrogen* before inserting the probe into liquid helium. This is usually good practice, except when the cryostat has *movable* parts; then the movable pieces freeze solid from the coating of liquid air that condenses on them during the transfer from liquid nitrogen into liquid helium. And we cannot beat the game by transferring the rig through the air quickly; I have tried. It takes only a fraction of a second for a film of liquid air to form, and there is no hope of breaking free the movable parts.

In such a case, the sample probe must be either precooled in the protective atmosphere of the test dewar with lengthy pretransfers of liquid nitrogen in and out of the dewar (with no exposure to air) or cooled all the way to 4.2 K from room temperature by lowering it

slowly (over a period of, say, 5–10 min) directly into liquid helium so the probe is precooled by the cold helium gas being boiled away. (During the *initial* cool-down, cold helium gas also can be *slowly* transferred into the dewar with the rig already in place.)

Slow-cooling an apparatus with cold helium gas may also be preferable to liquid-nitrogen cooling when liquid nitrogen could be trapped in the interstices of an apparatus (such as pockets or cooling channels). Slow-cooling with cold helium gas is not as efficient as liquid-nitrogen precooling, but at least it utilizes the enthalpy of the evaporating cold gas to precool the apparatus (Appendix A1.6b). The savings in cryogen obtained by slow-cooling can be considerable, and it is always amazing to me how sometimes people just plunge the probe into the bath with clouds of expensive helium gas billowing out of the dewar.

1.5.2 VARIABLE-TEMPERATURE HIGH-CURRENT MEASUREMENT CRYOSTATS

The easiest method to vary the temperature of a sample is to immerse it in a liquid cryogen and then change the temperature of the cryogen by pumping (partially evacuating) the vapor space above the fluid. Although the temperature ranges are restricted (as previously shown in Fig. 1.2), they are precisely the ranges of interest for many practical applications.

If sample tests are being conducted in a background magnetic field [Fig. 1.14(a)], pumping the large helium bath surrounding the magnet can be expensive. In such a case, a double-dewar arrangement is much more efficient [Fig. 1.14(b)]. This nested-dewar system creates a helium reservoir for the sample that is thermally isolated from the large magnet bath. An inlet valve at the bottom of the insert dewar can be opened and closed to allow liquid from the outer helium bath to flow into the inner sample-dewar space. By pumping just on the small inner volume of liquid and not the entire magnet chamber, the sample temperature can be lowered with reduced cryogen loss.

To reach temperatures well *above* the cryogenic-liquid range, there is no choice but to flow copious amounts of cold cryogenic *gas* over high-current samples (similar in concept to that described for low-current measurements in Sec. 1.4.6). The design and operation of such a variable-temperature apparatus for critical-current testing at high current levels are described later in Sec. 9.4.3. Sometimes, if the test current is not too high and the current contacts have very low resistance, the sample can be thermally anchored to the variable-temperature head of a commercially available cryocooler or liquid-flow cryostat *with high refrigeration power*. With either variable-temperature technique, the important point is to provide high cooling capacity for the sample and adequate thermal mass for stability.

Additional examples of high-current cryostats for various types of critical-current testing are described in Sec. 9.4.3.

1.5.3 MEASUREMENTS NEAR THE SUPERFLUID-TRANSITION TEMPERATURE

Because of the transformation from normal to superfluid helium (Sec. 1.2.2), special cryostat and refrigerator designs are needed to efficiently cool large apparatus near the superfluid-transition temperature.

Lambda-point refrigerator

For cooling powers of less than about 1 W, a lambda-point refrigerator is available commercially. In the simplest refrigerator, the temperature is lowered to about 2.2 K, just *above* the lambda point. Figure 1.15 shows the necessary components of such a refrigerator. Liquid helium in the lower part of the dewar is cooled by a coiled copper tube located just above the superconducting magnet or other test apparatus (labeled *lambda-point refrigerator coils* in Fig. 1.15). A vacuum pump attached to one end of the coiled tube draws liquid continuously through a needle valve located at the inlet end of the tube (required pumping capacity is typically about 10–20 L/s, depending on the cooling power needed). In this tube there is a two-phase mixture of liquid and gas. As the pumped liquid helium changes to gas, the latent heat of vaporization of liquid helium absorbs heat from the bath.

The liquid flow rate through the tube can be adjusted by using the needle valve, which determines the refrigeration power. When initially cooling the system from 4.2 K, high flow rates are used to rapidly cool the system, whereas after the base temperature is attained, the flow rate can be throttled back to make refrigeration more economical. It is especially inefficient to try to pump below the lambda point, which is impossible to do with this system and which wastes a lot of liquid helium in the attempt.

Because cold liquid helium is more dense than warm liquid helium, the cold liquid sinks to the bottom of the dewar, cooling the apparatus *below* the cooling coil with convection currents. However, the liquid *above* the cooling coil is not cooled very much. Because of the low thermal conductivity of normal He I [$<$20 mW/(m·K)] and its tendency to stratify, a strong temperature gradient is set up in the region immediately above the refrigerator coil. Thus, the surface of the helium at the top of the dewar remains near 4.2 K, whereas the helium below the coil is

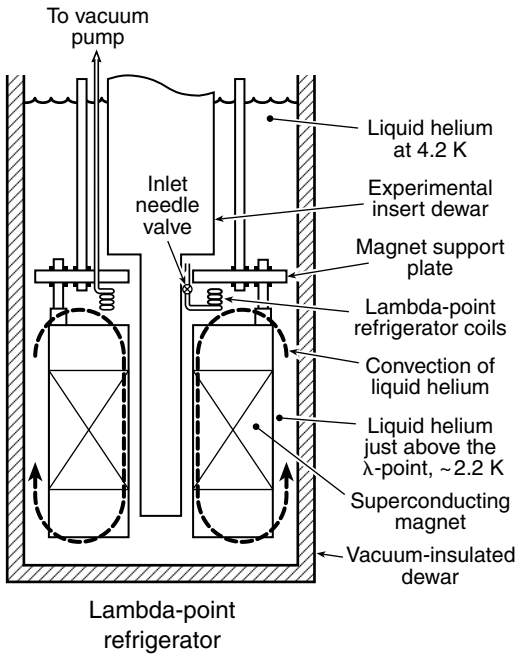

Fig. 1.15 Cross-sectional view of the components of a lambda-point refrigerator for operating continuously at temperatures just above the superfluid-transition temperature (2.177 K) (adapted from Oxford Instruments 2000). In this diagram, the refrigerator is being used to cool a superconducting magnet.

kept nearly isothermal at about 2.2 K by the mixing action of the strong convection currents in this region. Because of the stirring action, the position of the apparatus to be cooled is not critical as long as it is located below the refrigerator coil.

For this type of refrigerator to work, the dewar and apparatus need to be designed so that the temperature gradient above the refrigerator coil is preserved and not short-circuited by high-thermal-conductivity materials crossing the gradient region. Thus, the dewar wall and apparatus supports in the region just above the coil need to be made of stainless steel or other low-thermal-conductivity material (and not aluminum, for example).

The advantage of the lambda-point refrigerator over simply pumping on the entire dewar is that it is more efficient, since only part of the liquid in the dewar is cooled. Also, the liquid reservoir can be refilled from the top without interrupting the operation of the system in the bottom of the dewar (since the top liquid is at 4.2 K and at atmospheric pressure). Of course when transferring new liquid helium, some care must be exercised not to disrupt the temperature gradient near the cooling coil by keeping the transfer tube well above the surface of the liquid helium (see Sec. 1.6.2 on techniques for transferring liquid helium).

The operating parameters of the lambda-point refrigerator can be determined only empirically, and they depend on the needle-valve opening, the size of the coiled tube, the capacity of the vacuum pump, and the dewar size. (Further details of operation are given with each system's product literature.)

To reach temperatures below the superfluid-transition point (2.177 K), a *separate insulated chamber* needs to be provided in the bottom of the dewar to thermally isolate superfluid He II from the normal He I in the upper part of the dewar. The insulation provided by helium stratification is lost when the helium becomes superfluid because of the very high thermal conductivity of superfluid He II, as well as a density inversion at the lambda point (see, for example, Van Sciver 1986). Such an insulating partition for operating *below* the lambda point is illustrated next for the saturated-liquid-container refrigerator.

Saturated-liquid-container refrigerator

A great advantage of testing below the superfluid lambda point (2.177 K) is the huge increase in thermal conductivity of liquid helium that occurs when it transforms into the superfluid phase, He II. He II thus provides perhaps the ultimate sample-cooling and sample-temperature uniformity.

Superfluid helium can be obtained simply by pumping on the entire dewar. This works fine for dipper-probe testing, but for large apparatus it is usually much more efficient and convenient to use a saturated-liquid-container refrigerator in conjunction with a Joule–Thompson (J–T) valve (Claudet et al. 1974). Figure 1.16 shows the necessary components of such a refrigerator, the most obvious being a fiberglass–epoxy composite (G-10) insulating plate (also called a "lambda plate") placed in the dewar to thermally isolate the upper and lower parts of the liquid-helium bath into separate He I and He II reservoirs. The two are hydraulically connected by a valve used to introduce normal helium into the superfluid bath as needed. This valve could consist of, for example, a conical spring-loaded Teflon-on-Teflon™ valve operated by a connecting rod to the room-temperature head of the cryostat. Opening this port also serves to fill the lower chamber with liquid helium at the start of the experiment.

The lower reservoir is cooled by a saturated-liquid container used in conjunction with a J–T evaporation valve. A vacuum pump draws He I liquid through the J–T valve into the saturated-liquid container. As the liquid expands abruptly through the J–T valve, it cools the container and the surrounding lower helium bath. A counterflow heat exchanger precools the incoming liquid for increased efficiency.

A good operating temperature of the subcooled He II bath is typically about 1.8 K, where superfluid helium is most efficient at removing heat from the apparatus being cooled. By using a high-capacity vacuum pump (1400 L/s), cooling powers up to about 37 W have been obtained (Pfotenhauer et al. 1997).

The saturated-liquid-container refrigerator is generally not available commercially as an "off-the-shelf" system; it needs to be designed and built on an individual basis. However, such a system is efficient and enables cryogenic apparatus, such as superconducting magnets, to be operated *continuously* below the lambda point in a very highly conducting thermal bath. That is, normal He I can be added to the upper bath while maintaining the lower He II reservoir at superfluid-helium temperatures.

When large electrical currents must be transmitted across the insulating lambda plate, the heat leak from the He I reservoir to the superfluid He II reservoir needs to be minimized.

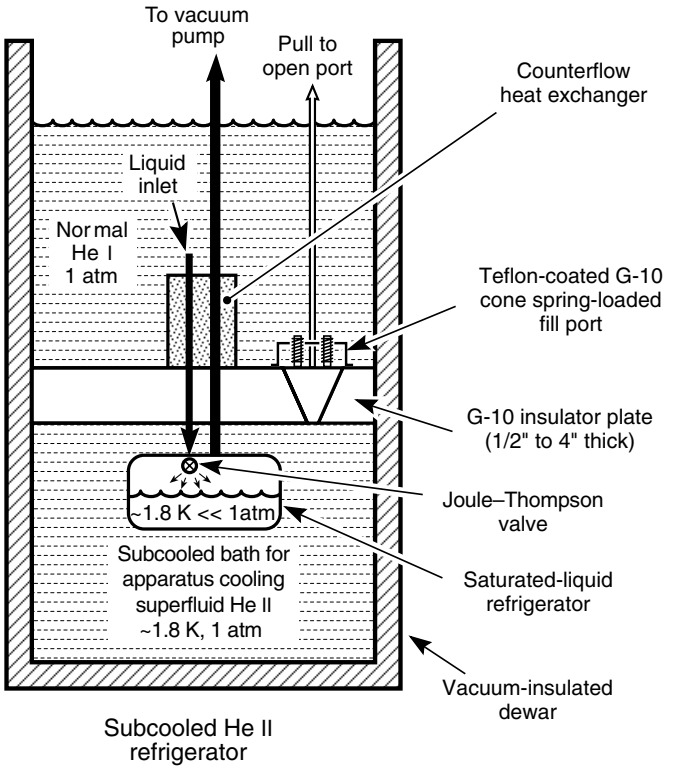

Fig. 1.16 Schematic diagram of the components of a saturated-liquid-container refrigerator for obtaining continuous high-cooling power at superfluid-helium temperatures (adapted from Pfotenhauer et al. 1997).

A high-current electrical lead that addresses this design challenge is described by Huang et al. (1992). It consists of a plug made of alternating copper and stainless-steel thin laminates with attached superconducting strands. The laminates minimize thermal conduction across the insulating plate, as well as provide a large heat capacity for over-current protection.

1.5.4 VARIABLE-ANGLE CRYOSTATS FOR MEASUREMENTS IN A MAGNETIC FIELD

Variable-angle measurements in a magnetic field represent a special class of cryostats, for either low- or high-current measurements. For most field-angle measurements, the axis of specimen rotation of interest usually lies not along the magnetic field, but perpendicular to it. This is the case for critical-current testing, as well as for many magnetic and optical experiments. The easiest way to make such measurements is to use a *radial-access* magnet, which has a perpendicular access port that permits the entire measurement probe to be rotated from above, as illustrated in Fig. 1.17.

This design permits use of a rotary seal operating at the top of the dewar at *room temperature*, which is less complex than a *cryogenic* rotating seal. If the dewar will be pumped to reduce the temperature of the cryogen, only a low-grade vacuum seal is needed, which works for pressures down to about 10^3 Pa for liquid-helium measurements, or 10^4 Pa for liquid-nitrogen measurements. In the simplest case, this seal can be just an O-ring, as depicted in Fig. 1.17. However, for precise angle control under vacuum, using an O-ring seal can be tricky because of friction from air-pressure loading on the seal when pumping. In this case, it is easiest to purchase one of the many commercial rotating vacuum seals that are available for use at room temperature.

To obtain *simultaneous* polar- and azimuthal-field angle measurements (not just rotation around a single axis, as shown in Fig. 1.17), a more complex gear mechanism is required

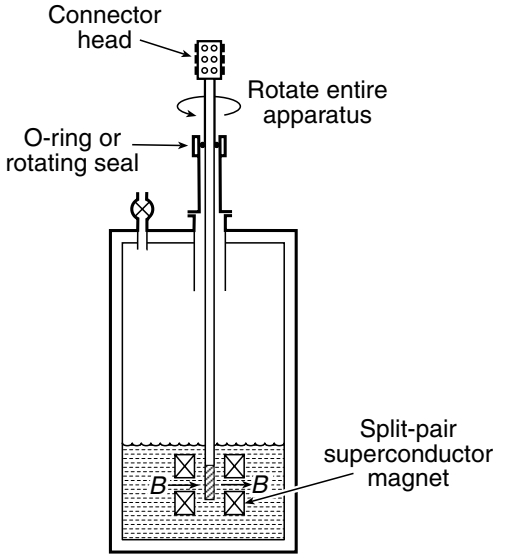

Fig. 1.17 Radial-access magnet arrangement for measuring the dependence of cryogenic properties on the angle of the magnetic field *B*. The entire measurement apparatus is simply rotated by using a room-temperature rotary seal.

that will operate within the confined space of the magnet bore. An innovative, compact, double-rotational-axes design is illustrated in Sec. 9.4.2.

Having surveyed a few basic measurement cryostats and the cooling options available for 300–1 K, we turn now to sequenced, in-depth design and construction techniques in the rest of the book. Perhaps the most important, initial step of the design process is that of heat transfer, treated in the next chapter. The addenda below call attention to a few practical pitfalls (many personally learned the hard way.)

1.6 Addenda: safety and cryogen handling

1.6.1 SAFETY: HOW WE CAN GO WRONG

By and large, cryogenics laboratories are relatively benign and most equipment is safe, but as a wise man once said: "*Anyone who thinks he has built a foolproof system has overlooked the ingenuity of fools*." And I might add wise people as well. So it pays to know how the rest of us have gotten into trouble. The following is certainly *not a complete list* (new failure modes are being invented daily) and it is only a list, *not a course in safety*. But the list may at least alert you to some potential failure scenarios, and sometimes it is intriguing to see the problems we have encountered. If you read nothing else in this section, at least have a look at the first few items—they are so common but the consequences are potentially severe. More information is included from time to time among the tips (→) in succeeding chapters, as well as in the book by Edeskuty and Stewart (1996). The best approach is to *talk about the details with an experienced person* who has "been there and done (or seen) that."

Cryogenic problems

For the most part, these problems are the most common, vexing, and potentially dangerous.

Warming up cryogenic apparatus after an experimental run: If gases condense into restricted spaces in your apparatus at low temperatures, these liquefied gases will suddenly vaporize and can blow the rig apart. *Make sure every cryogenic vacuum space (especially insulating dewar jackets) is equipped with an overpressure port* (a Richards valve, for example, Richards 1954). These usually work quite well. However, it is a good idea to protect every vacuum space with two such blow-off valves for redundancy; on one occasion I had a stainless-steel dewar with a slow cryogenic leak in the vacuum jacket that let some liquid helium into the vacuum space. On warming the dewar after the experiment, the single pressure relief valve apparently failed. I was lucky. The outer wall of the dewar held the pressure, but the inner dewar wall buckled into a twisted, shriveled stainless-steel mass (but it was quite an objet d'art).

Liquid-cryogen storage vessels: Never leave the valve at the top open to air for more than a few seconds when starting and stopping a transfer of liquid. Close it off so the storage vessel vents through a pressure relief valve; otherwise, air will be cryopumped (condensed) into the neck of the dewar, freeze, and form an "ice" plug that blocks the escape of gas from the boiling liquid

inside. The vessel becomes a virtual pressure bomb. *I have seen the aftermath of a storage dewar that exploded, and it was not a pretty sight.*

If you have a dewar you suspect may be ice plugged, get some experienced help! It can be cleared by thrusting a hollow copper pipe *rapidly* down the neck of the dewar (so the pipe does not have time to cool and become stuck). When the ice block is melted, watch out for the rush of escaping gas through the tube! (Do not use a large solid rod or it can become a missile.) Wear thick, insulating gloves and glasses, since when the block clears, one heck of a stream of high-pressure freezing cold helium gas will shoot up the dewar neck. Have a copper pipe of the right size on hand that fits down the neck of your storage dewars (preferably equipped with a metal disk shield to protect your hand—sort of like a sword and hilt).

Transferring liquid cryogens: Because it is such an important topic when starting to work in a cryogenics laboratory, a step-by-step procedure for transferring cryogenic liquids is given in the second addendum, Sec. 1.6.2. Despite this discussion, it is important to have someone knowledgeable initially *show* you how to do it and then, even more importantly, *watch* you the first several times you do it yourself. Too many things can, and will, go wrong. Also, with a newly constructed cryostat, it is especially important to have expert help to learn the times and pressures required for filling it.

As standard practice, wear gloves and protect your eyes with goggles or glasses when transferring liquid cryogens (especially helium) from one dewar to another—always. It is embarrassing, but several times I have not followed my own advice (just to speed things up) and have paid the price with a few skin burns (no eye damage, fortunately). Learn from the school of hard knocks—*it is not worth it!* Have the gloves and glasses on hand. The critical time is when removing a cold transfer tube—you have a meter length of cold steel and a jet of freezing gas to contend with.

Liquid nitrogen exposed to air for a long time: In such a situation, *liquid oxygen* can be condensed into the dewar, which is highly combustible if it comes into contact with anything that can serve as a fuel (including lubricants in fittings). Likewise, be careful working with oxygen gas. For example, gas pressure regulators that have previously been used with oil-pumped gases can be a combustion hazard when used with oxygen.

Less common cryogenic problems

Liquid hydrogen: This is not a common cryogen anymore because of the explosive danger of the boil-off gases as they mix with air. The flammable mixture range is from 4.1–75% hydrogen gas (at standard temperature and pressure) (Edeskuty and Stewart 1996). The boil-off hydrogen gas, therefore, needs to be carefully vented outdoors or else collected. Just beware. Once, we had an entire wall of a hydrogen research laboratory blow out (it was designed for that possibility, and no one was hurt).

Superconducting magnet leads: Do not disconnect them when the magnet is energized. The inductively stored energy in a superconducting coil is tremendous and can generate extremely high voltage across the magnet terminals. This can be a fatal mistake. Make sure superconducting magnets are equipped with an integral resistor/diode protection circuit to clamp the voltage at a low level (usually only about 10 V).

Vacuum foibles

Pressure relief valves: All vacuum systems should have two blow-off valves on them, even if there is no reason to suspect the system will be overpressurized. Too often something unexpected happens, such as having a gas-bottle pressure regulator turned too high when backfilling a system with gas to open it. Vacuum windows, for example, are designed for vacuum, not overpressure, and they can easily blow out.

Vacuum pump exhaust: Vent oil vapor to the outside, not into the laboratory. Also, beware of gases purged from capture-type pumps, particularly cryogenic pumps that use liquid-nitrogen-cooled sorbants or refrigerator-cooled sorbing arrays. Oxygen pumps are a special class; they entail explosion danger if lots of oxygen is pumped onto activated charcoal, which can be instantaneously ignited by the oxygen.

Vacuum view ports: Wear goggles or at least safety glasses, or at a minimum *some* kind of glasses. Taking them off to see better may result in not seeing at all.

Glass dewars: Do not even try to pull a vacuum on them. Unknowingly, one of our reviewers did this when he first started working in a cryogenics lab. It seemed reasonable at the time. As he later commented, "It is not that obvious if you have never thought about it. I was lucky not to lose an eye."

Unhealthy materials

Heavy metals: In general, avoid ingesting or inhaling vapors that might contain heavy metals, such as lead in solders, white lead oxide, cadmium in brazing alloys and solders, beryllium and beryllium–copper in the form of *dust*. Solder, braze, and work with such materials under a ventilation hood. Also, wash your hands after working with oxide superconductor materials, including Y- and Bi- based compounds. Avoid skin contact with Tl-based superconductors.

Solder flux: It is best to wear goggles and solder under a ventilation hood (or install a suction venting tube) to evacuate flux smoke that can cause allergies and irritate nasal passages. Soldering fluxes are corrosive and form corrosive by-products such as oxides and chlorides, on surfaces. Thoroughly rinse and clean up *acid* flux that is commonly used when soldering stainless steel. The possibility of eye damage is serious, and acid burns of your skin are no fun. Over the years, I have aerated a few very nice shirts with acid holes.

Lead: Beware; it can show up in unexpected places, such as in high-temperature lubricants for stainless-steel bolts.

Fiberglass–epoxy materials: Avoid breathing the glass dust produced in machining, filing, or sanding such composites. Keep the part wet during machining with a water-based cutting coolant to prevent glass dust from flying, or, if the part has to be machined dry, use a vacuum with an extension tube right at the cutting tool to continuously suck up the dust as it is being created. Use a dust mask and wear goggles to protect your eyes.

Beryllium–copper: Handling Cu–2%Be in *solid* form poses no special health risk. However, in machining Cu–2%Be, take care to avoid the production of *fine dust particles* or *fumes* that

could be inhaled and cause a serious lung disorder. Machining is fine if *sharp* cutting tools and a *coolant* such as a water-based cutting lubricant are used. Stamping, drilling, turning, milling, boring, hardening heat treatments, and other operations that produce only *large* particles or turnings (and no dust or fumes) present no unusual risks from the beryllium exposure. Before machining Cu–2%Be, however, be sure to check the latest detailed safety information about Cu–2%Be that is available, for example, from Brush Wellman (http://www.brushwellman.com/).

The primary hazards associated with beryllium–copper are those processes that generate small airborne dust, fumes, or mists having diameters less than 10 μm (0.0004 in.), at which size they are invisible to the naked eye. Likely inhalation hazard is produced by de-burring, grinding, polishing, buffing, welding, annealing, honing, sawing, lapping, high-speed machining, electrical discharge machining (EDM), and abrasive blasting. (Note: This list is not all-inclusive, and specific processes performed at your facility must be evaluated to ensure that proper work practice and engineering controls are implemented. This information was obtained from Brush Wellman's beryllium health and safety facts at http://www.brushwellman.com/; this or another source of safety facts should be consulted for more complete information.) Beryllium by itself (not alloyed with 98% copper) is nasty stuff, however! It is much more hazardous than Cu–2%Be and needs to be machined in a glove box with careful safety precautions.

1.6.2 TRANSFERRING CRYOGENIC LIQUIDS

Liquid nitrogen

The latent heat of vaporization of liquid nitrogen is quite high (161 J/mL, from Appendix A1.5). Thus, it is fairly easy to transfer liquid nitrogen with *un*insulated tubing. Just be sure to choose tubing that does not shatter too readily when frozen. Some forms of rubber tubing work fine; others break easily. Stainless-steel tubing of course will work, but is generally not needed unless vacuum-jacketed insulated tubes are required for efficient liquid transfers over long lengths ($\gtrsim$10 m).

Generally, liquid nitrogen can be ordered commercially and provided in portable storage dewars. These storage dewars are usually the self-pressurizing type, and all you need to do is open the valve to start the transfer. Some dewars, however, need to be pressurized from a cylinder of high-pressure nitrogen gas; the gas is delivered at low pressure (about 1 atm) through a pressure-reducing regulator to the vapor space above the liquid in the storage dewar. The pressure forces liquid nitrogen up a transfer tube inserted into the bottom of the dewar.

Precool large, high-mass superconducting magnets or cryostats with liquid nitrogen *slowly*. That is, transfer the cold gas/liquid over a period of an hour or more for larger systems and let the cold gas do the initial cooling. Otherwise, thermal shock or different thermal-contraction rates can damage cryogenic systems.

Liquid helium

The latent heat of vaporization of liquid helium is 60 times lower than that of liquid nitrogen (only 2.6 J/mL, from Appendix A1.5). Thus, unlike liquid nitrogen, it is not an easy substance to handle. In fact, the first time I tried to transfer liquid helium I went through half a dewar of liquid helium before someone with experience told me to stop transferring. Later, I found in the bottom of my measurement dewar a little liquid nitrogen (which I had not completely blown out of the dewar after filling the dewar with liquid nitrogen to precool my apparatus). I had used all that precious liquid helium just to freeze the residual nitrogen into a solid block. An expensive lesson. Ask someone with experience to show you and watch you as you transfer liquid helium the first several times.

Precisely because helium is not cheap, it usually pays to *precool* the apparatus with liquid nitrogen (just be sure to blow out *all* of it before transferring helium, unlike the practice of some people who will remain nameless). As insurance, it helps to blow a little warm nitrogen gas into the bottom of the dewar, after removing the liquid nitrogen, to evaporate any liquid that might remain puddled in the bottom of the dewar. Also, design the apparatus so that when you pressurize the dewar to blow the liquid nitrogen out, you do not leave liquid trapped in pockets in your rig, such as closed-ended screw holes (make them so they are self-draining).

Because the latent heat of vaporization is low, liquid helium requires the transfer line to be *thermally insulated* with a vacuum jacket. Although the simplest insulated transfer lines are rigid, it is worth the investment in a *flexible* stainless-steel bellows line like that shown in Fig. 1.18.

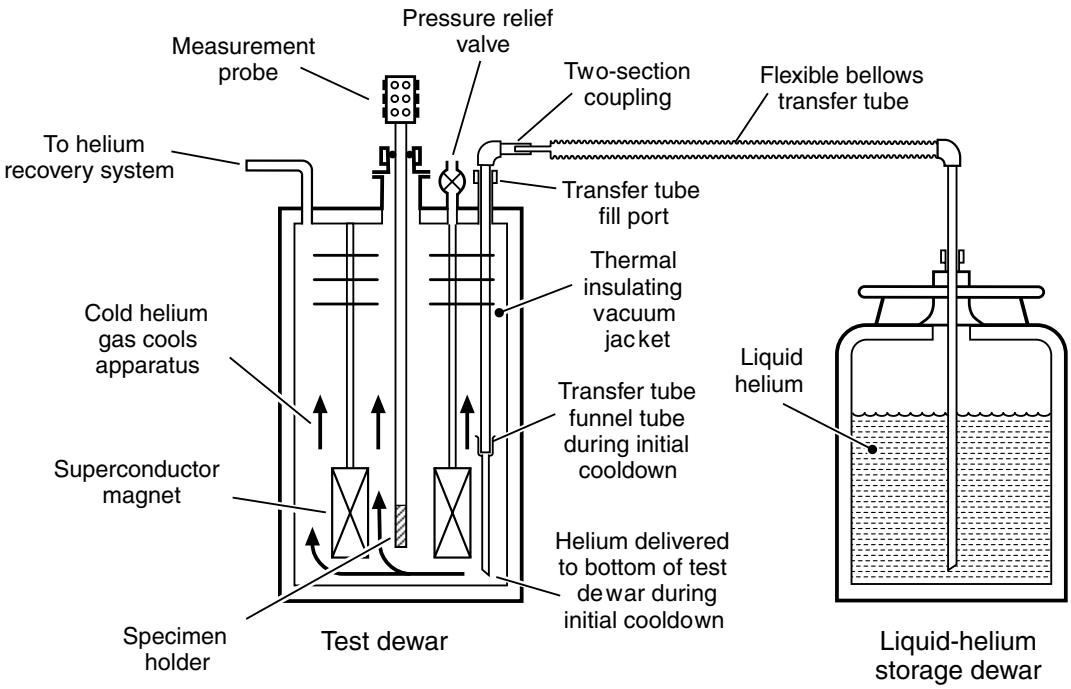

Fig. 1.18 Transferring liquid helium from a storage dewar into a test dewar. The transfer tube must be double walled (not shown), with the space between the walls evacuated to thermally insulate the inner fluid line from the outside world.

This allows the two helium vessels to be moved around slightly, so they do not have to be so precisely positioned. Some transfer lines come in *two sections*, one part inserted into the test dewar and the other into the storage dewar, joined by a coupling (illustrated in Fig. 1.18). This two-section transfer line is especially convenient for *re*transferring helium (in laboratories where helium is not recovered), described in more detail below.

Although only a small amount of heat is needed to evaporate liquid helium, cold helium *gas* has a very high *enthalpy* and can provide a lot of cooling power as it is warmed to room temperature (over six times that of nitrogen gas when warmed from its boiling temperature; see Appendix A1.6a). Thus, it pays when filling a measurement dewar initially to *slowly* transfer helium to the bottom of the receiving dewar so that first only cold gas will pass over and cool the apparatus, thereby utilizing the gas's large cooling power.

Procedure for transferring liquid helium

Following is a list of the basic steps for *initially* transferring liquid helium into a warm measurement dewar and magnet system (which usually also contains the measurement probe if the probe has a large mass):

1. Use *gloves* to protect your hands from frostbite and *goggles* for your eyes.
2. *Precool* the apparatus with liquid *nitrogen*, if possible, to save liquid helium. Blow out all the liquid nitrogen before transferring helium and keep the dewar sealed so air does not condense back into the cooled system. It is best not to take more than a few minutes between blowing out the liquid nitrogen and starting the transfer of liquid helium so that air does not have much of a chance to enter the dewar in the interim.
3. *Slowly* transfer helium to the bottom of the dewar, in order to utilize the cooling power of the cold gas as it flows over the warm system. A rough indicator for the appropriate flow rate is that the helium recovery line should not be frosted more than a few meters along its length, and no liquid air should be condensing and dripping from the outside of the line. (In laboratories where helium is *not* recovered, the cold plume of gas exiting the dewar into the air should not be more than about 10–20 cm long.) Do not freeze the top plate, since the dewar seals can crack and electrical connectors can short from frost and water condensation.
4. During the *initial* filling operation, deliver the helium to the *bottom* of the dewar. Since helium is lighter than nitrogen or air, the cold gas then flows up along the warm components of the apparatus. For complex rigs, this may require inserting the end of the transfer tube into a funnel fixture atop a permanently installed tube that transmits the helium to the bottom of the apparatus, as illustrated in Fig. 1.18.
5. When liquid starts condensing (i.e. "collects") in the bottom of the dewar, the gas flow rate exiting the system suddenly drops to a low level. Ice on the recovery line starts to melt (or the exhaust plume suddenly decreases in size). It then pays to *increase the transfer rate* by raising the pressure in the storage dewar (to typically about 0.3 atm). Why? Because slow gas cooling is no longer much of a help (the rig has already reached

liquid-helium temperature), and transferring liquid over a longer time results in increased losses in the transfer tube.

6. Monitor when to stop the liquid-helium transfer by using either a commercially available liquid-level sensor, or the inexpensive "thumper" tube described in Sec. 2.8.2. The latter is inserted temporarily into the measurement dewar through a separate port in the dewar top plate and used to detect the liquid level by the change in frequency of pressure oscillations in the tube that occurs when the tip of the tube is at the liquid-helium surface (described in more detail in Sec. 2.8.2).

The above procedure changes when *adding liquid helium* to a measurement dewar that already has liquid helium in it. The following procedure is designed to minimize loss of existing liquid in the dewar:

- In laboratories where helium gas is *recovered*, insert the transfer line into the dewar, but keep the end of the tube well *above* the liquid helium so that the warm gas initially passing through the transfer line does not boil off the liquid helium. *Precool* the transfer line with cold helium gas by keeping the initial flow rate low. When the flow rate of gas exiting the dewar reduces (indicating that the line is cold and has liquid helium coming out the end), increase the helium-transfer rate for efficiency.
- In laboratories where helium gas is *not recovered*, it is easiest to precool the transfer line by starting the transfer with the exit end of the line *not* in the test dewar at all. That way, you can see exactly when the line is cold, indicated by a dense plume of helium gas shooting out the end of the transfer line. When this happens, quickly wipe off the end of the transfer tube with a rag to remove the ice that will build up there and immediately insert the transfer tube into the test dewar. Keep the end of the tube *above* the liquid helium level (i.e. do not insert it into the funnel extension in Fig. 1.18), so as not to blow the initial helium gas coming through the transfer line into the liquid at the bottom of dewar. To implement this procedure, it helps considerably to have a flexible (bellows-type) transfer line and, better yet, a two-section bellows line like that illustrated in Fig. 1.18. The two-section arrangement is quite convenient since, after the long section from the storage dewar has cooled, it can be immediately inserted into the coupling at the end of the short section, which is already in position in the test dewar.

Helium-transfer problems

Problems are often encountered when learning how to transfer liquid helium. At the risk of sounding like a broken record, the absolutely best approach is to get someone knowledgeable to help. Just so you are forewarned, I have listed a few of the more common problems below.

Recovery (or exhaust) line does not get cold enough

This indicates that the transfer rate is much lower than it should be. Causes include:

- Pressure applied to the storage dewar may be too low. Increase the pressure. Also, check that there is not a high back pressure on the dewar's exhaust line leading to the helium recovery system.

- The storage dewar may be empty, or the liquid level has dropped below the bottom of the transfer tube in the storage dewar. Be sure to measure the liquid helium level in the storage dewar before you begin the transfer. Usually, when the liquid level dips below the end of the transfer tube, this situation is indicated by pressure in the dewar dropping suddenly or by the flow rate of gas into the storage dewar suddenly increasing as the pressurizing gas vents through the transfer tube. An extension can be added to the transfer tube to reach the bottom of deep storage dewars, but limit the length of the extension to about 30–50 cm to keep helium loss low.
- The transfer tube may be blocked. Usually this occurs by pushing the tube into ice that has built up on the bottom of the storage dewar. Remove the transfer tube; warm and dry it by blowing room-temperature helium gas through it. Then reinsert the transfer tube into the storage dewar, only this time, not so close to the bottom.
- The transfer tube may have a "soft" vacuum jacket that no longer provides adequate insulation. This is usually indicated by the outside of the transfer tube becoming cold and covered with frost or ice. The inner and outer tubes of the transfer line may also be touching; the telltale for "touches" is icy patches on the outside of the line.

The test dewar does not seem to cool fast enough

Remember that it takes a long time to cool slowly from room temperature to about 77 K (which is why we usually precool with liquid nitrogen). This is because the heat capacity of most materials is high at room temperature, but decreases rapidly as T^3 as temperature is lowered. Thus, cooling usually proceeds much faster below about 40 K or 50 K. If cooling is taking exceptionally long, causes include:

- The transfer rate may be slow because the pressure in the storage dewar is too low. Check the length of the frosted section of the recovery line (or the size of the cold gas plume coming out of the dewar's exhaust port), as described in the procedure above.
- The measurement apparatus may not have been adequately precooled.
- The vacuum jacket of the measurement dewar may have gone "soft," no longer providing adequate thermal insulation. Check whether the outside of the dewar is cold or frosted (it should be at room temperature). If so, the system needs to be slowly warmed to room temperature and the vacuum leak fixed. Be careful. Remember in this situation that liquid air may have condensed into the vacuum jacket, so make sure the dewar's vacuum jacket has an overpressure relief valve (see Sec. 1.6.1 above).
- Liquid nitrogen may still remain in the bottom of the dewar, or be trapped in pockets in a poorly designed test apparatus (see Sec. 1.6.1 above). Thus, we come full circle back to the central issue—good cryostat design.

Further information on helium-transfer problems and solutions is given in the short booklet entitled *Practical Cryogenics*, listed in the Further reading section below.

1.7 References

1.7.1 FURTHER READING

GENERAL INTRODUCTORY TEXTS ON LOW-TEMPERATURE REFRIGERATION AND CRYOSTAT DESIGN:

Techniques for refrigeration over the cryogenic range (from 300 K to less than 1 mK), and an introduction to cryogenic properties of solids and liquid helium:

Kent, A. (1993). *Experimental Low-Temperature Physics*, American Institute of Physics, Melville, New York.

Properties of liquids and solids at low temperature and refrigeration techniques:

Pobell, F. (1996). *Matter and Methods at Low Temperatures*, 2nd edition, Springer-Verlag, Berlin.

Information on refrigeration techniques, specific types of measurement cryostats, and low-temperature properties of materials:

Seeber, B., ed. (1998). *Handbook of Applied Superconductivity*, Parts D, E, and F, Institute of Physics Publishing, Bristol, UK.

White, G. K., and Meeson, P. J. (2002). *Experimental Techniques in Low-Temperature Physics*, 4th edition, Oxford University Press, Oxford, UK.

A short, readable introduction to cryogenic technology:

Practical Cryogenics, An Introduction to Laboratory Cryogenics (2000), available from Oxford Instruments, Superconductivity, Tubney Woods, Abingdon, Oxon, OX13 5QX, UK.

TEXTBOOKS ON CRYOGENIC ENGINEERING:

Barron, R. F. (1985). *Cryogenic Systems*, Oxford University Press, New York.

Scott, R. B. (1963). *Cryogenic Engineering*. Reprinted (1988) by Met-Chem. Research, Inc., P.O. Box 3014, Highmar Station, Boulder, CO 80307.

Timmerhaus, K. D., and Flynn, T. M. (1989). *Cryogenic Process Engineering*, Plenum Press, New York.

REFERENCE BOOK ON CRYOGENIC ENGINEERING:

Flynn, T. (1997). *Cryogenic Engineering*, Marcel Dekker, New York.

EDITED SERIES OF ARTICLES ON CRYOGENIC ENGINEERING AND EXPERIMENTAL TECHNIQUES:

Richardson, R. C., and Smith, E. N., eds. (1988). *Experimental Techniques in Condensed Matter Physics at Low Temperatures*, Addison-Wesley, Reading, MA.

Weisend, J. G., II, ed. (1998). *Handbook of Cryogenic Engineering*, Taylor & Francis Publishers, London.

SPECIALTY INFORMATION ON CRYOGENIC REFRIGERATORS:

Ackermann, R. W. (1997). *Cryogenic Regenerative Heat Exchangers*, Plenum Press, New York.

Kays, W. M., and London, A. L. (1984). *Compact Heat Exchangers*, 3rd edition, McGraw-Hill, Columbus, OH.

Organ, A. J. (1997). *The Regenerator and the Stirling Engine*, Mechanical Engineers Publications Ltd., London.

Radebaugh, R. (2003). "Pulse Tube Cryocoolers" in *NATO Advanced Study Institute on Low Temperature and Cryogenic Refrigeration—Fundamentals and Applications*, eds. Kakac, S., Smirnov, H., and Avelino, M. R. Kluwer Academic Publishers, Dordrecht.

Walker, G. (1983). *Cryocoolers*, Plenum Press, New York.

Walker, G., and Bingham, E. R. (1994). *Low-Capacity Cryogenic Refrigeration*, Oxford University Press, Oxford.

LIQUID-HELIUM AND SUPERFLUID-HELIUM PROPERTIES:

Eisberg, R., and Resnick, R. (1985). *Quantum Physics of Atoms, Molecules, Solids, Nuclei, and Particles*, 2nd edition, Sec. 11.10, John Wiley & Sons, Somerset, New Jersey.

McClintock, P. V. E., Meredith, D. J., and Wigmore, J. K. (1992). *Low-Temperature Physics: An Introduction for Scientists and Engineers*, Blackie, Glasgow, UK.

Van Sciver, S. W. (1986). *Helium Cryogenics*, Plenum Press, New York.

Wilks, J., and Betts, D. S. (1987). *An Introduction to Liquid Helium*, Clarendon Press, Oxford.

CRYOGENIC TECHNIQUES *BELOW 1 K*:

Betts, D. S. (1976). *Refrigeration and Thermometry below One Kelvin*, Sussex University Press, Brighton, UK.

Lounasmaa, O. V. (1974). *Experimental Principles and Methods below 1 K*, Academic Press, London, UK.

Pobell, F. (1996). *Matter and Methods at Low Temperatures*, 2nd edition, Springer-Verlag, Berlin.

Richardson, R. C., and Smith, E. N., eds. (1988). *Experimental Techniques in Condensed Matter Physics at Low Temperatures*, Addison-Wesley, Reading, MA.

VACUUM EQUIPMENT:

An introduction to vacuum pumps is given at the beginning of Chapter 10 of White and Meeson (2002); Hofmann, A. (1998), in Chapter D11.2, "Some aspects of cryogenic pumps," of Seeber, B. ed., *Handbook of Applied Superconductivity*, pp. 867–874, Institute of Physics Publishing, Bristol, UK; and in Chapter 2 of *Practical Cryogenics, An Introduction to Laboratory Cryogenics* (2000), available from Oxford Instruments, Superconductivity, Tubney Woods, Abingdon, Oxford, OX13 5QX, UK.

An updated list of vacuum equipment suppliers is given each year, for example, in the *Physics Today Buyers' Guide*, American Institute of Physics, http://www.physicstoday.org/guide/. The companies listed can be an excellent source of information about vacuum pumps and equipment.

SAFETY:

Edeskuty, R. J., and Stewart, W. F. (1996). *Safety in the Handling of Cryogenic Fluids*, Plenum Press, New York.

Richardson, R. N. (1998), in Chapter D12, "Safety with cryogens," of *Handbook of Applied Superconductivity*, ed. B. Seeber, pp. 875–888, Institute of Physics Publishing, Bristol, UK.

1.7.2 CHAPTER REFERENCES

Ackermann, R. W. (1997). *Cryogenic Regenerative Heat Exchangers*, Plenum Press, New York.

Anlage, S. M. (1988). Stanford University, California, personal communication.

Claudet, G., Lacaze, A., Roubeau, P., and Verdier, J. (1974). "The design and operation of a refrigerator system using superfluid helium," in *Proceedings of the 5th International Cryogenic Engineering Conference*, pp. 265–267, IPC Science and Technology Press, Guildford, UK.

Cryo Industries (2002). Manchester, NH; used by permission.

Edeskuty, R. J., and Stewart, W. F. (1996). *Safety in the Handling of Cryogenic Fluids*, Plenum Press, New York.

Eisberg, R., and Resnick, R. (1985). *Quantum Physics of Atoms, Molecules, Solids, Nuclei, and Particles*, 2nd edition, John Wiley & Sons, Somerset, New Jersey.

Huang X., Eyssa, Y. M., Pfotenhauer, J., and Lokken, O. (1992). "He I–He II electrical lead transition," *IEEE Trans. Appl. Supercond.* 3, 881–883.

Katti, R. S., Jacobsen, R. T, Stewart, R. B., and Jahangiri, M. (1986). "Thermodynamic properties for neon for temperatures from the triple point to 700 K at pressures to 700 MPa," *Adv. Cryog. Eng.* 31, 1189–1197.

Lemmon, E. W. (2003). Unpublished data. National Institute of Standards and Technology, Boulder, CO.

Lemmon, E.W., Jacobsen, R. T., Penoncello, S. G., and Friend, D. G. (2000) "Thermodynamic properties of air and mixtures of nitrogen, argon, and oxygen from 60 to 2000 K at pressures to 2000 MPa," *J. Phys. Chem. Ref. Data* 29, 1–54.

McCarty, R. D., and Arp, V. D. (1990). "A new wide range equation of state for helium," *Adv. Cryog. Eng.* 35, 1465–1475.

Oxford Instruments (2000). *Practical Cryogenics, An Introduction to Laboratory Cryogenics*. Oxford Instruments, Superconductivity, Abingdon, Oxford, OX13 5QX, UK.

Pfotenhauer, J. M. (2002). University of Wisconsin, Madison, WI, personal communication; data were evaluated from the temperature-dependent internal energy of liquid helium and the enthalpy of the exiting gas.

Pfotenhauer, J. M., Lokken, O. D., Christianson, O. R., and Daly, E. F. (1997). "He II refrigeration system performance in the SMES proof of principle experiment," *Cryogenics* 37, 711–717.

Radebaugh, R. (2002). "Cryocoolers and high T_c devices," Chapter 9 in *Handbook of High Temperature Superconductor Electronics*, ed. N. Khara, Marcel Dekker, New York.

Radebaugh, R. (2003a). National Institute of Standards and Technology, Boulder, CO, personal communication.

Radebaugh, R. (2003b). "Pulse Tube Cryocoolers" in *Low Temperature and Cryogenic Refrigeration*, eds. S. Kakac, H. Smirnov, and M. R. Mila, Kluwer Academic, Dordrecht, The Netherlands.

Richards, R. J. (1954). "A high vacuum seal-off valve," *Rev. Sci. Instrum.* 25, 520.

Russek, S. E. (1990). National Institute of Standards and Technology, Boulder, CO, personal communication.

Sample, H. H., and Rubin, L. G. (1978). "Magnetic field induced temperature changes in cryogenic liquids: N_2, Ar, and He^4," *Cryogenics* 17, 223–229.

Schmidt, R., and Wagner, W. (1985). "A new form of the equation of state for pure substances and its application to oxygen," *Fluid Phase Equilibria* 19, 175–200.

Span, R., Lemmon, E. W., Jacobsen, R. T., Wagner, W., and Yokozeki, A. (2000). "A reference quality thermodynamic property formulation for nitrogen," *J. Phys. Chem. Ref. Data*, 29(6), 1361–1433.

Swift, G. W. (1988). "Thermoacoustic engines," *J. Acoustic Soc. Amer.* 84, 1145–1180.

Tegeler, C., Span, R., and Wagner, W. (1999). "A new equation of state for argon covering the fluid region for temperatures from the melting line to 700 K at pressures up to 1000 MPa," *J. Phys. Chem. Ref. Data*, 28(3), 779–850.

Van Sciver, S. (1986). *Helium Cryogenics*, Plenum Press, New York.

Younglove, B. A. (1982). "Thermophysical properties of fluids. I. Argon, ethylene, parahydrogen, nitrogen, nitrogen trifluoride, and oxygen," *J. Phys. Chem. Ref. Data* 11, Suppl. 1, 1–11.

2 Heat Transfer at Cryogenic Temperatures

If you get it right on paper,
it'll be right when you build it.

– Susan Wright,
Mother of Orville & Wilbur Wright,
Pioneers of Aviation. (Reynolds 1950)

2.1 Introduction

Heat transfer is at the crux of most cryogenic designs. After machining an apparatus, we can get away with a few modifications, but for any kind of success, the heat flow into and out of the sample has to be, at least, in the right ballpark. I have seen rigs that do not stand a ghost of a chance of working because little or no effort was spent getting the heat-transfer design right in the first place. If you do not look at any other chapter in this book, this is the place where it pays to spend a little time, especially with the examples at the chapter end, Sec. 2.9.

Heat transfer occurs in three basic ways, depending on the medium: *conductive* heat transfer through solids (Sec. 2.2), *convective* heat transfer through liquids and gases (Sec. 2.3), and *radiative* heat transfer through space (Sec. 2.4). We can do a pretty good job predicting heat conduction through solids. However, convection and radiation are a little more problematic, but we can make reasonable estimates. The challenge is variability among materials—that is, handbook values of the accommodation coefficients for gas conduction and surface emissivity for radiation can differ significantly from material to material, depending on surface texture, tarnish, and so on.

In addition to heat conduction through solids, liquids, and space, heat transfer across *interfaces* often plays a significant role in experiment design. For example, heat conduction across liquid/solid interfaces is crucial for direct immersion experiments (Sec. 2.5), and good heat transfer across solid/solid interfaces is imperative for cryocoolers and variable-temperature cryostats in order to thermally anchor samples, wiring, and thermometers (Sec. 2.6). Sometimes the only option for cooling long or irregularly shaped samples is by heat transfer across solid/gas interfaces (Sec. 2.7).

Several not-so-obvious heat sources can also play a role, such as Joule heating, thermoacoustic oscillations, superfluid-helium creep, and gas desorption (Sec. 2.8).

We consider, in turn, each of these heat-transfer mechanisms and then, at the end of this chapter, show how they all come together by calculating the heat budget for a practical measurement probe (Sec. 2.9). What is important are the calculational principles, which can be extended readily to other types of apparatus.

2.2 Heat conduction through solids

The conduction heat flow $\dot{q}_{\text{cond}}$ through a small element of a solid bar, tube, or any other cryostat member is given by

$$\dot{q}_{\text{cond}} = \lambda(T)\, A\, \mathrm{d}T/\mathrm{d}x, \tag{2.1}$$

where A is its cross-sectional area, $\mathrm{d}T/\mathrm{d}x$ is the temperature gradient along the element, and $\lambda(T)$ is the temperature-dependent thermal conductivity of the material. (In this book, we have represented thermal conductivity by the symbol λ, but the symbol k is also common.) If we have the typical situation where the cryostat part has a *uniform* cross-sectional area, then we can integrate Eq. (2.1) to obtain the relatively simple expression:

$$\dot{q}_{\text{cond}} = A/L \int_{T_1}^{T_2} \lambda(T)\, dT = (A/L)\,\overline{\lambda}\,\Delta T, \tag{2.2}$$

where L is the length of the element, A its cross-sectional area, and T_1 and T_2 are the temperatures at the ends of the element. As shown on the right side of Eq. (2.2), a mean thermal conductivity $\overline{\lambda}$ is sometimes also defined for specific temperature intervals:

$$\overline{\lambda} \equiv \Delta T^{-1} \int_{T_1}^{T_2} \lambda(T)\, dT, \quad \text{Mean thermal conductivity}$$

where the interval is given by $\Delta T \equiv T_2 - T_1$.

Values of the thermal conductivity $\lambda(T)$ are shown in Fig. 2.1 for some common technical materials used in cryostat construction. There is quite a range, over six orders of magnitude, depending on the material. It is easy to see why materials such as stainless steel, with its relatively low thermal conductivity, are commonly used for the structural components of a cryostat to keep the influx of heat low.

Because of the strong temperature dependence of $\lambda(T)$, cryostat design can be simplified with general tabulations of the thermal conductivity *integral* $\int \lambda(T)\ \mathrm{d}T$ in Eq. (2.2). Appendix A2.1 lists thermal-conductivity integrals [with reference to 4 K, $\int_{4\,\text{K}}^{T_2} \lambda(T)\ \mathrm{d}T$] for a number of common technical cryostat materials. From these tabulated values we can determine the heat flow through a solid member of uniform cross-sectional area A and length L between two *arbitrary* temperatures T_1 and T_2 by taking differences between the 4 K integrals. That is, from Eq. (2.2),

$$\dot{q}_{\text{cond}} = A/L \int_{T_1}^{T_2} \lambda(T)\, dT = A/L \left[\int_{4\,\text{K}}^{T2} \lambda(T)\, dT - \int_{4\,\text{K}}^{T1} \lambda(T)\, dT \right]. \tag{2.3}$$

Most of the handbook values of thermal conductivity (Fig. 2.1) or the integrals (Appendix A2.1) do not vary much among different samples of the same material, except for

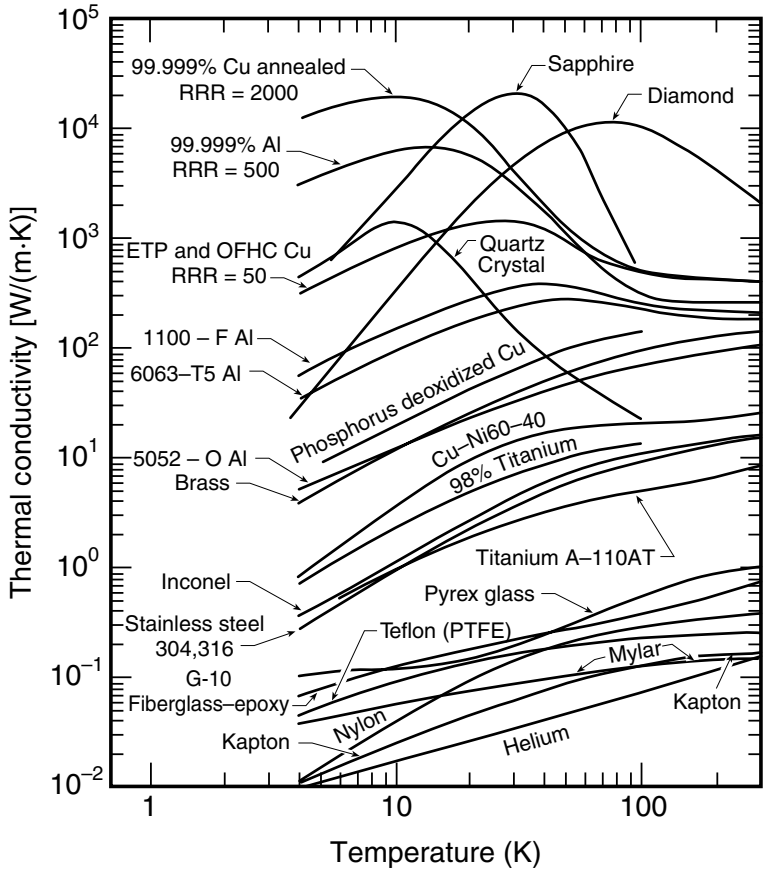

Fig. 2.1 Thermal conductivity of some common solids as a function of temperature (compiled from data in Radebaugh et al. 2001, Johnson 1960, White and Meeson 2002, and *Cryo. Mat. Prop. Prog.* 2001). Tabulated data for these and additional materials are given in Appendix A6.7.

high-purity metals. The conductivity of pure metals at low temperatures varies all over the map, depending on their defect content, as illustrated by the various copper materials in Fig. 2.1. An easy way, however, to approximately determine the low-temperature thermal conductivity of a high-purity metal is to measure the low-temperature *electrical* resistivity ρ of the material (which is much easier to measure than λ) and then calculate λ from the Wiedemann–Franz–Lorenz law:

$$\lambda \approx L_N T/\rho, \tag{2.4}$$

where L_N is the Lorenz number, 2.44×10^{-8} V^2/K^2. (This is described in more detail in Sec. 6.4.2.) Equation (2.4) also shows why the thermal conductivity of high-purity metals in Fig. 2.1 has a peak, since the increase in electrical resistivity at high temperatures suppresses electronic heat conduction in this regime.

2.3 Heat conduction through gases (and liquids)

Calculations of heat conduction through gases are not as accurate as through solids, but some estimate is needed in designing apparatus when exchange gas is deliberately introduced into a vacuum space to thermally connect two parts of the apparatus. This is the case, for example, when exchange gas is introduced to speed cool-down of the sample space, or to provide variable heat transfer to the cryogen bath when a variable-temperature cryostat needs to span a large temperature range (an example calculation is given in Sec. 2.9.2). Gas cooling is also sometimes used to help achieve thermal uniformity in long, low-thermal-conductivity samples that cannot be heat-sunk along their entire length.

There are two very different regimes of heat transfer through gas, depending on the pressure of the gas. In the *hydrodynamic* regime, near atmospheric pressure, the mean free path l of the gas molecules is limited by collisions with other gas molecules. At very low pressures, on the other hand, the mean free path of the molecules can become comparable to the distance between the hot and cold surfaces in the cryostat. In this *free-molecule* regime, the gas molecules travel from the hot wall (usually the apparatus) to the cold wall (in contact with the cryogen) without colliding with other molecules.

The transition between these two regimes occurs when l is approximately equal to the distance d between the hot and cold walls in the measurement cryostat. The mean free path can be determined from the relation (Frost 1975)

$$l = 2.87 \times 10^{-3}\, T^{j+1} / P, \tag{2.5}$$

where l is in centimeters, T is the temperature in kelvins, P is the pressure in pascals, and the exponent, $j+1$, has a value of 1.147 for helium (the most commonly used exchange gas because of its low condensation temperature). Table 2.1 shows the pressure of helium gas where l becomes equal to 1 cm. Note that the gas pressure at which the transition occurs decreases with temperature.

Table 2.1 **Transition between *hydrodynamic* and *free-molecule* behavior for helium gas when the hot-to-cold wall separation *d* is 1 cm. The crossover pressure for a separation other than 1 cm can be determined by multiplying the pressure by [1 cm/*d* (cm)].**

Temperature	Helium Gas Pressure	
[K]	[Pa]	[mm Hg]
4	1.4×10^{-2}	1.1×10^{-4}
10	4.0×10^{-2}	3.0×10^{-4}
15	6.4×10^{-2}	4.8×10^{-4}
20	8.9×10^{-2}	6.7×10^{-4}
30	1.4×10^{-1}	1.1×10^{-3}
50	2.6×10^{-1}	1.9×10^{-3}
77	4.2×10^{-1}	3.1×10^{-3}
100	5.7×10^{-1}	4.2×10^{-3}
150	9.0×10^{-1}	6.8×10^{-3}
200	1.2×10^{0}	9.4×10^{-3}
250	1.6×10^{0}	1.2×10^{-2}
300	2.0×10^{0}	1.5×10^{-2}

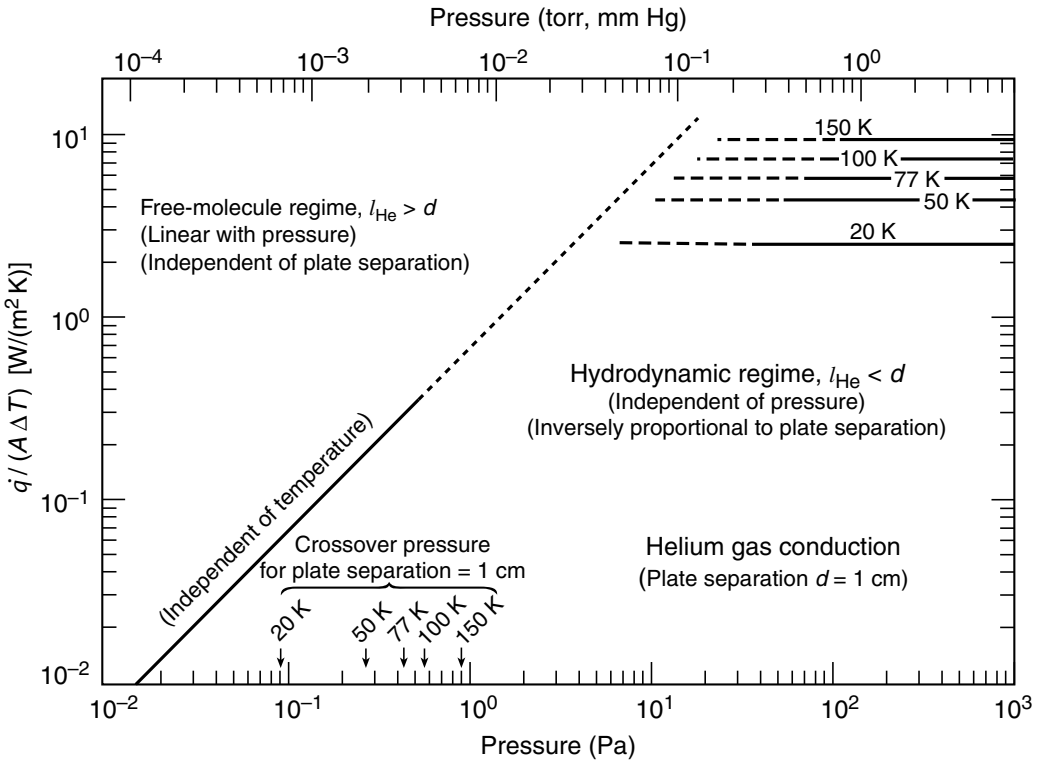

Fig. 2.2 Heat conduction through helium gas between two parallel copper plates spaced 1 cm apart as a function of pressure at various gas temperatures. The heat conduction shows a linear dependence on gas pressure below about 1 Pa and no dependence at higher pressure. The crossover pressure is inversely proportional to the plate separation d [determined by setting $l = d$ in Eq. (2.5)].

Heat conduction through gases behaves very differently in the two pressure regimes. At higher pressures, where the mean free path l of the gas molecules is limited by collisions with other gas molecules, l is inversely proportional to the gas pressure. Then the thermal conductivity λ is *independent of pressure* since $\lambda \propto l\,N$, where N is the number of gas molecules per unit volume (i.e. N is directly proportional to the pressure, making the product of l and N independent of pressure). This is illustrated by the horizontal lines in the hydrodynamic regime on the right side of Fig. 2.2, which shows the heat conduction between two parallel copper plates as a function of the helium gas pressure in the intervening space.

At very low pressures, on the other hand, where the gas molecules travel from the hot wall to the cold wall without colliding with another molecule, the heat conduction is proportional to the number of molecules present. Hence heat conduction varies *linearly with the gas pressure*, as illustrated by the sloped line on the left (low-pressure) side of Fig. 2.2. In this free-molecule regime, varying the gas pressure between hot and cold surfaces in a cryostat provides a convenient heat switch for either thermally coupling or decoupling different parts of the cryostat (e.g. during cool-down).

2.3.1 NORMAL PRESSURE (HYDRODYNAMIC CASE)

The gas heat conduction $\dot{q}_{\text{gas}}$ between two plates of surface area A, separation d, and temperature difference ΔT can be estimated in the hydrodynamic case by a simple one-dimensional heat-transfer relation (similar to that for conduction through solids):

$$\dot{q}_{\text{gas}} = \bar{\lambda} A \Delta T / d, \quad \text{(independent of pressure; } l \ll \text{cryostat dimensions)} \tag{2.6}$$

where $\bar{\lambda}$ is the mean value of the temperature-dependent thermal conductivity of the gas between the two boundary temperatures. Equation (2.6) represents a lower limit on the heat conduction because we have neglected convection currents, which can significantly increase the rate of heat conduction. (Ways to reduce convection include limiting the plate separation to a small gap and filling the space with glass wool, cotton, or paper wipes.)

The thermal conductivity defined by Eq. (2.6) can be used to represent heat conduction through cryogenic *liquids*, as well as cryogenic gases. Figure 2.3 shows the thermal conductivity of both cryogenic gases and liquids as a function of temperature. Note that the thermal conductivity of a liquid is about 3–15 times higher than that of its gaseous phase.

The gas data in Fig. 2.3 show that the magnitude of λ usually increases with temperature, and that gases with a heavier molecular weight have a lower value of λ. In general, the thermal conductivity of a gas is simply proportional to its specific heat:

$$\lambda = \text{c}\, C_V, \quad \text{(independent of pressure for } l \ll d) \tag{2.7}$$

where C_V is the constant-volume specific heat per gram of gas and c is a proportionality constant that has a value between 1.5 and 2.5 for most common cryogenic gases (helium, hydrogen, nitrogen, and oxygen).

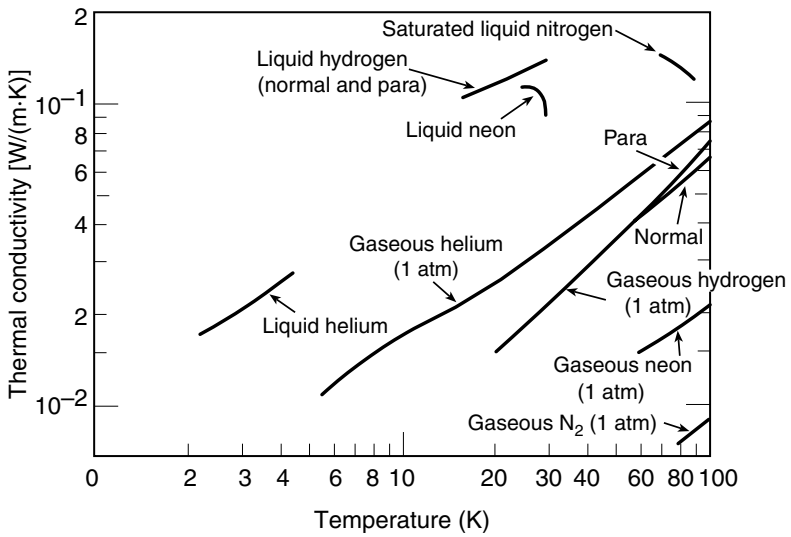

Fig. 2.3 Thermal conductivity of cryogenic *gases* and *liquids* as a function of temperature [gas data are measured at atmospheric pressure (~100 kPa) in the hydrodynamic regime, where λ is essentially independent of pressure]. Data are from Johnson (1960) and Goodall (1970); liquid neon data are from Loechtermann (1963).

2.3.2 LOW PRESSURE (FREE-MOLECULE CASE)

At low gas pressures, on the other hand, the heat conduction between two concentric cylindrical or spherical surfaces with a temperature difference ΔT is independent of the separation between the two surfaces; it is given by Knudsen (1910, 1930) and Kennard (1938).

$$\dot{q}_{\text{gas}} = \text{k}\, a_0\, P\, A_i\, \Delta T, \text{ [watts]} \quad \text{(linear with pressure, } l \gtrsim \text{surface separation)} \tag{2.8}$$

where k is a constant with values 2.1, 4.4, and 1.2 for helium, hydrogen, and air, respectively (White and Meeson 2002), and P is the pressure of the gas in the space between the two surfaces, expressed in pascals and measured with a pressure gauge at room temperature. (For more details on this point, see the discussion in Corruccini 1959 and in White and Meeson 2002.) A_i is the area of the inner cylindrical surface in square meters, and ΔT is expressed in kelvins.

The dimensionless number a_0 in Eq. (2.8) is related to the accommodation coefficients a_1 and a_2 of the inner and outer surfaces by the relation: $a_0 = a_1\, a_2/[a_2 + (A_1/A_2)\,(1 - a_2)\, a_1]$, where A_1 and A_2 are the areas of the inner and outer surfaces, respectively. The accommodation coefficient accounts for a molecule leaving a surface with an energy different from the surface temperature. Perfect accommodation is represented by a coefficient with a maximum value of 1.

Depending on the surface material, surface condition, type of gas, and temperature, accommodation coefficients have been reported ranging from about 0.3 to 1.0 at cryogenic temperatures. (For more information, see the cryogenic-engineering texts recommended at the end of this chapter.) For estimation purposes, however, assuming an accommodation coefficient of $a_1 \approx a_2 \approx 0.5$ is reasonable for most of the gases usually encountered in cryogenic design. The value of a_0 to use in Eq. (2.8) then becomes (after simplifying) $a_0 = 0.5/[1 + (A_1/A_2)\, 0.5]$.

For the other common geometry of *two parallel plates*, we can use Eq. (2.8) with $A_1 = A_2$, which leads to $a_0 = 0.33$.

2.4 **Radiative heat transfer**

In a cryostat, the radiative transfer of heat into the test section can be significant because of the great difference in temperature between various parts of the cryostat. So it is important to place radiation shields (typically made of metal or aluminum-coated Mylar™) between the hot and cold surfaces to intercept the heat flow. Radiative heat transfer strongly depends on the surfaces' *emissivity* ε (related to the *reflectivity* R_f by $\varepsilon \equiv 1 - R_f$). The emissivity can vary from a value near unity for heavily oxidized surfaces, to low values approaching zero for polished metallic surfaces.

The radiative heat flow from a surface is given by the Stefan–Boltzmann equation, $\dot{q}_{\text{rad}} = \sigma \varepsilon A T^4$, where ε is the emissivity of the surface at temperature T, A is the area of the surface, and σ is the Stefan–Boltzmann constant [5.67×10^{-8} W/(m^{2}K^4)]. The net heat exchange between *two* surfaces is given by

$$\dot{q}_{\text{rad}} = \sigma \boldsymbol{E} A (T_2^{\,4} - T_1^{\,4}), \tag{2.9}$$

where $\sigma \equiv 5.67 \times 10^{-8}$ W/(m^{2}K^4), subscripts 1 and 2 refer to the cold and warm surfaces, respectively, A is an area factor depending on the geometry (see Table 2.2), and $\boldsymbol{E}$ is a factor between 0 and 1 (Table 2.2), which involves the emissivities of the two surfaces and depends on whether they are specular (mirror-like) (where $\varepsilon \ll 1$ and $\boldsymbol{E} \ll 1$) or diffuse (where $\varepsilon \approx 1$ and $\boldsymbol{E} \approx 1$). (By diffuse, we mean that the intensity of the heat radiating from the surface is proportional to the cosine of the angle between the direction of emission and the surface normal.)

For spheres and cylinders, the mode of reflection at the outer enclosing surface determines whether to use the specular- or diffuse-reflection formula (the type of reflection at the inner enclosed surface does not matter). For parallel plates, the mode of reflection at both surfaces is irrelevant (as is evident from Table 2.2). In practice, the distinction between specular and diffusive reflection is not great, with $\boldsymbol{E}$(specular)/$\boldsymbol{E}$(diffuse) typically ranging from 0.5–1. (More information is given in Scott 1963.)

Other practical vessel shapes, such as short cylinders with ends, are well approximated by the concentric-sphere formula above by using E for diffuse reflection (with A_1 and A_2 taken as the total areas of the inner and outer surfaces facing the insulating space).

The value of emissivity (or reflectivity) to use in estimating radiative heat transfer is highly variable among different materials, since it depends on their surface condition. This is the weak point in applying Eq. (2.9). As a guide, Appendix A2.2 gives values of the emissivity at room temperature for materials typically used in cryostat construction.

The values tabulated there are appropriate for radiation wavelengths of 10 μm and larger, because this is the range of relevance for cryogenic design. That is, the heat radiating from a surface is distributed over a range of wavelengths, but generally peaks at a wavelength λ_m in micrometers given by

$$\lambda_m T = 2900 \ [\mu\text{m K}], \tag{2.10}$$

where T is the temperature of the material. Thus, for cryostat design, we are concerned mainly with radiation wavelengths in the range of about 10 μm at room temperature to about 700 μm at 4 K.

As seen in Appendix A2.2, the emissivities of highly polished, highly conducting metallic surfaces (such as those of Ag, Cu, Au, and Al) are very low, about 0.01. (That is, they are highly reflecting and excellent materials for radiation shields.) This is because the emissivity scales as the square root of a material's resistivity (from the classical model of Drude 1900)

Table 2.2 **Values of *E* and *A* for use in Eq. (2.9).**

Term in Eq. (2.9)	Parallel Plates	Long Coaxial Cylinders or Concentric Spheres
A	Area of the smaller plate	Area of the enclosed (inner) surface, A_1
$\boldsymbol{E}$ for specular reflection	$\varepsilon_1\varepsilon_2 / (\varepsilon_2 + \varepsilon_1 - \varepsilon_1\varepsilon_2)$	$\varepsilon_1\varepsilon_2 / (\varepsilon_2 + \varepsilon_1 - \varepsilon_1\varepsilon_2)$
$\boldsymbol{E}$ for diffuse reflection	$\varepsilon_1\varepsilon_2 / (\varepsilon_2 + \varepsilon_1 - \varepsilon_1\varepsilon_2)$	$\varepsilon_1\varepsilon_2 / [\varepsilon_2 + (A_1/A_2)(\varepsilon_1 - \varepsilon_1\varepsilon_2)]$

A_1 and A_2 are the areas, facing the insulating space, of the inner and outer surfaces, respectively.

$$\varepsilon \equiv 1 - R_f = 365\,(\rho/\lambda_r)^{0.5}, \tag{2.11}$$

where ρ is the dc electrical resistivity in ohm-meters, and λ_r is the radiation wavelength in micrometers. Thus, at cryogenic temperatures where the resistivity of pure metals becomes quite low, ε will be reduced to values even below the room temperature range of ~0.01– ~0.03 given in Appendix A2.2. More-resistive metals, such as brass, lead, nickel, or stainless steel, typically have room-temperature emissivity values slightly above this, in the range ~0.03– ~0.1, and do not change much at lower temperatures. Most nonmetallic surfaces, such as phenolic or glass, have very high emissivities of about 0.9.

The state of surface finish or polish also has a great effect on the emissivity (reflectivity), as seen in Appendix A2.2. If metallic surfaces are highly oxidized and dull, the emissivity can be increased by more than an order of magnitude with a corresponding loss in reflectivity; values from 0.3–0.6 are typical. Therefore, designs that depend on low ε are at risk from surface degradation, whether it occurs from oxidation, fingerprints, pump oil, or whatever.

From Eq. (2.9), we see that the radiative heat-transfer rate scales as $T_2^4 - T_1^4$ and is therefore strongly dependent on the temperature difference between the two surfaces. Thus, multiple radiation shields that break the temperature gradient into smaller steps significantly lower the radiative heat flow into the cryostat's lower-temperature sections. For example, a copper tube can be placed around the cryostat's sensitive sample region and thermally anchored at an intermediate temperature (usually liquid-nitrogen temperature) to shroud the inner sample chamber from radiation, as shown by the example in Sec. 2.9.3 below. Also, it is common to place several radiation shields, usually stainless steel or copper plates, in the upper part of the main bore of the cryostat to block room-temperature radiation from shining down the access port to the cryogenic sample chamber (shown, for example, in Fig. 1.14).

With N "floating" (not thermally anchored) metallic radiation shields, the radiative heat transfer is reduced by a factor of about $1/(N+1)$ (Scott 1963). The plates are often cooled by cold gas flowing over them from an evaporating cryogenic liquid, which further lowers the radiative heat influx. Helically twisted strips can also be inserted into large-bore tubes to block direct radiation paths without too much effect on gas conductance when pumping.

It helps to use dull or black (absorbing) radiation shields in noncritical parts of the cryostat (such as the neck of the dewar) to absorb scattered light that might otherwise find its way to the heat-sensitive parts. Save the polishing or gold plating (to obtain low emissivity) for the sensitive parts, such as the sample area, to provide extra insurance against radiation absorption at the critical point.

2.4.1 SUPERINSULATION/MULTILAYER INSULATION

In constructing "superinsulated" dewars, typically 30–80 layers of a thin high-reflectivity material, such as aluminized Mylar™, are placed between the hot and cold walls of the dewar's vacuum jacket, so they completely surround and protect the inner parts of the dewar from room-temperature radiation. Multilayer insulation (also known as MLI) is so efficient that it allows liquid-helium dewars to be operated without the radiative protection of a second outer

dewar filled with liquid nitrogen, as used to be common. Multilayer insulation is also very effective for protecting sensitive spaces in a measurement cryostat and is sometimes wrapped around the sample-holder area to provide radiative insulation (an example is given below in Sec. 2.9.2).

The heat transfer through MLI scales inversely with the thickness of the MLI stack, and so the performance of MLI can be represented by a *mean apparent thermal conductivity*, as illustrated for several types of MLI in Fig. 2.4. Figure 2.4 shows that if the vacuum jacket of the dewar is evacuated to below about 10^{-2} Pa, the apparent thermal conductivity of MLI blankets can approach extremely low levels: 10^{-5} W/(m·K) (which is three orders of magnitude off the bottom of the thermal conductivity chart in Fig. 2.1).

Multilayer insulation comes in many forms, but perhaps the shield of choice is commercially made by vapor-depositing a layer of aluminum on one or both sides of thin (5–76 μm) ethylene-glycol-dimethyl-terepthalate film (Mylar™) or polyimide film (Kapton™). Optimal insulation is obtained with an aluminum coating more than about 80 nm thick (Nast 2000). (Gold coating does not provide any improvement and is much more expensive.) These high-reflectivity sheets can be alternated with spacer layers made of silk or Nylon™ net to minimize solid conduction across the stack, or aluminized Mylar™ can be simply crinkled to minimize the points of contact. The more layers used, the lower the radiative heat transfer; but if the MLI is compressed too tightly to fit into a given space, the increase in solid conduction dominates the decrease in radiative heat-transfer rate. For best results, the layer density typically should be about 30 layers/cm. (Further discussion is given, for example, by Timmerhaus and Flynn 1989, and Flynn 1997.)

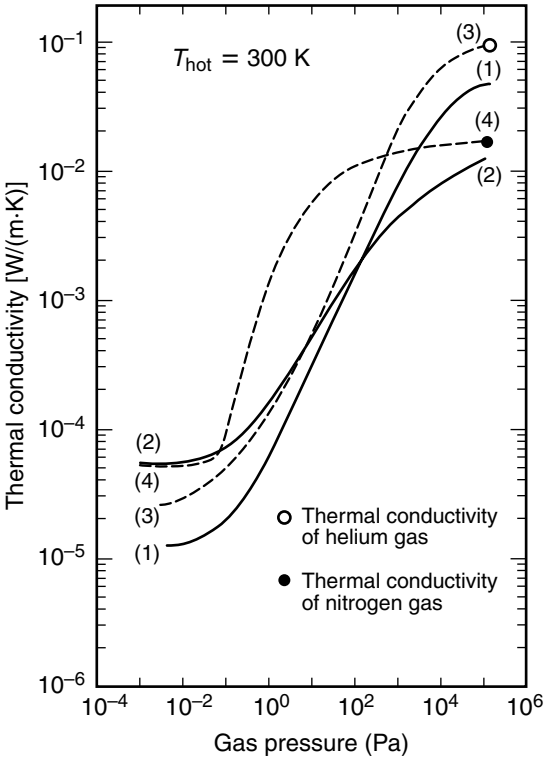

Fig. 2.4 Mean apparent thermal conductivity of various MLI as a function of gas pressure in a vacuum space, with a hot-wall temperature T_{hot} = 300 K. The MLI is composed of aluminized Mylar™ layers separated by various insulating spacer layers: (1) Al foil + fiberglass paper (with residual helium gas in the vacuum space) and a cold-wall temperature T_{cold} = 20 K; (2) Al foil + fiberglass paper (with residual nitrogen gas) T_{cold} = 77 K; (3) double-aluminized Mylar™ + Dexiglas (with helium gas) T_{cold} = 77 K; and (4) crinkled Mylar™ (NRC-2) (with nitrogen gas) T_{cold} = 79 K. (Compiled by Nast 2000 from data in Little 1963, Lockheed 1964, and Boberg 1964.)

Initial evacuation of the MLI-filled vacuum jacket of a superinsulated dewar can take a long time because of gas adsorbed on the great surface area of MLI blankets. Usually the dewar's vacuum jacket is baked out at an elevated temperature for an extended time while pumping, to help remove as much of the adsorbed residual gases as possible. A "getter" material, such as activated charcoal, can also be enclosed in the vacuum jacket to trap residual desorbed gas.

When *cooling* superinsulated dewars for routine use, the insulation may require several hours to reach thermal equilibrium. Consequently, it pays to start precooling superinsulated dewars well in advance of use. Typical procedure is to fill the dewar with liquid nitrogen, leave it overnight, *thoroughly* remove the liquid nitrogen the next morning, and then refill it with liquid helium.

2.5 Heat conduction across *liquid/solid* interfaces

The most efficient way to cool a test sample is just to immerse it in a cryogenic liquid. For high-current measurements, this immersion technique is absolutely crucial for cooling the sample and resistive electrical connections. However, the Achilles heel for liquid cooling is not heat conduction through the liquid, but heat transfer across the *liquid/solid interface* between the liquid and the sample. The problem is that efficient cooling is lost if the liquid loses contact with the sample surface. That is, at a high enough heat flux, *film* boiling commences at the liquid/solid interface, and the (relatively) hot solid surface becomes covered by a film of gas that effectively blankets the sample surface. This typically reduces the heat-transfer rate between the sample and cryogen by about an order of magnitude.

2.5.1 LIQUID-HELIUM / SOLID INTERFACES

Figure 2.5 shows the properties of heat transfer across liquid/solid interfaces for liquid helium at 4.2 K. The heat-transfer characteristic evolves as follows. At low heat flux ($\ll 10^3$ W/m^2) in the *nonboiling* regime, heat transfer is dominated by convection currents in the helium liquid bath. Vertical surfaces have the greatest heat-transfer rate (dashed lines in Fig. 2.5), whereas upward-facing surfaces have greatly reduced heat transfer, and downward-facing surfaces are the worst situation because trapped gas bubbles can insulate the surface.

As the heat flux rises above ~10^3 W/m^2, *nucleate boiling* commences, and the heat-transfer rate increases because many small bubbles form at the surface of the solid and stir up the surface layer of liquid helium as they rise off the surface of the solid. The heat-transfer rate still depends somewhat on the orientation of the surface, but it can be represented reasonably well by the solid lines for three pressures in Fig. 2.5. The heat-transfer rate at atmospheric pressure in the nucleate-boiling regime is given approximately by $\dot{q}/A \cong 6 \times 10^4\ \Delta T^{2.5}$ [(W/m^2)(K$^{-2.5}$)]. To account for variations in the heat-transfer rate that arise from different conditions of surface smoothness and orientation, Schmidt (1981) has suggested a conservatively low value of $\dot{q}/A \gtrsim 1 \times 10^4\ \Delta T^{2.5}$ [(W/m^2)(K$^{-2.5}$)] for use in engineering applications.

Finally, at a *critical heat flux* of about 10^4 W/m^2, *film boiling* begins, and the solid surface becomes insulated with a film of gas. The temperature difference ΔT between the metal surface

and liquid helium jumps abruptly (at constant heat flux) from about 0.5 K (shown by the circle at the upper end of the 1 atm nucleate-boiling curve) to about 10 K or more (depending on the surface geometry) onto the second set of film-boiling curves shown in the high ΔT region of Fig. 2.5. In the reverse situation, when the temperature of the solid surface is reduced from high ΔT values, film boiling persists down to relatively low ΔT (shown by the circles at the lower end of each film-boiling curve in Fig. 2.5). At this point, nucleate boiling begins again, and ΔT drops abruptly (at constant heat flux) back to the nucleate-boiling set of curves.

The main point is that liquid helium provides much better cooling at heat flux rates below about 10^4 W/m^2.

The bottom line summary for liquid-helium/solid interfaces (see Fig. 2.5):

1. At low heat flux ($<10^4$ W/m^2 or $\Delta T \lesssim 0.5$ K) in the nucleate-boiling regime, the average heat-transfer rate for liquid helium at atmospheric pressure (from Fig. 2.5) is about

$$\dot{q}/A = 6 \times 10^4 \, \Delta T^{2.5} \quad [(\mathrm{W/m^2})(\mathrm{K^{-2.5}})]. \tag{2.12}$$

Heat-transfer rate across liquid-helium/solid interfaces at low heat flux

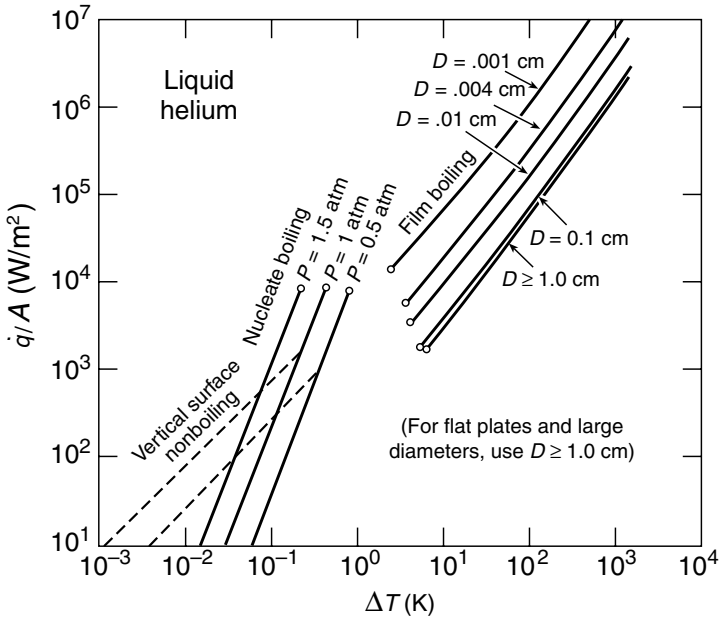

Fig. 2.5 Heat transfer from a metal surface to liquid helium, showing *nonboiling* curves, *nucleate-boiling* curves (for various pressures), and *film-boiling* curves (for various wire diameters D). (Adapted from correlation summaries by Richards et al. 1961 and Brentari et al. 1965 and from data summaries by Touloukian 1948, 1970. The 1 atm and 0.5 atm pressure nonboiling curves for vertical surfaces were determined from data by Karagounis 1956, the nucleate-boiling curves from a correlation by Kutateladze 1952, and the film-boiling curves from a correlation by Breen and Westwater 1962.) The predicted *critical heat flux* is shown by a circle at the top of the nucleate-boiling curves; the points of minimum film boiling at the bottom of the film-boiling curves are from correlations by Zuber and Tribus (1958).

Alternatively, a conservatively low heat-transfer rate can be used for engineering applications to cover nearly all variations in surface texture and orientation (Schmidt 1981):

$$\dot{q}/A \gtrsim 1 \times 10^4 \, \Delta T^{2.5} \quad [(\mathrm{W/m^2})(\mathrm{K}^{-2.5})].$$

Conservative low heat-transfer rate across liquid-helium/solid interfaces

2. The critical heat flux for the transition from nucleate to film boiling is about $\dot{q}/A \gtrsim 10^4$ W/m^2, above which the temperature difference between the solid and liquid jumps by more than an order of magnitude, from about 0.5 K typically to more than 10 K, depending on the diameter of the solid.

2.5.2 LIQUID-NITROGEN / SOLID INTERFACES

For liquid nitrogen, a similar situation occurs, except that the critical heat flux and temperature differences are much higher, as shown in Fig. 2.6. In the *nucleate-boiling* regime at low heat flux, the heat-transfer rate can be represented reasonably well at different pressures by the set of solid lines at $\Delta T \lesssim 10$ K in Fig. 2.6. At 1 atm of pressure, the heat-transfer rate is given approximately by $\dot{q}/A \equiv 5 \times 10^2 \, \Delta T^{2.5}$ $[(\mathrm{W/m^2})(\mathrm{K}^{-2.5})]$, although experimentally, the rate can span an order of magnitude because of variations in material, surface condition, and orientation (Richards et al. 1961; Seader et al. 1965).

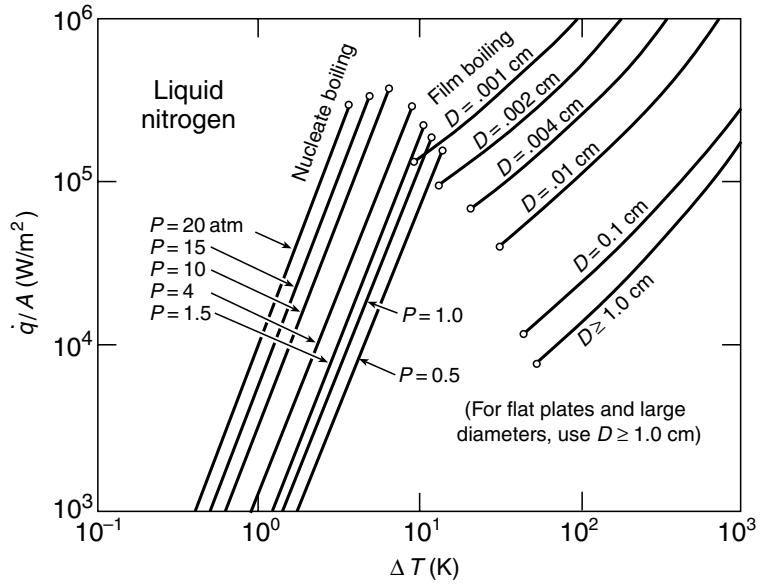

Fig. 2.6 Heat transfer from a metal surface to liquid nitrogen, showing *nucleate-boiling* curves (for various pressures) and *film-boiling* curves (for various wire diameters D). (Adapted from correlation summaries by Richards et al. 1961 and data summaries by Touloukian 1948, 1970; the nucleate-boiling curves are from a correlation by Kutateladze 1952 and the film-boiling curves from a correlation by Breen and Westwater 1962.) The predicted *critical heat flux* is shown by a circle at the top of the nucleate-boiling curves; the points of minimum film boiling at the bottom of the film-boiling curves are from correlations by Lienhard and Wong (1964), and Zuber and Tribus (1958).

At a *critical heat flux* of about $\dot{q}/A \gtrsim 2 \times 10^5$ W/m^2, *film boiling* begins and the solid surface becomes insulated with a film of gas. At this transition, the temperature difference ΔT between the metal surface and liquid nitrogen jumps (at constant heat flux) from about 10 K to hundreds of degrees. (That is why you can stick your finger into liquid nitrogen without freezing it, at least momentarily.) The film-boiling heat-transfer rates that occur above the critical heat flux are shown by the second set of curves in the high ΔT region of Fig. 2.6. In the reverse situation, when the temperature of the solid surface is reduced from high values of ΔT, film boiling persists down to relatively low ΔT (shown by the circles at the lower end of each film-boiling curve in Fig. 2.6), at which point nucleate boiling begins again and ΔT drops abruptly (at constant heat flux) to the nucleate-boiling set of curves.

Again, the main point is that liquid nitrogen provides much better cooling at heat flux rates below about 2×10^5 W/m^2.

The bottom line summary for liquid-nitrogen/solid interfaces (see Fig. 2.6):

1. At low heat flux ($< 2 \times 10^5$ W/m^2 or $\Delta T \lesssim 10$ K) in the nucleate-boiling regime, the average heat-transfer rate for liquid helium at atmospheric pressure is about (from Fig. 2.6)

   $$\dot{q}/A \cong 5 \times 10^2 \, \Delta T^{2.5} \quad [(\mathrm{W/m^2})(\mathrm{K^{-2.5}})]. \tag{2.13}$$

   Heat-transfer rate across liquid nitrogen/solid interfaces at low heat flux

   Experimentally, however, the range of rates is about 10^2–$10^3 \, \Delta T^{2.5}$(W/m^2), depending on surface condition and orientation (Richards et al. 1961).

2. The critical heat flux for the transition from nucleate to film boiling is about $\dot{q}/A \gtrsim 2 \times 10^5$ W/m^2, above which the temperature difference between the solid and liquid jumps by more than an order of magnitude, from about 10 K typically to more than 100 K, depending on the diameter of the solid.

Paradoxically, the cooling effectiveness of liquid nitrogen is both better and worse than that of liquid helium. Liquid nitrogen has an advantage in that the critical heat flux for transition to film boiling is 20 times higher than that for liquid helium (2×10^5 W/m^2 vs. 10^4 W/m^2) and the transition ΔT is about 20 times higher (10 K vs. 0.5 K). On the other hand, if we want to limit heating to a given ΔT between the solid and the liquid coolant, the *heat-transfer rate* of liquid nitrogen is about two orders of magnitude lower than that of liquid helium in the important *nucleate-boiling regime* {$5 \times 10^2 \, \Delta T^{2.5}$ [(W/m^2)(K$^{-2.5}$)] vs. $6 \times 10^4 \, \Delta T^{2.5}$ [(W/m^2)(K$^{-2.5}$)]}. This becomes a factor, for example, in limiting Joule heating at contacts in liquid nitrogen for critical-current measurements (Sec. 8.5.3).

For temperatures *below 1 K*, an extensive compilation of thermal boundary resistivities between liquid ^{3}He or ^{4}He and various solids is given in Lounasmaa (1974). Further information on heat transfer in helium over the entire cryogenic range is given by Van Sciver (1986).

2.6 Heat conduction across *solid/solid* interfaces

The thermal conduction at the boundary between two metal surfaces is surprisingly low at cryogenic temperatures, and it gets worse as the temperature is reduced. The boundary resistance at

such joints is usually the dominant factor limiting heat flux at low temperatures when thermally anchoring sample holders to cooled refrigerator stages, wires to heat sinks, or thermometers to sample-support structures. It is also a major consideration in pressed-contact thermal switches, which are used, for example, in heat-capacity experiments to change the sample temperature quickly and then, after switching, to provide thermal isolation for the heat-capacity measurement.

The heat flow across the interface between two solids, such as copper to copper, cannot be predicted very well from the *electrical* resistance of the interface. The heat flow is often 10^2–10^5 times higher than that predicted for electronic heat conduction from the Wiedemann–Franz–Lorenz law, Eq. (2.4). Presumably this results from strong heat conduction across the interface by crystal-lattice vibrations (phonons).

Figure 2.7 shows a compilation of the thermal conductance across various types of solid/solid interfaces. Solder joints generally have the highest thermal conductance, followed by varnish, grease, and finally pressure joints (depending on the force).

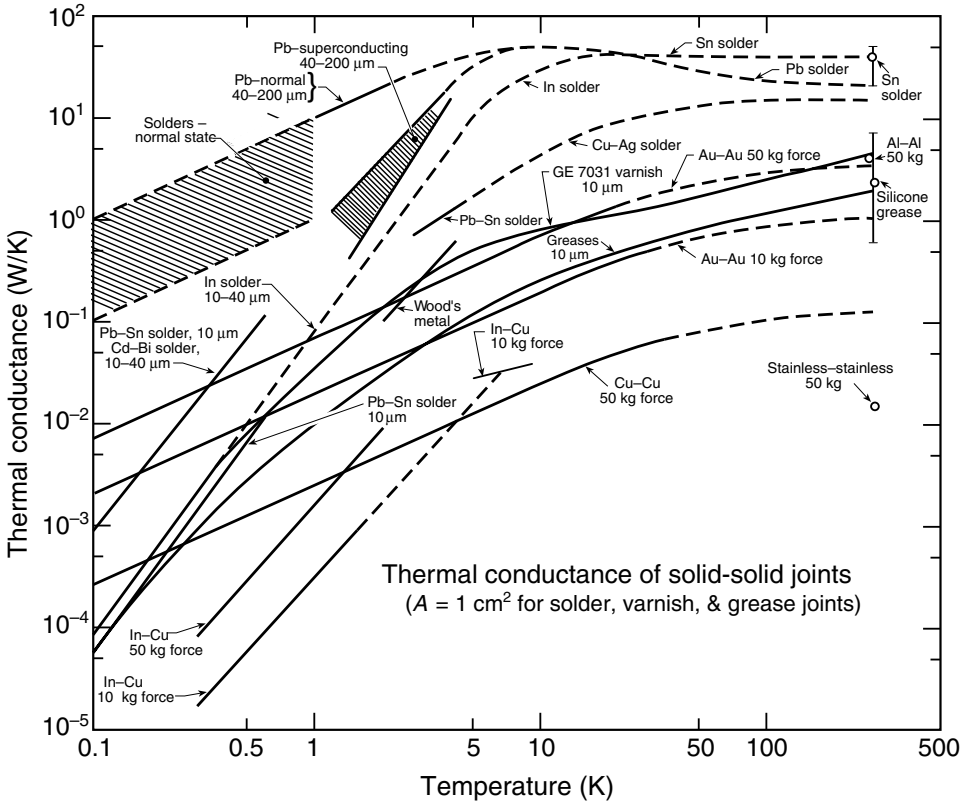

Fig. 2.7 Thermal conductance as a function of temperature for solder, varnish, grease, and pressure joints. *The conductance is per square centimeter of contact area for the solder, varnish, and grease joints.* However, the curves for *pressure* joints give the total conductance of the joint, independent of the contact area, but dependent on the total *force* applied. Dashed lines are estimates of the conductance in temperature regions where no data were available. Approximate thickness of solder, varnish, and grease joints is indicated in micrometers. [Compiled by Radebaugh et al. 1977 from the following references: Solder joints ($T < 1$ K): Anderson and Peterson 1970 and Steyert 1967. Solder joints (1 K $< T <$ 4 K): Challis and Cheeke 1964 and Barnes and Dillinger 1966. Solder joints (room temperature): Yovanovich and Tuarze 1969 and Yovanovich 1970. Grease and varnish joints: Anderson and Peterson 1970, Ashworth et al. 1973, McTaggart and Slack 1969, Sauer et al. 1971a, b. Pressure contacts: Colwell 1969, Berman and Mate 1958, Sauer et al. 1971a, b, and Gmelin 1967.]

2.6.1 SOLDER JOINTS

Solder joints are generally the best thermally conducting interfaces. For very high-thermal-conductivity joints, pure *indium* solder is a good choice. Figure 2.8 shows the thermal conductivity for a Cu/In/Cu joint formed between 99.999% pure copper and ETP copper. A second Be/In/Cu joint was made between beryllium and ETP copper. Both joints show about the same thermal conductivity. They were made by first tinning the two surfaces with generous amounts of 99.99% pure indium. The parts were then pushed and rubbed together as heat was applied to the joint. The joint thickness was on the order of 25 μm. These results for indium-solder joints are somewhat higher than the data shown in Fig. 2.7. The conductance per unit area of contact approached 100 W/(cm^2 K) in the 20 K regime. These data also show that, even though it is difficult to wet beryllium with indium, successful solder joints to beryllium can still be made.

2.6.2 VARNISH AND GLUE JOINTS

Varnish and glue joints are usually the next best techniques (after soldered joints) for high thermal conductance. Common varnishes and glues include IMI 7031 varnish (formerly GE 7031 varnish) or Epibond 121 epoxy. At very low temperatures, even the thermal boundary resistivity between

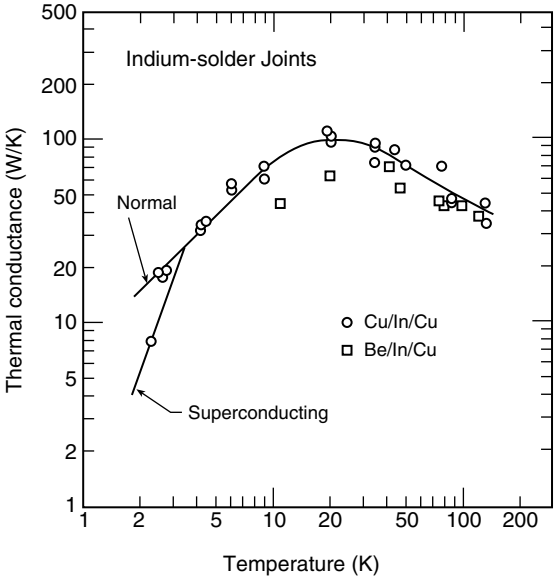

Fig. 2.8 Thermal conductance as a function of temperature for indium-solder joints. *The conductance is per square centimeter of contact area*. The Cu/In/Cu joint was made between 99.999% pure copper and ETP copper; the Be/In/Cu joint was made between beryllium and ETP copper. Thermal conductance across the two types of joints was about the same, even though the base materials being joined had significantly different purity and thermal conductivity. The normal state was produced by applying a magnetic field. (From Radebaugh 1977 and Radebaugh et al. 1977.)

glued Mylar™/metal interfaces becomes important. A compilation of thermal boundary resistivities for Mylar™ glued to several metals (W, Cu, Al, Mg, and Pb) is given by Lounasmaa (1974).

2.6.3 PRESSED CONTACTS AND HEAT SWITCHES

Experimentally, the thermal conductance has been found to *increase approximately linearly with pressure* and, consequently, unlike solder and glued joints, the heat flow across a pressed contact is insensitive to changes in contact area for a given total *force* pressing the two surfaces together. Thus, to make a good thermal connection between two solid surfaces (such as when thermally anchoring copper heat sinks to sample holders), a high force is necessary, usually supplied by bolting the two parts together.

Typical measured values of the thermal conductance across contacts, with 445 N (100 lb) total force applied, are given in Appendix A2.3. The heat flow across such contacts has been observed to increase with temperature in the 1–4 K range as T^y, where $y \approx 1.3$ for Cu/Cu and Au/Au, and $y \approx 3$ for sapphire/sapphire (from Berman and Mate 1958). Combining this temperature dependence with the observation that the conductance varies linearly with force F, we obtain an empirical expression for the heat flow across pressed solid/solid interfaces below 4.2 K:

$$\dot{q}_{\text{pressed solid/solid contact (T)}} = \dot{q}_{\text{pressed solid/solid contact (100 lb, 4.2 K)}} (F / 445\ \text{N})\ (T / 4.2\ \text{K})^y, \qquad (2.14)$$

where y has values between 1.3 and 3, depending on the material. Equation (2.14) can be used with the heat conductance data and y values in Appendix A2.3 to predict $\dot{q}$ over the *liquid-helium* temperature range.

The $\dot{q}$ values in Appendix A2.3 show that gold/gold pressure contacts (with well-polished, well-mated surfaces) have the highest heat conductance, presumably because of the lack of an oxide boundary layer. To achieve good thermal conduction across other metal interfaces, the surfaces are often electroplated with gold. Conversely, to substantially decrease the thermal conductance, such as when fabricating insulating supports, it helps to use a thin layer of manganese dioxide dust at the interface and utilize as many interfaces as possible, such as a stack of thin disks (Mikesell and Scott 1956).

Table 2.3 summarizes the main techniques for improving the thermal conductance across pressure contacts. The amount of pressure applied to the joint determines which is the best technique. Three categories are listed. Low-pressure joints (less than the yield strength of pure indium, <1 MPa) are usually those where no external force is applied or the joints are held together with a single screw. (Bolt-holding strengths are given in Appendix A3.4.) The copper bobbin heat sinks shown in Fig. 1.7, for example, would fall under this category. For such low-pressure joints, the behavior of the conductance across the joint is completely altered by applying thermal *grease* to the joint interface (such as Apiezon N™ grease or Cry-Con™ thermal grease; supplier information listed in Appendix A1.7 under Thermometers and accessories). With grease, the thermal conductance depends on the contact *area* (as we might normally expect for thermal conductivity), instead of the *force* used to press the two solid surfaces together.

Table 2.3 **Techniques for increasing thermal conductance across pressure contacts.**

Type of Pressure Contact	Main Method for Improving Thermal Conductance Across the Joint
Low pressure	Grease applied to the contact interface (such as Apiezon™ N grease)
Moderate pressure ($>$ yield strength of pure indium $\gtrsim$ 1 MPa)	Pure indium foil (0.05–0.1 mm thick) compressed between two bolted parts
High force (see example calculation below)	Gold plating parts before bolting together

When the joint pressure is greater than the yield strength of pure indium, the thermal conductance of the joint can be greatly improved by placing a thin (0.05–0.1 mm thick) piece of pure indium foil between the two parts before bolting them together. Joint pressure needs to be greater than the yield strength of pure indium so that the indium flows. The use of indium foil also converts the nature of pressure joints so that their thermal conductance scales with the contact area (rather than with the applied force).

Finally, for very high pressures (usually requiring multiple bolts and thick, distortion-free pressure plates), gold plating the parts before bolting them together produces excellent thermal conductance across the pressure contact. Such high-pressure, gold-plated joints can produce, for example, a thermal conductance of 70 W/K for Ni/Au contacts at 77 K under 20 kN force (5000 lb). In this case, the thermal conductance scales with the force and not the area, so the metal-to-metal force data in Fig. 2.7 apply.

2.6.4 TO GREASE, OR NOT TO GREASE?

As noted in Table 2.3, thermal conductance across *low*-pressure solid/solid joints can be increased greatly by applying a thermal grease (such as Apiezon N™ grease) to the surfaces. This is especially helpful for thermally anchoring samples, wire heat sinks, thermometers, or their respective holders (but does not apply, of course, to interfaces that need to be mechanically opened and closed at cryogenic temperatures, such as heat switches or cryo-changeable sample holders, because the grease freezes on cooling). However, there is a joint pressure limit beyond which grease does not help, and in fact makes the joint thermal conductivity worse. The crossover pressure between grease or no grease giving the best performance can be determined from the data in Fig. 2.7. The limit depends on the metals being joined, the force available, and the contact area. This is shown in the following example.

Example: A small copper bobbin heat sink at 4.2 K with a 5 mm diameter base (Fig. 1.7) is bolted to a copper base structure with a small 0–80 stainless-steel bolt (M1.6 metric bolt; metric equivalents are given in Appendix A3.4). Should we grease the interface or not?

From Appendix A3.4 we find that the maximum force that can be developed with a factor of two safety margin for an 0–80 (M1.6) stainless-steel bolt screwed into copper is about 50 lb (222 N)

[which we have approximated from the load limit for aluminum, which should be a good assumption for machined, nonannealed copper: (108 lb) (0.5 safety factor) ≈ 50 lb]. Thus, at 4.2 K the heat-flow rate from the bobbin's foot into the copper support structure with no grease is about [from Eq. (2.14) and the Cu/Cu joint data in Appendix A2.3 or Fig. 2.7]

$$(\dot{q}/\Delta T)_{\text{pressed solid/solid contact }(F,\,T)} = (\dot{q}/\Delta T)_{\text{pressed solid/solid contact (100 lb, 4.2 K)}}(\text{F}/100\,\text{lb})$$
$$= (10^{-2}\,\text{W/K})\,(50\,\text{lb}/100\,\text{lb}) = 5 \times 10^{-3}\,\text{W/K}.$$

However, when thermal grease (or varnish) is applied to the 5 mm diameter foot before it is screwed in place, we find from the conductance data for grease in Fig. 2.7 that the heat-flow rate at 4.2 K across the joint is about

$$(\dot{q}/\Delta T)_{\text{grease contact }(A)} = (\dot{q}/\Delta T)_{\text{grease contact (1 cm}^2\text{)}}(A/1\ \text{cm}^2)$$
$$= (10^{-1}\,\text{W/K})\,[\pi(0.25\,\text{cm})^2/(1\,\text{cm}^2)] = 2 \times 10^{-2}\,\text{W/K},$$

which is four times the conductance of that with no grease.

For a larger contact area, the increase in thermal conductance with grease is proportionately greater. The message is clear: Whenever possible, use grease with *low* pressure, or *large-area* thermal contacts to lower the thermal boundary resistance.

However, if *high force* is available and the *contact area is limited*, better thermal conductance is obtained without using grease. This would occur in the above example at loads greater than about 200 lb (91 kg) [which would require at least about a 4–40 (M3) size screw, from Appendix A3.4]. If the parts were *gold plated*, the crossover load would occur at even lower force levels. Appendix A2.3 and Fig. 2.7 show that the thermal conductance of Au/Au pressure joints is about 20 times higher than that of Cu/Cu joints. Thus, the use of gold plating would lower the crossover load in the above example to only about 10 lb (4.5 kg), in which case even a 0–80 (M1.6) stainless-steel screw joint would be better without grease.

2.7 Heat conduction across *solid/gas* interfaces

When sample temperatures need to be controlled outside the range of liquid cryogens, helium or nitrogen exchange gas is often used. Hence data on heat transfer by gas convection are needed to evaluate sample cooling under these conditions.

For the common case of *free*-convective heat transfer, the gas surrounding a solid is heated by the solid, which lowers the gas density and gives rise to buoyant forces that cause the heated gas to rise. This buoyancy effect is the driving force for free convection. The heat-transfer rate $\dot{q}_{\text{conv}}$ between a solid and gas with temperatures that differ by ΔT is given by

$$\dot{q}_{\text{conv}} = h\,\text{A}_{\text{surf}}\,\Delta T, \tag{2.15}$$

where h is the convective heat-transfer coefficient and A_{surf} is the surface area of the solid.

The free-convective heat-transfer coefficient for helium gas near 4.2 K and for nitrogen gas near 77 K is given for horizontal cylindrical solids in Figs 2.9 and 2.10, respectively. Comparing the gas heat-transfer rates with the liquid heat-transfer rates in Figs 2.5 and 2.6, we see that *liquid* cooling is several orders of magnitude more efficient than *gas* cooling for both helium and nitrogen (up to the transition between nucleate and film boiling).

The heat-transfer rate under forced convection can be much greater than that for free convection. Further information on convective cooling in general is given by Kreith and Bohn (2001), or Incropera and DeWitt (2002).

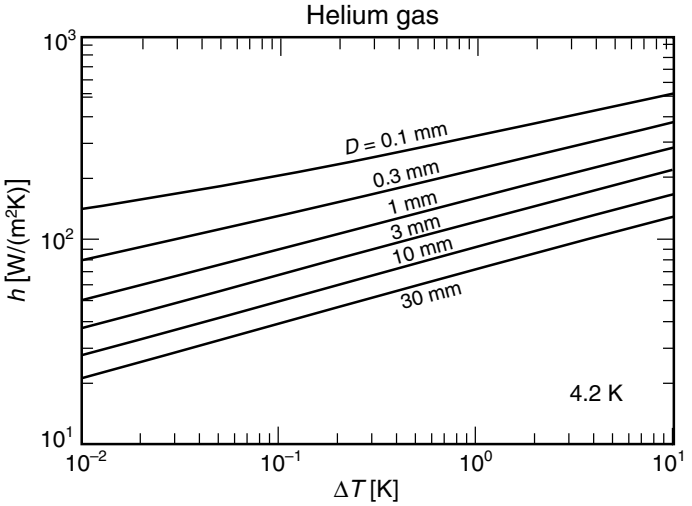

Fig. 2.9 Free-convective heat-transfer coefficient h for heat transfer between helium gas and horizontal cylindrical solids of diameter D at 4.2 K, for use with Eq. (2.15). (Data evaluated by Marquardt 2002 from free-convection correlation data for fluids and gases compiled by McAdams 1954 and reproduced by Kreith and Bohn 2001.)

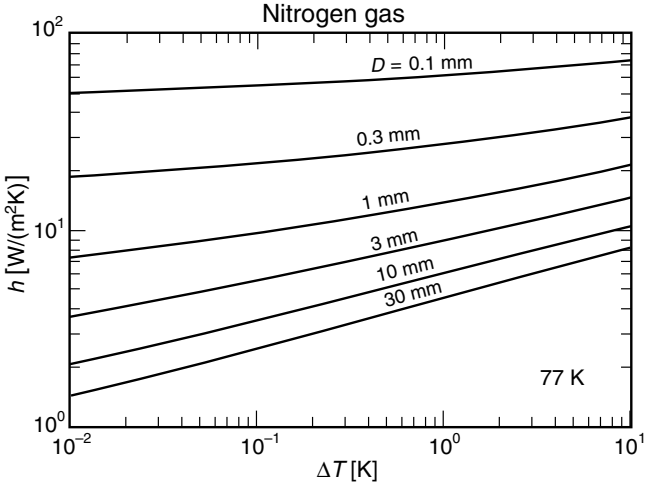

Fig. 2.10 Free-convective heat-transfer coefficient h between nitrogen gas and horizontal cylindrical solids of diameter D at 77 K, for use with Eq. (2.15). (Calculated by Marquardt 2002 from free-convection correlation data for fluids and gases compiled by McAdams 1954 and reproduced by Kreith and Bohn 2001.)

2.8 Other heat sources

Some less obvious, but quite important, sources of heat input can significantly affect the thermal design of measurement rigs. These include Joule heating, thermoacoustic oscillations, superfluid-helium creep, and gas desorption.

2.8.1 JOULE HEATING

Joule heating [the heat generated in a resistance R (ohms) carrying current I (amperes): $\dot{q}$ (watts) $= I^2R$] seems trivial enough, but it is one of the most vexing problems for transport measurements. Joule heating can occur anywhere along the electrical current path—in the cryostat current leads, in the test-sample contacts, and in the sample itself. Unfortunately, unwanted Joule heating sources are often not recognized until after the apparatus has been built and tested.

Joule heating in the *sample and its contacts* can be reduced by designing the cryostat to provide good sample cooling (described in Secs 7.3.1 and 7.4.1) and by making low-resistance sample contacts (described in Chapter 8). When this is not possible, a less satisfactory approach is to use pulsed-current techniques (Sec. 9.2.1), where heating in the sample and contacts is kept low by using a pulsed sample current with a low duty cycle. In small geometries (especially thin films) the pulse length can be very short. It is possible, but difficult, to work with pulses lasting only about 1 μs. However, this often introduces its own set of problems, especially when interpreting ac data for use in dc applications.

Joule heating in the *current leads* can be minimized at the cryostat-design stage by optimizing the choice of the cross-sectional area of the leads. The optimum size is a compromise between making the wire large enough that its resistance and Joule heating is sufficiently low, but not so large that a great amount of heat flows from outside the cryostat through the lead down to the sample. The optimum cross-sectional area for copper conductors is discussed in Sec. 4.9.1, but it always leads to the same minimum heat flux per ampere for design purposes (McFee 1959):

$$\dot{q}_{\min}/I = 84 \text{ mW/A}, \quad \text{(heat flux for a } \textit{pair} \text{ of optimally sized conductors, 290}-4 \text{ K)} \quad (2.16a)$$

$$\dot{q}_{\min}/I = 18 \text{ mW/A}. \quad \text{(heat flux for a } \textit{pair} \text{ of optimally sized conductors, 77}-4 \text{ K)} \quad (2.16b)$$

Equations (2.16a) and (2.16b) show that there is a significant payoff in terms of reduced heat influx at 4 K (where refrigeration is expensive) obtained by heat-sinking the instrumentation leads at 77 K (where refrigeration is much cheaper).

For high-current leads (as opposed to tiny instrumentation leads), other more expensive and voluminous solutions can considerably reduce helium consumption. For the temperature range from room temperature to 4 K, *vapor-cooled leads* (Sec. 4.9.2) are commercially available, which reduce the heat influx by about 40 times compared with that of optimally

sized solid copper wires [Eq. (2.16a)]. *High-T_c superconducting leads* (Sec. 4.9.3) can also be used to give an even greater reduction in heat leak over that of optimized copper wire in the low-temperature range from about 60–4 K.

Joule heating can also come from less obvious sources, such as induced eddy currents that occur when a background magnetic field is changed. It pays to avoid highly conducting current paths in the plane perpendicular to the applied field. For example, the high-conductivity copper shield illustrated in Fig. 1.8 is needed to promote temperature stability in the sample region by reducing gas convection currents and serving as a radiation buffer. However, it can also be the source of significant amounts of eddy current heating in magnetic-field measurements. This transient heating can be reduced by partially slitting the shield, as illustrated in Fig. 1.8.

2.8.2 THERMOACOUSTIC OSCILLATIONS

Unwanted heating can also stem from helium itself. The first effect involves thermally excited pressure oscillations (sometimes called *Taconis* oscillations) in tubes that have a closed end at a high temperature, typically room temperature, and an open end in cold helium gas or liquid helium (Keesom 1942, Taconis et al. 1949). This situation occurs more often than we might at first expect in cryostat construction, because we usually leave the bottom of structural tubes open so liquid nitrogen or helium can drain out. Thermoacoustic oscillations can spontaneously start in these helium-gas-filled cryostat tubes and consume hundreds of milliliters of liquid helium per hour. Typically, they occur in smaller tube diameters, up to about 1 cm diameter, but I have seen them occur in tubes as large as 8 cm in diameter.

So if liquid-helium consumption suddenly becomes higher than expected, it may be Taconis oscillations—listen carefully for a low-pitched tell-tale hum. The oscillations can be interrupted, at least temporarily, by pulling the apparatus out of the liquid. They can be permanently damped by drilling small holes (~2 mm diameter) into the side walls of long structural tubes every 5 cm or so along their length. (However, room-temperature air should not be allowed to enter the support tube of a dipper probe, for example, when it is raised out of a liquid-helium dewar, so some consideration needs to be given to the placement of the holes, preferably restricting them to the lower part of the main support tube.)

➔ These same oscillations are sometimes quite useful: they form the basis for pulse-tube cryocoolers (Sec. 1.4.5) and the simple liquid-helium level detector illustrated in Fig. 2.11. The latter is, perhaps, the most popular, cheap, level detector available. It is made from a small-diameter (~3 mm) stainless-steel tube with a rubber pipette bulb slipped over the top end. The bottom of the tube is bevel-cut to reduce the chance of plugging the end with ice that may be on the dewar bottom. Alligator clips are a convenient way to mark positions along the tube to aid in measuring liquid depth.

The tube is lowered slowly into the liquid-helium dewar until the bottom end is submerged. The rubber pipette bulb will then start to thump and vibrate from the Taconis oscillations set up in the tube. When we slowly raise the tube, the oscillations suddenly increase in frequency at the point where the lower end of the tube emerges from the liquid-helium surface, thus giving a simple indicator of the liquid-helium level in the dewar.

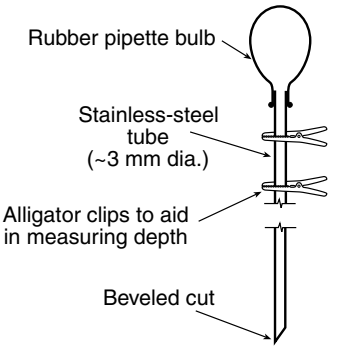

Fig. 2.11 "Thumper" liquid-helium level detector based on thermoacoustic oscillations.

2.8.3 SUPERFLUID-HELIUM CREEP

Another liquid-helium problem occurs in pumping superfluid helium below the lambda point. Superfluid He II will spontaneously climb the walls of its container until it evaporates in the warmer upper region of the dewar (Fig. 1.5). The rate of helium loss through creep is determined by the minimum *perimeter* of the walls covered by the helium film and the smoothness of the walls (since the thickness of the film is constant). For smooth, clean *metal* surfaces, the creep rate is about 2×10^{-7} L/s/cm of perimeter. For *glass* surfaces, the loss rate can vary from three times lower than this (for clean glass surfaces) to three times higher (if adsorbed layers of air are on the glass surface).

This evaporative loss limits the ultimate temperature that can be reached by pumping on a superfluid-helium bath, as described in Sec. 1.2. The efficiency of reaching low temperature with pumped He II can be significantly increased by placing a plate containing a small-diameter ($\lesssim$1 mm) hole just above the liquid helium to limit the creep rate (Ambler and Kurti 1952; White and Meeson 2002). Of course, this constriction also contributes to pumping inefficiency. Where possible, it is best to have a separate superfluid chamber as illustrated earlier in Fig. 1.16.

2.8.4 ADSORPTION AND DESORPTION OF EXCHANGE GAS

The final helium effect we consider is temperature drift associated with gas adsorption on the cold surfaces of cryostat parts. This temperature drift is a concern mainly for measurements that are sensitive to *small* heat loads, such as precision calorimetry below 10 K or adiabatic demagnetization cryostats below 1 K. Small but significant amounts of energy are consumed in gas desorption if a cryostat part is raised in temperature or exposed to a vacuum. For instance, glass cooling from 3–2 K will adsorb about 30×10^{-6} mol/m^2 of gas, which requires an energy of about 300 J/mol or about 10 mJ/m^2 to desorb. Thus, if helium is used as an exchange gas for cooling a calorimeter vessel, the gas desorption that occurs on warming will consume a small, but significant, amount of energy, giving a false value for the heat capacity of the sample.

Another example is exchange gas used to cool an adiabatic demagnetization apparatus. (For a description of this refrigeration technique, see Further reading in Sec. 2.10.1 on refrigeration techniques below 1 K.) The gas desorbed from the warm wall will adsorb on the cold salt pill, giving an apparent "heat leak." In these situations, a solution to the adsorption and desorption problem is not to use exchange gas, but rather mechanical or superconducting heat switches for cooling.

At temperatures below 1 K, other heat sources also become significant, including mechanical vibration, radioactive heating, electromagnetic radiation from neighborhood radio stations, and so on. Again, please refer to the Further reading on the subject given at the end of Chapters 1 and 2.

2.9 **Examples of heat-transfer calculation**

To illustrate how the heat inputs from these various sources come together in a practical way, we estimate the heat budget for a dipper probe under several different modes of operation, shown in Fig. 2.12. The examples are intended to illustrate the basic integration of heat-transfer analysis, which should be useful in the design of a wide range of low-temperature apparatus, not just dipper probes.

2.9.1 CASE 1: SIMPLE DIPPER PROBE IMMERSED IN LIQUID HELIUM

For the first case, shown in Fig. 2.12(a), we consider a sample on the end of a probe immersed directly in liquid helium. This is a very useful measurement cryostat because it can be simply

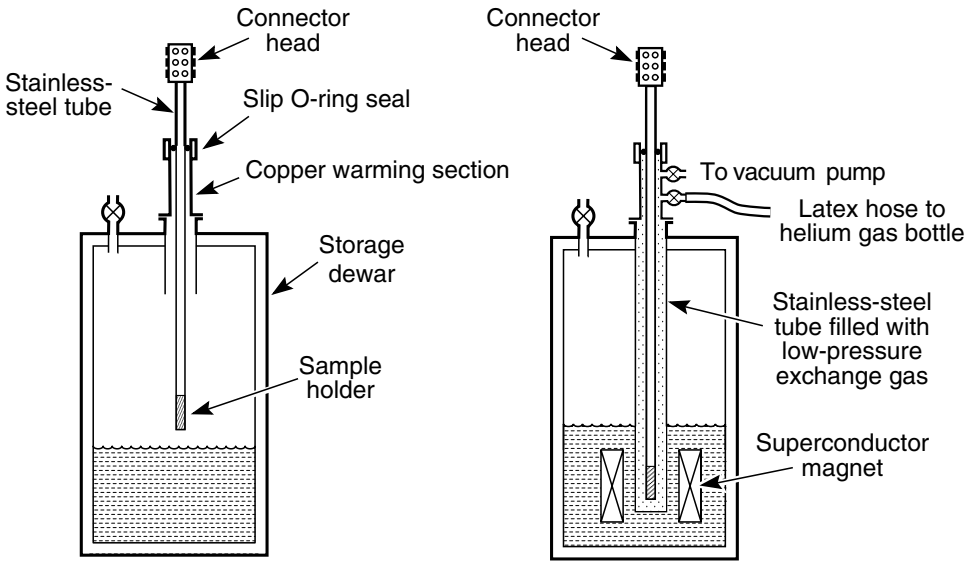

Fig. 2.12 Different modes of operation for a dipper measurement cryostat. (a) Measurements in a cryogenic-liquid shipping dewar; (b) variable-temperature operation in a high-field superconducting magnet.

inserted into a liquid-helium shipping dewar without having to transfer liquid helium into a separate dewar.

Let us assume it is constructed by attaching the sample to a high-thermal-conductivity holder made of ETP copper, which, in turn, is attached to the end of a support tube of low thermal conductivity, such as stainless steel. Further, let us assume that the stainless-steel tube is 2 cm in diameter with a 0.4 mm wall thickness and spans a distance of 1.5 m between the top of the shipping dewar and the surface of the liquid helium. The tube is slipped through an O-ring seal at the top of the dewar. In this way, the sample can be lowered into the liquid helium for testing at 4 K, or raised into the ullage space just above the liquid helium, where variable temperature can be obtained by adjusting the distance between the sample and liquid-helium surface. After testing, we can withdraw the sample into a warming chamber at the top to provide a moisture-free environment for heating it back to room temperature (Fig. 1.9).

The probe is constructed with all the instrumentation leads running down the center of the stainless-steel tube from the connector head at the top of the cryostat. The leads that provide electrical service to the sample (such as voltage taps) consist of 10 pairs of tightly twisted wires, each wire having a diameter of 0.127 mm (#36 American Wire Gauge AWG, or about 0.125 mm diameter; closest metric wire sizes are given in Appendix A4.1b). Also, we assume that there are two additional quad cables (eight wires total) of phosphor-bronze wire (#36 AWG or ~0.125 mm diameter) for the thermometers, and, finally, a separate pair of larger copper leads whose size is optimized for the sample transport current (which, we assume, will not exceed 500 mA).

We want to know the total liquid-helium consumption from:

(1) heat conduction from room temperature down the stainless-steel support tube to the immersed sample holder;

(2) heat conduction through the instrumentation leads;

(3) heat input from the pair of transport current leads.

In addition, we want to know:

(4) the heat input from radiation, and whether radiation shields are needed.

1. We evaluate the heat conduction down the stainless-steel tube from Eq. (2.3) by using the thermal conductivity integral $\int \lambda(T)\, dT$ from Appendix A2.1, which is 3.06 kW/m for stainless steel between 300 K and 4 K. We find

$$\dot{q}_{ss} = (A/L)\int_{4\,K}^{300\,K} \lambda(T)\, dT$$

$$= \pi(0.02\ \text{m})(0.0004\ \text{m})(1.5\ \text{m})^{-1}(3.06\ \text{kW/m})$$

$$= 51\ \text{mW}.$$

Actually, convective cooling of the stainless-steel tube by boil-off gas will slightly lower the amount of heat input through the stainless-steel tube.

2. The sensitive instrumentation leads are made of copper to minimize the interference of thermoelectric voltages with the small dc voltages being sensed by these wires. We find from

Appendix A2.1 a value of 162 kW/m for the thermal conductivity integral from 4–300 K for ETP copper, which is the type of copper commonly used in wire manufacture. There are 10 pairs of instrumentation leads sized at #36 AWG (~0.125 mm), which is about the smallest wire size that can be conveniently handled [about the size of a human hair, which is actually about #40 AWG (~0.080 mm)].

Phosphor-bronze wire was chosen for the eight thermometer leads because thermoelectric voltages are not as much of a concern at the voltage levels needed for thermometry. Because the operating current for the temperature sensors is modest, on the order of a few milliamperes, a #36 AWG (~0.125 mm) phosphor-bronze wire will suffice (optimally sized *copper* leads would be too small to handle; see the last two columns of the table in Appendix A4.1a). Since the heat leak through phosphor-bronze leads is expected to be small, we need only an approximate value, and for that Constantan will do—namely 5.16 kW/m from Appendix A2.1. The cross-sectional area of a #36 AWG (~0.125 mm) wire is 0.0127 mm^2 (from Appendix A4.1a), and taking the length of the leads spanning the temperature gradient to be 1.5 m, we calculate from Eq. (2.3):

$$\text{20 copper leads:} \quad \int_{4\,\mathrm{K}}^{300\,\mathrm{K}} \lambda \, dT = 162\ \mathrm{kW/m} \quad \text{and} \quad \dot{q}_{\mathrm{Cu\ wire}} = 27.4\ \mathrm{mW}$$

$$\text{8 phosphor-bronze leads:} \quad \int_{4\,\mathrm{K}}^{300\,\mathrm{K}} \lambda \, dT = 5.16\ \mathrm{kW/m} \quad \text{and} \quad \dot{q}_{\mathrm{Ph.Br.\ wire}} = 0.35\ \mathrm{mW}.$$

3. Joule heating in the *instrumentation* leads can be ignored because the service current is typically only about a milliampere. For the pair of larger *transport-current* leads, however, it is well worth optimizing their size to handle the 500 mA transport current [which, as described in Sec. 4.9.1, gives an optimum cross-sectional area of 1.5×10^{-7} m^2, or approximately a #25 AWG (~0.450 mm) wire; alternatively, this can be determined from Appendix A4.1a by scaling down the optimum current levels tabulated there for 1 m long copper wires by the longer length of our leads (1.5 m)]. For the pair of leads, we have from Eq. (2.16a) a total heat input of

$$\dot{q}_{\mathrm{current\ leads}} = 84\ \mathrm{mW/A} \times 0.5\ \mathrm{A} = 42\ \mathrm{mW}.$$

These leads could be sized somewhat smaller, depending on the percentage of time the leads are carrying transport current, since the conductive heat leak occurs all the time, whereas the Joule heating may occur over a smaller duty cycle. Sections 4.9.2 and 4.9.3 have more information on leads for significantly higher current. The results would simply be added to the heat budget of any such cryostat.

Thus, to summarize the first three sources of heat input, the greatest conductive heat influx will occur through the copper instrumentation leads, the current leads, and the stainless-steel support tube. In comparison, a negligible amount enters through the

phosphor-bronze thermometer leads. Adding the heat input from these sources, we find that the total conducted heat for this simple dipper probe will be about 0.12 W. Since the rate of liquid-helium consumption (Appendix A1.6a) is about

1.4 L/(Wh),	Consumption of liquid *helium* at atmospheric pressure	(2.17)

we find that the helium boil-off rate will be about 0.17 L/h, which is perfectly acceptable for a dipper probe.

A similar heat budget could be calculated at liquid-nitrogen temperature, where the boil-off rate would be even less, since the thermal gradient from room temperature is smaller, and the rate of liquid-nitrogen consumption from Appendix A1.6a is about

0.022 L/(Wh).	Consumption of liquid *nitrogen* at atmospheric pressure	(2.18)

The cost of liquid helium is about equal to that of table wine. Liquid nitrogen is much less expensive, cheaper than milk.

4. In addition, we consider the heat influx from radiation. For the present example of a sample holder immersed directly in liquid helium, radiant heat will be intercepted by the liquid bath, and so the sample is protected; that is, radiant heat will not significantly warm the sample holder and affect the measurement. However, the radiation influx from the dewar's room-temperature top plate will contribute to liquid-helium loss.

In the *worst* case, we can estimate this loss by assuming that the inner walls of the dewar are perfectly reflecting and funnel all radiation leaving the warm top plate to a perfectly absorbing liquid-helium bath [$\boldsymbol{E} = 1$ in Eq. (2.9)]. If the diameter of the top plate and dewar is 30 cm, for example, we find from Eq. (2.9) that the heat influx would be

$$\begin{aligned}\dot{q}_{\text{rad max}} &= \sigma \boldsymbol{E} A(T_2^4 - T_1^4) \\ &= [5.67 \times 10^{-8}\,\text{W/(m}^2\,\text{K}^4)]\pi(0.15\,\text{m})^2 \times [(293\,\text{K})^4 - (4.2\,\text{K})^4] = 29\,\text{W},\end{aligned}$$

which is far too high.

In the *best* case, all the heat radiating down from the top plate that strikes the dewar wall is absorbed, and only the radiation subtended by the solid angle of the liquid-helium surface actually reaches it:

$$\dot{q}_{\text{rad min}} \cong (29\,\text{W})[\pi(10.5\,\text{m})^2]/[2\pi(1.5\,\text{m})^2] = 0.15\,\text{W},$$

which is still quite high. So either way, the radiative heat input needs to be intercepted by *radiation shields*.

For example, a radiation shield thermally anchored to liquid nitrogen at 77 K will reduce the heat input to the liquid helium by a factor of about $(77/293)^4 \cong 0.0048$, resulting in an acceptable radiative heat load. Radiation baffles cooled to temperatures lower than 77 K by evaporating helium gas can further reduce the radiation input.

Perhaps the most common technique is to use multiple radiation shields in the neck of the dewar, as illustrated in Fig. 1.14. The number of "floating" metallic radiation shields N (not thermally anchored) will reduce the radiative heat transfer by a factor of about $1/(N+1)$ (Sec. 2.4). (More information can be found in Scott 1963 or Incropera and DeWitt 2002.) In practice, the reduction is less than this factor because of necessary openings in the shields for wiring, helium transfer tubes, and so on.

Thus, for large-diameter dewars, radiation shields are essential. For smaller-diameter dewars, or storage dewars with a small neck and top plate, the heat input is reduced by the area of the top plate, and the radiation heat input usually can be managed without radiation baffles. If a storage dewar has a wide neck (which can be a convenience for some larger dipper probes), the increased neck size will result in a continuous heat load, whether in use or not. The loss can be reduced by inserting a baffled arrangement of some sort into the neck when the dipper probe is not in use.

For superconductor critical-current measurements (where the transport current density through the sample is typically more than 10^5 A/cm^2), we would also be concerned about Joule heating at the sample current *contacts*. To obtain accurate data, we would normally limit the rise in sample temperature from this source of heat to less than about 100 mK. [Such a temperature rise corresponds, for example, to a decrease of about 2% in the critical current of Nb–Ti at liquid-helium temperature (4.2 K) and 0 T (or about a 5% decrease at 7 T).] Joule-heating calculations for contacts are treated in Sec. 8.5 for the cases of Nb–Ti and Nb_3Sn cooled by liquid helium, as well as for high-T_c superconductors cooled by liquid nitrogen. There, we find that the requirement of keeping the sample temperature rise to less than 100 mK in liquid helium results in a Joule heat production of about 10 mW, which does not significantly alter the heat budget calculated above in steps 1 to 3. (The requirements on contact *area* to keep the sample temperature within 100 mK of the liquid-helium bath can be quite stringent, however, as described in Sec. 8.5.)

2.9.2 CASE 2: DIPPER PROBE OPERATED IN VARIABLE-TEMPERATURE MODE IN A SUPERCONDUCTING MAGNET

Now suppose we want to use our same dipper probe to make high magnetic-field measurements at *variable* temperature from 20–100 K. We assume the ETP copper sample holder has a 2 cm^2 cross-sectional area for thermal conduction along its length, and that it is equipped with a resistance heater and thermometer 1 cm away from the sample. We further assume that all instrumentation leads are well thermally anchored to the sample holder before the leads are attached to the sample (Sec. 4.4). What is a simple way to vary the temperature?

The dipper-probe location is fixed in the middle of the magnet, so adjusting the height of the sample holder above the helium bath is not an option. Another effective way of varying the temperature is to insert the apparatus into a single-walled stainless-steel tube containing helium exchange gas, as shown in Fig. 2.12(b). The pressure of the gas surrounding the sample holder can be changed to vary the thermal coupling of the sample holder to the liquid bath. When the coupling is set in the right range, the temperature of the sample can be controlled by using only a moderate amount of power delivered to the sample-holder heater. This single-walled design has the added advantage that it avoids the use of a *double*-walled vacuum-jacketed insert dewar, which would consume much of the valuable space within the bore of a superconducting magnet.

We assume for this example that there is a 3 mm space between the tube wall and the copper sample holder, and that the holder has a surface area of 100 cm^2. We want to know:

(1) The cooling power of the helium exchange gas at *atmospheric* pressure. (This is a preliminary calculation to see if the cooling power falls in an acceptable range; otherwise, we will calculate the next step.)

(2) The desired exchange-gas pressure to achieve the right cooling power. The cooling rate must be slightly greater than the heat input of ~0.1 W expected for the dipper rig (which we calculated in Case 1).

(3) The radiative heat flow between the 100 cm^2 surface area of the copper base structure and the surrounding 4 K wall of the stainless-steel tube.

(4) The maximum expected temperature difference between the thermometer and sample, resulting from heat flow along the sample holder.

1. At atmospheric pressure (10^5 Pa), the helium gas conduction shown in Fig. 2.2 is clearly in the hydrodynamic regime and, therefore, independent of pressure. We assume the gas temperature is intermediate between the temperature of the sample holder and liquid bath. Thus, when the sample holder is at 20 K (the minimum cooling situation), we find from Fig. 2.3 that, for helium gas at an intermediate temperature of about 12 K, the mean thermal conductivity $\bar{\lambda}$ is about 0.018 W/(m·K). We assume convection currents have been suppressed (by a small convection gap or the use of filling material in the gap). Then from Eq. (2.6) we find the gas-cooling rate across a gap d is

$$\begin{aligned}\dot{q}_{gas\ 20\,K-4\,K} &= \bar{\lambda}\, A\, \Delta T/d \\ &= [0.018\ \mathrm{W/(m\cdot K)}]\ (0.01\ \mathrm{m^2})\ (16\ \mathrm{K})/(0.003\ \mathrm{m}) \\ &\cong 1\ \mathrm{W},\end{aligned}$$

whereas for a sample temperature of 100 K, and a mean $\bar{\lambda}$ of about 0.05 W/(m·K), the gas-cooling rate will rise to about

$$\dot{q}_{\mathrm{gas\ 100\,K-4\,K}} = [0.05\ \mathrm{W/(m\cdot K)}](0.01\ \mathrm{m^2})\ (96\ \mathrm{K})/(0.003\ \mathrm{m}) \cong 16\ \mathrm{W}.$$

For either temperature, this is an excessive gas-cooling rate, and the resistance-heater power required to maintain the sample-holder temperature will generate a high heat flow into the helium bath, which will consume too much liquid helium and probably also result in unacceptably high temperature gradients along the copper sample holder. So it would definitely pay to lower the cooling rate by reducing the helium exchange-gas pressure.

2. Next, we look at what level of exchange-gas pressure would reduce the cooling rate to about 0.2 W. This exchange-gas cooling power is chosen because it is only moderately above the previously calculated ~0.1 W total expected heat influx to the cold end of the cryostat. At this cooling rate, only a modest amount of power must be delivered to the sample-holder resistance heater to achieve and control the sample temperature. That is, 0.2 W (gas-cooling power) − 0.1 W (conductive heat influx down the probe) ≅ 0.1 W of resistance-heater power is needed to stabilize the sample temperature. (In practice, it does not pay to make the cooling power margin any smaller than 0.1 W because the gas cooling power must be kept high enough to overcome eddy current heating during magnet ramping or contact Joule heating during the measurements. On the other hand, raising the cooling margin above 0.1 W requires more make-up power delivered to the resistance heater on the sample holder, which can generate a significant temperature gradient between the thermometer and sample. Thus, the chosen exchange-gas cooling power 0.2 W represents a compromise between these two requirements.)

To determine the target pressure needed to reduce the cooling to ~0.2 W, we start by using the free-molecule relation Eq. (2.8) (for the low-pressure regime in Fig. 2.2),

$$\dot{q}_{\text{gas}} \cong 2.1\, a_0 P A_i \Delta T.$$

For the accommodation coefficient, we use an approximate value of $a_1 = a_2 = 0.5$ and assume the parallel-plate approximation (since the gap is small compared with the radii of the sample-support rod and the exchange-gas tube), for which case $a_0 = 0.33$ [see discussion following Eq. (2.8)]. Thus, to achieve a $\dot{q}_{\text{gas}}$ of 0.2 W, we find by rearranging Eq. (2.8) that we need an exchange-gas pressure

$$P = (0.2\ \text{W})[(2.1)(0.33)(0.01\ \text{m}^2)(16\ \text{K})]^{-1} = 1.8\ \text{Pa}$$

at 20 K, and about 0.3 Pa at 100 K.

However, we assumed that the pressure is in the free-molecular region, which is not reached until the molecular mean free path is reduced below 3 mm (the spacing between the walls). For the 20 K case, at an intermediate gas temperature of 12 K, we find from Eq. (2.5) that the transition to the free-molecular regime does not occur until the pressure is reduced to about

$$P < 2.87 \times 10^{-3}\, T^{n+1}/L = (2.87 \times 10^{-3})(12^{1.147})/(0.3\ \text{cm}) = 0.17\ \text{Pa}.$$

So to lower the exchange-gas coupling, the pressure will have to be reduced at least to this level. In practice, the optimum level is achieved by trial and error, but Eq. (2.5) shows that a level below about 0.1 Pa gives an initial target to shoot for in lowering the thermal coupling of the exchange gas.

A convenient way to obtain an exchange-gas pressure in this target range is first to evacuate the probe (at room temperature) and then to incrementally introduce a small quantity of helium gas until the right pressure is reached. Small quantities of gas are easily measured out by pinching the helium-gas hose shut close to the valve at the head of the probe and then opening the valve to introduce the gas [see "Latex hose" in Fig. 2.12(b)]. A rule of thumb that indicates whether the exchange-gas pressure is about "right" is that the time required to precool small probes such as this to 77 K (by immersion in liquid nitrogen) should be about 20–30 min.

➔ A similar exchange-gas technique can also accelerate the cooling of a sample chamber isolated by a vacuum jacket (which otherwise would take many hours to cool). In the vacuum space, include adsorbent charcoal (a "getter" material), contained in a small porous container (say, about 1 cm diameter by about 3 cm long) equipped with a heater and thermometer. To rapidly cool the sample chamber, the gas is desorbed from the charcoal by heating the container, poisoning the vacuum isolation, and providing good thermal coupling to the surrounding cryogenic bath. To restore vacuum for thermal isolation, the heater is simply switched off, and the charcoal readsorbs the residual gas from the vacuum space.

3. The *radiant* heat flow from the copper sample holder to the 4 K stainless-steel tube wall can be estimated from Eq. (2.9) by using approximately equal areas for the inner and outer cylinders. We use emissivity values from Appendix A2.2: $\varepsilon_1 = 0.02$ for a polished copper sample holder; $\varepsilon_2 = 0.07$ for the stainless-steel tube wall. So, when the copper sample holder (which has a 100 cm^2 surface area) is at 25 K, we estimate that the radiant heat flow will be

$$\begin{aligned}\dot{q}_{\text{rad}} &= \sigma A\,(T_2^{\,4} - T_1^{\,4})\,\boldsymbol{E} = \sigma A\,(T_2^{\,4} - T_1^{\,4})\,\varepsilon_1\varepsilon_2/(\varepsilon_1+\varepsilon_2-\varepsilon_1\varepsilon_2)\\ &= [5.67\times 10^{-8}(\text{W/m}^2\,\text{K}^4)](0.01\ \text{m}^2)[(25\ \text{K})^4-(4.2\ \text{K})^4](0.016)\\ &= 0.0035\ \text{mW},\end{aligned}$$

and, similarly, at 100 K

$$\dot{q}_{\text{rad}} = 0.9\ \text{mW}.$$

This level of radiant heat cooling of the sample holder is not a problem.

However, for highly oxidized copper ($\varepsilon_1 = 0.6$ from Appendix A2.2, corresponding to $\boldsymbol{E} = 0.07$), the radiant heat transfer to the stainless-steel surface would rise to about 4 mW at 100 K. [If the copper is neither polished nor highly oxidized, an intermediate value should be used because the lowest emissivity dominates $\boldsymbol{E}$ in Eq. (2.9).] If the variable temperature measurements were extended to higher temperatures, the radiant heat input would become significant for highly oxidized copper, amounting to about 300 mW for sample temperatures approaching room temperature. In the latter case, some radiation shielding between the sample holder and helium-cooled tube wall would be essential.

In any case, radiation shielding is desirable to minimize nonuniform cooling of the sample-holder assembly from radiation, as well as to break up convection currents in the exchange-gas gap. Shielding is easily provided by wrapping at least five layers of half-aluminized Mylar™ around the copper sample holder in the exchange-gas space (see Sec. 2.4.1 for more information on MLI insulation).

4. Finally, we check on the maximum expected temperature difference between the thermometer and sample, assuming both are well thermally anchored to the sample holder. (The situation where only the sample *ends* are thermally anchored to the holder is described in Sec. 7.3.1, where we calculate the limits on sample length required to maintain temperature uniformity along the sample.)

We assume a generous heat flow of 0.1 W along the 2 cm^2 cross-sectional area copper base structure. This flow might arise from heat introduced by the heater, as well as from heat-sinking the current leads and instrumentation wires. This underscores the importance of not placing the heat sinks for the leads in such a place where their heat will flow between the sample and thermometer locations along the copper base structure. It is best to put the sample plus thermometer in a thermal "dead end" [as described in Sec. 5.3.3 (Fig. 5.13)] and to keep the thermometer and sample close to each other.

In the present example, the separation was assumed to be 1 cm. Using 400 W/(m·K) as a lower limit for the thermal conductivity of ETP copper at all temperatures above ~7 K (from Fig. 2.1), we find from Eq. (2.2) that the temperature difference ΔT between the sample and thermometer would be less than

$$\Delta T_{\text{sample thermometer}} = \dot{q}_{\text{cond}}\, L/(\bar{\lambda}\, A)$$
$$\leq (0.1\ \text{W})(0.01\ \text{m})/\{[400\ \text{W/(m}\cdot\text{K)}](0.0002\ \text{m}^2)\} = 13\ \text{mK}.$$

We have assumed good thermal contact of both the sample and thermometer to the copper holder, which can be ensured by using thermal grease (as described above and in Secs 5.3.1 and 5.3.2 on thermally anchoring thermometers and samples). This result (13 mK) is not insignificant, and it illustrates the importance of using high-thermal-conductivity copper for the sample holder, rather than brass, for example, which has a thermal conductivity about a hundred times less than that of ETP copper. With a brass sample holder, the temperature difference between the sample and thermometer in this instance would be more than 1 K at low temperatures.

As a footnote to Case 2, another technique to provide cooling to the sample holder for a probe slipped inside a submerged single-wall tube is to use beryllium–copper finger stock. The finger stock is attached to the probe above the sample holder and scrapes along the inside of the stainless-steel tube into which it is slipped, thus providing a low-thermal-conductivity conduction path between the sample holder and cryogenic bath. The space inside the stainless-steel single-wall tube is completely evacuated. The right amount of cooling power is a trial-and-error process (obtained by adjusting the size and spring tension of the fingers), but once established, this provides a simple and reproducible method of thermally connecting the

probe to the bath for variable-temperature operation over a specific temperature range (by using a resistive heater attached to the sample holder). Radiation shielding is still needed to provide an isothermal sample space, especially when the temperature difference between the probe and bath becomes high, as calculated in Step 3.

2.9.3 CASE 3: VARIABLE-TEMPERATURE SAMPLE CHAMBER

With variable-temperature operation, temperature uniformity along the sample length can be improved by placing the sample in its own separate isothermal chamber, as illustrated schematically in Fig. 2.13. In this way, the sample can be completely surrounded with radiation shields in a static gas or vacuum environment. A separate sample chamber is particularly helpful for low-thermal-conductivity samples that cannot be thermally attached along their length to a highly conducting sample holder.

In this case, the addition of helium exchange gas to the isothermal chamber will help promote temperature uniformity along the sample length. However, the cooling power of the exchange gas is relatively small compared with that provided by direct immersion in liquid

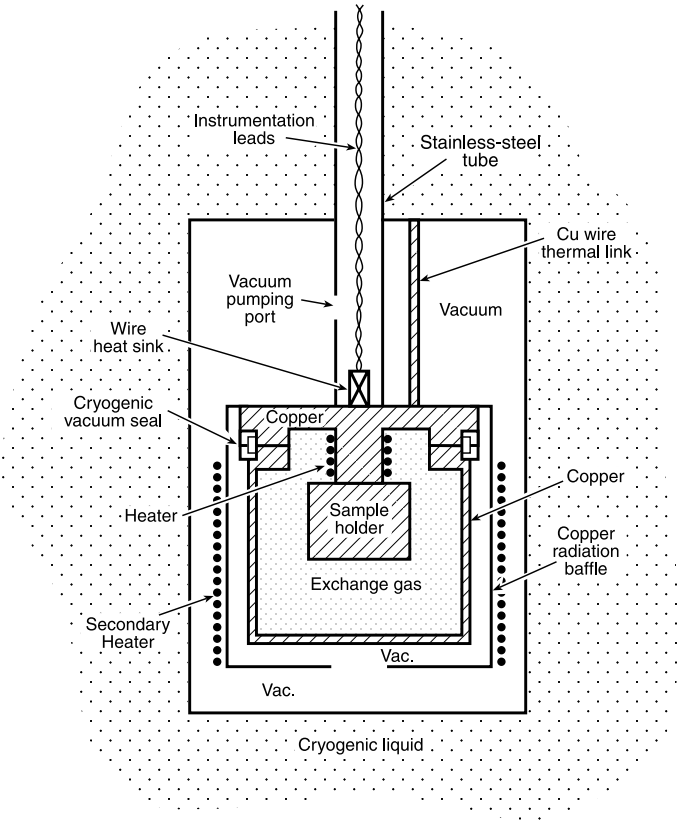

Fig. 2.13. Schematic diagram of vacuum-jacketed variable-temperature sample chamber.

cryogens (Sec. 2.7). Nevertheless, exchange gas can be effective in promoting temperature uniformity for such low-thermal-conductivity samples, if Joule heating and the heat input from external sources are kept low.

The same heat analysis described for Cases 1 and 2 applies to designing this type of apparatus, although the main thermal link is via the current leads and the stainless-steel tube connecting the sample chamber to the helium bath (see Fig. 2.13). The conductive heat flow is calculated from Eq. (2.3), just as above. If a stronger thermal link than stainless steel is needed between the sample chamber and cryogen bath, the support tube can be made of brass or copper. Better yet, a separate copper wire or brass link can be added to provide a parallel connection to the surrounding bath, as illustrated by the extra copper-wire thermal link in Fig. 2.13. With this approach, the cross-sectional area of the wire can be varied to adjust the heat-transfer rate without having to remake the structural connection supporting the sample chamber.

Thermal radiation down the support tube is determined as for Case 1 (item 4), and contact heating is calculated as in Sec. 8.5. To help promote temperature uniformity and minimize temperature gradients in the sample, a secondary heater can also be wound onto the radiation baffle to raise the temperature of the radiation shield to maintain low power in the main sample-holder heater.

Make sure the instrumentation wires are brought to sample temperature before attaching them to the sample. This is best done by thermally anchoring them first to the copper housing of the sample chamber with the wire heat sink schematically shown in Fig. 2.13. Then thermally attach the wires to the sample holder and, finally, to the sample.

A practical consideration in using such a variable-temperature sample chamber is making the cryogenic vacuum seal shown in Fig. 2.13, which needs to be done after the sample is mounted in the sample chamber. This is not much of a problem if the sample can withstand soft-solder or bismuth-alloy temperatures (about 60–200°C; see Appendix A3.7), but becomes more of a challenge for heat-sensitive samples. In that case, practical vacuum seals using indium O-rings can be useful, as described in Sec. 3.7.4.

2.10 References

2.10.1 FURTHER READING

GENERAL TEXTBOOKS ON HEAT-TRANSFER AND CRYOGENIC-ENGINEERING:

General discussion of heat transfer with practical examples:

White, G. K., and Meeson, P. J. (2002). *Experimental Techniques in Low-Temperature Physics*, 4th edition, Oxford University Press, Oxford, UK.

Edited series of articles on cryogenic engineering and heat transfer:

Weisend, J. G. II, ed. (1988). *Handbook of Cryogenic Engineering*, Taylor & Francis Publishers, London.

Radiation shielding and other cryogenic engineering issues are treated in the classic text:

Scott, R. (1959). *Cryogenic Engineering*, Van Nostrand Reinhold, New York.

Reference information on heat transfer in cryogenic engineering:
Flynn, T. (1997). *Cryogenic Engineering*, Marcel Dekker, New York.
Timmerhaus, K. D., and Flynn, T. M. (1989). *Cryogenic Process Engineering*, Plenum Press, New York.

Good historical background for a general readership:
Mendelssohn, K. (1966). *The Quest for Absolute Zero, the Meaning of Low Temperature*, World University Library, McGraw-Hill Book Co, NY.

HELIUM:

Barron, R. F. (1985). *Cryogenic Systems*, Oxford University Press, New York.
Scott, R. (1959). *Cryogenic Engineering*, Van Nostrand Reinhold, New York.
Timmerhaus, K. D., and Flynn, T. M. (1989). *Cryogenic Process Engineering*, Plenum Press, New York.
Van Sciver, S. W. (1986). *Helium Cryogenics*, Plenum Press, New York.

HEAT TRANSFER AND THERMAL BOUNDARY RESISTIVITIES BELOW 1 K:

Lounasmaa, O. V. (1974). *Experimental Principles and Methods Below 1 K*, Academic Press, London.
Pobell, F. (1996). *Matter and Methods at Low Temperatures*, 2nd edition, Springer-Verlag, Berlin.

2.10.2 MATERIAL PROPERTY INFORMATION ON THE INTERNET

Fluid properties are available on the Internet for a fee from http://www.nist.gov/srd/ and can be purchased on CD from http://www.cryodata.com/.
Emissivities of many materials at room temperature are available on the Internet at no cost from http://www.electro-optical.com/.

2.10.3 CHAPTER REFERENCES

Ambler, E., and Kurti, N. (1952). "Film transfer in helium II below 1 K," *Philos. Mag.* 43, 1307.
Anderson, A. C., and Peterson, R. E. (1970). "Selection of a thermal bonding agent for temperatures below 1 K," *Cryogenics* 10, 430.
Ashworth, T., Loomer, J. E., and Kreitman, M. M. (1973). "Thermal conductivity of Nylon™ and Apiezon™ greases," *Adv. Cryog. Eng.* 18, 271.
Barnes, L. J., and Dillinger, J. R. (1966). "Thermal resistivity at Pb–Cu and Sn–Cu interfaces between 1.3 and 3.1 K," *Phys. Rev.* 141, 615.
Battelle (1977). *Handbook on Materials for Superconducting Machinery; Mechanical, Thermal, Electrical, and Magnetic Properties of Structural Materials*, MCIC-HB-04, Metals and Ceramics Information Center, Battelle–Columbus Laboratories, Columbus, OH.
Berman, R., and Mate, C. F. (1958). "Thermal contact at low temperatures," *Nature* 182, 1661.
Boberg, J. E. (1964). "Storage of cryogenic fluids for long duration spacecraft missions," in *Progress Report 17410*, p. 21, Lockheed Corp., California.
Breen, B. P., and Westwater, J. W. (1962). "Effects of diameter of horizontal tubes in film-boiling heat transfer," *Chem. Eng. Prog.* 58, 67.

Brentari, E. G., Giarratano, P. J., and Smith, R. V. (1965). *Boiling Heat Transfer for Oxygen, Nitrogen, Hydrogen, and Helium*; NBS Technical Note 317. US Government Printing Office, Washington, DC.

Challis, L. J., and Cheeke, J. D. N. (1964). "Thermal conduction across cooper-lead-copper sandwiches at helium temperatures," *Proc. Phys. Soc.* (London) 83, 109.

Childs, G. E., Ericks, L. J., and Powell, R. L. (1973), *Thermal Conductivity of Solids at Room Temperature and Below, A Review and Compilation of the Literature*, NBS Monograph p. 131. US Government Printing Office, Washington, DC.

Colwell, J. H. (1969). "The performance of a mechanical heat switch at low temperatures," *Rev. Sci. Instrum*. 40, 1182, and the references cited therein.

Corruccini, R. J. (1959). "Gaseous heat conduction at low pressures and temperatures," *Vacuum* 7–8, 19.

Cryogenic Materials Properties Program Compact Disk (2001). Release B-01, Cryogenic Information Center, 5445 Conestoga Ct., Ste. 2C, Boulder, CO 80301-2724, Ph. (303) 442-0425, Fax (303) 443-1821.

Drude, P. (1900). "*Zur Elektronentheorie der Metalle,*" *Ann. Phys*. 1, 566 and 3, 369.

Flynn, T. (1997). *Cryogenic Engineering*, Marcel Dekker, New York.

Frost, W. (1975). *Heat Transfer at Low Temperatures*, Plenum Press, New York.

Gmelin, E. (1967). "A cryostat for measuring heat capacities from 1.2 to 300 K and measurements of the specific heat of magnesium oxide below 36 K," *Cryogenics* 7, 225.

Goodall, D. H. J. (1970). Wall data chart, A.P.T. Division, Culham Science Centre, Abingdon, Oxfordshire, UK.

Incropera, F. P. and DeWitt, D. P. (2002). *Introduction to Heat Transfer*, 4th edition, John Wiley & Sons, New York.

Johnson, V. (1960). *A Compendium of the Properties of Materials at Low Temperature, Part I, Properties of Fluids; Part II, Properties of Solids*, Wright Air Development Division (WADD) Technical Report 60-56. National Bureau of Standards, MD.

Karagounis, A. (1956). "Heat transfer coefficient for liquid helium" (in French), *Bull. Inst. Intern. Froid.*, Annexe 2, pp. 195–199.

Keesom, W. H. (1942). *Helium*, p. 174, Elsevier, Amsterdam.

Kennard, E. H. (1938). *Kinetic Theory of Gases*, McGraw-Hill, New York.

Knudsen, M. (1910). "Eine Revision der Gleichgewichtsbedingung der Gase. Thermische Molekularströmung," *Ann. Phys.*, 31, 205–229.

Knudsen, M. (1910). "Ein absolutes Manometer," *Ann. Phys.*, 31, 809–842.

Knudsen, M. (1910). "Thermischer Molekular druck der Gase in Röhren," *Ann. Phys.*, 31, 1435–1448.

Knudsen, M. (1930). *Ann. Phys*., 5 Folge, Band 6, Heft 2, 6–185.

Kreith, F., and Bohn, M. S. (2001). *Principles of Heat Transfer*, 6th edition, Brooks/Cole, Pacific Grove, CA.

Kutateladze, S. S. (1952). "Statistical science and technical publications of literature on machinery," *Atomic Energy Commission Translation 3770*, Technical Information Services, Oak Ridge, TN.

Lienhard, J. H., and Wong, P. T. Y. (1964). The dominant unstable wave-length and minimum heat flux during film boiling on a horizontal cylinder," *J. Heat Transfer, Trans. ASME*, Sec. C, 86, 220–226.

Little, Arthur D., Inc. (1963). Report 65008-00-03, p. 36, Boston, MA.

Lockheed Missiles and Space Co., Inc. (1964). Thermophysics Laboratory, unpublished data, Lockheed-Martin Corp., Sunnyvale, CA.

Loechtermann, E. (1963). "Thermal conductivity of liquid neon," *Cryogenics* 3, 44–45.

Lounasmaa, O. V. (1974). *Experimental Principles and Methods Below 1 K*, Academic Press, London.

Mann, D. (1978). *LNG Materials and Fluids, A User's Manual of Property Data in Graphic Format*. National Bureau of Standards, US Government Printing Office, Washington, DC.

Marquardt, E. (2002). *National Institute of Standards and Technology*, Boulder, CO, personal communication.

McAdams, W. H. (1954). *Heat Transmission*, 3rd edition, McGraw-Hill, New York.

McFee, R. (1959). "Optimum input leads for a cryogenic apparatus," *Rev. Sci. Instrum.* 30, 98–102.

McTaggart, J. H., and Slack, G. A. (1969). "Thermal conductivity of General Electric No. 7031 Varnish," *Cryogenics* 90, 384.

Mikesell, R. P., and Scott, R. B. (1956). "Heat conduction through insulating supports in very low temperature equipment," *J. Res. Natl. Bur. Stand. (U.S.)* 57, 371–378.

Nast, T. (2000). "Thermal performance of MLI systems, from tank calorimeter testing," in *Cryogenic Techniques for Applied Superconductivity*, Tutorial Short Course. Applied Superconductivity Conference 2000; Lockheed-Martin, Palo Alto, CA, unpublished.

Radebaugh, R. (1977). "Thermal conductance of indium solder joints at low temperatures," *Rev. Sci. Instrum.* 48, 93–94.

Radebaugh, R., Siegwarth, J. D., Lawless, W. N., and Morrow, A. J. (1977). *Electrocaloric Refrigeration for Superconductors*, NBSIR 76-847, National Institute of Standards and Technology, US Government Printing Office, Washington, DC.

Radebaugh, R., Bradley, P. E., Marquardt, E., Lewis, M. A., and Siegwarth, J. D. (2001). Materials Properties, http://www.cryogenics.nist.gov/, based principally on compilations by Battelle (1977); see also Childs et al. (1973), Johnson (1960), Mann (1978), Schramm et al. (1973), Simon et al. (1992), and Touloukian (1970).

Reynolds, Q. (1950). *The Wright Brothers, Pioneers of American Aviation*, Random House, New York.

Richards, R. J., Steward, W. G., and Jacobs, R. B. (1961). *A Survey of the Literature on Heat Transfer from Solid Surfaces to Cryogenic Fluids*, Technical Note 122, National Bureau of Standards Technical Note, US Government Printing Office, Washington, DC.

Sauer, H. J., Jr., Remington, C. R., Stewart, W. E., Jr., and Lin, J. T. (1971a). "Thermal contact conductance with several interstitial materials," *Proceedings XI International Thermal Conductivity Conference*, p. 22, Albuquerque, New Mexico.

Sauer, H. J., Jr., Remington, C. R., and Heizer, G. A. (1971b). "Thermal contact conductance of lubricant films," *Proceedings XI International Thermal Conductivity Conference*, p. 24, Albuquerque, New Mexico.

Schmidt, C. (1981). "Review of steady state and transient heat transfer in pool boiling helium I," *Stability of Superconductors*, pp. 17–32, International Institute Refrigeration. Commission A 1/2, Saclay, France.

Schramm, R. E., Clark, A. F., and Reed, R. P. (1973). *A Compilation and Evaluation of Mechanical, Thermal, and Electrical Properties of Selected Polymers*, NBS Monograph 132, National Bureau of Standards, US Government Printing Office, Washington, DC.

Scott, R. B. (1963). *Cryogenic Engineering*, reprinted (1988) by Met-Chem. Research, Inc., P.O. Box 3014, Highmar Station, Boulder, CO 80307.

Seader, J. D., Miller, W. S., and Kalvinskas, L. A. (1965). "Heat transfer to boiling cryogenic fluids—liquid hydrogen, nitrogen and oxygen," *NASA Report CR-243*, US Government Printing Office, Washington, DC.

Simon, N. J., Drexler, E. S., and Reed, R. P. (1992). *Properties of Copper and Copper Alloys at Cryogenic Temperatures*, NIST Monograph 177, National Institute of Standards and Technology, US Government Printing Office, Washington, DC.

Steyert, W. A. (1967). "Thermal transport across superconducting solder joints near 0.1 K," *Rev. Sci. Instrum.* 38, 964.

Taconis, K. W., Beenakker, J. J. M., Nier, A. O. C., and Aldrich, L. T. (1949). "Measurements concerning the vapor-liquid solutions of He^3 and He^4 below 2.19 K," *Physica* 15, p. 733.

Timmerhaus, K. D., and Flynn, T. M. (1989). *Cryogenic Process Engineering*, Plenum Press, New York.

Touloukian, Y. S. (1970–1977). *Thermophysical Properties of Matter, The Thermophysical Properties Research Center Data Series*, Plenum Press, New York.

Touloukian, Y. S., Hawkins, G. A., and Jakob, M. (1948). "Heat transfer by free convection from heated vertical surfaces to liquids," *Trans. Amer. Soc. Mech. Eng.* 70, 13–18.

Van Sciver, S. W. (1986). *Helium Cryogenics*, Plenum Press, New York.

White, G. K., and Meeson, P. J. (2002). *Experimental Techniques in Low-Temperature Physics*, 4th edition, Oxford University Press, Oxford, UK.

Yovanovich, M. M. (1970). "A correlation of the minimum thermal resistance at soldered joints," *J. Spacecraft* 7, 1013.

Yovanovich, M. M., and Tuarze, M. (1969). "Experimental evidence of thermal resistance at soldered joints," *J. Spacecraft* 6, 855.

Zuber, N. and Tribus, M. (1958). "Further remarks on the stability of boiling heat transfer," *Report 58-5*, Department of Engineering, University of California, Los Angeles.

3 Cryostat Construction

Measure twice, cut once.
or
Cut twice and it's still too short.

– Old machine-shop adages

3.1 Introduction

The head of our graduate-school machine shop was an ex-drill (no pun intended) sergeant. To get a pass to use the equipment, we had to complete a machine course consisting of turning a piece of brass into a bolt, including using a lathe to cut threads and setting up a dividing head on a milling machine to mill a hexagonal head on one end. After an embarrassing number of hours of Herculean effort and mistakes, I succeeded in making a bolt that I could have bought at a hardware store for 50 cents. That exercise was incalculably useful in motivating me to strive for simple, shop-friendly apparatus designs. For example, I was impressed with how much faster it is to turn parts on a lathe rather than to machine them on a mill (especially since it is so easy to draw right-angle designs, which unfortunately require a mill to fabricate). So design it *round* whenever possible (unless using a computer-numerically controlled mill). The exercise also underscored for me the efficiency of designing an apparatus around *commercially* available parts whenever possible. Inevitably, there are too many custom parts in a research cryostat that take twice as long to make as we initially thought. So whenever possible, buy and modify. It really pays (and it is fun) to come up with a design that utilizes commercially available stuff. Save the custom machining effort for the truly one-of-a-kind parts.

Again, the general approach is to first get the design right on paper (especially the thermal design, Chapter 2), mechanically construct the apparatus (the present Chapter 3), and then wire the rig (Chapter 4)—essentially the same approach used in building a house.

So where is it best to start the mechanical design? The sample holder. Generally, I have found it easiest to work from the sample-support structure outward, keeping in mind the boundary condition that the whole apparatus has to fit in the available real estate (such as within a dewar or the small bore of a high-field magnet). This generally means first thinking about how the sample will be mounted on the holder (see Chapter 7 for the special problems of designing sample holders for transport measurements). Next, consider how the holder will be mechanically supported, thermally isolated, and electrically wired. Continue this process, working outward (and usually upward) until eventually reaching the top mounting flange for the apparatus. It is usually best to settle on a standardized design for the mounting flange itself; this enables interchangeability among several dewar/magnet work stations in a given laboratory.

After getting a general idea of what our design will look like, and before proceeding with any specific shop drawings and construction design, we first have to *select materials* for each cryostat part (Sec. 3.2). The material properties need to be appropriate for the particular measurement

to be made (e.g. high strength, low flexure, low thermal contraction, high or low thermal conduction, or low magnetic susceptibility). Usually, lighter and less massive is better, unless high forces are part of the measurement. If forces are an issue, buckling of the compressive structural members also must be considered (see "Mechanical properties" in Sec. 3.2.2). As a general rule, choose materials with a high thermal diffusivity (Sec. 6.1.4) to make the rig thermally cycle faster.

Consult with knowledgeable shop personnel *initially*, not after the fact. Their suggestions can save a lot of time and money, especially if they will be doing the machining and assembly.

The process is *iterative*. That is, think with them about your high-level goals, then have a first look at the cryostat details, then go back to the high-level goals again, and then revisit the details. This cycling process is the quickest way to a design that works.

Also do not get locked into a specific design idea or part too quickly. For example, you may have been given a chamber and so, to save money, you commit to designing your apparatus around it. But after getting further into the design you find that the cost of adapting everything to fit that particular chamber exceeds the cost of buying a new chamber that fits your needs. Do not make any irrevocable decisions until you have thought about the design for awhile and have a better overall perspective.

Chapter contents: The first part of this chapter covers techniques common to the construction of most cryostats: materials selection in Sec. 3.2 and joining techniques in Sec. 3.3. These are then integrated into a practical construction example for a dipper probe in Sec. 3.4. Specialty construction topics are considered next: sizing parts for mechanical strength (Sec. 3.5), mechanical motion at cryogenic temperature (Sec. 3.6), and, finally, vacuum techniques and cryogenic seals (Sec. 3.7). High- and ultrahigh-vacuum techniques are less commonly needed (but critical for dewar design as well as surface science and microscopy apparatus); they are treated separately as addenda in Sec. 3.8.

3.2 Material selection for cryostat parts

This section provides an *introduction* to selecting materials, just to get the cryostat construction process started. The *physics* of the properties of solids at low temperatures is treated in Chapter 6, along with more extensive and detailed cryogenic-property data (contained both in the figures of Chapter 6 and the data tables of Appendix 6).

3.2.1 ROOM-TEMPERATURE INTUITION GENERALLY DOES NOT WORK

A number of general guidelines in material selection sometimes run counter to our room-temperature intuition. It helps to dispel some of these notions right up front. For example:

- *Metals feel colder to the touch than ceramics and therefore have a greater heat capacity*. Not true. In fact, glass and ceramic materials generally hold an amount of heat comparable to that of metals over most of the cryogenic temperature range (see, for example, Fig. 3.3). (Metals feel colder to the touch because they usually have a thermal conductivity much greater than those of ceramics and glass, see Fig. 3.1.) Ceramics also take a lot more *time* to cool than metals because their lower thermal conductivity makes it more difficult to extract heat from their interior (see thermal diffusivity comparison in Sec. 6.1.4). So it usually pays to avoid

ceramic parts in cryostat construction (unless they are specifically needed for low thermal contraction or electrical insulation).

- *Copper provides great cooling power at low temperatures.* True at room temperature, but not in the cryogenic range. It does not even come close to liquid helium for providing cooling power and heat capacity at very low temperatures. To absorb temperature transients and keep a sample's temperature rise to less than 1 K, liquid helium, gram for gram, outranks copper 200,000 to 1. That is, 1 g of liquid helium will absorb over 20 J when it boils at 4.2 K (Appendix A1.5), whereas 1 g of copper absorbs a minuscule 10^{-4} J/K in the liquid-helium temperature range (Sec. 6.1.1). That is why directly immersing a sample in liquid helium is the easiest way to stabilize and control its temperature. (Pure copper does, however, have excellent thermal conductivity at low temperature, which makes it a great material for a sample holder that must *conduct* heat to an energy sink, such as liquid helium.)
- *Materials become brittle when they are frozen.* Sometimes, but metals with a *face-centered-cubic* (f.c.c.) crystal structure like copper, aluminum, and brass are wonderfully ductile over the entire low-temperature range. We used to do a cryogenic "magic" show in the local secondary school system as part of an outreach program, where among other experiments, we would let the students freeze whatever they wanted (within limits) in liquid nitrogen.

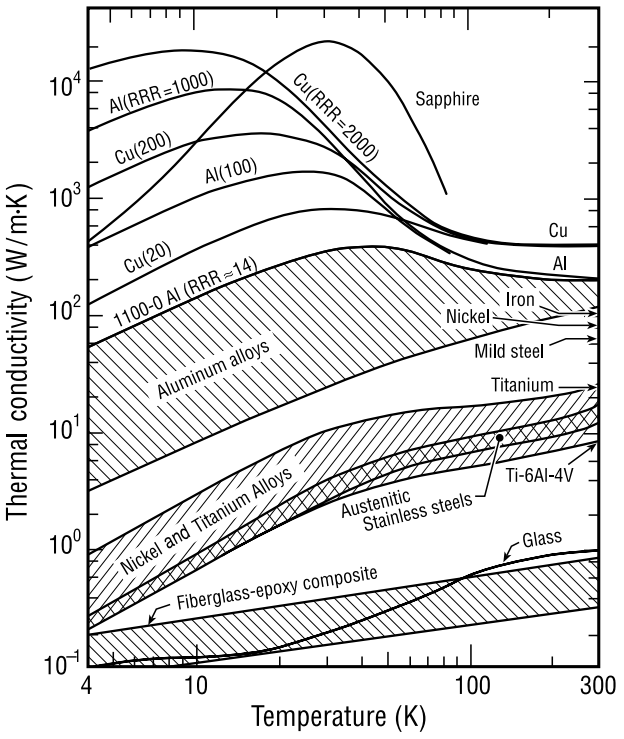

Fig. 3.1 Thermal conductivity of selected classes of materials (adapted from Hust 1983). The conductivities of nearly pure metals are similar at room temperature but differ widely at low temperatures, depending on their purity, as represented by the residual-resistance ratio (RRR) labeling these curves. (The higher the RRR, the purer the material and the higher the low-temperature thermal conductivity, as described in Sec. 6.3.4). Arrows along the right scale indicate the room-temperature values for several common metals. *Tabulated* data for these and additional materials are given in Appendix A6.7.

They loved to see rubber bands snap in two and use a liquid-nitrogen-temperature banana as a hammer. However, I remember one student who froze a copper penny and whaled away on it with a hammer over and over again to break it in half. He just could not get that thing to snap. I tried to tell him about f.c.c. metals, but it did not matter. He was absolutely convinced it should break, and he was going to make it happen. *Nonmetallic* materials that do not embrittle at low temperature include paper, Kapton™, and Teflon™. But watch out for epoxy. It is notorious for cracking at temperatures only slightly below room temperature, where, in fact, it undergoes a ductile-to-glass structural transition.

- *Solder is fairly soft.* Not so at cryogenic temperatures. When cooled to liquid-nitrogen temperature, its yield strength increases many times over. This is also a general characteristic of f.c.c. metals: they rise in strength on cooling, as described later in this section. However, these mechanical changes are mostly finished by 77 K. This is also true of thermal contraction. So, if your measurement rig survives cooling in liquid nitrogen, not much will happen (mechanically) on further cooling to liquid-helium temperature.

3.2.2 PERSONALITIES OF MATERIALS AT LOW TEMPERATURES

Usually, the choice of cryostat-construction materials is a compromise among several competing design needs. (An example is given in Sec. 3.4, later in this chapter.) In the present section, we introduce the key cryogenic material properties and indicate a few preferences for materials well suited to cryostat construction. Properties are listed in order of priority, with the first ones relevant to most cryostat designs, and the latter ones more applicable to specialized test apparatus.

Thermal conductivity

Handbook values of thermal conductivity are useful for many materials, such as glass, stainless steel, and brass, but not for *nearly pure* metals. Below liquid-nitrogen temperature, the thermal conductivity of relatively pure materials depends strongly on the *defect* content of the material, as Fig. 3.1 shows for different purities of copper. It is highly variable from sample to sample. The higher the purity, the higher the thermal conductivity. The relative purity is operationally quantified in Fig. 3.1 by labeling the curves with the material's electrical residual-resistance ratio, RRR (RRR $\equiv R_{293\,\mathrm{K}}/R_{4\,\mathrm{K}}$), which is described in more detail in Sec. 6.3.4. Appendix A6.7 tabulates the thermal conductivity of many of the materials described below.

High-thermal-conductivity parts, such as sample holders, are commonly made from electrolytic-tough-pitch (ETP) copper (Unified Numbering System UNS C10300) or from oxygen-free copper (UNS C10100 or C10200) (e.g., OFHC™). More information is given on the properties of these materials in Appendix A3.1. ETP and oxygen-free copper both have about the *same* thermal conductivity, roughly a thousand times greater than that of stainless steel at 4.2 K (see Fig. 2.1). However, ETP copper is more readily available (as sheet, rod, wire, and wire-braid) than oxygen-free copper and so is more commonly used for high-thermal-conductivity parts in cryogenic apparatus. Also, ETP copper is somewhat easier to machine than oxygen-free copper. (Use *very* sharp cutting tools for pure copper.) Oxygen-free copper is needed only if the copper part will be subjected to hydrogen brazing, because ETP copper contains about 0.3% oxygen, which reacts with the hydrogen and makes the joint weak and porous.

If money is not a problem, then 99.999% pure ("five-nines" purity) copper will improve the thermal conductivity by another factor of 20 or more at liquid-helium temperature (see Appendix A3.1). However, there is almost no advantage above liquid-nitrogen temperature, since the conductivity in this temperature regime is dominated by thermal vibrations of the atomic lattice (phonons) rather than by impurities.

If the part (such as a transport-measurement sample holder) must have high thermal conductivity as well as be electrically *insulating*, then the common solution is to coat ETP copper with a thin, electrically insulating layer, such as IMI 7031 varnish. If that will not work, then sapphire is among the highest thermally conducting insulators (see Fig. 3.1); it is also the material of choice for sample support in many optics measurements because of its optical transparency. (Incidentally, sapphire can be purchased already cut to shape for less money than might be expected.) Another high-thermal-conductivity insulator is beryllium oxide (beryllia), which is used for thermometer-lead heat sinks (Sec. 5.3.1).

Copper *tubes* are generally not available from ETP copper, but from phosphorus-deoxidized copper, which has a low-temperature thermal conductivity about 1/30 that of ETP copper (Appendix A3.1). Copper tubes from oxygen-free copper are not commonly available, but can be purchased from a few specialty suppliers, given in the supplier list in Appendix A1.7 under Materials, Copper.

Low-thermal-conductivity parts (for sample isolation and cryostat support) are usually made from austenitic stainless steel [American Iron and Steel Institute (AISI) 304, 316, and 321]. Stainless steel is the workhorse material for cryostat *support* structures because, in addition to its low thermal conductivity, it is mechanically tough, relatively inexpensive, and readily available as thin-wall tubing (which has a low cross-sectional area to limit heat influx into the cryostat). Heat conduction along stainless-steel tubes of different sizes is listed for convenience in Appendix A3.2. For magnetic measurements, however, materials such as titanium are preferred over stainless steel because they have a lower magnetic susceptibility (see below). Other common metals with low thermal conductivity include Cu–10%Ni and Inconel 625.

Nonmetallic construction materials usually have low thermal conductivity and include fiberglass–epoxy composites (G-10), polyimide (Kapton™), Mylar™, Nylon™, phenolic resins filled with fiber (e.g. paper, cloth, Tufnol™), ceramics (Macor™), and glass. Beware that *bulky* parts made from these materials have a long cool-down time [on the other hand, stainless-steel and metallic-alloy tubes usually have a thin wall (0.1–0.15 mm is typical) and therefore cool-down time is not a problem].

➔ Avoid breathing the glass dust in machining fiberglass–epoxy composite materials (keep the part wet during machining with a water-based coolant, see Sec. 1.6.1). Or use the popular paper- or cloth-filled phenolic composites instead.

➔ Some ceramics, such as Macor™, are *machinable* with ordinary metal-working tools, which is a great advantage in fabricating electrically insulating parts for a vacuum

chamber, for example. The microstructure of such machinable ceramics consists of a highly interlocked array of two-dimensional mica crystals dispersed within a brittle glassy matrix. When they are machined, mica crystals localize the fractures by deflecting, branching, and blunting the cracks. The machining resolution is, consequently, proportional to the size of the mica crystals, which are typically about 20 μm in diameter.

Thermal contraction

The thermal contraction of construction materials needs to be matched approximately, or the forces that develop between the various structural members can rip the rig apart. For example, the difference in thermal contraction between stainless-steel and aluminum-alloy support structures can cause a cryostat to self-destruct. Also, when selecting coaxial cables, beware that the different contraction rates between the center conductor and the dielectric material can cause end connections to break (Sec. 4.8). Sometimes, even small differential contraction forces can be a problem, particularly in sample holder design (Secs 7.3.2 and 7.4.2).

Figure 3.2 shows the total thermal expansion (contraction) $\Delta L/L$ for various construction materials as they are cooled below room temperature (295 K). As seen in Fig. 3.2, most of

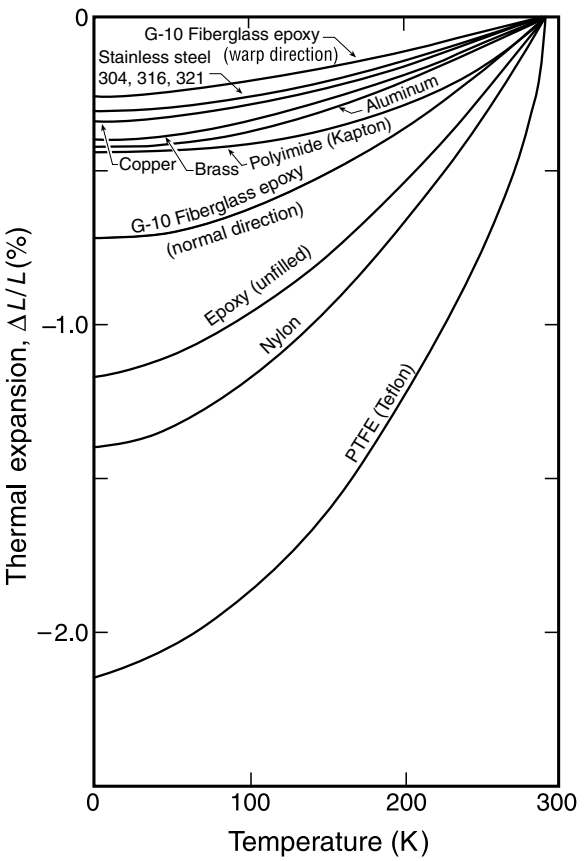

Fig. 3.2 Thermal expansion of selected construction materials (from Radebaugh et al. 2001 and the references listed therein). Data for these and additional materials are given in Figs 6.4–6.9 and tabulated in Appendix A6.4.

the thermal contraction occurs on cooling from room temperature to liquid-nitrogen temperature, with relatively little more occurring at still lower temperatures. Whereas the thermal contraction at low temperature is highly nonlinear, above room temperature the thermal expansion tends to be linear. So Appendix A6.4 tabulates the total $\Delta L/L$ for many construction materials at low temperatures and the *slope* at room temperature, so you can calculate the approximate thermal expansion at still higher temperatures.

High thermal contraction (~1% or more) (in engineering units this would be 10^{-2} in./in. or 10^{-2} m/m): Resins, epoxy, and plastics contract the most, typically between 10 and 20 mm per meter of length when cooled from room temperature to below ~50 K. The most notorious material commonly used is silicone rubber, which contracts more than 4%. More data on thermal contraction are given in Sec. 6.2 and Appendix A6.4.

Moderate thermal contraction: Metals and alloys are next, with length changes of about 2–4 mm per meter. Within this metallic group, ***a***luminum contracts the most (0.415% between 293 and 4 K), followed by ***b***rass (0.369% for 70/30 brass), then ***c***opper (0.324%), and finally ***s***tainless steel (0.306% for AISI 304L).

➔ A simple mnemonic to keep this order in mind is to remember your "ABCs."

Polyimide (Kapton™) is one of the few polymers with a thermal contraction in the same range as that of metals; see Fig. 3.2.

Low thermal contraction: Glasses and ceramics change the least, only several tenths of a millimeter per meter, and so they are often used for components that need dimensional stability such as optical mirrors and lenses, or for the critical parts in thermal-expansion-measurement apparatus. The thermal expansion *coefficients* for a number of low-contraction materials are given in Sec. 6.2.

Heat capacity

Heat capacity is a measure of the amount of heat that has to be extracted from a material to lower its temperature by a degree. Usually heat capacity is normalized by mass, which is called the *specific heat*, but in Fig. 3.3 we have plotted *volumetric* heat capacity because it is better suited to selecting materials for apparatus construction, where we are interested more in enclosing a structure (volume and strength) than saving mass.

Figure 3.3 shows that heat capacity decreases dramatically at cryogenic temperatures, compared with that at room temperature. For most materials, it drops approximately as T^3 at temperatures below liquid-nitrogen temperature (77 K). Consequently, cooling proceeds excruciatingly slowly from room temperature down to about 77 K and then really picks up pace at lower temperatures. At cryogenic temperatures, it is possible to change the temperature of metal parts by many degrees in a matter of seconds, a great time savings. The disadvantage from a measurements standpoint is that fluctuations in sample temperature become greater in the liquid-helium temperature range.

Appendix A6.2 presents tabulated values of the specific heat of many of the materials described below.

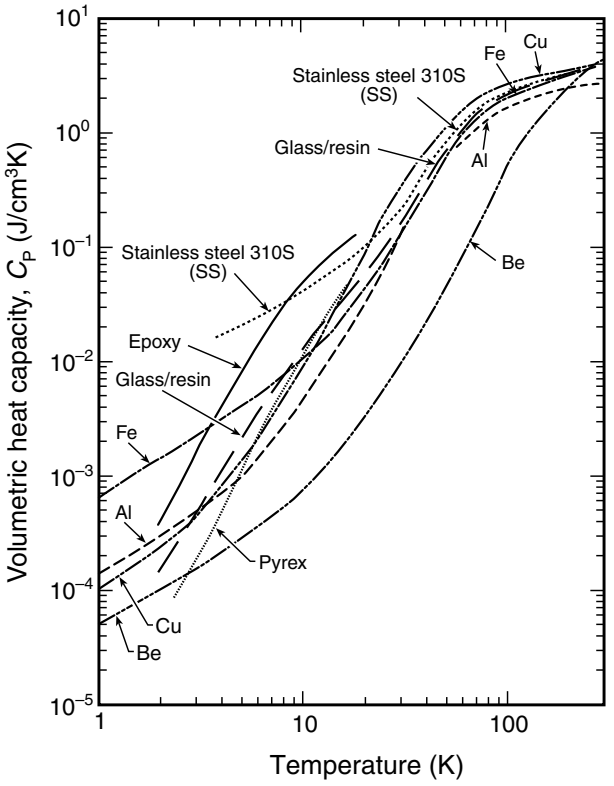

Fig. 3.3 *Volumetric* heat capacity (at constant pressure, C_P) of several types of materials at cryogenic temperatures, showing an approximate T^3 temperature dependence below ~77 K (from Corruccini and Gniewek 1960, Chang 1970, and Touloukian 1966, and a compilation by Goodall 1970, renormalized per unit volume using the room-temperature density of each material, which is relatively independent of temperature). Specific heat data (referenced to *mass*) are plotted in Fig. 6.1 and tabulated in Appendix A6.2.

High heat capacity: On a volume basis (Fig. 3.3), the heat capacity of most common construction materials is fairly comparable. On a mass basis (see Sec. 6.1.1), ceramics and resin-filled composites (such as glass-, boron-, or graphite-epoxy composites) have a specific heat about an order of magnitude greater than that of metals over most of the cryogenic temperature range. Because ceramics, glasses, and resin-filled composites usually have a low thermal conductivity as well, they are apt to have thermal gradients between their surface and core. Thus, it requires a very long time for them to come to thermal equilibrium when temperature is changed.

Low heat capacity: Metals tend to have a slightly lower volumetric heat capacity than that of insulators over much of the cryogenic temperature range, except below about 10 K, where heat storage in the metals' conduction electrons becomes relatively significant (described in more detail in Sec. 6.1).

Mechanical properties

Fracture toughness is usually the principal mechanical concern; that is, we do not want to use structural materials that embrittle on cooling. This restricts the use of most of the iron alloys like

Table 3.1 **Commonly used metallic elements and alloys of the f.c.c., b.c.c., and h.c.p. crystal structures.**

Elements	Alloys
Face-centered-cubic (f.c.c.) crystal structure	
Copper	Austenitic stainless steels (e.g. AISI 304, 310,
Aluminum	316; see Appendix A6.9 for compositions)
Nickel	Brass ($<$ 30 at% Zn)
Lead	
Silver	
Gold	
Platinum	
Body-centered-cubic (b.c.c.) crystal structure	
Iron	Ferritic stainless steels
Molybdenum	Carbon steel
Tungsten	Nickel steels ($<$ 10 at% Ni)
Niobium	Nb–Ti ($<$ 40 at% Ti)
Vanadium	
Chromium	
Lithium	
Sodium	
Potassium	
Hexagonal-close-packed (h.c.p.) crystal structure	
Zinc	
Cadmium	
Titanium	
Cobalt	
Magnesium	
Beryllium	

Source: Read (1983).

Fe–Ni steels, which (*iron*ically) are the most popular structural alloys at room temperature. In fact, this caveat effectively applies to all metals having a body-centered-cubic (b.c.c.) crystal structure, as well as to most materials having a hexagonal-close-packed (h.c.p.) crystal structure.

Table 3.1 lists common metals of each crystal type. Unlike b.c.c. and h.c.p. materials, metals and alloys with a f.c.c. crystal structure remain ductile and tough over the entire range of cryogenic temperatures. The f.c.c. crystal lattice is the optimum atomic arrangement to ease plastic deformation, and thus f.c.c. materials (such as copper, aluminum, their alloys, and austenitic stainless steels) not only have excellent ductility at room temperature, but they also remain ductile at low temperatures. They are generally the materials of choice for cryogenic structural parts. This is not to say that materials like titanium (h.c.p.) and niobium (b.c.c.) cannot be very useful in cryostats; we just need to be more careful about stressing them.

Yield strength is the next most important mechanical property for selecting structural parts. Yield strength is the stress at which a material starts to deform plastically. If a material is subjected to stress higher than its yield strength, it permanently deforms and becomes mechanically unreliable. (A more detailed discussion, including definitions and mechanical-property data for common technical materials, is given Sec. 6.6.1.)

The stress at which a material fractures or fails, the *ultimate strength*, is also considered in mechanical design, but usually it is not the limiting factor because common design practice

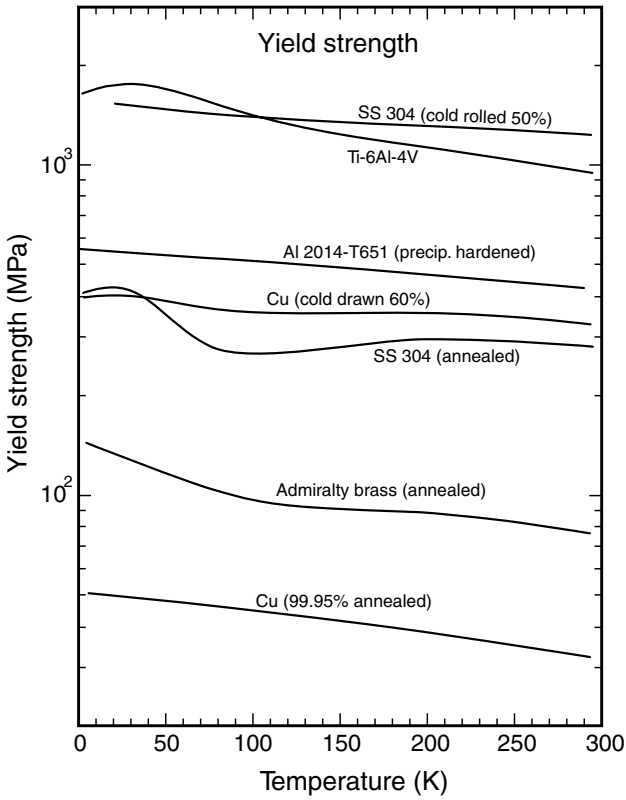

Fig. 3.4 Temperature dependence of the yield strength of several cryostat materials. (Data compiled from Battelle 1977, Read and Reed 1979, Tobler 1976, Smith and Rutherford 1957, Warren and Reed 1963, Schramm et al. 1973, and Soffer and Molho 1967.) Yield strength data for additional materials are given in Figs 6.17–6.18 and tabulated in Appendix A6.10.

dictates that stress on parts normally be kept well below the *yield* strength. (A conservative target of half of the yield strength is common.)

Figure 3.4 compares the yield strength of several common cryostat structural materials. The general shape of the curves in Fig. 3.4 shows that the yield strength of most structural materials *increases* slightly on cooling. Be aware that the amount of *cold work* in the material dramatically affects the yield strength, as is illustrated, for example, by the "cold rolled 50% (strain)" vs. "annealed" data for 304 stainless steel (SS) or copper in Fig. 3.4. This comes about because dislocations are introduced that strengthen a material when it is strained beyond its yield point during rolling and forming operations. Appendix A6.10 tabulates the mechanical properties of many of the materials described below.

High yield strength: The structural "all stars" are the austenitic stainless steels [Fe–Cr–Ni alloys, such as the American Iron and Steel Institute (AISI) 300-series stainless steels, particularly types 304, 310, and 316]. They are particularly tough, readily available, easy to fabricate, and have a good history of cryogenic use. Their disadvantages are that they are more expensive and have a lower yield strength than the traditional ferritic Fe–Ni steels, but Fe–Ni steels are usually unacceptable for cryogenic use because their low fracture toughness is low, as mentioned at the beginning of this subsection. (It is best to avoid either the austenitic or ferritic steels, however, if *magnetic* measurements are being made; see the next section on magnetic susceptibility.) Aluminum alloys are also a good structural choice, especially in high magnetic fields (with a susceptibility 2–3 orders of magnitude lower than that

of stainless steel) and when machinability is a consideration (quicker to cut than stainless steel).

Elastic strain limit: Cryostat parts that must withstand considerable flexure should be made from materials with a high elastic strain limit at their point of yielding. Good candidates are the precipitation-strengthened aluminum alloys, such as aluminum 2219-T85 and beryllium–copper alloys, such as Cu–2%Be (UNS C17200). (See the note on safely machining beryllium copper at the end of Sec. 1.6.1.) These alloys can strain a large amount (about 0.6% and 1.0%, respectively) before they start to plastically yield. In contrast, materials that become brittle at low temperatures, such as the b.c.c. metals and epoxies, do not plastically deform; instead, they crack and break. Generally, they have only a small region of reversible elastic strain preceding their fracture. Epoxy materials, in fact, usually crack when stretched only 0.2% of their length, which places severe limitations on the forces they can tolerate at cryogenic temperatures. Thick layers of epoxy are generally more prone to cracking than thin layers or filled epoxies.

Except for fracture toughness, the mechanical properties of most materials improve (become stronger) at lower temperatures. Chapter 6 presents the temperature dependence of mechanical-property data over the cryogenic temperature range for many common construction materials.

Magnetic susceptibility

Magnetic susceptibility (i.e. how readily a material becomes magnetized in an applied magnetic field) can be important in selecting construction materials for measurement cryostats where magnetization of the cryostat parts can significantly influence the results. This occurs, for example, in *magnetometers* or apparatus involving *electron beams*. In critical situations, use only materials with low magnetic susceptibility. Magnetic materials can show up in unexpected places—screws, welds, and springs (see the tip below).

In high magnetic fields, magnetic forces on cryostat parts can become significant. Even "nonmagnetic" stainless steel is not exempt, since the magnetic susceptibility of stainless steel is surprisingly high. A calculation in Sec. 6.5.2 shows that the magnetic force acting on a 2 cm diameter rod of AISI 316 stainless steel (such as might be used in mechanical testing for transmitting loads into a high-field magnet) is nontrivial, amounting to about 290 N (65 lbf) in the magnetic-field gradient of a typical 12 T magnet. With *ferromagnetic* materials, the magnetic forces become extremely high, so these materials are usually avoided entirely in high-field applications (except when needed for magnetic-field shaping).

The *mass* susceptibility is useful for small parts where the sample mass is more easily determined than volume. The *volume* susceptibility is useful for structural parts with well-defined shapes (such as tubes, rods, sheets, and blocks) where the volume is well defined. The mass susceptibility at 1.6–4.2 K of a variety of materials is tabulated in Appendix A6.8a, and the volume susceptibility of common structural materials is given at room temperature, 77 K, and 4.2 K in Appendix A6.8b.

These lists are especially useful for selecting materials in magnetically sensitive measurements like magnetometry, or in mechanical experiments where we do not want magnetic forces acting on the cryostat parts. So, for example, instead of using AISI 316 stainless steel [which has a 4.2 K volume susceptibility of about 1.6×10^{-2} (SI units), from Appendix A6.8b], we might choose another structural material like titanium, which has a volume susceptibility about a thousand times lower.

➔ Commercially available stainless-steel parts, such as screws, are usually made of AISI 304 stainless steel, which, when strained at low temperatures, can partially transform to a ferromagnetic phase (see Sec. 6.5.2) that has a much greater magnetic loading than the paramagnetic parent material. This is also true of *welded* 304 stainless steel: the welded material partially transforms to a ferromagnetic phase (Appendix A6.8c). When welding, the combination of 316 L stainless steel (with the DIN 17441-1.4404 composition) and a Grinox T-51 weld metal produces the lowest magnetization (Swenson and Markiewicz 2000). (Welding techniques are described in the next section.) However, the best option is to silver-solder or soft-solder stainless-steel joints, rather than to weld them, if they will be used in high magnetic fields.

3.3 **Joining techniques**

3.3.1 INTRODUCTION

Parts can be joined either *reversibly* with bolts, grease, or varnish, for example, or *permanently* with epoxy, welding, brazing, or solder. An introduction to each of these techniques follows, along with considerations for their use at cryogenic temperatures.

A brief description of "sticky stuff," such as tapes, adhesives, and glues that adhere well at cryogenic temperatures, is included as the last subtopic in this section, and Appendix A3.10 lists suitable materials.

Seals for *vacuum* applications (as well as methods for adapting commercial vacuum seals for cryogenic use) are presented in Sec. 3.7.4.

Temporary joining techniques

In the case of *bolting*, the main concern with cryostat parts is loosening of the joint from differential thermal contraction as parts made of different materials are cooled. For example, it usually works well to use a combination of brass (or aluminum) screws and copper parts. As illustrated in Fig. 3.5 for a copper heat-sink post, the brass screw will contract more than the

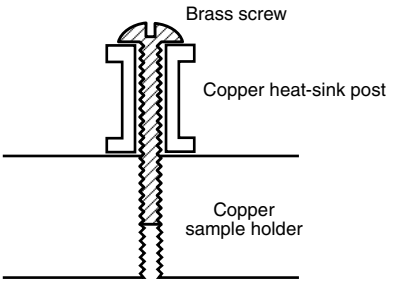

Fig. 3.5 Example of choosing materials that will tighten a joint on cooling. The brass screw contracts more than the copper heat-sink post, increasing the pressure holding the post against the sample holder.

copper part on cool-down (remember the ABCs mnemonic of Sec. 3.2). So after cooling, the extra thermal contraction of the screw will tighten the copper post against the sample holder body, thereby increasing the thermal contact between the two parts. Reverse the role of the materials, and we get loose joints.

If we are not so fortunate as to have the copper/brass-screw combination illustrated below (e.g. a stainless-steel screw and copper part), all is not lost. We can simply slip several Invar washers under the stainless-steel screw head. Since Invar has almost no contraction on cooling (Fig. 6.8), it can compensate for the difference in contraction between the copper part and the stainless screw. Just be sure to provide enough Invar length so the copper–Invar combination contracts less than a similar length of stainless steel. Belleville washers (springy, conical washers) can also be used to keep such a screw combination tight.

➔ There are few things so discouraging as having a stainless-steel screw seize in a stainless part. (In an attempt to get it out, we then compound the problem by twisting the screw head off.) To prevent galling of stainless-steel screws in stainless parts, use *stainless screws that are silver or nickel plated* or lubricate them with a *dry lubricant such as* MoS_2 *or* WSe_2. This is especially important for stainless-screw joints that are often remade. (Sources of such screws are listed in Appendix A1.7 under Vacuum accessories, Screws.)

As extra insurance, it helps to design flanges with through-bolts and nuts, rather than flanges with dead-end tapped holes; this makes it easier to machine-out seized bolts. Excessively long thread engagement, of more than a few threads (see Appendix A3.4) aggravates the seizure problem. Also, it is good practice to place washers under both bolt heads and nuts to help prevent galling damage to the flanges and enable more accurate tightening of bolts with a torque wrench.

Thermal conductance across bolted joints can be significantly improved by cleaning the surfaces before they are joined by sanding (moving the parts back and forth on sandpaper laying on a flat surface) to provide a smooth, flat finish with surface roughness of less than about 8 μm. Other techniques for enhancing the thermal conductance (discussed in Sec. 2.6) include the use of gold against gold (or against gold-plated copper), which reduces surface oxidation and gives high thermal conductance, as does an indium gasket, which cold-welds the parts together and fills in gaps and irregularities between the two surfaces. The thermal conductance (in units of W/K) for solid/solid pressure joints (without grease or indium gaskets) depends only on the *total force* pressing the two pieces together, and not the area of the joint. Thermal conductance data for several common metal combinations are given in Appendix A2.3 and in Fig. 2.7 of the previous chapter on heat transfer.

Grease is also an effective medium for joining parts temporarily. On cooling, the grease freezes; on rewarming, it allows easy disassembly. Thermal conductance across grease joints is proportional to the surface area (rather than total force), and it can be increased by minimizing the joint thickness and adding pure copper powder to the grease. Copper-powder-filled grease is available commercially from Cry-Con, or it can be made fairly easily by adding copper powder to Apiezon N™ grease (as much powder as possible while still maintaining the ability of the

grease to flow). Suppliers of both types of grease are listed in Appendix A1.7 under Thermometers and accessories.

IMI 7031 *varnish* (formerly GE 7031) provides a semipermanent bond. It usually helps to thin the varnish with ethanol. Acetone can also be used as a thinner, but it makes the varnish rather stringy. Thermal conductance for varnish is about the same as for grease joints. Values are given as a function of temperature in Fig. 2.7.

Permanent joining techniques

Epoxy joints: Epoxy works well to bond epoxy-based materials such as G-10 and G-11 fiberglass composites, but care must be used since epoxy is brittle at low temperatures and will easily crack from thermal stress. That is, epoxy contracts more on cooling than most materials, as Fig. 3.2 shows, and the differential contraction can highly stress epoxy joints.

Joint integrity is improved by degreasing and preferably etching or abrading surfaces before joining. Also, machine tight fits where possible to minimize the thickness of the epoxy bond.

The contraction problem can be mitigated by using special glass-filled epoxies, such as Stycast 2850 FT™, which has an average thermal contraction that is decreased to match that of copper through the addition of low-thermal-contraction ceramic powder to the epoxy. (It is not easily machined, however, because of the SiC or alumina filler.) Stycast 2850 FT™ has a fairly high viscosity, so it is best to use it in applications where good flow is not required.

If a low-viscosity epoxy is needed, Stycast 1266™ is an unfilled epoxy that works well at low temperatures. Although it has a high thermal contraction, it flows well when it is applied and thereby provides strong thin joints if the parts can be pressed together during curing. Also, the crack resistance of Stycast 1266™ can be improved by heating the joint to 90°C for 4 h after the epoxy has hardened. Eccobond 27 also works well as an unfilled epoxy. It is robust and is among the best for adherence. (Further information is given in Appendix A3.10.)

Other epoxies that are successfully cycled to liquid-helium temperature include Armstrong and Crest. "Five minute" epoxy does not work well at low temperatures. (Tricks for using epoxy to make electrical wire seals, which usually are notoriously unreliable at cryogenic temperatures, are treated in the chapter on wiring, Sec. 4.7.2.)

Metal joints: There are two general types of permanent metal joints. In the first type—welding, the metal surfaces are fused by melting or pressing them together without any intermediary metal. In the second type—brazing and soldering, a softer intermediary metal with a lower melting temperature is used to bond the parts. Welding works where the metals to be joined are similar or where they readily form alloys. Brazing and soldering, in contrast, permit dissimilar metals to be joined.

The main difference between brazing and soldering is that the melting temperature of the intermediary metal is higher with brazing. As a result, surface alloying with the base materials is much more extensive with brazing and the joint is usually stronger than with solder joints. Soldering, nevertheless, is popular precisely because it is simpler and can be carried out at lower temperatures; it also works well with many copper-based materials. Brazing is preferred for structurally strong stainless-steel joints, especially in high magnetic fields since welded stainless-steel joints are usually magnetic. Silver-soldering (essentially a form of brazing with a high-temperature torch) is usually faster than brazing; it also works well with stainless steel, but only if the stainless steel part is being joined to a higher-thermal-conductivity material

such as copper or brass (which acts to spread the heat of the torch and avoids locally overheating low-thermal-conductivity stainless steel).

Welding and brazing techniques are usually needed for ultrahigh-vacuum joints ($< 10^{-5}$ Pa, or $< 8 \times 10^{-8}$ torr), since soft-solder melts at the bake-out temperatures required to remove adsorbed gases from such systems. However, solder joints work just fine for most cryostat vacuum jackets [where only $\lesssim 10^{-3}$ Pa ($< 8 \times 10^{-6}$ torr) is needed for thermal insulation] or for pumped liquid-cryogen dewars that just need to be roughly evacuated to $\lesssim 10^{2}$ Pa ($\lesssim 8 \times 10^{-1}$ torr) to change the cryogen temperature (described earlier in Fig. 1.2).

Most metal-joining techniques require the use of high temperature, so the main principle in planning apparatus assembly is to make the joints that require the highest temperature first, and then work down in temperature so the apparatus does not fall apart when subsequent joints are made. Sounds trivial, but it takes some forethought when assembling a rig. In the following discussion on metal-joining techniques, we proceed in that order, starting with welds, and then going down in temperature to brazing, silver-soldering, and finally, soft-soldering.

3.3.2 WELDING

Welding can be carried out in several ways: oxygen–acetylene welding, electric-arc welding, electron-beam welding, laser welding, spot welding, and cold-pressure welding.

Oxygen–acetylene welding: This is one of the most common welding techniques: the metal parts are fused together in the very hot flame of an oxygen–acetylene torch. But the molten metal can take up gas, creating a porous joint. Severe surface oxidation of the metal can also provide a large surface area for trapping gas, making this joining technique inappropriate for use in high-vacuum systems.

Electric-arc welding: In traditional arc welding, one electrode is a welding rod that conducts electric current to heat the parts being welded (the parts are electrically connected to ground, which forms the other electrode). The welding rod is consumed and provides filler material for filling the weld-prep groove. The material used for the consumable electrode rod must be chosen with care to provide a weld composition compatible with the materials being welded. Traditional arc welding has the same problems as oxygen–acetylene welding, however, in that the welds are porous and oxidation is severe.

To mitigate these problems, another form of arc welding (sometimes called TIG welding, short for ***t***ungsten–***i***nert-***g***as welding) has been developed, which is very popular for stainless-steel vacuum systems and joining stainless-steel tubing. In this form of welding, the electric arc is struck in a protective atmosphere of an inert gas such as argon. The tungsten electrode is surrounded by a ceramic tubular shield through which argon gas is passed. A dc technique is used for steel, with the electrode negative and the work piece positive. For aluminum, an ac arc is used. The method does not work as well for metals that oxidize easily, such as molybdenum and tantalum, because the heated area of the work piece just outside the protective gas will still oxidize significantly. For such metals, the welding has to be carried out in an argon-filled box. Electric-arc welding heats only a small area, and therefore, differential heating of the joint area can generate significant strain and distortion, which has to be relieved by annealing afterward.

Also, if dimensional tolerances are important, the joint needs to be remachined after welding to remove distortion.

Electron-beam welding: In this technique, a focused beam of high-energy (> 10 kV) electrons is used to heat the parts to the fusion temperature. Because electrons are easily scattered by air, this method has to be carried out in a vacuum to accommodate the electron beam. Thus, the technique limits the parts to sizes small enough to fit within a vacuum chamber. It is also relatively expensive, but precise and reliable. It is particularly useful for welding metals with a high melting temperature that readily oxidize, such as joints between tungsten parts, for example. The total absence of gas eliminates gas entrapment, making very good joints for vacuum applications.

Laser-beam welding: This method is similar to electron-beam welding, except that the energy source is a laser beam instead of an electron beam. The advantage over electron-beam welding is that a vacuum environment is unnecessary.

Electrical resistance (spot) welding: This technique is usually restricted to small areas, since the metals are joined by pressing them together and passing a high current through the joint. The joint area needs to be small and the resistance high so that Joule heating melts the metals locally to form a fusion weld. Consequently, the technique is usually used for spot welding delicate components. The welds are strong, and they do not incorporate gas so the technique is useful in high-vacuum systems. Nickel, iron, and alloys of these metals, such as stainless steel, are well suited to spot welding. On the other hand, high-conductivity metals, such as silver and copper, are difficult to spot weld. Aluminum is also not suitable because its prevalent oxide layer electrically insulates the joint interface.

Pressure welding: This method is appropriate mainly for softer pure metals, such as copper or silver, but it has been used with harder metals by using an intermediate softer metal, such as indium or lead, between the hard-metal surfaces. The surfaces of the parts must be very clean and free of oxide. They are brought together under pressure to form a diffusion bond, either at room temperature, or sometimes at reduced pressure at elevated temperatures. Very high pressure ($> 10^8$ Pa) is required to form the diffusion bond, so this technique is not appropriate for large components. It is useful mainly for joining flat surfaces in situations where heating of the components must be avoided, as in the attachment of windows in vacuum systems.

Friction welding: This method is used mainly to make transition joints between dissimilar metals, such as stainless steel and aluminum. One piece is spun at high speed on a lathe, for example, and the other stationary piece is then jammed onto it, momentarily generating a lot of frictional heat at the interface. The resulting joint between the two metals is quite strong.

Beware that any of these welding techniques can lead to joint embrittlement, a problem that can become exacerbated at low temperatures particularly if b.c.c. phases are formed (Sec. 6.6.5 and Appendix A6.8c). For the most part, welds of chromium-containing austenitic stainless steels made with common welding processes are satisfactory at cryogenic temperatures, although the toughness of the weld is usually somewhat lower than that of the base metal. This degradation is due to the incorporation of precipitates of chromium carbides at the grain boundaries of the welded material that reduce the fracture toughness of the weld at low

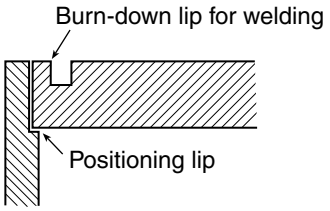

Fig. 3.6 Burn-down lip machined into a circular plate to increase welded-joint reliability.

temperatures. Toughness loss from this source can be mitigated by using weld filler metals with low carbon, such as 308L and 316L stainless steel (containing a maximum of ~0.04% C). Also, it helps *not* to follow normal welding practice, wherein the weld metal chemistry is balanced to provide 4–10% ferrite to avoid microfissuring. Since ferrite is a b.c.c. phase and therefore brittle at low temperature, weld toughness can be improved by keeping the ferrite content low. Oxygen and nitrogen pickup during welding also reduces toughness, so it is important to use inert-gas-shielded welding processes or flux to reduce oxide and nitrogen inclusions.

Where possible, the parts to be welded should be machined with a burn-down ring for the highest joint reliability, as shown in Fig. 3.6. The main point is to have two welding lips of about equal size so both parts are heated reasonably uniformly. A good welder can weld two parts of dissimilar size, but it pays to make a shop-friendly design where you are assured of a reliable joint. It also helps weld uniformity if the welds are cylindrical so the parts can be rotated in a fixture under the welding electrode, as opposed to requiring the welder to manually move the welding tip around the part.

3.3.3 BRAZING

Brazing is used when a lower joining temperature is needed than for welding, or in tight situations where access to the surfaces for welding is not available. For stainless steel, brazing also results in a nonferromagnetic joint (unlike welded stainless joints), and so brazing is better suited for high-magnetic-field apparatus.

In brazing, the pieces to be joined are held together in a jig. Brazing metal is applied around the joint in the form of a wire, foil, powder, or paste. The brazing metal is then melted by a furnace or radio-frequency induction heating, and it fills the joint. For a good braze, the parts must be fitted with fairly close tolerances, usually about 0.02–0.07 mm (~0.001–0.003 in.), so the molten brazing material wicks into the gap by capillary action. Special gap fillers can also be used when larger clearances, up to 1.5 mm, are needed.

Brazing fillers are selected to melt at a lower temperature than the base materials being brazed, and ideally they form an alloy with the base material that has a higher remelt temperature than the brazing material alone. This makes it possible to perform subsequent brazing operations. Brazing materials are usually alloys of silver, gold, copper, palladium, and nickel. Nickel alloys are especially well suited to joining stainless-steel parts.

Brazing can be carried out in air if a flux is used (so-called *hard* silver-soldering, which is described in the next section), or in a controlled atmosphere or vacuum furnace without the need for flux. Since it results in a very clean, nonporous joint, vacuum brazing is preferable for ultrahigh-vacuum joints. This technique usually requires a high-vacuum furnace, less than

$\sim 10^{-3}$ Pa, that is capable of reaching temperatures up to about 1400°C. An argon atmosphere is commonly used when vacuum brazing is difficult. The argon eliminates contaminants and inhibits out-gassing. Brazing is sometimes also carried out in hydrogen, which results in a very clean joint; however, beware of these beautiful joints, because sometimes hydrogen embrittlement of the base material can occur, as well as porosity [hydrogen brazing does not work, for example, with ETP (UNS C10300) copper, which contains too much oxygen].

Appendix A3.6 lists several common material combinations along with braze materials that work well for each combination. When brazing stainless steel, the oxide layer on the stainless surface decomposes only above 950°C, so higher-melting temperature brazing materials must be used, such as the gold compounds listed in the upper group in Appendix A3.6. For stainless-to-copper joints, the 35%Au–65%Cu compound works very well, but be aware that it requires temperatures slightly above 1010°C, and copper melts at 1083°C, so the furnace temperature needs to be controlled fairly precisely. Stainless steel can also be brazed at lower temperatures by using the other braze materials listed in the top group of Appendix A3.6. If need be, brazing temperatures lower than 950°C can be used if the stainless-steel parts are first plated with copper or nickel, but sometimes the plating layers delaminate.

3.3.4 SOLDERING

This is the most common and easiest method of joining metals. Soldering is an art all experimentalists should learn well, whereas welding and brazing are usually left to specialists.

Not much is needed in the way of equipment, and the parts do not need to be heated to high temperature. Since joining temperatures are low, soldering needs to be done only following all the other joining techniques in cryostat assembly. Again, remember that solder is not appropriate for ultrahigh-vacuum joints, because the relatively high temperature (up to 450°C) of the final degassing vacuum bake exceeds soft-solder melting temperatures. However, soldering works perfectly well for most cryogenic vacuum spaces.

Techniques for soldering are most easily learned by getting someone to show you how to do it. Choosing the right solder and flux for the job, however, is something it pays to read about. There are three broad classes of solder, depending on their melting temperatures:

(1) high-temperature *hard solders*, also called *silver-solder* because of their silver content;

(2) low-temperature lead- and tin-based *soft-solders*;

(3) very-low-temperature bismuth-based solders.

Appendix A3.7 presents general information on composition, melting temperature, and fluxes for each class, along with an extra class of "specialty" solders for potable water, aluminum, thin noble-metal films, and low thermoelectric voltage. Solder flux is generally needed to remove the oxide layer on the materials being soldered in order to get the solder to wet the surface. The required flux depends on the materials being soldered (described below and in Appendix A3.8). Use the mildest flux that will do the job.

Preclean the part to be soldered with steel wool, sandpaper, or a file. Whenever possible, "pre-tin" the parts before soldering them together. That is, heat the individual parts above the solder's melting temperature, and coat them with flux and a film of solder. This ensures that

they are evenly wet with solder before making the actual joint. Do not overheat, or the surface can burn and become difficult to solder. It helps during heating to keep testing the temperature of the part by using the solder as a fixed-point thermometer. That is, when the part readily melts the solder, it is up to temperature and does not need to be heated further.

The minimum joint clearance gives the strongest joint. This can be obtained by heating "pretinned" parts above the solder's melting temperature, pressing them together face-to-face with moderate (hand) pressure, removing the heat, and holding or clamping them together for a few seconds until the solder solidifies. *Fitted* parts should be machined with the minimum spacing needed to enable solder to flow into the gap, about 0.05–0.13 mm (0.002–0.005 in.). The gap should not be greater than about 0.15 mm (0.006 in.), at which point the joint starts to weaken.

My preferences for solder materials follow (with composition given in weight percent):

- *For the early stages of apparatus construction (especially where structural parts will be subjected later to soft-solder temperatures)*: hard-silver-solder with Safety Silv #56 (56%Ag–22%Cu–17%Zn–5%Sn), flux coated, cadmium-free silver-solder, which is one of the best free-flowing, ductile silver-solders (T_{melt} = 618–649°C).
- *For most mechanical joints*: 96%Sn–4%Ag eutectic solder (T_{melt} = 221°C). It is easy to solder and has relatively high strength. This solder is sometimes referred to as "soft silver-solder." (Because it also stays bright and shiny, a common trade name is Staybrite™.)
- *For electrical wiring*: 63%Sn–37%Pb or 63%Sn–36.65%Pb–0.35%Sb eutectic solder (T_{melt} = 183°C); or 93%Pb–5.2%Sn–1.8%Ag for a higher-melting-temperature solder (T_{melt} = 299°C). The antimony in the alternative lower T_{melt} solder minimizes embrittlement and cracking, a potential problem that can occur in high-tin solders after repeated thermal cycling to cryogenic temperatures. *Be sure to use pure rosin flux with all electronic connections*; see the tip in the next subsection. (Supplier information is given in Appendix A1.7 under Soldering materials.)

Specialty solders:

- *For soldering aluminum:* 95%Zn–5%Al eutectic solder (T_{melt} = 382°C).
- *For low thermoelectric voltage joints*: 97%In–3%Ag eutectic solder (T_{melt} = 143°C); this solder has a thermoelectric power much closer to that of copper than soft-solders containing lead or tin (see Appendix A4.6b).
- *For soldering thin noble-metal films:* 97%In–3%Ag eutectic solder (T_{melt} = 143°C), which results in much less leaching and dissolution of these thin films than soft-solders containing tin.

Avoid the weak, brittle, low-melting-temperature bismuth-based solders if possible (unless needed for making vacuum seals around heat-sensitive samples). If a low-melting-temperature solder is needed, In–48%Sn (T_{melt} = 118°C) is more robust and wets better than many bismuth-based solders.

Figure 3.7 shows the thermal conductivity of several solder materials. Generally, they behave like most metal alloys, such as brass or Constantan, with a thermal conductivity in the range of 1 W/(mK) to 100 W/(mK). Joints made of solder generally have higher thermal conductance than pressure, grease, or adhesive joints, as shown in Fig. 2.7. Very high thermal conductance can be achieved by joining parts with pure indium solder, as shown in Fig. 2.8.

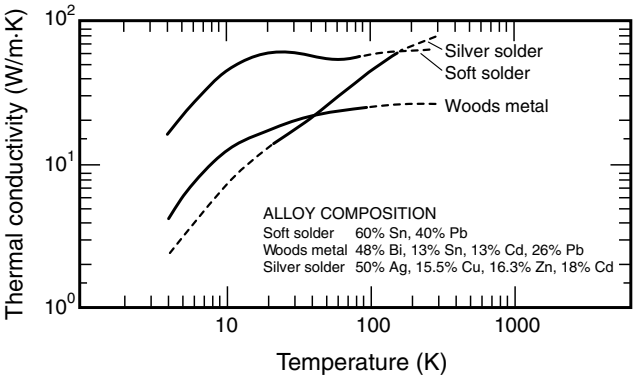

Fig. 3.7 Bulk thermal conductivity of common solder materials. Dotted lines indicate extrapolated values (from Johnson 1960 and D. H. J. Goodall 1970; soft-solder, R. Berman et al. 1955; and silver-solder, Powell and Coffin 1954).

➔ When soft-soldering stainless steel with a torch, beware that the stainless has low thermal conductivity, so it is easy to develop hot spots. Consequently, *a gas torch should not be used directly on stainless steel*. However, if the part being joined to stainless steel has good thermal conductivity, such as copper or brass, it is fine to heat the high-conductivity part with a torch, which, in turn, *uniformly* heats the stainless steel.

If neither material to be joined has a good thermal conductivity, there is no choice but to pre-tin the individual stainless-steel parts with solder applied with a soldering iron having a large copper tip, or by heating the stainless steel with a large piece of copper on a hot plate. The pre-tinned parts are then placed in contact and joined by heating them again with a large soldering iron.

Highly corrosive solder flux (containing hydrochloric acid) must be used to get solder to pre-tin or "wet" stainless steel. Be sure to thoroughly wash away the acid flux after soldering. (See next section on corrosion from flux residue.)

The right flux

To cut through the tough oxide layer on most metallic surfaces, a heat-activated soldering flux is usually used to clean the surface during soldering to enable the solder to wet the metal. Appendixes A3.7 and A3.8 list fluxes for various metals and alloys. Use noncorrosive *pure* rosin flux whenever possible (not "activated" rosin flux) for easy-to-solder metals such as copper and copper alloys, and especially for soldering copper electronic circuits. After soldering, clean away the flux with isopropanol.

A mildly corrosive flux, such as ZnCl flux or "activated" paste flux (which contains chlorides), usually works for harder to solder metals, as listed in Appendix A3.8. After soldering, however, *wash away the flux* with water or isopropanol.

➔ *Bête-noire of soldering: corrosion caused by flux residue*. Unfortunately, not all the chloride flux can be washed away, since tiny flux globules are entrapped inside the solder as it solidifies. After several years, the chlorides diffuse along grain boundaries to the surface and react with ambient moisture to form HCl, which will eventually eat through electronic circuits and perforate thin (0.1 mm) stainless-steel tubing. For *thin-walled* stainless steel, weld or braze the parts instead of soldering them.

For electronics with *fine wiring and films*, use pure rosin-core solder or "unactivated" rosin dissolved in alcohol. With such thin materials, do not use the "activated" rosin flux that contains chlorides (the type sometimes referred to as RA or RMA or supplied in small tin cans), or "mild" zinc-chloride flux, or any other kind of flux containing chlorides.

For stainless-steel parts (that are not thin), a highly corrosive acid flux such as HCl must be used to cut through the tough surface oxide layer. After soldering, it is best to wash away the acid flux with water. Then be sure to neutralize the acidity by rinsing the area with a weak base solution of baking soda, followed by rinsing with hot water or an ammonia/detergent/water solution.

Beryllium and titanium cannot be soft-soldered, except perhaps with pure (but very weak) indium, which will wet almost anything. The best solution for titanium is to vacuum-deposit palladium onto it (it sticks nicely), and then it solders easily.

For hard (silver) solder, use a fluoride or boric acid flux. It should be washed off with hot water after soldering.

Superconducting properties of solder

Many common solder materials become superconducting at low (liquid-helium) temperature. Measurement artifacts can occur at the critical temperature or critical magnetic field of the solder. For example, the solder used to attach a sample-stage can form a superconducting ring that distorts applied dc magnetic fields. Fortunately, in high-field experiments (>1 T), the superconducting properties of solder usually play no role because the critical field for most solders is only a few tenths of a tesla, so the magnetic field suppresses the superconducting transition throughout the experiment. However, beware of superconducting solder artifacts at low fields in swept-field or variable-temperature experiments, especially those arising at soldered voltage taps in transport measurements (described in Sec. 4.5.3). Superconducting critical temperatures and critical fields for a few common soldering materials are listed in Appendix A3.9.

Low-melting-temperature solders

Low-melting-temperature solders ($\leq 100°C$) can sometimes be weak and brittle if they contain bismuth. However, these solders are quite useful when soldering temperatures must be kept very low, as in soldering vacuum cans around sensitive samples. With these solders, the mechanical design of the solder joint is especially important. Most of these bismuth-based solders, listed in Appendix A3.7 under the category "Very low-melting-temperature solders,"

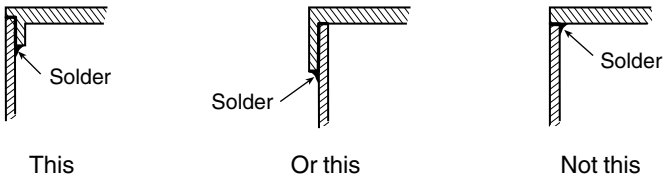

Fig. 3.8 Design joints so they have large soldered-surface areas for mechanical strength, especially with joints subjected to bending stress and soldered with low-melting-temperature ($\lesssim$100°C) bismuth-based alloys.

expand on solidification and continue to change for several hours after soldering. Interlocking joints or seals are much stronger than butt joints when subjected to bending stress, as illustrated in Fig. 3.8. In fact, always avoid butt joints for any kind of soldering.

Parts made of copper or brass can be soldered fairly well with low-melting-temperature solders, but the pieces must be pre-tinned ahead of time with a soldering iron and zinc chloride flux that is heated to a temperature high enough to activate the flux ($\gtrsim$ 300°C).

Soldering aluminum—a tough case

Soldering aluminum has three strikes against it (but it is not out): (1) aluminum has a tough, tenacious, refractory oxide on its surface that makes solder-wetting difficult, (2) aluminum solders generally flow poorly, and (3) aluminum reacts with Pb–Sn solders and corrosion forms at the interface. Problem 1 is solved by using reactive fluxes containing zinc chloride, tin chloride, or both. They must be heated to their reaction temperature (280–380°C) to work, however. Problem 2 requires special techniques to produce flow into certain types of joints. Problem 3 is resolved by using special solders, such as Sn–Zn or Zn–Al alloys (see the category "Specialty solders" in Appendix A3.7). Where possible, it is better to avoid soldering aluminum and use welding instead.

3.3.5 STICKY STUFF

In constructing cryogenic apparatus, there seems to be an endless need for sticky stuff: tapes, adhesives, and glues that stick, hold, and do not crack on cooling. The applications range from holding wires in place, to vacuum seals, to providing a protective overwrap for wire coils.

Many tapes used at room temperature, especially those with a resin or plastic base, become brittle and crack when cooled. However, several tape materials are quite durable at low temperature and survive thermal cycling quite well. Some tapes, such as common masking tape, actually stick better after several thermal cycles, but become brittle and difficult to remove later.

It is fairly simple to try whatever you have on hand by taping or gluing two pieces of copper together and dipping the joint in liquid nitrogen a few times to see whether it survives thermal cycling. Many common household glues, such as model airplane cement, work surprisingly well at low temperature. Others, such as "5 minute" epoxy, crack and debond on cooling to cryogenic temperatures.

A representative listing of epoxies, tapes, glues, and other adhesives that work at low temperature is given in Appendix A3.10, along with comments on their properties and application. (Epoxy vacuum seals for cryogenic *wiring* are described in Chapter 4, Sec. 4.7.2.)

3.4 Construction example for a basic dipper probe

To illustrate construction philosophy and procedure, we consider the design and fabrication of the general-purpose dipper probe shown in Figs 1.6 and 1.7. Although this is a relatively basic apparatus, the same approach and techniques apply well to the substructures of far more complex rigs. The approach described in the introduction to this chapter—starting with the sample-support structure and then working outward until ultimately reaching the connector box at the top of the probe—works well both for the design and for the actual machining and assembly of parts.

To give an overview of the construction process, we first summarize the generic construction steps (including references to wiring and thermometer installation, which will be described more thoroughly in later chapters). Following this summary, we apply the procedure to the construction of a dipper probe.

1. *Sketch the concept of the design*: Generally, I like to start with a simple sketch of the sample holder, laying out the mechanical support and electrical leads. It helps at this early stage of the process to aim for a design that can be fairly easily *disassembled* in case a part needs to be altered later. This applies, for example, to the method of joining the electrical connector head in Fig. 1.6 to the top of the support tube, the attachment of the sample holder to the bottom of the probe, the scheme for anchoring wire heat sinks to the sample holder, and the method used to attach radiation shields to the neck of the probe. For instance, in a larger rig, such as that shown in Fig. 1.14, the radiation baffles can be clamped (instead of soldered) to the probe's stainless support tubes so that they can be easily removed later if extra holes need to be machined through them for additional support tubes (or extra holes can be machined through the shields in the first place to accommodate additional tubes if needed later).

After sketching the main parts, I like to design an effective scheme for thermally anchoring the sample to the holder, especially if the sample will not be immersed directly in a liquid cryogen (Chapter 7). Then choose a thermometer (Chapter 5) and decide on the relative location of the thermometer, sample, and heater (see examples shown in Sec. 4.4). The main goal is to provide a uniform sample temperature and measure it accurately. This also includes heat-sinking the instrumentation leads (Sec. 4.4). If high-current leads are needed (Sec. 4.9), the design may center on accommodating these rather large leads, along with a construction scheme to make the leads accessible and demountable. If mechanical tests are being conducted, then the loading mechanism is usually a central issue.

2. *Select materials for the job*: Guidelines are given earlier in this chapter; detailed properties of materials are given in Chapter 6 and tabulated in the appendixes to Chapter 6.

3. *Size the parts*: For example, the wall thickness of the main support structure must minimize heat transfer (Chapter 2), yet provide sufficient structural support.

4. *Make the simplest construction drawings* that will get the job done, and have them reviewed by the machinists.

Get up-front feedback from colleagues; rarely will a design not be improved. And especially, show the design to the head of the machine shop before metal gets cut! Your rig will work far better (and the parts will be ready sooner).

5. *Assemble the parts mechanically*: To ensure the rig does not fall apart during construction, start with the highest temperature joining techniques first (welds, if used) and proceed down in temperature through brazing, hard-solder, and then soft-solder. Check any vacuum spaces for leaks (Sec. 3.7.3).

6. *Wire the rig*, including installation of thermometers.

7. *Give the apparatus its notorious "first run."* This is perhaps the most important part of the whole process. It calls for persistence and creativity to fix problems. (An apparatus that works the first time is definitely cause for celebration, since it is rare.) Run reality checks on the data and calibrate the apparatus.

To illustrate the process, we now apply the first five steps to the construction of the basic dipper probe shown in Fig. 1.7 (step 6 on wiring and thermometer installation is treated in Chapters 4 and 5, respectively; step 7 we learn from experience):

1. *Sketch design*: For a sketch of the sample holder, the schematic layout shown in Fig. 4.2 (sample, heat sinks, and thermometer) is a good place to start. In this example, the copper sample holder or platform is round, and is turned to fit into the end of support tube, where it will be soldered in place. The instrumentation leads are run down the middle of the support tube, through a hole in the top of the sample support, before they are attached to copper heat-sink posts, and eventually to the thermometer and sample.

The support tube that runs from the top of the dewar to the sample holder is a simple stainless-steel tube that passes through the O-ring vacuum coupling at the top of the dewar (or warming chamber) and is then joined to a connector box at room temperature, as illustrated in Fig. 1.6. If at all possible, the sample holder at the bottom of the tube should be of the same diameter as the support tube or smaller, so it will fit through the slip O-ring seal at the top of the dewar for easy removal. (With a larger sample holder on the bottom of the support tube, it would still be possible to use an O-ring seal around the support tube, but the parts for the O-ring seal would have to be slipped onto the support tube *before* the sample holder and connector head are attached to the tube ends.)

The room-temperature connector box can be permanently attached to the top of the support tube with solder, or a flange can be soldered to the top of the support tube onto which the connector box is then screwed or clamped (a more detailed description of different designs for connector boxes is given in Sec. 4.7.1). The screwed-flange option allows for flexibility if there is a design change, or, as has happened to me, if the entire rig must be rewired. Demountability can also be built into the sample holder attachment scheme at the bottom of the support tube by using a screw assembly or set screws.

2. *Select materials*: We start with the sample holder material, which for many applications must have a high thermal conductivity to ensure uniformity of the sample temperature. We choose ETP copper (UNS C10300) because it is easy to find commercially and has a high

thermal conductivity at low temperature compared with other commonly available forms of copper (see Appendix A3.1). High-purity (99.99% pure) copper would provide even greater thermal conductivity, but it is expensive and not so readily available.

However, if we were going to electrically test samples only by immersing them directly in liquid helium or liquid nitrogen, the sample holder would not need to have high thermal conductivity. In this case, it would be simpler to use a (thin-walled) fiberglass–epoxy composite (G-10) tube for the sample holder. The liquid cryogen provides the needed temperature uniformity for the sample, and the use of an insulating material such as G-10 would eliminate the need to electrically insulate the sample from a holder made of copper.

For the main support tube, we prefer a thin-walled stainless-steel tube rather than a fiberglass–epoxy tube such as G-10 or G-11, because stainless steel

(1) is readily available as very thin-walled tubing, down to a wall thickness of 0.1 mm (0.004 in.) or smaller;

(2) is stronger than fiberglass–epoxy composites, and therefore we can use a tube with a smaller cross-sectional area; the thinner tube-wall thickness also keeps the thermal conductance down the stainless tube comparable to that of a fiberglass–epoxy tube [even though the thermal conductivity of stainless-steel is somewhat higher than that of fiberglass–epoxy composites (Fig. 3.1)];

(3) consumes less liquid refrigerant when being cooled; stainless steel has a heat capacity per unit volume about the same as G-10 over most of the cryogenic temperature range (compare stainless steel vs. epoxy in Fig. 3.3 from room temperature to ~20 K), and therefore the smaller volume of stainless-steel material reduces the overall heat capacity of the support tube;

(4) thermally cycles much faster than G-10 because of its reduced overall heat capacity and higher thermal conductivity (this is discussed in more detail in Sec. 6.1 on thermal diffusivity).

If the rig were more complex and incorporated vacuum spaces (e.g. to provide thermal isolation or to protect reactive samples), then the construction materials should also be chosen to be compatible with good vacuum design, as described in detail in Sec. 3.7.

3. *Size the parts*:

Heat-leak sizing—The size and wall thickness of the stainless-steel support tube require a little thought. Looking at Appendix A3.2, we see that a stainless-steel tube 2.5 cm (1 in.) in diameter with a wall thickness of 0.5 mm (0.020 in.) would have a heat leak over an ~100 cm length between room temperature and 4 K of about 0.12 W [where we have scaled up the result listed for a 0.15 mm (0.006 in.) wall thickness to 0.5 mm (0.020 in.), and the length from 10 to 100 cm]. This is an acceptable heat leak (see Sec. 2.9.1), and the wall thickness is great enough that the tube will not be too easily dented.

Next we consider the cross-sectional area of the ETP-copper sample holder that will be adequate for variable-temperature testing in the vapor space above a cryogenic liquid, or in a gas-filled tube. The main requirement is to provide a sample holder with a cross section along its length that is large enough so that the sample, thermometer, and heater are all

thermally well connected. An example calculation for sizing an ETP-copper sample holder for this case was given in Sec. 2.9.2, where we found a cross-sectional area of roughly 2 cm^2 to be adequate.

Mechanical sizing—If we were making mechanical measurements in which the main support tube were under mechanical compression, the concern would be that the tube not buckle under the load. The calculation of the tube size in this case is treated in Sec. 3.5.2. Sizing of parts to withstand vacuum and pressure loading is also a common design consideration, and it is treated in Sec. 3.5.4.

4. *Construction drawings*: For such a simple probe as this, the construction drawings can be made by hand or with a relatively modest computer drafting program, depending on the simplest drawings that your shop will accept. For more complex rigs that have to be constructed commercially, or for computer-numerical-control (CNC) machining, a good set of computer drawings is essential. The same may be true for the critical parts of a simple rig.

For the dipper probe in Fig. 1.6, we used a combination of hand sketches for the tube, top flange, and top electrical connector box, and an AutoCAD drawing for the sample holder and the details of a positioning spacer frame for aligning the sample and contact pins (shown schematically in Sec. 7.4.1).

5. *Mechanical assembly*: No welding or brazing was used in assembling this probe, but if we had, we probably would have used electric-arc TIG welding for the stainless-to-stainless joints (because it avoids oxidation and porosity) and brazing for the copper-to-stainless joints (probably with 35%Au–65%Cu brazing compound in an argon atmosphere to produce high-quality welds). Because it is simple, we instead used solder to join the copper sample holder to the bottom of the support tube, as well as to attach the vacuum-seal flange to the top of the support tube (see Sec. 4.7.1). We needed joints that would support only rough-to-medium vacuum levels in order to pump on the cryogenic bath to lower its temperature, and for such joints, soldering works quite well. In soldering the parts onto the ends of the stainless-steel tube, it helps to leave a small lip when turning these pieces so the support tube bottoms against the lip and automatically positions itself during soldering (as shown, for example, in Fig. 3.6). Since the support tube is stainless steel, we used acid solder flux (washed away after soldering), and applied the soldering iron to the copper sample holder (when making the bottom joint) and to the brass flange (for the top joint), rather than to the stainless steel to ensure uniform heating of the stainless tube.

We finished the mechanical assembly by bolting the connector box to the top flange. Copper heat-sink posts, shown in Fig. 3.5, were screwed to the sample holder (with brass screws so the joints tightened on cool-down). Then we electrically wired the rig and added thermometers, using techniques described in Chapters 4 and 5.

Much more complex rigs follow the same procedure, except that they are often designed around some special requirement. The fastest route to learning techniques for special features is to talk with those who have constructed similar apparatus. They usually love to explain it. Also, ask for citations to good instrumentation articles, as well as recommendations to other experimentalists with experience in that specialty. If yours is a first-of-a-kind apparatus, break it into subsystems and just start trying out designs one system at a time. The rig may be unique, but it is surprising how often the overall cryogenic design and construction process are similar among different cryostats.

3.5 Sizing of parts for mechanical strength

Often an apparatus must support vacuum pressure, or tolerate the magnetic forces associated with large-scale superconductor critical-current testing, or withstand the high loads of a mechanical measurement. In such cases, we need to calculate the size of parts on the basis of *mechanical* considerations. Four general guidelines are recommended when sizing parts for mechanical strength.

1. Dimension critical parts so the maximum expected stress is kept to less than about half the material's yield strength (Sec. 3.5.1).
2. Keep support-tube walls thick enough to avoid buckling if the tubes are subjected to compression (Euler buckling criterion, Sec. 3.5.2).
3. Limit flexure to an acceptable level (deflection formulas for beams and circular plates, Sec. 3.5.3).
4. Size the thickness of cryostat walls so they can withstand the maximum loading they will experience from pressurization or evacuation (Sec. 3.5.4).

Many other calculations can be done, but these four guidelines have served me well over the years to get the size of parts approximately right (from a mechanical standpoint), without over-designing a one-of-a-kind rig.

3.5.1 YIELD STRENGTH

Generally we want to make the parts large enough that they do not start to deform plastically under load. This usually results in structural failure. The load F_y at which a part will yield is given by

$$F_y \equiv \sigma_y A,$$

where σ_y is the yield strength of the material and A is the cross-sectional area of the part along its length. A conservative (but common) rule of thumb is to use a factor-of-two safety margin, wherein a part is sized so that the maximum stress it experiences is less than half its yield strength. For less critical components, the design stress can be pushed to higher levels, up to 70–80% of the yield strength, depending on your comfort level.

Example: Suppose we are designing a small mechanical test apparatus to apply tensile loads up to 1000 N to a test specimen immersed in liquid helium, as shown in Fig. 3.9. We want to determine the diameter to use for the pull rod to allow a safety margin of a factor of two. For this particular example, let us assume that the tests will be carried out in a magnetic field.

We would like to use AISI 316 stainless steel for the pull rod because its fracture toughness is high (Sec. 6.6.1), but unfortunately, like most stainless steels, AISI 316 has a magnetic susceptibility that

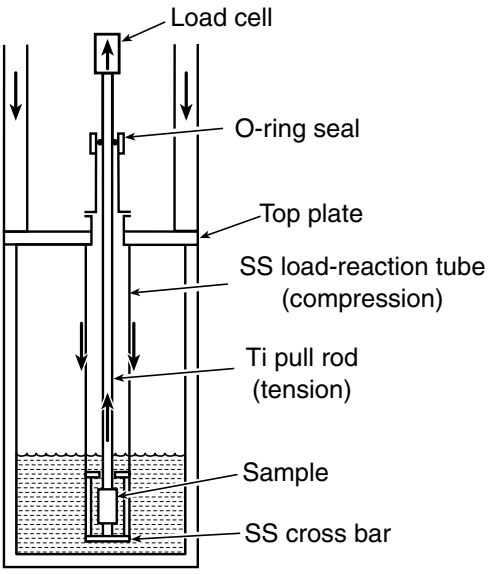

Fig. 3.9 Schematic illustration of a mechanical test apparatus, showing titanium pull rod and stainless-steel (SS) load-reaction tube.

will subject it to significant magnetic forces. So we settle for a commercially pure, cold-drawn Ti or Ti–6%Al–4%V because its magnetic susceptibility is very low [about three orders of magnitude less than that of stainless steel at 4.2 K (Appendix A6.8b)]. The yield strength of commercial, unalloyed titanium is about 500 MPa at room temperature (Sec. 6.6.1), rising to over 1 GPa at low temperature (Ti–6%Al–4%V would be stronger, but more susceptible to brittle fracture at higher stress levels). This application is a "weak-link" situation (as with the strength of a chain), so, although there is a temperature gradient along the rod, we use the lower room-temperature value for σ_y.

To provide a factor-of-two safety margin, we size our pull rod for twice the expected load. This gives a minimum cross-sectional area for the pull rod of

$$A_{\min} = F_y / \sigma_y = 2000\,\text{N} / 500\,\text{MPa} = 4 \times 10^{-6}\,\text{m}^2,$$

which for a solid rod would correspond to a diameter of 2.2 mm. We might want to size the rod larger to reduce the mechanical compliance of the rig, but this represents a minimum diameter for mechanical safety.

3.5.2 EULER BUCKLING CRITERION

Buckling comes into play in the design of long cryostat parts that will be loaded in compression. For example, in the simple mechanical testing apparatus of Fig. 3.9, the tensile load on the sample must be balanced by an opposing compressive load on the stainless-steel load-reaction tube. On the one hand, we want to make this reaction tube as thin as possible to minimize the heat leak into the cryostat, but, on the other hand, not so thin that it will buckle under compression. Usually, the buckling stress for compression is considerably more limiting than the tensile yield strength.

The buckling limit can be determined from the Euler formula for long tubes (e.g. Beer and Johnston 1981):

$$F_{cr} = C\,\pi^2\,E\,I_m / L^2, \quad \text{Euler buckling criterion} \tag{3.1}$$

where F_{cr} is the critical load for buckling; the dimensionless constant $C = 0.25$ (assuming one end of the tube is fixed and the other free); E is the Young's modulus of elasticity; L is the length of the tube, and I_m is the moment of inertia of a tube (about its center axis) having an outer diameter (D_o) and an inside diameter (D_i), given by

$$I_m = \pi\,(D_o^4 - D_i^4) / 64. \tag{3.2}$$

For *thin*-walled tubes of wall thickness d and diameter D (i.e. $d \ll D$), Eq. (3.2) reduces to approximately

$$I_m \cong \pi\,D^3\,d / 8. \tag{3.3}$$

Substituting Eq. (3.3) into Eq. (3.1), we see that the critical buckling load F_{cr} scales as the diameter cubed and inversely as the length squared.

Here we see the trade-off between heat flux and mechanical constraints. Choosing the dimensions of the compression tube is critical—if it is too long and thin, the tube collapses under compression; if it is too short and fat, its thermal conductance makes the rig a liquid-helium hog.

Example: Consider again the example cryostat design shown in Fig. 3.9 for testing relatively small loads. We want to size the load tube so that it will not buckle under the maximum compressive load of 1000 N. Suppose the tube is 2.5 cm in diameter and 75 cm long. We want to calculate the minimum tube-wall thickness d to avoid buckling failure.

We use an AISI 316 stainless steel for the tube material, since we are not especially concerned about magnetic forces on this static tube (as opposed to the *movable* pull rod). From Appendix A6.10 we see that the Young's modulus for AISI 316 stainless steel is 195 GPa at room temperature, and it increases by less than 10% on cooling to cryogenic temperatures. Inserting these values into Eqs (3.1) and (3.3), we find that the minimum wall thickness to prevent buckling is

$$\begin{aligned} d &= 8\,F_{cr}\,L^2\,[C\,\pi^3\,E\,D^3]^{-1} \\ &= 8\,(2000\text{ N})(0.75\text{ m})^2\,[0.25\,\pi^3\,(195\text{ GPa})(0.025\text{ m})^3]^{-1} = 0.4\text{ mm}. \end{aligned} \tag{3.4}$$

Since buckling would be fatal, we have again used a safety margin of a factor of two in the calculation, taking F_{cr} to be 2000 N. This also gives us a little more wall thickness to prevent denting and local buckling.

From Appendix A3.2, we see that such a tube will have a maximum heat leak of about 330 mW (assuming that the temperature gradient along the support tube occurs over a relatively short length of about 30 cm). From Eq. (2.17), we find that this heat leakage generates a maximum liquid-helium boil-off rate of about 0.46 L/h. This rate of liquid-helium consumption could be significantly reduced by venting the cold helium vapor up through the reaction tube, thereby utilizing the enthalpy of the cold gas to reduce the mean temperature of the tube (Appendix A1.6a).

Often such mechanical test rigs need to be designed to handle loads much higher than that given in this example. Shortening the compression tube and choosing a larger diameter would help meet the buckling criterion and reduce the liquid cryogen loss. This is because we see from Eq. (3.4) that F_{cr} scales as $D^3\,d$, whereas the heat leak scales as the tube's cross-sectional area $\pi\,D\,d$, so the ratio of critical buckling load to heat leak improves as the square of the tube diameter D. We eventually run into trouble playing this game, however, because as we scale up D, the reduced requirement on tube thickness d can become so small that the tube will dent easily and buckle locally.

3.5.3 DEFLECTION OF BEAMS AND PLATES

To limit flexure of a part to an acceptable level, we use standard deflection formulas for beams and plates. There are so many cases, it is beyond the scope of this book to list them all here. However, with just a few formulas, we can at least make a reasonable estimate of part size for most situations. An extensive tabulation of formulas for the many forms of *beam* deflection is given in Table 3, p. 96 of Roark and Young (1975). A similar tabulation of formulas for deflection of *circular plates* is given in Table 24 of the same text (p. 332, Roark and Young 1975).

A situation that often arises is that of a cantilever beam, as shown by the drawings in Fig. 3.10(a), where the left end of the beam is free, and the right end, fixed. In this case, the deflection y at the free end of the bar is given by the following equation (from Table 3, p. 96 of Roark and Young 1975):

$$y = -W L^3 / (3\,E\,I_m), \quad \text{Deflection of a cantilever beam} \tag{3.5}$$

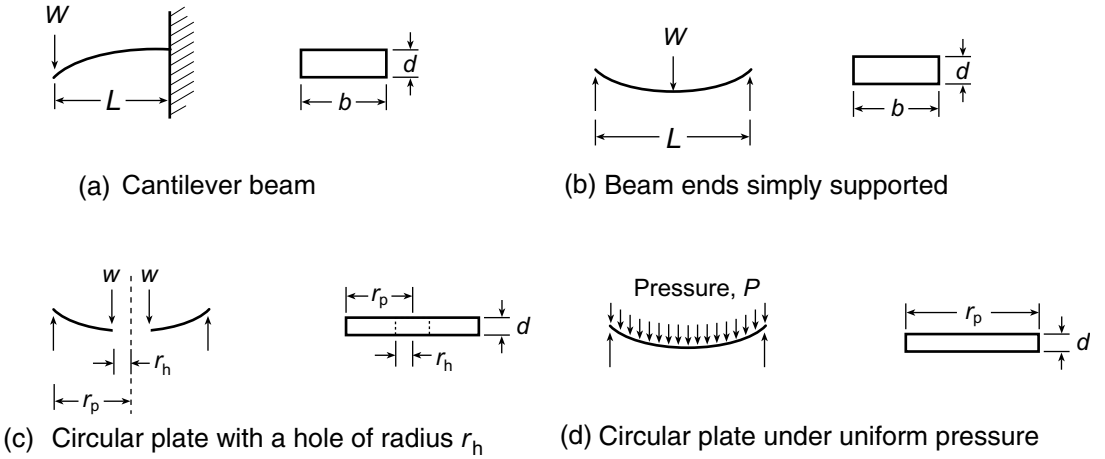

Fig. 3.10 Geometry of beams and circular plate corresponding to the deflection formulas given by Eqs (3.5) through (3.10). Deflection sketches are shown on the left and the *cross-sectional* dimensions of the beams and circular plate are defined on the right of each subfigure.

where the negative sign indicates a downward deflection, W is the total load applied at the end of the beam, E is the Young's modulus of the beam material, L is the length of the beam, and I_m is the area moment of inertia about the centroidal axis of the beam cross section. For a rectangular bar of width b and thickness d, I_m is given by

$$I_m = b\,d^3 / 12 \tag{3.6}$$

(from Table 1, p. 64 of Roark and Young 1975).

When *both* ends of the beam are simply supported and the load is applied at the middle of the beam [as shown by Fig. 3.10(b)], the deflection at the center of the bar is given by

$$y = -W L^3 / (48\,E\,I_m), \quad \text{Deflection of beam simply supported at both ends} \tag{3.7}$$

(from Table 3, p. 97 of Roark and Young 1975).

Example: Using the same example of the mechanical test apparatus shown in Fig. 3.9 and a load of 1000 N, we want to determine the thickness d of the stainless-steel cross bar at the bottom of the apparatus required to keep the deflection at the middle of the bar less than 0.02 mm. (This is a fairly stringent deflection limit, but in mechanical testing, such a small limit helps keep the overall compliance of the rig at an acceptably low level.) Let us make the beam out of AISI 316 stainless steel and assume it has a length $L = 2.5$ cm (to match the compression load-tube diameter) and a cross-sectional width $b = 1$ cm.

To determine the required beam thickness d, we substitute Eq. (3.6) into Eq. (3.7) and solve for d:

$$\begin{aligned} d &= [W L^3 / (4\,b\,E\,y)]^{1/3} \\ &= \{(1000\text{ N})(0.025\text{ m})^3 / [4\,(0.01\text{ m})(195\text{ GPa})(2 \times 10^{-5}\text{ m})]\}^{1/3} = 4.7\text{ mm}. \end{aligned} \tag{3.8}$$

So we would probably choose to make the bar about 5 mm thick to keep the midpoint deflection to this small value (0.02 mm). Note from Eq. (3.8) that the required beam thickness d is directly proportional to the beam length L.

A similar calculation of deflection can be done for the cryostat top plate in Fig. 3.9. The mechanical situation is illustrated by Fig. 3.10(c) [except that the direction of the load is reversed from that shown in Fig. 3.10(c)]. Here we use the deflection formula for a flat circular plate of constant thickness d, plate radius r_p, and central-hole radius r_h, and assume the worst-case situation where the outer edge of the plate is simply supported and the central hole is free. Assume that the load tube subjects the plate to a uniform annular *line load* of w (units of newtons per meter of circumference) at the hold radius r_h. Then the deflection y of the plate at the hole radius is given by

$$y = K_y\,w\,r_p^{\,3} / K_p, \quad \text{Deflection of a circular plate with a central hole} \tag{3.9}$$

(from Table 24, p. 334 of Roark and Young 1975), where K_p is the plate constant

$$K_p = E\,d^3 / [12(1 - \nu^2)], \tag{3.10}$$

with E the Young's modulus of elasticity, d the plate thickness, and ν Poisson's ratio (generally about 0.3). Values of the dimensionless constant K_y to use in the circular plate deflection formula [Eq. (3.9)] depend on the ratio of the plate radius r_p to the central-hole radius r_h, and are given by (Table 24, p. 334, Roark and Young 1975):

Table 3.2 **Values of K_y for use in Eq. (3.9), giving the deflection y of a circular plate subjected to a uniform annular line load, where r_p is the plate radius and r_h is the central-hole radius.**

r_h/r_p	0.1	0.3	0.5	0.7	0.9
K_y	−0.0364	−0.1266	−0.1934	−0.1927	−0.0938

Example: For a top plate made of AISI 316 stainless steel, with a radius $r_p = 4.2$ cm (1.7 in.) and hole radius $r_h = 1.25$ cm (0.5 in.) subjected to the same 1000 N total load {corresponding to a line load $w = 1000$ N / $[(2\pi)\ (0.013\ \text{m})] = 12$ kN/m} and the same rather stringent requirement that its deflection be less than 0.02 mm, we find from Eqs (3.9) and (3.10) that we would need to make the plate at least about 7 mm thick. This thickness scales mainly with the plate radius r_p, so larger plates would need to be correspondingly thicker.

Thus, we have arrived at a mechanical design that consistently limits the flexure to the same low value at each of the main cross members (the bottom cross bar and the cryostat top plate).

3.5.4 PRESSURE AND VACUUM LOADING

For cylinders that will be subjected to pressure, the container walls and end plates need to be thick enough that the hoop stress and axial stress they experience is less than the yield strength of the material from which they are made. For a typical thin-walled cylindrical pressure vessel with radius r and wall thickness d, the hoop stress it will experience around its circumference from an internal gas pressure P is given simply by

$$\sigma_{\text{hoop}} = P\,r / d, \quad \text{Cylinder hoop stress} \tag{3.11}$$

(e.g. Higdon et al. 1985). Similarly, the axial stress it will experience along its length is

$$\sigma_{\text{axial}} = P\,r / (2\,d), \quad \text{Cylinder axial stress} \tag{3.12}$$

(e.g. Higdon et al. 1985). The cylinder wall should be thick enough that the hoop stress is kept less than about 50% of the yield strength of the material being used. Note that the hoop stress around the cylinder, Eq. (3.11), is twice the stress along the axis of the cylinder, Eq. (3.12). *Thus, a longitudinal joint running the length of the cylinder needs to be twice as strong as a transverse (or girth) joint.*

Example: Suppose we want to raise the temperature of a cryogenic bath by pressurizing our measurement dewar (Sec. 1.2). Let us assume we have a AISI 304 stainless-steel dewar with a radius of 30 cm and a wall thickness of 1.5 mm (which is close to the minimum needed for welding). How high can we safely take the pressure?

From Appendix A6.10, we use a conservative value for the yield strength of AISI 304 stainless steel, namely 240 MPa, which applies to *annealed* 304 at *room temperature* (which allows for the reduced strength of the heat-affected zone around welds). Furthermore, we take 50% of this value (120 MPa) as a safety margin. Using the more limiting expression for cylindrical hoop stress (rather than axial stress), we find from [Eq. (3.11)] that the limiting overpressure is

$$P = \sigma_{\text{hoop}}\, d / r = (120\ \text{MPa})\ (1.5 \times 10^{-3}\ \text{m}) / (0.3\ \text{m}) = 6 \times 10^5\ \text{Pa}.$$

That is an overpressure of about 6 atm. However, an overpressure of 1 atm (total pressure of 2 atm or 200 kPa for the vapor pressure vs. temperature data in Appendix A5.1, corresponding to 5.04 K for boiling liquid helium or 83.6 K for boiling liquid nitrogen) is about the limit I would be comfortable with in our laboratory, especially since gas explosions are much more dangerous than hydrostatic bursting. Also, vessels usually fail at their seams, not in the base metal, as in this calculation. Seals, connectors, and other appendages can also blow out. All of which is why I suggest limiting dewar overpressure to about 1 atm. Just make sure to design the entire dewar *system* to take the pressure, use a regulator on the dewar vent to control pressure, and equip the dewar with an emergency pressure-relief valve.

Vacuum applications are just the inverse of the above internal pressure situation, with the outside pressure trying to implode the tube, rather than explode it. The same hoop and axial stress formulas above apply, except that a more conservative safety margin should be used to limit the hoop stress to less than about 20–25% of the material's annealed yield strength because of buckling concerns. Thus, a wall thickness of about 1.5 mm for stainless steel would work for vacuum loading as well. This is not precise—but, again, the philosophy for a one-of-a-kind research apparatus is not to spend an inordinate amount of time designing but to get to a reasonable solution fairly quickly by making a conservative design estimate and trying it out. For more critical situations, precise mechanical limits are given in section 8 of the ASME Boiler and Pressure Vessel Code (1998).

For circular end plates of uniform thickness d and radius r_p, subjected to a uniform pressure P, a conservative estimate is to assume the edges are not fixed, but simply supported, as illustrated by Fig. 3.10(d). Then the bending stress σ_B at the center of the plate is given by the following equation (from Table 24, p. 363, Roark and Young 1975):

$$\begin{aligned}\sigma_B &= (3/8)\,(3 + \nu)\, P\, r_p^{\,2} / d^2 \\ &\cong 1.24\, P\, r_p^{\,2} / d^2,\end{aligned} \qquad \text{Bending stress at center of circular plate} \quad (3.13)$$

where the approximate numerical value given above was evaluated assuming the Poisson's ratio of the plate material has the typical value $\nu = 0.3$. From the standpoint of structural

failure, the main concern is to keep the bending stress σ_B less than the yield strength of the material (again, typically 50–80% of σ_y, depending on your comfort zone and the criticality of the part).

Aside from structure failure, there may be experiments where deflection or bowing of the plate is also important (especially mechanical testing experiments as described in the previous section, or experiments requiring precise optical alignment). The deflection y at the center of a circular plate simply supported at the outer circumference and subjected to uniform pressure P is given by the following equation (from Table 24, p. 363, Roark and Young 1975):

$$\begin{aligned} y &= -(3/16)(5+\nu)(1-\nu^2)(1+\nu)^{-1} P r_p^{\,4} / (E d^3) \\ &\cong -0.70\, P r_p^{\,4} / (E d^3), \end{aligned} \qquad \text{Deflection at center of circular plate} \quad (3.14)$$

where E is the Young's modulus of the plate material, and the approximate numerical value was calculated by assuming a Poisson's ratio $\nu = 0.3$.

Example: The failure criterion of Eq. (3.13) is, of course, less stringent than the flexure criterion of Eq. (3.14). For example, if we have a vacuum-chamber end plate with a fairly large radius of 30 cm made of AISI 304 stainless steel [which has a room-temperature Young's modulus of about 200 GPa and a conservative (annealed) yield strength of 240 MPa (from Appendix A6.10)], and if we assume a 50% safety margin for the yield stress, we find that the structural limit of Eq. (3.13) requires the plate thickness to be about 1 cm. However, from Eq. (3.14) we find that such a plate under vacuum loading would deflect about 3 mm at its center. To reduce the deflection to a smaller value, say, 0.1 mm for a dimensionally sensitive apparatus, we find from Eq. (3.14) that the plate thickness would need to be increased to a hefty 3 cm.

When designing bolted flanges, only a few (4–6) bolts are needed for rubber O-ring *vacuum* seals, since the vacuum uniformly applies all the force needed to compress rubber O-rings. On the other hand, for *pressure* applications with flexible O-rings, more bolts are needed, typically four bolts for very small flanges ($\lesssim$ 1 in.), and 8–12 bolts for bigger flanges. The bolts should be sized to meet the maximum load limits given in Appendix A3.4. The bolt spacing around the circumference of the flange can be determined from the hex-head sizes also listed in Appendix A3.4. For indium O-rings or Teflon™ gaskets that have little spring-back, up to 16 bolts may be needed, but more than that starts to get expensive to machine and is usually not necessary.

3.6 Mechanical motion at cryogenic temperature

Sometimes experiments require control of mechanical motion at cryogenic temperatures, such as to activate mechanical switches, align parts, rotate the test sample, or apply stress

and strain to parts. The two basic approaches to introducing mechanical motion into cryostats are:

1. Convey mechanical motion down the cryostat from room temperature (such as via rotating shafts, pull or push rods, long thin screwdrivers, and cord drives).
2. Drive the motion electrically at low temperature with a motor widget (such as a motor or piezoelectric transducer).

If there is a choice, it generally pays to go with choice #1. Why? Because it is easier to debug things at room temperature than at low temperature.

With the first approach, reliable mechanical drivers have to be designed into the cryostat from the outset, since they usually require a straight-shot access down the rig along with a dynamic seal (Sec. 3.7.4). Typically, the shaft is attached to a gear mechanism at the bottom and driven at the top, either by hand (the simplest), a room-temperature motor, or a computer-controlled stepper motor.

Small gears, screw threads, and worm gears work fine at low temperature, so long as they are *degreased*. They usually have some annoying backlash that makes them hard to adjust. However, this backlash can also be a benefit to prevent disturbing vibrations from being transmitted down the drive shaft, by setting the gear in the middle of the backlash zone.

If flexibility is needed, cords (such as in the tuner mechanism of old radios) can be used to reach odd-angle locations in the rig.

As described in Sec. 6.5.2, beware that magnetic forces acting on mechanical drives can be substantial. So when designing mechanical drives to operate in high-field magnets, choose a drive rod material that has a low magnetic susceptibility (Appendix A6.8b).

Low-temperature motors can work well, but they are prone to creating trouble. They introduce magnetic fields, dissipate power into the measurement zone, and take up valuable space.

Piezoelectric transducers are traditionally weak and subject to high-voltage breakdown. However, new mechanical actuators and linear motors based on magnetostrictive devices are being developed that work quite well at cryogenic temperatures (listed in Appendix A1.7 under Mechanical actuators).

For all cryogenic moving parts, whether mechanically or electrically driven, beware of the "dastardly frozen-air film" (see the tip in Sec. 1.5.1).

➔ When machining parts that are supposed to slip or slide over each other, allow enough clearance. The required gap varies with the type of fit desired and the diameter of the part. A rough guide is given in Appendix A3.5. For more critical work, look up the gap specified in the *Machinery's Handbook* (2000).

Be sure to adjust the gap for any difference in thermal contractions between the materials from which the two parts are made.

Extra clearance is also needed for parts that might become covered with a layer of frost. For example, in the design of a measurement probe that will be repeatedly reinserted into a cold dewar, allow at least 1 mm (preferably 2 mm) clearance between the outside of the probe and the inner dewar wall to avoid potential binding and seizing.

3.7 Vacuum techniques and seals for cryogenic use

3.7.1 INTRODUCTION TO CRYOGENIC VACUUM TECHNOLOGY

Vacuum is needed in measurement cryostats for a variety of reasons. The least-demanding reason is to reduce the vapor pressure above cryogenic liquids, in order to lower the bath temperature (Fig. 1.2). For this application, only a *rough* vacuum is required. For example, a pressure of about 100 Pa will lower the temperature of liquid ^{4}He to ~1.2 K, which is about as low as we commonly go with ^{4}He cooling. Such a vacuum can be obtained fairly easily with a high-volume mechanical roughing pump. However, there are experiments where a *high* or *ultrahigh* vacuum is needed, for example, to protect reactive material surfaces or to allow charged particles (such as electrons and ions) to pass unimpeded across large distances. Figure 3.11 shows the approximate pressure range of each of these vacuum types as well as the typical vacuum requirements for a number of applications.

For the most part, cryogenic researchers are spoiled by automatic *cryopumping* (described below). As a result, the practical steps for good vacuum design at low temperatures are quite simple:

(1) Make the vacuum spaces leak tight (Sec. 3.7.3).

(2) Use good cryogenic vacuum seals (Sec. 3.7.4).

(3) Make the pumping lines big enough (Sec. 3.7.5).

(4) Be aware that glass and fiberglass dewars require regular flushing and repumping because of helium-gas permeation (see the subsection "Permeation of gases through materials" in

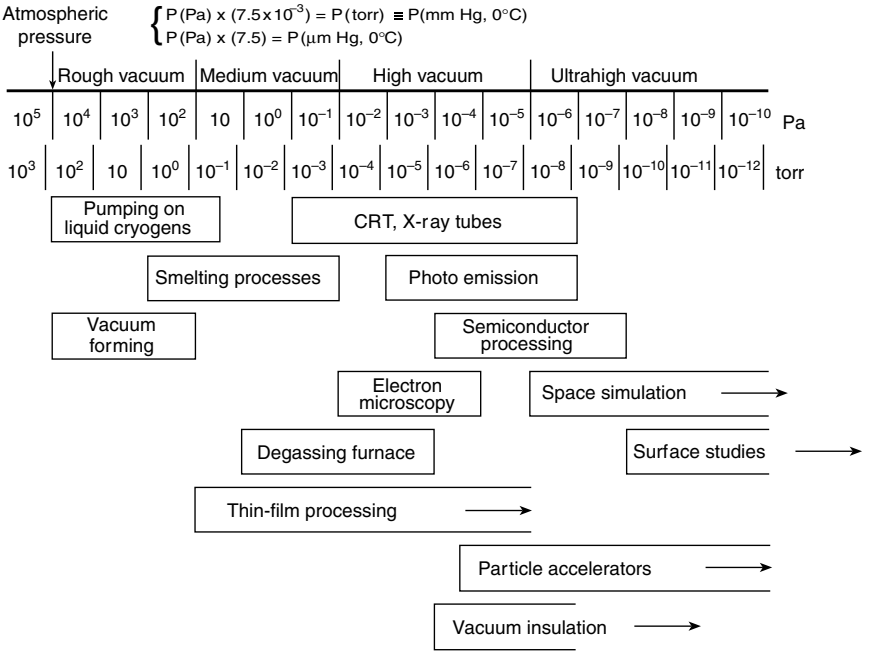

Fig. 3.11 Vacuum requirements for various applications (adapted from Weston 1985).

Sec. 3.8.3 of the addendum). Likewise, metal dewars also require occasional repumping because of hydrogen-gas permeation; repumping intervals are typically lengthened by incorporating activated charcoal or a molecular sieve in the vacuum space to getter desorbed or permeated gases.

(5) For high-vacuum (HV) or ultrahigh-vacuum (UHV) systems, more specialized techniques are required, but the basic approach is still simple (look at the introduction to HV techniques described in the addendum, Sec. 3.8)—Design the vacuum spaces so that they do not contain volatile polymers (see "Degassing of materials" subsection in Sec. 3.8.3); and read a good equipment supplier's catalogue for information about the selection of effective vacuum equipment.

3.7.2 PREPARING CRYOGENIC VACUUM SPACES

Most vacuum spaces that will be cooled to cryogenic temperatures are evacuated *before* cooling, and then sealed off. This is because at low temperatures the rate of desorption of gas trapped on the surface of materials is extremely low. In fact, cold surfaces act as a trap for any residual gas remaining in the chamber after cooling. As the apparatus is cooled, the cold surfaces act as perfect pumping surfaces where condensable gases stick. This provides a "cryopumping" action that lowers the partial pressure of most gases in the system (except gases with a low condensation temperature, such as helium, hydrogen, and neon). Surfaces cooled to liquid-helium temperatures are the best cryopumping surfaces, condensing all gases except helium.

Thus, to evacuate a vacuum-jacketed measurement apparatus or sample space for use at liquid-helium temperature, all we need to do is obtain a *rough* vacuum at room temperature, cool it, and let cryopumping take care of the rest. However, to obtain good vacuum insulation, we still need to purge the vacuum spaces of helium gas as much as possible, to less than about 10^{-3} Pa. The equilibrium pressure of helium in atmospheric air is about 5.3×10^{-1} Pa, so rough-pumping generally works fine. However, in laboratories that often use liquid helium, the partial pressure of helium in the air can be much higher. Both residual helium and water vapor can be eliminated by evacuating and backfilling the vacuum space several times with dry nitrogen gas (obtained from the boil-off of a liquid-nitrogen storage dewar, for example) and then rough-pumping the system a final time before cooling.

➔ Make sure the vacuum space is equipped with a pressure-release vent, burst valve, or Richards valve (Richards 1954). Beware that if a slow leak occurs in the vacuum space, cryopumping can accumulate a significant amount of liquid gas in the closed space, which on warming will rapidly evaporate and overpressure the container. If there is no pressure-release system, the container becomes a virtual bomb. I have seen leaky vacuum-jacketed stainless-steel dewars turned into bloated, distended, contorted pieces of junk when such a valve was not used or was blocked. So make sure all cryogenic vacuum jackets are equipped with a Richards valve (which combines a vacuum pumping port with a pressure-release feature) or some similar pressure-release valve.

Incidentally, I once had a Richards valve fail to properly release as it should in an overpressure situation, and ultimately fire its core across the lab like a bullet. So aim the valve accordingly! For Richards valves with diameters larger than a couple of centimeters, it is a good idea to tether the core to the valve body with a stainless-steel chain or stainless-steel wire. (A small bolt screwed into the tapped hole in the center of the core acts as a good anchoring point.)

➔ Vacuum pumps containing oil, such as diffusion pumps, can create a horrendous clean-up mess if oil enters the vacuum spaces and coats the inner surfaces of a cryostat. This can happen after pumping over a period of time without a proper cryogenic vacuum-line trap, or suddenly if, for example, the wrong vacuum valve is opened accidentally. Although they are more expensive, newer *oiless* pumps (such as scroll pumps, turbo pumps, and cryopumps) as well as Roots blowers (which contain only a small amount of oil) can be used instead of oil-filled vacuum pumps to avoid this possibility (see Further reading, Sec. 3.9.1). However, an oil diffusion pump system in the hands of a knowledgeable researcher can do very well. But woe to the experimentalist who lets a learner loose on the system.

For internal parts that need to be cooled efficiently (such as a sample holder), it is best to leave a partial pressure of nitrogen gas in the thermal-isolation vacuum jacket, because the partial pressure of gas accelerates the cooling of the inner apparatus parts by heat transfer through the gas. This is especially helpful in the "slow-cooling regime" above 77 K, where the heat capacity of most materials is large. When the system reaches temperatures below the liquid-nitrogen regime, the residual nitrogen gas in the vacuum jacket automatically condenses, producing the high vacuum needed for good thermal isolation of the inner apparatus parts. It is best to leave at least ~100 Pa of nitrogen gas in the vacuum space at room temperature, so that during cooling, the gas pressure (which will decrease as $T/295$ K on cooling from room temperature) stays above about 10 Pa for good thermal coupling (as shown, for example, in Fig. 2.2).

3.7.3 LEAK DETECTORS

A lot of time can be spent (especially during construction) checking for, finding, and fixing leaks in the vacuum system. Leak detectors based on mass spectrometry can significantly shorten this process and are well worth learning to use. The leak detector is itself a vacuum system (with a diffusion or turbo pump) that incorporates a mass spectrometer tuned to detect helium ions. The leak detector is attached to the vacuum space being tested, and then helium gas is sparingly sprayed externally around the joints and seals. Helium gas is used because of its light mass, which results in rapid diffusion through small leaks into the vacuum space. The helium diffuses through the vacuum system to the leak detector, where its presence is signaled, indicating that the part being sprayed has a leak.

It is best to connect the leak checker to the system with a flexible metal hose as large in diameter as is convenient to reduce the helium-detection response time (and to speed evacuation of the system, if the leak detector also provides vacuum pumping for the system under test). Rubber tubing can be used for the connections but rubber is best avoided because rubber hose usually is smaller in diameter than metal hose, and because helium can diffuse slowly through the rubber-tube walls (thereby contributing to the background level of helium in the system).

Start by leak-checking the hose and connections to the system and then work outward from the detector through the system. It helps to localize leaks by using only a small quantity of gas and spraying it momentarily through a small needle valve (attached to a flexible hose from an auxiliary helium-gas bottle) and then waiting a few seconds for the detector to respond to any possible leaks before moving on to the next joint. Since helium gas rises, check from the top of the apparatus to the bottom, again, working your way away from the detector through the system. Large leaks can introduce so much helium into an apparatus that it may take a long time to purge the system, so again, limit the quantity of gas being sprayed about. If a very large leak is present, it may not be possible to evacuate the system enough to use the mass spectrometer detector. In this case, lightly *pressurize* the system being tested, then squirt soapy water on the suspected joints and look for soap bubbles that might form from leaking gas.

Finding a single leak is not the end of the story. After fixing the leak, smaller leaks can then be found. This is a lengthy, iterative process that can be shortened by temporarily plugging the first leak found with a temporary leak sealant.

Several final suggestions are offered. Closed-cell Styrofoam should be avoided inside the vacuum space because helium that diffuses into the closed cells can take effectively forever to diffuse back out to restore a low background helium level. Also, maintain the leak detector. It can be very frustrating to discover you need to service it just at the time you are also confronted with leak problems. Lastly, there is no substitute for skill in the welding and soldering department. It can save a lot of painful leak checking.

➔ For example, accidentally overheating a stainless-steel vacuum wall during soldering with a torch can make the wall porous and cause vacuum leaks. This can be easily avoided with good soldering practice (see the tip on soldering stainless steel and low-thermal-conductivity parts in Sec. 3.3.4).

3.7.4 CRYOGENIC VACUUM SEALS

In general, avoid *cryogenic* vacuum seals when designing an apparatus if a room-temperature seal can be used for the job. Commercial room-temperature vacuum seals [such as O-ring seals, ISO (International Standards Organization) flanges, quick couplings, and VCR (e.g. Cajon) vacuum seals] are relatively inexpensive, quick, and reliable. For example, when samples need to be routinely inserted into a vacuum space, try to design the measurement probe so that the samples can be inserted simply through a seal that remains at room temperature, such as the slip O-ring seal at the top of the cryostat shown in Fig. 2.12.

There are many circumstances, however, where a room-temperature seal is not an option, such as for demountable cryogenic vacuum fixtures and low-temperature sample chambers

(as illustrated in Fig. 2.13). Then some form of *cryogenic* vacuum seal must be used. It usually saves time to buy commercial seals that work at cryogenic temperatures or adapt commercial room-temperature seals for cryogenic use. (Examples of cryogenic vacuum seals for *electric-wire lead-throughs* are presented in Chapter 4, Sec. 4.7.2, Wiring and connections.)

Commercial vacuum seals for cryogenic use

Several commercial room-temperature seals are directly usable, or can be adapted, for cryogenic use. Most *metal* seals work well without any modification. On the other hand, seals with *rubber* components become brittle, but sometimes the rubber parts can be replaced with metal fittings.

For relatively small vacuum tubing (2–12 mm diameter, or 3/32–1/2 in.), commercial VCR seals (such as Cajon connectors) work at cryogenic temperatures if they are fitted with a copper metal gasket or, still better (from a thermal contraction standpoint), a stainless-steel gasket plated with silver. Tungsten–inert-gas welding is usually used to join the stainless-steel tubing on either side of VCR seals.

Commercial metal C-ring seals also work well at low temperatures (see list of specialty suppliers in Appendix A1.7 under the heading Vacuum accessories). The ring, shown in Fig. 3.12, is made of Inconel or stainless steel with its cross section in the shape of a C. It is coated with a soft metal such as silver, lead, or indium to provide a reliable seal between the ring and the flanges. The open part of the C is placed so that it faces the higher pressure side of the seal, as illustrated in Fig. 3.12. Sometimes, C-ring seals can be used in regular rubber O-ring grooves (but for optimum sealing performance, it is best to follow the manufacturer's guidelines in designing the flange grooves). C-rings, like other metal seals, such as VCR or KK seals, can be reused with some success, but for complete reliability, the gasket should be replaced each time.

Swage tubing connectors are less reliable at cryogenic temperatures. Also, ISO vacuum seals with elastomer seals are not suited for cryogenic use. However, ISO series flanges (KF, NW, through large flanges) can be adapted for use at low temperatures by replacing the elastomer seal with a metal seal (normally used for UHV systems).

Dynamic seals, such as reciprocating and rotary seals, can be fitted with spring-loaded PTFE (Teflon™) (polytetrafluoroethylene, a type of Teflon™) seals also having a C cross section (suppliers listed in Appendix A1.7 under Vacuum accessories). The core of the C has a canted-coil spring that presses the seal against the O-ring flanges, giving it flexibility at low temperatures so that it functions effectively like a rubber O-ring would at room temperature. Some of these spring-loaded polymer seals can be used in regular rubber O-ring grooves; others require slightly different dimensions than those of common rubber O-rings. Again, check with the manufacturers' guidelines. In some applications, solid PTFE (Teflon™) O-rings can be substituted for rubber O-rings, such as in the slip-vacuum seal at the top of the warming chamber illustrated in Fig. 1.9.

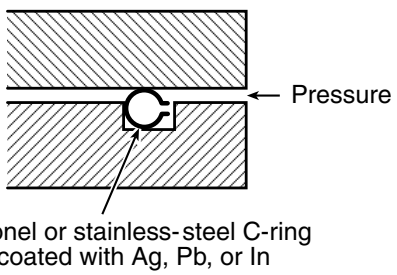

Fig. 3.12 Metal C-ring seal.

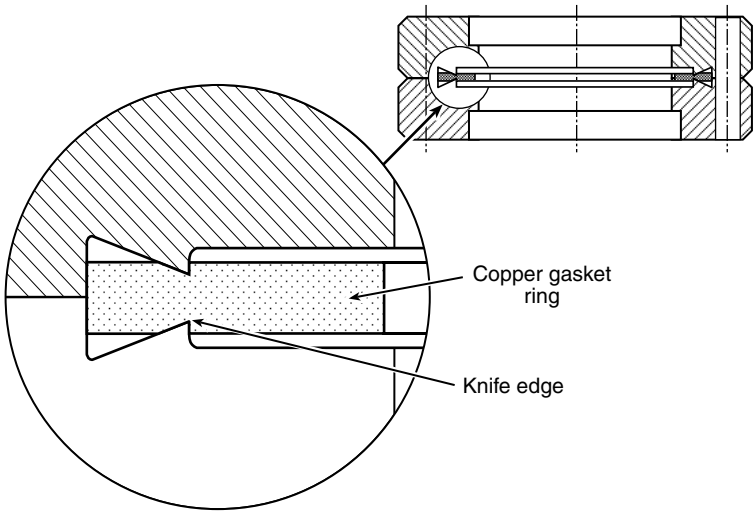

Fig. 3.13 Design of the ConFlat^R flange seal (reprinted by permission of Varian, Inc.).

When larger cryogenic vacuum seals are needed, a commercial ConFlat^R seal (shown schematically in Fig. 3.13) works well when cycled to cryogenic temperatures. The seal's squashable compression ring is made of copper, which has a f.c.c. crystal structure that does not become brittle on cooling (as discussed in Sec. 3.2.2). This is convenient, but requires that the cryostat be designed around relatively large, robust pressure flanges. Copper wire seals also work at cryogenic temperatures.

Indium O-ring vacuum seals

Sometimes commercial seals are not the right shape, too bulky, or not readily adaptable for joining particular cryostat parts. Then custom-made indium O-ring compression seals will do the job. The indium seals illustrated in Figs 3.14 and 3.15 are relatively easy to machine, and they function well at cryogenic temperatures. They do not need to be as large and robust as ConFlat^R seals because pure indium wire is soft and deforms at a lower pressure than copper gasket material, so the flanges do not have to supply so much mechanical pressure. Indium O-ring seals survive cycling to cryogenic temperatures, are very reliable, and can be incorporated easily into cryostat parts.

The indium compression ring is formed simply by wrapping a piece of pure indium wire (~1 mm in diameter) around the lip of the lower stainless-steel tube in Fig. 3.14 and then the wire ends are overlapping or simply twisted, as shown in the detail of Fig. 3.15. (Suppliers of pure indium wire are listed in Appendix A1.7 under Vacuum accessories.) The indium O-ring is then squashed between the faces of the two stainless-steel flanges. The pressure on the O-ring needs to be uniform, so the flanges must be thick enough to keep deflection within acceptable tolerance (see Fig. 3.14 and Sec. 3.5.3 on sizing parts). The flanges are screwed together with, typically, 6–12 bolts (depending on the flange size) arranged around the flange's circumference to apply uniform pressure (see Appendix A3.4 for hex-head sizes to provide adequate space between heads). For larger flanges, up to about 16 bolts can be used, beyond which the cost of machining usually becomes expensive.

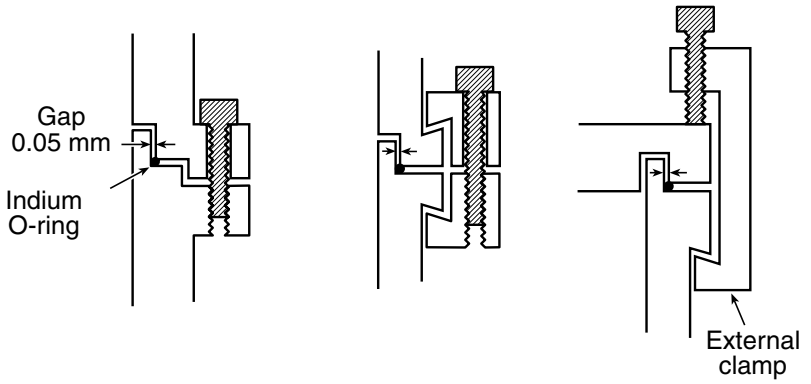

Fig. 3.14 Indium O-ring seal designs. Each diagram is a cross section of just one side of a circular seal. In the first design, a bolt flange is machined into the two stainless-steel tubes to be joined. In the second and third designs, external clamps are used to bolt the two pieces together.

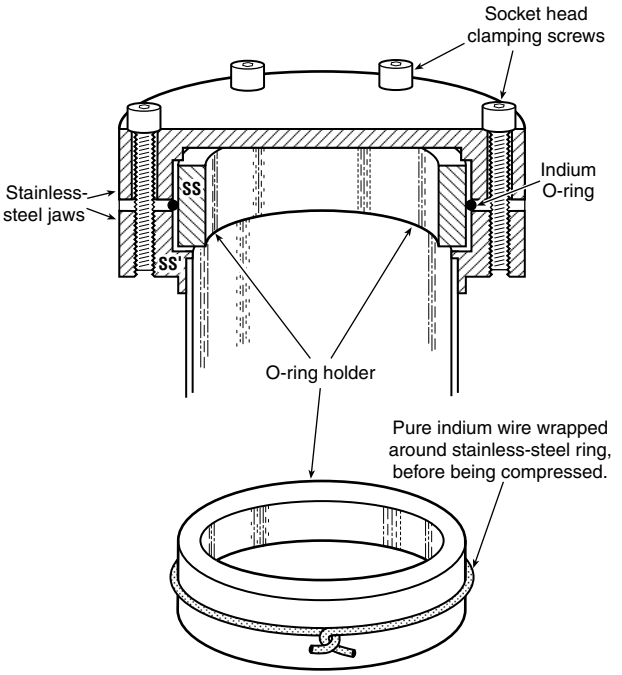

Fig. 3.15 Cut-away view of indium O-ring cryogenic vacuum compression seal. The O-ring is formed by wrapping pure indium wire around the stainless-steel ring; the ring is then placed in the apparatus and the O-ring is squashed by bolting together the two stainless-steel jaws.

To ensure uniform pressure, progressively hand-tighten the bolts that join an indium O-ring seal with an Allen wrench, sequentially tightening bolts on opposite sides of the bolt circle in a "star" pattern. No need to tighten too much, but it does help to leave the seal at room temperature for about an hour to let the indium creep, and then tighten the bolts some more. Also, make sure the indium O-ring wire and all parts are free of dirt and oil from your skin (wear clean, no-powder gloves, or handle with tissues).

If the joint will be *seldomly* disassembled, clean both indium and stainless-steel surfaces well with alcohol so they form a good diffusion bond. This usually results in indium diffusion bonding to the stainless-steel surfaces. If, on occasion, the joint needs to be remade and some residual indium remains bonded to the parts, it does not hurt to leave it there and wrap the new indium O-ring over the residue (as long as it is dirt-free).

On the other hand, if the joint will be *repeatedly* made, first clean all parts well and then rub a very small amount of vacuum grease into the surface of the stainless-steel pressure faces to aid in disassembly. If the flanges are stuck together, they can be separated by (carefully!) inserting a sharp knife blade between the flanges. For large flanges (> 5 cm), it helps to design several equally spaced threaded holes into *one* of the flanges, and fit them with "jacking bolts" that can evenly push the two flanges apart for disassembly.

The clamping designs shown in Fig. 3.14 work well with rigid stainless-steel tubes and end plates. The radial gap indicated in Fig. 3.14 (0.05 mm) needs to be machined with a fairly close tolerance to make the seal robust and avoid having the seal shift if stressed. The pressure faces need to be machined flat to about the same tolerance. In the first design of Fig. 3.14, the lips of the two tubes to be joined are machined with a *double* step to avoid having the indium metal extrude into the clamping screw threads, where it could diffusion-bond the bolt to the cryostat part.

Another way to avoid indium extrusion into the bolt area is to clamp the two stainless-steel parts with *external clamps*, as shown in the second and third designs of Fig. 3.14. The use of external clamps also usually simplifies the machining of the main cryostat parts (and if a stainless-steel bolt seizes, just the clamp can be taken to the shop to spark cut the bolt out, without trying to carry out that tricky operation on the main apparatus). In the third design illustrated in Fig. 3.14, the external clamps are individual screw C-clamps placed equally around the circumference of the O-ring flange. In the second design of Fig. 3.14, the external clamp is a circular clamp *ring*. For simplicity, it can be turned as one solid continuous ring and then orthogonally cut into four parts, first slicing the ring around its circumference to create the two top and bottom rings shown in the middle panel of Fig. 3.14, and then cutting each ring along a diameter so that the two halves can be placed around the cryostat tubes to be joined.

When an indium O-ring seal will be repeatedly made and remade each time the cryostat is used, such as the vacuum seal on a sample chamber, it is convenient to wrap the indium wire around a *separate* stainless-steel ring, as shown in Fig. 3.15. This allows the stainless-steel ring to be removed from the apparatus where it can be easily cleaned and refitted with a fresh indium O-ring each time.

3.7.5 VACUUM-DUCT SIZING (HYDRODYNAMIC FLOW)

Sizing requirements for vacuum ducts depend on whether the flow through the duct is hydrodynamic (high pressures, such as when pumping on a cryogenic bath) or free-molecular (low pressures, such as in surface-science experiments). Table 2.1 shows that, for typical duct diameters on the order of centimeters, the crossover between the two pressure regimes occurs in the range of 10^0–10^{-2} Pa (in the medium-vacuum range of Fig. 3.11). Here we consider duct sizing for the case of hydrodynamic flow, which is quite common in cryostat design for sizing pumping lines to change the temperature of a liquid-helium bath or when operating a dilution

refrigerator, where the cooling power is proportional to the gas molar flow rate. (Vacuum duct sizing under conditions of free-molecular flow are more specialized and are treated in the addenda on HV and UHV techniques.)

The most critical requirement for sizing vacuum ducts occurs at the low-pressure end of the hydrodynamic regime where flow is laminar. For this case, the pressure drop across a tube of length L and diameter D is given by (e.g. see Kays and London 1984) Poiseuille's law:

$$P_1^2(\mathrm{Pa}^2) - P_2^2(\mathrm{Pa}^2) = [256\,\mathrm{R}\,\nu(\mathrm{Pa{\cdot}s})\,T(\mathrm{K})/\pi]\,L(\mathrm{cm})\,D^{-4}(\mathrm{cm}^{-4})\,\dot{n}\,(\mu\mathrm{mol/s}), \tag{3.15a}$$

Pressure drop for laminar flow through a tube

where P_1 and P_2 are the pressures at either end of the tube in Pa; R is the universal gas constant (8.31441 J mol^{-1} K^{-1}); ν is the viscosity of the gas in Pa s; T is the gas temperature in kelvins, and $\dot{n}$ is the gas molar flow rate in μmol/s.

Typically, cryostat duct designs require that the pressure drop across the tube be small compared with the level of pressure (that is, $\Delta P \ll P_1 \cong P_2$). Then we can substitute $P_1^2 - P_2^2 \cong 2P\,\Delta P$ into Eq. (3.15a) to obtain

$$\Delta P\,P\,(\mathrm{Pa}^2) = [128\,\mathrm{R}\,\nu(\mathrm{Pa{\cdot}s})\,T(\mathrm{K})/\pi]\,L(\mathrm{cm})\,D^{-4}(\mathrm{cm}^{-4})\,\dot{n}\,(\mu\mathrm{mol/s}). \tag{3.15b}$$

Small pressure-drop approximation for laminar flow through a tube

Functionally, Eqs (3.15a or b) show that the *diameter* of the tube has a much greater effect on the flow impedance than does its *length*. It also shows that the flow impedance of vacuum ducting improves at lower temperatures. That is, $P_1^2 - P_2^2$ is proportional to the product of the viscosity ν and temperature T. The viscosity of a nearly ideal gas such as helium is proportional to $T^{2/3}$ over most of the cryogenic temperature range, so the pressure drop across a vacuum conduit scales with temperature as

$$P_1^2 - P_2^2 \propto T^{5/3}.$$

So, somewhat surprisingly, the most restrictive conditions on vacuum-conduit sizing occur at room temperature, not at cryogenic temperatures.

Thus, a worst-case expression is obtained by evaluating Eqs (3.15a or b) at room temperature. For example, the viscosity of ^{4}He gas is 20 μPa s at 300 K, for which case Eq. (3.15a) reduces to simply

$$P_1^2 - P_2^2\,(\mathrm{Pa}^2) = (4.0)\,L(\mathrm{cm})\,D^{-4}(\mathrm{cm}^{-4})\,\dot{n}\,(\mu\mathrm{mol/s}). \tag{3.16}$$

Pressure drop for laminar flow of ^{4}He at 300 K through a tube

Equation (3.16) is a useful, practical expression for sizing vacuum ducting in most liquid-helium cryostats under conditions of hydrodynamic flow.

3.8 Addenda: high and ultrahigh vacuum techniques

The requirements for achieving HV ($< 10^{-1}$ Pa) or UHV ($< 10^{-5}$ Pa) place severe requirements on materials selection and cryostat design. This is the situation, for example, in surface-science experiments, where sample surfaces need to be protected from contamination or corrosion, or in cryogenic scanning microscopes, where particles must pass unimpeded across large distances.

For such experiments, the vacuum requirements are often the starting place for cryostat design. Cryogenic vacuum ducts and seals are usually large and dominate the available space in such systems, so the rest of the design usually has to flow around them. Also, construction materials have to be chosen that have low out-gassing rates. It does not do any good to design a great cryostat and then fill its vacuum spaces with volatile wire insulation and varnish (degassing rates and vapor pressures of some common cryostat materials are given in Appendixes A3.12 and A3.13).

Where an UHV is needed, joining techniques such as TIG welding, furnace brazing, or hard-silver-soldering must be used in assembling the apparatus (described in Sec. 3.3). Soft-solder joints (lead- and tin-based) are unacceptable, because they will melt during the high-temperature apparatus bake-out (described later in this section) that is required to reach UHV levels. Also, the corrosion caused by trapped solder-flux residue can eventually perforate thin stainless-steel tubes, as well as introduce residual gas into UHV systems. Avoid brass and other commonly used construction materials containing zinc or other metals with high vapor pressure in UHV systems (see Appendix A3.13). For UHV systems, special techniques are also needed for preparing, handling, and cleaning surfaces, including the proper use of gloves and clean tools.

We now introduce some of the main design considerations for HV and UHV systems. A wealth of additional information is available from the primary suppliers of vacuum equipment (Sec. 3.9.1).

3.8.1 VACUUM-DUCT SIZING (FREE-MOLECULAR FLOW)

In the case of HV and UHV systems, *free-molecular conditions* apply (i.e. the mean free path of the gas molecules is smaller than the dimensions of the vacuum duct). Under these conditions, it is convenient to use the gas volume flow rate Q through the duct, expressed in units of (Pa m^3/s). [The gas *volume* flow rate Q is related to the gas *molar* flow rate $\dot{n}$ (used in Sec. 3.7.5) by $Q \equiv \dot{n}\,\mathrm{R}T$.] For free-molecular flow, Q is directly proportional to the pressure difference $(P_1 - P_2)$ across the vacuum duct,

$$P_1 - P_2 = C^{-1}\,Q\ (\mathrm{Pa\ m^3/s}), \quad \text{Pressure drop for free-molecular flow through a duct} \tag{3.17}$$

The proportionality constant C depends on the physical dimensions of the duct and is known as the *conductance*. It is measured in units of volume per second, having SI units (m^3/s).

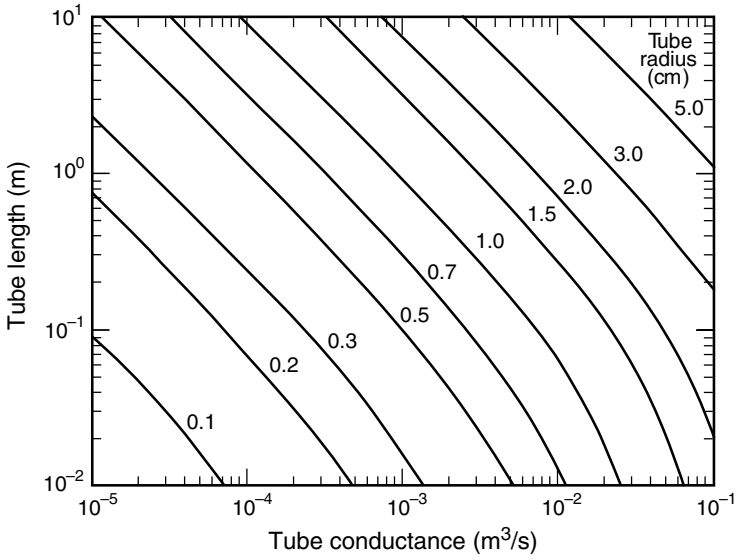

Fig. 3.16 Conductance of cylindrical tubes at room temperature under conditions of free-molecular flow (from Clausing 1932).

We see from the defining equation (3.17) that when two ducts (with conductances C_1 and C_2) are connected together, the total conductance C of the combination is given by the usual parallel and series formulas

$$C = C_1 + C_2, \quad \text{Parallel connection}$$

$$1/C = 1/C_1 + 1/C_2. \quad \text{Series connection}$$

For an *orifice* having no thickness and a diameter much smaller than the mean free path of the gas molecules, the conductance through the opening is given by

$$C_{\text{orifice}} = A\,(k_B\,T / 2\pi m)^{1/2}, \quad \text{Conductance through an orifice} \tag{3.18}$$

where A is the area of the orifice, k_B is Boltzmann's constant, and m is the (mean) molecular mass for the particular gas in the vacuum vessel.

For *tubes*, on the other hand, the conductance C depends on the ratio of tube length to radius. Figure 3.16 is a useful graph for determining the conductance at room temperature.

3.8.2 PUMP SPEED AND ULTIMATE PRESSURE

For HV and UHV systems, the ultimate pressure achievable depends on more than just adequate vacuum-duct sizing. There are *fundamental* pumping speed limits for vacuum

chambers. To understand this, we first need to consider the nature of vacuum pumps. Most practical pumps operate continuously, so that if a constant rate of gas Q flows into the pump, then an associated constant pressure P_{pump} will develop in the pump. The pumping capability of a vacuum pump is conveniently quantified in terms of the ratio of Q and P

$$S_{\text{pump}} \equiv Q / P_{\text{pump}}, \quad \text{Pump speed} \tag{3.19}$$

where Q is the gas volume flow rate (in units of Pa m^3/s) and S_{pump} is known as the *pump speed*. The pump speed is a useful quantity because for many pumps S_{pump} remains fairly constant over the working pressure range of the pump. As with conductance through ducts, pump speed also has units of gas conductance, m^3/s.

The pumping speed at the chamber is always less than the speed at the pump. From Eq. (3.17) we see that if we attach a pump to a vacuum chamber with pressure P_{chamber}, the flow of gas Q through the vacuum ducting (having a conductance C) produces a pressure drop between the chamber and pump of

$$P_{\text{chamber}} - P_{\text{pump}} = Q / C. \tag{3.20}$$

We can define a pumping speed for the chamber S_{chamber} by the relation

$$S_{\text{chamber}} \equiv Q / P_{\text{chamber}}, \tag{3.21}$$

which is similar to Eq. (3.19). Substituting Eqs (3.19) and (3.21) into Eq. (3.20), and eliminating Q (since, from conservation of matter, the gas flow rate from the chamber and through the pump will be the same), we have

$$S_{\text{chamber}} = S_{\text{pump}} \left[C/(S_{\text{pump}} + C)\right] = S_{\text{pump}} / \left[1 + (S_{\text{pump}}/C)\right] < S_{\text{pump}}. \tag{3.22}$$

Chamber pumping speed

From Eq. (3.22), it follows that the pumping speed of the chamber is always less than the speed of the vacuum pump, being limited by the conductance of the duct connecting the two. Equation (3.22) can be used to determine the derating of the pump speed at the cryostat chamber, and it emphasizes the importance of adequate vacuum duct conductance C. However, even when the size of the conductance C equals the pump speed, S_{chamber} is still only half S_{pump}. Only when the pump is directly attached to the chamber (as in most HV or UHV systems), so that $C \geq \infty$, can all the pump speed be utilized. However, the chamber pumping speed is only half the problem.

The ultimate pressure reached in the cryostat chamber P_{ult} is a combination of S_{chamber} and the gas influx from leaks and virtual leaks Q_{i},

$$P_{\text{ult}}\,(\text{Pa}) = Q_{\text{i}}\,(\text{Pa m}^3/\text{s}) / S_{\text{chamber}}\,(\text{m}^3/\text{s}). \quad \text{Ultimate chamber pressure} \tag{3.23}$$

Equation (3.23) is the crux of vacuum technology. It underscores the importance of limiting the leakage rate Q_i into the chamber, since S_{chamber} is fundamentally limited and can never be made big enough to overcome a high Q_{i}.

To illustrate the limits on S_{chamber}, consider the best possible situation where the pump is directly attached to the chamber, that is, $C = \infty$ in Eq. (3.22), so we utilize the full speed of the vacuum pump ($S_{\text{chamber}} = S_{\text{pump}}$). Further assume that we have a *perfect* vacuum pump in which all the molecules that strike the pump-inlet area stick permanently. In this case, S_{pump} is limited only by the rate Q_{max} at which molecules flow to that inlet area. It is worth emphasizing that pumps do not suck, they just collect.

The maximum molecular flow rate can be obtained from kinetic theory, which gives (see, for example, Weston 1985)

$$Q_{\text{max}} = P\,(k_{\text{B}}\,T\,/\,2\pi m)^{1/2}\,A, \tag{3.24}$$

where m is the molecular mass of the gas molecules in the system, and A is the surface area. So with a perfect vacuum pump, attached directly to the chamber, the maximum pumping speed of the chamber $S_{\text{chamber max}}$ would be limited to the ratio of $Q_{\text{max}}\,/\,P$ given by Eq. (3.24). We simply cannot do any better than

$$S_{\text{chamber max}} \equiv Q_{\text{max}}/P = (k_{\text{B}}\,T\,/\,2\pi\text{m})^{1/2}\,A. \quad \text{Chamber maximum pumping speed} \tag{3.25}$$

Example: Suppose we have a high-vacuum chamber with a perfect pump attached directly to a 10 cm $\times$ 10 cm area of the chamber, that is, 10^{-2} m^2. We wish to find the maximum pumping speed for this chamber.

Inserting the mass of a nitrogen molecule into Eq. (3.25), we find that the maximum pumping speed per unit area at room temperature is

$$S_{\text{chamber max}}/A = (k_{\text{B}}\,T\,/\,2\pi m)^{1/2} = 100 \text{ m/s}. \tag{3.26}$$

So for our example, where we have allocated an area of 10^{-2} m^2 to the pump, we find from Eq. (3.26) that the maximum possible pump speed $S_{\text{chamber max}}$ would be about

$$S_{\text{chamber max}} = (100 \text{ m/s})\,(10^{-2} \text{ m}^2) = 1 \text{ m}^3\text{/s}.$$

Thus, even with a perfect pump, we see from Eq. (3.23) that the main difference between an UHV and a rough-vacuum system is simply the total rate of gas influx Q_{i}. For the above example, where we have an area of 10^{-2} m^2 available for pumping corresponding to a maximum pumping speed of 1 m^3/s, Eq. (3.23) shows we must limit the gas load to about 10^3 Pa m^3/s for a rough vacuum of 10^3 Pa, or 1 Pa m^3/s for a medium vacuum of 1 Pa, or 10^{-4} Pa m^3/s for a high vacuum of 10^{-4}, or, finally, 10^{-8} Pa m^3/s for an ultrahigh vacuum of 10^{-8} Pa. It is all determined by the effective leak rate.

So, aside from choosing a good pump and having adequate ducting, *the main task of good vacuum design is simply to limit the total gas influx rate Q_{i} to a level consistent with the ultimate pressure we wish to achieve*. How to limit Q_{i} is the subject of the rest of this addendum.

3.8.3 SOURCES OF GAS IN A VACUUM SYSTEM

Vacuum vessel leaks

Most solids are adequately leak tight for vacuum-chamber construction. Leaks usually occur at *joints*. The usual joining techniques, including soldering, brazing, and welding, work well. For HVs and UHVs, however, the vacuum system usually has to be heated to temperatures as high as 450°C to extract adsorbed gas from the vacuum-chamber surfaces (see the following subsection on degassing), and therefore low-melting-temperature materials like soft-solder should be avoided. In this case, brazing or welding works well.

Be aware, especially with cryostats, that vacuum joints and seals can be subjected to stress and fatigue not only from pressure differences and vibrations, but also from thermal cycling. This can lead to failure, which places an extra premium on utilizing good cryogenic vacuum joints and seals (Secs 3.3 and 3.7.4).

Virtual leaks

These usually arise from gas trapped in the vacuum system. For example, when a cryostat is assembled (normally at atmospheric pressure), a screw in a blind hole will trap gas at the bottom of the hole. Then when the vacuum vessel is evacuated, this trapped gas will leak into the vacuum chamber along the thin helical crack formed by the screw thread. Ultimately, all the gas will escape through the screw thread, but this can take a *very* long time.

Example: Suppose the volume V of trapped gas is 10^{-6} m^3 and the conductance C of the screw thread is 10^{-12} m^3/s. The time t it will take to remove the gas is approximately given by

$$t = V/C = 10^6 \text{ s},$$

or about 10 days.

Thus, the problem with virtual leaks is not that they limit the system's ultimate pressure, but that they lengthen the time to achieve it.

Virtual leaks such as this can usually be avoided through good vacuum design. For example, where blind screw holes are needed, use commercially available *vented* screws that have a hole machined through their center to enable the gas to escape quickly (suppliers are listed in Appendix A1.7 under Vacuum accessories). Alternatively, a slot can be cut into the threads along the length of the screw, to provide a high-conductance channel.

Use welding designs that avoid cavities where dirt and gas can be trapped on the vacuum side of the joint. Figure 3.17 shows some examples of correct and incorrect welding practice for vacuum applications. The main design principle is to use continuous welding on the vacuum side of the joint. Any additional welds needed for strength should be intermittent on the atmospheric side.

Degassing of materials

The surfaces of most solids usually contain adsorbed gas—an extremely thin layer of water vapor and gas molecules that adheres to the surface. This trapped gas is not a problem for

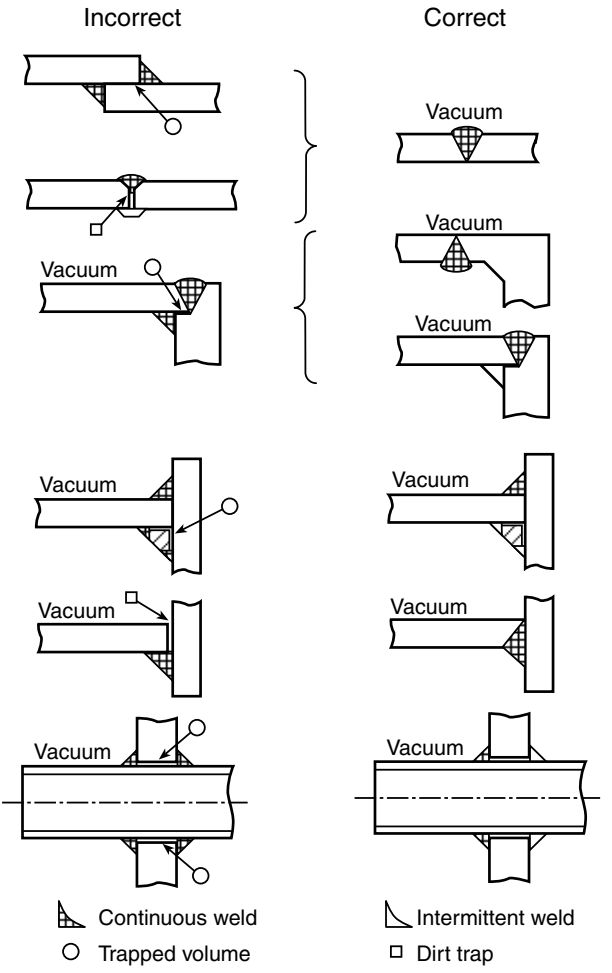

Fig. 3.17 Examples of correct and incorrect welding practice for vacuum applications (from Kronberger 1958).

rough- or medium-vacuum systems, but can significantly degrade HV and UHV systems. This is particularly true of surfaces that are heavily oxidized, or rough surfaces that provide a lot of surface area for adsorption of water vapor. Gases are also usually dissolved throughout the bulk of a solid material and can be released into the vacuum system, especially from material near the vacuum surface.

Both adsorbed and dissolved gases will be released into the vacuum system at a rate dependent on the total amount of gas sorbed, how it is bound, and the temperature. For example, the gas influx per area from borosilicate glass is about 10^{-5} (Pa m^3/s)/m^2 at room temperature. Metal surfaces, on the other hand, that have a thin layer of surface oxide can have an initial degassing rate at room temperature an order of magnitude higher, 10^{-4} (Pa m^3/s)/m^2. (Of course, if these materials are part of a *cryogenic* vacuum space, the degassing rate will become negligible after cooling to very low temperatures.) Figure 3.18 shows the release of adsorbed gas from several materials into a vacuum space at room temperature as a function of time. Polymers, including wire insulation, are not commonly used in UHV systems because of their large degassing rates and sensitivity to bake-out temperatures. Degassing rates for several polymers, Neoprene™ and Araldite™ epoxy, are included in Fig. 3.18 for comparison.

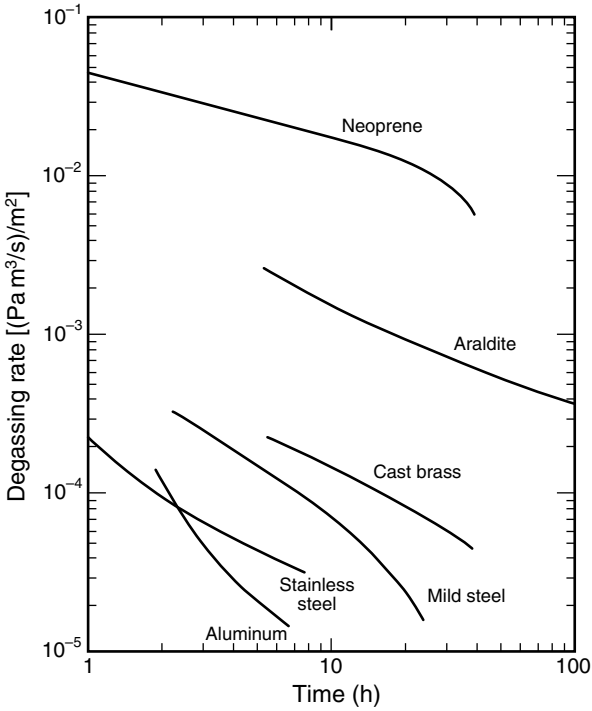

Fig. 3.18 Degassing rate for *un*treated metals, compared with Neoprene™ plastic and Araldite™ epoxy (from Blears et al. 1960). Degassing rates for addition synthetic materials are tabulated in Appendix A3.12.

Example: To show the influence of the high degassing rate of such materials, consider a vacuum vessel at room temperature that contains a relatively small Neoprene™ part with a surface area of 10 cm^2. Assume that the vacuum chamber is equipped with a perfect vacuum pump directly connected to the system (i.e. $S_{\text{chamber}} = S_{\text{chamber max}}$), with a 5 cm × 5 cm area allocated to the pump. We want to determine the ultimate pressure of the vacuum system after 10 h of pumping.

From Eq. (3.26), we find that the chamber has a maximum pumping speed at room temperature of

$$S_{\text{chamber max}} = (k_B T / 2\pi m)^{1/2} A = (100 \text{ m/s})\,(5 \times 10^{-2} \text{m})^2 = 2.5 \times 10^{-1} \text{ m}^3/\text{s}.$$

Figure 3.18 shows that after 10 h of pumping, Neoprene™ has a degassing rate of about 1.5×10^{-2} (Pa m^3/s)/m^2. From the principal vacuum-design equation, Eq. (3.23), we thus find that the ultimate pressure of the vacuum system will be limited by the 10 cm^2 Neoprene™ part to

$$P_{\text{ult}} = Q_i / S_{\text{chamber max}}$$
$$= [1.5 \times 10^{-2} \text{ (Pa m}^3\text{/s)/m}^2]\,(10 \times 10^{-4} \text{ m}^2) / (2.5 \times 10^{-1} \text{ m}^3/\text{s}) = 6 \times 10^{-5} \text{ Pa},$$

a pressure outside the UHV range (see Fig. 3.11). Smaller, imperfect pumps would have correspondingly higher ultimate pressures. Even after 100 h of pumping, the degassing rate of Neoprene™ is still on the order of 10^{-2} (Pa m^3/s)/m^2, so extra pumping time is not much help.

Fortunately, for UHV systems, the degassing rate at room temperature can be greatly accelerated by *baking* the vacuum system while it is under vacuum. Ideally, this is done in two

steps: a preassembly bake of the parts at as high a temperature as possible, and then a post-assembly bake of the entire vacuum system.

A system bake with heater tapes wrapped around the equipment at a moderate temperature of 150–250°C for several hours will release most of the water vapor adsorbed on the surface of metals or glasses. After this initial rapid evolution of gas, further heating produces a slower but more persistent release of gases dissolved in deeper layers within the bulk of the material. Since the rate of diffusion of these dissolved gases out of the material depends exponentially on temperature, it helps to use the highest temperature that the system can tolerate to shorten the process. Baking at up to 400–450°C for 16 h is recommended for UHV systems. Degassing rates of stainless steel, for example, decrease many orders of magnitude after such a bake-out process, from about 10^{-4} (Pa m^3/s)/m^2 for the untreated metal (see Fig. 3.18) down to the 10^{-10}–10^{-12} (Pa m^3/s)/m^2 range after vacuum baking. Ceramics also should be baked at 450°C for several hours. The resulting degassing rate at room temperature is then quite low, on the order of 10^{-11} (Pa m^3/s)/m^2.

Synthetic materials, such as plastics, elastomers, and epoxy resins, are sometimes needed in vacuum systems for their high elasticity or their low coefficient of friction (to make lubrication-free bushings). Unfortunately, most of these materials have degassing rates that are relatively high (see Appendix A3.12). Initial degassing rates are about 10^{-3}–10^{-4} (Pa m^3/s)/m^2 and they cannot be reduced to much below 10^{-5}–10^{-6} (Pa m^3/s)/m^2 even after 24 h of pumping at the relatively low baking temperatures they can tolerate without deforming or decomposing. On re-exposure to the atmosphere, these materials rapidly reabsorb water vapor.

The best of these synthetic materials are the ones that can be baked at the highest temperatures. Viton™ A, PTFE (Teflon™), Mycalex™, and polyimide (Kapton™ as sheets, films, or wire insulation; and Vespel™ as blocks) can be used in continuously pumped vacuum systems below 10^{-6} Pa. Polyimide has the lowest degassing rate of any of these synthetic materials; after it is baked at 300°C, the rate is reduced to the 10^{-8} (Pa m^3/s)/m^2 range. It is, therefore, of particular interest as a gasket material, and it is one of the best flexible materials for electric-wire insulation in vacuum systems. Also, unlike most polymers, it has a thermal expansion coefficient close to those of metals like brass and aluminum. Some care should be exercised in the design of seals using polyimide, however, since it experiences permanent distortion if compressed by more than 20%.

Teflon™ (PTFE) also can be heated to 300°C, and it is useful as a bushing material for moving parts to minimize friction against other materials (but do not overheat it or fluorine gas can be released). Kalrez and Viton E60C are among the best O-ring materials for UHV systems, since they can be baked at temperatures up to 300°C, and afterward their degassing rates are in the 10^{-8} (Pa m^3/s)/m^2 range. Viton A can be baked up to 200°C, and it is useful as an O-ring material in systems down to 10^{-7} Pa. An epoxy that works well in vacuum applications is Varian Torr Seal.

Vapor pressure of solids

Materials selected for use in vacuum systems must have a vapor pressure over their working temperature range well below the desired ultimate pressure. Figures 3.19(a) and (b) plot the temperature dependence of the vapor pressure of some representative metals, with the

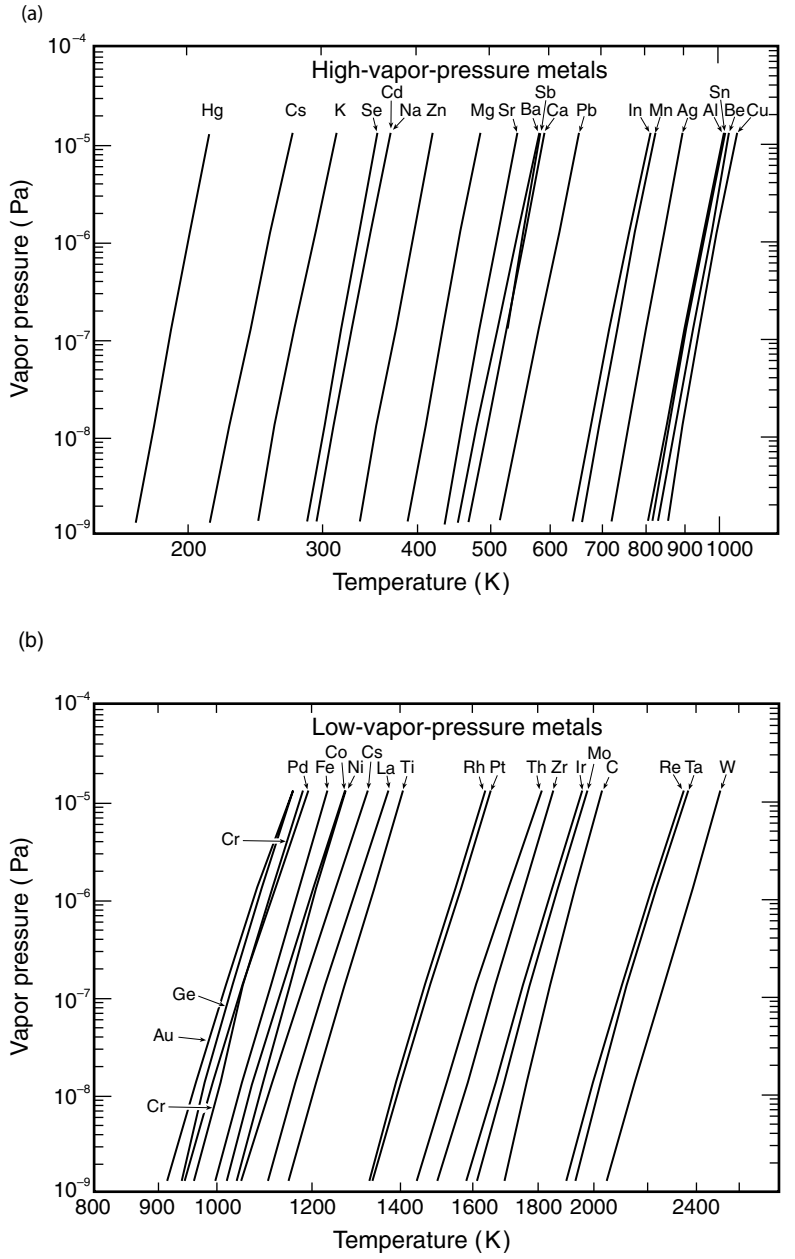

Fig. 3.19 Vapor pressure curves of metals: (a) high-vapor-pressure metals; (b) low-vapor-pressure metals (adapted from Honig 1962 and 1969). Data are tabulated in Appendix A3.13.

most problematic materials being those in the high-vapor-pressure group, Fig. 3.19(a). Appendix A3.13 lists the temperatures at which metals reach a specified vapor pressure (the tabulation is given in terms of temperature because of the steep dependence of vapor pressure on temperature). The lower the boiling temperature of a material, generally, the higher its vapor pressure.

The left side of Fig. 3.19(a) shows a number of metals that have vapor pressures above 10^{-9} Pa at 500 K, which initially may not seem like much of a problem. For degassing HV and UHV systems, however, materials need to be raised to temperatures as high as about 450°C. For such systems, common metals such as cadmium, zinc, magnesium, and their alloys should be avoided. Cadmium is often overlooked; it sometimes occurs in cadmium-plated screws and other parts.

Sometimes materials need to be raised to extremely high temperatures, such as for filament emitters in vacuum systems. Tungsten is commonly used for this purpose. Although it has one of the lowest vapor pressures [see Fig. 3.19(b)], it still has a vapor pressure of about 10^{-7} Pa when used as a filament emitter operating at 2000°C (2273 K).

Permeation of gases through materials

Permeation of gases through the vacuum vessel walls is usually not a significant problem if the vacuum system is pumped continuously and kept at room temperature. However, this is usually not the case with cryogenic vacuum chambers and dewar vacuum jackets, which are typically evacuated at room temperature and then sealed off before cooling to take advantage of the efficiency of cryopumping. During the time the vacuum chamber is closed off, gas permeation through the chamber walls can become significant. This is especially true of helium gas permeation through glass and hydrogen permeation through some metals (such as Mu-Metal, a high magnetic permeability nickel alloy used for shielding magnetic fields). Glass dewars used to be the norm for cryogenic measurements, but they have been largely replaced by stainless steel or metal-lined fiberglass–epoxy dewars because of the helium-permeation problem (as well as their fragility).

Glass: Glass materials have an irregular crystalline structure with openings in which gas atoms can be sited. Thus, the permeation of gas through glass depends on the porosity of the microstructure and the size of the gas molecules. Helium, with its small molecular diameter, has the highest permeation rate through glass of any of the gases. The rate of gas permeating through glass with a wall thickness d and area A is given by

$$Q_i = \mathrm{K}\,(A/d)\,(P_2 - P_1), \quad \text{Gas permeation rate through glass, ceramic, or synthetic materials} \tag{3.27}$$

where P_1 and P_2 are the gas pressures on each side of the wall and K is the permeation constant of the material in question, with units of m^2/s. Since K depends on a diffusion process, it increases exponentially with temperature. Values of K are given for several types of Corning™ glasses as a function of temperature in Fig. 3.20. Fused silica is the least dense and therefore has the highest permeation rate.

Ceramics: Ceramic materials have a porous microstructure, so gas permeates through them in the same way it permeates glass, as described by Eq. (3.27). Pore size and the size of gas molecules play significant roles, with helium again having the highest permeation rate. Values of the permeation rate K for helium through several ceramics are plotted in Fig. 3.21. Gases other than helium have lower permeation rates. Since ceramics are formed by a sintering process,

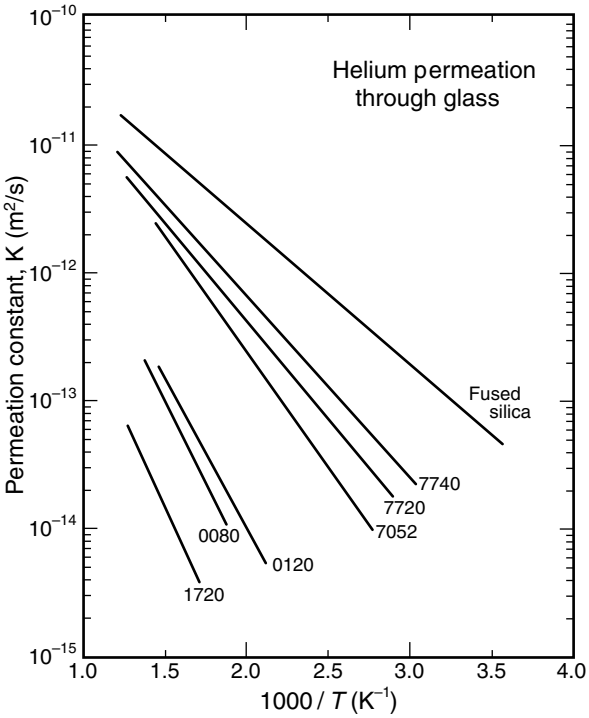

Fig. 3.20 Permeation constant K for helium through several Corning™ glasses as a function of temperature for use with Eq. (3.27) (from Weston 1985, based on data from Altemose 1961). Additional gas permeation rates are given for synthetic materials at room temperature in Appendix A3.14.

they usually are quite porous, with a 10% pore volume being common. They also contain a proportion of glassy phase material that bonds the crystal aggregates together and seals the pores. The amount of glassy phase present has a marked influence on the material's permeability and can be varied to deliberately close or open pores. The former situation minimizes permeation, the latter facilitates degassing. As Fig. 3.21 shows, gas permeation through many ceramics is quite low when extrapolated to typical service temperatures and, therefore, not a significant problem in achieving UHV.

Synthetic materials: For synthetic materials, gas permeation rates also follow the same functional relationship given in Eq. (3.27), since gas diffusion proceeds via pores in a material's microstructure. The permeability of synthetic materials is quite high. Room-temperature values of K are given for various combinations of gas and material in Appendix A3.14. For synthetic materials, permeation rates are typically several orders of magnitude greater than for the worst glass, fused silica. Interestingly enough, it is evident in Appendix A3.14 that the permeation rate for helium through many synthetic materials is not a lot greater than that of hydrogen or nitrogen. Thus, nitrogen permeation can be as serious a problem as helium permeation in these materials, if not more so, because of its much greater partial pressure in the air ($\sim 7.9 \times 10^4$ Pa for nitrogen vs. $\sim 5.3 \times 10^{-1}$ Pa for helium). The high permeation rate for PTFE (Teflon™) in Appendix A3.14 is a result of the difficulty of manufacturing this material with a low pore density. Where these synthetic materials are completely surrounded by a vacuum, as in gasket and

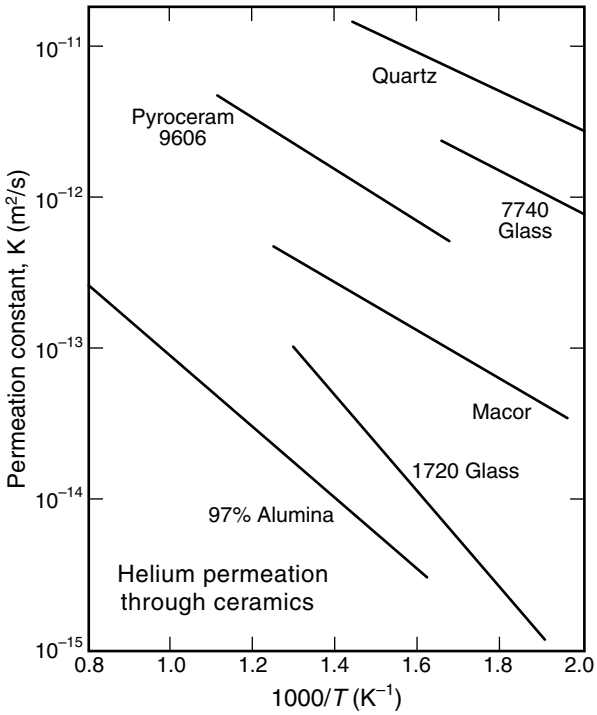

Fig. 3.21 Permeation constant for helium gas through several ceramics as a function of temperature, for use with Eq. (3.27) (from Weston 1985, based on data for Pyroceram and alumina from Miller and Shepard 1961, and for Macor™ from a Corning™ data sheet). Additional permeation rates are given for synthetic materials at room temperature in Appendix A3.14.

bushing applications, gas permeation is not a problem, of course. In such cases, the greater concern is with the degassing rate of the material.

Metals: Unlike glasses, ceramics, and synthetic materials, metallic materials are crystalline in nature and do not have a porous microstructure; consequently, only those gases that are soluble in the metal will permeate it. Thus, *inert* gases such as helium will not permeate metals, even at elevated temperatures. Hydrogen and oxygen, however, are soluble in many metals and will permeate most to some extent. For diatomic molecular gases such as hydrogen, the molecules dissociate on adsorption at the high-pressure metal surface, and diffuse through the metal as atoms, recombining on the other side during desorption. For such diatomic gases, the flow rate of gas Q_i permeating a metal wall having thickness d and area A is given by (Weston 1985)

$$Q_i = \mathrm{K}\,(A/d)\,(P_2^{1/2} - P_1^{1/2}), \quad \text{Gas permeation rate through metals} \qquad (3.28)$$

where P_1 and P_2 are the gas pressures on either side of the metal wall. K is the permeation constant for metals, which is different from that for glass, ceramics, and synthetic materials; it has SI units of $(m^2/s)\,(Pa)^{1/2}$. Hydrogen has the highest diffusion rate, and it is the main concern in vacuum design.

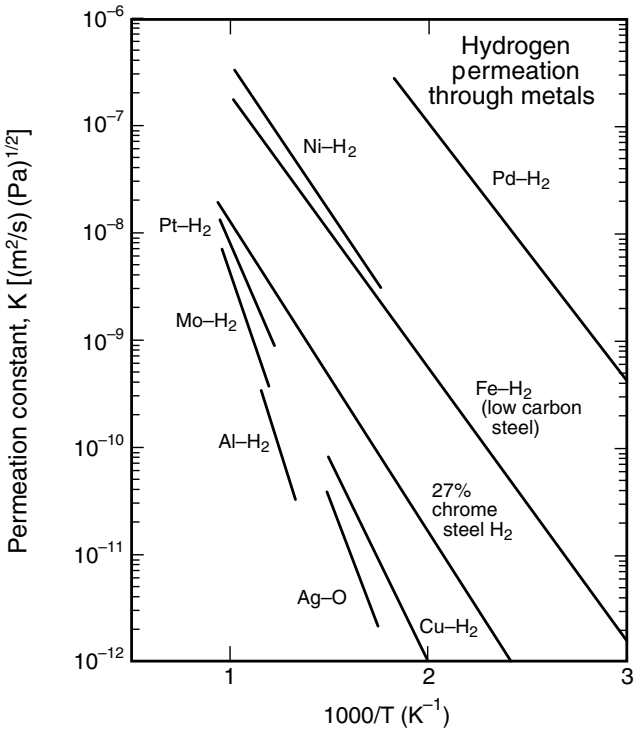

Fig. 3.22 Permeation constant K for hydrogen through several metals as a function of temperature, for use with Eq. (3.28) (from Weston 1985, based on data from Norton 1962). Note that the permeation constant in metals has units differing from those for microporous glasses, ceramics, and synthetic materials [Figs 3.20 and 3.21 are for use with Eq. (3.27)].

Figure 3.22 gives values of K for hydrogen permeation through various metals as a function of temperature, along with the special case of the Ag–O system. The permeation rate of hydrogen is highest through palladium (thus, heated palladium makes a great filter for obtaining pure hydrogen). This is followed by high permeation rates for nickel and iron [which would also include Mu-Metal, since it is mainly a combination of nickel and iron, 76%Ni–14%Fe–5%Cu–3%Cr–2%(Mn,Si,P,S)]. The permeation constant for 27% chromium steel is about two orders of magnitude lower still, but it cannot be ignored in UHV systems or in sealed vacuum vessels left at room temperature for long periods of time without vacuum pumping. Although the permeation rate of hydrogen through copper is about an order of magnitude lower than that for steel, copper is unsuitable as a UHV vessel material because, on heating to bake-out temperatures, its surface oxidizes heavily, causing scaling that flakes off.

The permeation rates of other gases through most metals are at least an order of magnitude lower than that for hydrogen, and they can be neglected for practical purposes. The exception is the permeation of *oxygen through silver* (see the data labeled Ag–O in Fig. 3.22). Because oxygen is highly soluble in silver, the permeation rate is much higher than even that of hydrogen. Consequently, a heated silver tube can be advantageously used to admit spectrographically pure oxygen to a vacuum system.

Examples of gas-permeability calculations:

Whereas degassing can be initially more of a problem than permeation, permeation of gases into a vacuum system is persistent and becomes more of a concern over long periods of time. Permeation especially affects sealed vacuum vessels, such as dewar vacuum jackets or sample chambers after they are initially evacuated and disconnected from a vacuum pump.

We now look at the pressure rise in an evacuated, sealed vessel due to gas permeation from the atmosphere through the dewar walls. From the conservation of mass in a vacuum vessel, we have

$$\mathrm{d}(PV) / \mathrm{d}t = Q_\mathrm{i} - Q_\mathrm{o}, \tag{3.29}$$

where Q_i is the rate of gas influx, and Q_o is the flow rate out of the chamber through the vacuum pump. After the pump is disconnected from the vacuum space, Q_o drops to zero. The gas influx from permeation is given for glass, ceramics, and synthetic materials by Eq. (3.27), where P_o is the pressure of gas on the outside of the vessel (assumed constant) and P_i is the pressure on the inside. We consider here the case where $P_\mathrm{o} \gg P_\mathrm{i}$; this is the practical situation for cryogenic dewar vacuum jackets, since by the time the inside pressure approaches the outside pressure, the vacuum space has long ceased to provide thermal isolation. Combining Eqs (3.27) and (3.29) under these conditions, we obtain

$$\mathrm{d}(PV)/\mathrm{d}t = \mathrm{K}\,(A/d)\,P_\mathrm{o}. \tag{3.30}$$

Assuming that the volume V of the vacuum space remains constant, Eq. (3.30) can be integrated to give the time dependence of the pressure P_i inside the vacuum space from gas permeation through the vessel walls,

$$P_\mathrm{i} = \mathrm{K}\,(A/V)\,d^{-1}\,P_\mathrm{o}\,t. \quad \text{Rate of pressure rise inside glass, ceramic, or synthetic vessels} \tag{3.31}$$

Here, V, A, and d are the vessel's volume, area, and wall thickness, K is the permeation constant for the particular gas/material in question, and P_o is the pressure of that gas outside the vacuum vessel. From Eq. (3.31) we see that for a constant wall thickness d, gas permeation becomes a greater problem as the size of a vessel is scaled down, since the rate of pressure rise is proportional to the ratio of the vessel's surface area to volume A/V.

Example: Suppose we want to determine how long it will take helium permeation from the atmosphere through the walls of a glass dewar to make the dewar's vacuum jacket "soft," that is, no longer providing good thermal isolation. Let us assume the worst case—that the dewar is made of silica glass. We assume further that the glass wall thickness is 2 mm, and that the dewar's vacuum jacket has a surface area of 0.6 m^2 and a volume of 2 L.

The partial pressure of helium naturally occurring in air is 5.3×10^{-1} Pa, which we use for P_o in Eq. (3.31). From Fig. 3.20 we find that the permeation constant K for helium through fused silica glass

is about 7×10^{-14} m^2/s at 20°C ($1000/T = 3.4$ K^{-1}). Thus, from Eq. (3.31) we find that the pressure inside the vacuum jacket will rise over time at a rate given by

$$\begin{aligned} P &= \mathrm{K}\,(A/V)\,d^{-1}\,P_\mathrm{o}t \\ &= (7 \times 10^{-14}\ \mathrm{m^2/s})\,(0.6\ \mathrm{m^2}/2 \times 10^{-3}\ \mathrm{m^3})\,(2 \times 10^{-3}\ \mathrm{m})^{-1}(5.3 \times 10^{-1}\ \mathrm{Pa})\,t \\ &= (5.5 \times 10^{-9}\ \mathrm{Pa/s})t. \end{aligned}$$

If we want to have good thermal isolation, we must maintain a vacuum in the dewar jacket low enough that the heat leak from conduction is $\ll 0.1$ W, which from Eq. (2.8) would correspond to a helium partial pressure $\ll 10^{-3}$ Pa (for a surface area of 0.6 m^2 and vacuum jacket spacing of several millimeters). Thus, because of the permeation of naturally occurring atmospheric helium, we had best purge and repump the vacuum jacket at least every

$$t \ll (10^{-3}\ \mathrm{Pa})\,/\,(5.5 \times 10^{-9}\ \mathrm{Pa/s}) = 2 \times 10^5\ \mathrm{s}$$

(i.e. every day, which would be onerous).

To make matters worse, if we use the dewar for liquid helium, the glass can come into contact with room-temperature helium gas (while we transfer liquid helium, or after the measurement, when the helium warms up in the dewar). Then the pressure P_o of helium gas seen by the glass vacuum jacket will be near atmospheric pressure (i.e. 1.0×10^5 Pa, not 5.3×10^{-1} Pa, the naturally occurring partial pressure of helium in air). In this case, the vacuum jacket will become soft in a matter of seconds! Now admittedly, we have calculated this permeation rate for the worst-case scenario—silica glass. Other choices of glass (see Fig. 3.20) would be several orders of magnitude better. However, even for these other glasses, we have only a few hours before the dewar will become soft if exposed to room-temperature helium gas. This explains, at least in part, the rise in popularity of stainless-steel dewars or metal-lined fiberglass–epoxy dewars. In the latter case, the thin (usually ~0.025 mm thick) stainless-steel lining is essential because of the same problem: helium permeation through fiberglass–epoxy composites.

A similar calculation can be performed for the permeation of *hydrogen* from the atmosphere through a *metal* vacuum vessel. In this case, we would use the partial pressure of hydrogen naturally occurring in air, which is 5×10^{-2} Pa, and Eq. (3.28) describing gas permeation for metals. From Eq. (3.29), this gives the pressure rise inside a metal vacuum vessel with time t as

$$P_\mathrm{i} = \mathrm{K}\,(A/V)\,d^{-1}\,P_\mathrm{o}^{1/2}\,t. \quad \text{Rate of pressure rise inside metal vessels} \qquad (3.32)$$

The permeation constant K for hydrogen through 27% Cr steel at 20°C, obtained by extrapolating the data in Fig. 3.22 to $1000/T = 3.4$ K^{-1}, is about 1×10^{-15} (m^2/s)(Pa)$^{1/2}$. For a dewar vacuum jacket of the same dimensions as that considered in the above example, we would find the rate of rise of the hydrogen pressure in the vacuum space from atmospheric permeation to be about 7×10^{-11} Pa/s, almost two orders of magnitude slower than that of helium permeation through silica glass. However, because of this hydrogen permeation, steel vacuum jackets still require occasionally purging and repumping after several months. [From Fig. 3.22 we see that the permeation rate of hydrogen through aluminum would be lower than that through steel, which is one of the reasons the outside (warm) dewar wall is often made of

aluminum. However, aluminum has a much higher thermal conductivity than steel, which is why the inside (cold) dewar wall is usually made of stainless steel or a metal-lined fiberglass-epoxy composite.]

Repumping intervals are usually lengthened by incorporating a getter material into the vacuum space to trap permeated gases, as well as gases desorbed from the surfaces of the multilayer insulation and vacuum jacket walls. The getter material is placed next to the (inner) cold wall of the dewar vacuum jacket to lower the getter's temperature for more effective trapping action. For dewars that are repumped every few years, activated charcoal is usually used as the getter because it can be easily reactivated by warming and pumping on the vacuum jacket. For dewars that must go longer without repumping, a molecular sieve is usually used because it does not saturate as quickly as activated charcoal; however, once saturated, the dewar's vacuum jacket has to be opened and the molecular sieve replaced.

3.9 References

3.9.1 FURTHER READING

MATERIAL PROPERTY DATA:

Heat capacity, thermal expansion, resistivity, superconducting parameters, thermal conductivity, magnetic susceptibility, and mechanical properties of many materials at cryogenic temperatures are tabulated in Appendixes A6.1 through A6.10 at the end of this book.

Classic multivolume source of handbook data:

Y. S. Touloukian et al., eds. (1970–1977). *Thermophysical Properties of Matter*, Plenum Press, New York.

General handbooks containing material property data:

(1972) *American Institute of Physics Handbook*. McGraw-Hill, New York.
(2002) *CRC Handbook of Chemistry and Physics*, 83rd edition. CRC Press, Boca Raton, FL.

Detailed review of material properties at low temperatures, as well as how they are measured:

Reed, R. P. and Clark, A. F., eds. (1983). *Materials at Low Temperatures*, ASM International, Materials Park, OH.

Compilations and handbook data on cryogenic properties, especially mechanical properties:

(1977) *Handbook of Materials for Superconducting Machinery*. MCIC-HB-04. Battelle Laboratories, Columbus, OH.

MEASUREMENT CRYOSTAT DESIGN:

An introductory review and literature references to specific types of measurement cryostats, including cryostats for measurement of heat capacity, thermal conductivity, thermal expansion, electric transport properties, optical and x-ray properties, and magnetic susceptibility:

White, G. K., and Meeson, P. J. (2002). Chapter 7 in *Experimental Techniques in Low-Temperature Physics*, 4th edition, Oxford University Press, Oxford, England.

Experimental techniques and apparatus specific to superconductor measurements:

Seeber, B., ed. (1998). *Handbook of Applied Superconductivity*, Institute of Physics Publishing, Bristol, England.

MACHINING:

A valuable reference for mechanical data on the strength of materials, dimensioning, fasteners, screws, gears, and you name it:

(2000) *Machinery's Handbook*, 26th edition, Industrial Press, Inc., New York.

VACUUM TECHNIQUES AND EQUIPMENT:

Introductory information on the various types of vacuum pumps:

White, G. K., and Meeson, P. J. (2002). *Experimental Techniques in Low-Temperature Physics*, 4th edition, beginning of Chapter 10, Oxford University Press, Oxford, England.

Vacuum equipment information is supplied in several excellent catalogues available from suppliers:

Physics Today Buyers Guide, American Institute of Physics, http://www.physicstoday. org/guide/.

Extensive tutorial and general information on vacuum technology is given, for example, in the Kurt J. Lesker catalogue.

Further information on ultrahigh-vacuum techniques, including materials selection, vacuum pump selection, pressure measurement, valves, and seals:

Weston, G. F. (1985). *Ultrahigh Vacuum Practice*, Butterworth, London.

VIBRATION ISOLATION:

Movshovich, R. (1988). "Vibration isolation," in *Experimental Techniques in Condensed Matter Physics at Low Temperatures*, eds. R. C. Richardson and E. N. Smith, Addison Wesley, Reading, MA.

Filinski, I., and Gordon, R. A. (1994). "The minimization of ac phase noise in interferometric systems," *Rev. Sci. Instrum*. 65, 575–586. This article has a good appendix describing the use of old inner tubes for vibration isolation.

3.9.2 PROPERTIES OF SOLIDS: INTERNET INFORMATION

Although information on the Internet is constantly changing, the following web sites are provided as starting points for locating additional on-line sources of information for many common construction materials.

Cryogenic properties (1–300 K) of many materials have been represented by empirical curve fits and are available free on the Internet at http://www.cryogenics.nist.gov/. Information for using the NIST fitting parameters to perform data calculations and make plots is also available at this web site.

Materials data along with fitting equations can be purchased on CD from http://www.cryodata.com/ (cryogenic properties of about 100 materials), and from http://www.jahm.com/(temperature-dependent properties of about 1000 materials, many at cryogenic temperatures).

Room-temperature data are available free on the Internet for about 10 to 20 properties of about 24 000 commercial materials at http://www.matweb.com/.

3.9.3 CHAPTER REFERENCES

Altemose, V. O. (1961). "Helium diffusion through glass," *J. Appl. Phys*. 32, 1309.

American Society of Mechanical Engineers, Boiler and Presure Vessel Code (1998), 28 volumes, NY, http://www.asme.org/.

Battelle (1977). *Handbook on Materials for Superconducting Machinery; Mechanical, Thermal, Electrical, and Magnetic Properties of Structural Materials*, MCIC-HB-04, Metals and Ceramics Information Center, Battelle, Columbus Laboratories, Columbus, OH.

Beer, R. P., and Johnston, E. R., Jr. (1981). *Mechanics of Materials*, p. 531, McGraw-Hill, New York.

Berman, R., Foster, E. L., and Rosenberg, H. M. (1955). "The thermal conductivity of some technical materials at low temperatures," *Brit. J. Appl. Phys*. 6, 181–182.

Blears, J., Greer, E. J., and Nightingale, J. (1960). "Factors determining the ultimate pressure in large high-vacuum systems," *Adv. Vac. Sci. Technol*. 2, 473.

Chang, S. S. (1970). "Heat capacity and thermodynamic properties of polyvinyl chloride," *J. Res. Natl. Bur. Stand*. 82, 9–17.

Childs, G. E., Ericks, L. J., and Powell, R. L. (1973). *Thermal Conductivity of Solids at Room Temperature and Below, A Review and Compilation of the Literature*. NBS Monograph 131. US Dept. of Commerce, US Government Printing Office, Washington, DC.

Clausing, P. (1932). "The flow of highly rarefied gases through tubes of arbitrary length." *Ann. Phys*. 12, 961 [English translation 1971, *J. Vac. Sci. Technol*. 8, 636–646.] Figure 3.16 reprinted by permission.

Corruccini, R. J., and Gniewek, J. J. (1960). *Specific Heats and Enthalpies of Technical Solids at Low Temperatures*. NBS Monograph 20, pp. 1–20. US Government Printing Office, Washington, DC.

Goodall, D. H. J. (1970). *Wall data chart*, A.P.T. Division, Culham Laboratory, Abingdon, Oxfordshire, England.

Higdon, A., Ohlsen, E. H., Stiles, W. B., Weese, J. A., and Riley, W. F. (1985). *Mechanics of Materials*, p. 160, John Wiley & Sons, New York.

Honig, R. E. (1962). "Vapor pressure data for the solid and liquid elements", *RCA Rev.* 23, 567–586.

Honig, R. E. (1969). "Vapor pressure data for the solid and liquid elements," *RCA Rev*. 30, 285.

Hust, J. G. (1983). "Thermal conductivity and thermal diffusivity," Chapter 4 in *Materials at Low Temperatures*, eds. R. P. Reed and A. F. Clark, ASM International, Materials Park, OH.

Johnson, V. (1960). *A Compendium of the Properties of Materials at Low Temperature, Part I. Properties of Fluids*; and *Part II. Properties of Solids*, Technical Report 60-56. National Bureau of Standards, Wright Air Development Division (WADD). US Government Printing Office, Washington, DC.

Kays, W. M., and London, A. L. (1984). *Pressure Drop Compact Heat Exchangers*, 3rd edition, McGraw-Hill, New York.

Kronberger, H. (1958). "Vacuum techniques in the atomic energy industry," *Proc. Inst. Mech. Eng.* 172, 113. Figure 3.17 reproduced by permission of the Council of the Institution of Mechanical Engineers.

Machinery's Handbook, 26th edition (2000), Industrial Press, Inc., New York.

Mann, D. (1978). *LNG Materials and Fluids, A User's Manual of Property Data in Graphic Format*. US Dept. of Commerce, US Government Printing Office, Washington, DC.

Miller, C. F., and Shepard, R. W. (1961). "Evaluation of Pyroceram code 9606 as a suitable envelope for vacuum devices operating at high ambient temperature," *Vacuum* 11, 58.

Norton, F. J. (1962). *Transactions of the 8th National Vacuum Symposium and Proc. 2nd International Congress on Vacuum Science Technology 1961*, Vol. 1, p. 8. Pergamon Press, Oxford; Elmsford, NY.

Powell, R. L., and Coffin, D. O. (1954). "Thermal conductivity of solids at low temperatures," *Adv. Cryog. Eng*. 1, 262–266.

Radebaugh, R., Bradley, P. E., Marquardt, E., Lewis, M. A., and Siegwarth, J. D. (2001). http://www.cryogenics.nist.gov/, based principally on compilations by Battelle 1977, Childs et al. 1973, Johnson 1960, Mann 1978, Schramm et al. 1973, Simon et al. 1992, and Touloukian et al. 1970–77.

Read, D. T. (1983). "Mechanical properties," Chapter 7 in *Materials at Low Temperatures*, eds. R. P. Reed and A. F. Clark, ASM International, Materials Park, OH.

Read, D. T., and Reed, R. P. (1979). "Toughness, fatigue crack growth and tensile properties of three nitrogen-strengthened stainless steels at cryogenic temperatures", In *The Metal Science of Stainless Steels*, eds. E. W. Collings and H. W. King, pp. 92–121, American Institute of Mining, Metallurgical, and Petroleum Engineers, New York.

Richards, R. J. (1954). "A high-vacuum seal-off valve," *Rev. Sci. Instrum*. 25, 520.

Roark, R. J., and Young, W. C. (1975). *Formulas for Stress and Strain*, McGraw-Hill, New York.

Schramm, R. E., Clark, A. F., and Reed, R. P. (1973). *A Compilation and Evaluation of Mechanical, Thermal, and Electrical Properties of Selected Polymers*. NBS Monograph 132. US Government Printing Office, Washington, DC.

Simon, N. J., Drexler, E. S., and Reed, R. P. (1992). *Properties of Copper and Copper Alloys at Cryogenic Temperatures*. NIST Monograph 177. US Government Printing Office, Washington, DC.

Smith, R. L., and Rutherford, J. L. (1957). "Tensile properties of zone refined iron in the temperature range from 298 to 4.2 K," *J. Met*. 9, 857–864.

Soffer, L. M., and Molho, R. (1967). *Cryogenic Resins for Glass-Filament-Wound Composites*. NASA Report N67–25076, Available from NTIS, Springfield, Virginia.

Swenson, C. A., and Markiewicz, W. D. (2000). "Magnetic characterization of austenitic stainless steel for nuclear magnetic resonance coils," *IEEE Trans. Appl Supercond*. 10, 736.

Tobler, R. L. (1976). "Cryogenic effects on the fracture mechanics parameters of ferritic nickel alloy steels," in *Materials Research for Superconducting Machinery*, Vol. 6, eds. R. P. Reed, H. M. Ledbetter, and E. C. Van Reuth, ADA036919, Available from NTIS, Springfield, Virginia.

Touloukian, Y. S. (1966). *Recommended Values of the Thermophysical Properties of Eight Alloys, Major Constituents and their Oxides*, Report No. CST-7590, pp. 271–343, Thermophysical properties Research Center, Purdue University, Lafayette, IN.

Touloukian, Y. S., Powell, R. W., Ho, C. Y., and Klemens, P. G., eds. (1970). *Thermophysical Properties of Matter*, The Thermophysical Properties Research Center Data Series, Plenum Press, New York.

Warren, K. A., and Reed, R. P. (1963). *Tensile and Impact Properties of Selected Materials from 20 to 300 K*. NBS Monograph 63, US Government Printing Office, Washington, DC.

Weston, G. F. (1985). *Ultrahigh Vacuum Practice*, Butterworth, London.

4 Wiring and Connections

Never hire a plumber who wears rubber boots or an electrician with scorched eyebrows.

–Ashley Cooper

4.1 Introduction

Cryostat wiring requires someone who is skilled and meticulous with his or her hands. It is fine detail work that, in many cases, is done by the experimentalist and not subcontracted outside the laboratory. In this chapter we focus on some of the techniques and pitfalls in wiring that hopefully will avoid "scorched eyebrows" (figuratively speaking). It takes great patience and a lot of practice to work effectively with fine #36 or #40 gauge wire and make clean, high-quality, miniature solder joints. So plan the wiring layout carefully, learn in noncritical situations, and allow plenty of time to do the job right. A wise colleague of ours once said, "It takes a long time to learn how to be this careful" (N. Missert). But the care exercised can save untold amounts of frustration later trying to work through a sea of problems, such as electrical shorts, thermoelectric-voltage drifts, noise, Joule heating, and unwanted heat flux introduced into the sample through the wiring leads.

In this chapter, we first describe the main guidelines for wiring a cryostat in Sec. 4.1. The key factor that ultimately determines the electrical performance of a cryostat is the *electrical layout*: what is twisted with what else, what is shielded, what shares a feed-through, and where joints are made. In effect, the cryostat is part of a low-noise electronic measurement system that must be designed at the outset.

Recommendations are also made for selecting the right wire material and gauge size in Sec. 4.2, and wire insulation in Sec. 4.3. These three choices spell success or failure in terms of thermoelectric-voltage drifts, heat leaks, and electrical shorts, respectively. Appendix A4.1a contains one of the more useful wire tables in making these choices, giving not only gauge size, area, and resistance per unit length, but also heat conduction and optimum current levels for wires of various materials and sizes. The nearest metric equivalents are tabulated in Appendix A4.1b.

The later sections of this chapter present details about heat-sinking (Sec. 4.4) and soldering techniques (Sec. 4.5), as well as information on specialty topics, including thermoelectric voltages (Sec. 4.6), vacuum electrical lead-throughs (Sec. 4.7), radio-frequency coaxial cable selection (Sec. 4.8), high-current leads (Sec. 4.9), and flexible current leads (Sec. 4.10).

4.1.1 GENERAL GUIDELINES

Several guidelines apply generally to cryostat wiring. First, select wires with *durable insulation*. Standard polyvinyl-formal insulation is soft, shorts if heated to soldering temperature,

dissolves when thermally anchored with varnish, and damages easily when twisted. Other than that, it is just fine. Wire insulation is discussed in Sec. 4.3 and Appendix A4.4.

Second, try to design the wiring layout so that leads carrying sensitive signals are separated from leads with big, noise-ridden signals. For example, in low-resistivity, high-current measurements (such as for bulk superconductor testing), keep the sensitive *voltage* leads separate from the current leads. This minimizes noise pickup in the voltage leads, which can be induced by variable high currents. For the same reason, try to keep the voltage-lead *heat sinks* separate from the current-lead sinks, since the heat influx from current leads can introduce thermoelectric-voltage noise.

On the other hand, for high-impedance, low-current measurements, keep the sensitive *current* leads separate from the voltage leads and any other noisy leads. Especially, avoid pulsed signals such as those carried by computer lines and the heater power lines of some temperature controllers. As a general rule, keep nonspecimen leads separate from specimen leads.

All instruments should be grounded at *one* point only. That is, they should be connected to ground through one path, like the branches of a tree, with the trunk being the ground. Avoid multiple ground points because they can lead to spurious voltages caused by currents flowing from one point to another through ground. If you have a choice, choose the ground point to be as close to the sample as possible, to minimize noise. Further information is contained in the very good book on grounding and shielding techniques by Morrison (1998).

The shields of plugs and sockets are unreliable for providing a continuous ground network. Always use an extra pin in a multipin connector for ground, not the shield. Thus, the right number of pins when selecting a connector for a four-wire transport measurement is five.

4.1.2 DC AND LOW-FREQUENCY ($\lesssim$10 kHz) WIRING

Non-rf leads (such as those used for thermometry and dc sample-voltage measurements) need to be *tightly twisted* together in corresponding pairs (voltage leads together, current leads together) to minimize "pickup" voltage and general laboratory noise. This is especially true in the high-field regions of magnets where even small magnetic-field variations or motion/vibration of the leads can induce voltages many times larger than the small microvolt signal voltages we are usually trying to measure. Twisting leads is much more effective than using coaxial cable for minimizing *magnetically* induced noise voltage (up to about 10 kHz) because the sheath of coaxial cables does not shield magnetic fields and the current distribution pattern in coaxial cables is never exactly symmetric.

➔ To be effective in minimizing induced voltages, the twist length (or pitch) has to be relatively short. I have found a twist length of $\leq$20 wire diameters (i.e. twist "bump" length of $\leq$10 wire diameters) to be a good compromise for making a twisted pair of #32 to #36 gauge (0.2–0.13 mm diameter) wire reasonably tight without damaging the wire insulation in the process.

Twisting is made easier by using a variable-speed electric drill with a hook in its chuck. The two ends of a length of wire are clamped in a vise (or other static support), and the middle of the wire is looped over the hook and pulled taut before twisting. The hook can be made by simply bending a solid heavy-gauge copper wire (say, #12 gauge, 2 mm

diameter) into a hook shape. By using such a soft, smooth hook material, the wires can be tensioned slightly during twisting without being severed. Be careful to keep the twisted pair stretched when letting the torque spring back afterward, or you will get a tangled mess. The slightly damaged ends of the twisted pair (where they are clamped as well as where they are wrapped around the hook) are cut off, and there you have it—a quick way to produce a very neat twisted pair.

For multiwire cables, it is good practice to first tightly twist *corresponding pairs* of wires before combining them into the final cable. Be sure to check for wire-to-wire shorts after twisting and *before* installing.

Thermoelectric voltages are the great nemesis for sensitive dc signals. For example, they must be dealt with in the case of high-current superconductor measurements where ac techniques cannot be used and the signal voltages are very small, typically less than a microvolt. Unwanted thermoelectric voltages are generated by changing temperature gradients along wires and across electrical joints. Techniques for minimizing them are described in detail in Sec. 4.6 and well worth the effort.

For ac measurements, on the other hand, thermoelectric voltages are not a problem because the alternating current averages out their effect. In fact, low-frequency ac methods are often used to sidestep the thermoelectric-voltage problem encountered in dc measurements and ought to be considered whenever practical, such as when the sample measurement current is relatively low ($\lesssim$100 mA), or when using resistance thermometers (a simple ac bridge circuit for use in these situations is detailed in Ekin and Wagner 1970). Similarly, lower signals can be extracted for dc measurements at moderately higher current ($\lesssim$10 A) by reversing the current with a hand-thrown knife switch. This reverses the sample signal but not the thermoelectric voltage, so the magnitude of the two voltage readings can be averaged to eliminate (to first order) slowly drifting thermoelectric voltages. This technique becomes too difficult at high current levels, however, and then the only practical approach is to pay particular attention to the techniques in Sec. 4.6.

4.1.3 AC HIGH-FREQUENCY WIRING

Detailed suggestions for selecting coaxial cables and techniques for heat-sinking them are described in Sec. 4.8. Here we offer some more general guidelines for the treatment of ac wiring (Colclough 2002).

As with dc wiring, it is best to twist current wires as pairs and voltage wires separately as pairs. Capacitive coupling between wires with different functions can be minimized by bundling them and routing them through separate plastic sleeves. Otherwise, bizarre and stubborn phase shifts can result from interwiring capacitance, which can become a problem when working with high-impedance samples or contacts. Also, use separate connectors and feed-throughs for the different wiring bundles.

A metal dewar provides good protection from high-frequency noise. Although the noise may be at a very different frequency from that of the measurement, it can cause considerable

interference. Use rf filters where possible to block unwanted noise, especially at the cryostat top. Filters that fit neatly between the plug and socket (especially the commercially available D-connector ones) are cheap and effective.

Watertight shield-to-shield connectors are needed to effectively keep out rf noise. Circular military-style connectors are not particularly well shielded. D-connectors (such as DB-25) are popular connectors that are well made, with gold plating and turned pins. Professional microphone connectors also work well. Leads carrying *differential* signals (which is desirable; see Morrison 1998) should be routed through adjacent pins in a single connector, never through separate BNC connectors.

Especially for large cryostats, it helps to design the sample holder so it can be unplugged from the main apparatus. This can make sample mounting much more convenient and flexible. Connectors that work at low temperatures include the cylindrical contact inserts from Fischer or Lemo, mini-D connectors, as well as better-quality IC plugs and sockets (for supplier information, see Appendix A1.7 under Connectors).

4.1.4 WIRING INSTALLATION TECHNIQUES

As noted at the outset, wiring a cryostat with wire only 0.1 mm in diameter is a tedious, tricky business that requires incredible craft, care, and patience. Try to get "someone who knows" to teach you and have him or her look over your work.

Following are several suggestions that may help (all learned the hard way):

- Learn to work with two pairs of very fine tweezers and a pointed scalpel, and *work under a magnifying lens*. That is, wear a strong magnification visor, or use a cheap binocular microscope (say, $\times 5$ to $\times 20$) or, better yet, a microscope with an inexpensive TV display.
- Hide your tweezers.
- Be sure to apply enough heat to solder joints to get the solder to become very liquid and *flow*. Learn to recognize good solder joints by looking (yes, with a microscope) for smooth concave contours of the solder and good wetting. Bad, under-heated solder joints are usually the source of most connection problems. Use a temperature-controlled soldering iron with adequate power for the task and a clean, pointed tip. Check for clearance from neighboring joints; pull the soldered wire to the side to prove that it cannot short to its neighbor.
- For fine-wire electronics, avoid "activated" rosin or "noncorrosive" flux. Do not believe the labels. They are all corrosive except pure rosin flux or "unactivated" rosin dissolved in alcohol (see the tip entitled "bête-noire of soldering" in Sec. 3.3.4).
- After a complex cryostat is wired, it can be difficult to make mechanical changes. Except for sensitive dc voltage leads, consider breaking the majority of the wires by using a plug-and-socket arrangement or soldered-terminal strip at strategic points in the cryostat. This can facilitate mechanical reworking of major cryostat sections that would otherwise be almost impossible. Electronic plugs and sockets with 1–2 mm pin spacing work fine.
- Try to anchor *all* solder connections with solder terminal strips or connectors. Where free-floating wire-to-wire connections cannot be avoided, twist the ends of large wires together for mechanical strength before soldering (unless frequent assembly and disassembly is contemplated). However, for small instrument wires [smaller than about #30 AWG

(~0.250 mm metric)], it is better to overlap them end-to-end. This technique creates a connection stronger than the wires themselves and also allows a piece of insulating tubing to be slipped over the joint.

- For mechanical protection, thread the wire leads through loose-fitting polyethylene or Teflon™ spaghetti tubing or spiral wrap.
- Try to run the wires inside stainless-steel cryostat support tubes for protection, shielding, and convenience. Still use sleeving, both to protect the wires from being cut by the sharp edges of the stainless tubing as well as to lower the stray capacitive coupling between the wires and metal.
- Tie free-floating wires to a support with some kind of a cord (e.g. dental floss, thread, string, plastic wire ties), tape, or BluTack™ (see Appendix A3.10 for further comments and supplier information). This provides protection and minimizes vibrationally induced pickup voltages. Loose wiring that is free to blow around is a source of noise and an accident waiting to happen.
- Before anchoring or gluing wires to the surfaces of a complex cryostat, it is well worth taking some time to prepare the surfaces so they do not cut through the wire insulation. File smooth curves on edges that the wires might touch, especially the edges of holes through which they will pass. Cover sharp corners with protective tape.
- Wires with weak insulation can be protected by pasting (with varnish) a layer of thin paper onto the surface before anchoring the wires with additional varnish (but beware, the varnish will soften polyvinyl-formal insulation until it is dry). Lens-cleaning tissue serves this purpose well because it is porous and is readily soaked with varnish. Cigarette paper is also okay. A layer of thin paper can also be placed on top of the wires for extra protection.
- Test all wiring for end-to-end continuity with an ohm meter. Also, make sure there is $> 20\ \mathrm{M}\Omega$ electrical isolation wire-to-wire and wire-to-chassis. If you use IMI 7031 varnish for insulating and attaching wires in place, do not try the isolation test until after the varnish dries; the wet varnish provides a high resistance path to ground, and you will fret needlessly.
- The canonical problem of low-temperature physics is figuring out which wire at the top of the apparatus corresponds to which at the bottom. Use a multimeter with a continuity beeper, and get one that has no delay between contact and beep, so that even a mere brush of the wire gets immediately noticed.
- Record your cryostat's wiring. We think we will not forget, but somehow 6 months later. . . .

4.2 **Wire selection**

4.2.1 WIRE SELECTION FOR CRYOSTAT DESIGN

Selecting the right wire size and material (and insulation, Sec. 4.3) can greatly affect heat load, thermoelectric-voltage drift, and Joule heating in the leads. Table 4.1 is a summary of the wires I have found useful as a starting point for specific cryostat-wiring applications.

Table 4.1 **Cryostat-wiring recommendations.**

Wiring Application	Wire Material	Typical Size (AWG and metric)[a]	Comments
Sample-voltage sensing	Copper	AWG: #34 – #40 (0.160–0.080 mm) typically #36 (0.127 mm)	For dc measurements (ref. Sec. 4.6): Use continuous leads (no connections) to reduce thermoelectric voltages by about an order of magnitude When connections are necessary, copper–copper joints minimize thermoelectric voltages
Thermometer leads and low-current sample leads	Phosphor bronze	AWG: #32 – #40 (0.202–0.080 mm) typically #36 (0.127 mm)	Phosphor bronze offers good thermal isolation (low λ) in a wire size convenient to handle Low magnetoresistance Easy to solder
Heater fabrication		AWG	Stable, high resistance is needed for heater wire
	Phosphor bronze	#36 (~0.127 mm) (~7 Ω/m at 4 K)	Phosphor bronze is easier to solder than Manganin, Constantan, or Nichrome (in order of increasing difficulty)
	Manganin	#36 (~0.127 mm) (~34 Ω/m at 4 K)	Phosphor bronze has the smallest magnetoresistance and volume susceptibility, so it is recommended for use in magnetic fields
	Constantan	#36 (~0.127 mm) (~39 Ω/m at 4 K)	
	Nichrome	#32 (~0.200 mm) (~34 Ω/m at 4 K) (the relatively larger wire size for Nichrome is needed to provide adequate surface area for dissipating heat)	
Heater power leads	Copper	AWG: #30 (~0.255 mm) (size depends on current; see Sec. 4.9.1 for optimum diameter)	Copper's low resistivity is needed to supply the higher currents required by heaters

[a] AWG: American Wire Gauge, see Appendix A4.1a. Wires are commonly available only in even gauges.
The conversion from inches to AWG is given by the equation: AWG gauge $= 30 - 20\log_{10}(d/0.01'')$, where d is the wire diameter in inches.
The nearest common *metric* wire sizes are tabulated in Appendix A4.1b.

4.2.2 WIRE MATERIAL PROPERTIES

As background reference data, Fig. 4.1 and Appendix A4.2 give the thermal conductivity and physical properties, respectively, of common wire materials at various temperatures. These temperature-dependent handbook data work well for "dirty" (highly resistive) wire materials, such as Constantan, Manganin, Nichrome, and phosphor bronze. Not so, however, for relatively pure conductors such as copper. As mentioned in Chapter 3, the resistivities of pure metals are fairly consistent near room temperature, but at lower temperatures, resistivities differ considerably depending on the level of defects in a wire.

The relative purity of conductors is commonly characterized by calculating the *ratio* of the room-temperature electrical resistivity $R_{293\,K}$ to the resistivity in the low-temperature limit $R_{\sim 4\,K}$—the so-called Residual Resistance Ratio, RRR $[\equiv R_{293\,K}/R_{\sim 4\,K} \equiv \rho_{293\,K}/\rho_{\sim 4\,K}]$. Sometimes the high reference temperature is taken as 20°C (293 K) or 22°C (295 K), and then again,

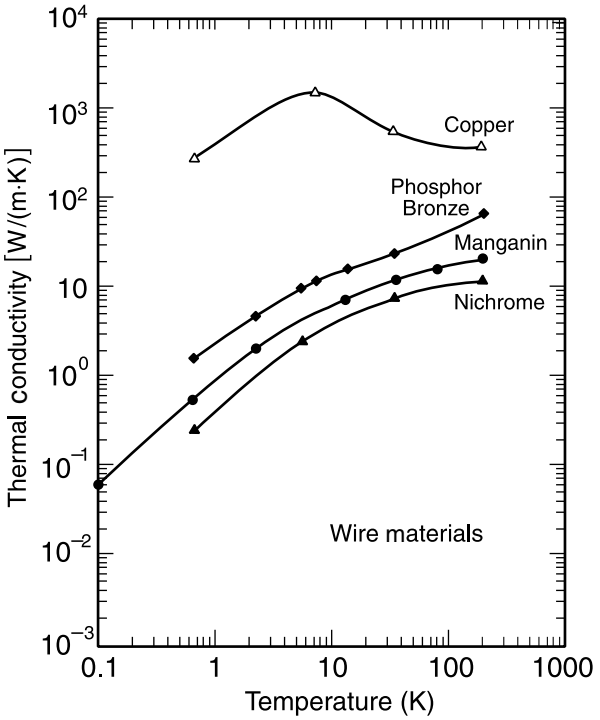

Fig. 4.1 Thermal resistivity of common wire materials (data compiled by Lake Shore Cryotronics 1995).

sometimes the ice point 0°C (273 K). (I prefer 20°C or 22°C, since these are closer to usual laboratory temperatures.) The specific temperature where the *low*-temperature resistance is measured is not particularly important, because the electrical resistivity is nearly independent of temperature in this regime. A value near the boiling point of liquid helium (~4.2 K) is usually used for convenience.

Example: We see from Appendix A4.2 that for electrolytic-tough-pitch (ETP) copper wire (common instrumentation wire), the resistance at low temperature (4 K) is 0.016 μΩ cm, whereas at room temperature (293 K) it is 1.71 μΩ cm, which gives a RRR of 1.71 / 0.016 = 107. A RRR of about 100 indicates a copper wire of moderate purity that is a good compromise between cost and performance in most wiring situations.

Note that the "dirty" alloy materials listed in Appendix A4.2 have RRR values barely above unity (i.e. the resistivity values listed there change very little between 293 and 4.2 K).

The RRR value becomes important when estimating Joule heating (I^2R) in leads at low temperature since the low-temperature resistance $R_{\sim 4\,\mathrm{K}}$ can be conveniently estimated from handbook values of the room-temperature resistance $R_{293\,\mathrm{K}}$ by using the identity $R_{\sim 4\,\mathrm{K}} \equiv R_{293\,\mathrm{K}}/\mathrm{RRR}$. (Room-temperature values of resistance per length are tabulated for common wire gauges and materials in Appendixes A4.1a and b.) The RRR is also useful for estimating the *thermal* conductivity of key cryostat parts, such as copper sample-holder materials, by using the Wiedemann–Franz–Lorenz law [see Eq. (2.4) and its discussion].

Appendix A4.3 tabulates some typical RRR values for several low-resistivity materials commonly used for wires and cryostat parts. We see in the table that annealing oxygen-free copper can make a difference in the RRR value (also, see the footnotes on annealing listed at the end of Appendix A3.1). Note that as-received copper grounding strap has a RRR only about one-quarter that of typical copper-wire material. When a measured RRR value is not available, 100 is a good approximate value to use for most copper instrumentation wire.

4.3 Insulation selection

Beware of the wire insulation you choose. One of my greatest frustrations in apparatus construction was having to rewire an entire cryostat because I used wires with insulation having a low thermal rating (polyvinyl formal). After fully wiring the apparatus and carefully winding and varnishing all the heat sinks, I needed to heat the copper sample support to make some solder connections. However, since the thermal rating of this insulation is lower than the melting temperature of almost every solder, the heat softened the insulation and shorted the leads to the heat sinks. Aargh! … Had to completely redo everything.

Thermal ratings of typical wire insulation materials are given in Appendix A4.4. Polyimide is now what I try to use, exclusively. It is tough, has a higher thermal rating, and, because it is bonded to the copper [unlike bare wire in tetrafluoroethylene (Teflon™) tubing], it provides good direct thermal contact for attaching the wires to heat sinks (next section).

Various chemical strippers are readily available for polyvinyl-formal insulation. Polyimide, on the other hand, is tougher to remove. It can be removed with a strong chemical stripper (for supplier information, see Appendix A1.7 under Wiring), but this is usually slow. From a practical standpoint, we have found that the best technique is to soften the section of polyimide you want to remove by holding it for a few seconds in a flame (match flame or cigarette lighter); then scrape off the weakened polyimide with a small wire brush or razor blade (drag the blade backwards along the conductor). The razor-blade technique gives a better defined transition between the insulated and bare sections of the wire so that it is easy to keep the wire well insulated right up to a solder terminal (to prevent accidental shorting to a neighboring terminal). The razor-blade method is also useful for stripping off bonded Teflon™ insulation. (Just be sure to practice the razor-blade method with some scrap pieces of wire first to learn not to nick the wires too much.)

Cotton overwrap (which is commercially available) is also a good insulation for protecting wires that are made with weaker insulation. The cotton soaks nicely with varnish for thermal anchoring and provides built-in mechanical protection.

4.4 Heat sinks for instrumentation leads

When a wire lead is attached to a sample or a thermometer, it brings with it not just an electrical connection, but a thermal connection as well. Heat-sinking the wire to the correct temperature before it is attached to a sensitive cryostat part may be as important as the part's mounting in determining its temperature. This is accomplished by thermally (but not electrically) anchoring wire leads to the sample holder before attaching them to a sample or thermometer.

For larger cryostats where there is room ($\gtrsim$2 cm diameter), the copper heat-sink post scheme shown in Figs 1.7 and 4.2 is a convenient, flexible arrangement for heat-sinking thermometer and instrumentation leads. Here, the leads are wrapped around copper heat-sink posts (or bobbins or tempering posts) before being attached to the sample. (For length of wrap needed, see Sec. 4.4.2 and the table in Appendix A4.5.) A rack of spring-loaded pins (such as "pogo pins" described in Sec. 7.4.3) might be used with this arrangement to make electrical contact with the sample. The thermometer is attached close to the sample, in this case, on the opposite side of the copper sample platform about 5 mm away, as illustrated schematically in Fig. 4.2.

If the measurement probe must be made smaller ($\lesssim$1.5 cm diameter), for example to fit into the small bore of a high-field magnet, then the heat-sinking scheme shown in Figs 1.8 and 4.3 can be used. Here, the instrumentation leads are brought to sample temperature by wrapping them around the main body of the sample-support rod itself, since there is not enough room for individual copper posts. The voltage and current leads can be kept separate by wrapping

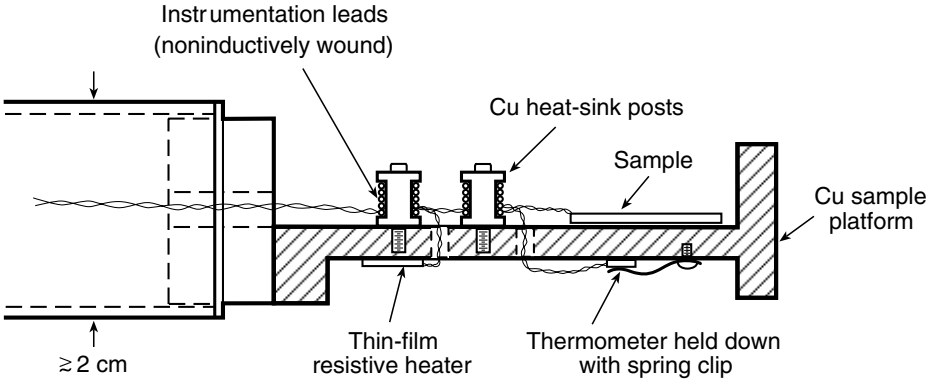

Fig. 4.2 Cross-sectional view of a heat-sink scheme for larger probes ($\gtrsim$2 cm diameter) where there is enough room to screw copper posts to the sample platform. The instrumentation leads are first twisted in pairs to minimize sensitivity to induced voltages and then noninductively wound onto the heat-sink posts (see Fig. 4.4 and the accompanying tip). Finally, they are cemented in place with varnish or epoxy.

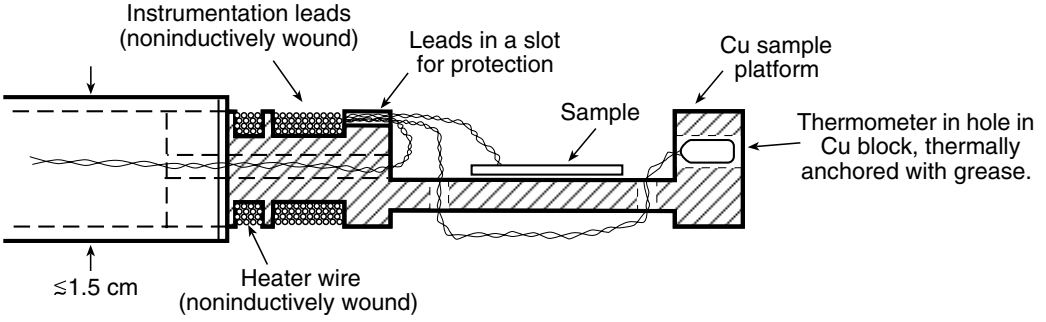

Fig. 4.3 Cross-sectional view of a heat-sink scheme for smaller probes ($\lesssim$1.5 cm diameter) that uses a groove cut around the circumference of the sample holder. Standard twisting and noninductive winding techniques are used, as described in the text.

the current leads around the probe's body in a location different from where the voltage leads are thermally anchored, as illustrated in Fig. 1.8.

If the cryostat will be used in a magnetic field, the instrumentation leads should also be *noninductively* wound around the copper bobbins using a scheme like that shown in Fig. 4.4 to further reduce magnetically induced voltages.

➔ The easiest way to noninductively wind instrumentation leads is to first twist pairs of voltage or current wires (by using, for example, the electric drill technique noted above) and then fold the cable into a loop, which is wound two-in-hand around the heat-sink post, as shown in Fig. 4.4.

4.4.1 WIRE-ANCHORING TECHNIQUES

An adhesive is needed to physically and thermally anchor the leads to the copper heat sink, such as varnish or epoxy (materials that work well are described in Appendix A3.10). Epoxy is permanent, whereas varnish can be removed (with ethanol or acetone) for lead replacement, if necessary. (Varnish softens polyvinyl-formal insulation, so use polyimide insulation when varnish is used for lead anchoring.) An alternative method is to tightly overwrap the leads on the heat sink with 3M Mylar™ tape, which is not as effective as varnish or epoxy, but, for temporary thermal anchoring, is relatively easy to remove.

Thick, soft wire insulations, such as bell-wire insulation, are not recommended because they thermally insulate the wire too much. Loose insulations, such as Teflon™ *tubing*, should also be avoided, because they prevent good thermal bonding directly to the wire. Wire insulations that work well for thermal anchoring are polyimide, polyvinyl formal, Teflon™ directly bonded to the wire, or cotton wrapping thoroughly soaked with varnish.

4.4.2 LENGTH OF WIRE NEEDED FOR THERMAL ANCHORING

The approximate length of wire required for good thermal anchoring to a heat sink depends on the wire material, as given in Appendix A4.5. A relatively short "tempering" length of a few

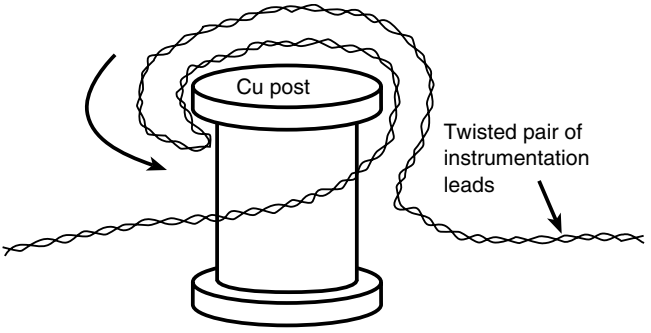

Fig. 4.4 Illustration of noninductive winding scheme for further minimizing induced voltages in instrumentation leads when making measurements in high magnetic fields.

centimeters is all that is needed for phosphor-bronze or Constantan leads, because the thermal resistance along their length is higher than that of copper wire. Such higher-resistance wires are great for thermometers and other low-current ($\lesssim$10 mA) devices. Copper conductors, on the other hand, are necessary for high-current leads to reduce Joule heating in the lead, or when continuous copper leads are needed for sensitive dc voltage measurements to minimize thermoelectric interference voltages. Then a much longer tempering length is required, which can range up to ~100 cm, depending on the wire size (Appendix A4.5).

4.4.3 BERYLLIUM-OXIDE HEAT-SINK CHIPS

A convenient way to provide excellent heat-sinking close to a thermometer or sample is to use beryllium-oxide heat-sink chips. The chips can also be used as a mechanical buffer layer to take up expansion mismatch between materials with a low expansion coefficient (e.g. a silicon diode sensor) and a material with a high expansion coefficient (e.g. copper or epoxy).

Figure 4.5 illustrates the chip, which is fully metalized on one side for soldering it to a copper heat sink, and patterned with terminal strips on the other side for making soldered lead connections. These chips provide effective electrical isolation from the sample mounting stage and, at the same time, good thermal conductivity (which is several times greater than that of copper in the liquid-nitrogen temperature range, but about a thousand times smaller than that of copper at lower, liquid-helium temperatures).

However, I suggest soldering the chips onto their own small copper platform, which can be screwed or greased to the larger copper base structure. This way, the small copper platform is easily *demountable*, so that the instrumentation leads can be soldered to the heat-sink chip. The thermal conductivity of the beryllium-oxide chip is so good that, if the chips are soldered or glued directly to the base structure of the apparatus, there is no way to solder leads to the other side of the chip unless the entire base structure is also heated to soldering temperature, with the attendant wire-insulation-softening problem noted above.

For use in a magnetic field, the plane of the chip should be oriented parallel to the field direction to minimize the effective loop area subject to induced voltages from field variations (see Fig. 4.5). For the same reason, twist the leads right up to where they are soldered to the

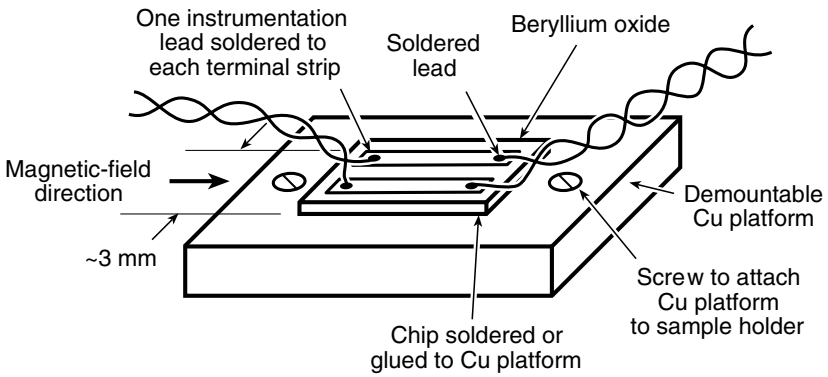

Fig. 4.5 Beryllium-oxide heat-sink chips for thermally anchoring instrumentation leads.

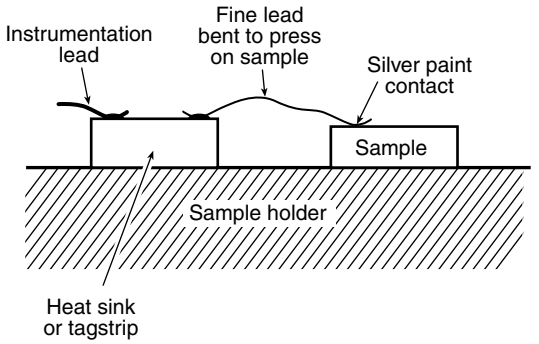

Fig. 4.6 Technique for attaching fine electrical leads to small samples, especially when using weak silver paint to contact the sample.

chip. Heat-sink chips have a magnetic susceptibility about the same as that of "nonmagnetic" stainless steel.

➔ To connect fine wires to small samples, especially with weak silver paint, consider first attaching the instrumentation lead to a (more substantial) heat sink or tagstrip, such as shown in Fig. 4.6. Then bend the wire with tweezers so that it presses on the sample in the right place. Finally, apply solder or silver paint to attach the lead to the small sample.

4.5 **Solder connections**

Much of the information on choosing the right solder for the job has already been tabulated in Appendix A3.7, depending on the materials to be soldered and the temperature that can be tolerated. Appendix A3.8 lists fluxes according to the type of metals being soldered. Superconducting properties of some solders are given in Appendix A3.9.

For wire connections I prefer the following solder and flux combinations:

- copper wires: 63%Sn–37%Pb or 63%Sn–36.65%Pb–0.35%Sb eutectic solders, with pure (not activated) rosin flux;
- aluminum wires: 95%Zn–5%Al with reaction flux;
- contact connections to thin-film, noble-metal surfaces: eutectic 97%In–3%Ag with no flux (see pp. 331–332).

Further information on these choices and their specific advantages are described in the following sections.

For soldering more difficult materials, such as Nichrome heater wire, eutectic 63%Sn–37%Pb can be used, but with a powerful acid flux, as indicated in Appendix A3.8. *After soldering, it is important to neutralize the residue of flux with a solution of baking soda and water, and then clean the area with soap and water, or alcohol.*

It is worth reemphasizing the need to use enough heat to make the solder flow easily and wet the lead in order to avoid resistive "cold" solder joints that are sometimes hard to detect. Enough heat is also needed to activate the flux to get clean, oxide-free surfaces.

4.5.1 SOLDER-JOINT CRACKING AFTER REPEATED THERMAL CYCLING

Wiring connections made with solders containing a high percentage of tin can embrittle and crack after repeated thermal cycling between room temperature and cryogenic temperatures. Although standard eutectic Pb–Sn soft-solder generally works, adding a small amount of antimony minimizes any potential problem, and so a good solder to use for copper-wire connections is 63%Sn–36.65%Pb–0.35%Sb eutectic solder (T_{melt} = 183°C) (with pure-rosin flux). When a higher-temperature solder is needed for electrical connections, the low-tin solder 93%Pb–5.2%Sn–1.8%Ag (T_{melt} = 299°C) works well.

4.5.2 SOLDERING TO THIN SILVER OR GOLD FILMS—THE MAGICAL DISAPPEARING ACT

When soldering to silver or gold film coatings on surfaces, avoid solders containing any tin, which acts as a strong leaching agent and often completely dissolves thin ($\lesssim$1 μm) noble-metal films. This is a problem especially for soldering to noble-metal contact pads, which are used for making electrical connections to high-T_c superconductors (Sec. 8.3.3). So, for thin noble-metal films, I like to use 97%In–3%Ag eutectic solder, heated to just above its melting temperature (143°C). Because it is a eutectic mixture, this combination will dissolve minimal additional silver, as long as the temperature is kept close to the eutectic melting temperature. Use no flux, but make sure the surfaces are well cleaned with alcohol.

4.5.3 SUPERCONDUCTING-SOLDER ARTIFACTS

The caveat described for structural solder joints in Sec. 3.3.4 also applies to electronic solder joints; beware that most common solders become superconducting at liquid-helium temperatures. I have seen too many papers of embarrassing "novel" effects that are just superconducting-solder artifacts.

For example, in variable-temperature measurements, *the contact points where voltage leads are attached to a test sample can shift their effective position at the critical temperature of the solder* as the solder blob suddenly provides a superconducting shunt for a portion of the sample. This produces a false change in the transport property being measured. The effect especially plagues transport measurements carried out at low current, in which case only a thin solder coating can carry the entire transport current.

A similar problem occurs in swept magnetic-field experiments. *At the point where the magnetic field exceeds the critical field of the solder, it suppresses the superconductivity of the solder coating the sample and changes the effective sample length between the voltage taps*, which can lead to some pretty weird magnetic-field effects. Fortunately for high-field testing, the superconducting properties of solders are usually not a problem because the critical field H_c of typical soldering materials is so low (e.g. H_c = 0.08 T for common 60%Sn–40%Pb solder) that the solder remains in the normal state. But do not get fooled at low fields!

Appendix A3.9 contains a list of the superconducting critical temperatures and critical fields for a few common soldering materials.

4.6 Sensitive dc voltage leads: techniques for minimizing thermoelectric voltages

The biggest problem for sensitive dc voltage measurements is the occurrence of spurious and constantly changing low-level thermoelectric voltages. These are generated by the temperature gradient between the hot and cold ends of electrical leads as they traverse the temperature difference between room temperature and the sample. However, if the return lead is made of the same material, if the material is homogeneous, and if there are no joints, then an equal and opposite thermoelectric voltage is produced that cancels the voltage generated by the down-lead. In this case, a voltmeter connected to the two leads at room temperature would sense, theoretically, no thermoelectric voltage.

The key is to use homogeneous wire material. Wire manufactured for thermocouple use is ideal, when it is available.

The other key is to *avoid solder joints* if possible, since the mismatch between the thermoelectric power of solder and the wire material is usually the main source of thermoelectric voltage. If corresponding pairs of joints in the up-lead and down-lead are not kept at exactly the same temperature, drifting thermoelectric voltages are introduced into the leads. Typical thermoelectric voltages of various materials *referenced to copper* are given in Appendix A4.6a (elements) and A4.6b (technical materials).

Example: If we use common 50%Sn–50%Pb solder to make joints in a pair of copper instrumentation leads, what level of thermoelectric voltages might we expect to have in this measurement probe?

From Appendix A4.6b, we see that a thermoelectric voltage of -0.30 mV will exist between 50%Sn–50%Pb solder and copper for two joints spanning the temperature range 0–100°C; this corresponds to an average thermoelectric power of -0.30 mV / 100°C $= -3$ μV/K. If we assume this average thermoelectric power is indicative of that over the cryogenic temperature range, we find that fluctuations of only 10 mK in the temperature of these joints would produce changing thermoelectric voltages on the order of 30 nV. Unless the joints are thermally anchored extremely well, precise dc voltage measurements in the 0.1 μV range would be difficult.

4.6.1 CONNECTION TECHNIQUES FOR LOW-THERMOELECTRIC VOLTAGES

The solution is to:

(1) minimize the number of joints in high-sensitivity voltage leads;

(2) keep corresponding joints at the same temperature;

(3) make the joints without any solder (direct copper-to-copper pressure contacts) or at least use a solder having a low thermoelectric voltage relative to copper (see Appendix A4.6b);

(4) keep the contacting surfaces clean and free of surface oxide.

To be effective, these low-thermoelectric techniques must be used all the way from the sample to the voltmeter. Usually joints can be eliminated everywhere except at the sample and voltmeter. That is, *continuous* leads can be run from the sample up through the probe and out

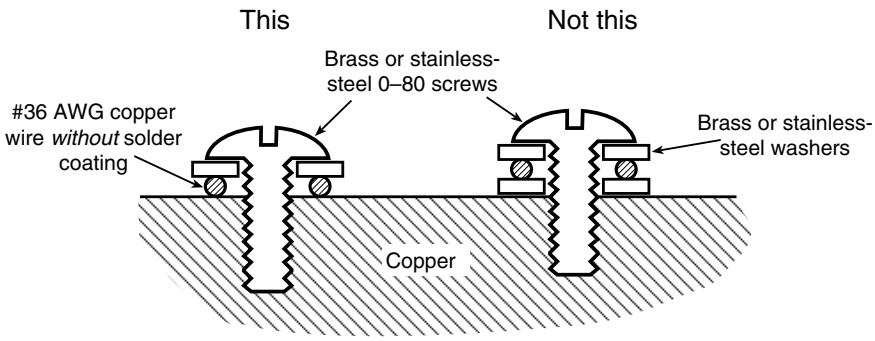

Fig. 4.7 When attaching a bare copper wire to a copper block, make sure that the wire is in direct contact with the block, not between washers, as is common, for example, with telephone-wire connectors. Clean the wire and the block with Scotch-Brite™ to remove the surface oxide.

through the "connector" box without any connections. In a typical measurement probe, I have found that eliminating connections in the sensitive voltage leads can lower thermoelectric interference levels by more than an order of magnitude.

Solderless joints can be made at both cryogenic and room temperature by using a direct pressure contact between a bare copper wire (untinned) and a copper block (e.g. with a screw and washer, as shown in Fig. 4.7), or with a spring-loaded pressure fixture, such as all-copper alligator clips (the type that are made without solder tinning and without teeth; suppliers are listed in Appendix A1.7 under Connectors). Be sure to clean the copper surfaces with a nonmetallic household abrasive pad such as Scotch-Brite™, since copper *oxide* on the contact surfaces can increase thermoelectric voltages by orders of magnitude. Gold-coating the contacts is also a very good technique, because gold eliminates the oxide layer on the surface of the contact and because gold has a thermoelectric voltage nearly identical to that of copper (see Appendix A4.6a). Silver also has a thermoelectric power nearly matching that of copper, but it readily oxidizes, defeating the purpose of contact plating.

If copper leads must be soldered together to get a good electrical contact, a solder such as indium, or the stronger In–3%Ag alloy, can be used. These solder materials have a thermoelectric power much closer to that of copper than lead-based soft-solder (a difference of about $-0.7\ \mu V/K$ for indium-based solders, versus $-3\ \mu V/K$ for 50Sn%–50%Pb solder; ref. Appendixes A4.6a and b). Traditional low-thermoelectric solders based on cadmium are not recommended because of their toxicity and poor wetting properties.

For some wiring jobs, wiring materials other than copper are needed, such as where heat conduction needs to be minimized down thermometer leads. In this case, materials such as phosphor bronze or Manganin are recommended over Constantan, because they have a smaller thermoelectric-power mismatch relative to the copper wires typically used in commercial thermometer sensors. For most thermometers, however, thermoelectric dc voltage perturbations are not a significant problem because thermometer signal levels are usually in the millivolt range. (Beware of *ac rectification* in thermometer diodes, though. Such rectification can be minimized by keeping diode-thermometer leads away

from ac sources, such as pulse-width-modulated power leads used in cryocontrollers, for example.)

4.6.2 VOLTMETER CONNECTIONS

For sensitive dc measurements, room-temperature connections to the voltmeter also need to be designed to minimize thermoelectric-voltage drift.

If a multiplexer switch is used to enable one voltmeter to read many different voltages, make sure it is the low-thermoelectric-voltage type. Generally, it is good to avoid a multiplexer, if possible, for it takes a lot of patience and time (on the order of 20 s) for the contacts to equilibrate in temperature before an accurate nanovolt reading can be made.

It is better to use a dedicated nanovoltmeter, make the connections once at the beginning of the measurement, and then give the connections plenty of time to come to thermal equilibrium before starting the measurements. The plus and minus connections should have a high thermal mass (to minimize drift) and be in good thermal contact with each other (to minimize the temperature difference between the connections).

The simplest method is shown in Fig. 4.8(a), which consists of attaching nontinned-copper alligator clips to the ends of nontinned-copper voltmeter leads with direct copper-to-copper crimp connections. At the beginning of each experimental run, the alligator clips are then simply clipped onto the copper test leads and the connections sandwiched between two bags of copper shot to give them thermal mass for temperature stability. The bags are made by filling cloth sacks with copper or brass shot. Again, to avoid the high thermoelectric voltages associated with copper oxide at the contact, make sure the copper connections are well cleaned.

A more sophisticated scheme (which is almost essential where there are many instrumentation leads) is to make a lightweight multiple connector at the end of the continuous-lead cable coming from the test apparatus, as illustrated in Fig. 4.8(b) and (c). The multiple connector is equipped with copper terminals attached to the continuous cryostat leads with copper crimp connections, or screws and washers (no solder, no tinned copper; just clean, unoxidized bare-copper to bare-copper). The leads from the voltmeter can then be clipped onto these tabs by using copper alligator clips, which can then be easily moved from one test lead to another to measure different samples. Be careful to orient the alligator clip so that the jaw to which the cryostat lead is directly attached is the one that contacts the copper tab on the terminal strip. The other jaw is not well connected to the cryostat lead, only poorly connected through the resistive spring and hinge pin of the alligator clip.

The third scheme shown Fig. 4.8(d) is a little slower to use, but gives extremely good temperature stability. It consists of two or more copper blocks (with mass for temperature stabilization) thermally connected together with grease. Thin mica or plastic sheets (similar to those used for thermally anchoring power transistors to heat sinks) are used to maintain electrical isolation between the blocks, yet provide good thermal connection. The leads are simply attached to the copper blocks with screws and washers, as shown in Fig. 4.8(d). It helps to place the blocks in a cardboard box, filled with paper tissue or other stuffing to minimize convective air currents.

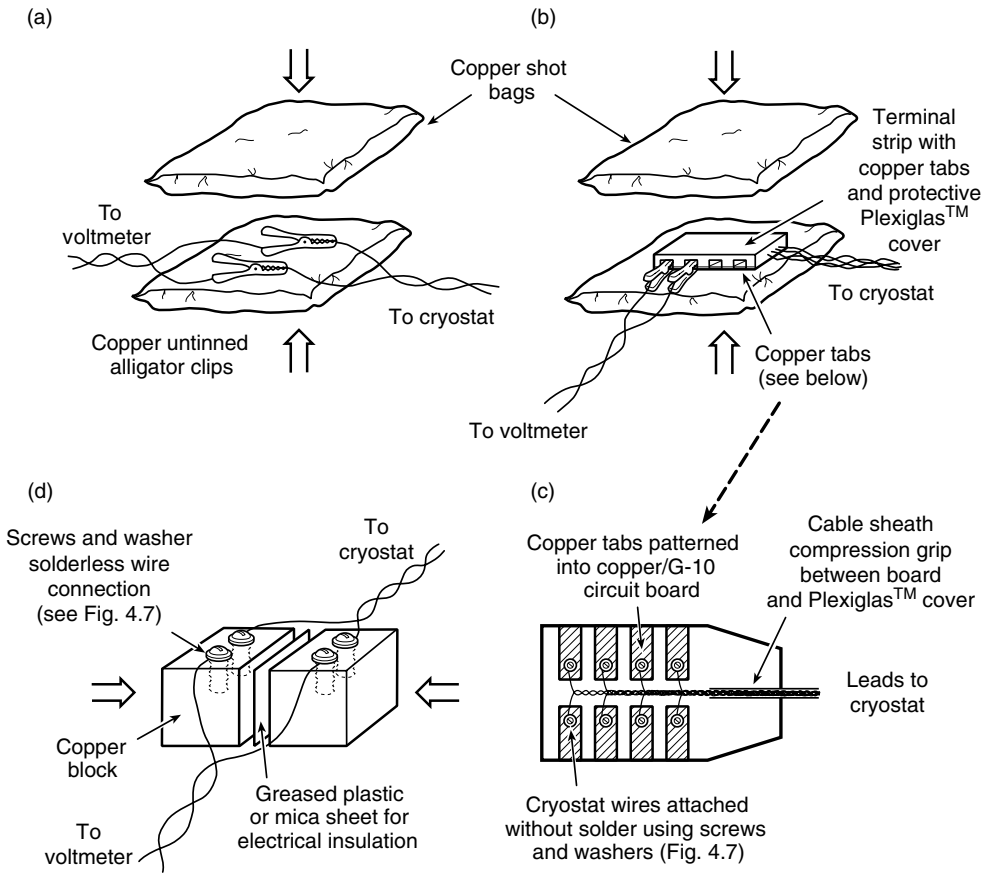

Fig. 4.8 Several schemes for making low-thermoelectric-voltage connections between the test apparatus leads and the leads from a sensitive voltmeter. Arrows indicate how the components are sandwiched together to make good *thermal* contact between the + and − connections. In illustration (d), the copper blocks are held together simply with a rubber band or insulating strap (not shown). All connections are copper-to-copper, without solder and without solder tinning of anything (leads, alligator clips, or copper washers). When attaching a bare copper wire to a copper tab or block, make sure the wire is in direct contact with the block, as shown in Fig. 4.7.

4.7 **Vacuum electrical lead-throughs**

4.7.1 ROOM-TEMPERATURE LEAD-THROUGHS

At the top of the measurement cryostat, the instrumentation leads and current leads must usually be fitted with a connector fixture as shown for the dipper probe in Fig. 1.6, for example. Usually, these connections need to at least hold a rough vacuum so the dewar can be pumped or to force boil-off helium gas through vapor-cooled current leads or through structural supports.

Commercial vacuum connectors are usually designed for use at room temperature and must be kept near room temperature so they do not become cold, brittle, and break. When cooled, most of these vacuum seals crack because of different thermal contraction rates between the various materials from which they are made. Also, connectors must be keep warm enough so they do not collect moisture and frost, which can short the connectors.

For the dipper probe of Fig. 1.6, this function is supplied automatically by the high thermal resistance of the stainless-steel support tube. On the other hand, for larger probes, such as those shown in Fig. 1.14, the needed thermal and moisture isolation can be provided by mounting the connectors on the ends of 4- to 6-cm-long standoffs of stainless-steel tubing protruding from the head plate.

The two basic types of connector boxes at the cryostat head are (1) the nonvacuum type, where the leads exiting the cryostat are vacuum-sealed before entering the connector box, and (2) the vacuum type, where the connector box is evacuated and individual vacuum-tight connectors are used where the leads exit the box.

Nonvacuum connector boxes

An example of a nonvacuum connector box is shown in Fig. 4.9(a). The instrumentation leads are vacuum-sealed at the top of the cryostat support tube before they enter the connector box, as shown by the detail in Fig. 4.9(b). The connector box is simply bolted onto a flange soldered to the top of the probe, and all connections are made to nonvacuum connectors mounted on the box.

The multiple-lead vacuum seal at the top of the cryostat support tube can be made by using wires with bonded insulation (such as polyimide or polyvinyl formal, rather than tube insulation, which makes it difficult to seal directly to the wire). The wires are passed through a hole in an epoxy–fiberglass (G-10) plug and permanently sealed in place with epoxy or, temporarily, with silicone caulk. The G-10 plug is usually vacuum-sealed to the sample-support tube with epoxy.

The advantage of this arrangement is simplicity in construction because multiple leads can be sealed all at once and nonvacuum-tight connectors can be used in the connector box. The disadvantage is that extra leads cannot be added easily to the probe nor can broken leads be replaced. Thus, it is wise to add a few extra pairs of leads as insurance when first wiring the probe. Also, remember to leave enough slack wire so that each connector can be demounted and pulled far enough out of the box to conveniently solder leads to the connector's terminals.

An advantage of leaving the top of the box clear of connectors, as shown in Fig. 4.9(a), is that it can be used to stand the cryostat stably upside down, which makes it very handy for working on the lower business end of the probe.

For small probes, a simple alternative to the connector box of Fig. 4.9 is the multipin connector arrangement shown in Fig. 4.10. It utilizes an ordinary nonvacuum-sealed D-connector or similar connector. The wiring is vacuum-sealed with epoxy where it exits the end of a small, ~6 mm diameter tube coming from the probe. The nice feature is that no connector box is needed; the backshell of the connector is simply clamped onto the stainless tube, and there is just enough space inside the metal backshell for the epoxy vacuum seal.

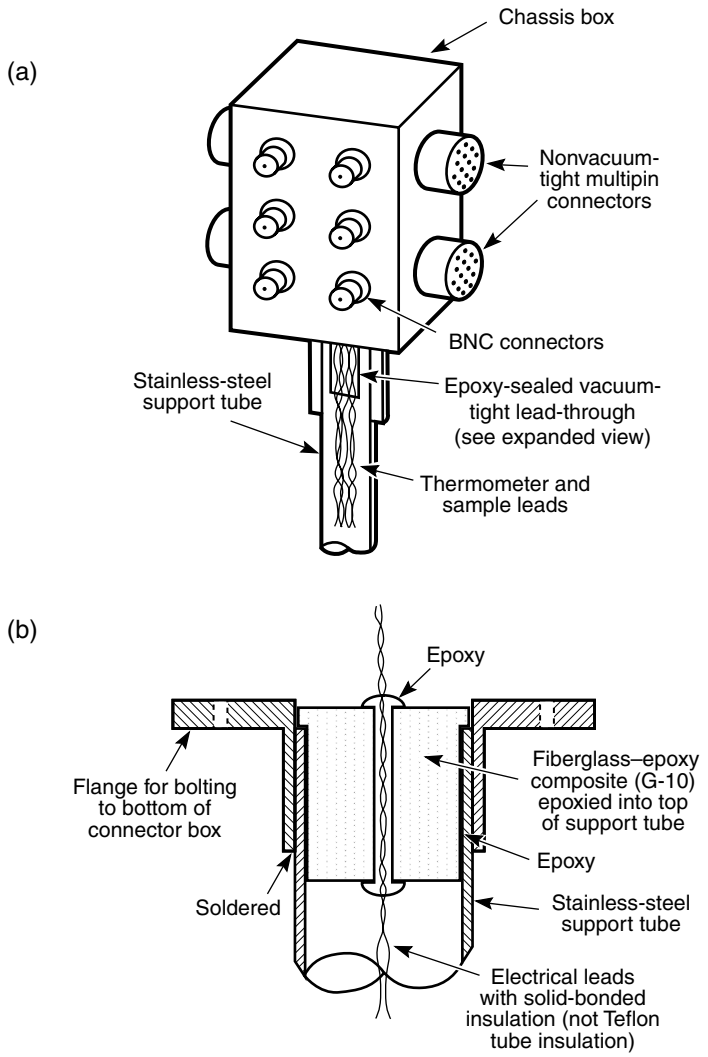

Fig. 4.9 Nonvacuum-tight connector box: (a) overview; (b) detail of epoxy vacuum seal for multiple leads at top of the support tube. The fiberglass–epoxy plug shown in (b) is best machined from a *rolled* fiberglass rod (with the glass fibers running around the circumference) so that the epoxy joint does not crack from stress generated by differential thermal contraction with the stainless-steel support tube.

Vacuum connector boxes

In the second type of design, the connector chamber itself is under vacuum, and commercial leak-tight (room-temperature) connectors are used where the wires exit the connector box, such as shown in Fig. 4.11. This scheme provides a lot of flexibility for adding new leads or replacing leads, should they become damaged. Thus, it is worth the extra fabrication complexity if the cryostat has many leads or if it might be modified for use with different experiments. It is also the best solution for flexible coaxial cables, which are difficult to vacuum-seal in a

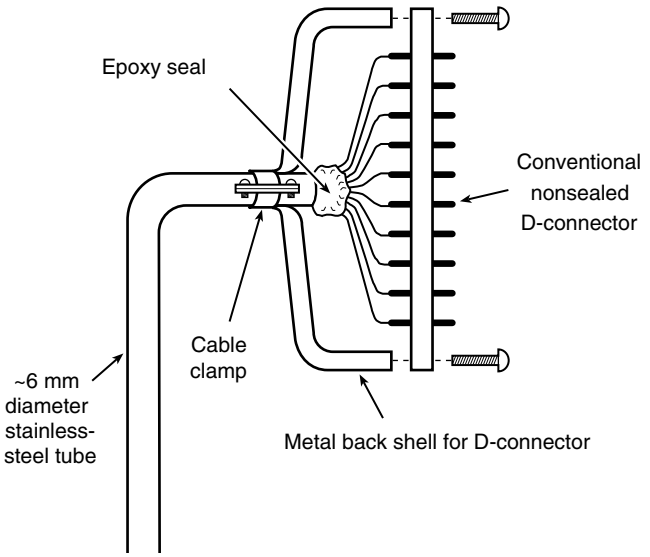

Fig. 4.10 Cross-sectional view of a conventional multipin D-connector adapted with a vacuum seal (Colclough 2002).

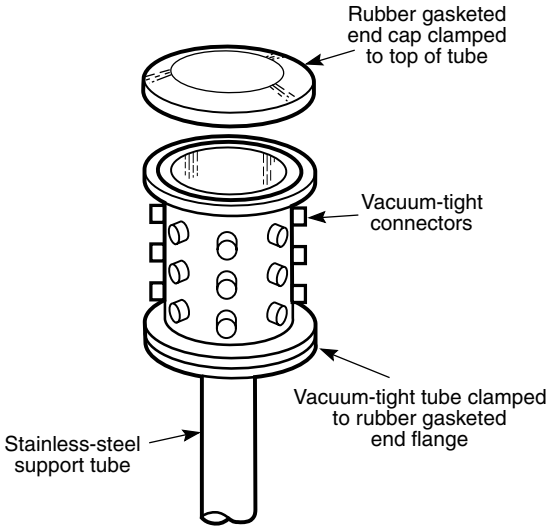

Fig. 4.11 Vacuum-tight connector chamber (about 5–8 cm inside diameter) with removable cover, made from commercially available vacuum fixtures (Mendez 1988).

custom seal arrangement such as Fig. 4.9(b). (Suppliers of commercial vacuum-tight coaxial lead-throughs are listed in Appendix A1.7 under Coaxial cables.)

As shown in Fig. 4.11, the vacuum-tight chamber can be made from a short section of a commercially available stainless-steel tube of diameter ~5–8 cm, which is equipped with decoupleable rubber-gasketed end flanges (such as Ladish Tri-Clover vacuum fixtures; see Appendix A1.7 under Vacuum accessories). This tube section is simply clamped onto the end of the probe's support tube; the top cover is also clamped so that it can be removed for easy

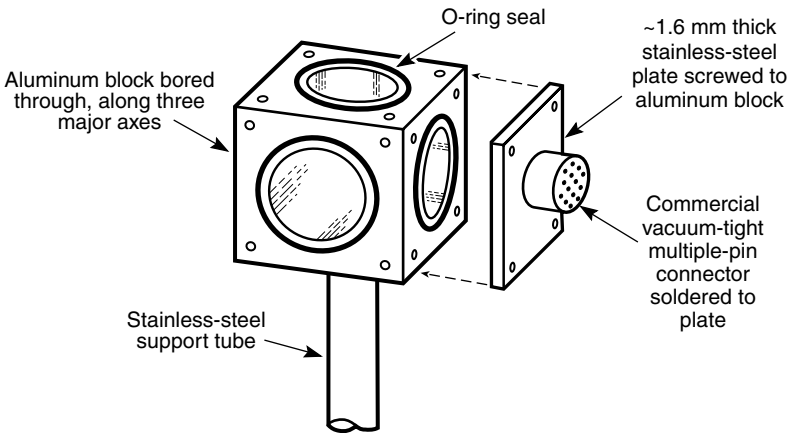

Fig. 4.12 Vacuum-tight aluminum connector box with removable plates for mounting commercial vacuum-tight multiple-pin connectors.

access to the instrumentation leads. Many commercial vacuum-tight connectors (such as single-pin BNC connectors) can be soldered into the tube wall, and the instrumentation wires coming from the cryostat are soldered to them inside the large-diameter tube section. Thus, the chamber acts as a convenient distribution point for cables, and it can be conveniently altered without having to make epoxy seals around new wiring.

Figure 4.12 shows an alternative vacuum-box design that I have found ideal for small probes, because it can be made lightweight and compact. The connector box is machined by boring out an aluminum cube in three orthogonal directions and fitting each flat with O-ring-sealed brass plates into which commercial hermetically sealed multipin connectors are soldered. As mentioned for nonvacuum boxes, be sure to allow enough slack in the wires so that the connectors can be demounted from the vacuum box for ease in soldering leads to the back of the connector's terminals.

Unlike the arrangements shown in Figs 4.9 and 4.11, an initial disadvantage of the designs of Figs 4.10 and 4.12 is that a separate distribution box has to be constructed to connect the multilead cable to the various laboratory instruments. However, the continuing advantage of this type of arrangement is that connections to the probe head can be made very easily at the start of each experimental run with only a few multipin connectors. Incidentally, when using multipin connectors, the *bayonet* type (which you simply insert and twist a partial turn to lock in place) is more convenient than the *screw* type for quick attachment (although for rf measurements it provides less shielding).

Vacuum lead-throughs for low-thermoelectric-voltage leads

For very sensitive voltage leads (discussed in Sec. 4.6), connections of any type introduce time-varying thermoelectric voltages that interfere with low-level voltage signals. When such sensitive leads need to be run *continuously* through a vacuum wall, the lead-through shown in Fig. 4.13 works well. The sensitive instrumentation leads are vacuum-sealed into a small (3 mm diameter) brass tube with epoxy. The tube is then slipped into a commercial quick-couple vacuum seal through the side of the connector box.

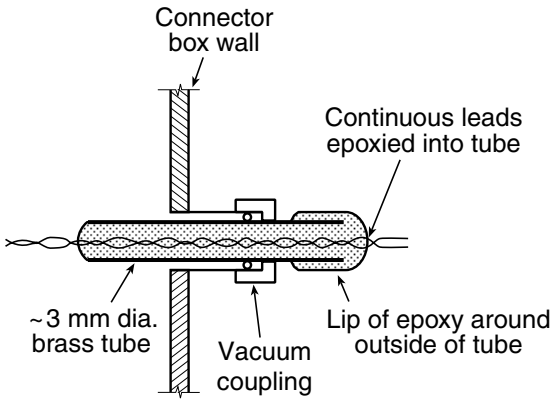

Fig. 4.13 Removable vacuum lead-through for *continuous* leads. The lip of epoxy provides a good vacuum seal and also prevents the tube from being sucked through the vacuum coupling; the epoxy lip can be conveniently made by using the technique shown below in Fig. 4.14.

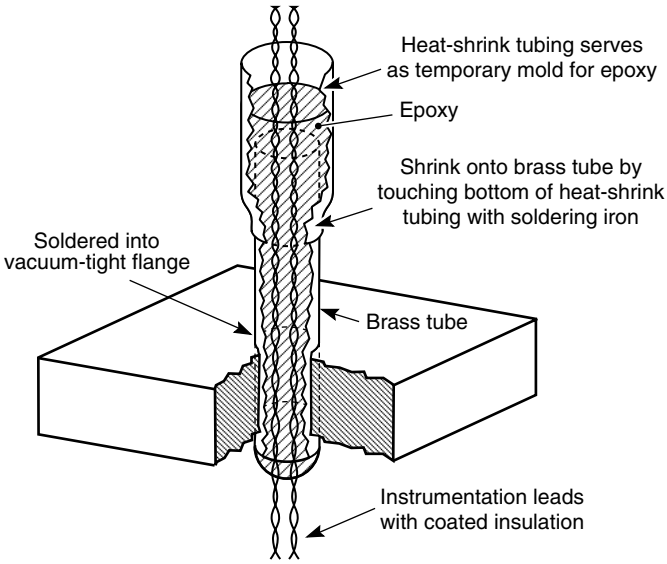

Fig. 4.14 Fabrication technique for cryogenic vacuum-tight electrical lead-through. Heat-shrink tubing serves as a mold for the epoxy and is later removed.

4.7.2 CRYOGENIC VACUUM LEAD-THROUGHS

When cooled to *cryogenic temperatures*, lead-throughs invariably leak if we simply epoxy the leads into a brass or stainless-steel tube by filling the tube with epoxy. This is because the epoxy contracts significantly more than the metal tube on cooling (Fig. 3.2), which cracks the bond between the epoxy and tube. An effective technique to solve the problem is to get the epoxy to coat both the inside and *outside* of a short length of *thin-walled* brass or stainless-steel tubing. Then on cooling, the epoxy on the outside of the tube contracts onto the tube, compressing it and keeping the tube from pulling away from the epoxy on the inside.

Figure 4.14 shows an effective vacuum electrical lead-through that utilizes this technique. An easy way to make a mold for the epoxy is to place a short length of heat-shrink tubing over the top part of the brass tube, then touch the bottom of the heat-shrink tubing with a solder iron to shrink it onto the brass tube, as shown in Fig. 4.14. Fill the brass tube and the heat-shrink mold with epoxy so that the epoxy surrounds the outside of the brass tube, forming an epoxy bead over the end of the tube. After the epoxy is cured, cut away the heat-shrink tubing with a sharp knife, and the result is a compact cryogenic vacuum lead-through. As extra insurance, it is best to use an epoxy with a filler (such as Stycast 2850FT) to better match the thermal contraction of brass. Also, it is good practice to keep the diameter of the brass tube as small as possible while still accommodating the electrical leads, thereby minimizing both the thickness of the brass tube wall and the thickness of the epoxy inside the tube.

Although I have had my share of the simple epoxy-in-a-tube lead-throughs fail, I have never had a leak in a cryogenic vacuum lead-through that was made with this outside–inside coating technique, even with many tens of instrumentation leads in a single lead-through. Just make sure the instrumentation leads are thoroughly coated with epoxy, and use wire that has a bonded adhesive insulation, such as polyimide, enamel, or varnish.

4.8 **Radio-frequency coaxial cables**

Choosing and providing heat sinks for cryogenic rf coaxial cables depends strongly on the measurement needs. Usually miniature coaxial cables are used because of their low heat conduction and flexibility. For applications at frequencies of 100 MHz and below, the terminations are not important and, therefore, cables with a solid dielectric can be used. This is a factor because repeated thermal contraction and expansion of the dielectric (usually Teflon™) tends to shift the position of the center connector longitudinally inside the coaxial sheath, which over a 1 m length usually forces the center pin of a typical SMA connector to protrude. Thus, the quality of the connector degrades with time, but the resultant signal reflections are not that significant at these lower frequencies.

On the other hand, at frequencies higher than about 1 GHz, the quality of the terminations becomes critical, and then coaxial cables made with an *expanded* dielectric such as Teflon™ tape wrapped around the central conductor are a better choice. The expanded dielectric accommodates the repeated thermal expansion and contraction better than solid dielectrics and reduces the stress on the connectors.

After choosing the type of dielectric (solid or expanded), the selection of the conductor material in the cable becomes a compromise between electrical attenuation and heat leak. In general, to minimize heat influx, choose the most resistive coaxial cable that will do the job electrically. The lowest heat leak is achieved with coaxial cables made of stainless steel, but they also have the greatest signal attenuation. On the other hand, coaxial cables made predominantly of copper have much better electrical properties, but high thermal-heat leak. (For loss specifications and other product information, see the catalogs of suppliers listed in Appendix A1.7 under Coaxial cables.)

4.8.1 HEAT-SINKING

Direct immersion in a liquid cryogen generally provides adequate heat-sinking for any of the cables, and it is especially recommended for expanded dielectric cables, where the central

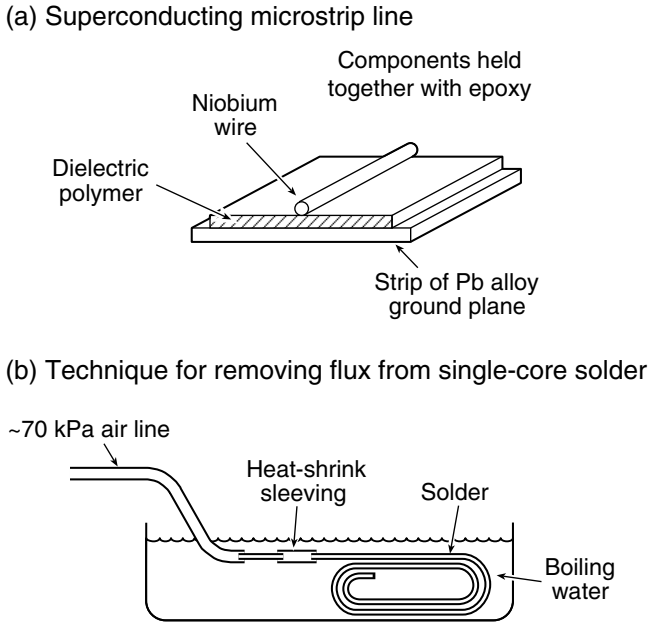

Fig. 4.15 Superconducting rf transmission lines: (a) cross section of a microstrip line made of niobium wire and a lead-alloy strip; (b) technique for removing flux for single-core solder wire to produce a superconducting coaxial cable (Colclough 2002).

conductor is not as well thermally connected to the outer sheath. As an extra precaution, the coaxial cable can be transitioned to a section of planar rf stripline like that shown in Fig. 4.15(a) (only it need not be superconducting). This provides direct cooling of the central conductor when the line is immersed in a cryogen.

On the other hand, when the cable is run through a *vacuum* rather than a liquid cryogen, a heat sink has to be provided to intercept the heat influx down the cable before it is attached to the test sample. This is best done by wrapping a miniature coaxial cable around a copper heat-sink post and anchoring the outer cable sheath with solder. Varnish is not as effective as solder for thermal attachment (see Fig. 2.7), but varnish suffices if heat sinking is provided over a greater length of cable. (Heat-sink lengths for coaxial cables can be approximately determined from Appendix A4.5 by using the combined cross-sectional area of the sheath and central conductor.)

Requirements for heat-sinking coaxial cables for use at temperatures below 1 K are much more stringent than above 1 K. In this case, the central conductor may need to be separately heat-sunk. Further information on techniques for temperatures below 1 K is given in Richardson and Smith (1988).

4.8.2 VACUUM-SEALING

Solid-dielectric cables are sufficiently leak-tight that they require no additional vacuum seals to maintain a rough vacuum for pumping on a liquid cryogen. To achieve a higher vacuum, however, hermetically sealed room-temperature coaxial connectors are needed.

Expanded dielectric cables are not leak-tight, even at the rough-vacuum level, and so they require room-temperature hermetic seals for almost any vacuum application.

4.8.3 SUPERCONDUCTING RF TRANSMISSION LINES

For the ultimate in low loss and high thermal resistance, a microstrip line can be made from superconducting materials. This is especially useful at very low temperature. Figure 4.15(a) shows such a superconducting transmission line. A niobium wire is insulated by a dielectric layer from a ground plane made of a strip of lead or lead-based alloy. Dielectric losses still occur in the insulator, however.

A superconducting coaxial cable or shielded twisted pair can also be made of superconducting materials by melting and blowing out the flux from single-core solder and using it as a superconducting tube. Removing the solder flux is easier than it might seem through the technique illustrated in Fig. 4.15(b), which utilizes boiling water and a low-pressure air line. Once air emerges from the single-core solder, flush it through with isopropanol by using the attached plastic tube and a syringe. Then feed a stiff phosphor-bronze wire (with smoothed end) through the solder tube (say, a 10–20 cm length) as a final measure for cleaning. To supply a center superconductor for the coaxial cable, use cyanoacrylate (super glue) to attach a small-diameter niobium wire (varnish insulated) to the phosphor-bronze wire (still in place), and pull the niobium wire back through the solder tube with the help of a coating of grease. Although it has a capacitance and a characteristic impedance that are not well controlled, the resulting superconducting coaxial cable is quite flexible and well suited for SQUID measurements or high-Q tuned circuits.

4.9 **High-current leads**

4.9.1 COPPER WIRE: OPTIMUM DIAMETERS

For high-current leads, the heat leak down the wires into the cryostat can be considerable. So, it pays to use leads as small in diameter as possible to minimize the heat influx. However, this is an exercise in compromise; if the current leads are made too small, Joule heating in the leads becomes a problem. The optimum wire diameter is somewhere in between and depends on the temperature range being spanned and the length of wire between the hot and cold ends. The optimum wire size is calculated by minimizing the *sum* of the heat conduction down the lead and the heat introduced by Joule heating in the lead. The results of this optimization procedure are plotted in Fig. 4.16.

More specifically, Fig. 4.16(a) gives the optimum size of copper wire to be used to carry current from an upper temperature T_{upper} to a lower temperature T_{lower}. For example, when the upper temperature is 290 K and the lower temperature is 4.2 K (liquid helium), Fig. 4.16(a) shows that the optimum occurs when

$$LI/A \cong 5 \times 10^6 \text{ A/m}, \tag{4.1}$$

Optimum copper-wire size for connections between 290 and 4.2 K (steady state)

where L is the length of the conductor, I is the current in the conductor, and A is the optimum cross-sectional area.

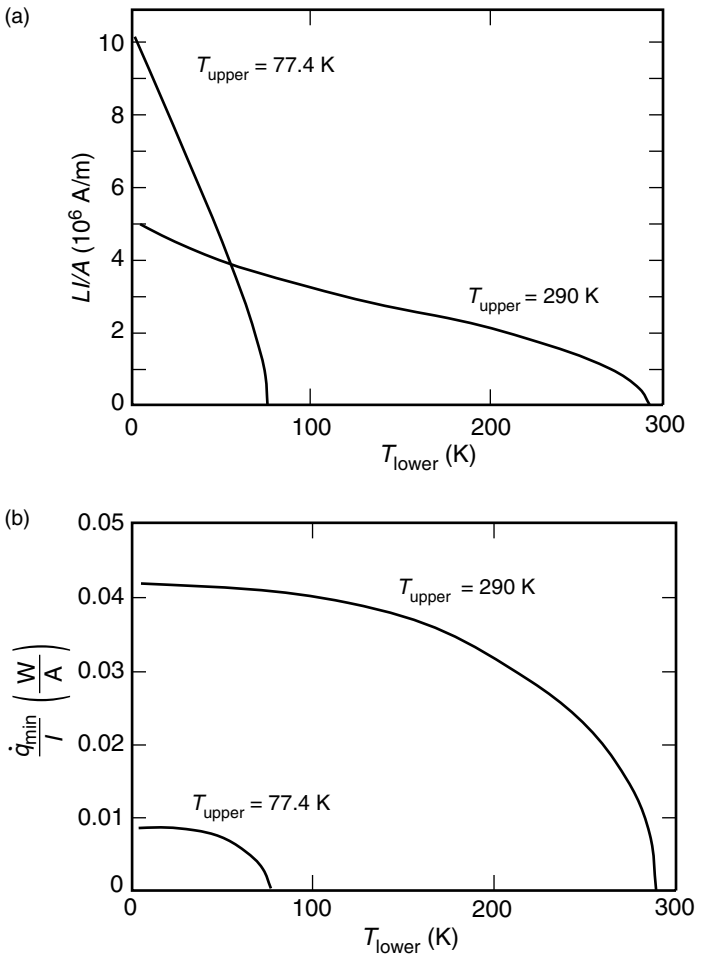

Fig. 4.16 Optimum wire diameter (a), and minimum heat input (b) for a single copper wire conducting current I from a region of the cryostat at temperature T_{upper} to a temperature T_{lower}. (We assume that the copper wire has a typical residual resistance ratio of 100 and that no heat transfers from the wire to the evaporating helium gas.) In graph (a), L is the length of the conductor between the upper and lower temperatures, and A is the optimum cross-sectional area. In graph (b), $\dot{q}_{min}$ is the corresponding minimum heat input (from McFee 1959).

Example: Thus, for the dipper probe described in Chapter 2, where the sample transport current is 500 mA and the wire length 1.5 m, the optimum cross-sectional area of the conductor is [from Eq. (4.1)], $A = 1.5 \times 10^{-7}$ m^2. From Appendix A4.1a, we see that this corresponds approximately to a #25 AWG (~0.450 mm diameter) wire.

From Fig. 4.16(a), we also find that for an upper temperature of 77 K (liquid-nitrogen temperature), the optimum size of copper wire is given by:

$$LI/A \cong 10 \times 10^6 \text{ A/m}. \tag{4.2}$$

Optimum copper-wire size for connections between 77 K and 4.2 K (steady state)

This corresponds to an optimum cross-sectional area A that is about half of that for the room-temperature leads (because of the enhanced conductivity of copper at low temperatures).

Figure 4.16(b) shows that this optimum wire sizing gives a minimum heat influx of

$$\dot{q}_{\text{copper leads}} / I = 84 \text{ mW/A}, \tag{4.3}$$

Heat flux through a *pair* of optimally sized copper leads, 290–4 K

and

$$\dot{q}_{\text{copper leads}} / I = 18 \text{ mW/A}. \tag{4.4}$$

Heat flux through a *pair* of optimally sized copper leads, 77–4 K

This is the source of the minimum heat-influx numbers for the pair of leads given in Eqs (2.16a) and (2.16b) for the dipper-probe design in Chapter 2.

From Eqs (4.3) and (4.4), we see that the minimum heat influx from the current leads can be significantly reduced if we intercept the heat at an intermediate temperature (where the refrigeration power required is much less than at 4.2 K). The minimum heat influx at 4.2 K from 77 K is less than one-fourth the heat influx from a lead spanning the entire temperature range from room temperature.

When the cross-sectional *area* differs from the optimum values of Fig. 4.16(a) by a small amount (10%), the increase in heat flux is not great (1%). However, the penalty becomes significant for larger differences. If the cross-sectional area differs from the optimum by a factor of four (wire diameter in error by a factor of two), the heat influx doubles (McFee 1959).

Optimum current levels for different wire gauge sizes are listed in the last column of the table in Appendix A4.1a.

Keep in mind that the data in Fig. 4.16 and Appendix A4.1a apply to a *steady-state* current in the lead; thus for intermittent, low-duty-cycle current needs, such as critical-current measurements, the Joule heating in the leads makes a smaller contribution over time than the steady heat flow down the lead. Thus, for operation at low-duty cycle, it is suggested that the wire size be shaded toward smaller values to reduce the background heat conduction down the leads.

Substituting materials such as brass or aluminum for copper will not change the minimum heat influx appreciably, because the ratio of electrical to thermal conductivity in metals is nearly a constant, given by the Wiedemann–Franz–Lorenz law [Eq. (2.4)]. However, the optimum wire diameter becomes larger as the conductivity of the material drops, which can be an advantage for *low-current* instrumentation leads. This is why phosphor bronze was chosen for the thermometer and instrumentation leads in the cryostat design example of Chapter 2 since this lower-conductivity material has an optimum wire size that is more manageable than pure copper leads. For example, a pure copper wire 1.5 m long, optimally sized for a small current of 1 mA, say, would have a cross-sectional area of only 3×10^{-10} m^2 from Eq. (4.1). This corresponds to a diameter of about 20 μm, or one-tenth of the area of a 40 gauge wire, which would be nearly impossible to handle.

4.9.2 VAPOR-COOLED LEADS, OR HOW TO BEAT THE WIEDEMANN–FRANZ–LORENZ LAW

Since the thermal and electrical conductivity by electrons in a metal are related by the Wiedemann–Franz–Lorenz law, it might seem that the minimum heat flux given in Fig. 4.16 cannot be beaten. But the results in Fig. 4.16 ignore the additional benefit of using the enthalpy of the cold evaporating helium gas to extract additional heat from the electrical leads. This effect can be considerable—if the surface area of the current leads is very large. That is, the heat influx to the helium bath can be greatly reduced by breaking up the optimal cross-sectional area given by Fig. 4.16 into many smaller wires, with a much increased surface area for helium-vapor cooling (as long as the wires are not tightly bundled together).

If the entire enthalpy of the evaporating gas were utilized, the theoretical minimum heat input (Joule heating plus heat conduction down the leads) is about (Lock 1969; Dresner 1995)

$$\dot{q}_{\text{vapor-cooled leads}} / I = 2.2 \text{ mW/A}. \tag{4.5}$$

Heat flux through a *pair* of vapor-cooled leads, 300–4 K

This represents about a factor of 40 reduction in heat input compared with the 84 mW/A for a pair of optimally sized solid-copper leads.

Thus, the additional size and cost of vapor-cooled leads becomes worthwhile at higher current levels ($\gtrsim$ 25 A). At 100 A, for example, the liquid-helium consumption rate for vapor-cooled leads is only 0.3 L/h [from Eq. (4.5) and Appendix A1.6a], compared with over 11 L/h for a pair of optimally sized solid-copper leads.

The heat influx *per ampere* given above is about the same over the whole range of commercially available vapor-cooled leads, from 50 A leads to behemoth 10 kA leads. (Several suppliers are listed in Appendix A1.7 under Current leads.)

Figure 4.17 shows the construction of a typical vapor-cooled current lead. Good vapor cooling of a large conductor surface is accomplished by filling a stainless-steel tube with many braided conductors, and providing holes at the top and bottom for helium gas to flow through the tube (Efferson 1967). Most of the temperature gradient occurs over the top 30–50 cm of a measurement cryostat, so the active length of vapor-cooled leads is usually less than half a meter.

A copper bus bar is attached to the bottom of the vapor-cooled section to carry the current the rest of the way into the liquid-helium bath (off the bottom of the illustration in Fig. 4.17). Losses in this copper bus bar can be reduced by sandwiching a superconductor in parallel with the copper bus. Then the Joule heating losses are reduced to zero in the lower part of the bus bar where the temperature drops below the superconductor's critical temperature. Not using a superconductor results in about a doubling of the loss mentioned above. So, while it helps significantly, it is not as important as the vapor-cooled section.

The great reduction in heat influx is realized only if there is a good flow of cold helium gas over the copper braid in the vapor-cooled section.

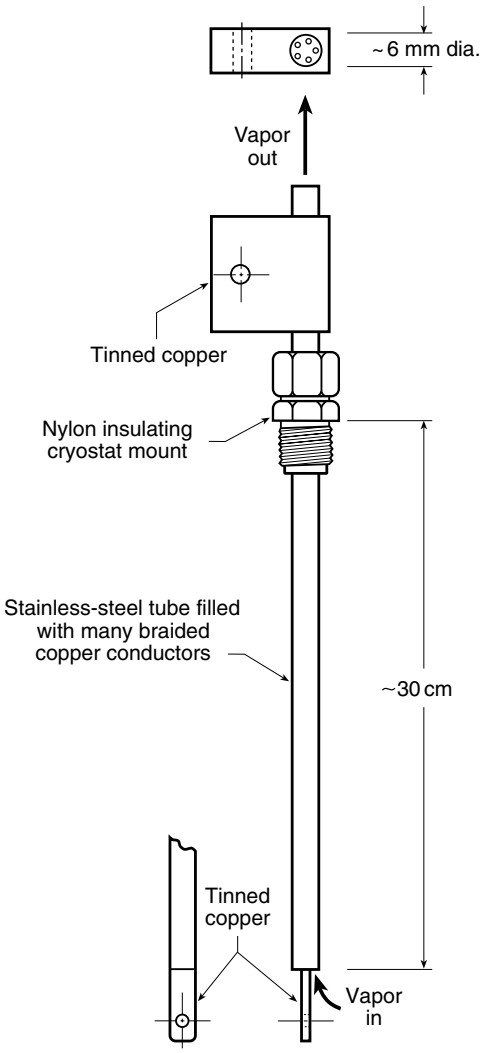

Fig. 4.17 Schematic illustration of 150 A vapor-cooled high-current lead (courtesy of Cryomagnetics, Inc.).

➔ When using vapor-cooled leads, all the escaping gas should be vented through the vapor-cooled leads. To make sure that the flow is not blocked by water vapor condensing and freezing in the vapor-cooled leads, monitor the flow rate of the effluent from the leads with a flow meter after the gas is warmed to room temperature.

A convenient way to prevent air from backing up into a vapor-cooled lead and freezing is to use the *inverted helium-gas trap* shown in Fig. 4.18 (also illustrated at the top of the overview illustration in Fig. 1.14). Since helium is lighter than air, the helium gas is trapped in the upper part of the tube, blocking air from diffusing back through the tube.

Even when not using vapor-cooled leads, such a helium-gas trap is useful to provide continuous venting of the dewar during and after an experimental run. If the dewar needs

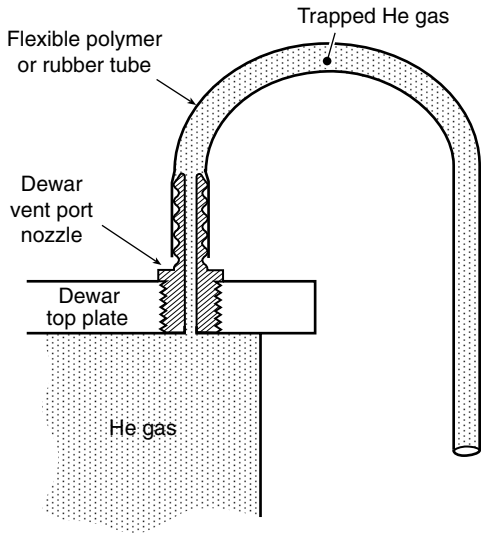

Fig. 4.18 Helium-gas trap for venting a dewar without allowing air to enter the dewar or vapor-cooled leads (where it would condense and freeze).

to be partially evacuated during the experiment (to reduce the temperature of the cryogenic liquid), pinch off the trap tubing. Then at the end of the experiment, back-fill the dewar with the same gas as the liquid coolant (in this case helium) and open the helium trap so that it can continue to vent the dewar, preferably to a helium-gas-recovery system.

Whether using a helium-gas trap or not, it is essential to provide overpressure relief for the overall dewar system. Use *two* commercial low-pressure relief valves to give redundancy, in case one of the valves freezes.

4.9.3 SUPERCONDUCTOR LEADS

The greatest reduction in heat influx at low temperatures is achieved with high-T_c superconducting (HTS) current leads. They can carry current densities orders of magnitude greater than copper can, with a thermal conductivity less than ~1/500 that of copper (Watanabe et al. 1996). The combination makes them ideal for high-current leads—the ultimate breakthrough of the Wiedemann–Franz–Lorenz limit.

Of course, with superconductors there are limits. The maximum current the lead can carry is limited by its critical magnetic field and critical temperature. However, below about 60 K, HTS materials do a marvelous job of transmitting current with minimum heat leak down the leads. $Bi_2Sr_2Ca_2Cu_3O_{10}$ (Bi-2223) is a popular current-lead material because it has a much higher critical-current density than $Bi_2Sr_2CaCu_2O_8$ (Bi-2212) in the higher-temperature range above ~30 K and, at present, it is less costly to fabricate into high-current leads than $YBa_2Cu_3O_7$ (YBCO).

Figure 4.19 shows the critical-current limits for Bi-2223 as a function of magnetic field at various temperatures. The data are given for a magnetic field applied *perpendicular*

to the axis of the current lead because this is the limiting orientation for these highly anisotropic superconducting materials. Figure 4.19 shows, for example, that an HTS lead with a 1 cm^2 cross-sectional area operating at 200 A has a magnetic-field limit of about 3 T when the warm end of the lead is at 54 K; the field limit reduces to 2 T at 58 K and 1.2 T at 63 K. Thus, HTS leads perform best when they are: (1) located in a low-field region of the cryostat, and (2) aligned with the field in the more favorable orientation along their length.

An added advantage of high-T_c superconducting leads is that they require no helium boil-off for cooling them (unlike vapor-cooled leads). This feature is significant because it enables the construction of practical, liquid-helium-free superconducting magnets cooled only by the cold second stage of a closed-cycle *cryocooler* (Watanabe et al. 1993). The HTS lead provides the vital current link between the first and second stages of the cryocooler.

Although relatively expensive, HTS leads become worth the extra cost over vapor-cooled current leads when the cost of liquid helium is high, or for liquid-helium-free cryocooled equipment. Further information on the use and system application of HTS current leads is given in Chang and Van Sciver (1998) and Pfotenhauer and Lawrence (1999).

Low-T_c superconductors can also be used as inexpensive current leads, except the magnetic-field and temperature levels are much more limited than those for high-T_c leads. A do-it-yourself superconducting, thermally isolating lead can be made from a multifilamentary low-T_c wire by etching away most of the copper, except at the ends (to make it easy to solder connections to the lead). (Field and current limits for Nb–Ti and Nb_3Sn, the two most common low-T_c wires, are given in Fig. 9.3 of Sec. 9.1.3.)

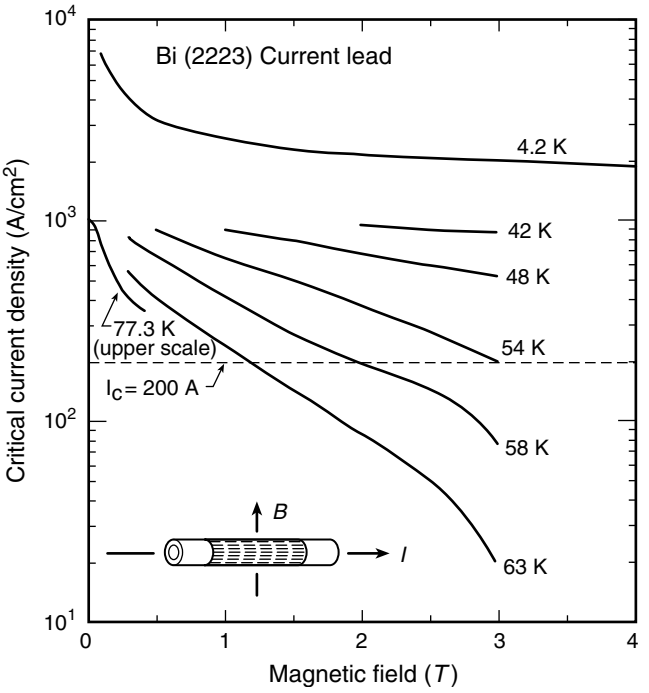

Fig. 4.19 Critical-current density as a function of magnetic field at various temperatures from 77–4.2 K for a $Bi_2Sr_2Ca_2Cu_3O_{10}$ current lead (from Watanabe et al. 1996). Data were obtained with the magnetic field applied in the least favorable orientation, perpendicular to the axis of the lead.

4.10 Flexible current leads

Transport measurements sometimes require flexible current connections between the sample and the current bus bars. In this situation, the flexible leads are inevitably the weak link that limit current. Examples of apparatus requiring flexible leads include cryostats for variable-angle measurements, sample holders for transport measurements where the sample must be cooled in a stress-free manner, and thermal contacts for vibration-sensitive experiments (such as SQUID measurements).

When wide-ranging multidimensional movement is necessary, such as in the field-angle apparatus of Fig. 9.12, the usual solution is to use a copper-wire *braid*. This can be obtained commercially in various sizes as grounding strap or cable sheathing. The required cross-sectional area of braid can be determined from Appendix A4.3, which shows that a typical copper ground-strap has a RRR of about 25 (i.e. its resistivity at liquid-helium temperatures is about 1/25th of its room-temperature value). Lower resistivity can be obtained with multiconductor braids of copper and silver wires, which are commercially available as loudspeaker cables. To minimize the overall electrical resistance, the braid is kept to the shortest length that will still permit the extent of motion required. The cross-sectional area, on the other hand, is maximized, consistent with the ease of bending needed.

Flexible leads are also needed for electrical connections to test samples requiring stress-free cooling. Figure 4.20 shows a flexible-lead design that works well for this situation, enabling the sample to thermally contract at a rate different from that of the sample holder. The free-floating flexible lead in Fig. 4.20 has a cross-sectional shape that is rectangular, to minimize stiffness in the direction of desired bending yet maximize its cross-sectional area for current conduction. At liquid-nitrogen temperature, copper is usually chosen for the flexible-lead material because copper is easy to solder and has a low electrical resistivity in this temperature range. At liquid-helium

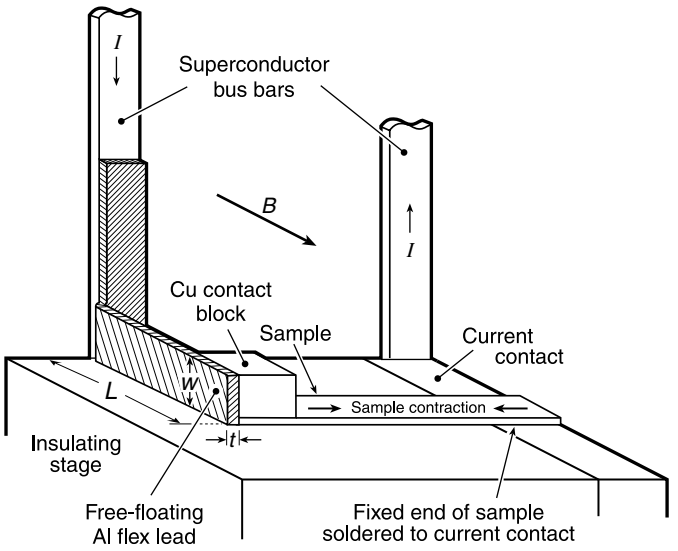

Fig. 4.20 Flexible high-current lead designed to accommodate small amounts of motion, such as cool-down strain from different thermal contraction rates between a test sample and holder (Kirkpatrick et al. 1999).

temperature, however, the purity of the material is far more important than the type of material (Sec. 6.3) and so *aluminum* is a better choice, because high-purity (> 99.9995% pure) aluminum is available commercially at a reasonably low price, having a RRR on the order of 5000 (roughly 50 times the RRR of oxygen-free copper; Appendix A4.3). With such a flexible lead, transport currents of many hundreds of amperes can be transported to the sample. To minimize the Lorentz force in high-field measurements, the current axis of the flexible lead should be aligned along the direction of the background magnetic field, as illustrated in Fig. 4.20.

Superconducting flexible leads can also be very effective. A low-T_c superconducting braid consisting of a mixture of fine copper and ductile Nb–Ti superconductor wires is available commercially (suppliers listed in Appendix A1.7 under Current leads). This mixed braid has the advantage that the copper serves to provide conduction (although limited) at high temperatures and magnetic fields, whereas the superconducting strands take over and provide resistance-free conduction if the lead is operated below the critical temperature and critical field of Nb–Ti (practical operating limits are ~8 K at zero magnetic field, or ~8 T in liquid helium). When operated in a magnetic field, the braid is also subjected to Lorentz forces that have to be kept low or else the force interferes with the motion of the apparatus. This restricts the use of unsupported, free-floating leads to low currents.

For electronic and other applications up to liquid-nitrogen temperature and slightly above, perhaps the ultimate flexible leads are the high-T_c *YBCO-coated conductor* tapes (suppliers listed in Appendix A1.7 under Superconducting wire). A thin (~1–2 μm) superconducting film of YBCO is deposited on a flexible (typically 50 μm thick) substrate tape (usually an alloy of nickel); the sandwich is completed by a 1–10 μm layer of silver deposited on top to provide stability and a low-resistivity bonding layer for making electrical contact with the superconductor layer (Sec. 8.4). Thermal conductivities of YBCO and the materials typically used in the construction of these coated conductors are given in Appendix A4.7. Note that the thermal conductance of the composite tape is dominated by the silver/copper stabilizer layer(s) and the substrate (depending on their relative thickness). Transport current can range up to about 100 A/mm of tape width, so relatively high currents can be transmitted by tapes of small (50 μm × 1 mm) cross-sectional area. The bending strain limit for YBCO composite tapes can range up to about 0.4%, corresponding to a rather remarkable minimum bend radius of only ~6 mm for these ceramic conductors.

4.11 References

4.11.1 FURTHER READING

ELECTRONIC NOISE REDUCTION:

Morrison, R. (1998). *Grounding and Shielding Techniques*, 4th edition, Wiley-Interscience, New York.

ELECTRONIC CIRCUIT DESIGN:

Horowitz, P., and Hill, W. (1995). *The Art of Electronics*, 2nd edition, Cambridge University Press, London; New York.

PRACTICAL WIRE AND COAXIAL CABLE:

(1995) *Temperature Measurement and Control*. Sec. 3. Lake Shore Cryotronics, Inc., Westerville, OH.
Richardson, R. C., and Smith, E. N., eds. (1988). *Experimental Techniques in Condensed Matter Physics at Low Temperatures*, Addison–Wesley, Reading, MA.

SOLDERING:

Summaries of data:
Solders and their properties—Appendix A3.7.
Fluxes and which materials to use them with—Appendix A3.8.
Superconducting properties of several common solders—Appendix A3.9.
Soldering techniques—Secs 3.3.4, 4.1.4 and 4.5.

Properties of solders and fluxes are described in greater detail in the review article:
Smith, J. F., and Borcina, David M., Lead Industries Association, Inc., New York.

Information on low-melting-temperature solder alloys:
Metals Handbook (1961). Vol. 1, *Properties and Selection of Materials*, 8th edition, ASM International, Materials Park, OH.

LOW-VOLTAGE MEASUREMENTS:

Yeager, J. and Hrusch-Tupta, M. A., eds., *Low Level Measurements*, 5th edition, available on request from Keithley Instruments, 28775 Aurora Road, Cleveland, OH 44139.

4.11.2 CHAPTER REFERENCES

Chang, H. M., and Van Sciver, S. W. (1998). "Thermodynamic optimization of conduction-cooled HTS current leads," *Cryogenics* 38, 729–736.
Colclough, M. (2002). University of Birmingham, UK, personal communication.
Dresner, L. (1995). *Stability of Superconductors*, pp. 188–193, Plenum Press, New York.
Efferson, K. (1967). "Helium cooled vapor current leads," *Rev. Sci. Instr.* 38, No. 12, 1776–1779.
Ekin, J. W., and Wagner D. K. (1970). "A simple ac bridge circuit for use in four-terminal resistance thermometry," *Rev. Sci. Instr.* 41, 1109.
Kirkpatrick, P. E., Ekin, J. W., and Bray, S. L. (1999). "A flexible high-current lead for use in high magnetic field cryogenic environments," *Rev. Sci. Instr.* 70, 3338–3340.
Lake Shore Cryotronics (1995). *Temperature Measurement and Control*, Lake Shore Cryotronics, Inc., Westerville, OH.
Lock, J. M. (1969). "Optimization of current leads into a cryostat," *Cryogenics* 9, 438–442.
McFee, R. (1959). "Optimum input leads for a cryogenic apparatus," *Rev. Sci. Instr.* 30, 98–102.
Mendez, E. (1988). SUNY, Stony Brook, New York, personal communication.
Metals Handbook (1961). Vol. 1, *Properties and Selection of Materials*, 8th edition, ASM International, Materials Park, OH.
Morrison, R. (1998). *Grounding and Shielding Techniques*, 4th edition, Wiley–Interscience, New York.
Pfotenhauer, J. M., and Lawrence, J. W. (1999). "Characterizing thermal runaway in HTS current leads," *IEEE Trans. Applied Supercond.* 9, 424–427.

Richardson, R. C., and Smith, E. N., eds. (1988). *Experimental Techniques in Condensed Matter Physics at Low Temperatures*, Addison–Wesley, Reading, MA.

Watanabe, K., Yamada, Y., Sakuraba, J., Fumiaki, H., Chong, C. K., Hasebe, T., and Ishihara, M. (1993). "$(Nb,Ti)_3Sn$ superconducting magnet operated at 11 K in vacuum using high-T_c $(Bi,Pb)_2Sr_2Ca_2Cu_3O_{10}$ current leads," *Jpn. J. Appl. Phys.* 32, L488–L490.

Watanabe, K., Awaji, S., Sakuraba, J., Watazawa, K., Hasebe, T., Jikihara, K., Yamada, Y., and Ishigara, M. (1996). "An 11-T liquid helium-free superconducting magnet." *Cryogenics* 36, 1019.

5 Temperature Measurement and Control

Man is fallen; nature is erect, and serves as a differential thermometer, detecting the presence or absence of the divine sentiment in man.

–Ralph Waldo Emerson

Would that we had such a "divine" thermometer. Instead, we engage in the more down-to-earth struggle of just trying to define and measure temperature accurately. The latest effort has resulted in The International Temperature Scale of 1990 (ITS-90) (Preston-Thomas 1990). Such temperature scales are based on primary thermometers and fixed-point thermometers (such as superconductor transition points).

A primary thermometer is one that expresses the temperature in terms of an equation of state involving no temperature-dependent quantities; examples include gas thermometers, acoustic thermometers, noise thermometers, and total radiation thermometers. Maintaining such primary standards is an expensive proposition, so these primary standards are transferred to secondary thermometers, most commonly resistance thermometers, such as high-purity platinum or high-purity Rh–Fe alloy. Such thermometers are also extremely expensive and so they, in turn, are used to calibrate working standards, which, in turn, are finally used to calibrate commercial thermometers for customer use.

We can bypass all this thermometer-calibration business if the sample we are measuring is immersed directly in a cryogenic liquid. Then the simplest method of determining sample temperature reasonably accurately is to monitor the vapor pressure of the liquid and determine the temperature from the standard tables given in Appendix A5.1. Recording the pressure *inside* the dewar is much better than measuring the pressure outside, because this procedure accounts for differences between internal and external pressure caused by flow restrictions in the dewar-venting system (see tip below). Also, note the approximate height of the liquid above the sample, because the hydrostatic head can significantly raise the temperature at the sample, especially for liquid nitrogen (see Appendix A5.1).

➔ The vapor-pressure measurement can be made simply by attaching a pressure meter to a ventilation port in the top plate of the dewar. Good measurement practice is to use at least a 1 m length of hose in making the connection to the port, so that the temperature of the gas at the gauge has warmed to room temperature. If a pressure reading within the dewar is not available, record the pressure from a barometer in your laboratory, or go to an Internet weather site and look up the atmospheric pressure in your location for the day the measurements were made (which will also be necessary if your pressure gauge is referenced to the ambient atmospheric pressure).

This vapor-pressure method is used quite frequently with bulk-superconductor measurements, for example, because they usually require the high cooling power of liquid helium or liquid nitrogen. However, the temperature ranges of such liquids are quite restricted (see Fig. 1.2 or Appendix A5.1).

For measurements outside these limited ranges or where more temperature accuracy is needed, a commercial cryogenic thermometer is usually used—the main subject of this chapter. The thermometer is directly or indirectly anchored thermally to the sample, as described in Sec. 5.3. Such commercial thermometers usually come in the form of resistors, diodes, or thermocouples. Unfortunately, there is no one ideal thermometer; each has its own characteristics. For example, the most accurate, reproducible thermometers are large, slow, and often fragile. On the other hand, thermometers with the greatest sensitivity cover only the smallest temperature range. So the first task is to select a thermometer appropriate for the specific job at hand.

In Sec. 5.1, we give an overview of thermometers and single out several that will serve well in most measurement situations. We then look at the selection of thermometers for use in high magnetic fields (Sec. 5.2), installation and checkout of thermometers (Sec. 5.3), and, finally, techniques for controlling temperature (Sec. 5.4).

For convenient reference later, a separate compendium of comments on the wide spectrum of available thermometers is given in an addendum to this chapter (Sec. 5.5), which is keyed to a quantitative tabulation of thermometer properties in Appendix 5.2.

5.1 Thermometer selection (1–300 K)

5.1.1 THERMOMETER OVERVIEW

A wide variety of sensors is available for cryogenic temperature measurements, each with its own advantages and disadvantages. It is easy to get into a situation of buying an expensive thermometer for its wonderful reproducibility (a germanium resistance thermometer, for example), only to discover later that we want to use it in a magnetic field, where it has a horrendous magnetic error (Sec. 5.2). So, it pays to check the broad range of characteristics in selecting a thermometer.

In keeping with the intended scope of this text, we consider thermometers for the temperature range above about 500 mK; information on thermometers for use at lower temperatures is given in the recommended reading at the end of this chapter.

Figures 5.1 through 5.4 show the temperature dependence of the output (resistance, voltage, or capacitance) of the basic types of sensors for the temperature range ~1– ~300 K:

1. *Resistance* thermometers come in two types: metallic and semiconductor-like.

   Metallic resistance thermometers have a temperature derivative that is positive, as shown in Fig. 5.1. They are highly reproducible and interchangeable, but they become less sensitive at lower temperatures.

   Semiconductor-like resistance thermometers, on the other hand, have a temperature derivative that is negative (like semiconductors), as shown in Fig. 5.2. They are much more variable from sensor to sensor than metallic sensors because their electrical resistivity depends on impurity doping levels and is also subject to differences in atomic-scale

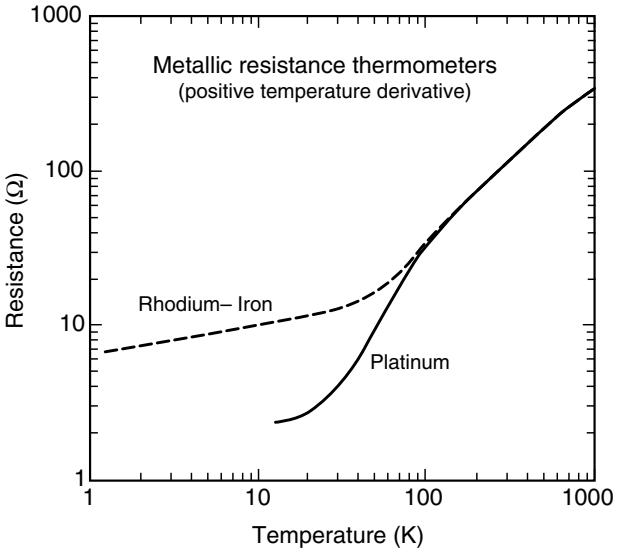

Fig. 5.1 Metallic resistance thermometers. The resistance vs. temperature characteristics of these sensors have a positive temperature derivative. Platinum resistance thermometers are highly reproducible and very popular for measurements above ~77 K. In the lower temperature range, below about 20 K, rhodium–iron resistance thermometers are more sensitive than platinum sensors. Both have excellent reproducibility. Standard platinum calibration tables are given in Appendixes A5.3a and A5.3b.

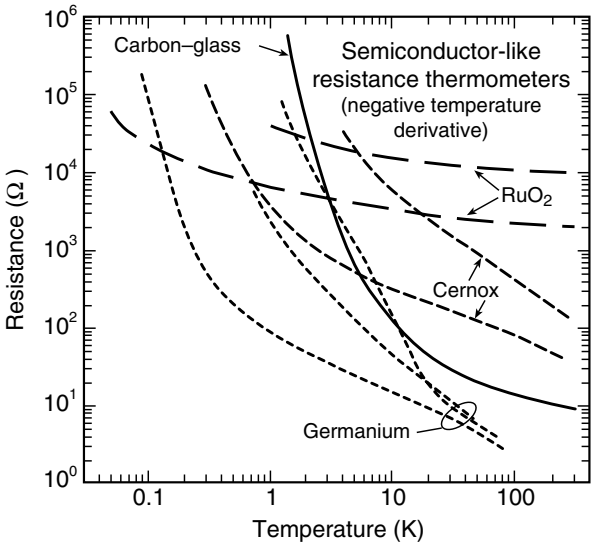

Fig. 5.2 Semiconductor-like resistance thermometers. The resistance vs. temperature curves of these sensors have a negative slope. They are significantly more sensitive than metallic resistance thermometers in the temperature range below about ~77 K.

configuration. Consequently, they usually require individual calibration. In contrast to metallic sensors, they have good sensitivity at low temperatures but become less sensitive at higher temperatures; thus, they should be picked for optimum sensitivity over the specific temperature range of interest.

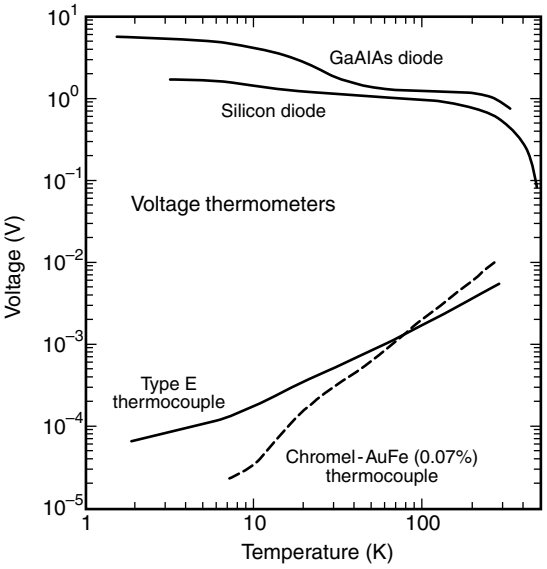

Fig. 5.3 Voltage thermometers. Diode sensors are relatively inexpensive utility thermometers that have an easily measured output. Thermocouples have a very low output voltage and, therefore, are more difficult to measure, but they are also inexpensive, cover a very wide temperature range, and are able to measure temperature at point locations. (Thermocouple voltages are shown referenced to zero at 0 K.) Standard diode and thermocouple calibration tables are given in Appendix A5.4.

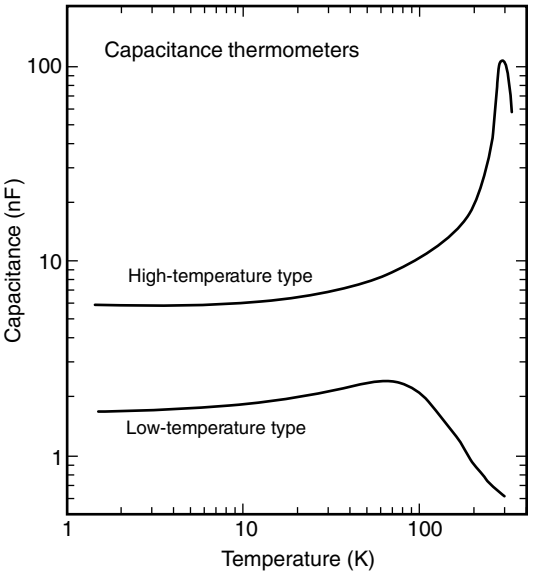

Fig. 5.4 Capacitance thermometers. These sensors are useful for holding temperature constant in experiments where magnetic field is swept.

2. Diode and thermocouple sensors have a *voltage* output, albeit with vastly different voltage magnitudes, as shown in Fig. 5.3.

   Diode thermometers have the most easy-to-read output signal, on the order of 1 V, but are not as accurate and reproducible as semiconductor or metal sensors.

   Thermocouples, on the other hand, have an output that is difficult to measure, since it is in the microvolt range. Their accuracy (except for differential measurements) is not as good as that of semiconductor or metal thermometers. However, when temperature does not have to be measured to a resolution better than about a degree, thermocouples provide

a small, quick-responding, and economical sensor that can be used over a very wide temperature range.

3. Finally, *capacitance* sensors, shown in Fig. 5.4, have the smallest magnetic-field errors; however, they are extremely irreproducible upon thermally cycling. So, they are not at all useful as thermometers, but rather as *control* sensors once a stable temperature is reached (e.g. for holding temperature constant during magnetic-field sweeps).

5.1.2 THERMOMETER-SELECTION CHARACTERISTICS

The main characteristics in selecting a thermometer are accuracy, reproducibility on thermal cycling, long-term calibration drift, magnetic-field errors, sensor size (speed of response), and, of course, cost. Appendix 5.2 quantitatively compares these characteristics for most of the useful thermometers over the range from 0.5 to 300 K.

Accuracy is usually the primary selection factor. It is limited by the *sensitivity* and *resolution* of the thermometer, which depend on temperature, as shown in Figs 5.5 and 5.6. These two figures are quite useful in the *initial* process of selecting a thermometer, showing the wide array of sensor responses in one glance.

Sensitivity, shown in Fig. 5.5, is defined as a dimensionless quantity that gives the relative change in a sensor's output, O, that corresponds to a given relative change in temperature, T; that is, $(\mathrm{d}O/O)/(\mathrm{d}T/T)$. For example, a *resistance* thermometer would have a dimensionless temperature sensitivity in terms of resistivity $(\mathrm{d}R/R)/(\mathrm{d}T/T)$, whereas a diode or thermocouple would have a sensitivity in terms of voltage $(\mathrm{d}V/V)/(\mathrm{d}T/T)$. A dimensionless sensitivity greater than about 0.1 is best.

One caveat, which is not evident from Fig. 5.5, concerns the *magnitude* of the signal. If the magnitude becomes very high or low, it can become a problem for the equipment to measure the output accurately. For example, the sensitivity curve of the gold–iron vs. Chromel thermocouple in Fig. 5.5 might indicate that it has a nearly flat sensitivity over the entire cryogenic temperature range, but in fact, the output voltage becomes very small at low temperatures and, therefore, difficult to measure. Or, in the case of semiconductor-like thermometers (such as germanium, carbon–glass, or zirconium–oxynitride), the resistivity of the sensor can climb to many megaohms at very low temperature and become difficult to measure. In another case, germanium or carbon–glass sensors, which require strain-free isolated packaging, have self-heating as a problem unless, as temperature is lowered, the measuring current is adjusted to maintain an output voltage of about 2 mV. This voltage level represents a compromise between signal level and power dissipation.

All of this is summarized in Fig. 5.6, which shows the resolution, or smallest relative change in temperature $\Delta T/T$ that can be measured, for several commercial thermometers *under typical operating conditions*. This is, admittedly, somewhat subjective, but it helps greatly with the selection process. The smaller $\Delta T/T$ is, the better. For most measurement cryostats, a relative temperature uncertainty $\Delta T/T$ less than ~0.1% is generally acceptable. However, for cryostats used in calibrations or for measuring and improving low-temperature thermometer scales, sensitivity and precision requirements become more extreme, less than ~0.01%. What is acceptable is usually a compromise between the desire for high sensitivity and the

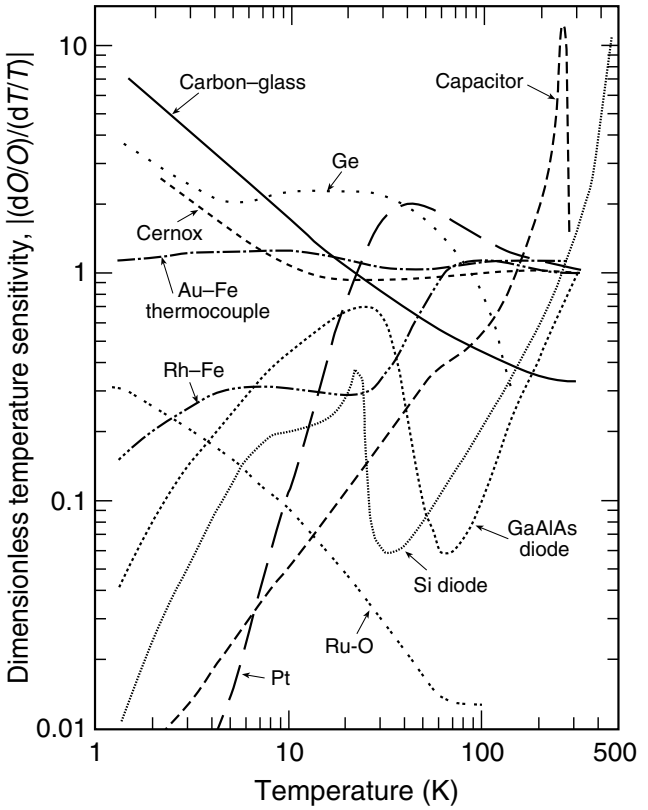

Fig. 5.5 Comparison of dimensionless sensitivity of various commercial cryogenic thermometers (given as an absolute value, since some of the sensitivities are negative) (from Lake Shore Cryotronics 2002 and product literature). The dimensionless sensitivity is defined as the relative change in a sensor's output dO/O from a given relative change in temperature dT/T; that is, $|(\mathrm{d}O/O)/(\mathrm{d}T/T)|$, or equivalently, $|\mathrm{d}\ln O/\ \mathrm{d}\ln T|$. The higher a curve's position on the plot, the better:

Au–Fe thermocouple: Thermocouple (KP Chromel vs. Au–0.07%Fe referenced to 0 K)
Capacitor: Capacitance thermometer
Carbon–glass: Carbon–glass resistor
Cernox™: Zirconium–oxynitride resistor
GaAlAs diode: GaAlAs diode operating at 10 μA
Ge: Germanium resistor
Pt: Platinum resistor
Rh–Fe: Rhodium–iron resistor
Ru–O: Ruthenium-oxide resistor
Si diode: Silicon diode operating at 10 μA

absence of other sensor characteristics (listed in Appendix A5.2) that may limit the accuracy, such as magnetic-field sensitivity.

The operating conditions listed in the caption to Fig. 5.6 are only typical and can be changed; for example, the output of a resistance sensor can be changed by choosing a different sensor resistance and operating it at a different measuring current. When using semiconductor-like sensors, choose the sensor best suited for the temperature range of interest. This is also the case

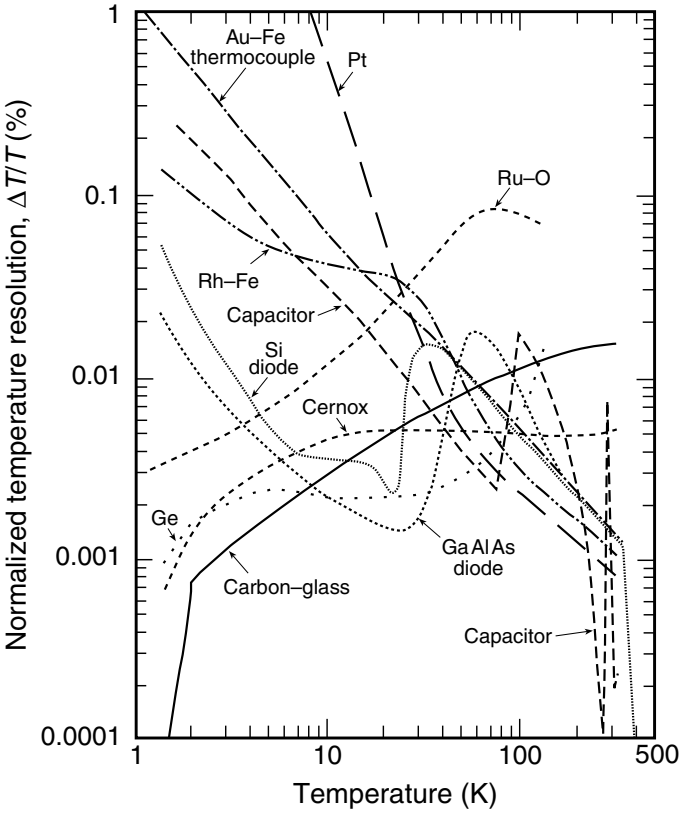

Fig. 5.6 Normalized temperature resolution of commercial cryogenic thermometers, $\Delta T/T$ (from Lake Shore Cryotronics 2002 and product literature). ΔT is the smallest temperature change that can be resolved under the typical operating conditions listed below; that is, the lower a curve's position on the plot, the better. The data assume a 5-1/2-digit voltage readout with a 0.1 μV resolution or a 5-digit capacitance readout with a 0.1 pF resolution:

Au–Fe thermocouple: Thermocouple (KP Chromel vs. Au–0.07%Fe referenced to 0 K).
Capacitor: Capacitance thermometer: 5 V at 5 kHz.
Carbon–glass: Carbon–glass resistor: 2 mV or 0.1 μA minimum operating current.
Cernox™: Zirconium–oxynitride resistor: 2 mV or 0.1 μA minimum operating current.
GaAlAs diode: GaAlAs diode operating at 10 μA.
Ge: Germanium resistor: 2 mV or 0.1 μA minimum operating current.
Pt: Platinum resistor: 100 μA operating current.
Rh–Fe: Rhodium–iron resistor: 300 μA operating current.
Ru–O: Ruthenium–oxide resistor: 10 μA operating current.
Si diode: Silicon diode operating at 10 μA.

for diode sensors. Diodes also have the complication of being nonohmic (i.e. they have a highly nonlinear voltage–current characteristic) and thus must be calibrated at a constant measuring current, typically 10 μA. Although the conditions used in Fig. 5.6 are only typical, nevertheless, it serves as a good guide to the resolution of a wide assortment of commercially available thermometers to aid in selecting a thermometer for a particular application.

5.1.3 GENERAL RECOMMENDATIONS; EXAMPLES OF THERMOMETER SELECTION FOR SEVERAL COMMON MEASUREMENT SITUATIONS

Out of the vast array of thermometer sensors available, we need a place to start, and so the following sensors are suggested for use in the common measurement situations listed next. Other sensors will certainly work for these applications, but these thermometers perform well and have the advantages described. Properties of other sensors are sometimes quite useful because of special requirements, such as rapid response, interchangeability, resistance to nuclear radiation, and cost. As noted in the introduction, a much more complete listing of sensor properties is given for reference purposes in the compendium at the end of this chapter (Sec. 5.5) and in the corresponding table (Appendix A5.2).

Temperature measurements in *zero* magnetic field

- The *most accurate* thermometer selection over the entire cryogenic temperature range is actually a *combination* of:

  Platinum resistance thermometer (PRT), 77–300 K

  Germanium or zirconium–oxynitride resistance thermometer, 0.5–77 K

For temperatures above liquid nitrogen, PRT is one of the best. The comparison given in Table 5.1 shows that PRTs have an accuracy of about ± 20 mK to ± 35 mK from 20 to 300 K, if individually calibrated. Because PRTs are so uniform and stable, they have a respectable accuracy even when used *without* individual calibration by using the standard calibration tables given in Appendix A5.3 (giving an accuracy for Class A PRTs of about ± 0.6 K at 70 K and ± 0.2 K at 300 K). Platinum sensors also have excellent reproducibility when *thermally cycled* between room temperature and cryogenic temperatures, as well as a low long-term calibration drift.

The germanium sensor has the best accuracy among any of the thermometers listed in Appendix A5.2 (about ± 5 mK below 10 K, and 0.07% of reading above 10 K). Its *reproducibility* when thermally cycled is among the best of any thermometer, and it is extremely stable against long-term calibration drift. Thus, it can serve as a secondary-standard thermometer. However, it has a very large magnetic-field error, and so it is not recommended for use in magnet applications. It is also relatively expensive, since each sensor must be individually calibrated.

The zirconium–oxynitride thermometer is a good alternative to the germanium thermometer for measurements in zero magnetic field. It also has the advantage of being an excellent sensor for use in magnetic fields (described below).

- For *simplicity*:

  Silicon diode thermometer 1.5–300 K

With one sensor, the entire cryogenic temperature range can be covered easily and relatively inexpensively. Silicon diodes do not have the best accuracy, but it is respectable (see Table 5.1). Silicon diodes also have reasonably good accuracy *without* individual calibration (± 1 K below 100 K and $\pm 1\%$ of reading above 100 K). If an accuracy of this magnitude is acceptable, diode thermometers are easily interchanged. Their output voltage is the highest among available thermometers, about 1 V, making the instrumentation readout very easy. However, their magnetic-field error is large, and so they are not recommended for use in magnet applications below about 60 K.

Table 5.1 **Properties of selected cryogenic thermometers (~1– ~300 K).***

A more complete listing of cryogenic thermometers and their properties is given in the addendum at the end of this chapter (Sec. 5.5) and in Appendix A5.2.

Sensor Type	Temperature Range	Accuracy[a] (± value)	Reproducibility[b] (± value)	Long-Term Calibration Drift	Inter-change-ability[c]	Magnetic Field Use	Best Use	Cost
Platinum resistance thermometer	77–800 K With impurity correction: 20–77 K (Appendix A5.3b)	Without individual calibration: 0.6 K at 70 K 0.2 K at 300 K With individual calibration: 20 mK at 70 K 35 mK at 300 K	10 mK from 77 K to 305 K	±10 mK/yr at 77 K to 237 K	Yes	Recommended above 70 K; error < 0.1% with standard correction given in Appendix A5.5	Measurements above 77 K Excellent reproducibility interchangeability, low magnetic field error Many shapes and sizes available	Low without calibration High with individual calibration
Zirconium–oxynitride resistance thermometer (Cernox™)	0.3–325 K	Must be individually calibrated 5 mK at 4.2 K < 0.1% at > 10 K	3 mK at 4.2 K	±25 mK/yr at 1 K to 100 K 0.05% of reading at 100 K to 300 K	No	Recommended Lowest error Standard correction given Appendix A5.6	One of the best sensors for use in magnetic fields Good sensitivity over a wide temperature range Fast response time as chip	High with individual calibration
Germanium resistance thermometer	0.05–100 K	Must be individually calibrated With individual calibration: 5 mK at < 10 K 0.07% at > 10 K	0.5 mK at 4.2 K	±1 mK/yr at 4.2 K ±10 mK/yr at 77 K	No	Not recommended	Secondary-standard thermometer Excellent reproducibility	High with individual calibration
Silicon diode thermometer	1.4–450 K	Without calibration: 1 K at < 100 K 1% at 100 K to 300 K With individual calibration: 20 mK at 1.4 K–10 K 50 mK at 10 K–330 K	5 mK at 4.2 K 20 mK at 77 K 15 mK at 300 K	±10 mK/yr at 4.2 K ±40 mK/yr at 77 K ±25 mK/yr at 300 K	Yes	Not recommended below ~60 K	Relatively inexpensive, interchangeable, easily measured output Small size	Medium for low accuracy High with individual calibration

* Compiled from data supplied by Lake Shore Cryotronics 2002, Besley (1993), Rubin (1999).

[a] Accuracy: the difference between the measured and true temperature value.

[b] Reproducibility: the change in apparent temperature when the sensor is subjected to repeated thermal cycling from room temperature.

[c] Interchangeability: the ability to substitute one sensor for another with little change in calibration.

- For *temperature indicators* to sense liquid cryogen levels:

  Carbon-composition resistors (1/8–1/2 W Allen-Bradley or Speer resistors)
  Silicon diodes

Although not listed in Table 5.1, these inexpensive thermometers are very useful when rough thermometry is needed for cryogen level sensing. Bias them with a measuring current high enough to produce self-heating in gas but not when immersed in liquid. When the liquid level reaches their position in the cryostat, the resistance changes abruptly, indicating the liquid level has reached that point. In classic liquid-filled dewar cryostats, it helps to put one liquid-level sensor right at the bottom of the dewar to determine when liquid helium first collects (indicating it is time to turn up the transfer pressure; see Sec. 1.6.2) as well as to indicate when all the nitrogen used to precool the dewar is really gone. Another can be placed near the top of the cryostat to avoid expensive overfilling accidents, and a few more can be spaced at useful intervals (such as at the top of superconducting magnets to give a red alert that the magnet is about to lose cooling!). Continuous liquid-level indicators are also available commercially (listed in Appendix A1.7 under Liquid-level monitors).

Temperature measurements in *magnetic fields*

- For the *entire cryogenic temperature range*:

  Zirconium–oxynitride (Cernox™) thermometer 0.3–325 K

Of the sensors listed in Appendix A5.2, the zirconium–oxynitride thermometer has the lowest overall magnetic-field error above liquid-helium temperature: less than 0.2% in a magnetic field of 2.5 T (described in more detail in Sec. 5.2.1). At temperatures where the magnetic-field error is largest, the error can be further reduced by applying universal magnetic-field corrections (outlined in Sec. 5.2.2). These thermometers also have excellent accuracy: ± 5 mK at 4.2 K and less than 0.1% of reading above 10 K (almost as good as the germanium sensors). Their reproducibility on thermal cycling is good, and long-term drift is acceptable. Zirconium–oxynitride thermometers are relatively expensive, since each sensor must be individually calibrated. But a single such thermometer can constitute an excellent all-purpose sensor that covers the entire cryogenic temperature range with low magnetic-field error. It is the one I usually choose for most of my measurement cryostats.

- For temperatures *above liquid-nitrogen temperature*:

  Platinum resistance thermometer 77–300 K

The platinum thermometer has a low magnetic-field error above liquid-nitrogen temperature: less than 0.03% in a magnetic field of 2.5 T (see Fig. 5.7). This error is not as low as that in zirconium–oxynitride, but platinum sensors have the advantage of excellent reproducibility and interchangeability.

- For temperature *control* in a changing magnetic field:

  Capacitance sensor 1–290 K

The capacitance sensor has a very large error on thermal cycling (> 500 mK), but once cooled to a given temperature, it is reasonably stable (± 10 mK) and has excellent stability in a magnetic field, less than 0.05% of reading over the entire temperature range from 2 to 300 K

(data from Appendix A5.2). This makes it useful as a *control element* in swept-magnetic-field experiments, to keep the temperature constant when changing magnetic field. However, the temperature in zero field has to be measured with another temperature sensor, and so the capacitance sensor should be used as a control element only. For adequate resolution, the capacitance sensor requires a high-quality capacitance readout (e.g. the 5-digit capacitance bridge from General Radio, the automatic capacitance bridge from Andeen-Hagerling, or the capacitance controller card from Lake Shore Cryotronics; supplier information is listed in Appendix A1.7 under Thermometers and accessories).

These are the combinations I have found to be the most useful for many measurement systems. There are other possibilities, however. Some unique situations may be better served with different sensors because of special factors, which are briefly described next.

5.1.4 SMALL SENSING ELEMENTS

Some applications require very *small* sensing elements, either because of limitations on cryostat space, small sample size, thermal mass, or the need for fast time response. For example, in a thermal conductivity measurement, the temperature gradient needs to be measured at well-defined positions along the sample, ideally at point locations. For such an application, thermocouples provide temperature sensing over the smallest dimensions, less than 0.1 mm for bare-wire butt-welded thermocouple junctions. Their use takes effort, however, because for accurate measurements, the thermoelectric voltage output must be measured with microvolt resolution, especially at temperatures below 40 K. If a thermocouple is needed, gold–iron vs. Chromel thermocouples are generally the best choice because they have about two to three times the sensitivity of the common thermocouple combinations in the low-temperature range. But beware: the magnetic-field corrections for gold–iron thermocouples are large and usually unpredictable, as described in Sec. 5.2.1. The Chromel vs. Constantan (Type E) thermocouple is not as sensitive to magnetic field, but requires even more precise voltage detection. Further description of thermocouples is given in the reference compendium, Sec. 5.5.

Thermal response time is also closely coupled with sensor size. The single most important factor determining thermal response time, however, is the sensor's packaging. Sensors that require bulky strain-free mounting and copper-canister packaging generally have the longest thermal response times, whereas bare-chip, thin-film sensors have the quickest response. Since response times are generally dominated by the specific packaging used for each type of sensor, the information is most easily found in supplier catalogues (listed in Appendix A1.7 under Thermometers and accessories). Typically, response times for sensors at 4.2 K vary from as short as a millisecond for bare-chip sensors, to about a second for canister and strain-free packages. At 77 K, response times are longer than at 4.2 K because the heat capacity of materials generally increases cubically with temperature over this range; at liquid-nitrogen temperature, response times typically vary from tens of milliseconds to several seconds.

For some measurements, small size is also necessitated because of *heat capacity* requirements. For example, in calorimetry, the addenda (the thermal mass of stuff in the calorimeter attached to the sample) must be held to a minimum, and so a thermometer with a small thermal mass is needed. In calorimetry, silicon bolometers (very sensitive resistance thermometers) are recommended over thermocouples because they combine low mass with

high sensitivity. Silicon-on-sapphire thermometers have also been developed for very fast response in cryogenic flow applications (Louie et al. 1986).

5.1.5 THERMOMETRY IN THE PRESENCE OF NUCLEAR RADIATION

Gamma radiation

Germanium, Cernox™, or rhodium–iron sensors have the best tolerance against gamma radiation. These sensors have an apparent temperature shift of ~5–25 mK after a dose of 1 Mrad of gamma radiation at either 4.2 K or room temperature. This is much less than the hundreds to thousands of millikelvins of temperature error observed for diodes and carbon–glass sensors at a comparable dose. Platinum-thermometer errors are moderate, about 75 mK at 300 K at a room-temperature dose. Summary tabulations of temperature errors induced by gamma radiation are given in Tables 4–10a and 4–10b of Holmes and Courts (1998).

Neutron radiation

As with gamma radiation, germanium, Cernox™, or rhodium–iron sensors are the least sensitive to *neutron* radiation. The temperature errors are in the range ~3–~25 mK when these sensors are irradiated with a total fluence of about 2×10^{12} neutrons/cm^2 at a flux in the 10^7 neutrons/(cm^{2}s) range, delivered at either 4.2 K or room temperature. The temperature shifts in diodes or carbon–glass sensors are, again, the greatest, hundreds to thousands of millikelvins, whereas platinum sensors are fairly stable, shifting about 40 mK in a room-temperature radiation test. Tabulations of temperature errors induced by neutron radiation are given in Tables 4–10c and 4–10d of Holmes and Courts (1998).

5.1.6 CALIBRATION

As noted at the outset of this chapter, the easiest calibration is simply to use the standard vapor-pressure vs. temperature curve for the common cryogens, tabulated in Appendix A5.1. [However, beware of the temperature stratification errors that can occur (see Appendix A5.1)]. Outside these restricted temperature ranges, the most convenient thermometers for the temperature range 1–300 K are those listed in Appendix A5.2. Some of these sensors are interchangeable and can be used with universal standard calibrations, whereas others are highly variable and must be calibrated on an individual basis.

The interchangeable group includes platinum resistance thermometers, ruthenium-oxide, diodes, and thermocouples. The most common calibration tables are given in the appendixes to Chapter 5:

Standard temperature tables

Vapor pressure vs. temperature for common cryogenic liquids, ITS-90 (Appendix A5.1).

Resistance vs. temperature for pure platinum thermometers (Appendix A5.3a for $T \geq 70$ K, and Appendix A5.3b for $T \leq 70$ K).

Voltage vs. temperature for a typical silicon diode and four thermocouples (Appendix A5.4).

Magnetic-field correction tables

Magnetic-field corrections for platinum resistance thermometers (for $T \geq 40$ K) (Appendix A5.5).

Magnetic-field corrections for zirconium–oxynitride (Cernox™) resistance thermometers ($2 \text{ K} \leq T \leq 300$ K) (Appendix A5.6).

Application notes for using these sensors and their calibrations are given in the reference compendium, Sec. 5.5.

When standard tables are not available or a higher level of accuracy is needed, sensors must be calibrated individually. Most thermometer manufacturers have calibration services—at a price. Considering the need for accuracy and the special design of calibration probes, such calibration services can be well worth the expense, especially if only a few sensors need to be calibrated.

However, when many thermometers must be calibrated or if frequent *re*calibrations are necessary, it may pay to set up an in-house calibration apparatus that utilizes a commercially calibrated secondary-standard thermometer, such as a Rh–Fe thermometer (which is best suited for the range from about 10 to > 300 K) or a germanium thermometer (best suited for the range from about 0.1 to 100 K).

Here are some do-it-yourself tips for thermometer calibration. The suggestions on fitting and interpolation techniques are useful, not just for thermometer calibrations, but for *any* data.

- Design a measurement apparatus that ensures the reference thermometer and the one being calibrated are really at the same temperature. Watch for time lags when increasing or decreasing temperature. Good examples of such apparatus are given by Plumb et al. (1977) and Sample et al. (1982).
- Choose the calibration points to get adequate coverage of any tricky points in the thermometer characteristic, for example at the knee in the silicon-diode curves around 20 K.
- It is a good idea to smooth and interpolate raw data before entering them into a temperature controller. If done right, this also eliminates nonmonotonically changing data, which will not work in many controllers.
- Do not blindly use a high-order polynomial to fit calibration data. An nth order polynomial will fit $n + 1$ data points exactly, noise and all! This produces oscillations in the fitted curve that are physically not real. Good-fitting functions that realistically represent the shape of most characteristics (without wiggles) are low-order polynomials or Chebyshev functions. Add fitting terms cautiously, paying attention to the residuals (the difference between data and fit). When the residuals start to look random, stop adding terms. A good reference for fitting and interpolating is Chapter 3 of Press et al. (2002).
- It is often helpful to break the data into several segments with different fits. Pick the break points where the characteristic changes shape. Join the segments so that both the connecting point and the derivative are the same. This is automatically implemented by using a *spline* fit. Add one spline piece for each segment (not each data point) and adjust the segment end points to minimize the deviation between the raw data and the fit.

All this may seem cumbersome, but the whole calibration process for a particular type of thermometer goes much more quickly the second time. Furthermore, the fitting techniques are extremely valuable tools that you will use the rest of your research career for representing data of any kind. I have seen too many published graphs with unrealistic, "overfitted" curves.

5.2 Selection of thermometers for use in high magnetic fields

5.2.1 COMPARISON OF MAGNETIC ERRORS FOR COMMERCIAL THERMOMETERS

Most cryogenic sensors have a relatively high magnetic-field error. Although the effect of magnetic field can be great, fortunately, these errors are usually reproducible and nearly universal, so greater accuracy can be obtained by applying magnetic-field correction factors to the best sensors. These correction factors are described in Sec. 5.2.2 and tabulated for the two most popular high-field sensors, platinum and zirconium-oxynitride, in Appendixes A5.5 and A5.6.

Figure 5.7 compares the percentage temperature error for common cryogenic thermometers in a magnetic field of 2.5 T. The errors are presented as absolute values since the error can be either positive or negative, depending on the type of sensor. From Fig. 5.7 we see that zirconium–oxynitride (Cernox™), carbon–glass resistors, and platinum resistors (above ~70 K) have the smallest magnetic-field errors. On the other hand, diode thermometers generally have the largest (and least reproducible) errors. In particular, GaAlAs diodes are not recommended for use in magnetic fields at temperatures below ~20 K, and Si diodes should not be used below ~60 K. The errors for all the thermometers shown in Fig. 5.7 generally decrease as temperature increases. For example, above 70 K the maximum magnetic-field errors for even the worst sensors are less than 0.5% (at 2.5 T). However, at low temperatures, the difference among sensors becomes quite large.

Magnetic-field *orientation* can also play a role, particularly for silicon-diode sensors. If a silicon-diode thermometer must be used in a magnetic field, the error can be reduced by aligning the diode so the junction is perpendicular to the magnetic field B (i.e. current flow across the junction is parallel to B). In the sensors with the best (lowest) magnetic-field error, orientation is less of a factor, but it can still be significant. The field-correction factors given in Appendixes A5.5 and A5.6 have been measured for specific orientations. So to minimize error and use the standard corrections, the sensors must be oriented as indicated in Table 5.2.

Although included in Fig. 5.7, *capacitance* sensors are a special case. They are very insensitive to magnetic field but are highly irreproducible after thermal cycling. Consequently, they are useful, not as thermometers, but as *control* elements for holding temperature constant when magnetic field is changed. In practical applications, they must be used in tandem with a calibration thermometer. That is, the calibration thermometer is used to determine the temperature in zero magnetic field, and then the capacitance sensor controls the temperature and keeps it constant as magnetic field is changed. Further information for how to best use capacitance sensors is given in the reference compendium (Sec. 5.5.10).

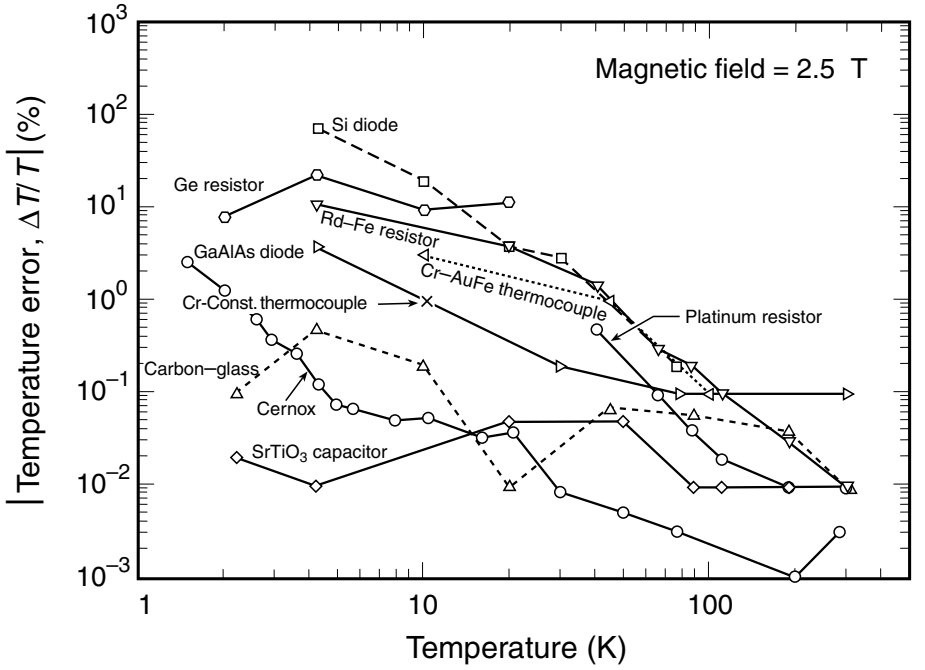

Fig. 5.7 Temperature error, $(T_{\text{apparent}} - T_{\text{actual}})/T_{\text{actual}}$ (%), (absolute value) of common cryogenic thermometers arising from a magnetic field of 2.5 T. For most sensors, the relative magnetic-field errors diminish as temperature increases. Diode sensors are generally the most affected by magnetic field. Capacitance thermometers are the least affected, but they have poor reproducibility. Cernox™ and carbon–glass sensors are the best thermometers for magnetic-field applications over the entire cryogenic range from 1 to 300 K, and platinum resistors are also excellent above liquid-nitrogen temperature. (GaAlAs diode data are for 2.0 T rather than 2.5 T.) (Compiled from data supplied by Lake Shore Cryotronics 1995 and 1991, product literature, and Rubin et al. 1986.)

Table 5.2 **Preferred orientation of thermometers in a magnetic field that minimizes error and corresponds to the correction factors in Appendixes A5.5 and A5.6.**

Sensor	Preferred Orientation
Carbon–glass	Long axis of package parallel to B (current flow parallel to B)
Platinum (wire wound)	Long axis of package parallel to B (package illustrated in Fig. 5.17 of the reference compendium, Sec. 5.5.1)
Platinum (film type)	No preferred orientation
Silicon diode	Junction plane perpendicular to B (i.e. the current flow across the junction is parallel to B)
Zirconium–oxynitride (Cernox™)	Film perpendicular to B (canister parallel to B)

➔ If the magnetic error of the *calibration* sensor is high, as with germanium sensors, for example, beware that it can be tricky to obtain "zero" magnetic field in some superconducting magnets because of remanent fields.

5.2.2 CORRECTING MAGNETIC TEMPERATURE ERROR IN THE BEST SENSORS

As mentioned in the general recommendations of Sec. 5.1.3, the *zirconium–oxynitride* (Cernox™) thermometer has the lowest overall magnetic-field error among common commercial sensors. Figure 5.8 shows the apparent temperature error of this sensor for magnetic fields as high as 32 T for the temperature range 2–77 K. The temperature error is typically less than about ± 2% from 4.2 to 10 K and less than 1% at higher temperatures. At temperatures and fields where the magnetoresistance is greatest, the error can be reduced by a factor of two to four through the use of magnetoresistance correction factors tabulated in Appendix A5.6. When even greater accuracy is needed, a particular sensor can be custom calibrated fairly easily in liquid helium or liquid nitrogen by recording its apparent temperature shift as a function of magnetic field while the bath temperature is held constant with a pressure regulator.

Carbon–glass thermometers also have small magnetic-field error, but have been largely supplanted by zirconium–oxynitride (Cernox™) sensors because their mounting is quite fragile (see Fig 5.18 in the reference compendium and the accompanying discussion). They also have generally larger magnetic-field errors than zirconium–oxynitride thermometers, as is evident from a comparison of Figs 5.8 and 5.9 (up to |–7%| error for carbon glass, versus up to |–2%| for zirconium–oxynitride at temperatures above 4.2 K and fields under 20 T). The effect

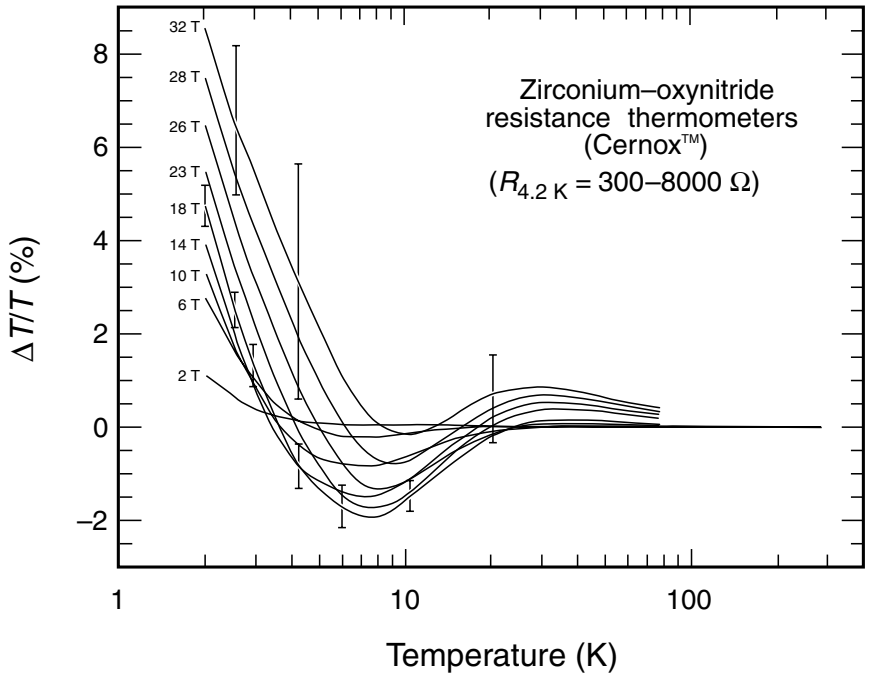

Fig. 5.8 Temperature error, $(T_{apparent} - T_{actual})/T_{actual}$ (%) at different magnetic fields for various zirconium–oxynitride thermometers (Cernox™) (300–8000 Ω at 4.2 K). Error bars for the 18 T and 32 T curves represent plus and minus one standard deviation among different sensors. These data were calculated and replotted as temperature error from magnetoresistance data of Brandt et al. (1999). A detailed tabulation of the magnetic-field corrections for zirconium–oxynitride sensors, along with examples of how to use the correction factors, is given in Appendix A5.6. Orientation of the sensor is such that the film is perpendicular to the magnetic field (canister parallel to the field).

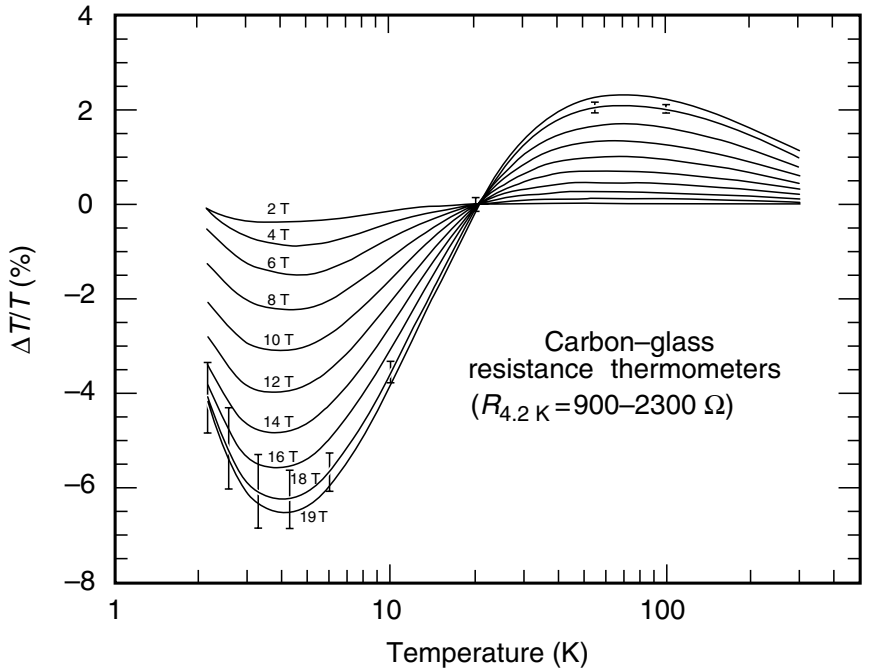

Fig. 5.9 Temperature error, $(T_{\text{apparent}} - T_{\text{actual}})/T_{\text{actual}}$ (%), at different magnetic fields, for a range of carbon–glass resistance thermometers (~900 – ~2300 Ω at 4.2 K). Error bars for the 18 T curve represent plus and minus one standard deviation. These data were calculated and replotted as temperature error from magnetoresistance data from Sample et al. (1982). The effect of magnetic field is somewhat larger than that of zirconium–oxynitride thermometers, but the data of Sample et al. (1982) can be used to reduce temperature error to a level comparable to that of zirconium–oxynitride sensors. Orientation of the sensor is such that the long axis of the thermometer case is parallel to the magnetic field (current through the sensor is parallel to the field).

of magnetic field on carbon–glass sensors is fairly consistent from sensor to sensor, however, so it can be reduced to a level comparable to that of zirconium–oxynitride sensors by applying correction factors, as discussed in the reference compendium, Sec. 5.5.5. Carbon–glass thermometers also have very good reproducibility.

Platinum resistance thermometers have only a small, magnetically induced temperature error above liquid-nitrogen temperature (about one-tenth the error of rhodium–iron resistors or silicon diodes, for example). Furthermore, the error (shown in Fig. 5.10) is nearly the *same* for different platinum resistance thermometers (both wire-wound and thick film, spanning a range of platinum purity, manufacturer, and ice-point resistance values from 100 to 500 Ω). Because the magnetoresistance is so consistent among different platinum sensors, universal correction factors can reduce magnetic-field error by about a factor of 10 over the entire useful temperature range. The corrections are simply percentage corrections to the temperature and are easier to apply than those for zirconium oxynitride, and so they are well worth using. Appendix A5.5 tabulates the standard correction factors and presents an example of their application. Magnetic-field effects at 19 T, for example, can be corrected to a very respectable $\Delta T/T$ uncertainty of ±0.2% at 77 K, decreasing to ±0.01% at 300 K. This is good enough for most applications and, in fact, is less than the interchangeability error for *industrial* platinum resistance sensors in zero field (see Appendix A5.3a).

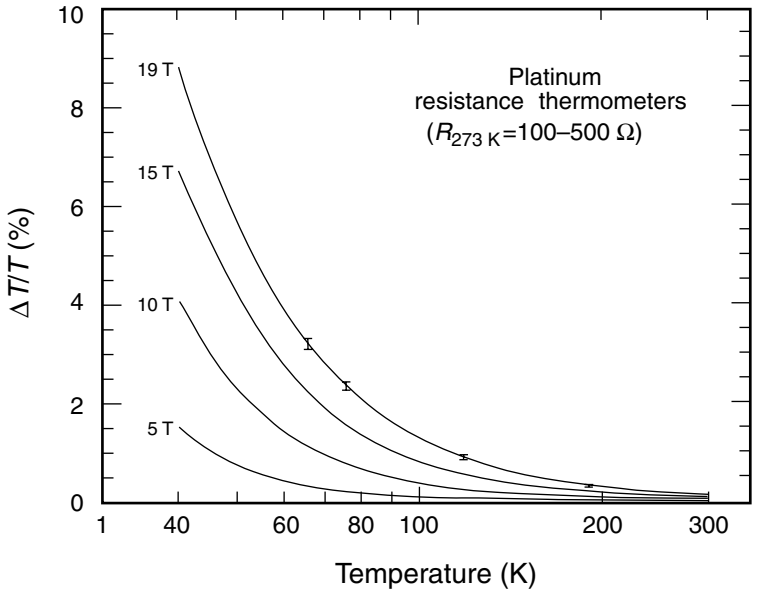

Fig. 5.10 Temperature error, $(T_{\text{apparent}} - T_{\text{actual}})/T_{\text{actual}}$ (%), at different magnetic fields, for platinum resistance thermometers (data calculated from magnetoresistance data by Brandt et al. 1988 and replotted here as temperature error). The standard deviation for this set of sensors is approximately ±10% of the magnetic-field correction at all fields and temperatures shown. A detailed tabulation of the magnetic-field corrections for platinum resistance sensors, along with examples of how to use the correction factors, is given in Appendix A5.5. Results apply equally well to both wire-wound and film-type platinum sensors. For wire-wound platinum sensors, the orientation is such that the long axis of the package is parallel to the magnetic field (an illustration of the package is shown in Fig. 5.17 in Sec. 5.5.1). Film-type platinum sensors depend little on orientation.

Although the magnetoresistance of wire-wound PRTs is dependent on orientation (see Table 5.2), a self-correcting platinum resistance sensor is also available utilizing platinum wire resistors of different orientation arranged in a bridge configuration (Nara et al. 1994).

5.3 Thermometer installation and measurement procedures

5.3.1 THERMAL ANCHORING OF THERMOMETERS AND THEIR LEADS

Invariably, errors in temperature measurements over the cryogenic range can be traced to poor thermal anchoring of thermometers to the samples being measured. Secondary to this are errors arising from thermometer instrumentation and calibration. The thermal connection between the thermometer and sample can be experimentally checked by using the procedure described in Sec. 5.3.6. It is an especially good idea to make this test during the initial checkout of a new cryostat or when changing to a different sample-mounting scheme.

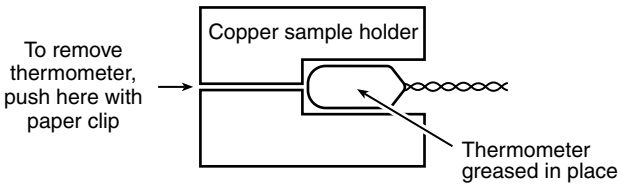

Fig. 5.11 Arrangement for removing thermometer canisters that are greased in place without pulling on the leads and possibly damaging them.

The important point is to make sure that the thermometer is well thermally anchored to the sample through a sample holder of high thermal conductance, or indirectly to the sample through a cryogenic bath with the thermometer and sample in close proximity. In a typical sample-holder installation, the thermometer canister is slipped into a hole drilled in a copper holder (or other material of high thermal conductivity), to which the sample is also thermally attached (see Figs 4.3 and 5.11). It is best if the hole for the thermometer is just large enough to closely fit the thermometer canister without much gap (clearance of $<$0.1 mm to 0.2 mm). Coat the canister with Apiezon N™ grease or Cry-Con™ grease to thermally attach it to the copper sample holder. For easy removal when using grease, it is best to drill a smaller hole all the way through the copper part, so the thermometer can be pushed out with a paper clip, as illustrated in Fig. 5.11. Pulling on the leads may damage the thermometer. Epoxy or varnish can be used to anchor the thermometer, but then the sensor is difficult to remove.

An alternative scheme for attaching flat thermometers is to use a beryllium–copper spring clip to press the sensor against the copper sample holder (see Fig. 4.2). A small amount of Apiezon N™ grease applied between the thermometer and copper block greatly enhances the thermal conduction between the two (Sec. 2.6.4). Thermometers can also be soldered or epoxied directly to the sample-holder copper block. When soldering, In or In–3%Ag are good soldering materials to use (see Sec. 3.3), since they have a relatively low melting temperature and are thus less likely to damage the sensor. Indium solders are also softer than Pb–Sn solders, so they better accommodate any strain from differential thermal contraction between the sensor and sample holder.

Thermally anchoring the *instrumentation leads* is just as important as anchoring the sensor itself, since about 75% of the thermal contact to packaged sensors is typically through their electrical leads, not their cases. Instrumentation leads need to be thermally anchored to the sample holder *before* they are attached to the thermometer leads (see, Sec. 4.4 on heat sinks for instrumentation leads, illustrated in Figs 4.2 through 4.5). This thermal anchoring serves to intercept the heat flow down the leads from points at higher temperature, which would otherwise be transmitted to the thermometer sensing element. Inadequate tempering of the thermometer leads raises the thermometer's temperature above that of the piece it is supposed to be measuring. Thermometer leads are usually heat-sunk along with the other instrumentation leads, as described in Sec. 4.4. For very sensitive measurements, it is advisable to anchor the leads at several places along their length from room temperature, with the final heat sink as close to the sample temperature as possible.

When space is available, *copper thermometer bobbins* are commercially available, which facilitate thermally anchoring leads, thermometer, and sample holder together all in one

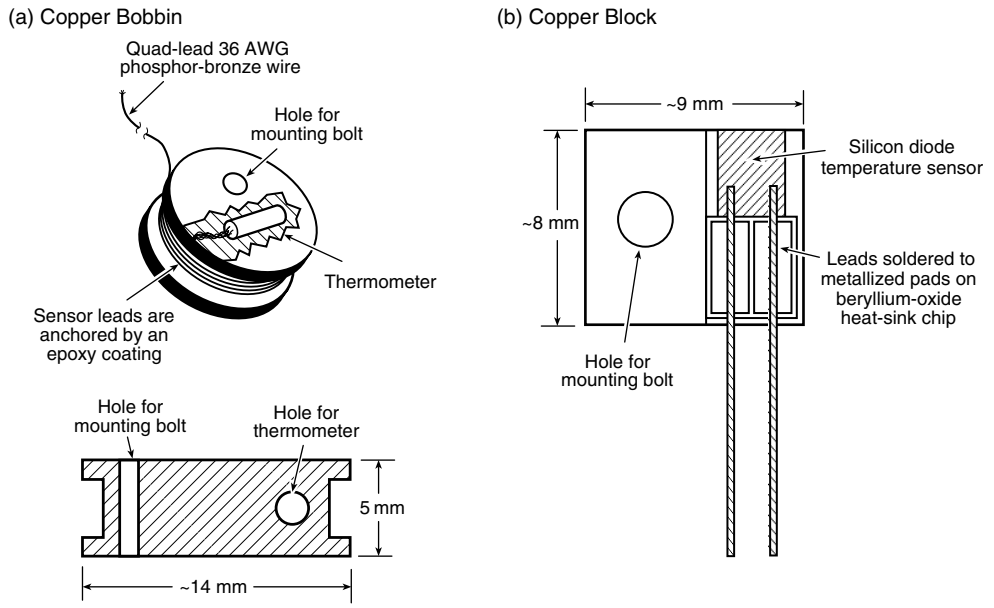

Fig. 5.12 Bolt-on copper bobbin (a), and copper block (b), for thermally anchoring a thermometer and its leads (adapted from Lake Shore Cryotronics 2002). For the bobbin technique, the thermometer leads are wrapped around the bobbin and thermally attached to it with varnish or epoxy. For the copper block technique, a beryllium-oxide chip with electric-terminal metallization on top can be used to thermally anchor the thermometer leads. To enhance the thermal contact between the bobbin/block and sample holder, a thin layer of thermally conductive grease is applied to the bottom of the bobbin/block before it is bolted in place.

assembly, as shown in Fig. 5.12. The thermometer is inserted into a hole in the copper bobbin with Apiezon N™ grease or Cry-Con™ thermally conductive grease, and the (electrically) insulated leads are wrapped around the bobbin and thermally anchored to it with varnish or epoxy. The thermometer bobbin can then be bolted to the sample holder. Thermal interfacial resistance between the thermometer bobbin and sample-holder body is significantly reduced by applying a thin ($\lesssim 0.05$ mm) coating of thermally conductive grease to the bottom of the bobbin before bolting it into place. (Supplier information for such grease is listed in Appendix A1.7 under Thermometers and accessories.) A bolt or screw made of brass is recommended, so that thermal contraction on cooling will tighten the joint. An added advantage of this bobbin arrangement is that the thermometer can be conveniently removed from the sample holder and protected, if necessary, when the sample holder needs to be heated for soldering. A similar arrangement utilizing a bolt-on copper thermometer block is also illustrated in Fig. 5.12.

5.3.2 THERMAL ANCHORING OF SAMPLES (WHILE MAINTAINING ELECTRICAL ISOLATION)

In the previous subsection, we treated the first part of the challenge—anchoring the thermometer. Now we look at the second part—thermally anchoring the sample. To accurately

measure the sample temperature, *both* the thermometer and sample must be thermally well anchored to the sample holder. This perennial temperature-measurement problem arises when the thermometer is thermally connected to the sample indirectly through the sample holder (as shown, for example, in Fig. 4.2 or 4.3). Complicating the situation is that the sample usually has to be *electrically* isolated from the sample holder (since, more often than not, the holder is made of highly conducting copper, which will electrically short the sample). That is, we want the sample to be simultaneously *electrically isolated* from, but *thermally well connected* to, the holder—a nice added challenge.

The electrical isolation problem is usually solved by using a thin layer of varnish, cigarette paper, Mylar™ or Kapton™ tape, or thin sapphire wafers:

Varnish, such as IMI 7031 varnish (formerly GE 7031), can be painted directly onto the copper sample holder to provide an electrically insulating layer. Application is easier if the varnish is first partially thinned with ethanol. Normal varnish curing time (12–24 h) can be shortened by using a heat lamp. If the varnish needs to be removed later, the same thinner can be used. This method is well suited to large or long samples, since large areas can be readily painted.

Cigarette paper can add some robustness to varnish (the paper is available commercially). This method is appropriate for situations where the soft varnish layer might be scratched. Thoroughly soak the paper with thinned varnish to adhere the thin paper to the copper sample holder as well as to provide good thermal conduction through the paper.

Mylar™- or Kapton™-based tape is perhaps the easiest to install. Simply stick it to the copper sample holder. "Yellow" Mylar™ tape (3M #56) is very thin, and its adhesion to copper actually improves with thermal cycling (application notes and supplier information are given in the table of sticky stuff, Appendix A3.10). Thin, adhesive-coated Kapton™ tape also works well. Both types of tape are more robust than a varnish layer alone.

Thin pieces of *sapphire* or *silicon wafer* can be greased to the sample holder. This method works best for electrically isolating small samples that do not require large sample holders.

After providing an insulating layer on the copper sample holder, the sample, in turn, needs to be thermally anchored to the electrically insulating layer. Sometimes we are lucky and the sample will not be damaged by stresses that can arise from the difference in thermal contraction between it and the sample holder. In this case, the sample can be attached directly to the holder with a high thermal conductivity grease (e.g. Apiezon N™ grease or Cry-Con™ thermal grease). Superconductors are a special case; they have such a low electrical resistivity that they can be soldered directly to metal-alloy sample holders (without the need for electrical insulation). The grease or solder techniques also work for strain-sensitive samples *if* the thermal contraction of the sample holder is carefully matched to that of the sample (see Appendixes A7.4 and A7.5).

When differential thermal contraction is a concern, the sample can be nonrigidly held onto the holder with an overlapping spiral wrap of Teflon™ tape. However, thermal contact to the sample holder is much worse than when using thermal grease or solder. (Wrapping with tape has the minor advantage, however, that after the experiment you do not have to clean gooey grease off the sample.) Alternatively, the sample can be tied to the sample holder with waxed dental floss, or a combination of dental floss with a Teflon™ tape overwrap.

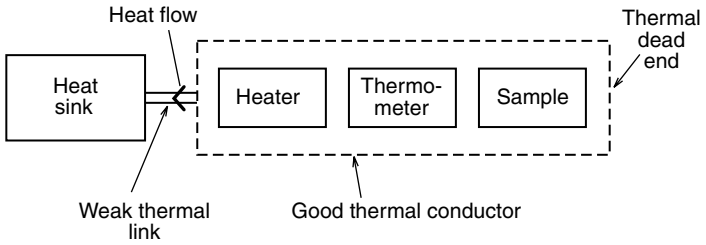

Fig. 5.13 Ideal arrangement for thermometer location.

When we cannot apply goo, glue, or grease to the sample, a thermal exchange gas (such as helium or nitrogen) can be used as a heat-transfer medium to help minimize thermal gradients along the sample, and between the sample and sample support. This exchange-gas convection technique helps to thermally contact samples that are delicate or have an unusual shape. Although thermal gradients are more of a problem than with either of the above techniques, they can be somewhat reduced by slipping a copper tube over the sample measurement area of the apparatus (Fig. 1.8) and wrapping a heater wire onto the tube to provide general heating of the entire sample region (Fig. 2.13).

5.3.3 THERMOMETER LOCATION

What is the best arrangement of thermometer, sample, and heater? Ideally, we would like all three to be in close thermal contact. This is usually accomplished by using a highly conducting copper sample holder (with a generous cross-sectional area), to which all three are thermally well connected (see the example calculation in Sec. 2.9.2, item 4). As discussed, however, thermal resistance between the thermometer, sample holder, and sample can present a problem. Then the best arrangement is to locate the sample and thermometer in a thermal dead end, with no heat flow, and hence no temperature gradient; see Fig. 5.13.

For ultimate temperature control, we want to locate the sensor close to the heater. On the other hand, to measure temperature accurately, we want the sensor close to the sample. The solution in critical situations is to use two thermometers—one for *control* near the heater and another for *measurement* near the sample.

An automatic temperature controller (see Sec. 5.4.3) may be essential to reduce temperature swings. In fact, whenever possible, use a properly tuned controller at cryogenic temperatures. A relatively simple but very effective tuning procedure is described in Appendix A5.7; the Ziegler–Nichols procedure provides the fastest thermal response while still preventing thermal oscillations.

5.3.4 THERMAL RADIATION AND EDDY-CURRENT HEATING

These are a couple of less-obvious sources of spurious sample heating. Too often, temperature errors trace their origin to these culprits.

Radiative heating is a significant problem in most cryogenic measurements because of the large temperature gradients that exist in cryostats (Sec. 2.4). It can be mitigated by choosing the location of the thermometer and sample so that they do not directly see surfaces at much higher or lower temperature. It is especially important to avoid a location that has a line-of-sight connection to a room-temperature surface, such as through a cryostat window or up a tube to the cryostat's top plate. Perhaps the easiest method to prevent radiative heat shining down a cryostat support tube is to place a bend or radiation baffle in the tube. The sample and sensor can also be shielded from seeing warm cryostat walls or windows by slipping a copper tube over the sample area (as shown in Fig. 1.8) or wrapping several layers of half-aluminized Mylar™ around the sample section.

In swept-magnetic-field experiments, induced eddy currents are a major source of extraneous heating. These occur, particularly, in large, highly conducting copper sample holders. Even a relatively thin copper tube slipped over the sample area (such as for radiation shielding) can be a significant source of unwanted heating from induced currents flowing around the tube's circumference. Such heating can be prevented by *slitting* the sample holder or tube along the direction of changing magnetic field to intercept the circulating currents; see Fig. 1.8. Alternatively, a tubular shield may be made with rolled copper foil, utilizing an overlapping but electrically insulating seam.

5.3.5 ELECTRICAL INSTRUMENTATION FOR THERMOMETER SENSORS

Some sensors, such as zirconium–oxynitride, carbon–glass, and germanium sensors, are packaged with *four* wires (two for current and two for voltage sensing); they must be measured with a four-lead technique. Other sensors, such as platinum resistors, are supplied with only *two* wires. Regardless of whether the sensor has two or four wires, an instrumentation-lead arrangement of the *four-lead* type should be used to eliminate the resistance of the instrumentation cables, which can be quite high since they run a long distance, from room-temperature instrumentation down through the cryostat to the thermometer. This is especially true for cryogenic thermometry, where blocking of heat conduction down the instrumentation cables necessitates the use of leads with a high electrical/thermal resistance. The high resistance of the instrumentation leads creates a problem by introducing significant spurious voltage along the leads, unless a four-lead measurement is made.

Figure 5.14 illustrates the four-lead measurement scheme. Two leads are used to connect the current source to the thermometer terminals, and two additional leads to connect the voltmeter. To minimize current-induced pickup in the voltage leads, the leads from the voltmeter are twisted together, separate from the pair of current-source leads (twisting is not shown in Fig. 5.14). High-resistance phosphor-bronze "quad" leads, discussed in Secs 4.2 and 4.4, work well for thermometer instrumentation because the high thermal resistance along their length minimizes unwanted heat conduction down the leads to the thermometer. These are offered commercially in a convenient package as four phosphor-bronze leads in a "quad" cable that can be attached to the four terminals of a thermometer.

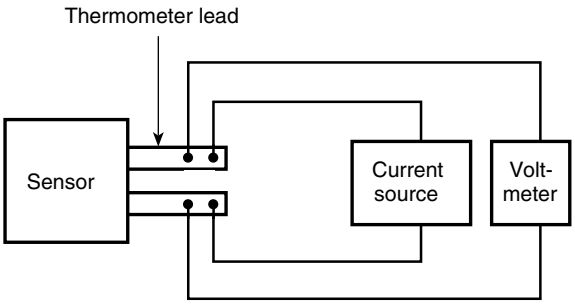

Fig. 5.14 Schematic diagram of a four-lead thermometer measurement used to reduce error from instrumentation-lead resistance. Resistance thermometers usually require a current supply that can be varied over a range of values (typically from 0.1 μA to 1 mA) to minimize self-heating effects and optimize the sensor output as its resistance changes with temperature. For diode thermometers, on the other hand, the current supply is usually a fixed source (typically 10 μA to match the diode calibration current). By using a low-frequency ac-current source, thermoelectric voltage interference can be eliminated.

➔ Read the manufacturer's instructions thoroughly before soldering to thermometer-sensor wires. The calibration of some sensors will be destroyed by heating the sensor to too high a temperature.

Thermometer sensors with only two wires necessitate doubling the instrumentation-lead connections; that is, the voltage and current leads are soldered two to each sensor wire, as illustrated in Fig. 5.14. The precise soldering point along the thermometer wire is usually not important, since the sensor wire resistance is small compared with that of the sensor element. Theoretically, there may be a slight advantage in connecting the voltmeter leads closer to the sensor body than the current leads, if there is space. If not, voltage and current leads can be simply soldered at the same location, because the difference is moot.

The reduction in error afforded by the four-lead scheme scales with the ratio of voltmeter resistance to thermometer resistance (see Sec. 7.2). Therefore, a voltmeter with a fairly high input impedance should be used. This is especially the case for semiconductor-like sensors, since at low temperatures their resistances can approach a megaohm (Fig. 5.2).

5.3.6 OPERATIONAL CHECKOUT

Self-heating problems

Self-heating from the sensor measuring current can cause significant errors in temperature readings. The effects are usually greatest at liquid-helium temperature and below, where thermal-contact boundary resistances are high. Self-heating can be corrected by using a low sensor current, but, on the other hand, too low a current reduces the signal-to-noise ratio of the thermometer and consequently degrades the temperature resolution. So what is the optimum sensor current? A nominal upper voltage limit is usually given in the supplier's literature to serve as a guideline in setting the thermometer current. This is a good place to

start, but, in practice, the optimum current depends on the thermal anchoring scheme used in a particular measurement cryostat. If uncertain, the following simple procedure works well for checking out *resistance* thermometers.

Under stable temperature conditions, start with a low sensor current and then increase the current until the resistance of the thermometer starts to rise from self-heating effects in the sensor. Optimum sensor current is just below the point where self-heating produces an observable increase in resistance. As a safety margin, choose a current lower by perhaps a factor of two.

For *diode* thermometers, on the other hand, such an experimental procedure is not possible because the current–voltage relationship is nonlinear and the sensor is calibrated at a given current specified by the supplier. In this case, the bias current recommended by the manufacturer must be used. Since no simple operational check for self-heating is possible, it is all the more important to use good installation and heat-sinking techniques in this case.

Electrical interference, if severe, can also lead to excessive thermometer heating. This happens either from spurious pickup signals that add to the excitation current, or a common-mode signal whereby all the thermometer leads go up and down in voltage together, and current flows through the capacitance of the thermal grounding of the thermometer. Both can be eliminated by good ac electrical practice (Sec. 4.1.3). In severe cases, one may wish to consider low-pass filtering all thermometry leads with multiway filters, which come conveniently built into commercial D-connector adapters.

A second, perhaps worse, effect of interference is a direct effect on the sensor's electrical measurement. This can take the form of driving the voltmeter a bit crazy, or more likely, a pickup signal that is rectified by diode thermometers into a dc voltage error. Again, the solution in such bad electrical environments is to use good ac wiring design, shielding, and low-pass filtering.

Direct check of the temperature error between thermometer and sample

In situations where the sample temperature is measured *indirectly* (e.g. the common situation of a thermometer and sample thermally connected through a sample holder), you would not know if you are getting good data unless you initially check new cryostats with a direct measurement of the temperature error. This is an important test. Attach a small thermometer to a typical sample (or similar dummy test sample) and then mount the specially instrumented sample into the rig, following the same thermal anchoring scheme that will be used in practice (thermal grease, Teflon™ tape, or whatever). Then, under typical experimental conditions, measure the difference between the cryostat and sample thermometers as a function of thermometer-sensor current and cryostat-heater power.

The difference between the two thermometer readings gives a measure of the cryostat's temperature error and serves to set workable limits on both the sensor and heater currents. Test both steady-state and transient errors. The transient measurement gives an indication of how much settling time is needed. If sample transport current is used in the measurement, include its level in the testing scheme as well, to make sure Joule heating is not affecting the sample temperature at high transport current. In cases where the error cannot be eliminated by setting appropriate limits on current levels, settling times, or both, the results can serve to determine the true sample temperature through the use of an error chart.

5.4 Controlling temperature

5.4.1 PUMPED LIQUID REFRIGERANTS

The simplest method for holding a temperature fixed is just to immerse the sample in a liquid cryogen, such as liquid helium (for the temperature range ~1.5– ~5 K) or liquid nitrogen (for the range ~63– ~83 K). As described in Sec. 1.2.1, the boiling temperature of the cryogenic liquid can be changed by varying the pressure of the saturated vapor above the liquid in the dewar. (Vapor pressure data are tabulated in Appendix A5.1 and plotted in Fig. 1.2). The temperature is lowered by partially evacuating the dewar with a vacuum pump, or raised by pressurizing the dewar (just make sure the dewar is mechanically designed to withstand the vacuum or applied pressure levels, and, when raising the temperature, place a heater in the bottom of the bath to break up temperature stratification in the liquid; see Sec. 1.2.1). Temperature stability is achieved by holding the vapor pressure steady with a manostat (pressure regulator), through which the vacuum pump is attached to the dewar. For liquid nitrogen, make sure the bath is not contaminated by condensation of oxygen from air, which invalidates the vapor-pressure calibration. [This requires not leaving the dewar open to air except for the short time it takes to insert measurement probes and, for long-running experiments, replacing the nitrogen with a fresh charge every few weeks (unless the dewar is operated as a closed system).]

This immersion cooling method is especially useful when high sample-heat loads are expected, such as for testing high-current superconductor samples where heating at resistive sample joints can cause significant errors in sample temperature. Fortunately, the maximum rates of heat transfer to cryogenic liquids are quite high, about $6 \times 10^4\ \Delta T^{2.5}$ W/m^2 for liquid helium, and $5 \times 10^2\ \Delta T^{2.5}$ W/m^2 for liquid nitrogen (see Sec. 2.5). However, this method for controlling temperature is limited to restricted temperature ranges (Fig. 1.2).

Temperatures between those of liquid helium and liquid nitrogen can be obtained in limited intervals by using liquid neon in the ~28– ~24.5 K range (but liquid neon is expensive) or liquid hydrogen in the ~21– ~14 K range (but hydrogen is potentially dangerous). For liquid neon, the vapor is collected and reused to save money. For liquid hydrogen, it is important to prevent the mixing of air with the hydrogen within the laboratory, in order to keep the vapor below the explosive mixture, which ranges from 4.1% to 75% hydrogen concentration (at standard temperature and pressure). (Hydrogen vapor is usually vented outdoors at the roof far away from ignition sources, where it is quickly reduced in concentration; for further information, see Edeskuty and Stewart 1996 and the references therein.)

5.4.2 RESISTANCE HEATERS

Temperatures outside these limited cryogen ranges are usually obtained by thermally anchoring a sample to a high-conductivity sample holder that is attached to a cold sink through a thermal resistance (Fig. 5.13). This method is also used when the sample must be thermally isolated and cannot be directly immersed in a cryogenic liquid, such as in heat-capacity measurements. Sample temperature is controlled by a resistive heater attached to the sample-holder assembly. Examples of such measurement cryostats were given in Sec. 1.4,

where solid or gas conduction provided the thermal link to the cold sink (usually a liquid cryogen bath or cryocooler cold stage).

The heater used to control the sample-holder assembly can be made, for example, by non-inductively winding heater wire around the sample holder (see Figs 4.2 through 4.4). Recommended heater wire materials are listed in Table 4.1: #36 AWG (~0.125 mm diameter) phosphor bronze or #32 AWG (~0.200 mm) Nichrome. [The difference in suggested gauge size arises from the fact that Nichrome is much more resistive than phosphor bronze and therefore should not be sized smaller than #32 gauge (~0.200 mm) to avoid inadequate surface area for dissipation of heat generated resistively within the wire.]

Example: What *length* heater wire should we use to make a heater from #36 AWG (~0.125 mm diameter) phosphor-bronze wire and power it with a temperature controller optimized for 25 Ω heaters?

We choose phosphor-bronze wire because it is much easier to solder than Nichrome. Appendix A4.2 shows that phosphor-bronze wire has a fairly constant bulk resistivity of about 11 μΩ cm at cryogenic temperatures (versus about 107 μΩ cm for Nichrome). Since a #36 AWG (~0.125 mm) wire has a cross-sectional area of 0.0127 mm^2 (from Appendix A4.1a), this corresponds to about

$$R/L = \rho/A = (11\ \mu\Omega\,\text{cm})/(0.0127\ \text{mm}^2) = 8.7\ \Omega/\text{m}.$$

Maximum power will be delivered to the heater if we choose the wire length to produce a matching 25 Ω impedance. This would require about a 2.9 m length of phosphor-bronze heater wire. In smaller apparatus, such a length may be difficult to accommodate. In this case we would either shorten the wire length (if we did not need the maximum controller power), use a wire of smaller diameter, or switch to Manganin, Constantan, or Nichrome (which have higher resistivities and can be used at larger diameters, Appendix 4.2).

The heater wire can be wound into a groove turned into the sample holder, as shown for example in Fig. 4.3. In this apparatus, we located the heater winding separate from the heat sink of the instrumentation leads so as not to introduce unwanted thermoelectric voltages into these sensitive leads. For the rig shown in Fig. 4.2, on the other hand, we used a *thin-film* resistive heater bonded to the flat back side of the copper sample platform. Suppliers for such thin-film heaters are listed in Appendix A1.7 under Heaters, thin film.

Depending on the power requirement, current is usually brought to the heater by using a heavier gauge copper wire (so the heating occurs in the heater, not in the current leads). For example, if an average heater current of about 0.25 A is needed, a heater power lead 1 m long would be optimally sized at #30 AWG (~0.250 mm), from Appendix A4.1a.

5.4.3 TEMPERATURE CONTROLLERS

A temperature controller is usually required to hold temperature steady with resistance heaters. At temperatures below about 30 K, the time constants are shortened to seconds because materials have low heat capacity in this regime. Under such conditions, it becomes tedious to continuously hold the temperature constant manually. At higher temperature, on the other hand, the time constants become so long that, with manual control, it becomes

difficult to not over-correct the temperature and cause oscillations. So, in either temperature regime, a controller is almost a necessity. For slow-temperature-drift measurements, a temperature controller is not required, but even here, it is convenient for programming a steady rate of temperature drift.

There are three main types of controllers—on–off, proportional, and proportional-integral-derivative (PID). Budget permitting, a PID controller is well worth the investment because it can control temperature much more precisely than the first two types.

- *On–off controllers* have a very simple principle of operation, as illustrated in Fig. 5.15. There is a dead band around the desired temperature (set point); when the temperature falls below the bottom end of the dead band, the heater power is turned fully on and it stays fully on until the thermometer sensor rises above the top of the dead band. Then power is turned off and it remains off until the temperature again falls below the bottom of the dead band (like a home furnace or air-conditioner thermostat). Depending on the width of the dead band, this can lead to significant temperature oscillations, and so the on–off controller is usually used only when precise control is not necessary (and budget is a factor). The output hardware for this type of system is either a mechanical or solid-state relay. The mechanical relay can be used when economy is important and cycle times are greater than about 10 s; however, for greater reliability or short cycle times, it is better to switch the electrical power on and off with a solid-state relay.
- *Proportional controllers* are generally preferred over the simple on–off controller because they greatly reduce the temperature oscillations. Proportional controllers decrease the average power delivered to the heater as the temperature approaches the desired set point. This slows the heating rate so that the system does not overshoot the set point and oscillate; instead, the system approaches the set point in a smooth manner and maintains a nearly stable temperature, as shown in Fig. 5.16. Variable power can be delivered to the heater by varying the current. It can also be varied by turning the power on and off for very short intervals (shorter than the thermal response time of the system) to vary the ratio of power-on time to power-off time. This latter scheme, however, should be avoided in accurate work because it leads to large amounts of electrical interference.

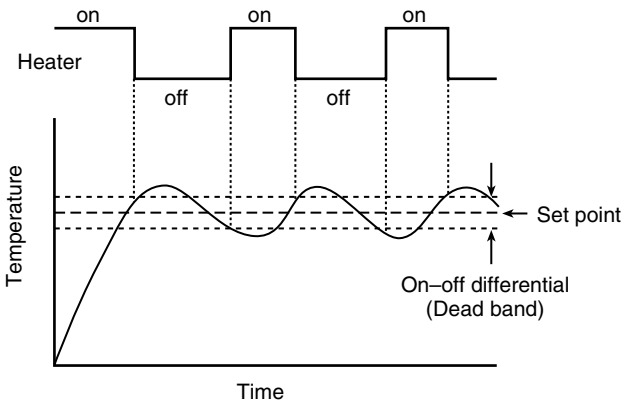

Fig. 5.15 On–off temperature controller operation (adapted from Omega Engineering 1992).

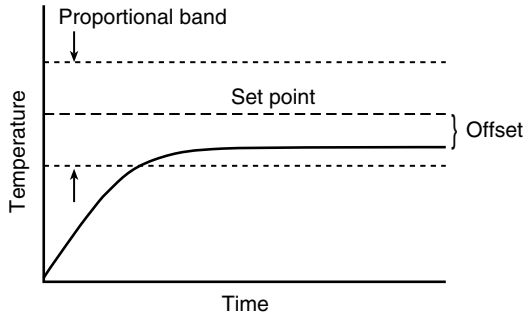

Fig. 5.16 Proportional controller operation.

The proportioning action takes place within a *proportional band*, with the set point at the middle of the band, as illustrated in Fig. 5.16. Outside the proportional band, the controller acts as an on–off controller, with the power fully on below the band, or completely off above the band. The width of the proportional band can be adjusted and needs to be carefully chosen to avoid sluggishness when the band is too large, or oscillations when the band is too small. The proportional band is usually expressed as a percent of the full-input range. It may also be referred to as *gain*, *G*, which is the reciprocal of the proportional band. Some controllers have a manual trim adjustment to zero the offset between the steady-state temperature and the set point (see Fig. 5.16).

- *Proportional-integral-derivative controllers* (PID) add two automatic adjustments to the proportional gain to greatly improve temperature control. They are especially well suited to systems where continual quick response is required to compensate for changes in additional energy sources (such as Joule heating). The first adjustment is automatic trim compensation: by adding *integral* control, the error signal between the set point and equilibrium temperature is integrated over time and eventually grows large enough that the offset or error is fully reduced to zero. (Effectively, this is an automatic version of the manual trim adjustment described above for proportional controllers.) The characteristic time constant t_i for this integration can be adjusted. The second adjustment, *derivative* control, compensates for load changes that take place rapidly. It is designed to reduce the undershoot and overshoot of temperature that occur in rapid transient conditions. It does this over a short time interval, t_d, which can also be varied.

  Tuning the PID controller is a matter of setting the gain *G*, the integral time t_i, and the derivative time t_d to get the best possible control for a given control system. An optimally tuned controller will provide a temperature that quickly tracks a rapid change in set point without much overshoot, oscillation, or droop below the set point. Some commercial products provide *automatic tuning* for changing these control parameters. This is useful, for example, to adapt the response of the system to the shorter time constants that occur as the cryostat is cooled to lower temperatures where the heat capacities of all the materials become much smaller. However, temperature controllers do not always have an automatic tuning feature, and it does not work well in some situations. In such situations, the relatively simple, but powerful, *Ziegler–Nichols method of tuning* (Ziegler and Nichols 1942) has been widely used for several decades as a quick and easy heuristic method to compute good settings for PID (and PI) controllers. A step-by-step procedure for manually optimizing PID controller settings in a given temperature range with the Ziegler–Nichols method is presented in Appendix A5.7.

When selecting a commercial temperature controller, it pays to check the following:

- *Resolution and absolute accuracy*: Is it adequate to meet your temperature-measurement needs?
- *Input modules*: Are they available for the particular sensors you want to use?
- *Sensor excitation level*: Can it be set low enough to avoid self-heating for a particular sensor and temperature range?
- *ac sensor excitation*: Is it available to avoid the effects of slowly drifting thermoelectric voltages?
- *Interpolation schemes*: What types are used to fit the calibration data? (See suggestion list in Sec. 5.1.6.) Can new calibrations be entered?
- *Preloaded calibrations*: Are they available for nonprecision work with interchangeable thermometers?
- *Heater power*: Is it adequate and a genuine analogue output (not pulsed, which causes electromagnetic interference for precise work)?
- *Computer interface*: Is it available? Is it electrically isolated from the cryogenic outputs to minimize interference?

5.5 Addendum: reference compendium of cryogenic-thermometer properties and application techniques

For convenient reference, we give here a detailed listing of the characteristics and best uses of commercial thermometers commonly used in the range ~1–~300 K. This compendium is provided, not as part of the main text, but as a separate reference for use with Appendix A5.2 in order to easily provide specific thermometer properties that may be of particular interest or to obtain a brief introduction to unfamiliar sensors. This more complete listing of commercially available thermometers is included here to supplement the most popular ones singled out earlier in the introductory general recommendations of Sec. 5.1.3. For ease in comparing the properties of different thermometers, their characteristics are tabulated *quantitatively* in Appendix A5.2. (The listing order of thermometers here corresponds to the order used in Appendix A5.2.)

5.5.1 PLATINUM RESISTANCE THERMOMETERS

Platinum resistance thermometers (PRTs) are the most popular thermometers above ~77 and can be used down to ~20 K with success, but in the lower temperature range they lose their advantage of interchangeability and sensitivity. Also, errors induced by magnetic fields ($\gtrsim 0.1$ T) significantly affect their accuracy below 30 K (see Fig. 5.7), so PRTs are not recommended for

magnetic-field use below this temperature. However, for temperature measurement at liquid-nitrogen temperature and above (whether in a magnetic field or not), they are by far the most reproducible, accurate, and inexpensive type of thermometer available. Often these thermometers will be used in tandem with a semiconductor-like thermometer (a zirconium–oxynitride sensor or germanium sensor, for example), with the PRT used above ~77 K and the semiconductor-like thermometer below. If needed, PRTs can be used for measurements to more than 800 K.

Platinum resistance thermometers are particularly convenient because of their interchangeability. That is, the calibration curves for PRT are standardized, and interface cards for these thermometers are readily available for direct computer readout of temperature. Industrial PRTs are accurate within about ± 1 K *without* individual sensor calibration, simply by using a standard PRT table (see Appendix A5.3a). This is a great cost saving. Since interchangeability is so good in the higher temperature range, a damaged sensor is easily replaced without recalibration. The accuracy and interchangeability of any given thermometer is mainly a matter of the *purity* of the platinum used in making the resistor and the care with which *strain* from handling and thermal contraction is eliminated in the mounting design. Consequently, PRTs are available in a wide range of quality, and which type is best depends on the temperature accuracy and reproducibility needed.

Industrial-grade PRTs are the least expensive. These thermometers are generally not recommended for use below about 70 K since they contain impurities that strongly affect the calibration at very low temperatures. (Impurity scattering significantly alters the temperature-dependent resistivity from phonon scattering, as described in the next chapter.) The calibration below 70 K must be individually matched to the purity level for the class of PRT in use. If a platinum thermometer must be used at such temperatures, a high-purity PRT is needed, or the *Z-value* scheme must be used, as described in Appendix A5.3b.

High-purity PRTs are available as *secondary standards* and have better accuracy than industrial-grade PRTs. These sensors are made from very high-purity platinum and are mounted strain-free to provide stability over time. The trade-off is that they cost considerably more than industrial-grade PRTs, and the strain-free mounting increases the thermal isolation of the sensor element from its case, thus making it more susceptible to self-heating. (This requires a lower measuring current, typically about 100 μA.) The strain-free package also increases the size of the sensor. Figure 5.17 shows a wire-wound platinum sensor, with the platinum wire wound around a central support structure.

The PRT is a *resistance* device, which usually means more sensitive voltage detection is needed than for *diode* sensors. However, as already noted, off-the-shelf instrumentation is readily available for PRTs from numerous suppliers, and standard calibrations with computer interface cards are common. Many digital multimeters and even some digital voltmeters have standard platinum calibration curves built in and can display temperature directly.

Magnetic-field errors are easily corrected by using the factors tabulated in Appendix A5.5 and the procedure outlined there. The consistency of the magnetoresistance effect among different platinum sensors leads to correction factors that can be universally applied to platinum resistance thermometers with very good results, consistently lowering the temperature error by about a factor of 10.

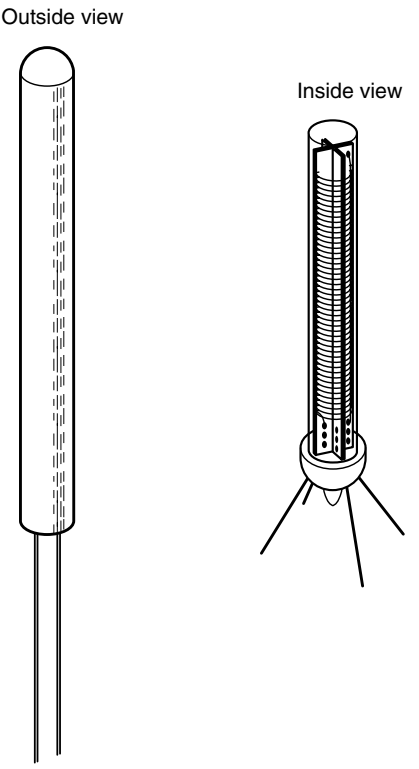

Fig. 5.17 Typical packaging for wire-wound platinum or rhodium–iron resistance thermometers used as standards, showing the outside copper canister and inside view of the wire-wound strain-free-mounting scheme (from Lake Shore Cryotronics 1995).

5.5.2 RHODIUM–IRON RESISTANCE THERMOMETERS

Rhodium–iron resistors are relatively new and behave like PRTs at higher temperatures. They are useful, however, because they are more sensitive than PRTs below 20 K, as shown in Figs 5.5 and 5.6. Also, rhodium–iron resistors can sensitively cover an incredible temperature range (0.5 K up to 900 K) with a *single thermometer*. Among low-temperature sensors, they also have the best reproducibility on thermal cycling, less than 0.1 mK at 4.2 K if they are high-purity and strain-free packaged. Consequently, rhodium–iron sensors can be used as a *secondary standard* over a very wide range of temperatures.

Magnetic fields are a problem, however, and rhodium–iron thermometers are not recommended for use in magnetic fields at temperatures below ~77 K (see Fig. 5.7).

Rhodium–iron sensors are offered in a wire-wound form, similar to the packaging scheme of high-purity PRTs shown in Fig. 5.17. For improved thermal contact to the sensing element, they are also offered in a film version deposited on a ceramic substrate.

5.5.3 GERMANIUM RESISTANCE THERMOMETERS

As mentioned previously, the main advantage of germanium resistance thermometers over other semiconductor-like resistance sensors is their reproducibility on thermal cycling,

which is typically less than ± 0.5 mK at 4.2 K. Consequently, they are recognized as a *secondary standard* for thermometry at cryogenic temperatures. They are smaller than most metallic (wire coil) thermometers, and more precise and accurate than silicon diodes. However, they have a very large magnetoresistance, about a hundred times larger than that of zirconium–oxynitride or carbon–glass thermometers; see Fig. 5.7. Thus, germanium resistance thermometers are recommended when absolute accuracy is needed in the 1–100 K temperature range, and when measurements are not made in a magnetic field. (A modified germanium resistance thermometer has also been developed that is less sensitive to magnetic field; nuclear irradiation converts germanium to arsenic or neighboring elements, which provides doping with an opposite magnetoresistance effect at low temperatures where the relative temperature error is greatest; Zarubin et al. 1990.)

One significant measurement note: These sensors must be strain-free mounted in a case to prevent thermal stress from changing the resistance of the sensor as it is cooled, as shown in Fig. 5.18. Unfortunately, this strain-free mounting reduces the thermal connection between the sensor and the case, making these sensors more sensitive to self-heating. Self-heating

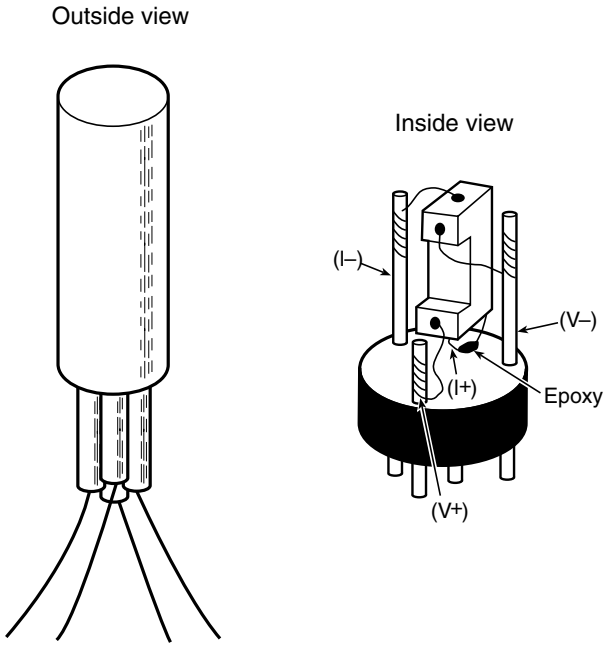

Fig. 5.18 Typical strain-free mounting for carbon–glass and germanium resistance thermometers (from Lake Shore Cryotronics 2002). For the carbon–glass resistance thermometer, the sensor base is supported by wires epoxied to the base, as shown in the inside view. For the germanium wires, the sensor base is epoxied directly to the package base. Both types of thermometers are sealed in a helium atmosphere, but at low temperatures, up to 70% of the thermal contact to the sensor occurs through the leads. The strain-free mounting scheme makes these thermometers very fragile; dropping a carbon–glass thermometer only a few centimeters can change its temperature response. The strain-free mounting also increases the thermal response time considerably. When soldering these thermometers into a cryostat, the sensing element is easily damaged by overheating the leads. So be careful with this type of thermometer if you have invested a lot in calibration.

effects require changing the measuring current in coarse steps for different temperature ranges to give an output voltage of about 2 mV.

Like other semiconductor-like thermometers, germanium sensors have relatively high resistance at the low end of their temperature range (Fig. 5.2), and thus they need a high input-impedance voltmeter for readout. The requirement of low self-heating also necessitates a much lower excitation current at low temperatures, especially below 1 K.

As is typical of all semiconductor-like resistance thermometers, their characteristics vary considerably from one thermometer to the next, which means that no universal calibration curves can be used; each thermometer must be calibrated individually at extra cost. This also means that their interchangeability is poor; that is, if we need to replace a thermometer, a new calibration curve must be generated for the replacement.

5.5.4 ZIRCONIUM–OXYNITRIDE RESISTANCE THERMOMETERS

Zirconium–oxynitride (Cernox™) is the best thermometer for temperature measurement in the presence of high magnetic fields. The magnetic-field correction for these sensors is typically less than 2% at 4.2 K in magnetic fields up to 20 T. When we do not want to use a combination of thermometers, this is also perhaps the best single thermometer for covering the entire cryogenic range, both below and above 100 K.

The chief advantage of zirconium–oxynitride thermometers over carbon–glass sensors is that Cernox™ thermometers are robust thin-film resistors that can be mounted in packages designed for excellent heat transfer to the sensing element. This results in much faster thermal response times than those for bulk devices requiring strain-free mounting. Also, these sensors are very stable under repeated thermal cycling and when exposed to extended ionizing radiation. Their only drawback is that their reproducibility errors on thermal cycling are somewhat greater than those of carbon–glass and germanium resistors, but still better than the rated accuracy of any of these sensors (see Appendix 5.2). Like other semiconductor-like thermometers, they must be individually calibrated.

Although the magnetic-field error of zirconium–oxynitride sensors is the lowest, it can be somewhat further reduced by applying universal correction factors tabulated in Appendix A5.6. These magnetoresistance corrections can reduce the error by a factor of two to four under some conditions, and give effectively no improvement under other circumstances because of the statistical variation in correction factors among individual sensors. Figure 5.8 shows that this correction procedure is most beneficial at temperatures below about 3 K and from about 6 K to 15 K, where the relative temperature errors are greatest. The correction factors given in Appendix A5.6 are applicable to zirconium–oxynitride sensors with 4.2 K resistances in the range 300–8000 Ω, and 4.2 K dimensionless sensitivities $(dR/R)/(dT/T)$ in the range -0.74 to -1.9, with -1.2 to -1.9 recommended. So try to purchase sensors in these common ranges.

As noted in Sec. 5.2.2, a more precise custom correction table can be obtained for any given sensor in the liquid-helium or liquid-nitrogen temperature range by using a pressure regulator to hold the bath temperature constant and recording its apparent temperature shift as the magnetic field is swept.

Data in Appendix A5.6 are given as relative *resistance* corrections (rather than temperature corrections) because Brandt et al. (1999) found that for zirconium–oxynitride sensors the standard deviations in resistance were much smaller than the standard deviations in temperature. [This results from the wide range of dimensionless sensitivities $S \equiv (dR/R)/(dT/T)$ of the individual sensors and the differing temperature dependences of S.] That is, the relative shift in resistance is first determined from the magnetoresistance data tabulated in Appendix A5.6. Then the temperature-dependent dimensionless sensitivity (supplied with the calibration data of a particular sensor) is used to calculate the equivalent shift in the sensor's apparent temperature. An example is given in Appendix A5.6.

The *orientation* of the magnetic field makes little difference in the calibration of zirconium–oxynitride thermometers at 77 K, but it becomes significant at 4.2 K (and there is no easy way to relate magnetoresistance for parallel and perpendicular orientations). Since the correction data of Brandt et al. were obtained for zirconium–oxynitride thermometers oriented with magnetic field *perpendicular* to the film surface (canister aligned parallel to the field), that is the best way to install these sensors if you think you may ever want to use these correction factors for improved accuracy.

5.5.5 CARBON–GLASS THERMOMETERS

The principal advantages of carbon–glass thermometers are that these sensors have small magnetic sensitivity and good reproducibility on thermal cycling, so they are well suited for measurement of temperature in high magnetic fields. However, carbon–glass sensors are quite fragile. They must be *strain-free* mounted in a case with support wires, as shown in Fig. 5.18. This mounting scheme decreases the thermal link to the case; it also makes carbon–glass sensors very susceptible to damage.

A comparison of the data in Figs 5.8 and 5.9 shows that carbon–glass thermometers generally have somewhat more magnetic-field error than zirconium–oxynitride sensors (at comparable fields). Nevertheless, a correction procedure similar to that just described for zirconium–oxynitride thermometers can be used to reduce the magnetoresistance error of carbon–glass thermometers to levels comparable to those of zirconium–oxynitride sensors. Correction factors are given by Sample et al. (1982) for carbon–glass resistance thermometers having 4.2 K resistance in the range 900–2300 Ω.

The *orientation* of the magnetic field does not have a large effect on these correction factors, which were determined for fields *parallel* to the long axis of the thermometer case (and therefore parallel to the sensor itself and to the sensor current). For magnetic fields *perpendicular* to the long axis of the thermometer case, an approximate simple correction can be obtained by multiplying the parallel temperature correction by 1.1 when the error is positive (above ~20 K) and by 0.98 when it is negative (below ~20 K).

5.5.6 BISMUTH–RUTHENATE AND RUTHENIUM-OXIDE THERMOMETERS

These thermometers are useful down to quite *low temperatures*, about 50 mK. At higher temperatures they are not as sensitive as other sensors, but they are, nevertheless, useful over

the temperature range 0.05–40 K, and especially well suited for sensitive temperature measurements below the lambda point of helium (2.2 K). They also have a small magnetic-field error at low temperature.

Another hallmark is the interchangeability of their calibration. However, because of the many proprietary formulations of bismuth–ruthenate or ruthenium-oxide materials, as well as inconsistencies from batch to batch, the calibration is applicable only *within one manufacturer's lot*. Sometimes the entire lot will be purchased by one customer and the lot calibration then used for the entire group.

These sensors are more easily damaged by thermal cycling at low temperature than other thermometers. Although they are fine during normal cooling and warming, they should not be used in an environment of large temperature excursions (such as when measuring heat-transfer characteristics in boiling cryogens).

5.5.7 SILICON DIODES

Silicon sensors are the sensor of choice for zero-magnetic-field "industrial" quality thermometry over the 4–300 K range. They are also readily interchanged, albeit with somewhat less accuracy than individually calibrated sensors. A "standard" calibration curve for a common silicon diode is given in Appendix A5.4. Silicon diodes are fairly inexpensive (if we do not specify close tolerance for interchangeability).

The small size of these sensors is another feature that can be very useful. They are roughly about one-fifth the size of other common thermometers, and so they are extremely useful when small thermal mass is needed (for rapid temperature response) or where space is restricted. For example, in the design of a magnetization apparatus, I needed a temperature sensor for a small single crystal (0.1 mm $\times$ 0.1 mm $\times$ 0.3 mm) that had to fit within the ~3 mm diameter bore of a SQUID magnetometer. In this measurement, I was trying to measure strain-induced shifts of only 1 mK in a critical temperature that was 90 K—that is, changes of 1 part in 100 000. Absolute accuracy was not critical. The silicon diode filled the bill exactly. By using a very stable current supply (stability of 1 part in 100 000), the sensor had the required sensitivity, particularly since these sensors involve measurement of relatively high voltages, typically about 1 V. Consequently, a silicon-diode sensor can have a greater *resolution* than a resistance thermometer, which typically operates at only the millivolt level. The silicon diode was smaller than any of the other high-resolution thermometers and made the measurement just possible.

Disadvantages of silicon sensors are that they do not provide the ultimate in *absolute* accuracy, and the reproducibility of these thermometers on thermal cycling is not quite as good as the other semiconductor-like thermometers. For high accuracy, each silicon sensor must be measured individually. (The calibration and operation of diodes must be at a given current, typically 10 μA, because they are "nonohmic" devices, wherein the resistance of the sensor changes with measuring current.) Also, beware of their sensitivity to magnetic field. As shown in Fig. 5.7, at liquid-helium temperature this can amount to several hundred percent!

5.5.8 GaAlAs DIODES

GaAlAs diodes are used in place of silicon diodes, mainly when sensitivity to magnetic field is a problem. GaAlAs diodes offer magnetic-field sensitivity about two orders of magnitude less than that of silicon diodes at liquid-helium temperatures and about an order of magnitude less at liquid-nitrogen temperature; see Fig. 5.7. Voltage sensitivity is higher than that of silicon diodes, but they are not as standardized as silicon diodes, and each sensor *must* be calibrated for any kind of reasonable accuracy. Cost is also higher than that of the silicon diodes, especially when the need for calibration is taken into consideration; however, if you are planning to buy a calibrated diode sensor anyway, the GaAlAs diode may be the better choice.

5.5.9 THERMOCOUPLES

At low temperatures, thermocouples are used less commonly than the other thermometers because their temperature resolution is not as good below about 20 K (see Fig. 5.6). This is mainly because their signal levels are in the microvolt range, which is more difficult to measure accurately than the relatively high millivolt signals of other sensors. Sometimes, however, thermocouples are the sensor of choice—for example, in situations where the temperature must be measured at a small point (such as in measurements of thermal conductivity). When precise temperature measurement is not needed, they are an inexpensive, convenient sensor for covering an extremely wide temperature range (1 K to more than 1000°C). In addition, they are very useful for controlling *differential* temperature, such as that between two temperature stages in some cryostats.

The most commonly used thermocouples at cryogenic temperatures are Au–Fe and Type E. Type K and Type T thermocouples are also used occasionally at low temperatures, but they are not as sensitive. Upper temperature limits are about 6°C for Au–Fe, 400°C for Type T, 1000°C for Type E, and 1400°C for Type K.

- Gold–iron 0.07% [Chromel (Ni–10wt%Cr) vs. Au–Fe (Au–0.07wt%Fe)] is the most widely used thermocouple below about 40 K because it has the highest sensitivity in this region (about 17 μV/K at 20 K). In addition to sensitivity, the materials used in gold–iron thermocouples have low thermal conductivity, which minimizes errors from heat conduction down the wires. However, Au–Fe thermocouples are not well suited for use in magnetic fields because they have a magnetic-field error that is about seven times larger than that of Type E thermocouples. Au–Fe thermocouples are also sensitive to work-hardening, which can change their calibration, and so they should be handled carefully. For *differential* measurements, Au–Fe thermocouple wire can be paired with a variety of positive elements, such as Chromel, copper, or "normal" silver (Ag–0.37wt%Au).
- Type E [Chromel (Ni–10wt%Cr) vs. Constantan (Cu–45wt%Ni)] thermocouples have the next highest sensitivity (8.5 μV/K at 20 K). The materials also have a low thermal conductivity and are resistant to corrosion in moist atmospheres. As noted above, Type E also have a much lower error in magnetic fields than Au–Fe, and so this is the type to choose when a thermocouple must be used in a magnetic field.

- Type K [Chromel (Ni–10wt%Cr) vs. Alumel (Ni–2wt%Al–2wt%Mn–1wt%Si)] thermocouples have half the sensitivity of Type E at 20 K (4.1 μV/K at 20 K). However, they are useful for covering an extremely wide range of temperature, from –270°C to 1372°C. The materials in Type K thermocouple also have low thermal conductivity and are resistant to corrosion in moist atmospheres.
- Type T [Copper vs. Constantan (Cu–45wt%Ni)] thermocouples are recommended for use in a vacuum, as well as in oxidizing, reducing, or inert environments down to about 90 K. Because the copper arm of the thermocouple has a high thermal conductivity, it is the most difficult to use in cryogenic measurements.

Appendix A5.4 gives "standard" temperature-vs.-voltage tables for these four types of thermocouples. Very detailed tables of thermoelectric voltage are given in Burns et al. (1993), and are readily available, for example, in the technical reference literature from Omega Engineering (2002).

When using these tables, the thermoelectric voltages for Type E, K, and T are normally referenced to 0°C, whereas Au–Fe is sometimes referenced to 0 K. The specific reference temperature does not really matter; just be sure to use the total *difference* in voltage between the temperature you are trying to measure and the reference temperature you choose. The reference temperature is room temperature when connecting the thermocouple directly to a voltmeter, or the temperature of a secondary junction if that setup is used (e.g. a reference junction immersed in ice water, liquid nitrogen, or liquid helium).

Use of thermocouples in magnetic fields is generally not recommended. The magnetic-field errors are relatively large and, unlike zirconium–oxynitride, platinum, or carbon–glass thermometers, the errors in thermocouples cannot be easily corrected. That is, the change in thermoelectric voltage with field depends in a complex way on both the temperature and magnetic field *along the position of the two thermocouple wires*. Thus, the correction will vary depending on cryostat design, magnetic-field location, and even in the same cryostat on changes in the cryogen liquid level.

When wiring a cryostat for use with thermocouples, dc techniques must be used because there is no ac option. The voltages are in the microvolt range, so take the same precautions with thermocouple instrumentation leads as recommended for sample voltage leads in Sec. 4.6.1. Perhaps the easiest readout is to use a voltmeter with a built-in program to determine the temperature for the standard thermocouple types. A good, detailed description of techniques for the practical use of thermocouples is provided in the technical reference information published by Omega Engineering (2002).

5.5.10 CAPACITANCE THERMOMETERS

The $SrTiO_3$ capacitance thermometer is useful only for *control* of temperatures in high magnetic fields. Its salient feature is that it has the lowest magnetic-field error of any sensor. However, capacitance sensors have a high reproducibility error ($>$500 mK) on thermal cycling, and so, in practice, they must be used in conjunction with another sensor used for calibration. As mentioned earlier, the calibration thermometer is used to set the temperature

in *zero magnetic field*, and then the capacitance sensor is used to *control* the temperature and keep it constant as magnetic field is changed. For temperatures below about 100 K, the zero-field calibration thermometer is typically chosen to be a stable, reproducible sensor, such as a germanium resistor, zirconium–oxynitride sensor, or carbon–glass resistor. For higher temperatures, a platinum resistance thermometer can be used.

Capacitance sensors have a region of zero sensitivity. There are two types from which to choose. Figure 5.4 shows that the first type of sensor has a region of insensitivity in the range 55–75 K. The second type of capacitance sensor has its insensitivity region at higher temperatures, near 300 K; however, this comes at the expense of reduced sensitivity below 55 K.

To control the temperature with any significant precision, the capacitance measurement has to be extremely sensitive. This makes capacitance sensors somewhat difficult to use in practice. Also, the *resistive* component of the $SrTiO_3$ capacitance sensor *is* dependent on magnetic field. Therefore, we need to use a bridge circuit to keep control errors less than a few tenths of a percent (suppliers of bridges adequate for the purpose are listed in Appendix A1.7 under Thermometers and accessories).

The voltage and frequency of the measuring current for capacitance thermometers should not be changed during a magnetic-field sweep, since this will cause the ferroelectric domains in the capacitance sensor to shift, giving rise to temperature errors. In practice this is not a problem; just be careful not to adjust the capacitance-sensor excitation during a magnetic-field ramp.

For magnetic-field applications below 1 K, a new type of capacitance temperature sensor has been developed that works well at temperatures down to 20 mK. Instead of a glass capacitor, the sensors are made from copper foil co-wound with Kapton™ sheets and cemented together with epoxy (Murphy et al. 2001).

5.5.11 CARBON RESISTANCE THERMOMETERS

As a final note, carbon-composition resistors, such as 1/2 W Speer resistors and 1/8 W Allen-Bradley resistors, have been used for many years as cheap thermometers for control in magnetic fields. However, their run-to-run reproducibility is not as good as thermometers developed more recently, and they have been replaced for magnetic-field use, in large part, by zirconium–oxynitride sensors. Nevertheless, they are still commonly used as an inexpensive thermometer for cryogen-level sensing, as described in Sec. 5.1.3.

5.6 References

5.6.1 FURTHER READING

GENERAL INFORMATION ON CRYOGENIC THERMOMETRY:

Schooley, J. F., ed. (1992). *Temperature, Its Measurement and Control in Science and Industry*, American Institute of Physics, c/o AIDC, 64 Depot Road, Colchester, VT 05446, Tel. 1-800-488-BOOK.

Courts, S., and Holmes, D. S. (1998). "Cryogenic instrumentation," in *Handbook of Cryogenic Engineering*, ed. J. G. Weisend II, Taylor & Francis Publishers, London.

DETAILED EXPLANATION OF PROPERTIES OF THERMOMETERS, MEASURING CIRCUITS, AND CALIBRATION TABLES:

Sparks, L. L. (1983). "Temperature, strain, and magnetic field measurements," Chapter 14 in *Properties of Materials at Low Temperatures*, eds. R. P. Reed and A. F. Clark, ASM International, Materials Park, OH.

Lake Shore Cryotronics (2002). "Reference guide," in *Temperature Measurement and Control*, pp. A-1 to A-63, Lake Shore Cryotronics, Inc., Westerville, OH; http://www.lakeshore.com/.

Omega Engineering (2002). "Technical reference section," in *The Temperature Handbook*, pp. Z-1 to Z-264, Omega Engineering, Inc., Stamford, CT; http://www.omega.com/.

Guideline for Realizing the International Temperature Scale of 1990 (ITS-90), NIST Tech Note 1265, US Government Printing Office, Washington, DC; contains formulas for determining vapor pressure vs. temperature for common cryogenic liquids.

NUMERICAL METHODS AND DATA-FITTING TECHNIQUES:

Press, W. H., Teukolsky, S. A., Vetterling, W. T., and Flannery, B. P. (2002). *Numerical Recipes: The Art of Scientific Computing*, 2nd edition Cambridge Univ. Press. Free on the Internet at http://www.nr.com. Interpolation and extrapolation techniques for fitting data are given in Chapter 3.

TEMPERATURE CONTROLLERS:

Swartz, J. M., and Rubin, L. G. (1985). "Fundamentals for usage of cryogenic temperature controllers," Application Note #3300, Lake Shore Cryotronics, Inc., Westerville, OH.

EFFECTS OF HIGH MAGNETIC FIELDS ON CRYOGENIC THERMOMETERS ARE DESCRIBED IN DETAIL IN:

Carbon resistors: Sample, H. H., Neuringer, L. J., and Rubin, L. G. (1974) "Low temperature thermometry in high magnetic fields. III. Carbon resistors (0.5–4.2 K); thermocouples." *Rev. Sci. Instrum*. 45, 64–73.

Carbon–glass thermometers: Sample, H. H., Brandt, B. L., and Rubin, L. G. (1982). "Low-temperature thermometry in high magnetic fields. V. Carbon-glass resistors," *Rev. Sci. Instrum*. 53, 1129–1136.

Cernox™: Brandt, B. L., Liu, D. W., and Rubin, L. G. (1999). "Low temperature thermometry in high magnetic fields. VII. Cernox™ sensors to 32 T," *Rev. Sci. Instrum*. 70, 104–110.

Instrumentation methods: Sample, H. H., and Rubin, L. G. (1977). "Instrumentation and methods for low temperature measurements in high magnetic fields," *Cryogenics* 17, 597–606.

Platinum thermometers: Brandt, B. L., Rubin, L. G., and Sample, H. H. (1988). "Low temperature thermometry in high magnetic fields. VI. Industrial-grade Pt resistors above 66 K; Rh–Fe and Au–Mn resistors above 40 K," *Rev. Sci. Instrum*. 59, 642–645.

Thermocouples: Sample, H. H., and Rubin, L. G. (1977). "Instrumentation and methods for low temperature measurements in high magnetic fields," *Cryogenics* 17, 597–606.

FOR INFORMATION ON THERMOMETRY BELOW 1 K:

Lounasmaa, O. V. (1974). *Experimental Principles and Methods Below 1 K*, Academic Press, NY.

Pobell, F. (1996). *Matter and Methods at Low Temperatures*, 2nd edition, Springer-Verlag, Berlin.

Richardson, R. C., and Smith, E. N., eds. (1988). *Experimental Techniques in Condensed Matter Physics at Low Temperatures*, Addison Wesley, NY.

5.6.2 **CHAPTER REFERENCES**

Beasley, L. M. (1993). National Measurements Laboratory, Sydney, Australia, personal communication.

Brandt, B. L., Rubin, L. G., and Sample, H. H. (1988). "Low-temperature thermometry in high magnetic fields. VI. Industrial-grade Pt resistors above 66 K; Rh–Fe and Au–Mn resistors above 40 K," *Rev. Sci. Instrum*. 59, 642–645.

Brandt, B. L., Liu, D. W., and Rubin, L. G. (1999). "Low temperature thermometry in high magnetic fields. VII. Cernox™ sensors to 32 T," *Rev. Sci. Instrum*. 70, 104–110.

Burns, G. W., Schroger, M. G., Strouse, G. F., Croarkin, M. C., and Guthrie, W. F. (1993). "Temperature-electromotive force reference functions and tables for the letter-designated thermocouple types based on the ITS-90," NIST Monograph 175, US Government Printing Office, Washington, DC.

Edeskuty, R. J. and Stewart, W. F. (1996). Safety in the Handling of Cryogenic Fluids, Plenum Press, New York.

Holmes, D. S. and Courts, S. S. (1998). "Cryogenic instrumentation" in *Handbook of Cryogenic Engineering*, ed. J. G. Weisend II, Taylor & Francis Publishers, London.

Lake Shore Cryotronics (1991). *Measurement and Control Technologies*, Lake Shore Cryotronics, Inc., Westerville, OH.

Lake Shore Cryotronics (1995, 2002). *Temperature Measurement and Control*, Lake Shore Cryotronics, Inc., Westerville, OH.

Louie, B., Radebaugh, R., and Early, S. (1986). "A thermometer for fast response in cryogenic flow," *Adv. Cryog. Eng*. 31, 1235–1246.

Murphy, T. P., Palm, E. C., Peabody, L., and Tozer, W. W. (2001). "Capacitance thermometer for use at low temperatures and high magnetic fields," *Rev. Sci. Instrum*. 72, 3462–3466.

Nara, K., Kato, H., and Okaji, M. (1994). "Design of platinum resistance thermometer with small magnetic-field correction," *Cryogenics* 34, 1007–1010.

Omega Engineering (1992, 2002). Temperature technical reference section in *The Temperature Handbook*, Omega Engineering, Inc., Stamford, CT; http://www.omega.com/.

Plumb, H. H., Besley, L. M., and Kemp, W. R. G. (1977). "Thermal cycling apparatus to test germanium thermometer stabilities," *Rev. Sci. Instrum*. 48, 419–423.

Press, W. H., Teukolsky, S. A., Vetterling, W. T., and Flannery, B. P. (2002). *Numerical Recipes: The Art of Scientific Computing*, 2nd edition, Cambridge Univ. Press. Free on the Internet at http://www.nr.com.

Preston–Thomas, H. (1990). "The international temperature scale of 1990 (ITS-90)," *Metrologia* 27, 107. Extensive information is also available on the Internet at http://www.its-90.com/.

Rubin, L. G. (1999). Francis Bitter National Magnet Laboratory, Cambridge, Massachusetts, personal communication, Cambridge Univ. Press.

Rubin, L. G., Brandt, B. L., and Sample, H. H. (1986). "Practical solutions to measurement problems encountered at low temperatures and high magnetic fields," *Adv. Cryog. Eng*. 31, 1221.

Sample, H. H., Brandt, B. L., and Rubin, L. G. (1982). "Low-temperature thermometry in high magnetic fields. V. Carbon-glass resistors," *Rev. Sci. Instrum*. 53, 1129–1136.

Zarubin, L. I., Nemish, I. Y., and Szmyrka–Grzebyk, A. (1990). "Germanium resistance thermometers with low magnetoresistance," *Cryogenics* 30, 533–537.

Ziegler, J. G., and Nichols, N. B. (1942). "Optimum settings for automatic controllers," *Trans. ASME* 64, 759–768.

6 Properties of Solids at Low Temperatures

Now fills thy sleep with perturbations.

– Shakespeare, Richard III

A summary of the cryogenic "personalities" of solid materials used in cryostat construction was presented in Chapter 3. Here we conclude Part I on cryostat design and material selection with a chapter describing the rest of the materials story—the *physics* of their properties and *tables of data* for cryostat design.

Emphasis is placed on showing the temperature dependence of these properties and highlighting useful expressions for estimating their values. More importantly, we try to give a feeling for how these expressions can be used in practical situations, illustrated by examples. In several cases, we delve a little deeper into the underlying physics where it provides an intuitive understanding of the physical property, as well as to clarify some common misunderstandings about the treatment of electric and heat transport at low temperatures. Further information on the fundamental physics of solids and detailed derivations are left to the excellent textbooks listed in Sec. 6.7.1.

We also look at the practical use of handbook data—when it is appropriate and when it is not. The graphs and the appendix tables of this chapter are some of the figures and charts I refer to the most when selecting materials for new apparatus designs. The old adage, "measure twice, cut once," applies as much to material selection as to design, maybe more so. It is really frustrating to pour your heart and soul into an apparatus, only to discover that a main cryostat member thermally contracts too much, or is too weak, or has a magnetic moment that interferes with the measurement. Often it means starting construction all over again.

The *graphs* in this chapter are intended to display at a glance the relative values of many materials; thus, they are useful for selecting materials and displaying the overall temperature dependence of the property. The complementary *data tables* in Appendixes A6.1 through A6.10 are provided because they facilitate reading specific values. These tables are collected in the appendix for easy access when later looking up data to design a cryostat. The table format also enables more materials to be included than can be clearly displayed in a graph, so if you do not see the material you want in a graph, you might check the corresponding appendix.

Properties of *adhesives* were given earlier in Appendix A3.10 as part of Chapter 3 on cryostat construction.

Further sources of cryogenic handbook values (both on the Internet and in the printed literature) are annotated at the end of the chapter.

The order of presentation of the first four properties (specific heat, Sec. 6.1; thermal expansion, Sec. 6.2; electrical resistivity, Sec. 6.3; and thermal conductivity, Sec. 6.4) has been chosen

because the underlying physics of each one logically flows into the next. The last two properties (magnetic susceptibility, Sec. 6.5, and mechanical properties, Sec. 6.6) are not always included in treatments of material properties, but they are absolutely crucial to the selection of materials for cryostat design.

6.1 Specific heat and thermal diffusivity

6.1.1 DESIGN DATA AND MATERIALS SELECTION

Figure 6.1 and Appendix A6.2 give the specific heat (heat capacity per unit mass at constant pressure, C_P) of a range of technical materials, from room temperature down to ~4 K. The figure shows that above about 100 K the specific heat decreases only slowly with temperature, but below ~100 K it decreases fairly rapidly, falling approximately as T^3 in most materials. Thus, most of the

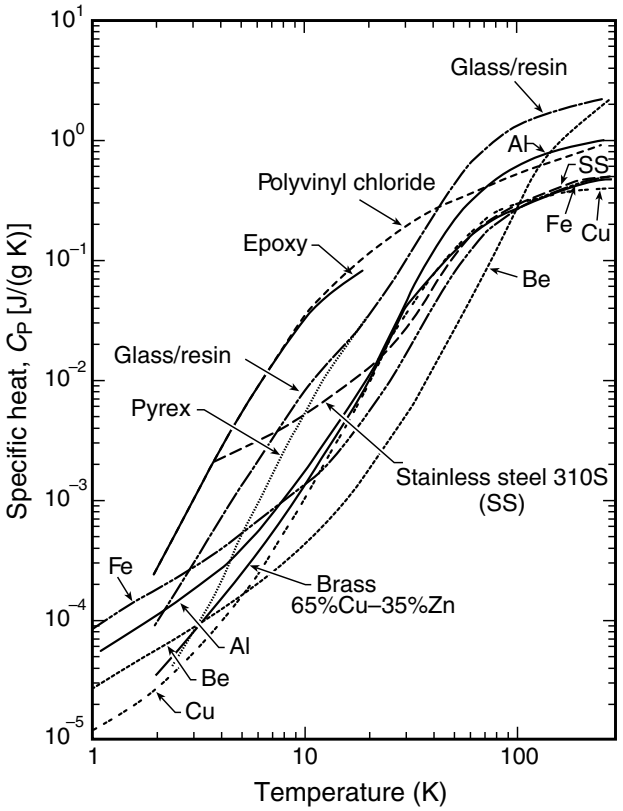

Fig. 6.1 Specific heat (heat capacity per unit mass at constant pressure, C_P) for technical materials at cryogenic temperatures (from Corruccini and Gniewek 1960, Chang 1977, Touloukian 1966, Johnson, Part II 1960, and White and Meeson 2002). *Volumetric* heat capacity (which is sometimes more convenient for larger cryostat structural parts) is given in Fig. 3.3. Tabulated values of specific heat for these and other materials are given in Appendix A6.2.

cool-down time for a cryogenic apparatus is spent reaching 100 K; the remaining cool-down process occurs relatively quickly because of the rapid drop in specific heat at lower temperatures.

This also means that with variable-temperature measurements, the temperature settling times are short below ~30 K, on the order of minutes, decreasing to seconds at liquid-helium temperature if the cryostat is correctly designed (i.e. by avoiding low thermal-diffusivity materials described in Sec. 6.1.4). However, above 100 K, the thermal response time of most cryostats is painfully slow (typically many tens of minutes). In this high-temperature regime, large heat capacities usually necessitate the use of an automatic temperature controller, since "human controllers" are usually not patient enough.

As seen in Fig. 6.1, the specific heats of glasses and resins are significantly greater than those for metals. This is why it generally pays to avoid massive parts made of glass-filled epoxy composites (such as G-10 or G-11) for cryostat construction. The combination of their high specific heat and low thermal conductivity usually results in lengthy cool-down times, as well as a lot of waiting for variable-temperature measurements to stabilize (Sec. 6.1.4).

Definitions: The terms used to define heat capacity can sometimes be confusing; they depend on how it is normalized:

	Term	Units
Heat capacity per unit mass	Specific heat	J/(kg K)
Heat capacity per unit volume	Volumetric heat capacity	J/(m^3 K)
Heat capacity per mole	Molar heat capacity	J/(mol K)
(to add to the confusion, this is sometimes also referred to as specific heat or heat capacity)		
Heat capacity of an entire object	Heat capacity	J/K

6.1.2 DEBYE MODEL

The Debye model is particularly useful for estimating the specific heat. Crystal-lattice vibrations, or perturbations called *phonons*, are the chief means of storing energy in solids and thus dominate the heat capacity of most solids over the cryogenic temperature range. The higher the temperature, the greater the magnitude of the atomic-lattice vibrations (which is what makes a material feel warm). The phonon contribution to the specific heat at constant volume C_V may be estimated by use of the Debye function,

$$C_V = 9Nk_B(T/\theta_D)^3 \int_0^{\theta_D/T} x^4 e^x (e^x-1)^{-2}\, dx \qquad (6.1)$$

$$[\equiv 9Nk_B(T/\theta_D)^3 \int_0^{\theta_D/T} x^4 (e^x-1)^{-1}(1-e^{-x})^{-1}\, dx],$$

where N is the number of atoms per unit volume (see Ziman 1960), k_B is Boltzmann's constant, and θ_D is the Debye temperature. The derivation of this famous formula is treated, for example, in Rosenberg (1988) or Ziman (1960) and is based on the elastic-continuum model of a solid, where energy is stored in the vibrational modes of the crystal lattice.

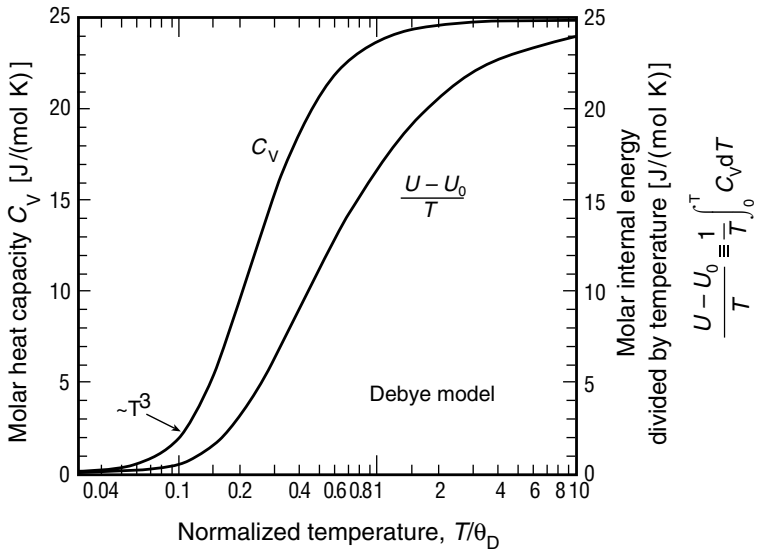

Fig. 6.2 Molar heat capacity at constant volume C_V and molar internal energy U (integrated molar heat capacity) as a function of temperature, from the Debye model. (The internal energy is divided by temperature to display the results in the same units as C_V.) (Values are from Furukawa et al. 1972.) The Debye model is useful for estimating heat capacity and internal energy in many solids, as illustrated in the example. Tabulations of the data in this figure are given in Appendix A6.3; values of the Debye temperature θ_D are given for many elements in Appendix A6.1.

This general function is relatively easy to use in estimating the temperature dependence of the specific heat C_V or integrated specific heat between any two temperatures. (The latter quantity is needed to determine how much refrigeration will be required to cool materials, as described below.) Values of the specific heat given by Eq. (6.1) are plotted as a function of T/θ_D in Fig. 6.2 and tabulated in Appendix A6.3 as molar heat capacity. To use this tabulation for any specific material, just look up the value of the Debye temperature θ_D for that element in Appendix A6.1.

Figure 6.2 shows that C_V is nearly constant at temperatures above θ_D, approaching the value 24.94 J/(mol K) (= 3R, where R is the molar gas constant, given in Appendix A1.2). However, at temperatures below about 0.2 θ_D, C_V changes to a T^3 dependence; more specifically, the model gives $C_V = 1944\,(T/\theta_D)^3$ J/(mol K) at low temperatures.

Although the Debye expression is derived for specific heat at constant *volume* C_V, the quantity that is usually *measured* (Fig. 6.1) is the specific heat at constant *pressure* C_P. The difference between C_P and C_V, however, is negligible at low temperatures and usually amounts to only ~1% at temperatures near $\theta_D/2$. So for most practical purposes, we can use the two interchangeably across the cryogenic range.

The Debye model predicts the specific heat data in Fig. 6.1 quite well. The main difference arises in nonsuperconducting metals at low temperatures ($\lesssim$10 K) where the specific heat starts to deviate from the T^3 phonon temperature dependence toward a more linear dependence on T. In this low-temperature region the phonon contribution is "frozen out," and the contribution to the specific heat from *conduction electrons* C_e becomes important.

At low temperatures, this electronic contribution C_e varies linearly with temperature,

$$C_e = cT, \tag{6.2}$$

where c is a proportionality constant. For highly conducting metals such as copper, silver, and gold, c is found to be relatively low, ~0.6 mJ/(mol K^2). However, it can rise to about 10 mJ/(mol K^2) for some of the transition metals.

6.1.3 ESTIMATING THE COST OF COOLING CRYOSTAT PARTS USING THE DEBYE MODEL

Although the Debye model (which considers only phonons) underestimates the specific heat in metals at low temperatures (because of the electronic contribution described above), it is nevertheless quite accurate for evaluating the specific heat at higher temperatures, precisely where the specific heat is greatest. Thus, the Debye model is particularly useful for estimating the *integrated* specific heat, or molar energy, of a cryostat part in order to determine how much refrigeration time or liquid cryogen the part will consume to cool it down. (Keep in mind, however, that for some specialty materials, large errors can occur when the Debye model is used if there are any other significant contributions to the specific heat, such as *magnetic* interactions or *phase transformations*. Such materials are sometimes quite useful, however, such as for cryocooler regenerators, Sec. 1.4.5.)

We now illustrate the simple power of the Debye model by estimating the energy cost of cooling common copper. The Debye expression for C_V can be integrated to obtain values of the molar internal energy U. The molar internal energy is divided by temperature (to remove most of the temperature dependence) and plotted in Fig. 6.2 and tabulated in Appendix A6.3 as

$$(U-U_0)/T \equiv T^{-1}\int_0^T C_V \, dT.$$

Example: Suppose we wish to know how much liquid helium it will take to cool 100 g of copper from room temperature, 293 K, to 4 K.

The Debye temperature $\theta_D = 310$ K for copper (from Appendix A6.1), and so at 293 K, $T/\theta_D = 0.95$. From Fig. 6.2 (or from the values in Appendix A6.3), we find that at $T/\theta_D = 0.95$

$$(U-U_0)/T \equiv T^{-1}\int_0^T C_V \, dT = 16.5 \text{ J/(mol K)}, \quad \left[\text{at } T = 293 \text{ K}\right]$$

and thus the molar internal energy is

$$U_{295\,K} - U_0 = (293 \text{ K})\ [16.5 \text{ J/(mol K)}] = 4.8 \text{ kJ/mol}.$$

On the other hand, at 4 K, where $T/\theta_D = 0.013$, $U_{4\,K} - U_0 \approx 0$. Therefore,

$$U_{295\,K} - U_{4\,K} \cong 4.8 \text{ kJ/mol}.$$

From Appendix A6.1 we find that 100 g of copper is about 1.6 mol, so the total energy that needs to be removed to cool 100 g of copper to 4 K is about (4.8 kJ/mol) × (1.6 mol) = 7.7 kJ.

From this estimate of the total energy needed for refrigeration, we can determine the amount of liquid helium that will be consumed. From Appendix A1.5, the latent heat of vaporization of liquid helium is 20.75 J/g or 2.6 J/mL. Thus, (7.7 kJ) / (2.6 kJ/L) ≅ 3 L of helium would be consumed to cool 100 g of copper from 293 to 4 K when using only the *latent heat of vaporization* of liquid helium: a profligate waste of helium!

On the other hand, if the full enthalpy of the helium *gas* warming from 4.2 K to room temperature is utilized, then much more cooling power is available. (That is, we use not just the heat of vaporization, but the cooling power of the cold *gas* as well.) The quantities of cryogen consumed when the entire enthalpy of the evaporated gas is utilized are tabulated in Appendix A1.6b for helium-, hydrogen-, and nitrogen-cooling of common structural materials: aluminum, copper, and stainless steel. From Appendix A1.6b we find that by using the full enthalpy of the helium gas, it would take only 0.08 L to cool the 100 g of copper, less than 1/30th the amount of liquid helium without gas cooling! The actual cryogen consumption will lie between these two extremes, depending on how the cryostat is cooled.

The cryogen consumption data given in Appendix A1.6b can be used to *estimate* the cost of cooling materials other than aluminum, copper, and stainless steel (for either the pessimistic case of latent heat only, or the optimistic case of fully utilizing the enthalpy of the evaporating gas). The Debye model is used to calculate the molar energy change of the new material relative to, say, copper, and the cryogen consumption values in the table are scaled accordingly.

Where possible, consumption of liquid helium can be significantly reduced by precooling a cryostat with liquid nitrogen before it is immersed in liquid helium. The latent heat of vaporization for nitrogen (161 J/mL, from Appendix A1.5) is 62 times greater than that of helium (2.59 J/mL). Liquid nitrogen is also cheaper and easier to handle.

For cryocoolers, the relative cooling *times* of the sample cold-stage can be similarly estimated from the molar energy of the materials (as calculated above) and the cooling power of the refrigerator.

6.1.4 THERMAL DIFFUSIVITY

Aside from the amount of energy that needs to be extracted from a given cryostat part, the other factor that affects the cooling rate is the part's *thermal diffusivity*. The thermal diffusivity is the ratio of a material's thermal conductivity to its specific heat,

$$D_t \equiv \lambda/(\delta\, C_P). \qquad \text{Thermal diffusivity} \quad (6.3)$$

Here λ is the thermal conductivity, C_P is the specific heat at constant pressure, and δ is the mass density of the material. Diffusivity has units of (m^2/s); that is, [W/(m K)] [kg/m^3]$^{-1}$ [J/(kg K)]$^{-1}$ = [m^2/s]. If a material has a low thermal conductivity and a high specific heat, hence a low D_t, the material effectively insulates itself and requires long times for extracting heat from its core.

Figure 6.3 shows typical thermal diffusivities for a range of technical materials. As seen in the figure, the thermal diffusivity generally rises as temperature is lowered, because the specific

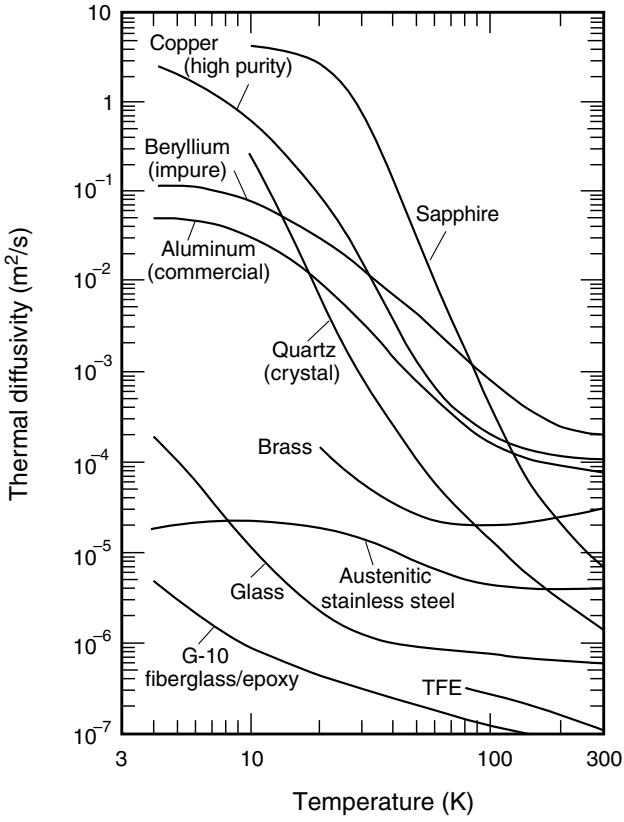

Fig. 6.3 Thermal diffusivity for selected technical materials (from Hust 1983 and calculated from the data in Appendixes A6.2 and A6.7). Although only a single curve is shown for high-purity copper (for clarity), this can be misleading because the thermal conductivity depends strongly on purity level (see Sec. 6.4.) The thermal diffusivity of additional materials can be calculated from Eq. (6.3) by using the data in Appendixes A6.2 and A6.7.

heat of most materials falls with temperature at a much greater rate ($\propto T^3$) than the low-temperature thermal conductivity ($\propto T$). The extreme rise in D_t for pure metals on cooling is attributed to their high electronic thermal conductivity. The values in Fig. 6.3 cover an enormous range, eight orders of magnitude.

A quantitative calculation of the cooling rates of materials immersed in a cryogen would involve many assumptions about heat transfer across solid–liquid interfaces, and D_t would have large variations that track the time-varying internal-temperature profile of the part. For most cryostat designs, it is probably not worth the effort, but the diffusivity values in Fig. 6.3 are quite useful for *comparisons* among materials.

For example, when selecting structural materials, we see from Fig. 6.3 that the thermal diffusivity of stainless steel is about two orders of magnitude higher than that of G-10 fiberglass–epoxy composites over most of the cryogenic temperature range. Thus, stainless-steel structural tubes can be cooled much more quickly than glass/resin tubes. The higher thermal diffusivity of stainless steel results from its thermal conductivity being higher than that of G-10 (see Sec. 6.4) and its specific heat lower (see stainless steel vs. glass/resin in Fig. 6.1). Also, stainless-steel structural

tubing has the added advantage over glass/resin composite tubes that it is quite robust and therefore is readily available in thin tubing-wall thicknesses (as thin as ~0.1 mm) with much less mass to cool.

6.2 Thermal expansion/contraction

6.2.1 DESIGN DATA AND MATERIALS SELECTION—GREAT DIFFERENCES AMONG RESINS, METALS, AND GLASSES

Thermal expansion/contraction is one of the more critical material parameters in the design of *cryogenic* apparatus. The entire apparatus will shrink on cooling, and any opposing structural supports or coaxial-cable components made of different materials can become highly stressed. Vacuum leaks may open. Drive trains can go limp. Dimensional tolerances of critical parts may be exceeded. Sample-holder contraction can stress samples, producing large unwanted changes in sample performance (Chapter 7). And the list goes on.

A general survey of Figs 6.4 through 6.7 shows that the length of materials changes the most at temperatures above ~50 K, whereas at lower temperatures, the thermal expansion curves flatten. So, if an apparatus survives cooling to liquid-nitrogen temperature, it should do fine when cooled further to liquid-helium temperature.

Handbook data for thermal expansion *near room temperature* are usually expressed conveniently in terms of the slope of the measured $\Delta L/L$ curve because of the linear dependence on temperature in this regime. The slope, or temperature coefficient of thermal expansion α, is defined by

$$\alpha \equiv (1/L)\, \mathrm{d}L/\mathrm{d}T. \quad \text{Temperature coefficient of thermal expansion} \tag{6.4}$$

Room-temperature values of α are given for many common elements in Appendix A6.1.

Although α is a convenient form for thermal expansion near room temperature, it becomes less useful at lower temperatures where the thermal expansion becomes nonlinear (approaching a constant length approximately as T^4 in metals and alloys). Thus, for cryogenic design, values of the *total thermal linear expansion* $\Delta L/L \equiv (L_{\mathrm{T}} - L_{293})/L_{293}$ are usually more useful. Figures 6.4 though 6.9 and Appendix A6.4 give data of $\Delta L/L$ as a function of temperature for common technical materials. Polymer resins and epoxies contract the most on cooling; metals and alloys are next; and "invars," glasses, and ceramics contract the least. Below, we consider each group of materials in turn.

Figures 6.4 through 6.7 show that for most materials their linear thermal expansion $\Delta L/L \equiv (L_{\mathrm{T}} - L_{293})/L_{293}$ varies with temperature linearly near room temperature, whereas at low temperatures the length change approaches zero (approximately as T^4 in metals and alloys). Most of the change in length occurs at temperatures above ~50 K.

Polymer resins: Polymer resins are commonly used in cryostats for the protective sleeving of cryostat wire bundles, coaxial-cable dielectrics, and epoxy bonds and seals. These materials

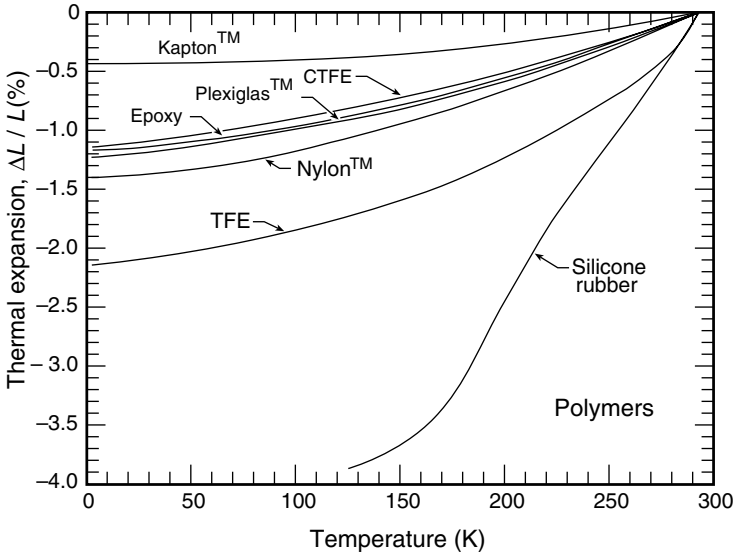

Fig. 6.4 Thermal linear expansion $\Delta L/L \equiv (L_T - L_{293})/L_{293}$ of common polymers (TFE = tetrafluoroethylene, Teflon™; CTFE = polychlorotrifluoroethylene, a type of Teflon™). (Data are from Clark 1983, Kirby 1956, Corruccini and Gniewek 1961, Laquer and Head 1952, and Radebaugh 2002.) Tabulated values of $\Delta L/L$ for these and other materials are given in Appendix A6.4.

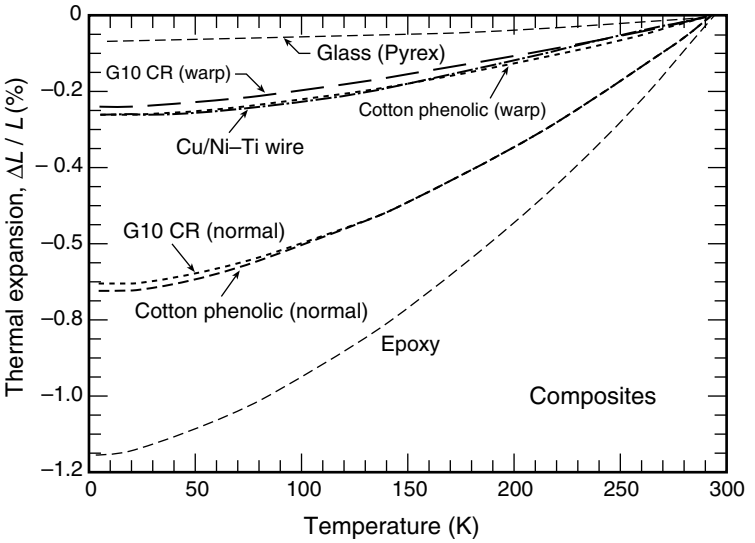

Fig. 6.5 Thermal linear expansion $\Delta L/L \equiv (L_T - L_{293})/L_{293}$ of selected composites, plus individual epoxy and glass components. [For glass–epoxy composites, G-10CR (*warp*) indicates the expansion along the glass–fiber direction, whereas G-10CR (*normal*) is transverse to the fiber direction.] (Compiled by Clark 1983 from data by Dahlerup-Peterson and Perrot 1979, Clark et al. 1981, Clark 1968, and Laquer and Head 1952.) Tabulated values for these and other materials are given in Appendix A6.4.

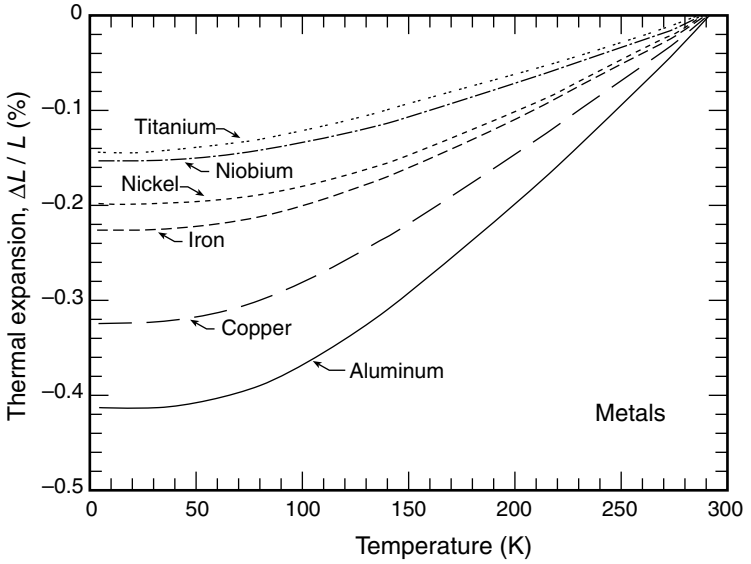

Fig. 6.6 Thermal linear expansion $\Delta L/L \equiv (L_T - L_{293})/L_{293}$ of common metals. (Compiled by Clark 1983 from data by Corruccini and Gniewek 1961, and Hahn 1970.) Tabulated values for these and other materials are given in Appendix A6.4.

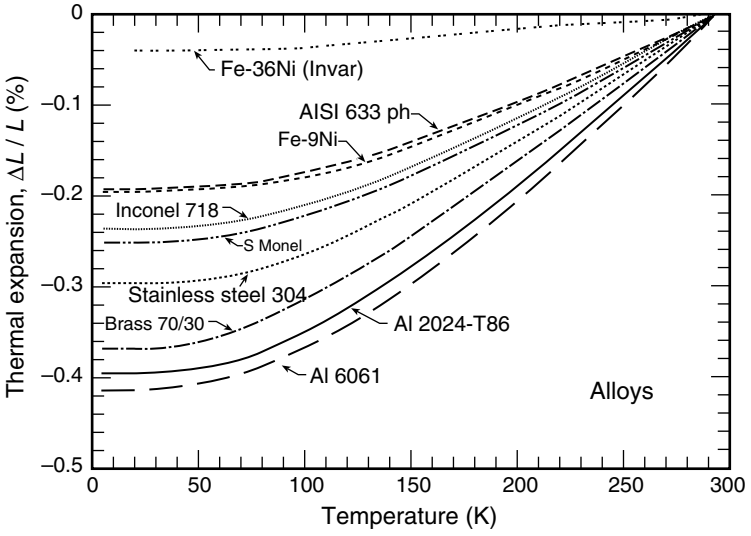

Fig. 6.7 Thermal linear expansion $\Delta L/L \equiv (L_T - L_{293})/L_{293}$ of common alloys. (Compiled by Clark 1983 from data by Clark 1968 and Arp et al. 1962.) Tabulated values for these and other materials are given in Appendix A6.4.

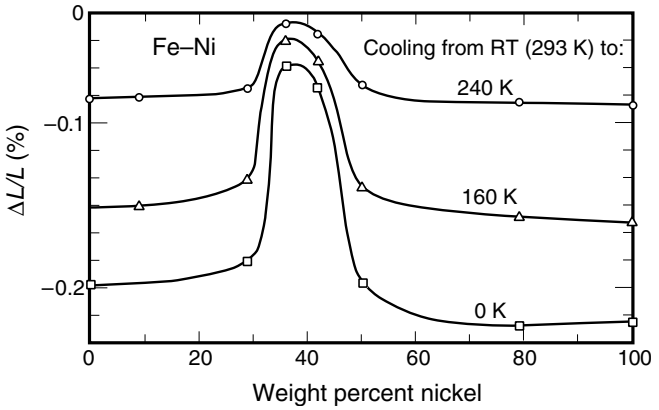

Fig. 6.8 Thermal expansion on cooling from room temperature for the Fe–Ni alloy system at different compositions, showing the "Invar" region near 36% Ni composition (from Clark 1968).

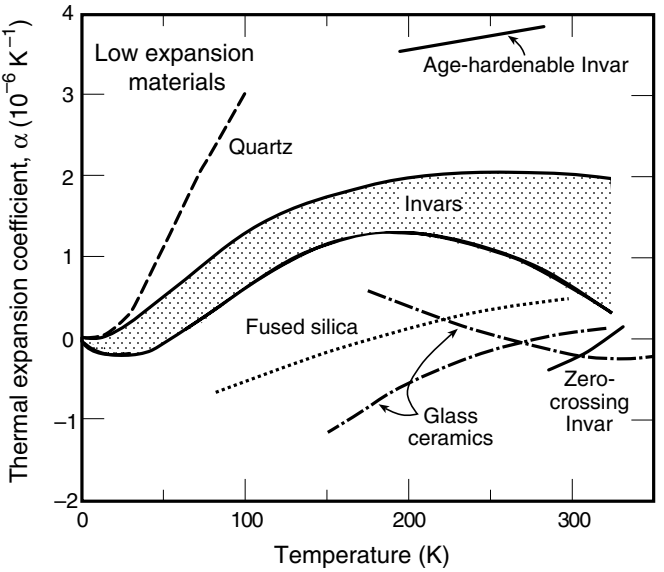

Fig. 6.9 Thermal expansion coefficient α as a function of temperature for low-expansion materials (from Clark 1983).

are made by linking together long chains or networks of smaller molecules. They can be either linked by a fairly *flexible* molecular structure into thermoplastics, such as fluorocarbons, vinyls, polyimides, polyethylenes, polycarbonates, or acrylics; or they can be joined by a fairly *rigid* molecular structure into thermosetting plastics such as epoxies, phenolics, polyesters, urethanes, or silicones. Therefore, the thermal linear expansion of polymers, shown in Fig. 6.4, varies over quite a range and has a wide spread in anisotropy, depending on the nature of the linking bonds. Fortunately, for any one epoxy system, different types and amounts of catalyst do not produce large differences in thermal expansion.

Polymers can also have a "glass" transition temperature T_g where they transform from an amorphous state at higher temperatures to a partially crystalline structure at low temperatures

that occupies a much smaller volume. This usually has dramatic effects on the thermal contraction, which is greatly enhanced as the material passes through T_g. An example is silicone rubber, which Fig. 6.4 shows is one of the all-time champions for contraction (and surprises).

Composites: As the name implies, composites are made by combining different materials together into a common structure. For cryostat structural materials, they often consist of strong reinforcing fibers in a matrix, such as glass fibers in epoxy, or boron fibers in aluminum. This makes for some highly anisotropic thermal-expansion properties. Actually, the thermal linear expansion of composites in cryostat design is relatively easy to understand: along the reinforcing fiber the expansion is dominated by the thermal expansion of the fiber, whereas perpendicular to the fibers, the thermal expansion takes on the character of the matrix material. Typically, the thermal expansion transverse to the fibers is two to five times larger than that along the fiber direction. This, of course, depends on the matrix material, the type of reinforcement, and the volume fraction of reinforcing fibers.

For example, as shown in Fig. 6.5, fiberglass-reinforced epoxy G-10CR (or G-10, or G11, not shown) has a thermal contraction along the fiber direction on cool-down to 4 K of about 0.25% (since it is dominated by glass in that direction), whereas transverse to the plane of the cloth, it is about 0.7% (since there are no glass fibers in this direction to oppose the large thermal contraction of the epoxy). Thus, in machining a G-10 sample holder, make sure the glass fibers run in the direction you want. For cylindrical G-10 tubes, the circumferential contraction becomes quite interesting, since it is the result of competing radial and circumferential forces, and the net result depends strongly on the thickness of the tubing wall (Sec. 7.3.2).

Filled composites are usually designed not for mechanical strength, but to achieve some other special property. For example, epoxy is sometimes filled with glass powder to reduce its thermal contraction. In other cases, fillers are added to raise the specific heat or to enhance the thermal conductivity of a base material. Filled composites differ from fiber-reinforced composites in that they have no preferred orientation or structure. The thermal expansion is usually isotropic and changes smoothly with the changing volume fraction of filler.

Pure Metals: Metals in their nearly pure form are most commonly used in cryostats for sample holders and electrical wiring (because their thermal and electrical conductivities are high). The spread of thermal expansion values for pure metals is relatively large because of their differing crystal structures. Data are given in Fig. 6.6 for common metals with cubic symmetry, plus polycrystalline titanium.

➔ A quick method for estimating the total thermal contraction of metals between room temperature and 4 K (or any temperature below about 50 K, for that matter) is the observation that

$$\Delta L/L\big|_{4\,\mathrm{K}}^{293\,\mathrm{K}}(\%) = \alpha_{293\,\mathrm{K}}\,(185\,\mathrm{K} \pm 15\,\mathrm{K})\;100,$$

where the $\pm$ value indicates the standard deviation of 85 metals and alloys (Clark 1983). The predictive accuracy of this expression is good enough for most engineering design and permits $\Delta L/L$ to be estimated for many metals simply by using the *room-temperature* coefficients of thermal expansion given in Appendix A6.1. The success of this method results from the validity of the Grüneisen relation (described below) and the Debye

model for most metals. However, it does not apply to Invar-type iron alloys (see below) and other materials having very low expansion.

Noncubic transition metals usually have thermal contraction coefficients that are highly anisotropic. For those with axial symmetry (tetragonal, hexagonal, or rhombohedral), the thermal contraction is described by two principal coefficients: α_c parallel to the symmetry axis, and α_a perpendicular to the axis. For metals such as zinc, the anisotropy is very large: $\alpha_c/\alpha_a = 9.5$. Other noncubic transition metals, however, are much less anisotropic: examples are zirconium, $\alpha_c/\alpha_a = 1.3$, and magnesium, with the lowest anisotropy $\alpha_c/\alpha_a = 1.07$. For polycrystalline materials, the observed α is given approximately by an average $\alpha = (2\alpha_a + \alpha_c)/3$.

Metallic alloys: These materials are most commonly used as structural members in cryostat construction. Generally, the thermal expansion of alloys is quite stable with compositional changes. A large change in composition of 10–20% is required to produce a significant (5%) change in the coefficient of thermal expansion. Also, the thermal treatment or mechanical condition of an alloy does not have a large effect on its thermal expansion, except for a few materials that precipitation-harden or undergo a crystalline structural change on cooling (Clark 1968). Thermal expansion data are shown for common alloys in Fig. 6.7.

One important exception to the "well behaved" properties of alloys is illustrated by the Fe–Ni system near the 36% Ni composition where the thermal contraction approaches zero, as shown in Fig. 6.8. This exception is caused by a crystal phase change from body-centered-cubic to face-centered-cubic. The low value of thermal contraction results from a balance between a lattice contribution and a magnetic one of opposite sign. Because of the (designed) invariance of length with temperature, this alloy composition was named *Invar*. Invar is commonly used in the production of glass-to-metal seals, since a seal made with most common metals would crack on cooling from the large mismatch in expansion for the two types of materials.

Glasses and ceramics: Glasses and ceramics have very low thermal expansion, as shown by the plot of thermal expansion coefficients in Fig. 6.9. (This graph shows the temperature coefficient of thermal contraction instead of the total change in length $\Delta L/L$, because the length changes are small, and sometimes they have a negative slope.) Because their thermal expansion is so low, glasses and ceramics are used extensively for optical components like mirrors and lenses that require extreme dimensional stability with changing temperature. They are also commonly used as electrical insulators.

Glasses are disordered structures that usually consist of a mixture of oxides bonded into a network. Among pure glasses and ceramics, quartz and fused silica have the lowest thermal expansion. By adding impurities, however, glasses can have their thermal expansion coefficients balanced to near zero or even made negative. The impurity ions are inserted into the open spaces of the network, which alters the nature of the bonds (White 1976).

6.2.2 ESTIMATING THERMAL EXPANSION BETWEEN ARBITRARY TEMPERATURES

In most materials without crystal-phase changes, the temperature dependence of the coefficient of thermal expansion α tracks that of the specific heat (either C_P or C_V, since they are nearly the same, for practical purposes). This was originally observed by Grüneisen, who

found that the ratio α/C_V *is nearly constant* at temperatures above $\theta_D/5$ for any given material; that is, $\alpha/C_V \equiv \gamma$, where γ is related to the Grüneisen parameter.

The corresponding temperature dependence of the two properties makes sense because crystal-lattice vibrations, which are the main mechanism for energy storage in solids, also give rise to thermal expansion. So, when data on the thermal expansion coefficient are not available, a reasonable estimate of α can be made using the temperature dependence of the Debye function for C_V. The total length change $\Delta L/L$ over an arbitrary temperature interval from T_1 to T_2 can then be evaluated from the heat-capacity integral (shown in Fig. 6.2). That is,

$$\Delta L/L\,|_{T1}^{T2} = \int_{T1}^{T2} \alpha \mathrm{d}T \approx \gamma \int_{T1}^{T2} C_V\,\mathrm{d}T = \gamma\left[\int_0^{T2} C_V\,\mathrm{d}T - \int_0^{T1} C_V\,\mathrm{d}T\right]. \tag{6.5}$$

Values of γ are most easily determined from room-temperature handbook data. Since the Debye function for C_V varies as T^3 at low temperatures, it follows from Eq. (6.5) that $\Delta L/L$ will vary approximately as T^4 at cryogenic temperatures. An example that uses Eq. (6.5) to estimate $\Delta L/L$ between any two arbitrary temperatures follows.

Example: Suppose we want to estimate the thermal contraction of a piece of copper when it is cooled from room temperature to 50 K, knowing only the *room-temperature* handbook values $\alpha = 16.5 \times 10^{-6}\ \mathrm{K}^{-1}$ and $C_V = 24$ J/(mol K) (from Appendix A6.1).

By using the same procedure described in the preceding section on specific heat, we first determine $\int_0^T C_V\,\mathrm{d}T$. That is, we find for copper that at 293 K, $T/\theta_D = 0.95$ ($\theta_D = 310$ K from Appendix A6.1), and thus (from Appendix A6.3)

$$\int_0^{293\,\mathrm{K}} C_V\,\mathrm{d}T = (293\ \mathrm{K})\left[16.5\ \mathrm{J/(mol\ K)}\right] = 4.83\ \mathrm{kJ/mol},$$

whereas at 50 K, where $T/\theta_D = 0.16$,

$$\int_0^{50\,\mathrm{K}} C_V\,\mathrm{d}T = (50\ \mathrm{K})\left[1.8\ \mathrm{J/(mol\ K)}\right] = 0.09\ \mathrm{kJ/mol}.$$

We can determine γ from the room-temperature value of the ratio α/C_V. Thus, we find from Eq. (6.5) that

$$\begin{aligned}\Delta L/L &\cong (16.5 \times 10^{-6}\ \mathrm{K}^{-1})(24\ \mathrm{J/mol\ K})^{-1}(4.83 \times 10^3\ \mathrm{J/mol} - 0.09 \times 10^3\ \mathrm{J/mol}) \\ &= 3.3 \times 10^{-3}.\end{aligned}$$

The measured value is 3.2×10^{-3}, in quite close agreement with the estimated value.

6.2.3 CALCULATING THERMAL STRESSES

Stress can build very quickly when cooling rigidly constrained members. To determine the stress generated on a part by thermal contraction, the basic principle is to equate any change in volume with the forces needed to return the material to its original shape. For example, with a simple rod constrained at both ends, a change in temperature ΔT would result in a change in length $\Delta L/L = \overline{\alpha}\Delta T$, where $\overline{\alpha}$ is the average coefficient of thermal contraction over the temperature

interval ΔT. The same change in length can be obtained by a tensile stress, $\sigma_{\text{tension}} = E\,(\Delta L/L)$, where E is the Young's modulus of elasticity. (Here we have assumed that the tensile stress is less than the yield strength of the material and thus it has not been deformed plastically; see Sec. 6.6.1.) Equating the two length changes gives a very simple expression for estimating the thermal stress experienced by the rod,

$$\sigma_{\text{tension}} = E\bar{\alpha}\Delta T. \quad \text{Thermal stress}$$

We see that the thermal stress is independent of the diameter of the rod or its length between constraints.

Thermal stresses developed from cooling have been extensively calculated for many other common shapes subject to various constraints. The stress in each case is essentially a variant of the basic equation above for a simple rod. The results of these calculations have been compiled by Roark and Young (1975), and a summary of the most useful relations is given by Clark (1983).

6.3 Electrical resistivity

6.3.1 DESIGN DATA AND MATERIALS SELECTION: DEPENDENCE OF ELECTRICAL RESISTIVITY ON TEMPERATURE AND PURITY

In this section, we delve a little deeper into the underlying physics of charge conduction in order to understand its temperature dependence and to develop a practical technique for estimating electrical resistivity, because it is so highly variable in commonly used pure metals at low temperatures. The relations considered here are also useful for estimating thermal conduction (Sec. 6.4), a quantity that is not only highly variable at cryogenic temperatures but more difficult to measure.

Electric charge is transported through metals by energetic electrons, whose freedom to move within the crystal lattice of a solid can be described at a fundamental level by a collective wave model (Ziman 1960). It is useful, however, to simplify this picture and understand the temperature dependence of the electrical resistivity (and heat conduction in the next section) in terms of "free" electrons by using the elementary kinetic theory of transport in metals. In this model (see, for example, Rosenberg 1988 or Ziman 1960), the electrical conductivity σ_e ($\equiv 1/\rho$, where ρ is the electrical resistivity) is given by

$$\sigma_e = Ne^2 l/(m\bar{\nu}), \quad \text{Electrical conductivity from kinetic theory} \tag{6.6}$$

where N is the number of conduction electrons per unit volume, e is the charge carried by an electron, m is the mass of an electron, $\bar{\nu}$ is the average velocity of the conduction electrons, and

l is the average distance (the mean free path) the electron travels before being scattered by an atomic-lattice perturbation.

The electrical conductivity of free electrons in a solid, where the electrons constitute a so-called "Fermi gas," is much smaller than the conductivity of a classical gas of similar density with the same scattering sites and charge, because the average electron velocity in solids [which appears as $\bar{\nu}$ in the denominator of Eq. (6.6)] is very high. The velocity (the Fermi velocity) is equivalent in thermal terms to a temperature greater than 20 000 K! (Ashcroft and Mermin 1976). This high velocity simplifies our understanding of the temperature dependence of the resistivity of a metal; in Eq. (6.6), N, e, and m are all constants, and since $\bar{\nu}$ is very high, it is also effectively not influenced by the thermal energy. This leaves the mean free path l of the electrons between collisions as the *primary factor determining the temperature dependence of the electrical conductivity*.

The mean free path is dominated by two distinctly different scattering mechanisms:

1. At *high* temperature, l is dominated by electron scattering from *thermal vibrations* (phonons) of the crystal lattice and, therefore, is strongly temperature-dependent. This determines the *ideal resistivity* of a metal $\rho_i(T)$ (Sec. 6.3.3).
2. At *low* temperatures (where the phonons are frozen out), l is limited mainly by electron scattering off chemical or physical crystal-lattice *imperfections* (impurities, vacancies, interstitials) and, therefore, is independent of temperature. This determines the *residual resistivity* ρ_{res} (Sec. 6.3.2).

The near constancy of the electrical resistivity is evident at low temperatures in Figs 6.10 and 6.11, where the resistivity approaches its residual value ρ_{res}, depending on the purity grade of the material. The higher a material's purity, the lower the value of ρ_{res} (and the lower the temperature where its resistivity becomes constant). We see from these example plots that for *nearly pure* metals, handbook values do not work. That is, we cannot simply look up the electrical resistivity of nearly pure metals since the resistivity is strongly dependent on the particular trace impurity levels in each sample.

6.3.2 RESIDUAL RESISTIVITY ρ_{res} AND DEFECT SCATTERING

Copper is a popular material for current leads and instrumentation wiring because of its relatively high electrical conductivity, low cost, and availability. (Silver is actually a better room-temperature conductor, but its cost is usually prohibitive). At low temperatures ($\lesssim$77 K), sample purity becomes the single most important practical factor in obtaining low resistivity, as shown for different grades of annealed copper and aluminum in Figs 6.10 and 6.11. Although aluminum has a higher room-temperature resistivity than copper, at liquid-helium temperatures, aluminum is a more cost-effective conductor than copper for high-current leads (ignoring strength and solder connection problems for the moment), because it is available in higher purity at lower cost.

The residual resistivity ρ_{res} of these conducting materials depends strongly on the amount of atomic-lattice defects in the material, determined by cold work from rolling and forming

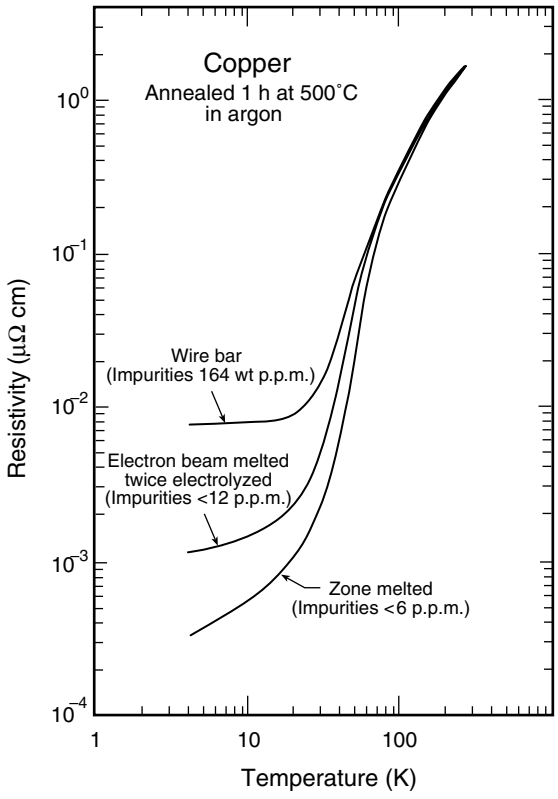

Fig. 6.10 Electrical resistivity of copper as a function of impurity content (p.p.m. ≡ parts per million). (Adapted from Goodall 1970 and Pawlek and Rogalla 1963.) Tabulated values are given for pure copper and OFHC copper in Appendix A6.5a.

(which introduces crystalline vacancies and dislocations), and heat treatments (which counter cold work by annealing out cold-work vacancies and dislocations). It also depends on the level of chemical impurities. Sometimes Nordheim's rule is useful in estimating the dependence of ρ_{res} on impurity concentration c (e.g. White 1976):

$$\rho_{res} = a\, c\, (1-c), \quad \text{Nordheim's rule} \tag{6.7}$$

where a is a proportionality constant that varies with impurity and the parent material. Equation (6.7) predicts that when the impurity concentration c is small, ρ_{res} varies approximately linearly with concentration. Thus, in nearly pure materials, only trace amounts of impurities can change c and ρ_{res} by orders of magnitude.

In practice, there are so many combinations of type and number of impurity and solute atoms, cold work, and heat treatments, that the best way to know the residual resistivity of a given material is just to measure it. The simplest method is to make a single, fixed-temperature resistivity measurement of a wire-shaped sample of the material immersed in liquid helium (described in Sec. 6.3.4).

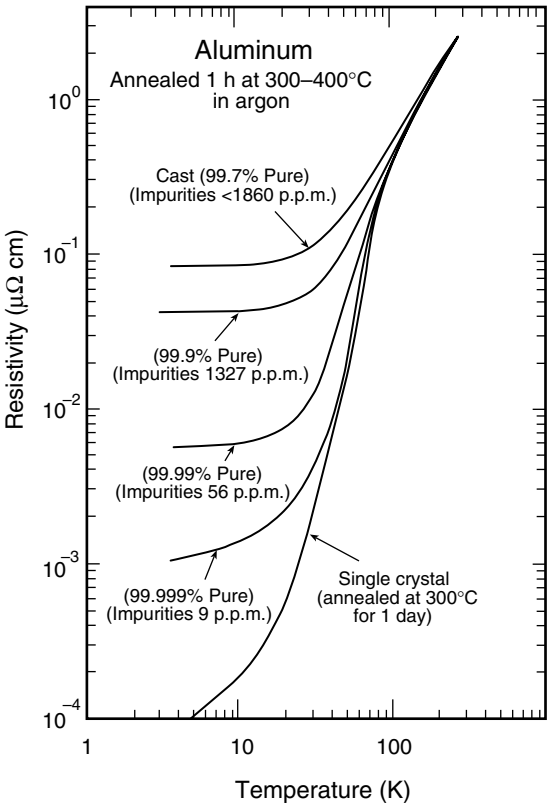

Fig. 6.11 Electrical resistivity of aluminum as a function of impurity content (p.p.m. ≡ parts per million). (Adapted from Goodall 1970, Pawlek and Rogalla 1963, and Aleksandrov and D'yakov 1963.)

6.3.3 IDEAL RESISTIVITY $\rho_i(T)$ AND PHONON SCATTERING

In contrast to the extremely variable, defect-determined ρ_{res}, the contribution of *thermal* vibrations (phonons) to the resistivity at high temperatures is a unique property of each element's crystal structure, and, therefore, it is designated as the *ideal* or *intrinsic* resistivity of a metal $\rho_i(T)$ because it is the resistivity we would measure in ideally pure (defect-free) samples. As an intrinsic characteristic, it does not depend (to first order) on how the particular sample has been fabricated, treated, or its impurity content. Values of $\rho_i(T)$ are shown for a number of "ideally pure" metals in Fig. 6.12 and tabulated in Appendix A6.5a.

We briefly consider the physical nature of the ideal resistivity to show the great variety of temperature dependences that are possible for $\rho_i(T)$ as well as to clarify the limitations of the Bloch–Grüneisen formula, which is sometimes given in textbooks to represent $\rho_i(T)$. From Eq. (6.6), we showed that the temperature dependence of $\rho_i(T)$ is determined mainly by the temperature dependence of the electronic mean free path l in a material. Unlike isotropic defect scattering, the temperature dependence of l from phonon scattering is strongly affected by the scattering *angle* between the colliding electron and phonon. This effect becomes increasingly important as temperature is lowered and is highly dependent on crystal structure,

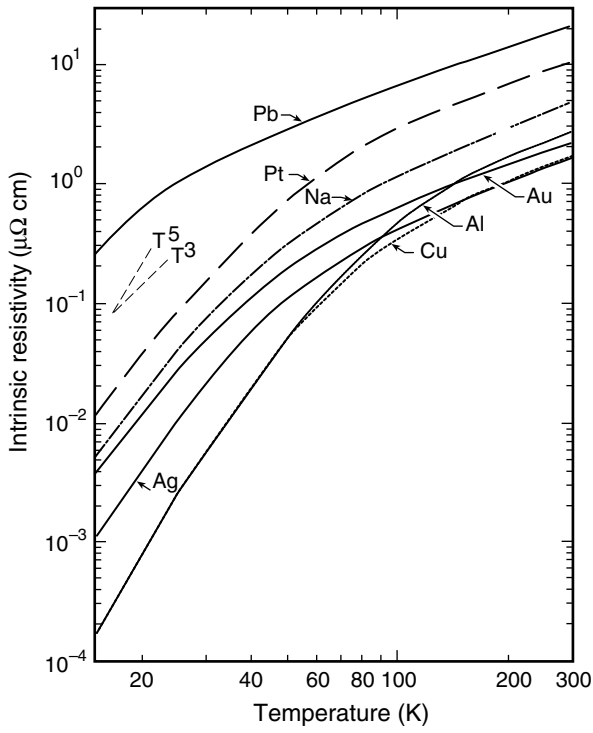

Fig. 6.12 Electrical resistivity of *ideally* pure elements at low temperature (from White 1987, p. 319). Appendix A6.5a gives tabulated values for these and additional pure metals.

making the calculation of $\rho_i(T)$ complex. Usually, simplifying assumptions are made that result in the famous Bloch–Grüneisen formula.

Bloch–Grüneisen formula: it does not work

The Bloch–Grüneisen expression for the ideal (phonon-generated) electrical resistivity can be expressed as (Bloch 1930; Ziman 1960)

$$\rho_i(T) \propto (T/\theta_D)^5 \int_0^{\theta_D/T} x^5 \,(e^x - 1)^{-1}\,(1 - e^{-x})^{-1}\,\mathrm{d}x. \tag{6.8}$$

At high temperatures, Eq. (6.8) gives a linear dependence of $\rho_i(T)$ on T, in fairly good agreement with measurements, and at low temperatures it transforms smoothly into a T^5 dependence. Whereas the Debye formula of Eq. (6.1) works surprisingly well for specific heat, the same cannot be said for the Bloch–Grüneisen formula of Eq. (6.8) for electrical resistivity.

The "fairly good" agreement between experimental values and the Bloch–Grüneisen formula often noted in textbooks results from presenting experimental data on a steep curve of ρ vs. T, where the difference between a T^3 and a T^5 dependence, for example, looks rather small

(see the inset in Fig. 6.12). But try plotting the measured ideal resistivity of metals over the cryogenic temperature range on a normalized graph of ρ/T^5 vs. T; the gross discrepancy in temperature dependence cannot be ignored. Sometimes Eq. (6.8) is artificially forced to fit resistivity data by defining an *effective* Debye temperature, but this is of small consequence since the effective temperature is extremely temperature dependent, varying by 50–80%, depending on the material.

The Bloch–Grüneisen formula actually describes quite accurately the *normal* scattering of electrons from phonons, but it makes the unjustified assumption of ignoring *umklapp* phonon scattering processes (sometimes called U-processes) described below. (This simplification was made mainly because umklapp scattering could not be treated quantitatively before the advent of computer numerical integration techniques.) Although not known at the time, the resistivity contribution from umklapp processes is actually many times greater than that from normal processes, even at room temperature and above.

Umklapp scattering

Umklapp (German for "flip over") scattering is an event where an electron is scattered not only by a phonon, but the metal's entire crystal lattice enters into the scattering process (more information is available in the further reading suggested in Sec. 6.7.1). Umklapp scattering is thus very powerful in changing the angle or direction of the velocity of an electron, which makes these scattering events far more effective than normal-phonon scattering in generating electrical resistance.

Unfortunately, umklapp processes do not have a simple *analytic* temperature dependence like normal processes; instead, they depend strongly on the crystal structure and phonon properties of each material. However, they can be accurately calculated by using the *numerical variational methods* described in the references of Sec. 6.7.1. For example, we find that in alkali metals, the umklapp processes freeze out at very low temperatures ($\lesssim$2 K), and then the temperature dependence becomes exponential, in very good agreement with measurements both in temperature dependence and absolute value (Ekin 1971). In metals such as aluminum, on the other hand, the temperature dependence from umklapp scattering is between T^3 and T^4 in the cryogenic temperature range (Lawrence and Wilkins 1972). The important point is that neither the temperature dependence nor the magnitude of the electrical resistivity can be represented by Eq. (6.8), even approximately, because it does not include the dominant effects of umklapp scattering. On the other hand, first principle's calculations of umklapp processes can determine the ideal resistivity $\rho_i(T)$ quite well when sufficient information is available on the phonon characteristics of a material.

From a practical standpoint, however, modeling each element's crystal structure and phonon band structure to evaluate the contribution of umklapp scattering is very time consuming and difficult. The net result is that there are no simple rules or temperature dependences to describe $\rho_i(T)$, and so, in practice, we use measured *handbook* values for $\rho_i(T)$. Fortunately, these are fairly accurate and universal because, as we have seen, $\rho_i(T)$ is uniquely determined by the fundamental properties of the metal's crystal structure.

6.3.4 MATTHIESSEN'S RULE—A SIMPLE METHOD OF ESTIMATING THE TOTAL ELECTRICAL RESISTIVITY OF NEARLY PURE METALS AT ARBITRARY TEMPERATURES

So how do we combine the defect and phonon contributions to the electrical resistivity? Fortunately, nature has been kind to us, and, to a reasonable approximation, the *total* electrical resistivity ρ is simply the sum of the resistivity contributions from defect scattering ρ_{res} and thermal vibrations $\rho_i(T)$:

$$\rho(T) \cong \rho_{res} + \rho_i(T). \quad \text{Matthiessen's rule} \tag{6.9}$$

Equation (6.9) is known as *Matthiessen's rule* (Matthiessen 1862). It says, in effect, that to a good approximation, the level of ρ_{res} does not affect $\rho_i(T)$, and vice versa. The two are simply additive.

The residual resistivity ρ_{res} is usually measured by mounting a sample of the material on a dipper probe such as that shown in Fig. 1.6. After measuring the sample's resistance at room temperature R_{RT}, the sample is dipped into a liquid-helium storage dewar, where it is remeasured to give $R_{4\,K}$. (For superconductors, the measurement is more complex and has to be carried out in a magnetic field high enough to suppress superconductivity or with a variable-temperature probe just above the critical temperature.) The results are usually expressed in terms of the material's *residual resistance ratio* (RRR):

$$\text{RRR} \equiv R_{RT}/R_{4\,K} = \rho_{RT}/\rho_{4\,K}. \quad \text{Residual resistance ratio} \tag{6.10}$$

The RRR is the preferred form of expressing these data because, unlike $\rho_{4\,K}$, it is a ratio that is easily determined without having to measure the test sample's length L and cross-sectional area A to determine ρ ($\equiv RA/L$).

Once the RRR of a sample has been measured, ρ_{res} can be determined by making the usually good assumption that $\rho_{res} \cong \rho_{4\,K}$, since there is typically little temperature variation below 4 K. Substituting Matthiessen's rule into Eq. (6.10), we obtain

$$\text{RRR} = (\rho_{i\,RT} + \rho_{res})/\rho_{res},$$

and therefore

$$\rho_{res} = \rho_{i\,RT}/(\text{RRR} - 1). \tag{6.11}$$

Thus, with Eq. (6.9) we can easily determine the approximate *total* resistivity of a sample of any purity over the *entire* cryogenic temperature range simply by combining handbook tabulations of $\rho_i(T)$ with our measured 4.2 K value of ρ_{res}. To save time, we can also estimate ρ_{res}

by using Eq. (6.11) with nominal values of RRR, which are tabulated for a number of common conductor materials in Appendix A4.3.

Example: Suppose we have a piece of copper wire, #36 gauge AWG (~0.125 mm) and 10 cm long. We wish to use it in an application where we need to know its approximate resistance at 50 K.

To determine ρ_{res}, we would mount a test sample of the wire on a dipper probe and measure its RRR. However, suppose for this purpose a rough estimate will suffice and so we use a typical RRR value of 110 for common copper wire from Appendix A4.3. From Eq. (6.11) we then find

$$\rho_{res} \cong \rho_{i\,RT}/(\text{RRR} - 1) = (1.69\ \mu\Omega\,\text{cm})/(110 - 1) \cong 15\ \text{n}\Omega\,\text{cm},$$

where we have obtained the handbook value of the ideal resistivity for copper at room temperature $\rho_{i\,RT}$ from either Appendix A6.1 or Appendix A6.5a. Then using Matthiessen's rule we find that, at 50 K, the total resistivity of the copper wire is about

$$\rho_{50\,K} \cong \rho_{res} + \rho_{i\,50\,K} = 15 + 49 = 64\ \text{n}\Omega\,\text{cm},$$

where $\rho_{i\,50\,K}$ was obtained from the handbook value for ideally pure copper in Appendix A6.5a.

Thus, the resistance of a 10 cm length of #36 gauge copper wire is about

$$R_{50\,K} = \rho_{50\,K} L/A$$
$$\cong (64\ \text{n}\Omega\,\text{cm})(10\ \text{cm})/(0.0127) \times 10^{-2}\text{cm}^2) = 5.0\ \text{m}\Omega,$$

where the cross-sectional area for #36 AWG (~0.125 mm) wire is given in Appendix A4.1a.

The same procedure could be used for any temperature and any arbitrary metal sample, so long as we have access to handbook values for its ideal resistivity and a single helium dip-test measurement to determine its RRR value.

This procedure, of course, assumes the validity of Matthiessen's rule, Eq. (6.9). In actual practice, deviations from this rule occur, as seen in the above example where the electrical resistivity underestimates the 84 nΩ cm actually measured at 50 K for a copper sample with RRR $\cong$ 100 (from Appendix A6.5a). The deviations occur because the scattering of electrons by impurity defects is usually *isotropic*, whereas umklapp scattering is *anisotropic* (occurring preferentially along high-symmetry directions of the crystal lattice). Umklapp and impurity scattering thus affect each other to second order as they "fight" over the *shape* of the Fermi surface (and the winner changes as their dominant roles change with temperature, which gives rise to the deviations) (Ekin and Bringer 1973). However, for most practical cases, Matthiessen's rule gives a reasonable approximation, and it serves as a great time-saving tool for estimating the highly variable total resistivity of nearly pure metals.

6.3.5 SUMMARY OF IMPORTANT POINTS FOR NORMAL METALS

- The electrical resistivity of metals arises from the scattering of electrons off perturbations in the atomic crystal lattice of the metal. These perturbations can be caused either by thermal vibration of the atoms in the crystal lattice (*phonons*), or by chemical and physical crystalline defects (*impurity atoms, vacancies, and dislocations*).
- At high temperatures, phonon scattering dominates the resistivity, giving rise to a temperature-dependent *ideal* resistivity $\rho_i(T)$, which is strongly dominated by *umklapp* scattering

of electrons off phonons. Thus, the ideal resistivity $\rho_i(T)$ is a unique complex characteristic for each metal. Although it can be calculated with numerical methods, it is more practical to determine $\rho_i(T)$ from handbook values tabulated from measurements of the metallic elements, given in Appendix A6.5a.

- At low temperatures, phonons are frozen out, leaving chemical and physical defects (such as cold-work dislocations) as the dominant scattering mechanism determining the resistivity. This *residual* resistivity ρ_{res} is *independent of temperature*, but highly dependent on a particular material's purity and annealing condition. Thus, it cannot be looked up in a handbook, but it is easily measured for any particular sample by a single fixed-temperature dip test in liquid helium.
- The total resistivity of *nearly pure* metals $\rho(T)$ is highly variable, but can be approximated by simply summing these two components: $\rho(T) \cong \rho_{res} + \rho_i(T)$, known as *Matthiessen's rule*. Figures 6.10 and 6.11 show examples of the family of experimentally measured curves obtained for various samples of copper and aluminum having different purities. The example calculation given above is a useful way of estimating the electrical resistivity of nearly pure metals at any temperature.
- For metal *alloys*, unlike nearly pure metals, handbook values can be used to give meaningful values of the total resistivity, since defect scattering is so dominant and not highly variable among samples of a given commercial alloy composition. Tabulations of the *total* resistivity for common metal alloys are given in Appendix A6.5b.

6.3.6 SUPERCONDUCTORS

Superconductors are a special class of electrical conductors that have their own set of characteristics distinct from normal conductors. The most commonly measured superconductor property, the critical current, is an *extrinsic* property, which cannot be found in a handbook. It has to be measured on a sample-by-sample basis. Techniques for this measurement are given some emphasis in the description of sample holders and contacts in Part II and are the detailed subject of Part III.

Superconductors also have *intrinsic* characteristics (critical temperature, critical field, magnetic-field penetration depth, and coherence length), which are nearly constant from sample to sample. The intrinsic characteristics of practical *high-field* superconducting alloys and compounds are tabulated in Appendix A6.6. Critical temperatures for superconducting *elements* are listed with the general tabulation of elemental properties in Appendix A6.1.

6.4 **Thermal conductivity**

6.4.1 DESIGN DATA AND MATERIALS SELECTION

As discussed in Chapter 2, the foundation of cryogenic apparatus construction is heat transfer, and the key material property of heat-transfer analysis is thermal conductivity. Figure 2.1 is reproduced here as Fig. 6.13 for convenience; it shows the thermal conductivity for a wide variety of materials commonly used in cryostat construction. Unlike the case for *electrical*

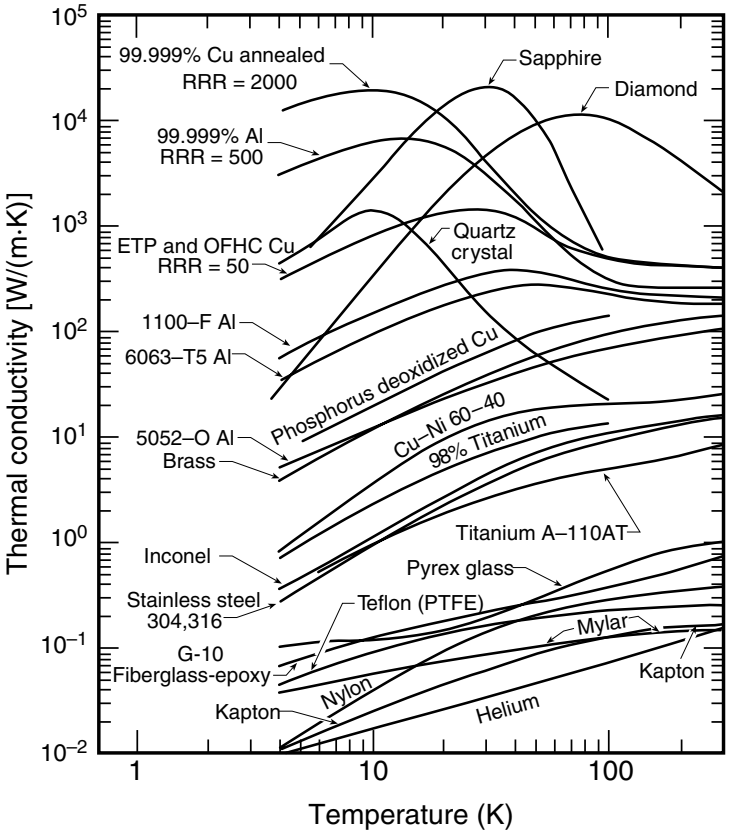

Fig. 6.13 Thermal conductivity of solids as a function of temperature (compiled from data in Radebaugh 2002, Johnson 1960, White and Meeson 2002, Childs et al. 1973, and Cryogenic Materials Properties Program Compact Disk 2001). For high-purity metals, the low-temperature thermal conductivity λ depends strongly on the level of trace impurities, as shown for the copper and aluminum data in the figure. Tabulated data for these and other materials are given in Appendix A6.7.

conductivity, where charge is carried by only one kind of carrier (electrons), *heat* is transported through solids by two kinds of carriers: electrons and phonons (lattice vibrations). Thus, we can write the thermal conductivity as

$$\lambda = \lambda_e + \lambda_p. \quad \text{Total thermal conductivity} \tag{6.12}$$

At first this may appear more complicated than electrical conductivity, but in practice most materials tend to be dominated by one or the other heat carrier—*metals and alloys by electron heat conduction* λ_e, and *insulators by phonon heat conduction* λ_p.

Near the top of Fig. 6.13 are the crystalline materials, sapphire and diamond, whose phonon heat conduction is very high at temperatures above about 10 K. These materials are especially useful when good thermal conduction is needed at the same time as electrical insulation, such as for sample holders. Also near the top of the figure are pure metals, where heat conduction by electrons dominates at all temperatures. Below these are metallic alloys, where electronic conduction still dominates but the thermal conductivity is limited by strong defect scattering from

alloying. Still lower on the chart are semiconductors and semimetals, such as bismuth, graphite, or antimony (not shown in the figure), for which heat conduction can be dominated by either electrons or phonons (although at low temperatures, phonons usually dominate because there the thermal energy is insufficient to excite electrons into the conduction band). Finally, at the bottom of Fig. 6.13 are noncrystalline insulators, amorphous glasses, resins, and polymers, where there is essentially no electron conduction, and heat is carried poorly by phonons in highly disordered structures.

Appendix A6.7 gives handbook values of λ for a number of technical materials over the cryogenic range. For the most part, handbook values of λ are fairly constant from sample to sample and can be used reliably. There are a few limitations, however, which we now consider.

6.4.2 ELECTRONIC THERMAL CONDUCTIVITY IN METALS

For *nearly pure metals*, we need to be careful about using handbook values. Similar to electrical conductivity, λ is dominated by phonon scattering at higher temperatures (above $\sim \theta_D/3$), and so, in this regime, handbook values and the data in Fig. 6.13 are fine to use. However, at low temperatures, once again, handbook values do not work. In this regime, phonon scattering is frozen out, and λ depends strongly on the level of defect scattering, which can vary widely with impurity content, cold work, and the annealing state of the particular sample. At low temperatures we need individually measured values of λ for each particular sample, a difficult task. However, there is a simple method of estimating λ at low temperatures.

The technique relies on the fact that, like electrical conductivity, thermal conductivity is represented well by the kinetic theory, which works for both types of heat carriers, electrons and phonons (Rosenberg 1988; Ziman 1960):

$$\lambda_i = (1/3) C_i \nu_i l_i. \quad \text{Thermal conductivity from kinetic theory} \tag{6.13}$$

Here, C_i, ν_i, and l_i are, respectively, the volumetric heat capacity, velocity, and mean free path of the ith carrier: electrons (e) or phonons (p).

Thus, in metals, the same electron scattering processes that limit electrical conductivity also limit λ_e, and so we would expect the two to be related. As described for electrical resistivity, the electron velocity at the Fermi level, ν_e in Eq. (6.13), is high and therefore affected little by temperature over the cryogenic range. On the other hand, C_e is proportional to T, as we saw from Eq. (6.2). Thus, in pure metals at high temperatures where the electron mean free path l_e varies as T^{-1}, the thermal conductivity is nearly *independent* of temperature [from the product of C_e and l_e in Eq. (6.13)]. On the other hand, in pure metals at low temperatures where l_e is dominated by defect scattering (and independent of temperature), the electronic thermal conductivity depends *linearly* on temperature (from the C_e term alone). These two temperature dependences (constant at high temperature and linear with respect to T at low temperatures) can be seen clearly in the data for Fig. 6.13 for pure metals and alloys.

Wiedemann–Franz–Lorenz law

So, in pure metals, how can we estimate the linearly temperature-dependent λ_e at low temperatures? A very useful relation results if we compare the kinetic theory expressions for the two types of transport. If we assume that l_e is similar for both types, we can eliminate l_e in Eqs (6.13) and (6.6) by taking their ratio:

$$\lambda_e/\sigma_e = (1/3)C_e m_e \nu_e^2/(Ne^2). \tag{6.14}$$

In an electron gas, the temperature dependence of the right side of Eq. (6.14) is given by the electronic specific heat (because everything else is constant or essentially constant, as described above). Evaluating C_e from Eq. (6.2) and the electron theory of gases (Rosenberg 1988), we obtain

$$\lambda_e/(\sigma_e T) = (\pi^2/3)\,(k_B/e)^2 \equiv L_N = 2.44 \times 10^{-8}\ \mathrm{V^2/K^2}. \tag{6.15}$$

Wiedemann–Franz–Lorenz law

Equation (6.15) is the famous *Wiedemann–Franz–Lorenz law*, where L_N on the right is the *Lorenz number*. This relation is well obeyed experimentally within a few percent at room temperature (where electron scattering from high-energy phonons dominates) as well as at low temperatures (where electron scattering from impurities dominates). (At intermediate temperatures, the experimentally measured Lorenz ratio in pure metals is lower than the Lorenz number L_N given above, because low-energy phonon scattering is more effective in limiting the flow of *heat* than that of *electric charge*. Tables of the temperature dependence of the Lorenz ratios for metals and alloys are given in Hust and Sparks 1983, and Madelung and White 1991, but they all tend approximately to L_N at room temperature and at low temperatures.)

Since the electrical conductivity is much *easier to measure* than the thermal conductivity, Eq. (6.15) is useful for experimentally estimating the thermal conductivity of pure metals at low temperatures, where handbook values serve no purpose.

Example: Suppose we wish to know the thermal conductivity at low temperatures of a piece of #36 gauge (~0.125 mm) copper wire (the same wire used in the example in Sec. 6.3).

Because the thermal conductivity is highly dependent on the amount of sample impurity and cold work at low temperatures, the only accurate method is to measure λ.

However, for practical purposes, a good estimate can be made by converting the electrical resistivity data on this conductor to thermal conductivity by using the Wiedemann–Franz–Lorenz law, Eq. (6.15). We simply take the value of $\rho_{res} = 15\ \mathrm{n\Omega\,cm}$ found in the example in Sec. 6.3 (corresponding to a RRR of 110) and calculate the thermal conductivity over the low-temperature range as

$$\lambda \cong L_N \sigma_e T = L_N T/\rho_{res}$$

$$\lambda \cong (2.44 \times 10^{-8}\ \mathrm{V^2/K^2})\,(15 \times 10^{-11}\ \Omega\,\mathrm{m})^{-1} T \approx 160\ T\ \mathrm{W/(m\cdot K)}.$$

This is in quite good agreement with the thermal conductivity data at low temperatures in Fig. 6.13 (close to, but slightly above the RRR = 50 curve for ETP copper).

6.4.3 PHONON THERMAL CONDUCTIVITY IN INSULATORS

As mentioned in the introduction to this section, heat conduction in insulators (where there are no free electrons) is mainly by phonons. The same is true for transition metals, where electron conduction is very limited. Unfortunately, the temperature dependence of the phonon (atomic-lattice) contribution to the thermal conductivity is not a simple analytic function. At high temperatures ($T > \theta_D/5$), the lattice conductivity λ_p is limited mainly by scattering of phonons by other phonons (because phonons are so energetic at these temperatures). At low temperatures, on the other hand, only low-energy long-wavelength lattice waves are left, and so phonon scattering in this regime is predominately off larger planar atomic irregularities, such as grain boundaries or dislocations (rather than off other phonons).

In practice, the handbook data given in Fig. 6.13 and Appendix A6.7 are, again, the best method of determining thermal conductivity. The values at higher temperatures are most universally applicable, because they depend only on scattering of phonons by phonons—an intrinsic property of the element's crystal structure. At lower temperatures, the conductivity may differ from sample to sample, depending on the amount and type of crystal defects present in the sample.

Dielectric crystals, such as quartz, alumina, and beryllia, are of special interest in cryogenic apparatus construction because they are electrically insulating, but they have a high thermal conductivity that can exceed 10^3 W/(m K) because of the strong heat conduction by phonons through these low-defect materials. Thus, they are useful as heat sinks for instrumentation leads or thermometer sensing leads, as illustrated for a beryllium-oxide chip in Fig. 4.5.

Amorphous solids (plastics, glass, and other materials with an amorphous structure, such as vitreous silica, vitreous germania, and vitreous selenium) are highly disordered and thus have very low thermal conductivity. At high temperature, we would expect the phonon mean free path in these materials to be limited by the scale of short-range order and, therefore, independent of temperature. Since the mean free path of the phonons l_p is nearly constant and the velocity of the phonons v_p is nearly constant (approximately that of sound), we would expect from Eq. (6.13) that the temperature dependence of λ_p in glasses would vary as that of the specific heat of the phonons C_p (i.e. nearly constant at high temperature and T^3-like at low temperature, from Secs 6.1.1 and 6.1.2). Figure 6.14 shows this dependence for λ approximately holds at higher temperatures, but at about 10 K an anomalous plateau develops, indicating that the mean free path of the phonons is no longer constant, but increases significantly as temperature is decreased. At lower temperatures ($T < 1$ or 2 K), λ resumes its decline, but falls approximately as T^2 (which is still slower than the decrease in heat capacity alone, indicating that l_p is still increasing, but at a slower rate). Thus, for engineering design purposes, handbook data is generally useful for estimating λ, but be aware that anomalous behavior typifies these noncrystalline solids.

6.5 **Magnetic susceptibility**

6.5.1 DESIGN DATA AND MATERIALS SELECTION

Magnetic susceptibility (the extent to which a material becomes magnetized in a magnetic field) can play an important initial-design role in measurement cryostats, especially in selecting

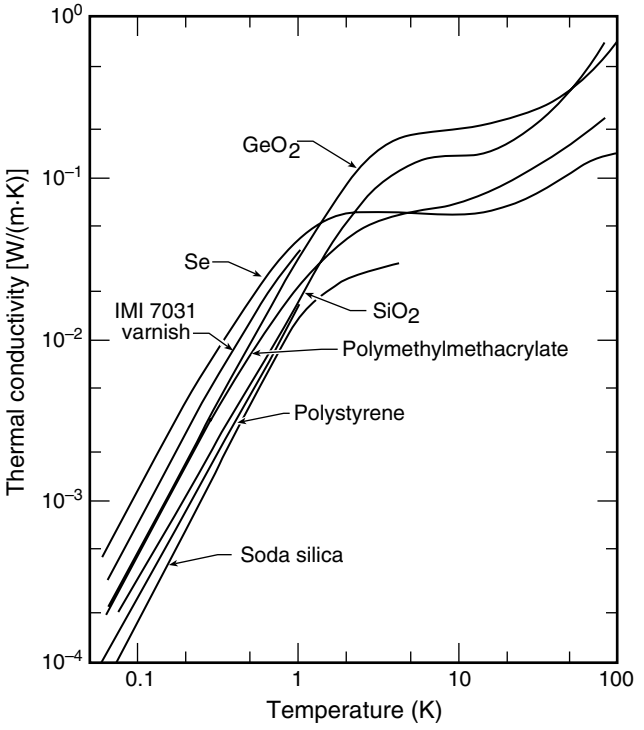

Fig. 6.14 Thermal conductivity of various amorphous solids: vitreous silica, vitreous germania, vitreous selenium, amorphous polystyrene, and amorphous polymethylmethacrylate (PMMA, Plexiglas™). (Adapted from Stephens 1973, and White and Meeson 2002.)

construction materials with small magnetic moments for sensitive magnetic measurements. For example, very low magnetic susceptibility is needed in measurements involving *electron beams* that can be diverted by small remanent magnetic moments in the cryostat materials, or for *magnetometer* measurements where the magnetization of the cryostat structure can mask that of small test samples. (Translucent drinking straws and colorless gelatin drug capsules, for instance, are good materials to use for magnetometer sample holders.) Likewise, cryostat parts with low magnetic susceptibility are important in *high-field measurements*, where magnetic forces can become significant. (*Ferromagnetic* materials, such as iron, cobalt, and nickel, are usually completely avoided in high-field cryostat construction, unless deliberately introduced for magnetic-field shaping.)

When determining the magnetic susceptibility of small parts, the sample mass is usually easier to figure than its volume, and so the *mass susceptibility* χ/ρ is more convenient to use for these situations. However, for large structural parts, the volume of the part is usually more readily known, and then the *volume susceptibility* χ is easiest to use. It is not hard, however, to convert between these two quantities [(mass susceptibility χ/ρ) $\equiv$ (volume susceptibility χ) / (density in kg/m^3)]. Appendices A6.8a and A6.8b give, respectively, the mass susceptibility χ/ρ (SI units of m^3/kg) and volume susceptibility χ (dimensionless SI units) of many materials commonly used in the construction of cryogenic apparatus.

6.5.2 HIGH-FIELD MEASUREMENTS—FORCES, FORCES

The magnetic forces acting on cryostat parts in a high magnetic field can be surprisingly high. Contrary to popular belief, the magnetic forces on "*nonmagnetic*" stainless steel, for example, are not negligible in high magnetic fields.

The magnetic force F (in newtons) on a cryostat part is determined in terms of *volume* susceptibility (χ) by the relation

$$F = \chi V B \nabla B / \mu_0, \quad \text{Magnetic force in terms of volume susceptibility} \quad (6.18a)$$

or equivalently, for *mass* susceptibility (χ/ρ), by the relation

$$F = (\chi/\rho)\, m B \nabla B / \mu_0, \quad \text{Magnetic force in terms of mass susceptibility} \quad (6.18b)$$

where $\mu_0 = 4\pi \times 10^{-7}$ H/m (the permeability of free space), V is the volume of the part in m^3, m is the mass of the part in kg, B ($\equiv \mu_0 H$) is the magnetic induction in free space in units of tesla T, ∇B is the gradient of the magnetic field in T/m, χ is the *volume* susceptibility of the material in dimensionless SI units [which is equal to 4π times the volume susceptibility in cgs units], and χ/ρ is the *mass* susceptibility of the material in SI units of m^3/kg [which is equal to ($4\pi \times 10^{-3}$ m^3/kg) times the mass susceptibility in cgs units].

Example: Consider the magnetic force acting on a long rod of "nonmagnetic" AISI 316 stainless steel with a diameter of 5 mm (~3/16 inch) when it is inserted into a 12 T solenoidal magnet with a bore 30 cm long. This is a common problem in cryostats where stainless-steel tubes or rods are used to support or manipulate a sample in the middle of a high-field magnet. The rod extends from outside the magnet to the middle of the magnet, so the magnet will try to draw the rod further into the high-field region. We want to know the approximate magnetic force acting on the rod.

From the material susceptibility values in Appendix A6.8b, we see that the volume susceptibility of 316 stainless steel at 4.2 K is 1.6×10^{-2} in SI units ($1.6 \times 10^{-2} / 4\pi = 1.3 \times 10^{-3}$ in cgs units). In most cryostats, the rod extends from room temperature down to the center of the magnet, so it traverses a magnetic-field gradient of 12 T in passing through a distance equal to about the magnet's length (from the magnet's center to about half the magnet's length beyond the end of the solenoid, where the field decays to a low value). That is, $\nabla B \approx (12\ \text{T} / 0.3\ \text{m}) = 40$ T/m. The average magnetic field over this gradient is about 6 T, and the volume of the rod in the gradient is $\pi\,(0.25\ \text{cm})^2\,(30\ \text{cm})$, which is 5.8×10^{-6} m^3. Substituting these values into Eq. (6.18), we find that the centering force acting on the 5 mm diameter rod is

$$\begin{aligned} F &= \chi V B \nabla B / \mu_0 \\ &\cong (1.6 \times 10^{-2})\,(5.8 \times 10^{-6}\ \text{m}^3)\,(6\ \text{T})\,(40\ \text{T/m})/(4\pi \times 10^{-7}\ \text{H/m}) \\ &= 18\ \text{N} \quad (\sim 4\ \text{lbf}). \end{aligned}$$

For such a relatively small volume of stainless steel, this is significant. Of course, the force, becomes greater as the volume of the part scales up or as the magnetic field becomes larger. For instance, a 2 cm diameter rod of AISI 316 stainless steel in a mechanical test cryostat would have a volume of 9.4×10^{-5} m^3 in the gradient region and a corresponding force of about 290 N (65 lbf). And remember this is *nonmagnetic* stainless steel! With *ferromagnetic* materials, the forces would be enormous. Equation (6.18) shows that the force scales approximately as the square of the magnetic field (assuming the field gradient is roughly proportional to field), and, thus, if the field were increased from 12 T to 20 T in this example, the loads would be $(20/12)^2 \approx 2.8$ times greater.

Thus, in high-field mechanical measurements (where we do not want magnetic forces acting on the moving cryostat parts) or in magnetically sensitive measurements (such as magnetometry), a far better choice than 316 stainless steel for construction material would be titanium or Ti–6%Al–4%V, which has a magnetic susceptibility three orders of magnitude smaller than either AISI 304 or 316 stainless steel (see Appendix A6.8b). (Suppliers of titanium tubes in less common sizes are listed in Appendix A1.7 under Materials, titanium.)

Also, beware that "nonmagnetic" austenitic stainless steels are unstable below room temperature and can transform into a *magnetic martensitic phase* when cooled, stressed, or welded (see Sec. 6.6.5 and Appendix A6.8c). Commercially available stainless-steel parts, such as screws, are usually made of AISI 304, which can partially transform to this magnetic phase when cooled to low temperatures. So avoid stainless-steel screws in critical situations. Also when welded, 304 stainless steel partially transforms to a magnetic phase, so it is best to *silver-solder* 304 stainless-steel joints if they will be subjected to high fields.

Whether austenitic stainless steels transform depends critically on the chemical composition of the steel and its processing history. Appendix A6.8c shows that, among austenitic stainless steels, only the 316LN and X6CrNi 1811 alloys have no ferromagnetic traces at 4.2 K when cooled or welded.

6.6 **Mechanical properties**

Mechanical properties enter strongly into material selection and cryostat design, determining, for example, the thicknesses of support structures and hence the heat leaks along their lengths (Sec. 3.5). Before considering the various mechanical properties of materials, it is worth reemphasizing that *fracture toughness* is the first selection factor for cryogenic service. As introduced in Sec. 3.2, structural parts are usually made from metals having a face-centered-cubic (f.c.c.) crystal structure, since these metals have a high fracture toughness over the entire cryogenic temperature range. For structural parts, the AISI 300 stainless steels are popular, especially alloys 304, 310, and 316 (compositions are given in Appendix A6.9). Other common f.c.c. metals include aluminum, copper, noble metals, and alloys, such as brass (additional f.c.c. metals are listed in Table 3.1).

On the other hand, metals that are body-centered-cubic (b.c.c.), such as chromium, iron, molybdenum, tantalum, tungsten, vanadium, and nickel steels, may be strong at room temperature, but beware that they become brittle at low temperatures. Metals that are hexagonal-close-packed (h.c.p.), such as beryllium, titanium, and zinc, have mechanical properties between those of f.c.c. and b.c.c. metals.

Resin materials, such as epoxy, are ductile at room temperature, but undergo a transition to a glass-like structure not far below room temperature, so they, too, become brittle. Although they are commonly used as fillers or adhesives in cryogenic applications, the forces on them need to be limited to keep the strain they experience below about 0.2%.

So, from a fracture toughness standpoint, f.c.c. metals are the most reliable, h.c.p. metals are also serviceable, but be careful when choosing to use b.c.c. metals and resin materials.

In addition to fracture toughness, many other mechanical parameters play a role in materials selection and parts design. Although the spectrum of mechanical properties can be complex, I have found the following short list to be effective in low-temperature design:

- tensile properties:
  - Young's modulus, E
  - yield strength, σ_y
  - elastic strain limit, ε_y
  - ultimate strength, σ_{ult}
- fracture toughness, K_{1c}
- fatigue tolerance
- creep.

We consider each in turn next.

6.6.1 TENSILE PROPERTIES

Before we look at tensile property data, we briefly review and define the Young's modulus, yield strength, elastic strain limit, and ultimate strength—all quantities used to describe the response of a material to a simple *tensile* force applied along the axis of a bar of the material. To generalize these properties for parts of different size, the axial force F is normalized by the part's cross-sectional area A and expressed as *stress* σ:

$$\sigma \equiv F/A. \quad \text{Stress} \tag{6.19}$$

The units (SI) for stress are *pascals* (Pa $\equiv$ N/m^2), and values are usually given in megapascals (MPa $= 10^6$ Pa) because the numbers in common situations are so large.

The stress-induced change in length ΔL is usually normalized by the part's length L and expressed as *strain* ε:

$$\varepsilon \equiv \Delta L/L, \quad \text{Strain} \tag{6.20}$$

(positive strain indicates elongation of the bar, and negative, strain compression). The units for strain are dimensionless, but for convenience and clarity, here we express the value as a percentage (%).

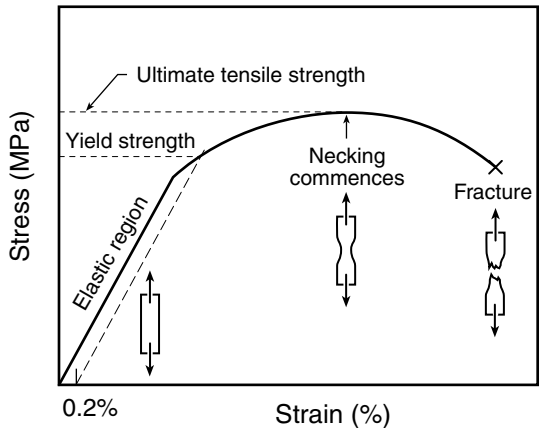

Fig. 6.15 The usual shape of the stress–strain curve for ductile materials when stressed axially (from Read 1983).

The relationship between axial stress σ and strain ϵ is illustrated for a typical metallic material in Fig. 6.15. When axial force is applied, the material at first deforms *elastically*; that is, it returns to its original size and shape when the force is removed. This results in the straight-line response of the material at the beginning of the diagram. The *slope* of this section of the curve determines the relative stiffness of the material and is designated as the *Young's modulus E*, usually expressed in gigapascals (GPa $= 10^9$ Pa):

$$E \equiv \sigma/\varepsilon. \quad \text{Young's modulus} \tag{6.21}$$

Values of the Young's modulus are shown for a selection of metals in Fig. 6.16 and for common structural alloys in Appendix A6.10. Figure 6.16 shows that the Young's modulus usually changes little with temperature, increasing only slightly as temperature is lowered.

The end of the elastic (linear) region in Fig. 6.15 is an important point and indicates the onset of yielding, where the material starts to plastically deform. The stress corresponding to this onset point is designated as the *yield strength* σ_y. For most structural designs, this is the stress level to be avoided! Often parts are sized so that the maximum stress they experience is no more than half the material's yield strength, giving a safety factor of two. Values of yield strength are usually determined by use of the 0.2% offset method, as illustrated in Fig. 6.15 (i.e. 0.2% more strain than that at the end of the elastic region). The temperature dependence of the yield strength of common technical materials is shown in Figs 6.17 and 6.18, and tabulated for a few common metal alloys and polymers in the last table of Appendix A6.10.

After fracture toughness, yield strength is generally the main mechanical design factor. Figures 6.17 and 6.18 show that the yield strength of most materials (both ductile and brittle) increases moderately as temperature is lowered. Unlike the Young's modulus, the yield strength is strongly affected by extrinsic factors such as the amount of cold work introduced into the material as it is rolled, pressed, or drawn to smaller cross-sectional area. This is illustrated by comparing the

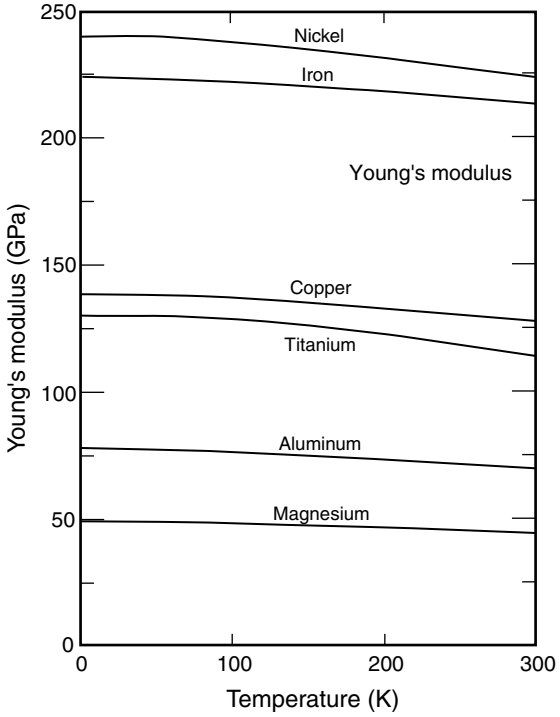

Fig. 6.16 Temperature dependence of the elastic (Young's) modulus for several metals (from Ledbetter 1983). Appendix A6.10 gives tabulated values, along with mechanical data for additional materials.

enormous differences between values of σ_y for annealed and cold-drawn materials, shown in Fig. 6.17 for copper and AISI 304 stainless steel.

The *elastic strain limit* (also called the *proportional limit* or *strain at yield*) is a significant design factor when choosing a material for a springy cryostat part that needs to bend elastically, such as spring clamps, extensometer arms, and bending beams. The elastic strain limit can be simply calculated as

$$\varepsilon_y = \sigma_y / E. \quad \text{Elastic strain limit} \tag{6.22}$$

Beryllium copper or precipitation-hardened aluminum alloys, for example, are materials having very high elastic strain limits, up to ~1.0%. They are great materials for cryogenic parts that need to flex without fatiguing or breaking.

Example: Suppose we want to determine the elastic limit of 2219 aluminum alloy used as a bending beam.

We find from Fig. 6.18 that, at 4 K, this alloy has the ideal combination of a relatively high yield strength $\sigma_y \cong 490$ MPa and from Appendix A6.10 a relatively low Young's modulus E = 86 GPa. From Eq. (6.22), this gives a high elastic limit ε_y of about (490 MPa) / (86 GPa) ≈ 0.6%. The 2000 series

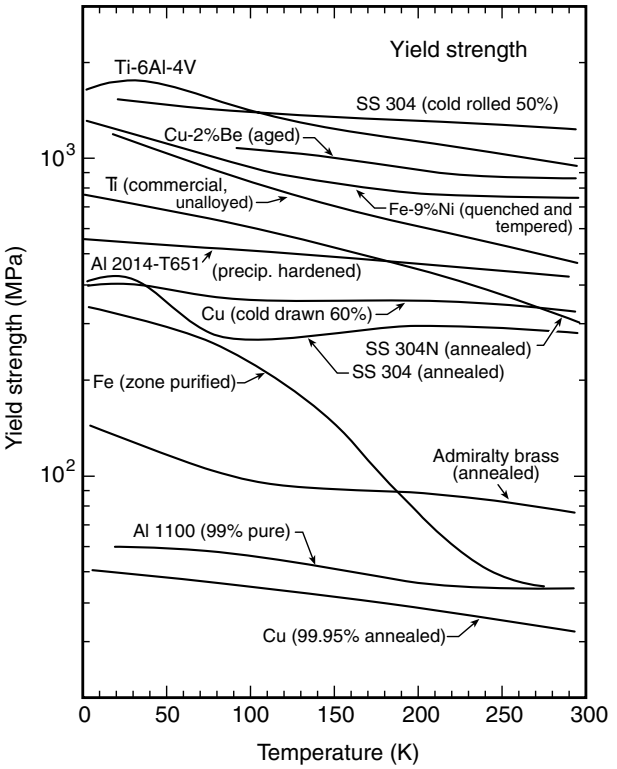

Fig. 6.17 Yield strength of common cryostat construction materials as a function of temperature. (Data compiled from Battelle 1977, Read and Reed 1979, Tobler 1976, Smith and Rutherford 1957, Warren and Reed 1963, Schramm et al. 1973, and Soffer and Molho 1967.) Appendix A6.10 gives tabulated values, along with mechanical data for additional materials.

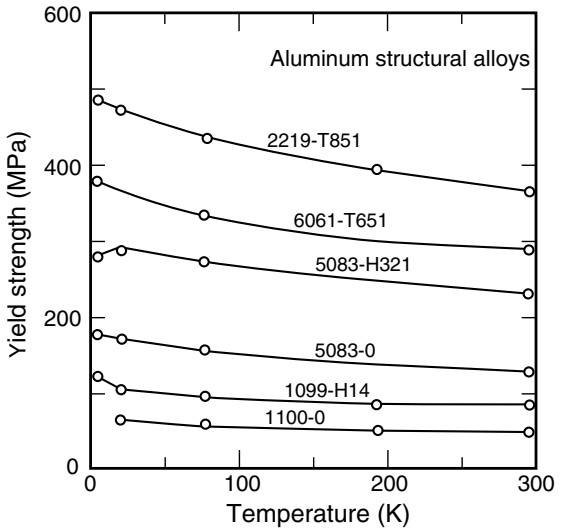

Fig. 6.18 Yield strength of structural aluminum alloys as a function of temperature (from Kaufman et al. 1968). Appendix A6.10 gives tabulated values, along with mechanical data for additional materials.

precipitation-hardened aluminum alloys have performed well for us in constructing sample-loading fixtures that can be flexed repeatedly at low temperatures.

Beryllium copper (Cu–2%Be, UNS C17200) is another material with a very high elastic limit. From the last table in Appendix A6.10, we find that it has a high yield strength at room temperature of about 1030 MPa and a Young's modulus of about 119 GPa, giving a very high elastic limit, about 0.9%.

The last tensile property, the *ultimate tensile strength*, is usually not as important in practice, especially if the yield-strength limit is respected. Figure 6.15 shows that when ductile materials are strained beyond their yield strength, stress increases until the ultimate tensile strength is reached. (Brittle materials, on the other hand, fail at low strain in the elastic region of Fig. 6.15.) At the ultimate strength, necking commences, and if the material is strained further, the load it will support decreases. (If load is being controlled rather than strain, the material will fail at the onset of necking.) Eventually, at high enough strain, ductile materials pull apart and fail, as indicated by the $\times$ in Fig. 6.15. Values of the ultimate strength for common cryostat materials

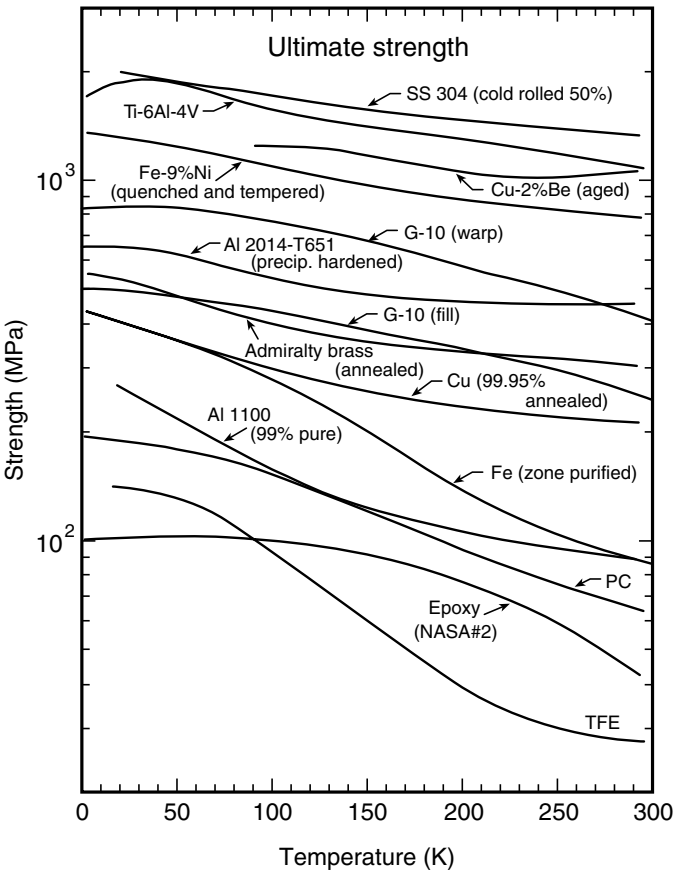

Fig. 6.19 Ultimate tensile strength of common cryostat construction materials as a function of temperature. (Data compiled from Battelle 1977, Read and Reed 1979, Tobler 1976, Smith and Rutherford 1957, Warren and Reed 1963, Schramm et al. 1973, Soffer and Molho 1967, and Kasen et al. 1980.)

are compared in Fig. 6.19. Similar to the yield strength, the ultimate strength generally increases at lower temperatures.

6.6.2 FRACTURE TOUGHNESS

As mentioned in the introduction, fracture toughness can be a show stopper in cryostat construction. The toughness parameter most commonly used for mechanical design is the plane-strain critical-stress intensity factor K_{1c} [for further information, see, for example, the introductory material in Ruffin (1996)]. Values of K_{1c} are shown for various construction materials in Fig. 6.20. This figure clearly shows the remarkable drop in fracture toughness around 100 K in b.c.c. materials, such as the very high-strength nickel steels (A203E, A553, and A645) and high-strength titanium alloys [Ti–6%Al–4%V, ELI Grade (ELI stands for a purer grade of titanium with extra-low interstitial element concentrations, which leads to higher

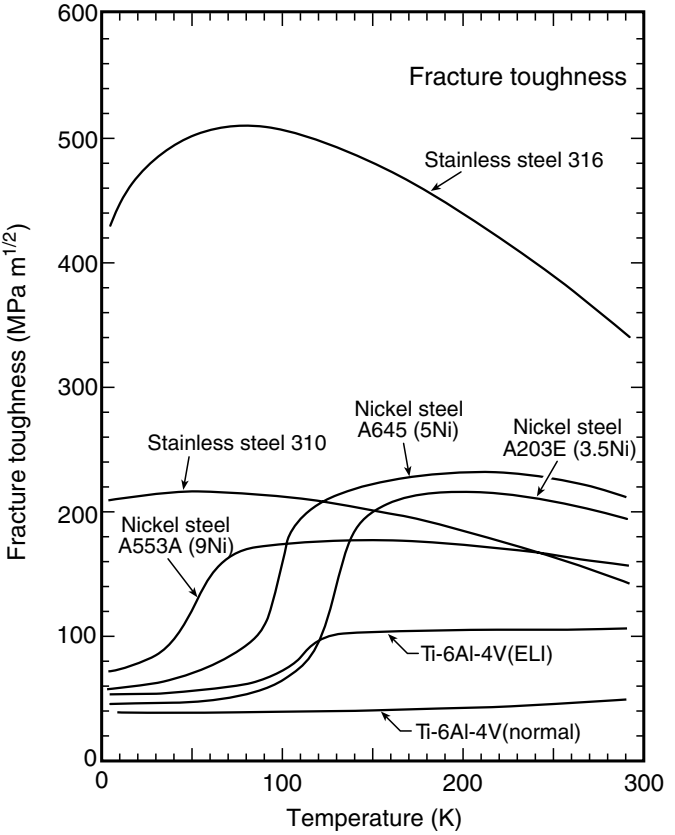

Fig. 6.20 Fracture toughness of various materials at low temperatures. Note that at low temperatures, the nickel steels (b.c.c. structure) decrease greatly in toughness and become brittle, whereas the austenitic stainless steels (f.c.c. structure) such as AISI 310 and 316 remain tough across the cryogenic temperature range. The Ti–6%Al–4%V alloys have an h.c.p. structure; their toughness drops more moderately. (Data compiled from Tobler and McHenry 1983, Mann 1978, and Fowlkes and Tobler 1976.) Tabulated data for some of these alloys are given in Appendix A6.10.

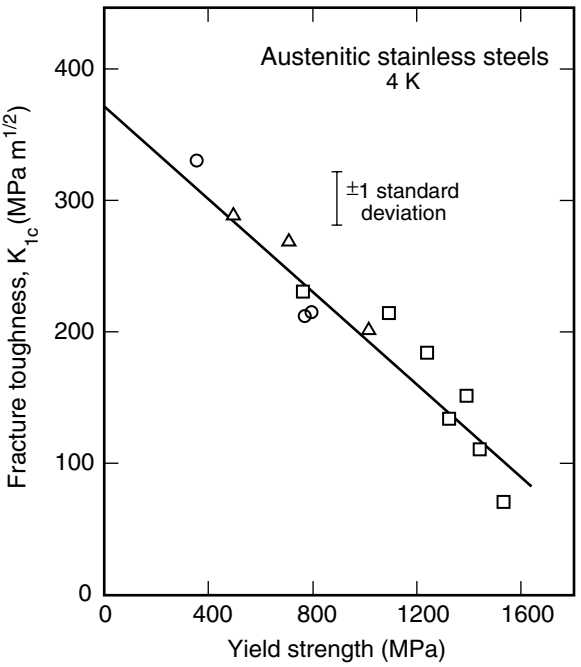

Fig. 6.21 Inverse relationship between fracture toughness and yield strength at 4 K for austenitic stainless steels (from Read and Reed 1981).

fracture toughness than for normal Ti–6%Al–4%V)]. On the other hand, austenitic stainless steels are exceptionally tough. These are alloys of iron and chromium with enough nickel or manganese to stabilize the fracture-resistant f.c.c. (austenitic) crystal structure. Figure 6.20 and the tabulated data in Appendix A6.10 show that the fracture toughness of austenitic AISI 310 and AISI 316 stainless steels do not exhibit a dip in toughness at low temperatures and have high strength as well. Thus, they make excellent structural materials for use at low temperatures.

Addition of nitrogen to the AISI 300 series steels increases their yield strength dramatically. For example, AISI 304 with additions of only 0.1–0.16 wt% nitrogen (designated AISI 304N), has approximately three times the yield strength of standard AISI 304 at 77 K. Furthermore, its strain-to-failure is higher at temperatures below 220 K. However, there is a trade-off: along with increased yield strength and strain-to-failure comes a significant loss in fracture toughness. Figure 6.21 shows that the toughness of austenitic stainless steels is generally *inversely proportional* to their yield strength.

6.6.3 FATIGUE

When materials are repeatedly stressed, they may eventually fail as a result of high-cycle fatigue damage. As a rough guide, fatigue effects can be avoided by keeping applied stress well below the yield strength.

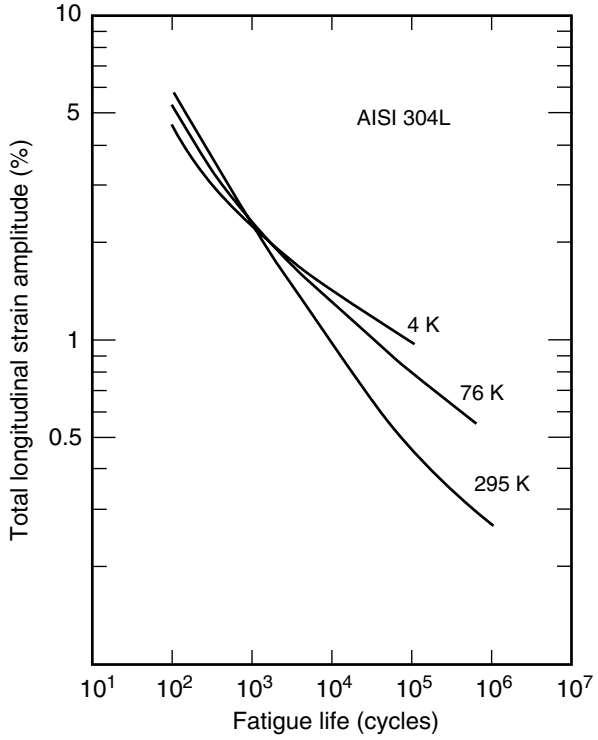

Fig. 6.22 Strain-cycling fatigue curves for AISI type 304L austenitic stainless steel at 295, 76, and 4 K(from Nachtigall 1975).

Figure 6.22 shows an example of the fatigue failure characteristics for AISI type 304L austenitic stainless steel when it is repeatedly strained beyond its yield point. [The L in 304L indicates low carbon (see Appendix A6.9), which is desirable to avoid precipitation of chromium carbides near grain boundaries that can lead to intergranular corrosion and loss of toughness.] The vertical axis of Fig. 6.22 shows the strain amplitude (alternate compressive and tensile strain, centered about zero) that is repeatedly applied to a notched test sample. This is plotted against the number of fatigue cycles the steel endured until it fractured. Figure 6.22 shows, for example, that at 4 K type 304L stainless steel can withstand about 10^5 cycles of 0.8% strain.

Fortunately, the *temperature dependence* of the fatigue performance of f.c.c. materials is in favor of cryogenic service. Figure 6.22 shows that the fatigue life improves significantly at high numbers of fatigue cycles when the material is cooled from room temperature to low temperature. Because of this improvement and the abundance of room-temperature fatigue data, room-temperature handbook results can be used as a conservative estimate to set low-temperature fatigue cycle limits. This does not work, however, with materials that become brittle (the non-f.c.c. metals). In this case, the important design point is the ductile-to-brittle transition, as indicated by the fracture toughness (Fig. 6.20).

6.6.4 CREEP

Creep (plastic flow of a material) may occur when a material is subjected to a constant load over a long period. Generally, creep is not a significant factor at cryogenic temperature, except possibly at stresses exceeding the yield strength. Even soft materials that normally creep at room temperature (such as Pb–Sn solder or indium) have negligible creep at liquid-nitrogen temperature because there the thermal energy is insufficient to activate deformation and plastic flow.

6.6.5 MECHANICAL PROPERTIES OF TECHNICAL MATERIALS: SYNOPSIS

We described above each of the main mechanical properties that enter into selecting materials for cryostat construction and presented a wide range of material data for each property. Here, we sort the information differently and conclude this section by summarizing the salient mechanical properties for each group of materials:

Copper and *aluminum:* These f.c.c. metals remain ductile at low temperatures and, in pure annealed form, have very low strength. However, when alloyed, their strength increases remarkably, especially for compositions that precipitation-harden when given a heat treatment, as illustrated in Fig. 6.17 for the pure and alloyed forms of aluminum and copper.

Steels: Remember that although b.c.c. materials such as 9-nickel steel are the structural champions at room temperature, they become brittle at low temperatures and fracture at low strain. The f.c.c. austenitic stainless steels, on the other hand, generally remain ductile at low temperatures. However, be aware that the f.c.c. austenitic phase is *metastable* in most of these alloys, and so the common stainless-steel materials (such as AISI 304, 310, and 316) can partially transform to a b.c.c. or h.c.p. martensitic phase when cooled, deformed, or welded (Reed 1983). If this happens, the alloy becomes stronger, but less tough. Also the martensitic crystal phase that is formed is magnetic, raising the magnetic susceptibility of these materials considerably, which might be a concern in magnetic fields (Sec. 6.5). Among the austenitic stainless steels, AISI 310 and 316 stainless-steel alloys are less likely to transform at low temperatures (Appendix A6.8c) and so are preferable to AISI 304, but they are not as readily available commercially. AISI 310 and 316 are excellent cryogenic structural materials, especially for compositions with high nitrogen (N) and low carbon (L) (Appendix A6.9), which give superior strength and corrosion resistance. The modified compositions are usually designated by adding an L and/or an N after the AISI type number, that is AISI 316LN. Unfortunately, the L and N grades are even less available commercially than the 310 and 316 alloys.

Titanium: Titanium and titanium alloys are sometimes preferred structural materials for cryogenic service because of their high strength, low thermal conductivity, and low thermal contraction. Also, they have a magnetic susceptibility much lower than that of stainless steel. However, because of their h.c.p. crystal structure, the toughness of very high-strength titanium alloys (the ELI grades in Fig. 6.20) can decrease severely around 77 K. The more useful materials include Ti–6%Al–4%V and Ti–5%Al–2.5%Sn alloys, along with commercially pure titanium. The yield strengths of Ti–6%Al–4%V and commercial, unalloyed titanium

are shown in Fig. 6.17 (Ti–5Al–2.5Sn, which is not shown, has a temperature dependence similar to that of Ti–6%Al–4%V, but about 20% lower).

Polymers: Polymers have cryogenic strengths well below those of the common structural materials, as illustrated in Fig. 6.19. They are usually characterized by a glass transition temperature T_g below which they lose ductility. Commonly observed values of T_g range from 220–370 K. Polymers can exist in either amorphous or crystalline states. Crystalline polymers usually have more strength than amorphous polymers, but become extremely brittle below T_g.

Glasses: Glasses have an amorphous structure with local order, but no long-range crystalline order. At high temperatures (800 K and above) they behave as viscous liquids, flowing gradually under applied stress, but their lack of long-range crystalline order inhibits the formation and motion of dislocations at low temperatures, where they are extremely brittle. Although, theoretically, the strength of glasses can be extremely high, around 10 GPa(!), their lack of ductility makes them very susceptible to scratches and other stress concentrators at the surface. As a result, their failure stresses are extremely variable, with a minimum of only about 35 MPa. In compression, glass is quite strong, with failure believed to be initiated by the presence of tensile components of stress that cannot be eliminated. The strength of glasses usually increases down to liquid-nitrogen temperature. Be aware that glasses may fracture from thermal stresses on rapid cooling because of their low thermal conductivity, which results in nonuniform contraction and internal stresses. Fatigue damage usually does not accumulate in glasses because of their elastic, brittle nature.

(*Sticky stuff*—useful tapes, adhesives, glues, and materials for tying things down at cryogenic temperatures are listed in Appendix A3.10.)

6.7 References

6.7.1 FURTHER READING

GENERAL TEXTBOOKS ON SOLID STATE PHYSICS:

A very readable introductory text:
Rosenberg, H. M. (1988). *The Solid State*, Oxford University Press, Oxford, UK.

Descriptions of transport properties of solids and derivations of useful transport formulas:
Ashcroft, N. W., and Mermin, N. D. (1976). *Solid State Physics*, Holt Rinehart and Winston, NY.
Kittel, C. (1986). *Introduction to Solid State Physics*, Wiley & Sons.

FURTHER INFORMATION ON ELECTRON AND PHONON INTERACTIONS:

Variational method of calculating the electrical resistivity:
Overview and derivation:
Ziman, J. M. (1960). *Electrons and Phonons*, Chapter 7, Oxford University Press, Oxford, UK.

Principles and numerical integration techniques for applying the variational method:
Ekin, J. W. (1971). "Electron–phonon umklapp interaction in the low-temperature electrical resistivity of potassium," *Phys. Rev. Lett.* 26, 1550–1553.

Ekin, J. W., and Maxfield, B. W. (1971). "Electrical resistivity of potassium from 1 to 25 K," *Phys. Rev*. B4, 4215–4225.

Deviations from Matthiessen's rule:

Extensive review article:

Bass, J. (1972). "Deviations from Matthiessen's rule," *Adv. Phys*. 21, 431–604.

Information on the fundamental role of umklapp processes in accounting for deviations from Matthiessen's rule:

Ekin, J. W., and Bringer, A. (1973). "Anisotropy in the electron–phonon umklapp interaction and deviations from Matthiessen's rule," *Phys. Rev*. B7, 4468–4478.

MATERIALS HANDBOOK DATA:

Heat capacity, thermal expansion, resistivity, superconducting parameters, thermal conductivity, magnetic susceptibility, and mechanical properties of many materials at cryogenic temperatures are tabulated in Appendixes A6.1 through A6.10 at the end of this book.

Classic 13-volume series:

Touloukian, Y. S., and Ho, C. Y., eds. (1970–1977). *Thermophysical Properties of Matter*, Plenum Press, NY.

Handbook data in more compact form:

Gray, D. E., ed. (1972). *American Institute of Physics Handbook*, McGraw-Hill, NY.

Linde, D. R., ed. (2002). *CRC Handbook of Chemistry and Physics*, 83rd edition, CRC Press LLC, Boca Raton, FL.

Metals Handbook, (1961). Vol. 1, *Properties and Selection of Materials*, 8th edition, ASM International, Materials Park, OH.

Source of many compilations and handbook data on cryogenic properties, especially mechanical properties:

Battelle (1977). *Handbook of Materials for Superconducting Machinery*, MCIC-HB-04. Battelle Columbus Laboratories, Columbus, OH.

Detailed review of material properties at low temperatures, as well as how they are measured:

Reed, R. P., and Clark, A. F., eds. (1983). *Materials at Low Temperatures*, ASM International, Materials Park, OH.

6.7.2 PROPERTIES OF SOLIDS: INTERNET INFORMATION

Information on the Internet is constantly changing, which is both an advantage and a disadvantage. The advantage is that new properties are continually being added as web sites are updated. The disadvantage is that, at some future time, the web address may be changed or discontinued. With this caveat, these web sites are provided as convenient online sources of additional information on properties of solids (at least at the moment). If they are discontinued, forwarding web address information is sometimes provided and, in any event, they can serve as a starting point for key words to search for new web sites that access similar material.

Cryogenic properties (1–300 K) of many solids, including thermal conductivity, specific heat, and thermal expansion, have been empirically fitted; the *equation parameters* are available free on the Internet at http://www.cryogenics.nist.gov/. Information for using the NIST fitting parameters to perform

data calculations and make plots is also available at this web site. An in-depth listing of the cryogenic *literature*, including references to the extensive database of cryogenic properties generated in the 1950s, is available from http://www.cpia.jhu.edu/.

Other sources of material data can be purchased on electronic media, which use their own fitting equations. These are available at http://www.cryodata.com/ (cryogenic properties of about 100 materials), and http://www.jahm.com/ (temperature-dependent properties of about 1000 materials, many at cryogenic temperatures).

Room-temperature data for about 10 to 20 properties of about 24 000 commercial materials are available free on the Internet at http://www.matweb.com/.

A database of high-T_c bulk superconductor properties has been compiled by Iwata University. Physical properties are tabulated at http://ikebehp.mat.iwate-u.ac.jp/database.html and mechanical properties at http://paris.mech.iwate-u.ac.jp/sc-bulk/database.html.

6.7.3 CHAPTER REFERENCES

Aleksandrov, B. N., and D'yakov, I. G. (1963). "Variation of the electrical resistance of pure metals with decrease of temperature," *Soviet Phys. JETP* 16, 603–608.

Arp, V., Wilson, J. H., Winrich, L., and Sikora, P. (1962). "Thermal expansion of some engineering materials from 20 to 293°K," *Cryogenics* 2, 230–235.

Ashcroft, N. W., and Mermin, N. D. (1976). *Solid State Physics*, Holt Rinehart and Winston, NY.

Battelle (1977). *Handbook on Materials for Superconducting Machinery; Mechanical, Thermal, Electrical, and Magnetic Properties of Structural Materials*, MCIC-HB-04, Metals and Ceramics Information Center, Battelle, Columbus Laboratories, Columbus, OH.

Bloch, F. (1930). "Zum elektrischen Widerstandsgesetz bei tiefen Temperaturen," *Z. Phys*. 59, 208–214.

Chang, S. S. (1977). "Heat capacity and thermodynamic properties of polyvinyl chloride," *J. Res. Natl. Bur. Stand*. 82, 9–17.

Childs, G. E., Ericks, L. J., and Powell, R. L. (1973). *Thermal Conductivity of Solids at Room Temperature and Below, A Review and Compilation of the Literature*. NBS Monograph 131. US Government Printing Office, Washington, DC.

Clark, A. F. (1968). "Low temperature thermal expansion of some metallic alloys," *Cryogenics* 8(5), 282–289.

Clark, A. F. (1983). "Thermal expansion," Chapter 3 in *Materials at Low Temperatures*, eds. R. P. Reed and A. F. Clark, ASM International, Materials Park, OH.

Clark, A. F., Fujii, G., and Ranney, M. A. (1981). "The thermal expansion of several materials for superconducting magnets," *IEEE Trans. Magn*. MAG-17, 2316–2319.

Corruccini, R. J., and Gniewek, J. J. (1960). *Specific Heats and Enthalpies of Technical Solids at Low Temperatures*. NBS Monograph 20, pp. 1–20. US Government Printing Office, Washington, DC.

Corruccini, R. J., and Gniewek, J. J. (1961), *Thermal Expansion of Technical Solids at Low Temperatures*. NBS Monograph 29, US Government Printing Office, Washington, DC.

Cryogenic Materials Properties Program Compact Disk (2001). Release B-01, Cryogenic Information Center, 5445 Conestoga Ct., Ste. 2C, Boulder, CO 80301–2724, Ph. (303) 442–0425, Fax (303) 443–1821.

Dahlerup-Peterson, K., and Perrot, A. (1979). *Properties of Organic Composite Materials at Cryogenic Temperatures*. ISR-BOM/79–39, CERN, Geneva, Switzerland.

Ekin, J. W. (1971). "Electron–phonon umklapp interaction in the low-temperature electrical resistivity of potassium," *Phys. Rev. Lett*. 26, 1550–1553.

Ekin, J. W., and Maxfield, B. W. (1971). "Electrical resistivity of potassium from 1 to 25 K," *Phys. Rev*. B4, 4215–4225.

Ekin, J. W., and Bringer, A. (1973). "Anisotropy in the electron–phonon umklapp interaction and deviations from Matthiessen's rule," *Phys. Rev*. B7, 4468–4478.

Fowlkes, C. W., and Tobler, R. L. (1976). "Fracture testing and results for a Ti–6Al–4V alloy at liquid helium temperatures," *Eng. Fract. Mech*. 8, 487–500.

Furukawa, G. T., Douglas, T. B., and Pearlman, N. (1972). "Heat capacities," Chapter 4e in *American Institute of Physics Handbook*, McGraw-Hill, NY.

Goodall, D. H. J. (1970). Wall data chart, A.P.T. Division, Culham Science Center, Abingdon, Oxfordshire, UK.

Hahn, T. A. (1970). "Thermal expansion of copper from 20 to 800 K—standard reference material 736," *J. Appl. Phys*. 41, 5096–5101.

Hust, J. G. (1983). "Thermal conductivity and thermal diffusivity," Chapter 4, in *Materials at Low Temperatures*, eds. R. P. Reed and A. F. Clark, ASM International, Materials Park, OH.

Hust, J. G., and Sparks, L. L. (1973). "Lorenz ratios of technically important metals and alloys," NBS Technical Note 634, National Bureau of Standards, US Government Printing Office, Washington, DC.

Johnson, V. (1960). *A Compendium of the Properties of Materials at Low Temperature, Part I, Properties of fluids*; and *Part II, Properties of solids*, WADD Technical Report 60–56. National Bureau of Standards and Wright Air Development Division, US Government Printing Office, Washington, DC.

Kasen, M. B., MacDonald, G. R., Beekman, D. H., and Schramm, R. E. (1980). "Mechanical, electrical, and thermal characterization of G-10CR and G-11CR glass-cloth/epoxy laminates between room temperature and 4 K," *Adv. Cryog. Eng. (Mater.)* 26, 235–244.

Kaufman, J. G., Bogardus, K. O., and Wanderer, E. T. (1968). "Tensile properties and notch toughness of aluminum alloys at –452 °F in liquid helium," *Adv. Cryog. Eng*. 13, 294–308.

Kirby, R. K. (1956). "Thermal expansion of polytetrafluoroethylene (Teflon™) from –190 to 300°C," *J. Res. Natl. Bur. Stand*. 57, 91–94.

Laquer, H. L., and Head, E. L. (1952). *Low Temperature Thermal Expansion of Plastics*. AECU-2161, Technical Information Service, Atomic Energy Commission, Oak Ridge, TN.

Lawrence, W. E., and Wilkins, J. W. (1972). "Umklapp electron-phonon scattering in the low-temperature resistivity of polyvalent metals," *Phys. Rev*. B6, 4466.

Ledbetter, H. M. (1983). "Elastic properties," Chapter 1 in *Materials at Low Temperatures*, eds R. P. Reed and A. F. Clark, ASM International, Materials Park, OH.

Madelung, O., and White, G. K., eds. (1991). *Landolt-Börnstein*, Vol. III/15c, Springer, Berlin.

Mann, D. (1978*). LNG Materials and Fluids, A User's Manual of Property Data in Graphic Format*, US Dept. of Commerce, NBS. US Government Printing Office, Washington, DC.

Matthiessen, A. (1862). "On the variation of the electrical resistance of alloys due to change of temperature," *Rep. Brit. Assoc*. 32, 136–139.

Nachtigall, A. J. (1975). "Strain cycling fatigue behavior of ten structural metals tested in liquid helium, liquid nitrogen, and ambient air," in *Properties of Materials for Liquefied Natural Gas Tankage*, ASTM STP 579, 378–396. Figure 6.22 was reprinted with permission, © ASTM International, Philadelphia.

Pawlek, F., and Rogalla, D. (1963). *Met. Phys*. 20, 603.

Radebaugh, R. (2002). http://www.cryogenics.nist.gov/, based principally on compilations by Battelle (1977), Childs et al. (1973), Johnson (1960), Mann (1978), Schramm et al. (1973), Simon et al. (1992), and Touloukian (1970–1977).

Read, D. T. (1983). "Mechanical properties," Chapter 7 in *Materials at Low Temperatures*, eds. R. P. Reed and A. F. Clark, ASM International, Materials Park, OH.

Read, D. T., and Reed, R. P. (1979). "Toughness, fatigue crack growth and tensile properties of three nitrogen-strengthened stainless steels at cryogenic temperatures," in *The Metal Science of Stainless Steel*, pp. 92–121, ASM International, Materials Park, OH.

Read, D. T., and Reed, R. P. (1981). "Fracture and strength properties of selected austenitic stainless steels at cryogenic temperatures," *Cryogenics* 21, 415–417.

Reed, R. P. (1983). "Martensitic phase transformations," Chapter 9 in *Materials at Low Temperatures*, eds. R. P. Reed and A. F. Clark, ASM International, Materials Park, OH.

Roark, R. J., and Young, W. C. (1975). *Formulas for Stress and Strain*, McGraw-Hill, NY.

Rosenberg, H. M. (1988). *The Solid State*, Oxford University Press, Oxford, UK.

Ruffin, A. C. (1996). *Fatigue and Fracture*, Vol. 19, ASM International Handbook Series, ASM International, Materials Park, OH.

Schramm, R. E., Clark, A. F., and Reed, R. P. (1973). *A Compilation and Evaluation of Mechanical, Thermal, and Electrical Properties of Selected Polymers*. NBS Monograph 132, US Government Printing Office, Washington, DC.

Simon, N. J., Drexler, E. S., and Reed, R. P. (1992*). Properties of Copper and Copper Alloys at Cryogenic Temperatures*. NIST Monograph 177, US Government Printing Office, Washington, DC.

Smith, R. L., and Rutherford, J. L. (1957). "Tensile properties of zone refined iron in the temperature range from 298 K to 4.2 K," *J. Met*. 9, 857–864.

Soffer, L. M., and Molho, R. (1967). *Cryogenic Resins for Glass-Filament-Wound Composites*, NASA Report N67–25076, US Government Printing Office, Washington, DC.

Sparks, L. L. (1983). "Specific heat," Chapter 2 in *Materials at Low Temperatures*, eds. R. P. Reed and A. F. Clark, ASM International, Materials Park, OH.

Stephens, R. B. (1973). "Low temperature specific heat and thermal conductivity of noncrystalline dielectric solids," *Phys. Rev*. B8, 2896–2905. Figure 6.14 was reprinted with permission, © 1973 by the American Physical Society.

Tobler, R. L. (1976). "Low temperature effects on the fracture behavior of a nickel base superalloy," *Cryogenics* 16, 669–674.

Tobler, R. L., and McHenry, H. I. (1983). "Fracture mechanics," Chapter 8 in *Materials at Low Temperatures*, eds. R. P. Reed and A. F. Clark, ASM International, Materials Park, OH.

Touloukian, Y. S. (1966). *Recommended Values of the Thermophysical Properties of Eight Alloys, Major Constituents and their Oxides*, Report No. CST-7590, 271–343, Thermophysical Properties Research Center, Purdue University, Lafayette, IN.

Touloukian, Y. S. (1970–1977). *Thermophysical Properties of Matter, The Thermophysical Properties Research Center Data Series*, Plenum, NY.

Warren, K. A., and Reed, R. P. (1963). *Tensile and Impact Properties of Selected Materials from 20 to 300 K*. NBS Monograph 63, US Government Printing Office, Washington, DC.

White, G. K. (1976). "Thermal expansion at low temperatures of glass-ceramics and glasses," *Cryogenics* 16, 487–490 and 606 (corrigenda).

White, G. K. (1987). *Experimental Techniques in Low-Temperature Physics*, Oxford University Press, Oxford, UK.

White, G. K., and Meeson, P. J. (2002). *Experimental Techniques in Low-Temperature Physics*, 4th edition, Oxford University Press, Oxford, UK.

Ziman, J. M. (1960). *Electrons and Phonons*, Oxford University Press, Oxford, UK.

This page intentionally left blank

Part II

Electrical Transport Measurements: Sample Holders and Contacts

Part I, which discussed probe construction and material selection, applies to cryogenic measurements generally. Part II focuses on electrical *transport* measurements and the special requirements they pose for the design of sample holders and contacts.

For *non*transport measurements such as magnetometry, sample holders are relatively simple because electrical leads do not have to be attached to the test specimen, and electromagnetic forces on the sample are insignificant. In this case, a straightforward commercial sample holder may consist simply of a glass or plastic capsule into which the sample is placed and kept from moving by lightly stuffing the capsule with cotton wool.

For transport measurements, on the other hand, electrical current must be introduced into the sample. The sample has to be securely fastened to the sample holder and good electrical contacts made directly to the sample without straining it. In this case, the details of sample mounting, thermal contraction, contacts to the sample, and heat extraction become a crucial part of the measurement.

In the following chapters, we focus increasingly on measurements of critical current for practical superconductors; this is one of the more common (and challenging) cryogenic measurements. However, many of the sample-holder and contact techniques apply, not just to critical-current measurements, but generally to almost any cryostat where current contacts are made to the sample, such as measurements of the Hall effect, thermoelectric power, and resistivity.

Sample shape: Most samples for transport measurements are formed, cut, or patterned into *long* shapes (wires, tapes, or strips) of uniform cross section. In the main text, we concentrate on this long-wire or tape geometry, because it is the most common for transport measurements. However, occasionally we need to measure *un*patterned films, arbitrarily shaped flat samples, or anisotropic single crystals. Useful, specialized methods are available for measuring the electrical-transport properties of these alternative geometries. Step-by-step procedures for carrying out such measurements are presented in Appendixes A7.1 through A7.3:

- *Unpatterned films:* A four-probe technique for measuring the sheet resistance of unpatterned films is given in Appendix A7.1. It is quite useful in the initial stages of characterizing films, obviating the need for film patterning at this stage.
- *Arbitrarily shaped flat samples:* The van der Pauw method, described in Appendix A7.2, enables characterization of new materials that may be available only in arbitrary shapes (provided they are flat).
- *Anisotropic samples:* The Montgomery method, described in Appendix A7.3, is useful for measuring anisotropic samples, such as single crystals, provided (as is usually the case) that the crystals are cut or cleaved along principal axes.

Multifilamentary configuration: *High-current superconductors* are usually fabricated with many very fine (typically 1–50 μm diameter) filaments of superconductor embedded in a "stabilizer" matrix of normal metal (such as copper or silver). A picture of this multifilamentary configuration is essential to understanding a number of topics in the remainder of the text, especially current-transfer voltages, which strongly affect sample-holder design for high-current superconductors (Sec. 7.3.4), contact fabrication (Secs 8.3.3 and 8.5.2), and data analysis (Sec. 10.2). If unfamiliar with the multifilamentary construction of high-current superconductors, please take a moment to refer to the brief introduction to this topic given in the addenda to this chapter, Sec. 7.5.2.

7 Sample Holders

The lotus, though lovely, requires its green leaves for support.

– Chinese Proverb

7.1 General principles for sample-holder design

I learned about sample holders the hard way during one of my first cryogenic measurements. Naively, I attached the ends of a metal test sample firmly to a Plexiglas™ base (hey, it was nice and shiny, and sure looked impressive under that sample). Then I precooled the assembly by dipping it into liquid nitrogen. When I pulled it out of the nitrogen to put it into liquid helium, I noticed the sample looked like someone had grabbed both ends and bent it into a colossal bow. I had no idea that the thermal contraction of acrylic plastic was so gigantic; it had completely buckled my sample . . . but it was the best-looking buckled sample I had ever seen. In another instance, I put a ceramic superconducting sample that was not quite flat on a very flat holder and ran high current through it in a magnetic field . . . . Cracked it all to pieces from the magnetic Lorentz force. The message—provide good mechanical support for high-current samples, and pick sample-holder materials carefully to match the thermal expansion of the sample (unless the sample is mounted in a strain-free manner; see Sec. 4.10).

An example of a simple but effective sample holder for measuring short, straight, high-current superconductors is shown in Fig. 7.1. Two copper pieces at the end of the holder act as a source of high-transport current for the sample. These copper blocks are separated by an insulator, which might consist of a piece of G-10 epoxy–fiberglass, since this has a total thermal contraction along the glass fiber direction that approximately matches that of high-T_c ceramic superconductors, such as YBCO. The sample rests flat against the G-10 insulator for support, and a twisted pair of voltage leads is soldered across the middle section of the sample. In this example, the temperature can be controlled by immersing the sample directly into a liquid cryogen, such as helium, neon, or nitrogen. Thus, with this rather simple arrangement, the main requirements of a sample mount are satisfied:

1. to provide uniform and stable *temperature control* of the sample;
2. to eliminate sample stress due to *differential thermal contraction* between the sample and holder;
3. to minimize *noise* from induced voltages and magnetic pickup by keeping the effective voltage-tap loop area as small as possible;
4. to provide well-designed current and voltage *contacts*, with enough space between each current contact and the nearest voltage lead to ensure that the current distribution is uniform in the region between the voltage taps;

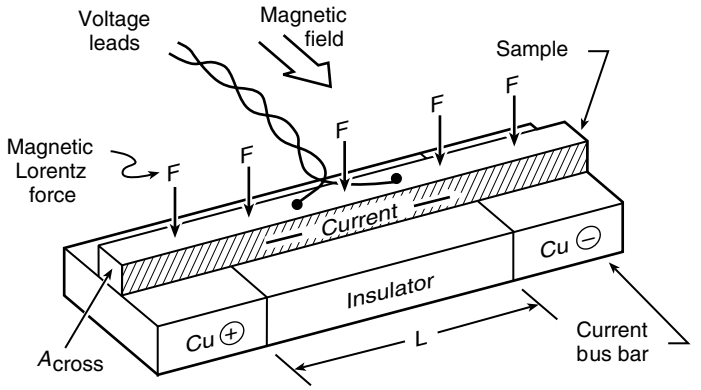

Fig. 7.1 Example of a sample holder for measuring critical current in short, straight samples.

5. to provide firm *mechanical support* for the sample, particularly for critical-current measurements where large, magnetic Lorentz forces are a major issue.

We will consider each of these factors in turn, for both bulk sample holders (Sec. 7.3) and thin-film sample holders (Sec. 7.4), along with examples and design techniques. First, however, we need to consider the general nature of *four-lead* measurements, since this technique determines the overall design of most transport-measurement sample holders.

The holder supports the sample against the magnetic Lorentz force F, and has a thermal contraction that matches that of the sample, eliminating the stress of differential thermal contraction. The long sample allows the current contacts to be located well away from the voltage-sensing leads so that they measure a *uniform* current distribution.

7.2 Four-lead and two-lead electrical transport measurements

One of the main challenges of cryogenic transport measurements (both bulk and thin film) is that large spurious voltages are generated by current flowing through the wires leading to the sample and through the joints where the leads are attached to the sample. In the two-lead method, only one pair of leads runs to the sample from the room-temperature instrumentation, in which case the voltmeter and current source share the same pair of leads, as illustrated in Fig. 7.2(a). The high current in these leads generates voltages along their length that are detected by the voltmeter, giving an erroneously high voltage V at the voltmeter,

$$V = (I - \varepsilon)(R_{\text{sample}} + 2R_{\text{contact}} + 2R_{\text{lead}}) - \varepsilon(2r_{\text{lead}}). \quad \text{Two-lead arrangement} \tag{7.1}$$

Here, I is the transport current supplied by the current source, ε is the current through the voltmeter, and the various resistances are defined by Fig. 7.2(a). Usually, $R_{\text{voltmeter}}$ is much larger than any of the other resistances in the circuit (typically, it is greater than $\sim 10^7\,\Omega$) and thus

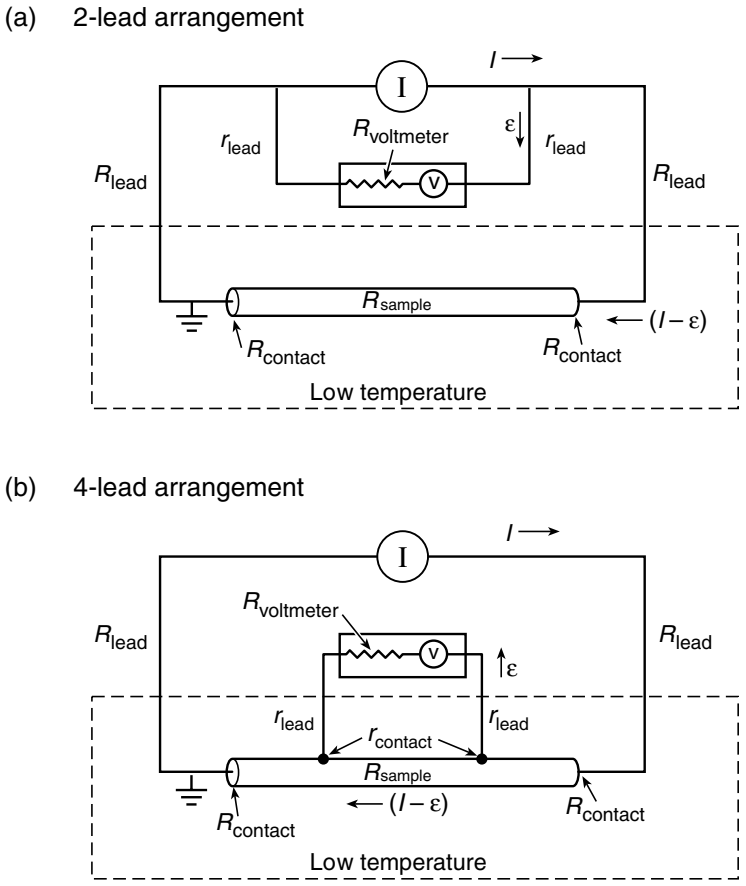

Fig. 7.2 (a) Two-lead arrangement and (b) four-lead arrangement for measuring transport properties.

$\varepsilon \ll I$, for which case Eq. (7.1) reduces to

$$V \cong I\,(R_{\text{sample}} + 2R_{\text{contact}} + 2R_{\text{lead}}). \tag{7.2}$$

Thus, the voltage detected at the voltmeter is not only that from the sample resistance R_{sample}, but artificially enhanced by voltages across the contact resistances R_{contact} and across the (usually) long instrumentation leads R_{lead}.

To avoid having these spurious voltages affect the voltmeter reading, a *separate* pair of twisted leads is usually run from the voltmeter, down the test probe (independent of the current leads), and attached directly across the central section of the sample, away from the current contacts. This so-called *four-lead* arrangement is diagrammed in Fig. 7.2(b).

In the four-lead case, the voltage measured by the voltmeter is given by

$$V = (I - \varepsilon)(R_{\text{sample}}) - \varepsilon(2r_{\text{contact}} + 2r_{\text{lead}}), \quad \text{Four-lead arrangement} \tag{7.3}$$

where I, ε, and the various resistances are defined by Fig. 7.2(b). Again, because $R_{\text{voltmeter}}$ is typically much larger than any of the other resistances in the circuit, $\varepsilon \ll I$ and Eq. (7.3) reduces to

$$V \cong I\,R_{\text{sample}}\,,$$

giving a true reading of sample voltage at the voltmeter. For this reason, almost without exception, a four-lead arrangement is used in both bulk and thin-film transport measurements, as well as in thermometry (Fig. 5.14).

Good wiring practice also calls for grounding the circuit at a *single* point, preferably close to the sample (not at the voltmeter), as shown in the circuit diagrams in Fig. 7.2. This minimizes the effect of currents flowing through ground paths. Make sure that the current and voltage leads are well isolated from each other and from ground (>10 MΩ). Also, for low-current measurements, shield the voltage leads from ac pickup, which can be rectified by bad contacts. These and other precautions to reduce voltage noise are described in Sec. 4.1.

7.3 **Bulk sample holders**

In this section, we describe techniques for meeting each of the five main design requirements, outlined at the beginning of this chapter, as they apply to sample holders for testing bulk (usually high-current) materials. (Holders for low-current thin-film samples are treated in Sec. 7.4.)

7.3.1 REQUIREMENT 1: SAMPLE TEMPERATURE UNIFORMITY AND CONTROL

When testing a sample immersed directly in a *liquid cryogen*, temperature measurement and uniformity along the length of the sample are usually not a problem (because of the excellent heat capacity and temperature uniformity of the liquid bath). The temperature of the liquid cryogen is usually varied by controlling the vapor pressure of the gas above the liquid (Sec. 1.2). To obtain a temperature that is *uniform* throughout the entire liquid bath, the temperature must be *monotonically* decreased (by lowering the vapor pressure of the gas). Then, as the liquid at the surface starts to cool, it becomes more dense and sets up natural convective stirring of the bath. On the other hand, if temperature is *raised* (by increasing the pressure of the gas vapor), a stable temperature stratification occurs throughout the depth of the liquid bath, where the top of the bath becomes warmer than the bottom. To break up this temperature stratification, the cryogenic liquid has to be stirred, or a resistive "bubbler" heater is placed in the bottom of the liquid bath to set up convective stirring (e.g. an inexpensive metal-film resistor with enough current passing through it to dissipate a few tens of milliwatts; metal-film resistors are used, as opposed to carbon resistors, because their resistance does not change much with temperature). This may sound trivial, but many weird (erroneous) effects trace their origin to neglect of the strong temperature stratification that can exist in cryogenic baths if the temperature is raised.

Temperature nonuniformity from variable convective cooling

When measurements cannot be carried out in a cryogenic liquid, we usually are faced with the challenge of maintaining sample-temperature uniformity in a *vacuum*, helium *vapor*, or other

such cryogenic gas. To illustrate, let us assume we have the common situation where the sample is surrounded by helium vapor, as with the dipper probe of Fig. 1.6 in the ullage space above the liquid surface. Further, let us assume that the ends of the sample are soldered to copper current contacts similar to those shown in Fig. 7.1, which are thermally anchored to a temperature-controlled base structure. In this case it is best to also thermally anchor the middle of the sample to a thermally conductive sample holder. However, this is not always possible if the sample is irregularly shaped or if the sample holder is an insulating material, as illustrated in Fig. 7.1.

In such a case, variable convective cooling along the sample can lead to nonuniform sample temperature if the gas temperature is uncontrolled and unknown, such as with the variable-temperature dipper probe of Fig. 1.6. One solution is to keep the sample length short enough that the sample's thermal conductivity will keep it uniform in temperature along its length and at the same temperature as the current contacts. But how short is short enough?

The answer depends on the thermal conductivity of the sample, compared with the convective heat-transfer rate to the variable-temperature gas wafting over the sample surface. In the absence of Joule heating (which we consider later) or another external heat source, the convective heat flow to the surrounding gas equals the conductive heat flow along the sample's length. That is,

$$\dot{q}_{\text{cond}} = \dot{q}_{\text{conv}},$$

and from Eqs (2.2) and (2.15),

$$\overline{\lambda} A_{\text{cross}} \Delta T_{\text{cond}}/(0.25\text{L}) = h A_{\text{surf}} \Delta T_{\text{conv}},$$

where $\overline{\lambda}$ is the mean thermal conductivity along the length of the sample of cross-sectional area A_{cross}, h is the convective heat-transfer coefficient between the surface of the sample and the cryogenic vapor, and A_{surf} is the cooled surface area. (In the above equation, we have approximated the conductive heat-transfer length as 25% of the total sample length L, because that is the mean distance heat has to travel from points within the sample to the nearest copper current contact.) Temperature control and uniformity will be achieved if the temperature difference along the sample ΔT_{cond} is small compared with the temperature difference between the sample surface and the surrounding vapor ΔT_{conv}; that is, we want $\Delta T_{\text{cond}}/\Delta T_{\text{conv}} \ll 1$.

From the above equation, this leads to the condition

$$h A_{\text{surf}} (\overline{\lambda} A_{\text{cross}})^{-1} (0.25\, L) \ll 1. \tag{7.4}$$

Condition for uniform sample temperature, assuming negligible Joule heating

When we apply this uniform-temperature condition to the common case of a round wire sample of length L and diameter D, we obtain from Eq. (7.4)

$$(h/\overline{\lambda})\,(L^2/D) \ll 1. \tag{7.4a}$$

Uniform-temperature condition for round wire samples, assuming negligible Joule heating

[Equation (7.4) is similar to the dimensionless Biot number ($\mathrm{Bi} \equiv h\ \vartheta/\lambda$, for example, Incropera and DeWitt 2002), but the condition is distinctly different, since the characteristic dimension ϑ for this long-sample situation is L^2/D, not the plate thickness that is normally used in applying the Biot number.] Note that the length of the sample enters in Eq. (7.4a) as the *square*; thus, it is difficult to maintain uniform temperature in long samples.

Example: Suppose the sample in Fig. 7.1 is a commercial superconducting wire containing ~50% copper as a stabilizer matrix (examples of typical conductor cross sections are shown in Fig. 7.24 of the addenda). Let us further assume the sample is a round wire (1 mm in diameter) that is suspended horizontally in helium vapor at a temperature near 4.2 K. (In practice, the sample shape and orientation do not make a great difference.) We want to determine how long we can make the sample and still maintain a controlled and uniform temperature along its length with only the ends of the sample thermally anchored to the temperature-controlled sample holder (assuming negligible Joule heating).

The first step is to determine the approximate thermal conductivity along the length of the sample, $\overline{\lambda}$. The value $\overline{\lambda}$ of will be dominated by the pure copper stabilizer, rather than by the other components of the superconductor composite (a result of the configuration of practical superconducting composites, as described in Sec. 7.5.2). We find the low-temperature thermal conductivity of a pure conductor, such as copper, most easily from its *electrical* resistivity ρ_{res} by using the Wiedemann–Franz–Lorenz law, as outlined in Sec. 6.4. We could measure ρ_{res} directly by using a simple dip test in liquid helium, but it is probably not worth the effort for approximation purposes. Invariably, commercial superconductors have a copper-stabilizer material with a RRR on the order of 100, which, from Eq. (6.11), corresponds to a low-temperature residual electrical resistivity of about

$$\rho_{\mathrm{res}} \cong \rho_{\mathrm{i\,295\,K}}/(\mathrm{RRR} - 1) = (1.69\ \mu\Omega\,\mathrm{cm})/(100 - 1) = 17\ \mathrm{n}\Omega\,\mathrm{cm}.$$

[Here, we have used the handbook value for the ideal resistivity $\rho_{\mathrm{i\ 295\ K}}$ of copper from Appendix A6.1.] From the Wiedemann–Franz–Lorenz law Eq. (6.15), this low-temperature electrical resistivity corresponds to a *thermal* conductivity λ for the copper in the sample of about

$$\begin{aligned}
\overline{\lambda}/(\sigma_{\mathrm{e}}T) &\equiv \overline{\lambda}/(\rho^{-1}T) = L_{\mathrm{N}} = 2.45 \times 10^{-8}\,\mathrm{V^2/K^2} \\
\overline{\lambda}(4.2\ \mathrm{K}) &= (2.45 \times 10^{-8}\,\mathrm{W\,\Omega/K^2})/(17 \times 10^{-11}\,\Omega\,\mathrm{m})^{-1}\,(4.2\ \mathrm{K}) \\
&= 6 \times 10^2\,\mathrm{W/(m{\cdot}K)}.
\end{aligned}$$

(This result agrees well with the value that happens to be listed in Appendix A6.7 for OFHC copper with RRR = 100; we went through this Wiedemann–Franz–Lorenz law procedure because it is much more useful for different materials and RRR values other than 100, where thermal conductivity data are generally not available.) Since the sample composite is only 50% copper, we can approximate the mean thermal conductivity of the sample $\overline{\lambda}$ as about $3 \times 10^2\,\mathrm{W/(m{\cdot}K)}$.

The convective heat-transfer coefficient h between the sample and helium gas at 4.2 K is obtained from Fig. 2.9, where we see that a horizontal rod of 1 mm diameter has a free (natural) convective coefficient h that is roughly equal to ~100 $\mathrm{W/(m^2K)}$ over several orders of magnitude of ΔT_{conv}.

Substituting this value of h and the mean thermal conductivity of the sample $\bar{\lambda}$ into the uniform-temperature criterion for round wire samples, Eq. (7.4a), and solving for L, we find that

$$L \ll (D\bar{\lambda}/h)^{0.5} = (1 \times 10^{-3}\,\text{m})^{0.5}[3 \times 10^{2}\ \text{W/(m·K)}]^{0.5}[100\ \text{W/(m}^2\,\text{K)}]^{-0.5}$$
$$\ll 5\ \text{cm} \quad \text{(or 50 wire diameters)}.$$

Therefore, temperature uniformity along the length of the sample would be achieved for sample lengths $\ll$ 5 cm (~50 wire diameters). This is a relatively short overall length for a sample with such a high thermal conductivity. Samples with lower thermal conductivity $\bar{\lambda}$ will have even shorter length requirements in helium vapor.

So, if the sample has a good thermal conductivity along its length and is relatively short ($\ll$50 diameters), the sample ends can be simply soldered to two copper blocks that are thermally anchored to a temperature-controlled base structure. On the other hand, if the uniform-temperature criterion of Eq. (7.4) is not met, either because the sample is too long or has a poor thermal conductivity, then we need to provide additional thermal anchoring of the sample along its length by attaching it to a high-thermal-conductivity sample *holder*. It can be made from a material such as sapphire (an electrical insulator) or, more commonly, high-conductivity pure copper, such as ETP copper (which can be electrically insulated from the sample by using the techniques described in Sec. 5.3.2). The condition for uniform sample temperature given in Eq. (7.4) is then applied to the length, cross-sectional area, and thermal conductivity of the sample *holder* (rather than just the sample alone). Representative thermal-conductivity data are given for a number of technical materials that can be used for sample holders in Fig. 2.1, and values are tabulated in Appendix A6.7.

The *time constant* for the thermal response of the sample holder can also be determined fairly easily if the uniform-temperature condition of Eq. (7.4) is met. In this case, we can assume that the entire sample holder is at a uniform temperature and therefore can be approximated by the "lumped capacitance" approximation. The thermal response of the sample holder is then given by its $R_{\text{th}}C_{\text{th}}$ time constant, where C_{th} is the thermal capacity (= mass times specific heat of the holder material) and R_{th} is the thermal resistance between the sample holder and cryostat heat sink [or, if the holder is cooled only by vapor, $R_{\text{th}} = (h A_{\text{surf}})^{-1}$ from Eq. (2.15)].

Temperature nonuniformity from Joule heating

Joule heating at electrical connections and within the sample can also be a major source of nonuniformity in sample temperature. This can occur whether the sample is liquid-cooled, end-conduction cooled, or gas cooled. Joule heating is perhaps the greatest challenge for most transport measurements.

Joule-heating errors are most easily minimized experimentally by raising the transport current through "ohmic" samples (i.e. they obey Ohm's law) until a noticeable change in resistance occurs, which indicates an unacceptable temperature shift. The experiment is then simply carried out at a transport current below this heat-affected level.

However, for samples that are not ohmic and have, instead, nonlinear voltage-current characteristics (such as superconductors), the option of operating at a lower current level is not available. In this case, the only choice is to maximize sample cooling and reduce contact resistance at the sample ends to an acceptable level.

How to achieve an acceptable level of Joule heating depends on the method of sample cooling. Three cases are quite common:

1. End-cooled samples with Joule heating distributed along the sample length. The result is a temperature rise in the middle of the sample given approximately by equating the rate of Joule heating to heat flow along the sample to the cooled ends,

$$\dot{q}_{\text{Joule}} = \dot{q}_{\text{cond}} = \overline{\lambda}\, A_{\text{cross}} \Delta T_{\text{cond}} / (0.25\, L),$$

   where ΔT_{cond} is the average temperature rise in the middle section of the sample and, similar to Eq. (7.4), $\overline{\lambda}$ is the mean thermal conductivity along a sample of length L and cross-sectional area A_{cross}. Here, the main options available for lowering ΔT_{cond} are to limit sample length L or (more commonly) to thermally anchor the sample to a sample holder with a high thermal conductivity, thereby increasing the effective A_{cross}, as described in the previous subsection.
2. Sample cooling with a high flow rate of temperature-controlled gas. In this case, the sample temperature is controlled by passing a continuous stream of temperature-controlled gas over the sample. The acceptable Joule heating level is usually determined empirically as a function of transport current and gas-flow rate. The main technique for limiting Joule heating errors is to increase the gas-flow rate. An example of a commercial (low-flow-rate) gas-flow cryostat for measurements with low Joule heating requirements was described in Sec. 1.4.6. An example of a custom-designed (high-flow-rate) cryostat that can handle the Joule heating loads of bulk superconductor critical-current testing is given in Sec. 9.4.3.
3. Liquid-cooled samples with high transport currents. This is the situation usually encountered in critical-current measurements. Here, the main Joule-heating problem is to keep the sample *contact* resistances low. This is accomplished by making high-quality contacts and designing the sample holder to provide enough cooled contact area. How to determine the minimum contact area for a particular type of superconductor is illustrated by several example calculations in Sec. 8.5.

Practical illustrations of bulk sample holders

To illustrate these various situations, let us consider the design of a sample holder for measuring the critical current of *long* superconductor samples. The most popular sample holder for this type of measurement is the tubular holder shown in Fig. 7.3 (also called a barrel, drum, cylinder, or "Rutherford" sample holder). The ends of the sample are soldered to two copper end rings to introduce high current into the sample. This is just a spiral variant on the generic sample holder illustrated in Fig. 7.1.

When the sample holder is immersed in a cryogenic *liquid*, temperature uniformity and control is usually not a problem, and the middle of the tubular holder can be fiberglass–epoxy or another insulator. In the case of superconductor testing, even moderately conducting alloy materials can be used without insulation (such as brass, stainless steel, beryllium copper, or

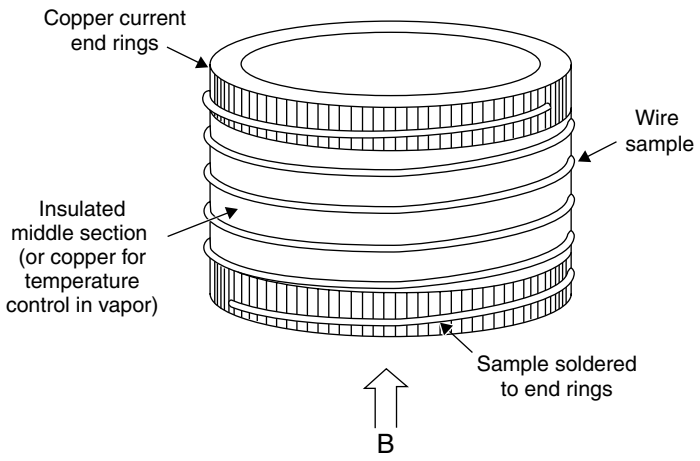

Fig. 7.3 Tubular sample mount for measuring coiled conductors in the small bore of a high-field solenoidal magnet. For testing in a liquid cryogen, the middle section does not have to be made from a high-conductivity material, and it can be chosen to match the thermal contraction of the sample. For testing in vapor, the middle section is usually made of copper to provide temperature uniformity along the sample.

Ti–6%Al–4%V) since the effective electrical conductivity of the superconductor is so much greater than that of the alloys.

However, when the holder is used in *vapor*, the middle section of the tube shown in Fig. 7.3 is usually made of relatively pure copper to thermally anchor the sample along its length. The copper middle section is electrically insulated from (but thermally connected to) the current end rings with insulation breaks, such as thin Kapton™ sheets, for example. The sample itself also needs to be electrically insulated from the copper middle section (to avoid current from bypassing the sample through the high-conductivity holder) by coating the surface of the copper middle section with either varnish, or cigarette paper soaked with varnish, or Mylar™, or thin Kapton™ tape. The sample can be *thermally* attached to this insulated coating in a reversible manner by using grease, such as Apiezon N™ grease, Cry-con™ thermal grease, or common silicone vacuum grease. The grease freezes on cooling and thaws on warming, so it can be easily removed. (Incidentally, frozen petroleum jelly is mechanically much weaker than frozen silicone vacuum grease and does not hold structurally as well at low temperatures.) For samples that might be remeasured, it is usually worth making a custom sample subholder on which the sample is permanently mounted. In this case, an epoxy such as Stycast 2850FT™ can be used, but once the epoxy sets, the sample is fixed.

When the difference in thermal contraction between the sample and holder is a concern (described in the next section), an in-between technique can be used to achieve some temperature stability along the sample length without firmly bonding the sample to the holder. The technique consists of taping the sample to a high-thermal-conductivity holder, such as varnished covered copper, with Teflon™ tape or dental floss, as described in Sec. 5.3.2 for thermometers. Alternatively, the sample can be sandwiched between two highly conductive supports, as with the sample mounts made of silver in Fig. 7.4 (useful for angle measurements described later in Sec. 9.4.2). Kapton™ or Teflon™ tape is wrapped around the assembly to

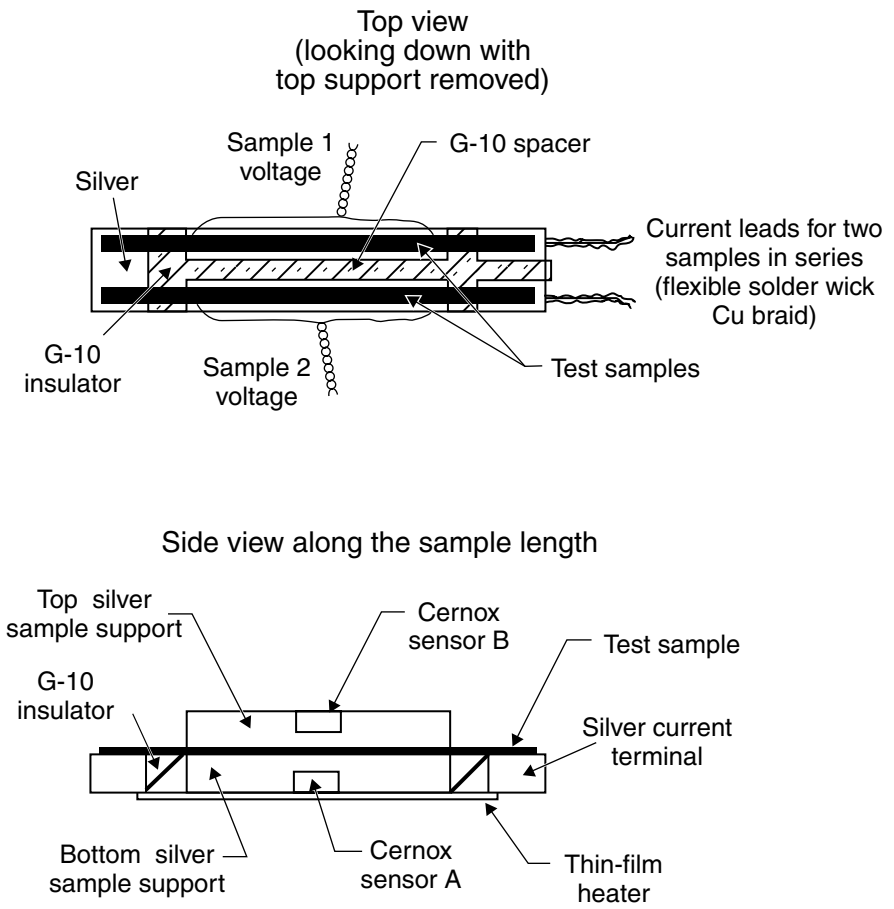

Fig. 7.4 Dual sample holder for variable-angle measurements, where the samples are sandwiched between two supports made of silver, to provide good thermal stability as well as to match the thermal expansion of the test samples (in this case, silver-sheathed bismuth-based HTS samples). A G-10 spacer is used to direct the flow of current through the two samples. The top support inserts into the bottom piece for alignment (not shown), and the entire "sandwich" is taped together with Teflon™ tape. The support pieces are equipped with a thin-film heater and two thermometers, one to control the heater and the other to monitor the sample temperature. (Adapted from Herzog et al. 1994.)

hold the top and bottom pieces together. Such a tape covering also helps promote temperature uniformity by protecting the sample from fluctuating convective gas currents.

7.3.2 REQUIREMENT 2: THERMAL CONTRACTION OF THE SAMPLE HOLDER AND STRAIN-FREE MOUNTING TECHNIQUES

As noted in the introduction, a mismatch in the thermal contraction between the sample and holder can significantly influence the measurement. In the case of brittle materials, such as high-T_c superconductors, the mismatch can potentially fracture the sample. The effect can also

be more subtle, as in low-T_c superconductors with an A15 crystal structure (see Appendix A6.6), where strain introduced by the sample holder can lower the apparent critical current by a substantial amount (reduction by 50% is not unusual) at high magnetic fields (see Sec. 10.5.1).

We can approach the thermal-contraction mismatch problem in several ways: (1) The simplest is to *select* a sample-holder material with a thermal contraction that approximately matches that of the sample. (2) When that is not possible, a composite sample holder can be made with a thermal contraction *engineered* to match the sample. (3) Failing all else, a universal floating mount with a *flexible current lead* can be made. We will consider each approach in turn.

Choosing a sample holder with a thermal contraction that matches the sample

When testing in a liquid cryogen, or when only the ends of the sample need be thermally anchored [i.e. the uniform-temperature condition is met, Eq. (7.4)], we do not need a sample-holder with a high thermal conductivity, and, thus, we are free to choose just about any sample-holder material for which the thermal contraction matches that of the sample. The holder material can be an alloy, fiberglass–epoxy composite, or pure conductor. Total thermal contractions on cooling from room temperature to 4 K and 77 K are collected for some of the common sample-holder materials in Appendix A7.4. To make material selection easier, the materials are arranged in ascending order of thermal contraction within each material group. For materials not listed in the table, the calculational technique given in Eq. (6.5) can be used to estimate $\Delta L/L$ between two arbitrary temperatures; for metals, the quick method given in the tip of Sec. 6.2.1 can also be used.

The upper reference temperature in the table of Appendix A7.4 is not given as the ice point, as is commonly tabulated, but rather room temperature (293 K), since that is where most sample mounting is done (unless you like cold hands). Also included in Appendix A7.4 is the room-temperature coefficient of thermal contraction $\alpha_{293\,\mathrm{K}}$, since samples are often *soldered* in place, which further raises the starting temperature for differential thermal contraction, up to the melting temperature of the solder (Appendix A3.7). At room temperature and higher, the thermal expansion of most materials is nearly linear, so that $\Delta L/L$ on cooling from some upper reference temperature T_u other than room temperature (but close to it) can be calculated simply from [ref. Eq. (6.4)]

$$\Delta L/L_{T_u-T} = \Delta L/L_{293\,\mathrm{K}-T} + \alpha_{293\,\mathrm{K}}\,(T_u - 293\ K). \tag{7.5}$$

(Below room temperature, α starts to decrease and is no longer constant, as can be seen from the slope of the thermal contraction data in Figs 6.4 through 6.7.)

The data in Appendix A7.4 show that insulating materials have a very wide range of thermal contraction, from ~0.06% for Pyrex™ glass, through ~1.2% for my good ol' buddy Plexiglas™, to over 2% for TFE (Teflon™). Also, notice the very large *anisotropy* in the thermal contraction of the G-10 fiberglass–epoxy composites and cotton–phenolic composites. Along the fiber direction (warp), the contraction is much (about one-third!) less than that perpendicular to the plane of the glass fibers. So think about the direction of the fibers before machining a fiberglass–epoxy sample holder.

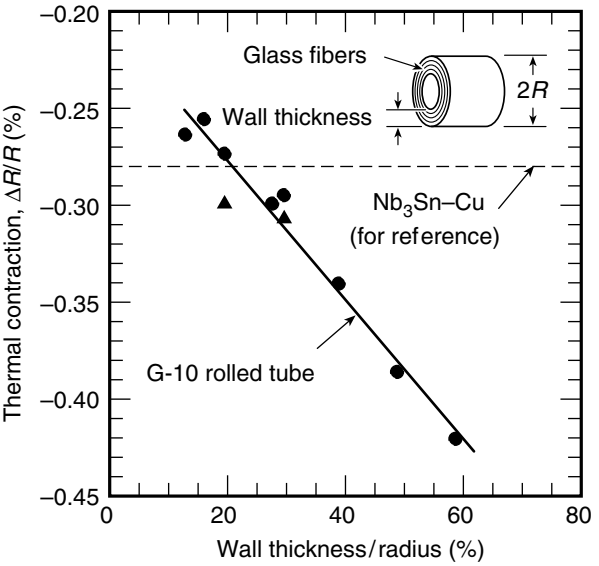

Fig. 7.5 Thermal contraction of the radius $\Delta R/R$ on cooling from 293 to 76 K for G-10 fiberglass–epoxy "rolled" tubes (where the glass fibers run around the tube circumference). Note the strong dependence of the thermal contraction for rolled tubes on the ratio of the tube's wall thickness to radius. For comparison, the thermal contraction of a Nb_3Sn superconductor is shown by the horizontal dashed line (from Goodrich et al. 1990).

Tubular sample holders of G-10 fiberglass–epoxy composites are a special case. Figure 7.5 shows the thermal contraction of the radius of "rolled" tubes (where the glass fibers run around the tube's circumference). As shown in Fig. 7.5, the radial thermal contraction of thin-wall tubes is much less than that for thick-wall tubes. This difference occurs because thin-wall rolled tubes behave like flat plates, whereas thick-wall tubes (or in the limiting case, solid rods) are dominated by the great contraction of the epoxy filler in the radial direction.

On the other side of the mismatch problem (the sample side), Appendix A7.5 gives the thermal contraction values for some of the more common *superconductor* materials. To illustrate the use of these two tables in selecting sample-holder materials, let us consider the ubiquitous challenge of designing a sample holder for transport measurements of Nb_3Sn superconductor samples in liquid helium. Sample-holder selection significantly affects the measured transport properties of this material (and of all the A-15 superconductors, for that matter), since at high magnetic fields the critical current can change by several tens of percent when the sample experiences a strain of only a few tenths of a percent (Sec. 10.5.1).

Example of selecting a sample-holder material for Nb_3Sn: When dip-testing a Nb_3Sn composite (typically containing 10% Nb_3Sn) in liquid helium, we see from Appendix A7.5 that the thermal contraction $\Delta L/L_{293\,K-4\,K}$ of the superconductor will be about 0.30% when it is cooled from 293 to 4 K. Fortunately, $\Delta L/L_{293\,K-4\,K}$ is usually in the range of 0.30% for most practical Nb_3Sn samples. [In Appendix A7.5 we see, for example, that $\Delta L/L_{293\,K-4\,K}$ decreases only a little (to 0.28%) if the volume fraction of the Nb_3Sn core is doubled from 10% to 20%.] So, 0.30% is our target value in selecting a sample-holder material. (For most materials, thermal contraction curves are similar enough that if the total $\Delta L/L$ from 293 K to 4 K is correct, the entire curve is approximately right, even at intermediate temperatures; see Figs 6.4 through 6.7.)

Let us look at several sample-holder material options for matching the 0.30% contraction of this test sample. If we have G-10 fiberglass–epoxy rolled tubes, and we trust that the volume fraction of epoxy to fiberglass filler is similar to that of the rolled tube composite whose data are shown in Fig. 7.5

(probably a good assumption), then we could use a tube with a wall thickness equal to about 20% of the radius, which will give us the desired match in thermal contraction between sample and holder.

We can also look at other more common (isotropic) choices for a sample-holder material by referring to those listed in Appendix A7.4. There we see that Ti–6%Al–4%V, which is sometimes used for testing Nb_3Sn, has a thermal contraction ($\Delta L/L_{293\,K-4\,K} = 0.173\%$) that is about half that of Nb_3Sn composites. This mismatch results in the sample being placed under a significant *tensile* strain of about 0.13% on cool-down, which artificially increases the sample's critical current because of the strain effect in the A-15 superconductors [about a 25% enhancement for Nb_3Sn at 16 T, for example (Sec. 10.5)].

On the other hand, we see from Appendix A7.4 that epoxying the Nb_3Sn sample onto 304 stainless steel (usually in the form of a thin-walled cylinder to minimize weight and cool-down time) gives a sample-holder thermal contraction of $\Delta L/L_{293\,K-4\,K} = 0.29\%$ to 0.31% (depending on the stainless-steel alloy), which would result in a nearly strain-free sample mount (mismatch of less than ~0.01%). Another good choice would be beryllium–copper (Cu–2%Be, UNS C17200), for which $\Delta L/L_{293\,K-4\,K} = 0.31\%$, corresponding to a mismatch of less than ~0.02%. Beryllium–copper also has the advantage that the sample can be easily soldered to the sample mount, rather than epoxied. (Beryllium–copper is relatively safe to machine if the practices given in the tip at the end of Sec. 1.6.1 are followed.)

For most high-field measurements of critical current, it is essential to firmly attach the sample to a sample holder of tubular shape in order to support the magnetic Lorentz forces acting on the sample, as well as to prevent sample motion, which can lead to noise and instabilities. The above example assumes that we adhere the sample to the holder with some kind of *room-temperature* adhesive, such as epoxy or vacuum grease. Now let us look at the case of *soldering* the sample to the holder, which raises our starting temperature for differential thermal contraction to the melting temperature of solder.

Example of Nb_3Sn soldered to the sample holder: If the Nb_3Sn wire is soft-soldered to a beryllium–copper (Cu–2%Be) sample holder, the sample mounting temperature will be raised to the melting temperature of soft-solder, about 183°C for common eutectic 63%Sn–37%Pb solder (from Appendix A3.7). (We do not need to worry about electrically isolating the sample from the holder because the superconductor's electrical conductivity is orders of magnitude greater than that of beryllium–copper or any of these alloys.) The 163 K increase above room temperature results in additional thermal expansion, which, from Eq. (7.5) and the value of α given in Appendix A7.4, gives a total $\Delta L/L$ for beryllium–copper of

$$\begin{aligned}\Delta L/L_{456\,K-4\,K} &= \Delta L/L_{293\,K-4\,K} + \alpha\,\Delta T \\ &= 0.0031 + (18.1 \times 10^{-6}\,K^{-1})(163\,K) \\ &= 0.0061\ (= 0.61\%). \qquad [\text{Cu–2\%Be}]\end{aligned}$$

On the other side of the mismatch calculation (the Nb_3Sn side), we use a value for α of about $17 \times 10^{-6}\,K^{-1}$, since the thermal expansion of practical Nb_3Sn composites is dominated by bronze ($\alpha = 18.8 \times 10^{-6}\,K^{-1}$, from Appendix A7.5) and copper (the thermal expansion of which is nearly equal to that of bronze: $\alpha = 16.7 \times 10^{-6}\,K^{-1}$). From Eq. (7.5), we then have for the Nb_3Sn composite a total $\Delta L/L$ of

$$\begin{aligned}\Delta L/L_{456\,K-4\,K} &= 0.0030 + (17 \times 10^{-6}\,K^{-1})(163\,K) \\ &= 0.58\%, \qquad [Nb_3Sn\ \text{composite}]\end{aligned}$$

which is still within 0.03% of that of the beryllium–copper sample holder. A similar result (a mismatch of only 0.03%) would be obtained if the sample-holder material were stainless steel, either AISI 304 or 316 (the latter is preferred because it is less magnetic; see Appendix A6.8c).

So, for testing Nb_3Sn wire, whether soldered, greased, or epoxied to the sample holder, beryllium–copper or stainless steel are excellent material choices for avoiding the artifacts of strain induced by the sample holder.

Turning to the high-T_c superconductors, we see from Appendix A7.5 that the thermal contraction of ceramic materials is smaller than that of metallic low-T_c superconductors. For example, polycrystalline YBCO has a $\Delta L/L_{293\ \mathrm{K}-4\ \mathrm{K}}$ of only 0.23%, compared with 0.30% for Nb_3Sn (whereas in the Cu–O plane, or *a–b* direction, the average $\Delta L/L_{293\ \mathrm{K}-4\ \mathrm{K}}$ for YBCO is only 0.16%). We see from Appendix A7.4 that if we mount a piece of this brittle material on stainless steel ($\Delta L/L_{293\ \mathrm{K}-4\ \mathrm{K}} = 0.30\%$), the differential thermal contraction would compress the sample on cool-down. On the other hand, the thermal contraction of Inconel 718 ($\Delta L/L_{293\ \mathrm{K}-4\ \mathrm{K}} = 0.24\%$) matches that of YBCO quite closely.

If an insulating sample holder is desired, a G-10CR sample holder *with the fiberglass parallel to the sample* (warp direction) would do the trick ($\Delta L/L_{293\ \mathrm{K}-4\ \mathrm{K}} = 0.24\%$). However, if the sample is soldered to copper bus bars embedded in a G-10 sample holder, the additional thermal expansion of the sample above room temperature must be accounted for, as in the example above. Fortunately, the room-temperature coefficient of thermal expansion for both Inconel and G-10CR (warp direction) ($\alpha \cong 13 \times 10^{-6}\ \mathrm{K}^{-1}$, from Appendix A7.4) is similar to that of polycrystalline YBCO ($\alpha \cong 12 \times 10^{-6}\ \mathrm{K}^{-1}$). However, for G-10 sample holders, keep in mind that, when heating to soldering temperature, the sample will expand more quickly than the sample holder because of G-10's low thermal diffusivity. This can be minimized by heating the G-10 sample holder slowly (on a hot plate, for example) so it will be warmed close to soldering temperature, thus keeping temperature equilibrium between the holder and sample, and avoiding tensile strain on the brittle ceramic during subsequent cool-down.

Composite sample holder with an engineered thermal expansion

When a sample-holder material with a thermal expansion matching that of the sample cannot be found easily, another approach is to make a composite sample holder that is engineered to match it. A composite of G-10 and copper works very nicely, as shown by the arrangement in Fig. 7.6.

Suppose, for example, we wish to measure an *a–b*-textured (i.e. crystalline grains aligned along the *a–b* directions) sample of YBCO using room-temperature contacts (such as pressure contacts of silver paint or indium, rather than soldered contacts). From Appendix A7.5 we find that the sample will have an average thermal contraction in the *a–b* plane $\Delta L/L_{293\ \mathrm{K}-4\ \mathrm{K}}$ of about 0.16%. From Appendix A7.4 we see that the thermal contraction of G-10CR in the warp direction ($\Delta L/L_{293\ \mathrm{K}-4\ \mathrm{K}} = 0.24\%$) is too large, but a smaller effective $\Delta L/L$ can be created by using the opposing combination of G-10CR and copper ($\Delta L/L_{293\ \mathrm{K}-4\ \mathrm{K}} = 0.32\%$). That is, in Fig. 7.6, we want

$$\Delta L_{\text{G-10}} - 2\Delta L_{\text{Cu}} = \Delta L_{\text{sample}}. \tag{7.6}$$

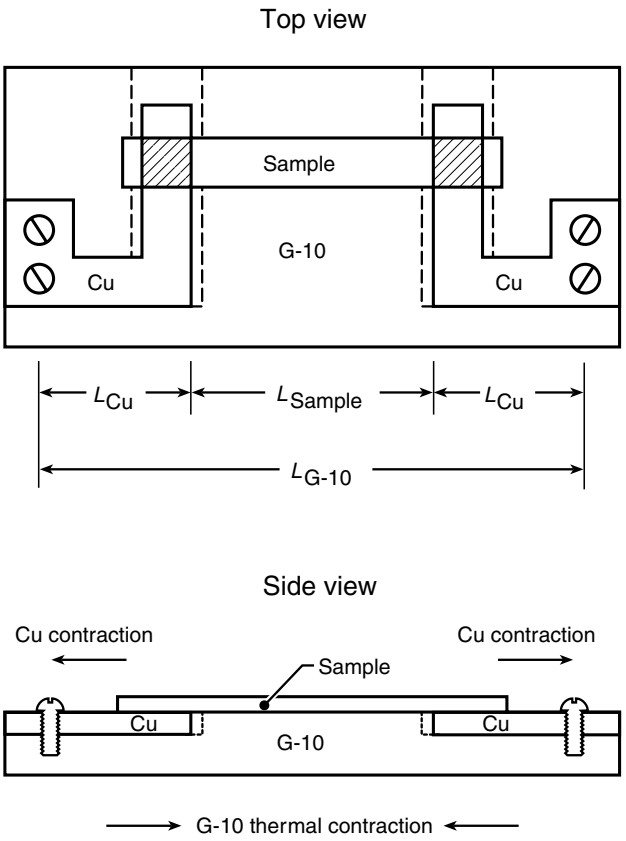

Fig. 7.6. Composite sample holder engineered to match the thermal contraction of the sample by use of a copper bus bar with a length given by Eq. (7.7). The sample is soldered to the two copper bus bars, but it is not attached to the G-10 support. The dashed lines indicate a small additional area that is cut out of the G-10 holder to accommodate the thermal contraction of the copper bus bars.

So we choose the relative lengths of copper and G-10CR in the sample holder to satisfy the condition

$$L_{\text{G-10}}(\Delta L/L)_{\text{G-10}} - 2L_{\text{Cu}}(\Delta L/L)_{\text{Cu}} = L_{\text{sample}}(\Delta L/L)_{\text{sample}}. \tag{7.7}$$

Example: Assume the YBCO sample length is 12 mm between the copper bus bars, and the G-10CR sample holder is 20 mm long between the screw anchor points for the copper bus bars ($L_{\text{G-10}}$ in Fig. 7.6). Then from Eq. (7.7) we have

$$(20\text{ mm})\,(0.24\%) - 2L_{\text{Cu}}(0.32\%) = (12\text{ mm})\,(0.16\%).$$

Thus, the thermal contraction of the holder will match that of the sample, if the length of the copper arms (L_{Cu} in Fig. 7.6) is 4.5 mm.

The right-angle bend in the copper arms of Fig. 7.6 could be omitted, but it provides a length orthogonal to the sample, which adds some flexibility to accommodate any residual mismatch in thermal contraction.

This engineered sample-holder approach also works if the test sample has a thermal contraction *larger* than G-10CR (but still smaller than that of copper). Such a situation can be accommodated simply by making the G-10CR holder with the copper arms flipped around (so the separation of the screw anchor points is shorter than the sample length, rather than longer).

If many different types of samples are being tested, or if repeated mounting and demounting will damage the sample or its contacts, it may pay to design a custom sample holder for each sample *that stays connected to the sample*. Each sample holder can then be designed to

1. match the thermal contraction of the sample;
2. eliminate the need to remake sample contacts.

This is particularly effective for experimental samples that are valuable and whose contact interface will degrade significantly if soldered and resoldered (see, for example, the subsection on soldering challenges for current contacts to high-T_c superconductors in Sec. 8.3.3).

Flexible current leads

If all else fails and we need to test a variety of samples with different thermal contraction coefficients, it may be simpler to design a sample holder for general use with a flexible current lead to avoid sample stress during cooling. An example of such a sample holder is illustrated in the section on flexible current leads, Sec. 4.10.

7.3.3 REQUIREMENT 3: INSTRUMENTATION WIRING—KEEP THE LOOP AREA SMALL

Next we turn to the problem of sample-holder *wiring*. For the voltage leads, surprisingly large voltages can be induced by time-varying magnetic fields passing through the small loop area formed between the two voltage leads. *Twisting* the voltage leads right up to the sample, as shown in Fig. 7.7, minimizes the effective loop area of the voltage taps. The twist reverses the sign of the induced voltage every half twist, largely canceling the overall effect. Also, to further reduce magnetically induced noise voltages, orient the remaining loop area where the leads attach to the sample so the area is *coplanar* to the direction of the magnetic field (Fig. 7.7).

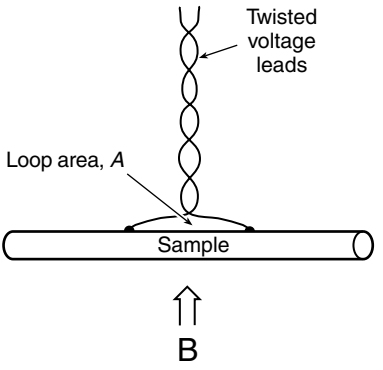

Fig. 7.7 Twist voltage leads close to the sample and align the effective loop area *A* coplanar with the direction of the magnetic field to reduce inductive noise voltage arising from magnetic-field variations or sample motion.

Usually, after attaching the voltage taps, I gently pull the twisted leads away from the sample along the direction of the applied background field to line up the plane of the remaining loop area with the field direction. This may sound like a trivial detail, but it makes a significant difference when testing in a high magnetic field.

Quantitatively, the induced voltage noise can be estimated from Faraday's law. If the loop area were aligned perpendicular to the applied magnetic field, the time rate of change of magnetic flux ϕ through the loop area A in Fig. 7.7 would be

$$V = \mathrm{d}\phi/\mathrm{d}t = A\,\mathrm{d}B/\mathrm{d}t, \tag{7.8}$$

where B is the magnetic field, and the sign of the voltage (from Lenz's law) is such so that it opposes the magnetic-field change.

Example: For a typical voltage-tap loop area A on the order of 1 cm^2, we can calculate the magnetic-field change $\mathrm{d}B/\mathrm{d}t$ that would induce a noise voltage of 0.1 μV (a typical voltage detection limit in short-sample superconductor testing),

$$\mathrm{d}B/\mathrm{d}t = A^{-1}V = (10^{-4}\,\mathrm{m}^2)^{-1}(10^{-7}\,\mathrm{V}) = 10^{-3}\,\mathrm{T/s}.$$

Thus, it does not take much of a change in magnetic field to induce voltages that are comparable to those we are trying to measure. For a typical background test field of 10 T, this would require a magnetic-field stability of better than 1 part in 10^4 per second.

So it really pays to make the area of the voltage-tap loop as small as possible and to align it coplanar with the magnetic-field direction. Similarly, very small *sample motion* or *vibration* can also induce noise voltage, since this is just an alternate way of producing $\mathrm{d}\phi/\mathrm{d}t$.

For a tubular-shaped sample holder, twisting the leads right up to the tube does not work. In the usual orientation, where the tube axis is parallel to the field (Fig. 7.3 or 7.8), the sample between the voltage taps makes N turns perpendicular to the field. This produces

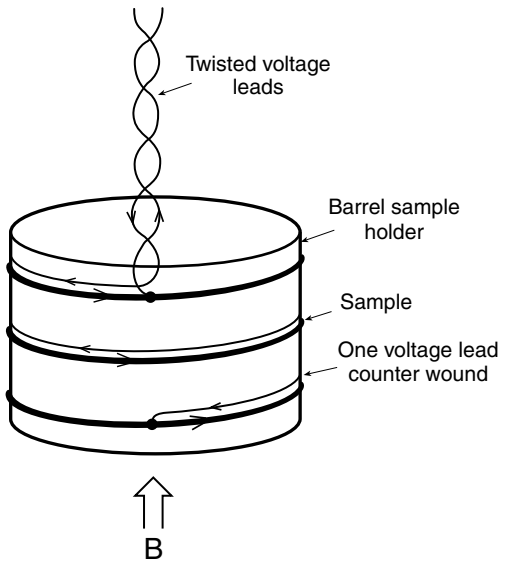

Fig. 7.8 Noninductive winding scheme, where one of the voltage leads is wound counter to the test sample to minimize the loop area and induced electromagnetic noise.

a large effective loop area perpendicular to the field that is N times the cross-sectional area of the cylinder. We can minimize this effective area by using a noninductive winding scheme in which one of the voltage leads is *wound counter* to the test sample, as shown in Fig. 7.8.

7.3.4 REQUIREMENT 4: VOLTAGE-TAP PLACEMENT AND CURRENT-CONTACT LENGTHS

When selecting wire for the voltage taps to the sample, it is best to use a wire with a diameter much less than the diameter of the sample (or its transverse dimension). Large voltage leads are hard to bend. If they are too large, it becomes a case of the tail wagging the dog—that is, the voltage lead can twist the test sample, bend it, or break the contact between the lead and sample. Usually I would use voltage leads as fine as I can conveniently handle, rarely larger than about #36 AWG (~0.125 mm). Sometimes, for very thin samples, even finer voltage wires are needed. In this case, an optical microscope helps when attaching the leads.

Whereas the material covered in this book up to this point has been applicable generally to testing most cryogenic samples, the remainder of this section focuses specifically on high-current superconductors. Since almost all practical high-current superconductors are *multifilamentary* in nature, this raises special considerations in selecting attachment points along the sample for the voltage taps. (Again, Sec. 7.5.2 gives a brief tutorial description of the unique multifilamentary geometry of high-current superconductors.)

Three lengths are important when testing *multifilamentary* composite samples, as illustrated in Fig. 7.9. If these are not correct, strange erroneous voltages can result. We first introduce each of the lengths and then describe the strange voltages that originate when the first two lengths are too short.

Length 1: The contact length (#1 in Fig. 7.9) determines the contact area between the current bus and sample. It should be large enough that Joule heating at the interface is limited to an acceptable level. (Example calculations of required contact areas are given in the next chapter, Sec. 8.5.) A further requirement on length #1 for twisted multifilamentary conductors is that the contact should extend over at least one twist length, also called the twist pitch [Fig. 7.24(a)]. This requirement ensures that current is distributed more uniformly among the outer filaments and helps eliminate erroneous voltages, as described under the following heading "twist-pitch effect."

Length 2: The distance between the end of the current-contact and the nearest voltage tap (the "current-transfer length," #2 in Fig. 7.9) must be sufficiently long that the current leaving the current contact can be distributed to all the inner filaments before it reaches the first voltage tap. When length #2 is too short, spurious voltages are seen by the voltage taps as current continues to cross the resistive matrix. Below, we look at the requirements on sample-holder design to avoid this problem.

Length 3: The voltage-tap separation determines the electric field *sensitivity* of the measurement: the greater the distance between the two voltage taps, the greater the potential difference that will be produced (for a given electric field along the sample length). Ideally, we would like length #3 to be as long as possible, but it is limited by lengths #1 and #2, and the available overall sample length.

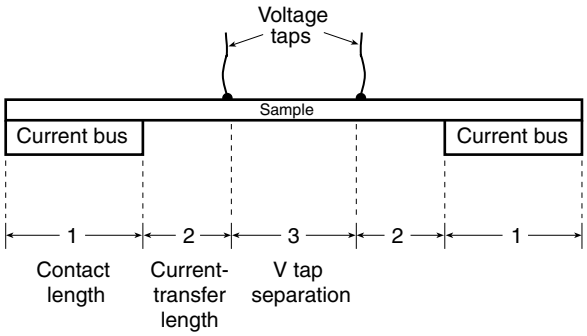

Fig. 7.9 Relevant lengths for voltage-tap placement and current-contact lengths.

We now look specifically at the *current-transfer length* (#2) and the *twist effect length* (#1). Length #3 is simply what is left over.

Strange voltages of the first kind: the current-transfer length

The sample holder needs to be designed so that the length (#2 in Fig. 7.9) between the current-bus contacts and the voltage taps is enough for current to cross the resistive matrix and uniformly fill the superconducting parts of the conductor. Otherwise, large current-transfer voltages will mask the intrinsic superconductor characteristic we are trying to measure. For homogeneous samples (i.e. no resistive matrix), the required length is about equal to the diameter of the sample. However, for nonhomogeneous samples, the required current-transfer length can be tens or even hundreds of sample-wire diameters long, especially in practical multifilamentary composite superconductors with very highly conductive filaments separated by a low-conductivity matrix (such as with Nb_3Sn/bronze composites or multilayer tape conductors).

Consider, for example, a typical multifilamentary Nb_3Sn composite [shown in cross section in Fig. 7.24(b) in Sec. 7.5.2]. Current introduced into the outer copper stabilizer must penetrate a considerable amount of resistive bronze to reach the inner superconducting filaments, a process that generates large spurious current-transfer voltages. The amount of current crossing the resistive matrix is greatest near the current contact and falls off as the square of the distance from the contact.

Often, the current-transfer voltage manifests itself as a large ohmic voltage, illustrated by the linear voltage–current characteristic in Fig. 7.10(b). Methods of extracting the intrinsic superconductor voltage from the current-transfer voltage are described in detail in Sec. 10.2 on critical-current data analysis. Here, we are concerned with how to reduce this spurious voltage in the first place through good sample-holder design. The technique is basically to make length #2 long enough. But how long is long enough?

That depends on how sensitive a measurement we wish to make. If we assume the resistivity detection limit of our measurement is $\rho^\star$, then, to a good approximation, the required current-transfer length $x_{\min}$ required to keep the current-transfer voltage small compared to our detection limit is given by the relation (Ekin 1978)

$$x_{\min} = D\,(0.1/n)^{0.5}\,(\rho_m/\rho^\star)^{0.5}, \quad \text{Current-transfer length} \tag{7.9}$$

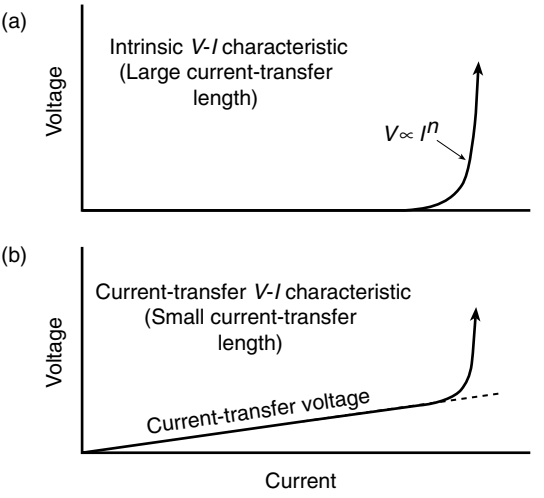

Fig. 7.10 Influence of current-transfer voltage on the voltage V vs. current I characteristic of a superconductor: (a) typical intrinsic V–I characteristic of a superconductor composite measured with a long current-transfer length between the voltage taps and current contacts; (b) V–I characteristic altered by a (typically linear) current-transfer voltage measured on a sample instrumented with a short current-transfer length (from Ekin 1978).

where D is the sample diameter and ρ_m is the sample's matrix resistivity. The parameter n is an index of the *nonlinearity* of the sample's intrinsic V–I characteristic (in the absence of current-transfer voltage), defined by

$$V \propto I^n. \quad \text{Definition of nonlinearity index } n \tag{7.10}$$

(The characteristic is linear for $n = 1$ and increasingly nonlinear for higher values of n. For good multifilamentary superconductors, n typically ranges from about 20 to 50; the higher the value, the better.) Equation (7.9) simply says that the current-transfer length is directly proportional to the wire diameter, which makes sense, since the greater the wire diameter D, the more matrix material there is to traverse, and the larger the required x_{min}. Similarly, a larger matrix resistivity ρ_m also requires a longer current-transfer length because the current crossing the matrix produces a larger voltage. The parameter n enters because a highly nonlinear V–I characteristic (high n value) will force current transfer to occur over a shorter distance.

Figure 7.11 shows a plot of Eq. (7.9) for determining current-transfer lengths in two common low-T_c superconductors, Nb–Ti/copper and Nb_3Sn/bronze. Current-transfer lengths are usually short for conductors having a matrix with a low resistivity, such as Nb–Ti/copper ($\rho_m \cong 1.4 \times 10^{-8}\ \Omega$cm), and about an order of magnitude greater in high-matrix-resistivity conductors, such as Nb_3Sn/bronze composites ($\rho_m \cong 2 \times 10^{-6}\ \Omega$cm).

Example: Suppose we are designing a sample holder to test multifilamentary Nb_3Sn conductors. In this material, n is typically about 30. We see from Fig. 7.11 that to measure a resistivity as low as $\rho^* = 10^{-12}\ \Omega$ cm will require a current-transfer length x_{min} of about 80 wire diameters. Thus, for a typical strand diameter of 0.6 mm, this would require a 5 cm length of conductor between the edge of the current contact and the voltage tap. Conductors with a slightly different transition parameter (n value) will not alter this much—an n of 40 would only shorten the current-transfer length to a little over 4 cm.

On the other hand, when testing Nb–Ti/copper composites, where the copper matrix has a resistivity ρ_m about 100 times lower than that of bronze, the required current-transfer length will be significantly shorter. Assuming the same sample diameter and resistivity detection limit $\rho^\star = 10^{-12}\,\Omega\,\text{cm}$, we find from Fig. 7.11 that the required current-transfer length is only ~0.4 cm.

For *tape* multilayer or multifilamentary conductors with a resistive matrix, approximately the same current-transfer-length relation applies (within a factor of about 2), but the relevant dimension is now the *thickness* of the tape d, which replaces the wire diameter D in Eq. (7.9).

More strange voltages: the twist-pitch effect

Very strange, even negative, voltages can occur in *twisted multifilamentary* samples if the current is not uniformly distributed among the filaments in the outer perimeter of the conductor (ref. Fig. 7.24). Fundamentally, the origin of this effect also stems from current-transfer voltages, except that in this case, the twist length of the multifilamentary composite plays a central role. Nonuniform injection of current into the outer ring of filaments at the current contacts occurs quite often in *short*-sample testing. Most laboratories have only a relatively small-bore solenoidal magnet, which usually necessitates short-sample lengths and, consequently, short current-contact lengths (length #1 in Fig. 7.9).

Figure 7.12 shows an actual example of what can happen in a such a short-sample test. These *V–I* data were obtained for a Nb–Ti sample with current contacts shorter than the sample's

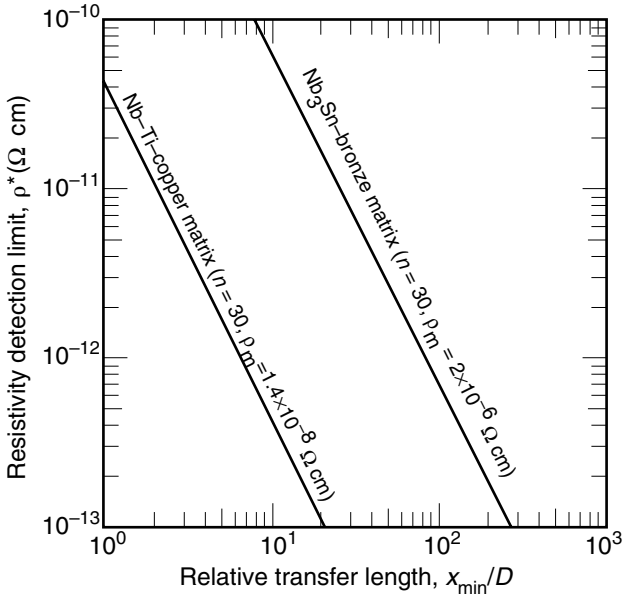

Fig. 7.11 Current-transfer length x_{min} for typical Nb–Ti and Nb_3Sn multifilamentary superconductors, determined from Eq.(7.9), where D is the wire diameter, and $\rho^\star$ is the resistivity limit (usually determined by the apparatus voltage-detection limit). Here, n is the nonlinearity index of the *V–I* characteristic (Eq. 7.10), and ρ_m is the resistivity of the superconductor's matrix material (from Ekin 1978).

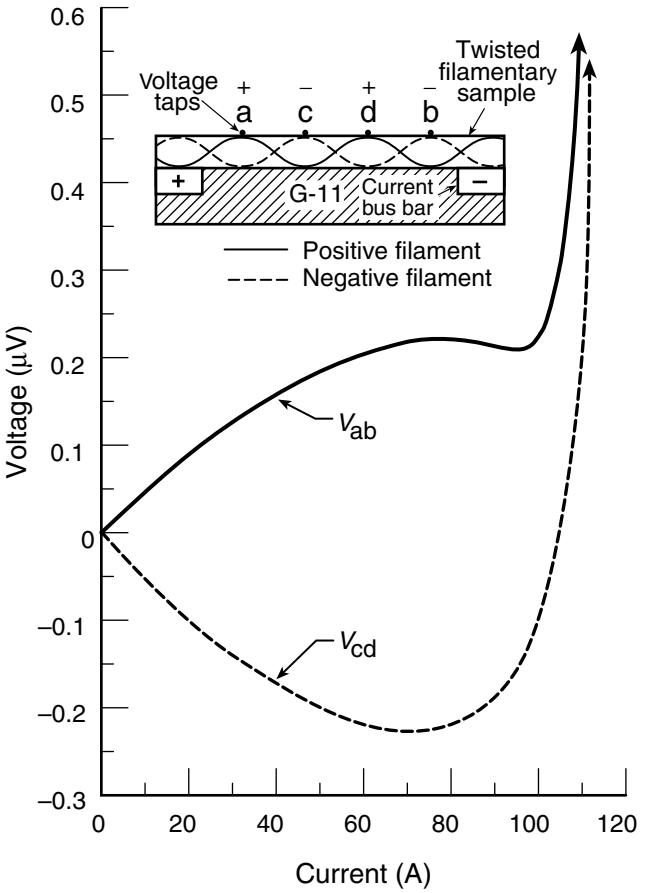

Fig. 7.12 Anomalous *V–I* characteristic of a short Nb–Ti sample, where the length of the current contact is less than a full twist pitch *and* there is an odd half-integer number of filament twists between the current contacts (from Goodrich et al. 1982).

filament twist pitch. As a result, the current from the positive contact is introduced predominately into a small portion of the filaments, represented by the solid line in the inset. Diametrically opposite to this group of filaments is another group, represented by the dashed line in the inset, in which the filaments are attached predominately to the negative current contact. Remember that this situation came about because the current contact was shorter than the filament twist pitch.

Strange negative, or positive, voltages can result from this setup. These voltages result from current crossing the composite from the positive filament group (solid line in the inset) to the negative filament group (dashed line). So if the voltage taps are placed at points *a* and *b* in Fig. 7.12, a significant (positive) current-transfer voltage is added to the intrinsic *V–I* characteristic of the sample (curve V_{ab} in Fig. 7.12). On the other hand, if the taps are placed at points *c* and *d*, a reverse (negative) current-transfer voltage reduces the intrinsic *V–I* characteristic, resulting in an apparent "negative resistance" (curve V_{cd}).

Either way, the measured *V–I* characteristic is erroneous. We can understand the strange shapes of the *V–I* curves in Fig. 7.12 if we take the conductor shown in the inset and imagine

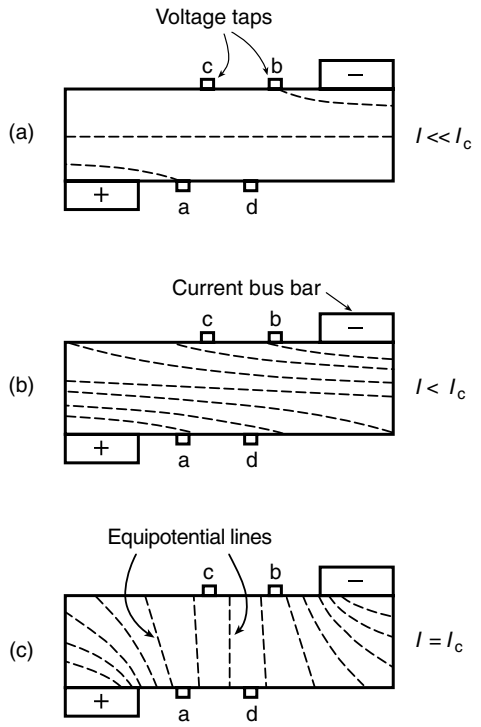

Fig. 7.13 Model of equipotential lines (dashed) for the superconductor test setup and data shown in Fig. 7.12: (a) current much less than I_c; (b) intermediate currents less than I_c; and (c) current near I_c (adapted from Goodrich et al. 1982).

how it would look if it were *untwisted*. Current injection would then be on opposite sides of the conductor, as illustrated in Fig. 7.13. At low current, the equipotential lines between the positive group of superconductor filaments (at the bottom of each drawing in Fig. 7.13) and the negative group (at the top of each drawing) are predominately oriented along the length of the conductor at first, shown by Fig. 7.13(a) and at higher current in Fig. 7.13(b). However, as the current approaches the critical current of the sample, the sample becomes more uniformly resistive and the equipotential lines rotate to the pattern illustrated in Fig. 7.13(c), and the curves in Fig. 7.12 approach the intrinsic *V–I* curve.

The solution to all this is to have a current contact with a length equal to an integral number of twist pitches (at least 1). In this way, the current is injected more uniformly into *all* the outer filaments as they spiral around the conductor where it contacts the current bus bar. The twist effect is then minimized, and we need contend only with the transfer length to get the current into the *inner* filaments (as discussed in the previous subsection). The twist effect is actually more of a problem for conductors with a homogeneous matrix, like Nb–Ti/Cu or the BSCCO/Ag conductors, than for Nb_3Sn conductors, which are usually fabricated with a high-conductivity copper *outer sheath* surrounding a lower-conductivity bronze matrix. For such a Nb_3Sn conductor, the copper sheath serves to uniformly distribute the current around the sample's circumference before the current tries to penetrate the resistive bronze matrix, thus minimizing the twist effect. (However, this is small compensation for the large current-transfer length that still must be accommodated in composites such as Nb_3Sn/bronze, where the matrix resistivity is so high). In any case, when measuring twisted multifilamentary conductors, try to make the length of the current contacts at least 1 twist pitch long.

7.3.5 REQUIREMENT 5: SUPPORT YOUR SAMPLE!

Particularly with high-current-superconductor measurements, the sample mount must be strong, and shaped to provide uniform support for the sample, because the magnetic Lorentz force can be tremendous. There are times when I have seen a sample bent into a contorted shape or snapped in two as a result of inadequate sample support. As shown in the example below, the magnetic force on a single superconductor strand can be on the order of 10 000 N/m. Thus, for long samples, the forces that need to be supported can accumulate to very high values. The key is to provide uniform support for the sample along its length.

The current *polarity* also needs to be correct (see Fig. 7.1) so that the sample is pressed against the support, not away from it. Sounds easy, but it is amazing how often this one will hurt us. From Maxwell's equations,

$$\mathbf{F}(\mathrm{N/m}) = \mathbf{I}(\mathrm{A}) \times \mathbf{B}(\mathrm{T}). \tag{7.11}$$

So, in Fig. 7.1, if the current direction crosses the magnetic-field direction, according to the right-hand rule, the force will be down, against the base. The magnitude of the force is calculated in the following typical example.

Example: Suppose we have a high-current measurement situation where a Nb_3Sn superconductor is carrying 500 A in a field of 12 T. From Eq. (7.11), this will produce a force of 6000 N/m. Not many samples could stand this force without external support. At lower magnetic fields where the critical current is higher, the Lorentz force will be even greater, peaking at field of about 5 T for Nb_3Sn.

Illustrations of both good and bad high-current superconductor mounts are shown in Fig. 7.14. For brittle, flat samples, the sample holder needs to be as flat as possible to match the sample's surface. When fabricating a mount constructed from several pieces, as shown in Fig. 7.14(a) or (b), it is easiest to flatten the support surface by milling the surface *after* assembly. As shown in Fig. 7.14(c) or (d), do not attempt to use non-flat samples or sample holders; there are too many potential problems. Good sample support is also essential to prevent sample motion, which can lead to thermal runaway in superconductor testing: As little as 1 μm of sample motion can initiate a thermal runaway process (Sec. 7.5.1).

Tubular-shaped holders for long samples (Fig. 7.3) present another set of challenges. The tube is usually located in the bore of a solenoidal magnet, and so the Lorentz forces will be either compressive or explosive off the tubular holder. Either way, without support, this force is contained by the axial strength of the wire itself. Applying Eq. (7.11) to a coil of wire, we find that the resulting hoop stress σ_{hoop} along the length of the sample is given by

$$\sigma_{\mathrm{hoop}} = J\,B\,r, \tag{7.12}$$

where J is the overall current density in the wire, B is the component of magnetic field perpendicular to the sample, and r is the radius of the winding. Whereas the perpendicular magnetic

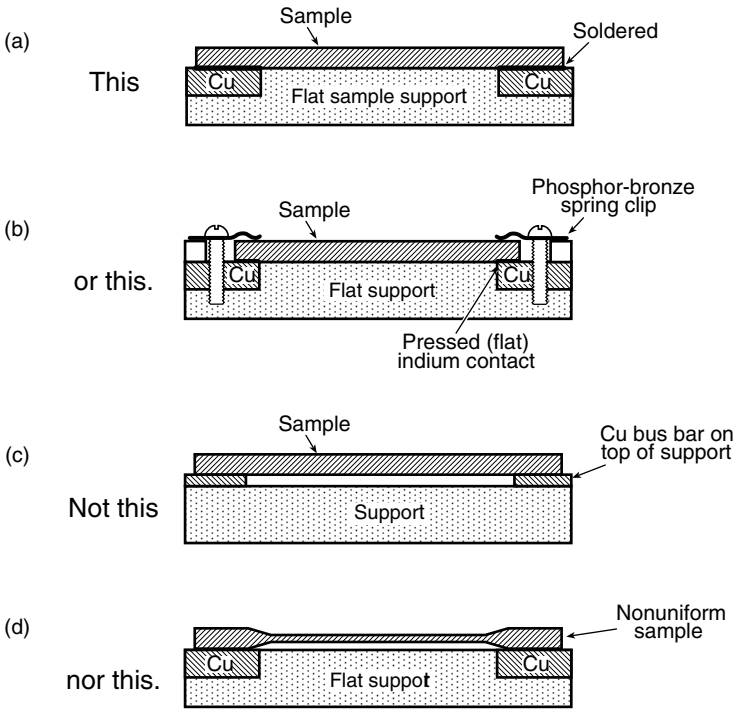

Fig. 7.14 Good and bad supports for high-current testing of short samples.

force pressing the sample against a flat support is mainly a concern for testing at high *current I* (previous example), the hoop stress along the sample length for the tubular geometry scales with the coil radius and current *density J*. Thus, when testing coil-shaped samples, the hoop stress in the sample can be a major consideration for any high-J sample, whether the sample cross-sectional area is large or small.

Example: Assume that the radius of the winding is 1 cm and that the critical-current density in a typical practical conductor is 10^9 A/m^2 at 12 T. Then, from Eq. (7.12),

$$\sigma_{\text{hoop}} = JBr = (10^9 \text{ A/m}^2)\,(12 \text{ T})\,(10^{-2} \text{ m}) = 120 \text{ MPa}.$$

So, even for a relatively small winding radius of 1 cm, the stress is considerable and will alter the properties of most high-field A-15 superconductors. For a larger winding radius, the hoop stress becomes even more of a concern.

To contain this hoop stress, the Lorentz force is usually directed inward, and the sample is immobilized (to avoid motion-generated premature quenches) by winding it under light tension (e.g. ~30 MPa for a typical Nb–Ti strand) or by "walking" the slack out of the conductor (described in the next section for Nb_3Sn strands). The sample can also be kept from moving by choosing a sample-holder material that contracts less than the sample on cool-down. (The latter technique is not recommended, however, because the strain introduced

into the sample can significantly affect the measurement results.) For strain-sensitive samples, often the best alternative is to immobilize them by soldering them in place (which is easy for Cu–2%Be sample holders) or affix them with epoxy such as filled Stycast 2850FT™.

There are two other caveats regarding stress in the design of sample holders: First, in *variable-angle* testing, the direction of the Lorentz force is rotated as the sample holder is rotated; thus, the sample must be provided with both good *side* support (for up to 180° rotation) and *top* support (for $>$ 180° rotation). Figure 7.4 shows an example of a variable-angle sample mount, where the sample is sandwiched between top and bottom supports (which, as noted earlier, also provide good temperature uniformity and control). Second, when the measurement requires *movable* parts, including the sample holder, the parts must be made of materials with a low magnetic susceptibility, or we may have unwanted erroneous extra forces acting on the sample. As shown in Sec. 6.5.2, avoiding ferromagnetic materials is not enough; it also takes low susceptibility to keep the magnetic forces on a cryostat part from becoming significant in the bore of a high-field magnet.

Finally, when designing tubular sample holders around which the superconductor is wrapped, make sure the *diameter of the holder* is large enough that bending strain in the sample is kept small. For a wire of diameter d (or a tape conductor of thickness d) and a sample holder of diameter D, this usually requires that the maximum bending strain $\varepsilon_{\text{bend}}$ at the outer surface of the sample be less than 0.1%; that is,

$$\varepsilon_{\text{bend}} \equiv d / D \leq 0.1\%.$$

For a conductor diameter of, say, 0.5 mm, this requires maintaining a bend diameter of greater than ~50 cm. If bending strain is increased above this level, the outer superconducting filaments in the composite sample can have their initial strain state permanently altered (due to yielding of the soft matrix material). At strain levels above about 0.2%, the superconducting filaments can start to fracture. (Ways to avoid this bending-strain problem are discussed in Sec. 7.3.6, which describes techniques for testing brittle samples when they must be bent around small mandrels to fit in the bore of a high-field magnet.) This bending requirement applies to both the brittle high-T_c oxide superconductors as well as the low-T_c compound superconductors (but not to ductile alloy superconductors like Nb–Ti).

7.3.6 PROCEDURES FOR MOUNTING LONG SUPERCONDUCTOR SAMPLES

As a final topic for high-current sample holders, we make a few specific comments about *procedures* commonly encountered in preparing and mounting long superconductor samples on tubular sample holders.

For testing long *ductile* samples such as Nb–Ti wire, it is often convenient to machine a threaded groove around the circumference of the tubular holder to automatically position the sample when winding it onto the holder, as illustrated in Fig. 7.15. In this illustration, the center section of the holder is a fiberglass–epoxy tube that has a relatively thin wall with the glass fibers running around the circumference of the tube. (The small wall thickness increases the cool-down rate and the fiberglass serves to match the sample's thermal contraction, although the latter

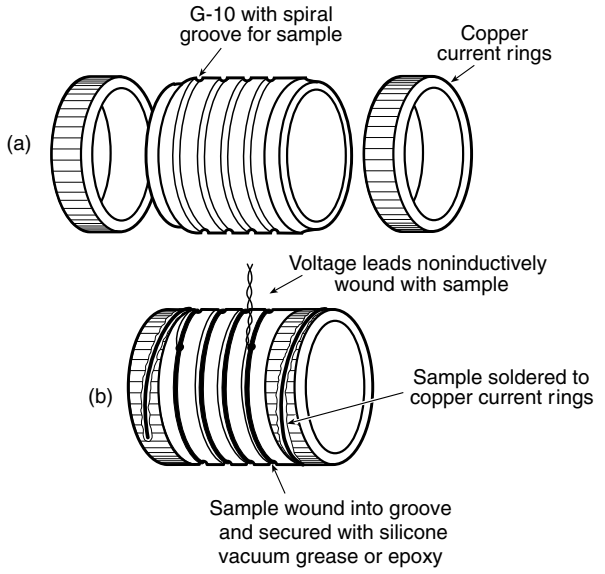

Fig. 7.15 Test mandrel for Nb–Ti superconductor: (a) exploded view of grooved fiberglass–epoxy thin-walled mandrel and copper current rings; (b) sample wound on the mandrel and held in place, with the ends soldered to copper current rings; voltage leads are noninductively wound with the sample.

is not so important with ductile Nb–Ti). After winding is complete, the sample is soldered to the copper end rings, and greased or epoxied into the groove for mechanical support. Similarly, for metallic sample holders, such as stainless steel, Ti–6%Al–4%V, or beryllium copper, it is helpful to machine a groove into the surface of the holder for alignment and automatic positioning.

For *brittle* samples, such as Nb_3Sn or Nb_3Al, the conductor is usually fabricated in a two-step process, where, first, a multifilamentary composite of ductile materials is drawn into long lengths and then, second, it is heat-treated to form the final brittle superconducting wire (see Sec. 7.5.2). This two-step process makes it possible to form the sample into a coil shape after step one, and then, in step two, heat-treat (or "react") it to form a (brittle) spiral coil that matches the tubular test mandrel.

For example, brittle Nb_3Sn conductors are typically formed by heat-treating an unreacted composite wire (consisting of niobium filaments in a Cu–Sn matrix) in vacuum at about 750°C to form the brittle Nb_3Sn compound. To prepare such conductors for critical-current testing in a high-field magnet, the unreacted wire is usually first wound onto a stainless steel (or Ti–6%Al–4%V) *heat-treatment* mandrel. The stainless-steel mandrel is prepared by first heating it in air to a temperature at least as high as it will see in service; this serves to oxidize the mandrel's surface, thereby providing a protective oxide layer that prevents the test sample from diffusion-bonding to the mandrel when the sample is heat-treated. (Ti–6%Al–4%V heat-treatment mandrels are usually prepared in a similar fashion by coating them with graphite spray and then heat-treating them at the service temperature to form a nonsticking surface.) As described above, a spiral groove is usually machined into the surface of the heat-treatment mandrel to position the sample and, in this case, to also keep it from sagging during the heat treatment.

Stainless-steel mandrels contract more than the test sample on cooling, leaving the test sample loose after the reaction heat treatment. (For Ti–6Al–4%V mandrels, the mandrel contracts less than the sample and so care must be taken that the sample ends remain loose so

the sample is not stretched on cooling.) The sample is then *carefully* screwed off the reaction mandrel and onto a *measurement* mandrel [stainless steel, beryllium copper (Cu–2%Be, UNS C17200), or Ti–6%Al–4%V]. The sample is tightened into place on the measurement mandrel by soldering one end to the copper current end piece and then carefully "walking" the slack out of the sample to the opposite end, where it is soldered to the other copper end piece.

➔ If Ti–6%Al–4%V is used for the *measurement* mandrel, keep in mind that the mismatch in thermal contraction compared with that of practical Nb_3Sn superconductors places the test sample under a tensile strain of about 0.13% on cooling to 4.2 K (described in the example in Sec. 7.3.2). Also, Ti–6%Al–4%V at 4.2 K is superconducting in magnetic fields < 2 T (Goodrich et al. 1994).

An alternative (and usually more convenient) scheme, which eliminates *transferring* the sample from the reaction mandrel to the measurement mandrel, is to react the sample directly on the measurement mandrel, as illustrated in Fig. 7.16. The central part of the holder works fine if it is stainless-steel or Ti–6%Al–4%V treated to prevent sticking, but the copper current end pieces cannot be heated in physical contact with the sample (which usually has a copper outer sheath), because the two copper surfaces will diffusion-bond together. Consequently, the copper end pieces are replaced temporarily by Ti–6%Al–4%V spacer rings during the heat treatment, as shown in Fig. 7.16. After reaction, the Ti–6%Al–4%V rings are removed and replaced with the copper end pieces. The three pieces are then bolted together with brass bolts extending down the bore of the central cylinder, which self-tighten as the holder is cooled (since brass contracts more than any of the other materials; see Appendix A6.4).

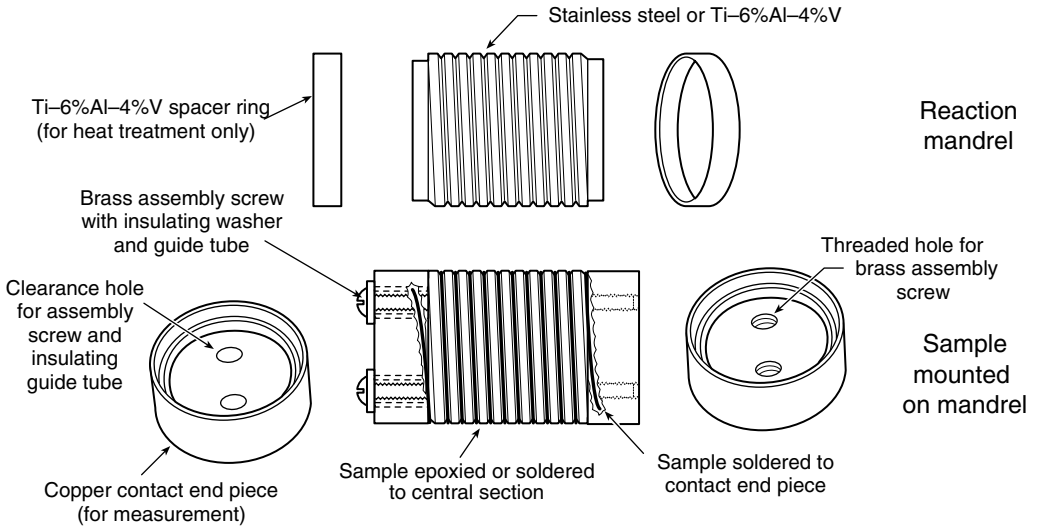

Fig. 7.16 Combination reaction-and-measurement mandrel for Nb_3Sn. The Nb_3Sn superconductor is heat-treated on the same mandrel used for measurements (typically made of stainless steel or Ti–6%Al–4%V). The copper end pieces are replaced by Ti–6%Al–4%V or stainless-steel spacer rings during reaction to keep the sample from sticking. After heat treatment, the copper end pieces are reinstalled to serve as current contacts.

As described above, the end of the test sample is then soldered to one of the copper end pieces, the slack is walked out of the sample, and the other end is soldered to the other copper end piece.

The cryostat's current down-leads (usually bus bars or copper rods) are best soldered to the copper-contact end pieces with a solder having a melting temperature higher than that used for sample mounting (Appendix A3.7). A solder of similar melting temperature can also be used if the joint is held together with screws that keep it from falling apart during the sample-soldering process.

The assembly shown in Fig. 7.16 has an additional advantage in that it forms a convenient, self-contained sample-and-holder combination that can be kept intact for retesting later or shipped to other laboratories for interlaboratory comparisons.

A final word: Extra care must be exercised when using any of these sample-mounting procedures with brittle samples: A-15 superconductors, high-T_c superconductors, or otherwise. Practice first on dummy samples. We are handling very brittle superconductor filaments embedded in a soft matrix. Damage can be pervasive, but completely *hidden*. It is a little like working with pencil leads embedded in soft clay. If we accidentally bend the sample, we would break the internal brittle filaments, but never know it (until we electrically tested it). If there is any doubt about whether such a brittle-filament sample has been damaged, I have found it saves time, in the long run, just to start over with a new sample. Better to have lost some time remounting the sample than to waste a day measuring a damaged sample, or worse yet, reporting data on a sample when only the person who mounted the sample knows it may have been bad.

7.4 Thin-film sample holders

In some respects, thin-film testing is easier than high-current, bulk-sample testing. The currents are much lower, typically less than 100–200 mA, so magnetic Lorentz forces are rarely a problem. Variable-temperature operation is relatively easy to obtain because Joule heating loads are usually small. Thus, the design of thin-film sample holders is concerned mainly with: (1) providing uniform and stable temperature control of the sample, and (2) avoiding sample stress introduced by differential thermal contraction. Additional sample-holder design requirements are: (3) providing lead attachments to thin-film contact pads, and (4) properly locating voltage contacts to minimize spurious current-transfer voltages and noise pickup. We consider techniques for meeting each of these requirements, next.

7.4.1 REQUIREMENT 1: TEMPERATURE CONTROL AND UNIFORMITY

Unless the thin-film test chip is immersed directly in a cryogenic liquid, the chip is usually pressed against a base structure made of high-conductivity copper by using a spring clip or spring-loaded pogo pins (described below), as illustrated in Fig. 7.17. Sometimes a thin layer

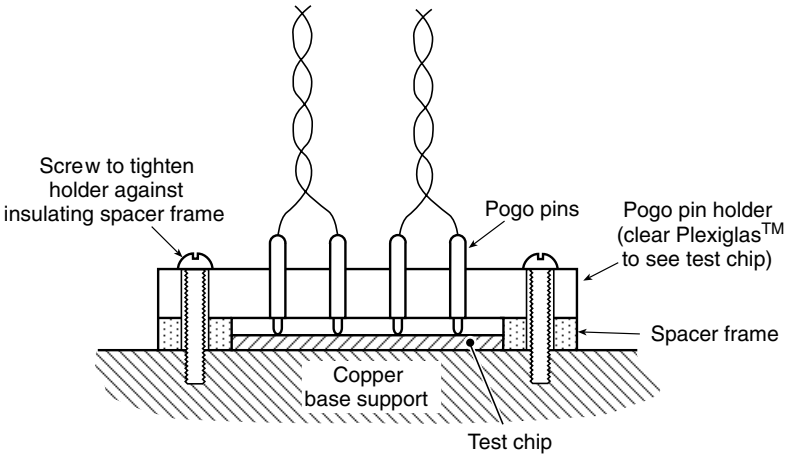

Fig. 7.17 Schematic illustration of spring-loaded pogo pins that press the test chip against a copper base support (pogo pins are described in Sec. 7.4.3). The pogo-pin holder is screwed against a spacer frame (made of Delrin™, for example), which surrounds the test chip. The thickness of the frame is designed to provide just enough gap between the test chip and pogo-pin holder so that the pogo pins are compressed to half their length; it also aligns the test chip for accurate contact between the pogo pins and the contact pads patterned on the chip.

of thermal conducting grease (such as Apiezon N™ grease) is used to enhance the thermal contact between the chip and copper base (described in more detail below). The base should be thick enough to provide good thermal conductance between the sample, thermometer, and heater. Two examples of such copper base structures are shown in Figs 4.2 and 4.3.

The total thermal resistance between the test film and copper base is usually dominated by the thermal boundary resistance between the chip and the base structure, rather than solid conduction through the substrate material. In Appendix A7.6 we have tabulated the thermal conductivity of common thin-film substrate materials. For example, we find from the data in Appendix A7.6 and Eq. (2.2) that the heat *conductance* across an MgO chip of 1 mm thickness, with a cross-sectional area of 1 cm^2, is about

$$\dot{q} / \Delta T = \lambda_{4.2\,K}(A/L) = [82\ W/(m{\cdot}K)]\,(10^{-4}\ m^2) / (10^{-3}\ m) \approx 8\ W/K$$

at 4.2 K. On the other hand, from Appendix A2.3, we find that at 4.2 K the heat conductance across solid *interfaces* pressed together is typically on the order of 10^{-1}–10^{-3} W/K for force loads of 445 N (100 lbf). Even if the interface conductance is near the upper end of this range (that of polished, well-mated surfaces), then, at the low force levels expected from a rack of spring-loaded pogo pins (a few newtons), the heat conductance across the interface will be in the range of only 10^{-3} W/K. [Here we have assumed that the thermal conductance is proportional to force, as described by Eq. (2.14).] Thus the heat conductance across the interface is several orders of magnitude larger than that across the MgO substrate.

The interface heat conductance can be improved if a thin (~10 μm thick) layer of thermal grease is used between the chip and sample holder. From Fig. 2.7, we find that the thermal conductance of a 1 cm^2 grease joint is about 10^{-1} W/K in the liquid-helium range, a hundred-fold

increase over the no-grease case. Even so, the interface is still the weak link in this example. At very low-power dissipation in the microwatt range, thermal grease is probably not necessary, but at higher-power dissipation levels, grease can significantly lower the temperature difference between the test chip and substrate.

Silver paste can also be used, but be aware that some do not work well at low temperatures; supplier information is given in Appendix A1.7. Also, indium works to enhance the heat conductance across the interface if the sample can be heated to the melting temperature of indium (157°C) and if the indium wets the chip and holder surfaces. Likewise, for samples that cannot be heated, an indium–gallium eutectic mixture (made by heating indium and gallium together on a hot plate) remains liquid at room temperature and freezes on cooling, thus providing good thermal contact. However, if mechanical stability is needed at room temperature, it must be provided by some mechanism other than indium–gallium. As with indium alone, wetting can be an issue depending on the chip and holder materials.

Designing the chip mount so that it provides a constant-temperature *radiation* environment around the sample also helps achieve temperature uniformity across the sample. This is not needed for dip testing in a liquid cryogen, of course, but for variable temperature operation, especially at higher temperatures, the radiant heat transfer scales as T^4 and becomes significant [Eq. (2.9)]. For a sample holder like that shown in Fig. 1.8, covering the sample compartment with a copper lid can provide good radiation shielding. The lid also acts to reduce variable *convective* cooling that can change the temperature of the small instrumentation wires leading to the sample. With radio-frequency instrumentation, the copper lid also provides electromagnetic shielding.

A second level of shielding against thermal radiation and convection can be supplied by a copper tube that slips over the entire assembly, as shown in Fig. 1.8.

7.4.2 REQUIREMENT 2: STRESS FROM DIFFERENTIAL THERMAL CONTRACTION

Differential thermal contraction is not a problem if the chip is not bonded to the base structure with thermal grease or other adhesive, but rather held in place with a spring clip, rack of pogo pins, or fuzz buttons (all described below). However, if power levels on the chip are high enough that grease must be used to heat-sink the chip to the base structure, the base can introduce considerable strain into the substrate material if the thermal contractions of the substrate and base material (usually copper) do not match. Ceramic substrates, such as those used for the high-temperature superconductors, have a thermal contraction on cooling from room temperature that is significantly smaller than that of copper. If the substrate is thin, this stress will be transmitted to the test film and can affect the measurement. Representative values of the thermal contraction of common substrate materials are included in Appendix A7.6.

7.4.3 REQUIREMENT 3: LEAD ATTACHMENT TO THE SAMPLE'S CONTACT PADS

To test thin films deposited on substrate chips, connections must be made to small contact pads that are usually patterned into the film (typically using photolithographic techniques).

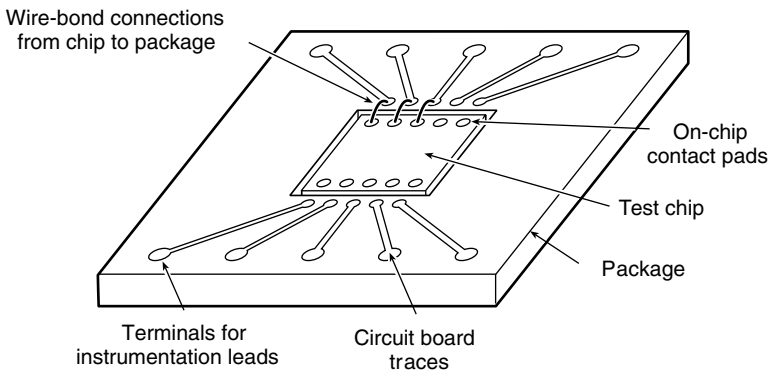

Fig. 7.18 Test chip located in a wire-bond chip carrier or package, showing connecting leads wire-bonded between the chip contact pads and the package terminal pads. (The density of contact pads is typically much higher than that shown in this simplified sketch.)

If the chip pattern is *one of a kind*, then it is usually easiest to make connections to the chip contact pads by using a commercially available wire-bond chip carrier or package that holds the test chip and surrounds it with many terminal pads, as shown in Fig. 7.18. The chip is electrically connected to the package with very small-diameter wires or ribbons that are wire-bonded onto the terminal pads, providing jumper connections between the small on-chip contact pads and the package terminal pads, as illustrated in Fig. 7.18. [Surprisingly, a typical wire-bond ribbon 0.05 mm $\times$ 0.25 mm and about 1 cm long immersed in liquid helium can carry up to about 200 mA before it burns out.]

On the other hand, if the chip's test pattern is one that will be *replicated* many times and if the on-chip contact pads are not too close together ($\gtrsim$1–2 mm spacing), it is usually more convenient to change test samples by using a standard arrangement of springy contact pins that matches the pattern of on-chip contact pads. These contact pins can be an array or rack of pogo pins, for example, as shown earlier in Fig. 7.17.

We will now look at some specific techniques for making and using wire bonds, pogo pins, and other high-density spring arrays for contacting on-chip contact pads.

Wire/ribbon bonds

Wire bonds are usually made with an ultrasonic pressure technique. Small-diameter (typically 0.05–0.25 mm) wire or ribbon leads, usually made of high-conductivity aluminum or gold, are welded to the chip contact pads with a small wedge-shaped tool, shown schematically in Fig. 7.19. Welding occurs when the tool presses the small-diameter wire against the bonding surface and ultrasonic energy is applied.

For strong wire bonding to occur, the substrate should be firmly supported during ultrasonic bonding, and the surfaces of the metal contact pads and the wire leads must be made of pure, soft materials that are very clean. Combinations of wire materials and thin metal surfaces that can be ultrasonically bonded are tabulated in Appendix A7.7. Beware that the combination of gold and aluminum is not durable because these two materials eventually

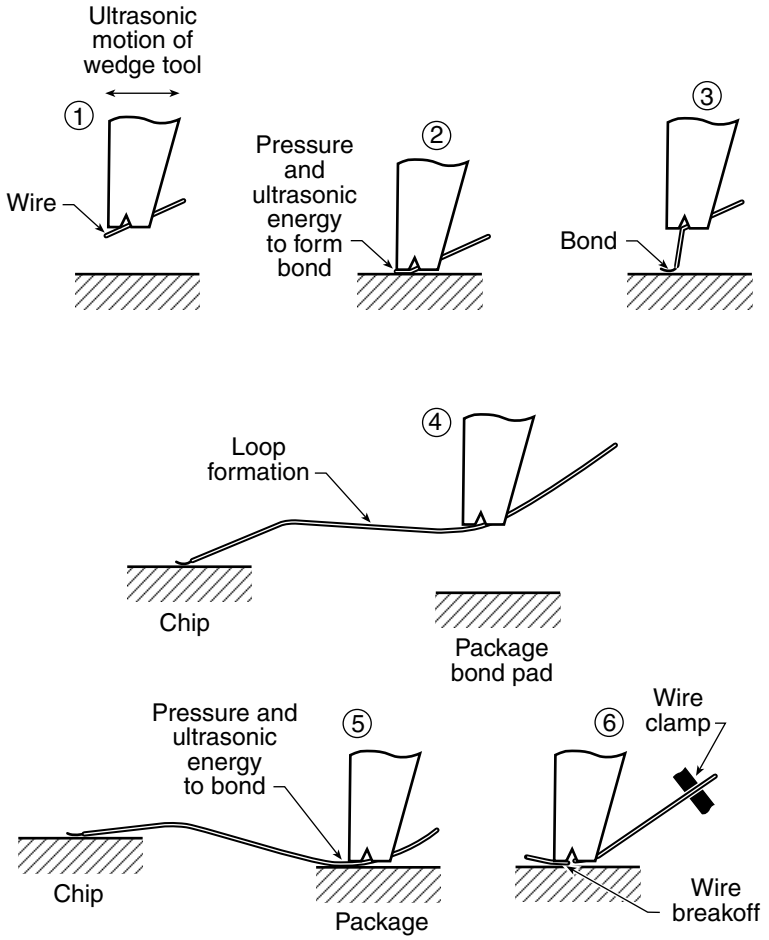

FIG. 7.19 Wire-bond procedure: (1) the wire or ribbon is positioned between the chip contact pad and an ultrasonically powered wedge tool; (2) pressure and ultrasonic energy are applied to make the on-chip bond; (3) the tool is raised and the wire paid out from a spool of wire (not shown); (4) the tool is moved to the contact pad on the package; (5) a second wire bond is made between the wire and the package pad; and (6) a wire clamp (part of the bonding tool) pulls back on the wire to break it at the heel of the bond (from Harmon 1997).

form a corrosive intermetallic compound $AuAl_2$, often referred to as the "purple plague" because of its characteristic color. Also, aluminum wire ultrasonically bonded to silver contact pads can be unreliable.

Gold usually wire-bonds poorly unless a *thermosonic* bonding technique is used. This is just a variant of the above *ultrasonic* method, wherein the chip is also heated typically to between 125°C and 220°C. With thermosonic bonding, ultrasonic energy can be kept small enough to minimize cratering damage to the chip. A comparison of the advantages and disadvantages of these wire-bond technologies is given in Sec. 2.6.4 of Harmon (1997). Harmon's book also contains useful information about additional details of wire-bonding, quality testing, and failure modes of wire bonds.

➔ If sample testing is carried out by immersion in a liquid cryogen, the chip carrier in Fig. 7.18 does not need to be made of a material of high thermal conductivity, in which case it can be custom-made fairly easily by use of a commercial circuit-board fabrication service. So they can be used with wire-bonding, order the boards with bare copper traces (without solder coating) or with "bondable gold" plating. The chip can be attached to the carrier with most of the adhesives listed in Appendix A3.10.

Pogo pins

Changing samples is made considerably simpler through the use of a standardized pattern of contact pads that are lithographically fabricated into the test films and contacted with a rack of spring-loaded pogo pins having a matching pattern. The rack of pins is simply pressed onto the test chip's pattern of contact pads, usually by screwing it in place, as shown in Fig. 7.17. Each pin consists of a spring-loaded pin in a tubular housing—a miniature "pogo stick"—as illustrated in Fig. 7.20. [Supplier information is given in Appendix A1.7 under Contacts (springy devices).]

For convenience, the pogo-pin holder can be made of clear Plexiglas™, which enables the test chip's contact pads to be seen as the rack of pins is centered over the chip and screwed down. The pogo pins are secured by press-fitting them into holes drilled in the holder. On cool-down, the Plexiglas™ holder contracts more than the pins (compare the thermal contraction data of Plexiglas™ in Fig. 6.4 with that of metals in Fig. 6.6), so the grip on the pins automatically self-tightens as temperature is lowered.

The ends of the pins are usually plated with gold to make good *electrical* contact with the array of contact pads on the chip. For most film applications, I prefer a rounded tip in order not to damage the film any more than necessary. The pressure applied to the test chip by the spring-loaded pins also helps to make good *thermal* contact between the chip and copper base support, as described Sec. 7.4.1.

In pressing the rack of pins onto the chip, a good guideline is to compress the pins about half their extension. This is a compromise between applying adequate pressure for all the pins to make good electrical contact, without having the rack of pins bottom out and

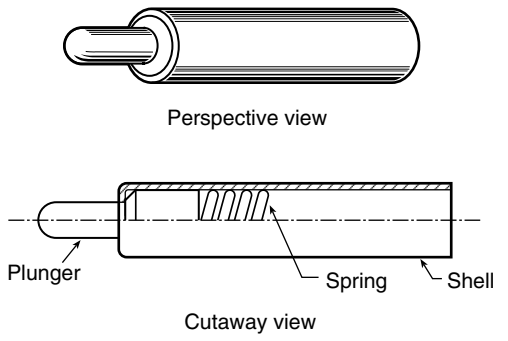

Fig. 7.20 Pogo pin for making electrical pressure contacts to small contact pads. The spring-loaded pins are available in a wide variety of sizes (from a fraction of a millimeter to several millimeters in diameter) and with differently shaped tips varying from flat to round to pointed. For decreased electrical contact resistance, tips can be coated with gold.

damage the test film. A convenient way to ensure this, as well as to accurately align the test chip and pogo-pin rack, is to machine a positioning spacer frame, as shown in Fig. 7.17. The frame simply rests on the copper base support and is thick enough that the pogo pins are compressed to half their length when the pogo-pin rack is screwed tightly against the spacer frame. The frame also serves to center the test chip under the rack of pogo pins.

When a high-thermal-conductivity copper holder is not needed (e.g. when dip testing in a liquid cryogen) an alternative scheme is to embed the contact pins into a sample-holder base made of an electrically insulating material. The sample chip can then be flipped over and placed face down on the bed of protruding pins; a pressure plate to hold it in place is the only free part. This scheme has the advantage that the instrumentation leads do not get flexed and are less susceptible to possible damage during sample changes. Alignment may be more of an issue but can be provided by a centering frame built into the base of the holder.

Other characteristics: Pogo pins have an *internal resistance* of about 30 mΩ at 77 K. This should present no problem for voltage contacts, since the voltage leads carry extremely small amounts of current (Sec. 7.2). However, for current contacts, this sometimes needs to be taken into consideration. For example, at 100 mA, the Joule heating at each pogo pin will be $\dot{q} = I^2R = (0.1\ \text{A})^2\,(0.03\ \Omega) = 0.3$ mW, which is an insignificant heat load for immersion testing in liquid helium, but may become a factor when testing in vapor or a vacuum.

Pogo pins also have a significant *magnetic susceptibility* arising from the spring material (Fig. 7.20). Consequently, they should not be used in sensitive magnetic measurements. However, I have used them at high-magnetic fields (~25 T) for thin-film transport-current testing without the magnetic forces becoming significant enough to affect the pin pressure on the chip.

Finally, during cool-down, be sure the pogo pins do not become coated with liquid air, which will freeze and prevent them from moving (see the tip in Sec. 1.5.1). Although they have their limitations, pogo pins are very convenient and are one of the most popular methods for making thin-film sample-holder connections.

Fuzz buttons

Another way of contacting on-chip contact pads with an array spacing somewhat finer than that for pogo pins is with fuzz buttons. Figure 7.21 shows an illustration of one of the fuzz

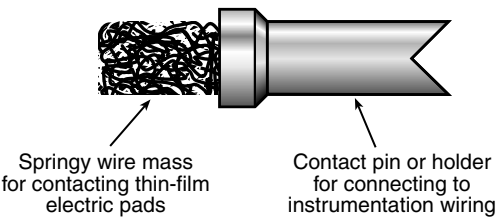

Fig. 7.21 Fuzz buttons for making electrical pressure contacts to small contact pads or device leads. Each fuzz button consists of a fine single strand of springy gold-plated beryllium–copper wire compressed into a springy wire mass with a cylindrical form. Diameters typically range from a few tenths of a millimeter to about a millimeter.

buttons. It consists of a very fine, single strand of gold-plated beryllium–copper wire that is compressed and crumpled into a springy cylindrical wire mass. The wire mass makes good electrical contact when its length is compressed about 20%, and it can be used again and again.

Each fuzz-button wire mass is packed into small contact cylinders or into an array of holes in a holder for making electrical contact with a matching array of on-chip contact pads. Typical diameters of fuzz-buttons range from a few tenths of a millimeter to about a millimeter. [Supplier information is also listed in Appendix A1.7 under Contacts (springy devices).]

Beryllium–copper microsprings

For very small test chips, or when we need to squeeze a high density of contacts onto a chip, sometimes there is not enough room for an array of pogo pins (~1.5–2 mm center spacing). Of course, a higher density of sample-holder contacts can be made using wire bonds, but often we would like the convenience of a standard array of springy contacts.

A very high-density array of spring contacts (with center spacing of ~0.5 mm or less) can be made by patterning a beryllium–copper circuit board and using it as a chip carrier (Hamilton 1982). Contact strip lines are photolithographically etched into a beryllium–copper sheet 0.05 mm thick that is bonded to a FR4 or G-10 circuit board, shown in Fig. 7.22. The Be–Cu clad circuit board can be self-made or custom ordered (Appendix A1.7 under Contacts). Springs for contacting the chip are formed by peeling up the last 1 mm end of each patterned beryllium–copper line and folding it back over a small mandrel (made by rounding the end of a blade of a jeweler's screwdriver). Contact is made to the on-chip pads by flipping the test chip over, aligning it, and pressing it down onto the beryllium–copper springs, as illustrated in Fig. 7.22.

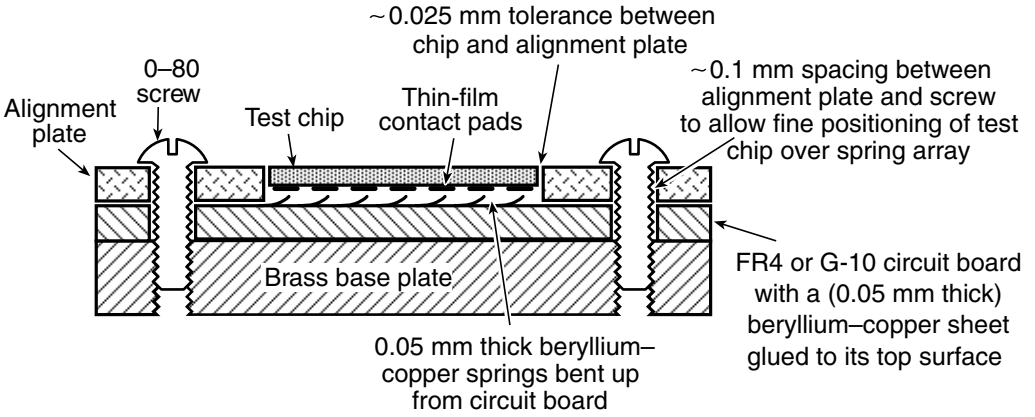

Fig. 7.22 Contact microsprings patterned into a 0.05 mm thick beryllium–copper sheet that is glued to a 1.6 mm FR4 or G-10 circuit board. (The number of contacts is much higher and the spacing much smaller than that shown in this simplified sketch.) Precise alignment between the test chip and contacts is provided by an alignment plate. The test chip is flipped upside down, dropped into the alignment frame, and pressed down against the microsprings with a spring-loaded pressure plate (not shown) (from Hamilton 1982).

To help center the on-chip contact pads on the springs, an alignment plate is screwed to the circuit board, as shown in Fig. 7.22. The frame has a cutout that is only about 0.025 mm larger than the test chip (which accommodates differences in thermal contraction). The test chip is then dropped into the closely matching cutout, and contact with the beryllium–copper springs is made by pressing the chip down onto the springs with a spring-loaded pressure plate (not shown in Fig. 7.22). The initial position of the alignment frame can be set by substituting a patterned glass microscope slide for the test chip and viewing the contact alignment through the glass. Contact resistivity can be lowered by gold-plating the beryllium–copper springs. Further details are provided by Hamilton (1982).

For rf measurements, it is possible to extend a ground plane right up to the signal lines by using the same microspring contact technique and a second beryllium–copper ground plane layer (Wire et al. 2001).

Thin-film transport measurements without patterning

When initially screening film properties, a lot of time can be saved if the sheet resistance, critical temperature, or critical current of superconducting films are measured without patterning them first. This gives an immediate sense of film quality without investing a lot of effort in photolithographically fabricating the usual transport-current strip-line geometry. Unpatterned measurements of sheet resistance and T_c are most easily obtained by the four-probe contact method described in Appendix A7.1, wherein four equally spaced in-line probes are pressed against the unpatterned film near its middle, as illustrated by the insets in Fig. A7.1.

Although this four-probe technique is the simplest for screening the sheet resistance or critical temperature of unpatterned films, for critical-*current* measurements there is usually no way to avoid patterning the films unless an *inductive* technique is used. Unlike the four-probe technique, the inductive technique is also nondestructive and avoids direct electrical connections to the film. The inductive technique can also be used to measure the critical temperature by sensing the abrupt change of the screening current in the sample that occurs at T_c when temperature is swept.

In the inductance technique, a coil of fine wire (encapsulated in an epoxy block) is pressed against the film surface with light spring pressure, as illustrated in the inset of Fig. 7.23(a) and in the cross-sectional view at the bottom of Fig. 7.23(b). (For convenience, the coil is embedded in the surface of the sample holder, and the test chip is flipped upside down and pressed down on top of it.) A low-distortion, sine-wave current I_{drive} drives the coil, which induces screening currents in the superconducting sample film. If I_{drive} is small enough, the superconducting screening currents are proportional to I_{drive}. As I_{drive} increases, however, a level is reached where the screening response of the sample film exceeds its critical current and the screening currents become nonlinear. This causes harmonic components to appear in the voltage across the drive coil. Only odd harmonics develop, since any nonlinearity cannot depend on the polarity of the current flow. Of these odd harmonics, the third has the best signal-to-noise ratio. The critical current of the sample film is detected most easily by the sudden upturn in the output of a lock-in amplifier set to detect the third-harmonic voltage of the drive coil, as illustrated by the experimental data in Fig. 7.23(a).

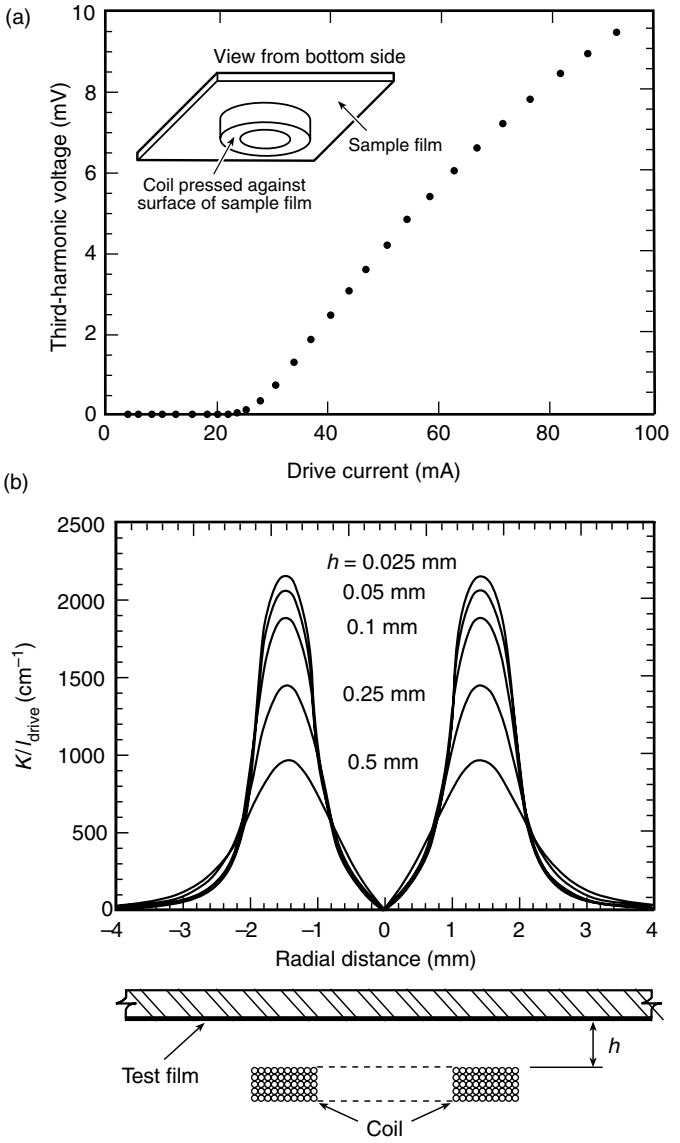

Fig. 7.23 (a) Experimental data plot of the third-harmonic voltage across the drive coil as a function of drive current at 1 kHz. The drive coil is pressed against the surface of the superconducting film, as illustrated in the inset. (b) Calculated dependence of K (the induced current per unit film thickness) normalized by the drive-coil current I_{drive}, as a function of radial distance from the center of the coil. Curves are shown for several values of the spacing h between the coil and film. Note that the peak induced-current density occurs very near the mean radius of the drive coil. A cross-sectional view of the drive coil in relation to the superconducting film is illustrated at the bottom of the figure. The data are for a 300-turn coil (25 μm diameter wire) having an inside radius of 1.05 mm, an outside radius of 1.95 mm, and an axial length of 0.46 mm (adapted from Claassen et al. 1991).

To determine the film's critical current, we need to know the relationship between I_{drive} and the induced sheet current K ($K \equiv I/d$, where I is the induced current in the film and d is the film's thickness). The ratio K/I_{drive} depends on the particular shape of the coil and the spacing between the coil and the superconducting film. Figure 7.23(b) shows the ratio calculated for a typical coil as a function of the spacing h between the coil and film. The critical current corresponds to the peak value of K, which occurs near the mean radius of the drive coil, as shown in Fig. 7.23(b).

Although Fig. 7.23(b) gives a reasonable estimate for K/I_{drive} for one particular coil geometry, for more precise, absolute values of film critical current, it is best to first calibrate a given coil and film configuration by comparing the inductive results with conventional (patterned) transport critical-current measurements made on the same test film.

For this one-coil inductive technique to work, two conditions must be met: First, the outer radius of the coil should be less than half the substrate size to minimize sensitivity to sample-edge effects or variations in the shape of the sample. Second, to make sure the magnetic field is perfectly shielded from the back side of the film by the induction currents, the film thickness d should not be too thin, $d \gg \lambda^2/D$, where λ is the magnetic penetration depth, D is the drive-coil diameter, and $d < \lambda$ for this relation to hold. These conditions are usually easily met in practice.

A two-coil method can also be used wherein a coil on one side of the film induces currents in a second receiving coil on the other side of the test sample. However, the single-coil method described above has several advantages over a two-coil mutual-inductance method: accurate alignment of the two coils is not required, and the induction fields do not have to pass through the substrate to reach the pickup coil.

Further details are given by Claassen et al. (1991). The third-harmonic technique and a comparison with conventional transport measurements are also described in the thesis by Stork (1996).

7.4.4 REQUIREMENT 4: VOLTAGE TAPS—NOISE PICKUP AND CURRENT-TRANSFER LENGTHS

To minimize electromagnetically induced noise and to reduce voltages from magnetic-field variations (when high-field testing), the voltage leads must be twisted in corresponding pairs, as close as possible to where they attach to the pogo pins or wire-bond terminals. The same voltage noise figures apply as those described by Eq. (7.8). For low-frequency testing, *twisted* instrumentation leads are better than coaxial cable to minimize induced noise from magnetic-field drift or ripple. The effective loop area formed by the twisted leads should also be *coplanar* with the background field, as illustrated earlier for wire samples in Fig. 7.7.

With regard to the *current-transfer length* for thin-film samples, the same considerations apply as described earlier for bulk composite samples (Sec. 7.3.4). That is, the distance between the position where current is injected into the thin-film test strip and where voltage is detected (indicated as length #2 in Fig. 7.9) must be long enough that current will uniformly fill the cross-sectional area of the film by the time it reaches the voltage tap.

For homogeneous films, a current-transfer length of several strip widths should be adequate to fill the width of the strip. However, for composite *multilayer* films, in which the superconducting layers are separated by more resistive layers, Eq. (7.9) can be used to approximately determine the current-transfer length needed to fill all the layers throughout the thickness of the sample. In using Eq. (7.9) for the multilayer-film case, D is replaced by the total thickness of the multilayer composite, and ρ_m is the resistivity of the interleaved resistive layers.

7.5 Addenda

To understand parts of the discussion involving high-current superconductors in Parts II and III of this text, it is important to be familiar with *thermal runaway* (Sec. 7.5.1) and how it leads to the stabilized *multifilamentary* geometry of practical superconductors (Sec. 7.5.2).

7.5.1 THERMAL RUNAWAY (QUENCH)

A superconductor strand of the size of a pencil lead carrying hundreds of amperes of current is a potential light-bulb filament. When a disturbance (such as a sample movement) locally heats a small portion of the superconductor into the resistive state, a thermal-runaway event can be triggered. Since superconductors are generally poor thermal conductors, the Joule heating in one small part of the superconductor heats surrounding superconductor material into a resistive state, and so it continues, with the resistive zone growing to fill the entire cross-sectional area of the superconductor strand and then propagating along the length of the conductor. At typical current densities of over 1000 A/mm^2, the Joule heating can literally vaporize the sample.

A thermal-runaway event is sometimes also called a *quench* because of the cloud of helium vapor that usually comes pouring out of the test dewar (as if a red-hot piece of metal were being quenched in water).

When a superconductor is carrying current close to its critical value, it does not take much of a disturbance to generate thermal runaway. Sample motion by only a fraction of a micrometer suffices.

The initiation of the thermal-runaway process and a quantitative description in terms of "minimum propagating zones" is given in the text by Wilson (1990).

7.5.2 MULTIFILAMENTARY GEOMETRY OF PRACTICAL HIGH-CURRENT SUPERCONDUCTOR COMPOSITES

Here, we simply present the geometric structure of practical superconductors to serve as a visual aid for the discussions of sample holders, contacts, and critical-current measurements

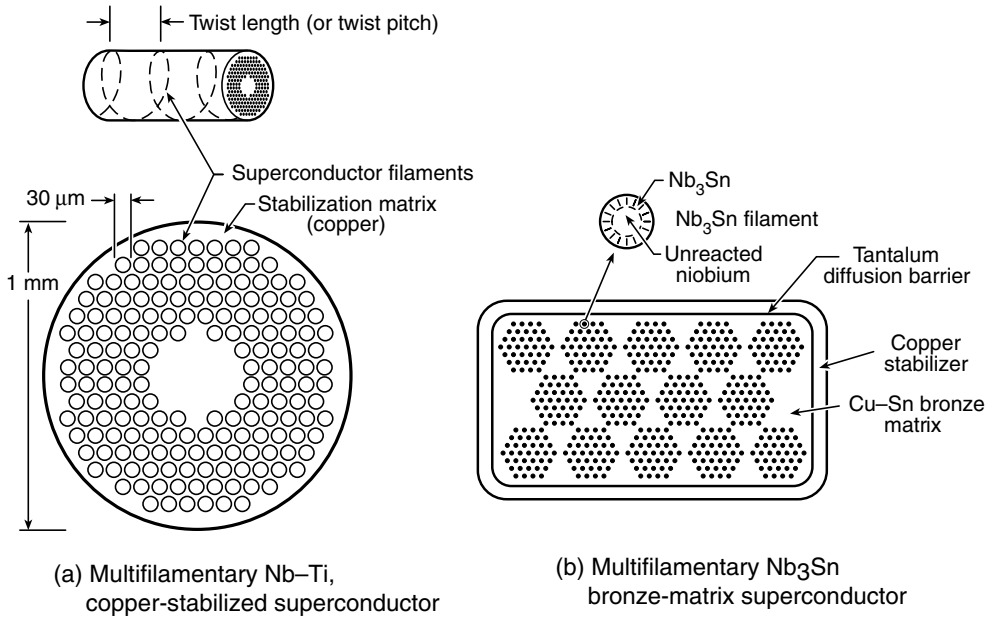

Fig. 7.24 Cross-sectional view of practical low-T_c superconducting composites: (a) Nb–Ti copper-stabilized multifilamentary superconductor; (b) Nb_3Sn bronze-matrix multifilamentary superconductor (adapted from Ekin 1983).

that are contained in Parts II and III of this book. More information about the intriguing techniques for fabricating practical low-T_c and high-T_c superconductors is given in Cardwell and Ginley (2002).

As illustrated by the cross-sectional views in Fig. 7.24(a) and (b), most practical superconductors are not single, large strands of superconducting material, but a *composite* structure consisting of

1. finely subdivided superconducting filaments,
2. which are embedded in a highly conductive normal-metal matrix (copper, aluminum, or silver, for example).

The conductive matrix stabilizes the superconductor against thermal runaway: If a disturbance locally raises the temperature of the superconductor filaments above their critical temperature and drives them into the normal resistive state, the copper will momentarily conduct the current and save the superconductor filaments from overheating. The copper stabilizer matrix also conducts away heat, protecting neighboring filaments from overheating.

The filaments in practical multifilamentary conductors are also usually *twisted* around the axis of the conductor [see Fig. 7.24(a)] in order to lower ac losses caused by changing current or magnetic field. (More information on ac losses is given in Wilson 1990 and Carr 2001.)

Figure 7.24(a) shows the configuration of a *ductile*, low-temperature Nb–Ti superconductor. It is made by stacking Nb–Ti rods into a large (typically 10–20 cm in diameter) copper cylinder, or billet. Then, through the miracle of metallurgy, this large billet is extruded and drawn into a wire more than a kilometer long and only ~1 mm in diameter, all the while preserving the complex composite structure shown in Fig. 7.24(a). Such a ductile composite can be bent into almost any shape for testing purposes.

Figure 7.24(b), on the other hand, shows the cross section of a *brittle*, low-temperature superconductor, such as Nb_3Sn. Because Nb_3Sn is brittle, it cannot be fabricated in the same way as a ductile superconductor. Rather, the constituent elements, niobium and tin, which in their pure form are ductile, are first fabricated along with copper into a billet (similar to Nb–Ti composites described above) and drawn into kilometer lengths of conductor. The composite wire is ductile at this stage, so it can be wound into a coil, after which the niobium filaments are heated to a high temperature (typically ~750°C) so that the niobium reacts with the tin in the billet to form brittle Nb_3Sn filaments.

All this takes care and practice, however. It is worth repeating that when these brittle samples are handled for testing, they can be easily damaged without your knowledge, because the matrix material is soft and ductile, and hides what is inside.

The brittle ceramic high-T_c superconductors have similar challenges with handling. Figure 7.25(a) illustrates the geometry of bismuth-based superconductors. The superconductor material is first ground into a fine powder, mixed, and inserted into a silver/silver-alloy billet. The composite billet is then drawn, rolled into a long tape, and heat-treated to make the superconductor compound, usually by repeatedly heating and pressing the composite tape. Because of the multiple heating-and-pressing steps, the untreated conductor is not simply wound into a final coil shape and then heat-treated. Instead, the brittle conductors are produced in long lengths and then wound onto large spools (to minimize bending strain) for shipping and handling.

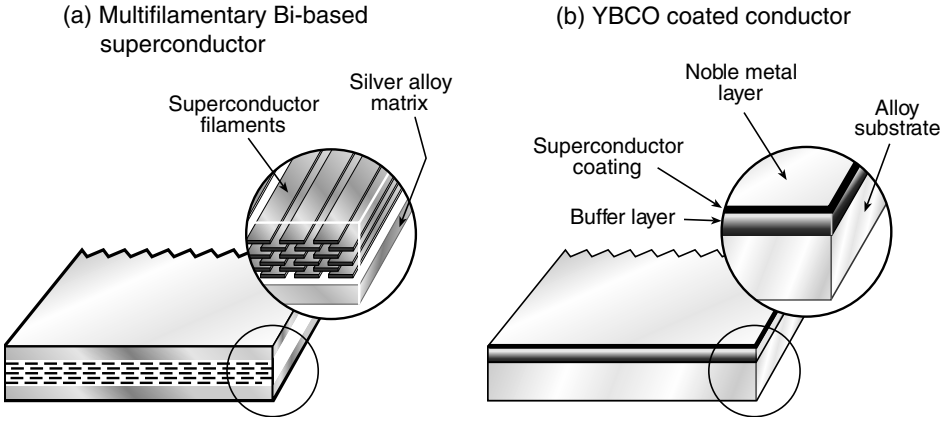

Fig. 7.25 Cross-sectional view of practical high-T_c superconducting composites: (a) multifilamentary $(Bi,Pb)_2Sr_2Ca_2Cu_3O_{10}$ silver-alloy sheathed high-T_c superconductor tape; (b) coated thick-film $YBa_2Cu_3O_7$ superconductor tape (from Banker 2003).

Figure 7.25(b) illustrates the composite nature of $YBa_2Cu_3O_7$ (YBCO) coated conductors. They are formed by depositing a YBCO film onto a structural alloy substrate, with a buffer layer in between. The YBCO film is typically 1–4 μm thick; to conduct high supercurrents, it must be nearly a single crystalline layer. The crystallinity is obtained either with a highly textured nickel-alloy substrate (produced by rolling and heat treatments) or by depositing a highly textured buffer layer onto a polycrystalline structural substrate (produced by ion-beam-assisted deposition). The crystalline structure is then transferred to the superconductor through epitaxial deposition of YBCO onto the buffer/substrate base. A noble metal layer is deposited on top of this "sandwich" to enable a good electrical connection to be made to the superconductor coating, which is the subject of the next chapter.

7.6 References

7.6.1 FURTHER READING

SUPERCONDUCTIVITY—COMPREHENSIVE REFERENCE TEXTS:

Cardwell, D., and Ginley, D., eds. (2002). *Handbook of Superconducting Materials*, Institute of Physics Publishing, Bristol, UK.

Evetts, J., ed. (1992). *Concise Encyclopedia of Magnetic & Superconducting Materials*, Pergamon Press, Oxford, UK.

Seeber, B., ed. (1998). *Handbook of Applied Superconductivity*, Institute of Physics Publishing, Bristol, UK.

SUPERCONDUCTING MAGNETS, AC LOSSES, SUPERCONDUCTOR STABILITY, AND THERMAL RUNAWAY:

Carr, W. J., Jr. (2001). *AC Loss and Macroscopic Theory of Superconductors*, 2nd edition, Taylor and Francis, NY.

Wilson, M. N. (1990). *Superconducting Magnets*, Oxford University Press, Oxford, UK.

STANDARD TEST METHODS FOR LONG SUPERCONDUCTOR SAMPLES:

Cu/Nb–Ti composite superconductors—IEC International Standard 61788-1, http://www.iec.ch/.

Nb_3Sn composite superconductors—IEC International Standard 61788-2, http://www.iec.ch/.

WIRE-BONDING TECHNIQUES:

Harmon, G. G. (1997). *Wire Bonding in Microelectronics: Materials, Processes, Reliability, and Yield*, McGraw-Hill, NY.

TRANSPORT MEASUREMENT TECHNIQUES FOR UNPATTERNED FILMS, ARBITRARILY SHAPED FLAT SAMPLES, AND ANISOTROPIC SAMPLES:

Unpatterned films—sheet-resistance measurements, Appendix A7.1

Arbitrarily shaped flat samples—Van der Pauw method, Appendix A7.2

Anisotropic samples—Montgomery method, Appendix A7.3

7.6.2 CHAPTER REFERENCES

Banker, A. (2003). American Superconductor Corp., Westborough, MA, personal communication.

Cardwell, D., and Ginley, D., eds. (2002). *Handbook of Superconducting Materials*, Institute of Physics Publishing, Bristol, UK. Part B focuses on processing techniques.

Carr, W. J., Jr. (2001). *AC Loss and Macroscopic Theory of Superconductors*, 2nd edition, Taylor and Francis, NY.

Claassen, J. H., Reeves, M. E., and Soulen, R. J. (1991). "A contactless method for measurement of the critical current density and critical temperature of superconducting films," *Rev. Sci. Instrum.* 62, 996–1004.

Ekin, J. W. (1978). "Current transfer in multifilamentary superconductors. I. Theory," *J. Appl. Phys.* 49, 3406–3409. See also the original numerical analysis of Wilson (1977).

Ekin, J. W. (1983). "Superconductors," Chapter 13 in *Materials at Low Temperatures*, eds. R. P. Reed and A. F. Clark, ASM International, Materials Park, OH.

Goodrich, L. F., Ekin, J. W., and Fickett, F. R. (1982). "Effect of twist pitch on short-sample V–I characteristics of multifilamentary superconductors," *Adv. Cryog. Eng. (Mater.)* 28, 571–580.

Goodrich, L. F., Bray, S. L., and Stauffer, T. C. (1990). "Thermal contraction of fiberglass–epoxy sample holders used for Nb_3Sn critical-current measurements," *Adv. Cryog. Eng. (Mater.)* 36A, 117–124.

Goodrich, L. F., Wiejaczka, J. A., Scrivastava, A. N., and Stauffer, T. C. (1994). *Superconductor Critical Current Standards for Fusion Applications*, NISTIR 5027, National Institute of Standards and Technology, US Government Printing Office, Washington, DC.

Hamilton, C. A. (1982). "High-speed, low-crosstalk chip holder for Josephson integrated circuits," *IEEE Trans. Instrum. Meas.*, IM-31, 129–131.

Harmon, G. G. (1997). *Wire Bonding in Microelectronics: Materials, Processes, Reliability, and Yield*. McGraw-Hill, NY.

Herzog, R., Evetts, J. E., Somekh, R. E., and Pullan, P. A. (1994). "Full angular critical current anisotropy of $YBa_2Cu_3O_7$ thin films," *Critical Currents in Superconductors*, 391, ed. Harald W. Weber, World Scientific Press, Singapore.

Incropera, F. P., and DeWitt, D. P. (2002). *Introduction to Heat Transfer*, 4th edition, John Wiley & Sons, NY.

Stork, F. J. B. (1996). "The thickness dependence of the morphology, ac and dc properties of laser ablated $YBa_2Cu_3O_{7-\delta}$ thin films." Master's thesis, University of Twente, Entschede, Netherlands.

Wilson, M. N. (1977). Report SMR/1, Rutherford Laboratory, Chilton, Didcot, UK.

Wilson, M. N. (1990). *Superconducting Magnets*, Oxford University Press, Oxford, UK.

Wire, M. S., Durand, D. J., Silver, A. H., Wagner, M. K., and Hamilton, C. A. (2001). "A multiple pin, flip-chip system for microwave and gigabit per second cryogenic device testing at variable temperatures," *Rev. Sci. Instrum.* 72, 1542–1547.

8 Sample Contacts

Skill is fine, and genius is splendid, but right contacts are more valuable than either.

– Archibald Mcindoe

8.1 Introduction

After designing an effective sample holder, we come to the crux of many transport measurements—making electrical contact directly to the test sample itself. If the contacts are resistive and there is significant Joule heating, sample temperature becomes impossible to control and measure. For many materials, sample contacts are straightforward, but not for the high-T_c oxide superconductors (HTS). They have a unique interfacial chemistry that is counterintuitive.

Problems can easily result. In early 1987, a few days after the announcement of the new high-T_c superconductor Y–Ba–Cu–O, and just a day before my semiannual allotment of time at the National Magnet Laboratory, I made the hasty decision to scrap all my plans for testing other materials and, instead, try to take a first look at the transport critical current of the new superconductors (all other critical-current measurement on HTS up to that time had been contactless magnetization experiments). I called everyone I knew for information about how to make electrical contact to the oxide superconductors, but no one had any idea. So, I tried the usual soldering technique with Pb–Sn solder, but that was unproductive. I had only Saturday night to find something that would work before leaving for the Magnet Lab, so I went to my old standby, indium, thinking that if it could wet glass, it would wet anything. But no luck.

Out of desperation I tried raising the temperature of the soldering iron a bit more and scratching the sample with the soldering tip *under* the molten indium and, voilà, it worked. I later learned it was not the greatest contact; in fact, it was pretty bad. But it was adequate for the early samples (which I soon discovered truly had zero *transport* resistance, but a terribly low critical current that became even worse in magnetic fields—so much for good utilization of my limited time at the high-field test facility). Eventually, however, this crude little discovery led to an improvement in contact resistivity by nine orders of magnitude and the pioneering patents for contacts to high-T_c superconductors (Ekin et al. 1990–1993). The spectacular improvement came about mainly from understanding the chemistry at the interface between the contacts and the sample.

In this chapter, we focus predominately on contact techniques for the more challenging high-T_c oxide superconductors. However, many of the topics are widely applicable to transport measurements on materials in general. Such topics include, for instance, techniques for soldering to thin noble-metal contact pads (in Sec. 8.3.3 under the heading Soldering) and methods for measuring specific-interface resistivity (Secs 8.3.4 and 8.4.3).

After the introduction, the chapter is divided into two major parts: the first describes techniques for fabricating contacts to *high-current* ($\gg$1 A) superconductors (Sec. 8.3); the second focuses on contacts to low-current *film* superconductors (Sec. 8.4). Thick-film, high-current conductors, such as Y–Ba–Cu–O (YBCO) "coated superconductors," are hybrids. Because they have the same surface-contacting requirements as thin films, they are treated, for the most part, with thin films in Sec. 8.4. (However, techniques in Sec. 8.3 on soldering and indium-pressed contacts pertain to coated conductors as well as bulk superconductors.)

Methods for accurately *measuring* contact resistivity are presented for high-current superconductors in Sec. 8.3.4 and for film superconductors in Sec. 8.4.3. This is especially useful when first starting a new contact fabrication process to provide feedback on the contact resistivity actually being achieved.

Finally, once the contact resistivity is known, we need a rough idea of the minimum contact *area* required to prevent sample overheating. This is important for planning the amount of contact length to allow in the initial design of a sample holder, particularly for critical-current measurements because the current densities and contact heating are so high. If heating is too great, the sample temperature rises to an unknown value and the data are useless. Operational heating checks can be made later, but it is difficult to arrange for more contact length if the space allowed in the sample holder is not at least approximately correct in the first place. Several calculational examples are given at the end of the chapter to illustrate a simple method for estimating the required minimum contact area (Sec. 8.5). Although the examples are given for critical-current measurements, the same calculational procedure applies to other types of transport measurements as well.

For these calculations to be valid, we also need to know the effect of *spreading resistance* within the contact pad. This is a concern particularly for contact pads that are thin, such as those usually deposited on high-T_c superconductors. Because of spreading resistance, the contact area we provide may be effectively much less than we think. This can produce severe overheating problems. An introduction to spreading-resistance effects and how to determine the true effective area of a contact is given in the last section, Sec. 8.6.

8.2 Definition of specific contact resistivity and values for practical applications

Before we launch into contact-fabrication techniques and the unique interfacial chemistry of high-T_c superconductors, we need to define a quantity to describe the resistance of a contact in a way that is independent of contact area: the specific contact-interface resistivity ρ_c:

$$\rho_c \equiv R_c A_c. \qquad \text{Specific contact resistivity} \tag{8.1}$$

Here, R_c is the contact resistance and A_c is the contact area. If, for example, we increase the area of a contact A_c, the measured contact resistance R_c would of course get proportionately smaller, but the $R_c A_c$ product remains the same. Thus, the $R_c A_c$ product ($\equiv \rho_c$) gives us a

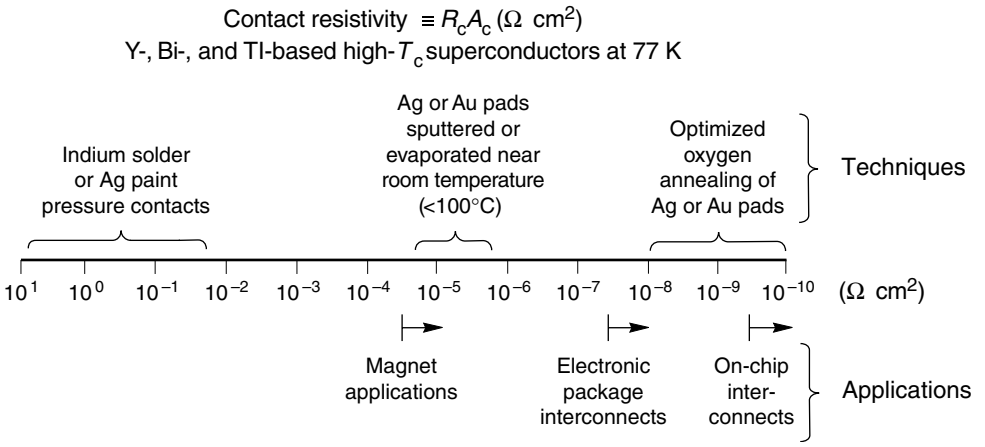

Fig. 8.1 Representative values of specific contact resistivity ($\rho_c \equiv R_c A_c$) for high-T_c superconductors. The lower half of the figure shows typical ρ_c requirements for particular applications. The upper half of the figure shows typical values of ρ_c that result from various contact-fabrication techniques.

means to quantify the specific resistivity of the contact interface independent of its area. Note that the contact resistivity ρ_c is measured in Ω cm^2 (that is *square* centimeters), not the usual Ω cm unit used for the *bulk* resistivity of materials ρ. (The two quantities could be mathematically related by $\rho_c \equiv \rho\, d$, where d is the thickness of the interface; however, for practical purposes, the "thickness" of an interface cannot be defined, and so the bulk resistivity of an interface is not a useful quantity.)

We can get a feeling for the contact-resistivity requirements in different applications by referring to the information below the line in Fig. 8.1.

- Superconductor applications, such as magnets and transmission lines, require a ρ_c less than 10^{-5}–10^{-4} Ω cm^2 to prevent unacceptably high heat and voltage generation at current connections. Values of ρ_c for transport critical-current *measurements* usually also fall in this range. Sometimes with short-sample measurements, pulsed-current methods can be used to minimize heating, and we can manage marginally high ρ_c values (of course, such techniques do not work in most applications, where current is usually steady state).
- Thin-film package interconnects, on the other hand, require nominal values of ρ_c in the range 10^{-8}–10^{-7} Ω cm^2.
- On-chip interconnects, where there are many contacts in series and the strip line width is narrow, present the most stringent requirements; in this case, an extremely low-contact resistivity in the range 10^{-10}–10^{-9} Ω cm^2 is necessary.

As a benchmark, the specific contact resistivity of two pieces of copper soldered together under moderate pressure with common eutectic Pb–Sn solder is quite low, about 4×10^{-9} Ω cm^2 (Goodrich and Ekin 1981). This is near the extreme right end of Fig. 8.1, and thus for conductors sheathed with copper or silver, the usual soft-soldering techniques adequately serve a wide range of magnet and transmission-line applications. However, when contacts are formed to bare high-T_c superconductors (bulk, film, or thick-film conductors), it

presents a different situation. Here the range of possible ρ_c values is enormous, spanning eight orders of magnitude, as indicated by the information above the line in Fig. 8.1. This great range results from the unique interfacial chemistry of high-T_c oxide superconductors. Depending on the contact technique, a semiconducting interface can be formed (described later), which produces highly resistive contacts.

An overview of ρ_c values for the entire range of HTS contact techniques is given in Appendix A8.1, along with comments on the common usage for each type of contact. The techniques giving the best (lowest) contact resistivity are listed first, with a soldered copper contact shown at the top of the list for reference. Common Pb–Sn soft-solder works fine for making contacts to low-T_c superconductors with a copper *sheath*, or for contacting bismuth-based high-T_c superconductor with a relatively thick (> 100 μm) silver sheath. Contacting YBCO and other oxide superconductors without a thick integral silver sheath is more challenging. As shown in the upper part of Appendix A8.1, the *in situ* technique (described below) gives the best contact resistivity. The *ex situ* technique is not far behind, provided it is oxygen annealed (and, for many applications, the *ex situ* method is the only one possible). However, beware that soldering copper wires or bus bars to any of these contacts can destroy their low resistivity. As shown in the lower part of Appendix A8.1, soldered contacts can have their contact resistivity degraded by many orders of magnitude; this damage can be mitigated, however, with the proper technique.

A detailed discussion of these techniques for bulk (high-current) samples is given next, with particular emphasis on the problematic case of bare oxide superconductors. The principles for making *film* contacts of high quality are similar to those discussed for bulk samples, but the techniques are somewhat different, as described in Sec. 8.4.

8.3 Contact techniques for *high-current* superconductors

8.3.1 OVERVIEW FOR HIGH-CURRENT SUPERCONDUCTORS

Contacts to oxide superconductors are more challenging if the superconductor is bare or covered by only a thin layer of silver (e.g. materials such as YBCO "coated conductors" or high-T_c superconductors that are unsheathed). Appendix A8.2 summarizes my preferences specifically for contacts to YBCO. The contact types are listed according to whether the methods are appropriate for *voltage* or *current* connections, because there are more possibilities for the relatively easy-to-make (low-current) voltage contacts than for the high-current contacts, where a lot more care is required to achieve low resistivity.

8.3.2 VOLTAGE CONTACTS

Wires used as voltage leads should be small in diameter—much thinner than the sample cross-sectional dimensions, if possible, so the voltage contact point is well defined. Thin voltage leads also reduce the chance of damaging the sample from handling, which can occur if

the voltage lead is so large that its strength becomes comparable to that of the sample. A thin voltage lead also minimizes the risk that it will be pulled off owing to differential thermal contraction during cooling.

Soldered voltage contacts

When attaching wire voltage leads, I prefer soldering, because it is robust and works well for copper-sheathed samples, silver-sheathed oxide superconductors, and (with the right solder) even bare oxide superconductors. Some samples, however, would be damaged by soldering (either chemically or thermally). Also, at times, soldering is inconvenient, such as when many similar samples need to be tested in rapid succession; in that case, spring-pressure voltage contacts are worth making, as described below under the heading "Pressure contacts."

When selecting a soldering material for voltage taps, a few precautions are in order. For copper-sheathed low-T_c superconductors, common eutectic Pb–63%Sn solder is fairly strong and works well (T_{melt} = 183°C). However, the heat from soldering can cause oxygen loss in high-T_c superconductors: *bismuth*-based superconductors above ~300°C, and *YBCO* above only ~150°C. The relatively high melting temperature of some soldering materials can also lead to thermal shock, especially in the case of sintered materials or bismuth conductors where the superconducting material can be fragile and porous. For *laminated* conductors with layers held together by solder (as part of the composite's internal makeup), the soldering temperature must be no greater than the lowest melting temperature of the internal soldering materials. Common solders with lower melting temperatures include eutectic In–3%Ag (143°C), pure indium (157°C), or Ostalloys® 158 or 162.

Melting temperatures of solders are included in the resistivity-of-materials table given in Appendix A8.4, and a more extensive listing is given in the general solder-properties table in Appendix A3.7.

As noted at the beginning of this chapter, Pb–Sn-based solders will not wet bare oxide superconductors, but indium-based solders will. However, *pure* indium (T_{melt} = 157°C) is extremely soft and weak, so indium-solder *alloys* are better choices, such as eutectic In–48%Sn (T_{melt} = 118°C) or eutectic In–3%Ag (T_{melt} = 143°C). Not only are they stronger than pure indium, but their soldering temperatures are (advantageously) lower.

After soldering voltage leads, I generally give the lead a gentle pull with a pair of tweezers after making the connection to make sure the connection is mechanically sound. A few times I have detected bad solder joints this way; in each case, the extra 10 s invested has saved me a couple hours of testing time.

Wetting the oxides

Solder flux is "death" for most bare, sintered oxide-superconductor materials. The flux wicks into the superconductor along grain boundaries and degrades the transport properties of the superconductor. However, for superconductors with bi-axially aligned grain boundaries, such as single crystals or high-quality thin films, there is no effective degradation since the grain boundaries are almost impervious to fluids such as water, solder flux, and photoresist processing chemicals. So for oxides that are not bi-axially aligned, use pure indium *without any solder flux*.

Indium will wet almost anything, including glass and ceramics. Just make sure the sample surfaces are clean … very clean.

Either pure indium or (stronger) indium alloys can be made to wet bare, bulk high-T_c superconductors by lightly scratching the sample surface with a soldering iron *under* the molten indium (again, with no solder flux). To avoid overheating the sample, I would suggest keeping the temperature of the soldering iron only about 30–50°C above the solder's melting temperature by using a variable-temperature soldering iron or by plugging the soldering iron into a variable power source.

An even more certain method of wetting bare, bulk high-T_c superconductors is to use an ultrasonic soldering iron. Operate the ultrasonic iron at very low ultrasonic power to keep from fracturing the sample. Also, for ultrasonic soldering to work well, the sample must be placed on a mechanically rigid surface. A drop of molten solder is applied to the hot tip of the ultrasonic soldering iron, and the vibration of the tip chips away at the brittle superconductor's surface beneath the molten solder drop, exposing a fresh surface that the solder readily wets. However, if the sample is very fragile, it is best to patiently scratch the oxide surface by hand under a drop of molten indium-based solder, as mentioned in the preceding paragraph.

Whereas ultrasonic soldering and scratching works well with brittle materials, ultrasonic soldering is surprisingly useless with copper leads, because copper is ductile, and the tough copper-oxide layer on the surface does not chip away. A mild ZnCl flux is needed to chemically cut through the copper-oxide coating on the surface and allow the indium-based solders to wet the copper surface. Thus, a chemical flux is essential for separately "tinning" copper leads with indium before soldering them to high-T_c superconductors. (After tinning, however, wipe all the excess flux off the copper leads before attempting to attach them to bulk-sintered oxide superconductors, or, once again, it is "death by flux.")

Pressure contacts

For quick sample changing or when many samples need to be tested, spring contacts are convenient. They are a little more work to fabricate initially, but they can be used to make voltage contacts to almost any sample material.

A "springy" material such as beryllium–copper spring stock is used to make contact with the sample by cutting and forming the alloy sheet into a spring or clip that presses on the sample surface with an arrangement such as that shown in Fig. 8.2. Contact pressure must be kept light ($\lesssim$0.5 N for small, brittle samples) so the sample will not be damaged; the sample also must be supported with a solid sample-holder base, as illustrated in Fig. 8.2.

If the contact resistance between the spring clip and the sample is too high, try coating the surface of the spring (where it will touch the sample) with a small drop of indium solder. Again, a mild flux is needed to get indium to wet copper-based materials, such as beryllium–copper, but be sure to thoroughly clean the residual solder flux off the indium before making a pressure contact to the superconductor. If silver or gold contact pads are going to be deposited on the superconductor for *current* connections (see below), it is convenient to also deposit an extra set of *voltage* contact pads on the superconductor at the same time. Such pads work well to lower the resistance of the spring-clip contact where it presses on the sample.

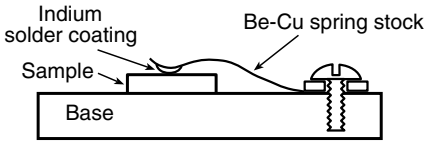

Fig. 8.2 Spring contact for convenient, quick changing of contacts when testing many samples.

Silver paint, paste, and epoxy

My least favorite contact methods are silver paint, silver paste, and silver-based epoxy. The joint is weak (for paint and paste), and the voltage contact usually ends up as a sizable blob. Annealing the silver paint or paste in oxygen by using the oxygen-annealing procedure described below can greatly improve the contact resistivity. However, the organic carrier used in compounding the silver paint or paste can wick in along pores and grain boundaries, degrading bulk-sintered samples (but again, it can be okay with high-quality, highly aligned thin-film superconductors). Nevertheless, these conductive compounds do serve to make electrical connections and are sometimes the only way of contacting small, delicate samples. Supplier information is given in Appendix A1.7.

8.3.3 CURRENT CONTACTS FOR OXIDE HIGH-T_c SUPERCONDUCTORS

These are the challenging connections. Because *current* contacts must carry much higher current than voltage contacts, the requirements on ρ_c are orders of magnitude more stringent. For silver-sheathed conductors, excellent low-resistivity current contacts can be made simply by *soldering* to the thick silver sheath, as long as the sheath is more than about 20 μm thick. But if the silver layer is only a few micrometers thick, or if the contact must be made directly to a bare oxide sample, then soldering does not work for high-current contacts because the resulting ρ_c is far too excessive.

Pressed-indium contacts

Pressing indium against the superconductor surface, without heating or soldering, forms a medium-grade contact that is sometimes useful for testing tape samples, such as YBCO-coated conductors. The advantage of this technique is that samples can be changed fairly quickly. It works well for initial screening of tape samples, provided the current is not too high (less than ~100 A/cm of tape width) and provided the sample does not need to be heated later for additional processing (because residual indium on the surface reacts with and degrades YBCO). (In the latter case, a soft annealed silver foil works in place of indium because of interfacial chemistry, as described below.)

With this pressed-foil technique, a copper current block with a thin intermediary soft-indium foil is pressed against the surface of the superconducting tape by tightening a pressure bolt, as illustrated in Fig. 8.3. Immediately before making the pressure current contact, clean the bottom of the copper block by sliding it back and forth over sandpaper on a flat surface. Also, both sides of the indium foil need to be scraped clean just before making the pressure

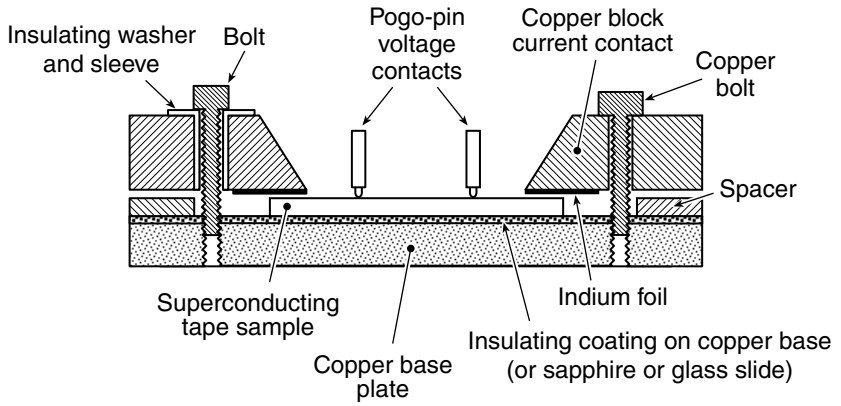

Fig. 8.3 Indium-pressure contacts for relatively low-current tapes (based on a design by Martin 2001). Clean copper current blocks are screwed against the surface of the tape with an intermediate layer of clean (freshly scraped) indium foil or soft, annealed silver foil. Voltage contacts can be made to the center portion of the tape sample with pogo pins (described in Sec. 7.4.3).

contact by drawing a razor blade backwards across the foil surface while the foil is laying on a flat surface.

High-current contacts—failures

For conductors carrying high current (several hundred amperes per centimeter of width), the interfacial resistivity of such pressed-indium contacts is too high. To reduce Joule heating to acceptable levels, a better contact is needed. The end of Appendix A8.2 lists my early attempts to find a better method of contacting oxide superconductors.

Everything I tried was a failure. But failures can be instructive. I found that Cu or Au–Cr (a great semiconductor-contact material) sputter-deposited onto a clean oxide-superconductor surface is terrible. Lead–tin solder does not form a bond at all. Most of the *voltage* contact methods at the top of Appendix A8.2 would also fail as current contacts. Silver paint adheres, but has a high interfacial resistivity, unless the paint is oxygen-annealed at high temperatures ($\gtrsim$400–500°C). Pure indium and indium-alloy solders, even when applied to a freshly exposed superconductor surface under molten solder, produce contacts with interfacial resistivities that are orders of magnitude too high for use in most high-current connections.

Interfacial chemistry

The underlying problem that all these "bad" contact materials have in common is a high affinity for oxygen. Figure 8.4(a) illustrates this with an Auger electron spectrograph (AES) depth profile of the interface between YBCO and a typical indium-alloy solder (In–2%Ag). The AES signal strength along the vertical axis indicates the relative amount of different elements at the interface; the sputter time along the horizontal axis indicates the relative position across the interface as the probe sputters through pure indium on the left side of the figure, into pure YBCO on the right side. The AES depth profile shows that indium does not end abruptly at the YBCO surface but, instead, diffuses far into the YBCO, reacting with the oxygen in the YBCO.

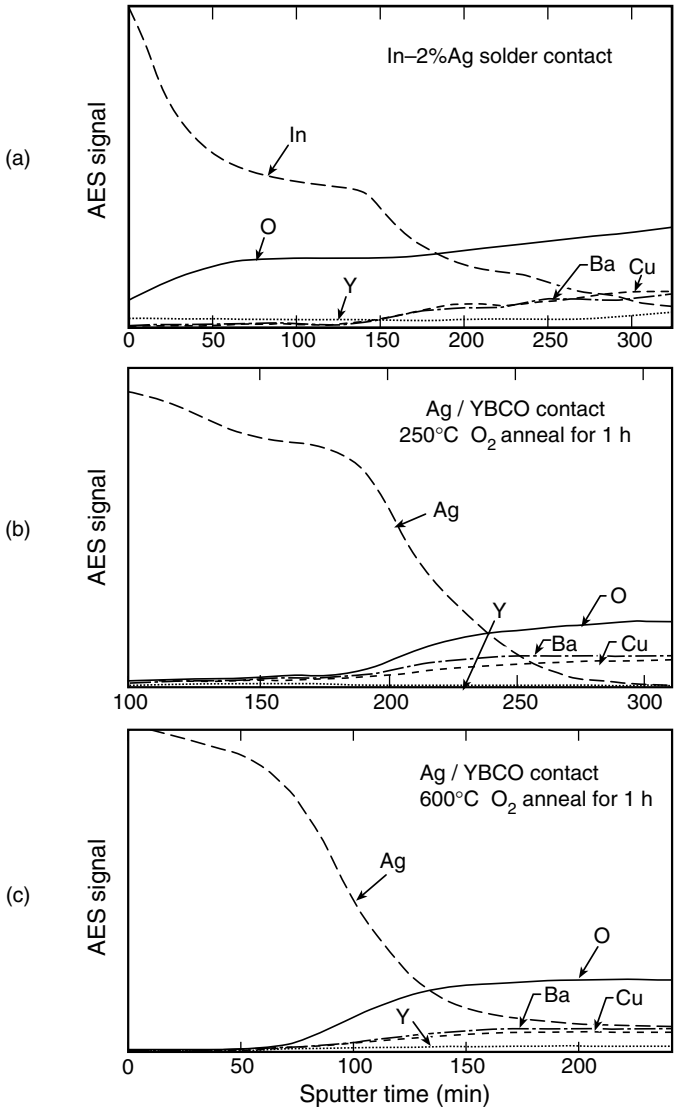

Fig. 8.4 Auger electron spectroscopy (AES) depth profile for three contacts to YBCO: (a) indium-solder contact; (b) Ag/YBCO contact [given an oxygen anneal at a very low temperature (250°C)]; and (c) Ag/YBCO contact fully oxygen-annealed at 600°C for 1 h. Relative amounts of each element are indicated by the Auger electron intensity, plotted along the vertical axis in arbitrary units; position across the interface is indicated by the ion sputter time plotted along the horizontal axis (from Ekin et al. 1988a).

This oxygen reaction causes two major problems: first, at the surface, the YBCO superconductor is depleted of its oxygen and ceases to be superconducting; second, the oxygen gets bound into an indium-oxide compound that forms a resistive barrier at the interface. The compound layer (indicated by the nearly constant oxygen and indium signals from about 50 to 150 min sputter time in Fig. 8.4), is probably In_2O_3, which is semiconducting. It has a band gap of 3.5 eV and a resistivity at liquid-nitrogen temperature that is orders of magnitude

higher than that of most metals. Thus, an interfacial In_2O_3 layer would explain the poor interfacial resistivity observed for In/YBCO contacts.

Similarly, lead, tin, chromium, and copper all readily form oxide compounds, which would explain the poor contact resistivities for these materials as well (listed in Appendix A8.2 under "Failures"). The ρ_c of silver paint is probably high because of a degradation of the superconductor surface by the organic carrier in the paint.

The solution is to use contact pads made from materials with a low affinity for oxygen—the *noble* metals. Verification of this is shown by the AES depth profile of an Ag/YBCO interface in Fig. 8.4(b). The oxygen signal decays very quickly into the silver, and there is no telltale section of nearly constant silver and oxygen signal levels, which would indicate the formation of an oxide-barrier compound [as in the In/YBCO depth profile in Fig. 8.4(a)]. The ρ_c values for sputter-deposited silver and gold contacts to YBCO are shown in the current-contact section of Appendix A8.2. These values are four to six *orders of magnitude* lower than those for the materials of high oxygen affinity presented at the end of Appendix A8.2.

Fabrication procedures for high-quality HTS current contacts

Thus, the trick for fabricating high-quality HTS contacts is to avoid formation of a resistive oxide-compound layer at the contact interface. A generic method that consistently yields high-quality, low-ρ_c contacts consists of the following four basic processing steps:

(1) *clean* the superconductor surface;

(2) use a *noble metal*, such as silver or gold, for the contact material;

(3) *oxygen-anneal* the noble-metal/superconductor interface (this step is not needed if ρ_c over $10^{-5}\ \Omega\ \text{cm}^2$ is acceptable;

(4) if current leads are to be *soldered* to the noble-metal pads, make sure the noble-metal pads are at least 7–10 μm thick and use a low-melting-temperature, low-leaching solder such as In–3%Ag (143°C).

Cleaning: The surface of YBCO reacts with water vapor and carbon dioxide to produce a resistive layer at the superconductor surface. The effect of this barrier on contact resistivity is shown in Fig. 8.5, where contacts were made to YBCO films that had been exposed for different times to air, CO_2, N_2, O_2, and vacuum *prior* to depositing a silver contact pad. As shown in Fig. 8.5, the ρ_c of such contacts rises rapidly for air exposure times $\gtrsim 1000$ min. So, the first step before depositing a noble-metal contact pad is to remove the degraded superconductor surface. This cleaning step is helpful, but not essential, if the contacts are later oxygen-annealed (described below).

To clean *bulk* samples, I like to lightly sand the surface where the contact pads will be made and then use low-energy sputter etching (a physical etching process carried out in a low-pressure argon atmosphere; see "Further reading") or ion milling (carried out in a vacuum, typically with argon ions accelerated from a source). The sputtering or milling cleans away the remaining degraded layer on the oxide-superconductor surface just before the noble-metal contact pads are deposited. It is best to carry out the sputtering or milling in the same vacuum system where the noble-metal pads will be later deposited, so the samples are not exposed to air between cleaning and deposition. (For *thin-film* samples, of course, no sanding is done; just the ion milling is performed.)

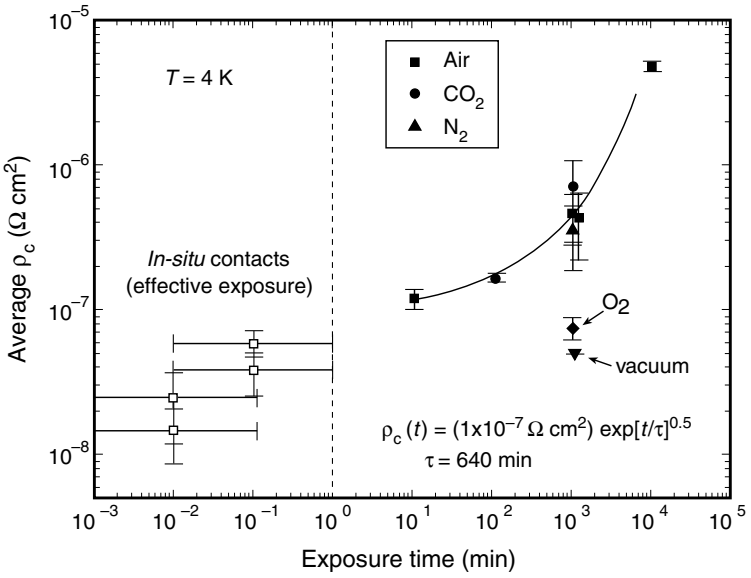

Fig. 8.5 Contact resistivity of Ag/YBCO interfaces at 4 K as a function of exposure time to air, CO_2, N_2, O_2, and vacuum (from Russek et al. 1994). The term "*in-situ* contacts," designating the data to the left of the vertical dashed line, refers to noble-metal contact pads deposited *in situ* on freshly fabricated superconductor surfaces not exposed to air. The "effective" exposure times for these *in situ* contacts result from the small residual partial pressure of water vapor in the vacuum chamber, which reacts with the sample surface during the period between the end of superconductor deposition and the start of noble-metal deposition.

It is important in this step to keep the ion-milling or sputter energy low to avoid destroying the weak crystal structure of the superconductor. However, if the energy is too low, the damaged surface material is not removed. An optimum reduction in ρ_c is achieved by ion milling or sputter etching with argon at about 200 V, which, at a typical ion current density of 0.5 mA/cm^2, will remove about 16 nm in about 2 min. (Further information is given in Sec. 8.4.2.)

Noble metal deposition: The noble-metal contact layer needs to be deposited onto the superconductor surface immediately after the superconductor surface is sputter-cleaned or ion-milled. As mentioned above, this step should be done preferably without exposure to air between the cleaning and deposition operations, or at least the intervening period should be limited to less than a few hours (see Fig. 8.5).

Silver or gold can be either thermally evaporated or sputtered onto the surface. The relatively higher energies of sputtering compared with those of evaporation can damage the superconductor's crystal structure at the surface. However, if the first few tens of nanometers of sputter deposition are carried out at a relatively low cathode voltage (e.g. $\lesssim$750 V) in argon at a reasonably high gas pressure of 1–2 Pa (to reduce the ion energy), sputtering produces a layer of noble metal strongly bonded to the superconductor surface with minimal surface damage. After a few tens of nanometers of noble metal are deposited, the sputter deposition energy (and rate) can be increased, since this initial layer then protects the superconductor surface.

Even with this variable-energy sputtering technique, the overall difference in deposition rate between sputtering and evaporation becomes important when depositing *thick* contact

pads. When copper wires or bus bars are soldered to the pads, the pad thickness needs to be about 7–10 μm thick. This keeps the solder from completely alloying through the pad and coming into contact with the sensitive oxide-superconductor surface (see "Soldering to noble-metal contact pads" below). Such a thick pad can take literally all day to deposit when sputtering, since sputter deposition rates are usually about 0.3–0.5 nm/s, whereas evaporation rates are typically 1–2 nm/s. So for speed and simplicity, it is usually best to deposit the noble-metal contact pad by *thermal evaporation*, typically from an inexpensive, resistively heated source. This usually produces ρ_c values of about 10^{-5} Ω cm^2 before oxygen annealing.

Oxygen annealing: It is possible to reduce ρ_c another three to four orders of magnitude (depending on how well the superconductor's surface has been cleaned prior to depositing the noble-metal contact pad) by annealing the contact pad in flowing oxygen after it is deposited. The resulting ρ_c is usually in the range 10^{-7}–10^{-8} Ω cm^2. A comparison of the AES depth profiles in Fig. 8.4(b) and (c) shows that, after oxygen annealing at 600°C, silver is diffused much farther into the superconductor (probably mainly along grain boundaries), thus providing better contact with the superconductor. Oxygen concentration near the YBCO surface is also enhanced.

Figure 8.6 shows the reduction of ρ_c obtained for Au/YBCO and Ag/YBCO contacts after annealing in oxygen at various temperatures. The annealing was carried out in flowing oxygen

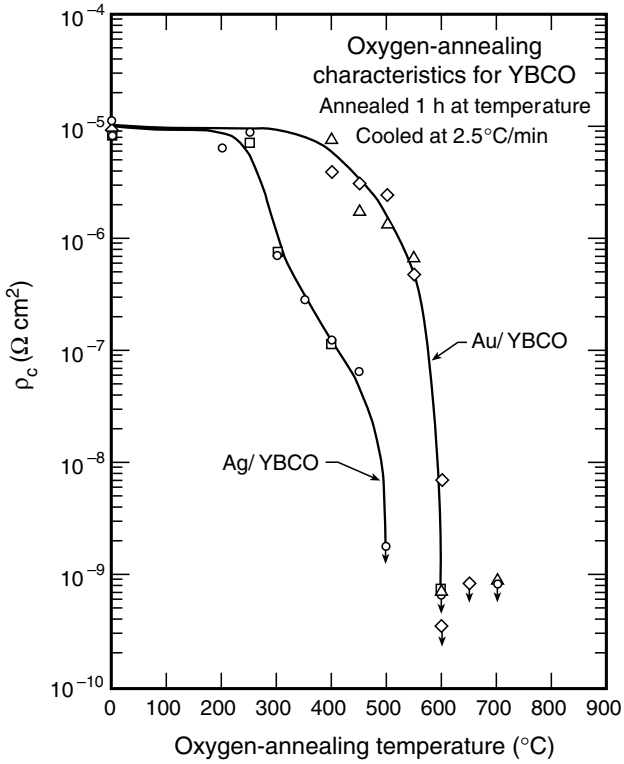

Fig. 8.6 Oxygen-annealing characteristic for silver and gold contacts on sintered bulk YBCO; annealing time was 1 h and oxygen was supplied at atmospheric pressure, flowing at a rate of about 2×10^{-6} m^3/s (~0.3 scfh, standard cubic feet per hour) (from Ekin et al. 1988a).

at atmospheric pressure for 1 h at each temperature. As seen in Fig. 8.6, a rapid reduction in ρ_c for gold contacts occurs at an annealing temperature about 100°C higher than that for silver, probably because higher temperatures are required for diffusion of gold. Another difference between the two noble metals is that oxygen readily diffuses through silver, whereas gold is impervious to oxygen. These and subsequent data indicate that the optimum condition for annealing Ag/YBCO contacts is about 30–60 min at about 500°C in flowing oxygen, whereas the optimum annealing temperature for Au/YBCO contacts is slightly higher, about 600°C. It is important not to anneal silver contacts at a temperature that is too high because the silver contact pad will completely diffuse into the YBCO and disappear. Annealing for longer than 1 h does not significantly improve ρ_c. Optimum annealing conditions are summarized for bulk-sintered HTS materials in Appendix A8.3. (For *film* superconductors, annealing times and temperatures are slightly lower, as described in Sec. 8.4.2.)

Oxygen-annealing curves for silver contact pads deposited directly on *bare* bulk-sintered *bismuth*-based superconductors are given in Fig. 8.7. Between 200°C and 400°C, the contact interface resistivity drops four orders of magnitude to the 10^{-9}–10^{-8} $\Omega\,cm^2$ range. The optimum

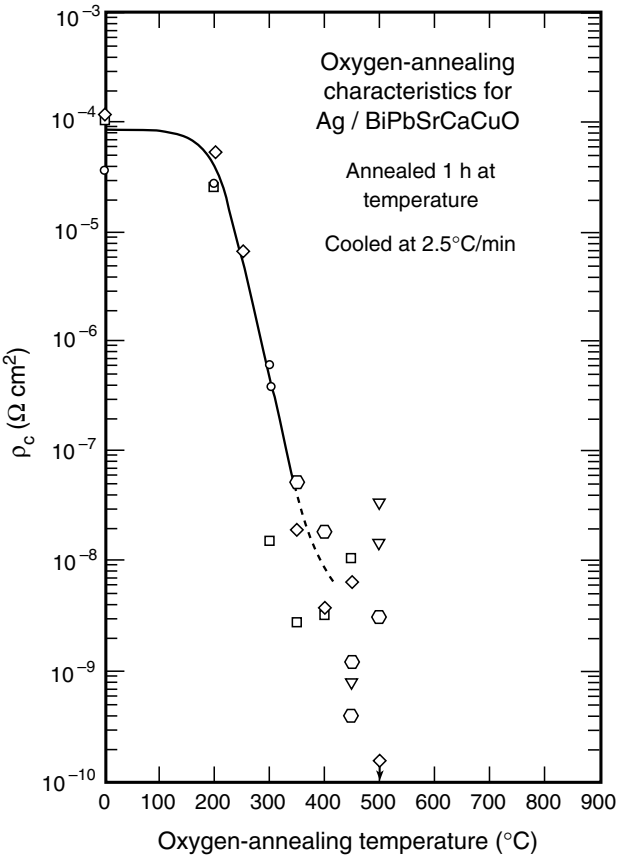

Fig. 8.7 Oxygen-annealing characteristic for silver contacts on bare bulk-sintered bismuth-based superconductors; annealing time was 1 h, and oxygen was supplied at atmospheric pressure, flowing at a rate of about 2×10^{-6} m^3/s (~0.3 scfh). (Ekin, unpublished data.)

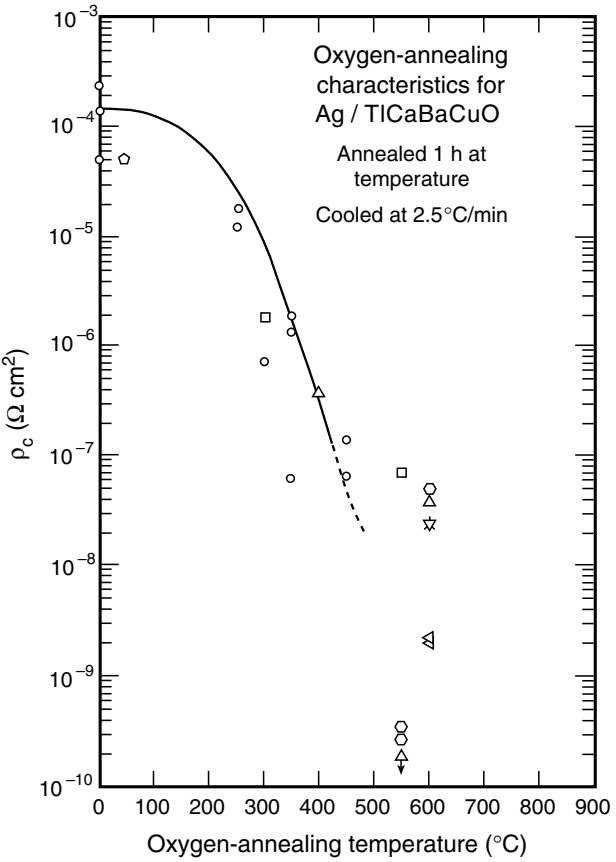

Fig. 8.8 Oxygen-annealing characteristic for silver contacts on bare bulk-sintered thallium-based superconductors; annealing time was 1 h, and oxygen was supplied at atmospheric pressure, flowing at a rate of about 2×10^{-6} m^3/s (~0.3 scfh). (Ekin, unpublished data.)

range of annealing temperature for silver contacts with bulk-sintered bismuth-based superconductors is lower than that for YBCO, about 350–400°C.

For silver contact pads on bare bulk-sintered *thallium*-based superconductors, the optimum annealing temperature range is about 500°C, as shown in Fig. 8.8. If too high a temperature is used, thallium loss results in a degraded superconductor (Siegal et al. 1999).

Figure 8.9 shows a typical tube-furnace arrangement for performing oxygen annealing. The sample (with contact pads already deposited on its surface) is placed in the tube furnace, and oxygen is fed into one end of the tube (on the left side of Fig. 8.9) through a flow valve at a low rate of about 2×10^{-6} m^3/s (~0.3 scfh). The oxygen flows down a small quartz tube inserted into a larger quartz tube holding the sample. In this way, the oxygen is warmed to furnace temperature before it flows back across the sample. Eventually, it vents through a flexible plastic tube with cotton or a paper tissue stuffed into its end to prevent backflow of air into the furnace tube. [At such a low flow rate (~2×10^{-6} m^3/s) no special precautions are usually needed for venting pure oxygen into a reasonably large laboratory space with normal room ventilation.] Air is purged from the sample tube by starting the oxygen flow at a high rate (say about 2–5 $\times 10^{-5}$ m^3/s) approximately 15 min before turning on the furnace; then the rate is reduced to the low value for

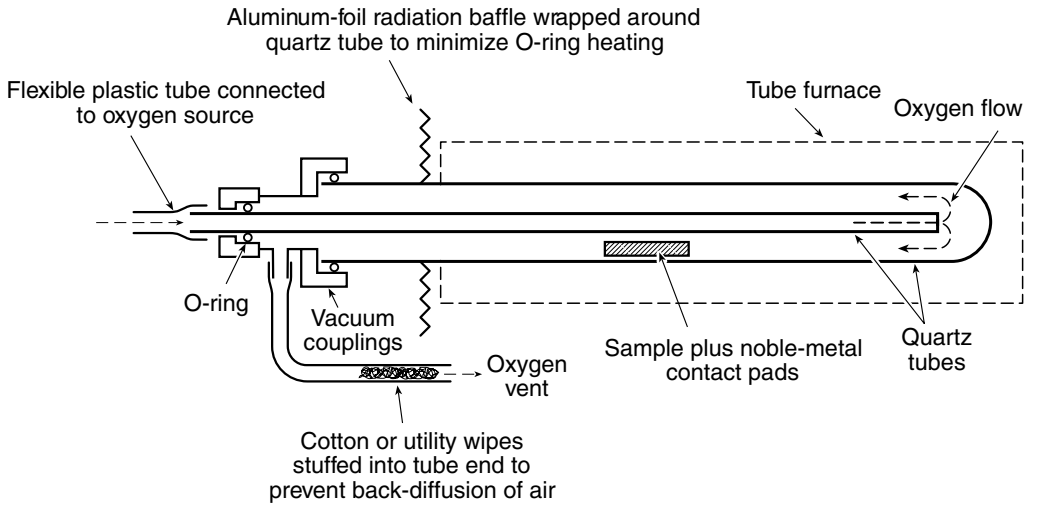

Fig. 8.9 Furnace arrangement for counter-flow oxygen annealing of high-T_c superconductor contacts, in which the oxygen is first warmed to the temperature of the furnace before it flows back across the sample.

the actual anneal (to save oxygen and to allow the flowing gas to warm to furnace temperature). After they are annealed, YBCO samples must be slowly cooled (typically 2.5°C/min), still in flowing oxygen to allow the crystal structure to take up its full complement of oxygen.

Soldering to noble-metal contact pads

Soldering to noble-metal contact pads is tricky. If not done correctly, the contact pad will become useless as a low-resistivity interface. The solder (usually indium-based) can partially alloy through the noble-metal contact pad, bringing oxygen-hungry indium in direct contact with the oxide superconductor, which forms the infamous indium-oxide barrier [Fig. 8.4(a)]. In the worst situation, molten indium can completely alloy with and dissolve thin noble-metal pads. The result is degradation of the interface resistivity of a perfectly good contact from 10^{-7} or 10^{-8} Ω cm^2 before soldering to typically 10^{-1}–10^{-3} Ω cm^2 after soldering.

Destruction of the noble-metal interface layer is avoided by using the following soldering technique:

1. Deposit a noble-metal contact pad at least 7–10 μm thick. (Thinner pads only ~0.2 μm thick are fine for attaching wire bonds to thin films, but not for soldering. For rapid, automated soldering and lamination, the thickness of the noble-metal layer can be reduced to a few micrometers, depending on the soldering temperature and time.)
2. Coat the noble-metal contact pad with a small amount of eutectic In–3%Ag solder or In–34%Bi, preferably *without* using solder flux (omitting the flux usually works for freshly deposited silver or gold). To minimize dissolving any more of the pad than necessary, adjust the soldering iron temperature so it is only about 30–50°C above the solder melting temperature (143°C for In–3%Ag or 72°C for In–34%Bi; data for other solders is given in Appendix A3.7). Avoid scratching the contact pad with the soldering iron. I have found that In–3%Ag generally works well because it has fairly high strength and contains no tin, which is a strong leaching agent for silver. Furthermore, since In–3%Ag solder already has exactly

the *eutectic* concentration of silver in it, minimal silver uptake should occur if the soldering temperature is kept close to the eutectic melting temperature. If a lower-temperature solder is needed, In–34%Bi works well, but it is not mechanically strong. If solder flux must be used to get the solder to wet older corroded silver pads, keep the amount to a minimum; for example, make a pointed wooden stick (by breaking the wooden stick of a cotton swab) and use it to apply a very small amount of flux to the area that needs to be wetted with solder. Clean away the residual flux with a cotton swab that has been moistened with a little water or alcohol.

3. Also pre-tin the copper wire or bus bar with In–3%Ag or In–34%Bi solder. In this case a mild solder flux such as zinc chloride is necessary to get the solder to wet the copper. Again clean away the flux with a cotton swab moistened with water or alcohol *before* attaching the copper conductor to the noble-metal contact pad.
4. Fuse the solder blob that is on the copper conductor to the solder-coated contact pad using *no* flux, with minimal heat (by using the moment at which the solder melts as an indicator of when the temperature reaches the melting temperature of the solder). Again, avoid scratching the contact pad.

Even when using this solder method, some indium degradation of the contact interface usually occurs. About the best ρ_c we can obtain when soldering is in the range of $10^{-6}\ \Omega\ \text{cm}^2$.

Silver-sheathed HTS materials

For a sample with an Ag or Ag–Mg sheath that is coprocessed with the superconductor (such as a bismuth-based superconductor tape), the resistivity of the Ag/HTS interface is typically very good, less than $10^{-8}\ \Omega\ \text{cm}^2$ (Appendix A8.1). Because the silver sheath of these samples is so thick (typically hundreds of micrometers), no particular care about leaching silver or diffusion of indium is required when soldering.

A solder should be chosen, however, that has a relatively low melting temperature, such as In–48%Sn (118°C), In–3%Ag (143°C), Pb–36%Sn–2%Ag (179°C), or standard eutectic Pb–63%Sn solder (183°C), so that heating does not result in oxygen loss from the superconductor crystal structure. As mentioned earlier in this chapter, the critical temperature and current of bismuth-based superconductors start to degrade from oxygen loss at temperatures above about 300°C. (A similar degradation from oxygen loss in YBCO materials heated in air starts to occur at temperatures of only about 150°C.) Also, be sure to choose a contact solder with a melting temperature lower than that of the solder used to fabricate laminated conductors. For structurally weak, porous materials, it is best to select a solder of lower melting temperature so that thermal shock from soldering does not structurally damage the superconductor.

8.3.4 MEASURING CONTACT RESISTIVITY

Measuring the contact resistivity of high-current superconductor samples is relatively easy, as illustrated by the configuration in Fig. 8.10. It consists of attaching an extra voltage lead to the current-contact pads being tested, in order to monitor the potential difference between the contact pad and any voltage tap on the superconductor. Such a scheme readily works, since at

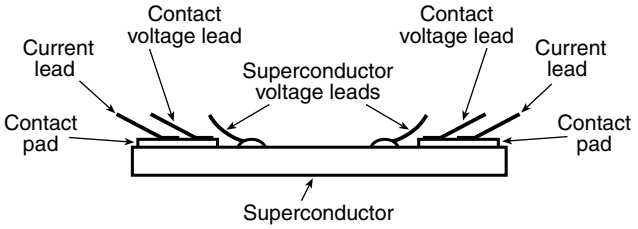

Fig. 8.10 Diagram of contact resistance measurement, showing extra voltage leads attached to each current pad close to a current lead. The potential difference between the extra voltage lead and a voltage tap placed anywhere on the superconductor can be used to monitor the voltage across the pad/superconductor interface.

a measuring current below the critical current, the superconductor has negligible resistance compared with the contact-pad interface resistance being measured. Thus, the superconductor is effectively equipotential, and a voltage lead attached *anywhere* on its surface will monitor the potential at the superconductor surface *under* the contact pads.

Keep in mind that the spreading resistance of the contact pad can limit the effective contact area, as discussed in Sec. 8.6. So it is important to attach the extra voltage lead *close* to where the current lead connects to the contact pad, especially if the contact pad is thin and the interface resistivity between the pad and superconductor is expected to be low. If the tap is *not* located well within the effective spreading distance ξ given by Eq. (8.8) in Sec. 8.6, then the tap will sense the voltage in a part of the contact pad where no current is flowing. The resulting reading will give an apparent contact resistance that is falsely low.

The *total* resistance of the contact/sample/contact combination can be monitored during an experiment by simply attaching voltage-monitoring leads to both contacts (see Fig. 8.10) and measuring the potential difference across the entire ensemble. This is always a good measurement practice, since it gives a warning if significant heating is occurring at either of the current contacts.

8.4 Contact techniques for *film* superconductors

8.4.1 OVERVIEW FOR FILM SUPERCONDUCTORS

In this section we focus on making contacts directly to thin-film superconductors—that is, the direct interface between a superconductor film and a contact pad deposited on its surface. *External* connections between the contact pad and the outside world [with wire bonds (ultrasonically welded microwires), pogo pins (spring-loaded contact pins), or microsprings, for example] are usually built into the sample-holder assembly and were described in Sec. 7.4.3.

Before presenting contact techniques specifically for oxide superconducting films, we make some brief observations about techniques for film samples in general:

- Contact pads for *thin* films are usually much thinner (usually 50–200 nm thick) than those for high-current *thick* films, because for thin films, connections to the outside world can be made using low-current wire bonds and pogo pins. In contrast, thick-film samples (such as YBCO-coated conductors) require contact pads 7–10 μm thick so they can be *soldered* to

high-current bus bars (see the earlier discussion on Soldering to noble-metal contact pads, near the end of Sec. 8.3.3).

- Gold is a popular material for film contact pads because it maintains a clean contact surface and does not tarnish like silver. However, the cost of gold becomes significant when depositing thick contact pads on high-current coated conductors. Then silver is a more economical choice.
- If ion-milling equipment is available, higher-quality contacts can be obtained by giving the surface of the superconductor a light cleaning etch with a low-voltage ion mill before depositing the noble-metal contact pads. It is best to deposit the contact pads immediately after the cleaning mill, before the surface has had time to degrade.
- When small contact pads ($\ll 1$ mm^2) are required, the noble-metal contact layer is usually deposited over the entire test-film surface and then patterned by using *photolithographic* techniques (an introduction to such patterning techniques is given, for example, in the books by Anner 1990 or Ghandhi 1983).
- When larger (>0.5 mm^2) contact pads are used, it is not necessary to use photolithographic techniques to define the shape of the contact pad. In this case, processing time can be saved in defining the pads by evaporating them through a *shadow mask*, which is made by a machine shop or with a photochemical etching technique.

Thin-film electronic applications can place fairly severe demands on the specific contact resistivity between the pad and film, as indicated on the chart in Fig. 8.1 at the beginning of this chapter. This is illustrated, for example, by the stringent requirement for on-chip interconnects, where thin-film transmission lines are on the order of a micrometer wide. This results in very small contact areas requiring contact-interface resistivity in the range of 10^{-9}–10^{-10} Ω cm^2.

We now look at methods for contacting oxide-superconductor films that can produce such high-quality contacts. For the most part, the same contact techniques and annealing procedures apply either to *thin* films used in electronic devices or to *thick*-film coated conductors used for power applications.

8.4.2 CONTACTS FOR OXIDE HIGH-T_C SUPERCONDUCTOR FILMS

To achieve high-quality contacts to oxide-film superconductors, the same interfacial chemistry problems have to be faced as discussed previously for bulk high-T_c materials in Sec. 8.3.3 under the heading "Interfacial chemistry." The contact pads must be made from a material with a low oxygen affinity, such as gold or silver. As described below, the main difference in technique between the bulk and film cases is that, for films, the optimum oxygen-annealing temperatures are slightly lower and annealing times are shorter. Another important distinction for film samples (vs. bulk samples) is that with films it is sometimes possible to use an *in situ* deposition technique to form contact interfaces of very high quality.

In situ vs. *ex situ* contacts

For some film applications, it is possible to deposit the noble-metal contact pad in the same vacuum chamber used to make the superconducting film, thereby not exposing the

superconductor surface to air before the contact pad is deposited. This so-called *in situ* technique results in the lowest values of ρ_c, usually in the range 10^{-8}–10^{-9} Ω cm^2, and it requires no oxygen-annealing step (Lee et al. 1990; Ekin et al. 1993).

Often the *in situ* process is *in*compatible with other film processing steps that commonly need to be performed on the superconductor film before contact pads are deposited. Then the *ex situ* contact technique is used, where the contact film is deposited after an intervening exposure of the superconductor surface to air or photoresist-processing chemicals. When exposed to air, some degradation of the YBCO surface results from reaction with water vapor and carbon dioxide, as shown earlier in Fig. 8.5. However, the degradation of the resulting ρ_c is gradual until 100–1000 min of air exposure, after which it increases rapidly.

As deposited, *ex situ* contacts usually have contact resistivity in the range 10^{-5}–10^{-1} Ω cm^2, depending on the quality of cleaning before deposition of the contact pad. However, subsequent oxygen annealing can be used to reduce the ρ_c of *ex situ* film contacts to the range 10^{-6}–10^{-7} Ω cm^2, which is almost as good as *in situ* contacts. (Oxygen annealing is not effective in further reducing the ρ_c of as-deposited *in situ* contacts.)

Cleaning etch

When a noble-metal contact pad is deposited onto a superconductor surface that has been exposed to air (i.e. an *ex situ* contact), it is best first to clean the superconductor film surface with a gentle, low-voltage ion mill. (For *in situ* contacts, no such cleaning is required, but because of the small residual water-vapor partial pressure in the vacuum chamber and impurities in process gasses, it is best to minimize the time between fabrication of the superconductor and deposition of the contact pad, preferably not to exceed 100–1000 min, as noted above.) As with bulk high-T_c superconductors, be aware that the ion energy must be kept low to avoid destroying the delicate crystal structure of the superconductor; too low an energy, however, results in no milling at all. Figure 8.11 shows a typical voltage dependence for the sputter yield, which is

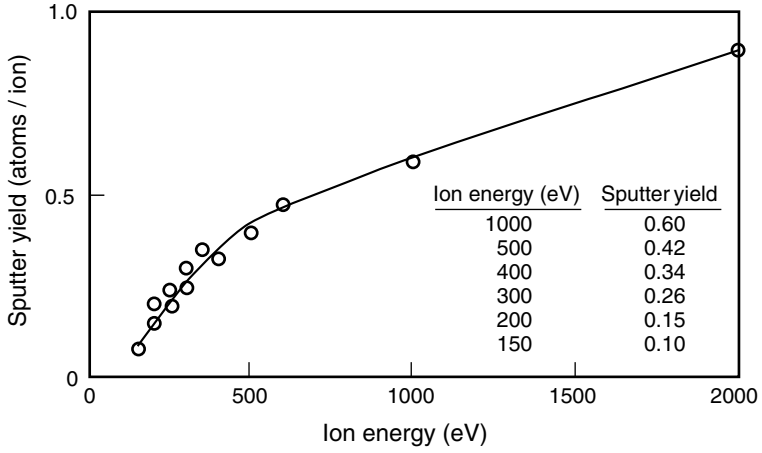

Fig. 8.11 Effect of ion energy on sputter yield (number of sputtered atoms per incident ion) (from Kaufman and Robinson 1989).

proportional to the milling rate. The results are shown for argon ions incident on silicon, but the relationship is similar for most physical-sputtering applications, such as ion milling and sputter etching. For cleaning YBCO with argon ions, an energy of about 200 eV is optimum.

The amount of material removed must be sufficient to clean the surface, but not so great that film samples are significantly thinned in the process. Milling away ~10 nm of a YBCO film surface is usually enough to remove the degraded surface layer.

Thickness monitors, such as resonant quartz-crystal monitors, are commercially available for measuring film thickness when *depositing* material, but such real-time measurements are not generally available when *removing* material (unless the quartz crystal is coated with the same material, which can occur when deposition and milling are carried out in the same chamber). Usually, ion-milling rates are experimentally determined for any particular system by using test films. For example, photoresist droplets can be placed on a test film and the film's surface ion-milled for a given time. After rinsing away the photoresist with acetone, mesas are left where the droplets protected the film. The step height at the edge of the mesas can then be measured with a sensitive depth gauge to calibrate the ion-milling rate.

An approximate milling rate can also be determined from *handbook* values. Milling rates using argon ions at 200 and 500 eV are tabulated in Appendix A8.5a for many of the *elements*, and in Appendix A8.5b for several *compounds*. Rates at other energies can be estimated by scaling the rates at 200 or 500 eV by use of Fig. 8.11. This yield curve will vary for different materials, especially at low voltages, but it can give at least a first approximation for how the milling rate will change with ion energy (accelerating voltage).

Example: Let us assume we wish to clean the surface of a YBCO film before depositing a noble-metal contact pad. We plan to clean the surface with an argon ion mill operating at a low energy of 200 eV. If we operate the ion mill at a current density of 0.5 mA/cm^2, how long should the surface be milled to remove about 15 nm of YBCO?

From Appendix A8.5b we find that, at 500 eV and 1 mA/cm^2, the argon etch rate for YBCO is about 45 nm/min. From Fig. 8.11 we estimate that at 200 eV this rate will be reduced to about (0.15/0.42) (45 nm/min) = 16 nm/min. The tabulated values in Appendix A8.5b are for a current density of 1 mA/cm^2, whereas we plan to operate our system at 0.5 mA/cm^2. Since the etch rate is directly proportional to the ion current density, the rate in our system will be about half this amount, or about 8 nm/min. Thus, to remove about 15 nm of material, our target time for milling would be ~2 min.

There is, of course, a proportional trade-off between milling time and ion current. So in practice, the ion current density can be adjusted to give a time that is convenient for any particular ion-milling operation. The important point is to keep the ion energy low, in the 200 eV range.

Sometimes photoresist processing occurs *before* the contact layer is deposited, as with the "lift-off" patterning technique (see, for example, Anner 1990). In this case, the superconductor's surface must be ion-cleaned after photoresist processing and sometimes not all the resist is completely removed, especially from very small areas. Unfortunately, it does not take much residual photoresist on the surface to give erroneously low milling depths in these "cleared" areas. A trick that helps alleviate this problem is to add about 10–20% oxygen to the argon gas used for milling in order to reactively ion-mill *organic* material. This preferentially increases

the milling rate for any residual photoresist without a commensurate rise in etch rate for the superconductor-film surface.

A minor disadvantage of this technique is that the oxygen can shorten the life of the filament in a Kaufman ion source. As the filament oxidizes, it also changes the operating conditions of the source by altering its electron emission properties. However, these problems are usually not significant compared with the importance of cleaning the superconductor surface of photoresist and solvents before contact pads are deposited. Often, this oxygen-activated cleaning is followed by a brief milling with pure argon to remove any oxides that might have formed.

Noble-metal deposition and thickness

Techniques for depositing gold or silver pads on films are similar to those described previously for bulk HTS contacts. Thermal evaporation is the easiest method. Typically, we use 99.99% ("four-nines pure") silver or gold evaporated from a resistively heated tungsten boat at a deposition rate of about 1 nm/s. Alternatively, electron-beam evaporation can be used, but this requires a greater initial outlay of funds for the deposition equipment. The pads do not have to be very thick, about 50–200 nm for ribbon-bond lead attachment or for pogo-pin contacts.

Film contact annealing

For *ex situ* contacts, the contact resistivity can be improved three to four orders of magnitude by annealing the contact pads in oxygen. As shown in the Auger depth profile in Fig. 8.4(c), oxygen annealing diffuses silver into the superconductor, probably mainly along grain boundaries, thereby increasing the effective contact area. The surface layers of YBCO are also reoxygenated.

Oxygen-annealing schedules for YBCO films are summarized, along with those for bulk samples, in Appendix A8.3. Figure 8.12 shows the reduction in contact resistivity that results from annealing 500 nm thick silver contacts to YBCO films in flowing oxygen at atmospheric pressure. With *ex situ* deposited films, the ultimate contact resistivity reached after annealing appears to be not quite as low as for bulk-sintered samples, probably because sintered superconductors have more grain-boundary surface area over which silver can diffuse. ("Melt-textured" bulk superconductors are expected to be an intermediate case because they are less porous than bulk-sintered samples.) Annealing times used were shorter than for bulk samples (10 min at full temperature for films vs. ~1 h for bulk samples).

Figure 8.12 shows that the optimum annealing temperature for thin ($\lesssim 1$ μm) silver pads on YBCO films is about 400°C, which is about 100°C lower than for bulk-sintered YBCO. The slightly reduced temperature is particularly important for thin films of silver, because the silver film starts to agglomerate or "ball up" at annealing temperatures above approximately 400°C. Figure 8.13 shows a silver film after oxygen annealing 10 min at 500°C; there is very little contact left. As the thickness of the silver film increases, the temperature limit to avoid agglomeration will also increase somewhat (Roshko et al. 1991).

For gold pads, on the other hand, agglomeration is not a problem (presumably because gold has a lower surface energy and higher melting temperature). Figure 8.14 shows the reduction in contact resistivity that results from annealing 350 nm thick gold contacts on YBCO films in

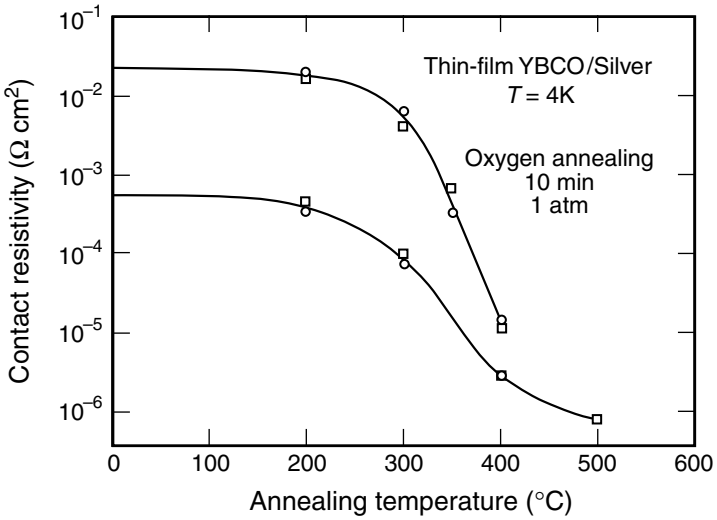

Fig. 8.12 Contact resistivity ρ_c as a function of annealing temperature for two silver thin-film contacts (500 nm thick) deposited *ex situ* on YBCO films (from Ekin et al. 1995). Annealing was carried out at atmospheric pressure in flowing oxygen for 10 min (after reaching annealing temperature). The contact resistivity starts to drop at an annealing temperature of about 250°C and shows marked improvement to less than $10^{-5}\ \Omega\ \text{cm}^2$ after annealing at approximately 400°C. At higher annealing temperatures, thin silver films agglomerate and electrical continuity is lost. The initial contact resistivity depends mostly on the exposure time of YBCO to air, as well as on the cleaning procedure before coating the superconductor surface with silver.

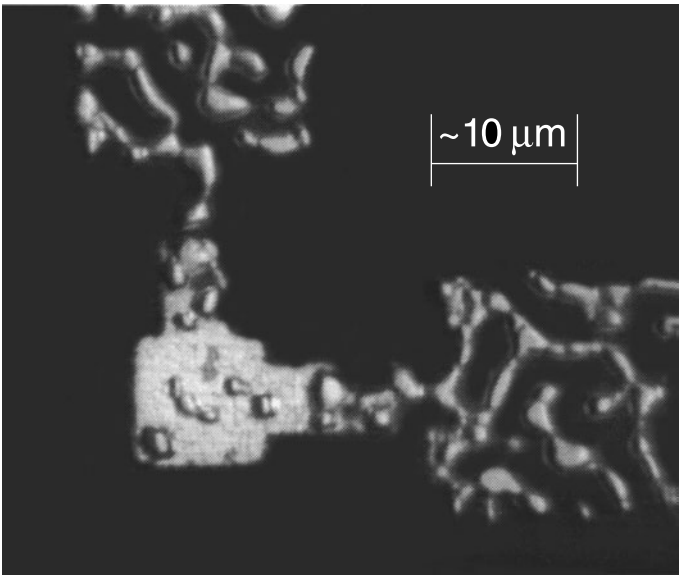

Fig. 8.13 Optical micrograph of silver film annealed at 500°C, showing extensive agglomeration of silver that results in loss of electrical continuity through the contact pad (from Ekin et al. 1995). The 500 nm thick silver film was deposited on a YBCO film, annealed at 500°C in oxygen for 10 min and cooled at a rate of 50°C/min.

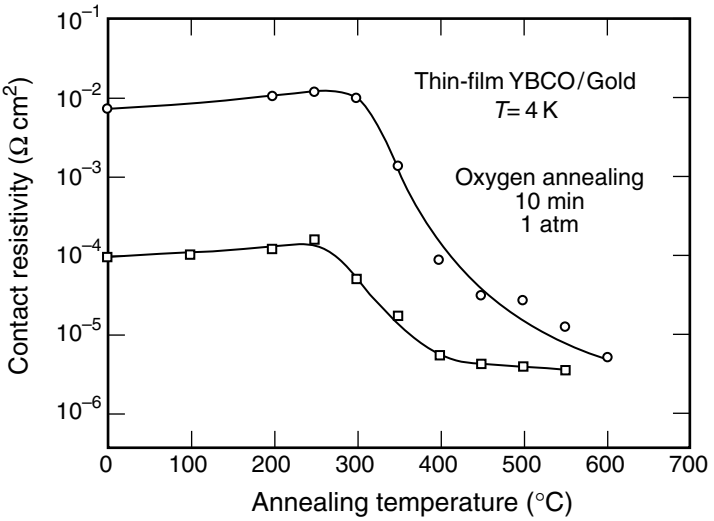

Fig. 8.14 Contact resistivity as a function of annealing temperature for two gold thin films (350 nm thick) deposited *ex situ* on YBCO films (from Xu et al. 1998). Annealing was carried out at atmospheric pressure in flowing oxygen for 10 min (after reaching annealing temperature). The optimum annealing temperature is about 50–100°C higher than that for silver contacts; see Fig. 8.12. Similar to silver contacts, the initial contact resistivity of each contact depends mostly on the YBCO air exposure time and cleaning procedure before coating with gold.

flowing oxygen at atmospheric pressure. The optimum oxygen annealing temperature for thin ($\lesssim$1 μm) gold contact pads on YBCO films is in the range 450–500°C, for 10–30 min.

The oxygen furnace described under "Fabrication procedures" in Sec. 8.3.3 for bulk samples works perfectly well for annealing film samples as well. Rapid thermal annealing can also be achieved with radiant heat lamps, but the initial temperature calibration must be done carefully by attaching a thermocouple to a dummy film–substrate combination that has emissivity and mass similar to those of the actual sample chip.

When annealing YBCO, cool the film slowly in oxygen, no faster than approximately 50°C/min, to avoid loss of critical current from oxygen disorder (Moeckly et al. 1993).

8.4.3 MEASURING FILM/CONTACT INTERFACE RESISTIVITY

When initially checking the performance of a new technique for depositing contact pads, the interface resistivity between the contact pad and superconductor film surface can be measured with one of the test patterns illustrated in Fig. 8.15. The simplest arrangement is a cross-strip geometry, shown in Fig. 8.15(a). The superconductor is patterned into a strip and a layer of contact material deposited on top. The contact layer is then patterned to form the cross strip. One arm of the superconductor strip and one arm of the contact-material strip are used to supply current through the interface formed where the two films cross [the arms labeled *I* in Fig. 8.15(a)]. The other two arms are used to detect the potential difference across the contact interface [labeled *V* in Fig. 8.15(a)]. When measuring very low interface *resistivity*, the

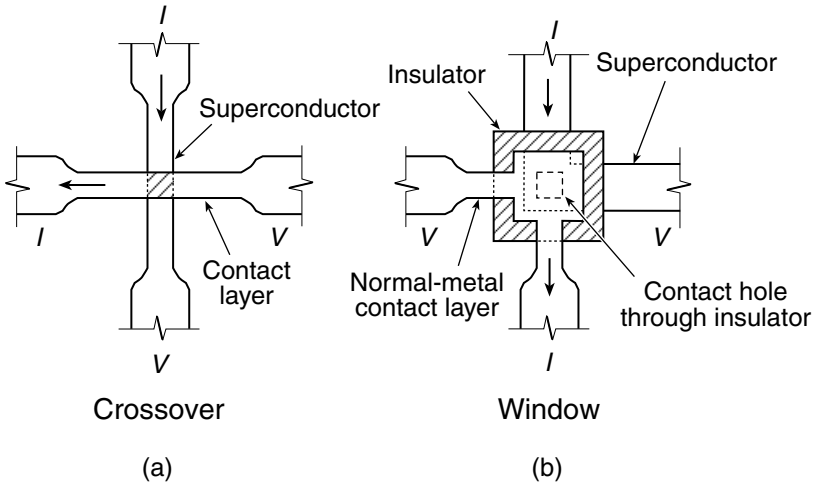

Fig. 8.15 Configurations for measuring film interface resistivity: (a) crossover configuration, for simplicity in patterning; and (b) window configuration, to minimize sheet-resistance effects in normal-metal overlayers [(b) adapted from Cohen and Gildenblat 1986].

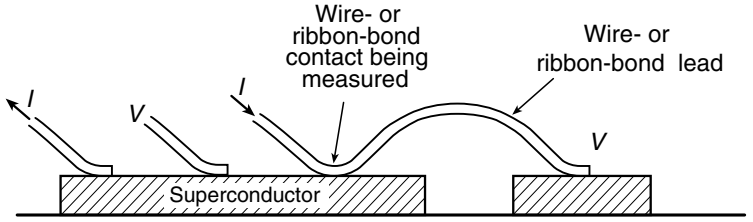

Fig. 8.16 Stitch-bond arrangement for measuring the contact resistivity of wire-bond or ribbon-bond connections.

crossover area needs to be kept small to obtain a contact *resistance* large enough to measure. This usually requires photolithographic patterning techniques.

The arrangement shown in Fig. 8.15(b) is more complex to fabricate, but it compensates for the spurious effect of voltages in contact layers made from normal metals. With this arrangement, current is not forced to make a 90° bend at the contact, as in the crossover configuration in Fig. 8.15(a). Instead, the current continues to flow in a straight, nearly symmetrical path, from the top of the diagram to the bottom, passing vertically through the contact hole in the insulator layer at the middle of the pattern (Cohen and Gildenblat 1986). The spurious effects of voltage in the normal metal are canceled (to first order) by the symmetrical pattern of flowing currents in the normal-metal layer and by the perpendicular configuration of voltage detection.

Wire-bond or ribbon-bond connections present a different set of measurement problems. To measure the quality of such connections, a stitch-bond arrangement can be used, as shown in Fig. 8.16. This configuration avoids the severe limitations on voltage-tap placement imposed by spreading-resistance effects (Sec. 8.6). A measurement of the overall contact resistance is obtained by introducing current into the ribbon bond and detecting voltage with the continuation of the bond lead to a separate voltage-contact pad. The return voltage tap can be located anywhere on the superconductor because the superconductor is effectively an equipotential surface (as long as the measuring current is well below the critical current).

8.5 Example calculations of *minimum contact area*

In designing a critical-current measurement, we need to know the minimum contact area required to prevent significant sample heating that can lead to false data or premature sample quenching. As noted in the introduction, this is especially important in the initial planning stage of a sample holder, when we must make sure adequate contact lengths have been allowed. This is hard to redo once the holder is built.

Although we illustrate the calculational procedure for critical-current measurements, it applies equally well to other types of transport measurements.

The calculation proceeds in two steps:

1. Determine the maximum contact resistance that can be tolerated to keep Joule heating below an acceptable level.
2. Calculate the minimum contact area needed to obtain this resistance value.

We illustrate this procedure first for *low-T_c* superconductors, such as Nb–Ti and Nb_3Sn operating in liquid helium. Then we give an example for *high-T_c* superconductors operating in liquid nitrogen (where cooling is very different from that in liquid helium). We also include a brief discussion of how the calculational procedure would be modified if the measurements were carried out in a gas or vacuum environment (rather than in liquid helium), such as on the cooled stage of a cryocooler.

8.5.1 Nb–Ti AT 4 K

Contacts immersed in liquid helium

Example: Suppose we wish to design a sample holder for a Nb–Ti critical-current test rig that will be cooled by direct immersion in liquid helium. We want to be able to handle transport currents up to about 600 A. Assume that common Pb–Sn eutectic solder is used to attach copper current bus bars or wires to the outer copper sheath of the test conductor.

The design question is: What is the *minimum contact area* we need to keep contact Joule heating at 600 A from raising the temperature of the sample contacts by no more than 0.1 K? This temperature rise corresponds, for example, to a decrease of about 2% in the critical current of Nb–Ti at 4.2 K and 0 T, or to a decrease of about 5% in a magnetic field of 7 T.

First, we consider the power generation $\dot{q}$ at the contacts that would give rise to a temperature difference ΔT of 0.1 K between the test sample and liquid helium. This is determined by the heat-transfer rate across the liquid/solid interface, which for nucleate boiling (i.e. below the critical heat flux for film boiling of 10^4 W/m^2 or $\Delta T \lesssim 0.4$ K) is given approximately by Eq. (2.12):

$$\dot{q} \cong 6 \times 10^4 \Delta T^{2.5} \times A_{\text{surf}} \, [(\text{W/m}^2)(\text{K}^{-2.5})], \tag{8.2}$$

where A_{surf} is the total cooled surface area. We make the worst-case approximation that the heat generated at the contact is dissipated into the liquid-helium bath only over the contact area, and we ignore the cooling of the contact that occurs from solid conduction along the current bus bar. So, if

we make the conservative assumption that the total cooled surface area A_{surf} is only the contact area A_c, we find from Eq. (8.2) that the contact Joule heating must be kept below

$$\dot{q} \cong 6 \times 10^4 \Delta T^{2.5} \times A_c[(\mathrm{W/m^2})(\mathrm{K^{-2.5}})]$$
$$\cong (6 \times 10^4)(0.1\ \mathrm{K})^{2.5} \times A_c \cong (1.9 \times 10^2\ \mathrm{W\,m^2})A_c.$$

The design critical current in our example is 600 A. Thus, from Ohm's law, the contact resistance must be kept below

$$R_c \leq \dot{q} I^{-2} \tag{8.3}$$
$$\leq (1.9 \times 10^2\ \mathrm{W/m^2})\, A_c\, (600\ \mathrm{A})^{-2} \cong (5 \times 10^{-4}\ \Omega/\mathrm{m^2})A_c.$$

Second, we determine the minimum contact area from Eq. (8.1), using for ρ_c the interfacial contact resistivity given at the top of Appendix A8.1 for two pieces of copper soldered together under moderate pressure with eutectic Pb–Sn solder:

$$A_c \geq \rho_c / R_c \tag{8.4}$$
$$\cong (4 \times 10^{-9}\ \Omega\,\mathrm{cm^2})/[(5 \times 10^{-8}\ \Omega/\mathrm{cm^2})\, A_c].$$

Therefore

$$A_c^2 \geq 8 \times 10^{-2}\ \mathrm{cm^4}$$

or

$$A_c \geq 0.28\ \mathrm{cm^2}.$$

Thus, for this example, the minimum contact area needed to keep the temperature rise less than 0.1 K would be about a quarter of a square centimeter. That is fairly small, as contacts go. From Eq. (8.2), we find this corresponds to a Joule heating level of about 5 mW.

Since we used worst-case assumptions in the calculation, a contact area that is even smaller would probably work. Note that the requirements on contact area become rapidly more stringent to achieve a temperature-difference ΔT smaller than 0.1 K between the sample contact and helium bath, because the nucleate-boiling heat-transfer rate for liquid helium scales as $\Delta T^{2.5}$ in Eq. (8.2).

Contacts in helium gas or vacuum

When measurements are carried out with the sample mounted on the cooled stage of a cryocooler, the sample is in a gas or vacuum environment (rather than in a liquid cryogen). In this case, the contacts will be cooled mainly by *solid conduction* along the current leads and through the sample holder. The calculation of the minimum contact area is carried out in the same way as above, except that Eq. (8.2) is replaced by Eq. (2.2) for solid conduction along the current bus bar and across joints to the cryocooler head.

Such measurements in a vacuum or gas environment usually require a contact area larger than that for the liquid-immersion case, because the rate of heat conduction through the joints and various sample mounting members is typically lower than that for solid/liquid interfaces.

In this case, the main factor limiting solid conduction is usually the thermal-boundary resistance at *joints*. The best joints are those made with solder, followed by varnish, grease, and pressure (see Fig. 2.7).

8.5.2 Nb_3Sn AT 4 K: RESISTIVE-MATRIX CONTRIBUTION

Another factor in calculating minimum contact areas for practical multifilamentary conductors is the heat generated in the *resistive matrix* surrounding the superconducting filaments. This can lead to an effective contact resistivity $\rho_{c\ eff}$ much larger than the ρ_c of a copper/solder/copper joint alone. In general, $\rho_{c\ eff}$ is given approximately by

$$\rho_{c\ eff} \cong \rho_c + \rho_{matrix}\, d, \tag{8.5}$$

where ρ_c is the *interface* resistivity of the contact given in Appendixes A8.1 and A8.2 (having units of $\Omega\ cm^2$), ρ_{matrix} is the *bulk* resistivity of the superconductor's matrix material given in Appendix A8.4 (having units of Ω cm), and d is the thickness of the matrix material between the sample surface and the superconducting filaments. Joule heating as current crosses the matrix material is usually not much of a problem for Nb–Ti superconductors (which have a relatively pure-copper matrix), but it becomes a significant factor when the matrix is a more resistive material, such as the *bronze* matrix in Nb_3Sn superconductors or the silver-*alloy*-sheath material in bismuth-based superconductors.

Example: Suppose the 600 A test sample in the example above is a Nb_3Sn multifilamentary composite conductor (rather than a Nb–Ti conductor) with a soldered contact length at least one twist-pitch long so that all filaments come into close proximity to the contact (this minimizes the effect of the twist-pitch effect described in Sec. 7.3.4). Furthermore, let us assume that the outermost Nb_3Sn filaments in the composite wire are separated from the high-conductivity copper stabilizer surface by a Cu–Sn bronze matrix layer that has an average thickness of about 0.1 mm. What is the minimum contact area requirement in this case?

Copper–tin bronze typically has a $\rho_{matrix} \cong 2 \times 10^{-6}\ \Omega$ cm, from Appendix A8.4. Thus, we see from Eq. (8.5) that the effective contact resistivity becomes much higher than that of just soldered copper-to-copper interfaces ($4 \times 10^{-9}\ \Omega\ cm^2$), namely,

$$\rho_{c\ effective} \cong 4 \times 10^{-9}\ \Omega\ cm^2 + (2 \times 10^{-6}\ \Omega\ cm)(0.01\ cm) \cong 24 \times 10^{-9}\ \Omega\ cm^2,$$

about six times higher. For the same contact resistance requirement as in the previous example [$R_c \leq (5 \times 10^{-4}\ \Omega/m^2)\ A_c$], this necessitates a larger contact area

$$A_c \geq \rho_c / R_c \cong (24 \times 10^{-9}\ \Omega\ cm^2)/[(5 \times 10^{-8}\ \Omega/cm^2) A_c]$$

(where we have again assumed the worst case that the current bus bar provides no additional cooling area). Solving for the contact area A_c, we obtain

$$A_c \geq 0.69\ cm^2.$$

Thus, the required area for Nb_3Sn contacts is generally larger than for Nb–Ti, in this case by a factor of about 2.5. This is a direct result of the bronze matrix in Nb_3Sn being more resistive than the pure-copper matrix in Nb–Ti conductors. [Note that the presence of an outer pure-copper sheath does not significantly affect the contact resistivity in either case, since, at 4 K, pure copper typically has a ρ_{matrix} much smaller than that of bronze, and the $\rho_{matrix}d$ contribution in Eq. (8.5) is much smaller than the specific contact resistivity ρ_c.]

8.5.3 HIGH-T_c SUPERCONDUCTORS AT 77 K

We conclude this section with an example of contact sizing for high-T_c superconductors in *liquid nitrogen*, where the cooling conditions are very different from those considered above for liquid helium. Again, we focus on critical-current testing, since these measurements usually pose the most demanding requirements on contacts. However, a similar calculational procedure applies to any of the many transport measurements carried out at low temperature. (Because contact pads deposited on YBCO conductors are usually thin, *spreading resistance* within the contact pad area can also be a problem, so the same example will be continued in the next section to illustrate the calculation of spreading-resistance effects.)

The calculation for sizing contacts to a bismuth-based superconductor (BSCCO) in liquid nitrogen would proceed in the same way as that illustrated next for YBCO, except the contact resistivity ρ_c will be that for silver/BSCCO instead of silver/YBCO (again, ρ_c values for the different cases are given in Appendix A8.1).

Example: Suppose we want to determine the size of the current connections needed to test a thick-film YBCO-coated conductor immersed in liquid nitrogen. Let us assume the critical current is about 150 A and that the total surface area of the contact and bus bar cooled by liquid nitrogen is 10 cm^2. We want the contact resistance to be small enough that Joule heating does not raise the sample temperature by more than 0.5 K. This temperature rise corresponds to about a 5% decrease in the critical current of YBCO at 77 K in self-field (from Sec. 10.4.4 or Appendix A10.1).

Proceeding as in the previous examples, the 0.5 K temperature rise places a limit on power generation, which is given by the solid/liquid heat-transfer rate for liquid nitrogen. Similar to Eq. (8.2), this is given approximately at low heat flux ($< 2 \times 10^5$ W/m^2 or $\Delta T \lesssim 10$ K) by Eq. (2.13):

$$\dot{q} \cong 5 \times 10^2 \, \Delta T^{2.5} \times A_{surf} \, [(\mathrm{W/m^2})(\mathrm{K^{-2.5}})]. \tag{8.6}$$

Comparing Eq. (8.6) with Eq. (8.2), we see, somewhat surprisingly, that the solid/liquid heat-transfer rate for liquid nitrogen is about two orders of magnitude *smaller* than that for liquid helium. Thus, contrary to popular belief, liquid nitrogen does not cool as well as liquid helium (for a given ΔT). To keep the contact size reasonably small, we need all the cooled surface area we can get, and so, for calculational purposes, we take into account the cooled surface area of the current bus bar as well as the contact area itself. This is an optimistic assumption, and so it must be treated carefully (unlike the previous liquid-helium calculations). In many cases, however, it is a reasonable assumption in liquid nitrogen, justified by the high rate of heat conduction along a typical copper bus bar compared with the smaller rate of surface cooling.

Of course, much more sophisticated heat-transfer calculations can be made, but using the combined cooled surface area of the contact *and* bus bar for A_{surf} (assumed to total 10 cm^2) in Eq. (8.6) gives us a quick, simple method of obtaining a rough estimate of the contact cooling rate,

$$\dot{q} \cong [(5 \times 10^2)(0.5\ \mathrm{K})^{2.5}] \times (10 \times 10^{-4}\ \mathrm{m}^2)[(\mathrm{W/m}^2)(\mathrm{K}^{-2.5})] \cong 88\ \mathrm{mW}.$$

For a 150 A test current, this limits the contact resistance (from Ohm's law) to about

$$R_c \leq \dot{q}\, I^{-2} = (88\ \mathrm{mW}) \times (150\ \mathrm{A})^{-2} = 3.9 \times 10^{-6}\ \Omega.$$

Next, we determine the minimum contact area needed to achieve this resistance by first estimating the total effective contact resistivity from Eq. (8.5):

$$\rho_{c\,\mathrm{eff}} \cong \rho_c + \rho_{\mathrm{pad}}\, d_{\mathrm{pad}}, \tag{8.7}$$

where ρ_c is the interface contact resistivity, and ρ_{pad} and d_{pad} represent the bulk resistivity and thickness of the soldered noble-metal contact pad. Assume that we have been careful to make good contacts for soldering; that is, we deposited thick (about 7–10 μm) silver contact pads on the sample ends and used In–3%Ag eutectic solder to attach current bus bars to the contact pads (Sec. 8.3.3). Then the soldered contact resistivity should be pretty good, about $\rho_c \cong 10^{-6}\ \Omega\,\mathrm{cm}^2$ (from Appendix A8.1).

For ρ_{pad}, we assume the worst case and take ρ_{pad} to be dominated by the bulk resistivity of In–3%Ag solder, since the contact pad will partially alloy with the In–3%Ag solder. From Appendix A8.4, we find for In–3%Ag solder that the bulk resistivity is 1.8 μΩ cm. (If we were to attach a wire bond to the pad instead, then we would use the bulk resistivity of pure silver.)

Substituting these quantities in Eq. (8.7) and taking the pad thickness to be 10 μm, we find that

$$\rho_{c\,\mathrm{eff}} = 10^{-6}\ \Omega\,\mathrm{cm}^2 + (1.8 \times 10^{-6}\ \Omega\,\mathrm{cm})(10^{-3}\ \mathrm{cm}) \cong 10^{-6}\ \Omega\,\mathrm{cm}^2.$$

That is, the effective contact resistivity is dominated by the interface and not by the bulk resistivity of the contact pad, even after soldering. [For BSCCOs made with high-resistivity sheaths of dispersion-strengthened silver, such as Ag–Mg, the added resistivity of the matrix must be taken into account by using Eq. (8.5) and the data in Appendix A8.4. The effect of the relatively thick dispersion-strengthened sheath is to significantly increase $\rho_{c\,\mathrm{eff}}$, similar to the above example for a bronze-matrix Nb_3Sn superconductor.]

Inserting this value for $\rho_{c\,\mathrm{eff}}$ into Eq. (8.4), we find the minimum contact area:

$$A_c \geq \rho_{c\,\mathrm{eff}} / R_c = (10^{-6}\ \Omega\ \mathrm{cm}^2) / (3.9 \times 10^{-6}\ \Omega) = 0.26\ \mathrm{cm}^2.$$

Thus, if the YBCO-coated conductor had a width of 3 mm, the required contact length would be about 1 cm.

This seems like a reasonably small contact-area requirement. However, the area scales quadratically with current [from Eq. (8.6), assuming the total cooled surface area of the bus bar does not increase]. So, a wider YBCO-coated conductor having the same bus-bar cooled surface area of 10 cm^2 and a critical current of, say, 500 A, would require a sample contact area of about (500 A/150 A)^2 × 0.26 cm^2 = 2.9 cm^2, more than 10 times larger than that of the 150 A conductor in the example above. If the width of the 500 A conductor were 1 cm, the required contact length would be about 3 cm.

Also, the requirement on contact area becomes considerably greater if we want to reduce the temperature difference ΔT between the test sample and the liquid-nitrogen bath to less than

0.5 K assumed in the above example. From Eq. (8.6), we see that the heat-transfer rate scales as $\Delta T^{2.5}$, so the required contact area increases as the power 2.5.

Thus, the minimum contact area for high-T_c superconductor (HTS) materials at 77 K is significantly greater than that for low-T_c superconductor (LTS) materials at 4 K, for comparable critical current and ΔT. (In the LTS examples above, we assumed $I_c = 600$ A and $\Delta T = 0.1$ K.) This increased area requirement stems from a combination of the reduced cooling rate of liquid nitrogen compared with that of liquid helium and the lower contact resistivities of soldered HTS contacts compared with those of copper-sheathed LTS materials.

Contacts in nitrogen gas or vacuum

For high-T_c superconductor contacts in a *vacuum*, the contact cooling is mainly by solid conduction along the current leads and sample holder to the cold stage of a refrigerator (subject, of course, to the power limitations of the refrigerator). The calculation is carried out in the same way as above, except that instead of Eq. (8.6), we substitute the heat-transfer rate for solid conduction along the current bus bar and across joints, Eq. (2.2).

As in the case of LTS testing at 4 K, the main factor limiting heat conduction through solids at liquid-nitrogen temperatures is usually the thermal-boundary resistance across *joints*. Figure 2.7 shows that at liquid-nitrogen temperature, the highest thermal conductance is obtained across solder joints [about 10–40 W/(cm^2 K)], followed by varnish joints [~2 W/(cm^2 K)] and grease joints [~1 W/(cm^2 K)]. Pressure joints typically have a lower thermal conductance (0.01–3 W/K), independent of area but dependent on the force applied to the joint and the surface condition of the parts, with gold plating being the best (Sec. 2.6).

In a vacuum, it is also important to conductively cool the middle of the sample. If a sample has a low thermal conductivity along its length, it must be thermally anchored to a high-thermal-conductivity sample holder with the techniques described in Sec. 7.3.1.

8.6 *Spreading-resistance* effect in thin contact pads and example calculations

There is still another caveat to sizing thin contact pads. We cannot assume that the contact pads will distribute the current *uniformly* over the entire contact area because their sheet resistance is relatively high. If the current is injected locally into the middle of a pad by a soldered wire, wire bond, or ribbon bond, the sheet resistance of the pad itself can limit the effective area of the contact pad to a *spreading distance* ξ around where the wire is attached to the pad, as illustrated in Fig. 8.17.

The spreading distance ξ is determined by the *sheet resistance* of the contact pad, R_s, and the contact interface resistivity ρ_c between the pad and superconductor. It is given approximately by (Ekin et al. 1993)

$$\xi \cong (\rho_c / R_s)^{0.5}, \quad \text{Spreading distance} \tag{8.8}$$

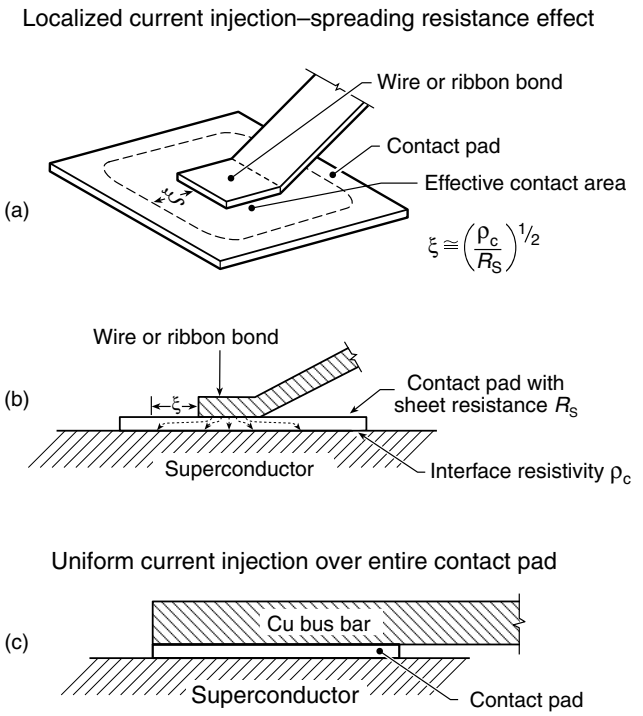

Fig. 8.17 Spreading-resistance effect in thin contact pads. When current is injected into the middle of the contact pad (using a soldered wire, wire bond, or ribbon bond, for example) the sheet resistance of the pad limits the effective contact area to a distance ξ around the injection area, as shown in (a) and (b). Effects of spreading resistance are not a problem when current is injected uniformly over the entire contact-pad area by a thick copper bus bar, for example, as shown in (c)—just make sure the resistance along the copper bus bar is much smaller than the contact resistance.

where the sheet resistance R_s is the quotient of the film's *bulk* resistivity ρ and thickness d (assumed to be uniform)

$$R_s \equiv \rho/d \quad [\Omega/\text{sq}]. \quad \text{Sheet resistance} \tag{8.9}$$

The sheet resistance is expressed in units of "ohms per square" (Ω/sq) because, physically, it corresponds to the in-plane resistance of a square-shaped piece of the film: 1 μm $\times$ 1 μm, 1 m $\times$ 1 m, or whatever, just so long as it is a *square*.

We illustrate the spreading-resistance effect with a couple of examples.

8.6.1 YBCO-COATED-CONDUCTOR CONTACTS

Example—Spreading resistance for a wire soldered to the middle of a contact pad: In the above example for YBCO-coated conductors, if we were to inject current locally at the middle of the contact pad, the effective contact area may be inadequate because of the spreading-resistance effect. Let us determine

the effective spreading distance ξ if we assume that current is injected into the contact pad via a wire soldered to the middle of the contact pad with In–3%Ag solder.

Assume that, in the process of soldering the wire to the middle of the contact pad, we are left with a relatively thick (1 mm) blob of solder uniformly coating the entire area of the pad. Then the solder layer is much thicker than the ~10 μm-thick pad and provides the main path for distributing current over the contact-pad area. We determine the approximate sheet resistance of the solder layer from Eq. (8.9); substituting the bulk resistivity of In–3%Ag solder from Appendix A8.4, we obtain

$$R_{\text{s solder layer}} \equiv \rho / d = 1.8\ \mu\Omega\,\text{cm} / 0.1\ \text{cm} = 1.8 \times 10^{-5}\ \Omega/\text{sq}.$$

As in the previous example, we assume the contact resistivity between the pad and superconductor is that of a relatively high-quality soldered contact having $\rho_c = 10^{-6}\ \Omega\text{cm}^2$. Then from Eq. (8.8) we have for the effective spreading distance

$$\xi \cong (\rho_c / R_s)^{0.5} = [(10^{-6}\ \Omega\,\text{cm}^2) / (1.8 \times 10^{-5}\ \Omega/\text{sq})]^{0.5} = 0.24\ \text{cm}.$$

So, regardless of how big a silver contact pad we deposit, if we inject current just at a point at its middle, it will function like a contact pad with a radius of only about 2.4 mm, significantly less than the 26 mm^2 contact area we needed in the previous example. Thus, to obtain an effective contact area of about 26 mm^2, we would need to use a low-resistance copper bus bar like that shown in Fig. 8.17(c) to spread the current uniformly over the entire area of the contact pad.

8.6.2 THIN-FILM CONTACTS

For thin-film devices where wire-bond, ribbon-bond, or pogo-pin connections can be used, the contact interface resistivity is usually lower than that for soldered contact pads, typically on the order of $10^{-8}\ \Omega\ \text{cm}^2$ or less. When the interface resistivity is so low, the spreading resistance of the contact pad usually limits the effective contact area to only the very small area just under the ribbon bond or pogo pin, and effectively none of the rest of the contact-pad area is utilized. This is illustrated in the following example.

Example—Spreading resistance for wire-bond or ribbon-bond contact pads: A typical wire-bond or ribbon-bond arrangement is illustrated in Fig. 8.17. We calculate the effective current-spreading distance ξ around the bond for an oxygen-annealed gold contact pad at 77 K, which we assume is 0.2 μm thick.

The sheet resistance R_s of the gold contact pad will be, from Eq. (8.9),

$$R_s \equiv \rho / t = (0.43\ \mu\Omega\,\text{cm}) / (2 \times 10^{-5}\ \text{cm}) = 2.1 \times 10^{-2}\ \Omega/\text{sq},$$

where we have used a bulk resistivity of 0.43 μΩcm at 77 K for evaporated gold (from Appendix A8.4). If the gold contact pad is a high-quality *in situ* deposited contact, it will have a low specific contact resistivity between the pad and superconductor of about $\rho_c = 10^{-8}\ \Omega\,\text{cm}^2$ (from Appendix A8.2). Thus, from Eq. (8.8), the effective current-spreading distance ξ around the ribbon bond will be only

$$\xi \cong (\rho_c / R_s)^{0.5} = [(10^{-8}\ \Omega\text{cm}^2) / (2.1 \times 10^{-2}\ \Omega/\text{sq})]^{0.5} = 7\ \mu\text{m}.$$

This is small compared to the contact size of a typical wire bond or ribbon bond (usually in the range 50–250 μm across). So for contact pads with a relatively low ρ_c, the contact area is effectively that of the ribbon-bond area alone. If the contact interface resistivity ρ_c is much higher than the 10^{-8} Ωcm^2 value assumed in this example, ξ will become correspondingly greater, and the contact pad will then assist in improving the contact resistance by providing a larger effective pad area.

Beware, however, when *measuring* the interface resistivity of thin-film contacts, that current-spreading effects can lead to significant error in the apparent value of ρ_c, because the spreading distance artificially extends the contact area if the geometry is not well defined. Furthermore, the voltage on the normal-metal side of the contact must be detected within ξ of the contact pad, or else the "measured" potential difference across the contact will appear erroneously low. Measurement configurations like those shown in Figs 8.15 and 8.16 are needed to ensure both accurate area determination and voltage detection.

8.7 References

8.7.1 FURTHER READING

DESCRIPTIONS OF THIN-FILM ETCHING, ION-MILLING, DEPOSITION, AND PATTERNING TECHNIQUES:

Anner, G. E. (1990). *Planar Processing Primer*, Van Nostrand Reinhold, NY.

Ghandhi, S. K. (1983). *VLSI Fabrication Principles*. Wiley, NY.

Vossen, J. L., and Kern, W. (1991). *Thin Film Processes II*, Academic Press, San Diego, CA.

WIRE BONDING:

Harman, G. G. (1997). *Wire Bonding in Microelectronics: Materials, Processes, Reliability, and Yield*, McGraw–Hill, NY.

THIN-FILM CONTACT MEASUREMENT TECHNIQUES:

Cohen, S. S., and Gildenblat, G. S. (1986). *VLSI Electronics 13, Metal-Semiconductor Contacts and Devices*, pp. 87–133, Academic Press, NY. The techniques described in this text are commonly used in the semiconductor industry but are adaptable to superconductor testing.

REVIEWS OF THE EARLY LITERATURE ON CONTACTS FOR HIGH-T_C SUPERCONDUCTORS:

Ekin, J. W. (1992). "Preparation of low-resistivity contacts for high-T_c superconductors," in *Processing and Properties of High-T_c Superconductors, Vol. 1 Bulk Materials*, ed. Sungho Jin, p. 371, World Scientific Press, Singapore.

Talvacchio, J. (1989). "Electrical Contact to Superconductors," *IEEE Trans. Components, Hybrids, Mfg. Tech.* 12, 21–31.

8.7.2 CHAPTER REFERENCES

Anner, G. E. (1990). *Planar Processing Primer*, Van Nostrand Reinhold, NY.

Cohen, S. S., and Gildenblat, G. S. (1986). "Metal–semiconductor contacts and devices," in *VLSI Electronics 13*, pp. 87–133, Academic Press, NY.

Ekin, J. W., Larson, T. M., Bergren, N. F., Nelson, A. J., Swartzlander, A. B, Kazmerski, L. L., Panson, A. J., and Blankenship, B. A. (1988). "High T_c superconductor/noble-metal contacts with surface resistivities in the 10^{-10} Ω cm^2 range," *Appl. Phys Lett.* 52, 1819–1821.

Ekin, J. W., Panson, A. J., and Blankenship, B. A. (1990–1993). "Method for making low resistivity contacts to high-T_c superconductors," US Patent 4,963,523 (1990); "High-T_c superconductor contact unit having low interface resistivity, and method of making," US Patent 5,015,620 (1991); "High-T_c superconducting unit having low contact surface resistivity," US Patent 5,149,686 (1992); "High-T_c superconductor contact unit having low interface resistivity," US Patent 5,179,071 (1993).

Ekin, J. W., Russek, S. E., Clickner, C. C., and Jeanneret, B. (1993). "*In situ* noble metal $YBa_2Cu_2O_7$ thin-film contacts," *Appl. Phys. Lett.* 62, 369–371.

Ekin, J. W., Clickner, C. C., Russek, S. E., and Sanders, S. C., (1995). "Oxygen annealing of ex-situ YBCO/Ag thin-film interfaces," *IEEE Trans. Appl. Supercond.* 5, 2400–2403.

Ghandhi, S. K. (1983). *VLSI Fabrication Principles*, Wiley & Sons, NY.

Goodrich, L. F., and Ekin, J. W. (1981). "Lap joint resistance and intrinsic critical current measurements on a Nb–Ti superconducting wire," *IEEE Trans. Magn.* 17, 69–72.

Kaufman, H. R., and Robinson, R. S. (1989). "Broad-beam ion source technology and applications," *Vacuum* 39, 1175–1180. Fig. 8.11 reprinted with permission from Elsevier.

Lee, M., Lew, D., C-B Eom, Geballe, T. H., and Beasley, M. R. (1990). "Anisotropic proximity coupling in small $Ba_2Cu_3O_7$ - normal-Pb junctions," *Appl. Phys. Lett*. 57, 1152–1154.

Martin, P. M. (2001). Oak Ridge National Laboratory, Oak Ridge, TN, personal communication.

Moeckly, B. H., Lathrop, D. K., and Buhrman, R. A. (1993). "Electromigration study of oxygen disorder and grain boundary effects in $YBa_2Cu_3O_7$ thin films," *Phys. Rev.* B47, 400–417.

Roshko, A., Ono, R. H., Beall, J. A., Moreland, J., Nelson, A. J., and Asher, S. E. (1991). "Morphology of silver on $YBa_2Cu_3O_7$ thin films," *IEEE Trans. Magn.* 27, 1616–1618.

Russek, S. E., Sanders, S. C., Roshko, A., and Ekin, J. W. (1994). "Surface degradation of superconducting YBCO thin films," *Appl. Phys. Lett.* 64, 3649–3651.

Siegal, M. P., Overmyer, D. L., Venturini, E. L., Padilla, R. R., and Provencio, P. N. (1999). "Stability of Tl–Ba–Ca–Cu–O superconducting thin films," *J. Mater. Res.* 14, 4482–4488.

Xu, Y., Ekin, J. W., Clickner, C. C., and Fiske, R. L. (1998). Oxygen annealing of YBCO/gold thin-film contacts," *Adv. Cryog. Eng. (Mater.)* 44, 381–388.

Part III

Superconductor Critical-Current Measurements and Data Analysis

Part I was general in nature, presenting design techniques common to most cryostats. Part II focused more specifically on electrical-transport measurements. In Part III, we further narrow the focus and bring together some of the material from the earlier chapters to illustrate the process of cryostat design for one particular low-temperature measurement—critical current. We also present an in-depth treatment of techniques for data analysis for this type of measurement.

The critical current of a superconductor is the principal engineering design parameter for most applications of these materials, whether they be high-current wires or thin films. Furthermore, critical current is an *extrinsic* property; that is, it depends strongly on the particular grain-boundary and defect structure of a superconductor material. Thus, the critical current varies greatly from sample to sample and cannot be simply looked up in a handbook. For both these reasons, critical-current measurements are among the most ubiquitous cryogenic measurements.

Chapter 9 presents techniques for critical-current-data *acquisition*. Although the focus is specifically on measurements of critical current, several of the topics discussed here are widely applicable to other types of measurements, especially the approach to initial instrument checkout, measurement troubleshooting, and the programming schemes for automating data acquisition.

Chapter 10, on the other hand, focuses on critical-current-data *analysis*—how to define a "critical" value of current and translate it to different magnetic fields, temperatures, and strains.

9 Critical-Current Measurements

One experiment is worth a thousand expert opinions.

–Unknown

9.1 Introduction

How frustrating it is to spend hours mounting a sample, hook up all the instrumentation leads, cool the apparatus, and then, in a fraction of a second, burn out your sample. The first time it happened to me, I found my wonderful sample reduced to a tiny molten blob lying in the bottom of the cryostat. Among other topics, this chapter looks at ways to avoid "meltdown."

Chapter 9 is divided into four sections:

1. In the *introduction* (Sec. 9.1) we describe the principal ways of defining critical-current *density* (which can lead to vastly different values) (Sec. 9.1.2). An overview is also given of the dependence of critical current on temperature, magnetic field, and strain (Sec. 9.1.3) and the main experimental configurations for measuring critical current (Sec. 9.1.4).
2. The *instrumentation* section (Sec. 9.2) offers suggestions of where to put your money when assembling a quality instrumentation system (Sec. 9.2.1) and techniques for checking out a new system (Sec. 9.2.2).
3. The *measurement procedures* section (Sec. 9.3) looks at general, time-proven troubleshooting tips (Sec. 9.3.1) as well as specific methods to avoid and identify critical-current measurement problems (Sec. 9.3.2). We also consider when it is appropriate to use automated data acquisition (and when not to) and map out the most effective programming strategies (Sec. 9.3.3). Sections 9.3.1 and 9.3.3, especially, have wide applicability to many types of measurements, not just critical current.
4. The last section (Sec. 9.4) illustrates specific *examples* of various types of cryostats for measuring critical current. There we flag the specific pitfalls and key design elements of each type.

For those interested mainly in *thin-film* measurements, the first three sections should be generally useful, as well as the thin-film cryostats for angle measurement in Sec. 9.4.2 and variable-temperature measurement in Sec. 9.4.3 (the rest of the examples in Sec. 9.4.3 are mainly relevant to high-current measurements). Looking back, most of the cryostat examples presented earlier in the text were illustrated with low-current thin-film probes; these were summarized in the introduction (Sec. 1.4) and in the sections referred to in the introductory checklist (Sec. 1.3.1).

For *high-current* measurements, essentially the entire chapter is relevant, including most of the new examples of cryostat designs given in Sec. 9.4.3.

Looking ahead, Chapter 10 contains a wide synthesis of useful information on analysis and transformations for *both* thin-film and bulk superconductor critical-current measurements.

As emphasized in the introduction to the book, the focus here is on common design problems. The information and examples are not intended to be a complete sourcebook. Rather, they are intended as an adjunct to the essential step of examining actual cryostats and talking with others specializing in your specific measurement field. There is no substitute for those connections, but the information given here should significantly shorten the learning curve.

9.1.1 TRANSPORT METHOD vs. CONTACTLESS METHODS OF MEASURING CRITICAL CURRENT

To put this chapter in context, we note that several methods exist for measuring critical current, but the most practical technique is the *transport* method. With the transport method (the focus of this chapter), a current I is passed through the sample and the electric-potential difference (voltage) V is measured along its length. Ideally, the superconductor V–I characteristic should be highly nonlinear. As illustrated in Fig. 9.1, at low transport current the superconductor has effectively zero resistance, but, at a critical value of current I_c, the voltage rapidly rises as the superconductor reverts to the normal resistive state. Ultimately, the transport method is the most trusted for determining I_c, but it requires care with current handling and contacts, as described in Chapters 7 and 8.

On the other hand, indirect methods for determining I_c include magnetization measurements and eddy-current testing [as described, for example, by Claassen et al. 1991; see Fig. 7.23(a) and (b) in Sec. 7.4.3]. These indirect methods are *contactless* techniques, in which current is electromagnetically induced in the sample, where it circulates within grains or small regions of the sample rather than along the entire sample length. Such contactless measurements are useful in the initial stages of characterizing new superconducting materials and production-line

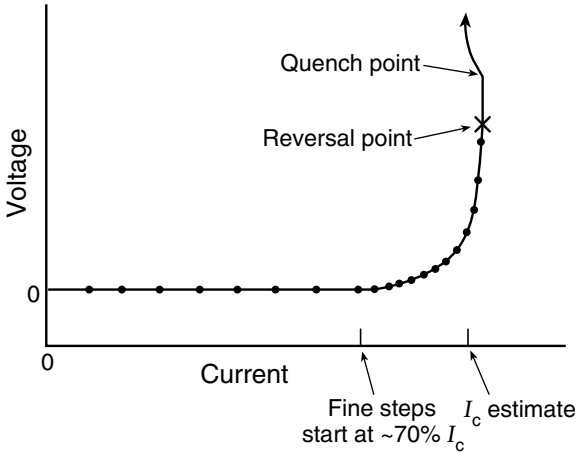

Fig. 9.1 Plot of voltage vs. current for a typical superconductor, showing regions of negligible resistance (at lower currents), the highly nonlinear critical-current regime, and the quench point where thermal runaway occurs.

testing for quality assurance. But the calculated I_c values that are inferred from such measurements generally have to be backed up by transport measurements, as witnessed by the incredible (orders of magnitude) difference between magnetization I_c and transport I_c that was found in the early development stages of oxide superconductors. The difference arises from a "weak link" effect in polycrystalline high-T_c superconductors (Sec. 10.3.4), wherein a strong barrier to conduction occurs at grain boundaries, even though within the grains the critical-current density can be very high. That is, transport measurements are *inter*granular in nature, whereas magnetization measurements are *intra*granular. So for most practical applications, beware of critical-current values determined by magnetization only.

9.1.2 DEFINING CRITICAL-CURRENT *DENSITY*

Before considering techniques for measuring critical current, we must first define what we mean by critical-current *density*. To make an equitable comparison between different superconductors, we divide the critical current by the cross-sectional area A of the conductor; this defines a critical-current density J_c ($\equiv I_c/A$). What area A to choose, however, depends on your purpose. Three areas are commonly used.

1. The *superconductor* critical-current density J_c is defined by using the cross-sectional area of just the superconductor material in the composite, illustrated, for example, by just the black dots in Fig. 9.2. All the other components of the composite conductor are ignored. The superconductor critical-current density is useful for determining the quality of the superconductor material itself, since it is independent of the quantity of stabilization material, diffusion barrier, bronze matrix, or other materials that may be present in practical composite superconductors.
2. The *nonstabilizer* (or noncopper) critical-current density J_n is usually the best way to define the critical-current density of low-T_c superconductors, because it takes into consideration everything in the superconducting composite except the stabilizer area, which is highly variable from application to application but essential to prevent thermal runaway (Sec. 7.5.1). The

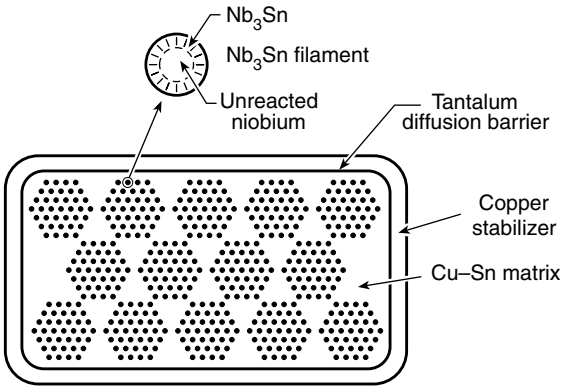

Fig. 9.2 Cross section of a practical multifilamentary Nb_3Sn superconducting composite, illustrating the various components that could be included in the area used to calculate critical-current *density*.

nonstabilizer critical-current density would include, for example, the area of the Cu–Sn bronze matrix and tantalum diffusion barrier in Fig. 9.2. The residual bronze material left over from the manufacturing process neither carries supercurrent nor provides stabilization in actual applications. Thus, it is "excess baggage." The nonstabilizer J_n would reflect the advantage of conductors designed to minimize this noncontributing material (left over from the manufacturing process), whereas the superconductor J_c would not. Therefore, J_n provides a common ground for comparing different fabrication techniques, which justly rewards techniques that produce a higher overall current-carrying fraction of the composite.

3. The *engineering* critical-current density J_e is an important parameter for designers who are selecting a superconductor for a particular application with a specified stabilization requirement. It is calculated simply by dividing I_c by the entire cross-sectional area of the composite conductor, including the stabilizer material. Thus, J_e fully derates the critical-current density for everything in the conductor, including the amount of stabilizer material the designer decides is needed for the particular application. The definition of J_e can also be expanded to include structural material, insulation, and coolant in the winding volume, giving a true overall critical-current density.

For high-T_c superconductors, such as $(Bi,Pb)_2Sr_2Ca_2Cu_3O_{10-x}$ (designated Bi-2223) and $Bi_2Sr_2CaCu_2O_{8+x}$ (Bi-2212), J_e is usually used when comparing conductors, since it includes the large area fraction of silver matrix, illustrated in Fig. 7.25(a). The silver serves as a stabilizer, but the amount of silver needed for fabrication of Bi-2223 and Bi-2212 is usually more than is required for stability. Comparisons in terms of J_e thus reward the efficiency of fabrication processes that minimize the amount of silver used.

On the other hand, for YBCO-coated conductors, J_c or J_n is usually used for conductor comparisons because, if J_e were used, the derating of the current density by the area of the substrate [an additional structural member, shown schematically in Fig. 7.25(b)] would be extremely variable, depending on the substrate thickness chosen. The thickness of the substrate is a design variable, and, for many applications, the substrate is needed for structural support and is not necessarily a liability.

Thus, there is no single "critical-current density." The choice depends on the conductor and the application. For critical-current data to be useful, the *area fractions* of the various components in the superconducting composite should be measured and specified along with the critical-current data.

➔ How do we measure the areas of the various components? For film tapes [like the coated conductor shown in Fig. 7.25(b)], the area of the superconducting layer is calculated from the product of the thickness of the film (determined by measuring it with a depth profiler) and the width of the tape or microbridge (measured under a microscope). In the case of bulk superconductors, the simplest (but approximate) method is to measure the final outer dimensions of the conductor and use the starting ratios of materials that went into the billet (which can be obtained from the manufacturer) to calculate the various areas (superconductor area or nonstabilizer area).

A potentially more accurate, but also more complicated, way to determine the relative areas in bulk superconducting composites is to measure the areas from a photograph taken

through a microscope (a photomicrograph) of a polished and etched cross-sectional surface of the conductor. However, this method can be prone to errors for conductors with many filaments, where the task of determining the area of all the filaments is formidable. Computer software for analyzing micrographs is improving and can ease the task.

For very precise measurement of the nonstabilizer area, a length of the sample can be weighed, the stabilizer matrix chemically etched away, the leftover filaments dried, and the sample reweighed. (Copper can be dissolved with a 50% solution of nitric acid and water, or with a mixture of one part NH_4OH, one part H_2O_2, and two parts H_2O, made fresh each time.) By using the overall density of the sample and the handbook value for the density of the stabilizer material (Appendix A6.1), we can calculate the ratio of stabilizer volume to total conductor volume. An accurate way to measure the overall sample density for this calculation is to use Archimedes' principle and measure the weight of a piece of the sample suspended by a light thread from a scale both in and out of distilled water (by using the density of water, 0.9982 g/cm^3 at 20°C).

9.1.3 THE OVERALL PICTURE: DEPENDENCE OF CRITICAL CURRENT ON MAGNETIC FIELD, TEMPERATURE, AND STRAIN

Figure 9.3 shows the classic three-dimensional plot of the dependence of critical-current density J_c on magnetic field B and temperature T for two common superconductors. (The data

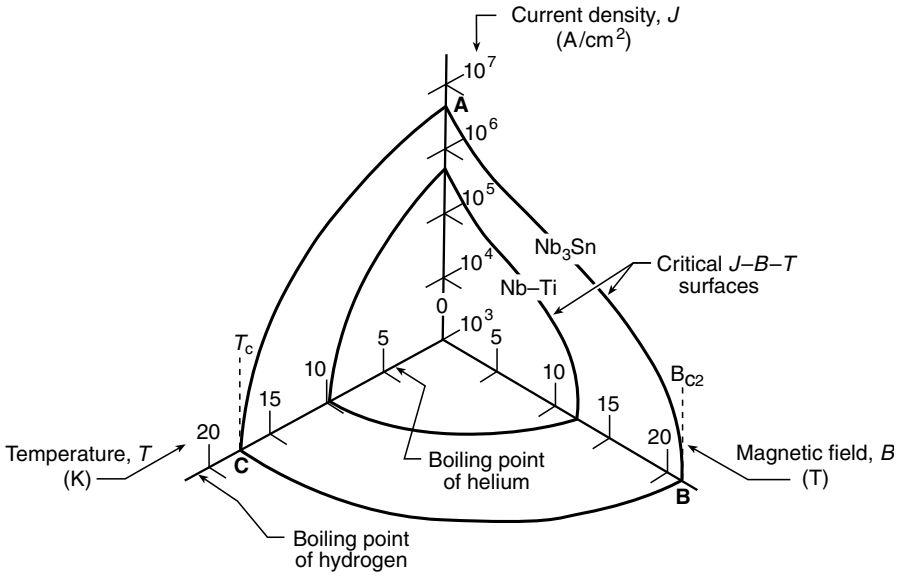

Fig. 9.3 Critical-current density J_c of two commercial low-T_c superconductors as a function of magnetic field B and temperature T. In the region between the origin and the critical J–B–T surface, the material is superconducting; above the surface, the superconductor reverts to its resistive state. (The three-dimensional surface for Nb–Ti is nested inside that for Nb_3Sn.)

shown for the current density correspond to the J_c of the superconducting layer itself, rather than to J_n or J_e; see previous section.) The plot defines a three-dimensional *critical surface*: below the surface, the material is superconducting; above the surface, the superconductor reverts to its resistive state. To be practical for large-scale applications, a superconductor typically should have $J_c \gtrsim 10^5$ A/cm^2. Thus, we see from Fig. 9.3 that at 4.2 K, Nb–Ti is useful up to magnetic fields of about 7–8 T, whereas Nb_3Sn can be used up to about 14–16 T. At higher temperatures, the magnetic-field limit drops rapidly. (Equations for precisely modeling the relationship between J_c, B, and T are given in Secs 10.3 and 10.4 for both high- and low-T_c superconductors.)

In most high-field superconductors, the critical current also depends *reversibly* on the mechanical strain it experiences. Similar to the surface in Fig. 9.3, we can define a critical J–B–ε surface at a particular operating temperature, like that shown for liquid-helium temperature in Fig. 9.4.

So from an experimental standpoint, the characterization of critical current is a multidimensional task of measuring J_c as a function of B, T, and ε.

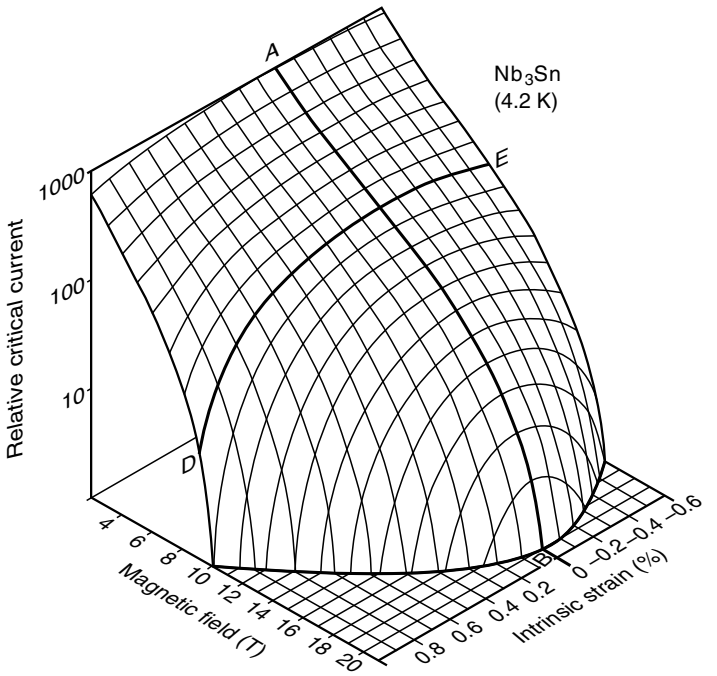

Fig. 9.4 Critical J–B–ε surface for commercial Nb_3Sn superconductors at 4.2 K, showing the relative dependence of critical current on magnetic field B and axial strain ε (from Ekin 1983b). The conductor is superconducting below this surface, but transforms *reversibly* into the resistive state above the surface. Line A–B represents the maximum (nearly strain-free) critical current as a function of magnetic field. Line D–E represents a typical J_c-vs.-ε curve at a given magnetic field.

9.1.4 TEST CONFIGURATIONS

The main design principle in choosing an experimental test configuration is to *begin with the end application in mind*. That is, design the test apparatus to mimic the configuration of currents, magnetic fields, and forces that the test sample will see in actual practice.

Transmission-line applications

For transmission-line applications, the test configuration is shown schematically in Fig. 9.5(a). The conductor is simply held at the expected operating temperature and current is passed through it while voltage is measured along a central length. The only magnetic field involved is the self-field of the superconductor (i.e. the field that is generated by the transport current in the conductor). The magnetic forces experienced by the conductor are much smaller than those in high-magnetic-field testing.

Magnet and rotating-machinery applications

For electromagnet applications, on the other hand, the conductor must be tested in a high magnetic field to simulate the operating conditions. Usually, the application requires that the magnetic field be applied *perpendicular* to the conductor's length [Fig. 9.5(b)], which, as nature would have it, produces the highest magnetic forces and brings into play all the mechanical-force considerations for sample holders described in Sec. 7.3.5.

The background magnetic field is usually supplied by one of the types of magnets illustrated in Fig. 9.6: either a solenoidal magnet [Fig. 9.6(a) and (b)], a split-pair magnet [Fig. 9.6(c)], or a race-track magnet [Fig. 9.6(d)]. The latter two magnets are useful for testing long, straight conductor samples, but the highest magnetic fields for test purposes are achieved least expensively with solenoidal magnets. Usually the desire for high field and minimum expense wins, and so the test configurations shown in Fig. 9.6(a) and (b) are the most common.

Short, straight sample (solenoidal magnet): The straight, transverse geometry shown in Fig. 9.6(a) is well suited when a short test piece is all that is available, such as with experimental

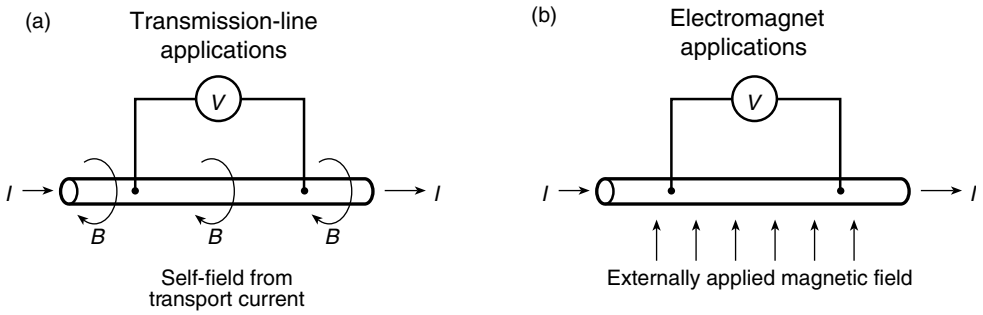

Fig. 9.5 Test configurations for critical-current measurement for (a) transmission lines and (b) electromagnet applications.

conductors. Sometimes this geometry is also necessary when a sample must be tested at high magnetic fields in a straight, unbent condition.

Coil sample (solenoidal magnet): When a longer sample is available that can be bent or reacted in a coil shape (Sec. 7.3.6), the test sample can be tested in the shape of a small coil that fits within the bore of the magnet, as illustrated in Fig. 9.6(b). This is the most desirable configuration since it allows a relatively *long length* of conductor to be tested in the confined space of a high-field solenoidal magnet. The sample is mounted on a tubular sample holder (Fig. 7.3) with a length that is usually kept short to ensure that the sample is in the most homogeneous part of the magnet.

Long, straight samples (split-pair and race-track magnets): Figure 9.6(c) and (d) show the arrangements for measuring the transport properties of long, straight samples with either a split-pair magnet or race-track magnet. These arrangements are mainly useful for critical-current measurements of large-diameter samples that cannot be easily bent into a small coil, and they also serve well for measurements as a function of magnetic-field angle since the sample is easily rotated in the background magnetic field.

With any of these configurations, the sample can be refrigerated with the same cryogenic liquid that cools the background superconducting magnet, or the sample can be thermally isolated from the magnet by a separate insert dewar, as illustrated in Fig. 1.14(b) for high-current samples or in Fig. 2.12(b) for low-current samples.

Thin-film electronic applications

Whereas the transport current for bulk-sample testing is usually relatively high (>>1 A) and necessitates an immersion cryostat, the test current for thin-film measurements is typically low enough that it permits the use of variable-temperature commercial cryocoolers of the type described in Secs 1.4.3 to 1.4.6. Thus, for thin films, critical-current testing as a function of temperature is much easier than for bulk samples.

Furthermore, thin-film testing is usually performed in zero magnetic field to simulate the operating conditions of electronic-chip applications. Occasionally, measurements are needed in high magnetic fields, in which case the test configuration shown in Fig. 9.6(a) is commonly used. This configuration also lends itself well to variable-angle testing (Sec. 9.4.2).

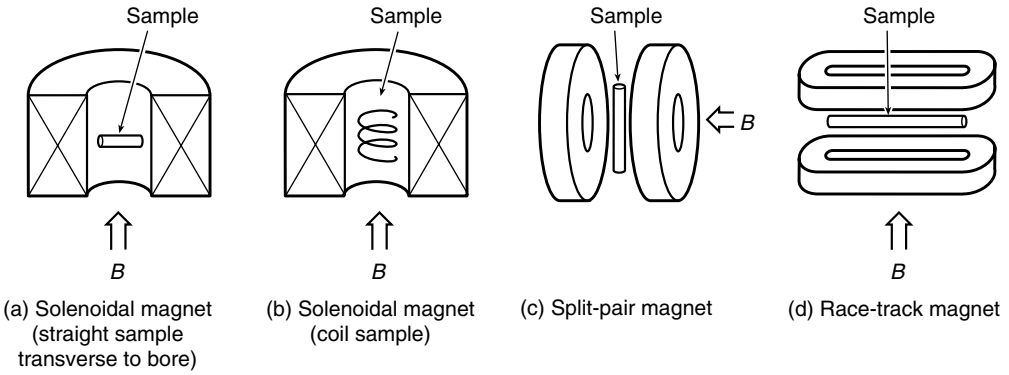

Fig. 9.6 Different types of background magnets and sample configuration for critical-current measurements in a transverse magnetic field.

Thick-film coated conductors, on the other hand, usually require the same test configurations illustrated above for bulk samples. That is, the test currents are high, and so the samples are usually cooled by direct immersion in a cryogen (rather than with a cryocooler), and long test lengths are needed (to provide low-resistance contacts and minimize current-transfer voltages, as described in Sec. 7.3.4).

9.2 Instrumentation

In this section we look at how to create an effective instrumentation system for critical-current measurements (Sec. 9.2.1) and methods of checking out a new system (Sec. 9.2.2).

9.2.1 SETTING UP A CRITICAL-CURRENT MEASUREMENT SYSTEM

The experimental setup for measuring critical current is a four-lead measurement of voltage vs. current, shown in Fig. 9.7. The main difference between critical-current measurements and voltage vs. current measurements of other materials is that the resistance we want to detect in a superconductor is very low, typically only 10^{-9}–10^{-10} Ω for bulk superconductors. Thus, since critical currents of superconducting strands are typically hundreds of amperes, the required voltage measurement is in the range 10–100 nV.

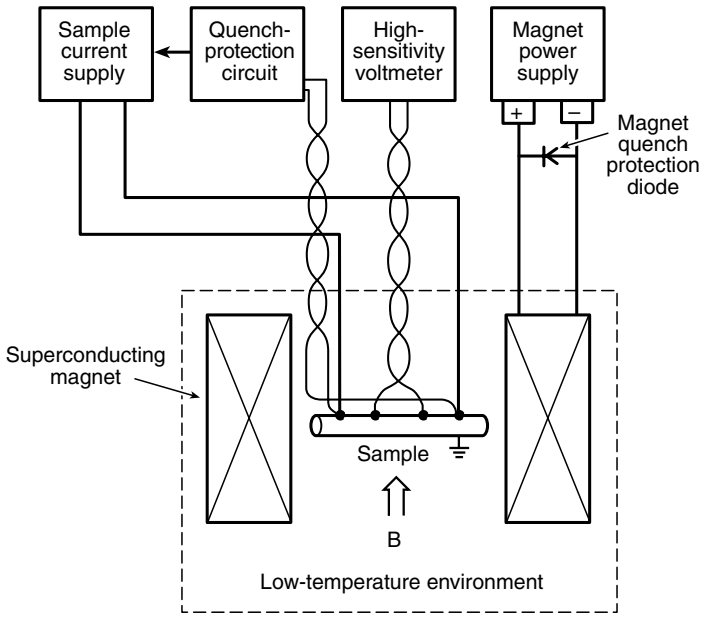

Fig. 9.7 Schematic diagram of instrumentation for critical-current measurements.

Handling the high currents needed for bulk superconductor testing does not pose much hazard in practice. It is current passing through our bodies that can kill us, but it takes voltage to get the current through our (relatively) high-resistance skin. So, for example, we can pick up 1000 A leads connected to a 12 V current supply and touch the copper with our bare hands without any problem. But sparks will fly if we touch the leads to any *conducting* metal. It is like working with a car battery: the main danger is sparks and arcs from contacting metals.

➔ So what is lethal in a cryogenic laboratory?

See Sec. 1.6.1 on safety, but two potential events bear emphasis:

1. A cryogenic liquid dewar with a vent that is blocked by ice. I have seen the result of such an explosion: the room lights were blown out, and the rollers on the bottom of the dewar left 1-cm-deep pits in the tile floor.
2. Disconnecting a current lead from an energized magnet that is not equipped with a protection circuit. I have not seen this yet, but it will ruin your day; the induced voltage across the magnet terminals can reach tens of kilovolts.

For *thin-film* superconductor measurements, the same instrumentation diagram shown in Fig. 9.7 applies; the main difference from bulk-sample measurements is that the current supply is much smaller, usually covering the low-current range from 1 μA to 1 A.

In the following subsections, we consider guidelines for buying or constructing each of the instruments in Fig. 9.7.

Sample current supply

To make precise critical-current measurements, the dc current supply shown in Fig. 9.7 must be stable and noise-free to within about 1 part in 10^4. This rigorous requirement arises because the *V–I* curve is so nonlinear. That is, the current must be held very steady on the steep part of the *V–I* curve in Fig. 9.1 to avoid generating a wildly noisy voltage signal at the sample.

Aside from generating voltage noise, current oscillations can also reduce the apparent dc critical current. As a general rule, a sinusoidal current ripple of a given percentage will reduce the apparent I_c by about the same percentage (Goodrich and Bray 1988). For example, a sinusoidal current ripple that is 1% of the dc current (or a *peak-to-peak* amplitude of 2%) will reduce the measured critical current by slightly less than 1%.

A low-noise current source that is stable to within 1 part in 10^4 usually requires series-transistor regulation. Figure 9.8 shows the basics of such a series-transistor current supply. The regulation is provided by a power transistor (or bank of transistors) through which all the current must pass, be it tens, hundreds, or thousands of amperes; so the power requirements on the transistors can be quite high. Also, if a filtered ac source is used to power the series transistors, the response of the transistors must be fast enough to actively filter out the ripple and voltage spikes.

Unfortunately, such low-noise supplies are relatively expensive. However, if a good, commercial, highly regulated current source is within your budget, go for it. It will save a lot of construction time and continuing maintenance. (Sources are listed in Appendix A1.7 under Current power supplies.) A quality floating current supply can also be constructed with a battery source for the

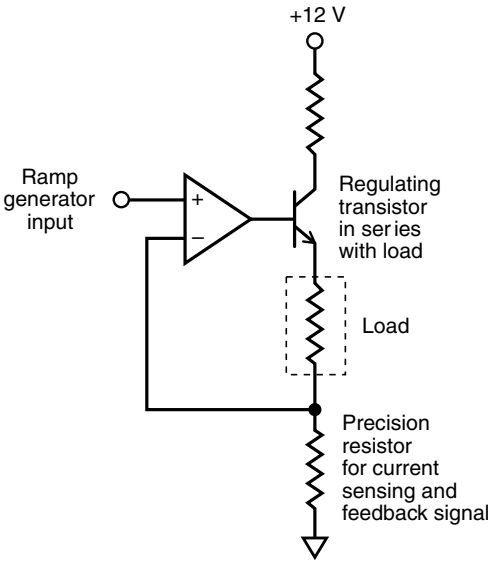

Fig. 9.8 Basic circuit diagram of a series-transistor-regulated current supply. Current through the load is controlled by a high-power regulating transistor in series with the measuring current. A differential amplifier regulates the current passing through the power transistor by comparing two voltages: (1) the signal from a controlling ramp generator, and (2) the feedback signal from a precision resistor in series with the sample current. Feedback resistors are added across the operational amplifier to prevent oscillations at higher frequencies.

series-transistors circuit. Such a battery supply has minimal noise, but it can be difficult to prevent it from oscillating, and the batteries require regular recharging and maintenance. An example of a battery-powered low-current (10 A) series-transistor supply is described by Bray and Goodrich (1990), and a high-current (1000 A) version by Bray et al. (1989).

Thermal-runaway protection circuits

Superconducting samples become very unstable near their critical current, where it takes only a small amount of sample motion or other disturbance to initiate a thermal-runaway event (Sec. 7.5.1). The entire process usually takes place in a fraction of a second.

When I was setting up our first superconductor measurements laboratory, I did not have an automatic protection circuit to shut down the sample current supply. So I ran the experiments with my trigger finger constantly poised on the power supply switch, ready to snap it off at the slightest sign of a rapid voltage rise across the sample. If I was too slow by a fraction of a second, my precious sample would melt into a shapeless blob. After a day of such tension, my nerves were frazzled, and it did not make for a great home life either. The moral of the story? Use an automatic quench-protection circuit and invest the time to set it up.

The input signal for the quench-protection circuit consists of a pair of leads connected to the sample-voltage leads or, preferably, a separate twisted pair of leads attached to the *current* terminals of the sample, as shown in Fig. 9.7. The latter technique serves to separate the quench detector from the sample voltage leads and thus helps to minimize noise at the high-sensitivity voltmeter. It also enables resistive zones to be detected in the current-transfer section outside the region between the voltage taps, which can be invaluable for identifying erroneous data (discussed in Sec. 9.3.2).

The circuit basically consists of an operational amplifier that compares the voltage across the length of the sample with a reference voltage. If the voltage across the sample suddenly exceeds the reference level, the output of the operational amplifier rapidly shuts down the current supply or actuates a "crowbar" circuitry (which shorts the supply's output). An example of a quench-protection circuit is described by Dubé and Goodrich (1986).

Voltmeter

For most *V–I* measurements, the voltmeter in Fig. 9.7 is the heart of the system. It must be sensitive, very sensitive: 1 μV is the minimum resolution; 0.1 μV is much better; and 0.01 μV is the best. A wealth of information is buried at low voltages near the start of the rise in the *V–I* characteristic, which is needed for engineering design data, problem identification, and basic physics studies of superconductors. The keys to gaining access to this information are good low-thermoelectric-voltage connections (Sec. 4.6.1), twisted leads (Sec. 4.1.2), and an excellent voltmeter. On a limited equipment budget, the high-sensitivity voltmeter is the item to buy.

To illustrate this point, consider the common situation of short-sample testing for superconductor-magnet design. In a typical test, a sample only a few centimeters long is used to predict the performance of a magnet containing wire with a length on the order of a kilometer. (The same would also be true of transmission lines that can have kilometer-long wires, or microelectronic chips, where the test length of film materials is usually a fraction of a millimeter compared with on-chip transmission lines that can total meters in length.) What is the sensitivity of the voltmeter required to extrapolate from such a short test sample to the full application length?

Example: Assume we are testing a 20 cm sample for application in an electromagnet where the length of the conductor will be 1 km and the operating current of the magnet will be 100 A. We wish to measure the *V–I* characteristics of the superconductor at low voltage levels where the power dissipation in the electromagnet is less than 1 W (1.4 L/h boil-off rate).

The 1 W dissipation limit requires the voltage along the entire length of conductor to be less than

$$V \leq 1\,\mathrm{W}/100\,\mathrm{A} = 10\,\mathrm{mV},$$

which corresponds to an electric field along the length of the conductor of

$$E = 10\,\mathrm{mV}/1\,\mathrm{km} = 10^{-7}\,\mathrm{V/cm}.$$

So for a 10 cm long voltage-tap separation in a typical 20 cm long sample test, the voltage needs to be detected at the 1 μV level, requiring a voltmeter sensitivity in the range 0.1–0.5 μV. For developmental samples where only a couple of centimeters may be available, the voltage-tap separation may be only 1 cm or less, which would require a voltmeter sensitivity in the range 0.01–0.05 μV.

However, a good voltmeter is not enough. As noted above, thermoelectric voltages need to be minimized by eliminating as many connections as possible between the voltage taps and the voltmeter through the use of *continuous* voltage leads. Those unavoidable connections (e.g. where the instrumentation leads are attached to the voltmeter) should be made with low-thermoelectric-voltage techniques. This requires the use of polished copper-to-copper connections (without solder, as illustrated in Fig. 4.7) and keeping corresponding pairs of connections close to the same temperature. Several schemes for making high-quality room-temperature connections to voltmeters are shown in Fig. 4.8.

Magnet power supplies

The magnet power supply shown in Fig. 9.7 for energizing the superconducting background magnet is surprisingly small when compared with power supplies for resistive electromagnets.

In steady-state operation, the superconductor requires no voltage for it to carry current, so the power supply needs to deliver only enough voltage to overcome the small potential differences across resistive joints in the leads that connect the magnet to the power supply. Usually, such magnet power supplies provide current on the order of 100 A and have a voltage capability of about 10 V, which is needed mainly to overcome the reactance of the winding (typically many tens of henries) when energizing the magnet. The higher the power-supply voltage, the shorter the charging time, which typically runs 5–30 min, depending on the inductance of the superconducting coil and its stability. The charging rate can be initially fast at low fields, but must be slowed considerably to prevent thermal runaway as the current approaches within 10–20% of the fully rated magnet current.

The main feature that distinguishes superconductor magnet power supplies from ordinary current supplies is their ability to (1) dissipate the energy stored in the magnet so that the magnet can be *dis*charged in a reasonable amount of time, and (2) clamp (i.e. limit) the voltage produced at the supply's output terminals if the magnet quenches. (For large magnet systems, a quench is quite an event—the heat suddenly generated in a large system can vaporize liquid helium and fill an entire lab with a cloud of helium-cooled water vapor, raise your voice by an octave, and result in suffocation if the lab air is not well vented.)

Both capabilities are met by a magnet-quench-protection diode connected across the supply's output terminals, as shown in the schematic diagram of Fig. 9.7. The polarity of the diode is such that during magnet charging the diode is reverse-biased and carries no current. During magnet discharging when the power supply is ramped down, the inductive voltage across the magnet coil forward-biases the diode, which turns on and provides a means of dissipating power owing to the voltage drop (~0.6 V) across the diode. Faster discharge rates can be obtained by placing several diodes in series to provide a greater voltage drop. More importantly, if the magnet were to quench, the diode would become forward-biased and short the output terminals of the magnet, thus clamping the otherwise huge voltage that would form across the magnet terminals.

Commercial power supplies for superconductor magnets have this type of circuitry built into them at the factory. Further information is given in the product literature listed in Appendix A1.7 under Magnets.

Pulsed-current measurements

When current-contact resistance is high, Joule heating at the sample contacts can affect the measurements. The heating can be mitigated by use of a pulsed-current measurement. Pulse techniques are also useful for marginally stable samples with low stabilizer-to-superconductor ratios (in which case, pulse techniques may be the only method of obtaining critical-current data).

In a typical pulsed-current measurement, the current is ramped quickly from zero up to some level; the voltage along the test sample is measured before the heat diffuses to the voltage contacts (Colclough et al. 1990); and the current is ramped back to zero again. To correct for voltage offset in the voltmeter or for thermoelectric-voltage drifts, the sample voltage is usually measured at zero current before and after the current pulse (or if the current is not too high, measured at forward and reverse polarities and averaged). Pulse duration is typically anywhere

from 1 ms to about 1 s. High ramp rates dictate the need for a sensitive differential amplifier with a bandpass range from dc to about 10 kHz and good common-mode voltage rejection throughout this range (Morrison 1998). Also, for such pulsed systems, the lead pairs should be carefully twisted to minimize their inductive reactance. Voltage and current waveforms are usually displayed and recorded through the use of a digital processing oscilloscope.

9.2.2 WIRING CHECK-OUT FOR A NEW SYSTEM

Induced voltage, ground loops, common-mode voltages, and thermoelectric voltages interfere with accurate, sensitive *V–I* measurements because these erroneous voltages change with current and time. For a new measurement system, these should be minimized and measured to determine the limits of error for the system.

First, plan the circuit so that common-mode voltage is minimized at the test sample by use of a single ground point *near* the sample, as illustrated in Fig. 9.7. This requires a floating current supply. (Further information on proper grounding techniques may be found in Morrison 1998.)

Also, keep the resistance of the voltage leads between the sample and the voltmeter low enough that the input impedance seen by the voltmeter does not exceed the low levels specified for sensitive voltmeters. Use pure-copper wire (rather than phosphor-bronze wire); the wire size can be relatively small, say, #36 AWG (~0.125 mm), so that heat leaks down the leads do not become too great. The use of pure-copper wire also reduces thermoelectric voltages.

The thermoelectric voltage and noise-voltage floor inherent in a new measurement apparatus can be directly measured by a cryogenic test with a superconducting test sample installed in the probe. The sample current is ramped to a level *well below* the expected critical current of the test sample and then held at that level, where the sample voltage should be zero. The noise and interference voltages in the apparatus can then be directly recorded. This *in situ* test also permits thermoelectric-voltage drifts to be determined by monitoring the voltage signal over several minutes (still at fixed low current). Their magnitude is a primary figure of merit for a good critical-current apparatus.

The time constant of the voltmeter and the effective inductance of the entire system can be measured by making a step change in the current (still well below the critical current) and measuring the settling time of the output signal. This will determine the rate at which the current can be ramped and, depending on the accuracy required, may indicate the necessity of a step-and-hold method of changing the current (Sec. 9.3.3).

9.3 **Measurement procedures**

After the setup and initial checkout of a new measurement system, we come to the fun part—smart ways to use the system in day-to-day testing. We start this section on measurement procedures with a few general troubleshooting tips applicable to most measurements (not just critical-current measurements) (Sec. 9.3.1). Then we outline specific time-proven procedures

for measuring critical current that minimize the chance of destroying your sample and pinpoint errors while taking data (not after the fact) (Sec. 9.3.2). Finally, we consider the merits and drawbacks of automatic data acquisition as well as effective algorithms for their use (Sec. 9.3.3).

9.3.1 GENERAL TROUBLESHOOTING TIPS

Gleaned from the "school of hard knocks," the following brief list of troubleshooting tips has general applicability, either for commissioning a new system or for working through problems that occasionally plague all systems (both new and old).

1. *Principle of known samples:* For a first measurement, use a sample that is already tested and well known. There are usually enough initial instrumentation problems without having to deal with a bad sample. It also lets you know immediately whether a new system is giving good data.
2. *Principle of subsystems:* Divide a new measurement system into parts and get each subsystem working on its own before combining them. It is too much to expect the entire system to work perfectly the first time. First runs with a new measurement system are notorious. Rejoice if you get any data at all.
3. *Principle of elimination:* Find out what is *not* the problem. Use the fission approach: if something is wrong, start splitting the system into a few large parts. For a start, see whether the problem (a short to ground, for example) is in the *cryogenic* part of the apparatus or in the *room-temperature* connections and cabling. Then progressively divide the remaining parts in two until the specific problem area is localized. This is much faster than systematically working one little step at a time, from one end of a long system to the other end (and faster still than the random approach!).
4. *Principle of substitution:* If you suspect the fault may be in a particular instrument, borrow a substitute to see if the problem goes away. (Take care not to damage the borrowed instrument, however.)
5. *Principle of bad connectors:* Get rid of them. Bad or intermittent connectors are the bane of the laboratory. If a bad BNC cable connector is found, for example, cut off the connector and trash it. Bad connectors cause headaches in the middle of an experiment just when we are under the most pressure. They are hard to find, and if we put the bad cable back on the lab bench, invariably, someone dutifully hangs it back up on the rack and, in a week or so, we get to enjoy the problem all over again. Spend the money to buy good commercially made connectors; making them correctly requires experience and skill, and it is such a small fraction of the total experiment cost.

9.3.2 CRITICAL-CURRENT MEASUREMENT PROCEDURES

Moving on from general troubleshooting tips, we now focus on procedures that are specific to measuring critical current. The most valuable of these are "real-time" techniques. These serve

to prevent and detect problems during data acquisition when it is not too late to make changes, or to abort the experimental run before investing a lot of time in a bad set of data.

The *V–I* curve reversal point

To determine the critical current accurately, especially to correct for current-transfer voltages (Sec. 10.2), we want to climb the *V–I* curve to as high a voltage as possible without quenching the sample. The reversal point, marked X in Fig. 9.1, is kind of a "chicken point" where we turn around the current before the voltage irreversibly flies off the chart. It depends on sample stability and the current magnitude. For high-current bulk samples, we usually cannot reach more than a few microvolts before triggering a quench, whereas for thin-film superconductors we often can reach the millivolt range (because the critical current is lower and because the ratio of cooled surface area to volume is greater).

In actual practice, the quench point is usually encountered accidentally in the course of taking data (especially the first curve), and then we adjust the reversal point accordingly. This requires a good thermal-runaway protection circuit (Sec. 9.2.1).

Sample stability

Sometimes samples are so unstable that sample quenching precludes getting any useful data at all. This is one of the biggest practical problems in critical-current measurements. You can save yourself a lot of wasted time by observing the following guidelines:

1. At liquid-helium temperature, it is very difficult to test samples that have a stabilizer-to-superconductor area ratio less than about 1:1, unless pulsed-current techniques are used. (The superconductor area to use in this ratio is that of the actual superconductor, not the noncopper area; these areas are defined in Sec. 9.1.2.) The sample should also be completely immobilized with solder, epoxy, or some other adhesive. If it must be left free to move (such as in electromechanical testing), electroplate extra copper onto the outside of the conductor to bring the stabilizer-to-superconductor ratio to at least 2:1, or do not even try to make the measurement.
2. Thermal runaway is less of a problem when testing in liquid nitrogen than in liquid helium [because the critical heat flux for the transition from nucleate to film boiling is 20 times higher in liquid nitrogen than in liquid helium (Sec. 2.5)]. Also, the relatively high heat capacity of solids at liquid-nitrogen temperature limits the temperature rise for a given energy input, so the experiment is much more tolerant of disturbances, such as sample motion.
3. Finally, thermal runaway is much less likely at high magnetic fields and temperatures where the critical current is low. This is the preferred regime for starting to take data on a new sample (item #3 in the measurement protocol below).

Data-acquisition protocol to avoid sample burnout and ensure good data

In performing routine critical-current measurements, the first *V–I* curve for each new sample is the trickiest. That is when sample meltdown is most likely to happen. There is also a host of

other systematic errors that can be easily detected at the outset of each experimental run, if you take just a few minutes to check for them. The following protocol, performed at the start of each data set, has always worked for me. (The few times I have not followed it, I have usually regretted my impatience.)

1. The first item in Table 9.1 checks the condition of the quench-protection system. For preventing sample destruction, this circuit is worth its weight in gold. This check means to *operationally* test it. That is, ramp the sample current up to a low value and hold it there; then simulate a voltage rise across the sample, such as by momentarily disconnecting one of the voltage leads to the input of the quench-protection circuit. Make sure the circuit rapidly resets the sample current to zero. (You would be amazed how many times a lead is not hooked up properly; then the first quench burns out the sample and many hours of labor have been wasted for lack of a 1-min check. After it happens to you, you will not again forget this simple test.)
2. The second item in Table 9.1 ensures that the sample is, in fact, superconducting (before wasting time ramping the background magnet to full field, only to find that the sample is bad). This test also provides a check of the noise-voltage floor [measured during the initial apparatus checkout (Sec. 9.2.2)].

Table 9.1 **Protocol checklist for high-current I_c measurements.**

1. Quench detector?	To ensure that it is functioning and set correctly, check it with an operational test by ramping the current to a low value (well below the expected critical current) and simulate a voltage rise at the input to the quench detector to make sure the circuit rapidly resets the sample current.
2. Bad sample?	Ramp the sample current to a low level (still well below the expected critical current) and make sure the sample is, in fact, superconducting. This check also provides an immediate indication of any problems with current-transfer voltages that may result from bad placement of the voltage taps (Sec. 7.3.4).
3. Safe zone for first curve?	Take the first V–I curve in a parameter space where the critical current is low (usually at high magnetic fields or high temperatures) so that an unexpected quench will not damage the sample. Then work toward higher values of critical current once the approximate value of I_c and the sharpness of the V–I characteristic are known.
4. Current reversibility?	Look for reversibility in the V–I curve between ramping current up vs. down; irreversibility is a sign of heat- or strain-affected data.
5. Magnetic-field reversibility?	Check that there is no difference in the critical-current data when approaching a given magnetic field from below or above. If a difference exists, the particular material under test may require approaching the magnetic field always from the same direction (usually from below). For a new superconductor, find this out at the *beginning* of the data set rather than halfway through, and avoid having to retake the data.
6. Lorentz-force reversibility?	As soon as possible during data acquisition, check that I_c is the same before and after taking data at the magnetic field where the Lorentz force is highest. If I_c has shifted, it may indicate that the sample was poorly supported and permanently strained during the measurement.

3. The third item is to take the first *V–I* measurement under conditions where we expect the critical current of the sample to be low; that is, where the risk of sample burnout is small. With most superconductors, this means starting at *high* magnetic fields. See what the *V–I* curve looks like there, and then approach the high-I_c regime cautiously by reducing the magnetic field in several steps. The problem at low magnetic fields is the challenge of very slowly approaching a high, *unknown* critical current without quenching the sample. The extra 10 min can save hours of work remounting a quench-damaged sample.
4. Check for hysteresis in the *V–I* curve. If the curve does not retrace itself when current is ramped both up and down, the data may be affected by sample heating (usually from poor current connections) or Lorentz-force strain (from inadequate sample support). Beware that this test is not always foolproof, especially at liquid-nitrogen temperatures. At such temperatures, the heat capacity of materials is generally so great and the transition to film boiling so delayed that heat-affected *V–I* data can be stable and reversible (without initiating a quench). This is a situation where the art of critical-current testing comes into play. We need other clues to detect excessive contact heating. One way is to look for a noticeable rise in the curvature of the *V–I* characteristic—a rise in the so-called *n* value [see Eq. (10.1a) in the next chapter]. Another foolproof way is to place an extra set of voltage taps across the current contacts at either end of the sample to monitor the total contact resistance (the leads installed for the quench-protection circuit work well for this purpose, see Fig. 9.7). Especially in starting with a new apparatus or new sample, this simple practice can save time acquiring erroneous data (or, worst yet, publishing it).
5. When testing superconductors that trap magnetic flux, the critical current can be significantly different depending on whether a magnetic field level is approached from below or above. The difference in the critical current of Bi-2223 samples, for instance, can amount to 40% at low temperatures (Goodrich and Stauffer 2001). As a general rule, the lower, more conservative value of critical current will limit a superconductor in service. Usually this occurs when approaching a given magnetic field from *lower* values.
6. Although this last item cannot be made at the outset of data acquisition, as soon as possible, check that the sample is not being damaged by Lorentz forces. This is done by seeing if data acquired at a common magnetic field reproduce after an intervening measurement at the field where the Lorentz force F_L is highest. For example, with Nb–Ti and Nb_3Sn at 4.2 K, check that data taken at 8 T are the same before and after an intervening measurement at 5 T (since F_L at 4.2 K is a maximum in both these materials at about 5 T).

Curve shape: the "who's who" in problem identification

The other tool we have to check data quality during acquisition is the *shape* of the *V–I* curve. It is a virtual "who's who" in problem identification.

Our benchmark is the ideal characteristic shown as curve *a* in Fig. 9.9. It is highly nonlinear; the greater its nonlinearity, the easier the determination of a precise critical current. (Ways of defining a "critical" value from this curve are presented in Sec. 10.1.) The curve should also be reversible, which indicates the absence of heating and strain effects.

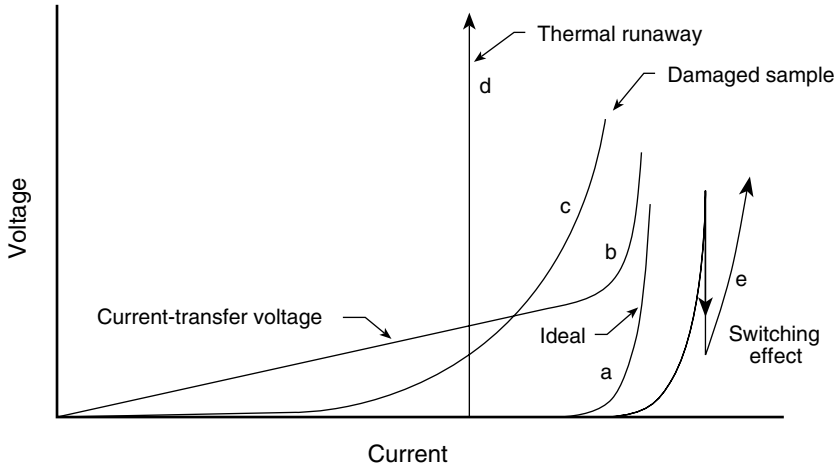

Fig. 9.9 *V–I* curve shapes: (a) ideal characteristic; (b) inadequate current-transfer length between current contacts and voltage taps; (c) damaged sample; (d) premature thermal runaway; and (e) switching effect that can occur when a resistive zone forms outside the voltage taps or when current suddenly transfers between poorly connected filaments or strands (adapted from Ekin 1983a and Goodrich et al. 1995).

Curve *b*, on the other hand, shows the shape that results from current-transfer voltages, which occur near current contacts as current passes through the sample's resistive matrix on its way to filling the innermost superconducting filaments. This indicates that the voltage taps are too close to the current contacts. The required current-transfer distance to leave between the two is given in Sec. 7.3.4, Eq. (7.9).

Curve *c* shows the gradual voltage onset that can occur when a superconductor sample is damaged, resistive, or inhomogeneous.

Curve *d* indicates the *V–I* characteristic obtained when wire movement, contact heating, or inadequate refrigeration causes premature thermal runaway in a marginally stable sample. This is the problem described in the Sample-stability subsection above. The voltage precipitously, *irreversibly* increases and the voltage flies off the scale. Unfortunately, curve *d* is also the shape obtained when a voltmeter is too crude to detect what is going on below the quench point. The flyaway current *may* be the true critical current; but, then again, it may be premature thermal runaway. You just do not know. The only way to tell is to use a more sensitive voltmeter.

Curve *e* illustrates a rather interesting switching effect that can occur in a couple of ways. First, it can result from an *alternative normal conducting path* paralleling the sample, such as a conductive sample holder. If a resistive zone forms *outside* the voltage taps, the voltage will not be detected by the voltmeter (if the resistive zone is stable and does not propagate into the sample region between the voltage taps). However, the sudden rise in sample resistance forces current to flow through the sample holder (or other alternative current path). The apparent *V–I* curve is shifted to higher current, with respect to the true curve, by the amount of current flowing through the conductive holder. Note that the true critical current of curve *e* is given by the *first* voltage rise, not the second rise (further description of this case is given by Goodrich et al. 1995). As a rule of thumb, this first type of switching phenomenon becomes a problem mainly when the *normal resistance of the sample is comparable to that of the sample holder*.

This can happen, for example, when testing very-small-diameter wire samples wound onto stainless-steel, titanium, or beryllium–copper sample holders.

Curve *e* can also indicate a second type of switching phenomenon that occurs between *poorly connected superconducting filaments or strands* within a short test sample. If current is not evenly injected into the filaments or strands, voltage may initially appear in some filaments or strands but not in others. Current will then be forced to transfer to the underutilized filaments or strands. Depending on which filaments or strands are monitored by the voltmeter, premature, unstable voltages can be detected. Unlike the previous case, the true critical current in this scenario is the rapid voltage rise that occurs *after* the current is forced to distribute evenly throughout the composite or cable, not the initial voltage rise that may occur in a few filaments or strands.

Fortunately, there is an easy way to diagnose which case applies and to determine the true critical current. Simply place an *extra pair of voltage taps on the current contacts* to monitor the *entire length* of the sample, not just the central test section or a subset of filaments or strands. The same valuable pair of voltage taps attached to the current contacts for the quench protection circuit can also serve this function.

Thus, a wealth of information is buried in the details of the *V–I* characteristics. (Again, this can be accessed only with a sensitive microvoltmeter, or else you are relegated to the no-man's land of curve *d*.) The shape of the *V–I* curve, I would submit, it is the only way of knowing you are getting reliable critical-current data.

9.3.3 AUTOMATIC DATA-ACQUISITION PROGRAMS

Automatic data acquisition systems have their time and place, and are not always appropriate, but for certain experiments they are a panacea for drudgery, and for others they make the impossible possible.

Introduction and general approach

Before considering techniques, I offer two overriding suggestions for the general approach to automatic data-acquisition systems.

First, in setting up a data-acquisition system, it is much better to buy smart *sub*systems rather than dumb subsystems connected to a smart central computer. I have tried it the second way, and it does not work very well. With smart peripheral equipment (such as digital multimeters, voltage-ramp generators, programmable power supplies, and programmable magnet supplies), the programming is divided automatically into manageable pieces, and often the needed software is automatically incorporated into the peripherals. This way there are many brains on the job, and the central controller does not get bogged down trying to keep track of everything at once. (Incidentally, this is also a very good management principle with people—that is, push responsibility *and* control to the lowest levels possible.)

A second general guideline is to beware of *overusing* automatically controlled data-acquisition systems. Although computer logging data is nearly always recommended over hand-logging data, automated data acquisition (where the computer also *controls* the experiment) is worth

the time required to set it up only if one of the following conditions is met:

1. The automatic data-acquisition system is used over and over on a number of experiments, not for one-of-a-kind experiments.
2. The experiment is so fast that it is beyond human response time.
3. The experiment is so slow that humans do not have the patience or stamina to take the data.
4. The volume of data per sample is extremely large.

So assuming our task fits one of these situations, we proceed (in the next two subsections) to look at different architectures for automated data acquisition, progressing from simple data loggers to fully automated control systems. Where to cut off the level of sophistication is your call—I have heard dreams of systems that do everything (including writing the publication), but invariably they take more time and effort than they are worth. I would suggest deciding up front what's "enough," and stick to it.

Program architecture: simple data loggers

With data loggers, the operator controls the independent variable(s) while the equipment automatically records the data output from one or more (usually "intelligent") instruments. Figure 9.10 shows the basic schematic diagram of a data-logging system designed for critical-current measurements. The sample current is passed through a low-resistance precision resistor in series with the sample, and the voltage across this resistor is measured to record the amount of transport current (x). A second high-sensitivity voltmeter measures the electric potential across the sample (y). The outputs of both voltmeters are digitally recorded, simultaneously, if possible. If a multichannel recording system is not available for simultaneous readings, the current level can be recorded immediately before and after the voltage reading, and the two current values are then averaged to give the approximate value at the time of the voltage reading.

For bulk superconductor measurements, the control (independent) variable is usually the current, whereas for thin-film devices it can also be the voltage. Either way, the same logging

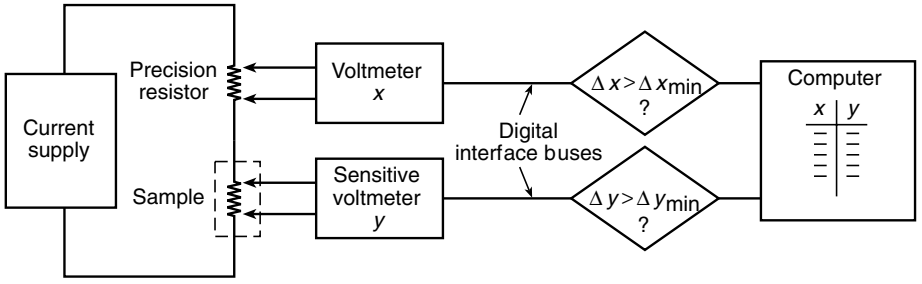

Fig. 9.10 Schematic diagram of a data-logging system, illustrated for the case of critical-current measurements. The same logging system is useful, however, for many other measurements, such as resistance vs. temperature or susceptibility vs. temperature, and it can be used to simultaneously log more than two variables. Data can be continuously streamed into the computer, or conditional comparators can trigger acquisition of individual data points when either variable (x or y in the figure) changes by more than a set minimum.

system is useful for measurements of voltage vs. current or whatever variables we wish. It can also be expanded to include simultaneous recordings of more than two variables, such as voltage, current, temperature, magnetic field, sample strain, and so on.

Two data-logging modes are possible:

1. data can be *continuously streamed* into memory;
2. the computer logger can be programmed to take readings only if there has been a *minimum change in one or more of the variables*.

The first mode is useful, for example, in recording fast current-vs.-voltage traces for thin-film devices, where the voltage applied to the device under test is ramped quickly. With such measurements, many I–V characteristics can be recorded and then averaged to improve the signal-to-noise ratio.

The second mode is useful in a slow temperature-drift experiment: for example, a dipper probe (Sec. 1.4.2) inserted into a storage dewar to measure the temperature dependence of a superconductor's magnetic susceptibility or resistance. With such slow measurements, the logger is capable of measuring at periods much shorter than the time it takes to vary the temperature. So it saves computer memory space and data reduction time to log data only if there has been some minimum change in either variable.

For example, when measuring the resistance vs. temperature characteristic of a superconductor with a drift dipper probe, the resistance changes slowly when the sample is first cooled from high temperatures, then very rapidly through the critical-temperature region. The data logger can be programmed to record data only if there is a significant change in *either* temperature or resistance (the Δx and Δy comparators shown schematically in Fig. 9.10). Thus, away from the critical temperature, data are taken only if the *temperature* has drifted by at least some minimum amount. On the other hand, near the critical temperature, changes in *resistance* take over and trigger data acquisition much more rapidly as the resistance drops precipitously. By this simple logic, memory is saved and rapid data logging automatically occurs right where it is needed (i.e. at the critical-temperature transition). Such a relatively simple automated data-acquisition system works very efficiently, and it can run almost unattended, with only occasional adjustments of the height of the dipper probe above the cryogenic liquid to control the rate of temperature drift.

Further refinements in data loggers are also possible. For example, when running an experiment, it is a tremendous help to have the *previous* curve displayed while the present curve is being recorded (as was traditionally provided by an x–y chart recorder). The previously recorded curves show approximately where the critical region is expected for the next curve. They also provide live feedback, instantly showing changes in shape that can help guide the progress of the experiment. So when it is available, select data-logging software that allows retention of the previous curve(s) on the screen during the recording of subsequent curves.

Program architecture: data acquisition with automated current control

Progressing to the next level of automation, namely, having the data-acquisition system also control the independent variable (current in this case), requires even closer scrutiny of the four conditions for investing time and money in such a system. Assuming that repetition or speed (fast or slow) is a prevalent factor that is worth the price, there are several ways to set up the control architecture for

critical-current measurements. Figure 9.11 shows three ways to automatically control the sample current:

1. Continuously *ramp* the current up and down, logging data points as you go.
2. *Step-and-hold* the current, waiting until transient voltages have settled before taking a data point.
3. *Pulse* the current, taking a data point during the flat top of each pulse.

The first method [Fig. 9.11(a)] is generally more useful for thin-film devices where data logging can proceed quickly because currents are low, voltages are relatively high, and, therefore, the time constant of the voltmeter can be relatively short. The second method [Fig. 9.11(b)] is generally more useful for bulk critical-current measurements, where high-sensitivity dc voltmeters usually require a long settling period and data-acquisition time to obtain a high signal-to-noise ratio at each data point. Although more complicated, a third method—the pulse technique [illustrated in Fig. 9.11(c)]—is sometimes needed for samples that require a short current-duty cycle, usually because the sample is unstable or there is a contact-heating problem. In this case, the current is ramped rapidly from zero to a given level and held there for a short time; the sample voltage and current are measured during this short interval, and then the current is returned to zero between data points. Method *b* is always preferred over *c*, which should be used only as a last resort.

Protocols for automatic current control: Since sample damage can occur even with the protection of a quench-detector circuit, it is best to minimize the possibility of thermal runaway by taking the *initial* curve *manually*, thereby carefully determining the actual value of I_c. Afterward, the controller program can use previous data obtained under similar conditions to estimate where to slow down the current-ramp rate as I_c is approached.

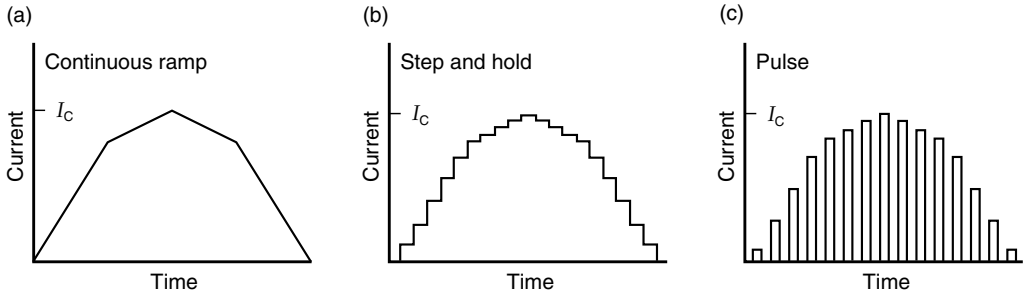

Fig. 9.11 Three methods of controlling current for critical-current measurements: (a) continuous ramp, with a slower ramp rate used at high currents near the critical current I_c; (b) step and hold, wherein the current is ramped quickly to a value, held there while the voltage is recorded, and then ramped quickly to the next value where the procedure is repeated; (c) pulse, wherein the current is returned to zero between each voltage reading. For all three methods, current is increased more quickly in the regime where changes in the superconductor voltage are small, say up to 70% of the estimated I_c, then more slowly (and carefully) through the superconductor-to-resistive transition. The point where the *V–I* curve is reversed (to avoid quenching the sample, as illustrated in Fig. 9.1) is usually set by the sample voltage reaching some predetermined level (e.g. 10 μV/cm for high-current samples).

An efficient protocol is to acquire data rapidly through the first part of the *V–I* curve where there is little change in voltage, say up to about 70% of the estimated I_c, as shown in Fig. 9.1. Thereafter, current is ramped slowly, and a much finer grid of data points is taken through the superconductor-to-resistive transition where the voltage rapidly rises. This change in data-acquisition rate is reflected in all three of the current-time charts depicted in Fig. 9.11.

Current-step size for the step-and-hold and pulse techniques is typically set to a fraction of the estimated I_c, say $I_c/20$ for the fast region and $I_c/200$ for the slow (critical) region. Current reversal can be automatically triggered when the sample voltage exceeds a given level, say 10 μV, at which point the current is automatically ramped down. To check for reversibility, the down-ramp protocol is the same as that for the up-ramp—that is, ramp back slowly through the transition region, then more rapidly to zero. If increased data-acquisition speed is important and the sample is mechanically well anchored, the current can be rapidly reset to zero immediately after the sample voltage has reached a predetermined voltage level.

A slightly more involved, but more adaptable, procedure is to use voltage feedback to control the current-ramp rate—sensing the rise in voltage and automatically slowing the current-step size or ramp rate as I_c is approached. This works well if the *V–I* curve is not very steep in the critical region and if the voltage rise can be detected quickly (without a lot of time averaging). However, problems result if the rise in the *V–I* curve is abrupt, since a step-and-hold program, for example, might jump beyond the critical current and quench the sample.

Such on-line voltage feedback can be used to control the current to give a *uniform* rise in voltage; that is, a voltage-step size that is constant. Empirically, current and voltage near the critical current are usually related by the very useful expression

$$\mathrm{d}V/V = n\,\mathrm{d}I/I, \tag{9.1}$$

where n is a nearly constant number, typically between 20 and 50. (This empirical relation is described more thoroughly in Sec. 10.1.3). Equation (9.1) simply says that superconductor *V–I* characteristics plotted on a log–log graph look approximately linear, with a slope of n. So to obtain a constant voltage step C_V, we set $\mathrm{d}V = C_V$ in Eq. (9.1), and obtain an expression for the required current-step size:

$$\Delta I/I = C_V/(nV). \tag{9.2}$$

That is, the program would adjust the relative size of the current step $\Delta I/I$ as V^{-1} to obtain a uniform rise in voltage (and good-looking data on a linear *V–I* graph). On the other hand, to obtain a constant *percentage* rise in voltage (for good-looking data on a log V vs. log I graph), we set $\mathrm{d}V/V = C_V$, in Eq. (9.1) and obtain

$$\Delta I/I = C_V/n. \tag{9.3}$$

All this sounds nice, but usually it is overkill and not worth the program complexity. It is interesting, though, to see from Eq. (9.3) that the simple approach of keeping the percentage current-step size $\Delta I/I$ constant through the narrow critical-current region (i.e. a nearly

constant ΔI, since I hardly changes) is ideal for acquiring uniformly spaced data on a *full-log* plot.

When developing such automated data-acquisition programs, it is helpful to test them at room temperature by using a superconductor simulator (see, for example, Goodrich et al. 1991). Such a device electronically simulates the low-resistance, highly nonlinear V–I characteristic of a superconductor (as well as the mutual inductance between the I and V taps), providing a convenient means to checkout various automatic-programming systems.

Computer averaging schemes for the step-and-hold approach: The step-and-hold approach has the added advantage that voltage sensitivity can be increased by automatically averaging a lot of voltage data at each current step. Your patience level determines the amount of averaging time—typically about 1 s for each point. However, there is a point of diminishing return at times over about 3 s where the drift in thermoelectric voltage starts to dominate any benefit from averaging. Initial effort spent minimizing thermoelectric voltages with the techniques described in Sec. 4.6 yields far more dividends than trying to deal with large voltage drifts every time data are taken.

There is also a trade-off between passive filtration and calculational averaging. Calculational averaging usually wins. That is, to enhance the signal-to-noise ratio for a small voltage, it is usually better to average a number of data points (each point taken with a relatively short data-acquisition time) than to use a *passive* filter with a long time constant to take one data point. To eliminate pickup of line-frequency noise, set integrating dc voltmeters to acquire data over a time interval that is an integer *multiple of the line frequency*, say, exactly 1 s. If the voltmeter does not integrate for such long times, then stream in data, acquiring each point over one line cycle (16.667 ms for 60 Hz or 20.00 ms for 50 Hz).

Another advantage of the step-and-hold method is that the computer can compute the average during the time it takes the system to ramp to the next current level and settle. As noted in Sec. 9.2.2, the settling time to allow for the step-and-hold approach can be experimentally determined by recording the response of the system to a step change in current. From the time profile, determine how long it takes for the transient voltages to decay below the system's noise floor; this needs to be done only once when initially checking out a new system.

9.4 Examples of critical-current measurement cryostats

The final section of this chapter is a collection of cryostat examples. The purpose is to highlight the key elements and pitfalls that affect how each cryostat is designed. Of necessity, this treatment is an overview, because the number of possible probes and their details would fill volumes. This chapter calls attention to critical design elements for several classes of probes, focusing attention on important compromise points that may not be so obvious at first.

Again, the best place to get more details for designing a particular type of apparatus is to search the technical literature for examples of similar cryostats. Journals specifically focusing on construction techniques are particularly useful, such as *The Review of Scientific Instruments*. If possible, follow up by contacting authors you trust and even consider a visit to their laboratory to see first-hand more of the details.

We start with a brief summary of previously discussed cryostat examples, especially those for measuring the dependence of critical current on magnetic-field magnitude. Then we consider examples of cryostats for the more specialized measurement of critical current as a function of *magnetic-field angle, temperature*, and *strain*. Continuity is not lost by skipping to the specific type of cryostat that interests you.

Thin-film cryostats: As mentioned in the introduction to this chapter, the cryostat examples described in this section are mostly of the *high*-current type (also pertinent to measuring thick-film coated conductors). A number of probes for *low*-current thin-film testing have already been considered (section references are summarized in Sec. 9.4.1). The main new information for thin-film probes is that given for field-angle measurements (Sec. 9.4.2) and variable-temperature measurements (Sec. 9.4.3).

9.4.1 CRITICAL CURRENT vs. MAGNETIC FIELD

The most common type of critical-current test is the measurement of I_c as a function of magnetic-field magnitude (e.g. curves A–B shown for Nb_3Sn in Figs 9.3 and 9.4). This dependence is highly variable from sample to sample, and thus it is the first characteristic usually measured for most superconducting materials. As noted in Sec. 9.1.4, magnetic field is usually applied *perpendicular* to the conductor to mimic the relationship between field and conductor in the high-field region of most magnets. This configuration is typically obtained with the testing arrangements shown earlier in Fig. 9.6.

Often, $I_c(B)$ data for engineering design are needed only at a fixed temperature, such as the boiling temperature of liquid helium or liquid nitrogen. In this case, many of the immersion cryostats already illustrated in Chapter 1 work well (Figs 1.6 through 1.13 for low-current testing and Fig. 1.14 for high-current testing). The critical design points for this type of cryostat were described earlier: low-loss electrical leads (Sec. 4.9), sample holders (Chapter 7), and sample contacts (Chapter 8). [Variable-temperature $I_c(B)$ cryostats are described below in Sec. 9.4.3.]

Good detailed sources of specific *procedures* for the measurement of I_c vs. B are outlined in the standards published by the International Electrotechnical Commission (IEC): Nb–Ti superconductors in IEC (1998), Nb_3Sn superconductors in IEC (1999), and Bi-2212 and Bi-2223 oxide superconductors in IEC (2000); also see the Further reading listings in Sec. 9.5.1.

9.4.2 CRITICAL CURRENT vs. THE ANGLE OF MAGNETIC FIELD

For some applications, especially those utilizing anisotropic materials such as the high-T_c superconductors, the $I_c(B)$ characteristic needs to be determined also as a function of the *angle* between the magnetic field and sample face, that is $I_c(B,\theta)$. Usually, the axis of field rotation lies along the sample axis, so the magnetic field is always perpendicular to the current direction. In this case, the easiest method of carrying out such measurements is to use a split-pair magnet, as illustrated in Fig. 9.6(c) (an overview of the cryostat and dewar is given in Fig. 1.17). This has the advantage that the entire measurement probe is rotated to obtain variable field angles, and consequently no flexible high-current *cryogenic* leads are needed (probe rotation is easily

accommodated by flexible copper cables at room temperature, where the cables can be large and the magnetic field is low). The down-leads into the cryogenic part of the probe are just the standard (rigid) high-current leads: vapor-cooled leads, solid copper/superconductor bus bars, or bulk high-T_c leads (Sec. 4.9).

However, for angle measurements at high magnetic fields ($\gtrsim$12 T), a solenoidal magnet is usually used rather than a split-pair magnet. (It is difficult to reach very high fields in split-pair superconducting magnets because the large magnetic force that draws the two magnet halves together places tremendous stress on the magnet's midplane windings; the high-field windings must be supported by thin structural plates without bending or microscopic movement—a difficult task.) Consequently, for high-field measurements, the design problems of the magnet are usually transferred to the measurement apparatus. It must (1) be very compact to fit into the bore of a high-field solenoidal magnet, (2) incorporate a rotation mechanism, and (3) have flexible high-current leads to accommodate sample rotation. The last item is usually the point on which the design succeeds or fails (Sec. 4.10).

Sometimes a full angular characterization is needed, that is, $I_c(B,\theta,\varphi)$. Figure 9.12 shows a unique compact rig with *double* rotational axes for measuring a sample's response to variations in both polar- and azimuthal-field angles (Herzog et al. 1994). This scheme is also useful for optical experiments and other measurements requiring full solid-angle control.

In this design, the cryostat measurement head is equipped with two worm gears connected to two room-temperature stepper motors, one for each axis of rotation. To measure the dependence of I_c on field angle in the conventional way (i.e. with the field always perpendicular to the direction of current flow), the φ worm gear in Fig. 9.12 is set so that the plane of the support frame is perpendicular to the magnetic field (the position illustrated in Fig. 9.12) and then the θ gear is rotated. On the other hand, to measure I_c as a function of the angle that the magnetic field makes with the current direction, the φ gear is rotated and *simultaneously* the θ gear is counter-rotating to keep the sample face parallel to the plane of the frame.

The apparatus is limited to low-current specimens because the full-angular sweep requires flexible cryogenic current leads, which, in high fields, are usually made from a copper braid or YBCO-coated conductors (Sec. 4.10). The braid is subjected to a Lorentz force, which must also be supported. However, for low-current or thin-film samples, the apparatus works well, providing great versatility in angular characterization.

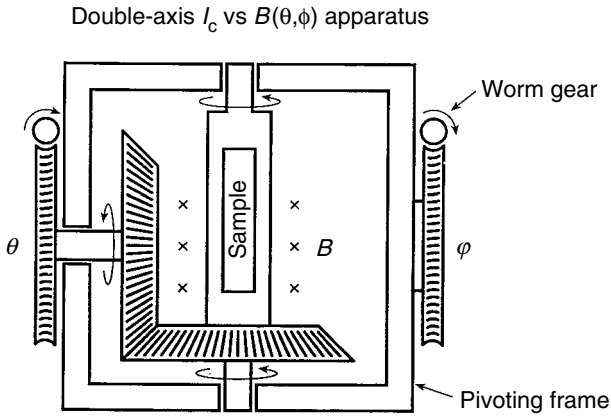

Fig. 9.12 Double-axis apparatus for full solid-angle measurements of low-current specimens in a solenoidal magnet (adapted from Herzog et al. 1994).

In carrying out such field-angle measurements, check for angle hysteresis at the start of data acquisition (to avoid later surprises!). If a sample shows hysteresis in the sweep of field *magnitude* (item 6 in Table 9.1), there will also be hysteresis in the sweep of field *angle*. Generally, the correct value of critical current is the lower branch of the field-angle hysteresis loop (since this will limit the superconductor in service).

9.4.3 CRITICAL CURRENT vs. TEMPERATURE

Variable-temperature measurements of the critical current are needed to measure the full $I_c(B,T)$ characteristic of a superconductor. That is, I_c vs. T curves of the type A–C in Fig. 9.3 can be combined with the more common I_c vs. B curves to map the entire critical surface. These data are needed to determine temperature margins for studies of superconductor stability. They are also required for designing magnets that operate at temperatures other than the canonical 4.2 K or 77 K, such as magnets conductively cooled by closed-cycle cryocoolers or by forced cryogen flow.

The simplest method to obtain variable-temperature measurements is to pump on the cryogen with a high-capacity (10–20 L/s) mechanical vacuum pump, as described in Sec. 1.2.1. This is convenient and works well, but over only the limited temperature ranges shown in Fig. 1.2. Also, a different liquid cryogen is required for each range.

To move beyond these narrow temperature bands requires giving up the high cooling power of direct immersion in a cryogenic liquid. Several alternative techniques are commonly used: allowing the sample-holder assembly to slowly drift in temperature in the ullage of a storage dewar, conductively connecting the sample to a variable-temperature refrigerator stage, or cooling the sample in flowing gas. These techniques were described in Sec. 1.4 for low-current cryostats and in Sec. 1.5 for high-current cryostats. Here we summarize the key points and bring together additional details.

Low-current variable-temperature cryostats

Dipper probes: For low-current measurements ($\lesssim$1 A), the variable-temperature techniques depicted in Fig. 2.12 are inexpensive and efficient. In Fig. 2.12(a), a dipper probe is used to raise and lower the sample in the stratified-temperature layer of cold gas above the liquid cryogen; temperature is varied by changing the distance between the sample holder and the surface of the liquid. Automatic data acquisition can occur while the temperature slowly drifts (see Fig. 9.10), or the temperature can be controlled by a resistive heater and feedback thermometer attached to the sample holder. However, the need to change the sample height in the dewar in order to vary the temperature precludes measurements in a high-field magnet, since the sample must remain in a fixed position at the center of the magnet.

In this case, the exchange-gas technique illustrated in Fig. 2.12(b) permits variable-temperature operation of the same dipper probe in a fixed position. The cooling rate of the sample is varied by controlling the pressure of the exchange gas that thermally couples the sample to the liquid-cryogen bath, as calculated in Case 2 of Sec. 2.9.

The key requirement in either case is to thermally anchor the sample to a highly conductive sample holder that has enough thermal mass to minimize temperature fluctuations. (Anchoring techniques are described in detail in Sec. 7.3.1 for bulk samples and in Sec. 7.4.1 for thin films.)

Liquid-flow cryostats: For current measurements below about 20 A, a variable-temperature liquid-flow cryostat (Fig. 1.10) is simple to operate and available commercially. Constant temperature is maintained with an automated temperature controller in conjunction with a feedback thermometer thermally anchored to the cold plate or, if possible, attached directly to the sample. (Use the heater-sample-thermometer arrangement shown in Fig. 5.13.)

The key requirement for temperature control is good thermal conduction between the sample and cold plate. To ensure stability and uniformity of the sample temperature, the cold plate should be made of a material having high thermal conductivity, such as ETP copper (Appendix A3.1). The thermal joint between the sample and cold plate should be soldered or greased to provide high heat conduction between the two (see Sec. 2.6). Temperature fluctuations are minimized by using a cold plate with sufficient mass to provide relatively high heat capacity. However, the heat capacity should not be so great that the time required to move between temperature settings becomes unreasonably long, especially if working in the upper cryogenic-temperature range, since the heat capacity grows as T^3. In practice, an optimal mass is usually determined by trial and error.

Cryocoolers: When cryogen conservation and simplicity of operation are important, a commercial cryocooler can be used (Sec. 1.4.4). They conductively cool the sample in a manner similar to that of liquid-flow cryostats, except the sample stage is cooled by a closed-cycle refrigerator rather than by continuously transferring a liquid cryogen from a storage dewar. Commercial cryocoolers at present provide up to about 1 W of cooling power at 4 K (although higher-power commercial units are being developed). However, vibration from the moving displacer in a Gifford–McMahon (G–M) cryocooler can introduce considerable noise for critical-current measurements in a magnetic field. For measurements where vibration is a problem, a pulse-tube cryocooler can be used instead (Sec. 1.4.5); vibration is two orders of magnitude less than when using typical G–M cryocoolers.

The important experimental requirement is the same as with liquid-flow cryostats: good thermal conduction between the sample and the cold sample stage. The sample must be thermally anchored to the cold head by means of joints having a high thermal conductivity (Sec. 2.6). Data on the thermal conductance of grease, adhesive, solder, and pressure joints are given as a function of temperature in Fig. 2.7. From the expected sample heating and joint thermal conductance, we can calculate the required joint area that is needed to limit the temperature drop across the joint to an acceptable level. If the sample is thermally anchored to the sample holder with only low contact pressure, as is often the case, vacuum grease can increase thermal conductance to the cold head by an order of magnitude (Sec. 2.6.4).

Gas-flow cryostats: In this case, sample cooling is provided by cold helium or nitrogen gas flowing over the sample. Cooling power can extend over a wide range, determined mainly by the gas volume flow rate. Therefore, this type of cryostat can function at both low and high measurement currents. Its operation is described in more detail in the following high-current section.

High-current variable-temperature cryostats

At high transport-current levels, the cooling requirement imposed by Joule heating in the contacts and sample becomes formidable. The key requirement for variable-temperature measurements

under such conditions is to use a very high rate of helium gas flow (~0.3 L/s) to adequately cool the sample, current contacts, and (preferably massive) sample holder.

Figure 9.13 shows an apparatus that has worked at over 400 A in the temperature range 4–120 K (Goodrich and Stauffer 2001). The dewar is lightly pressurized so that liquid helium flows into a heater chamber at the rate of 1–3 L/h, where it is vaporized and heated to approximately the desired sample temperature by a resistive heater. [Alternatively, the cryostat's vapor-cooled current leads could be attached to a vacuum pump at the outlet of the vapor-cooled leads, as illustrated in Fig. 9.13, so that liquid helium is drawn into the heater chamber; in either case, a manostat should be used to control the pressure. Only a slight pressure (or vacuum)

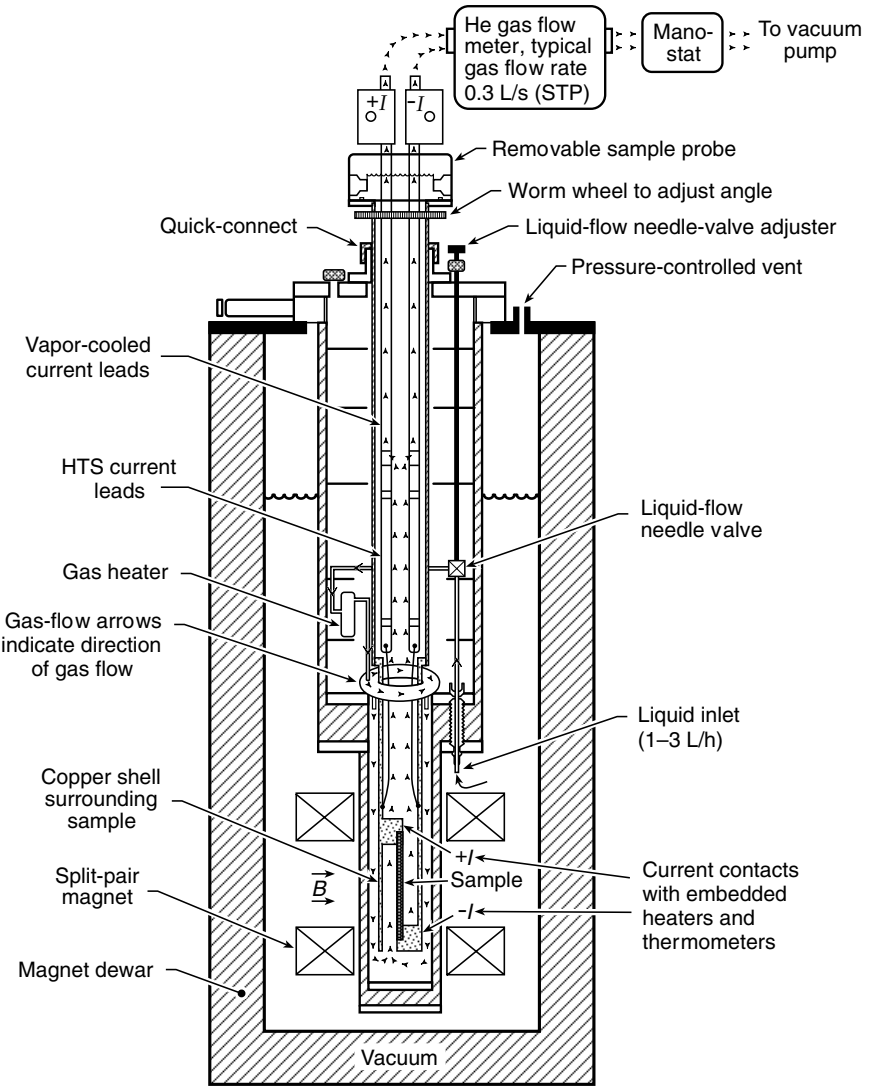

Fig. 9.13 High-current helium-gas-flow cryostat for measuring critical current at variable temperature and magnetic-field angle (from Goodrich and Stauffer 2001).

is needed: ~20 torr (2.7 kPa) for steady-temperature operation or about 50–100 torr (6.7–13.3 kPa) when changing sample temperature.]

As illustrated in Fig. 9.13, the preheated gas is then distributed by a ring duct so that it flows symmetrically over the outside of a copper shell surrounding the sample, which serves to further condition the gas temperature. The copper shell also serves as a radiation shield, thermal mass, and current contacts. (To perform the last function, the shell is symmetrically split along its length into + and − current leads.) Final temperature control of the sample is obtained by two resistive heaters attached to the two halves of the copper shell. After the gas passes over the outside of the copper shell, it is channeled to the inside of the shell at the bottom of the cryostat, where it then flows up along the sample. Higher in the cryostat, the cool gas then passes over high-T_c current leads and finally through vapor-cooled current leads before exiting the cryostat. The sample is anchored by solder joints only at each end (not along its entire length).

Temperature is controlled by feedback signals from two resistance thermometers attached to the copper current shells that surround the sample. The gas inlet heater supplies most of the power for warming the cryogen to near the desired temperature—up to ~2 W to achieve temperatures over 50 K. This enables the power to the resistive copper-shell heaters to be kept low, below 0.1–0.3 W, so that the sample temperature and uniformity can be controlled to within about 50 mK.

Temperature uniformity and control can be further enhanced by using a current-pulse method for critical-current measurements to minimize Joule heating at the contacts. In such a case, current is delivered in a series of ~1 s long pulses, as illustrated in Fig. 9.11(c). The current-ramp rate up and down is kept in the range 0.7–4 kA/s, since at faster ramp rates ($\gtrsim$10 kA/s) sample vibration from quick application of the Lorentz force creates significant voltage noise as well as eddy-current heating.

Again, the main cryostat elements are the high-volume flow of temperature-controlled helium gas, the gas preheater chamber, and the counter-flow design that equilibrates large quantities of helium gas to the sample temperature before the gas directly cools the sample. With such a design, the cryostat can handle surprisingly high currents (hundreds of amperes) without spurious Joule heating over the entire cryogenic-temperature range.

9.4.4 CRITICAL CURRENT vs. AXIAL STRAIN

Strain has a large *reversible* effect on the critical current of most practical *low-T_c* superconductors. The effect is illustrated by curve D–E in Fig. 9.4 for Nb_3Sn, which shows that either tensile (+) or compressive (−) strain as small as several tenths of one percent will *reversibly* decrease I_c by 50% or more at high magnetic fields. The relative I_c degradation from strain increases greatly as the magnetic field approaches the critical magnetic field of the superconductor, as evidenced by the increasing curvature of the I_c-vs.-strain curves at higher fields in Fig. 9.4.

Notice that the I_c-vs.-strain curves have a maximum where the intrinsic strain in the superconductor material is zero. However, superconducting composite wires, as fabricated, do not automatically come with I_c at this peak value. Instead, the various materials in the composite contract with temperature at different rates, which typically places the superconducting component of the composite in an initial compressive (−) strain state. The amount of built-in

strain is called the wire's initial *prestrain*. It depends on the design of the composite wire and thus varies considerably from conductor to conductor.

The objective of good engineering is to design an application so that, on average, all the fabrication and thermal contraction forces take the conductor from its initial prestrain state to an intrinsic strain of about −0.1% to −0.2%, just on the compressive side of the ridgeline A–B in Fig. 9.4. That way, the critical current is almost optimum, and there is still a strain margin of safety before magnetic tensile forces pull the critical current too far down the precipitous tensile side of the ridge in Fig. 9.4. Thus, for engineering purposes, the prestrain as well as the shape of the I_c-vs.-strain characteristic need to be measured for most superconducting wires. The first type of strain-measurement cryostat (described next) enables both to be measured.

Stress-free cooling cryostats

With this type of cryostat, the sample is cooled in a *stress-free* manner. That is, the sample is not soldered, bonded, or constrained by the sample holder during cool-down (which otherwise would alter the intrinsic prestrain state of the sample).

In the cryostat shown in Fig. 9.14, the ends of the sample are soldered to two grips, one of which is movable; the other, fixed. This arrangement allows the sample to thermally contract

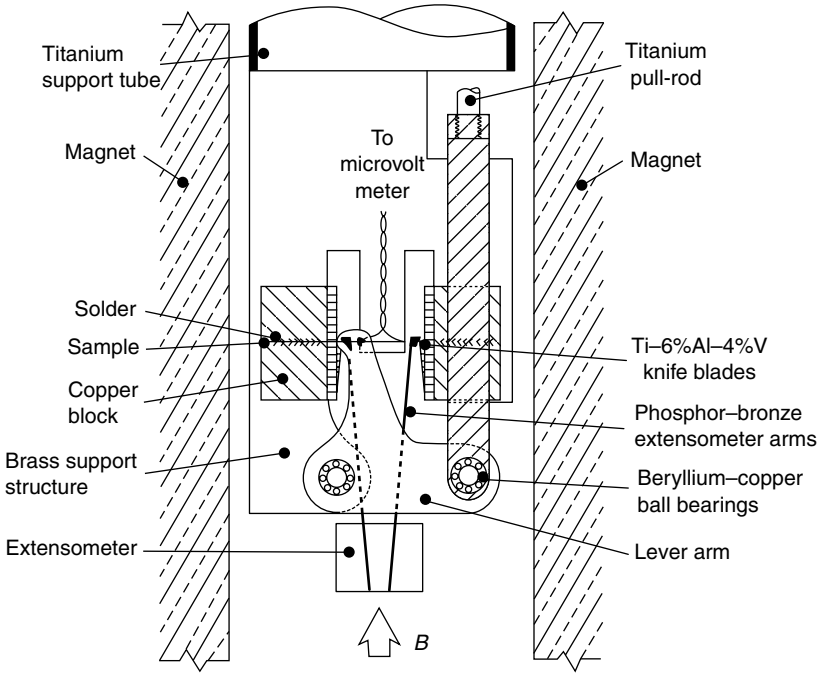

Fig. 9.14 Apparatus for measuring critical current as a function of axial strain and magnetic field (from Ekin 1980a). The sample is soldered to two copper current blocks, one of them movable so that the sample is cooled in a stress-free manner (thus enabling the intrinsic prestrain of the superconductor to be determined). Load is applied to the sample by a lever mechanism that pushes on the (left) movable current block. Sample strain is measured with an extensometer riding on knife blades attached to the two current blocks.

at its own rate during cool-down without being constrained. Each "solder grip" is made of pure copper (labeled "Copper block" in Fig. 9.14) and serves the dual function of supplying current as well as tensile stress to the sample. A platform under the sample provides support for the Lorentz force the sample will experience during testing.

With this straight-sample geometry, the sample usually needs to be kept short (a few centimeters in length) so it fits transverse to the magnetic field in the bore of high-field solenoidal magnets. For such short sample lengths, strain in the test specimen cannot be measured remotely (outside the cryostat), because the compliance in the meter-long pull rod running up the support structure will overwhelm any attempt to measure the small elongation in a sample only a few centimeters long. The only accurate method in this case is to measure strain *at the sample*. This can be accomplished by gluing a strain gauge to the sample, but such a technique usually does not work for thin tape or small wire superconductors, because the sample is locally strengthened over the region where the strain gauge is affixed. Thus, the crux of such a test apparatus hinges on a method for accurately measuring strain at the sample.

For the cryostat shown in Fig. 9.14, strain is measured by a light-spring-constant, nonmagnetic extensometer (whose arms are viewed edge-on in the figure). The ends of the extensometer arms ride on two knife blades attached to the sample grips. The arms are made of nonmagnetic flexible Be–Cu strips to which four strain gauges are attached and wired in a Wheatstone-bridge configuration. With such an extensometer, sample displacements less than 5 μm can be measured, even in the presence of significant cryostat vibration. Since the strain measurement is typically made at high fields, the extensometer, as well as all *movable* parts, must be made of materials having very low magnetic susceptibility (Appendix A6.8) in order to minimize spurious magnetic forces. The magnetic force, which is trying to pull cryostat parts into the magnet, can become substantial. As described in Sec. 6.5.2, for example, the centering force on a relatively small "nonmagnetic" AISI 316 stainless-steel pull rod that is 5 mm in diameter amounts to 18 N (4 lbf) in a 12 T magnet; this quickly scales up to a force of 50 N in a 20 T magnet. So instead of stainless steel, materials with very low susceptibility must be used, such as titanium, phosphor bronze, and aluminum alloys. (Suppliers of less common tube and rod sizes are listed in Appendix A1.7 under Materials.)

Another example of a cryostat that provides stress-free cooling for I_c-strain measurements is based on the use of a split-pair magnet, such as that shown in Fig. 9.6(c). This configuration can accommodate large-diameter conductors and is usually the only method of testing big superconducting cables. The sample is passed through a radial access port in the magnet and attached to a load train that leads to the top of the cryostat. Stress is applied from outside the cryostat with a mechanical actuator, either a conventional screw-mechanical-test system (which controls displacement) or a servohydraulic system (which utilizes high-pressure oil applied to a piston actuator to control either displacement, force, or sample strain).

Since this type of cryostat can accommodate long samples, the displacement that corresponds to a given sample strain is much larger and easier to measure than that in short-sample cryostats. However, the active region for critical-current measurement is still restricted to just the bore diameter of the magnet. Also, for multifilamentary strands, the current-transfer region must be at full field (Sec. 7.3.4).

Bending-beam cryostats

The second general category of cryostats for I_c-vs.-strain measurements are those utilizing a bending beam or spring. The sample is soldered or otherwise attached to the outer edge of a beam, and then the beam is flexed or bent to apply strain to the sample. Both compressive as well as tensile strain can be applied with this technique, but, unlike the stress-free cooling cryostats just described, the intrinsic prestrain cannot be directly measured.

Two configurations are in common use: a long sample soldered to a flexible coil spring, such as that shown in Fig. 9.15, or a short, straight sample soldered to a U-bending-beam, as shown in Fig. 9.16. In the coil method, strain is applied to the sample by twisting or untwisting the spring, whereas with the U-bending beam the backbone of the U is flexed by applying force to the ends of the two long arms.

For samples that can be fabricated in the shape of a coil (e.g. Nb_3Sn), the coil-spring method has an advantage over the U-beam in that it provides a long sample length that enables more sensitive measurements of the electric field along the superconductor to be made, and it

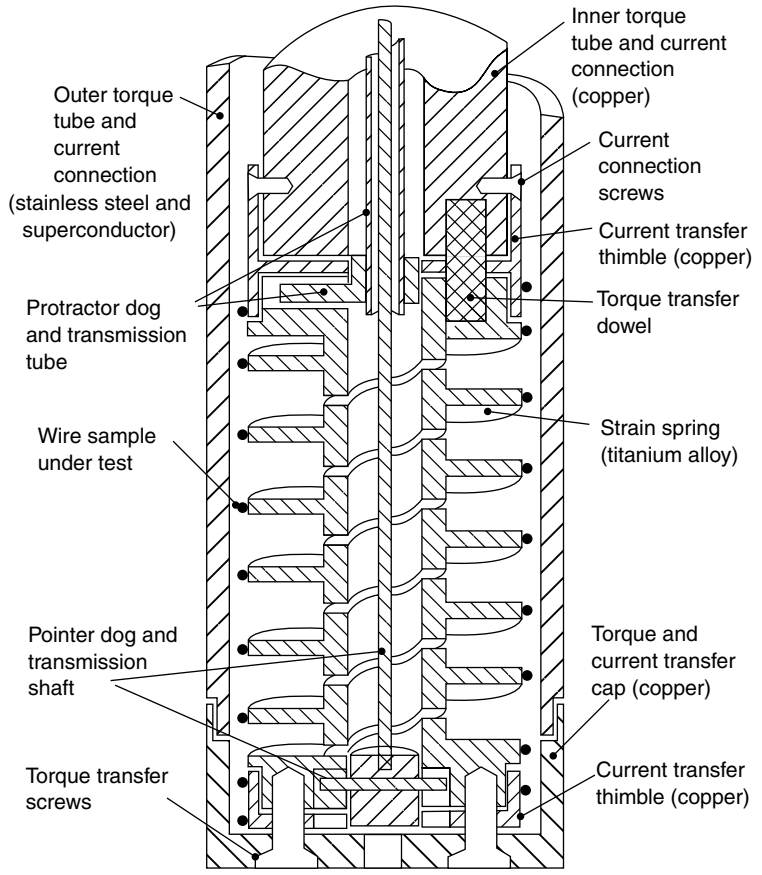

Fig. 9.15 Coil sample holder for measuring the effect of strain on the critical current of long superconductor samples (from Walters et al. 1986). The sample is soldered to a spring, which is twisted and untwisted through small angles to apply axial strain to the superconductor. Sample strain is measured by the angle of rotation of the coil.

reduces current-transfer effects. For samples fabricated nearly straight (e.g. YBCO), the U-beam has an advantage over the coil-spring in that samples can be tested in a nearly straight condition without bending the sample. In either case, the sample is firmly soldered to a bending beam, so these cryostats are easier to use than stress-free-cooling cryostats because sample motion is eliminated, and the beam automatically provides support for the Lorentz force.

However, the disadvantage of bending-beam cryostats remains that the thermal contraction of the beam dominates that of the sample after the two materials are joined, so sample *prestrain* cannot be directly measured. A rough estimate can be made if the difference in thermal contraction between the sample and bending-beam materials are known from independent thermal-contraction measurements made on the sample and holder separately. Much better, a bending-beam material can be chosen that has a thermal contraction that closely matches that of the sample. For example, a good coil-spring material for testing Nb_3Sn/copper–bronze superconductors is Cu–2%Be (UNS C17200), as discussed in Sec. 7.3.2, since both materials have about the same thermal contraction when cooled to cryogenic temperatures from soft-soldering temperatures (compare the data in Appendix A7.5 with those in Appendix A7.4).

➔ Cu–2%Be that is cold-worked and precipitation-hardened at 315°C for 2 h (temper TH04) has a very high elastic strain limit, about 1.0% at 4.2 K (0.9% at room temperature). Thus, it is a good material for avoiding yielding of the beam and the possible introduction of nonuniform strain into the test sample, unlike beam materials, such as brass, which have a much lower elastic strain limit. Also, Cu–2%Be is easily soldered. For all these reasons (matched thermal contraction, high elastic strain limit, and solderability), Cu–2%Be is an excellent choice for the bending-beam material when testing Nb_3Sn strands. (See the safety tip on machining beryllium copper at the end of Sec. 1.6.1.)

Recently, procedures have been developed for indirectly determining the prestrain with bending-beam probes (Uglietti et al. 2003). The most obvious technique of soldering the sample

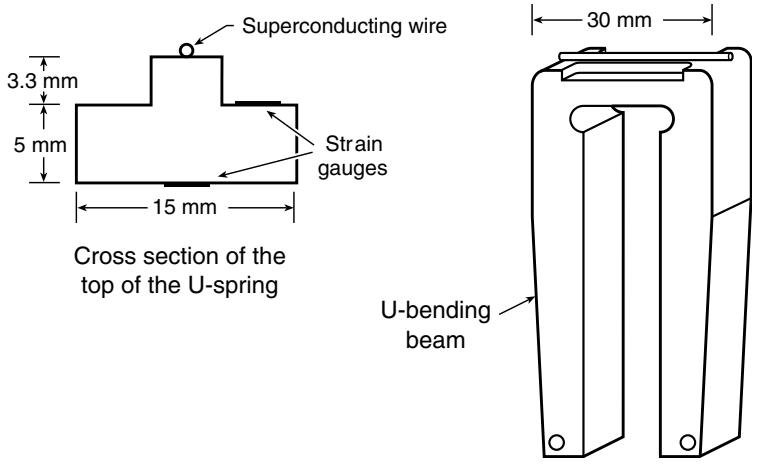

Fig. 9.16 U-bending beam for measuring strain effects on short samples (from ten Haken et al. 1995). The sample is soldered to the bending beam, and the backbone of the U is flexed by applying force to the two arms. Strain is measured by strain gauges bonded to the flexed section at the top of the U-spring.

only at its ends and leaving it slack during cool-down (to achieve stress-free cooling) does not work because nonuniform strain develops if the sample is longer than a few centimeters. That is, some sections of the sample are strained more than others because the backlash or slack in the sample is not uniform over the whole sample length. So instead, the prestrain is determined by a two-step process. First, the sample is soldered only at its ends to the copper current leads and sufficient slack is left over the middle of the sample so that it is not strained during cool-down. A stress-free value of I_c can then be measured. The sample is then warmed and uniformly soldered to the coil spring along its entire length. [Gold plating can be used to facilitate soldering to Ti-alloy beam materials (Uglietti et al. 2003).] The assembly is then recooled, and strain is adjusted until I_c matches the stress-free value of I_c, indicating that the stress-free strain has been reached. Of course, this procedure works only if I_c is strongly (and reversibly) dependent on strain, as is the case for Nb_3Sn at high fields, but it will not for conductors where I_c is initially nearly independent of strain, as with Bi-based conductors, YBCO, or Nb_3Sn conductors with small prestrain (near the peak in the I_c vs. ε curve). For the latter cases, a *strain*-free cooling procedure must be used where the sample is soldered to the spring along its entire length and then sample strain is carefully and continually adjusted during cool-down to match that of a strain gauge attached to an unstrained reference sample of the conductor located in the same thermal environment (Uglietti et al. 2003).

Variable-temperature strain measurements

To measure I_c as a function of temperature, strain, and magnetic field, the temperature of the sample and strain mechanism must be varied inside the bore of a background magnet. This is usually accomplished either by conductively cooling the sample through the sample holder or by convectively cooling the sample with a high-volume flow rate of cold gas. Such cryostats enable a direct determination of the four-dimensional J–B–T–ε critical surface—quite an extensive test matrix.

Figure 9.17 shows an example of a conduction-type cryostat (Cheggour and Hampshire 2000). The sample is soldered to a Cu–2%Be coil spring, which anchors it both thermally and mechanically. The spring-and-sample assembly is thermally isolated from the surrounding helium bath by vacuum, but it is thermally linked to the bath via the current leads. Temperature is varied between 6 and 20 K with a Constantan heater wrapped around a copper sleeve that is slipped over the coil spring. The heater and sleeve are also wrapped with about 10 layers of aluminized Mylar to provide radiative insulation.

Current is generally limited to about 25 A when this cryostat is operated in vacuum because, otherwise, excessive heat is generated in the leads and contacts, which produces thermal gradients along the sample. Higher current levels up to about 85 A have been reached with thicker current leads thermally connecting the spring-and-sample assembly to the surrounding helium bath.

Ring-coil hoop-stress measurements

Superconducting magnets are usually a *composite* structure (i.e. the combination of superconductor, insulation, fiberglass, and epoxy), and so for engineering design purposes, electromechanical information is sometimes needed on the ensemble of components. For such

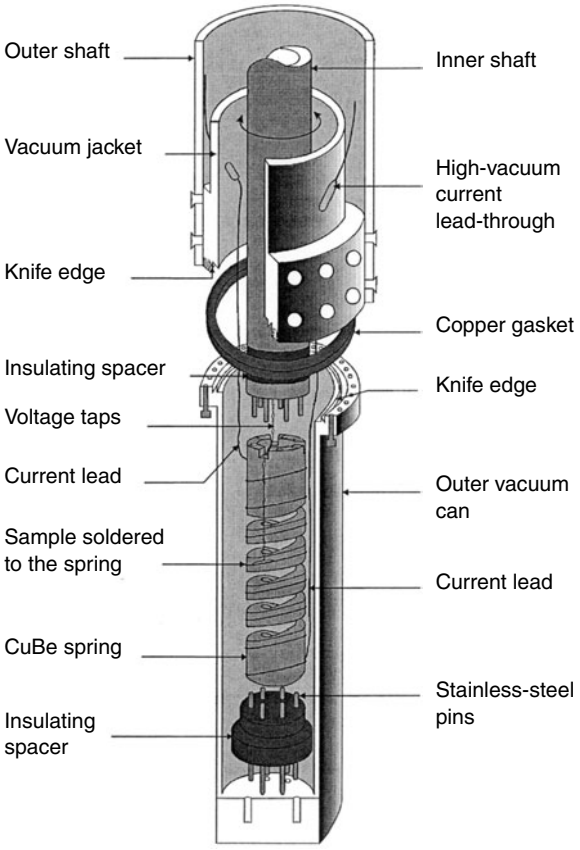

Fig. 9.17 Coil sample holder designed for measuring the effect of strain on critical current at both variable temperature and magnetic field (from Cheggour and Hampshire 2000).

measurements, fixtures are required that can test ring-shaped composite coils that are wound and potted with fiberglass and epoxy to mimic the internal structure of the magnet.

Ideally, we would like to utilize the Lorentz force that develops when such a test coil is placed in the bore of a large background magnet and energized with current (a good example of such a test apparatus is given by Schwartz et al. 1997). This type of coil-test fixture has the advantage that the method of force application matches that of an actual magnet. However, in practice, the hoop stress σ_{hoop} is limited by the test coil's critical-current density J_c [since $\sigma_{\text{hoop}} = J_c Br$, where B is the background magnetic field and r is the test-ring radius (Sec. 10.5.1)]. Thus, the hoop stress is not an independent test parameter that can be varied over a range of values; rather it is restricted to this one value at the test-ring's critical-current density [although, in principle, σ_{hoop} could be varied by a series of time-consuming measurements of test coils with different radii].

Another idea is the cone apparatus shown in Fig. 9.18. This loading apparatus is designed to apply any level of hoop stress to a test coil by pressing vertically on two large slit cones that function like Belleville washers, pushing radially outward on the sample coil. Figure 9.18(a)

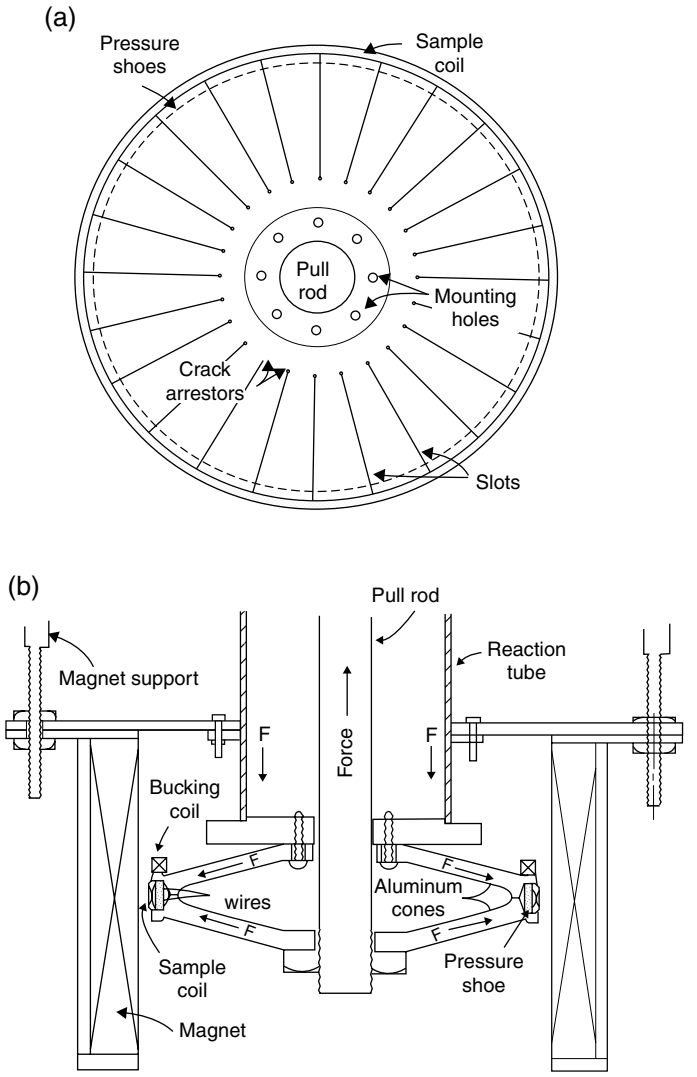

Fig. 9.18 Loading apparatus for applying hoop stress to a superconducting composite coil: (a) top view of cone assembly; (b) cross-sectional view (from Ekin et al. 1980). (See the cover photo of this textbook.)

shows a top view of the cone-coil assembly and Fig. 9.18(b) a cross-sectional side view. The cones are made of a material with a high elastic strain limit [such as aluminum alloy 2219-T6, or Cu–2%Be (UNS C17200-TH04); mechanical properties are given in Appendix A6.10]. The most reliable (and easiest) method of measuring hoop strain in the test coil is with two strain gauges epoxied to the circumference of the test ring, spaced 90° apart to compensate for any bending strain that might be introduced by eccentricity in the test ring. The stress is not as uniformly distributed as with the Lorentz-force method noted above, but pressure shoes (shown in Fig. 9.18) can be added at the ends of the cone fingers to improve uniformity. The significant advantage of this cryostat is that much higher hoop stress can be applied to the composite test coil and controlled as an *independent* variable.

9.4.5 CRITICAL CURRENT vs. BENDING STRAIN

The final type of mechanical-test fixture we consider is that for measuring I_c degradation from bending strain. This is a very practical measurement needed for most superconductors to determine the minimum radius of spools used during superconductor fabrication and to set bending-strain limits when winding superconductors into coils and cables for applications.

The most common test method is to cut a series of samples from the same billet and bend them onto a set of curved sample holders, each holder machined with a different radius. The set of critical-current values then gives an I_c vs. bending-strain plot. To get data on the same conductor (thereby eliminating sample-to-sample variations inherent in a series of different samples), a single sample must be mounted on the sample holder with the least amount of curvature, cooled, measured, warmed, and then progressively remounted on the holder with the next greatest curvature to acquire the entire set of data. This technique is simple in concept but time-consuming in practice, and it is liable to create sample damage from so much mounting and remounting of the same sample.

Another method for varying the radius on a single sample *in situ*, without having to mount and remount it, is to use the bending fixture shown in Fig. 9.19. This offers a significant savings in measurement time and sample handling compared with a series of fixed-curvature holders. The sample is clamped (or soldered) into two grips, which are moved in such a way that the sample is uniformly bent into the shape of a progressively tighter circular arc.

Figure 9.19 illustrates three bending positions of the test sample. The sample ends are always oriented tangent to the circular arc. The motion of the two grips is coupled with a transmission to provide a synchronous opposite-turning motion as indicated in Fig. 9.19. The smallest possible bending radius r_{min} determines the distance separating the sample grips and, therefore, the sample length is $L_s = \pi\, r_{min}$. The distance between the turning axes of the sample grips is $L_a = 2\, r_{min}$, and the axes are located in-line with the sample when it is straight, a distance $(L_s - L_a)/2$ away from the inside edge of the clamps.

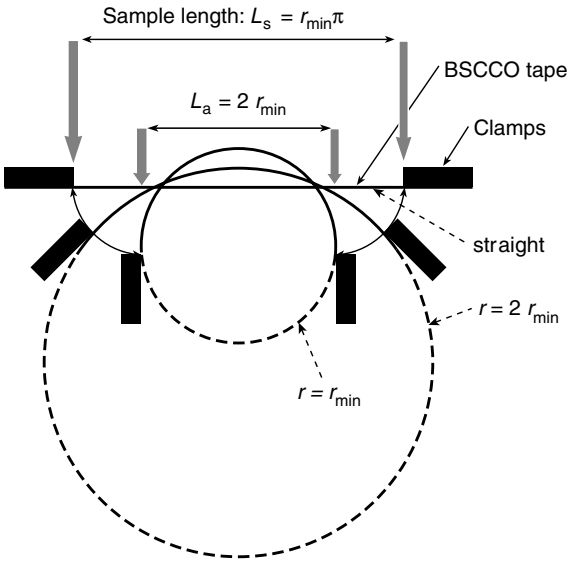

Fig. 9.19 Illustration of fixture for continuous bend testing (from Goldacker et al. 2002). Three bending positions of the sample are illustrated. Labels are defined as follows: r is the bending radius, r_{min} is the minimum bending radius, L_s is the sample length, and L_a is the distance and location (shown by vertical arrows) of the grip turning axes.

To prevent sample damage, the sample should be held with clamps with edges that are tapered and not sharp where they contact the sample. After mounting the sample in the straight position, avoid straining the sample during cooling by setting a slight bend in the sample during cool-down so it is not held taut between the two clamps. This will automatically accommodate any strain from differential thermal contraction between the holder and sample. (For the same reason, the sample should not be fully straightened until warmed again.) Alternatively, the sample clamps can be tightened with the sample under liquid nitrogen after cooling to 77 K, but this is not as convenient as using the slight-bending trick.

If the sample is delicate or easily damaged, soldering is a preferred mounting technique compared with clamping, or even with clamping using soft indium foil around the sample. However, be sure to set the rig to a slightly bent position immediately after the solder solidifies to employ the same technique described above so that thermal contraction of the sample during cooling to room temperature does not axially strain the sample.

The only limitation of the apparatus is that the method is ill-suited for measurements in a magnetic field since the sample is free-standing and unsupported against Lorentz forces. However, the important parameter is the irreversible bending-strain limit where permanent damage occurs, and this limit is independent of magnetic field. So for most practical purposes, operation at zero field gives the important data and is not a limitation.

Again, the significant advantage of this technique is that all the bending data are obtained with only one sample mounting, which saves time and minimizes the chances of sample damage. All data are also obtained on a single sample, so sample-to-sample scatter is eliminated. Furthermore, bending strain can be introduced either at room temperature (i.e. warming between each cryogenic data point) or in a continuous series of low-temperature measurements (again, giving a considerable savings in thermal-cycling time). Finally, this design permits measurements of bending fatigue, since the sample can be repeatedly bent and straightened in a controlled manner. All in all, it represents a unique design that offers a number of advantages over the usual series of fixed-curvature sample holders.

9.5 References

9.5.1 FURTHER READING

STANDARD TEST SPECIFICATIONS:

Detailed standard test procedures have been developed by the International Electrotechnical Commission (IEC) for measurements of the critical-current of Nb–Ti (IEC 61788-1), Nb_3Sn (IEC 61788-2), and Ag-sheathed Bi-2212 and Bi-2223 (IEC 61788-3). The test standards are available for purchase on the Internet at http://www.iec.ch/ or http://web.ansi.org. Other superconductor specifications are also available at this site for measuring the following:

Residual-resistance ratio of the matrix of Nb–Ti composite superconductors (IEC 61788-4) and Nb_3Sn composite superconductors (IEC 61788-11).

Matrix-to-superconductor volume ratio of Cu/Nb–Ti composite superconductors (IEC 61788-5) and Nb_3Sn composite superconductors (IEC 61788-12).

Room-temperature mechanical tensile test of Cu/Nb–Ti composite superconductors (IEC 61788-6).

Ac-loss measurements by magnetometer (IEC 61788-13) and by alternating transverse magnetic field (IEC 61788-8).

Critical-temperature measurements (IEC 61788-10).

Microwave surface resistance (IEC 61788-7).

Definitions of superconductor terms (IEC 60050-815).

EDITED SERIES OF ARTICLES ON CHARACTERIZATION TECHNIQUES FOR HIGH-T_C AND LOW-T_C SUPERCONDUCTORS:

Cardwell, D. A., and Ginley, D. S., eds. (2003). *Handbook of Superconductors, Vol. II, Characterization, Applications and Cryogenics*, Part D, Institute of Physics Press, Bristol, UK.

Seeber, B. (1998). *Handbook of Applied Superconductivity*, Part B, Institute of Physics Publishing, Bristol, UK.

INTRODUCTORY SUMMARIES AND ARTICLES ON MEASUREMENTS IN SUPERCONDUCTORS:

General introductions:

Campbell, A. M. (1992). "Measurements in superconducting materials," in *Concise Encyclopedia of Magnetic and Superconducting Materials*, ed. J. Evetts, pp. 305–314, Pergamon Press, Oxford; Elmsford, NY.

Critical-current measurements:

Goodrich, L. F. and Fickett, F. R. (1982). "Critical-current measurements: a compendium of experimental results," *Cryogenics* 22, 225–241.

Mechanical-property measurements:

Ekin, J. W. (1980). "Mechanical properties and strain effects in superconductors," Chapter 7 in *Superconductor Materials Science: Metallurgy, Fabrication, and Applications*, eds. S. Foner and B. B. Schwartz, pp. 455–510, NATO Advanced Study Institutes Series, Plenum Press, NY.

9.5.2 CHAPTER REFERENCES

Bray, S. L., and Goodrich, L. F. (1990). "Current supply for high-T_c superconductor testing," *Meas. Sci. Technol.* 1, 491–494.

Bray, S. L., Goodrich, L. F., and Dubé, W. P. (1989). "Battery-powered current supply for superconductor measurements," *Rev. Sci. Instrum.* 60, 261–264.

Cheggour, N., and Hampshire, D. P. (2000). "A probe for investigating the effects of temperature, strain, and magnetic field on transport critical currents in superconducting wires and tapes," *Rev. Sci. Instrum.* 71, 4521–4530.

Claassen, J. H., Reeves, M. E., and Soulen, R. J. (1991). "A contactless method for measurement of the critical current density and critical temperature of superconducting films," *Rev. Sci. Instrum.* 62, 996–1004.

Colclough, M. S., Abell, J. S., Gough, C. E., Rickets, J., Shields, T., Wellhofer, F., Vinen, W. F., Alford, N. McN., and Button, T. (1990). "Pulsed critical current measurements on YBCO wires and screen-printed films," *Cryogenics* 30, 439–444.

Dubé, W. P., and Goodrich, L. F. (1986). "Quench detector circuit for superconductor testing," *Rev. Sci. Instrum.* 57, 680–682.

Ekin, J. W. (1980). "Strain scaling law for flux pinning in practical superconductors. Part 1: Basic relationship and application to Nb_3Sn superconductors." *Cryogenics* 20, 611–624.

Ekin, J. W. (1983a). "Superconductors," Chapter 13 in *Materials at Low Temperatures*, eds. R. P. Reed and A. F. Clark, pp. 465–513, ASM International, Materials Park, OH.

Ekin, J. W. (1983b). "Four dimensional J–B–T–ε critical surface for superconductors," *J. Appl. Phys.* 54, 303–306.

Ekin, J. W., Schramm, R. E., and Superczynski, M. J. (1980). "Training of epoxy-impregnated superconductor windings," *Adv. Cryog. Eng. (Mater.)* 26, 677–683.

Goldacker, W., Schlachter, S. I., Nast, R., Reiner, H., Zimmer, S., Kiesel, H., and Nyilas, A. (2002). "Bending strain investigations on BSCCO(2223) tapes at 77 K applying a new bending technique," *Adv. Cryog. Eng. (Mater.)* 48, 469–476.

Goodrich, L. F., and Bray, S. L. (1988). Current ripple effect on superconductive dc critical current measurements," *Cryogenics* 28, 737–743.

Goodrich, L. F., Srivastava, A. N., and Stauffer, T. C. (1991). "Simulators of superconductor critical current: design, characteristics, and applications," *J. Res. Natl. Inst. Stand. Technol.* 96, 703–724.

Goodrich, L. F., Wiejaczka, J. A., and Srivastava, A. N. (1995). "Anomalous switching phenomenon in critical-current measurements when using conductive mandrels," *IEEE Trans. Appl. Supercond.* 5, 3442–3444.

Goodrich, L. F., and Stauffer, T. C. (2001). "Hysteresis in transport critical-current measurements of oxide superconductors," *J. Res. Natl. Inst. Stand. Technol.* 106, 657–690.

Herzog, R., Evetts, J. E., Somekh, R. E., and Pullan, P. A. (1994). "Full angular critical current anisotropy of YBCO thin films," *Proc. 7th International Workshop on Critical Currents in Superconductors*, ed. H. Webber, pp. 391–394, World Scientific Press, Singapore.

IEC (1998). *Superconductivity—Part 1: Critical current measurement—dc critical current of Cu/Nb–Ti composite superconductors*, IEC 61788-1, International Electrotechnical Commission, Geneva, Switzerland.

IEC (1999). *Superconductivity—Part 2: Critical current measurement—dc critical current of Nb_3Sn composite superconductors*, IEC 61788-2, International Electrotechnical Commission, Geneva, Switzerland.

IEC (2000). *Superconductivity—Part 3: Critical current measurement—dc critical current of Ag-sheathed Bi-2212 and Bi-2223 oxide superconductors*, IEC 61788-3, International Electrotechnical Commission, Geneva, Switzerland.

Morrison, R. (1998). *Grounding and Shielding Techniques*, 4th edition, Wiley-Interscience, NY.

Schwartz, J., Amm, B. C., Garmestani, H., Hilton, D. K., Hascicek, Y. (1997). "Mechanical properties and strain effects in $Bi_2Sr_2CaCu_2O_x$/AgMg composite conductors," *IEEE Trans Appl. Supercond.* 7, 2038–2041.

ten Haken, B., Godeke, A., and ten Kate, H. H. J. (1995). "The influence of compressive and tensile axial strain on the critical properties of Nb_3Sn conductors," *IEEE Trans. Appl. Supercond.* 5, 1909–1912.

Uglietti, D., Seeber, B., Abacherli, V., Pollini, A., Eckert, D., and Flukiger, R. (2003). "A device for critical current versus strain measurements up to 1000 A and 17 T on 80 cm long HTS and LTS technical superconductors," *Supercond. Sci. Technol.* 16, 1000–1004.

Walters, C. R., Davidson, I. M., and Tuck, G. E. (1986). "Long sample high sensitivity critical current measurements under strain," *Cryogenics* 26, 406–412.

10 Critical-Current Data Analysis

Poems reveal secrets when they are analyzed.

– Diane Wakoski

Have you ever looked at the voltage–current curve of a superconductor and tried to see *the* critical current? Except in rare cases, it does not just leap out at you. Because the voltage–current characteristic is a curve, the value of the critical current (I_c) depends on the definition. It also depends on the magnetic field, the temperature, and the strain the superconductor experiences (as illustrated earlier in Figs 9.3 and 9.4). This chapter is an introduction to sorting through all the possible definitions and variables.

We begin with methods of *defining* critical current that are practical (Sec. 10.1). Then we look at the notorious problem of *current-transfer* voltages and how to correct them (Sec. 10.2); all too often, these extraneous voltages interfere with obtaining good critical-current data on *short*, high-current samples, but there are effective ways to extract the underlying intrinsic I_c data.

In the main part of the chapter we present analytic representations of the critical current for use in application design and for accurate intercomparisons of data obtained on different conductors, in different locations, and at different magnetic fields, temperatures, and strain levels. Even simply comparing liquid-helium or liquid-nitrogen temperature data from different laboratories is not always trivial. Superconductors almost always perform better in our laboratory, for instance, because we test at about 1600 m above sea level, where liquid helium boils at about 4.0 K instead of 4.2 K, and liquid nitrogen at 76 K instead of 77 K. It may not sound like much, but at high magnetic fields, a fraction of a degree can make a significant difference in the results. So how do we correct for this?

In developing analytic forms for this purpose and, more generally, for application design, we consider, in turn, each of the three primary critical-current variables:

Magnetic field B (Sec. 10.3): A synthesis of $I_c(B)$ data is given for practical conductors of both high- and low-T_c materials, along with examples of how to analytically model the effect of magnetic field. We also contrast the very different effects of magnetic field on I_c in high-T_c vs. low-T_c superconductors.

Temperature T (Sec. 10.4): This is the problem alluded to above. Compilations of $I_c(B,T)$ data are given for a number of superconducting materials, including variable-temperature data for *high-current* superconductors, which is usually not so readily available. We also describe the linear method for interpolating and extrapolating the temperature dependence of the critical current, along with its limitations. [In a later section on scaling laws, we present a much more general technique for analytically modeling the effects of temperature (Sec. 10.6).]

Strain ε (Sec. 10.5): Scaling laws are introduced to model the very significant (and sometimes subtle) effects of strain on the critical current, $I_c(B,\varepsilon)$. In this and the last sections, we focus mainly

on low-T_c superconductors where a growing database is available. (For high-T_c superconductors, intrinsic reversible strain effects have only recently been observed, and they are just beginning to be understood and systematized.)

Transformation method: Finally, a new method is introduced to simplify the application of scaling laws, pertinent to all three variables: field, temperature, and strain. This renormalization technique significantly reduces the number of scaling variables required to predict performance in difficult-to-reach regions of the I_c-parameter space. Practical in-depth examples illustrate the effective use of the scaling laws in each case: Sec. 10.6 for $I_c(B,\varepsilon)$ and $I_c(B,T)$ data sets, and Sec. 10.7 for unified three-dimensional $I_c(B,T,\varepsilon)$ data sets.

A summary of these scaling laws and transformation relations is given in Appendix A10.2b for quick reference.

10.1 Practical critical-current definitions

The first consideration in I_c-data analysis is to choose a definition for determining the critical current from voltage vs. current (V–I) curves. Sounds easy enough. Figure 10.1 shows a hypothetical set of V–I characteristics obtained at different magnetic fields. There is usually a narrow current region where the voltage of a superconductor rises quickly. However, there is no one "critical" current. It is generally defined to lie somewhere in the region where the voltage takes off vertically, but this can cover quite a range of current. Thus, the exact value of I_c depends on the definition. There are three commonly used criteria for determining critical current: the electric-field, resistivity, and offset criteria.

10.1.1 ELECTRIC-FIELD CRITERION

This is my favorite all-around definition of critical current because it is the most used criterion, it is well understood, and it facilitates intercomparisons of data. It is also "equipment based." That is, it allows us to take maximum advantage of the sensitivity of a given voltmeter, and (unlike the resistivity criterion) the voltage where the critical current is determined does not change with the magnitude of critical current or the diameter of the sample that is being tested.

A critical voltage level is chosen [e.g. the 0.86 μV horizontal line in Fig. 10.1(a)], and the critical current is defined as the current at which the V–I curves intersect this criterion line, illustrated by the light-vertical-dashed lines in Fig. 10.1(a). Of course, the voltage generated depends on the length of superconductor between the two voltage taps (illustrated in Fig. 9.5), so the critical level is usually expressed as an *electric field* along the conductor [e.g. $E_c = 0.1$ μV/cm in Fig. 10.1(a)]. This criterion facilitates interlaboratory comparisons of data and makes the data useful for engineering design purposes.

Ideally, the value of the electric field is chosen to match the requirements that will be placed on the superconductor in actual applications. In *short* sample testing, however, the criterion is often chosen to correspond to a voltage slightly above the noise floor of the experimental equipment being used, and then rounded off to a convenient electric-field value.

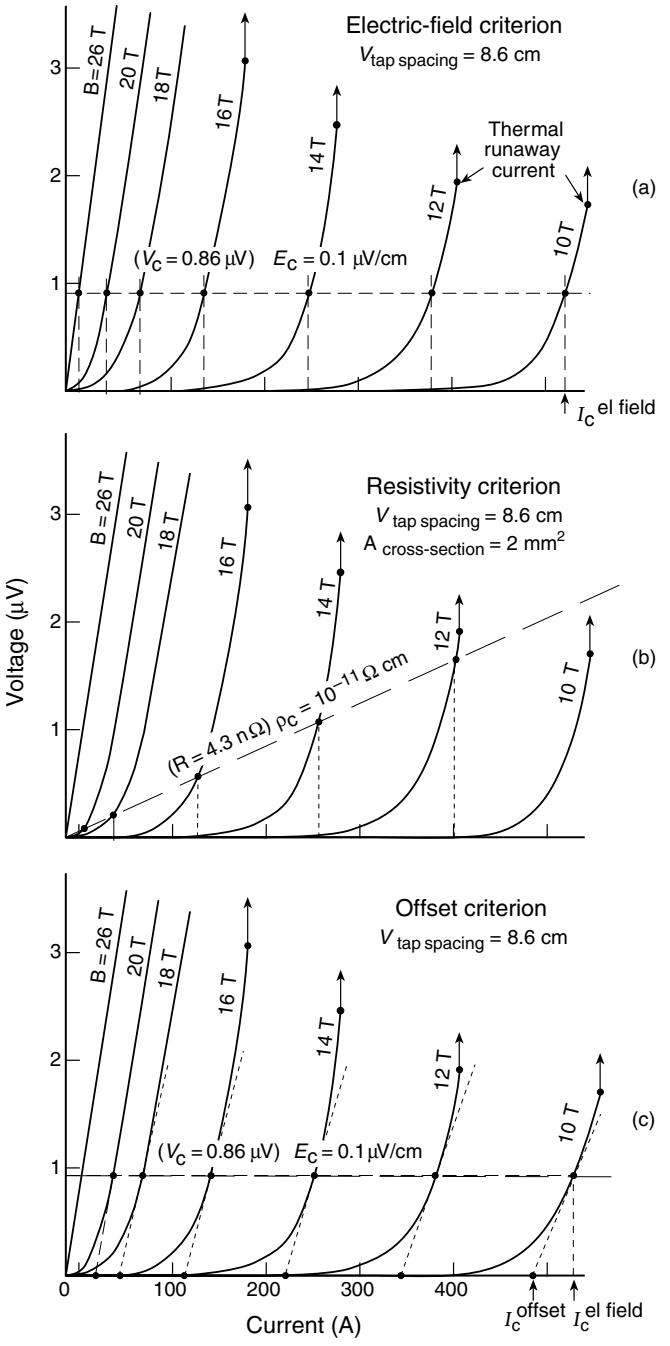

Fig. 10.1 Methods for determining the critical current from a set of *V*–*I* curves obtained at different magnetic fields: (a) electric-field criterion, (b) resistivity criterion, and (c) offset criterion (adapted from Ekin 1989).

Example: Suppose we have measured the typical set of *V–I* curves shown in Fig. 10.1. Each curve is obtained at a different magnetic field and the current range is quite large, from hundreds of amperes at low magnetic fields, to tens of amperes at high magnetic fields. Assume that the spacing between voltage taps attached to this sample is 8.6 cm. Our problem is to choose an electric-field *criterion level* E_c for determining the critical current.

We want the *voltage* corresponding to E_c to be above the voltage noise level for our measurement system, which, for a well-designed wiring layout (Sec. 4.6) and a high-sensitivity voltmeter, is typically less than ~0.1 μV. We also want to set the criterion level high enough that the *V–I* curves are rising rapidly as they cross the criterion line, so that I_c is accurately defined.

From a practical standpoint when choosing a criterion, we sort of work backwards. From Fig. 10.1(a), it appears that a good voltage criterion would be in the range of 1 μV. We want to choose a convenient electric-field criterion level that corresponds to a voltage in this range. Given that the voltage-tap spacing is about 8.6 cm, we choose the nearest rounded-off electric-field criterion value of 0.1 μV/cm (= 0.86 μV/8.6 cm). That is, we choose a voltage criterion of 0.86 μV, shown by the horizontal dashed line marked as E_c = 0.1 μV/cm in Fig. 10.1(a). That is about the optimum electric-field criterion for this measurement system and sample length. We could also try analyzing the data at a more sensitive criterion of 0.01 μV/cm, but the results would start to get noisy and less well-defined.

The critical-current values for each curve are obtained by dropping a vertical line down to the current axis from the point where each *V–I* curve crosses the criterion line. Since each *V–I* curve corresponds to a different magnetic field, the resulting I_c values may be plotted as a function of magnetic field, shown in Fig. 10.2 by the curve labeled "E_c = 0.1 μV/cm."

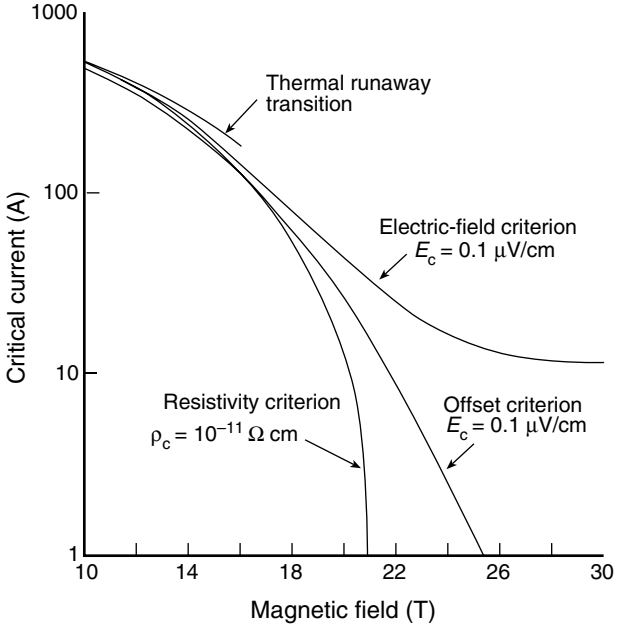

Fig. 10.2 Illustration of the critical current of a superconductor as a function of magnetic field that results from using different criteria.

The electric-field criterion presents problems, however, if the relative take-off in the *V–I* characteristics becomes gradual, or ohmic, as illustrated by the high-field curves in Fig. 10.1(a). In this typical situation, the I_c defined by the electric-field criterion never goes to zero, even when superconductivity is fully suppressed. For example, the 26 T *V–I* "curve" in Fig. 10.1 has no curvature and is completely ohmic, but the defined I_c is still finite. This produces an artificial high-field "tail" in the I_c vs. field plot of Fig. 10.2, with I_c approaching a constant level instead of zero.

Generally, this situation arises whenever current-sharing conduction by the normal stabilizer material in the conductor composite approaches that of the superconducting material. This occurs in all superconductors when I_c approaches zero, such as at high levels of magnetic field, temperature, or strain. It also occurs over a wide range of operating conditions in highly stabilized superconductors containing a lot of normal-conducting matrix material, such as BSCCO/silver conductors or conductors with relatively large amounts of copper-stabilizer material. Additionally, it presents a problem in experimental superconducting materials with low critical-current densities. Current sharing through the matrix material and sample holder can be subtracted if it is known, but this procedure becomes complex in magnetic fields because of the high magnetoresistance of pure stabilizer materials. The *offset* criterion described in Sec. 10.1.3 was defined precisely to take care of these difficulties.

10.1.2 RESISTIVITY CRITERION

The resistivity criterion is, perhaps, the next most popular criterion. A resistivity criterion of $10^{-11}\ \Omega$ cm is illustrated by the sloped dashed line through the origin in Fig. 10.1(b). The critical current is defined as the current at which the *V–I* curves intersect this sloped-criterion line.

A critical value of resistivity ρ_c is chosen which, ideally, would match the engineering requirements for the superconductor. For example, in most magnet applications a value of ρ_c in the 10^{-12}–$10^{-13}\ \Omega$ cm range would be desirable. As illustrated in the example below, however, the value of ρ_c in short-sample testing is usually limited to a higher value because of voltmeter sensitivity, especially for short samples at low values of J_c.

Example: Assume that the voltage tap spacing for our particular sample mount is again 8.6 cm, and, furthermore, that the sample has a cross-sectional area of 2 mm^2. Figure 10.1(b) shows our *V–I* data. We want to choose a convenient resistivity criterion level for analysis purposes that takes full advantage of the voltage sensitivity of our system, but also is high enough that the *V–I* curves are rising rapidly in the vicinity of the criterion line so that I_c is defined accurately.

From Fig. 10.1(b), we see that there is no resistance that is ideal for all the *V–I* curves, but a value around 5 nΩ would at least work well for the *V–I* curves at the midrange of the magnetic field *B*. Thus, we choose a convenient ρ_c value of $1 \times 10^{-11}\ \Omega$ cm, which corresponds to a resistance of 4.3 nΩ [for our particular sample length and cross-sectional area, $R_c = \rho_c L/A = (1 \times 10^{-11}\ \Omega\ \text{cm})(8.6\ \text{cm})/(0.02\ \text{cm}^2) = 4.3\ \text{n}\Omega$]. A line of this slope is marked $\rho_c = 10^{-11}\ \Omega$ cm in Fig. 10.1(b). Critical-current values are obtained from the intersection points of the *V–I* curves with the resistivity-criterion line; the resulting $I_c(B)$ curve is illustrated in Fig. 10.2 for comparison with the curve determined by the electric-field criterion.

The resistivity criterion is often used for magnet engineering purposes to select among different conductors over a limited magnetic-field range (where I_c is not changing too much). The ρ_c criterion has the appearance of being the most fundamental because it takes into account not only conductor length (as does the electric-field criterion), but also conductor cross-sectional area. The resistivity is actually an effective resistivity, one that an equivalently sized "normal" conductor would have at that voltage and current. Usually, the entire conductor cross-sectional area is used in applying the ρ_c criterion, not just the superconductor fraction. (Section 9.1.2 describes the various areas that are typically used in the definition of a critical-current *density*.)

The ρ_c criterion is not well suited for measuring the I_c of a specific superconductor over a wide range of current, however. As illustrated in Fig. 10.1(b), the criterion dips below the sensitivity of the voltmeter at high magnetic fields, and at low magnetic fields the required voltage is so high that it is beyond the point of thermal runaway. This is particularly a problem when measuring critical current as a function of temperature or magnetic field, where I_c can vary by many orders of magnitude.

10.1.3 OFFSET CRITERION

The difficulties of both the above criteria are averted by the offset criterion (Ekin 1989). That is, unlike the resistivity criterion, the offset criterion is useful over a wide range of current, and it does not encounter the definition problems of the electric-field criterion in regions where the superconductor characteristic is becoming ohmic (linear). The offset criterion is very similar to the electric-field criterion but, as illustrated in Fig. 10.1(c), the critical current is obtained by taking the *tangent* to the *V–I* curve at a given electric-field level (instead of dropping a vertical line to the abscissa as with the electric-field criterion). The critical current is defined by the intersection of these tangent lines with the current axis, as shown by the dots along the current axis in Fig. 10.1(c).

The electric-field level where the tangent is taken is usually chosen to be comparable to that used for the ordinary electric-field criterion.

Example: In this example, we apply the offset criterion to the *V–I* curves shown in Fig. 10.1 for comparison with the other two criteria. We will use the same electric-field level E_c as for the electric-field definition, except now we take tangents to the data curves where they intersect the E_c line. As illustrated in Fig. 10.1(c), the points where these tangent lines intersect the current axis define the critical current.

The resulting critical-current data are plotted in Fig. 10.2 for comparison with the results of the other two criteria. Note that there is not much difference in the three criteria at low magnetic fields where the normal-matrix conduction is relatively small compared to that of the superconducting material. However, the difference becomes significant at high magnetic fields. It is immediately apparent in Fig. 10.2 that the resistive "tail" of the curve defined by the electric-field criterion is removed by the offset criterion, and, unlike the resistivity criterion, this criterion enables an accurate determination of I_c over the entire magnetic-field range.

Another unique feature is that at high magnetic fields where the *V–I* curves are nearly ohmic (linear) the offset values of I_c are insensitive to the particular criterion level chosen, unlike the electric-field or resistivity criteria. This can be seen in the high-field data of Fig. 10.1(c), where, if we mentally raise or lower the E_c criterion line, we still obtain approximately the same tangent line with about the same slope and offset I_c intercept.

As noted in the example, the difference between the offset criterion and electric-field criterion becomes negligible at high critical-current density in Fig. 10.2. For most practical purposes the two are identical except where the superconductor characteristic starts to become ohmic. We can see this mathematically by first introducing the following simple (but very useful) empirical expression, which is found to approximate the *V–I* of most practical superconductors over an extended range of voltage:

$$V = \mathrm{c}\, I^n \tag{10.1a}$$

or, alternatively, in terms of electric field E

$$E = \mathrm{k}\, I^n. \tag{10.1b}$$

Here, c (or k) is a proportionality constant, and the exponent n is an index of the degree of nonlinearity. For a good multifilamentary superconducting wire at low magnetic fields, n is usually quite high, in the range from 20 to 50. As the *V–I* characteristic starts to become ohmic, on the other hand, n reduces to unity. In most practical superconductors, n is nearly constant over a fairly wide voltage range (usually an order of magnitude or more), which is what makes Eqs (10.1a) or (10.1b) useful.

To express the quantitative difference between $I_c^{\text{el field}}$ and I_c^{offset}, we differentiate Eq. (10.1a) and find that the slope of the *V–I* characteristics in Fig. 10.1 is given by

$$\mathrm{d}V/\mathrm{d}I = n\,\mathrm{c}\, I^{n-1} = n\, V/I. \tag{10.2}$$

[Incidentally, if we rearrange Eq. (10.2), we find the source of Eq. (9.1) used in the discussion on data-acquisition techniques, Sec. 9.3.3, namely $\mathrm{d}V/V = n\,\mathrm{d}I/I$.] Evaluating Eq. (10.2) at the voltage-criterion level V_c, we find that the slope of the *V–I* characteristic at V_c is given by

$$(\mathrm{d}V/\mathrm{d}I)_c = n\, V_c/I_c^{\text{el field}}. \tag{10.3}$$

On the other hand, referring to the geometric construction in the bottom right portion of Fig. 10.1(c), we see that

$$I_c^{\text{el field}} = I_c^{\text{offset}} + V_c\,(\mathrm{d}V/\mathrm{d}I)_c^{-1}. \tag{10.4}$$

Finally, substituting Eq. (10.3) for $(\mathrm{d}V/\mathrm{d}I)_c$ in Eq. (10.4) we find that

$$I_c^{\text{el field}} = I_c^{\text{offset}} + n^{-1}\, I_c^{\text{el field}}.$$

or (Ekin 1989)

$$I_c^{\text{offset}} = I_c^{\text{el field}}\,(1 - n^{-1}). \tag{10.5}$$

Thus, for highly nonlinear *V–I* characteristics (large *n*), the difference between $I_c^{\text{el field}}$ and I_c^{offset} becomes negligible. On the other hand, when the *V–I* characteristic becomes completely ohmic ($n = 1$), we see from Eq. (10.5) that I_c^{offset} becomes zero, as it should be when all superconductivity is lost. In practice, the offset criterion can be used in place of the electric-field criterion, giving essentially comparable I_c values where the *V–I* curves have a sharp transition, but with the advantage of eliminating the false "tail" at high fields and temperatures.

With Eq. (10.5), the correction is very easy to apply to $I_c^{\text{el field}}$ data with a spreadsheet program by using *n* values evaluated at the same electric-field criterion level. *The correction is particularly important for situations where there are significant parallel conducting paths (e.g. through the conductor matrix or sample holder) and where the critical current becomes low (e.g. near the critical temperature, near the upper critical field, or at high strains)*. For example, it is often significant for Bi-based superconductors, which have a relatively large amount of silver matrix material and relatively low values of the irreversible strain limit ε_{irr} (giving rise to a sharp drop-off in critical current and *n*). *The need for the correction is signaled quite readily by low values of n and becomes particularly important to make when n dips below about 5 or 10*. It is surprising how may times this simple correction for alternative current-path conduction eliminates erroneous artifacts in the data.

10.1.4 SUMMARY OF THE ADVANTAGES AND DISADVANTAGES OF THE DIFFERENT CRITERIA

1. The *electric-field* criterion [illustrated in Fig. 10.1(a)] is instrument friendly, allowing data to be taken near a voltmeter's maximum sensitivity for wide-ranging values of magnetic field, temperature, or strain. Therefore, it is a very popular criterion. However, the defined I_c is artificially enhanced by current conduction through the normal components of a superconducting composite if a correction for current sharing is not made. Thus, this criterion is not very useful under conditions where the *V–I* characteristic starts to become more linear (such as in highly stabilized composites and bismuth-based superconductors, where there is typically a lot of normal silver conduction, or at high magnetic fields approaching the critical field).
2. The *resistivity* criterion [Fig. 10.1(b)] is, perhaps, the most commonly used definition for engineering a magnet and is often used to select among different conductors for a *specific* magnet application. The resistivity criterion is not well suited, however, for measuring the critical current of a superconductor over a wide range of magnetic fields. At high fields (corresponding to low-current levels) it can require a voltage below the noise floor of the voltmeter, and at low fields (high currents) it can require a voltage above the thermal-runaway limit.
3. The *offset* criterion [Fig. 10.1(c)] combines some of the better features of both. It defines a superconducting I_c that approaches zero when the *V–I* characteristic of a conductor becomes ohmic, unlike the electric-field criterion. Furthermore, unlike the resistivity criterion, it is useful for evaluating I_c over a wide range of current.
4. Unfortunately, a fourth criterion, the *thermal-runaway* current, is also sometimes utilized [see the points in Fig. 10.1(a) through (c) where the voltage spikes upward off the scale].

This criterion is irreproducible, incapable of comparison with other work, and strongly dependent on the specific conductor cooling conditions (other than that, it is just fine). As a criterion for the critical current, it is anathema. Do not use it!

10.1.5 TRANSFORMING TO A MORE SENSITIVE CRITERION

Often, the critical current needs to be determined at a more sensitive criterion level than where it was measured, for example, to determine practical engineering values of I_c for magnet design. This is especially true for critical-current data obtained from short samples where it is difficult to achieve high electric-field sensitivity. The restriction of short samples is quite common and occurs, for example, in test probes where a short sample length is required to fit within a small measurement space (e.g. transverse to the bore of a high-field magnet) or in the development of new materials where typically only a small length of an experimental material is available.

The technique described below, for changing from one criterion level to another, is simple and effective provided that the *V–I* curves can be modeled by the simple power-law relationship given in Eqs (10.1a) or (10.1b). That is, it works *so long as n is nearly constant over the range of interest*.

For the electric-field criterion, the technique consists simply of evaluating Eq. (10.1a) at the old and new criterion levels, and taking their ratio. That is,

$$I_{c1}/I_{c2} = (V_{c1}/V_{c2})^{1/n} = (E_{c1}/E_{c2})^{1/n}, \tag{10.6}$$

Criterion dependence of the critical current for electric-field and offset criteria

where the indices 1 and 2 refer to two different criterion levels of critical voltage V_c or critical electric field E_c. Equation (10.6) also works for scaling I_c values determined by the offset criterion, since I_c values determined by the two types of criteria are related simply by the constant proportionality factor, $(1-n^{-1})$, given by Eq. (10.5).

For the resistivity criterion, we find a similar expression by using ohm's law and substituting $V_c = I_c R_c$ or $E_c = \rho_c I_c/A$ into Eq. (10.6)

$$I_{c1}/I_{c2} = (R_{c1}/R_{c2})^{1/(n-1)} = (\rho_{c1}/\rho_{c2})^{1/(n-1)}, \tag{10.7}$$

Criterion dependence of the critical current for the resistivity criterion

where the indices 1 and 2 refer to two different criterion levels of critical resistance R_c or critical resistivity ρ_c.

Remember that these relationships assume that the *V–I* characteristic is described well by Eqs (10.1a) or (10.1b), and that the exponent n is reasonably constant. Experience has shown that extrapolations of an order of magnitude in criterion level can generally be trusted and provide quite accurate results, especially if $n \geq 20$. Fortunately, most *practical* conductors have values of n in this range.

How is the *n* value determined and how do we know it is reasonably constant? Probably the easiest way is to plot the *V–I* curve on logarithmic coordinates and see how linear the relationship is. The slope of the data is the *n* value in the $V = c\, I^n$ relationship. Determining the *n* value is an important supplement to I_c data, since it provides a quality factor for the sharpness of the *V–I* characteristic as well as a convenient method of determining I_c at other criteria levels, as we have just seen. The process of determining *n* for each *V–I* curve is greatly simplified by digitally acquiring the *V–I* data on a computer (see Sec. 9.3.3).

Example: Suppose we have critical-current data that was obtained at an electric-field criterion of 1 μV/cm. Further, assume that we have determined the *n*-value of the *V–I* characteristic to be about 35 from a plot of log *V*–log *I*. We wish to calculate the approximate value of I_c at a more sensitive criterion of 0.1 μV/cm.

From Eq. (10.6) we find that

$$I_c^{0.1\ \mu V/cm}/I_c^{1\ \mu V/cm} = (0.1\ \mu V/cm\ /\ 1\ \mu V/cm)^{1/35} = 0.936.$$

Thus, for a steep *V–I* curve with an *n* value of 35, the critical current decreases by only 6.4% even though the E_c criterion changes by an order of magnitude. The same result is obtained for the offset criterion, and a very similar result is obtained from Eq. (10.7) for the resistivity criterion. At high magnetic fields where *n* becomes smaller, the change in I_c value would, of course, be greater than the few percent change in this example. Such a small correction is typical, however, for most practical situations.

10.2 Current-transfer correction

10.2.1 INTRODUCTION

Sometimes we obtain *V–I* characteristics with sloped baselines like those shown in Fig. 10.3. This sloped baseline usually arises in short-sample testing of superconductors with a resistive matrix where *the separation between the current contact and voltage tap is small.* (This was illustrated in Fig. 7.9 by the part of the test sample labeled "current transfer length.")

These spurious voltages arise because in practical composite superconductors, large voltages are generated near the current contacts where current crosses the resistive matrix to penetrate to the inner superconducting filaments. If voltage taps are located too close to the current contacts, these *current-transfer* voltages can strongly affect the measured *V–I* characteristic.

It is best to avoid these voltages in the first place through good sample-holder design, as described in detail in Sec. 7.3.4. (Specifically, the separation between the voltage taps and current contacts required to minimize current-transfer voltages was given by Eq. (7.9) and evaluated specifically for Nb_3Sn and Nb–Ti composites in Fig. 7.11.)

Sometimes, however, the current-transfer voltages cannot be avoided because of limited testing space, for example, in the bore of a high-field magnet. Then we obtain *V–I* characteristics that have sloping baselines like those shown in Fig. 10.3. The shape of the current-transfer characteristic depends on the distribution of filaments in the conductor. Sometimes the effect results in a linearly sloped baseline [Fig. 10.3(a)], sometimes a gentle curve [Fig. 10.3(b)]. It can also produce a segmented baseline [Fig. 10.3(c)] when there are discrete rings of filaments in the conductor cross section.

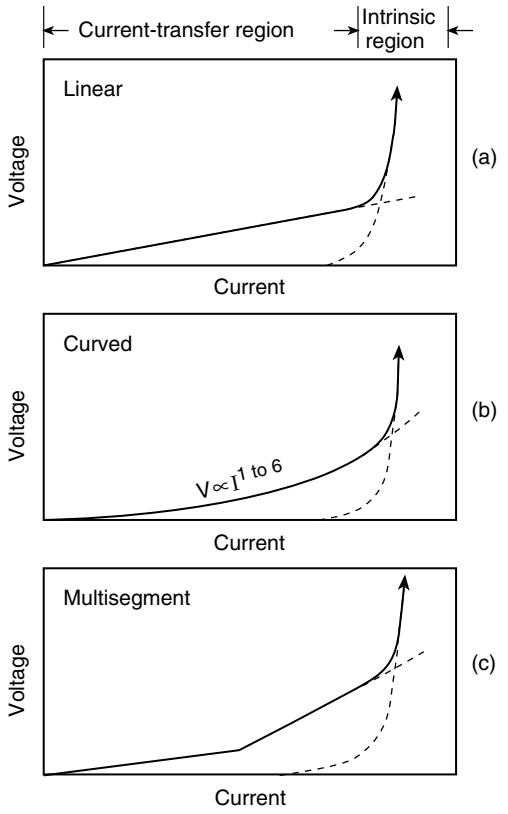

Fig. 10.3 Illustration of *V–I* curves affected by current-transfer voltage at low-current levels.

With such alterations of the *V–I* curve, we need to correct for the current-transfer voltages to extract the intrinsic *V–I* characteristic of the superconductor. The best all-around technique to accomplish this, in my opinion, is the *back-extrapolation* method (Sec. 10.2.2), which requires acquiring *V–I* data to high voltages. When high-voltage data cannot be obtained because of thermal runaway, then we must use the *baseline method* (Sec. 10.2.3).

10.2.2 BACK-EXTRAPOLATION CORRECTION METHOD: EXTEND THE *V–I* CURVE TO HIGH VOLTAGE

In general, the usual empirical relation $V = C\,I^n$ works pretty well for fitting *V–I* characteristics, both in the *current-transfer region* of the *V–I* curve (the low-current region labeled at the top of Fig. 10.3) as well as in the *intrinsic region* (the high-current region also shown at the top of Fig. 10.3), but with different values of n. In the intrinsic region, n is quite high (typically 20–50 as noted above), but it is considerably lower in the current-transfer region of the *V–I* curve. Various model calculations predict different values of n. For example, the two-cylinder current-transfer model (Wilson 1977; Ekin 1978) predicts an n of 1, whereas the anisotropic continuum model (Dresner 1978) predicts an n of 2. Experimentally n values in the current-transfer region have been observed anywhere from 1 to 6. Consequently, it is best *not* to use the data in this low-current

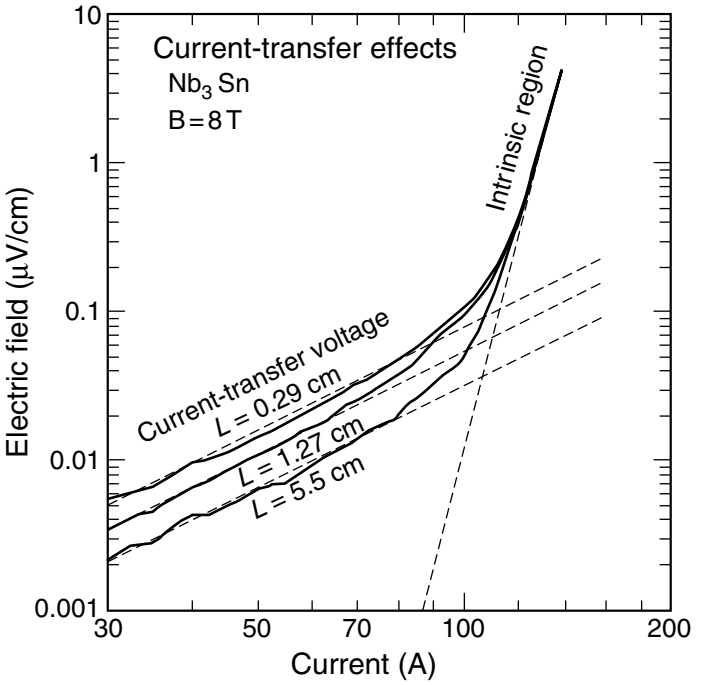

Fig. 10.4 Log–log plot of electric field vs. current (*E–I*) for a short Nb_3Sn sample, showing current-transfer effects for different values of *L*, the length between the current contacts and voltage taps (length #2 in Fig. 7.9).

region and, instead, fit the data in the high-current intrinsic region. This relation can then be back-extrapolated to low voltages to obtain the "true" *V–I* curve (with current-transfer voltages removed). This method is illustrated by the dashed lines in Fig. 10.3. It helps to visualize the technique by plotting the data in full-log space, as illustrated by actual test data in Fig. 10.4.

Example: From the *E–I* characteristics shown in Fig. 10.4, we wish to determine I_c at sensitive electric-field criteria levels of 0.1 μV/cm and 0.01 μV/cm, both well below the current-transfer voltages that mask this part of the curve.

Fortunately, this is a fairly stable sample, and so we are able to take data to a relatively high electric-field level (about 5 μV/cm) without quenching the superconductor (a higher electric field would be even better). Looking at the log *V*–log *I* plot, we see a fairly distinct "break point" at about 100 A. Using the empirical relation Eq. (10.1b), we fit the high-current data that are above and away from the "break point" (where the effect of the current-transfer voltage is negligible). We find from the slope of the data on the log–log plot in Fig. 10.4 that *n* is about 20 (illustrated by the steep dashed line in Fig. 10.4). Next we evaluate I_c at a high electric-field criterion above the "break point," say 1 μV/cm, and find (from Fig. 10.4) that I_c is about 127 A. Substituting these values of *n* and I_c into Eq. (10.6), we can then find I_c at other *E* levels. Thus, for the criterion of 0.1 μV/cm,

$$I_{c1}/127\ \text{A} = (0.1\ \mu\text{V/cm} / 1\ \mu\text{V/cm})^{1/20}$$
$$I_{c1} = 113\ \text{A}.$$

Similarly, at the more sensitive criterion of 0.01 μV/cm,

$$I_{c1}/127\ \text{A} = (0.01\ \mu\text{V/cm} / 1\ \mu\text{V/cm})^{1/20}$$
$$I_{c1} = 101\ \text{A}.$$

The higher the value of n, the more reliable this method. Generally, for n values above 20, I_c values can be extracted at voltage levels that are about an order of magnitude below the current-transfer voltages. A comparison of I_c values obtained from this back-extrapolation technique with data taken directly on a long sample of the same conductor (data free of current-transfer voltages) shows that the two results agree within a few percent.

The bottom line: try to take data to high voltages whenever current transfer is affecting the baseline of a *V–I* characteristic. The main caveats for using this back-extrapolation technique are to make sure the *V–I* (or *E–I*) curve fits Eq. (10.1a) [or Eq. (10.1b)] well, and that n is not too low ($\gtrsim$10, preferably $\gtrsim$20). The method works equally well for high-T_c or low-T_c superconductors.

10.2.3 BASELINE METHOD: WHAT TO DO IF THERMAL RUNAWAY PREVENTS EXTENDING THE *V–I* CURVE TO HIGH VOLTAGES

Sometimes the *V–I* curve cannot be extended to high voltage (well above the current-transfer voltage) because of thermal runaway, such as when the sample has a minimum amount of stabilizer or disturbances are large because of sample motion. Then the baseline method is our only choice. This involves fitting the lower current-transfer region of the *V–I* curve (e.g. below the "break-point" in Fig. 10.4) to the same Eq. (10.1b), and determining n in the current-transfer region. An approximation to the intrinsic *V–I* characteristic is then obtained by *subtracting* this current-transfer baseline from the measured data beyond the "break point." This can also be illustrated by using the log–log plot in Fig. 10.4.

Example: Suppose we wish to determine the intrinsic critical current from the data in Fig. 10.4 at a moderate electric-field criterion of 0.1 μV/cm by using the baseline method instead of the back-extrapolation method.

If we fit the data below the "break point" with the empirical relation Eq. (10.1b), we find an effective n value of 2.2. The intrinsic voltage does not interfere much with this determination because the rapidly falling intrinsic voltage is negligible compared with the current-transfer voltage in this region. If the data contain multiple current-transfer segments [as in Fig. 10.3(c)], it is best to use the data segment nearest to the break point and avoid fitting across different segments. As noted earlier, such segments occur when there are just a few discrete rings of filaments in the conductor cross section.

From the fit in this low-current region we extrapolate the current-transfer characteristic to higher electric-field levels (see dashed lines in Fig. 10.4) and then subtract it from the measured electric field to obtain an approximation to the "true" intrinsic *V–I* characteristic. If we constructed such an intrinsic curve from the data in Fig. 10.4, we would find that, at a criterion of 0.1 μV/cm, $I_c = 110$ A and, at 0.01 μV/cm, I_c would be in the range ~84 – ~92 A, depending on which curve we used in Fig. 10.4. The I_c value for a 0.1 μV/cm criterion is close to that obtained with the back-extrapolation technique. However, the nearly two-orders-of-magnitude extrapolation to a 0.01 μV/cm criterion falls significantly below the I_c value obtained from the more accurate back-extrapolation technique.

Errors introduced by the baseline method become greater as the criterion level is lowered, but the procedure at least gives an indication of I_c at such sensitive criteria, which could not be obtained otherwise.

10.3 Magnetic-field dependence of critical current

10.3.1 INTRODUCTION

We now switch from methods of determining I_c, to analytically modeling it. These analytic representations have proven to be invaluable for data comparisons and application designs. We start with the effects of magnetic field, which play a dominant role in determining the critical current for applications such as magnets, transformers, and rotating-machinery.

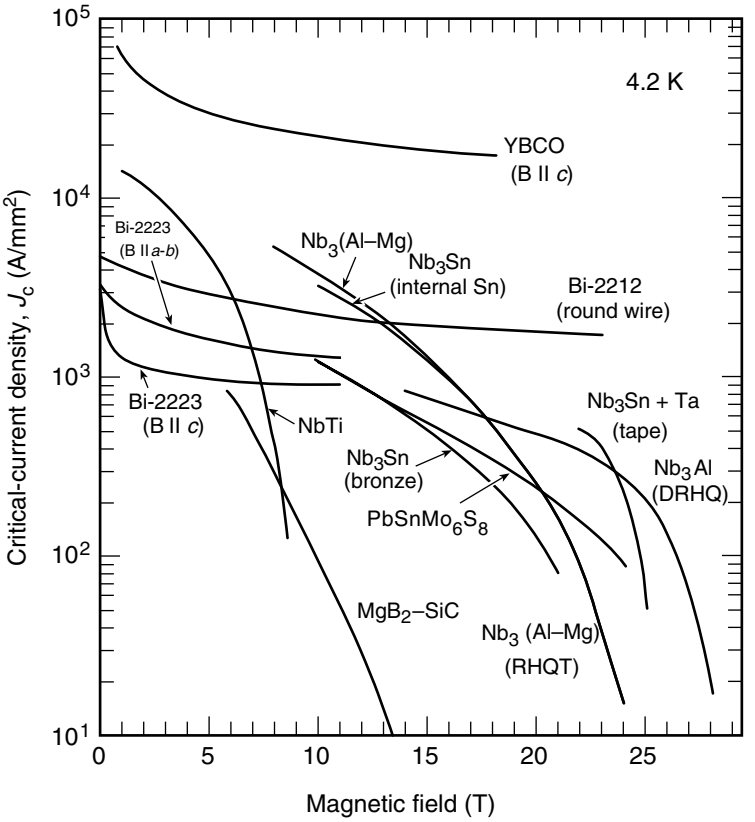

Fig. 10.5 Critical-current density as a function of magnetic field for a number of high-current-density superconductors at *liquid-helium* temperature (from a compilation by Lee 2002, 2005). The critical-current density J_c is normalized by the superconductor area alone or by the nonstabilizer area, not by the overall conductor area (see definitions in Sec. 9.1.2). Note that the high-T_c superconductors are very anisotropic with respect to magnetic-field orientation, with J_c being much higher for field parallel to the *a*,*b*-axes than to the *c*-axis of the superconductor.

YBCO: /Ni/YSZ ~1 μm thick microbridge (Foltyn et al. 1999).

Bi-2223: rolled 85-filament tape (American Superconductor 6/1996).

$PbSnMo_6S_8$ (Chevrel phase): wire with 20% superconductor in 14-turn coil (Cheggour et al. 1997).

Bi-2212: 427-filament round wire (Hasagawa et al. 2000).

MgB_2–SiC: 10wt% SiC doped (Dou et al. 2002).

Nb_3Al–Mg: 84-filament RHQT Nb/Al–Mg(0.6 μm) (Iijima et al. 1999).

Nb_3Al: DRHQ with intermediate cold work, core J_c (Kikuchi et al. 2001).

Nb_3Sn (internal tin): high-J_c design CRE1912, OI-STG (Zhang et al. 1999).

Nb–Ti: APC strand Nb–47wt%Ti with 24vol%Nb pins (24 nm nominal diameter) (Heussner et al. 1997).

Magnetic field can change the critical current of a superconductor by orders of magnitude, as shown in Fig. 9.3. For most of these applications, the magnetic-field characteristic at a fixed temperature (curve A–B in Fig. 9.3) is the primary engineering curve used to set the operating current of superconducting coils. As mentioned in the introduction to Part III, this curve is highly variable from sample to sample because it is *extrinsic* in nature; that is, it depends strongly on how a particular superconductor is fabricated. Thus, because of both its extrinsic nature and its engineering importance, the critical-current vs. magnetic-field dependence is perhaps the most frequently measured characteristic of a superconductor.

Figure 10.5 shows the J_c–B characteristics at 4.2 K of many of the best high-field superconductors. If the temperature is raised to 77 K, however, all but YBCO and Bi-2223 are eliminated from the plot, as shown by the data in Fig. 10.6.

In magnet design, it is often necessary to model the shape of these curves to make accurate interpolations between data points (and sometimes limited extrapolations). To do this, we first need to understand the important role of magnetic-vortex *pinning* in determining I_c.

That is, practical type II superconductors are penetrated by magnetic field in the form of localized magnetic vortices—regions of circulating screening supercurrents that localize the magnetic field in a small normal core at the middle of each vortex, as illustrated in Fig. 10.7.

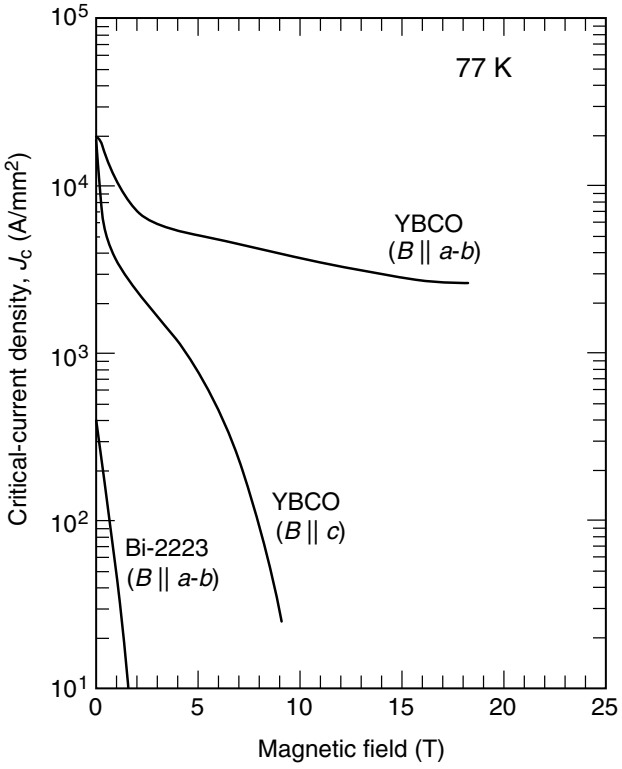

Fig. 10.6 Critical-current density as a function of magnetic field for high-T_c superconductors at *liquid-nitrogen* temperature (from a compilation by Lee 2002). The critical-current density J_c is normalized to the superconductor area alone (see definitions in Sec. 9.1.2). Again, note strong anisotropy, with J_c being much higher for field parallel to the *a*,*b*-axes than to the *c*-axis of the superconductor.
YBCO: /Ni/YSZ ~1 μm thick microbridge, 75 K (Civale et al. 2004; Foltyn et al. 1999, 2003; Macmanus-Driscoll et al. 2004; and a compilation by Lehndorff 2001); Bi-2223: 77 K (Hayashi et al. 1997).

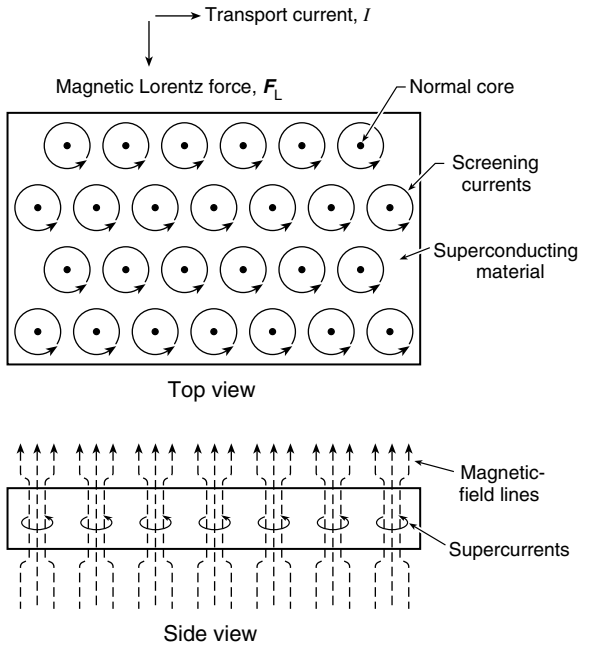

Fig. 10.7 Representation of a vortex lattice in a Type II superconductor. The normal cores are represented by dots; the screening currents by circles. The side view shows the distortion of an applied uniform magnetic field as it is channeled through each vortex core by the screening supercurrents, leaving most of the superconducting material free of field. Arrows at the top of the figure show the direction of the magnetic Lorentz force F_L acting on the vortex array when a transport current I is applied in the direction shown. (From Ekin 1983.)

The diameter of the normal core is determined by the superconductor's coherence length, typically only a few nanometers across. (Values of the coherence length are listed for most of the important high-field superconductors in the last column of Table A6.6.) If electric current is being transported along the superconductor from left to right in Fig. 10.7, this results in a magnetic Lorentz force

$$F_L = I \times B, \tag{10.8}$$

(vector cross product), which acts on each vortex and tries to make them move at right angles to the current I and magnetic field B (downward in the example given in Fig. 10.7). Once vortex motion occurs, energy will be dissipated and the superconductor becomes resistive, even though much of the material may still be superconducting. Thus, from a practical standpoint, the critical current is limited by the ability of the superconductor to *pin* these magnetic vortices in place (by defects in the material), not by the complete disappearance of superconductivity in the material. [This gives rise to the difference between the so-called *depinning* current and the *pair-breaking* current. The depinning current is the practical limit. A good introduction to this topic is given, for example, in Chapter 12 of the book by Rose Innes and Rhoderick (1976).]

The role of vortices and pinning gives rise to several definitions of the *critical magnetic field* in practical high-field superconductors. First, we summarize these definitions and then in the following sections give several practical examples of their use in magnetic-field interpolations and extrapolations.

H_{c1}: The *lower critical field*. A low-magnetic field, typically $\leqslant$80 kA/m (0.1 T), where magnetic field first penetrates a superconductor in the form of single vortices. H_{c1} is determined from magnetization measurements. This quantity is used very little in describing

practical high-field superconductors, since the presence of magnetic field within a type II superconductor does not produce energy dissipation and resistance; only vortex *motion* does, as described above.

H_{c2}: The *upper critical field*. The applied magnetic field where superconductivity is totally suppressed. H_{c2} is the magnetic field at which the density of vortices becomes so high that the normal cores start to overlap, which is determined completely by the superconductor's coherence length. H_{c2} can be measured either by (1) a *magnetization* measurement where it corresponds to the applied magnetic field at which flux completely fills the superconductor, or (2) a *resistivity* measurementt where it corresponds to the applied magnetic field at which the normal resistivity first starts to drop (as measured by a very low transport current typically in the milliampere range). In *in*homogeneous superconductors (which is the typical practical case), H_{c2} represents the magnetic field where the best material in the composite conductor first starts to transition into the superconducting state.

H_{c2}^{*}: The *effective upper critical field* or *effective depinning field*. The applied magnetic field that reduces the critical current to zero due to a loss of vortex pinning. Usually this is determined by extrapolating the Lorentz-force vs. magnetic-field curve to zero, without any weighting of the data (an example is given in Sec. 10.3.3). H_{c2}^{*} is smaller than H_{c2} because it takes into account the loss of pinning from inhomogeneities that occur in all practical superconducting wires. From a technological standpoint, H_{c2}^{*} is more useful than H_{c2} because it represents an effective average over the distribution of H_{c2} values in the conductor, not just the very best material. It is precisely this effective average that determines the critical current and thus the upper end of the I_c–H curve.

Sometimes the magnetic field where the critical current extrapolates to zero is referred to as the *scaling field*, H^{*}. This is more applicable to situations where distant extrapolations are made from data that do not extend to very high fields ($\leqslant$70% H_{c2}^{*}); such extrapolations obtained from lower magnetic fields are inaccurate and highly dependent on the assumed form of the extrapolation (examples are given in Sec. 10.3.4). Nevertheless, values of the scaling field H^{*} determined from data at moderate magnetic fields are still useful to accurately represent data up to these moderate fields, but they should not be used at high magnetic fields where the effective upper critical field H_{c2}^{*} (extrapolated from high-field data) gives more accurate results. Also, their values should not be considered as representative values of the upper-critical field H_{c2} or of the effective average upper critical field H_{c2}^{*}.

The effective upper critical field H_{c2}^{*} was defined in 1980, well before the advent of high-T_c superconductors and the *irreversibility field*, a similar term used to describe the depinning characteristics of HTS materials.

H_{irr}: The *irreversibility field*. The applied magnetic field where pinning is lost, as indicated by the loss of irreversibility in the magnetization curve. Similar to H_{c2}^{*}, H_{irr} is a measure of the practical depinning limit of a superconductor, except it is usually determined from magnetization measurements instead of transport-current measurements.

The difference between H_{c2} and the two *depinning* critical fields (H_{c2}^{*} and H_{irr}) is typically less than a tesla in relatively homogeneous low-T_c superconductors, but it can reach several teslas in *in*homogeneous low-T_c superconductors and many teslas in high-T_c superconductors near

the critical temperature because of thermal fluctuations (further details on these effects are given in Further reading in Sec. 10.8.1).

The standard (SI) unit for H is *amperes per meter* (A/m), which is not commonly used in characterizing superconductors. Consequently, magnetic field is often expressed in terms of the magnetic induction in free space B ($\equiv \mu_0 H$), which has the more common SI unit of *tesla*. (In free space, 1 T corresponds to 7.958×10^5 A/m.) Thus, in this text we use the corresponding terms: B_c, B_{c2}, B^*_{c2}, and B_{irr}.

10.3.2 GENERAL FUNCTION FOR THE MAGNETIC-FIELD DEPENDENCE OF CRITICAL CURRENT IN LOW-T_c SUPERCONDUCTORS

As summarized above, the I_c–B curve of practical low-T_c superconductors is determined by magnetic-vortex *pinning*, and B^*_{c2} determines the upper end of this curve. We now use these concepts to give a few practical examples of how to accurately interpolate and moderately extrapolate I_c–B data.

Pinning theories (e.g. Narlikar and Dew-Hughes 1966; Fietz and Webb 1969; Campbell and Evetts 1972; Hampshire and Taylor 1972; Kramer 1973; Kroeger et al. 1980) suggest that the magnetic-field dependence of the critical Lorentz force F_L has the general form

$$F_L \equiv I_c B = k f(b). \quad \text{Representation of the critical Lorentz force} \tag{10.9}$$

where k is a proportionality constant and $f(b)$ is a general pinning function having the form

$$f(b) = b^p (1 - b)^q. \quad \text{General pinning function} \tag{10.10}$$

Here, p and q are exponential constants, and b is the *reduced* magnetic field (magnetic field B normalized by B^*_{c2}):

$$b \equiv B/B^*_{c2}. \quad \text{Reduced magnetic field (definition)} \tag{10.11}$$

Examples of the magnetic-field dependence of F_L of several practical low-T_c superconductors are shown in Fig. 10.8, along with fits to these data (solid curves) by using Eq. (10.9) with Eqs (10.10) and (10.11). The fit of this general functional form is excellent. The overall shape of the F_L–B curve is determined mainly by the exponential constants: p and q. Although p and q vary from sample to sample (depending on crystal structure, impurity content, annealing conditions, and processing parameters), they are nearly independent of the superconductor's temperature (Fietz and Webb 1969) and strain state (Ekin 1980a), as well as the combination of both (Cheggour and Hampshire 1999). This constancy is the essence of the powerful scaling laws described in Sec. 10.5.

Typical values of the fitting parameters B^*_{c2}, p, and q are tabulated for many practical superconductors in the fifth column of Appendix A10.2a. These are not handbook values because

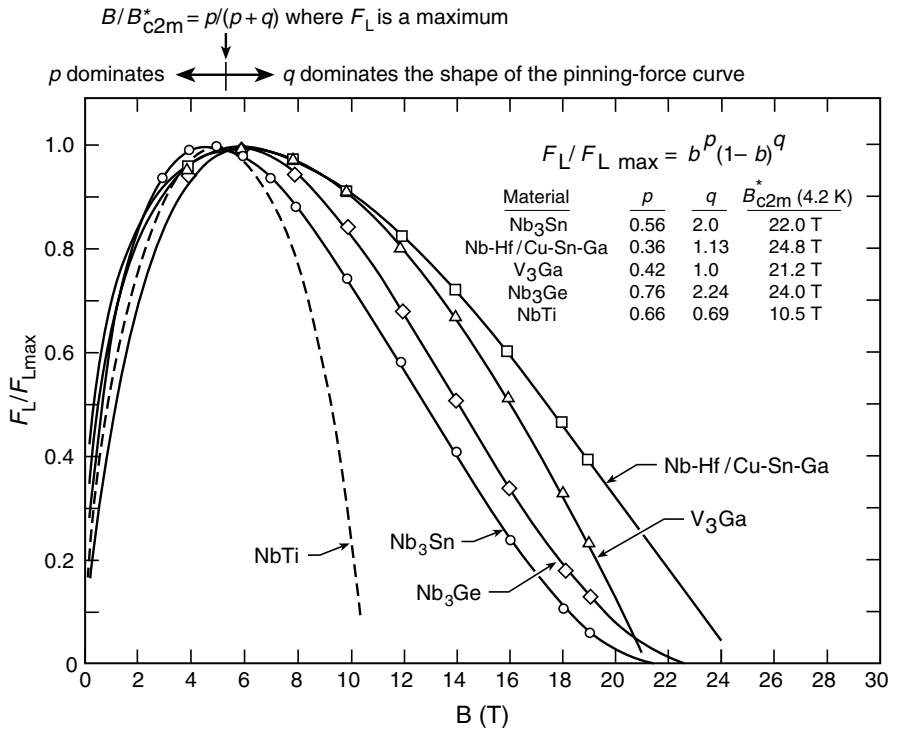

Fig. 10.8 Critical Lorentz-force density F_L of several high-field superconductors fitted by using the general pinning-force parameters of Eqs (10.9)–(10.11): p, q, B^*_{c2} and k (from Ekin 1981b). The Kramer model (Kramer 1973), which predicts $p = 0.5$ and $q = 2.0$, has limited applicability and works only for some high-field superconductors, such as *binary* Nb_3Sn.

B^*_{c2}, in particular, can change from sample to sample depending on the pinning structure, additive content, and homogeneity of the superconductor. However, the values serve as a good starting point for determining the parameters in Eq. (10.9) when only limited data are available, as described in the next section.

10.3.3 METHOD FOR MAGNETIC-FIELD INTERPOLATIONS AND EXTRAPOLATIONS

Sometimes when making interpolations and extrapolations from available I_c–B measurements, the data are forced to fit one particular pinning theory, such as the Kramer model (Kramer 1973), which predicts $p = 0.5$ and $q = 2$. This is a mistake. In practice, the Kramer model works only for a few types of high-field superconductors, such as binary Nb_3Sn, and has very limited success or none at all in representing other materials, as shown in Fig. 10.8. Even for Nb_3Sn with small amounts of additional elements, we see from the Nb–Hf/Cu–Sn–Ga sample in Fig. 10.8 and the data tabulated in Appendix A10.2a that the additives significantly lower q below the value of 2 appropriate for binary Nb_3Sn. When data are not available for

ternary Nb_3Sn with additives, the data in Appendix A10.2a suggest that $q \approx 1.6$ is a good default value for many practical Nb_3Sn materials with common titanium and tantalum additives (provided the conductor is not highly inhomogeneous; see Sec. 10.3.4). For the superconductors listed in Appendix A10.2a with crystal structures other than A-15, q can range from 1 to 3 or more.

Thus, when possible, it is best not to use the Kramer model ($p = 0.5$ and $q = 2$), but rather the more general pinning form given by Eq. (10.9) and determine the actual p and q values for a given type of superconductor, each with its unique additive concentrations and heat-treatment conditions. Precise values of these parameters are important for magnet design and enable Eq. (10.9) to accurately interpolate and extrapolate values of J_c at different magnetic fields. (So the moral of the story is—"mind your p's and q's.")

The easiest way to determine the parameters in Eq. (10.9) is to use a multiple-parameter least-squares fitting function, which is now available on most personal computers as part of a spreadsheet program. The following fitting process takes only a few minutes once the data are entered into the spreadsheet.

Up to four parameters are being determined simultaneously in Eq. (10.9). If the range of data is limited, accuracy and consistency are improved if the fit is selectively carried out with fewer than four, as follows. At low fields, the shapes of the pinning-force curves in Fig 10.8 are determined mainly by p and, at high fields, predominantly by q. The crossover field for the two regimes is where the Lorentz force rises to a maximum at

$$b_{max} = p / (p + q). \tag{10.12}$$

For many low-T_c superconductors, this crossover field occurs at about 20% of B^*_{c2} (about 5 T in Nb_3Sn at 4.2 K, for example). Thus:

1. If data cover a large range of magnetic field (from $0.1 \leqslant b \leqslant 0.75$), all four parameters (k, B^*_{c2}, p, and q) can be accurately determined simultaneously by a multiple-parameter fitting routine (initial parameter guesses can be based on the tabulated values in Appendix A10.2a).
2. In magnet design, however, data are often available only at high magnetic fields (e.g. over 5 T in Nb_3Sn) simply because that is the region of greatest interest for many magnet applications. In this case, it is best to use a nominal value of p from Appendix A10.2a to represent the low-field data. Magnetic-field interpolations above b_{max} are not affected much by the value chosen for p.
3. Similarly, for low-field applications less than b_{max}, such as superconducting transmission lines or magnetic-resonance-imaging (MRI) magnets, data are usually obtained only in the low magnetic-field regime. In this case, it is best to use a nominal value of q from Appendix A10.2a to determine the other three free parameters. Data interpolations at low fields are not affected much by the choice of q.
4. B^*_{c2} is the hardest parameter to determine accurately, unless data are available above ~70% of B^*_{c2}. Again, if data are not available for such high-field levels, critical-current interpolations at liquid-helium temperature can be carried out at fields well below B^*_{c2} with little loss of accuracy by using the nominal 4.2 K values of B^*_{c2} listed in Appendix A10.2a.

The use of Eq. (10.9) may look like it requires a lot of time, but, as mentioned above, it takes only a few minutes in practice.

Example: Critical-current data obtained for a ternary Nb_3Sn conductor (made with niobium-alloy filaments containing 7.5 wt% tantalum) are shown in the first two columns of Table 10.1. The experimentally measured Lorentz force $F_L \equiv I_c B$ is calculated in the third column. The fourth column contains the Lorentz force calculated from Eq. (10.9) with the values of the four parameters p, q, B^*_{c2}, and k given near the bottom of the spreadsheet. The difference Δ between the calculated and experimental values for the Lorentz force is calculated in the fifth column, and the square of this difference Δ^2 is given in the sixth.

To optimize the parameter values for the best fit, simply sum the Δ^2 values of the sixth column (sum = 11.21) and then use the spreadsheet's multiparameter fitting routine (in this case the Solver™ subroutine in Excel™) to minimize this sum by varying the parameters you designate as free. Unfortunately, when simultaneously fitting many parameters, it is easy to get into a local minimum in the parameter space that is not the absolute minimum. So when starting the fitting procedure with a new data set, it helps to first set the parameters to known values that are reasonable, and then free them up one at a time over a series of fits to get into the right part of the parameter space. As a general rule, however, it is best to keep the number of free-fitting parameters to the absolute minimum needed for a good fit, as we shall now demonstrate.

The optimal parameter set for this conductor (listed at the bottom of Table 10.1) is tabulated in the first row of Table 10.2. The parameter p was not fit and instead set to a standard value (obtained from Appendix A10.2a) because these data did not extend to a low-enough magnetic field to accurately determine p. The results of this three-parameter fit are shown by the solid line in Fig. 10.9. The fit is excellent, with a root-mean-square (rms) deviation [$\equiv (\text{sum}/N)^{0.5}$, where N is the number of data points] for the Lorentz force of only about 1.2 A·T, as listed in the seventh column of Table 10.2.

Table 10.1 **Spreadsheet example of determining fitting parameters p, q, B^*_{c2}, and k in Eq. (10.9) for the pinning force of a $(Nb–2wt\%Ta)_3Sn$ sample measured at 4.2 K.**

B [T]	I_c [A]	$F_L \equiv I_c B$ [A·T]	$k f(b)$ [A·T]	Δ [A·T]	Δ^2 [(A·T)^2]
8	126.43	1011.4	1009.8	−1.6	2.6
9	105.82	952.4	954.0	1.6	2.8
10	88.78	887.8	887.9	0.1	0.0
12	61.11	733.3	733.8	0.5	0.2
14	40.26	563.6	563.6	0.0	0.0
16	24.58	393.3	391.4	−1.9	3.4
18	12.73	229.1	230.6	1.5	2.1
19	8.38	159.2	159.0	−0.2	0.1
	p = 0.50			sum	= 11.2
	q = 1.63			rms error	= 1.2
	B^*_{c2} = 22.61			rms % error	= 0.035%
	k = 3462				

Notes:

The rms error $\equiv (\sum\Delta^2/N)^{1/2}$, where N is the number of data points in the fit.
The rms % error $\equiv 100(\sum\Delta^2/N)^{1/2}/k$.

Table 10.2 **Comparison of results for different numbers of free parameters**

p	q	B^*_{c2} [T]	k [A·T]	# Free parameters	Rms error [A·T]	Comments
(0.50)	1.63	22.61	3462	3	1.2	Optimum (minimum) number of free parameters
0.46	1.56	22.40	3238	4	1.0	Small change in rms error for additional free parameter → too many free parameters and inconsistent values
(0.50)	(2.0)	24.54	3945	2	11.4	Large rms error → too few free parameters; Kramer function does not fit the data well

Notes:
Values of p and q in parentheses were assigned "Kramer" values and not treated as free parameters.
Again, the rms error $\equiv (\Sigma\Delta^2/N)^{1/2}$, where N is the number of data points in the fit.

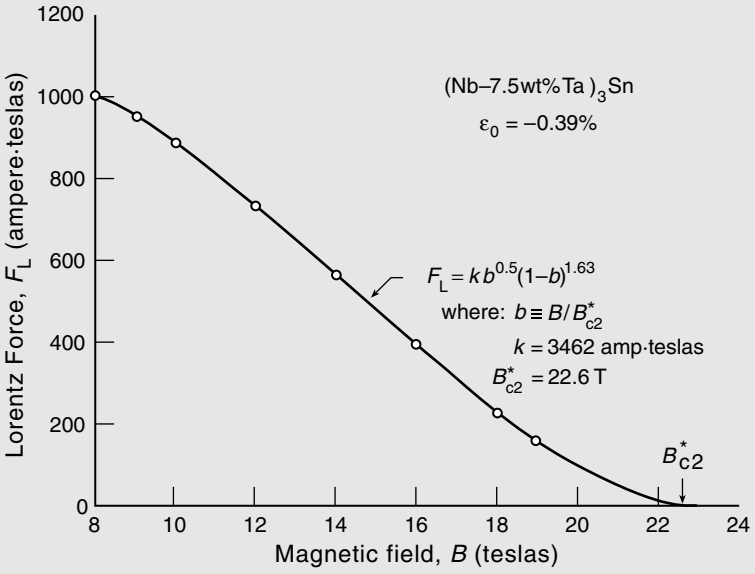

Fig. 10.9 Example showing a three-parameter (q, B^*_{c2}, and k) fit (solid curve) of the general pinning-force function Eq. (10.9) to the critical-current data of Table 10.1 (open circles).

(Here we have expressed the Lorentz force in units of ampere-teslas, which is equivalent to N/m.) This amounts to an rms error of only 0.1–0.8% in the Lorentz force.

Although these data were not taken at a low enough field to accurately determine the value of the exponent p, a second fit was made by simultaneously optimizing all *four* parameters, with results shown in the second row of Table 10.2. The four-parameter fit did not significantly reduce the rms deviation, *indicating that too many free parameters were being used in the fit*. This can lead to large variations in the parameter values and they lose significance.

The third row of Table 10.2 shows the results of a *two*-parameter fit wherein we fixed $p = 0.5$ and $q = 2.0$ (effectively the Kramer function). In this case, there was an order-of-magnitude rise in the rms deviation from about 1 A·T to over 11 A·T, indicating the inadequacy of the Kramer model to

describe ternary Nb_3Sn with additives. Furthermore, the value of B^*_{c2} jumped to over 24.5 T (beyond the right edge of Fig. 10.9). [This value is unrealistically high for a temperature of 4.2 K, given the relatively high value of compressive prestrain (−0.39%) where these data were obtained (the effect of strain is described in Sec. 10.5).] When data are forced to fit the Kramer model, the resulting value of B^*_{c2} does not represent the conductor's effective depinning field; rather, it should be considered an arbitrary scaling field B^*, useful only for fitting data below about 70% of B^*_{c2} (i.e. < 16 T in this case).

As shown in the example above, the reduction of q below the Kramer value of 2 in ternary Nb_3Sn conductors becomes important for magnetic-field interpolations and extrapolations above ~0.7 B^*_{c2}. This is illustrated more clearly by a second example at higher magnetic fields, shown in Fig. 10.10, where J_c data for another Nb_3Sn conductor (made with Nb–2wt%Ta alloy filaments) are replotted on a so-called "Kramer plot," with $J_c^{0.5}\,B^{0.25}$ as the ordinate. On such a plot, the Kramer values ($p = 0.5$ and $q = 2$) give a pinning-force curve that is a straight line intersecting the abscissa at B^*_{c2}, shown by the dashed line in Fig. 10.10. [This can be seen as follows: $J_cB \propto b^{0.5}(1-b)^2 \rightarrow (J_cB)^{0.5} \propto (B/B^*_{c2})^{0.25}(1-B/B^*_{c2}) \rightarrow J_c^{0.5}B^{0.25} \propto (B^*_{c2})^{-0.25} \times (1-B/B^*_{c2})$; that is, $J_c^{0.5}B^{0.25}$ is proportional to $1 - B/B^*_{c2}$.] The deviation of the data below the (straight line) Kramer dependence is clearly evident at fields of 18 T and above in Fig. 10.10.

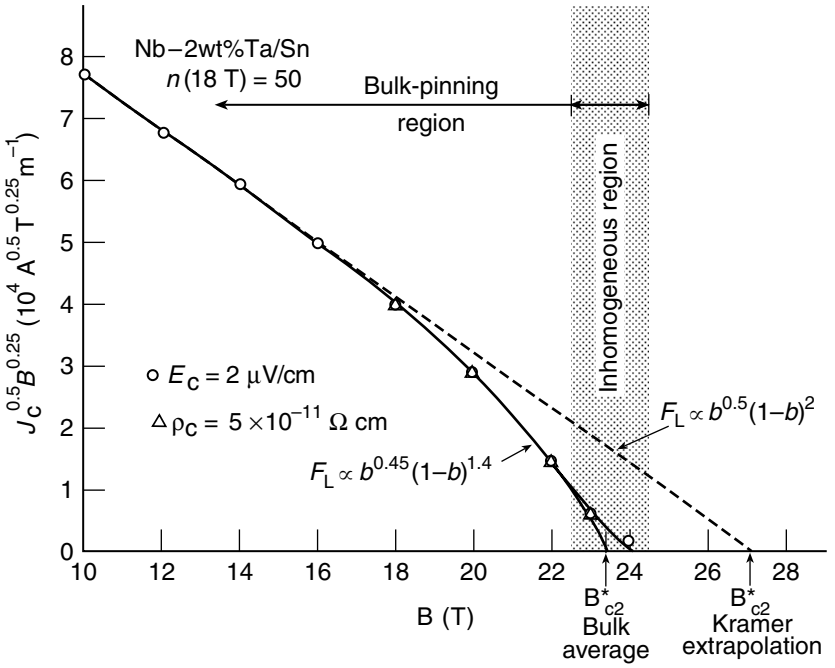

Fig. 10.10 Deviation of the high-field flux-pinning curve from the Kramer-model expression in a high-quality (high-n) Nb_3Sn sample with tantalum additions. A straight-line extrapolation with this type of "Kramer" plot overvalues B^*_{c2} by about 4 T for this conductor. On the other hand, a fit to the general pinning expression in Eq. (10.9) gives $q = 1.4$ and a more accurate effective depinning field of $B^*_{c2} = 23.4$ T. Data obtained with a resistivity criterion (triangles) do not differ significantly from those obtained with an electric-field criterion (circles), except near B^*_{c2}. (From Ekin 1985.)

The decrease of q below 2 is independent of the criterion used to determine J_c. For this sample, the resistive transition index n [defined in Eq. (10.1)] had a very high value of 50 at 18 T, indicating this to be a high-quality, homogeneous sample. For such a high-n value, Fig. 10.10 shows that there was no significant difference in the J_c values determined with either a resistivity criterion (triangles) or electric-field criterion (circles); they both resulted in the same curve shape (except very near B^*_{c2}). Notice the artificially high B^*_{c2} of about 27 T that would be obtained with a Kramer extrapolation compared with the more realistic effective depinning field of about 23.5 T obtained from a fit to the general pinning function, Eq. (10.9).

Again, the main point is that J_c–B interpolations (and minor extrapolations) are generally much more accurate with Eq. (10.9) than those obtained from the Kramer model, usually with errors less than a few tenths of a percent. (To minimize error when making *extrapolations*, it is best to keep the extrapolation within 10–20% of the highest or lowest available data points.)

10.3.4 EFFECT OF B_{c2} INHOMOGENEITY ON THE SHAPE OF THE I_c–B CHARACTERISTICS OF LOW-T_c SUPERCONDUCTORS

Inhomogeneities that are inherent to the fabrication process of practical superconductors can also have a considerable effect on magnetic-field interpolations and extrapolations, especially at high magnetic fields. Variations in the upper critical field can result, for example, from tin gradients across the Nb_3Sn reaction layer (Godeke et al. 2003). The effect of such inhomogeneities on the effective upper critical field can be an important factor, for example, in the selection of Nb_3Sn conductors for high-frequency nuclear-magnetic-resonance (NMR) magnets, which operate close to the upper critical field.

The effect at high fields is illustrated in Fig. 10.11 by a Kramer plot of critical current for a hydrogen-doped Nb_3Sn sample containing 0.2 at% hydrogen in the Nb_3Sn reaction layer. Note that the value of the transition index n for this sample was quite low, only 12 at 18 T (compared with $n \approx 50$ at 18 T for the Nb–2wt%Ta/Sn sample shown in Fig. 10.10). This low value of n at high fields suggests that the sample is quite inhomogeneous with a wide range of B_{c2} values. Such a wide range can lower the effective upper critical field as well as distort the pinning-force curve, producing a "tail" or region of positive curvature ($q > 2$) that is evident in Fig. 10.11 starting at about 18 T. The tail results from different portions of the sample progressively becoming resistive as the applied magnetic field increases.

The region where this tailing effect becomes significant (i.e. where the curve changes from negative curvature to positive curvature) is shown by shading in Fig. 10.11. This is much wider than the corresponding shaded region of positive curvature in Fig. 10.10, indicating a relative narrow distribution of B_{c2} values for the high-n sample.

Because of the low n-value and suspected large B_{c2} inhomogeneities for the hydrogen-doped sample, it is quite possible that even this sample has a significantly lower q than the $q = 2$ value typifying binary Nb_3Sn. The start of the decrease below the $q = 2$ line in Fig 10.11 can be seen in the range between 14 and 18 T, before the tailing effect starts. Such a lower value of q would be consistent with those of the other ternary Nb_3Sn samples listed in Appendix A10.2a.

Thus, care needs to be exercised in drawing conclusions about intrinsic high-field pinning characteristics from inhomogeneous samples. Generally, inhomogeneities in the upper

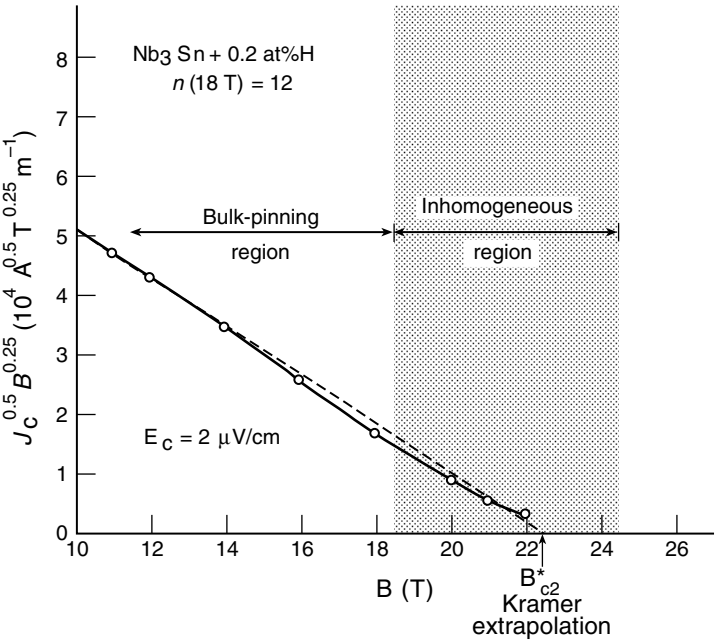

Fig. 10.11 Kramer plot of a low-n Nb_3Sn sample with hydrogen additions, showing a depressed value of the effective depinning field B^*_{c2} due to material inhomogeneities. Such a wide distribution of B_{c2} inhomogeneities also distorts the pinning-force curve at high fields, creating a tailing effect with artificially high values of the pinning-function exponent q. (From Ekin 1985.)

critical field lower the effective depinning field B^*_{c2} and, paradoxically, raise q to abnormally high values (3 or more in some Nb_3Sn samples), which can mask the true extent of depression of B^*_{c2} when extrapolating its value.

10.3.5 EFFECT OF WEAK LINKS ON THE SHAPE OF THE I_c–B CHARACTERISTICS OF HIGH-T_c SUPERCONDUCTORS

In high-T_c superconductors, there is an additional effect of *weak links* that strongly affects the magnetic-field dependence of the transport critical current in these materials. Small imperfections in the crystal lattice, especially grain boundaries, can block the flow of supercurrents at very low magnetic fields ($B \ll 1$ T). Uncorrected, weak-link limitations render high-T_c superconductors useless for most applications. As we shall now see, this is perhaps the greatest challenge for the manufacture of practical high-T_c superconductors.

Figure 10.12 presents the first *transport* critical-current data measured in YBCO. These data clearly show the severe degradation of the transport current in these early sintered samples at very low magnetic fields. In Fig. 10.12, we also see the contrasting results of critical current determined from *magnetization* measurements in the same conductors at the same magnetic fields (indicated by the light dashed line in the upper part of the figure). These data showed that the *intra*granular J_c was significantly higher than the *inter*granular transport J_c in these samples and indicated that grain boundaries were responsible for the weak-link behavior. (Magnetization is determined mainly by currents circulating *within* each grain; further information on this technique of determining the critical current is given, for example, in Kroeger et al. 1975.)

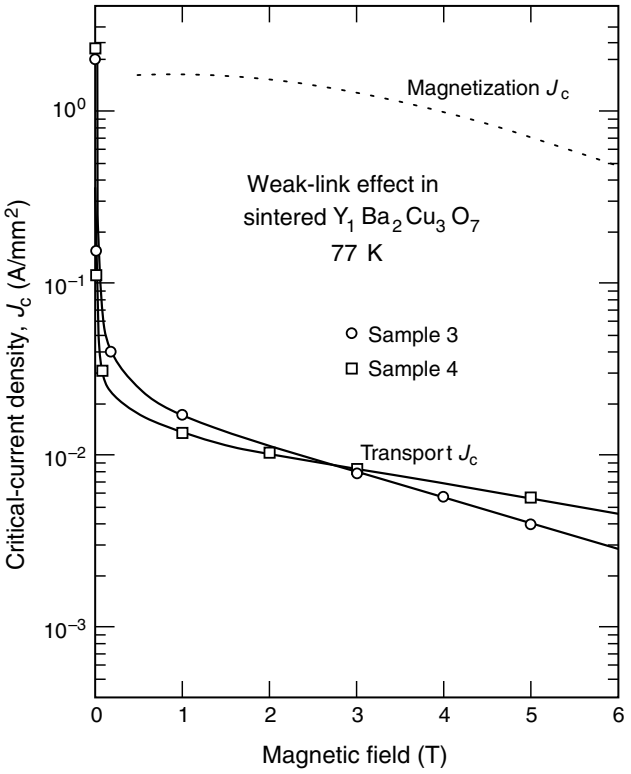

Fig. 10.12 The first measurement of the *transport* critical current as a function of magnetic field in granular YBCO, demonstrating extreme weak-link behavior (Ekin et al. 1987). The solid curves show that the *inter*granular transport J_c is sharply suppressed by the application of very low (millitesla) magnetic fields. At the same time, magnetization measurements show that the *intra*granular J_c (light dashed line) is significantly higher than the intergranular transport J_c and thus implicates grain boundaries as the source of the weak links.

The weak-link behavior results from the low charge-carrier density in high-T_c superconductors and their short superconducting coherence length (the range over which superconducting electron pairing can occur; see Further reading section at the end of this chapter). The 0 K coherence length of YBCO, for example, is only about 1.5 nm in the *a* or *b* crystallographic direction (Larbalestier et al. 2001), and just ~0.5 nm in the *c* direction. Thus, coherence is lost between the superconducting pairs of electrons as they cross very small crystalline imperfections on the order of a grain-boundary thickness.

In YBCO superconductors, grain boundaries that are misaligned by more than about 4° start to become weak-linked (Dimos et al. 1988, 1990). When misaligned by more than 10–15° (as in the early sintered YBCO conductors) the low-magnetic-field behavior of the transport J_c becomes completely dominated by *Josephson tunneling* across the grain boundaries. (An introduction to the Josephson effect is also given in the introductory reading suggested at the end of this chapter.)

Figure 10.13 shows this quantitatively. Transport J_c data for sintered YBCO samples are plotted on an expanded logarithmic magnetic-field scale to illustrate more clearly the very low-magnetic-field behavior. The solid line in Fig. 10.13 is the result of a calculation of Josephson tunneling across grain boundaries. It describes the data quite well without any fitting parameters, relying only on the experimentally measured average grain size in the sample. These data

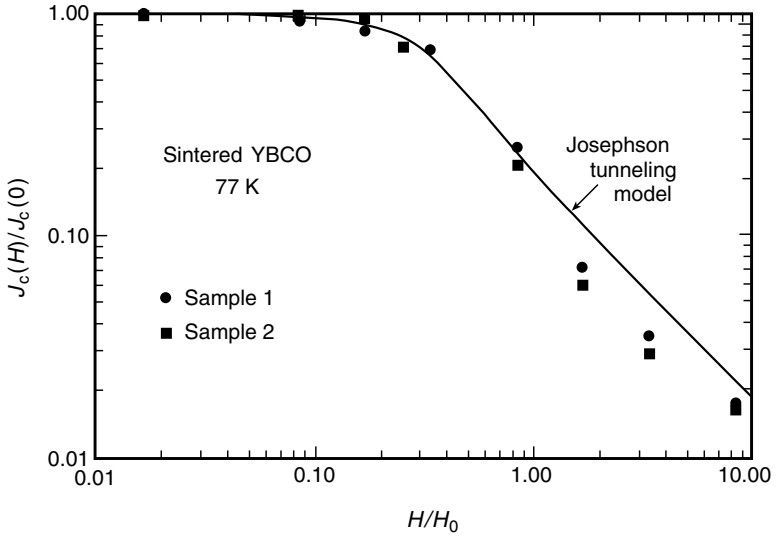

Fig. 10.13 Transport critical-current density vs. applied field normalized to a characteristic magnetic field H_0. The solid line depicts the result of a Josephson tunneling model for current transport across grain-boundary weak links, which fits the data well *without adjustable parameters*. The weak-link decoupling field H_0 used in the model is given by Eq. (10.13) and has a value of only about 1 mT in typical YBCO materials at temperatures of 77 K and below (from Peterson and Ekin 1988).

show that the characteristic magnetic field H_0, where J_c is degraded by weak-link decoupling, is given by (Peterson and Ekin 1988):

$$H_0 = \phi_0/(\mu_0 dL). \quad \text{Weak-link decoupling field} \tag{10.13}$$

Here, ϕ_0 is the flux quantum, μ_0 is the magnetic constant, L is the average grain diameter in the material, and d is the effective thickness of the grain boundary (which is approximately twice the London magnetic penetration depth; further information is given in the reference). Evaluating these parameters for typical YBCO materials having an average grain size of about 10 μm, we find that the decoupling field H_0 is only about 1 mT over the practical temperature range from liquid-helium to liquid-nitrogen temperature.

The important point is that grain-boundary weak links severely degrade the critical current at an extremely low characteristic field, given by Eq. (10.13). As we shall see, the solution is grain *alignment*. Consequently, from a practical standpoint, the main challenge of fabricating practical high-T_c conductors is (1) to minimize the effects of grain-boundary weak links through a high degree of grain alignment, and (2) to achieve this over very long lengths.

10.3.6 IMPROVEMENT OF J_c–B CHARACTERISTICS FROM GRAIN ALIGNMENT IN HIGH-T_c SUPERCONDUCTORS

Figure 10.14 shows the immense improvement in the J_c–B characteristics as techniques have been developed for grain alignment in high-T_c superconductors. Three types of high-T_c

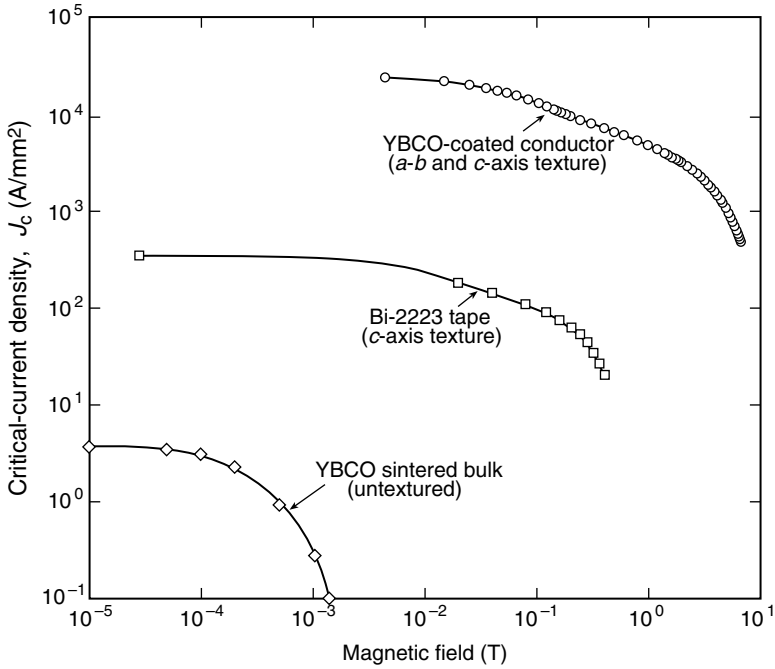

Fig. 10.14 Critical-current density vs. magnetic field of an early YBCO-bulk sample (Ekin et al. 1987), a high-quality Bi-2223 tape (van der Laan 2004), and a YBCO-coated conductor (Civale 2005). All data were obtained at about 77 K and, for the tape conductors, magnetic field was applied perpendicular to the wide side of the tape. (Adapted from van der Laan 2004.)

superconductors are illustrated, with different degrees of grain alignment or *texturing*. At the bottom of the plot is a representative J_c–B curve of an untextured sintered YBCO conductor, the case just illustrated in Fig. 10.13.

In the middle of Fig. 10.14 is a typical J_c–B curve for Bi-2223, showing the considerable enhancement in critical-current density resulting from *c-axis* texturing. With *c*-axis texturing, the *c*-axes of the superconducting grains are aligned, providing paths of in-plane electrical connectivity along the superconductor. Such in-plane connectivity is important for achieving high critical-current density because of the very small coherence length in the *c*-direction, as described in the previous section. The critical-current density is enhanced by about two orders of magnitude over that obtained in sintered samples, and high values of J_c extend to magnetic fields two orders of magnitude higher than for untextured materials. Still, only a small fraction of the grain-boundary cross-sectional areas are carrying supercurrents in these conductors.

Full current-carrying potential can be approached only with in-plane grain alignment (both *a-b* and *c*-axis texturing), as illustrated for a biaxially aligned YBCO-coated conductor at the top of Fig. 10.14. The required degree of in-plane texture is difficult to achieve, but it has been made possible with improvements in conductor fabrication technology. Two processes are mainly being developed for commercial use, one wherein a *textured buffer* layer is first

deposited on a structural substrate, which then serves as a template for epitaxially depositing a superconducting film on top [the so-called ion-beam-assisted-deposition (IBAD) process], the other where the *substrate* is textured by a rolling and heating process [rolling-assisted-biaxially textured substrates (RABiTS)]. [Further information on these fabrication processes is given, for example, in the book edited by Goyal (2004), listed in the Further reading section.]

Although the current densities within the superconducting layer of YBCO-coated conductors are significantly higher than those for Bi-2223 conductors, the overall engineering current densities are comparable, because the YBCO coating is only about 0.8–2.5 μm thick compared with a substrate thickness of about 50 μm. This gives a relatively low filling factor of 1–5%, whereas that of Bi-2223 tapes exceeds 40%. Nevertheless, the high-magnetic-field performance and mechanical properties of YBCO-coated conductors are significantly improved over those of bismuth superconductors, thus providing strong impetus to develop these superconductors.

Practical YBCO-coated conductors have a very high degree of grain alignment—they are effectively mosaic single crystals approaching a kilometer in length. If the average grain alignment is off by more than 10° to 15°, the grain boundaries are dominated by Josephson weak-link conduction (Chisholm and Pennycook 1991), and we are back to the sintered YBCO situation. For average grain misalignments between about 4° and 8°, the grains are no longer completely weak-linked. In this case, the vortex pinning at grain boundaries changes character and is augmented by interactions with intragranular vortices, which supports significantly higher critical-current densities at higher magnetic fields (Gurevich 2002). On the other hand, for grain alignment better than about four degrees, the full cross-sectional area of the grain boundary carries supercurrents (Polyanskii et al. 1996, Feldmann et al. 2000). In such a case, the grain boundaries support extremely high critical-current densities (up to 4×10^4 A/mm^2 at 77 K in zero applied magnetic field). [A detailed review of grain-boundary effects in high-T_c superconductors has been written, for example, by Hilgenkamp and Mannhart (2002), listed in the Further reading section.]

Thus, it is not bulk pinning that determines the magnetic-field behavior of high-T_c superconductors, but rather the quality of their grain boundaries. (For *low*-T_c superconductors, on the other hand, there is effectively no loss of superconducting coherence across grain boundaries and, in fact, the grain boundaries play the important beneficial role of providing vortex-pinning sites.) Unlike low-T_c superconductors, the vortex pinning in high-T_c superconductors is also highly *anisotropic*. Consequently, the J_c–B dependence of technical high-T_c superconductors is strongly dependent on the orientation of the magnetic field relative to the superconductor crystal axes. It also depends on the magnetic-vortex state, which changes with temperature, magnetic field, and the type of pinning within the a,b-axes. (In-depth reviews on this subject are given by Blatter et al. 1994 and Brandt 1995, also listed in the Further reading section.)

So in summary, our information regarding these complex magnetic-field effects in high-T_c superconductors is introductory and incomplete at present, and certainly not well systematized for technological conductors. Because of the very recent advent of long-length, high-J_c fabrication techniques, detailed studies of weak-link conduction processes in *practical* high-T_c superconductors is an active field of research still in its early stages of development.

10.4 Temperature dependence of critical current

10.4.1 INTRODUCTION

Along with the magnetic-field effects just discussed, temperature also plays a dominant role in determining critical-current magnitude. Temperature is usually the first parameter to be fixed in most superconductor applications. Historically, it was usually chosen to be the boiling point of liquid helium or (with the recent progress in high-T_c superconductors) the boiling temperature of liquid nitrogen. Increasingly, however, the development of commercial cryocoolers is enabling operation at temperatures other than these fixed levels. Even the fixed levels are not so fixed, because with immersion measurements in a liquid cryogen, significant temperature differences can occur at different locations. As mentioned in the introduction, superconductors typically perform better in our laboratory at the base of the Rocky Mountains, where reduced atmospheric pressure results in helium boiling 0.2° lower than at sea level and nitrogen boiling about a degree lower. All this creates the need for temperature corrections to put measurement results from different laboratories on an equal footing, as well as the need for analytic temperature modeling for use in application designs.

In this section we present variable-temperature data for practical superconductors and describe a common "linear" technique for interpolating (and moderately extrapolating) the J_c–T dependence of a superconductor. This simple method enables measurements carried out at a convenient temperature (such as liquid-helium temperature) to be used to approximately predict critical currents at other temperatures.

However, before we treat J_c–T curves, such as that labeled A–C in Fig. 9.3, we first need to highlight the temperature dependence of the critical *field* of a superconductor, curve B–C in the base plane of Fig. 9.3. We start our consideration of temperature effects there because, in the highly variable world of critical-current data, the B_{c2}–T curve is the one intrinsic characteristic that is common from superconductor to superconductor. It serves as perhaps the single most useful handbook curve for determining the temperature and magnetic-field limits for practical applications.

10.4.2 CRITICAL FIELD VS. TEMPERATURE

Figure 10.15 shows the temperature dependence of the upper critical field ($B_{c2} \approx B^*_{c2}$) for many of the practical low-T_c superconductors. Except for the MgB_2 data, Fig. 10.15 is a rather old figure (1974), but nevertheless still useful because most of the superconductor advancements since then have been to increase J_c, not to change the B_{c2}–T curve. Figuratively speaking, the base of the critical surface in Fig. 9.3 remains a fairly stable foundation for the variable critical-current superstructure above it. In the intervening decades, the main noteworthy change in the base plane data has been the addition of third and fourth element additions to Nb_3Sn to increase the 4.2 K value of B^*_{c2} from about 21 T to about 25 T, and the addition of a new superconductor (but old material), MgB_2.

As mentioned in the introductory definitions to Sec. 10.3, there is usually not much difference (less than about a tesla) between the upper critical field (B_{c2}) and the *depinning* critical field (B^*_{c2} or B_{irr}) in low-T_c superconductors (except for MgB_2). For high-T_c superconductors, however, there can be a much larger difference. The important practical parameter is the latter, the depinning critical field, since it determines the ability of the superconductor to carry current. It is an extrinsic parameter that varies with magnetic-field orientation and doping.

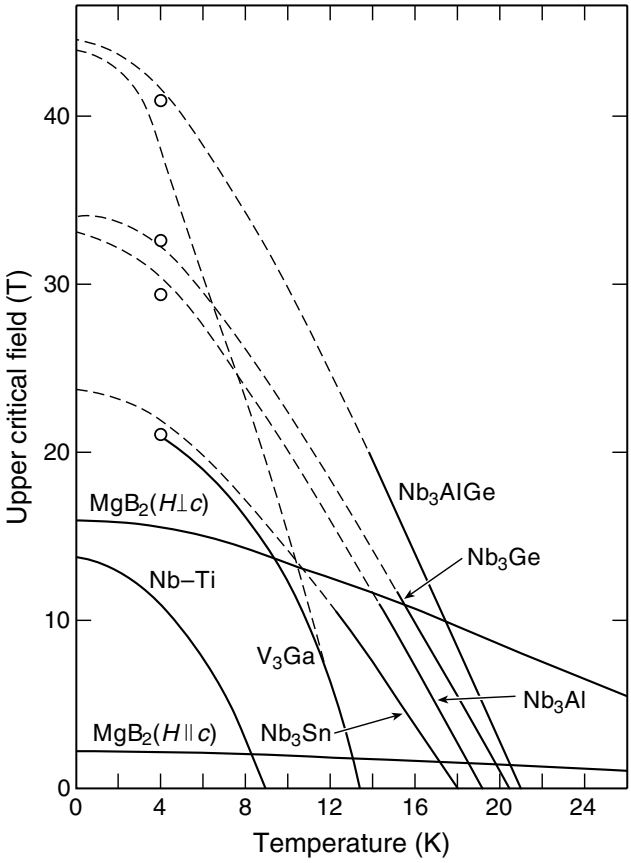

Fig. 10.15 Upper critical field vs. temperature for several low-T_c superconductors. The high- field open-circle data points at 4.2 K were obtained with pulsed fields. The solid lines correspond to data obtained in dc fields, and the dashed lines were calculated (assuming no paramagnetic limiting). (Adapted from Fietz and Rosner 1974.)

Figure 10.16 shows values of B_{irr} for optimized high-T_c superconductors, as well as MgB_2. From Fig. 10.16, we see that Bi-2212 has application only at temperatures below the liquid-nitrogen range. On the other hand, Bi-2223 accesses the liquid-nitrogen range but is limited to low-field applications; Bi-2223 can nevertheless be used for transmission lines and transformers over this range. YBCO, Hg-1212, and Tl-1223 have application potential in both high and low magnetic fields at liquid-nitrogen temperature, enabling their use in liquid-nitrogen-cooled motors, generators, and electromagnets.

10.4.3 CRITICAL CURRENT vs. TEMPERATURE

Comparisons among different samples measured at different temperatures often need to be normalized to a common temperature, especially at temperatures above $T_c/2$ where the J_c–T curve (curve A–C in Fig. 9.3) becomes increasingly sensitive to temperature as it approaches the B_{c2}–T curve in the base plane of the figure.

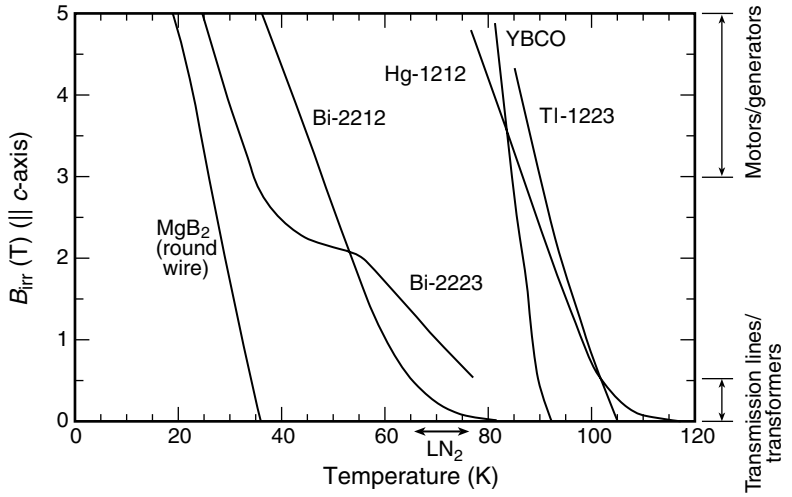

Fig. 10.16 Irreversibility field (parallel to the *c*-axis) vs. temperature for several high-T_c superconductor films (from Christen 2000) and round-wire data for high-pressure sintered polycrystalline MgB_2 (from Kumakura et al. 2001).

It is worth reemphasizing that for precise critical-current measurements, such normalization is not possible unless the sample temperature is recorded at the time of the critical-current measurement. This usually happens automatically for variable-temperature cryostats, where the temperature is recorded by a thermometer attached to the sample holder. On the other hand, for the more common case of I_c measurements in boiling-liquid helium or nitrogen, the vapor pressure above the liquid in the dewar must be recorded, from which we determine the temperature with the vapor-pressure table in Appendix A5.1. As described in Chapter 5, note the pressure inside the dewar as well as the approximate height of the liquid above the sample, because the hydrostatic head can significantly raise the temperature at the sample, especially for denser liquid nitrogen (see Appendix A5.1). Better yet, monitor the temperature at the sample with a cryogenic thermometer thermally connected to the sample or sample holder (Sec. 5.3.1).

With the measurement temperature in hand, it is then possible to convert the critical-current data from the arbitrary measurement temperature to a standard temperature such as the boiling temperature of liquid helium or liquid nitrogen at atmosphere pressure (4.230 K and 77.36 K, respectively). For small corrections, perhaps the most common technique is the *linear* method, described next. This technique applies mainly to low-T_c superconductors. A more general technique, which has potential applicability to high-T_c superconductors as well, utilizes the temperature scaling law to convert an entire J_c–B curve (linear or not) from one temperature to another. The scaling technique is described in Sec. 10.6.3.

10.4.4 LINEAR METHOD FOR CALCULATING TEMPERATURE CHANGES IN THE CRITICAL CURRENT

In this section, we illustrate the linear interpolation technique. This method consists of approximating the temperature dependence of the critical current of common technical superconductors with a linear relationship. However, the technique does not work well for all

superconductors, but for many of the low-T_c superconductors it has utility for corrections over a limited temperature range. It is useful mainly because it is so simple.

For example, J_c–T data are shown for several *low*-T_c superconductors at constant magnetic-field levels in Figs 10.17 through 10.19. The data in these linear plots show that for many of the common low-T_c superconductors, a linear fit is a fairly good approximation for interpolating between data points in A-15 superconductors such as Nb_3Sn and V_3Ga, and in Nb–Ti at higher magnetic fields. (Note that the J_c–T data shown earlier in Fig. 9.3 appear nonlinear because they were plotted on a semi-log plot.) Usually, the linear relationship breaks down close to where J_c approaches zero because of material inhomogeneities, but this regime is of little practical importance since critical-current densities there have usually dropped below usable levels.

For *high*-T_c superconductors, on the other hand, J_c does not usually decrease linearly with temperature, except for some YBCO conductors at 0 T. Figure 10.20 shows J_c–T data for several HTS materials at zero magnetic field. Figures 10.21 through 10.23 show in-field data

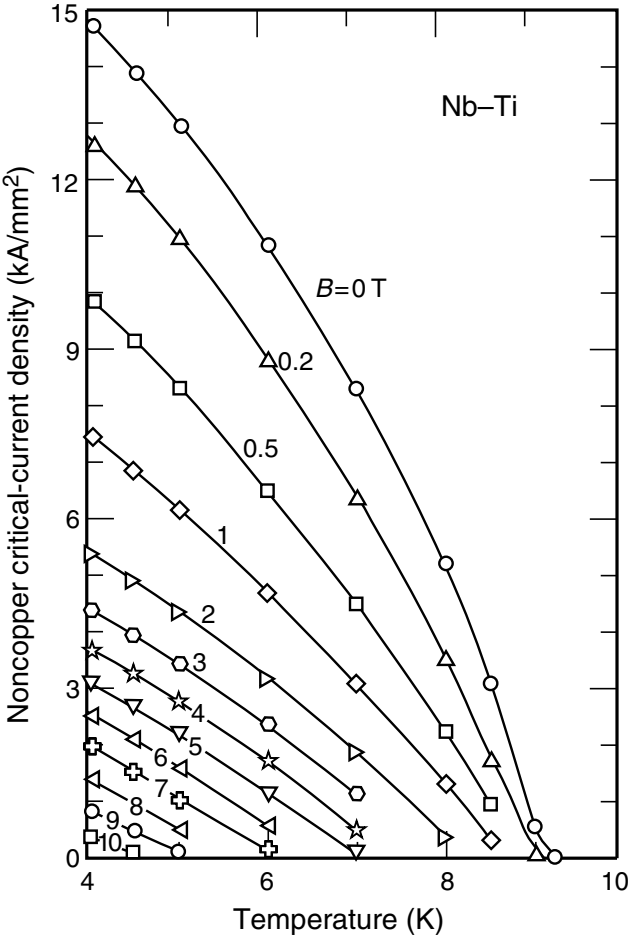

Fig. 10.17 Temperature dependence of the critical-current density of a Nb–Ti/Cu multifilamentary wire at different magnetic fields, showing the approximately linear decrease of J_c with temperature at higher magnetic-field levels (from Goodrich and Stauffer 2003).

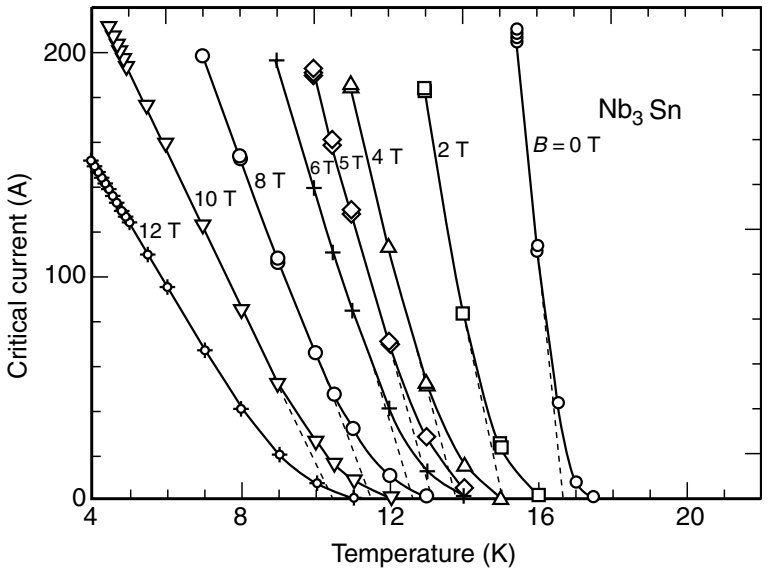

Fig. 10.18 Temperature dependence of the critical current of Nb_3Sn multifilamentary wire at different magnetic fields (from Goodrich et al. 1998).

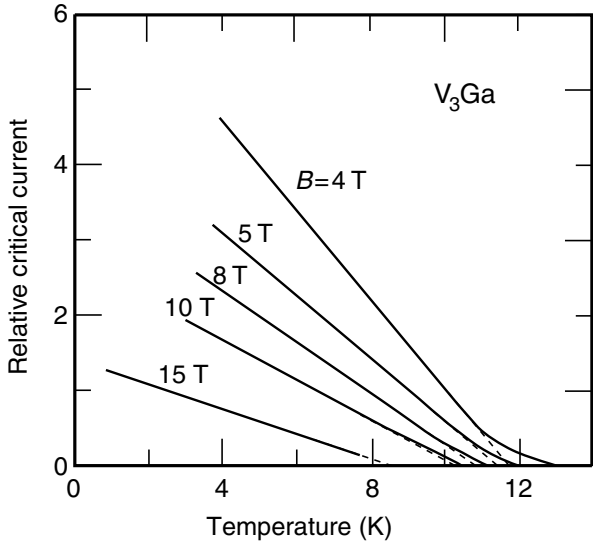

Fig. 10.19 Temperature dependence of the critical current of V_3Ga at different magnetic fields (from Iwasa and Montgomery 1975).

for YBCO, Bi-2212, and Bi-2223. None of them show a linear relationship, except possibly YBCO at zero field. Interpolating along these J_c–T curves thus requires data that are spaced fairly closely, and each curve should be fit to a nonlinear function.

For low-T_c superconductors (and possibly YBCO at 0 T), the most accurate way to apply the linear-temperature method is to measure I_c at two temperatures near the desired temperature

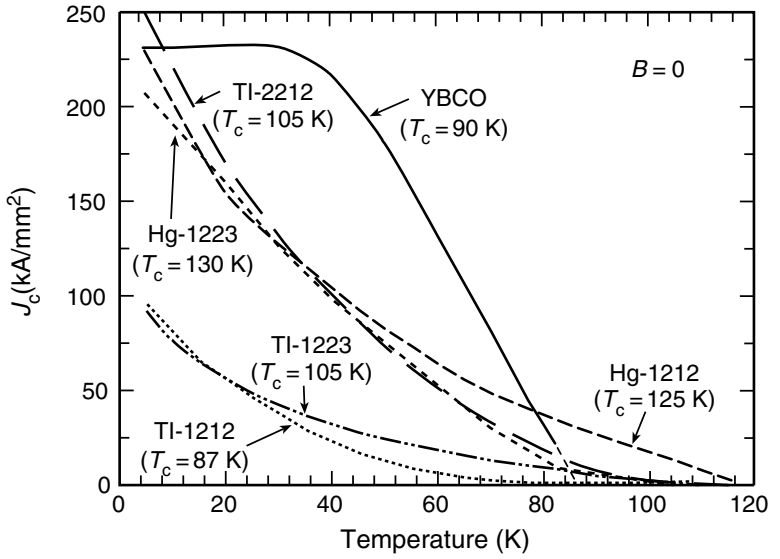

Fig. 10.20 Temperature dependence of the critical current of several high-T_c superconducting thin films at zero magnetic field (from Wu 2000).

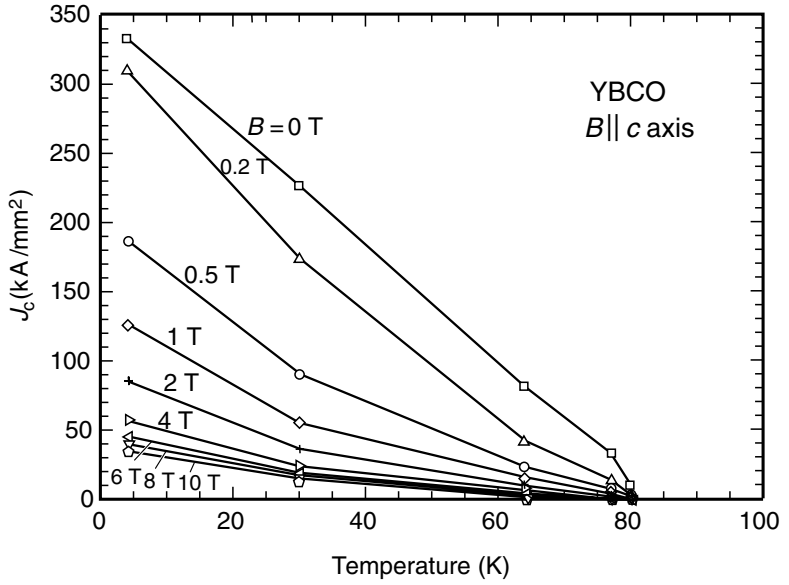

Fig. 10.21 Temperature dependence of the critical current of a YBCO-coated conductor at different magnetic fields (from Feenstra and Verebelyi 1999).

and interpolate or extrapolate by using the measured slope. For example, with samples directly immersed in a liquid cryogen such as liquid helium, the dewar can be partially evacuated to lower the cryogen temperature a degree or two. The dewar can also be overpressured about 1 atm to raise the temperature a degree to get a measurement of the slope of the I_c–T characteristic.

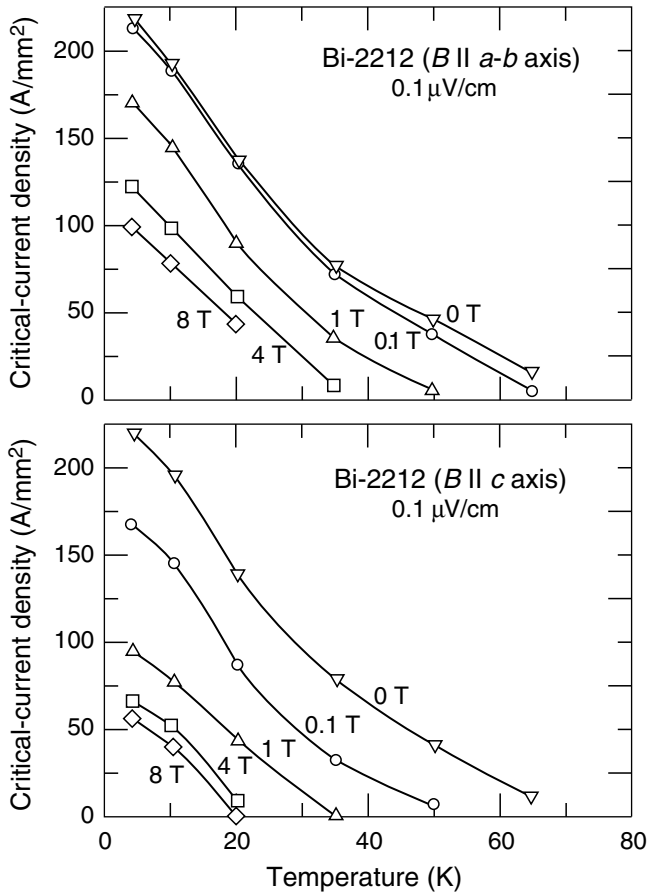

Fig. 10.22 Temperature dependence of the critical current of a Bi-2212 multifilamentary tape at different magnetic fields: upper graph—field parallel to *a–b* plane; lower graph—field parallel to *c* axis (from Goodrich and Stauffer 2001).

➔ It is worth reemphasizing that, when raising the temperature of the liquid cryogen, be sure the dewar is designed to withstand the overpressure and protect the dewar with two *pressure-relief valves* (two for redundancy in case one freezes). To break up temperature stratification, also be sure to heat the liquid cryogen with a bubbler resistance heater placed in the *bottom* of the dewar (see Sec. 1.2.1 for details).

Although this variable-temperature process is the most accurate, it takes extra measurement time, which, unfortunately, is why it usually is not used.

The more common (and less accurate) method is to make the correction in terms of tabulated "standard" values of an *effective critical temperature* T_c^* at each magnetic field. The effective critical temperature is the temperature at which the critical current extrapolates to zero along a straight-line approximation. This is shown for the data in Figs 10.17 through

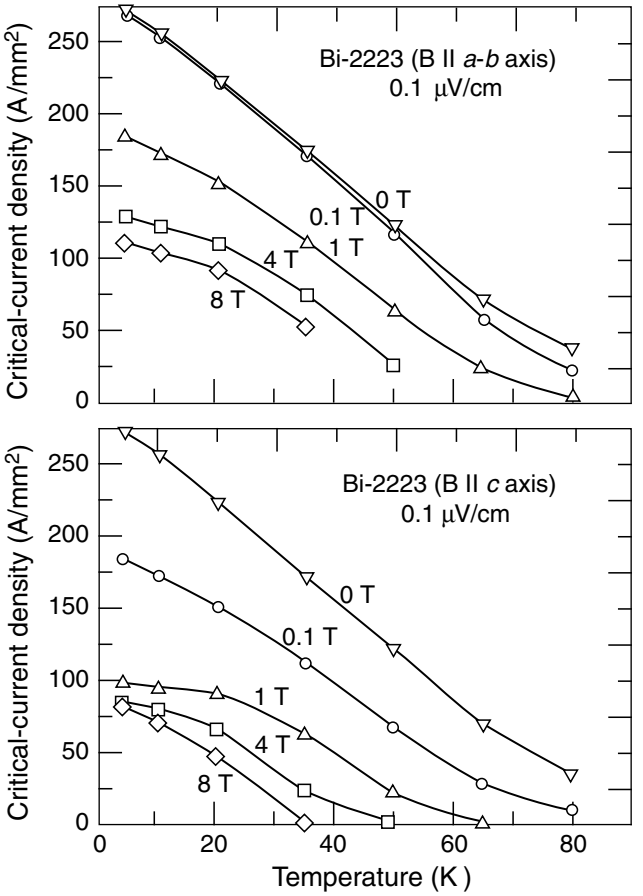

Fig. 10.23 Temperature dependence of the critical current of a Bi-2223 multifilamentary tape at different magnetic fields: upper graph—field parallel to *a*–*b* plane; lower graph—field parallel to *c* axis (from Goodrich and Stauffer 2001).

10.19, and for the zero-field curve in Fig. 10.21. Although critical current is highly variable from sample to sample, T_c^* is a more consistent material property and so handbook values are generally useful, albeit with less accuracy than an interpolation between two closely spaced measured values. Approximate values of T_c^* have been compiled in Appendix A10.1 for most of the technical low-T_c superconductors.

With a single known value of $I_c(T_1)$ at temperature T_1, handbook values of T_c^* can be used to approximately determine $I_c(T)$ at an arbitrary temperature T:

$$\frac{I_c(T)}{I_c(T_1)} = \frac{T_c^* - T}{T_c^* - T_1}. \quad \text{Linear approximation} \tag{10.14}$$

Example: Assume that we have just completed the measurement of I_c–B on a Nb–Ti superconductor immersed in liquid helium. Furthermore, we have been diligent in our attention to details and hooked up a little electric sensor and measured the pressure in the vapor space above the liquid helium to be 104 kPa (1.04 bar)—that is, the lab is near sea level, it is a beautiful day with a high pressure outside, and we checked to ensure that there was no restriction of helium-vapor flow as it vented our dewar. Our pressure corresponds to a helium-sample temperature of 4.258 K (from Appendix A5.1, neglecting any hydrostatic head correction).

Suppose we measured the critical current under these conditions to be 375 A at 7 T. We want to compare this value with data for similar conductors obtained in other laboratories, so we need to normalize the data to the boiling temperature (4.230 K) of liquid helium at standard atmospheric pressure.

To make the correction with Eq. (10.14), we first look up the effective critical temperature T_c^* for Nb–Ti from Appendix A10.1, where we find that T_c^* at 7 T is 6.16 K (for the 4.0–4.5 K temperature range). This gives an I_c value corrected to 4.230 K of

$$I_c(4.230\text{ K}) = I_c(T_1)\frac{T_c^* - 4.230\text{ K}}{T_c^* - T_1}$$
$$= (375\text{ A})\frac{6.16 - 4.230}{6.16 - 4.258} = 380.5\text{ A}.$$

The correction is not over a great temperature range (only 28 mK), and so it is insensitive to the exact value we use for T_c^*. (For example, a 50 mK error in T_c^* would produce an error of only 0.15 A in the calculated I_c.) On the other hand, the calculated change of +5 A in I_c with temperature is significant from the standpoint of comparing data on equal terms for conductor selection and magnet design.

Corrections are much greater, of course, when comparing data measured at sea level with data measured at higher elevations. For example, a mile above sea level the boiling temperature of liquid helium is about 4.0 K, which would correspond to a considerably greater I_c correction to sea level (4.230 K) of −40 A in the above example.

We shall have more to say in Sec. 10.6.3 about a general method of making such temperature corrections based on the scaling laws, which does not require a linear $I_c(T)$ relationship.

10.5 Strain-induced changes in the critical current

10.5.1 INTRODUCTION

Stress and strain impact most things in life, and superconductors are no exception. These mechanical parameters often operate behind the scene, affecting the critical current without being recognized. The effects can be profound, however.

Substantial stress on superconductors in both magnet and transmission-line applications arises from several sources:

1. *Fabrication*: In power transmission cables or magnet construction, the superconducting wire is subjected to bending stress as it is wound onto the cable core or into the magnet coil. The conductor also experiences axial stress from pretensioning during coil winding, as illustrated in Fig. 10.24.

2. *Thermal contraction*: As the superconducting wire is cooled from the heat-treatment temperature to the operating temperature, different materials within the composite wire and within the cable or magnet structure thermally contract at different rates. The mismatch in contraction between structural materials and superconductors (such as stainless steel working against Nb_3Sn) can generate compressive strains up to 0.9%, leading to large critical-current reductions.
3. *Magnetic force*: When an electromagnet is energized, the magnetic Lorentz force acting on the superconductor can generate significant forces within the magnet windings, particularly in large magnets. In a solenoidal magnet, the magnetic *hoop* stress σ_{hoop} generated in each current-carrying turn of the coil is given by (Fig. 10.25)

$$\sigma_{\text{hoop}} = JBr, \tag{10.15}$$

where J is the engineering current density (see definition in Sec. 9.1.2), B is the magnetic-field strength, and r is the radius of the winding. In small research magnets ($r \leqslant 3$ cm), the magnetic

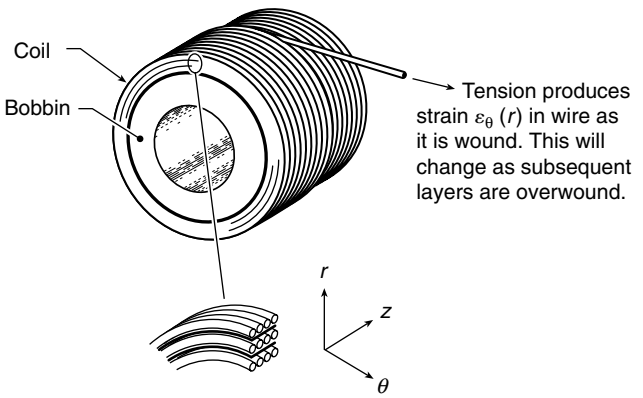

Fig. 10.24 Illustration of bending strain and pretensioning axial stress incurred during magnet winding (from Arp 1977).

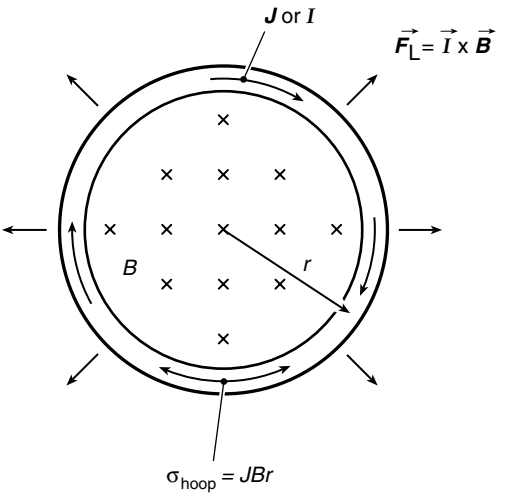

Fig. 10.25 Representation of a current-carrying loop showing the transport current density J (or current I), the associated magnetic field B, and the resultant hoop stress σ_{hoop} generated by the Lorentz force F_L acting on the winding (Ekin 1981a).

hoop stress acting along the axis of the conductor is typically less than ~100 MPa and usually does not present a serious problem. But in larger magnets, where the magnet bore can be several meters in diameter, we see from Eq. (10.15) that the magnetic hoop stress increases in proportion to the radius of the winding and can become greater than the ultimate tensile strength of superconducting composite wire.

In such large magnets, the magnetic hoop stress in the superconductor windings must be contained with an outer casing of structural material or with distributed reinforcement within the winding pack. This arrangement subjects the superconductor to additional *transverse* stress as the magnetic Lorentz force presses the conductor against the containment structure.

The response of the critical current to these stresses and strains ranges from little or no effect in some superconducting materials, to extreme sensitivity in others. For example, in ductile alloy superconductors, such as Nb–Ti, not much happens until eventually the wire breaks, usually at strains well above 1%. This explains the greater popularity of Nb–Ti for magnet construction, but Nb–Ti is restricted to magnetic fields less than about 8 T at 4.2 K (see Fig. 10.5). For high-magnetic-field (>10 T at 4.2 K) or high-temperature (>10 K) applications, the only choice is to use brittle superconductors such as Nb_3Sn or the high-T_c ceramic materials, both of which are considerably affected by strain.

Reversible strain effect

Strain can produce a large *reversible* change in the critical current of most practical superconductors, including low-T_c superconductors with the A-15 crystal structure (such as Nb_3Sn, V_3Ga, and Nb_3Al); Chevrel-phase superconductors (such as $PbMo_6S_8$); and high-T_c superconductors (such as YBCO), where the effect is significant particularly at liquid-nitrogen temperatures and above.

The effect is not introduced simply through fracture of the superconductor; it is an intrinsic effect. The abscissa of Figure 10.26 shows axial strain (applied longitudinally along the axis of the conductor) and its effect on the critical current of Nb_3Sn. As the applied strain is increased, the critical current at first rises, reaches a maximum at ε_m, and then decreases. Figure 10.26 shows that an axial strain of only 0.2% applied to this particular Nb_3Sn wire at 14 T changes the critical current by more than 20%. So the effect is not subtle. Remove the strain, and the critical current again *reversibly* retraces itself. This reversible behavior continued in this conductor up to an applied strain of about 0.8% (more on this limit in the next section).

Figure 10.26 is similar to the family of curves (e.g. curve D–E) shown in the three-dimensional plot of Fig. 9.4, except in Fig. 10.26 where all the curves are collapsed onto the I_c–ε plane. Also, the abscissa of the raw data in Fig. 10.26 is expressed in terms of the strain ε *applied* to the composite wire, rather than the *intrinsic* strain ε_0 of Fig. 9.4, which is defined as

$$\varepsilon_0 \equiv \varepsilon - \varepsilon_m. \quad \textit{Intrinsic} \text{ strain definition} \tag{10.16}$$

The intrinsic strain ε_0 is a useful parameter because it allows us to express axial-strain results more universally in terms of a quantity that more nearly represents the strain experienced by just the superconducting component of the composite conductor. That is, the other materials in the composite wire place the superconducting material under compressive prestrain ε_m, a

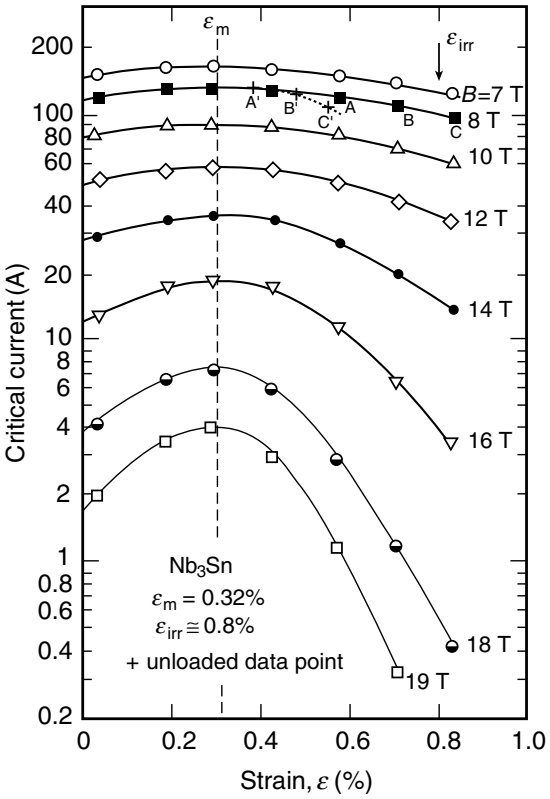

Fig. 10.26 Critical current I_c of a Nb_3Sn conductor as a function of axial strain for different magnetic fields applied perpendicular to the current direction (from Ekin 1980a, 1984). Data points designated by a + symbol (and labeled by primed letters) denote the I_c measured after unloading from the data point labeled by the corresponding unprimed letter. The strain ε_m (where I_c is a maximum) is 0.32% for this sample, and the irreversible damage strain limit ε_{irr} (where the curve becomes irreversible upon unloading) is about 0.8%.

variable quantity that depends on the relative amounts and properties of the materials in the composite. These changeable effects are effectively eliminated by the definition of Eq. (10.16), as shown below by the fact that data from different composites normalized to their peak values fall on nearly the same intrinsic strain curve.

From the definition given by Eq. (10.16), we see that the intrinsic strain is zero at ε_m (the strain where I_c is a maximum in Fig. 10.26), positive to the right of ε_m where the superconducting material in the composite is under axial *tension*, and negative to the left of ε_m where the superconducting material is under axial *compression*. We will use the intrinsic strain parameter extensively in the rest of this chapter to formulate general expressions that remove the variability of the compressive prestrain from sample to sample. Three-dimensional-strain effects (Hoard et al. 1980; Welch 1980; ten Haken et al. 1994; Markiewicz 2004) are actually incorporated in this representation of axial strain, as described in Sec. 10.5.5.

In low-T_c superconductors, the reversible-strain effect is a fundamental property of superconductors with a soft crystal structure at low temperatures, such as the A-15 and Chevrel-phase crystal structures. It does not occur in superconducting materials with more robust crystal

structures like the B1 or Laves-phase superconductors. More technically, the magnitude of reversible strain effects correlates closely with the degree of phonon anharmonicity or lattice softening in the crystal structure (Ekin and Welch 1985). These effects are significant in crystal structures such as the A-15 and Chevrel-phase structures, which are on the verge of transforming from a cubic crystal structure to a martensitic structure. On the other hand, the B1 or Laves-phase materials are very stable with no detectable lattice softening. Recently, the effects of phonon anharmonicity on the critical temperature have been calculated by Markiewicz (2004) and shown to quantitatively account well for the observed strain effect. The results of this calculation will be considered briefly in Sec. 10.5.5.

The intrinsic reversible strain effect strongly influences the use of most practical low-T_c superconductors, as well as the liquid-nitrogen operation of high-T_c superconductors (Cheggour et al. 2003, 2005). It becomes a major design consideration for large magnets and for rotating machinery such as generators and motors.

Irreversible strain limit

As alluded to above, the reversible behavior of the data in Fig. 10.26 ceases when the conductor is strained beyond an *irreversible* strain limit ε_{irr}. We can see this transition by focusing on the 8 T curve in Fig. 10.26. After the sample is loaded to point A, it is then unloaded and the strain springs back to point A′. (It does not spring back all the way to zero strain because some materials in the composite have been plastically deformed in tension.) When the critical current is measured after unloading, we find that it has *reversibly* returned to point A′, that is, it falls on the original I_c–ε curve. When the sample is loaded to point B, the corresponding unloaded point B′ still falls fairly well on the original curve. But after loading to point C, the unloaded critical current C′ has fallen significantly below the original curve, indicating that the wire has been *irreversibly* damaged in loading from point B to C. If we had continued this curve to higher strains, the drop in the unloaded critical current would have been even more pronounced. Thus, the irreversible strain limit ε_{irr} for this wire occurs between strain points B and C, or about 0.8%.

The irreversible limit ε_{irr} corresponds to the strain where the superconducting filaments in the composite wire start to crack and are permanently damaged. It is an important engineering parameter that represents an overriding limit to everything else we say here about the reversible effects of strain. It can be taken as a handling limit or design limit that must not be exceeded at any point in the life of the superconductor (device fabrication, cool-down, or operation).

Typically, the irreversible strain plays a more limiting role in the bismuth-based high-T_c superconductors than it does in YBCO-coated conductors or Nb_3Sn wires, because bismuth superconductors have a weaker plate-like structure. Figure 10.27 shows the irreversible strain effect in an early Bi-2223 multifilamentary tape. The data show that, in *tension*, the ε_{irr} limits are fairly small, typically in the range of only 0.2–0.4%. Similar results are obtained in Bi-2212. More-recently fabricated Bi-based superconductors have considerably higher critical-current densities than those of the early bismuth conductors, but the strain limits are still comparable. For YBCO films, on the other hand, ε_{irr} is significantly higher, about 0.4–0.6% depending on the fabrication process (Cheggour et al. 2005). For multifilamentary Nb_3Sn wires, tensile ε_{irr} limits are typically about 0.6–0.7% (corresponding to *intrinsic* irreversible strains ε_{0irr} of about +0.3 to +0.5%), but ε_{irr} can range to well over 1% in very fine filament composites (Ekin 1984).

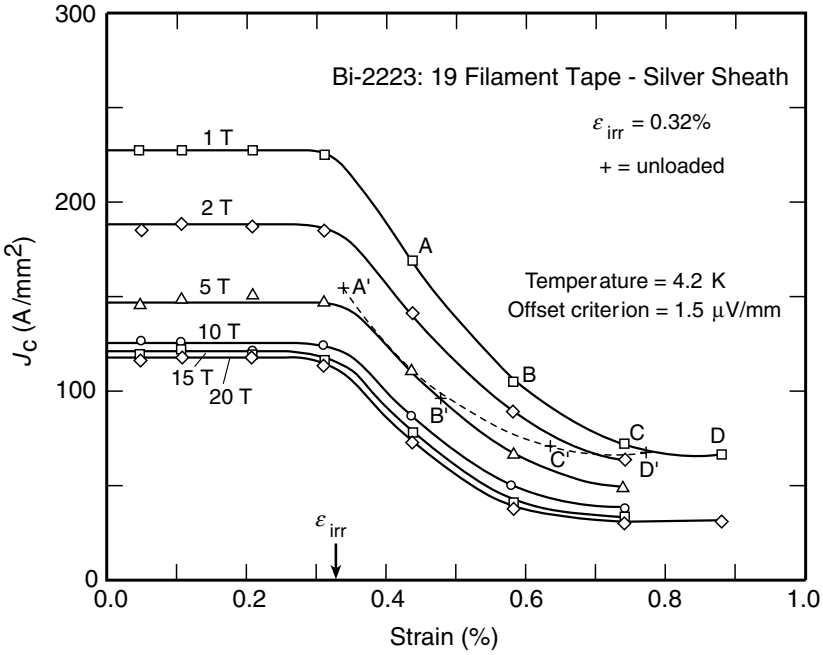

Fig. 10.27 Effect of strain on the critical current of a Bi-2223 superconductor, illustrating the field-*in*dependent irreversible strain limit ε_{irr} where the superconductor is permanently damaged (from Ekin et al. 1992). Data points designated by a + symbol (labeled by primed letters) denote J_c determined after unloading from the data point labeled by the corresponding unprimed letter. Magnetic field was parallel to the tape surface and perpendicular to the current direction.

The value of ε_{irr} in *compression* is also an important application design factor for the plate-like bismuth-based superconductors, where irreversible degradation of the critical current starts at compressive strains much less than 0.1% in both Bi-2212 and Bi-2223 (ten Haken et al. 1995, 1996). In comparison, YBCO films have compressive values of ε_{irr} typically exceeding 1%. The same high-compressive strain tolerance (>1%) also characterizes the low-T_c compounds. High-compression tolerance is a great advantage, since such materials can be fabricated like prestressed concrete (figuratively speaking). That is, they can be combined with structural materials having a large thermal contraction that places the superconductor under high-compressive strain, producing a larger tensile-strain range in service.

For the remainder of this chapter we focus mainly on *reversible* strain effects, keeping in mind that all the reversible effects we discuss are valid only for strains less than the irreversible damage limit ε_{irr}. First, we briefly consider *bending* strain, and then we consider in detail reversible *axial*-strain effects, because they are usually the main design consideration in practical applications. Axial-strain data can also be used to calculate bending strain effects.

10.5.2 BENDING STRAIN EFFECTS

Perhaps the first and most basic mechanical test of a superconductor for characterizing its fitness for applications is the effect of bending strain on the conductor's critical current. Bending

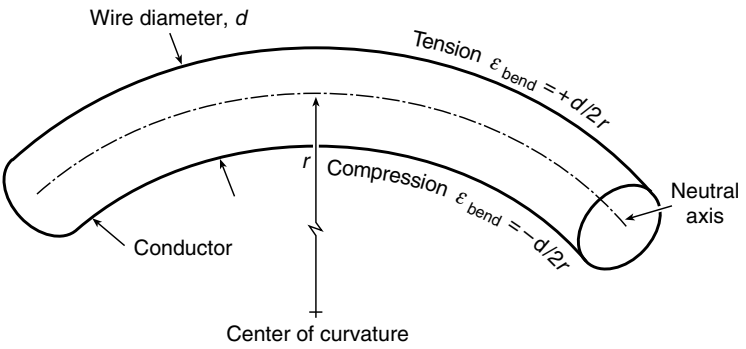

Fig. 10.28 Illustration of strain distribution introduced into a conductor from bending. Tensile strain occurs along the outside of the bend, compressive strain along the inside, and zero strain along the neutral axis (from Ekin 1981a).

strain is the simplest electromechanical effect to measure but more of a challenge to interpret, because bending produces a *distribution* of strains across the cross section of the conductor. Figure 10.28 illustrates the effect of bending strain. When a conductor of thickness d is bent around a radius r, the maximum *tensile* strain ε_{bend} along the outside of the bend is equal to

$$\varepsilon_{bend} = d/2r. \quad \text{Maximum bending strain} \tag{10.17}$$

The maximum *compressive* strain along the inside of the bend has the same magnitude given by Eq. (10.17) but the opposite sign (assuming there is no sample yielding; that is, the so-called *neutral axis* is in the middle of the conductor as illustrated in Fig. 10.28). The smaller the bending radius, the more severe the strain acting on the filaments and the greater the decrease in critical current.

The effect of bending is not very great in ductile *alloy* superconductors, such as Nb–Ti, where the conductor is so strain-tolerant it can be bent into a relatively sharp hairpin shape with little effect on the critical current. However, for brittle superconductors, such as Nb_3Sn and the high-T_c superconductors, both reversible degradation and irreversible breakage of the filaments can occur from bending strain, as shown in Fig. 10.29.

The reversible effect of bending strain on I_c is represented by dashed curves in Fig. 10.29. These bending-strain degradation curves were calculated from axial-strain data utilizing the distribution integrals given in Ekin (1980b). The calculation involves averages over the distribution of filaments within a superconducting strand and, since the strands are usually twisted, it also takes into account that each filament sees alternate tensile and compressive strain. A comparison of bending degradation with axial-strain degradation in multifilamentary wires shows that, as a general rule, it takes about *twice as much bending strain as axial strain to produce the same I_c degradation*. (That is, axial strain has more of an effect than bending strain because with axial strain, all the filaments are uniformly affected, not just those away from the neutral axis as with bending strain.)

The bending effect is predicted from axial data quite well up to the irreversible strain limit ε_{irr} (as determined by axial-strain measurements). Beyond ε_{irr}, however, bending permanently damages the superconducting filaments and I_c drops precipitously below the curve calculated

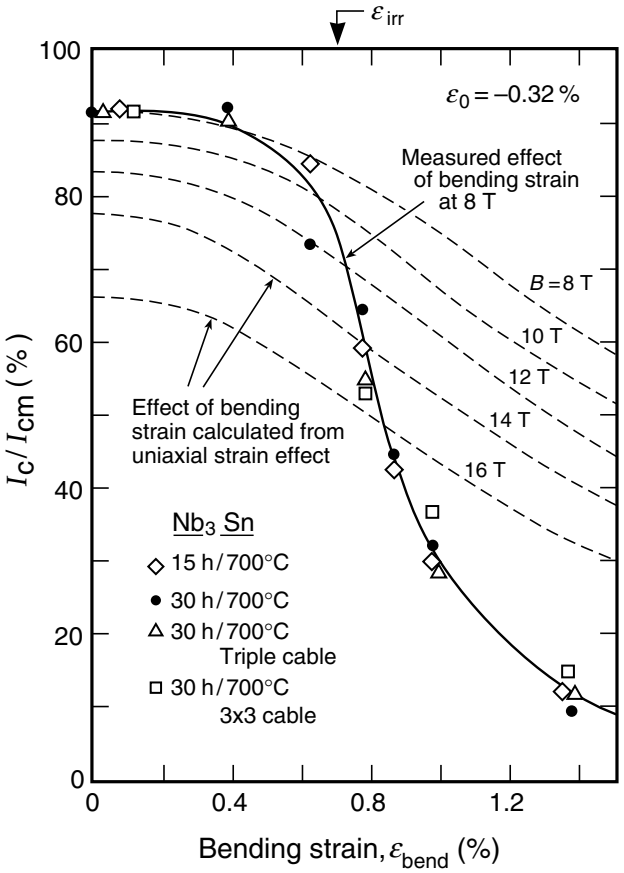

Fig. 10.29 Dependence of critical current on bending strain for Nb_3Sn superconductors measured at 8 T (solid curve is a guide to the eye for the experimental data). Dashed curves show the reversible effect of bending strain on the critical current, calculated from axial-strain measurements. The sharp drop in critical current from bending strain occurs at the irreversible strain limit where filament breakage begins (from Ekin 1980b).

at 8 T. These data illustrate that the single most important parameter for bending strain is the irreversible strain limit. Since ε_{irr} is independent of magnetic field, it can be simply measured at zero magnetic field, for example with the very efficient bending-test apparatus shown in Fig. 9.19.

The ensemble of calculated curves in Fig. 10.29 also illustrates that the *reversible* decrease of I_c from bending strain does not change much with magnetic field. This is also a nice simplification, since a measurement of the effect of bending strain at a single magnetic field can serve to indicate its effect at neighboring fields.

10.5.3 AXIAL-STRAIN EFFECTS

Reversible changes in the critical current from *axial* strain (i.e. uniform stress and strain applied along the axis of a superconductor) form the basis for most of the electro-mechanical designs of superconducting magnets and transmission lines (within the damage limits set

by ε_{irr}). Axial-strain effects are thus the main focus of the remaining sections of this chapter. Apparatus for such measurements were shown in Figs 9.14 through 9.17 of Sec. 9.4.4.

Because critical current is strongly affected by axial strain, the comparison of critical-current data is strongly dependent on the prestrain level of each superconductor. As noted earlier, the prestrain is highly variable from conductor to conductor, since it is determined by the mismatch in thermal contraction rates of the particular materials in the composite. All too often, critical-current values are compared without first normalizing the data to a common intrinsic strain level. Usually, comparisons are made in terms of I_c–B data obtained on a conductor in its initial (as-received) condition regardless of the internal strain state of the superconductor filaments. What is needed for comparisons on an equal basis is a method of transforming critical-current data to the same intrinsic strain.

The scaling laws introduced in the remainder of this text form very powerful, general tools for analytically treating these strain effects. The resulting analytic expressions are useful for addressing the data comparison problem just mentioned, as well as for application design, particularly the design of large magnets or high-field systems where magnetic forces become a significant design factor. (As we will see, the scaling relations are also very useful for modeling temperature effects and combined strain-and-temperature effects.)

In the following material, we shall narrow the focus to reversible strain effects in *low-*T_c superconductors, since much more strain-effect data are available for these materials, and the underlying mechanisms are much better understood at present than for high-T_c superconductors. Strain effects in high-T_c superconductors are more complex since they are affected not only by strain-induced changes in bulk pinning (as for low-T_c materials) but also by strain effects on the grain boundaries, a research area that is only beginning to be investigated.

Where sufficient scaling data are available, good statistical data correlations are observed. However, complete data correlations for advanced types of low-T_c superconductors are still being measured. The scaling law treatment described here is therefore offered as a useful, consistent framework that should serve to systematize future data. The data correlations available so far have yielded the "standard" scaling parameter values tabulated in Appendix A10.2a (described in more detail below), and they should at least form a practical starting point for a growing database of scaling-parameter values that will develop over time.

In Secs 10.5.4 through 10.5.7 we first focus on strain scaling, and then, in the remaining sections of the text, on temperature scaling and unified strain-and-temperature scaling. In Sec. 10.6 we also introduce an alternative transformation method for data comparisons and magnet design that is much simpler to use than the usual straight application of scaling laws. With this method, a set of $I_c(B)$ data obtained at one strain level can be transformed to another strain level with far fewer scaling parameters. Whichever technique is used, the basis in both cases rests on the scaling laws, which we now introduce starting with the strain scaling law.

10.5.4 STRAIN SCALING LAW FOR LOW-T_c SUPERCONDUCTORS

The scaling laws have their basis in the common pinning-force behavior of a given class of superconductors. The strain scaling law describes the effects of strain on the Lorentz force F_L—the magnetic force (per unit length) acting on each magnetic vortex in the superconductor.

[The Lorentz force was introduced earlier in Eq. (10.8) of Sec. 10.3.1; the critical value of the Lorentz force corresponds to where flux motion starts, that is, $F_L \equiv I_c B$.]

The magnetic-field dependence of the critical Lorentz force is an important characteristic that determines the usefulness of various superconducting materials, especially at high magnetic fields where the differences can be substantial. A comparison of this characteristic for a number of high-field superconductors was shown earlier in Fig. 10.8.

The strain scaling law is simply the observation that the *shape* of the F_L–B curves in Fig. 10.8 is not altered by strain. Mathematically, this can be stated as (Ekin 1980a)

$$F_L \equiv I_c B = g(\varepsilon) f(b). \tag{10.18}$$

Strain scaling law (SSL) (Valid for fixed temperature $T \ll T_c$)

valid for fixed temperature $T \ll T_c$ (e.g. at 4.2 K in Nb_3Sn). In Eq. (10.18), $g(\varepsilon)$ is a *function of strain only* (not magnetic field) and $f(b)$ is an arbitrary pinning-force function that depends only on the *reduced* magnetic field

$$b \equiv \frac{B}{B^*_{c2}(\varepsilon)},$$

where $B^*_{c2}(\varepsilon)$ is the strain-dependent effective upper critical field at temperature $T \ll T_c$. Thus, in the general representation of $f(b)$ given by Eq. (10.10) [i.e. $f(b) = b^p(1-b)^q$], the exponents p and q are *independent of strain and magnetic field*. The usefulness of the strain scaling law stems from the fact that strain enters only through the function $g(\varepsilon)$ and its effect on the critical field $B^*_{c2}(\varepsilon)$ and does not otherwise affect $f(b)$. That is all the strain scaling law entails, but it is very powerful for modeling and predicting the effects of strain on practical superconductors, as we shall illustrate below.

The parameterization of the strain function $g(\varepsilon)$ is quite simple at moderate intrinsic strains, that is, within about $\pm 0.5\%$ of the peak in the $I_c(\varepsilon)$ curve. This strain range is important from a technological standpoint, because it is the strain range where superconductor critical currents are highest and therefore where most magnets are designed. (The case of high-compressive strains is more complex. However, it is sometimes important for certain applications and is described separately in Sec. 10.5.6.) Within this moderate strain range on each side of the peak in $B^*_{c2}(\varepsilon)$, $g(\varepsilon)$ can usually be simply represented as a power of $B^*_{c2}(\varepsilon)$,

$$g(\varepsilon_0) = g(0)\left[\frac{B^*_{c2}(\varepsilon_0)}{B^*_{c2}(0)}\right]^s. \tag{10.19}$$

Parameterization of prefactor $g(\varepsilon)$ using $B^*_{c2}(\varepsilon)$ at $T \ll T_c$

$\varepsilon_0 \equiv \varepsilon - \varepsilon_m \quad (-0.5\% < \varepsilon_0 < \varepsilon_{0irr})$

where $g(0)$ and $B^*_{c2}(0)$ are the values of $g(\varepsilon_0)$ and $B^*_{c2}(\varepsilon_0)$ at $\varepsilon_0 = 0$, and s is an exponential constant, all of which are independent of strain and magnetic field (Ekin 1980a). Values of s are tabulated in Appendix A10.2a for many of the A-15 superconductors at liquid-helium temperature.

The applicability of Eq. (10.19) is, of course, limited to tensile strains below the point where superconductor filament breakage starts to occur. Typically, the intrinsic irreversible strain limit ε_{0irr} has a value between +0.3% and +0.5% for Nb_3Sn, as described in Sec. 10.5.1. In the following sections, we will use a nominal value for ε_{0irr} of +0.4% to represent the upper strain limit of validity of Eq. (10.19), keeping in mind that this can vary depending on the individual conductor. (Usually, composites with large filament diameters or fused filament clusters have lower values of ε_{0irr}, whereas conductors with small filament diameters, such as Nb_3Al or certain Nb_3Sn conductors, have larger irreversible strain limits.)

Substituting Eq. (10.19) into Eq. (10.18), and substituting Eq. (10.10) for $f(b)$, we find the strain scaling law can be parameterized by the relatively straightforward expression

$$I_c B = g(0)\left[\frac{B^*_{c2}(\varepsilon_0)}{B^*_{c2}(0)}\right]^s b^p (1-b)^q.$$

Parameterization of the SSL using $B^*_{c2}(\varepsilon)$ at $T \ll T_c$

(Valid for fixed temperature $T \ll T_c$ and $-0.5\% < \varepsilon_0 < \varepsilon_{0irr}$) (10.20)

This is a great simplification. With Eq. (10.20), the problem of determining the strain dependence of the critical current of most low-T_c superconductors at liquid-helium temperature is reduced to knowing the strain dependence of $B^*_{c2}(\varepsilon_0)$, a nearly universal function for each class of superconductor.

10.5.5 NEARLY UNIVERSAL EFFECT OF STRAIN ON THE UPPER CRITICAL FIELD

Figure 10.30(a) shows the effect of axial strain on the upper critical field $B^*_{c2}(\varepsilon_0)$ at 4.2 K for a number of binary Nb_3Sn superconductors. The data correlation shows that the effect of elastic strain on B^*_{c2} at moderate strains ($-0.5\% < \varepsilon_0 < +0.5\%$) is nearly universal for different multifilamentary wires made from the same superconducting material. It depends on neither the fabrication details of the wire nor its specific composite geometry.

Figure 10.30(b) shows the close correlation between the functions $g(\varepsilon_0)$ and $B^*_{c2}(\varepsilon_0)$ over this strain range. For binary Nb_3Sn, this leads to simply $s = 1$ in Eqs (10.19) and (10.20). For other types of conductors the two functions are also simply related by Eq. (10.19), with s not necessarily unity. Values of s for a number of types of conductors are given in Appendix A10.2a. [Occasionally, data for some conductors are characterized by unsymmetrical values of the parameter s; that is, s^- for compressive intrinsic strain ($\varepsilon_0 < 0$) and s^+ for the tensile side ($\varepsilon_0 > 0$). Further data correlations are needed to see if such unsymmetrical values of s are "standard" for particular superconductor classes.]

Similar to the data correlation in Fig. 10.30(a), Fig. 10.31 presents correlations of $B^*_{c2}(\varepsilon_0)$ for *ternary* Nb_3Sn superconductors with additives (Ti, Hf, Ga, Ta, or H), as well as for most of the other high-field A-15 superconductors. These data show that ternary Nb_3Sn conductors can have a $B^*_{c2}(\varepsilon_0)$ strain sensitivity comparable to that of binary Nb_3Sn (for small amounts of additives) or significantly larger (for larger amounts of additives). (The effect of additives to enhance the strain sensitivity is described in more detail at the end of this section.) Figure 10.31 also shows that, among A-15 superconductors, the upper critical field of Nb_3Al has the smallest intrinsic sensitivity to axial strain, about one-fifth that of Nb_3Sn.

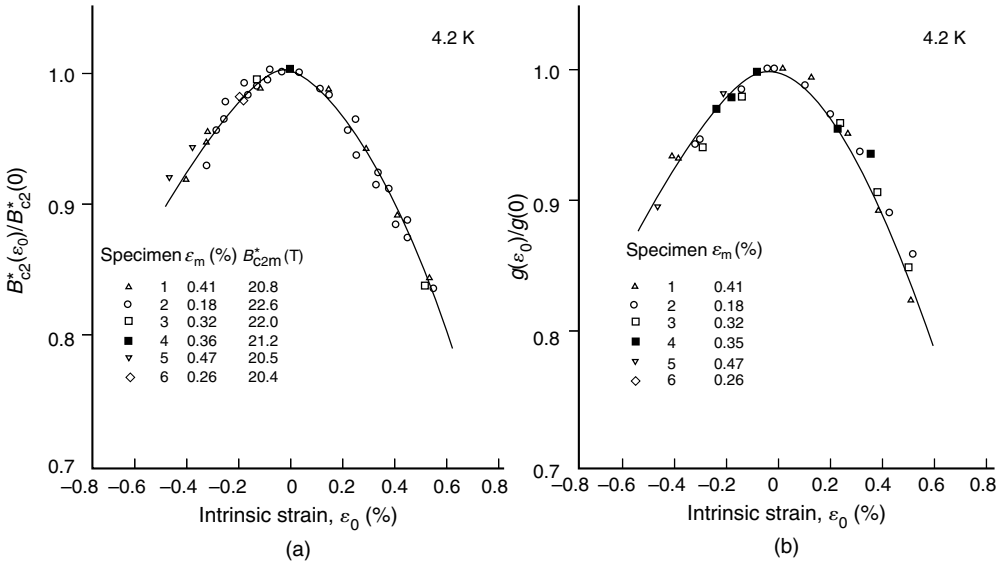

Fig. 10.30 Correlation of data for binary multifilamentary Nb_3Sn wires showing the nearly universal effect of axial strain on (a) the effective upper critical field $B^*_{c2}(\varepsilon_0)$ at 4.2 K and (b) the strain-scaling prefactor $g(\varepsilon_0)$ in Eq. (10.18). The results are shown in terms of the *intrinsic* strain ε_0 experienced by the superconducting material, defined as $\varepsilon_0 \equiv \varepsilon - \varepsilon_m$, where ε_m is the strain at the maximum. For each sample, $B^*_{c2}(\varepsilon_0)$ and $g(\varepsilon_0)$ are normalized by their maximum values at B^*_{c2} ($\varepsilon_0 = 0$) and $g(\varepsilon_0 = 0)$, respectively. The solid curves in each figure are generated from the power-law expressions of Eqs (10.21) and (10.22), respectively. For the case of binary Nb_3Sn, the normalized correlation curves for both functions are nearly identical (from Ekin 1980a).

All the data in Figs 10.30 and 10.31 can be empirically fit by the same simple power-law expression:

$$\frac{B^*_{c2}(\varepsilon_0)}{B^*_{c2}(0)} = 1 - a|\varepsilon_0|^u \qquad (-0.5\% < \varepsilon_0 < +0.4\%) \tag{10.21}$$

$$= 1 - a|\varepsilon_0|^{1.7}, \quad \text{Power-law representation of } B^*_{c2}(\varepsilon_0)$$

where

1. ε_0 is defined as the intrinsic strain of the superconductor ($\varepsilon_0 \equiv \varepsilon - \varepsilon_m$).
2. $B^*_{c2}(0)$ is the maximum value of B^*_{c2} that occurs at $\varepsilon_0 = 0$.
3. a is the *strain-sensitivity parameter*, which is approximately the same for superconductors of the same class of materials (i.e. made from the same superconducting material and additive concentrations). Values of a are tabulated in Appendix A10.2a for many of the technical high-field superconductors. The curves in Fig. 10.31 are slightly steeper for tension (+) than compression (−), and so the parameter a^+ is used to characterize the tensile side of the peak ($\varepsilon_0 > 0$), and a^- is used for the compressive side ($\varepsilon_0 < 0$). (The fundamental origin of the difference is described below.)

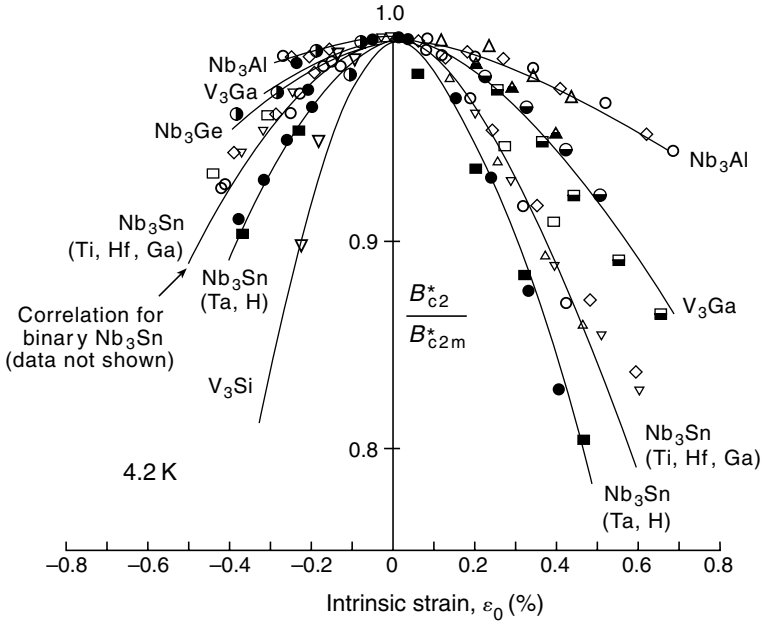

Fig. 10.31 Data correlations showing the nearly universal effect of axial strain on the effective upper critical field $B^*_{c2}(\varepsilon_0)$ of different types of bronze-process A-15 multifilamentary superconductors at 4.2 K (from Ekin 1984). The correlation curve for binary Nb_3Sn from Fig. 10.30(a) is redrawn here without the data shown in Fig. 10.30(a) so as not to mask the ternary Nb_3Sn data. The correlation for binary Nb_3Sn also well represents ternary Nb_3Sn conductors with small amounts of additives, such as titanium (~0.6 at%), hafnium, or gallium. On the other hand, the strain dependence of Nb_3Sn with larger amounts of additives, such as tantalum (0.2 at%) or hydrogen, leads to an *increased* strain sensitivity of $B^*_{c2}(\varepsilon_0)$ as shown by the steeper curve labeled Nb_3Sn (Ta,H). (Further data for the strain sensitivity of different ternary Nb_3Sn conductors are tabulated in Appendix A10.2a.) Note that only compressive data are shown for Nb_3Ge and V_3Si.

4. The exponent u in Eq. (10.21) is a nearly universal constant that consistently has a value of about 1.7 over the intrinsic strain range ($-0.5\% < \varepsilon_0 < +0.4\%$) for all the multifilamentary A-15 and Chevrel-phase superconductors listed in Appendix A10.2a. (It was unambiguously measured to be about $u = 1.7$ over this strain range by measuring the slope of a plot of $\log\{1-[B^*_{c2}(\varepsilon_0)/B^*_{c2}(0)]\}$ vs. $\log|\varepsilon_0|$ for many samples of each type of superconductor.)

The strain prefactor $g(\varepsilon_0)$ can also be represented at moderate strains with the simple power-law expression for $B^*_{c2}(\varepsilon)$; that is, substituting Eq. (10.21) into Eq. (10.19), we have

$$g(\varepsilon_0)=g(0)\left[\frac{B^*_{c2}(\varepsilon_0)}{B^*_{c2}(0)}\right]^s=g(0)[1-a|\varepsilon_0|^{1.7}]^s, \quad (-0.5\% < \varepsilon_0 < +0.4\%). \tag{10.22}$$

The characterization of the strain dependence of the prefactor $g(\varepsilon_0)$ in terms of $[B^*_{c2}(\varepsilon_0)]^s$ holds only for moderate strains ($-0.5\% < \varepsilon_0 < \varepsilon_{0\text{irr}}$). At high-compressive strains ($\varepsilon_0 < -0.5\%$) this relation generally breaks down (see Sec. 10.5.6).

The near universality of $B^*_{c2}(\varepsilon_0)/B^*_{c2}(0)$ and its power-law dependence at moderate intrinsic strains arise as a natural consequence of the effects of phonon anharmonicity on the superconducting energy gap; that is, it is a fundamental property of the crystal structure. This is shown by Fig. 10.32(a), which gives the results of a basic calculation by Markiewicz (2004) of the strain dependence of the critical temperature $T_c(\varepsilon)$ that arises from phonon anharmonicity in binary Nb_3Sn solid-filament wires and tape conductors. [The strain dependence of $T_c(\varepsilon)$ is related to $B^*_{c2}(\varepsilon)$ as described in Sec. 10.7.1.] The model results are fit well by a power law at moderate strains and, furthermore, are accurately represented by the canonical power-law exponent $u = 1.7 \pm 0.1$ for both tensile and compressive intrinsic strains. This is shown unambiguously in Fig. 10.32(b), where the model results are replotted so that the slope yields the power-law exponent without any adjustable parameters.

[More technically, the value of u at moderate intrinsic strains is determined by phonon anharmonicity through the principal part of the *second* invariant of the crystal lattice's deviatoric strain tensor. The other terms of the strain tensor (the hydrostatic term and the higher-order deviatoric-strain invariants) play a negligible role in determining u over the intrinsic peak regime (Ekin 2007). The asymmetry (i.e. the difference between the values of a^- and a^+) is also explained by the anharmonicity model, which shows that it stems mainly from the *third* invariant of the deviatoric strain tensor (Markiewicz 2004).]

Thus, at moderate strains $-0.5\% < \varepsilon_0 < \varepsilon_{0irr}$ where most magnets are designed, the consistent power-law behavior of $T_c(\varepsilon)$ and $B^*_{c2}(\varepsilon)$ arises as a physical consequence of phonon anharmonicity of the crystal lattice (through the second invariant).

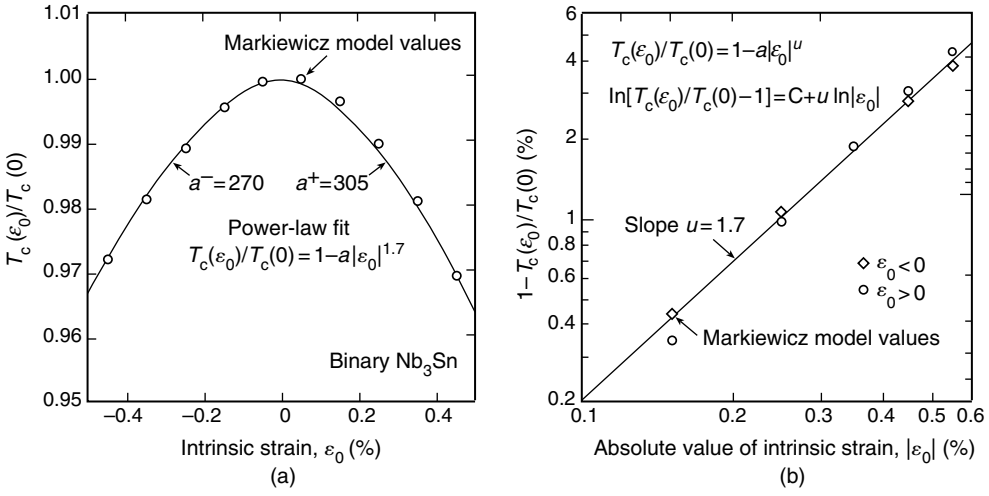

Fig. 10.32 Fundamental basis of the power law at moderate intrinsic strains ($-0.5\% < \varepsilon_0 < \varepsilon_{0irr}$): (a) Strain dependence of the critical temperature of binary Nb_3Sn calculated by introducing phonon anharmonicity into the McMillan/Kresin equation (from Markiewicz 2004). The model shows that the power-law dependence given by Eq. (10.21) arises mainly through the principal part of the second invariant of the deviatoric strain tensor. (b) Calculated results replotted as $\ln\{1 - [T_c(\varepsilon_0)/T_c(0)]\}$ vs. $\ln|\varepsilon_0|$, showing that the anharmonicity model gives the canonical power-law exponent $u = 1.7 \pm 0.1$ without any adjustable parameters for both tensile and compressive intrinsic strains.

Since ε_m is fixed experimentally by the strain where $B^*_{c2}(\varepsilon)$ is a maximum, and since u consistently has a value of ~1.7, the strain dependence of $B^*_{c2}(\varepsilon)$ over the moderate intrinsic strain range can be represented by one *free* fitting parameter, a. For a couple of decades, a has served as a strain-sensitivity parameter to characterize and compare the strain sensitivities of various conductors.

The parameter a is nearly the same for conductors of a given class of superconductors. Appendix A10.2a lists values of a for the most common types of practical superconductors: *solid-filament* multifilamentary *wires*.

In using the data of Appendix A10.2a, note that:

1. Additives can change the value of a, as shown by the two curves for Nb_3Sn in Fig. 10.31. These data and the tabulated values of a in Appendix A10.2a show that conductors made from *ternary* Nb_3Sn conductors have a greater intrinsic strain sensitivity than those made from *binary* Nb_3Sn. This appears to be a fundamental result of an increase in crystal-lattice anharmonicity with additive content.
2. For conductors that do not have *solid* filaments, values of a will differ from those listed in Appendix A10.2a. In general, wires with *tubular* filaments (or bundles of filaments that fuse into tubular structures after reaction) with bronze material in the core have significantly increased a values. This is a result of three-dimensional strain effects (Welch 1980; Hoard et al. 1980; ten Haken 1994; Markiewicz 2004), which produce increased deviatoric strain for the case of tubular filaments.
3. As noted above, the strain sensitivity is slightly smaller for compressive strains than for tensile, characterized by a value of a^- less than that of a^+. For Nb_3Sn, typically $a^-/a^+ \approx 0.75$. Generally, magnets are designed on the compressive side of the peak ($\varepsilon_0 < 0$), because this operating point provides a greater strain margin during fabrication and operation for avoiding irreversible damage at ε_{irr}. Thus, a^- is usually the more important parameter from the standpoint of application design (unless enough bending strain is present that the spread in strains extends over the peak to the tensile side).

It is worth repeating that Eq. (10.21) is valid only within the *intrinsic* peak region: $-0.5\% < \varepsilon_0 < +0.4\%$. This simple parameterization serves well for most technological designs but not all, as discussed next.

10.5.6 HIGH-COMPRESSIVE-STRAIN RANGE

Although the high-compressive-strain range ($\varepsilon_0 < -0.5\%$) is not the usual strain regime for most magnet designs, it can become significant for large magnets in which the superconducting material is subjected to thermally induced strains from structural materials with high thermal contraction rates. For example, if the superconductor is thermally reacted within a conduit of stainless steel, the superconducting filaments will be subjected to large compressive strains which develop during cool-down from the heat-treatment temperature. At high enough compressive strains ($\varepsilon_0 < -0.5\%$), $B^*_{c2}(\varepsilon_0)$ and $T^*_{c2}(\varepsilon_0)$ deviate from a simple power law (ten Haken 1994). Experimentally, the strain dependences of $B^*_{c2}(\varepsilon_0)$ and $T^*_{c2}(\varepsilon_0)$ are seen to exhibit an inflection, with the curves transitioning from a negative second derivative to a

positive one at high-compressive strains (Cheggour and Hampshire 2002; Keys and Hampshire 2003). The Markiewicz model shows that a contribution to this positive curvature arises from the third invariant of the deviatoric strain tensor (briefly described below).

However, yielding of the soft matrix materials (e.g. copper and bronze) in practical conductors at such high-compressive-strain levels may also contribute to the positive curvature, although sufficient data are not available to determine this at present. Because yielding effects are *extrinsic* (i.e. they vary from sample to sample), the fitting parameters in this regime would then lack universality for a given class of materials (unlike the intrinsic strain-sensitivity parameter a). The parameter values would then depend on factors particular to a given conductor, such as the type of matrix alloy used in their construction, annealing condition, Kirkendall voids, the internal filament pattern, and twist pitch.

It would therefore be advantageous to ensure that extrinsic parameters at high-compressive strains do not affect the intrinsic parameters at moderate strain levels. After considering a number of forms, I have found a useful relation that accomplishes this is obtained by simply adding a term to the intrinsic power law—a term that operates only at high-compressive strains,

$$\frac{B^*_{c2}(\varepsilon_0)}{B^*_{c2}(0)} = 1 - a|\varepsilon_0|^{1.7} + a_1|\varepsilon_0 - \varepsilon_0'|^{a_2}\, I(\varepsilon_0 < \varepsilon_0'), \tag{10.23}$$

where

$$I(\varepsilon_0 < \varepsilon_0') \equiv \begin{cases} 1 & \text{if } \varepsilon_0 < \varepsilon_0' \\ 0 & \text{if } \varepsilon_0 > \varepsilon_0' \end{cases}.$$

Here, $I(\varepsilon_0 < \varepsilon_0')$ is an *indicator function*, which is zero except at high-compressive strains: $\varepsilon_0 < \varepsilon_0'$, with $\varepsilon_0' = -0.005$ for Nb_3Sn. [This is readily programmed into spreadsheet programs with a conditional clause of the form: IF($\varepsilon_0 < -0.5\%$, 1 if true, 0 if false).]

In addition to the upper critical field, this form also represents the critical temperature well at high-compressive strains, as shown in Fig. 10.33 by the close fit of Eq. (10.23) to the strain effects induced by phonon anharmonicity at high-compressive strains.

Again, the salient feature of Eq. (10.23) is that *variations in the high-compression extrinsic fitting parameters* (a_1 *and* a_2) *do not change the value of the intrinsic parameter* a *characterizing the peak region*. This feature precludes the inconsistency of multiple parameters collectively altering each other, such as with a polynomial fitting function where all the parameters change whenever there is a shift in any one of those characterizing the extrinsic high-compressive-strain regime. The values of such interdependent parameters also change with the *range* of strain being fit. In contrast, the form given by Eq. (10.23) preserves a as a single, standard parameter for characterizing the strain sensitivity of superconductors over the intrinsic peak range ($-0.5\% < \varepsilon_0 < 0.4\%$) independent of extrinsic effects or the fitting range.

This form also has the advantage that a continues to serve as a nearly universal parameter for each superconductor class, useful not only for magnet design, but also for identifying erroneous data from outlier values of a.

Turning to the prefactor term $g(\varepsilon_0)$ in Eq. (10.18), at high-compressive strains ($\varepsilon_0 < -0.5\%$) the simple relationship between $g(\varepsilon_0)$ and $B^*_{c2}(\varepsilon_0)$ given by Eq. (10.19) breaks

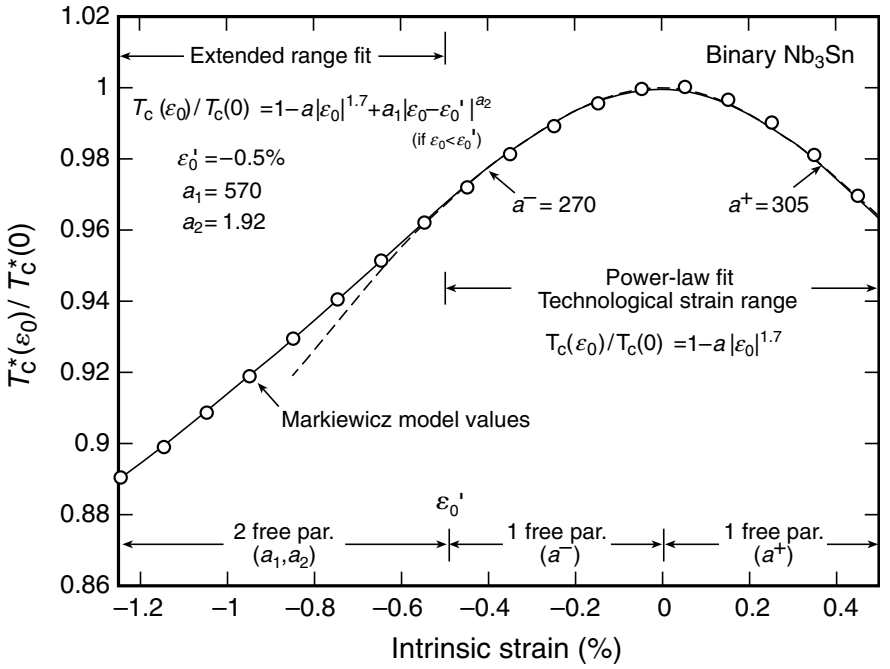

Fig. 10.33 Critical temperature of binary Nb_3Sn calculated over an extended strain range from a three-dimensional deviatoric strain model by Markiewicz (2004, 2005). The solid curve shows an extended-range fit of the model results with an expression of the same form as Eq. (10.23) for the effective upper critical field. Fitting forms of this type are useful for analytically representing the strain dependence at high compression while preserving a consistent value of the parameter a for characterizing the intrinsic peak region ($-0.5\% < \varepsilon_0 < 0.4\%$) where most magnets are designed. In the Markiewicz model, the transition to a positive second derivative at high-compressive strains mainly arises from the third invariant of the deviatoric strain tensor. Extrinsic factors, such as copper and bronze yielding or conductor damage at very high compressive strains, may also contribute to a positive curvature.

down; that is, $g(\varepsilon_0)/g(0) \neq [B^*_{c2}(\varepsilon_0)/B^*_{c2}(0)]^s$ (Ekin 2007). Thus, in this regime we represent $g(\varepsilon_0)$ by an expression of the same form as $B^*_{c2}(\varepsilon_0)$, but with its own set of fitting parameters

$$\frac{g(\varepsilon_0)}{g(0)} = [1-a|\varepsilon_0|^{1.7}]^s + g_1|\varepsilon_0-\varepsilon_0'|^{g_2} I(\varepsilon_0<\varepsilon_0'), \tag{10.24}$$

where

$$I(\varepsilon_0<\varepsilon_0') \equiv \begin{cases} 1 & \text{if } \varepsilon_0<\varepsilon_0' \\ 0 & \text{if } \varepsilon_0>\varepsilon_0' \end{cases}.$$

As before, $I(\varepsilon_0 < \varepsilon_0')$ is an indicator function, which is zero except at high-compressive strains: $\varepsilon_0 < \varepsilon_0'$, with $\varepsilon_0' = -0.005$ for Nb_3Sn. We use this particular form because it preserves the values of both a and s for the intrinsic peak region, that is, a has the same value as in Eq. (10.23)

and s has the same value as in Eq. (10.22). However, the values of g_1 and g_2 are not consistently related to those of a_1 and a_2 in Eq. (10.23). Rather, they are additional free fitting parameters needed to represent $g(\varepsilon_0)$ in this extrinsic high-compressive-strain range.

Again, "make things as simple as possible . . . ." Use the high-compression representation of $B^*_{c2}(\varepsilon_0)$ and $g(\varepsilon_0)$ in Eq. (10.18) only if necessary. For the many applications at moderate intrinsic-strain levels, it is not needed. This happens seamlessly with Eqs (10.23) and (10.24), because the indicator function automatically drops the extra term in each case, reducing these relations to the simpler fundamental power-law expression over the intrinsic peak region.

10.5.7 EXAMPLE: APPLICATION OF THE STRAIN SCALING LAW

We now illustrate a reliable procedure for determining the *values* of the strain-scaling parameters. Although we focus on the intrinsic peak region ($-0.5\% < \varepsilon_0 < +0.4\%$) in this example, the same step-by-step process would also apply to data that extend to high-compressive strains [except that Eqs (10.23) and (10.24) would be used to parameterize $B^*_{c2}(\varepsilon_0)$ and $g(\varepsilon_0)$, respectively].

Example: Table 10.3 shows critical-current data, measured at 4.2 K as a function of both magnetic field and strain, for a Nb_3Sn wire conductor. Although this is a binary superconductor with $B^*_{c2}(0)$ lower than that of ternary Nb_3Sn, we use this particular sample for illustration purposes because the compressive prestrain ε_m is high and so the data cover a fairly wide range of strain.

We want to use the strain scaling law to obtain a general analytic expression $I_c(B,\varepsilon)$ for these data.

Since the data fall within the intrinsic peak range, we utilize the simpler power-law parameterization of the strain scaling law. (The values obtained for the scaling parameters, however, could also be utilized straight away in the more general expression if we later wanted to extend the treatment to high-compressive strains.) We repeat here Eqs (10.20) through (10.22) for convenient reference:

Parameterization of the strain scaling law

(Valid for fixed temperature $T \ll T_c$ and $-0.5\% < \varepsilon_0 < \varepsilon_{0irr}$):

$$I_c(B,\varepsilon) = B^{-1} g(\varepsilon) b^p (1-b)^q = B^{-1} g(0) \left[\frac{B^*_{c2}(\varepsilon_0)}{B^*_{c2}(0)}\right]^s b^p (1-b)^q$$

$$= B^{-1} g(0) (1 - a|\varepsilon_0|^{1.7})^s \, b^p (1-b)^q \tag{10.25a}$$

where

$$\frac{B^*_{c2}(\varepsilon_0)}{B^*_{c2}(0)} = 1 - a|\varepsilon_0|^{1.7}, \tag{10.25b}$$

$$\varepsilon_0 \equiv \varepsilon - \varepsilon_m, \tag{10.25c}$$

$$b \equiv \frac{B}{B^*_{c2}(\varepsilon_0)}. \tag{10.25d}$$

1. The first step is to determine the *strain-independent* exponents p and q from one of the $I_c(B)$ data subsets. A spreadsheet example of this four-parameter fitting process was given earlier in Table 10.1 of Sec. 10.3.3 (within the context of illustrating magnetic-field interpolations). The same procedure is used here. Note that the fit is made to the Lorentz force ($I_c B$) and *not* the critical current alone, so that excessive weight is not given to fitting I_c data at low fields (where I_c is much greater than at high fields).

For this first step, select a reliable $I_c(B)$ curve at a strain level well within the reversible strain range (i.e. away from ε_{irr}). The $I_c(B)$ curve measured at the initial strain or an $I_c(B)$ curve near the peak is fine. A large range of magnetic fields is also desirable for determining both p and q, but any low-field data that might be affected by heating should be omitted before making the fit. (One way to identify such heat-affected data is to look for a rise in the n value as current is increased; generally, the n value should remain nearly constant in the vicinity of I_c.) If the data do not extend to low enough fields [i.e. $B/B^*_{c2} < b_{max} \approx 5$ T; see Eq. (10.12)], p cannot be accurately determined and it is far better to use a standard value for p than to rely on an erroneous fitted value. This is the case for the data in Table 10.3, which extend down to only ~ 7 T. So from Appendix A10.2a we use the standard value $p = 0.5$. The four-parameter fitting routine illustrated in Table 10.1 gives values of $p = 0.5$ and $q = 1.8$ for this conductor. Notice that the best value for q is less than the Kramer value ($q = 2$), even though this is a binary Nb_3Sn conductor. However, the exact values of p and q have very little effect on the resulting value of the parameter a, which we will determine in step (3).

2. Next, fix the values of the exponents p and q with the values determined in step (1) and, with a two-parameter fit, determine the values of $B^*_{c2}(\varepsilon)$ and $g(\varepsilon)$ for *each* measured strain. These values are shown in a box for each strain in Table 10.3. Note that the rms errors in Table 10.3 do not increase significantly even at the highest strain ($\varepsilon = 0.93\%$, that is, $\varepsilon_0 = 0.51\%$). This is a good test to make sure that ε_{irr} has not been exceeded and that data affected by damage are not included in the fit. A quick look at the Δ values of the individual data points also shows that there is no obvious heat-affected data included. Such heat-affected data points will fall significantly below the fitted curves (especially where I_c is highest, near the peak strain ε_m and at the low-field end of the F–B curves).

3. It is usually best to plot the $B^*_{c2}(\varepsilon)$ data obtained in step (2) on a graph similar to that shown in Fig. 10.34(a) (but without the normalization) to visually determine the peak strain ε_m and $B^*_{c2}(\varepsilon_m)$. This determines these two parameters independently of the fitting process and avoids errors that can accompany a multiparameter fitting process, especially when data are not available on a fine strain grid. After fixing ε_m and $B^*_{c2}(\varepsilon_m)$, values of a^- and a^+ are then determined from a two-parameter spreadsheet fit of Eq. (10.25b) to $B^*_{c2}(\varepsilon_0)/B^*_{c2}(0)$, with a different value of a for each side of the peak to accommodate the asymmetry: a^- for ($\varepsilon_0 < 0$) and a^+ for ($\varepsilon_0 > 0$).

A preferred procedure (once enough data are available) is to determine a consistent value for a^-/a^+, which is approximately a constant for a given superconductor class (e.g. for nearly all the Nb_3Sn conductors, binary and ternary alike, this ratio usually falls in the range of 0.70 to 0.75). By fixing the ratio a^-/a^+, finer adjustments to ε_m and $B^*_{c2}(\varepsilon_m)$ can be obtained by including ε_m and $B^*_{c2}(\varepsilon_m)$ as fitting parameters, without unduly increasing the number of free parameters. The solid curve in Fig. 10.34(a) shows the results and quality of such a fit for the $B^*_{c2}(\varepsilon)$ data for this sample.

4. The proportionality constant $g(\varepsilon_m)$ [$\equiv g(\varepsilon_0 = 0)$ in Eq. (10.25a)] is determined with the same procedure as that for evaluating $B^*_{c2}(\varepsilon_m)$, that is, visually from a plot of $g(\varepsilon)$ [e.g. the triangle symbols in Fig. 10.34(a)].

For binary Nb_3Sn, the strain dependence of $g(\varepsilon)$ over the intrinsic peak range corresponds almost identically to that of $B^*_{c2}(\varepsilon)$, as shown for this sample by the correspondence of the two data sets in Fig. 10.34(a) (and earlier for the data correlations in Fig. 10.30). For other types of conductors the two functions are not necessarily the same, but they are usually simply related by the exponential constant s.

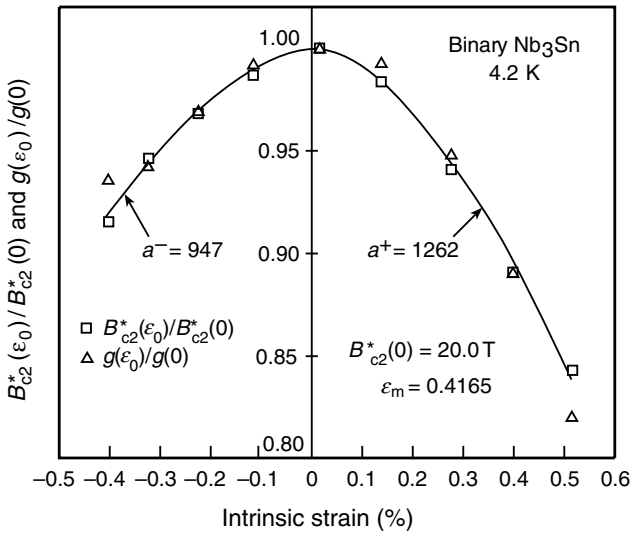

(a)

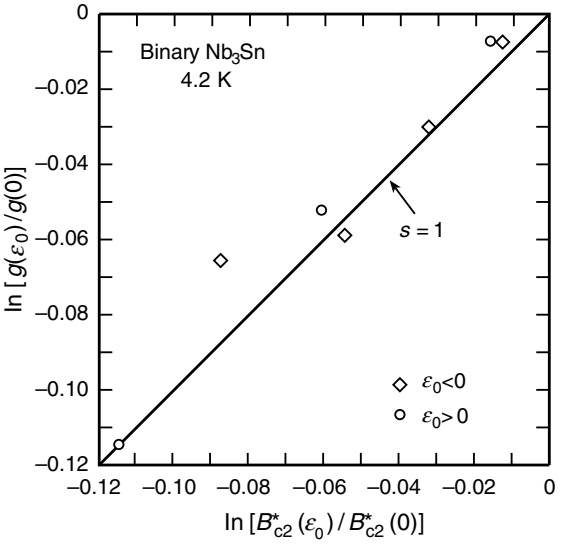

(b)

Fig. 10.34 (a) Fit of the power-law expression Eq. (10.21) to the normalized values of $B^{*}_{c2}(\varepsilon_0)$ (square symbols) obtained by fitting the data in Table 10.3 strain-point by strain-point. Normalized values of $g(\varepsilon_0)$ (triangles) from the fits in Table 10.3 are nearly identified to those of $B^{*}_{c2}(\varepsilon_0)$ and hence the scaling parameter $s \approx 1$ for this sample. (b) Logarithmic plot of $g(\varepsilon_0)/g(\varepsilon_0 = 0)$ vs. $B^{*}_{c2}(\varepsilon_0)/B^{*}_{c2}(\varepsilon_0{=}0)$, the slope of which gives the parameter s in Eq. (10.19), independent of the values of ε_m, $B^{*}_{c2}(\varepsilon_0{=}0)$, or $g(\varepsilon_0 = 0)$. [The data are normalized in the plot for dimensional reasons, but the slope is unaffected by the values used for the normalization constants $g(0)$ and $B^{*}_{c2}(0)$.]

The exponent s can be evaluated independent of the values of ε_m, $B^*_{c2}(\varepsilon_m)$, or $g(\varepsilon_m)$ from the slope of a log–log plot of $B^*_{c2}(\varepsilon)$ vs. $g(\varepsilon)$. This is illustrated by the plot of $\ln[g(\varepsilon_0)/g(\varepsilon_0 = 0)]$ vs. $\ln[B^*_{c2}(\varepsilon_0)/B^*_{c2}(\varepsilon_0 = 0)]$ in Fig. 10.34(b) where we see that $s \approx 1$. [The data are normalized in Fig. 10.34(b) for dimensional reasons, but the values of the normalization constants do not affect the slope.]

Thus, the magnetic-field and strain dependence of the critical current $I_c(B,\varepsilon)$ for this particular superconductor is characterized by Eqs (10.25a–d) with the following scaling parameter values:

$$\begin{aligned} p &= 0.5 \text{ (standard value)},\\ q &= 1.8,\\ \varepsilon_m &= 0.416\%\\ B^*_{c2}(\varepsilon_m) &= 20.0 \text{ T},\\ g(\varepsilon_m) &= 3970 \text{ A} \cdot \text{T},\\ a^- &= 947,\\ a^+ &= 1262,\\ s &= 1.0. \end{aligned}$$

This procedure of determining $B^*_{c2}(\varepsilon_0)$ and $g(\varepsilon_0)$ strain-point by strain-point results in values of $B^*_{c2}(\varepsilon_0)/B^*_{c2}(0)$ and $g(\varepsilon_0)/g(0)$ that are consistent and not codependent on other parameter values. It is worth reemphasizing that the resulting parameter values determined for a^-, a^+, and *s do not depend on the precise values of p and q* used to carry out the fits. [However, the parameter $B^*_{c2}(0)$ is significantly affected by the value of q, and $g(0)$ by p and q (unless the data extend to low enough fields to directly measure $g(0)$ at the peak in the F_L curve). There is no way to get around this except to use the transformation method given in the next section.]

The bottom line: To obtain consistent scaling parameter values, use high-leverage subsets of data that determine each parameter as uniquely as possible; the procedures given above avoid the errors inherent in concurrently fitting multiple parameters.

➔ Beware of trying to fit with too many free parameters *simultaneously*. In the above example, if we optimize all the parameters at the same time (rather than building the parameter set one step at a time), significant errors can result. The problem with globally fitting all the parameters at once is that they can work against each other in strange ways. You can get a great fit, but parameters that are interdependent do not stand on their own for comparison purposes. They lose consistency.

The procedure given above has the following advantages:

1. No "a priori" assumptions are made about the form of $B^*_{c2}(\varepsilon)$ and $g(\varepsilon)$. This becomes important when $g(\varepsilon)$ is not well characterized by the form given in Eq. (10.19), or when the conductor is damaged, or when the low-field data is affected by heating. In all these cases, a simultaneous fit usually covers up the situation and the resulting values of a may be anomalous or completely erroneous, and, worse yet, it is not obvious that there is anything different. *You cannot see what is happening with a simultaneous fitting procedure.*

2. No a priori assumptions are made about the prestrain ε_m. With the step-by-step procedure outlined above, ε_m is not determined until *after* all the $B^*_{c2}(\varepsilon)$ and $g(\varepsilon)$ values are obtained. Relatively small errors in the value of ε_m can significantly affect the a values in a simultaneous fitting process. With the procedures given in step (3), ε_m is determined independently of the other parameters.
3. The parameter values are insensitive to the *range* of strain being fit. With a multiparameter fit, you can go beyond the damage strain limit ε_{irr} and not know it, thus affecting all the other parameter values. Also, for fitting ranges that are asymmetrical about the peak in $B^*_{c2}(\varepsilon)$, the long side can dominate the short, giving erroneous values for the short side.

I have seen every one of these errors in the many ways I have tried to determine scaling parameter values. Interdependent multiparameter fits can hide a multitude of mistaken values. The resulting parameter values are inconsistent and untrustworthy, especially when many parameters are involved.

This is not to say to never fit multiple parameters simultaneously. The important point is to limit the number of *free* parameters. More than four free parameters is usually too many. The greater the number of adjustable parameters, the greater the potential errors. This becomes particularly important, for example, with the larger parameter set used with the unified strain-and-temperature scaling law (Sec. 10.7). The only reliable way of consistently determining such a large number of parameters is to break down the fitting task into smaller steps and chose high-leverage subsets of data appropriate for each parameter, as outlined in the fitting methods given in Sec. 10.7.4.

➔ In a similar vein, please note that a general enhancement in consistency and accuracy is obtained by considering up front which parameters can be determined accurately and which cannot from a given set of data. When faced with the usual situation of data obtained over a finite range, it is an exercise in futility to try to determine parameters that are outside the available range (e.g. it takes low-field data to fit p, high-field data to fit q). Again, when data are limited, it is far better to use standard values for out-of-range parameters than to obtain grossly inaccurate fitted values.

You can tell when too many free parameters are being used if the rms error of the fit is not significantly reduced by adding a parameter. (This was evident when we attempted to make p a free parameter in the second row of Table 10.2 on p. 416.) Additional adjustable parameters may seem advantageous because they offer increased fitting accuracy, but the greater number also leads to inconsistencies in the rest of the values, and the entire parameter set becomes unreliable.

Bottom line: Fitting accuracy alone is not an overarching goal; the greater accomplishment is to use the minimum number of parameters possible for the task (another example of "less is more.")

Table 10.3 **Spreadsheet example illustrating step (2) for determining $B^*_{c2}(\varepsilon)$ and $g(\varepsilon)$ at each strain point of an $I_c(B,\varepsilon)$ data set for a Nb_3Sn sample at 4.2 K.**

Values are determined by a two-parameter fit to the strain scaling law, $I_cB = g(\varepsilon)\, f(b)$, with $f(b) = b^p(1–b)^q$ and strain-independent exponents: $p = 0.5$ and $q = 1.8$ [determined in step (1) of the example]. The rms error is defined as $(\Sigma\Delta^2/N)^{1/2}$, and the rms % error is defined as $100(\Sigma\Delta^2/N)^{1/2}/g(\varepsilon_m)$, where N is the number of data points in the fit, and the maximum value $g(\varepsilon_m)$ was determined in step (4) of the example. The strain at maximum $\varepsilon_m = 0.416\%$ was determined in step (3).

Constant values of scaling parameters used with Eqs (10.25a)–(10.25d) in determining the values of $B^*_{c2}(\varepsilon)$ and $g(\varepsilon)$ for each measured strain:

$p = 0.5$ and $q = 1.8$; $\varepsilon_m = 0.416\%$; $B^*_{c2}(\varepsilon_m) = 20.0$ T; $g(\varepsilon_m) = 3970$ A·T.

ε [%]	ε_0 [%]	B [T]	I_c [A]	$F_L \equiv I_cB$ [A·T]	$g(\varepsilon)f(b)$ [A·T]	Δ [A·T]	Δ^2 [(A·T)^2]
0.01	−0.406	6.78	144.2	978	983	5.1	26
		7.75	116.0	899	898	−0.5	0
		9.68	73.5	711	700	−11.2	126
$B^*_{c2}(0.01\%) = 18.39$		11.62	41.8	486	487	1.3	2
$g(0.01\%) = 3704$		13.56	20.5	278	287	8.6	74
		15.50	7.6	118	122	4.0	16
		17.43	1.8	32	18	−13.8	190
						rms error = 7.9 A·T	
						rms % error = 0.20%	
0.09	−0.326	6.78	148.1	1004	1009	4.5	20
		7.75	119.2	924	929	5.0	25
		9.68	77.8	754	739	−14.9	222
$B^*_{c2}(0.09\%) = 18.96$		11.62	46.0	535	531	−4.3	19
$g(0.09\%) = 3741$		13.56	23.6	320	330	10.1	101
		15.50	9.7	150	158	8.0	64
		17.43	2.8	49	39	−10.4	108
						rms error = 8.9 A·T	
						rms % error = 0.23%	
0.19	−0.226	6.78	154.1	1045	1049	4.9	24
		7.75	125.2	970	971	1.5	2
		9.68	81.7	791	783	−7.7	59
$B^*_{c2}(0.19\%) = 19.39$		11.62	49.9	580	575	−5.3	28
$g(0.19\%) = 3850$		13.56	27.1	368	370	2.2	5
		15.50	11.6	180	191	10.7	115
		17.43	3.7	65	59	−6.1	37
						rms error = 6.2 A·T	
						rms % error = 0.16%	
0.30	−0.116	6.78	158.3	1073	1083	9.9	99
		7.75	130.5	1011	1007	−4.4	20
		9.68	85.6	829	821	−7.5	56
$B^*_{c2}(0.30\%) = 19.77$		11.62	53.1	617	612	−5.0	25
$g(0.30\%) = 3939$		13.56	29.7	403	405	2.5	6
		15.50	13.6	210	221	10.5	110
		17.43	4.8	84	79	−5.3	28
						rms error = 7.0 A·T	
						rms % error = 0.18%	

Table 10.3 ***Continued***

ε [%]	ε_0 [%]	B [T]	I_c [A]	$F_L \equiv I_c B$ [A·T]	$g(\varepsilon)f(b)$ [A·T]	Δ [A·T]	Δ^2 [(A·T)^2]
0.43	0.014	6.78	161.3	1094	1097	3.1	10
		7.75	132.3	1025	1023	−2.3	5
		9.68	86.9	841	840	−0.9	1
$B^*_{c2}(0.01\%) = 20.03$		11.62	54.7	636	633	−2.8	8
$g(0.01\%) = 3967$		13.56	31.3	425	427	1.8	3
		15.50	15.2	235	240	4.7	22
		17.43	5.6	98	94	−4.1	17
						rms error = 3.1 A·T	
						rms % error = 0.08%	
0.55	0.134	6.78	158.8	1076	1082	5.4	29
		7.75	129.7	1005	1005	−0.1	0
		9.68	85.1	824	818	−5.8	33
$B^*_{c2}(0.55\%) = 19.70$		11.62	53.0	616	609	−6.9	48
$g(0.55\%) = 3940$		13.56	29.1	394	401	7.0	50
		15.50	13.9	215	217	1.4	2
		17.43	4.3	76	76	0.3	0
						rms error = 4.8 A·T	
						rms % error = 0.12%	
0.69	0.274	6.78	147.8	1002	1012	10.0	100
		7.75	120.2	931	930	−0.9	1
		9.68	77.2	747	737	−10.3	106
$B^*_{c2}(0.69\%) = 18.84$		11.62	46.4	539	526	−12.4	155
$g(0.69\%) = 3765$		13.56	23.1	313	324	10.5	110
		15.50	9.0	140	152	11.6	134
		17.43	2.4	42	34	−8.1	66
						rms error = 9.8 A·T	
						rms % error = 0.25%	
0.81	0.394	6.78	134.2	910	922	12.4	153
		7.75	107.7	835	836	1.0	1
		9.68	68.0	658	637	−20.7	427
$B^*_{c2}(0.81\%) = 17.84$		11.62	37.6	437	428	−8.8	77
$g(0.81\%) = 3537$		13.56	16.2	219	236	17.2	296
		15.50	5.0	78	85	7.6	58
		17.43	1.0	17	4	−13.0	168
						rms error = 13.0 A·T	
						rms % error = 0.33%	
0.93	0.514	6.78	118.7	805	819	13.7	188
		7.75	94.6	733	730	−3.8	14
		9.68	57.2	553	532	−21.5	464
$B^*_{c2}(0.93\%) = 16.88$		11.62	28.4	330	331	0.9	1
$g(0.93\%) = 3255$		13.56	10.2	138	156	18.3	336
		15.50	2.6	40	34	−5.6	32
						rms error = 13.1 A·T	
						rms % error = 0.33%	

10.6 Transformation method for simplified application of scaling relations

The classic method of using the strain scaling law illustrated above entails a lot of data acquisition and scaling-parameter analysis. Let us introduce a powerful alternative method for applying scaling relations, which eliminates the need for so much effort, *regardless of the parameterization scheme used*. In fact, it eliminates the need to know the pinning-force function $f(b)$ altogether, along with the parameters p and q [for $f(b)$], as well as $B^*_{c2}(0)$ and $g(0)$.

The technique is especially useful for transforming a *single* I_c–B curve from one strain level to another, without the need to first fit it to a pinning-force function, extrapolate a value of $B^*_{c2}(0)$, or measure a complete set of $I_c(B,\varepsilon)$ characteristics. The method is particularly accurate and simple for nearby strain transformations in the intrinsic peak region, where handbook values of just two scaling parameters, a and s, can be effectively utilized to carry out the transformation.

Figure 10.35 shows an example of a typical data comparison between two Nb_3Sn superconductors measured in the as-cooled strain state. Taken at face value, we would conclude from the (solid) curves in Fig. 10.35 that Sample 2 has a higher critical-current density than Sample 1. As it turns out, however, Sample 1 has a greater initial compressive prestrain ($\varepsilon_0 = -0.4\%$), which reversibly lowers its I_c value relative to Sample 2 (where the prestrain is smaller, ($\varepsilon_0 = -0.18\%$). As we shall see, Sample 1 is, in fact, the better conductor at high fields.

In Sec. 10.6.1 we derive a general renormalization transformation that is the basis for the simplified method, and then in Sec. 10.6.2, we illustrate its use by obtaining a quick, simple solution to the problem presented in Fig. 10.35. In Sec. 10.6.3 we show how the same transformation method can be applied to temperature scaling and, later in Sec. 10.7.5, to combined temperature-and-strain scaling (since all the scaling relations have the same general form).

10.6.1 TRANSFORMATION METHOD

The core of the strain scaling law, introduced in Sec. 10.5.4, is the strain invariance of the shape of the general pinning function $f(b)$ [i.e. p and q in Eq. (10.18) are effectively independent of strain].

With this key feature, we are now in a position to quickly transform a set of I_c–B data obtained at one strain level to another [without needing to first determine the pinning-force function $f(b)$ or the parameters: $p, q, B^*_{c2}(0)$, and $g(0)$].

Referring back to Fig. 10.35, we express the I_c–B curve measured for Sample 1 (in its original strain state ε_1) in terms of the strain scaling law [Eq. (10.18)]

$$I_c(B,\varepsilon_1) = (B)^{-1} g(\varepsilon_1) f[B/B^*_{c2}(\varepsilon_1)], \tag{10.26}$$

and its renormalized I_c–B curve (dashed line) at the target strain ε_2 by

$$I_c(B',\varepsilon_2) = (B')^{-1} g(\varepsilon_2) f[B'/B^*_{c2}(\varepsilon_2)]. \tag{10.27}$$

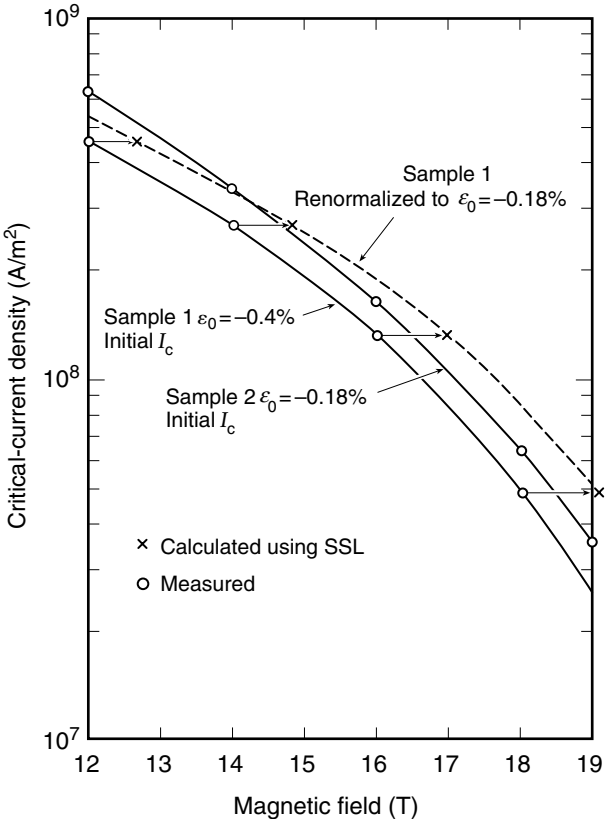

Fig. 10.35 $J_c(B)$ curves measured for two binary Nb_3Sn superconductors in the as-cooled strain state. Sample 1 has an initial compressive strain $\varepsilon_0 = -0.4\%$, and Sample 2 has a smaller initial compressive prestrain of $\varepsilon_0 = -0.18\%$. The dashed curve shows the data for Sample 1 transformed to $\varepsilon_0 = -0.18\%$ strain by using the transformation method, thus enabling a comparison to be made with the data of Sample 2 on an equal basis, that is, at the same intrinsic strain level.

In the second equation, we have purposely used a different variable B' to represent the magnetic field.

Since the shape of the function f is the same for both expressions, they can be related by making a simple coordinate transformation in Eq. (10.27), setting

$$B' = \beta B, \quad \text{Magnetic-field transformation} \tag{10.28}$$

where the factor β is defined by the ratio

$$\beta \equiv \frac{B^*_{c2}(\varepsilon_2)}{B^*_{c2}(\varepsilon_1)}. \tag{10.29}$$

Then, substituting Eq. (10.28) into Eq. (10.27) gives

$$I_c(B',\ \varepsilon_2) = (\beta B)^{-1} g(\varepsilon_2)\ f\left(\frac{\beta B}{B^*_{c2}(\varepsilon_2)}\right)$$

$$= (\beta B)^{-1} g(\varepsilon_2)\ f\left(\frac{B}{B^*_{c2}(\varepsilon_1)}\right),$$

and we can eliminate the function f by substituting Eq. (10.26) for $f[B/B^*_{c2}(\varepsilon_1)]$ to obtain

$$I_c(B',\ \varepsilon_2) = \beta^{-1} \frac{g(\varepsilon_2)}{g(\varepsilon_1)}\, I_c(B, \varepsilon_1), \tag{10.30}$$

Critical-current transformation for fixed $T \ll T_c$

Over the intrinsic peak region ($-0.5\% < \varepsilon_0 < +0.4\%$) where Eq. (10.19) holds {i.e. $g(\varepsilon) = g(0)\ [B^*_{c2}(\varepsilon)]^s$}, Eq. (10.30) can be further simplified to

$$I_c(B',\ \varepsilon_2) = \beta^{s-1} I_c(B, \varepsilon_1), \tag{10.31}$$

Critical-current transformation for fixed $T \ll T_c$ and ($-0.5\% < \varepsilon_0 < +0.4\%$)

where, again, $\beta \equiv B^*_{c2}(\varepsilon_2)/B^*_{c2}(\varepsilon_1)$.

Strain-scaling transformations

Thus, we can easily renormalize any I_c–B curve measured at strain ε_1 to obtain a corresponding I_c–B' curve at another strain ε_2 by using the magnetic-field and critical-current transformations summarized below:

Strain-scaling transformations:

Magnetic-field transformation:

$$B' = \{\beta\} B, \tag{10.32}$$

Critical-current strain transformation [for constant $T \ll T_c$ (e.g. $T \leq$ ~6 K in Nb_3Sn)]:

Over the intrinsic range ($-0.5\% < \varepsilon_0 < +0.4\%$),

$$I_c(B',\ \varepsilon_2) = \{\beta^{s-1}\}\, I_c(B, \varepsilon_1), \tag{10.33}$$

$$\beta \equiv \frac{B^*_{c2}(\varepsilon_2)}{B^*_{c2}(\varepsilon_1)} = \frac{1 - a|\varepsilon_{02}|^{1.7}}{1 - a|\varepsilon_{01}|^{1.7}}. \tag{10.34}$$

For the extended strain range including high-compressive strains ($\varepsilon_0 < -0.5\%$),

$$I_c(B', \varepsilon_2) = \left\{\beta^{-1}\frac{g(\varepsilon_2)}{g(\varepsilon_1)}\right\} I_c(B,\varepsilon_1), \tag{10.35}$$

$$\beta \equiv \frac{B^*_{c2}(\varepsilon_2)}{B^*_{c2}(\varepsilon_1)}.$$

Although we have used Eqs (10.21) and (10.22) to parameterize the ratios $B^*_{c2}(\varepsilon_1)/B^*_{c2}(\varepsilon_2)$ and $g(\varepsilon_2)/g(\varepsilon_1)$ over the moderate intrinsic strain range, any other parameterization scheme for $B^*_{c2}(\varepsilon)$ and $g(\varepsilon)$ in the strain scaling law of Eq. (10.18) would also work with this simplified transformation method. Likewise, for high-compressive strains, the ratios $B^*_{c2}(\varepsilon_1)/B^*_{c2}(\varepsilon_2)$ and $g(\varepsilon_2)/g(\varepsilon_1)$ in Eq. (10.35) can be readily parameterized by Eqs (10.23) and (10.24), respectively, but any other high-compression representation of these ratios also works.

Thus, the transformation method eliminates the pinning-force function $f(b)$, along with its parameters p and q, as well as $B^*_{c2}(0)$ and $g(0)$. The constant factors needed to carry out transformations are enclosed in brackets { } in the equation set above. For the common strain range ($-0.5\% < \varepsilon_0 < 0\%$) where most magnets are designed, we need only two parameters, a^- and s, instead of the half dozen listed in the example of Sec. 10.5.7. Again, values of these two scaling parameters are nearly universal for a given class of conductors made from a given superconducting material with the same additive content and filament shape. Standard values are listed in Appendix A10.2a for a number of common superconductor classes.

10.6.2 EXAMPLE: TRANSFORMATION METHOD FOR CALCULATING STRAIN CHANGES IN THE CRITICAL CURRENT

Let us see how this transformation method works in a simple, practical example.

Example of strain transformation at 4.2 K: As proposed at the outset of this section, suppose we have the typical problem of comparing two sets of I_c–B data for two binary Nb_3Sn conductors measured at 4.2 K in the as-cooled strain state (the data shown in Fig. 10.35 are tabulated in Table 10.4).

At first glance, the critical current of Sample 2 appears to be significantly higher than that of Sample 1 over the entire range of high magnetic fields. However, we appreciate that the particular level of prestrain in a conductor can strongly affect its critical-current data, especially at high magnetic fields.

Assume we know that the two conductors have dissimilar prestrains, approximately $\varepsilon_0 = -0.4\%$ for Sample 1 and $\varepsilon_0 = -0.18\%$ for Sample 2. Often, this information is available from a strain

measurement on a similar conductor with the same type of construction. It can also be obtained from a relatively quick measurement of a *single* I_c–ε curve at some convenient magnetic-field level (even zero field), since the prestrain is independent of magnetic field.

To make a comparison of these two sets of high-field data on an equal strain basis, we convert the data for Sample 1 to the same intrinsic strain as Sample 2. We use Eq. (10.33) [rather than Eq. (10.35)] because both sets of data were obtained at strains that fall within the moderate strain range on either side of the peak.

The value of the transformation parameter $\beta \equiv B^*_{c2}(\varepsilon_2)/B^*_{c2}(\varepsilon_1)$ is determined from Eq. (10.34) by substituting the values $\varepsilon_{01} = -0.4\% = -0.004$, $\varepsilon_{02} = -0.18\% = -0.0018$, and the "standard" value $a^- = 900$ for binary Nb_3Sn (from Appendix A10.2a). (If the conductor were ternary Nb_3Sn, a larger a^- value would be used corresponding to that type and level of additive, as listed in Appendix A10.2a; or a refined value of a^- could be used if it were available from strain data measured specifically for this conductor.) This substitution gives

$$\beta = \frac{1-a|\varepsilon_{02}|^{1.7}}{1-a|\varepsilon_{01}|^{1.7}} = \frac{1-900|-0.0018|^{1.7}}{1-900|-0.004|^{1.7}} = 1.060.$$

Thus, to transform the data for Sample 1, we simply multiply the B data in the first column of Table 10.4 by β [the factor enclosed in brackets { } in Eq. (10.32)] and the $I_c(\varepsilon_0 = -0.4\%)$ data in the second column by β^{s-1} [the factor enclosed in brackets in Eq. (10.33)] to calculate $I_c(\varepsilon_0 = -0.18\%)$ vs. B', shown by the two right-hand columns in Table 10.4. The value of s for Nb_3Sn from Appendix A10.2a is about 1, so $\beta^{s-1} = 1$ and consequently, the I_c values in our data table do not change at all. We need only transform the magnetic field B by the factor β. [For materials other than Nb_3Sn where $s \neq 1$ (see Appendix A10.2a), values of I_c in the fourth column of Table 10.4 would change, of course.]

That is the complete process. It takes only a few minutes. No need to spend several days measuring and analyzing a large set of two-dimensional $I_c(B, \varepsilon)$ curves to transform the data to a common strain level for comparison. The results tabulated in the two right-hand columns of Table 10.4 are plotted as a dashed line in Fig. 10.35, where we see in this actual example that Sample 1 is the better performing conductor at fields above 14 T.

Incidentally, the transformed $I_c(B)$ data (dashed line) fit the data actually measured for Sample 1 at this strain level to within 2% (less than our experimental error).

Table 10.4 **Data sheet example for the strain transformation of the J_c–B data for Sample 1 in Fig. 10.35 from $\varepsilon_0 = -0.4\%$ to $\varepsilon_0 = -0.18\%$ [with the transformation factor $\beta = 1.060$ obtained by evaluating Eq. (10.34) and $s = 1$ from Appendix A10.2a].**

Measured at $\varepsilon_0 = -0.4\%$		Transformed to $\varepsilon_0 = -0.18\%$	
B	$J_c(-0.4\%)$	B'(T) $= \beta B$ $= 1.060\,B$	$J_c(-0.18\%) = \beta^{s-1} J_c(-0.4\%)$ $= (1.060)^0 J_c(-0.4\%)$ $= J_c(-0.4\%)$
[T]	[10^8 A/m^2]	[T]	[10^8 A/m^2]
12	4.62	12.72	4.62
14	2.71	14.85	2.71
16	1.34	16.97	1.34
18	0.485	19.09	0.485
19	0.253	20.15	0.253

Notice that this method is not dependent on the detailed shape of the I_c–B curve, or on some extrapolation method for obtaining a value of B^*_{c2} from our measured I_c–B data (thus a Kramer extrapolation and its sometimes unrealistic values of B^*_{c2} are not an issue). It relies solely on the strain scaling law, Eq. (10.18), and the nearly universal dependence of B^*_{c2} on axial strain, parameterized in Eq. (10.21). [Other parameterizations could have been substituted equally well for $B^*_{c2}(\varepsilon)$ in Eq. (10.33) for moderate intrinsic strains, or for $B^*_{c2}(\varepsilon)$ and $g(\varepsilon)$ in Eq. (10.35) for high-compressive strains.] For the many sets of data we have measured, transformed values of I_c have consistently been within 3% of directly measured values, and usually the difference is less than 1% or 2%.

The method is also useful to transform data to a common strain level if a sample is mounted on a sample holder having a thermal contraction different from that of the superconductor. Such a mismatch can significantly shift the initial prestrain. As a typical example, Nb_3Sn samples measured on Ti–6%Al–4%V sample holders are strained by about 0.13% on cool-down from room temperature to 4.2 K because of the difference in thermal contraction rates between Ti–6%Al–4%V and Nb_3Sn composites (typically $\Delta L/L = 0.17\%$ vs. 0.30%, from Appendixes A7.4 and A7.5, respectively). The Ti–6%Al–4%V sample holder stretches the sample by this amount, which reduces the compressive prestrain and shifts the critical current toward the peak (strain-free) value. The relatively simple procedure illustrated in the example above can be used to transform the critical current back by 0.13% strain to provide a valid comparison with data obtained on a better matched sample-holder material, such as 304 stainless steel or Cu–2%Be (UNS C17200). The change is significant, especially at high magnetic fields ($B \gtrsim 0.5\, B^*_{c2}$). (The β factor for the strain correction is 0.971, so data measured on Ti–6%Al–4%V sample holders should be reduced by approximately half a tesla at magnetic fields over ~14 T when comparisons are made with data measured on more closely matched stainless-steel holders.)

As another example, when comparing I_c for a number of different types of sample-holder materials, it would be helpful to express all data at the peak, nearly strain-free $I_c(\varepsilon_m)$ value. No problem. This can be done by using Eq. (10.33) with ε_2 set equal to ε_m.

10.6.3 TEMPERATURE SCALING LAW

The same transformation method can be used to simplify the application of the temperature scaling law. Unlike the linear method described in Sec. 10.4.4, the transformation method does not require a linear relationship between J_c and T for its use. Thus, it is applicable to many more types of superconductors, and it is independent of the temperature range (i.e. there is no need for dual sets of T^*_c values, as given for Nb–Ti in Appendix A10.1).

Again, the transformation equations are based on scaling, this time on the temperature scaling law (TSL). The TSL states that temperature does not change the shape of a superconductor's pinning-force function $f(b)$. Mathematically, this can be written as (Fietz and Webb 1969)

$$F_L \equiv I_c B = h(T) f(b), \tag{10.36}$$

Temperature scaling law (TSL) (Valid for fixed strain)

where $h(T)$ is a *function of temperature only* (not magnetic field) and $f(b)$ is an arbitrary pinning-force function that depends only on the *reduced* magnetic field:

$$b \equiv \frac{B}{B^*_{c2}(T)},$$

where $B^*_{c2}(T)$ is the temperature-dependent effective upper critical field (at a fixed strain). The important point is that the exponents p and q in the general pinning function $f(b) = b^p(1–b)^q$ are *independent of temperature and magnetic field*.

The temperature function $h(T)$ can be simply parameterized for low-T_c superconductors as a power of $B^*_{c2}(T)$,

$$h(T) = h(0)\left[\frac{B^*_{c2}(T)}{B^*_{c2}(0)}\right]^{\eta}, \quad \text{Parameterization of prefactor } h(T) \text{ using } B^*_{c2}(T) \qquad (10.37)$$

where $h(0)$ and $B^*_{c2}(0)$ are the values of $h(T)$ and $B^*_{c2}(T)$ at $T = 0$, and η is an exponential constant, all of which are independent of temperature and magnetic field (Fietz and Webb 1969). For practical multifilamentary Nb_3Sn conductors, $\eta \approx 3$ is typical, but values have been reported ranging from about 2.5 to 3.5 (Kramer 1973; Kroeger et al. 1980; Cheggour and Hampshire 2002; Keys and Hampshire 2003).

Thus, the TSL can be parameterized by the relatively simple expression (Fietz and Webb 1969):

$$I_c B = h(0)\left[\frac{B^*_{c2}(T)}{B^*_{c2}(0)}\right]^{\eta} f(b). \qquad (10.38)$$

Parameterization of the TSL using $B^*_{c2}(T)$ (Valid for fixed strain)

With Eq. (10.38), the information for determining the effect of temperature on critical current is reduced mainly to knowing the temperature dependence of $B^*_{c2}(T)$. From data obtained so far, this appears to be a nearly universal function for a given type of superconductor. A summary of the TSL and parameters for its use with Nb_3Sn are given in Appendix A10.2a and in the comments immediately preceding the table.

Expressions for $h(T)$ other than Eq. (10.37) have been proposed (e.g. Hampshire et al. 1985; Summers et al. 1991; Godeke et al. 2001; and Keys and Hampshire 2003; a synopsis of these is given in Ekin 2007). However, whatever the form of $h(T)$, the transformation method described next can be used to simplify the application of the temperature scaling relation without the need to first measure the general pinning-force function $f(b)$ or determine the parameters: p, q, $B^*_{c2}(0)$, and $h(0)$.

Temperature-scaling transformations

Similar to the development of the strain transformation given above, we eliminate $f(b)$ to find the transformation equations that enable us to renormalize an I_c–B curve measured at

temperature T_1 to obtain a corresponding I_c–B' curve at a different temperature T_2. The transformation equations are summarized as follows:

Temperature-scaling transformations:

Magnetic-field transformation:

$$B' = \{\beta\}B, \tag{10.39}$$

Critical-current temperature transformation (for constant strain):

$$I_c(B',T_2) = \left\{\beta^{-1}\frac{h(T_2)}{h(T_1)}\right\} I_c(B,T_1). \tag{10.40}$$

With the parameterization of Eq. (10.37), this simplifies to

$$I_c(B',T_2) = \{\beta^{\eta-1}\} I_c(B,T_1). \tag{10.41}$$

For this set of equations,

$$\beta \equiv \frac{B^*_{c2}(T_2)}{B^*_{c2}(T_1)} = \frac{1-(T_2/T^*_c)^\nu}{1-(T_1/T^*_c)^\nu}. \tag{10.42}$$

To carry out the transformation with the parameterization of Eq. (10.37), we need know only the factor β. From theory (Werthamer et al. 1966), $B^*_{c2}(T)$ has the general form

$$B^*_{c2} = B^*_{c2}(0)\,[1-(T/T^*_c)^\nu], \tag{10.43}$$

where T^*_c is the effective critical temperature at which the critical current extrapolates to zero, about 17.5 K for multifilamentary Nb_3Sn (at small intrinsic strain) (Goodrich et al. 1998; Cheggour and Hampshire 2002; Keys and Hampshire 2003). The exponent ν is a parameter that has been observed experimentally in multifilamentary Nb_3Sn to have a strain-independent value of about 1.5 (Cheggour and Hampshire 2002). This is also the value expected from WHH theory (Werthamer et al. 1966). Substituting this form into the factor β gives

$$\beta \equiv \frac{B^*_{c2}(T_2)}{B^*_{c2}(T_1)} = \frac{1-(T_2/T^*_c)^\nu}{1-(T_1/T^*_c)^\nu}, \tag{10.44}$$

which is the source of the parameterization shown in Eq. (10.42) above. Thus, all that is needed to carry out temperature transformations are the scaling parameters ν, η, and T^*_c. The only requirement is that the transformations be carried out at constant strain or at low levels of strain ($\varepsilon_0 \approx 0$) where T^*_c is only weakly dependent on strain.

With other expressions for $h(T)$, the same simplified method works to transform I_c–B data from one temperature to another by substituting the alternative expressions for $h(T)$ into the transformation factor enclosed in brackets { } in Eq. (10.40), with the scaling factor β still

given by Eq. (10.42). Here we have focused on the form of $h(T)$ given by Eq. (10.37) since, for technological purposes, it is the simplest and, for low-T_c superconductors such as Nb_3Sn, gives the same result within experimental error as more complex expressions for fitting measured values of $h(T)$ (Ekin 2007).

In summary, this method provides an easy way to transform I_c–B characteristics measured at a convenient temperature (e.g. 4.2 K) to other temperatures not so readily accessible. Again, the advantages are that the pinning-force function $f(b)$ and the parameters $B^*_{c2}(0)$ and $h(0)$ do not need to be determined and, unlike the linear-extrapolation method described in Sec. 10.4.4, this method is useful for superconductors generally, since it is not restricted to those with a linear relationship between I_c and T. Only three temperature-scaling parameters (ν, η, and T^*_c) are needed.

For Nb_3Sn, where $\nu \approx 1.5$ is a nearly universal constant for many different types of conductors (described in more detail in Sec. 10.7.2), the transformations can be carried out with only two parameters: T^*_c and η. Again, typical values for Nb_3Sn are $T^*_c \approx 17.5$ K and $\eta \approx 3$. As shown in the example at the end of Sec. 10.7.5, errors in the transformed $I_c - B$ values are small for nearby transformations even for relatively large uncertainties in the scaling parameter values.

10.7 Unified strain-and-temperature scaling law and transformations

There are times when we want to make a strain transformation, but the temperature is not far enough away from T_c for the strain scaling law to work (e.g. $T > 4.2$ K for Nb_3Sn). Other times we want to transform both strain and temperature, but then the TSL will not work. For these situations, the *unified* strain-and-temperature scaling law is needed. It also serves as a tool for magnet design by analytically representing the dependence of critical current on all three variables: magnetic field, temperature, and strain [i.e. $I_c(B,T,\varepsilon)$]. As with the strain scaling law and temperature scaling law, the application of the unified scaling law can be greatly simplified by the transformation technique. We illustrate this in Sec. 10.7.5 with a practical example of magnet design at temperatures above 4.2 K using 4.2 K data. First, however, we introduce the unified scaling law and give a consistent scheme for parameterizing it for use in magnet design and modeling critical-current data.

10.7.1 UNIFIED SCALING LAW—BASIC RELATION

The unified strain-and-temperature scaling law (USL) was postulated some time ago (Ekin 1980a) but not experimentally confirmed until recently with the advent of combined strain and temperature critical-current measurements (Cheggour and Hampshire 1999; Ekin 2007). Basically, it states that neither strain nor temperature change the shape of a superconductor's pinning-force function $f(b)$. It is expressed by the following set of equations (Ekin 1980a)

Unified strain-and-temperature scaling law:

$$F_L \equiv I_c B = K(T,\varepsilon_0)\, f(b) = K(T,\varepsilon_0) b^p (1-b)^q \tag{10.45}$$

with variables

$$\varepsilon_0 \equiv \varepsilon - \varepsilon_m, \qquad \text{Intrinsic strain}$$

$$b \equiv \frac{B}{B^*_{c2}(t,\varepsilon_0)}, \qquad \text{Reduced magnetic field} \tag{10.46}$$

$$t \equiv \frac{T}{T^*_c(\varepsilon_0)}, \qquad \text{Reduced temperature} \tag{10.47}$$

where

$$\frac{B^*_{c2}(t,\varepsilon_0)}{B^*_{c2}(0,0)} = \frac{B^*_{c2}(0,\varepsilon_0)}{B^*_{c2}(0,0)} \frac{B^*_{c2}(t,0)}{B^*_{c2}(0,0)}, \tag{10.48}$$

$$\frac{T^*_c(\varepsilon_0)}{T^*_c(0)} = \left(\frac{B^*_{c2}(0,\varepsilon_0)}{B^*_{c2}(0,0)} \right)^{1/w}, \tag{10.49}$$

and p, q, w, $B^*_{c2}(0,0)$, and $T^*_c(0)$ are scaling constants.

Here, $B^*_{c2}(t, \varepsilon_0)$ is the effective upper critical field, postulated to be separable into strain and reduced-temperature parts as expressed by Eq. (10.48).

The function $T^*_c(\varepsilon_0)$ is the *strain-dependent* effective critical temperature, which can be parameterized by Eq. (10.49) with the strain-dependent part of the effective upper critical field at 0 K (the relationship holds in terms or either applied strain ε or intrinsic strain ε_0). Recently, Eq. (10.49) has been shown to be a rather general relationship. This is shown in Fig. 10.36 for different types of Nb_3Sn conductors; the exponent w has the value of about 3 in binary as well as ternary conductors, over both the moderate strain and high-compressive strain ranges. [This general correspondence between $T^*_c(\varepsilon_0)$ and $B^*_{c2}(0,\varepsilon_0)$ probably stems from their common dependence on the strain-dependent superconducting energy gap (but with additional strain-dependent contributions to B^*_{c2} entering through terms such as the Ginsburg–Landau constant and the electron–phonon coupling constant) (Ekin 2007).]

The heart of the USL Eq. (10.45) comprises two key points: (1) the prefactor $K(T,\varepsilon_0)$ is a *function of temperature and strain only* (not magnetic field), and (2) the pinning-force function $f(b)$ depends only on the *reduced* magnetic field b and does not otherwise depend on temperature or strain [i.e. the exponents p and q in the general pinning function $f(b) = b^p (1-b)^q$ are independent of *both* strain and temperature]. Because of this shape-invariance of $f(b)$, the USL

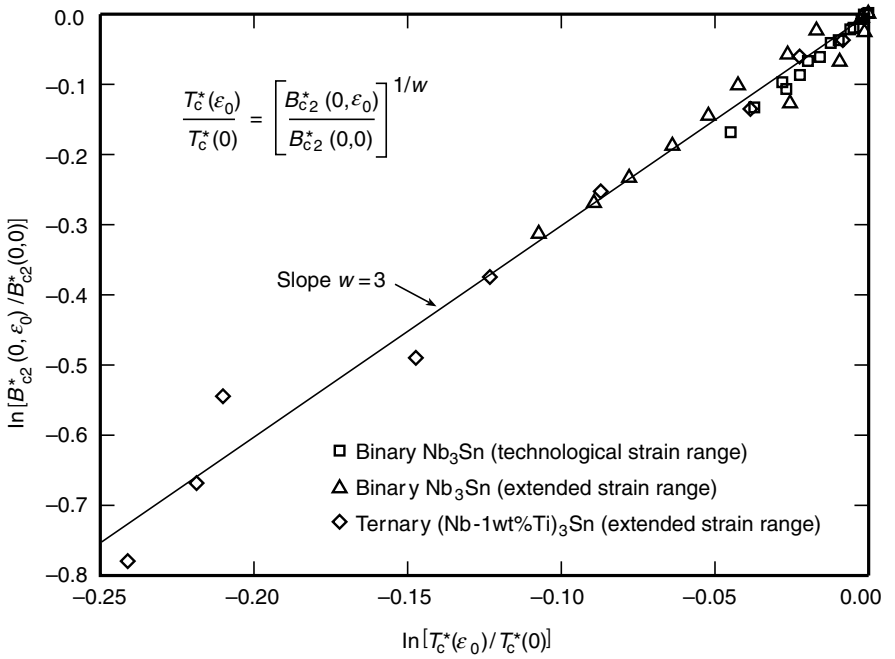

Fig. 10.36 Data correlation of the strain dependence of $T_c^*(\varepsilon_0)$ and $B_{c2}^*(0,\varepsilon_0)$ for binary and ternary Nb_3Sn conductors at moderate strains *and* high-compressive strains. The solid line has a slope of 3, showing that the exponent value $w \approx 3$ in Eq. (10.49) holds for these Nb_3Sn conductors *independent of additives and strain range* (extending from $-1.8\% < \varepsilon_0 < +0.25\%$). (From Ekin 2007; data analyzed from the following sources: □ Ekin 1980a; △ Cheggour and Hampshire 2002; ◇ Keys and Hampshire 2003.)

provides a powerful tool for modeling the combined magnetic-field, temperature, and strain dependence of the critical current, as shown below.

In the next subsection, we simplify the USL into separable form and then parameterize it with a consistent parameter set for use at both moderate strains (Sec. 10.7.2) and high-compressive strains (Sec. 10.7.3). Of practical importance, we also describe how to accurately determine these parameter values from either limited or complete sets of $I_c(B,T,\varepsilon)$ data (Sec. 10.7.4). Finally, we reduce the number of parameters and simplify the application of the USL with the transformation method (Sec. 10.7.5).

Separable form

The USL can be simplified by a further postulate (also confirmed by recent observations) that the prefactor $K(T,\varepsilon_0)$ in Eq. (10.45) is itself separable into strain- and temperature-dependent parts (Ekin 1980a)

$$K(T,\varepsilon_0) = g(\varepsilon_0)h(t), \tag{10.50}$$

$$F_{\mathrm{L}} \equiv I_{\mathrm{c}}B = g(\varepsilon_0)h(t)\,f(b), \tag{10.51}$$

Unified scaling law (USL)—separable form

where $g(\varepsilon_0)$ is the same prefactor described earlier for the strain scaling law [a function of only intrinsic strain], and $h(t)$ is the same prefactor as in the TSL [a function of only *reduced* temperature $t \equiv T/T_{\mathrm{c}}^{*}(\varepsilon_0)$]. This separation of functional dependences greatly facilitates the practical application of the USL, enabling the definition of a *separable parameter set*.

The set of equations (10.45) through (10.49) and the separable form, Eq. (10.51), provide the mathematical *framework* for the unified strain-and-temperature scaling law. In the following sections we parameterize the USL in terms of physically measurable quantities. We focus on the easiest-to-use parameterization scheme, the original separable set, although several other empirical representations of $K(T, \varepsilon_0)$ in Eq. (10.45) have also been subsequently proposed for use with the above relationship. It turns out, they all fit the available $I_{\mathrm{c}}(B, t, \varepsilon)$ data equally well within experimental error. Although the alternative representations are not usually given in separable form, they can be broken down into separate strain and temperature expressions, $g(\varepsilon_0)$ and $h(t)$, for use with Eq. (10.51). However, the parameters employed are commingled with respect to strain and temperature. [A synthesis of the various representations and analyses in terms of $g(\varepsilon_0)$ and $h(t)$, showing their close correspondence, is detailed in Ekin (2006).]

The separable parameter set, summarized next, is based on extensive scaling data. It takes full advantage of the separability of Eq. (10.51) and, for engineering design, offers three principal advantages over other parameterization schemes:

1. It is simple.
2. All the parameters can be measured or determined independently.
3. The scaling parameters are not commingled with respect to strain and temperature, so they have consistent values that can be determined one at a time.

From a practical point of view, the strain-and-temperature independence of the separable parameter set parallels the way data are often obtained, facilitating their determination from independent strain and temperature experiments. For example, measurements show that the strain term $g(\varepsilon_0)$ is effectively independent of temperature; unnecessary complications are thus created if the strain term is characterized by the interplay of both temperature- and strain-based parameters, since whenever one parameter is updated, all the others have to be changed. With the separable parameter set, whenever new temperature data become available, the parameters characterizing the temperature function $h(t)$ in Eq. (10.51) can be updated without effectively altering the strain parameters, and, vice versa, new strain data effectively change only the strain parameters characterizing $g(\varepsilon_0)$ and not the temperature parameters. *In this way the USL can be constructed one term at a time, without revising all the parameter values whenever additional data become available.* (Details of this building process are given in Sec. 10.7.4.)

Their independence also has the advantage that the parameter values are unaffected by changes in the range of strain over which the fits are carried out. Both features

(range independence as well as strain-and-temperature separability) provide parameter values that are *consistent*, leading to nearly universal values that stand alone for a given class of conductors.

10.7.2 PARAMETERIZATION OF THE UNIFIED STRAIN-AND-TEMPERATURE SCALING LAW OVER THE INTRINSIC PEAK RANGE ($-0.5\% < \varepsilon_0 < +0.4\%$)

Most technological applications are designed within the moderate strain range $-0.5\% < \varepsilon_0 < +0.4\%$ (assuming $\varepsilon_{irr} \geq +0.4\%$) where the simplest and easiest-to-use scaling representations of $g(\varepsilon_0)$ and $h(t)$ are given in terms of the strain- and temperature-dependent parts of the effective upper critical field [Eq. (10.48)]. This representation was used earlier with the SSL and TSL [Eqs (10.19) and (10.37), respectively]. Substituting these into Eq. (10.50) we find

$$K(T,\varepsilon_0) = g(\varepsilon_0)\, h(t) = \mathrm{C}\left[\frac{B^*_{c2}(0,\varepsilon_0)}{B^*_{c2}(0,0)}\right]^s \left[\frac{B^*_{c2}(t,0)}{B^*_{c2}(0,0)}\right]^\eta, \tag{10.52}$$

where the proportionality constant C is defined as $\mathrm{C} \equiv K(0,0)$. Therefore, from Eq. (10.51), the critical current as a function of magnetic field, temperature, and axial strain is given by the following representation (Ekin 1980a):

Unified scaling law for the intrinsic peak range ($-0.5\% < \varepsilon_0 < +0.4\%$):

$$I_c(B,t,\varepsilon_0) = \mathrm{C}\, B^{-1}\left[\frac{B^*_{c2}(0,\varepsilon_0)}{B^*_{c2}(0,0)}\right]^s \left[\frac{B^*_{c2}(t,0)}{B^*_{c2}(0,0)}\right]^\eta b^p(1-b)^q, \tag{10.53}$$

where

$$\frac{B^*_{c2}(t,\varepsilon_0)}{B^*_{c2}(0,0)} = \frac{B^*_{c2}(0,\varepsilon_0)}{B^*_{c2}(0,0)}\,\frac{B^*_{c2}(t,0)}{B^*_{c2}(0,0)}, \tag{10.54}$$

$$\frac{T^*_c(\varepsilon_0)}{T^*_c(0)} = \left[\frac{B^*_{c2}(0,\varepsilon_0)}{B^*_{c2}(0,0)}\right]^{1/w},$$

and C is a proportionality constant [$\mathrm{C} \equiv K(0,0)$].

There are a number of ways to parameterize $B^*_{c2}(0,\varepsilon_0)$ and $B^*_{c2}(t,0)$, and they all would work with Eqs (10.53) and (10.54). Again, the simplest and easiest to use are the parameters introduced with the SSL and TSL [Eqs (10.21) and (10.43)]. Substituting these into Eq. (10.52) gives

$$K(T,\varepsilon_0) = \mathrm{C}(1-a|\varepsilon_0|^{1.7})^s\,(1-t^\nu)^\eta \tag{10.55}$$

and, therefore, the critical current as a function of magnetic field, temperature, and axial strain can be parameterized by the following set of equations:

Parameterization of the unified scaling law for the intrinsic peak range ($-0.5\% < \varepsilon_0 < +0.4\%$):

$$I_c(B,t,\varepsilon_0) = C\,B^{-1}(1-a|\varepsilon_0|^{1.7})^s\,(1-t^\nu)^\eta\,b^p(1-b)^q, \tag{10.56}$$

where

$$B^*_{c2}(t,\varepsilon_0) = B^*_{c2}(0,0)(1-a|\varepsilon_0|^{1.7})(1-t^\nu), \tag{10.57}$$

$$\frac{T^*_c(\varepsilon_0)}{T^*_c(0)} = (1-a|\varepsilon_0|^{1.7})^{1/w}. \tag{10.58}$$

Again, C is a proportionality constant and the variables are defined by:

$\varepsilon_0 \equiv \varepsilon - \varepsilon_m$, Intrinsic strain (where ε is the applied strain and ε_m is the applied strain at the peak, all in absolute units, not percent)

$b \equiv \dfrac{B}{B^*_{c2}(t,\varepsilon_0)}$, Reduced magnetic field

$t \equiv \dfrac{T}{T^*_c(\varepsilon_0)}$. Reduced temperature

[*Technical note*: The proportionality "constants" used in earlier sections are not actually constant. Rather, the constant k, used in Eq. (10.9) to parameterize the magnetic-field dependence of a single I_c–B curve, represents $k = C\,(1-a|\varepsilon_0|^{1.7})^s\,(1-t^\nu)^\eta$ in Eq. (10.56) and is actually constant only for fixed T and ε_0. On the other hand, the proportionality constant $h(0)$, used in Eq. (10.38) to parameterize the TSL, represents $h(0) = C\,(1-a|\varepsilon_0|^{1.7})^s$ in Eq. (10.56) and is constant only for fixed strain. Finally, the proportionality constant $g(0)$, used in Eq. (10.20) to parameterize the SSL, represents $g(0) = C\,(1-t^\nu)^\eta$ and is approximately constant only if T is fixed and $T \ll T^*_c(\varepsilon_0{=}0)$, (e.g. 4.2 K in Nb_3Sn). The only proportionality constant that is truly constant is C in Eq. (10.56).]

Thus, with Eqs (10.56) through (10.58), the general functional dependence of $I_c(B,t,\varepsilon)$ can be expressed in terms of the following separable parameter set:

From $I_c(B)$ data:	p, q	characterizing the magnetic-field dependence
From $I_c(B,\varepsilon)$ data:	ε_m	characterizing the compressive prestrain
"	$a^-, a^+, B^*_{c2}(0,0)$	characterizing $B^*_{c2}(0,\varepsilon_0)$
"	s	characterizing $g(\varepsilon_0)$
From $I_c(B,t)$ data:	ν	characterizing $B^*_{c2}(t,0)$

"	$w, T_c^*(0)$	characterizing $T_c^*(\varepsilon_0)$
"	η	characterizing $h(t)$
	C	proportionality constant

Detailed methods of measuring or estimating these parameters from separate strain or temperature data are described in Sec. 10.7.4.

Most of these scaling parameters have nearly universal values *for a given class* of superconductors (i.e. those made from the same superconducting material, with the same additive content and filament shape). This can be seen by looking at each parameter in turn:

- The parameter ν is a nearly universal constant, at least for the technological Nb_3Sn conductors that have been tested so far, including both binary and ternary Nb_3Sn, at both low and high intrinsic strains. Although data are limited, the parameter w also appears consistent:

  $\nu = 1.5$ independent of Nb–Sn phase inhomogeneity, measurement method, and strain range, as shown for the data in Figs 10.37 and 10.38.

  $w \simeq 3$ independent of additive content and strain range, as shown for the data in Fig. 10.36.

- The parameters p, q, a, and s have reasonably standard values for individual classes of conductors. These are tabulated in Appendix A10.2 for the data correlations available so far.

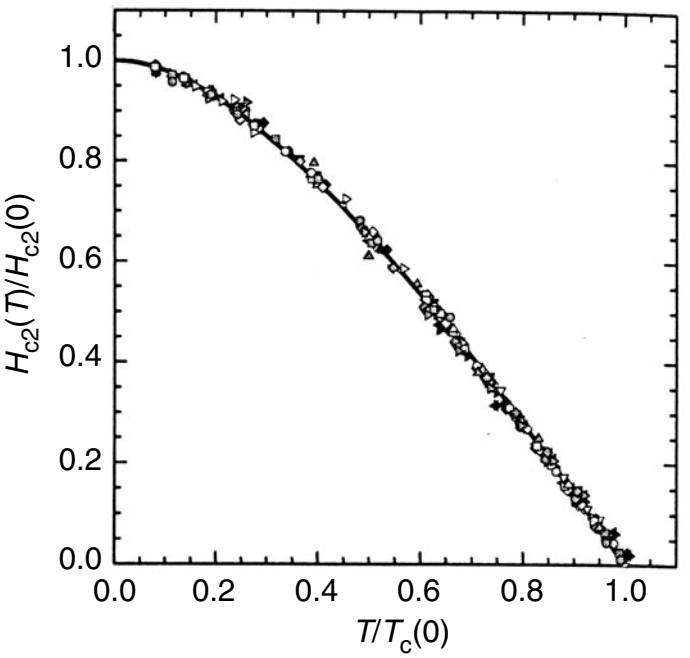

Fig. 10.37 Correlation of data for the temperature dependence of the upper critical field $H_{c2}(T)$ for a number of Nb_3Sn samples covering a range of Nb–Sn phases. Upper-critical-field data were obtained both from resistivity measurements and from Kramer extrapolations at various resistivity and electric-field criteria. The solid curve is a Maki–DeGennes description, with an exponent $\nu = 1.5$, showing that the value 1.5 holds for Nb_3Sn for a *range of Nb–Sn phases, independent of the measurement method* used to determine $H_{c2}(T)$. (From Godeke et al. 2005.)

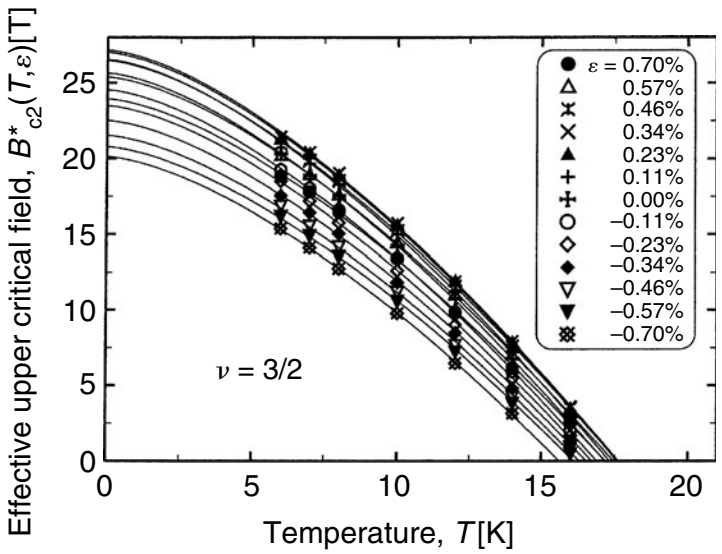

Fig. 10.38 Effective upper critical field $B^*_{c2}(T,\varepsilon_0)$ as a function of temperature T and applied strain ($\varepsilon = \varepsilon_0 + 0.33\%$), obtained for a bronze-processed Nb_3Sn multifilamentary wire. Solid curves represent the function $B^*_{c2}(T,\varepsilon_0) = B^*_{c2}(0,\varepsilon_0)\{1-[T/T^*_c(\varepsilon_0)]^\nu\}$, with $\nu = 1.5$, showing that the value 1.5 holds for Nb_3Sn *independent of the applied strain*. (From Cheggour and Hampshire 2002.)

- The temperature parameter η is not yet statistically well established for specific conductor classes. (This is the original temperature exponent in the Fietz and Webb TSL, Sec. 10.6.3.) Values have been reported ranging from 2.5–3.5 for Nb_3Sn, for example, covering a number of different conductor types. Hopefully, more standard values of η can be determined as variable-temperature data correlations become available for well-characterized superconductor classes.
- This leaves C, $T^*_c(0)$, $B^*_{c2}(0,0)$ and ε_m as the only effective *free* parameters needed to accommodate the variable pinning structure, homogeneity, and prestrain of individual conductors.

[The simplified transformation method described in Sec. 10.7.5 further reduces this free set to just $T^*_c(0)$ and ε_m.]

10.7.3 GENERAL PARAMETERIZATION OF THE UNIFIED STRAIN-AND-TEMPERATURE SCALING LAW FOR STRAINS EXTENDING TO HIGH COMPRESSION ($\varepsilon_0 < -0.5\%$)

For magnets designed with superconductors reacted within stainless-steel conduits or other structural materials that have high thermal contraction rates, the high-compressive-strain range ($\varepsilon_0 < -0.5\%$) becomes relevant. In the following, we focus mainly on Nb_3Sn because high-compressive-strain data are more available for this superconductor, but the same parameterization would be applicable to any of the technological low-T_c superconductors (although possibly with different values of the scaling parameters).

The temperature-scaling parameterization of Fietz and Webb (1969) given by Eq. (10.37), that is, $h(t)/h(0) = [B^*_{c2}(t,0)/B^*_{c2}(0,0)]^{\eta}$, holds quite well at high-compressive strains with approximately the same constant value of η as for the intrinsic peak range (Cheggour and Hampshire 2002). However, as described in Sec. 10.5.6, the strain-scaling parameterization given by Eq. (10.19), that is, $g(\varepsilon_0)/g(0) = [B^*_{c2}(0,\varepsilon_0)/B^*_{c2}(0,0)]^s$, no longer applies at high-compressive strains, with s ceasing to be a constant for $\varepsilon_0 \lesssim -0.5\%$ (Ekin 2007). Also, extrinsic effects such as compressive yielding of some of the conductor components may start to play a role.

So, for high-compressive strains we use the more general expression

$$K(T,\varepsilon_0) = g(\varepsilon_0)h(t) = g(\varepsilon_0)\left[\frac{B^*_{c2}(t,0)}{B^*_{c2}(0,0)}\right]^{\eta}, \tag{10.59}$$

where $g(\varepsilon_0)$ is left as an arbitrary strain function. Therefore, from Eq. (10.51), we have the following representation of the USL:

Unified scaling law for strains extending to high compression ($\varepsilon_0 < -0.5\%$):

$$I_c(B,t,\varepsilon) = B^{-1}g(\varepsilon_0)\left[\frac{B^*_{c2}(t,0)}{B^*_{c2}(0,0)}\right]^{\eta} b^p(1-b)^q, \tag{10.60}$$

where

$$\frac{B^*_{c2}(t,\varepsilon_0)}{B^*_{c2}(0,0)} = \frac{B^*_{c2}(0,\varepsilon_0)}{B^*_{c2}(0,0)}\,\frac{B^*_{c2}(t,0)}{B^*_{c2}(0,0)}, \tag{10.61}$$

$$\frac{T^*_c(\varepsilon_0)}{T^*_c(0)} = \left[\frac{B^*_{c2}(0,\varepsilon_0)}{B^*_{c2}(0,0)}\right]^{1/w}.$$

Here we have represented $T^*_c(\varepsilon_0)$ by Eq. (10.49) since this relation still holds well at high-compressive strains, as shown by the high-compression data in Fig. 10.36.

The temperature-dependent part of the effective upper critical field $B^*_{c2}(t,0)$ in Eqs (10.59) through (10.61) is parameterized well by Eq. (10.43) at high-compressive strains, as shown by the data in Fig. 10.38. Substituting Eq. (10.43) into Eq. (10.59) gives

$$K(T,\varepsilon_0) = g(\varepsilon_0)\,(1-t^{\nu})^{\eta}, \tag{10.62}$$

and, therefore, the following set of equations serve to parameterize $I_c(B,t,\varepsilon)$ over an extended strain range, including high-compressive strains ($\varepsilon_0 < -0.5\%$):

Parameterization of the unified scaling law for strains extending to high compression ($\varepsilon_0 < -0.5\%$):

$$I_c(B,t,\varepsilon_0) = B^{-1}g(\varepsilon_0)\,(1-t^{\nu})^{\eta}\,b^p(1-b)^q, \tag{10.63}$$

where

$$B^*_{c2}(t,\varepsilon_0) = B^*_{c2}(0,\,\varepsilon_0)\,(1-t^{\nu}), \tag{10.64}$$

$$\frac{T_c^*(\varepsilon_0)}{T_c^*(0)} = \left[\frac{B_{c2}^*(0,\varepsilon_0)}{B_{c2}^*(0,0)}\right]^{1/w}. \tag{10.65}$$

Again, the variables are defined by:

$\varepsilon_0 \equiv \varepsilon - \varepsilon_m$, Intrinsic strain (where ε is the applied strain and ε_m is the applied strain at the peak, all in absolute units, not percent)

$b \equiv \dfrac{B}{B_{c2}^*(t,\varepsilon_0)}$, Reduced magnetic field

$t \equiv \dfrac{T}{T_c^*(\varepsilon_0)}$. Reduced temperature

This leaves $B_{c2}^*(0,\varepsilon_0)$ and $g(\varepsilon_0)$ to be parameterized. As described in Sec. 10.5.6, both deviate from a simple power law at high-compressive strains and therefore need additional parameters to represent them in this regime. *Any parameterization of $B_{c2}^*(\varepsilon_0)$ and $g(\varepsilon_0)$ would work with Eqs (10.63)–(10.65)*, including empirical multiparameter fitting functions such as a fourth-order polynomials (Keys and Hampshire 2003) or the form proposed by Ten Haken et al. (1999).

Here we use the convenient parameterization introduced earlier for the strain scaling law [similar to Eqs (10.23) and (10.24)],

$$\frac{B_{c2}^*(0,\varepsilon_0)}{B_{c2}^*(0,0)} = 1 - a|\varepsilon_0|^{1.7} + a_1|\varepsilon_0 - \varepsilon_0'|^{a_2} I(\varepsilon_0 < \varepsilon_0'), \tag{10.66}$$

$$\frac{g(\varepsilon_0)}{C} = [1 - a|\varepsilon_0|^{1.7}]^w + g_1|\varepsilon_0 - \varepsilon_0'|^{g_2} I(\varepsilon_0 < \varepsilon_0'), \tag{10.67}$$

where the proportionality constant C has the same value as in Eq. (10.56), and the indicator function is given by

$$I(\varepsilon_0 < \varepsilon_0') \equiv \begin{cases} 1 & \text{if } \varepsilon_0 < \varepsilon_0' \\ 0 & \text{if } \varepsilon_0 > \varepsilon_0'. \end{cases}$$

(As noted in Sec. 10.5.6, this is readily programmed in spreadsheet programs with a conditional clause.) This form deconvolutes the intrinsic-peak and high-compressive strain regimes, and therefore leads to consistent parameter values that do not change with the strain range being fitted (Sec. 10.5.6). In particular, the intrinsic "strain-sensitivity parameter" a in these extended-range functions for $B_{c2}^*(0,\varepsilon_0)$ and $g(\varepsilon_0)$ remains the same as that characterizing the intrinsic peak regime. An example of the use of this extended-range fitting form was illustrated earlier in Fig. 10.33 for critical temperature at high-compressive strains.

Thus, to treat the extended-strain regime, four free parameters (a_1, a_2, g_1, and g_2) are added, resulting in the following (still separable) parameter set:

From $I_c(B)$ data:	p, q	characterizing the magnetic-field dependence
From $I_c(B,\varepsilon)$ data:	ε_m	characterizing the compressive prestrain

From $I_c(B,\varepsilon)$ data:	$a^-, a^+, a_1, a_2, B^*_{c2}(0,0)$	characterizing $B^*_{c2}(0,\varepsilon_0)$
"	s, g_1, g_2	characterizing $g(\varepsilon_0)$
From $I_c(B,t)$ data:	ν	characterizing $B^*_{c2}(t,0)$
"	$w, T^*_c(0)$	characterizing $T^*_c(\varepsilon_0)$
"	η	characterizing $h(t)$
	C	proportionality constant

Specific methods of evaluating these scaling parameters for both the intrinsic peak range and the extended strain range are given next.

10.7.4 METHODS FOR DETERMINING PARAMETER VALUES

Having defined the simplest parameter set for the intrinsic peak range and a more general set for the extended strain range, we now come to the practical task of determining the parameter *values*. With the separable parameter set, they all can be individually measured or estimated from limited data. It is important to determine them this way, rather than fitting many parameters simultaneously to a large multidimensional data set, to avoid errors inherent in a codependent fitting process (see the example given in Sec. 10.5.7). The procedures outlined below are designed to use high-leverage subsets of data to determine *consistent* parameter values that can stand alone for comparison with those of other conductors.

As a general rule try to avoid fitting more than *four free* parameters simultaneously (as shown earlier in the example of Sec. 10.5.7). Yes, it is true that larger simultaneously fit parameter sets work together for one conductor, but the individual parameter values are arbitrary, meaningless, and highly inconsistent compared with parameter values determined using the data-subset approach below.

If you have available a complete set of parameter values for an individual conductor, you can skip the rest of this section without the text losing continuity and just use them with Eq. (10.56) or Eq. (10.63) to determine $I_c(B,t,\varepsilon)$ over the intrinsic peak range or the extended-strain range, respectively. The same holds true for using them with the *transformation equations* described in Sec. 10.7.5. Just make sure the parameter values you use were obtained from high-leverage subsets of data as outlined below, not from a simultaneous global-fitting process.

On the other hand, if no parameter values are available for an individual conductor, the use of standard parameter values, such as those given in Appendix A10.2a, work for many purposes (especially nearby transformations), and, again, you can skip the rest of this section.

We consider several cases, depending on the available data, starting with a minimal amount of data and progressing to more complete data sets, the way data usually unfold for a new conductor.

1. *Method for making $I_c(B,t,\varepsilon)$ estimates when no variable-strain or variable-temperature data are available*: In this case, at least an initial estimate of $I_c(B,t,\varepsilon)$ can be obtained with nearly universal parameter values, applicable to a given class of superconductors for treating the intrinsic peak range. Standard correlation values for the parameters p, q, a^-, a^+, and s are listed in Appendix A10.2a for a number of A-15 and Chevrel superconductor classes.

For Nb_3Sn, quite generally, $\nu = 1.5$ and $w = 3$, as shown by Figs 10.36 through 10.38; and, although less standard, the values $\eta \approx 3$ and $T_c^*(0) = 17.5$ K are good first approximations. The parameter $B_{c2}^*(0,0)$ can be estimated from the approximate values of $B_{c2}^*(4.2K,0)$ given in Appendix A10.2a by using Eq. (10.57); that is, $B_{c2}^*(0,0) = B_{c2}^*(4.2K,0)[1-(4.2K/17.5K)^{\nu}]^{-1} = 1.13\, B_{c2}^*(4.2K,0)$.

That leaves the variables ε_m and C, which depend strongly on the particular technique used to fabricate a given conductor. The compressive prestrain ε_m can be determined from a measurement of $I_c(\varepsilon)$ at a single magnetic field or estimated from $I_c(\varepsilon)$ data obtained for a similar conductor. The proportionality constant C can be determined reliably only from an I_c measurement on the conductor in question, usually a single $I_c(B)$ curve or even just one I_c data point measured at, say, liquid-helium temperature at one magnetic-field level in the as-cooled prestrain state.

2. *Single $I_c(B)$ curve*: From a single $I_c(B)$ curve measured at a fixed temperature and strain, we can determine the parameters p and q, which characterize the magnetic-field dependence of the Lorentz force $F_L \equiv I_c B$. As described for the strain scaling law in the example of Sec. 10.5.7, the most reliable values of p and q are obtained from an $I_c(B)$ curve at a temperature $T \ll T_c^*(0)$ to minimize the effects of B_{c2} inhomogeneity (Sec. 10.3.4). Also, the curve should preferably be at a strain not too far from $\varepsilon_0 \approx 0$, to avoid B_{c2} inhomogeneity effects when $B_{c2}^*(\varepsilon)$ and $T_c^*(\varepsilon)$ are severely depressed by high-compressive strains, and to avoid filament breakage at high tensile strains. Standard values must be used to fill out the rest of the parameter set, as in case (1), which is at least useful for estimates of $I_c(B,t,\varepsilon)$.

3. *Set of $I_c(B,\varepsilon)$ data*: From a set of $I_c(B,\varepsilon)$ data at a fixed temperature T_1, we can determine all the strain parameters. Again, it is preferable to have a data set where $t_1 = T_1 / T_c^*(0) \ll 1$, such as 4.2 K for Nb_3Sn, in order to minimize inhomogeneity effects.

We start by determining $B_{c2}^*(T_1,\varepsilon)$ and the general prefactor $K(T_1,\varepsilon)$ in Eq. (10.45) as a function of strain. Values for $B_{c2}^*(T_1,\varepsilon)$ and $K(T_1,\varepsilon)$ are determined by fixing p and q, as described in case (2) above, and then making independent two-parameter fits of $B_{c2}^*(T_1,\varepsilon)$ and $K(T_1,\varepsilon)$ to the F_L–B curves at *each* strain point, exactly as shown in Table 10.3 for the strain-scaling example Sec. 10.5.7. The fits are made to the *Lorentz force* rather than I_c so that the low-field data are not unduly weighted.

From the $B_{c2}^*(T_1,\varepsilon)$ data, we can then determine the parameters ε_m, a^-, a^+, and the peak value $B_{c2}^*(t_1,\varepsilon_m)$ with a spreadsheet fit using Eq. (10.57) (at constant t_1). The procedure is exactly that described in step (3) of the example for the strain scaling in Sec. 10.5.7, illustrated in Fig. 10.34a. It is best to plot the data and visually determine the best values for ε_m and $B_{c2}^*(t_1,\varepsilon_m)$. Then, use the fitting routine to determine only the two parameters: a^- and a^+. Otherwise, with four adjustable parameters, the fitting routine can sometimes produce unrealistic parameter values (unless the data are precisely measured with a fine strain grid).

From the value of $B_{c2}^*(t_1,\varepsilon_m)$ we can also estimate the zero-temperature parameter $B_{c2}^*(0,\varepsilon_0=0)$ (where we have switched to intrinsic strain as the strain variable, since we now know ε_m). From Eq. (10.57), we see that the peak value $B_{c2}^*(t_1,0)$ is equal to $B_{c2}^*(0,0)\,(1-t_1^{\nu})$, from which we can calculate $B_{c2}^*(0,0)$ with "standard" values for $T_c^*(0)$ and ν [e.g. $T_c^*(0) = 17.5$ K and $\nu = 1.5$ for Nb_3Sn]. The error in $B_{c2}^*(0,0)$ is minimal if $t_1 = T_1/T_c^*(0) \ll 1$.

[For example, when $T_1 = 4.2$ K, a misestimate of 0.5 K in the value of $T_c^*(0)$ for Nb_3Sn produces an error in the calculated value of $B_{c2}^*(0,0)$ of only 0.5%.]

The $K(T_1,\varepsilon)$ data give the parameter s. For $t_1 = T_1/T_c^*(0) \ll 1$, the term $[B_{c2}^*(t,0)]^\eta$ in Eq. (10.52) is effectively independent of strain. {For example, a relatively large strain of $\varepsilon_0 = -0.4\%$ changes $[B_{c2}^*(t,0)]^\eta$ by only 1.6% at $T_1 = 4.2$ K for Nb_3Sn.} Consequently, when $T_1/T_c^*(0) \ll 1$, we obtain from Eq. (10.52) that $K(T_1,\varepsilon_0)/K(T_1,0) \approx [B_{c2}^*(T_1,\varepsilon_0)/B_{c2}^*(T_1,0)]^s$, and therefore the value of s can be determined directly (without any other fitting parameters) from the slope of a plot of $\log[K(T_1,\varepsilon)]$ vs. $\log[B_{c2}^*(T_1,\varepsilon)]$. This was illustrated earlier in Fig. 10.34(b) for the strain scaling law.

Thus, a single set of $I_c(B,\varepsilon_0)$ data at a temperature $T_1 \ll T_c^*(0)$ gives almost all the scaling parameters: p, q; ε_m; $a^-, a^+, B_{c2}^*(0,0)$; and s! At least for Nb_3Sn, the primary remaining unknown scaling parameters are η and $T_c^*(0)$, since the nearly universal values $\nu = 1.5$ and $w \simeq 3$ apply to most Nb_3Sn conductors. Lacking temperature data, the values $\eta \approx 3$ and $T_c^*(0) \approx 17.5$ K for Nb_3Sn are useful for estimating $I_c(B,t,\varepsilon)$ data, with minimal errors at temperatures $T_1 \ll T_c^*(0)$. The proportionality constant C for this particular parameter set can be obtained from a single value of I_c, preferably near $\varepsilon_0 = 0$. [A refined value of C could also be obtained from a *one*-parameter fit of C in Eq. (10.56) to the entire data set of $F_L \equiv I_c B$ values.]

Extended strain range: For data extending to compressive strains $\varepsilon_0 < -0.5\%$, we determine a series of values of $B_{c2}^*(T_1,\varepsilon_0)$ and $K(T_1,\varepsilon_0)$ at each strain, exactly as described above. For $T_1/T_c^*(0) \ll 1$, Eq. (10.62) gives $K(T_1,\varepsilon_0)/K(T_1,0) = [g(\varepsilon_0)/C]\ \{1-[T_1/T_c^*(\varepsilon_0)]^\nu\}^\eta / \{1-[T_1/T_c^*(0)^\nu\}^\eta \approx g(\varepsilon_0)/C$ and, therefore, the normalized functional dependence of $g(\varepsilon_0)/C$ for use in Eq. (10.63). However, the simple parameterizations of $B_{c2}^*(T_1,\varepsilon_0)$ and $K(T_1,\varepsilon_0)$ in terms of a and s, respectively, do not hold. Instead, we must employ extra parameters for the extended strain range and fit the two functions independently. We use Eq. (10.66) to parameterize $B_{c2}^*(0,\varepsilon_0)/B_{c2}^*(0,0)$ and Eq. (10.67) to parameterize $g(\varepsilon_0)/C$, because these expressions preserve the consistency of the parameter values (a and s) for the moderate strain range where many designs are carried out. For the high-compressive-strain range, however, four parameters are added (a_1, a_2, g_1, and g_2).

Thus, a single set of $I_c(B,\varepsilon_0)$ data at a temperature $T_1 \ll T_c^*(0)$ also serves to determine nearly all the scaling parameters over the extended strain range. The primary remaining unknown parameters are still η and $T_c^*(0)$, at least for the Nb_3Sn conductors evaluated thus far (where consistent values $\nu = 1.5$ and $w \simeq 3$ hold at high-compressive strains). For Nb_3Sn, the values $\eta \approx 3$ and $T_c^*(0) \approx 17.5$ K still work well at high-compressive strains for estimating $I_c(B,t,\varepsilon)$ data with minimal errors at temperatures $T_1 \ll T_c^*(0)$.

4. *Set of $I_c(B,T)$ data*: From $I_c(B,T)$ data measured at a fixed strain ε_1 (preferably near $\varepsilon_0 \approx 0$), we can determine all the temperature parameters.

Again, we start by determining $B_{c2}^*(T,\varepsilon_1)$ and the general prefactor $K(T,\varepsilon_1)$ in Eq. (10.45) as a function of temperature, similar to case (3), except now we are fitting at a series of variable temperatures, not strains. We break the fitting process into high-leverage subtasks to get consistent parameter values. The pinning-force exponents p and q are determined with the procedure described in case (2), and then independent two-parameter fits to the F_L–B curves are made at *each* temperature to determine a set of values for $B_{c2}^*(T,\varepsilon_1)$ and $K(T,\varepsilon_1)$. The fitting procedure proceeds just like the spreadsheet example for strain scaling shown earlier in

Table 10.3. Again, the fits are made to F_L, rather than I_c, so that the low-field data are not unduly weighted.

The $K(T,\varepsilon_1)$ data give the parameter η. From Eq. (10.52), $K(T,\varepsilon_1)/K(0,\varepsilon_1) = [B^*_{c2}(T,\varepsilon_1)/B^*_{c2}(0,\varepsilon_1)]^\eta$, since the term $B^*_{c2}(0,\varepsilon_0)$ is independent of temperature, so the value of η can be determined without any other fitting parameters from the slope of a plot of $\log[K(T,\varepsilon_1)]$ vs. $\log[B^*_{c2}(T,\varepsilon_1)]$.

From the $B^*_{c2}(T,\varepsilon_1)$ data, we can refine the standard value of the parameter ν. From Eq. (10.57) we have $B^*_{c2}(T,\varepsilon_1)/B^*_{c2}(0,\varepsilon_1) = (1-t^\nu)$, and so a three-parameter spreadsheet fit of the $B^*_{c2}(T,\varepsilon_1)$ data to this function gives ν, $T^*_c(\varepsilon_1)$, and $B^*_{c2}(0,\varepsilon_1)$, as illustrated by any one of the curves in Fig. 10.38. If the $I_c(B,T)$ data do not cover an extensive temperature range, more reliable values of $T^*_c(\varepsilon_1)$ and $B^*_{c2}(0,\varepsilon_1)$ are obtained with a two-parameter fit using a standard value for ν (e.g. $\nu=1.5$ for Nb_3Sn).

If ε_m and a are known from variable strain data (case 3), the value obtained for $T^*_c(\varepsilon_1)$ can be used to estimate $T^*_c(0)$ from Eq. (10.58) with a standard value for w (e.g. $w\approx 3$ for Nb_3Sn). The resultant error in $T^*_c(0)$ is minimal if $|\varepsilon_{01}|$ is less than about 0.1% to 0.2%.

Summarizing, $I_c(B,T)$ data at a fixed strain determine η and ν. If values for ε_m and a are available [e.g. from $I_c(B,\varepsilon_0)$ data], $T^*_c(0)$ can be determined as well. The most important function of $I_c(B,T)$ data, however, is to fix the parameter η [because it is not as well established as ν, and a precise value of $T^*_c(0)$ becomes important only at temperatures approaching $T^*_c(0)$].

Nota bene: From cases (3) and (4), we see that if measurements of both $I_c(B,\varepsilon)$ and $I_c(B,T)$ are available, the entire parameter set can be obtained for an individual conductor. The only exception is the parameter w, but it appears to be a constant with a nearly universal value, as evidenced by data correlations for Nb_3Sn conductors. The use of separate strain and temperature measurements and equipment represents a considerable savings in measurement time and specialized apparatus compared with determining the parameter values from a large three-dimensional $I_c(B,T,\varepsilon)$ data set. This is one of the principal advantages of separable parameters.

5. *Complete set of $I_c(B,T,\varepsilon)$ data*: The parameterizations of $B^*_{c2}(T_i, \varepsilon_j)$ and $K(T_i, \varepsilon_j)$ are carried out *independently* for individual pairs of temperature and strain (T_i and ε_j) by using the high-leverage procedures outlined in (3) and (4) above. Avoid the temptation to make a simultaneous fit of all the parameters. This is quick, especially with the larger parameter set of the unified scaling law, but it leads to inconsistent parameter values that depend on the fitting range and do not stand alone for comparison with those of other conductors. It also opens the door to using fitting relations that are not valid. There is no way to see what is going on without determining individual $B^*_{c2}(T_i, \varepsilon_j)$ and $K(T_i, \varepsilon_j)$ values for each pair of T_i and ε_j.

Individually determine as many parameters as possible with appropriate data *sub*sets as outlined in the steps above, and thus limit the number of remaining free parameters to just a few (ideally, just the overall proportionality constant C) when making a final global fit to the entire data set. Again, when adequate data are not available to determine some of the parameters, use standard values for these, rather than compromise the rest of the parameter set with highly inaccurate fitted values for the out-of-range parameters.

A complete set of $B^*_{c2}(T_i, \varepsilon_j)$ data offers the advantage over cases (3) and (4) above in that values of $T^*_c(\varepsilon_j)$ and $B^*_{c2}(0, \varepsilon_j)$ can be *directly* determined from a fit of Eq. (10.64) to the $B^*_{c2}(T_i, \varepsilon_j)$ data, as illustrated by the intercepts of the curves with the axes in Fig. 10.38. Then, from a

logarithmic plot of $T_c^*(\varepsilon_j)/T_c^*(0)$ vs. $B_{c2}^*(0, \varepsilon_j)/B_{c2}^*(0,0)$, the parameter w in Eq. (10.49) can be determined. Also, from the shape of the curves in Fig 10.38, the strain-independence of the parameter ν can be verified.

A complete set of $K(T_i, \varepsilon_j)$ data can also be used to check the functional dependences of $g(\varepsilon_0)$ and $h(t)$, as well as the constancy of p and q. Remember that at high temperatures, inhomogeneities in B_{c2} may increase the apparent value of q, as illustrated in Sec. 10.3.4. In this regard, the fitting procedures described above are quite robust and, independent of the precise values of the constants p and q, give consistent values for the rest of the parameters. [Again, the exception is the parameter $B_{c2}^*(0,0)$, which depends strongly on the value of q, as illustrated in Sec. 10.3.4.]

Thus, the unified scaling law works with a large range of available data, be it a single $I_c(B)$ curve, separate strain and temperature data, or a complete $I_c(B,T,\varepsilon)$ data set. With separable parameters and robust fitting procedures, consistent parameter values are obtained and can easily be updated for use with Eq. (10.56) for the intrinsic peak range or with Eq. (10.63) for the extended strain range. Typically, the better part of a month (or more) is required to obtain a complete set of $I_c(B,T,\varepsilon)$ data. For a new type of conductor, such an investment of time may be worth it to convince yourself that the unified scaling law works and to verify the value of the scaling parameter w. But, to determine customized scaling parameters for other conductors of the same type, considerable time can be saved by using the separable parameter set and two subsets of data [$I_c(B, \varepsilon)$ and $I_c(B,T)$], each taking only about one day to measure.

10.7.5 TRANSFORMATION METHOD FOR SIMPLIFIED APPLICATION OF THE UNIFIED SCALING LAW

In this last section we look at a method to reduce the number of parameters and streamline the entire unified-scaling process. We utilize the same transformation method developed earlier, except that now we extend it to the USL to carry out *combined* strain-and-temperature transformations.

The transformation equations given below in Eqs (10.68) and (10.69) work *regardless of the parameterization scheme used to represent* $K(T, \varepsilon)$. Here, we illustrate the technique with the original separable-parameter representation because it is consistent and easy to use, but the same two equations work by substituting any other representation of $K(T,\varepsilon)$ in Eq. (10.69).

The transformation method is particularly useful for utilizing a single $I_c(B)$ curve obtained at a convenient temperature and strain to obtain sets of $I_c(B,T, \varepsilon)$ data at less accessible temperatures and strains. The results are quite accurate, especially if the transformations are to nearby temperatures and strains. The method is particularly useful for saving time and effort in utilizing 4.2 K data to design applications operating at temperatures in the neighborhood above 4.2 K, such as cable-in-conduit magnets or magnets refrigerated with cryocoolers. This is illustrated at the conclusion of this section with a practical example.

Unified-scaling transformations

Similar to the development of the transformations given in Sec. 10.6.1, we eliminate $f(b)$ by utilizing the USL [Eq. (10.45)] to find scaling factors that allow us to renormalize an I_c–B curve measured at a given strain ε_1 and temperature T_1 to obtain a corresponding I_c–B' curve at a different strain ε_2 and temperature T_2. As shown in the example at the end of this section, the transformation is carried out in a spreadsheet program simply by multiplying a column of magnetic-field values and a column of corresponding critical-current values by the two constant prefactors enclosed in brackets { } below:

Unified scaling transformations:

Magnetic-field transformation:

$$B' = \{\beta\}B. \tag{10.68}$$

Critical-current unified transformation:

$$I_c(B',T_2,\varepsilon_2) = \left\{\beta^{-1}\frac{K(T_2,\varepsilon_2)}{K(T_1,\varepsilon_1)}\right\} I_c(B,T_1,\varepsilon_1), \tag{10.69}$$

where

$$\beta \equiv \frac{B^*_{c2}(t_2,\varepsilon_2)}{B^*_{c2}(t_1,\varepsilon_1)}, \tag{10.70}$$

and

$$\frac{B^*_{c2}(t,\varepsilon_0)}{B^*_{c2}(0,0)} = \frac{B^*_{c2}(0,\varepsilon_0)}{B^*_{c2}(0,0)}\,\frac{B^*_{c2}(t,0)}{B^*_{c2}(0,0)}, \tag{10.71}$$

$$\frac{T^*_c(\varepsilon_0)}{T^*_c(0)} = \left(\frac{B^*_{c2}(0,\varepsilon_0)}{B^*_{c2}(0,0)}\right)^{1/w}. \tag{10.72}$$

As before, the variables are defined by

$\varepsilon_0 \equiv \varepsilon - \varepsilon_m$, Intrinsic strain (where ε is the applied strain and ε_m is the applied strain at the peak, all in absolute units, not percent)

$b \equiv \dfrac{B}{B^*_{c2}(t_1,\varepsilon_0)}$, Reduced magnetic field

$t \equiv \dfrac{T}{T^*_c(\varepsilon_0)}$. Reduced temperature

Below we parameterize $K(T, \varepsilon_0)$ with the same separable parameter set used for the strain and temperatue scaling laws, considering first the intrinsic peak range and then the case of strains extending into the high compressive range. However, *any other representation of the*

prefactor $K(T, \varepsilon_0)$ in the general unified scaling law [Eq. (10.45)] would work to carry out simplified scaling transformations with Eqs (10.68) and (10.69).

Intrinsic peak range ($-0.5\% < \varepsilon_0 < +0.4\%$)

For the common case of data within the intrinsic peak range ($-0.5\% < \varepsilon_0 < +0.4\%$), we have [Eq. (10.52)]

$$K(T,\varepsilon_0) = C\left[\frac{B^*_{c2}(0,\varepsilon_0)}{B^*_{c2}(0,0)}\right]^s \left[\frac{B^*_{c2}(t,0)}{B^*_{c2}(0,0)}\right]^\eta. \quad (-0.5\% < \varepsilon_0 < +0.4\%)$$

Substituting this expression for $K(T, \varepsilon_0)$ in Eq. (10.69) and utilizing the separable parameter set given by Eqs (10.21) and (10.43), the bracketed { } transformation factors in Eqs (10.68) through (10.72) become:

Parameterization of unified transformation factors for $-0.5\% < \varepsilon_0 < +0.4\%$:

Magnetic-field factor, for use with Eq. (10.68):

$$\beta = \frac{B^*_{c2}(0,\varepsilon_{02})\, B^*_{c2}(t_2,0)}{B^*_{c2}(0,\varepsilon_{01})\, B^*_{c2}(t_1,0)} = \left(\frac{1-a|\varepsilon_{02}|^{1.7}}{1-a|\varepsilon_{01}|^{1.7}}\right)\left(\frac{1-t_2^\nu}{1-t_1^\nu}\right). \tag{10.73}$$

Critical-current factor, for use with Eq. (10.69):

$$\begin{aligned}\beta^{-1}\frac{K(T_2,\varepsilon_2)}{K(T_1,\varepsilon_1)} &= \left[\frac{B^*_{c2}(0,\varepsilon_{02})}{B^*_{c2}(0,\varepsilon_{01})}\right]^{s-1}\left[\frac{B^*_{c2}(t_2,0)}{B^*_{c2}(t_1,0)}\right]^{\eta-1} \\ &= \left(\frac{1-a|\varepsilon_{02}|^{1.7}}{1-a|\varepsilon_{01}|^{1.7}}\right)^{w-1}\left(\frac{1-t_2^\nu}{1-t_1^\nu}\right)^{\eta-1},\end{aligned} \tag{10.74}$$

where

$$\left(\frac{T^*_c(\varepsilon_0)}{T^*_c(0)}\right)^w = \frac{B^*_{c2}(0,\varepsilon_0)}{B^*_{c2}(0,0)} = 1-a|\varepsilon_0|^{1.7}. \tag{10.75}$$

Thus, for the common design strain range ($-0.5\% < \varepsilon_0 < +0.4\%$), the task of transforming both strain and temperature with Eqs (10.68) and (10.69) is reduced to evaluating these two prefactors from the scaling parameters: $\nu, w, \eta, s, a^-, a^+, T^*_c(0)$, and ε_m.

For Nb_3Sn, quite universally, $\nu = 1.5$ and, approximately, $w \simeq 3$, as shown previously by the data correlations given in Figs 10.36 through 10.38. Three of the remaining parameters (s, a^-, and a^+) have standard values for given classes of Nb_3Sn conductors (listed in Appendix A10.2a), leaving only the need for estimates of η, $T^*_c(0)$, and ε_m to carry out most combined strain and temperature transformations. With time and additional data, consistent standard values of the temperature scaling law parameters η and $T^*_c(0)$ may also be established for given classes of conductors.

High-compressive-strain range

As discussed in Sec. 10.7.3, Eq. (10.72) and the relationship $h(t)/h(0) = [B^*_{c2}(t,0)/B^*_{c2}(0,0)]^\eta$ still holds at high-compressive strains with approximately the same values of w and η as for the intrinsic peak range. However, as described in Sec. 10.5.6, the relationship $g(\varepsilon_0)/g(0) = [B^*_{c2}(0,\varepsilon_0)/B^*_{c2}(0,0)\,]^s$ no longer applies, with s ceasing to be a constant for $\varepsilon_0 \lesssim -0.5\%$ (Ekin 2007).

Thus, for high-compressive strains we substitute the more general expression [Eq. (10.59)]

$$K(T,\varepsilon_0) = g(\varepsilon_0)\left[\frac{B^*_{c2}(t,0)}{B^*_{c2}(0,0)}\right]^\eta,$$

into Eq. (10.69) to obtain the following set of equations for carrying out unified strain and temperature transformations for strains extending into the high-compressive-strain range.

Parameterization of unified transformation factors for extended strains, including $\varepsilon_0 < -0.5\%$:

Magnetic-field factor, for use with Eq. (10.68):

$$\beta = \frac{B^*_{c2}(0,\varepsilon_{02})\,B^*_{c2}(t_2,0)}{B^*_{c2}(0,\varepsilon_{01})\,B^*_{c2}(t_1,0)} = \frac{B^*_{c2}(0,\varepsilon_{02})}{B^*_{c2}(0,\varepsilon_{01})}\left(\frac{1-t_2^\nu}{1-t_1^\nu}\right). \tag{10.76}$$

Critical-current factor, for use with Eq. (10.69):

$$\begin{aligned}\beta^{-1}\frac{K(T_2,\varepsilon_2)}{K(T_1,\varepsilon_1)} &= \frac{g(\varepsilon_{02})}{g(\varepsilon_{01})}\left[\frac{B^*_{c2}(0,\varepsilon_{02})}{B^*_{c2}(0,\varepsilon_{01})}\right]^{-1}\left[\frac{B^*_{c2}(t_2,0)}{B^*_{c2}(t_1,0)}\right]^{\eta-1} \\ &= \frac{g(\varepsilon_{02})}{g(\varepsilon_{01})}\left[\frac{B^*_{c2}(0,\varepsilon_{02})}{B^*_{c2}(0,\varepsilon_{01})}\right]^{-1}\left(\frac{1-t_2^\nu}{1-t_1^\nu}\right)^{\eta-1},\end{aligned} \tag{10.77}$$

where

$$\frac{T^*_c(\varepsilon_0)}{T^*_c(0)} = \left(\frac{B^*_{c2}(0,\varepsilon_0)}{B^*_{c2}(0,0)}\right)^{1/w}. \tag{10.78}$$

As described in Sec. 10.5.6, $B^*_{c2}(0,\varepsilon_0)$ and $g(\varepsilon_0)$ both deviate from a simple power law at high-compressive strains, and therefore additional parameters are needed to represent them in this regime. *Again, any parameterization of* $B^*_{c2}(0,\varepsilon_0)$ and $g(\varepsilon_0)$ *work to evaluate the transformation factors given by Eqs (10.76) and (10.77).*

Here we use the extended-range parameterization of Sec. 10.5.6 because it has the advantage that it preserves the consistency of the parameter values over the intrinsic peak range. That is,

$$\frac{B^*_{c2}(0,\varepsilon_0)}{B^*_{c2}(0,0)} = 1 - a|\varepsilon_0|^{1.7} + a_1|\varepsilon_0 - \varepsilon_0'|^{a_2} I(\varepsilon_0 < \varepsilon_0'), \tag{10.79}$$

$$\frac{g(\varepsilon_0)}{g(0)} = [1-a|\varepsilon_0|^{1.7}]^s + g_1|\varepsilon_0-\varepsilon_0'|^{g_2} I(\varepsilon_0<\varepsilon_0'), \tag{10.80}$$

where the indicator function is defined by

$$I(\varepsilon_0<\varepsilon_0') \equiv \begin{cases} 1 & \text{if } \varepsilon_0<\varepsilon_0' \\ 0 & \text{if } \varepsilon_0>\varepsilon_0'. \end{cases}$$

[Again, the indicator function $I(\varepsilon_0 < \varepsilon_0')$ is readily programmed in spreadsheet programs with a conditional clause of the form IF($\varepsilon_0 < \varepsilon_0'$, 1 if true, 0 if false); for Nb_3Sn, $\varepsilon_0' \approx -0.005$.] This representation adds four parameters (a_1, a_2, g_1, and g_2) to treat the extended strain range. The intrinsic strain-sensitivity parameter a in these extended-range functions retains the same consistent value as that characterizing the intrinsic peak regime.

No extra parameters are needed for $T_c^*(\varepsilon_0)$, since Eq. (10.78) still holds with the same value of w over both the moderate strain and high-compressive-strain ranges.

Thus, for carrying out combined strain and temperature transformations at high compressive strains ($\varepsilon_0 < -0.5\%$), the two transformation constants given by Eqs (10.76) and (10.77) are evaluated from the scaling parameters: ν, w, η, a^-, a_1, a_2, s, g_1, g_2, $T_c^*(0)$ and ε_m. As noted in the previous subsection, the parameters ν, w, s, a^-, and a^+ have standard values for given classes of Nb_3Sn conductors (listed in Appendix A10.2a), and, with further data correlations, consistent values of the temperature scaling parameters η and $T_c^*(0)$ may also become available.

Example: Transformation method for calculating combined strain-and-temperature changes in the critical current

We conclude by giving an example to show the simplicity of this transformation method for combined strain-and-temperature transformations in a practical situation. We start with the same data used to illustrate the strain-only transformation in the example of Sec. 10.6.2, except now we consider an example with temperature transformations added. This is a common situation encountered in the design of magnets operating at temperatures above 4.2 K, such as cryocooled magnets or cable-in-conduit magnets.

Example: Unified strain-and-temperature transformation: Suppose we have the I_c–B curve shown for sample 1 in Fig. 10.35 (the data are tabulated in the first two columns of Table 10.5). These data were obtained by making measurements under the easiest conditions possible—by cooling the sample in liquid helium and measuring I_c–B with the conductor in its prestrain state (in this case, about $\varepsilon_0 = -0.4\%$ as determined from a single I_c–ε curve on this or a similar conductor).

Further, suppose we are considering this conductor for a high-field cryocooled magnet that will operate at 5.5 K. Our problem is that we need I_c–B data at 5.5 K at a series of possible design strains, but we have data for this conductor only at 4.2 K at one strain level (the as-cooled strain state).

We could, of course, measure the needed data from a combined variable-strain and variable-temperature experiment, but this is a fairly complex measurement and requires very specialized

Table 10.5 **Data-sheet example for combined strain-and-temperature transformation of I_c–B data at $T = 4.2$ K and $\varepsilon_0 = -0.4\%$, to $T = 5.5$ K and $\varepsilon_0 = -0.18\%$.**

Measured at $\varepsilon_0 = -0.4\%$ and $T = 4.2$ K		Calculated at $\varepsilon_0 = -0.18\%$ and $T = 5.5$ K	
B	$J_c(4.2\text{ K}, -0.4\%)$	$B' = \beta B$ $= 0.993\,B$	$J_c(5\text{ K}, -0.18\%) =$ $0.877\,J_c(4.2\text{ K}, -0.4\%)$
[T]	[10^8 A/m^2]	[T]	[10^8 A/m^2]
12	4.62	11.92	4.05
14	2.71	13.90	2.38
16	1.34	15.89	1.18
18	0.485	17.87	0.425
19	0.253	18.87	0.222

The magnetic-field transformation factor is $\beta = 0.993$ from Eq. (10.73), and the critical-current transformation factor is $\beta^{-1}\,K(T_2, \varepsilon_2)/K(T_1, \varepsilon_1) = 0.877$ from Eq. (10.74).

equipment. The experiment is all the more difficult because the desired temperature is only slightly above liquid-helium temperature. (That is, regulating the temperature with a gas-cooled apparatus at high currents is extremely difficult this close to 4.2 K because of the small ΔT available for cooling. An example of such a specialized variable-temperature apparatus with high cooling power was illustrated in Fig. 9.13.)

We illustrate the method for a single transformation of the I_c–B curve of sample 1 from 4.2 K and -0.4% intrinsic strain, to 5.5 K and -0.18%. (This is the same target strain considered for the example in Sec. 10.6.2, so we can compare the results with those obtained earlier.) However, any desired strain (or series of strains) at 5.5 K is easily calculated in the same way with a spreadsheet program.

Equations (10.73) through (10.75) are the simplest parameterization for this case (since high-compressive strains are not an issue). The transformation factor β for magnetic field is evaluated by substituting the initial variable values ($\varepsilon_{01} = -0.4\% = -0.004$ and $T_1 = 4.2$ K) and the target values ($\varepsilon_{02} = -0.18\% = -0.0018$ and $T_2 = 5.5$ K) into Eq. (10.73), with values of $T_c^*(\varepsilon_0)$ obtained from Eq. (10.75). Since this is a binary Nb_3Sn conductor, we use the nearly universal parameter values for this class of Nb_3Sn superconductors from Appendix A10.2a: $\nu = 1.5$, $w = 3$, $s = 1$, and $a^- = 900$, as well as the approximate values $\eta = 3$ and $T_c^*(0) = 17.5$ K.

These values work well for such nearby transformations. If distant transformations are involved or greater accuracy is needed, the high-leverage methods given in Sec. 10.7.4 describe how to use even limited strain and temperature data to more precisely determine the parameters for a particular conductor [s, a^-, and ε_m for characterizing the conductor's strain dependence, and $T_c^*(0)$ and η for characterizing its temperature characteristics].

With the standard parameter values for binary Nb_3Sn, $T_c^*(\varepsilon_0)$ is evaluated from Eq. (10.75) for the source and target strains:

Effective critical temperatures:

$$T_c^*(\varepsilon_0) = T_c^*(0)(1 - a|\varepsilon_0|^{1.7})^{1/w}$$

$$T_c^*(-0.004) = (17.5\text{ K})\,[1 - 900|-0.004|^{1.7}]^{1/3} = 17.05\text{ K}$$

$$T_c^*(-0.0018) = (17.5\text{ K})\,[1 - 900|-0.0018|^{1.7}]^{1/3} = 17.39\text{ K}$$

and then from Eq. (10.73) we obtain

Magnetic-field transformation factor

$$\begin{aligned}\beta &= \left(\frac{1-a|\varepsilon_{02}|^{1.7}}{1-a|\varepsilon_{01}|^{1.7}}\right)\left(\frac{1-t_2^{\nu}}{1-t_1^{\nu}}\right)\\ &= \left(\frac{1-900|-0.0018|^{1.7}}{1-900|-0.004|^{1.7}}\right)\left(\frac{1-(5.5\text{ K}/17.39\text{ K})^{1.5}}{1-(4.2\text{ K}/17.05\text{ K})^{1.5}}\right)\\ &= 0.993.\end{aligned}$$

Note that this value of β is smaller than that obtained in the earlier example of Sec. 10.6.2 ($\beta=1.060$) because the transformation to higher temperature compensates the transformation to smaller intrinsic strain.

Next, we calculate the transformation factor for the critical-current values from Eq. (10.74). As noted above, the value of the strain exponent s for binary Nb_3Sn is about 1, so the exponent $s - 1 = 0$ in the strain part of Eq. (10.74) does not play a role (although it would, to varying degrees, for the other conductor classes listed in Appendix A10.2a where s is not unity). The value of the temperature exponent η is approximately 3 for Nb_3Sn conductors in general, and so the exponent $\eta - 1 = 2$ in the temperature part of Eq. (10.74). Evaluating Eq. (10.74), we find

Critical-current transformation factor

$$\begin{aligned}\beta^{-1}\frac{K(T_2,\varepsilon_2)}{K(T_1,\varepsilon_1)} &= \left(\frac{1-a|\varepsilon_{02}|^{1.7}}{1-a|\varepsilon_{01}|^{1.7}}\right)^{s-1}\left(\frac{1-t_2^{\nu}}{1-t_1^{\nu}}\right)^{\eta-1}\\ &= \left(\frac{1-(5.5\text{ K}/17.39\text{ 1})^{1.5}}{1-(4.2\text{ K}/17.05\text{ 1})^{1.5}}\right)^{2}\\ &= 0.877.\end{aligned}$$

Thus, to transform the data for Sample 1, we simply multiply the B data in the first column of Table 10.5 by 0.993 to obtain B', and the $I_c(T=4.2\text{ K}, \varepsilon_0=-0.4\%)$ data in the second column by 0.877 to calculate $I_c(T=5.5\text{ K}, \varepsilon_0=-0.18\%)$. The results are tabulated in the two right-hand columns of Table 10.5.

That's it. The entire process can be done quickly in a spreadsheet program and gives sufficiently accurate results for this purpose, perhaps more accurate than most variable-temperature measurement equipment are capable of providing at temperatures so close to 4.2 K. The principal error stems from not having yet established standard values of the conductor's temperature exponent η for each conductor class. Even if the conductor's actual η differed from the estimated value by a large amount, say 20%, the error in the transformed I_c at 5.5 K would be only about 3.5%.

In summary, the transformation approach provides a way to transform I_c–B characteristics measured at a convenient temperature and strain (such as 4.2 K and the as-cooled strain state) to other temperatures and strains not so readily accessible. Therefore, it represents a powerful, but relatively simple technique for data comparisons and magnet design.

Sometimes, all that is needed is an estimate of an I_c–B curve at a different strain and temperature. Other times, precise data may be needed, but the target strains and temperatures are nearby. In either case, the transformation method is ideally suited *with the nearly universal values* of the separable parameter set given in Appendix A10.2a.

If precise data are needed for distant transformations, refined parameter values specific to a given conductor can be obtained, as described in Sec. 10.7.4, from only limited strain data $I_c(B,\varepsilon)$ or temperature data $I_c(B,T)$ [not necessarily the entire three-dimensional $I_c(B,T,\varepsilon)$ data set]. As more extensive data become available for a specific conductor, the separable strain and temperature parameters can be independently updated.

It bears reemphasizing that this method depends on neither the shape of the I_c–B curve nor the extrapolation method used to obtain B^*_{c2} (thus Kramer extrapolations and the sometimes unrealistic values of B^*_{c2} are not a problem). The method relies on only the unified scaling law Eq. (10.45) and would readily work with any other parameterization of the general prefactor $K(T,\varepsilon_0)$ in Eq. (10.45).

EPILOGUE

Thus, with the practical measurement and analysis of critical current, we complete this narrative on experimental techniques in an exciting space very far from our ambient environment—the world of cryogenics.

Cold indeed, and labor lost:
Then farewell heat, and welcome frost!

– William Shakespeare,
The Merchant of Venice, Act 2

10.8 References

10.8.1 FURTHER READING

DESCRIPTIONS OF TYPE II SUPERCONDUCTIVITY AND THE ROLE OF MAGNETIC VORTICES AND PINNING IN DETERMINING THE CRITICAL CURRENT:

Orlando, R. P., and Delin, K. A. (1991). *Foundations of Applied Superconductivity*, Addison-Wesley Publishing, Reading, MA (out of print, but available as a used book on the Internet); a clear, comprehensive text.

Rose Innes, A. C., and Rhoderick, E. H. (1976). *Introduction to Superconductivity*, International Series in Solid State Physics, Vol. 6, Pergamon Press, Oxford; Elmsford, NY (also out of print, but available used on the Internet); a lucid introductory treatment of type II superconductivity and magnetic vortices is given in Part II, starting with Chapter 12.

Tinkham, M. (2004). *Introduction to Superconductivity*; 2nd edition, Dover Publications, New York; a thorough, more advanced textbook.

INTRODUCTIONS TO THE JOSEPHSON EFFECT:

Matisoo, J. (1981). *Scientific American*, Nov. 25, 50–65.

Orlando, R. P., and Delin, K. A. (1991). *Foundations of Applied Superconductivity*, Addison-Wesley Publishing, Reading, MA (out of print, but available as a used text on the Internet); see the first several pages of Chapter 8.

Ruggiero, S. (1999). "Tunneling and Josephson Junctions." in *The Encyclopedia of Electrical and Electronics Engineering*, John G. Webster (ed.) John Wiley & Sons, Somerset, New Jersey.

Tinkham, M. (1992). "Josephson effects in weak links" in the *Concise Encyclopedia of Magnetic & Superconducting Materials*, ed. J. Evetts, Pergamon Press, Oxford, UK.

FLUX PINNING AND CRITICAL CURRENTS IN HIGH-T_C SUPERCONDUCTORS:

Overview article

Larbalestier, D., Gurevich, A., Feldmann, D. M., and Polyanskii, A. (2001). "High-T_c superconducting materials for electric power applications," *Nature* 414, 368–377; an insightful article giving an overview of superconductor fabrication techniques, flux pinning, critical-current densities, grain-boundary effects, anisotropy, and current percolation paths.

Detailed reviews and articles

Blatter, G., Feigel'man, M. V., Geshkenbein, V. B, Larkin, A. I., and Vinokur, V. M. (1994). "Vortices in high-temperature superconductors," *Rev. Mod. Phys.* 66, 1125–1388; a detailed review of the literature on vortices and pinning.

Brandt, E. H. (1995). "The flux-line lattice in superconductors," *Rep. Prog. Phys.* 58, 1465–1594; an accessible review of magnetic-flux-line lattices and pinning in both low- and high-T_c superconductors.

Goyal, A., ed. (2004). *Second-Generation HTS Conductors*, Kluwer Academic Publishers, Dordrecht; articles on techniques for fabricating second-generation high-current YBCO superconductors.

Hilgenkamp, H., and Mannhart, J. (2002). "Grain boundaries in high-T_c superconductors," *Rev. Mod. Phys.* 74, 485–549; detailed review article focusing on grain-boundary effects.

THE DEPINNING CRITICAL FIELD—DETERMINATION IN TWO WAYS:

From extrapolating I_c vs. B curves to zero current, called the *effective critical field* B^*_{c2}:

Ekin, J. W. (1980a). "Strain scaling law for flux pinning in practical superconductors. Part 1: Basic relationship and application to Nb_3Sn superconductors." *Cryogenics* 20, 611–624.

From magnetization curves, called the *irreversibility field* B_{irr}:

Suenaga, M., Ghosh, A. K., Xu, Y., and Welch, D. O. (1991). "Irreversibility temperatures of Nb_3Sn and Nb-Ti," *Phys. Rev. Lett.* 66, 1777.

Yershurun, Y., and Malozemoff, A. P. (1988). "Giant flux creep and irreversibility in an Y-Ba-Cu-O crystal: An alternative to the superconducting-glass model," *Phys. Rev. Lett.* 60, 2202.

BENDING STRAIN EFFECTS AND THEIR RELATION TO AXIAL STRAIN EFFECTS:

Ekin, J. W. (1980b). "Strain scaling law and the prediction of uniaxial and bending strain effects in multifilamentary superconductors," in *Filamentary A15 Superconductors*, eds. M. Suenaga and A. F. Clark, pp. 187–203, Plenum Press, New York. This edited volume also contains several other good articles in the "Mechanical Properties" section, which treat prestress and strain effects in practical low-T_c superconductors.

10.8.2 CHAPTER REFERENCES

American Superconductor (1996). Westborough, MA 01581.

Arp, V. D. (1977). "Stresses in superconducting solenoids," *J. Appl. Phys.* 48, 2026–2036.

Campbell, A. M., and Evetts, J. E. (1972). "Flux vortices and transport currents in type II superconductors," *Adv. Phys.* 21, 199.

Cheggour, N., Decroux, M., Gupta, A., Fischer, O., Perenboom, J. A. A. J., Bouquet, V., Sergent, M., and Chevrel, R. (1997). "Enhancement of the critical current density in Chevrel phase superconducting wires," *J. Appl. Phys.* 81, 6277–6284.

Cheggour, N., and Hampshire, D. P. (1999). "Unifying the strain and temperature scaling laws for the pinning force density in superconducting niobium–tin multifilamentary wires," *J. Appl. Phys.* 86, 552–555. Note that the treatment of the parameter *m* in this article should not be identified with the parameter *s* used in Sec. 10.7.2 of this textbook or with the strain exponent *n* used in the unified strain-and-temperature scaling law postulated in the last section of Ekin (1980a). (The difference is that in the 1980a article, the unified scaling law was postulated to have a separable form that expresses the strain- and temperature-scaling functions with different constant exponent: *n* and *v*, respectively. In this 1999 article, on the other hand, the same exponent *m* is applied to both the temperature and strain functions, which gives a nonconstant value of *m*.) Moreover, when the data and relations of this article are re-expressed in separable form and evaluated, they effectively reduce to that in Ekin (1980a), providing experimental confirmation of the original postulate of the unified scaling law (Ekin 2007).

Cheggour, N., and Hampshire, D. P. (2002). "The unified strain and temperature scaling law for the pinning force density of bronze-route Nb_3Sn wires in high magnetic fields," *Cryogenics* 42, 299–309. See the previous reference's note regarding the treatment of the parameter *m* in this article, which is not the same as the parameter *s* used in Sec. 10.7.2 of this textbook.

Cheggour, N., Ekin, J. W., Clickner, C. C., Verebelyi, d. T., Thieme, C. L. H., Feenstra, R., and Goyal, A. (2003). "Reversible axial-strain effect and extended strain limits in Y–Ba–Cu–O coatings on deformation-textured substrates," *Appl. Phys. Lett.* 83, 4223–4225.

Cheggour, N., Ekin, J. W., and Thieme, C. L. H. (2005). "Magnetic-field dependence of the reversible axial-strain effect in Y-Ba-Cu-O coated conductors," *IEEE Trans. Appl. Supercond.* 15, 3577–3580.

Cheggour, N., Ekin, J. W., Xie, Y. Y., Selvamanickam, V., Thieme, C. L. H., and Verebelyi, D. T. (2005). "Enhancement of the irreversible axial-strain limit of Y–Ba–Cu–O coated conductors with the addition of a Cu layer," *Appl. Phys. Lett.*, 87, 212505-1–212505-3.

Chisholm, M. F., and Pennycook, S. J. (1991). "Structural origin of reduced critical currents at $YBa_2Cu_3O_{7-\delta}$ grain boundaries," *Nature* (London) 351, 47.

Christen, D. K. (2000). Oak Ridge National Laboratory, Oak Ridge, Tennessee, personal communication.

Civale, L. (2005). Los Alamos National Laboratory, Los Alamos, New Mexico, personal communication.

Civale, L., Maiorov, B., Serguis, A., Willis, J. O., Coulter, J. Y., Wang, H., Jia, Q. X., Arendt, P. N., Jaime, M., MacManus-Driscoll, J. L., Maley, M. P., and Foltyn, S. R. (2004). "Understanding high critical currents in $YBa_2Cu_3O_7$ thin films and coated conductors," *J. Low Temp. Phys.* 135, 87.

Dimos, D., Chaudhari, P., Mannhart, J., and Legoues, F. K. (1988). "Orientation dependence of grain-boundary critical currents in $YBa_2Cu_3O_{7-\delta}$ bicrystals," *Phys. Rev. Lett.* 61, 219–222.

Dimos, D., Chaudhari, P., and Mannhart, J. (1990). "Superconducting transport properties in $YBa_2Cu_3O_{7-\delta}$ bicrystals," *Phys. Rev.* B 41, 4038–4049.

Dou, S. X., Soltanian, S., Horvat, J., Wang, X. L., Zhou, S. H., Ionescu, M., Liu, H. K., Munroe, P., and Tomsic, M., (2002). "Enhancement of the critical current density and flux pinning of MgB_2 superconductor by nanoparticle SiC doping," *Appl. Phys. Lett.* 81, 3419–3421.

Dresner, L. (1978). "Distribution of current among the filaments of a multifilamentary superconductor close to the inputs leads," *Cryogenics* 18, 285–288.

Ekin, J. W. (1978). "Current transfer in multifilamentary superconductors: Part I—theory," *J. Appl. Phys.* 49, 3406–3409.

Ekin, J. W. (1980a). "Strain scaling law for flux pinning in practical superconductors. Part 1: Basic relationship and application to Nb_3Sn superconductors," *Cryogenics* 20, 611–624. The "Unified strain and temperature scaling relation" postulated in the last section of this article is distinct from the "Strain

scaling law" formulated in the first part. Two of the parameters in this original article have been changed in this text to avoid confusion with other symbols in the text or in recent literature. The following parameters in Eqs (10.56)–(10.58) of this text that have been relabeled from the original article (all other parameter labels remain the same as in Eqs 13–18 of the original article): $n \rightarrow s, \nu \rightarrow \eta$.

Ekin, J. W. (1980b). "Strain scaling law and the prediction of uniaxial and bending strain effects in multifilamentary superconductors," in *Filamentary A15 Superconductors*, eds. M. Suenaga and A. F. Clark, pp. 187–203, Plenum Press, New York.

Ekin, J. W. (1981a). "Mechanical properties and strain effects in superconductors," in *Superconducting Materials Science: Metallurgy Fabrication and Applications*, eds. S. Foner and B. B. Schwartz, pp. 455–510, Plenum Press, New York.

Ekin, J. W. (1981b). "Strain scaling law for flux pinning in Nb–Ti, Nb_3Sn, Nb–Hf/Cu–Sn–Ga, V_3Ga and Nb_3Ga." *IEEE Trans. Magn.* MAG-17, 658–661.

Ekin, J. W. (1983). "Superconductors," Chapter 13 in *Materials at Low Temperatures*, eds. R. P. Reed and A. F. Clark, ASM International, Materials Park, OH.

Ekin, J. W. (1984). "Strain effects in superconducting compounds," *Adv. Cryog. Eng.* 30, 823–836.

Ekin, J. W. (1985). "High-field flux pinning and the strain scaling law," in *Proceedings International Symposium on Flux Pinning and Electromagnetic Properties of Superconductors*, eds. T. Matsushita, K. Yamafuji, and F. Irie, pp. 267–271, Matsukuma Press, Fukuoka, Japan.

Ekin, J. W. (1989). "Offset criterion for determining superconductor critical current," *Appl. Phys. Lett.* 55, 905–907.

Ekin, J. W. (2007). *Cryogenics*, to be published.

Ekin, J. W. and Welch, D. O. (1985). "Abstract," in *Proceedings of the Sixth International Cryogenic Materials Conference*, August 12–16, Cambridge, MA.

Ekin, J. W., Braginski, A. I., Panson, A. J., Janocko, M. A., Caponne. D. W., II, Zaluzec, N. J., Flandermeyer, B., de Lima, O. F., Hong, M., Kwo, J., and Liou, S. H. (1987). "Evidence for weak link and anisotropy limitations on the transport critical current in bulk polycrystalline $Y_1Ba_2Cu_3O_x$," *J. Appl. Phys.* 62, 4821–4828.

Ekin, J. W., Finnemore, D. K., Li, Q., Tenbrink, J., and Carter, W. (1992). "Effect of axial strain on the critical current of Ag-sheathed Bi-based superconductors in magnetic fields up to 25 T," *Appl. Phys. Lett.* 61, 858–859.

Feenstra, R., and Verebelyi, D. T. (1999). Oak Ridge National Laboratory, Oak Ridge, Tennessee, personal communication.

Feldmann, D. M., Reeves, J. L., Polyanskii, A. A., Kozlowski, G., Biggers, R. R., Nekkanti, R. M., Maartense, I., Tomsic, M., Barnes, P., Oberly, C. E., Peterson, T. L., Babcock, S. E., and Larbalestier, D. C. (2000). "Influence of nickel substrate grain structure on $YBa_2Cu_3O_{7-\delta}$ supercurrent connectivity in deformation-textured coated conductors," *Appl. Phys. Lett.* 77, 2906–2908.

Fietz, W. A., and Rosner, C. H. (1974). "Advances in superconducting magnets and materials," *IEEE Trans. Magn.* MAG-10, 239–259.

Fietz, W. A., and Webb, W. W. (1969). "Hysteresis in superconducting alloys—temperature and field dependence of dislocation pinning in niobium alloys," *Phys. Rev.* 178, 657–667.

Foltyn, S. R., Jia, Q. X., Arendt, P. N., Kinder, L., Fan, Y., and Smith J. F. (1999). "Relationship between film thickness and the critical current of $YBa_2Cu_3O_{7-\delta}$-coated conductors," *Appl. Phys. Lett.* 75, 3692–3694.

Foltyn, S. R., Arendt, P. N., Jia, Q. X., Wang, H., MacManus–Driscoll, J. L., Kreiskott, S., DePaula, R. F., Stan, L., Groves, J. R., and Dowden, P. C. (2003). "Strongly coupled critical current density values achieved in $Y_1Ba_2Cu_3O_{7-\delta}$ coated conductors with near-single-crystal texture," *Appl. Phys. Lett.* 82, 4519–4521.

Godeke, A., Krooshoop, H. J. G., Knoopers, H. G., ten Haken, B., and ten Kate, H. H. J. (2001). "Experimental verification of the temperature and strain dependence of the critical properties in Nb_3Sn wires," *IEEE Trans. Appl. Supercond.* 11, 1526–1529.

Godeke, A., Jewell, M. C., Golubov, A. A., ten Haken, B., and Larbalestier, D. C. (2003). "Inconsistencies between extrapolated and actual critical fields in Nb_3Sn wires as demonstrated by direct measurement of H_{c2}, H^* and T_c," *Supercond. Sci. Technol.* 16, 1019–1025.

Godeke, A., Jewell, M. C., Fischer, C. M., Squitieri, A. A., Lee, P. J., and Larbalestier, D. C. (2005). "The upper critical field of filamentary Nb_3Sn conductors," *J. Appl. Phys.* 97, 93909–1–93909–12.

Goodrich, L. F., and Stauffer, T. C. (2001). "Hysteresis in transport critical-current measurements of oxide superconductors," *J. Res. Natl. Inst. Stand. Technol.* 106, 657–690.

Goodrich, L. G., and Stauffer, T. C. (2003). National Institute of Standards and Technology, Boulder, CO, unpublished.

Goodrich, L. F., Medina, L. T., and Stauffer, T. C. (1998). "High critical-current measurements in liquid and gaseous helium," *Adv. Cryog. Eng.* 44, 873–880.

Gurevich, A. (2002). "Nonlinear dynamics of vortices in easy flow channels along grain boundaries in superconductors," *Phys. Rev.* B65, 214531–1–214531–16.

Hampshire, D. P., Jones, H., and Mitchell, E. W. J. (1985). "An in depth characterization of $(NbTa)_3Sn$ filamentary superconductor," *IEEE Trans. Magn.* MAG-21, 289–292.

Hampshire, R. G., and Taylor, M. T. (1972). "Critical supercurrents and the pinning of vortices in commercial Nb-60 at-% Ti.," *J. Phys. F* 2, 89.

Hasagawa, T., Ohtani, N., Koizumi, T., Aoki, Y., Nagaya, S., Hirano, N., Motowidlo, L., Sokolowski, R. S., Scanlan, R. M., Dietderich, D. R., and Hanai, S. (2000). "Improvement of superconducting properties of Bi-2212 round wire and primary test results of large capacity Rutherford cable," *IEEE Trans. Appl. Supercond.* 11, 3034–3037.

Hayashi, K., Hahakura, S., Saga, N., Kobayashi, S., Kato, T., Ueyama, M., Kaneko, T., Hikata, T., Ohkura, K., and Sato, K. (1997). "Development of Ag-sheathed Bi2223 superconducting wires and their application to magnets," *IEEE Trans. Appl. Supercond.* 7, 2201–2206.

Heussner, R. W., Marquardt, J. D., Lee, P. J., and Larbalestier, D. C. (1997). "Increased critical current density in Nb–Ti wires having Nb artificial pinning centers," *Appl. Phys. Lett.* 70, 901–903.

Hilgenkamp, H., and Mannhart, J. (2002). "Grain boundaries in high-T_c superconductors," *Rev. Mod. Phys.* 74, 485–549.

Hoard, R. W., Scanlan, R. M., and Hirzel, D. G. (1980). "Maximsuper: A computer program to assist in the design of multifilamentary superconducting composites," *Adv. Cryog. Eng.* 26, 578–588.

Iijima, Y., Kikuchi, A., Inoue, K., and Takeuchi, T. (1999). "Multifilamentary wire fabricated by rapid-heating/quenching process," *IEEE Trans. Supercond.* 9, 2696–2701.

Iwasa, Y., and Montgomery, B. (1975). "High-field superconducting magnets," in *Applied Superconductivity* 2, ed. V. L. Newhouse, pp. 387–487, Academic Press, New York.

Keys, S. A., and Hampshire, D. P. (2003). "A scaling law for the critical current density of weakly- and strongly-coupled superconductors, used to parameterize data from a technological Nb_3Sn strand," *Supercond. Sci. Technol.* 16, 1097–1108.

Kikuchi, A., Iijima, Y., Inoue, K., Kosuge, M., and Itoh, K. (2001). "Rapidly-heating/quenching process," *IEEE Trans. Appl. Supercond.* 11, 3984–3987.

Kramer, E. J., (1973). "Scaling laws for flux pinning in hard superconductors," *J. Appl. Phys.* 44, 1360–1370.

Kroeger, D. M., Koch, C. C., and Charlesworth, J. P. (1975). "Comparison of methods for measuring flux gradients in type-II superconductors," *J. Low Temp. Phys.* 19, 493.

Kroeger, E. M., Easton, D. S., DasGupta, A., Koch, C. C., and Scarbrough, J. O. (1980). "The effect of strain upon the scaling law for flux pinning in bronze process Nb_3Sn," *J. Appl. Phys.* 51, 2184–2192.

Kumakura, H., Tadano, Y., Fujii, H., Togano, K., Kito, H., and Ihara, H. (2001). "Critical current densities and irreversibility fields of MgB_2 bulks," *Physica C* 363, 179–183.

Larbalestier, D., Gurevich, A., Feldmann, D. M., and Polyanskii, A. (2001). "High-T_c superconducting materials for electric power applications," *Nature* 414, 368–377.

Lee, P. J. (2002 and 2005). http://www.asc.wisc.edu/plot/plot.htm.

Lehndorff, B. R. (2001). *High-T_c Superconductors for Magnet and Energy Technology*, Springer, Berlin.

Markiewicz, W. D. (2004). "Elastic stiffness model for the critical temperature T_c of Nb_3Sn including strain dependence," *Cryogenics* 44, 767–782.

Markiewicz, W. D. (2005). National High Magnetic Field Laboratory, Tallahassee, Florida, personal communication.

MacManus-Driscoll, J. L., Foltyn, S. R., Jia, Z. X., Wang, H., Serquis, A., Civale, L., Maiorov, B., Hawley, M. E., Maley, M. P., and Peterson, D. E. (2004). "Strongly enhanced current densities in superconducting coated conductors of $BaZrO_3$-doped $YBa_2Cu_3O_{7-x}$", *Nature Materials* 3, 439.

Narlikar, A. V., and Dew-Hughes, D. (1966). "Superconductivity of deformed niobium-alloys," *J. Mater. Sci.* 1, 317.

Norton, D. P., Goyal, A., Budai, J. D., Christen, D. K., Kroeger, D. M., Specht, E. D., He, Q., Saffian, B., Paranthaman, M., Klabunde, E., Lee, D. F., Sales, B. C., and List, F. A. (1996). "Epitaxial $YBa_2Cu_3O_7$ on biaxially textured nickel (001): an approach to superconducting tapes with high critical current density," *Science* 274, 755–757.

Peterson, R. L., and Ekin, J. W. (1988). "Josephson-junction model of critical current in granular $Y_1Ba_2Cu_3O_{7-\delta}$ superconductors," *Phys. Rev.* B 37, 9848–9851.

Polyanskii, A. A., Gurevich, A., Pashitski, A. E., Heinig, N. F., Redwing, R. D., Nordman, J. E., and Larbalestier, D. C. (1996). "Magneto-optical study of flux penetration and critical current densities in [001] tilt $YBa_2Cu_3O_{7-\delta}$ thin-film bicrystals," *Phys. Rev.* B 53, 8687–8697.

Rose Innes, A. C., and Rhoderick, E. H. (1976). *Introduction to Superconductivity*, International Series in Solid State Physics, Vol. 6, Pergamon Press, Oxford; Elmsford, NY. (out of print, but available used on the Internet).

Summers, L. T., Guinan, M. W., Miller, J. R., and Hahn, P. A. (1991). "A model for the prediction of Nb_3Sn critical current as a function of field, temperature, strain, and radiation damage," *IEEE Trans. Magn.* 27, 2041–2044.

ten Haken, B. (1994). *Strain Effects on the Critical Properties of High-Field Superconductors*, Ph.D. dissertation, University of Twente, Enschede, The Netherlands.

ten Haken, B., ten Kate, H. H. J., and Tenbrink, J. (1995). "Compressive and tensile axial strain reduce critical currents in Bi-2212 conductors," *IEEE Trans. Magn.* 5, 1298–1301.

ten Haken, B., Godeke, A., Schuver, H. J., and ten Kate, H. H. J. (1996). "Strain reduced critical current in Bi-2223/Ag superconductors under axial tension and compression," *Adv. Cryog. Eng.* 42, 651–658.

ten Haken, B., Godeke, A., and ten Kat, H. H. J. (1999). "The strain dependence of the critical properties of Nb_3Sn conductors," *J. Appl. Phys.* 86, 3247–3253.

van der Laan, D. C. (2004). *Flux Pinning and Connectivity in Polycrystalline High-Temperature Suerconductors*, Ph.D. dissertation, University of Twente, Enschede, The Netherlands.

Welch, D. O. (1980). "Alteration of the superconducting properties of A15 compounds and elementary composite superconductors by nonhydrostatic elastic strain," *Adv. Cryog. Eng.* 26, 48–65.

Werthamer, N. R., Helfand, E., and Hohenberg, P. C. (1966). "Temperature and purity dependence of the superconducting critical field, H_{c2}. III. Electron spin and spin-orbit effects," *Phys. Rev.* 147, 295–302.

Wilson, M. N. (1977). Rutherford Laboratory Report SMR/1. Chilton, Oxfordshire, England. (unpublished).

Wu, J. (2000). University of Kansas, Lawrence, Kansas, personal communication.

Zhang, Y., McKinnell, J. C., Hentges, R. W., and Hong, S. (1999). "Recent development of niobium–tin superconducting wire at OST," *IEEE Trans. Appl. Supercond.* 9, 1444–1446.

Appendix

Data Handbook of Material Properties and Cryostat Design

This page intentionally left blank

APPENDIX

DATA HANDBOOK OF MATERIAL PROPERTIES AND CRYOSTAT DESIGN

The following tables provide handbook data for cryostat design and measurements. In many cases the tables serve as a ready collection of *general design information* for quick reference, including SI conversion factors sorted by function, cooling power data, suppliers of specialty parts, heat conduction down stainless-steel tubing, strengths of bolts, metric equivalents, vacuum-design data, wire properties, magnetic-correction factors for thermometers, and so on. In other cases, the tables provide a convenient aid in *material selection*, presenting, at a glance, a condensed overview of the temperature dependence of the properties of many materials (sorted by type of material and property). Once a material is selected, more detailed information can then be obtained for that particular material by referring to the extensive references accompanying each table or to the Internet data sources given in Sec. 6.7.2.

A detailed Appendix Table of Contents is included on the inside of the back cover for convenient reference. The appendix tables are divided into categories corresponding to each chapter, starting with general information and properties of cryogenic fluids, continuing with heat transfer, construction, wiring, thermometers, properties of solids, sample holders, contacts, and ending with information useful for critical-current analysis. The text sections indicated in parentheses with each appendix table contain specific information on the application and interpretation of the data in that table.

Default nomenclature: Alloy compositions in this book are given in *weight* percent (e.g. 2wt%Al or 2%Al) unless specifically indicated as *atomic* percent (e.g. 2at%Al).

A1 General information and cryogen properties (ref. Chapter 1)

A1.1 TERM–ABBREVIATION–ACRONYM DECODER

When starting in a new field, the jargon can sometimes be daunting. The following is only a brief introductory list, given in practical terms, but it may be useful to help clarify a few of the more commonly used terms, abbreviations, and acronyms.

An accessible multilingual website containing introductory information on *polymers* and their designations is http://www.pslc.ws/macrog/index.htm.

AISI American Iron and Steel Institute, a designation system for steel alloys (Appendix A6.9)

Alumel A high electrical-resistivity nickel alloy used for thermocouples consisting of Ni–2%Al–2%Mn–1%Si.

ASTM Formerly known as the American Society for Testing and Materials, ASTM International provides a global forum for consensus standards for materials, products, systems, and services.

AWG American Wire Gauge, a designation system for wire size. Appendix A4.1a lists physical information by AWG wire size. Corresponding *metric* wire sizes are given in Appendix A4.1b.

Bi-2212 A common abbreviation for the high-T_c superconductor material $Bi_2Sr_2CaCu_2O_{8+\delta}$ (where, typically, $\delta << 1$). The name is derived from the subscripts of the first four elements in the compound

formula. This superconductor is also sometimes referred to as BSCCO (pronounced "bisco") ($T_c \approx 90$ K.)

Bi-2223 A common abbreviation for the high-T_c superconductor $(Bi, Pb)_2Sr_2Ca_2Cu_3O_{10-\delta}$; also sometimes referred to as BSCCO. ($T_c \approx 110$ K.)

Chromel A high electrical-resistivity nickel alloy commonly used for resistive wiring and thermocouples, consisting of Ni–10%Ni.

Constantan Another high electrical-resistivity alloy commonly used for resistive wiring and thermocouples, consisting of Cu–45%Ni.

Critical current I_c The maximum amount of current that can be carried by a superconductor before it starts to become resistive. Good commercial superconductors can carry over 1000 A/mm^2 in the presence of a 12 T magnetic field applied perpendicular to the wire.

Critical magnetic field There are several definitions of critical magnetic field, described in Sec. 10.3.1. Generally, the so-called *upper critical field* H_{c2} is the practical quantity for low-T_c superconductors, corresponding to the magnetic field above which all superconductivity is suppressed. H_{c2} values at 0 K for low-T_c materials range up to about 30 T. Typical values are tabulated for practical superconductors in Appendix A6.6 and plotted vs. temperature in Fig. 10.15. The so-called irreversibility or depinning field H_{irr} is the practical quantity for high-T_c superconductors, plotted vs. temperature in Fig. 10.16.

Critical temperature T_c The temperature below which a superconductor must be cooled before it becomes superconducting. Typical values for practical low-T_c materials range from about 10–40 K; for high-T_c materials, from about 90–130 K. Values are tabulated for the most common superconductors in Appendix A6.6.

Cryocooler A cryogenic refrigerator.

Cryogen Another name for a *cryogenic liquid*, such as liquid helium ($T_{boil} = 4.2$ K), liquid neon ($T_{boil} = 27$ K), or liquid nitrogen ($T_{boil} = 77$ K). The physical properties of common cryogens are given in Appendix A1.5.

CTFE Polychlorotrifluoroethylene, a type of Teflon™.

ELI Ti–6Al–4V Extra Low Interstitial form of Ti–6Al–4V. The mechanical properties of titanium strongly depend on interstitial elements (especially oxygen, nitrogen, and carbon), which affect particularly the fracture toughness. ELI grade is a purer form of titanium with a greater fracture toughness.

Ethylene glycol dimethyl terepthalate Mylar™.

ETP copper Electrolytic-Tough-Pitch copper [designated by the Unified Numbering System (UNS) as C10300]. This is the copper commonly used to make ordinary copper wire.

Eutectic mixture The alloy composition with the lowest melting temperature; eutectic compositions are particularly useful as solder materials.

FEP Fluorinated ethylene propylene, a type of Teflon™.

G-10, G-11 Designations for fiberglass–epoxy composites (commonly used as commercial electronic circuit boards) made from layers of fiberglass cloth filled with epoxy.

Hastelloy C A corrosion-resistant nickel alloy consisting of 54%Ni–17%Mo–15%Cr–5%Fe–4%W.

HTS High-T_c (high-critical-temperature) superconductors. Copper-oxide materials having critical temperatures ranging to over 100 K. Also referred to as *oxide* superconductors or *ceramic* superconductors. Examples are: $YBa_2Cu_3O_{7-x}$ ($T_c = 92$ K), $Bi_2Sr_2CaCu_2O_{8+x}$ ($T_c = 85$ K), $(Bi,Pb)_2Sr_2Ca_2Cu_3O_{10-x}$ ($T_c = 110$ K), $(Tl, Pb)_1(Ba,Sr)_2Ca_2Cu_3O_{10+x}$ ($T_c = 115$ K), and $HgBa_2Ca_2Cu_3O_{8+x}$ ($T_c = 135$ K).

ISO International Standards Organization.

ITS-90 The International Temperature Scale of 1990.

KF flange *Klein Flange,* meaning "small flange"; a flexible O-ring vacuum coupling.

LTS Low-T_c (low-critical-temperature) superconductors. These materials (usually with niobium as the core element) have critical temperatures up to about 40 K and are based on a phonon-coupling mechanism between superconducting pairs of electrons. Common examples are: Nb–Ti ($T_c = 9.5$ K), Nb_3Al ($T_c = 15$ K), NbN ($T_c = 16$ K), Nb_3Sn ($T_c = 18$ K), Nb_3Ge ($T_c = 23$ K), and MgB_2 ($T_c = 39$ K).

Lambda point The temperature (2.177 K) where normal ^{4}He (also designated as He I) transforms into superfluid helium ^{4}He (also designated as He II); see Sec. 1.2.2.

Manganin An alloy commonly used for cryostat wiring and heaters in nonmagnetic applications, consisting of Cu–13%Mn–4%Ni.

Martensitic phase transformation A change in the atomic structure of a metal to a new crystalline phase that is usually harder and more brittle. In stainless steels commonly used in cryogenic apparatus, such as AISI 304, 310, and 316, the martensitic phase transformation is precipitated by cooling to low temperatures or by applied stress (Sec. 6.6.5). The martensitic phase of the metal has a lower fracture toughness and is usually ferromagnetic.

Monel A high-strength, corrosion-resistant, nickel alloy consisting of Ni–30%Cu.

***n* value** An index of the nonlinearity or sharpness of the voltage–current (V–I) curve near the critical current of a superconductor. It is defined by the relation $V = cI^n$ (Sec. 10.1.3). Good superconductors have n values above 20–30.

Nichrome A highly resistive alloy commonly used for heater wiring, consisting of Ni–20%Cr.

OFHC™ copper A type of oxygen-free copper [designated by the UNS as C10200; a higher-purity type is designated as C10100].

PCTFE Polychlorotrifluoroethylene.

PET Polyethylene terephthalate, Mylar™.

Phosphor bronze An alloy commonly used for cryostat and thermometer instrumentation wiring composed of Cu–5%Sn–0.2%P (Grade A).

PMMA Polymethyl methacrylate, Plexiglas™.

Polyamide Nylon™.

Polyimide Kapton™.

Phonon A wave-like displacement of the atoms from their equilibrium positions in a solid, usually thermally generated.

Poisson's ratio A term used in mechanics (Secs 3.5.3 and 3.5.4) that is the (negative of the) ratio of the *lateral* strain to *longitudinal* strain when a beam is uniformly and elastically stressed along the longitudinal axis. (It simply expresses the fact that the beam becomes narrower as it is stretched, to approximately conserve its volume.) The Poisson's ratio of metals is typically about 1/3, with values ranging from 0.28–0.42 for most materials.

PTFE Polytetrafluoroethylene, a type of Teflon™.

Quench A colloquial term for a thermal runaway event; see Thermal runaway.

SI The international system of units (Système International d'Unités).

SQUID Superconducting Quantum Interference Device. A very sensitive magnetometer able to detect magnetic flux as small as a fraction of magnetic flux quantum Φ_0 ($= 2.0678 \times 10^{-15}$ Wb).

TFE Tetrafluoroethylene, Teflon™.

Thermal runaway (quench) A process wherein a small part of a superconductor carrying very high current densities is momentarily heated into the resistive state (by sample movement, friction, or some other disturbance). The resulting electrical (Joule) heating in this portion of the superconductor then heats additional surrounding superconductor material into the resistive state, resulting in a thermal-runaway process with an ever-growing resistive zone and rapidly increasing Joule heating. When measuring the critical current of a superconducting strand, the Joule heating typically locally melts the superconductor unless the current is shut off quickly (in less than a second). More information is given in Sec. 7.5.1.

Type I superconductors Superconducting materials where magnetic field uniformly penetrates the material, suppressing superconductivity at relatively low magnetic fields (typically much less than 1 T). This is the original type of superconductivity discovered in 1911 by Onnes. It was not until nearly 50 years later that practical (high-field) Type II superconductivity was discovered.

Type II superconductors Superconductors wherein magnetic field is localized by circulating supercurrents, confining the field to small regions (vortices) and thereby leaving most of the superconductor free of magnetic field; see Fig. 10.7. This second type of superconductivity, which was discovered half a century after Type I superconductors, allows superconductivity to persist to much higher magnetic fields and comprises the practical superconducting materials from which most of today's applications are fabricated. Paradoxically, Type II superconductors have a much lower electrical conductivity in the normal (nonsuperconducting) state than that of Type I superconductors (which are typically pure metallic elements).

YBCO The term commonly used for the high-T_c material $YBa_2Cu_3O_{7-\delta}$ ($T_c \approx 92$ K), also sometimes referred to as simply *123* because of the subscripts of the first three elements in the compound.

A1.2 FUNDAMENTAL CONSTANTS

Fundamental Physical Constants

Quantity	Symbol	Value
Avogadro constant	N_A	$6.022\,141\,99 \times 10^{23}$ mol^{-1}
Boltzmann constant	$k_B = R/N_A$	$1.380\,650\,3 \times 10^{-23}$ J/K
Electric constant	$\varepsilon_0 = 1/\mu_0 c^2$	$8.854\,187\,817 \times 10^{-12}$ F/m
Electron volt	eV	$1.602\,176\,463 \times 10^{-19}$ J
Elementary charge	e	$1.602\,176\,463 \times 10^{-19}$ C
Lorenz constant (Sec. 6.4.2)	$L_N = (\pi^2/3)\,(k_B/e)^2$	2.443×10^{-8} V^2/K^2
Magnetic flux quantum	$\Phi_0 = h/2e$	$2.067\,833\,637 \times 10^{-15}$ Wb
Molar gas constant	R	8.314 472 J/(mol K) = 8.314 472 Pa m^3/(mol K)
Magnetic constant	μ_0	$4\pi \times 10^{-7} = 1.2566 \times 10^{-6}$ N/A^2 = 1.2566 μV s/(A m) = 1.2566 μWb/(A m) = 1.2566 μH/m
Newtonian constant of gravitation	G	6.673×10^{-11} m^3/(kg s^2)
Planck's constant	h	$6.626\,068\,76 \times 10^{-34}$ J s
Speed of light in vacuum	c	$2.997\,924\,58 \times 10^{8}$ m/s
Stefan–Boltzmann constant (Sec. 2.4)	$\sigma = (\pi^2/60)k_B{}^4/(h/2\pi)^3 c^2$	$5.670\,400 \times 10^{-8}$ W/(m^2 K^4)

Source: *CRC Handbook of Chemistry and Physics* (2002), 83rd edition, CRC Press LLC, Boca Raton, FL.

Useful approximate equivalents

Pressure: 1 atm (≡ 760 torr) → ~10^5 Pa
Temperature: 11 000 K → ~1 eV
Wavelength: 12 000 Å → ~1 eV

A1.3 SI CONVERSION FACTORS

SI: Système International d'Unités (International System of Units)

To convert from	to	multiply by
ACCELERATION		
ft/s^2	meter per second^2 (m/s^2)	3.048 000 E−01
free fall, standard	meter per second^2 (m/s^2)	9.806 650 E+00
in/s^2	meter per second^2 (m/s^2)	2.540 000 E−02
AREA		
acre	meter^2 (m^2)	4.046 873 E+03
barn	meter^2 (m^2)	1.000 000 E−28
circular mil	meter^2 (m^2)	5.067 075 E−10
ft^2	meter^2 (m^2)	9.290 304 E−02
in^2	meter^2 (m^2)	6.451 600 E−04
mi^2 (US statute mile)	meter^2 (m^2)	2.589 988 E+06
section	meter^2 (m^2)	2.589 988 E+06
township	meter^2 (m^2)	9.323 957 E+07
yd^2	meter^2 (m^2)	8.361 274 E−01
BENDING MOMENT OR TORQUE		
dyne centimeter	newton meter (N m)	1.000 000 E−07
kgf·m	newton meter (N m)	9.806 650 E+00
ozf·in	newton meter (N m)	7.061 552 E−03
lbf·in	newton meter (N m)	1.129 848 E−01
lbf·ft	newton meter (N m)	1.355 818 E+00
CAPACITY (*see* VOLUME)		
DENSITY (*see* MASS PER UNIT VOLUME)		
ELECTRICITY AND MAGNETISM[a]		
ampere hour	coulomb (C)	3.600 000 E+01
EMU of capacitance	farad (F)	1.000 000 E+09
EMU of current	ampere (A)	1.000 000 E+01
EMU of electric potential	volt (V)	1.000 000 E−08
EMU of inductance	henry (H)	1.000 000 E−09
EMU of resistance	ohm (Ω)	1.000 000 E−09
ESU of capacitance	farad (F)	1.112 650 E−12
ESU of current	ampere (A)	3.335 6 E−10
ESU of electric potential	volt (V)	2.997 9 E+02
ESU of inductance	henry (H)	8.987 554 E+11
ESU of resistance	ohm (Ω)	8.987 554 E+11
gauss	tesla (T)	1.000 000 E−04
gilbert	ampere (A)	7.957 747 E−01
maxwell	weber (Wb)	1.000 000 E−08
oersted	ampere per meter (A/m)	7.957 747 E+01

(Continued)

A1.3 (*Continued*)

To convert from	to	multiply by
ENERGY (includes WORK)		
British thermal unit (thermochemical)	joule (J)	1.054 350 E+03
calorie (thermochemical)	joule (J)	4.184 000 E+00
electron volt	joule (J)	1.602 176 E−19
erg	joule (J)	1.000 000 E−07
ft lbf	joule (J)	1.355 818 E+00
kilocalorie (thermochemical)	joule (J)	4.184 000 E+03
kW h	joule (J)	3.600 000 E+06
W h	joule (J)	3.600 000 E+03
W s	joule (J)	1.000 000 E+00
FLOW (*see* MASS PER UNIT TIME or VOLUME PER UNIT TIME)		
FORCE		
dyne	newton (N)	1.000 000 E−05
kilogram-force (kgf)	newton (N)	9.806 650 E+00
kilopond-force	newton (N)	9.806 650 E+00
kip (1000 lbf)	newton (N)	4.448 222 E+03
ounce-force (avoirdupois)	newton (N)	2.780 139 E−01
pound-force (lbf)	newton (N)	4.448 222 E+00
poundal	newton (N)	1.382 550 E−01
FORCE PER UNIT AREA (*see* Pressure)		
FORCE PER UNIT LENGTH		
lbf/in	newton per meter (N/m)	1.751 268 E+02
lbf/ft	newton per meter (N/m)	1.459 390 E+01
HEAT		
Btu (thermochemical) in/s ft^2 °F (*k*, thermal conductivity)	watt per meter kelvin (W/m K)	5.188 732 E+02
Btu (thermochemical) in/h ft^2 °F (*k*, thermal conductivity)	watt per meter kelvin (W/m K)	1.441 314 E−01
Btu (thermochemical)/ft^2	joule per meter^2 (J/m^2)	1.134 893 E+04
Btu (thermochemical)/h ft^2 °F (*C*, thermal conductance)	watt per meter^2 kelvin (W/m^2 K)	5.674 466 E+00
Btu (thermochemical)/lb	joule per kilogram (J/kg)	2.324 444 E+03
Btu (thermochemical)/lb °F (*c*, specific capacity)	joule per kilogram kelvin (J/kg K)	4.184 000 E+03
Btu (thermochemical)/s ft^2 °F	watt per meter^2 kelvin (W/m^2 K)	2.042 808 E+04
cal (thermochemical)/cm^2	joule per meter^2 (J/m^2)	4.184 000 E+04
cal (thermochemical)/cm^2 s	watt per meter^2 (W/m^2)	4.184 000 E+04
cal (thermochemical)/cm s °C	watt per meter kelvin (W/m K)	4.184 000 E+02
cal (thermochemical)/g	joule per kilogram (J/kg)	4.184 000 E+03

A1.3 (*Continued*)

To convert from	to	multiply by
cal (thermochemical)/g °C	joule per kilogram kelvin (J/kg K)	4.184 000 E+03
°F h ft^2/Btu (thermochemical) (*R*, thermal resistance)	kelvin meter^2 per watt (K m^2/W)	1.761 102 E−01
ft^2/h (thermal diffusivity)	meter^2 per second (m^2/s)	2.580 640 E−05
LENGTH		
angstrom	meter (m)	1.000 000 E−10
astronomical unit	meter (m)	1.495 98 E+11
fermi (femtometer)	meter (m)	1.000 000 E−15
foot (ft)	meter (m)	3.048 000 E−01
inch (in.)	meter (m)	2.540 000 E−02
light year	meter (m)	9.460 528 E+15
micron	meter (m)	1.000 000 E−06
mil	meter (m)	2.540 000 E−05
mile (US statute)	meter (m)	1.609 347 E+03
pica (printer's)	meter (m)	4.217 518 E−03
point (printer's)	meter (m)	3.514 598 E−04
rod	meter (m)	5.029 210 E+00
yard (yd)	meter (m)	9.144 000 E−01
LIGHT		
footcandle	lumen per meter^2 (lm/m^2)	1.076 391 E+01
footcandle	lux (lx)	1.076 391 E+01
MASS		
grain	kilogram (kg)	6.479 891 E−05
gram	kilogram (kg)	1.000 000 E−03
hundredweight (long)	kilogram (kg)	5.080 235 E+01
hundredweight (short)	kilogram (kg)	4.535 924 E+01
ounce (avoirdupois)	kilogram (kg)	2.834 952 E−02
pound (lb) (avoirdupois)	kilogram (kg)	4.535 924 E−01
slug	kilogram (kg)	1.459 390 E+01
ton (assay)	kilogram (kg)	2.916 667 E−02
ton (long, 2240 lb)	kilogram (kg)	1.016 047 E+03
ton (metric)	kilogram (kg)	1.000 000 E+03
ton (short, 2000 lb)	kilogram (kg)	9.071 847 E+02
MASS PER UNIT VOLUME (includes DENSITY and MASS CAPACITY)		
g/cm^3	kilogram per meter^3 (kg/m^3)	1.000 000 E+03
oz (avoirdupois)/gal (UK liquid)	kilogram per meter^3 (kg/m^3)	6.236 027 E+00
oz (avoirdupois)/gal (US liquid)	kilogram per meter^3 (kg/m^3)	7.489 152 E+00
oz (avoirdupois)/in^3	kilogram per meter^3 (kg/m^3)	1.729 994 E+03
lb/ft^3	kilogram per meter^3 (kg/m^3)	1.601 846 E+01
lb/in^3	kilogram per meter^3 (kg/m^3)	2.767 990 E+04

(*Continued*)

A1.3 (*Continued*)

To convert from	to	multiply by
lb/gal (UK liquid)	kilogram per meter^3 (kg/m^3)	9.977 644 E+01
lb/gal (US liquid)	kilogram per meter^3 (kg/m^3)	1.198 264 E+02
ton(long, mass)/yd^3	kilogram per meter^3 (kg/m^3)	1.328 939 E+03
POWER		
Btu (thermochemical)/s	watt (W)	1.054 350 E+03
Btu (thermochemical)/min	watt (W)	1.757 250 E+01
Btu (thermochemical)/h	watt (W)	2.928 751 E−01
cal (thermochemical)/s	watt (W)	4.184 000 E+00
cal (thermochemical)/min	watt (W)	6.973 333 E−02
erg/s	watt (W)	1.000 000 E−07
ft lbf/h	watt (W)	3.766 161 E−04
ft lbf/min	watt (W)	2.259 697 E−02
ft lbf/s	watt (W)	1.355 818 E+00
horsepower (550 ft lbf/s)	watt (W)	7.456 999 E+02
kilocalorie (thermochemical)/min	watt (W)	6.973 333 E+01
kilocalorie (thermochemical)/s	watt (W)	4.184 000 E+03
PRESSURE OR STRESS (FORCE PER UNIT AREA)		
atmosphere (normal = 760 torr)	pascal (Pa)	1.013 25 E+05
atmosphere (technical = 1 kgf/cm^2)	pascal (Pa)	9.806 650 E+04
bar	pascal (Pa)	1.000 000 E+05
centimeter of mercury (0°C)	pascal (Pa)	1.333 22 E+03
centimeter of water (4°C)	pascal (Pa)	9.806 65 E+01
dyne/cm^2	pascal (Pa)	1.000 000 E−01
foot of water (39.2°F)	pascal (Pa)	2.989 070 E+03
gram-force/cm^2	pascal (Pa)	9.806 650 E+01
inch of mercury (32°F)	pascal (Pa)	3.386 389 E+03
inch of mercury (60°F)	pascal (Pa)	3.376 85 E+03
inch of water (39.2°F)	pascal (Pa	2.490 82 E+02
inch of water (60°F)	pascal (Pa)	2.488 4 E+02
kgf/cm^2	pascal (Pa)	9.806 650 E+04
kgf/m^2	pascal (Pa)	9.806 650 E+00
kgf/mm^2	pascal (Pa)	9.806 650 E+06
kip/in^2 (ksi)	pascal (Pa)	6.894 757 E+06
millibar	pascal (Pa)	1.000 000 E+02
millimeter of mercury (0°C)	pascal (Pa)	1.333 224 E+02
poundal/foot^2	pascal (Pa)	1.488 164 E+00
lbf/ft^2	pascal (Pa)	4.788 026 E+01
lbf/in^2 (psi)	pascal (Pa)	6.894 757 E+03
psi	pascal (Pa)	6.894 757 E+03
torr (mm Hg, 0°C)	pascal (Pa)	1.333 22 E+02

A1.3 (*Continued*)

To convert from	to	multiply by
SPEED (*see* VELOCITY)		
STRESS (*see* PRESSURE)		
TEMPERATURE		
degree Celsius (°C)	kelvin (K)	$t_K = t_C + 273.15$
degree Fahrenheit (°F)	kelvin (K)	$t_K = (t_F + 459.67)/1.8$
degree Rankine	kelvin (K)	$t_K = t_R/1.8$
degree Fahrenheit (°F)	degree Celsius (°C)	$t_C = (t_F - 32)/1.8$
kelvin (K)	degree Celsius (°C)	$t_C = t_K - 273.15$
TIME		
day (mean solar)	second (s)	8.640 000 E+04
day (sidereal)	second (s)	8.616 409 E+04
hour (mean solar)	second (s)	3.600 000 E+03
minute (mean solar)	second (s)	6.000 000 E+01
year (calendar)	second (s)	3.153 600 E+07
TORQUE (*see* BENDING MOMENT)		
VELOCITY (includes SPEED)		
ft/h	meter per second (m/s)	8.466 667 E−05
ft/min	meter per second (m/s)	5.080 000 E−03
ft/s	meter per second (m/s)	3.048 000 E−01
in/s	meter per second (m/s)	2.540 000 E−02
km/h	meter per second (m/s)	2.777 778 E−01
knot (international)	meter per second (m/s)	5.144 444 E−01
mi/h (US statute)	meter per second (m/s)	4.470 400 E−01
mi/min (US statute)	meter per second (m/s)	2.682 240 E+01
mi/s (US statute)	meter per second (m/s)	1.609 344 E+03
mi/h (US statute)	km/h	1.609 344 E+00
VISCOSITY		
centipoises	pascal-second (Pa s)	1.000 000 E−03
centistokes	meter^2 per second (m^2/s)	1.000 000 E−06
ft^2/s	meter^2 per second (m^2/s)	9.290 304 E−02
poise	pascal-second (Pa s)	1.000 000 E−01
poundal·s/ft^2	pascal-second (Pa s)	1.488 164 E+00
lb/ft·s	pascal-second (Pa s)	1.488 164 E+00
lbf·s/ft^2	pascal-second (Pa s)	4.788 026 E+01
slug/ft·s	pascal-second (Pa s)	4.788 026 E+01
stoke	meter^2 per second (m^2/s)	1.000 000 E−04
VOLUME (includes CAPACITY)		
acre-foot	meter^3 (m^3)	1.233 489 E+03
barrel (oil, 42 gal)	meter^3 (m^3)	1.589 873 E−01

(*Continued*)

A1.3 (*Continued*)

To convert from	to	multiply by
board foot	meter^3 (m^3)	2.359 737 E−03
bushel (US)	meter^3 (m^3)	3.523 907 E−02
cup	meter^3 (m^3)	2.365 882 E−04
fluid ounce (US)	meter^3 (m^3)	2.957 353 E−05
foot^3	meter^3 (m^3)	2.831 685 E−02
gallon (Canadian liquid)	meter^3 (m^3)	4.546 090 E−03
gallon (UK liquid)	meter^3 (m^3)	4.546 092 E−03
gallon (US dry)	meter^3 (m^3)	4.404 884 E−03
gallon (US liquid)	meter^3 (m^3)	3.785 412 E−03
inch^3	meter^3 (m^3)	1.638 706 E−05
liter	meter^3 (m^3)	1.000 000 E−03
ounce (UK fluid)	meter^3 (m^3)	2.841 307 E−05
ounce (US fluid)	meter^3 (m^3)	2.957 353 E−05
peck (US)	meter^3 (m^3)	8.809 768 E−03
pint (US liquid)	meter^3 (m^3)	4.731 765 E−05
quart (US liquid)	meter^3 (m^3)	9.463 529 E−04
tablespoon	meter^3 (m^3)	1.479 000 E−05
teaspoon	meter^3 (m^3)	4.929 000 E−06
ton (register)	meter^3 (m^3)	2.831 685 E+00
yard^3	meter^3 (m^3)	7.645 549 E−01
VOLUME PER UNIT TIME (includes FLOW)		
ft^3/min	meter^3 per second (m^3/s)	4.719 474 E−04
ft^3/s	meter^3 per second (m^3/s)	2.831 685 E−02
in^3/min	meter^3 per second (m^3/s)	2.731 177 E−07
yd^3/min	meter^3 per second (m^3/s)	1.274 258 E−02
gal (US liquid)/day	meter^3 per second (m^3/s)	4.381 264 E−08
gal (US liquid)/min	meter^3 per second (m^3/s)	6.309 020 E−05
WORK (*see* ENERGY)		

Source: Selected excerpts from *Metric Practice Guide*, Designation: E 380–74 (1974), American Society for Testing and Materials, 100 Barr Harbor Drive, West Conshocken, PA 19428–2959; updated with data from SI10–02 IEEE/ASTM SI 10 *American National Standard for Use of the International System of Units (SI): The Modern Metric System* (2002), SI10–02 IEEE/ASTM SI 10, 100 Barr Harbor Drive, West Conshocken, PA 19428–2959.

[a] ESU means electrostatic cgs unit. EMU means electromagnetic cgs unit.

A1.4 MAGNETIC UNITS: EQUIVALENCY TABLE

Symbol	Quantity	Conversion from Gaussian and cgs emu to SI[a]
Φ	Magnetic flux	$1\,\text{Mx} = 1\,\text{G cm}^2 \rightarrow 10^{-8}\,\text{Wb} = 10^{-8}\,\text{V s}$
B	Magnetic flux density, magnetic induction	$1\,\text{G} \rightarrow 10^{-4}\,\text{T} = 10^{-4}\,\text{Wb/m}^2$
H	Magnetic field strength	$1\,\text{Oe} \rightarrow 10^3/(4\pi)\,\text{A/m}$
m	Magnetic moment	$1\,\text{erg/G} = 1\,\text{emu} \rightarrow 10^{-3}\,\text{A m}^2 = 10^{-3}\,\text{J/T}$
M	Magnetization	$1\,\text{erg/(G cm}^3) = 1\,\text{emu/cm}^3 \rightarrow 10^3\,\text{A/m}$
$4\pi M$	Magnetization	$1\,\text{G} \rightarrow 10^3/(4\pi)\,\text{A/m}$
σ	Mass magnetization, specific magnetization	$1\,\text{erg/(G g)} = 1\,\text{emu/g} \rightarrow 1\,\text{A m}^2\text{/kg}$
j	Magnetic dipole moment	$1\,\text{erg/G} = 1\,\text{emu} \rightarrow 4\pi \times 10^{-10}\,\text{Wb m}$
J	Magnetic polarization	$1\,\text{erg/(G cm}^3) = 1\,\text{emu/cm}^3 \rightarrow 4\pi \times 10^{-4}\,\text{T}$
χ, κ	Volume susceptibility[b]	$1 \rightarrow 4\pi$
$\chi_\rho, \chi/\rho$	Mass susceptibility[c]	$1\,\text{cm}^3\text{/g} \rightarrow 4\pi \times 10^{-3}\,\text{m}^3\text{/kg}$
μ	Permeability	$1 \rightarrow 4\pi \times 10^{-7}\,\text{H/m} = 4\pi \times 10^{-7}\,\text{Wb/(A m)}$
μ_r	Relative permeability	$\mu \rightarrow \mu_\text{r}$
w, W	Energy density	$1\,\text{erg/cm}^3 \rightarrow 10^{-1}\,\text{J/m}^3$
N, D	Demagnetizing factor	$1 \rightarrow 1/(4\pi)$

Source: Table based on R. B. Goldfarb and F. R. Fickett (1985), NBS STP 696, National Bureau of Standards. US Government Printing Office, Washington, DC.

[a] Gaussian units are the same as cgs emu for magnetostatics; Mx = maxwell, G = gauss, Oe = oersted, Wb = weber, V = volt, s = second, T = tesla, m = meter, A = ampere, J = joule, kg = kilogram, H = henry.

[b] Volume susceptibility is dimensionless but is sometimes expressed in cgs units as emu/cm^3 or emu/(cm^3 Oe).

[c] Mass susceptibility is sometimes expressed in cgs units as emu/g or emu/(g Oe).

A1.5 PROPERTIES OF COMMON CRYOGENIC FLUIDS (SEC. 1.2)

Additional data on the vapor-pressure vs. temperature dependence of these cryogenic fluids are given in Appendix A5.1.

Fluid: property	^{3}He	^{4}He	H_2[a] (Para)	H_2[a] (Normal)	Ne	N_2	Ar	O_2	CH_4 (Methane)
Molecular weight	3.0160	4.0026	2.0159	2.0159	20.179	28.013	39.948	31.999	16.043
Critical temp. [K]	3.324	5.195	32.93	33.18	44.49	126.2	150.7	154.6	190.6
Critical pressure [atm]	1.145	2.245	12.67	12.98	26.44	33.51	47.99	49.77	45.39
Boiling point [K]	3.191	4.230	20.27	20.27	27.10	77.35	87.30	90.20	111.7
Melting point [K]	—	4.2 (at 140 atm)	13.80	13.95	24.56	63.15	83.81	54.36	90.72
Liquid density at B.P. [g/mL]	0.05722	0.1247	0.07080	0.07080	1.207	0.8061	1.395	1.141	0.4224
Gas density at 0°C and 1 atm [g/L]	0.1345	0.1785	0.08988	0.08988	0.8998	1.250	1.784	1.429	0.7175
Vapor density at B.P. [g/L]	24.51	16.76	1.339	1.339	9.577	4.612	5.774	4.467	1.816
Liquid thermal conductivity at B.P. [mW/(m·K)]	—	18.66	103.4	103.4	155.0	145.8	125.6	151.6	183.9
Liquid isobaric specific heat at B.P. [J/(g K)]	24.80	5.299	9.659	9.667	1.862	2.041	1.117	1.699	3.481

Latent heat of vaporization at B. P.	7.976 J/g (0.4564 J/mL)	20.75 (2.589)	445.4 (31.54)	445.4 (31.54)	85.75 (103.5)	199.2 (160.6)	161.1 (224.9)	213.1 (243.1)	510.8 (215.8)
Latent heat of fusion at M.P. [J/g]	—	30.5	—	58.2	16.6	25.5	27.8	13.8	58.7
Vapour pressure of solid at M.P. [kPa]	—	—	7.04	7.20	43.46	12.52	68.89	0.146	11.5
Magnetic susceptibility [10^{-6} cm^3/mol][b] (+ ≡ paramagnetic)	—	−2.20 (gas)	−5.44 (liq., 20.3 K)	−3.99 (gas, ≳293 K)	−6.96 (gas)	−12.0 (gas)	−19.32 (gas)	+3 449 (gas) +7 699 (liq., 90K) +10 200 (sol., 54 K)	−17.4

B.P. ≡ boiling point; M.P. ≡ melting point.

Principal source of data: E. W. Lemmon, NIST, evaluated from equations of state referenced in Appendix A5.1.

Data on solids:

V. Johnson (1960), NBS, Wright Air Development Div. (WADD) Technical Report 60–56, Part II. US Government Printing Office, Washington, DC.

D. H. J. Goodall (1970), A.P.T. Division, Culham, Culham Science Center, Abingdon, Oxfordshire, UK.

K. Timmerhaus and T. Flynn (1989), *Cryogenic Process Engineering*, Plenum Press, New York.

[a] Hydrogen can exist in two different molecular forms: higher-energy *ortho*hydrogen (nuclear spins aligned) and lower-energy *para*hydrogen (nuclear spins opposed). The equilibrium ratio is determined by temperature: at room temperature and above, hydrogen consists of about 25% para and 75% ortho (so-called *normal* hydrogen), but at the atmospheric boiling temperature of liquid hydrogen (20.27 K) and below, the equilibrium shifts almost completely to parahydrogen (99.79% para and 0.21% ortho at 20.27 K).

[b] *CRC Handbook of Chemistry and Physics* (2002), 83rd edition, CRC Press, Boca Raton, FL.

A1.6a COOLING POWER DATA FOR ^{4}He, H_2, AND N_2 (SEC. 1.2)

Tabulated values are consumption rates resulting from 1 W dissipated directly in the indicated cryogenic liquid at atmospheric pressure.

Cryogenic liquid	Volume of liquid boiled off from 1 W [L/h]	Flow of gas at 0°C, 1 atm from 1 W [L/min]	Enthalpy change at 1 atm pressure [J/g]
^{4}He	1.377	16.05	87 (4.2–20 K) 384 (4.2–77 K) 1542 (4.2–300 K)
H_2	0.1145	1.505	590 (20–77 K) 3490 (20–300 K)
N_2	0.0225	0.243	233.5 (77–300 K)

Source: Data compiled from:
V. Johnson (1960), NBS, Wright Air Development Div. (WADD) Technical Report 60–56, Part II, US Government Printing Office, Washington, DC.
D. H. J. Goodall (1970), A.P.T. Division, Culham Science Center, Abingdon, Oxfordshire, UK.

A1.6b COOLING POWER DATA: AMOUNT OF CRYOGENIC FLUID NEEDED TO COOL COMMON METALS (SEC. 1.2)

	Cryogenic fluid:	^{4}He (T_b = 4.2 K)		H_2 (T_b = 20.3 K)		N_2 (T_b = 77.3 K)
	Initial temp. of metal	300 K [L/kg]	77 K [L/kg]	300 K [L/kg]	77 K [L/kg]	300 K [L/kg]
Using the latent heat of vaporization only	Aluminum	58	2.6	5.4	0.25	1.01
	Copper	27	1.8	2.4	0.17	0.46
	Stainless steel	30	1.2	2.8	0.12	0.54
Using both the latent heat and the enthalpy of the gas	Aluminum	1.60	0.22	1.03	0.14	0.64
	Copper	0.80	0.15	0.51	0.092	0.29
	Stainless steel	0.80	0.10	0.52	0.064	0.34

Source: Determined from data by J. B. Jacobs (1962), *Adv. Cryog. Eng.* 8, 529.
For temperature combinations other than those given in this table, see Jacobs (1962, reference above).
T_b is the boiling temperature at atmospheric pressure.

A1.7 SUPPLIERS OF SPECIALTY PARTS AND MATERIALS

The following is a list of suppliers of specialty parts and materials for constructing measurement cryostats. It is provided as a convenience to save time locating less-common items. These are not complete listings of suppliers and information can change over time, but at least they are a place to start. They may also serve as points of reference if contact information has changed.

Updated supplier information is listed for *cryogenic* instrumentation annually each December in the *Cold Facts Buyer's Guide*, Cryogenic Society of America, http://www.cryogenicsociety.org/. Suppliers for *general physics* instrumentation are updated each August in the *Physics Today Buyers Guide*, American Institute of Physics, http://www.physicstoday.org/guide/.

Trade names, products, and companies cited here do not constitute or imply endorsement by NIST or by the US government, and do not imply that they are the best available for the purpose.

Adhesives (see Appendix A3.10)

Coaxial cables for cryogenic applications (Secs 4.7.1 and 4.8)

Solid dielectric coaxial cables for lower frequency applications (<1 GHz) where dimensional stability of the terminations on thermal cycling is not needed (see Sec. 4.8):

Axon Cable Inc., 390 E. Higgins Rd., Suite 101, Elk Grove Village, IL 60007, Tel. 708-806-6629, Fax. 708-806-6639, http://www.axon-cable.com/. Supplier of miniature coaxial cable; stock number SM50 comes standard with Teflon™ dielectric and jacket; PXC47K08 can also be supplied with a Teflon™ jacket.

Lake Shore Cryotronics, Westerville, OH 43081, Tel. 614-891-2244, Fax. 614-818-1600, http://www.lakeshore.com/.

Micro-Coax, 206 Jones Blvd., Pottstown, PA 19464–3465, Tel. 610-495-0110, 800-223-2629, Fax. 610-495-6656, http://www.micro-coax.com/.

Oxford Instruments–Cryospares, Witney, Oxfordshire, UK OX29 4TL, Tel. +44(0)1865 881437, Fax. +44(0)1865 884045, http://www.oxinst.com/cryospares/.

Precision Tube, Coaxitube Div., 620 Naylor Mill Road, Salisbury, MD 21801, Tel. 410-546-3911, Fax. 410-546-3913, http://www.precisiontube.com/. Catalog contains helpful information on the electrical selection of coaxial cables.

RS, United Kingdom, Tel. +44-1536-201201, Fax. +44-1536-201-501, http://www.rs-components.com. Supplier of miniature coaxial cable with Teflon™ dielectric and jacket; "RF cable MCX" stock numbers: 388–530 (50 Ω), 388–546 (75 Ω).; (for low frequencies, where impedance matching is not a concern, the 75 Ω might be better since the capacitance is a bit lower).

Storm Products Co., Microwave Sales Office, 10221 Werch Drive, Woodridge, IL 60517, Tel. 630-754-3300, 888-347-8676, Fax. 630-754-3500, http://www.stormproducts.com/.

Expanded dielectric coaxial cables for higher frequency applications (>1 GHz) where dimensional stability of the terminations on thermal cycling is needed (see Sec. 4.8):

Storm Products Co., Microwave Sales Office, 10221 Werch Drive, Woodridge, IL 60517, Tel. 630-754-3300, 888-347-8676, Fax. 630-754-3500, http://www.stormproducts.com/; expanded dielectric coaxial cables, for example cable #421–193.

Complete cryogenic measurement systems (Sec. 1.4)

Cryo Industries; 11124 S. Willow St., Manchester, NH 03103; Tel. 603-621-9957; cryo@cryoindustries.com; http://www.cryoindustries.com/.

Janis Research Co.; 2 Jewel Dr., P. O. Box 696, Wilmington, MA 01887–0696; Tel. 978-657-8750, http://www.janis.com/.

Oxford Instruments; Witney, Oxfordshire, UK OX29 4TL, Tel. +44(0)1865 881437, Fax. +44(0)1865 884045, http://www.oxinst.com/.

Precision Cryogenic Systems, Inc.; 1171 West Rockville Rd., Indianapolis, IN 46234; Tel. 317-272-0880, http://www.precisioncryo.com/.

Conductive epoxies and pastes (Secs 7.4.1 and 8.3.2)

Silver-based epoxy

Ted Pella, Inc., P.O. Box 492477, Redding, CA 96049–2477, Tel. 800-237-3526; Fax. 530-243-3761, http://www.TedPella.com/.

Silver paste

Ted Pella, Inc., P.O. Box 492477, Redding, CA 96049–2477, Tel. 800-237-3526; Fax. 530-243-3761, http://www.TedPella.com/.

Connectors (Secs 4.1, 4.6, 4.7, 4.8)

Alligator clips: smooth, flat jaws; 7/32" jaw opening, #20 wire or smaller; crimp connection:

Mueller Electric Co., part number (PN) BU-34C, http://www.muellerelectric.com/ (distributed by Allied Electronics, Inc., PN 860-4340, Tel. 800-433-5700, http://www.alliedelec.com/ or Newark Electronics, PN 28F497, Tel. 800-263-9275, http://www.newark.com/).

Rf connectors

Fischer Connectors, Tel. 1-800-551-0121, http://www.fischerconnectors.com/

Lemo Connectors, http://www.lemousa.com/.

Vacuum lead-throughs (room temperature)

Cerama-Seal, 1033 State Route 20, New Lebanon, NY 12125, Tel. 10518-794-7800, Fax 518-794-8080, http://www.ceramaseal.com/.

Detoronics Corp., 10660 East Rush St., So. El Monte, CA 91733–3432, Tel. 818-579-7130, Fax 818-579-1936, http://www.detoronics.com/.

Contacts (springy devices) (Sec. 7.4.3)

Beryllium–copper clad circuit board for making microsprings

Specialty order from Q-Flex, 1220 S. Lyon St., Santa Ana, CA 92705, Tel. 714-835-2868, Fax. 714-835-4772, http://www.q-flex.com/.

Fuzz buttons

Techknit, Cranford, NJ, http://www.fuzzbuttons.com/.

Pogo pins

Emulation Technology, Inc., Santa Clara, CA, http://www.emulation.com/pogo/.

Cryogenic accessories and consumables

Lake Shore Cryotronics, Westerville, OH 43081, Tel. 614-891-2244, Fax. 614-818-1600, http://www.lakeshore.com/.

Oxford Instruments–Cryospares, Witney, Oxfordshire, UK OX29 4TL, Tel. +44(0)1865 881437, Fax. +44(0)1865 884045, http://www.oxinst.com/cryospares/.

Current leads (Secs 4.9 and 4.10)

Flexible superconducting braid

Supercon Inc., 830 Boston Turnpike, Shrewsbury, MA 01545, http://www.supercon-wire.com/ (by special order).

Low-T_c and high-T_c superconductors—see Superconducting wire

Vapor-cooled leads

American Magnetics Inc., P.O. Box 2509, 112 Flint Road, Oak Ridge, TN 37831–2509, USA, http://www.americanmagnetics.com/.

Cryomagnetics Inc., 1006 Alvin Weinberg Drive, Oak Ridge, TN 37830, USA, http://www.cryomagnetics.com/.

Current power supplies; low-ripple, series-transistor regulated (Sec. 9.2)

Alpha Scientific Electronics, Hayward, CA, 510-782-4747, http://www.alphascientific.com/.

Inverpower Controls Ltd., Burlington, Ontario, Canada, 905-639-4692, http://www.inverpower.com/.

Walker LDJ Scientific Inc., Worcester, MA 01606, 508-852-3674, http://www.walkerscientific.com/ (current $\leq$ 500 A).

Dewars for measurement systems—metal and fiberglass–epoxy

American Magnetics Inc., P.O. Box 2509, 112 Flint Road, Oak Ridge, TN 37831–2509, USA, http://www.americanmagnetics.com/.

Cryomagnetics Inc., 1006 Alvin Weinberg Drive, Oak Ridge, TN 37830, USA, http://www.cryomagnetics.com/.

International Cryogenics, 4040 Championship Drive, Indianapolis, IN 46268, Tel. 317-297-4777, Fax. 317-297-7988, http://www.intlcryo.com/.

Janis Research Co., 2 Jewel Dr., P. O. Box 696, Wilmington, MA 01887–0696, Tel. 978-657-8750, http://www.janis.com/.

Oxford Instruments, Witney, Oxfordshire, UK OX294TL, Tel. +44(0)1865 881437, Fax. +44(0)1865 884045, http://www.oxinst.com/.

Precision Cryogenic Systems, Inc., 7804 Rockville Road, Indianapolis, IN 46214, Tel. 317-273-2800, Fax. 317-273-2802, prcry@iquest.net, http://www.precisioncryo.com/.

Tristan Technologies, Inc., 6185 Cornerstone Court East, Suite 106, San Diego, CA 92121, Tel. 877-436-1389, http://www.tristantech.com/.

Heaters, thin film (Secs 1.4, 5.4, 7.3.1, and 7.4.1)

Minco Products, Inc., 7300 Commerce Lane, Minneapolis, MN 55432–3177, Tel. 763-571-3121, Fax. 763-571-0927, Info@minco.com, http://www.minco.com/.

Liquid-level monitors (Sec. 1.6.2)

Janis Research Co., 2 Jewel Dr., P. O. Box 696, Wilmington, MA 01887–0696, Tel. 978-657-8750, http://www.janis.com/.

Lake Shore Cryotronics, Westerville, OH 43081, Tel. 614-891-2244, Fax. 614-818-1600, http://www.lakeshore.com/.

Oxford Instruments, Witney, Oxfordshire, UK OX29 4TL, Tel. +44(0)1865 881437, Fax. +44(0)1865 884045, http://www.oxinst.com/.

Lubricants (see Appendix A3.11)

Magnets, superconducting (Secs 1.4, 1.5, 9.1.4, and 9.2.1)

American Magnetics Inc., P.O. Box 2509, 112 Flint Road, Oak Ridge, TN 37831-2509, USA, http://www.americanmagnetics.com/.

American Superconductor Corp., Two Technology Dr., Westborough, MA 01581, Tel. 508-836-4200, Fax. 508-836-4248, http://www.amsuper.com/ (high-T_c magnets).

Cryomagnetics Inc., 1006 Alvin Weinberg Drive, Oak Ridge, TN 37830, http://www.cryomagnetics.com/.

Oxford Instruments, Witney, Oxfordshire, UK OX294TL, Tel. +44(0)1865 881437, Fax. +44(0)1865 884045, http://www.oxinst.com/.

SuperPower, Inc., 450 Duane Ave., Schenectady, NY 12304, Tel. 518-346-1414, Fax. 518-346-6080, http://www.igc.com/superpower/ (high-T_c magnets).

Materials, less common and specialty sizes (Secs 3.2, 3.4, 6.5.2, 7.3, and 7.4)

Metals—general supplier of high-purity metals and metallic compounds

ESPI, 1050 Benson Way, Ashland, OR 97520, Tel. 800-638-2581, Fax. 800-488-0060, http://www.espimetals.com/.

Copper—high conductivity, oxygen free; (see Appendix A3.1 for a listing of the various types)

Copper & Brass Sales, Tel. 800-926-2600, Fax. 888-926-2600, http://www.copperandbrass.com/ (OFHC™ copper tubes).

Farmer's Copper & Industrial Supply, 800-231-9450, Fax. 409-765-7115, http://www.farmerscopper.com/ (OFHC™ copper tubes).

McMaster–Carr, http://www.mcmaster.com/.

Fiberglass–epoxy composite tubes; custom sizes (made from G-10, G-11, G-13)

A & M Composites, P.O. Box 3281, Big Spring, TX 79721, Tel. 432-267-6525, Fax. 432-267-6599, http://www.amcctx.com/.

Microwave circuit board (TMM™) (with a thermal-expansion coefficient less than that of G-10 circuit board, so as to give better dimensional stability)

Rogers Corp., One Technology Dr., P.O. Box 188, Rogers, CT 06263-0188, Tel. 860-774-9605, Fax. 860-779-5509, http://www.rogers-corp.com/

Titanium tubes—less common sizes.

Titanium Sports Technologies (TST), 1426 E. Third Ave., Kennewick, WA 99336, Tel. 509-586-6117, http://www.titaniumsports.com/.

Mechanical actuators and linear motors (Sec. 3.6)

Energen, Inc., 170 Cabot St., Suite 301, Lowell, MA 01854, Tel. 978-259-0100, Fax. 978-259-0105, http://www.energeninc.com/index.htm.

Soldering materials (Secs 3.3.4, 4.5, 4.6, 8.3.2, and 8.3.3)

Indium-alloy solders

Indium Corp. of America, Indalloy® solders, Tel. 315-853-4900 or 800-4-INDIUM, askus@indium.com, http://www.indium.com/.

Lake Shore Cryotronics, Ostalloy® solders, Westerville, OH 43081, Tel. 614-891-2244, Fax. 614-818-1600, http://www.lakeshore.com/.

Umicore Indium Products, Ostalloy® solders, http://www.thinfilmproducts.umicore.com/.

Solder flux

- Combined solder and flux paste:
  Fusion Automation, Inc., http://www.fusion-inc.com/ Model SSX-430-830.
  Multicore Kester 135, http://www.kester.com/.
- Mild flux:
  Alpha HF260, http://www.alphametals.com/distributors/pdfs/2001134214.pdf.
  Litton ESF33, http://www.amsuper.com/products/library/003-TechNote_Soldering.pdf.
- Unactivated rosin flux:
  Kester, Tel. 800-253-7837, Fax. 847-390-9338, technicalservice@kester.com, http://www.kester.com/ designated "Plastic core" RNA (rosin non-activated).

Solder with antimony to minimize embrittlement and cracking at cryogenic temperatures

Kester, Tel. 800-253-7837, Fax. 847-390-9338, technicalservice@kester.com, http://www.kester.com/.

Strain gauges, accessories, and gauge adhesives for cryogenic service (Sec. 9.4.4)

Vishay Intertechnology, Inc., Vishay Micro-Measurements Division, http://www.vishay.com/.

Sticky stuff: (see Appendix A3.10)

Superconducting wire (Secs 4.9 and 4.10, Chapters 9 and 10)

Updated links to superconductor suppliers are available at http://superconductors.org/Links.htm.

Low-T_c (Nb–Ti and Nb_3Sn)

Alstom Magnets and Superconductors, 90018 Belfort Cedex, France, Tel. +33 (0)3 84 55 32 26, Fax. +33 (0)3 84 55 70 93, http://www.powerconv.alstom.com/.

Bochvar, 5 ulitsa Rogova, Moscow 123060, Tel. (095) 190-49-93[1], 190-82-97[2], Fax. (095) 196-41-68, e-mail: post@bochvar.ru, http://www.bochvar.ru.

European Advanced Superconductor (EAS), Ehrichstraße 10, 63450 Hanau, Germany, Tel. (+49) (6181) 43 84-41 00, Fax. (+49) (6181) 43 84-44 00, http://www.advancedsupercon.com/.

Furukawa Electric, 6-1, Marunouchi 2-chome, Chiyoda-ku, Tokyo 100, Japan, Tel. 81-3-3286-3001, Fax. 81-3-3286-3747,3748, http://www.furukawa.co.jp/english.

Kobe Steel, Ltd., Shinko Building, 10–26, Wakinohamacho, 2-chome, Chuo-ku, Kobe, Hyogo 651-8585, Japan, Tel. 81-78-261-511, Fax. 81-78-261-4123, http://www.kobelco.co.jp/english.

Outokumpu, http://www.outokumpu.com/.

Oxford Superconducting Technology, 600 Milik St., P.O. Box 429, Carteret, NJ 07008–0429, Tel. 732-541-1300, Fax. 732-541-7769, http://www.oxford-instruments.com/.

Shape Metal Innovations (SMI); Nb_3Sn powder-in-tube (PIT) process, Tel. +31 53 4340704, JLSMI@worldonline.nl.

Sumitomo, One North Lexington Ave., White Plains, NY 10601, Tel. 914-467-6001, Fax. 914-467-6081, http://www.sumitomoelectricusa.com/.

Supercon Inc., 830 Boston Turnpike, Shrewsbury, MA 01545, http://www.supercon-wire.com/.

Western Superconducting Material Technology Corp., P.O., Box 51, Xi'an Shaanxi, 710016 P.R. China.

Low-T_c (MgB_2)

Columbus Superconductor S.R.L., Corso F. Perrone 24, 16152 Genova, Italy, Tel. +39 (0)10 65 98 784, Fax. +39 (0)10 65 98 732. (*Ex-situ* process.)

Diboride Conductors, http://www.diboride.biz/.

Hyper Tech Research, Inc., 110 E. Canal St., Troy, OH 45373-3581, Tel. 937-332-0348, http://www.hypertechresearch.com/. (*In-situ* process.)

High-T_c (Bi-2212)

Oxford Superconducting Technology, 600 Milik St., P.O. Box 429, Carteret, NJ 07008-0429, Tel. 732-541-1300, Fax. 732-541-7769, http://www.oxford-instruments.com/.

Showa Electric Wire and Cable Co., Ltd., http://www.swcc.co.jp/eng/index.htm.

High-T_c (Bi-2223)

American Superconductor Corp., Two Technology Drive, Westborough, MA 01581, Tel. 508-836-4200, Fax. 508-836-4248, http://www.amsuper.com/.

European Advanced Superconductor (EAS), Ehrichstraße 10, 63450 Hanau, Germany, Tel. (+49) (6181) 43 84-41 00, Fax. (+49) (6181) 43 84-44 00, http://www.advancedsupercon.com/.

Innova Superconductor Technology Co. Ltd, 7 Rongchang Dongjie, Longsheng Industrial Park, Beijing 100176, P.R. China.

Sumitomo, One North Lexington Ave., White Plains, NY 10601, Tel. 914-467-6001, Fax. 914-467-6081, http://www.sumitomoelectricusa.com/.

Trithor GmbH, Heisenbergstrasse 16, D-53359 Rheinbach, Germany, Tel.: +49 (0) 2226-90 60—0, Fax. +49 (0) 2226-90 60—900, http://www.trithor.com/.

High-T_c (YBCO)

American Superconductor Corp., Two Technology Drive, Westborough, MA 01581, Tel. 508-836-4200, Fax. 508-836-4248, http://www.amsuper.com/.

Fujikura, http://www.fujikura.co.jp/ie_e.html.

SuperPower, 450 Duane Avenue, Schenectady, NY 12304, Tel. 518/346-1414, Fax. 518/346-6080, http://www.igc.com/superpower/.

Theva GmbH, Rote-Kreuz-Str. 8, D-85737 Ismaning Germany, Tel. +49 89 923346-0, Fax. +49 89 923346-10, info@theva.com, http://www.theva.com/.

Thermometers and accessories (Chapter 5)

Beryllium-oxide high-thermal-conductivity chips

Lake Shore Cryotronics, Westerville, OH 43081, Tel. 614-891-2244, Fax. 614-818-1600, http://www.lakeshore.com/.

Capacitance bridges

Automatic bridges—Andeen–Hagerling Inc., Cleveland, OH, Tel. 440-349-0370, Fax. 440-349-0359, http://www.andeen-hagerling.com/.

Capacitance controller card—Lake Shore Cryotronics, Westerville, OH 43081, Tel. 614-891-2244, Fax. 614-818-1600, http://www.lakeshore.com/.

General Radio capacitance bridges (5 digit) available from IET Labs Inc., Westbury, NY, Tel. 800-899-8438, Fax. 516-334-5988, http://www.ietlabs.com/ or Tucker Electronics, Dallas, TX, Tel. 800-527-4642, Fax. 214-348-0367, http://www.tucker.com/.

Grease—thermally conducting

Apiezon N™ grease—Apiezon Products, M & I Materials Ltd., Manchester, UK, Tel. +44 (0)161 864 5419, Fax. +44 (0)161 864 5444, http://www.apiezon.com/.

Cry-Con™ grease—available, for example, from Janis Research Co., Accessories and Ancillary Equipment, http://www.janis.com/.

Thermometers for cryogenic temperatures and calibration services

Lake Shore Cryotronics, Westerville, OH 43081, Tel. 614-891-2244, Fax. 614-818-1600, http://www.lakeshore.com/.

Oxford Instruments—Cryospares, Witney, Oxfordshire, UK OX29 4TL, Tel. +44(0)1865 881437, Fax. +44(0)1865 884045, http://www.oxinst.com/cryospares/.

Scientific Instruments, Inc., West Palm Beach, FL 33407, Tel. 561-881-8500, Fax. 561-881-8556, http://www.scientificinstruments.com/.

Tinsley Manufacturing, supplier of rhodium–iron resistance thermometers in wire form.

Temperature controllers

Lake Shore Cryotronics, Westerville, OH 43081, Tel. 614-891-2244, Fax. 614-818-1600, http://www.lakeshore.com/.

Oxford Instruments, Witney, Oxfordshire, UK OX29 4TL, Tel. +44(0)1865 881437, Fax. +44(0)1865 884045, http://www.oxinst.com/.

Thermocouple wire (Secs 5.1.1, 5.1.2, 5.1.4, 5.1.6, and 5.5.9)

Omega Engineering, P.O. Box 4047, Stamford, CT 06907-0047, 800-848-4286 or 203-359-1660, Fax. 203-359-7700, http://www.omega.com/.

River Bend Technology Centre, Northbank, Irlam, Manchester UK, M44 5BD, http://www.omega.co.uk/.

Vacuum accessories (Secs 3.3.1 and 3.7)

C-ring metal seals

American Seal and Engineering Co., P.O. Box 1038, Orange, CT 06477, 800-878-2442, http://www.ameriseal.com.

Garlock–Helicoflex, P.O. Box 9889, Columbia, SC 20290, Tel. 800-713-1880, http://www.helicoflex.com.

Hydrodyne, 325 Damon Way, Burbank, CA 91505, Tel. 818-841-9667, http://www.hydrodyne.com.

Nicholsons Sealing Technologies Ltd., Hamsterley, Newcastle upon Tyne, UK, NE17 7SX, Tel. +44 (0)1207 560505, http://www.nicholsons.com.

Dynamic seals: O-rings, spring-loaded PTFE

Bal Seal Engineering Co., Inc., 620 West Ave., Santa Ana, CA 92707-3398, Tel. 714-557-5192.

Vacuum flanges and fixtures: Ladish Tri-Clover, and ISO KF; available from general vacuum-equipment suppliers such as

Duniway Stockroom Corp., Tel. 800-446-8811, http://www.duniway.com/.

Kurt J. Lesker Co., Tel. 800-245-1656, http://www.lesker.com/.

O-rings, indium wire

Indium Corp. of America, 1676 Lincoln Ave., Utica, NY 13503.

O-rings, metal

Perkin Elmer, Beltsville, MD, Tel. 301-937-4010.

Screws (silver-plated to prevent galling, precleaned, and optionally vented for vacuum systems)

McMaster–Carr, http://www.mcmaster.com/.

U-C Components, Morgan Hill, CA, http://www.uc-components.com/.

Wire (Secs 4.1, 4.2, and 4.3)

Phosphor-bronze twisted-wire pairs for thermometer leads

Lake Shore Cryotronics, Westerville, OH 43081, Tel. 614-891-2244, Fax. 614-818-1600, http://www.lakeshore.com/ Quad-Twist™ cryogenic wire.

Pure indium wire for indium O-rings

Indium Corp. of America, Tel. 315-853-4900 or 800-4-INDIUM, askus@indium.com, http://www.indium.com/.

Stripper (chemical) for polyimide (Kapton™) wire insulation

Miller–Stephenson chemical, George Washington Hwy., Danbury, CT 06810, Tel. 203-743-4447, Fax. 203-791-8702, support@miller-stephenson.com, MS-111 stripping agent.

A2 **Heat transfer (ref. Chapter 2)**

A2.1 THERMAL CONDUCTIVITY INTEGRALS FOR TECHNICAL CRYOSTAT MATERIALS (SEE ALSO FIG. 2.1 IN SEC. 2.2)

The thermal conductivity integrals tabulated below are referenced to 4 K. Steady-state heat conduction $\dot{q}_{\mathrm{cond}}$ through a solid member of uniform cross section A and length L may be determined between two arbitrary temperatures T_1 and T_2 by taking the difference between the two corresponding 4 K integral values:

$$\dot{q}_{\mathrm{cond}} \equiv A/L \int_{T_1}^{T_2} \lambda(T)\,\mathrm{d}T = A/L \left\{ \int_{4\,\mathrm{K}}^{T_2} \lambda(T)\,\mathrm{d}T - \int_{4\,\mathrm{K}}^{T_1} \lambda(T)\,\mathrm{d}T \right\},$$

where $\lambda(T)$ is the temperature-dependent thermal conductivity.

Data for materials other than those tabulated may be estimated well enough for cryostat-design purposes by using data for similar materials, especially if they have a low thermal conductivity and do not contribute much to the total heat influx. For example, most commercial glasses, as well as many plastics and disordered polymers can be represented (within a factor of about two) by the integral values given for Pyrex™. Values for Manganin can be approximated by those given for Constantan, and values for Inconel and Monel alloys are between those of stainless steel and Constantan.

Greater care must be given to the highly conducting materials. Phosphorus deoxidized copper is the type of copper used most often in pipe, rods, and bars. ETP copper is the material from which copper electrical wires are usually made.

The temperature dependence of the thermal conductivity of additional cryostat construction materials is given in Appendix A6.7.

Thermal Conductivity Integrals

	$\int_{4\mathrm{K}}^{T} \lambda\,\mathrm{d}T$ [kW/m]									[W/m]			
	Copper		Copper alloys		Aluminum			Stainless steel	Const-antan	Glass	Polymers		
T[K]	ETP[a]	Phos. deox.	Be/Cu 98 Cu 2 Be	German Silver 60 Cu 25Zn 15 Ni	Common pure 99 Al[a]	Mn/Al 98.5 Al 1.2 Mn plus traces	Mg/Al 96 Al 3.5 Mg plus traces	Average types 303, 304, 316, 347		Average Pyrex™ Quartz Boro-silicate	Teflon™	Perspex™	Nylon™
6	0.80	0.0176	0.0047	0.00196	0.138	0.0275	0.0103	0.00063	0.0024	0.211	0.113	0.118	0.0321
8	1.91	0.0437	0.0113	0.00524	0.342	0.0670	0.025	0.00159	0.0066	0.443	0.262	0.238	0.0807
10	3.32	0.0785	0.0189	0.010	0.607	0.117	0.0443	0.00293	0.0128	0.681	0.44	0.359	0.148

15	8.02	0.208	0.0499	0.030	1.52	0.290	0.112	0.00816	0.0375	1.31	0.985	0.669	0.410
20	14.0	0.395	0.0954	0.0613	2.76	0.534	0.210	0.0163	0.0753	2.00	1.64	1.01	0.823
25	20.8	0.635	0.155	0.102	4.24	0.850	0.338	0.0277	0.124	2.79	2.39	1.44	1.39
30	27.8	0.925	0.229	0.153	5.92	1.23	0.490	0.0424	0.181	3.68	3.23	1.96	2.08
35	34.5	1.26	0.316	0.211	7.73	1.67	0.668	0.0607	0.244	4.71	4.13	2.59	2.90
40	40.6	1.64	0.415	0.275	9.62	2.17	0.770	0.0824	0.312	5.86	5.08	3.30	3.85
50	50.8	2.53	0.650	0.415	13.4	3.30	1.24	0.135	0.457	8.46	7.16	4.95	6.04
60	58.7	3.55	0.930	0.568	17.0	4.55	1.79	0.198	0.612	11.5	9.36	6.83	8.59
70	65.1	4.68	1.25	0.728	20.2	5.89	2.42	0.270	0.775	15.1	11.6	8.85	11.3
76	68.6	5.39	1.46	0.826	22.0	6.72	2.82	0.317	0.875	17.5	13.0	10.1	13.1
80	70.7	5.89	1.60	0.893	23.2	7.28	3.09	0.349	0.943	19.4	13.9	11.0	14.2
90	75.6	7.20	1.99	1.060	25.8	8.71	3.82	0.436	1.11	24.0	16.3	13.2	17.3
100	80.2	8.58	2.40	1.23	28.4	10.2	4.59	0.528	1.28	29.2	18.7	15.5	20.4
120	89.1	11.5	3.30	1.57	33.0	13.2	6.27	0.726	1.62	40.8	23.7	20.0	26.9
140	97.6	14.6	4.32	1.92	37.6	16.2	8.11	0.939	1.97	54.2	28.7	24.7	33.6
160	106	18.0	5.44	2.29	42.0	19.4	10.1	1.17	2.32	69.4	33.8	29.4	40.5
180	114	21.5	6.64	2.66	46.4	22.5	12.2	1.41	2.69	85.8	39.0	34.2	47.5
200	122	25.3	7.91	3.06	50.8	25.7	14.4	1.66	3.06	103.0	44.2	39.0	54.5
250	142	35.3	11.3	4.15	61.8	33.7	20.5	2.34	4.06	150.0	57.2	51.0	72.0
300	162	46.1	15.0	5.32	72.8	41.7	27.1	3.06	5.16	199.0	70.2	63.0	89.5

Sources:

V. Johnson (1960), NBS, Wright Air Development Div. (WADD) Technical Report 60-56, Part II. US Government Printing Office, Washington, DC.

D. H. J. Goodall (1970), A.P.T. Division, Culham Science Center, Abingdon, Oxfordshire, UK.

[a] The high thermal conductivity of nearly pure metals is variable and strongly depends on their impurity content; see Sec. 6.4.2.

A2.2 EMISSIVITY OF TECHNICAL MATERIALS AT A WAVELENGTH OF ABOUT 10 μm (ROOM TEMPERATURE) (SEC. 2.4)

Material	Emissivity		
	Polished	Highly oxidized	Common condition
Metallic			
Ag	0.01		
Cu	0.02	0.6	
Au	0.02		
Al	0.03	0.3	
Brass	0.03	0.6	
Soft-solder			0.03
Nb, crystalline, bulk			0.04
Lead	0.05		
Ta	0.06		
Ni	0.06		
Cr	0.07		
Stainless steel			0.07
Ti			0.09
Tin (gray), single crystal			0.6
Nonmetallic			
IMI 7031 varnish			0.9
Phenolic lacquer			0.9
Plastic tape			0.9
Glass			0.9

Sources:

American Institute of Physics Handbook (1972), 3rd edition, Chapter 6, McGraw-Hill, New York.

M. M. Fulk, M. M. Reynolds, and O. E. Park (1955), *Proc. 1954 Cryogenic Eng. Conf.*, Nat. Bur. Stands. (US) Report No. 3517, p. 151. US Government Printing Office, Washington, DC.

W. H. McAdams (1954), *Heat Transmission*, 3rd edition, McGraw-Hill, New York.

W. T. Ziegler and H. Cheung (1957), *Proc. 1956 Cryogenic Engineering Conference*, National Bureau of Standards, p. 100. US Government Printing Office, Washington, DC.

Emissivities of additional materials at room temperature are available in the technical reference section of *The Temperature Handbook* (2002), p. Z-171. Omega Engineering Inc., Stamford, CT (http://www.omega.com/).

A2.3 HEAT CONDUCTANCE ACROSS SOLID INTERFACES PRESSED TOGETHER WITH 445 N FORCE (45 kgf OR 100 lbf) (SEC. 2.6)

Heat conductance at a force level F other than 445 N can be determined by multiplying these data by the ratio F / 445 N. In addition to these data, see Fig. 2.7 for heat conductance values covering a wide range of temperatures (0.1–300 K) for pressed contacts of gold/gold, indium/copper, copper/copper, and stainless/stainless. Data are also given in Fig. 2.7 for solder, grease, and varnish joints.

Heat conductance across solid interfaces pressed together with 44 N force (100 lbf)

Interface materials	4.2 K	77 K	y [a]
Gold/gold	2×10^{-1} W/K[b]		1.3[b]
Copper/copper	1×10^{-2} W/K[c]	3×10^{-1} W/K[c]	1.3[b]
Steel/steel	5×10^{-3} W/K[c]	3×10^{-1} W/K[c]	
Sapphire/sapphire	7×10^{-4} W/K[b]		3[b]

[a] Values of y are for calculating the heat conductance at temperatures below 4.2 K by using Eq. (2.14) in Sec. 2.6.

[b] R. Berman and C. F. Mate (1958), *Nature* 182, 1661.

[c] R. Berman (1956), *J. Appl. Phys.* 27, 318.

A3 **Cryostat construction (ref. Chapter 3)**

A3.1 HIGH-THERMAL-CONDUCTIVITY CONSTRUCTION-METAL PROPERTIES: RRR, THERMAL CONDUCTIVITY, AND ELECTRICAL RESISTIVITY (SEC. 3.2.2)

The thermal conductivities of additional construction materials are shown in Fig 2.1 and tabulated in Appendix A6.7.

Material	RRR [a,f] ($\equiv \rho_{293\,K}/\rho_{4\,K}$)	$\lambda_{293\,K}$ [g] [W/(m·K)]	$\lambda_{4.2\,K}$ [f,h] [W/(m·K)]	$\rho_{293\,K}$ [f,g] [μΩ cm]	$\rho_{77\,K}$ [f] [μΩ cm]	Use	Comments
Copper							
High purity (99.999% pure)[c,d]	~2000	394	~11300	1.68	0.19	Very high thermal-cond. parts	Thermal conductivity can be increased by annealing; see footnotes c and d
Oxygen-free[c,d,e] Grade C10100 [b,c,d] (99.99% pure)	~150	394	~850	1.72	0.19	High thermal-cond. foil, rods, plates, and tubes	Thermal conductivity can be increased by annealing; see footnotes c and d
Electronic grade C10200[b,c,d] (99.95% pure)	~100	390	~560	1.72	0.19		
ETP Grade C11000[b,c]	~100	390	~560	1.71	—	High thermal-cond. rods, plates, wire, and wire braid	ETP ≡ electrolytic-tough-pitch copper Contains about 0.3% oxygen—cannot be used for hydrogen brazing Thermal conductivity of cold-worked ETP copper can be increased by annealing; see footnote c
Phosphorus deoxidized Grade C12200	3–5	339	~14–24	2.03	—	Tubes	
Brass Free cutting brass Grade C36000	~2.5	125	~4.5	7.2	4.7		
Beryllium copper, annealed Grade C17000–C17300	1.5–2.5	~84 depends on processing	~1.8–3.0	6.4–10.7 depends on processing	4.2–8.5 depends on processing		

A3.1 **High-thermal-conductivity construction-metal properties** (***Continued***)

Material	RRR [a,f] ($\equiv \rho_{293\,K}/\rho_{4\,K}$)	$\lambda_{293\,K}$ [g] [W/(m·K)]	$\lambda_{4.2\,K}$ [f,h] [W/(m·K)]	$\rho_{293\,K}$ [f,g] [μΩ cm]	$\rho_{77\,K}$ [f] [μΩ cm]	Use	Comments
Aluminum							
99.999% high purity	~1000	235	~3400	2.76	0.23		
Grade 1100	~14	222	~45	—	—		
Grade 6063	~7	218	~22	—	—		
Grade 5052	~1.4	138	~2.8	4.93	—		

[a] RRR $\equiv \rho_{293\,K}/\rho_{4\,K}$, the residual resistivity ratio, $\lambda \equiv$ thermal conductivity; $\rho \equiv$ electrical resistivity. The listed RRR values are nominal and can vary by about 50% from sample to sample for the purer grades, depending on the amount and type of impurities as well as cold-work condition.

[b] UNS grade numbers for metals and alloys.

[c] The thermal and electrical conductivity of *deformed* and *cold-worked* high-purity, oxygen-free, and ETP copper can be increased (depending on the amount of cold work) by annealing. Heat in vacuum ($\lesssim 10^{-4}$ torr) or argon at about 500°C for about an hour. If vacuum or argon are not readily available, copper can be heated in air, but a surface scale forms, which can be removed afterward with dilute nitric acid.

[d] Although this is not commonly done, further increase in the thermal and electrical conductivity can be obtained by oxidizing the magnetic iron impurities in high-purity and oxygen-free copper (but not in ETP copper, which contains too many impurities other than iron). The RRR of oxygen-free copper is typically increased from ~100 as received, to ~800 after oxidation; the RRR of high-purity (99.99%) copper is typically increased from ~1500 as received, to more than 10 000 after oxidation. Heat the copper part at about 1000°C in oxygen at about 0.13–1.3 Pa (10^{-3}–10^{-2} torr) pressure. About a day of annealing is required for small parts, up to a month for large copper billets [ref. F. R. Fickett (1974), *Mater. Sci. Eng.* 14, 199–210].

[e] Sources of oxygen-free copper are not as plentiful as ETP copper, especially in tube form. However, if high-thermal-conductivity tubes are needed or if hydrogen brazing is to be done, oxygen-free copper is required. Suppliers of oxygen-free copper are listed in Appendix A1.7 under Material, copper.

[f] From C. A. Thompson, W. M. Manganaro, and F. R. Fickett (1990), *Cryogenic Properties of Copper*, Wall Chart, NIST, and the references cited therein. US Government Printing Office, Washington, DC.

[g] *Metals Handbook* (1961), Vol. 1, *Properties and Selection of Materials*, 8th edition, ASM International, Materials Park, OH.

[h] Calculated from the Wiedemann–Franz–Lorenz law, Eq. (2.4): $\lambda = L_N T / \rho$, where L_N is the Lorenz constant; this results in $\lambda(4.2\ K) = \lambda(293\ K)\,(\rho_{293\,K}/\rho_{4\,K})\,(4.2\ K/293\ K)$.

A3.2 HEAT CONDUCTION ALONG THIN-WALLED STAINLESS-STEEL TUBING (SEC. 3.2.2)

The heat conduction values tabulated in this table may be simply scaled to lengths other than 10 cm (inversely proportional) and wall thicknesses other than those listed in column 2 (directly proportional).

The tabulated values of conducted heat assume no gas cooling of the tubing. If the gas boiled off by the conducted heat were to cool the tubing with 100% efficiency, the resultant heat flow would be 1/10 of the values given for $T = 77$ K and 1/32 of those for $T = 300$ K.

Heat conduction along thin-walled stainless-steel tubing

Tube O.D.	Wall thickness	Cross-sectional area	Heat conducted along 10 cm of tubing with one end at 4 K and the other at:	
			T = 77 K	T = 300 K
[inches]	[inches (mm)]	[cm^2]	[mW]	[mW]
1/8	0.004 (0.10)	0.0098	3.1	30
3/16	0.004 (0.10)	0.0149	4.7	45
1/4	0.004 (0.10)	0.020	6.3	61
3/8	0.004 (0.10)	0.045	14	137
1/2	0.004 (0.10)	0.060	19	184
5/8	0.006 (0.15)	0.075	24	230
3/4	0.006 (0.15)	0.091	29	277
1	0.006 (0.15)	0.121	38	370
1 1/4	0.010 (0.25)	0.251	80	770
1 1/2	0.010 (0.25)	0.302	96	924
2	0.015 (0.38)	0.604	191	1847

Sources:

V. Johnson (1960), NBS, Wright Air Development Div. (WADD) Technical Report 60-56, Part II. US Government Printing Office, Washington, DC.

D. H. J. Goodall (1970), A.P.T. Division, Culham Science Center, Abingdon, Oxfordshire, UK.

A3.3 PIPE AND TUBING SIZES (SEC. 3.5)

Nominal size	Type K copper tubing		Brass pipe		Steel and PVC pipe, Schedule 40		Soft copper refrigeration tubing	
[inches]	Internal diameter	External diameter	Internal diameter	External diameter	Internal diameter	External diameter	Internal diameter	External diameter
1/8	NA[a]	NA	NA	NA	0.269	0.405	0.065	0.125
1/4	0.30	0.375	0.410	0.540	0.364	0.540	0.190	0.250
3/8	0.40	0.500	0.545	0.675	0.493	0.675	0.311	0.375
1/2	0.53	0.625	0.710	0.840	0.622	0.840	0.436	0.500
5/8	0.65	0.750	NA	NA	NA	NA	0.555	0.625
3/4	0.75	0.875	0.920	1.050	0.824	1.050	0.680	0.750
1	1.00	1.125	1.185	1.315	1.049	1.315		
1-1/4	1.25	1.375	1.530	1.660	1.380	1.660		
1-1/2	1.48	1.625	1.770	1.900	1.610	1.900		
2	1.96	2.125	2.245	2.375	2.067	2.375		
2-1/2	2.44	2.625	2.745	2.875	2.469	2.875		
3	2.91	3.125	3.334	3.500	3.068	3.500		
3-1/2	3.39	3.625	3.810	4.000	3.548	4.000		
4	3.86	4.125	4.296	4.500	4.026	4.500		
5	4.81	5.125	5.298	5.562	5.047	5.562		
6	5.74	6.125	6.309	6.625	6.065	6.625		

All dimensions are in inches.

Source: From B. Brandt (2002), National High-Field Magnet Laboratory, Florida State University, personal communication.

[a] NA ≡ Not available.

A3.4 SCREW AND BOLT SIZES, HEXAGON SOCKET-HEAD SIZES, AND LOAD LIMITS (SEC. 3.3.1)

Maximum load and minimum engaged thread length are determined for stainless-steel (SS) bolts assuming a yield strength of 414 MPa (60 ksi). Hexagon socket-head diameters and heights are given to facilitate laying out bolt circles on vacuum flanges.

Screw and bolt sizes, hexagon socket-head sizes, and load limits

Screw[a] size—Number of threads per inch	Major diam. [inches (mm)]	Nearest standard metric size	Maximum[b] load (SS bolts) [lbf (kN)]	Engaged length[c] (SS into SS) [inches (mm)]	Number[c] engaged threads (SS into SS)	Engaged length (SS into Al) [inches (mm)]	Number engaged threads (SS into Al)	Socket head diameter[d] [inches]		Socket head height[d] [inches]		Tap drill size (inch, number, and letter drills)	Clearance drill size (number and inch drills)
								Max	Min	Max	Min		
0–80	0.0600 (1.524)	M1.6 × 0.35	108 (0.48)	0.0328 (0.833)	2.6	0.0654 (1.66)	5.2	0.096	0.091	0.060	0.057	3/64	51
1–64	0.0730 (1.854)	M2 × 0.4	157 (0.70)	0.0396 (1.01)	2.5	0.0786 (2.00)	5.0	0.118	0.112	0.073	0.070	53	47
1–72	”	”	167 (0.74)	0.0407 (1.03)	2.9	0.0831 (2.11)	6.0	”	”	”	”	53	47
2–56	0.0860 (2.184)	”	222 (0.99)	0.0471 (1.20)	2.6	0.0938 (2.38)	5.3	0.140	0.134	0.086	0.083	50	42
2–64	”	”	236 (1.05)	0.0482 (1.22)	3.1	0.0100 (0.25)	6.4	”	”	”	”	50	42
3–48	0.0990 (2.515)	M2.5 × 0.45	292 (1.30)	0.0539 (1.37)	2.6	0.0107 (0.27)	5.2	0.161	0.154	0.099	0.095	47	37
3–56	”	”	314 (1.40)	0.0558 (1.42)	3.1	0.115 (2.93)	6.5	”	”	”	”	46	37
4–40	0.1120 (2.845)	M3 × 0.5	362 (1.61)	0.0602 (1.53)	2.4	0.118 (2.99)	4.7	0.183	0.176	0.112	0.108	43	31
4–48	”	”	396 (1.76)	0.0625 (1.59)	3.0	0.129 (3.27)	6.2	”	”	”	”	3/32	31
5–40	0.1250 (3.175)	”	477 (2.12)	0.0688 (1.75)	2.8	0.139 (3.53)	5.6	0.205	0.198	0.125	0.121	38	29
5–44	”	”	499 (2.22)	0.0703 (1.79)	3.1	0.145 (3.68)	6.4	”	”	”	”	37	29
6–32	0.1380 (3.505)	M4 × 0.7	545 (2.42)	0.0741 (1.88)	2.4	0.144 (3.65)	4.6	0.226	0.218	0.138	0.134	36	27
6–40	”	”	609 (2.71)	0.0775 (1.97)	3.1	0.161 (4.08)	6.4	”	”	”	”	33	27
8–32	0.1640 (4.166)	”	841 (3.74)	0.0914 (2.32)	2.9	0.186 (4.73)	6.0	0.270	0.262	0.164	0.159	29	18
8–36	”	”	884 (3.93)	0.0932 (2.37)	3.4	0.196 (4.98)	7.1	”	”	”	”	29	18
10–24	0.1900 (4.826)	M5 × 0.8	1 050 (4.68)	0.103 (2.61)	2.5	0.201 (5.11)	4.8	0.312	0.303	0.190	0.185	26	9
10–32	”	”	1 200 (5.34)	0.109 (2.76)	3.5	0.230 (5.83)	7.3	”	”	”	”	21	9
12–24	0.2160 (5.486)	”	1 450 (6.45)	0.120 (3.05)	2.9	0.244 (6.20)	5.9	—	—	—	—	16	2
12–28	”	”	1 550 (6.88)	0.123 (3.13)	3.5	0.261 (6.62)	7.3	—	—	—	—	15	2

(Continued)

A3.4 Screw and bolt sizes (*Continued*)

Screw[a] size—Number of threads per inch	Major diam. [inches (mm)]	Nearest standard metric size	Maximum[b] load (SS bolts) [lbf (kN)]	Engaged length[c] (SS into SS) [inches (mm)]	Number[c] engaged threads (SS into SS)	Engaged length (SS into Al) [inches (mm)]	Number engaged threads (SS into Al)	Socket head diameter[d] [inches] Max	Socket head diameter[d] [inches] Min	Socket head height[d] [inches] Max	Socket head height[d] [inches] Min	Tap drill size (inch, number, and letter drills)	Clearance drill size (number and inch drills)
1/4–20	0.2500 (6.350)	M6 × 1.0	1 910 (8.49)	0.138 (3.51)	2.8	0.278 (7.05)	5.6	0.375	0.365	0.250	0.244	7	17/64
1/4–28	”	”	2 180 (9.71)	0.146 (3.71)	4.1	0.318 (8.07)	8.9	”	”	”	”	3	17/64
5/16–18	0.3125 (7.938)	M8 × 1.25	3 150 (14.0)	0.177 (4.48)	3.2	0.366 (9.30)	6.6	0.469	0.457	0.312	0.306	F	21/64
5/16–24	”	M8 × 1.0	3 480 (15.5)	0.185 (4.69)	4.4	0.405 (10.3)	9.7	”	”	”	”	I	21/64
3/8–16	0.3750 (9.525)	M10 × 1.5	4 650 (20.7)	0.214 (5.43)	3.4	0.451 (11.5)	7.2	0.562	0.550	0.375	0.368	5/16	25/64
3/8–24	”	M10 × 1.0	5 270 (23.4)	0.226 (5.75)	5.4	0.511 (12.3)	12.3	”	”	”	”	Q	25/64
7/16–14	0.4375 (11.112)	M12 × 1.75	6 380 (28.4)	0.251 (6.37)	3.5	0.530 (13.5)	7.4	0.656	0.642	0.438	0.430	U	29/64
7/16–20	”	M12 × 1.25	7 120 (31.7)	0.263 (6.68)	5.3	0.592 (15.0)	11.8	”	”	”	”	25/64	29/64
1/2–13	0.5000 (12.700)	M12 × 1.75	8 510 (37.9)	0.289 (7.34)	3.8	0.619 (15.7)	8.1	0.750	0.735	0.500	0.492	27/64	33/63
1/2–20	”	M12 × 1.25	9 600 (42.7)	0.305 (7.74)	6.1	0.698 (17.7)	14.0	”	”	”	”	29/64	33/64
9/16–12	0.5625 (14.288)	M16 × 2.0	10 900 (48.6)	0.327 (8.30)	3.9	0.706 (17.9)	8.5	—	—	—	—	31/64	37/64
9/16–18	”	M16 × 1.5	12 200 (54.2)	0.343 (8.72)	6.2	0.788 (20.0)	14.2	—	—	—	—	33/64	37/64
5/8–11	0.6250 (15.875)	M16 × 2.0	13 600 (60.3)	0.364 (9.25)	4.0	0.790 (20.1)	8.7	0.938	0.921	0.625	0.616	17/32	41/64
5/8–18	”	M16 × 1.5	15 400 (68.3)	0.385 (9.78)	6.9	0.894 (22.7)	16.1	”	”	”	”	37/64	41/64
3/4–10	0.7500 (19.050)	M20 × 2.5	20 100 (89.3)	0.442 (11.2)	4.4	0.973 (24.7)	9.7	1.125	1.107	0.750	0.740	21/32	49/64
3/4–16	”	M20 × 1.5	22 400 (99.5)	0.464 (11.8)	7.4	1.09 (25.6)	17.4	”	”	”	”	11/16	49/64

Al=aluminum, SS=stainless steel

[a] ANSI screw thread standard.

[b] It is good practice to derate these maximum loads by about a factor of two safety margin.

[c] To prevent galling and seizing, especially for stainless steel into stainless steel, use silver-plated stainless-steel bolts or coat them with MoS_2. Sources of such screws are listed in Appendix A1.7 under Vacuum accessories, Screws.

[d] From R. O. Parmley, ed. (1997), *Standard Handbook of Fastening and Joining*, McGraw-Hill, NY.

A3.5 CLEARANCES FOR VARIOUS TYPES OF FITS

When machining parts that need to slip or slide over each other, the required gap varies with the type of fit desired and the diameter of the part. The following table can be used as a rough guide. For more critical parts, follow the detailed specifications in the *Machinery's Handbook* (2000), Industrial Press, Inc., New York.

Be sure to adjust the gap for any difference in thermal contractions between the two materials.

The clearance gaps tabulated below are appropriate only for moving parts that are protected from repeated air exposure. Beware of liquid air films that can freeze movable parts (see the tip in Sec. 1.5.1 for preventing this). Also, the gap between a dip probe and the inner wall of a dewar (or the bore of a magnet) must be much larger than the clearances indicated below. A 1–2 mm (or larger) gap is needed to accommodate frost that can form on surfaces during repeated insertion and removal of probes from a dewar.

Clearances for various types of fits

Type of fit	Approximate gap for a 1/8th inch (3.2 mm) diameter shaft [10^{-3} inch]	Approximate gap for a 1 inch (25 mm) diameter shaft [10^{-3} inch]	Approximate gap for a 5 inch (127 mm) diameter shaft [10^{-3} inch]
Running fit	0.3	1	2
Sliding fit	0.15	0.5	1
Push fit	<0.1	<0.3	<0.4

A3.6 COMMON BRAZE MATERIALS (SEC. 3.3.3)

Braze materials	T_{melt} [°C]	Comments	Materials commonly joined
35%Au–65%Cu	990–1010	For the first two braze materials, make gap 0.02–0.08 mm (0.001–0.003 inch)	For any of the braze materials in the group: SS to SS and SS to Cu[a]
50%Au–50%Cu	955–970		
82%Au–18%Ni eutectic	950	(Trade name: NIORO) For NIORO, make gap 0.10–0.13 mm (0.004–0.005 inch)	
72%Ag–28%Cu	780	Eutectic mixture (Trade name: CUSIL)	For any of the braze materials in this group: Cu to Cu[a]
63%Ag–27%Cu–10%In	685–730	(Trade name: INCUSIL 10)	
61.5%Ag–24%Cu–14.5%In	630–705	(Trade name: INCUSIL 15)	

Notes:
Braze materials available in wire, sheet, powder, and preforms.
Braze stop material (STOPYT) can be used to control unwanted flow.
Braze materials available from WESGO Division, GTE Prod. Corp., 477 Harbor Blvd., Belmont, CA 94022.

[a] Be aware that copper melts at about 1083°C.

A3.7 SOLDER: PHYSICAL PROPERTIES (SEC. 3.3.4)

Solder materials are generally ordered within each tabulated group according to melting temperature. Additional data on the electrical resistivities of selected solders at 295 K, 77 K, and 4 K are given in Appendix A8.4.

To make strong solder joints, hold the parts together with hand pressure while the solder is still molten, until it solidifies. For machined pieces, the gap between the parts should be as noted in the table, generally in the range of about 0.05–0.13 mm (0.002–0.005 in.).

Suppliers of specialty solders are given under the heading of Soldering materials in Appendix A1.7.

Solder: Physical Properties

Solder	Composition [percent by weight]	Melting temperature	Mass density [g/cm^3]	Electrical cond. [% of Cu]	Thermal cond. @ 85°C [W/m·K]	Thermal coef. of expansion @ 20°C [10^{-6}]	Tensile strength [MPa]	Comments	Flux
Hard (silver) solder group (Ag–Cu alloys)								Gap should be about 0.05–0.1 mm (0.002–0.004 in.)	Fluoride flux, Borax, or Boric acid mixed to a paste with alcohol (Wash with hot water after soldering; see Sec.3.3.4)
	56Ag–22Cu–17Zn–5Sn (Safety Silv #56)	618–649°C 1144–1200°F	9.21					Flows freely, ductile	
	45Ag–30Cu–25Zn (ASTM Grade 4)	675–745°C 1247–1373°F						Strong	
	20Ag–45Cu–35Zn (ASTM Grade 2)	775–815°C 1427–1499°F						Flows readily on melting	
	70Ag–20Cu–10Zn (ASTM Grade 7)	725–755°C 1337–1391°F						Malleable and ductile	
	Ag	960°C 1760°F							
Soft–solder group (alloys of Sn and Pb)								Gap should be about 0.05–0.13 mm (0.002–0.005 in.)	*See Table 3.8 to match flux and metal:* *Mild*: Rosin, rosin in alcohol, paste of petroleum jelly, ZnCl and NH_4Cl *Stronger, corrosive*: $ZnCl_2$ (Zn dissolved in HCl)

								Stainless-steel flux, *highly corrosive*: ZnCl with excess HCl, H_3PO_4 (after soldering, neutralize these fluxes with baking soda and wash with water)
63Sn–37Pb (60Sn–40Pb)	183°C 361°F	8.4	11.5	50	25.0	52	Eutectic mixture, high-quality, general-purpose solder used in electronics	Use pure (not "activated") rosin flux for electrical Cu connections, Sec. 3.3.4
63Sn–36.65Pb–0.35Sb	183°C 361°F						Eutectic mixture, general-purpose solder used for *electrical connections* at low temperatures. Sb helps inhibit embrittlement and cracking from cryogenic thermal cycling	Use pure (not "activated") rosin flux for electrical Cu connections, Sec. 3.3.4
96.5Sn–3.5Ag	221°C 430°F	7.50	16.0	33	30.2	39	Eutectic mixture; stronger than Pb–Sn solders (a common trade name is Staybrite™)	
93Pb–5.2Sn–1.8Ag	299°C 570°F						Used for *electrical connections* when a higher melting temperature is needed. Low Sn helps inhibit embrittlement and cracking from cryogenic thermal cycling	Use pure (not "activated") rosin flux for electrical copper connections, Sec. 3.3.4

(Continued)

A3.7 Solder: physical properties (*Continued*)

Solder	Composition [percent by weight]	Melting temperature	Mass density [g/cm^3]	Electrical cond. [% of Cu]	Thermal cond. @ 85°C [W/m·K]	Thermal coef. of expansion @ 20°C [10^{-6}]	Tensile strength [MPa]	Comments	Flux
	97.5Pb–1.0Sn–1.5Ag	309°C 588°F						Eutectic higher-melting-temperature solder; widely used in semiconductor assembly	
	92.5Pb–5In–2.5Ag	300–310°C 572–590°F	11.02	5.5	25	25.0	31	Higher-melting-temperature solder with minimal Au-leaching properties	
	95Pb–5Sn	308–312°C 586–593°F	11.06	8.8	23	30.0	28	Low-cost high-melting-temperature solder. Not recommended for Ag- or Au-plated parts because Sn aggressive dissolves Ag and Au films	
Specialty solder group									
Solders compatible with drinking water	95.5Sn–3.5Cu–1Ag	214–228°C 417–442°F						Pb-free solder for potable water Cu pipes; flows well	Any of the mild fluxes
Solders for aluminum	10Sn–90Zn	199°C 390°F	7.27	15.0	61		55	Solders Al; eutectic with lowest melting temp	Reaction flux: contains $ZnCl_2$, tin chloride, or both; must be heated 280–380°C to work

	60Sn–40Zn	199–340°C 390–644°F						Solders Al; low melting temp.	Reaction flux
	95Zn–5Al	382°C 720°F	6.6					Solders Al; high joint strength	Reaction flux; no flux needed for electronic applications
Solders for thin noble-metal films	66.3In–33.7Bi	72°C 162°F	7.99					Eutectic; very low melting temperature solder for thin Ag or Au films and contacting high-T_c superconductors; low strength	Mild $ZnCl_2$ solution for soldering to Cu; no flux needed for Ag if surfaces are freshly made and clean
	97In–3Ag	143°C 290°F	7.38	23.0	73	22.0	5.5	Eutectic; low leaching solder for thin Ag or Au films and contacting high-T_c superconductors	Mild $ZnCl_2$ solution for Cu; no flux needed for Ag if surfaces are freshly made and clean
Solders for difficult-to-solder materials	52In–48Sn	118°C 244°F	7.30	11.7	34	20.0	11.8	Eutectic; low melting temperature; higher yield strength; Sn leaches Ag or Au films	Mild $ZnCl_2$ solution for Cu
	50In–50Sn	116–126°C 241–259°F	7.30	11.7	34	20.0	11.8	Wets glass readily	
	In	157°C 315°F	7.31	24.0	86	29.0	1.9	Low strength; wets glass	No flux needed for wetting glass, but clean surfaces required; mild $ZnCl_2$ flux needed for soldering to Cu-based materials
	62Sn–36Pb–2Ag	179°C 354°F	8.41	11.9	50	27.0	44	Eutectic; higher strength, moderate melting-temperature solder	

(Continued)

A3.7 Solder: physical properties (*Continued*)

Solder	Composition	Melting temperature	Mass density	Electrical cond.	Thermal cond. @ 85°C	Thermal coef. of expansion @ 20°C	Tensile strength	Comments	Flux
	[percent by weight]		[g/cm^3]	[% of Cu]	[W/m·K]	[10^{-6}]	[MPa]		
Solders for low thermoelectric voltage	70Cd–30Sn							Very low thermo-electric power with respect to copper near room temperature. Contains cadmium, and fumes are TOXIC.	
	97In–3Ag	143°C 290°F						Eutectic; a NON-TOXIC alternative to low thermo-electric voltage Cd-based solder; In and Ag have thermoelectric powers close to Cu; stronger than pure In	Mild $ZnCl_2$ solution for soldering to Cu
Very low melting-temp. solder group (Alloys of Bi with Pb, Sn, Cd, and In)								As a class, Bi-based solders expand on solidification and are weak and brittle	Corrosive $ZnCl_2$ solutions usually required; pre-tin parts at higher temp. ($\gtrsim$300°C) to activate flux
	49Bi–18Pb–12Sn–21In	58°C 136°F	9.01	2.43	10	23.0	43	Eutectic alloy; expands slightly on solidification and then shrinks slowly over several hours	
	50Bi–25Pb–12.5Sn–12.5Cd (Wood's metal)	65–70°C 149–158°F	9.60	3.1			31	Contains Cd, and fumes are TOXIC. Similar to Ostalloy® 158	

50Bi–26.7Pb–13.3Sn–10Cd (Cerrobend)	70°C 158°F	9.58	4.0	18	22.0	41	Contains Cd, and fumes are TOXIC	
66.3In–33.7Bi	72°C 162°F	7.99					Eutectic; very low melting temperature solder for thin Ag or Au films and contacting high-T_c superconductors; low strength	Mild $ZnCl_2$ solution
55.5Bi–44.5Pb (Cerrobase)	124°C 255°F	10.44	4.0	4		44	Contracts slightly on solidification	

Sources:

Indium Corp. of America, http://www.indium.com/.

J. Ross (2002), Canfield Corp., personal communication.

A3.8 SOLDER FLUXES FOR SOFT-SOLDERING COMMON METALS AND ALLOYS (SEC. 3.3.4)

Material	Flux		
	Mild[a]	Corrosive[b]	Special flux and/or solder[c]
Aluminum			•
Aluminum–bronze			•
Beryllium–copper		•	
Brass	•	•	
Copper	•	•	
Copper–chromium		•	
Copper–nickel		•	
Copper–silicon		•	
Gold	•		
Inconel	•		
Lead	•	•	
Magnesium			•
Monel		•	
Nickel		•	
Nichrome			•
Platinum	•		
Silver	•	•	
Stainless steel			•
Steel		•	
Tin	•	•	
Tin–zinc	•	•	
Zinc		•	

[a] *Mild fluxes*: rosin, rosin in alcohol, paste of petroleum jelly, zinc chloride, or ammonium chloride. After soldering, wash away flux with a solution of soap and water, or isopropanol. Be aware that fluxes other than pure rosin, or rosin dissolved in alcohol, will leave chloride residues trapped in the solder that eventually react with ambient moisture to form hydrochloric acid, which attacks electronic circuits and perforates thin (0.1 mm) stainless-steel tubing. For soldering copper electronic circuitry, use only pure rosin flux, not "activated" rosin flux or pastes. See Sec. 3.3.4 for more information.

[b] *Corrosive flux*: zinc chloride solution (zinc dissolved in hydrochloric acid). After soldering, wash away flux with water or isopropanol; then neutralize the pH by blotting the area with a baking soda/water solution or ammonia/detergent/water solution.

[c] *Special flux and/or solder*: Appendix A3.7 has information on highly corrosive stainless-steel soldering fluxes as well as types of solders and fluxes that work with aluminum. After soldering, wash away corrosive acid fluxes with water or isopropanol; then neutralize the pH by blotting the area with a baking soda/water solution or ammonia/detergent/water solution.

Source: Information from J. F. Smith and D. M. Borcina, Lead Industries Assoc., Inc., New York.

A3.9 SOLDER: SUPERCONDUCTING PROPERTIES (SEC. 3.3.4)

Solder [wt%]	T_c [K]	H_c (1.3 K) [T]	Melting temperature [°C]
60Sn–40Pb	7.05	0.08	182–188
50Sn–50Pb	7.75	0.20	182–216
30Sn–70Pb	7.45	0.15	182–257
95Sn–5Sb	3.75	0.036	232–240
50In–50Sn	7.45	0.64	117–125
50In–50Pb	6.35	0.48	180–209
97.5Pb–1.0Sn–1.5Ag	7.25	0.11	309

$T_c \equiv$ superconducting transition temperature of the solder
$H_c \equiv$ superconducting critical field of the solder
Source: W. H. Warren and W. G. Bader (1969), *Rev. Sci. Instrum.* 40, 180–182.

A3.10 STICKY STUFF FOR CRYOGENIC APPLICATIONS (SEC. 3.3.5)

Material	Application and comments
Epoxies	
Araldite Type 1™ [a]	
Eccobond 2™ [b]	Low-viscosity, unfilled epoxy. Robust and good adhesion at cryogenic temperatures
Scotch-Weld DP-460™ [c]	High-performance urethane, two-part epoxy, Duo-Pak™ cartridge
Silver-based epoxy [d]	Electrically and thermally conductive epoxy
Stycast 1266™ [e]	Low-viscosity, unfilled epoxy. High thermal expansion, but thin films of this epoxy do not crack and provide good adhesion at cryogenic temperatures. Crack resistance can be improved by heating to 90°C for 4 h after epoxy has hardened
Stycast 2850 FT™ [e]	High-viscosity epoxy; filled with silica powder to provide a low thermal expansion matching that of copper
Tapes	
Fiberglass electrical tape	Tough under cryogenic cycling and withstands cycling to higher temperatures when soldering
Kapton™ tape	A robust tape, well suited for providing tough, durable electrical insulation between cryostat parts
Masking tape	All-purpose tape. The adhesion improves with thermal cycling. Tape becomes brittle with age and eventually becomes difficult to remove
Mylar™ electrical tape (3M #56*f*, "yellow" tape) [f]	Maintains adhesion better than Kapton™ tape upon cryogenic cycling, but thinner (10^{-3} in.) and therefore better suited for applications where strength is not paramount. Commonly used for electrically isolating samples from Cu sample holders. Dielectric strength is 5500 V

(Continued)

Sticky stuff (*Continued*)

Material	Application and comments
Teflon™ pipe-thread tape	Excellent for wrapping wires to support structure for mechanical support, or fastening samples to sample holders, especially where you do not want to deal with sticky tape that is hard to remove. For the same reason, this is also the best tape for corralling fine delicate wires. To protect small wires from mechanical damage, place a layer of tape *under* the wires as well as over them when wrapping them to a support structure
Varnish and glues	
Bostik™ multibond glue [g]	All-purpose glue that holds well at cryogenic temperatures. Easier to work with if thinned with acetone or methyl-ethyl-ketone
Duco™ household cement (model-airplane glue)	All-purpose glue that survives thermal cycling well. Can be thinned or removed with acetone. Not good for wires because the acetone dissolves varnish insulation. Good for sticking samples to the sample rod in a vibrating sample magnetometer
IMI 7031™ varnish (formerly GE 7031™ varnish)[h]	Easier to work with if thinned to the consistency of water with ethanol (acetone also acts as a thinner, but it makes the varnish stringy and eats wire insulation). Baking the varnish under a heat lamp decreases drying time
Loctite™ [i]	Low viscosity adhesive used in machine shops as a substitute for lock nuts, interference fits, or silver-soldering. Good for securing tight-fitting metal parts. Cures at room temperature, but can be loosened by moderate heating with a torch. Works OK at cryogenic temperatures
White Shellac	Useful for adhering sapphire to sapphire
Miscellaneous	
Apiezon™ black wax [j]	Meltable adhesive
Beeswax and Alox 350™ (T_{melt}=38–43°C), and Alox 2138F™ (T_{melt}=71°C) [k]	Low-strength fillers. Although they yield at low stress, they are sometimes useful as magnet-coil filling agents to minimize the probability of thermal-runaway events that can otherwise result from microfracturing of epoxies used to impregnate superconducting coils
BluTack™[l]	A gummy clay-like adhesive for generally attaching leads to support structures or mechanically holding almost anything in place
Dental floss (waxed or no-wax)	Excellent for tying things together (like samples to samples holders) and overwrapping fragile instrumentation leads wound onto heat sinks. Waxed floss is a little easier to stick in place during wrapping and tying
Silver paste[d]	Electrically and thermally conductive weak adhesive

Suppliers of specialty materials include:

[a] Ciba Specialty Chemicals Corp, 4917 Dawn Ave., East Lansing, MI 48823, Tel. 517-351-5900, Fax. 517-351-9003, http://www.araldite.com/.

[b] Emerson and Cuming Corp., http://www.emersoncuming.com/.

[c] 3M, http://www.3M.com/; distributed by MSC Industrial Supply, PN: 65861684, (Duo-Pak cartridge PN: 65861569), Tel. 800-645-7270, http://www.mscdirect.com/; or McMaster–Carr Supply Co., PN: 7467A26, http://www.mcmaster.com/.

[d] Ted Pella, Inc., P.O. Box 492477, Redding, CA 96049-2477, Tel. 800-237-3526; Fax. 530-243-3761, http://www.TedPella.com/.

[e] Emerson and Cuming, http://www.emersoncuming.com/.

[f] Essex Brownell Inc., 4670 Shelby Drive, Memphis, TN 38118, Tel. 800-805-4636, Fax. 219-461-4165; or from http://www.mpsupplies.com/3mtape56.html.

[g] Bostik Pty Ltd., 51–71 High Street, Thomastown, Vic., Australia 3074, Tel 3-465-5211.

[h] Insulating Materials Inc., 1 W. Campbell Rd., Schenectady, NY 12306, Tel. 518-395-3200, Fax. 518-395-3300; small quantities available from Lake Shore Cryotronics, Westerville, OH 43081, Tel. 614-891-2244. Fax. 614-818-1600, http://www.lakeshore.com/.

[i] Loctite, a Hendel Company, http://www.loctite.com/.

[j] Apiezon Products, M&I Materials Ltd., P.O. Box 136, Manchester, M601AN, England. Tel. +44-161-875-4442, http://www.apiezon.com/.

[k] Alox Corp., Niagara Falls, NY.

[l] Bostik Findley, http://www.bostikfindley-us.com/.

A3.11 SLIPPERY STUFF FOR CRYOGENIC APPLICATIONS

Material	Application and comments
Lubricant coatings	
Graphite	Available as dry powder or spray-on coatings
Molybdenum disulfide	Spray coatings; good for higher forces
Teflon™	Spray coatings, low coefficient of friction
Thicker lubricant coatings	
Emralon ® [a]	Flurocarbon lubricant in an epoxy mixture for thicker lubricating coatings or for making cast parts with a low coefficient of friction
Bearing materials	
Kel-F™ [b]	Polychlorotrifluoroethylene. Stronger than Teflon™
Nylon™	Stronger than Teflon™, but higher coefficient of friction
Teflon™	Polyamide, low coefficient of friction, but softer than other materials
Teflon™ bearing materials reinforced with Nylon™, fiberglass, and other materials	
Flurogold ® [c]	Reinforced Teflon™
Parmax ® [d]	High strength polymer, similar uses as Torlon™
Rulon ® [b]	Teflon reinforced with Nylon, fiberglass, or other materials; available in various formulations. Type J has the lowest coefficient of friction of the Rulon® series. Applications include retainer rings for cryogenic ball-bearing raceways
Teflon-coated Kapton™ [e]	Useful, for example, as a cryogenic gasket material since the Teflon™ coating deforms for good sealing, but the stronger Kapton™ base keeps the gasket from extruding
Torlon™ [e]	PolyAmide-Imide (Teflon™-Kapton™ combination) high strength polymer used for wear and friction parts. Capable of performing under continuous stress at temperatures to 260°C. Low coefficient of linear thermal expansion and high creep resistance provide good dimensional stability. Available as sheet, rod, or tube

[a] Acheson Colloids Co., http://www.achesonindustries.com/.
[b] San Diego Plastics, Inc., http://www.sdplastics.com/.
[c] Granor Rubber and Engineering, http://www.granor.com.au/, Conroy & Knowlton Inc., http://conroyknowlton.com/materials.htm.
[d] Mississippi Polymer Technologies, http://www.mptpolymers.com/.
[e] Boedeker, http://www.boedeker.com/.

A3.12 DEGASSING RATES OF SYNTHETIC MATERIALS (SEC. 3.8.3)

Degassing rates of *metals* are given in Fig. 3.18.

Material	Degassing rate at room temperature before baking [Pa m^3/(s m^2)]	Baking temperature [°C]	Degassing rate at room temp. after 24 h bake [Pa m^3/(s m^2)]
Araldite ATI™ epoxy [a]	3.4×10^{-4}	85	—
Mycalex™ [a]	2.7×10^{-6}	300	—
Nylon 31™ [a]	1.1×10^{-4}	120	8.0×10^{-7}
Perspex™ [a]	1.3×10^{-5}	85	7.8×10^{-6}
Polythene™ [a]	4.0×10^{-4}	80	6.6×10^{-6}
PTFE (Teflon™) [b]	2.0×10^{-4}	—	4.7×10^{-7}
Viton A™ [a]	1.3×10^{-4}	200	2.7×10^{-6}
Polyimide (Kapton™)[c]	—	200*	6.6×10^{-8}
	—	300*	4.0×10^{-8}
Kalrez™ [d]	—	300	4.0×10^{-8}
Viton E60C™ [d]	—	150	$\sim 1 \times 10^{-6}$
	—	300	3.0×10^{-8}

Source: G. F. Weston (1985), *Ultrahigh Vacuum Practice*, Butterworth, London.

[a] R. S. Barton and R. P. Govier (1965), *J. Vac. Sci. Tech.* 2, 113.
[b] B. B. Dayton (1959), *Trans. 6th Nat. Symp. Vac. Technol., I*, p. 101.
[c] P. W. Hait (1967), *Vacuum* 17, 547.
[d] L. DeChernatony (1977), *Vacuum* 27, 605.
* 12 h bake.

A3.13 VAPOR PRESSURES OF METALS (SEC. 3.8.3)

Tabulated values in the three right-hand columns are expressed as the temperature required to produce the vapor pressures indicated at the head of each column.

These data are plotted in Fig. 3.19(a) and (b).

Vapor pressures of metals

Metal	Melting temperature [K]	Temperature [K] giving a vapor pressure P		
		$P = 1.33 \times 10^{-9}$ Pa	$P = 1.33 \times 10^{-7}$ Pa	$P = 1.33 \times 10^{-5}$ Pa
Ag Silver	1234	721	800	899
Al Aluminum	932	815	906	1015
Au Gold	1336	915	1020	1150
Ba Barium	983	450	510	583
Be Beryllium	1556	832	925	1035
C Carbon	—	1695	1845	2030
Ca Calcium	1123	470	524	590
Cd Cadmium	594	293	328	368
Ce Cerium	1077	1050	1175	1325

Vapor pressures of metals (*Continued*)

Metal	Melting temperature [K]	Temperature [K] giving a vapor pressure P		
		$P = 1.33 \times 10^{-9}$ Pa	$P = 1.33 \times 10^{-7}$ Pa	$P = 1.33 \times 10^{-5}$ Pa
Co Cobalt	1768	1020	1130	1265
Cr Chromium	2176	960	1055	1175
Cs Cesium	302	213	241	274
Cu Copper	1357	855	945	1060
Fe Iron	1809	1000	1105	1230
Ge Germanium	1210	940	1030	1150
Hg Mercury	234	170	190	214
In Indium	429	641	716	812
Ir Iridium	2727	1585	1755	1960
K Potassium	336	247	276	315
La Lanthanum	1193	1100	1220	1375
Mg Magnesium	923	388	432	487
Mn Manganese	1517	660	734	827
Mo Molybdenum	2890	1610	1770	1975
Na Sodium	371	294	328	370
Ni Nickel	1725	1040	1145	1270
Pb Lead	601	516	580	656
Pd Palladium	1823	945	1050	1185
Pt Platinum	2043	1335	1480	1655
Re Rhenium	3463	1900	2100	2350
Rh Rhodium	2239	1330	1470	1640
Sb Antimony	903	447	526	582
Se Selenium	490	286	317	356
Sn Tin	505	805	900	1020
Sr Strontium	1043	433	483	546
Ta Tantalum	3270	1930	2120	2370
Th Thorium	1968	1450	1610	1815
Ti Titanium	1940	1140	1265	1410
W Tungsten	3650	2050	2270	2520
Zn Zinc	693	336	374	421
Zr Zirconium	2128	1500	1665	1855

Source: From G. F. Weston (1985), *Ultrahigh Vacuum Practice*, Butterworth, London, who extracted the data from compilations by R. E. Honig (1962), *RCA Rev*. 23, 567; and R. E. Honig (1969), *RCA Rev*. 30, 285.

A3.14 GAS PERMEATION CONSTANT AT ROOM TEMPERATURE FOR SYNTHETIC MATERIALS [FOR USE WITH EQ. (3.27) OF SEC. 3.8.3]

Additional gas permeation rates are given for:

- helium through glass in Fig. 3.20
- helium through ceramics in Fig. 3.21
- hydrogen through metals in Fig. 3.22.

Material	Permeation constant K in [m^2/s] at 23°C				
	Nitrogen	Oxygen	Hydrogen	Helium	Argon
Polythene™ [a]	9.9×10^{-13}	3.0×10^{-12}	8.2×10^{-12}	5.7×10^{-12}	2.7×10^{-12}
PTFE (Teflon™)[a]	2.5×10^{-12}	8.2×10^{-12}	2.0×10^{-11}	5.7×10^{-10}	4.8×10^{-12}
Perspex™ [a]	—	—	2.7×10^{-12}	5.7×10^{-12}	—
Nylon 31™ [a]	—	—	1.3×10^{-13}	3.0×10^{-13}	—
Polystyrene™ [a]	—	5.1×10^{-13}	1.3×10^{-11}	1.3×10^{-11}	—
Polystyrene™ [b]	6.4×10^{-12}	2.0×10^{-11}	7.4×10^{-11}	—	—
Polyethylene™ [b]	$6–11 \times 10^{-13}$	$2.5–3.4 \times 10^{-12}$	$6–12 \times 10^{-12}$	$4–5.7 \times 10^{-12}$	—
Mylar 25-V-200™ [b]	—	—	4.8×10^{-13}	8.0×10^{-13}	—
CS2368B (Neoprene™)[a]	2.1×10^{-13}	1.5×10^{-12}	8.2×10^{-12}	7.9×10^{-12}	1.3×10^{-12}
Viton A™ [a]	—	—	2.2×10^{-12}	8.2×10^{-12}	—
Polyimide (Kapton™)[c]	3.2×10^{-14}	1.1×10^{-13}	1.2×10^{-12}	2.1×10^{-12}	—

Source: G. F. Weston (1985), *Ultrahigh Vacuum Practice*, Butterworth, London.

[a] J. R. Bailey (1964), *Handbook of Vacuum Physics*, Vol. 3, Part 4, Pergamon Press, Oxford; Elmsford, NY.
[b] D. W. Brubaker and K. Kammermeyer, *Ind. Eng. Chem.* 44, 1465 (1952); 45, 1148 (1953); 46, 733 (1954).
[c] D. E. George, in an article by W. G. Perkins (1973), *J. Vac. Sci. Technol.* 10, 543.

A4 Cryogenic apparatus wiring (ref. Chapter 4)

A4.1a WIRE GAUGE SIZE, AREA, RESISTIVITY, HEAT CONDUCTION, AND OPTIMUM CURRENT (SECS 4.1, 4.2, AND 4.9.1)

To obtain the resistance-per-length for wire materials other than copper, multiply the room-temperature values for copper in the fourth column of the table by the ratio $\rho_{293\ K}/\rho_{Cu\ 293\ K}$, where $\rho_{293\ K}$ and $\rho_{Cu\ 293\ K}$ are the resistivity values of the new material and copper, respectively. Ratio values for several common wire materials at room temperature follow the table.

At 77 K and 4.2 K, the resistance-per-length may be similarly calculated by using the low-temperature resistivity data given in Appendix A4.2.

In practice, resistivity values may vary from those tabulated below because of different impurity concentrations, alloy concentrations, and heat treatments.

American Wire Gauge (AWG) and *Brown & Sharpe* (B&S) are the same gauge.

The nearest common *metric* wire sizes are given in Table A4.1b.

A4.1a Wire gauge size, area, resistivity, heat conduction, and optimum current

American wire gauge (AWG) or Brown & Sharpe (B&S)	Diameter 20°C[a]	Cross-sectional area at 20°C[a]	Resistance of annealed copper wire at 20°C[a]	Heat conducted along 1 m of copper wire between the indicated temperatures[b] [W]			Optimum current for 1 m of copper wire with one end at 4 K and the other at temperature T_{upper}[c] [A]	
	[mm]	[mm^2]	[Ω/km]	300–4.2 K	300–76 K	76–4.2 K	T_{upper} = 290 K	T_{upper} = 77 K
0000	11.68	107.2	0.161	17.4	10.0	7.35	536	1072
000	10.40	85.03	0.203	13.8	7.94	5.83	425	850
00	9.266	67.43	0.256	10.9	6.30	4.62	337	674
0	8.252	53.48	0.322	8.66	5.00	3.67	267	535
1	7.348	42.41	0.407	6.87	3.96	2.91	212	424
2	6.543	33.63	0.513	5.45	3.14	2.31	168	336
3	5.827	26.67	0.646	4.32	2.49	1.83	133	267
4	5.189	21.15	0.815	3.43	1.98	1.45	106	212
5	4.621	16.77	1.03	2.72	1.57	1.15	84	168
6	4.115	13.30	1.30	2.15	1.24	0.912	66	133
7	3.665	10.55	1.63	1.71	0.985	0.724	53	106
8	3.264	8.366	2.06	1.36	0.781	0.574	42	84
9	2.906	6.634	2.60	1.08	0.620	0.455	33	66
10	2.588	5.261	3.28	0.852	0.491	0.361	26	53
11	2.305	4.172	4.13	0.676	0.390	0.286	21	42
12	2.053	3.309	5.21	0.536	0.309	0.227	16	33
13	1.828	2.624	6.57	0.425	0.245	0.180	13	26
14	1.628	2.081	8.28	0.337	0.194	0.143	10	21
15	1.450	1.650	10.4	0.267	0.154	0.113	8.2	16
16	1.291	1.309	13.2	0.212	0.122	0.0898	6.5	13
17	1.150	1.038	16.6	0.168	0.0969	0.0712	5.2	10
18	1.024	0.8231	21.0	0.133	0.0769	0.0565	4.1	8.2
19	0.9116	0.6527	26.4	0.106	0.0610	0.0446	3.3	6.5
20	0.8118	0.5176	33.3	0.0838	0.0483	0.0355	2.6	5.2

21	0.7230	0.4105	42.0	0.0665	0.0383	0.0282	2.0	4.1
22	0.6439	0.3255	53.0	0.0527	0.0304	0.0223	1.6	3.2
23	0.5733	0.2582	66.8	0.0418	0.0241	0.0177	1.3	2.6
24	0.5105	0.2047	84.2	0.0332	0.0191	0.0140	1.0	2.0
25	0.4547	0.1624	106	0.0263	0.0152	0.0111	0.81	1.6
26	0.4049	0.1288	134	0.0209	0.0120	0.00884	0.64	1.3
27	0.3606	0.1021	169	0.0165	0.00954	0.00700	0.51	1.0
28	0.3211	0.08098	213	0.0131	0.00756	0.00556	0.40	0.81
29	0.2859	0.06422	268	0.0104	0.00600	0.00440	0.32	0.64
30	0.2548	0.05093	339	0.00825	0.00476	0.00349	0.25	0.51
31	0.2268	0.04039	427	0.00654	0.00377	0.00277	0.20	0.40
32	0.2019	0.03203	538	0.00519	0.00299	0.00220	0.16	0.32
33	0.1798	0.02540	679	0.00411	0.00237	0.00174	0.13	0.25
34	0.1601	0.02014	856	0.00326	0.00188	0.00138	0.10	0.20
35	0.1426	0.01597	1080	0.00259	0.00149	0.00110	0.080	0.16
36	0.1270	0.01267	1360	0.00205	0.00118	0.000869	0.063	0.13
37	0.1131	0.01005	1720	0.00163	0.000939	0.000689	0.050	0.10
38	0.1007	0.007967	2160	0.00129	0.000744	0.000546	0.040	0.080
39	0.08969	0.006318	2730	0.00102	0.000590	0.000433	0.032	0.063
40 [d]	0.07988	0.005010	3440	0.000812	0.000468	0.000344	0.025	0.050

[a] Data obtained partially from calculations (see following footnotes) and partially from tabulations in the *CRC Handbook of Chemistry and Physics* (1987; 2002), CRC Press, Inc., Boca Raton, FL; and from the *Machinery's Handbook* (2000), 26th edition, Industrial Press, New York.

[b] Heat conduction for a length other than 1 m is obtained by dividing the values in the table by the desired wire length (in meters). In obtaining the values for heat conduction, it was assumed that there was no gas cooling of the wire. If helium gas boil-off were used to cool the wire with maximum efficiency, the resultant heat flow would be 1/12 of the values given for an upper temperature of 300 K, and 1/4 of the values shown for 77 K. Calculations were based on the thermal conductivity integrals of ETP copper, Appendix A2.1. From V. Johnson (1960), National Bureau of Standards; Wright Air Development Division (WADD) Technical Report 60-56, Part II; and D. H. J. Goodall (1970), A.P.T. Division, Culham Laboratory, Abingdon, Oxfordshire, UK.

[c] Optimum current is for steady-state operation. For wires that carry current with only a low duty cycle, the optimum current should be adjusted to a higher value because in that case the Joule heating is intermittent, whereas the heat flow down the current lead is continuous. Optimum current for a length other than 1 m is obtained by dividing the values in the table by the desired wire length (in meters). Values were calculated from Eqs (4.1) and (4.2) in Sec. 4.9.1, which were derived by R. McFee (1959), *Rev. Sci. Instrum*. 30, 98–102.

[d] For wire sizes smaller than #40 AWG, the diameter can be calculated by using a ratio of 1:1.123 for consecutive AWG sizes.

Room-temperature resistivities for several common wire materials relative to copper

These ratios can be used to obtain the resistance-per-length for wire materials other than copper by multiplying the room-temperature values given for copper in the fourth column of the above table by the ratio $\rho_{293\ \mathrm{K}}/\rho_{\mathrm{Cu}\ 293\ \mathrm{K}}$. (Calculated from Appendix A4.2 and the *CRC Handbook of Chemistry and Physics* 2002.)

Material	$\rho_{293\ \mathrm{K}}/\rho_{\mathrm{Cu}\ 293\ \mathrm{K}}$
Aluminum	1.579
Brass (70%Cu–30%Zn)	3.62
Constantan	29
Manganin	28
Nichrome	64
Phosphor bronze	7.5
Platinum	6.26
Silver	0.946
Tungsten	3.15

A4.1b WIRE GAUGE: METRIC AND AMERICAN WIRE GAUGE (AWG) SIZE COMPARISON (SECS 4.1 AND 4.2)

Wire gauge: metric and AWG size comparison

AWG or B & S	Nearest common metric gauge wire diameter at 20°C [mm]	Metric wire cross-sectional area at 20°C [mm]	Resistance of annealed copper wire at 20°C [Ω/km]
5	4.750	17.72	1.0
6	4.250	14.19	1.2
7	3.750	11.04	1.5
8	3.350	8.814	1.9
9	2.800	6.158	2.8
10	2.500	4.910	3.5
11	2.240	3.941	4.3
12	2.000	3.142	5.4
13	1.800	2.545	6.7
14	1.600	2.011	8.5
15	1.400	1.539	11.1
16	1.250	1.227	13.9
17	1.120	0.9852	17.4
18	1.000	0.7854	21.8
19	0.900	0.636	26.9
20	0.800	0.503	34.0
21	0.710	0.396	43.2
22	0.630	0.312	54.8
23	0.560	0.246	69.4
24	0.500	0.196	87.1
25	0.450	0.159	108
26	0.400	0.126	136
27	0.355	0.0990	173
28	0.315	0.0779	219
29	0.280	0.0616	278
30	0.250	0.0491	348
31	0.224	0.0394	434
32	0.200	0.0314	544
33	0.180	0.0255	672
34	0.160	0.0201	850
35	0.140	0.0154	1110
36	0.125	0.0123	1390
37	0.112	0.00985	1740
38	0.100	0.00785	2180
39	0.090	0.0064	2700
40	0.080	0.0050	3400

A4.2 PHYSICAL PROPERTIES OF COMMON WIRE MATERIALS (SEC 4.2)

Wire materials: composition, resistivity, melting temperature, thermal expansion, magnetoresistance, and magnetic susceptibility

Wire material	Chemical composition	Resistivity[a] at 293 K, 77 K, 4.2 K [μΩcm]	Melting range[a]	Coef. thermal expansion[a] [°C^{-1}]	Magnetores.[a] $\Delta R/R_0$ @ 4.2 K and 10 T (perpendicular to wire)[d]	Volume susceptibility[a] [SI]
Copper (ETP)	100 wt% Cu	1.68 0.21 ~0.02	1056–1083°C	1.68×10^{-5} (20–100°C)	188%[f]	3.2×10^{-5} @R.T.[b] 2.5×10^{-5} @4.2 K[b]
Constantan	55 wt% Cu 45 wt% Ni	49.9	1300–1340°C[c]	1.5×10^{-5} (20–100°C)	−2.56%	Ferromagnetic[d] Ferromagnetic[d]
Manganin	83 wt% Cu 13 wt% Mn 4 wt% Ni	48.2 45.4 42.9	1100–1160°C[c] (85 wt%Cu– 15wt%Mn)	1.9×10^{-5} (20−100°C)	−2.83%	0.0027 @R.T.[d] 0.022 @76 K[d] 0.0125 @4.2 K[d]
Nichrome	80 wt% Ni 20 wt% Cr	109 107 106	1400°C	1.73×10^{-5} (20–1000°C)	0.69%	5.2×10^{-4} @R.T.[d] 8.3×10^{-4} @76 K[d] 5.6×10^{-3} @4.2 K[d]
Phosphor bronze A	94.8 wt% Cu 5 wt% Sn 0.2 wt% P	12.8 11.0 10.7	950–1050°C	1.78×10^{-5} (20–300°C)	4.5%[e,g]	-5.2×10^{-5} @R.T.[d] -4.7×10^{-5} @76 K[d] -3.3×10^{-5} @4.2 K[d]

[a] Except where otherwise cited, data were compiled from *Metals Handbook*, (1961), Vol. 1, *Properties and Selection of Materials* (1995), 8th edition, American Society for Metals, Materials Park, OH; *Temperature Measurement and Control*, Lake Shore Cryotronics, Inc., Westerville, Ohio; and C. A. Thompson, W. M. Manganaro, and F. R. Fickett (1990), *Cryogenic Properties of Copper*, Wall Chart, NIST, and the references cited therein.

[b] F. R. Fickett (1992), *Adv. Cryog. Eng. (Mater.)*, 38B, 1191–1197.

[c] T. B. Massalski, ed. (1990), *Binary Alloy Phase Diagrams*, ASM International, Materials Park, OH.

[d] M. Abrecht, A. Adare, and J. W. Ekin (2006), *Rev. Sci. Inst.*, to be published. Susceptibilities at 4.2 K were determined from magnetization vs. magnetic-field data; room-temperature and 76 K susceptibilities were calculated from the magnetization measured at $H = 100$ Oe, except where noted.

[e] The magnetoresistance of phosphor bronze varies with (trace) impurities in the wire.

[f] The magnetoresistance of pure copper is strongly dependent on its purity; it can be determined from a normalized "Kohler" plot, such as that shown in Fig. 5.16 of F. R. Fickett, Chapter 5 in *Materials at Low Temperatures*, eds. R. P. Reed and A. F. Clark, ASM International, Materials Park, OH.

[g] At 76 K and 10 T, the magnetoresistance of phosphor bronze is much smaller than at 4 K, decreasing to about $\Delta R/R_0 = 0.08\%$ (Abrecht et al. 2006, footnote d).

A4.3 RESIDUAL RESISTANCE RATIO (RRR) OF SELECTED WIRING AND CONDUCTOR MATERIALS (SEC. 4.2)

RRR values of additional materials are tabulated in Appendix A3.1.

Material	Resistivity at 293 K [μΩcm]	Resistivity at 4 K [μΩcm]	RRR ($\rho_{293\,K}/\rho_{4\,K}$)
Copper ETP (common wire, rod, and plate material)	1.68	~0.015	~110
Oxygen-free copper [a,b] 99.95% pure; annealed ~500°C for ~1 h in argon or vacuum ($\lesssim 10^{-4}$ torr)	1.68	~0.010	~160
Oxygen-free copper [a] 99.95% pure; unannealed	1.71	~0.038	~45
Copper ground strap [a] (1/4 in. wide flexible braid)	1.74	~0.070	~25
Silver foil [a] (rolled)	1.61	~0.019	~85
Aluminum 99.9995% [c] (pure rolled foil annealed 350°C for 1 h)	2.65	~0.0005	~5000

RRR $\equiv R_{293\,K}/R_{4\,K} = \rho_{293\,K}/\rho_{4\,K}$

[a] Measured by R. McDonough (1995), unpublished data, National Institute of Standards and Technology, Boulder, CO.

[b] See annealing information in footnote c of Appendix A3.1.

[c] Measured by P. Kirkpatrick (1997), unpublished data, National Institute of Standards and Technology, Boulder, CO.

A4.4 WIRE INSULATION: THERMAL RATINGS (SEC. 4.3)

Wire insulation	Thermal rating	
Polyvinyl Formal (Formvar™)	105°C	221°F
Tetrafluoroethylene (Teflon™)	200°C	392°F
Polyimide (Kapton™)	220°C	428°F

Source: *Temperature Measurement and Control* (2002), Sec. 3, Lake Shore Cryotronics, Inc., Westerville, OH.

A4.5 THERMAL ANCHORING: REQUIRED WIRE LENGTHS (SEC. 4.4)

Tabulated values give the tempering length required to bring the designated wire material to within 1 mK of the heat-sink temperature T_s.

T_1 is the temperature where the lead was last thermally anchored.

Thermal anchoring: required wire lengths

			Tempering length for various wire gauges[a] [cm]			
Material	T_1 [K]	T_s [K]	0.005 mm^2 (#40 AWG)[b] (~0.080 mm)[c] [cm]	0.013 mm^2 (#36 AWG) (~0.125 mm) [cm]	0.032 mm^2 (#32 AWG) (~0.200 mm) [cm]	0.21 mm^2 (#24 AWG) (~0.500 mm) [cm]
Copper	300	80	1.9	3.3	5.7	16.0
	300	4	8.0	13.8	23.3	68.8
Phosphor	300	80	0.4	0.6	1.1	3.2
bronze	300	4	0.4	0.7	1.3	3.8
Manganin	300	80	0.2	0.4	0.4	2.1
	300	4	0.2	0.4	0.7	2.0
Stainless	300	80	0.2	0.3	0.6	1.7
steel 304	300	4	0.2	0.3	0.5	1.4

Source: D. S. Holmes and S. S. Courts (1998), Chapter 4 in *Handbook of Cryogenic Engineering*, ed. J. G. Weisend II, Taylor & Francis, Philadelphia, PA; based on an earlier calculation by J. G. Hust (1970), *Rev. Sci. Instrum.* 41, 622–624. (The difference in values between the earlier and later evaluations for copper stems from the use of mean thermal conductivity values by Hust and thermal-conductivity integrals by Holmes and Courts.)

[a] The calculated results pertain to wires with thin, well-bonded insulation such as Formvar or polyimide (not Nylon™ or Teflon™ sleeve insulation) in a vacuum environment (i.e. not cooled by surrounding gas). The insulation-plus-adhesive layer attaching the wire to the heat sink is assumed to have a thickness about equal to the wire diameter and a thermal conductivity typical of varnish, namely 0.01, 0.02, and 0.05 W/(m K) at 4, 20, and 78 K, respectively. The length of untempered conductor between T_1 and T_s is assumed to be 25 cm; however, increasing this length by a factor of 10 shortens the required tempering length by a factor of less than two.

[b] American Wire Gauge (Appendix A4.1a).

[c] Nearest metric wire size (Appendix A4.1b).

A4.6a THERMOELECTRIC VOLTAGES OF SOME ELEMENTS RELATIVE TO COPPER (SEC. 4.6)

Tabulated thermoelectric voltages are *relative to copper* with the reference junction at 0°C.

A positive sign means that, in a simple thermoelectric circuit, the resultant voltage direction produces a current from the material to the copper at the reference junction (0°C).

Values have been *ordered by their absolute magnitude* at −100°C or, when not available, at +100°C. Thus, the higher a material's position in the table, the closer its thermoelectric voltage matches that of copper.

Thermoelectric voltages of some elements relative to copper

Element	−200°C [mV]	−100°C [mV]	0°C [mV]	+100°C [mV]	+200°C [mV]
Gold	−0.02	−0.02	0	+0.02	+0.01
Silver	−0.02	−0.02	0	−0.02	−0.06
Iridium	−0.06	+0.02	0	−0.10	−0.34
Rhodium	−0.01	+0.03	0	−0.06	−0.22
Carbon	—	—	0	−0.06	−0.29
Indium	—	—	0	−0.07	—
Zinc	+0.12	+0.04	0	0.00	+0.06
Cadmium	+0.15	+0.06	0	+0.14	+0.52
Thallium	—	—	0	−0.18	−0.53
Tungsten	+0.62	+0.22	0	+0.36	+0.79
Lead	+0.43	+0.23	0	−0.32	−0.74
Cesium	+0.41	+0.24	0	—	—
Tin	+0.45	+0.25	0	−0.34	−0.76
Cerium	—	—	0	+0.38	+0.63
Tantalum	+0.40	+0.27	0	−0.43	−0.90
Magnesium	+0.56	+0.28	0	−0.32	−0.73
Platinum	+0.19	+0.37	0	−0.76	−1.83
Aluminum	+0.64	+0.43	0	−0.34	−0.77
Molybdenum	—	—	0	+0.69	+1.36
Thorium	—	—	0	−0.89	−2.09
Lithium	−0.93	+0.63	0	+0.06	—
Sodium	+1.19	+0.66	0	—	—
Rubidium	+1.28	+0.83	0	—	—
Calcium	—	—	0	−1.27	−2.96
Palladium	+1.00	+0.85	0	−1.33	−3.06
Mercury	—	—	0	−1.36	−3.16
Potassium	+1.80	+1.15	0	—	—
Cobalt	—	—	0	−2.09	−4.91
Nickel	+2.47	+1.59	0	−2.24	−4.93
Antimony	—	—	0	+4.13	+8.31
Bismuth	+12.58	+7.91	0	−8.10	−15.40
Germanium	−45.81	−26.25	0	+33.14	+70.57
Silicon	+63.32	+37.54	0	−42.32	−82.40

Source: Calculated from thermal emf data compiled in the *American Institute of Physics Handbook* (1972), 3rd edition, Chapter 4, McGraw-Hill, New York.

A4.6b THERMOELECTRIC VOLTAGES OF SELECTED TECHNICAL MATERIALS RELATIVE TO COPPER (SEC. 4.6)

Tabulated thermoelectric voltages are *relative to copper* with the reference junction at 0°C.

A positive sign means that in a simple thermoelectric circuit the resultant voltage direction produces a current from the material to the copper at the reference junction (0°C).

Values have been *ordered by their absolute magnitude* at +100°C. The higher a material's position in the table, the closer its thermoelectric voltage matches that of copper.

Thermoelectric voltages of selected technical materials relative to copper

Technical Material	−200°C [mV]	−100°C [mV]	0°C [mV]	+100°C [mV]	+200°C [mV]
Silver coin (90%Ag–10%Cu)	—	—	0	+0.04	+0.07
60%Ni–24%Fe–16%Cr	—	—	0	−0.09	+0.18
Copper–beryllium	—	—	0	−0.09	−0.21
Manganin	—	—	0	−0.15	−0.28
Yellow brass	—	—	0	−0.16	−0.34
Copper coin (95%Cu–4%Sn–1%Zn)	—	—	0	−0.16	−0.35
Phosphor bronze	—	—	0	−0.21	−0.49
Solder (50%Sn–50%Pb)	—	—	0	−0.30	—
Solder (96.5%Sn–3.5%Ag)	—	—	0	−0.31	—
18–8 Stainless steel	—	—	0	−0.32	−0.79
80%Ni–20%Cr	—	—	0	+0.38	+0.79
Spring steel	—	—	0	+0.56	+0.80
Gold–chromium	—	—	0	−0.93	−2.15
Iron	−2.73	−1.47	0	+1.13	+1.71
Alumel	+2.58	+1.66	0	−2.05	−4.00
Chromel P	−3.17	−1.83	0	+2.05	+4.13
Nickel coin (75%Cu–25%Ni)	—	—	0	−3.52	−7.84
Constantan	+5.54	+3.35	0	−4.27	−9.28

Source: Calculated from thermal emf data compiled in the *American Institute of Physics Handbook* (1972), 3rd edition, Chapter 4, McGraw-Hill, New York.

A4.7 THERMAL CONDUCTIVITY OF YBCO-COATED CONDUCTORS (SEC. 4.10)

The thermal conductivity of YBCO-coated conductors (e.g. for flexible current leads; see Sec 4.10) is tabulated in terms of each of the major components of these composite conductors. For any particular YBCO conductor, the total thermal conductivity along the length of the composite conductor λ_{total} is the sum of the contribution of each component λ_i weighted by its fractional cross-sectional area. Thus, for tape conductors

$$\lambda_{\text{total}} = \sum (d_i/D)\,\lambda_i,$$

where d_i is the layer thickness of the ith component and D is the total thickness of the tape.

Thermal conductivity of component materials of YBCO-coated conductors

Material	Thermal conductivity [W/(m·K)]				
	20 K	50 K[a]	90 K[a]	110 K	295 K
YBCO($a-b$) 123 phase[b] (Calc. from melt-textured data)	14	27	22	21	~18
YBCO(c) 123 phase[b] (Calc. from melt-textured data) ($\lambda_{a-b}/\lambda_c \approx 6.3$)	3.5	4.4	3.2	3.0	~2.8
YBCO($a-b$) 123 + 40% 211 phase[b] melt textured	10	19	16	15	~14
YBCO[c] sintered	5	8	5	5	5
Ag[d]	Depends on Ag purity (Sec. 2.2)	1180	620	560	450
Cu (RRR = 100)[e]	2430	1220	497	452	397
Inconel 625 [f] $\lambda = 24.7992 \times 10^{-6}\,T^2 + 1.989348 \times 10^{-2}\,T + 7.899798$ (valid 116–1255 K)				7.4	9.8
Hastelloy C-276[f] UNS N10276 $\lambda = 3.565928 \times 10^{-6}\,T^2 + 1.349819 \times 10^{-2}\,T + 5.726708$ (valid 105–811 K)				7.0 (100 K)	10
Nichrome[f] UNS N06003 (77.3%Ni, 21%Cr) $\lambda = 2.099567 \times 10^{-6}\,T^2 + 1.480732 \times 10^{-2}\,T + 8.265973$ (valid 273–1073 K)					13

[a] The abrupt rise in thermal conductivity below T_c is due to condensation of electrons into superconducting pairs, eliminating them as scatterers of phonons, and thus enhancing the dominant phonon contribution to the thermal conductivity.

[b] M. Ikebe, H. Fujishiro, T. Naito, K. Noto, S. Kohayashi, and S. Yoshizawa (1994), *Cryogenics* 34, 57–61.

[c] A. Jezowski, J. Mucha, K. Rafalowicz, J. Stepien-Damm, C. Sulkowski, E. Trojnar, A. J. Zaleski, and J. Klamut (1987), *Phys. Lett. A* 122, 431–433.

[d] Calculated from the resistivity of silver (Appendix A6.5a) by using the Wiedemann–Franz Law (Sec. 2.2) for electronic thermal conduction ($\lambda = L_N\,T/\rho$, where $L_N = 2.44 \times 10^{-8}\ V^2/K^2$).

[e] Cryogenic Materials Properties Program CD, Release B-01 (June 2001), Cryogenic Information Center, 5445 Conestoga Ct., Ste. 2C, Boulder, CO 80301-2724; Tel. (303) 442-0425, Fax (303) 443-1821.

[f] R. Radebaugh et al. (2003), http://www.cryogenics.nist.gov/ and the references listed therein.

A5 Temperature measurement tables and controller tuning (ref. Chapter 5)

A5.1 VAPOR PRESSURE VS. TEMPERATURE (ITS-90) FOR CRYOGENIC LIQUIDS (SECS 5.1.6 AND 5.4.1)

Values are tabulated from 200 kPa (~2 atm) down to the triple point (i.e. the solidification temperature). A table of triple points follows the vapor-pressure table. Atmospheric pressure is 101.325 kPa, corresponding to 760 mm Hg at 0°C and standard gravity.

Stratification: Because of temperature stratification within the cryogenic liquid, these vapor pressure data are useful when lowering the temperature of a cryogenic liquid (pumping on cryogenic bath), but not when raising the temperature (pressurizing the bath). In the latter case, the bottom of the bath is much colder than the surface unless a resistive heater is used to establish thermal equilibrium throughout the depth of the liquid. This can take a half hour or more depending on the heater power. Further information and methods to ensure accurate temperature measurements in cryogenic liquids are given in Secs 1.2.1 and 5.4.1. The techniques to minimize temperature stratification in the cryogen liquid are particularly important.

Hydrostatic pressure head: Even when pumping on cryogenic fluids, be aware that after reaching a given pressure, the temperature at the sample depth in a static bath can increase slowly from the hydrostatic pressure of liquid above the sample. If there is a lot of turbulent mixing of the cryogenic liquid, such as from bubbles that occur during pumping or from a relatively large steady-state heat leak into the bath, the error is minimal. However, if the liquid is static for a while (tens of minutes or more), the temperature at the sample location beneath the liquid surface can rise.

This hydrostatic pressure-head correction can be significant, especially for the case of the more dense cryogens, such as liquid nitrogen. The correction is given by $\Delta P = \delta h$, where ΔP is the hydrostatic pressure increase, δ is the mass density of the cryogenic liquid, and h is the height of liquid above the sample. From the cryogen mass densities tabulated in Appendix A1.5 and the SI conversion factors in Appendix A1.3, we find that the pressure increase amounts to about 1.22 kPa at a depth of 1 m in liquid helium, and about 7.90 kPa at the same depth in liquid nitrogen. At atmospheric pressure, for example, this corresponds to a temperature correction of +13 mK in liquid helium, and a correction of +536 mK in liquid nitrogen. The temperature correction increases at lower bath pressures. Thus, for approximate temperature measurement, vapor-pressure data are fine, but for accuracies better than those just noted, it is safest to use a cryogenic thermometer in close thermal proximity to the sample (Sec. 5.3.1).

Note that neither of these errors (stratification or pressure head) occurs in *superfluid* helium (i.e. at temperatures below the dashed line in the ^{4}He column below). Superfluid helium has an extremely high thermal conductivity (see Sec. 1.2.2) and thus, in this case, vapor-pressure data serve to determine sample temperature very accurately.

An extensive tabulation of additional physical properties of cryogenic liquids is given in Appendix A1.5.

Vapor pressure vs. temperature for cryogenic liquids

Pressure [kPa]	^3He [b] [K]	^4He [c] [K]	Para* H_2 [d] [K]	Ne [e] [K]	N_2 [f] [K]	Ar [h] [K]	O_2 [i] [K]	CH_4 [j] [K]
200		5.036	22.805	29.558	83.626	94.290	97.245	120.622
190		4.970	22.596	29.357	83.115	93.722	96.672	119.894
180		4.901	22.379	29.148	82.584	93.130	96.077	119.137
170		4.829	22.153	29.931	82.030	92.514	95.454	118.347
160		4.754	21.918	28.703	81.451	91.869	94.805	117.521
150		4.676	21.672	28.466	80.845	91.194	94.123	116.655
140		4.594	21.413	28.216	80.207	90.483	93.406	115.744
130		4.507	21.142	27.952	79.533	89.732	92.649	114.782
120		4.416	20.855	27.672	78.819	88.936	91.845	113.762
110	3.269	4.319	20.550	27.376	78.059	88.087	90.989	112.674
105	3.224	4.269	20.389	27.219	77.659	87.641	90.538	112.102
101.325	3.191	4.230	20.268	27.100	77.355	87.302	90.196	111.667
100	3.178	4.216	20.224	27.057	77.244	87.178	90.070	111.508
95	3.130	4.162	20.053	26.888	76.812	86.696	89.584	110.890
90	3.080	4.106	19.875	26.713	76.363	86.195	89.077	110.248
85	3.028	4.048	19.689	26.530	75.895	85.672	88.549	109.576
80	2.974	3.988	19.496	26.339	75.405	85.124	87.995	108.874
75	2.918	3.925	19.293	26.138	74.891	84.550	87.414	108.137
70	2.859	3.859	19.081	25.927	74.349	83.945	86.802	107.360
65	2.797	3.790	18.857	25.704	73.777		86.155	106.540
60	2.732	3.717	18.620	25.466	73.170		85.467	105.668
58	2.705	3.687	18.522	25.367	72.916		85.180	105.303
56	2.677	3.656	18.421	25.266	72.655		84.884	104.929
54	2.649	3.624	18.317	25.162	72.387		84.580	104.543
52	2.620	3.591	18.211	25.054	72.111		84.268	104.147
50	2.590	3.558	18.101	24.944	71.826		83.945	103.738
48	2.559	3.524	17.988	24.830	71.533		83.612	103.316
46	2.528	3.489	17.871	24.712	71.230		83.268	102.880
44	2.495	3.452	17.750	24.590	70.916		82.912	102.429
42	2.462	3.415	17.627		70.591		82.543	101.962
40	2.427	3.377	17.498		70.254		82.160	101.476
38	2.392	3.337	17.364		69.903		81.762	100.971
36	2.355	3.295	17.226		69.537		81.346	100.445
34	2.317	3.252	17.081		69.155		80.912	99.895
32	2.277	3.208	16.929		68.755		80.456	99.318
30	2.236	3.161	16.770		68.334		79.978	98.712
29	2.214	3.137	16.689		68.116		79.729	98.397
28	2.193	3.112	16.604		67.891		79.473	98.073
27	2.170	3.087	16.517		67.660		79.210	97.740
26	2.147	3.061	16.428		67.422		78.938	97.396
25	2.124	3.035	16.336		67.177		78.659	97.042
24	2.100	3.008	16.243		66.923		78.370	96.677
23	2.075	2.979	16.145		66.661		78.071	96.299

(Continued)

Vapor pressure vs. temperature for cryogenic liquids (*Continued*)

Pressure [kPa]	^{3}He [b] [K]	^{4}He [c] [K]	Para* H_2 [d] [K]	Ne [e] [K]	N_2 [f] [K]	Ar [h] [K]	O_2 [i] [K]	CH_4 [j] [K]
22	2.049	2.951	16.044		66.390		77.762	95.908
21	2.023	2.921	15.940		66.109		77.441	95.502
20	1.996	2.890	15.832		65.817		77.108	95.080
19	1.968	2.858	15.719		65.513		76.761	94.641
18	1.939	2.825	15.602		65.196		76.399	94.183
17	1.909	2.791	15.481		64.864		76.020	93.704
16	1.878	2.755	15.354		64.516		75.623	93.201
15	1.846	2.718	15.220		64.151		75.205	92.673
14	1.812	2.679	15.080		63.765		74.763	92.115
13	1.776	2.638	14.931		63.356		74.296	91.523
12	1.739	2.594	14.773				73.798	90.894
11	1.699	2.549	14.605				73.265	
10	1.658	2.500	14.424				72.690	
9	1.613	2.448	14.230				72.067	
8	1.565	2.392	14.018				71.383	
7	1.513	2.331					70.625	
6.5	1.485	2.298					70.213	
6	1.455	2.263					69.773	
5.5	1.424	2.227					69.301	
4	1.318	2.087					67.633	
3.5	1.277	2.039					66.960	
3.0	1.231	1.986					66.201	
2.5	1.181	1.926					65.327	
2.0	1.123	1.858					64.290	
1.8	1.097	1.827					63.814	
1.6	1.068	1.793					63.290	
1.4	1.038	1.757					62.707	
1.2	1.004	1.716					62.049	
1.0	0.966	1.670					61.289	
0.9	0.946	1.644					60.859	
0.8	0.923	1.616					60.387	
0.7	0.898	1.585					59.860	
0.6	0.871	1.551					59.266	
0.5	0.841	1.512					58.578	
0.45	0.824	1.490					58.188	
0.4	0.806	1.467					57.760	
0.35	0.786	1.441					57.281	
0.3	0.763	1.411					56.741	
0.25	0.739	1.378					56.115	
0.2	0.710	1.339					55.368	
0.15	0.675	1.292					54.439	
0.1	0.631	1.230						
0.09	0.620	1.214						

(Continued)

Vapor pressure vs. temperature for cryogenic liquids (*Continued*)

Pressure [kPa]	^{3}He [b] [K]	^{4}He [c] [K]	Para* H_2 [d] [K]	Ne [e] [K]	N_2 [f] [K]	Ar [h] [K]	O_2 [i] [K]	CH_4 [j] [K]
0.08	0.609	1.197						
0.07	0.596	1.179						
0.06	0.582	1.158						
0.05	0.566	1.134						
0.04	0.547	1.106						
0.03	0.524	1.072						
0.02		1.026						
0.01		0.956						
0.008		0.935						
0.006		0.910						
0.004		0.875						
0.002		0.822						

Footnotes are listed after next table.

Boiling temperature and triple points for cryogenic liquids[a]

Cryogenic liquid	Boiling temperature (ITS-90) 1 atm (101.325 kPa, 760 mm Hg)	Triple point	
		Temperature (ITS-90)	Pressure
	[K]	[K]	[kPa]
^{3}He[b]	3.1905	—	
^{4}He[c]	4.230	2.1768[†]	4.856
H_2 (para)* [d]	20.268	13.80	7.04
Neon[e]	27.100	24.557	43.46
Nitrogen [f]	77.355	63.151	12.52
Liquid air [g]	78.903	59.75[‡]	5.26
Argon[h]	87.302	83.806	68.89
Oxygen[i]	90.196	54.359	0.146
Methane[j]	111.67	90.694	11.70

Footnotes and references for both of the above tables:

* Hydrogen can exist in two molecular forms: higher-energy orthohydrogen (nuclear spins aligned) and lower-energy parahydrogen (nuclear spins opposed). The equilibrium ratio is determined by temperature: at room temperature and above, hydrogen consists of about 25% para and 75% ortho (so-called "normal" hydrogen), but at the atmospheric boiling temperature of liquid hydrogen (20.27 K) and below, the equilibrium shifts almost completely to parahydrogen (99.79% para and 0.21% ortho at 20.27 K). The boiling temperatures of parahydrogen and normal hydrogen are nearly equal.

† Superfluid λ point.

‡ Solidification point.

[a] Data were evaluated by E. W. Lemmon (2003) from equations of state given in references c through j; National Institute of Standards and Technology, Boulder, CO, personal communication.

[b] E. W. Lemmon (2002), National Institute of Standards and Technology, Boulder, CO, personal communication.

[c] R. D. McCarty and V. D. Arp (1990), *Adv. Cryog. Eng.* 35, 1465–1475.

[d] B. A. Younglove (1982), *J. Phys. Chem. Ref. Data* 11 (Suppl. 1), 1–11.

[e] R. S. Katti, R. T. Jacobsen, R. B. Stewart, and M. Jahangiri (1986), *Adv. Cryog. Eng. (Mater.)* 31, 1189–1197.

[f] R. Span, E. W. Lemmon, R. T. Jacobsen, W. Wagner, and A. Yokozeki (2000), *J. Phys. Chem. Ref. Data* 29(6), 1361–1433.

[g] E. W. Lemmon, R. T. Jacobsen, S. G. Penoncello, and D. G. Friend (2000), *J. Phys. Chem. Ref. Data* 29(3), 1–54.

[h] C. Tegeler, R. Span, and W. Wagner (1999), *J. Phys. Chem. Ref. Data* 28(3), 779–850.

[i] R. Schmidt and W. Wagner (1985), *Fluid Phase Equilibria* 19, 175–200.

[j] U. Setzmann and W. Wagner (1991), *J. Phys. Chem. Ref. Data* 20(6), 1061–1151.

A5.2 PROPERTIES OF CRYOGENIC THERMOMETERS (~1 – ~300 K) (SECS 5.1.2, 5.1.3, AND 5.5)

This table is designed for use in conjunction with the reference compendium, Sec. 5.5, where comments on the properties and practical use of each type of thermometer are given (in corresponding order).

Properties of cryogenic thermometers (~1 – ~300 K)

Sensor type	Temp. range	Accuracy* (± value)	Reproducibility† (± value)	Long-term calibration drift	Inter-change-ability‡	Magnetic field use	Best use	Cost
Metallic Resistance Sensors (positive temperature coefficient):								
Platinum	77–800 K With impurity correction: 20–77 K (Appendix A5.3b)	Without individual calibration: 0.6 K at 70 K 0.2 K at 300 K With individual calibration: 20 mK at 77 K 35 mK at 300 K 55 mK > 330 K 200 mK > 480 K	10 mK from 77 to 305 K	±10 mK/yr from 77 to 273 K	Yes	Recommended above 70 K; error < 0.1% with standard correction factors given in Appendix A5.5	Measurements above 77 K Excellent reproducibility interchange-ability, low mag. field error Many shapes and sizes	Low without calibration High with individual calibration
Rh–Fe	0.5–900 K	With individual calibration: 10 mK at 4.2 K 25 mK at 100 K 35 mK at 300K	10 mK from 1.4 K to to 325 K High purity, strain-free: 0.1 mK at 4.2 K	±20 mK/yr from 1.4 to 325 K	No	Not recommended below ~77 K	Secondary standard thermometer Measurements over a wide temp. range down to 0.5 K	High with individual calibration
Semiconductor-like Resistance Sensors (negative temperature coefficient):								
Germanium	0.05–100 K	Must be individually calibrated With individual calibration: 5 mK at < 10 K 15 mK at < 20 K 35 mK at < 50 K	0.05 mK at 4.2 K	±1 mK/yr at 4.2 K ±10 mK/yr at 77 K	No	Not recommended	Secondary standard thermometer Excellent reproducibility	High with individual calibration

Zirconium–oxynitride (Cernox™)	0.3–420 K	Must be individually calibrated With individual calibration: 5 mK at 4.2 K 20 mK at 20 K 50 mK at 100 K 140 mK at 300 K 230 mK at 400 K	3 mK at 4.2 K	±25 mK/yr over the range 1–100 K 0.05% of reading 100–300 K	No	Recommended Lowest error Correction factors given in Appendix A5.6	One of the best sensors for use in mag. fields Good sensitivity over wide temp. range Fast response time as chip	High with individual calibration
Carbon–glass	1– ~325 K	Must be individually calibrated With individual calibration: 5 mK at <10 K 20 mK at 20 K 55 mK at 50 K	0.75 mK at 4.2 K	−5 mK/yr at 4.2 K −30 mK/yr at 15 K −100 mK/yr at 77 K −600 mK/yr at 300 K	No	Recommended Correction factors given by Sample et al. (1982)	One of the best sensors for use in mag.fields High sensitivity at 4.2 K, low sens. >100 K Fragile; calib. easily invalidated	High with individual calibration
Bi ruthenate/ ruthenium oxide	0.05–40 K	With individual calibration: 5 mK at 0.05 K 7 mK at 1.4 K 11 mK at 4.2 K 77 mK at 20 K 470 mK at 77 K 1.7 K at 200 K 7 K at 300 K	10 mK at 4.2 K	±15 mK/yr at 4.2 K	Yes, but only within each lot	Recommended	Most useful below 20 K Calibration interchangeability (20–40 mK) for sensors of the same lot	High with individual calibration
Diode Voltage Sensors:								
Silicon diode	1.4–475 K	Without calibration: 1 K at < 100 K 1% at 100–475 K With individual calibration: 20 mK 1.4–10 K 55 mK 10–475 K	5 mK at 4.2 K 20 mK at 77 K 15 mK at 300 K	±10 mK/yr at 4.2 K ±40 mK/yr at 77 K ±25 mK/yr at 300 K	Yes	Not recommended below ~60 K	Relatively inexpensive, easily measured, interchangeable thermometer Small size	Medium without calibration High with individual calibration
GaAlAs diode	1.4–325 K	Must be individually calibrated With individual calibration: 15 mK at < 20 K 50 mK at 50 K 110 mK at 300 K	5 mK at 4.2 K	±15 mK/yr at 4.2 K ±50 mK/yr over the range 77 to 330 K	No	Acceptable error (~10 times less than Si diode, but >10 times greater error than Cernox™)	When diode sensor is required in mag. field	High with individual calibration

(Continued)

A5.2 Properties of cryogenic thermometers (~1 – ~300 K) (*Continued*)

Sensor type	Temp. range	Accuracy* (± value)	Reproducibility† (± value)	Long-term calibration drift	Inter-change-ability‡	Magnetic field use	Best use	Cost
Special Purpose Sensors:								
Thermocouples			20 mK at 77 K	—	Yes		Low mass sensor	Requires low dc voltage measurement
Chromel–AuFe (0.07%)	1.4–325 K					Not recommended	-Chromel–AuFe for lower temp. range	
Type E (Chromel–Cu Ni)	3–1274 K	1.7 K from 73 to 273 K				Difficult to use in magnetic field	-Type E for higher temp. range	
Capacitance sensor	1–290 K	Used as transfer control element only, not absolute measurement	>500 mK; 10 mK after cooling and stabilizing	±1 K/yr	No	Recommended for temperature *control*	Excellent magnetic field stability for temp. control	Sensor: medium Requires capacitance measurement

Definitions:

* Accuracy: The difference between the measured and true temperature value.

† Reproducibility: The change in apparent temperature when the sensor is subjected to repeated thermal cycling from room temperature.

‡ Interchangeability: The ability to substitute one sensor for another with little change in calibration.

Sources: Information compiled from *Temperature Measurement and Control* (2000, 2002), Lake Shore Cryotronics, Westerville, OH; L. M. Besley (1993), National Measurements Laboratory, Sydney, Australia; and L. G. Rubin (2002), Francis Bitter National Magnet Laboratory, Cambridge, MA.

References for magnetic-field calibration:

Carbon resistors: H. H. Sample, L. J. Neuringer, and L. G. Rubin (1974), *Rev. Sci. Instrum.* 45, 64–73.
Carbon–glass thermometers: H. H. Sample, B. L. Brandt, and L. G. Rubin (1982), *Rev. Sci. Instrum.* 53, 1129–1136.
Cernox™: B. L. Brandt, D. W. Liu, and L. G. Rubin (1999), *Rev. Sci. Instrum.* 70, 104–110.
Platinum thermometers: B. L. Brandt, L. G. Rubin, and H. H. Sample (1988), *Rev. Sci. Instrum.* 59, 642–645.
Thermocouples: H. H. Sample and L. G. Rubin (1977), *Cryogenics* 17, 597–606.

A5.3a PLATINUM RESISTANCE THERMOMETER (PRT) RESISTIVITY vs. TEMPERATURE *ABOVE* 70 K (SECS 5.1.3, 5.1.6, AND 5.5.1)

This table gives a standard calibration of the temperature dependence of PRTs for use above liquid-nitrogen temperature. This calibration is not recommended at lower temperatures, however, because the role of impurity resistivity increases in the low-temperature range. A standard calibration below 70 K that compensates for varying impurity resistivities is given in the next table, Appendix A5.3b.

For platinum thermometers having an ice-point resistance $R_{273\ \mathrm{K}}$ other than 100 Ω, multiply the resistance values in this table by the ratio of the ice-point resistance to 100 Ω. For example, for a 500 Ω PRT, multiply all the values in the table by 5 to obtain the calibration for such a thermometer.

Calculation of temperature values (ITS-90): Temperatures other than those listed in the table can be calculated according to DIN EN 60751 for Class A and Class B PRTs {alpha $\equiv [R_{100°\mathrm{C}} - R_{0°\mathrm{C}}]/[100\,R_{0°\mathrm{C}}] = 0.00385$}, where the temperature T is in kelvins:

For $T < 273.15$ K (0°C):

$$R(T) = R_0\,[1 + A\,(T - 273.15) + B\,(T - 273.15)^2 + C\,(T - 373.15)\,(T - 273.15)^3]$$

For $T \geq 273.15$ K (0°C):

$$R(T) = R_0\,[1 + A\,(T - 273.15) + B\,(T - 273.15)^2],$$

where the constants in these two equations have the values

$$\mathrm{A} = 3.9083 \times 10^{-3}/\,°\mathrm{C}$$
$$\mathrm{B} = -5.775 \times 10^{-7}/\,°\mathrm{C}^2$$
$$\mathrm{C} = -4.183 \times 10^{-12}/\,°\mathrm{C}^4$$
$$R_0 = 100\ \Omega.$$

Interchangeability tolerance:

$$\text{Class A: } \Delta T(\mathrm{K}) = \pm(0.15 + 0.002\,|T - 273.15|)$$
$$\text{Class B: } \Delta T(\mathrm{K}) = \pm(0.3 + 0.005\,|T - 273.15|).$$

DIN EN 60751 resistance vs. temperature (ITS-90) for platinum resistance thermometers.

(Thermometer resistance at 273.15 K is 100 Ω, alpha[a] = 0.00385.)

T [K]	R [Ω]	Interchangeability tolerance Class A, B [K]	T [K]	R [Ω]	Interchangeability tolerance Class A, B [K]	T [K]	R [Ω]	Interchangeability tolerance Class A, B [K]
60	12.80		140	46.71		225	81.04	
65	14.98		145	48.77		230	83.02	
70	17.16	±0.6, ±1.3	150	50.82	±0.4, ±0.9	235	85.00	
75	19.32		155	52.87		240	86.98	
80	21.47		160	54.91		245	88.95	
85	23.62		165	56.95		250	90.92	±0.2, ±0.4
90	25.75		170	58.98		255	92.89	
95	27.88		175	61.01		260	94.85	
100	30.00	± 0.5, ±1.2	180	63.03		265	96.81	
105	32.12		185	65.05		270	98.77	
110	34.22		190	67.06		273.15	100.00	
115	36.32		195	69.07		275	100.72	
120	38.41		200	71.07	±0.3, ±0.7	280	102.67	
125	40.49		205	73.07		285	104.62	
130	42.57		210	75.07		290	106.57	
135	44.64		215	77.06		295	108.51	
			220	79.05		300	110.45	±0.2, ±0.4

[a] Alpha $\equiv (R_{100°C} - R_{0°C})/100\, R_{0°C}$.

A5.3b PLATINUM RESISTANCE THERMOMETER (PRT) RESISTIVITY vs. TEMPERATURE *BELOW* 70 K (SECS 5.1.3, 5.1.6, AND 5.5.1)

This table provides a calibration for PRTs if they must be used for thermometry below ~70 K (such as a when a platinum film-type sensor is used for a rapid time response). In this low-temperature range, differences in impurity levels in the thermometers lead to significant errors in the standard calibration table (Appendix A5.3a). Consequently, the temperature should be determined by calculating the Z-ratio (defined below).

With this scheme, the impurity resistivity of an individual PRT can be compensated. The PRT's resistance is first measured at or near liquid-helium temperature in order to determine its impurity resistivity $R_{4.2\,\mathrm{K}}$. This is then used with the measured resistance of the sensor R_T to determine the ratio:

$$Z \equiv (R_T - R_{4.2\,\mathrm{K}})/(R_{273\,\mathrm{K}} - R_{4.2\,\mathrm{K}}),$$

where $R_{273\,\mathrm{K}}$ is the sensor's ice-point resistivity. The value of this Z-ratio can then be used to determine temperature from the following table.

Values of $\Delta Z/\Delta T$ are also provided to facilitate interpolation between tabulated temperature values.

This Z-ratio procedure has a typical error of about ± 25 mK down to 30 K, below which temperature the error increases to about ± 120 mK at 14 K (Besley and Kemp 1978). Use below 14 K is not recommended.

Z-ratio for PRTs

T [K]	$10^6\,Z$	$10^6\,\Delta Z/\Delta T$ [K^{-1}]
14.0	908.7	256
14.5	1043.5	284
15.0	1192.9	314
15.5	1358.2	347
16.0	1540.4	382
16.5	1740.3	418
17.0	1958.9	457
17.5	2197.2	497
18.0	2456.2	539
18.5	2736.7	583
19.0	3039.7	629
19.5	3366.1	677
20.0	3716.7	726
21.0	4493.6	829
22.0	5376.0	937
23.0	6368.3	1049
24.0	7474.2	1164
25.0	8696.8	1282
26.0	10038	1401
27.0	11500	1522
28.0	13083	1644
29.0	14788	1766
30.0	16615	1887

(Continued)

Z-ratio for PRTs (*Continued*)

T [K]	$10^6\,Z$	$10^6\,\Delta Z/\Delta T$ [K^{-1}]
31.0	18562	2007
32.0	20628	2126
33.0	22812	2242
34.0	25111	2356
35.0	27523	2468
36.0	30045	2576
37	32674	2681
38	35406	2783
39	38238	2880
40	41166	2974
42	47293	3151
44	53758	3311
46	60528	3456
48	67572	3586
50	74862	3701
52	82368	3803
54	90065	3892
56	97929	3970
58	105937	4037
60	114071	4095
65	134839	4205
70	156050	4274
75	177535	4316
80	199174	4337
85	220881	4344
90	242600	4342
95	264293	4334
100	285935	4322

Source: Table values were calculated by L. M. Besley and R. C. Kemp (1978), *Cryogenics* 18, 497–500, from data on 50 high-quality platinum thermometers. Data were compiled by C. G. Kirby and R. E. Bedford, and J. Kathnelson (1975), *Metrologia* 11, 117–124, and J. P. Compton and S. D. Ward (1975), *Temperature Measurement*, p. 91, Institute of Physics London Conference Series No. 26. See also the discussion and summary given in G. K. White (1989), *Experimental Techniques in Low-Temperature Physics*, pp. 100–104, Oxford University Press, Oxford.

A5.4 DIODE AND THERMOCOUPLE VOLTAGE-VS.-TEMPERATURE TABLES (SECS 5.1.3, 5.1.6, 5.5.7, AND 5.5.9)

Silicon diode[a] DT-470 Curve 10		Thermocouple[b] Chromel vs. Au–0.07at%Fe		Type E[c] Thermocouple Chromel vs. Constantan		Type K[d] Thermocouple Chromel vs. Alumel		Type T[e] Thermocouple Copper vs. Constantan	
[K]	[V]	[K]	[mV]	[K]	[mV]	[K]	[mV]	[K]	[mV]
1.4	1.6981	1.4	−5.298	3.0	−9.836	3.0	−6.458	3.0	−6.258
2.0	1.6879	3.0	−5.281	5.6	−9.830	6.0	−6.455	6.5	−6.252
3.8	1.6390	4.8	−5.259	9.0	−9.818	10.0	−6.449	11.0	−6.240
9.0	1.4505	7.0	−5.223	13.5	−9.796	14.5	−6.438	16.5	−6.218
12.0	1.3681	10.5	−5.174	19.0	−9.757	19.5	−6.421	22.0	−6.189
15.5	1.2946	19.0	−5.032	25.0	−9.701	25.0	−6.395	29.0	−6.140
20.0	1.2144	26.0	−4.193	32.0	−9.620	32.0	−6.353	38.0	−6.062
24.0	1.1360	48.0	−4.549	40.0	−9.507	40.0	−6.291	48.0	−5.954
25.0	1.1246	58.0	−4.381	50.0	−9.337	48.0	−6.215	60.0	−5.800
26.0	1.1190	70.0	−4.173	60.0	−9.135	58.0	−6.102	75.0	−5.575
27.0	1.1152	80.0	−3.995	70.0	−8.903	65.0	−6.010	90.0	−5.320
28.0	1.1121	90.0	−3.813	80.0	−8.648	75.0	−5.863	105	−5.034
32.0	1.1026	100	−3.627	90.0	−9.367	85.0	−5.699	120	−4.719
36.0	1.0949	110	−3.437	105	−7.906	95.0	−5.516	135	−4.377
44.0	1.0809	120	−3.244	120	−7.394	105	−5.317	155	−3.878
60.0	1.0527	135	−2.948	135	−6.839	120	−4.988	175	−3.328
77.35	1.0203	150	−2.645	150	−6.240	135	−4.624	195	−2.734
100	0.9755	165	−2.337	170	−5.383	150	−4.227	220	−1.930
120	0.9338	180	−2.042	190	−4.456	165	−3.799	245	−1.059
140	0.8907	200	−1.600	210	−3.470	185	−3.187	270	−0.125
170	0.8240	220	−1.169	235	−2.161	205	−2.526	300	+ 1.062
200	0.7555	245	−0.623	260	−0.767	230	−1.646	330	+2.325
230	0.6856	270	−0.071	290	+0.995	260	−0.519	360	+3.664
273.15	0.5833	300	+0.599	320	+2.843	295	+0.869	395	+5.310
320	0.4707	305	+0.716	350	+4.770	350	+3.130	430	+7.042
360	0.3734	310	+0.843	385	+7.115	395	+5.000	470	+9.111
400	0.2746	315	+0.994	420	+9.557	460	+7.616	510	+11.276
440	0.1746	320	+1.194	460	+12.443	510	+9.613	555	+13.805
475	0.0906	325	+1.484	475	+13.557	575	+12.279	575	+14.968

Source: Data from Lake Shore Cryotronics, Inc. (2002), *Temperature Measurement and Control*, Westerville, OH.

[a] Accuracy: 1 K at <100 K, 1% at 100–475 K. Reproducibility: ±5 mK at 4.2 K, ±20 mK at 77 K, ±15 mK at 300 K. See Appendix A5.2 for more information.

[b] For accuracy information, refer to L. L. Sparks and R. L. Powell (1973), *J. Res. Nat. Bur. Std*. 76A, 263–283. Thermocouple voltages are referenced to zero at 273 K.

[c] Accuracy: 1.7 K from 73 to 273 K. See Appendix A5.2 for more information. Thermocouple voltages are referenced to zero at 273 K.

[d] Accuracy: 2.2 K from 73 to 273 K. Thermocouple voltages are referenced to zero at 273 K.

[e] Accuracy: 1.0 K from 73 to 273 K. Thermocouple voltages are referenced to zero at 273 K.

A5.5 MAGNETIC-FIELD CORRECTION FACTORS FOR PLATINUM RESISTANCE THERMOMETERS (PRTs) (SECS 5.1.6, 5.2, AND 5.5.1)

These magnetic-field correction factors were calculated from magnetoresistance data obtained by Brandt et al. (1988) and are tabulated here as relative temperature errors $(T_{\text{apparent}} - T_{\text{actual}})/T_{\text{actual}}$ [%]. The corrections were nearly the same for measurements on thirteen PRTs of varying purity (alpha = 3.85–3.925 $\times$ 10^{-3}/°C), as well as varying construction types (wire-wound and thick-film types), manufacturers, and ice-point resistances (100–500 Ω). For all the sensors, the *standard deviation* of the correction is simply about ±10% of the correction value itself, irrespective of temperature or magnetic field.

Example: Suppose we wish to correct the reading of a PRT that indicates an apparent temperature of 100 K in a magnetic field of 10 T.

From the table below we see that, at 100 K and 10 T, this temperature reading would actually be too high by 0.40%. Thus, the actual temperature would be 100 K / (1 + 0.004) = 99.6 K. The standard deviation for this correction would be about 10% of the correction (0.1% $\times$ 0.40%), or only 0.04% (i.e. 0.04 K).

The *orientation* of the magnetic field has a negligible effect on these correction factors for film-type PRTs, but the effect is significant for wire-wound PRTs. The data below correspond to wire-wound PRTs oriented with the applied magnetic field parallel to the long axis of their package (see Fig. 5.17). Thus, to use the table, it is recommended that wire-wound PRTs be installed with this orientation. Alternatively, when the sensor must be used in varying field orientations, a thin-film PRT is preferred.

Magnetic-field correction factors for PRTs

Tabulated values are $(T_{\text{apparent}} - T_{\text{actual}})/T_{\text{actual}}$ [%] at magnetic field B.

The standard deviation of these corrections is about ±10% of the tabulated values.

T [K]	B = 5 T [%]	B = 10 T [%]	B = 15 T [%]	B = 19 T [%]
40	1.5	4.1	6.7	8.9
50	1.05	2.9	5.0	6.7
60	0.59	1.8	3.2	4.5
70	0.27	0.97	1.9	2.8
80	0.18	0.67	1.4	2.1
90	0.13	0.50	1.0	1.6
100	0.11	0.40	0.85	1.4
120	0.068	0.26	0.57	0.91
150	0.038	0.16	0.35	0.56
200	0.019	0.085	0.19	0.31
220	0.017	0.074	0.17	0.28
250	0.015	0.058	0.14	0.22
300	0.010	0.030	0.080	0.13

Source: Correction factors calculated from magnetoresistance data from B. L. Brandt, L. G. Rubin, and H. H. Sample (1988), *Rev. Sci. Instrum.* 59, 642–645.

A5.6 MAGNETIC-FIELD CORRECTION FACTORS FOR ZIRCONIUM–OXYNITRIDE RESISTANCE THERMOMETERS (SECS 5.1.6, 5.2, AND 5.5.4)

These magnetoresistance correction factors were interpolated to even temperature values by using a cubic-spline fit to magnetoresistance data measured by Brandt et al. (1999). The corrections are applicable to a wide range of zirconium–oxynitride (Cernox™) resistance thermometers having 4.2 K resistances from about 300 to 8000 Ω, and 4.2 K dimensionless sensitivities $(dR/R)/(dT/T)$ in the range −0.74 to −1.9 (with −1.2 to −1.9 recommended).

The data are presented as the percentage change in *resistance* rather than *temperature* (unlike platinum in Appendix A5.5), because Brandt et al. found that, for zirconium–oxynitride sensors, the standard deviations in resistance were much smaller than the standard deviations in temperature. [This results from the wide range of dimensionless sensitivities $S \equiv (dR/R)/(dT/T)$ of the individual sensors and the differing temperature dependences of S.] The standard deviation of the magnetoresistance correction is given as a ± quantity below each magnetoresistance correction. The standard deviations show that this correction procedure is most beneficial at temperatures below about 3 K and from about 6 to 15 K.

Example: Let us assume that a particular zirconium–oxynitride thermometer indicates an apparent temperature of about 10 K in a magnetic field of 16 T. We wish to correct for the magnetoresistance error of this particular sensor.

From the table below, we see that, at 10 K and 16 T, the sensor's resistance would exceed its zero-field resistance by 1.40%. We use the dimensionless sensitivity $S \equiv (dR/R)/(dT/T)$ supplied with the calibration data for our particular sensor to calculate the equivalent shift in its apparent temperature. For our sensor, suppose that $S = -1.16$ at 10 K. Then, we would calculate $(T_{\text{apparent}} - T_{\text{actual}})/T_{\text{actual}} = (1.40\%)/(-1.16) = -1.21\%$ and accordingly adjust the apparent temperature reading by this percentage to obtain the actual temperature. Since $T_{\text{apparent}} - T_{\text{actual}}$ is negative at 10 K and 16 T, the apparent temperature is lower than the actual temperature, and it would need to be *increased* by 1.21% to give the actual temperature. From the standard deviation of ±0.30 for the resistivity correction at 10 K and 16 T, we find the standard deviation of the temperature correction is ±0.26%.

At liquid-nitrogen temperatures, the effect of magnetic-field *orientation* on these correction factors was observed to be insignificant. However, at 4.2 K the situation was more complex, giving rise to a positive orientation effect in some sensors, negative in others (e.g. apparent temperature shifts of −0.2% to +0.4% were observed at 16 T; Brandt et al. 1999). Since the tabulated corrections were determined for a field *perpendicular* to the film surface (canister aligned parallel to the field), it is best to orient these sensors accordingly so they can be used with the correction data.

A5.6 Magnetic-field correction for zirconium–oxynitride (Cernox™) resistance thermometers

Tabulated values are $[R(B) - R(0)]/R(0)$ [%] at magnetic field B.

The standard deviation of the correction is shown as a ± factor (also in percent) below each correction.

T [K]	B=2 T [%]	B=4 T [%]	B=6 T [%]	B=8 T [%]	B=10 T [%]	B=12 T [%]	B=14 T [%]	B=16 T [%]	B=18 T [%]	B=20 T [%]	B=23 T [%]	B=26 T [%]	B=29 T [%]	B=32 T [%]
2	−2.20	−4.47	−5.52	−6.10	−6.61	−7.19	−7.85	−8.59	−10.12	−10.39	−10.96	−12.87	−14.87	−16.92
	±0.39	±1.08	±1.58	±1.83	±1.90	±1.79	±1.59	±1.35	±1.09	±0.85	±1.00	±1.28	±1.80	±2.35
2.5	−1.21	−2.55	−3.09	−3.25	−3.35	−3.55	−3.88	−4.14	−5.07	−5.65	−6.31	−8.06	−9.87	−11.74
	±0.25	±0.77	±1.20	±1.46	±1.55	±1.51	±1.35	±1.13	±0.86	±0.59	±1.40	±1.80	±2.25	±2.76
3	−0.65	−1.42	−1.65	−1.57	−1.43	−1.37	−1.47	−1.69	−2.17	−2.73	−3.42	−5.00	−6.73	−8.55
	±0.16	±0.52	±0.88	±1.12	±1.24	±1.24	±1.15	±0.98	±0.76	±0.57	±1.73	±2.16	±2.62	±3.12
3.5	−0.38	−0.76	−0.80	−0.57	−0.28	−0.06	0.02	−0.11	−0.34	−0.75	−1.57	−3.02	−4.63	−6.34
	±0.11	±0.35	±0.64	±0.87	±1.00	±1.04	±1.00	±0.92	±0.79	±0.71	±1.92	±2.37	±2.84	±3.30
4.2	−0.17	−0.30	−0.20	0.11	0.50	0.82	1.07	1.06	1.02	0.79	0.03	−1.20	−2.63	−4.22
	±0.03	±0.20	±0.42	±0.61	±0.73	±0.81	±0.81	±0.85	±0.74	±0.72	±2.03	±2.50	±2.97	±3.43
5	−0.09	−0.07	0.10	0.42	0.82	1.20	1.47	1.62	1.22	1.55	1.00	0.06	−1.23	−2.65
	±0.02	±0.15	±0.31	±0.44	±0.55	±0.59	±0.64	±0.67	±0.65	±0.68	±1.89	±2.37	±2.84	±3.30
6	−0.08	0.02	0.21	0.51	0.90	1.29	1.61	1.85	2.01	1.96	1.69	0.91	−0.12	−1.26
	±0.02	±0.07	±0.19	±0.31	±0.40	±0.45	±0.51	±0.55	±0.58	±0.68	±1.87	±2.31	±2.78	±3.25
7	−0.06	0.03	0.23	0.52	0.89	1.26	1.60	1.88	2.26	2.08	1.88	1.29	0.48	−0.48
	±0.01	±0.03	±0.11	±0.21	±0.27	±0.34	±0.39	±0.45	±0.53	±0.66	±1.75	±2.17	±2.62	±3.08
8	−0.05	0.03	0.24	0.52	0.85	1.19	1.52	1.80	1.97	2.03	1.78	1.38	0.73	−0.11
	±0.02	±0.03	±0.07	±0.13	±0.18	±0.24	±0.30	±0.37	±0.48	±0.62	±1.53	±1.95	±2.38	±2.81
9	−0.04	0.02	0.21	0.46	0.76	1.07	1.37	1.63	1.71	1.86	1.62	1.32	0.78	0.08
	±0.03	±0.03	±0.06	±0.10	±0.14	±0.18	±0.24	±0.32	±0.44	±0.57	±1.36	±1.76	±2.16	±2.56
10	−0.05	0.01	0.16	0.38	0.64	0.92	1.18	1.40	1.54	1.65	1.43	1.17	0.72	0.16
	±0.03	±0.04	±0.06	±0.09	±0.12	±0.15	±0.21	±0.30	±0.40	±0.52	±1.23	±1.59	±1.96	±2.34
12	−0.05	−0.01	0.08	0.23	0.43	0.66	0.85	1.01	1.21	1.24	1.04	0.81	0.48	0.09
	±0.02	±0.04	±0.05	±0.08	±0.11	±0.13	±0.18	±0.26	±0.34	±0.43	±1.02	±1.31	±1.62	±1.95
15	−0.03	−0.03	0.02	0.12	0.24	0.37	0.50	0.61	0.70	0.76	0.48	0.32	0.07	−0.27
	±0.02	±0.03	±0.05	±0.06	±0.08	±0.11	±0.15	±0.20	±0.26	±0.33	±0.77	±0.99	±1.23	±1.48

20	−0.03	−0.04	−0.04	−0.01	0.03	0.09	0.13	0.17	0.20	0.22	−0.03	−0.17	−0.37	−0.65
	±0.01	±0.02	±0.03	±0.05	±0.06	±0.08	±0.11	±0.14	±0.18	±0.23	±0.51	±0.67	±0.83	±1.00
30	−0.01	−0.02	−0.03	−0.04	−0.04	−0.05	−0.05	−0.07	−0.09	−0.12	−0.35	−0.49	−0.64	−0.83
	±0.00	±0.01	±0.01	±0.02	±0.03	±0.05	±0.07	±0.09	±0.11	±0.13	±0.27	±0.34	±0.42	±0.51
40	0.00	−0.01	−0.01	−0.02	−0.04	−0.06	−0.08	−0.10	−0.14	−0.17	−0.38	−0.50	−0.61	−0.76
	±0.00	±0.00	±0.01	±0.01	±0.02	±0.03	±0.04	±0.05	±0.07	±0.08	±0.16	±0.19	±0.24	±0.29
50	0.00	−0.01	−0.02	−0.03	−0.05	−0.06	−0.08	−0.11	−0.14	−0.17	−0.32	−0.41	−0.51	−0.63
	±0.00	±0.00	±0.01	±0.01	±0.02	±0.02	±0.03	±0.04	±0.05	±0.06	±0.10	±0.13	±0.16	±0.19
60	−0.01	−0.02	−0.03	−0.04	−0.05	−0.07	−0.09	−0.11	−0.13	−0.16	−0.27	−0.34	−0.43	−0.53
	±0.00	±0.01	±0.01	±0.02	±0.02	±0.03	±0.04	±0.05	±0.07	±0.08	±0.07	±0.10	±0.12	±0.14
70	−0.01	−0.01	−0.02	−0.03	−0.04	−0.06	−0.08	−0.10	−0.12	−0.15	−0.23	−0.30	−0.37	−0.45
	±0.01	±0.01	±0.01	±0.02	±0.02	±0.03	±0.05	±0.06	±0.08	±0.09	±0.06	±0.07	±0.09	±0.11
77	0.00	−0.01	−0.02	−0.02	−0.04	−0.05	−0.07	−0.09	−0.11	−0.13	−0.21	−0.27	−0.34	−0.41
	±0.01	±0.01	±0.01	±0.01	±0.02	±0.03	±0.04	±0.06	±0.07	±0.08	±0.05	±0.06	±0.07	±0.09
80	0.00	−0.01	−0.01	−0.02	−0.03	−0.04	−0.06	−0.08	−0.10	−0.12	−0.20	−0.26	−0.33	−0.40
	±0.01	±0.01	±0.01	±0.01	±0.02	±0.02	±0.03	±0.04	±0.06	±0.07	±0.05	±0.06	±0.07	±0.09
90	0.00	0.00	−0.01	−0.02	−0.02	−0.03	−0.04	−0.05	−0.06	−0.07	−0.18	−0.23	−0.29	−0.34
	±0.00	±0.00	±0.01	±0.01	±0.01	±0.01	±0.00	±0.00	±0.00	±0.00	±0.04	±0.04	±0.04	±0.06
100	0.00	0.00	−0.01	−0.01	−0.02	−0.03	−0.02	−0.03	−0.03	−0.04	−0.15	−0.20	−0.25	−0.29
	±0.00	±0.00	±0.01	±0.01	±0.01	±0.01	±0.02	±0.03	±0.04	±0.04	±0.04	±0.02	±0.02	±0.04
120	0.00	0.00	−0.01	−0.01	−0.02	−0.02	−0.01	−0.01	−0.01	−0.02	−0.09	−0.13	−0.17	−0.18
	±0.00	±0.00	±0.01	±0.01	±0.01	±0.01	±0.03	±0.04	±0.06	±0.06	±0.02	±0.02	±0.02	±0.00
150	0.00	0.00	0.00	0.00	−0.01	−0.01	−0.02	−0.02	−0.03	−0.03	0.08	0.09	0.10	0.16
	±0.00	±0.00	±0.01	±0.01	±0.01	±0.01	±0.01	±0.01	±0.01	±0.01	±0.08	±0.12	±0.16	±0.17
200	0.00	0.00	0.00	0.00	−0.01	−0.01	−0.01	−0.01	−0.02	−0.02	0.27	0.35	0.41	0.56
	±0.01	±0.01	±0.01	±0.01	±0.01	±0.01	±0.01	±0.01	±0.01	±0.02	±0.17	±0.25	±0.33	±0.35
250	0.00	0.00	0.00	0.00	0.00	−0.01	−0.01	−0.01	−0.01	−0.01	0.47	0.60	0.72	0.96
	±0.01	±0.01	±0.01	±0.01	±0.01	±0.01	±0.01	±0.01	±0.01	±0.02	±0.26	±0.37	±0.49	±0.53
300	0.00	0.00	0.00	0.00	0.00	0.00	0.00	0.00	0.00	0.00	0.67	0.85	1.02	1.35
	±0.01	±0.01	±0.01	±0.01	±0.01	±0.01	±0.01	±0.01	±0.01	±0.02	±0.35	±0.50	±0.65	±0.71

Source: These temperature corrections were interpolated to even temperature values by using a cubic-spline fit to magnetoresistance data measured by B. L. Brandt, D. W. Liu, and L. G. Rubin (1999), *Rev. Sci. Instrum.* 70, 104–110.

A5.7 TEMPERATURE-CONTROLLER TUNING WITH THE ZIEGLER–NICHOLS METHOD (SEC. 5.4.3)

Temperature controllers do not always have an auto-tuning feature, and, even if they do, it does not work well for some applications. Here we describe a time-proven, relatively simple, step-by-step procedure for manually optimizing a proportional-integral-differential (PID) controller's settings of gain G, integral time t_i, and the derivative time t_d for a specific system. The settings for a proportional-integral (PI) controller and a simple proportional (P) controller are also given. The optimum settings enable a controller to react quickly to a change in heat demand without much overshoot, oscillation, or droop below the set point (Sec. 5.4.3).

Before describing the tuning procedure, we first define a few terms.

Definitions

Cycle time (sometimes referred to as *duty cycle*): This denotes the time it takes an on–off or time-proportional controller to complete an on–off cycle, illustrated in Fig. 5.15. This applies only to time-proportional controllers and not to analog voltage or current controllers.

Proportional band, and gain: Let P_b be the proportional band around the set point (see Fig. 5.16), usually expressed as a percent of full scale. This is also referred to as the *gain, G*, which is the reciprocal of the proportional band; that is, $G \equiv 1/P_b$.

Integration-time constant (sometimes called *reset*): Let t_i be the characteristic time constant for integration to eliminate the offset error. (The offset error is the steady-state difference between the system temperature and the set point, illustrated in Fig. 5.16).

Derivative-time constant (sometimes called *rate*): Let t_d be the characteristic time constant to correct transient disturbances in the system with a minimum of overshoot or undershoot.

(The terms *proportional band, reset*, and *rate* are those generally used in the field of industrial controls, whereas *gain, integration-time constant*, and *derivative-time constant* are the terms employed by physicists and the companies that sell controllers to them.)

Procedure

1. The tuning procedure is easier to observe with a recorder or scrolling data-acquisition display to monitor the process temperature, since the time constants for cycling may be as long as 30 min or more.
2. For time-proportional controllers only, adjust the cycle time to a short time so that the system will not be limited in its time response because of the duty cycle of the heater power.
3. Set the gain to a small value (proportional band to a large value) so the system is overdamped to start with.
4. Turn the integral (reset) and derivative (rate) controls *off*.
5. Enter the set point where control is desired and wait until the temperature is close to that point, or use the manual heater control (manual reset) to reach a temperature near the set point. When the sample temperature is close to the desired temperature, increase the gain (decrease the proportional band) until the system just becomes unstable and starts to oscillate. This is easiest to observe by looking directly at the output power to the heater. Let us denote this critical value of the gain as G'.
6. Measure the time period of the oscillations; denote this as t'.
7. Initial optimum values, G and t_i, for optimum stable control are calculated from the following table by using the measured values of G' and t'. These values are given for three types of controllers: P, PI, and for PID.

8. After entering these initial values into the controller and turning on the integral and derivative control, the parameters can be fine tuned. If overshoot occurs in response to step changes in the set-point temperature, it can be eliminated by decreasing the derivative (rate) time constant t_d. When changes are made in the derivative time constant, a corresponding change should also be made in the integral time constant to keep their *ratio* about the same as that given in the table.
9. For time-proportional controllers only, increase the cycle time after satisfactory tuning has been achieved to extend the contactor life of the power supply. Increase the cycle time as much as possible without causing the system to breaking into oscillation when the heater power cycles on and off.

Calculation of control parameters for critical damping with the Ziegler–Nichols tuning formula.

Control type [a]	PID	PI	P
Proportional gain	$G = 0.6\ G'$	$G = 0.45\ G'$	$G = 0.5\ G'$
Integral time (reset time constant)	$t_i = 0.5\ t'$	$t_i = 0.85t'$	
Derivative time (rate time constant)	$t_d = 0.125\ t'$		

[a] PID ≡ proportional-integral-differential control, PI ≡ proportional-integral control, and P ≡ proportional control.

Sources:

J. G. Ziegler and N. B. Nichols (1942), *Trans. ASME* 64, 759–768.

P. B. Deshpande and R. H. Ash (1981), "Computer process control," ISA pub., USA.

For large time constants, where the Ziegler–Nichols method becomes time-consuming, a refinement that improves performance based on set-point weighting has been suggested by C. C. Hang, K. J. Astrom, and W. K. Ho (1991), *IEEE Proc.-D* 138, 111–118.

If a computer is available to monitor the temperature, it is easy to implement an improved form of PID control with software described by C. K. Chan (1988), *Rev. Sci. Instr.* 59, 1001–1003.

A good reference for understanding PID control at cryogenic temperatures is E. M. Forgan (1974), *Cryogenics* 14, 207–214.

A6 **Properties of solids at low temperature (ref. Chapter 6)**

Additional sources of materials data in the literature and on the Internet are given in the further reading and web sites listed in Secs 6.7.1 and 6.7.2, respectively.

A6.1 ELEMENTS: PHYSICAL PROPERTIES AT ROOM TEMPERATURE

For anisotropic elements, polycrystalline values are listed unless otherwise noted.

Elements: Physical properties at room temperature.

Element	Atomic weight	Crystal structure	Density (298 K) [g/cm^3]	Debye temp. θ_D [a] (295 K) [K]	Specific heat (at const. press.) (298 K) [J/(g K)]	Coef. of thermal linear expansion (298 K) [10^{-6} K^{-1}]	Electrical resistivity (295 K) [$\mu\Omega$ cm]	Thermal conductivity (300 K) [W/m·K)]	Magnetic susceptibility [d] [10^{-6} SI]	Superconducting transition temperature [e] [K]
Aluminum	26.98	f.c.c.	2.70	380	0.904	23.1	2.67	237	20.8	1.175
Antimony	121.76	Rhombohedral	6.68	210	0.207	11.0	41.3[b]	24.3	−68.3	
Arsenic	74.91[c]	Rhombohedral	5.73[b]	290	0.329	5.6[b] (293 K)	29[b]	37[c]	−5.4	
Barium	137.33	b.c.c.	3.62	110	0.205	20.6	33.5	18.4	0.1	
Beryllium	9.013	h.c.p.	1.85	920	1.82	11.3	3.62	200	−23.1	0.026
Bismuth	208.98	Rhombohedral	9.79	120	0.122	13.4	116[b]	7.87	−165.0	
Boron	10.81	Hexagonal	2.535	1300	1.277	8.3	1012[c]	30[c]	−19.7	
Cadmium	112.41	h.c.p.	8.69	175	0.231	30.8	7.27[b]	96.8	−19.0	0.517
Calcium	40.08	f.c.c.	1.54	210	0.646	22.3	3.38	98[c]	19.4	
Carbon										
Graphite	12.01	Hexagonal	2.22	400	0.709	3	10^2–10^6 [c]	200	−13.9	
Diamond	12.01	Diamond	3.51	2000	0.4715	1.18	10^{12} [c]	990		
Cesium	132.91	b.c.c.	1.93	45	0.242	97	20.6	35.9	5.1	
Chromium	52.00	b.c.c.	7.15	480	0.450	4.9	12.5	93.7	290.5	
Cobalt	58.93	h.c.p.	8.86	380	0.421	13.0	5.80[b]	100	ferro	
Copper	63.55	f.c.c.	8.96	310	0.385	16.5	1.69	401	−9.7	
Gallium	69.72	Orthorhombic	5.91	240	0.374	18	14.85[b]	40.6	−23.2	1.083

Germanium	72.59	Diamond	5.32	400	0.3219	6.1	5×10^{7} [c]	64	−10.7	
Gold	196.97	f.c.c.	19.3	185	0.129	14.2	2.23	317	−34.5	
Hafnium	178.49	h.c.p.	13.3	210	0.144	65.9	33.3	23	66.4	0.128
Indium	114.82	Tetragonal	7.31	110	0.233	32.1	8.75[b]	81.6	−8.2	3.408
Iridium	192.22	f.c.c.	22.5	290	0.131	6.4	5.07[b]	147	36.8	0.112
Iron	55.85	b.c.c.	7.87	400	0.449	11.8	9.71	80.2	ferro	
Lead	207.20	f.c.c.	11.3	88	0.127	28.9	20.9	35.3	−15.8	7.196
Lithium	6.94	b.c.c.	0.534	360	3.57	46	9.36	84.7	13.6	
Magnesium	24.30	h.c.p.	1.74	330	1.024	24.8	4.43	156	11.8	
Manganese	54.94	Cubic (complex)	7.43	410	0.479	21.7	144	7.82	869.7	
Mercury	200.59	Rhombohedral	13.534	110 (220 K)	0.139	60.4	95.9[b]	83.4	−21.4	4.154[a]
Molybdenum	95.94	b.c.c.	10.2	380	0.251	4.8	5.39	138	96.2	0.915
Nickel	58.69	f.c.c.	8.90	390	0.445	13.4	7.01	90.7	ferro	
Niobium	92.91	b.c.c.	8.57	250	0.265	7.3	14.5[b]	53.7	241.1	9.25
Osmium	190.23	h.c.p.	22.59	400	0.130	5.1	9.13[b]	87.6	16.3	0.66
Palladium	106.42	f.c.c.	12.0	290	0.244	11.8	10.6	71.8	766.6	1.4
Platinum	195.08	f.c.c.	21.5	225	0.133	8.8	10.6	71.6	266.7	
Potassium	39.10	b.c.c.	0.89	98	0.757	83.3	7.28	102.4	5.7	
Rhenium	186.21	h.c.p.	20.8	275	0.137	6.2	18.6[b]	47.9	94.9	1.697
Rhodium	102.91	f.c.c.	12.4	350	0.243	8.2	4.78[b]	150	154.9	
Rubidium	85.47	b.c.c.	1.53	61	0.364	90	12.9	58.2	3.8	
Ruthenium	101.07	h.c.p.	12.1	450	0.238	6.4	7.37[b]	117	59.4	0.49
Selenium (gray)	78.96	Hexagonal	4.81	250	0.293	17.89 ($\parallel$c) 74.09 ($\perp$c)	$>10^{12}$ [c] $\sim10^{7}$ [c]	0.45 ($\parallel$c) 0.13 ($\perp$c)	−17.1	
Silicon	28.09	Diamond	2.328	700	0.702	2.49	$>10^{10}$ [c]	124	−3.2	
Silver	107.87	f.c.c.	10.5	220	0.235	18.9	1.60	429	−23.8	
Sodium	22.99	b.c.c.	0.97	160	1.225	71	4.81	141	8.5	
Strontium	87.62	f.c.c.	2.64	140	0.306	22.15	13.3	35.3	34.3	
Tantalum	180.95	b.c.c.	16.4	230	0.140	6.3	13.2	57.5	177.5	4.47
Tellurium	127.61	Hexagonal	6.23	180	0.197	18.0[c]	0.4×10^{6} [c]	3.38	−23.4	

Continued

Elements: Physical properties at room temperature (*Continued*)

Element	Atomic weight	Crystal structure	Density (298 K) [g/cm^3]	Debye temp. θ_D[a] (295 K) [K]	Specific heat (at const. press.) (298 K) [J/(g K)]	Coef. of thermal linear expansion (298 K) [10^{-6} K^{-1}]	Electrical resistivity (295 K) [$\mu\Omega$ cm]	Thermal conductivity (300 K) [W/m·K)]	Magnetic susceptibility[d] [10^{-6} SI]	Superconducting transition temperature[e] [K]
Thallium	204.38	h.c.p.	11.8	94	0.129	29.9	16.4[b]	46.1	−36.4	2.38
Thorium	232.04	f.c.c.	11.7	140	0.118	11.0	15[b]	54.0	61.4	1.38
Tin	118.71	Tetragonal	7.26	160	0.227	22.0	11.0[b]	66.6	−28.9	3.722
Titanium	47.88	h.c.p.	4.51	360	0.522	8.6	43.1[b]	21.9	178	0.40
Tungsten	183.84	b.c.c.	19.3	315	0.132	4.5	5.33[b]	174	69.9	0.0154
Uranium	238.03	Orthorhombic	19.1	160	0.116	13.9	25.7[b]	27.6	411.3	0.2
Vanadium	50.94	b.c.c.	6.0	380	0.489	8.4	19.9	30.7	429.5	5.40
Zinc	65.39	h.c.p.	7.14	240	0.388	30.2	5.94	116	−12.6	0.85
Zirconium	91.22	h.c.p.	6.52	250	0.278	5.7	42.4	22.7	107.5	0.61

Source: Unless otherwise noted, data are from the *CRC Handbook of Chemistry and Physics* (2002), 83rd edition, CRC Press, Boca Raton, FL.

[a] Values of the Debye temperature θ_D are from G. K. White (1987), *Experimental Techniques in Low-Temperature Physics*, Oxford University Press, Oxford, determined from specific heat data in the range $\theta_D/2-\theta_D$. These data were compiled from the *American Institute of Physics Handbook* (1972), 3rd edition, McGraw-Hill, New York; Touloukian et al., ed. (1970–1977), *Thermophysical Properties of Matter*, Plenum Press, New York; *Landolt–Börnstein*, Springer-Verlag, Berlin, 1968, 1971, etc.; and K. A. Gschneidner (1964), *Solid State Phys.* 16, 275–476.

[b] American Inst. of Physics Handbook (1972), 3rd edition, coordinating ed. D. E. Gray, Table 9d, p. 9–39, McGraw Hill, NY.

[c] G. K. White. and P. J. Meeson. (2002), *Experimental Techniques in Low-Temperature Physics*, 4th edition, Oxford University Press, Oxford.

[d] Magnetic susceptibility data were recalculated from molar susceptibilities given in the *CRC Handbook of Chemistry and Physics* (2000), 81st edition, CRC Press, Boca Raton, FL; and from compilations given in *Landolt–Börnstein, Numerical Data and Functional Relationships in Science and Technology*, New Series, II/16 (1986); III/19, subvolumes a to i2 (1986–1992); and II/2, II/8, II10, II11, and II12a, (1966–1984), Springer-Verlag, Heidelberg; *Tables de Constantes et Donnees Numerique* (1957), Vol. 7, *Relaxation paramagnetique*, Masson, Paris.

[e] Superconducting critical temperatures are from B. W. Roberts (1978), "Properties of selected superconductive materials," 1978 Supplement, *NBS Technical Note* 983, U.S. Government Printing Office, Washington, DC; tabulated in the *CRC Handbook of Chemistry and Physics* (2000), 81st edition, CRC Press, Boca Raton, FL. Note that thin films of these elements generally have higher critical temperatures than those listed here for bulk materials (see the CRC handbook).

A6.2 SPECIFIC HEAT vs. TEMPERATURE OF TECHNICAL MATERIALS (SEC. 6.1)

To convert these values of specific heat at constant pressure to *volumetric* heat capacity, multiply each value by the density of the material (densities of elements are given in Appendix A6.1).

Specific Heat C_P [J/(g K)] ≡ [10^{-3} J/(kg K)]

Material	4 K	10 K	20 K	30 K	50 K	77 K	100 K	150 K	200 K	300 K
Metals										
Al [a]	0.00026	0.00140	0.0089	0.032	0.142	0.336	0.481	0.684	0.797	0.902
Cu [a,b]	0.00009	0.00088	0.0070	0.027	0.097	0.192	0.252	0.323	0.356	0.386
Fe [a]	0.00038	0.00124	0.0045	0.012	0.055	0.144	0.216	0.323	0.384	0.447
In [a]	0.00095	0.0155	0.061	0.108	0.162	0.191	0.203	0.219	0.225	0.233
Nb [a]	0.00040	0.00220	0.0113	0.035	0.099	0.167	0.202	0.239	0.254	0.268
Ni [a]	0.00050	0.00162	0.0058	0.017	0.068	0.163	0.232	0.328	0.383	0.445
Si [a]	0.000017	0.00028	0.0034	0.017	0.079	0.177	0.259	0.425	0.556	0.714
Ti [a]	0.00032	0.00126	0.0070	0.025	0.099	0.218	0.300	0.407	0.465	0.522
W [a]	0.00004	0.00023	0.0019	0.008	0.332	0.682	0.089	0.114	0.125	0.136
Alloys										
Al 2024 [e]	—	—	—	—	—	0.478	0.534	0.639	0.736	0.855
Al-6061-T6 [f]	0.00029	0.00157	0.0089	0.033	0.149	0.348	0.492	0.713	0.835	0.954
Brass (65wt%Cu–35wt%Zn) [g]										
(yellow brass)	0.00015[e]	—	0.011	0.041	0.118	0.216	0.270	0.330	0.360	0.377
Constantan (60wt%Cu–										
40wt%Ni) [a]	0.00049	0.00169	0.0068	0.022	0.083	0.175	0.238	0.322	0.362	0.410
Inconel (77wt%Ni–15wt%Cr–										
7wt%Fe) [e]	—	—	—	—	—	0.275	0.291	0.334	0.369	0.427
Stainless steel 304L [f]	0.0017	0.0047	0.016	—	—	—	—	—	—	—
Stainless steel 310 [d]	0.0020	0.0052	0.017	0.01	0.10	0.20	0.25	0.35	0.40	0.48
Ti–6wt%Al–4wt%V [e]	—	—	—	0.007	0.098	0.217	0.300	0.410	0.477	0.529
Polymers and composites										
Epoxy (Stycast 2850FT™) [h]	0.0005	0.0063	0.0226	0.042	0.083	0.154	0.240	—	—	—
Epoxy (CY221) [c]	—	0.022	0.085	0.170	0.270	0.400	0.480	—	1.000	1.300
G-10CR [f] glass/resin	0.0020	0.0154	0.047	0.081	0.149	0.239	0.317	0.489	0.664	0.999
Glass/resin (S 901Glass/										
NASA Resin 2) [i]	0.00064	0.0067	0.028	0.050	0.094	0.169	0.262	0.56	0.96	1.94
Plexiglas™ (PMMA) [c]	—	0.017	0.080	0.147	0.280	0.420	0.550	—	0.920	—
Polyamide (Nylon™) [f]	0.0016	0.020	0.100	0.200	0.380	0.574	0.717	0.984	1.21	1.62
Polyimide (Kapton™) [f]	0.00079	0.0117	0.0579	0.116	0.224	0.338	0.414	0.537	0.627	0.755
Teflon™ (PTFE) [c]	—	0.026	0.079	0.126	0.210	0.310	0.392	0.550	0.677	0.870
Ceramics and nonmetals										
AlN [e]	—	—	—	—	—	0.074	0.139	0.305	0.471	0.739
Apiezon N™ [f]	0.00203	0.0243	0.0925	0.172	0.332	0.522	0.657	0.913	1.201	—
Carbon (diamond)[a]	—	0.00002	0.0001	0.000	0.002	0.008	0.020	0.084	0.195	0.518

(Continued)

Specific Heat C_p [J/(g K)] ≡ [10^{-3} J/(kg K)] (*Continued*)

Material	4 K	10 K	20 K	30 K	50 K	77 K	100 K	150 K	200 K	300 K
Ice [a]	0.00098	0.0152	0.114	0.229	0.440	0.689	0.882	1.230	1.570	—
MgO [a]	—	—	0.0022	0.006	0.024	0.101	0.208	0.465	0.680	0.940
Pyrex™ [a]	0.00020	0.0042	—	—	—	—	—	—	—	—
Sapphire (Al_2O_3) [e]	—	0.00009	0.0007	0.003	0.015	0.060	0.126	0.314	0.502	0.779
SiC [e]	—	—	—	—	—	0.052	0.107	0.253	0.405	0.676
Silica glass (SiO_2), Quartz crystal (SiO_2) [a]	—	0.00070	0.0113	0.035	0.097	0.185	0.261	0.413	0.543	0.745
$SrTiO_3$ [e]	—	—	—	—	—	0.181	0.246	0.358	0.439	0.536
ZrO_2 [e]	—	—	—	—	—	0.100	0.153	0.261	0.347	0.456

[a] R. J. Corruccini and J. J. Gniewek (1960), National Bureau of Standards Monograph 21, US Government Printing Office, Washington, DC.
[b] C. Y. Ho and A. Cezairliyan (1988), *Specific Heat of Solids*, Hemisphere Publishing Corp., New York.
[c] G. Hartwig (1994), *Polymer Properties at Room and Cryogenic Temperatures*, Plenum Press, New York.
[d] L. L. Sparks (1983), Chapter 2 in *Materials at Low Temperatures*, eds. R. P. Reed and A. F. Clark, ASM International, Materials Park, OH.
[e] Y. S. Touloukian and E. H. Buyco (1970), *Specific Heat*, Vols 4 and 5, Plenum Press, New York.
[f] R. Radebaugh et al. (2003), http://www.cryogenics.nist.gov/ and the references listed therein.
[g] G. K. White and P. J. Meeson (2002), *Experimental Techniques in Low-Temperature Physics*, 4th edition, Oxford University Press, Oxford.
[h] C. A. Swenson (1997), *Rev. Sci. Instrum.* 68, 1312–1315.
[i] E. W. Collings and R. D. Smith (1978), *Adv. in Cryog. Eng.* 24, 290–296.

A6.3 DEBYE MODEL VALUES OF THE MOLAR HEAT CAPACITY AND MOLAR INTERNAL ENERGY AS A FUNCTION OF TEMPERATURE (SECS 6.1.2 AND 6.1.3)

Tabulated values of the molar heat capacity are at constant volume, designated as C_V . Molar internal energy U is obtained by integrating the heat capacity, tabulated here as $(U - U_o)/T \equiv T^{-1} \int_0^T C_V \, dT$ and plotted in Fig. 6.2.

Values of the Debye temperature θ_D are tabulated for common elements in Appendix A6.1.

Molar heat capacity and molar internal energy

T/θ_D	θ_D/T	C_V [J/(mol K)]	$(U-U_o)/T \equiv T^{-1}\int_0^T C_V \, dT$ [J/(mol K)]
∞	0.0	24.94	24.94
10	0.1	24.93	24.02
5	0.2	24.89	23.12
2.5	0.4	24.74	21.40
2.0	0.5	24.63	20.58
1.667	0.6	24.50	19.78
1.25	0.8	24.16	18.25
1.0	1.0	23.74	16.82
0.833	1.2	23.24	15.48
0.714	1.4	22.66	14.24
0.625	1.6	22.02	13.08
0.556	1.8	21.33	12.00
0.500	2.0	20.59	11.00
0.400	2.5	18.60	8.83
0.333	3.0	16.53	7.07
0.286	3.5	14.48	5.66
0.250	4.0	12.55	4.53
0.222	4.5	10.78	3.64
0.200	5.0	9.195	2.93
0.1667	6.0	6.625	1.94
0.143	7.0	4.760	1.31
0.125	8.0	3.447	0.912
0.111	9.0	2.531	0.654
0.100	10.0	1.891	0.481
0.0909	11.0	1.440	0.363
0.0833	12.0	1.117	0.281
0.0769	13.0	0.882	0.221
0.0714	14.0	0.707	0.177
0.0625	16.0	0.474	0.119
0.0556	18.0	0.333	0.083
0.0500	20.0	0.243	0.061
0.0400	25.0	0.124	0.031
0.0333	30.0	0.072	0.018

Source: From G. T. Furukawa, T. B. Douglas, and N. Pearlman (1972), Chapter 4e in *American Institute of Physics Handbook*, McGraw-Hill, New York.

A6.4 THERMAL EXPANSION/CONTRACTION OF TECHNICAL MATERIALS (SEC. 6.2)

The total linear contraction from room temperature to the indicated temperature T is defined as

$$\Delta L/L \equiv (L_{293\,\mathrm{K}} - L_{\mathrm{T}})/L_{293\,\mathrm{K}}.$$

The coefficient of linear expansion at room temperature is defined as

$$\alpha \equiv (1/L)\, \mathrm{d}L/\mathrm{d}T.$$

Since the thermal expansion/contraction is approximately linear above room temperature, the total contraction from an upper reference temperature T_{u} above room temperature (such as soldering temperature) to a low temperature T can be determined approximately from

$$\Delta L/L_{T_u - T} = \Delta L/L_{293\,\mathrm{K}-T} + (\alpha_{293\,\mathrm{K}})(T_{\mathrm{u}} - 293\ \mathrm{K}).$$

Data on Invar, glasses, ceramics, and other materials having a very low thermal contraction are given in Figs 6.8 and 6.9. Thermal contraction data at 4 K and 77 K for a few additional materials are tabulated in Appendixes A7.4 and A7.5.

Thermal expansion/contraction of technical materials

Material	$\Delta L/L$ at 4 K [%]	$\Delta L/L$ at 40 K [%]	$\Delta L/L$ at 77 K [%]	$\Delta L/L$ at 100 K [%]	$\Delta L/L$ at 150 K [%]	$\Delta L/L$ at 200 K [%]	$\Delta L/L$ at 250 K [%]	α at 293 K [$10^{-6}\,\mathrm{K}^{-1}$]
Metals								
Ag [b]	0.413	0.405	0.370	0.339	0.259	0.173	0.082	18.5 [h]
Al [a]	0.415	0.413	0.393	0.370	0.295	0.201	0.097	23.1 [b]
Au [b]	0.324	0.313	0.281	0.256	0.195	0.129	0.061	14.1
Be [b]	0.131	0.131	0.130	0.128	0.115	0.087	0.045	11.3 [d]
Cu [a]	0.324	0.322	0.302	0.282	0.221	0.148	0.070	16.7 [i]
Fe [a]	0.198	0.197	0.190	0.181	0.148	0.102	0.049	11.6 [b]
Hg [b,*]	0.843	0.788	0.788	0.592	0.396	0.176	*	57.2 *
In [b]	0.706	0.676	0.602	0.549	0.421	0.282	0.135	32.0
Mo [b]	0.095	0.094	0.090	0.084	0.067	0.046	0.022	4.8 [d]
Nb [a]	0.143	0.141	0.130	0.121	0.094	0.063	0.030	7.3 [d]
Ni [a]	0.224	0.223	0.212	0.201	0.162	0.111	0.053	13.4 [d]
Pb [b]	0.708	0.667	0.578	0.528	0.398	0.263	0.124	29
Ta [b]	0.143	0.141	0.128	0.117	0.089	0.059	0.028	6.6
Sn [b] (white) [r]	0.447	0.433	0.389	0.356	0.272	0.183	0.086	20.5
Ti [a]	0.151	0.150	0.143	0.134	0.107	0.073	0.035	8.3 [b]
W [b]	0.086	0.085	0.080	0.075	0.059	0.040	0.019	4.5
Alloys								
Al-6061-T6 [c]	0.414	0.412	0.389	0.365	0.295	0.203	0.097	22.5
Brass (65%Cu–35%Zn) [b] (yellow brass)	0.384	0.380	0.353	0.326	0.253	0.169	0.080	19.1 [b]
Constantan (50%Cu–50%Ni) [b]	—	0.264	0.249	0.232	0.183	0.124	0.043	13.8 [b]

Thermal expansion/contraction of technical materials (*Continued*)

Material	$\Delta L/L$ at 4 K [%]	$\Delta L/L$ at 40 K [%]	$\Delta L/L$ at 77 K [%]	$\Delta L/L$ at 100 K [%]	$\Delta L/L$ at 150 K [%]	$\Delta L/L$ at 200 K [%]	$\Delta L/L$ at 250 K [%]	α at 293 K [$10^{-6}\,K^{-1}$]
Cu–2%Be–0.3%Co (Beryllium copper, Berylco 25) [b]	0.316	0.315	0.298	0.277	0.219	0.151	0.074	18.1 [b]
Fe–9%Ni [a]	0.195	0.193	0.188	0.180	0.146	0.100	0.049	11.5
Hastelloy C [q]	0.218	0.216	0.204	0.193	0.150	0.105	0.047	10.9 [c]
Inconel 718 [a]	0.238	0.236	0.224	0.211	0.167	0.114	0.055	13.0 [k]
Invar (Fe–36%Ni) [a]	—	0.040	0.038	0.036	0.025	0.016	0.009	3.0 [k]
50%Pb–50%Sn solder [a]	0.514	0.510	0.480	0.447	0.343	0.229	0.108	23.4 [d]
Stainless steel (AISI 304) [b]	0.296	0.296	0.281	0.261	0.206	0.139	0.066	15.1 [l]
Stainless steel (AISI 310) [b]	—	—	—	0.237	0.187	0.127	0.061	14.5
Stainless steel (AISI 316) [b]	0.297	0.296	0.279	0.259	0.201	0.136	0.065	15.2 [l]
Ti–6%Al–4%V [a]	0.173	0.171	0.163	0.154	0.118	0.078	0.036	8.0 [m]
Superconductors								
Bi-2212 *a,b*-axes [u,y]	0.152	0.150	0.139	0.132	0.106	0.074	0.036	8.3
Bi-2212 *c*-axis [u,y]	0.295	0.289	0.266	0.250	0.199	0.136	0.064	15.1
Bi-2223 *a,b*-axes [z,u,y]	0.15	0.15	0.14	0.13	0.11	0.07	0.04	8.3
Bi-2223 *c*-axis [z,u,y]	0.30	0.29	0.27	0.25	0.20	0.14	0.06	15
Bi (2223)/Ag tape [g] ($\geq$ 2nd cool-down)	—	0.31	0.30	0.28	0.22	0.15	0.07	13
Bi-2223/61%Ag-alloy tape [w,x]			0.24					
Nb_3Sn [a]	0.16	0.16	0.14	0.13	0.095	0.065	0.03	7.6 [t]
Nb_3Sn(10vol%)/Cu wire [s]	0.30		0.28					
Nb–45%Ti [a]	0.188	0.184	0.169	0.156	0.117	0.078	0.038	8.2
Nb–Ti/Cu wire [a]	0.265	0.262	0.247	0.231	0.179	0.117	0.054	12.5
YBCO *a*-axis [f]	—	—	0.12	0.12	0.10	0.070	0.04	7.4
YBCO *b*-axis [f]	—	—	0.16	0.15	0.13	0.10	0.05	9.6
YBCO *c*-axis [f]	—	—	0.34	0.33	0.25	0.17	0.09	17.7
Polymers								
Epoxy [a]	1.16	1.11	1.028	0.959	0.778	0.550	0.277	66
Epoxy (Stycast 2850FT™) [e]	0.44	0.43	0.40	0.38	0.32	0.225	0.12	28
CTFE (Teflon™) [a]	1.135	1.070	0.971	0.900	0.725	0.517	0.269	67 [b]
TFE (Teflon™) [a]	2.14	2.06	1.941	1.85	1.600	1.24	0.750	250 [n]
PMMA (Plexiglas™) [a]	1.22	1.16	1.059	0.99	0.820	0.59	0.305	75[o]
Polyamide (Nylon™) [a]	1.389	1.352	1.256	1.172	0.946	0.673	0.339	80
Polyimide (Kapton™) [c]	0.44	0.44	0.43	0.41	0.36	0.29	0.16	46
Composites [a]								
G-10CR epoxy/glass ($\parallel$ glass fibers)	0.241	0.234	0.213	0.197	0.157	0.108	0.052	12.5
G-10CR epoxy/glass (normal)	0.706	0.690	0.642	0.603	0.491	0.346	0.171	41 [p]

(Continued)

Thermal expansion/contraction of technical materials (*Continued*)

Material	$\Delta L/L$ at 4 K [%]	$\Delta L/L$ at 40 K [%]	$\Delta L/L$ at 77 K [%]	$\Delta L/L$ at 100 K [%]	$\Delta L/L$ at 150 K [%]	$\Delta L/L$ at 200 K [%]	$\Delta L/L$ at 250 K [%]	α at 293 K [10^{-6}K^{-1}]
Ceramics and nonmetals								
Al N ($\parallel a$-axis) [q]	—	—	0.032	0.031	0.028	0.020	0.011	3.7
Al N ($\parallel c$-axis) [q]	—	—	0.025	0.025	0.022	0.017	0.009	3.0
C (diamond) [b]	0.024	0.024	0.024	0.024	0.023	0.019	0.011	1.0
Glass (Pyrex™)	0.055	0.057	0.054	0.050	0.040	0.027	0.013	3.0 [o]
MgO[b]	0.139	0.139	0.137	0.133	0.114	0.083	0.042	10.2
Quartz ($\parallel$ optic axis) [b]	—	—	—	0.104	0.085	0.061	0.030	7.5
Sapphire (Al_2O_3) [m] ($\parallel c$-axis)	—	0.079	0.078	0.075	0.066	0.048	0.025	5.4 [q]
Si [b]	0.022	0.022	0.023	0.024	0.024	0.019	0.010	2.32
α-SiC (polycrystalline) [q]	—	—	0.030	0.030	0.029	0.024	0.013	3.7
Silica glass [b]	−0.008	−0.005	−0.002	−0.0001	0.002	0.002	0.002	0.4

Definitions: $\Delta L/L \equiv (L_{293\,K} - L_T)/L_{293\,K}$; $\alpha \equiv (1/L)\,\mathrm{d}L/\mathrm{d}T$.

* For mercury, all data are referenced to its solidification temperature, 234 K.

[a] A. F. Clark (1983), Chapter 3 in *Materials at Low Temperatures*, ASM International, Materials Park, OH.

[b] R. J. Corruccini, and J. J. Gniewek. (1961), *Thermal Expansion of Technical Solids at Low Temperatures*, National Bureau of Standards Monograph 29, US Government Printing Office, Washington, DC.

[c] R. Radebaugh, et al. (2001), http://www.cryogenics.nist.gov/ and the references listed therein.

[d] *CRC Handbook of Chemistry and Physics* (2001), 82nd edition, CRC Press, Boca Raton, FL.

[e] C. A. Swenson (1997), *Rev. Sci. Instrum*. 68, 1312–1315.

[f] Calculated from data by H. You, J. D. Axe, X. B. Kan, S. Hashimoto, S. C. Moss, J. Z. Liu, G. W. Crabtree, and D. J. Lam (1988), *Phys. Rev*. B38, 9213–9216.

[g] N. Yamada, K. Nara, M. Okaji, T. Hikata, T. Kanedo, and N. Sadakata (1998), *Cryogenics* 38, 397–399.

[h] V. J. Johnson, ed. (1961), *Properties of Materials at Low Temperature, Phase 1*, US Government Printing Office, Washington, DC.

[i] T. A. Hahn (1970), *J. Appl. Phys*. 41, 5096–5101.

[j] N. J. Simon, E. S. Drexler, and R. P. Reed (1992), *Properties of Copper and Copper Alloys at Cryogenic Temperatures*, NIST Monograph 177, US Government Printing Office, Washington, DC; N. Cheggour and D. P. Hampshire, *Rev. Sci. Instr*. 71, 4521–4529 (2000).

[k] A. F. Clark (1968), *Cryogenics* 8, 282–289.

[l] *Handbook on Materials for Superconducting Machinery* (1974, 1976), National Bureau of Standards, US Government Printing Office, Washington, DC.

[m] V. Arp, J. H. Wilson, L. Winrich, and P. Sikora (1962), *Cryogenics* 2, 230–235.

[n] R. K. Kirby (1956), *J. Res. Natl. Bur. Stand*. 57, 91–94.

[o] H. L. Laquer and E. L. Head (1952), *Low Temperature Thermal Expansion of Plastics*. AECU-2161, Technical Information Service A.E.C., Oak Ridge, TN.

[p] A. F. Clark, G. Fujii, and M. A. Ranney (1981), *IEEE Trans. Magn*. MAG-17, 2316–2319.

[q] Y. S. Touloukian, *Thermal Expansion* 12, 1248.

[r] Tin is anisotropic. Mean values were calculated as 1/3($\parallel$) + 2/3($\perp$), where ($\parallel$) and ($\perp$) signify the contraction parallel and perpendicular to the tetragonal axis. White tin is the ordinary ductile variety; it may transform to brittle gray tin (with a diamond-type lattice) at low temperatures, but usually it does not because of impurity stabilization. (See ref. b for more information.)

[s] L. F. Goodrich, S. L. Bray, and T. C. Stauffer (1990), *Adv. Cryog. Eng. (Mater.)* 36A, 117–124.

[t] D. S. Easton, D. M. Kroeger, W. Specking, and C. C. Koch (1980), *J. Appl. Phys*. 51, 2748.

[u] M. Okaji, K. Nara, H. Kato, K. Michishita, and Y. Kubo (1994), *Cryogenics* 34, 163.

[v] S. Ochiai, K. Hayashi, and K. Osamura (1991), *Cryogenics* 31, 959.

[w] E. Harley (2004), American Superconductor Corp., personal communication.

[x] J. P. Voccio, O. O. Ige, S. J. Young, and C. C. Duchaine (2001), *IEEE Trans. Appl. Supercon*. 11, 3070–3073.

[y] M. Mouallem-Bahout, J. Gaudé, G. Calvarin, J.-R. Gavarri, and C. Carel, (1994), *Mater. Lett*. 18, 181–185.

[z] Data are for Bi-2212 oriented crystals, but the atomic structures of the Bi-2223 and Bi-2212 phases are close enough that the Bi-2212 crystal data should approximately apply to both.

A6.5a IDEAL ELECTRICAL RESISTIVITY vs. TEMPERATURE FOR PURE METALS (SEC. 6.3)

The *ideal* resistivity $\rho_i(T)$ is tabulated below for *ideally* pure metals. The *total* resistivity $\rho(T)$ of *nearly* pure metals is approximated by summing the temperature-dependent ideal resistivity $\rho_i(T)$ and the temperature-*in*dependent residual resistivity ρ_{res} (that arises from defects). This is expressed as Matthiessen's rule:

$$\rho(T) \equiv \rho_{res} + \rho_i(T).$$

(Deviations from Matthiessen's rule are briefly described in Sec. 6.3.4.)

In nearly pure metals, ρ_{res} is highly variable from specimen to specimen, because ρ_{res} depends on trace impurity levels and cold-work conditions. Therefore, it must be measured on an individual material basis (typically with a dip test in liquid helium) or estimated from such a measurement on a similar material. The total resistivity is then calculated from the above equation.

The *Residual Resistance Ratio* (RRR $\equiv R_{RT}/R_{4\,K} = \rho_{295\,K}/\rho_{4\,K}$) is often used as an indicator of sample purity for pure metals [i.e. the residual resistivity $\rho_{res} \approx \rho_{4\,K} = \rho_{i\,295\,K}/(\text{RRR}-1)$]. The higher the value of RRR, the lower ρ_{res}, and the more defect-free the metal. (Appendix A3.1 lists RRR values for common conductor materials, which can be used to estimate ρ_{res}; an example is given in Sec. 6.3.4.)

Values of the ideal resistivity $\rho_i(T)$ tabulated below were determined experimentally by assuming the validity of Matthiessen's rule and subtracting the measured value of ρ_{res} from precise measurements of the total $\rho(T)$ measured for very pure metals.

For convenience, the *total* resistivities of two oxygen-free copper (OFHC) samples are also listed, one with RRR $\cong$ 100, and the other 60% cold-drawn. Unlike the rest of the data, entries for these two material listings are not *ideal* resistivities and apply only to copper samples of comparable RRR or cold work.

Resistivity data at room temperature for additional elements are given in Appendix A6.1.

A6.5a Pure metal ideal resistivity ρ_i [$\Omega\,m \times 10^{-8} \equiv \mu\Omega\,cm$]

Pure metal	10 K	20 K	50 K	77 K	100 K	150 K	200 K	250 K	295 K
[RRR $\equiv \rho_{RT}/\rho_{4\,K}$]									
Ag (RRR = 1800)[a]	0.0001	0.003	0.103	0.27	0.42	0.72	1.03	1.39	1.60
Al (RRR = 3500)[a]	—	0.0007	0.047	0.22	0.44	1.01	1.59	2.28	2.68
Au (RRR = 300)[b]	0.0006	0.012	0.20	0.42	0.62	1.03	1.44	1.92	2.20
Cu (RRR = 3400)[k]	—	0.0010	0.049	0.19	0.34	0.70	1.05	1.38	1.69
Cu(OFHC) (RRR $\cong$ 100)[i] (*total* ρ)	0.015	0.017	0.084	0.21	0.34	0.70	1.07	1.41	1.70
Cu (OFHC) (60% cold drawn)[i] (*total* ρ)	0.030	0.032	0.10	0.23	0.37	0.72	1.09	1.43	1.73
Fe (RRR = 100)[c]	0.0015	0.007	0.135	0.57	1.24	3.14	5.3	7.55	9.8
In (RRR = 5000)[d]	0.018	0.16	0.92	1.67	2.33	3.80	5.40	7.13	8.83
Nb (RRR = 213)[e]	—	0.062	0.89	2.37	3.82	6.82	9.55	12.12	14.33
Ni (RRR = 310)[c]	—	0.009	0.15	0.50	1.00	2.25	3.72	5.40	7.04
Pb (RRR = 14000,[f] RRR = 10^5)[g]	—	0.53[f]	2.85[f]	4.78[f]	6.35[g]	9.95[g]	13.64[g]	17.43[g]	20.95[g]
Pt (RRR = 600)[c]	0.0029	0.036	0.72	1.78	2.742	4.78	6.76	8.70	10.42
Ta (RRR = 77)[c]	0.0032	0.051	0.95	2.34	3.55	6.13	8.6	11.0	13.1
Ti (RRR = 20)[h]	—	0.020	1.4	4.45	7.9	16.7	25.7	34.8	43.1
W (RRR = 100)[j]	0.0002	0.0041	0.150	0.56	1.03	2.11	3.20	4.33	5.36

(Footnotes continued)

A6.5a Pure metal ideal resistivity ρ_i [$\Omega\,m \times 10^{-8} \equiv \mu\Omega\,cm$] *(continued)*

[a] R. S. Seth and S. B. Woods (1970), *Phys. Rev*. B2, 2961; J. Bass, ed. (1982), *Landolt–Börnstein*, Vol. III/15a, *Metals: Electronic Transport Phenomena*, Springer-Verlag, Berlin.

[b] D. Damon, M. P. Mathur, and P. G. Klemens (1968), *Phys. Rev*. 176, 876; J. Bass, ed. (1982), *Landolt–Börnstein*, Vol. III/15a *Metals: Electronic Transport Phenomena*, Springer-Verlag, Berlin.

[c] G. K. White and S. B. Woods (1959), *Philos. Trans. Roy. Soc*. A251, 273; J. Bass, ed. (1982), *Landolt–Börnstein*, Vol. III/15a, *Metals: Electronic Transport Phenomena*, Springer-Verlag, Berlin.

[d] G. K. White and S. B. Woods (1957), *Rev. Sci. Instrum*. 28, 638; J. Bass, ed. (1982), *Landolt–Börnstein*, Vol. III/15a, *Metals: Electronic Transport Phenomena*, Springer-Verlag, Berlin.

[e] J. M. Abraham, C. Tete, and B. Deviot (1974), *J. Less-comm. Met*. 37, 181; J. Bass, ed. (1982), *Landolt–Börnstein*, Vol. III/15a, *Metals: Electronic Transport Phenomena*, Springer-Verlag, Berlin.

[f] B. N. Aleksandrov and I. G. D'Yakov (1963), *Sov. Phys. JETP* (English Transl.) 16, 603–608; *Zh. Eksp. Teor. Fiz*. (1962) 43, 399; J. Bass, ed. (1982), *Landolt–Börnstein*, Vol. III/15a, *Metals: Electronic Transport Phenomena*, Springer-Verlag, Berlin.

[g] J. P. Moore and R. S. Graves (1973), *J. Appl. Phys*. 44, 1174; J. Bass, ed. (1982), *Landolt–Börnstein*, Vol. III/15a, *Metals: Electronic Transport Phenomena*, Springer-Verlag, Berlin.

[h] R. J. Wasilewski (1962), *Trans. Met. Soc. AIME* 224, 13; J. Bass, ed. (1982), *Landolt–Börnstein*, Vol. III/15a, *Metals: Electronic Transport Phenomena*, Springer-Verlag, Berlin.

[j] J. G. Hust (1976), *High Temp.– High Press*. 8, 377–390.

[k] J. S. Dugdale (1965), unpublished data, University of Leeds, Leeds, UK.

A6.5b TOTAL ELECTRICAL RESISTIVITY vs. TEMPERATURE FOR TECHNICAL ALLOYS AND COMMON SOLDERS (SEC. 6.3)

For *alloys*, values of the *total* resistivity $\rho(T)$ are tabulated [i.e. $\rho(T) \equiv \rho_{res} + \rho_i(T)$], since there is little specimen-to-specimen variation in the residual resistivity contribution from defects.

Resistivities of solder alloys at room temperature are tabulated in Appendix A3.7.

A6.5b Alloy total resistivity ρ_i [$\Omega\,m \times 10^{-8} \equiv \mu\Omega\,cm$]

Alloy	10 K	20 K	50 K	77 K	100 K	150 K	200 K	250 K	295 K
Al 1100–0	0.08	0.08	0.16	0.32	0.51	1.07	1.72	2.37	2.96
Al 5083–0	3.03	3.03	3.13	3.33	3.55	4.15	4.79	5.39	5.92
Al 6061–T6	1.38	1.39	1.48	1.67	1.88	2.46	3.09	3.68	4.19
Hastelloy C	123	123	123	124	—	—	126	—	127
Inconel 625	124	124	125	125	—	—	127	—	128
Inconel 718	108	108	108	109	—	—	114	134	156
Berylco 25 (Cu–2%Be–0.3%Co)	6.92	6.92	7.04	7.25	7.46	7.96	8.48	8.98	9.43
Phosphor bronze A	8.58	8.58	8.69	8.89	9.07	9.48	9.89	10.3	10.7
Cartridge brass (70%Cu–30%Zn)	4.22	4.22	4.39	4.66	4.90	5.42	5.93	6.42	6.87
CuNi 30 (67Ni–30Cu) (Monel)	36.4	36.5	36.6	36.7	36.9	37.4	37.9	38.3	38.5
Ti–6%Al–4%V	—	147	148	150	152	157	162	166	169
Stainless steel (304 L)	49.5	49.4	50.0	51.5	53.3	58.4	63.8	68.4	72.3
Stainless steel (310)	68.6	68.8	70.4	72.5	74.4	78.4	82.3	85.7	88.8
Stainless steel (316)	53.9	53.9	54.9	56.8	58.8	63.8	68.9	73.3	77.1
Invar (Fe–36%Ni)	50.3	50.5	52.1	54.5	57.0	63.3	70.0	76.5	82.3

Source: Values were interpolated with a cubic spline fit to data obtained by A. F. Clark, G. E. Childs, and G. H. Wallace (1970), *Cryogenics* 10, 295–305.

A6.6 SUPERCONDUCTOR PROPERTIES (SEC. 6.3.6)

Property values of these high-field superconductors are representative because there is some variation with sample composition, inhomogeneities, and impurity levels.

Additional data on critical-temperature values of superconducting *elements* are included in the general table of Appendix A6.1

Superconductor properties

Superconductor	Crystal structure*	Lattice constants [Å]†			T_c [K]	$\mu_0 H_{c2}(0\ \mathrm{K})$ [T]	$\lambda_{GL}(0\ \mathrm{K})$‡ [nm]	$\xi_{GL}(0\ \mathrm{K})$ζ [nm]
		a	*b*	*c*				
Low T_c								
Nb–Ti [e]	A2				9.3 [j]	13	300	4
V_3Ga [e]	A15	4.816 [n]	—	—	15	23	90	2–3
V_3Si [e]	A15	4.722 [n]	—	—	16	20	60	3
Nb_3Sn [e]	A15	5.289 [n]	—	—	18	23	65	3
Nb_3Al [o]	A15	5.187 [n]	—	—	18.9	32		
Nb_3Ga [o]	A15	5.171 [n]	—	—	20.3	34		
$Nb_3(Al_{75}Ge_{25})$ [b]	A15				20.5	41		
Nb_3Ge [e]	A15	5.166 [n]	—	—	23	38	90	3
NbN [e]	B1				16	15	200	5
$V_2(Hf,Zr)$ [o]	C15				10.1	24		
$PbMo_6S_8$ [e]	Chevrel				15	60	200	2
MgB_2	hexagonal	3.086[m]	—	3.521[m]	39	~16 (*a*, *b*)[l] ~2.5 (*c*)	140[k]	5.2[k]
High T_c [a]								
$La_{1.85}Sr_{0.15}CuO_{4-\delta}$ [e]	I4/mmm	3.779	3.779	1.323	40	50	80 (*a*, *b*) 400 (*c*)	~4 (*a*, *b*) 0.7 (*c*)
$YBa_2Cu_3O_{7-\delta}$ [d] (YBCO)	Pmmm	3.818	3.884	11.683	90	670 (*a*, *b*) 120 (*c*)	150 (*a*, *b*) 900 (*c*)	~2 (*a*, *b*) 0.4 (*c*)
$Bi_2Sr_2CaCu_2O_{8-\delta}$ [d] (Bi-2212)	A2aa	5.410	5.420	30.930	90	280 (*a*, *b*) 32 (*c*)	300 (*a*, *b*)	~3 (*a*, *b*) 0.4 (*c*)
$(Bi,Pb)_2Sr_2Ca_2Cu_3O_{10+\delta}$ (Bi-2223)	Perovskite (orthorhombic)	5.39	5.40	37	110			
$Tl_2Ba_2CaCu_2O_{8+\delta}$ [d,p] (Tl-2212)	I4/mmm	3.856	3.856	29.260	110		215 (*a*, *b*) 480 (*c*)	2.2 (*a*, *b*) 0.5 (*c*)
$Tl_2Ba_2Ca_2Cu_3O_{10-\delta}$ [d,p] (Tl-2223)	I4/mmm	3.850	3.850	35.88	125	120	205 (*a*, *b*) 480 (*c*)	1.3 (*a*, *b*)
$HgBa_2Ca_2Cu_3O_{8+\delta}$ [a]	Pmmm	3.85	—	15.85	133	160[q]		1.42 (*a*, *b*)[q]

Notation:

* Crystal structures for the low-T_c superconductors are listed here mostly by the Strukturbericht designation, whereas for the high-T_c materials they are mostly listed by the Space group designation. Tables of cross lists to different nomenclatures are given in the appendixes to the *ASM Handbook* (1992), Vol. 3, *Alloy Phase Diagrams*, ASM International, Materials Park, OH.

† (*a*, *b*) refers to magnetic field, penetration depth, or coherence length being coplanar with the *a*, *b* crystallographic direction or Cu–O planes (usually parallel to the flat faces of practical conductors); (*c*) refers to an orientation along the *c*-axis; that is, perpendicular to the Cu–O planes (usually perpendicular to the flat faces of most practical conductors).

‡ The penetration depth $\lambda_{GL}(0\ \mathrm{K})$ is the constant prefactor in the Ginzburg–Landau expression $\lambda_{GL}(T) = \lambda_{GL}(0\ \mathrm{K})(1 - T/T_c)^{-0.5}$.

ζ The coherence length $\xi_{GL}(0\ \mathrm{K})$ is the constant prefactor in the Ginzburg–Landau expression $\xi_{GL}(T) = \xi_{GL}(0\ \mathrm{K})(1 - T/T_c)^{-0.5}$.

(References continued)

References:

[a] *CRC Handbook of Chemistry and Physics* (2002), 83rd edition, CRC Press, Boca Raton, FL.

[b] G. Bogner (1977), "Large scale applications of superconductivity," in *Superconductor Applications: SQUIDS and Machines*, eds. B. B. Schwartz and S. Foner, Plenum, New York.

[c] B. W. Roberts (1978), *Properties of Selected Superconducting Materials*, NBS Technical Note 983, US Government Printing Office, Washington, DC.

[d] T. Datta (1992), "Oxide superconductors: physical properties," in *Concise Encyclopedia of Magnetic and Superconducting Materials*, ed. J. Evetts, pp. 414–423, Pergamon Press, Oxford; Elmsford, NY.

[e] R. J. Donnelly (1981), in *Physics Vade Mecum*, ed. H. L. Anderson, American Institute of Physics, p. 118–132, New York, NY; T. P. Orlando and K. A. Delin (1991), *Foundations of Applied Superconductivity*, Addison-Wesley, Reading, MA.

[j] L. F. Goodrich and T. C. Stauffer (2003), unpublished data, National Institute of Standards and Technology, Boulder, CO.

[k] D. K. Finnemore, J. E. Ostenson, S. L. Bud'ko, G. Lapertot, and P. C. Canfield (2001), *Phys. Rev. Lett*. 86, 2420–2422.

[l] P. C. Canfield and G. W. Crabtree (2003), *Physics Today* 56, 34–40.

[m] T. Vogt, G. Schmneider, J. A. Hriljac, G. Yang, and J. S. Abell (2001), *Phys. Rev*. B 63, 220505/1–3.

[n] M. Weger and I. B. Goldberg (1973), p. 2–178 in *Solid State Physics*, Vol. 28, eds. H. Ehrenreich, F. Seitz, and D. Turnbull, Academic Press, New York, NY.

[o] J. W. Ekin (1983), Chapter 13 in *Materials at Low Temperatures*, eds. R. P. Reed and A. F. Clark, ASM International, Materials Park, OH.

[p] E. Bellingeri and R. Flükiger (2003), in *Handbook of Superconducting Materials*, Vol. 1, eds., D. A. Cardwell and D. S. Ginley, Institute of Physics Publishing, pp. 993–1027, Philadelphia, PA.

[q] J. Schwartz and P. V. P. S. S. Sastry (2003), in *Handbook of Superconducting Materials*, Vol. 1, eds., D. A. Cardwell and D. S. Ginley, Institute of Physics Publishing, pp. 1029–1048, Philadelphia, PA.

A6.7 THERMAL CONDUCTIVITY vs. TEMPERATURE FOR SELECTED METALS, ALLOYS, GLASSES, AND POLYMERS (SEC. 6.4)

Additional thermal-conductivity data for various amorphous solids (vitreous silica, germania, selenium) and amorphous materials (polystyrene and PMMA) are shown in Fig. 6.14. Thermal conductivity integrals are tabulated for selected cryostat construction materials in Appendix A2.1. Properties of metals with very high thermal conductivities are given in Appendix A3.1.

Thermal conductivity [W/(m·K)]

Material	4 K	10 K	20 K	40 K	77 K	100 K	150 K	200 K	295 K
Metals and alloys									
Al 5083[a]	3.3	8.4	17	33	55	66	85	99	118
Al 6061-T6[a]	5.3	14	28	52	84	98	120	136	155
Beryllium–copper[a]	1.9	5.0	11	21	36	41	41	31	9.7
Brass (UNS C36000) (61.5wt%Cu–35.4wt%Zn–3.1st%Pb)[b]	2.0	5.7	12	19	29	40	47	64	86
Brass (68wt%Cu–32wt%Zn)[d]	3.0	10	22	38	53	—	—	—	—
Copper OFHC (RRR ≈ 100)[a]	630	1540	2430	1470	544	461	418	407	397
Inconel 718[a]	0.46	1.5	3.0	4.7	6.4	7.1	8.1	8.7	9.7
Invar[b]	0.24	0.73	1.7	2.6	4.2	6.2	7.6	10	12
Manganin (Cu–12wt%Mn–3wt%Ni)[d]	0.44	1.4	3.2	6.8	11	—	—	—	—
Soft-solder (Sn–40wt%Pb)[d]	16	43	56	53	53	—	—	—	—
Stainless steel 304,316[a]	0.27	0.90	2.2	4.7	7.9	9.2	11	13	15
Ti (6%Al–4%V)[a]	—	—	0.84	1.9	3.5	3.8	4.6	5.8	7.4
Polymers									
G-10CR (Normal)[a]	0.072	0.11	0.16	0.22	0.28	0.31	0.37	0.45	0.60
G-10CR (Warp)[a]	0.073	0.14	0.20	0.27	0.39	0.45	0.57	0.67	0.86
HDPE[c]	0.029	0.090	—	—	0.41	0.45	—	—	0.40
Kevlar 49[a]	0.030	0.12	0.29	0.59	1.0	1.2	1.5	1.7	2.0
PMMA (Plexiglas™)[c]	0.033	0.060	—	—	—	0.16	0.17	0.18	0.20
Polyamide (Nylon™)[a]	0.012	0.039	0.10	0.20	0.29	0.32	0.34	0.34	0.34
Polyimide (Kapton™)[a]	0.011	0.024	0.048	0.083	0.13	0.14	0.16	0.18	0.19
Polyethylene terepthalate (Mylar™)[b]	0.038	0.048	0.073	0.096	0.12	—	—	—	—
PVC[c]	0.027	0.040	—	—	—	0.13	0.13	0.13	0.14
PTFE (Teflon™)[a]	0.046	0.10	0.14	0.20	0.23	0.24	0.26	0.27	0.27

(Continued)

Thermal conductivity [W/(m·K)] (*Continued*)

Material	4 K	10 K	20 K	40 K	77 K	100 K	150 K	200 K	295 K
Ceramics and nonmetals									
Alumina (Al_2O_3, sintered)[d]	0.49	5.6	24	80	157	136	93	50	—
Macor™ [e]	0.075	0.25	0.60	—	—	—	—	—	—
MgO (crystal)[d]	82	1130	2770	2160	507	294	135	91	61
Pyrex™ glass[d]	0.10	0.12	0.15	0.25	0.45	0.58	0.78	0.92	1.1
Sapphire (Al_2O_3, synthetic crystal)[d,f]	230	2900	15700	12000	1100	450	150	82	47
α-SiC (single crystal, $\perp$ to c-axis)[d]	27	420	2000	4700	4000	3000	1500	950	510
SiO_2 crystal (avg. of $\parallel$ and $\perp$ to c-axis)[d]	185	1345	545	134	43	30	18	13	9

[a] Cryogenic Materials Properties Program CD, Release B-01 (June 2001), Cryogenic Information Center, 5445 Conestoga Ct., Ste. 2C, Boulder, CO 80301-2724, Ph. (303) 442-0425, Fax (303) 443-1821.
[b] R. Radebaugh et al. (2003), http://www.cryogenics.nist.gov/ and the references listed therein.
[c] G. Hartwig (1994), *Polymer Properties at Room and Cryogenic Temperatures*, Plenum Press, New York.
[d] Y. S. Touloukian and E. H. Buyco (1970), *Thermal Conductivity*, Vols 1 and 2, Plenum Press, New York.
[e] W. N. Lawless (1975), *Cryogenics*, 15, 273–277.
[f] For sapphire, the direction of heat flow is 60° to the hexagonal axis; values are thought to be accurate to within 10–15% at temperatures above 60 K, but highly sensitive to small physical and chemical variations below 60 K.

A6.8a MAGNETIC MASS SUSCEPTIBILITY FROM 1.6 K TO 4.2 K OF MATERIALS COMMONLY USED IN CRYOSTAT CONSTRUCTION (SEC. 6.5)

Mass susceptibility is useful for small samples or irregularly shaped parts where the mass of the sample is more easily determined than its volume. It is not difficult, however, to convert between the two with the relation

$$(\text{mass susceptibility } \chi/\rho) \equiv (\text{volume susceptibility } \chi) \,/\, (\text{density in kg/m}^3).$$

Mass susceptibility is defined as $\chi/\rho \equiv \sigma/H$, where σ is the magnetic moment per unit mass and H is the magnetic intensity.

The coefficients B and C tabulated below (fourth and fifth columns) are used to calculate mass susceptibility in the temperature range 1.6–4.2 K through the Curie law

$$\chi/\rho \equiv B + (C/T).$$

Mass susceptibility χ/ρ has been evaluated at 4.2 K in the third column.

Values are tabulated in SI units (mks). To convert to cgs units, divide the values in this table by $4\pi \times 10^{-3}$ to get χ/ρ in cm^3/g; see Appendix A1.4.

Magnetic mass susceptibility χ/ρ from 1.6 K to 4.2 K

Material	Supplier	χ/ρ at 4.2 K $[10^{-8}\,m^3/kg]$	B at 1.6–4.2 K $[10^{-8}\,m^3/kg]$	C at 1.6–4.2 K $[10^{-8}\,m^3K/kg]$
Dielectric structural materials				
Alumina[a]	Alcoa	2.8	1.0 ± 0.8	7.5 ± 2
Alscobond Y-725™ and catalyst[c]	Alloy Supply Co.	−9.4	−3.3 ± 0.1	−25.5
Bakelite™, type 950[c]	Thiokil Chemical Co.	0.3	0.7 ± 0.16	−1.8
Epibond 100A™ [b]	Furane Plastics, Inc.	−0.5	−0.5 ± 0.1	0.1 ± 0.2
Epibond 104™ [a]	”	60	30 ± 3	160 ± 10
Epibond 121™ [a]	”	0.4	0.1 ± 1	1 ± 3.1
Glass				
Plate 7740[a]	Corning Glass Co.	14	3.8 ± 1	44 ± 5
Test tubes, Pyrex™ [a]	”	7.3	2.5 ± 1	20 ± 4
Tubing 7740[a]	”	5.6	2.0 ± 1	15 ± 4
Lava, grade A[c]	American Lava Corp.	−21.1	−4.2 ± 0.7	−71
Nylon™ 101, type 66[b]	Polypenco Ltd.	−0.81	−0.79 ± 0.01	−0.08 ± 0.03
PTFE (Teflon™) [b]	”	−0.40	−0.41 ± 0.01	0.06 ± 0.01
Resin 3135 w/catalyst 7111[c]	Crest Products Co.	1.24	1.44 ± 0.2	−0.86
Resin 3170 w/catalyst 7133[c]	”	0.53	0.59 ± 0.017	−0.25
Resin 7343 w/catalyst 7139[c]	”	1.70	2.24 ± 0.18	−2.24
Quartz[a]		3	4 ± 1.9	−4.4 ± 4.4
Silica				
No washing[a]	Fisher Scientific Co.	1.2	1.8 ± 0.5	−2.3 ± 2.3
Acid washing[a]		−0.1	−0.3 ± 0.9	0.6 ± 1.9
Stycast 2850GT™ w/catalyst No. 9[a]		27	19 ± 5	33 ± 9
Tufnol™, Carp brand[b]	Tufnol Ltd.	0.5	−0.3 ± 0.3	3.0 ± 0.5
Fibrous materials				
Absorbent cotton[a]	New Aseptic Labs, Inc.	570	380 ± 40	800 ± 100
Felt[a]	McMaster-Carr	60	42 ± 16	75 ± 50
Pyrex wool™ [a]	Corning Glass Co.	240	150 ± 30	380 ± 50
Thread (white)[a]	Coates and Clark Co.	−15.3	−19 ± 16	15 ± 38
Fluids				
Apiezon “J”™ oil[a]	James G. Biddle Co.	−0.19	−0.04 ± 0.18	−0.6 ± 4
Apiezon “N”™ grease[a]	”	−0.5	0.1 ± 1.5	−2.5 ± 0.4
Aquadag™ [a]	Colloids Corp.	15	15 ± 2	0.1 ± 5
RTV-102™ adhesive[c]	General Electric	0.79	1.2 ± 0.5	−1.62
Silicone-oil 50 cs[a]	Dow-Corning	1.7	1.6 ± 1.6	0.1 ± 4
GE 7031™ Varnish-toluene				
(1:1 mixture)[a]	General Electric	0.4	3 ± 2	−9 ± 4

(Continued)

Magnetic mass susceptibility χ/ρ from 1.6 K to 4.2 K (*Continued*)

Material	Supplier	χ/ρ at 4.2 K $[10^{-8}\,m^3/kg]$	B at 1.6–4.2 K $[10^{-8}\,m^3/kg]$	C at 1.6–4.2 K $[10^{-8}\,m^3K/kg]$
Metals				
Brass[a]	Central Steel and Wire Co.	−235	−226 ± 25	−38 ± 13
Copper magnet wire				
Formex insulated[a]	Anaconda Copper Co.	0.04	0.04 ± 1.3	0.01 ± 1.9
Sodereze insulated[a]	Phelps Dodge Inc.	0.1	0.6 ± 0.9	−2.0 ± 2.1
Evanohm				
Double silk covered[a]	Wilbur B. Driver Co.	86.0	−3.8 ± 7.5	377 ±38
Formex insulated[a]	”	155	11 ± 18	603 ± 75
Manganin, enamel insulated[a]	Driver-Harris Inc.	147	151 ± 13	−16 ± 4
Phosphor bronze[c]	Central Steel and Wire Co.	2.1	2.9 ± 1.1	−3.3
Beryllium copper Berylco 25[c]	Meier Brass and Aluminum	254	254 ± 1.9	0.0
Stainless steels				
303[a]	Central Steel and Wire Co.	148	144 ± 19	13 ± 13
304[a]	”	134	136 ± 11	−7.2 ± 6
316[a]	”	361	392 ± 31	−130 ± 25
321[a]	”	133	126 ± 13	31 ± 13
347[a]	”	215	250 ± 120	−150 ± 190
Sheets and tapes				
Kapton™ H film[c]	Du Pont	0.8	1.3 ± 0.7	−2.1
Mylar™ [a]	Du Pont	63	63 ± 9	1.9 ± 8
Paper				
White[a]	W. M. Morgan Putnam Co.	4	−0.3 ± 3	18 ± 9
Black (photographic)[a]	”	3	1 ± 4	6 ± 8
Tapes				
Cellophane™ [a]	Minn. Mining and Mfg. Co.	0.7	0.1 ± 2	2 ± 6
Glass #27[a]	”	30	9 ± 2	88 ± 10
Masking (Tuck Tape)[a]	Technical Tape Corp.	11	10 ± 2	3 ± 5
Special				
Cupro-Nickel (70–30)[a]	Superior Tube Co.	480	480 ± 100	
Eccosorb LS-22™ foam sheet[c]	Emerson and Cuming Inc.	−0.6	1.2 ± 0.9	−7.7
Germanium resistor[c]	Cryocal Inc.	6330	6380 ± 48	−215
Inconel™ [a]	Superior Tube Co.	2.6×10^5	$(3.3 \pm 0.25)\times10^5$	$(-2.9 \pm 0.25)\times10^5$
SC-13™ flexible silver micropaint[a]	Microcircuits Co.	1.5×10^4	$(1.3 \pm 0.9)\times10^4$	$(0.87 \pm 0.09)\times10^4$
Rubber (Neoprene™)[a]	Microdot Inc.	35	16 ± 24	78 ± 56

[a] G. L. Salinger and J. C. Wheatley (1961), *Rev. Sci. Instrum.* 32, 872–874.
[b] R. J. Commander and C. B. P. Finn (1970), *J. Phys. E: Sci. Instrum.* 3, 78–79.
[c] D. M. Ginsberg (1970), *Rev. Sci. Instrum.* 41, 1661–1662.

A6.8b MAGNETIC VOLUME SUSCEPTIBILITY AT 293 K, 77 K, AND 4.2 K OF STRUCTURAL MATERIALS COMMONLY USED IN CRYOSTAT CONSTRUCTION (SEC. 6.5)

Volume susceptibility is useful for structural parts with well-defined shapes (such as tubes, rods, sheets, and blocks) where the volume of the part is readily determined. (In contrast, mass susceptibility is utilized in situations where the mass is easier to determine, such as with small or irregularly shaped parts.) The two quantities are simply related by

$$(\text{mass susceptibility } \chi/\rho) \equiv (\text{volume susceptibility } \chi) \,/\, (\text{density in kg/m}^3).$$

Volume susceptibility is defined by $\chi \equiv M/H$, where M is the magnetic moment per unit volume and H is the magnetic intensity.

Values in the table below are tabulated in SI units (mks). To convert to cgs units, divide these values by 4π (from Appendix A1.4).

Magnetic volume susceptibility χ at 293 K, 77 K, and 4.2 K

Material	Condition	Density [10^3 kg/m^3]	χ(293 K) [SI units]	χ (77 K) [SI units]	χ (4.2 K) [SI units]
Aluminum alloys					
Pure Al[c]		2.70	2.07×10^{-5}		2.52×10^{-5}
2014[c]		2.79	1.80×10^{-5}		1.72×10^{-5}
Copper alloys					
99.999% pure Cu[b]	Cold drawn, etch, and annealed		-9.34×10^{-6}	-9.18×10^{-6}	-8.67×10^{-6}
99.96% pure Cu[b]	As formed		-7.32×10^{-6}	-8.55×10^{-6}	-9.32×10^{-6}
Oxygen-free Cu[b]			-9.14×10^{-6}	-9.32×10^{-6}	-8.93×10^{-6}
ETP copper [c]		8.92	3.22×10^{-5}		2.53×10^{-5}
Beryllium copper [c] (Cu–2%Be)		8.33	1.56×10^{-3}		1.82×10^{-3}
Phosphor bronze A[c] (94.8%Cu–5%Sn–0.2%P)		8.95	-5.86×10^{-6}		-5.56×10^{-6}
90%Cu–10%Ni[b]			1.69×10^{-5}	1.57×10^{-5}	2.21×10^{-5}
Brass, plain (cartridge) [c] (70%Cu–30%Zn)			8.52	-3.48×10^{-6}	-6.14×10^{-5}
Brass, free-cutting[c] (61.5%Cu–35.4%Zn–3.1%Pb)		8.52	1.12×10^{-2}		-1.4×10^{-2}
Manganin[j] (83%Cu–13%Mn–4%Ni)			2.7×10^{-3}		1.26×10^{-2}
Constantan[j] (Cu–45%Ni)			0.45		4.3
Titanium alloys					
Ti		4.51[f]	1.78×10^{-4}[e]		
Ti–6%Al–4%V		4.41[c]	1.80×10^{-4}[c]		-8.27×10^{-6}[c]

(Continued)

Magnetic volume susceptibility χ at 293 K, 77 K, and 4.2 K (*Continued*)

Material	Condition	Density [10^3 kg/m^3]	χ(293 K) [SI units]	χ (77 K) [SI units]	χ (4.2 K) [SI units]
Stainless steels					
304		7.86[g]	2.7×10^{-3}[h]	5.5×10^{-3}[h]	
304 L	Fully softened	7.86[g]	2.6×10^{-3}[h]	4.9×10^{-3}[h]	
304 N		7.86[g]	2.6×10^{-3}[h]	5.2×10^{-3}[h]	4.8×10^{-3}[d]
309[a]	Fully softened		2.1×10^{-3}	6.2×10^{-3}	2.4×10^{-2}
	sensitized		2.6×10^{-3}	6.7×10^{-3}	2.1×10^{-2}
310[a]	Fully softened	7.85[g]	2.2×10^{-3}	8.3×10^{-3}	F
	sensitized		2.3×10^{-3}	1.2×10^{-2}	F
310 S		7.85[g]	2.6×10^{-3}[h]	9.5×10^{-3}[h]	
316		7.97[g]	3.0×10^{-3}[c,h]	7.7×10^{-3}[h]	1.6×10^{-2}[d]
316 L		7.97[g]	3.0×10^{-3}[h]	8.0×10^{-3}[h]	
316 LN[a]	Fully softened	7.97[g]	2.6×10^{-3}	6.9×10^{-3}	1.1×10^{-2}
	sensitized		3.5×10^{-3}	7.2×10^{-3}	1.1×10^{-2}
Nickel alloys[i]				*Maximum susceptibility* at:	value:
Inconel 718-1153				19 K	13
Inconel 718-1094				16 K	3.2
Inconel 718-1				15 K	3.8
Inconel 625				$<$ 5 K	0.0032
Nichrome (Ni–20Cr)[j]			5.2×10^{-4}		5.75×10^{-3}
Polymers					
Acrylic[c]		1.05	-6.98×10^{-6}		-2.65×10^{-6}
Nylon[c]		1.15	-9.04×10^{-6}		-7.46×10^{-6}
Composites[c]					
G10CR		1.83	2.63×10^{-6}		5.34×10^{-4}
G11CR		1.90	2.59×10^{-6}		4.58×10^{-4}
Linen phenolic		1.35	-4.26×10^{-6}		2.93×10^{-6}
Miscellaneous[c]					
Hardwood		0.63	6.09×10^{-6}		1.22×10^{-5}
Quartz		2.21	-1.03×10^{-5}		-9.27×10^{-6}

F ≡ Ferromagnetic at this temperature.

[a] D. C. Larbalestier and H. W. King (1973), *Cryogenics* 13, 160–168.

[b] *Handbook on Materials for Superconducting Machinery* (1977), MCIC-HB-04, Battelle, Columbus, OH.

[c] F. R. Fickett (1992), *Adv. Cryog. Eng. (Mater.)* 38, 1191–1197.

[d] E. W. Collings and R. L. Cappelletti (1985), *Cryogenics* 25, 713–718.

[e] *Landolt-Börnstein* (1986), New Series, II/16, *Diamagnetic Susceptibility*, Springer-Verlag, Heidelberg; *Landolt–Börnstein* (1986–1992), New Series, III/19, Subvolumes a to i2, *Magnetic Properties of Metals*, Springer-Verlag, Heidelberg; *CRC Handbook of Chemistry and Physics* (2000), 81st edition, CRC Press, Boca Raton, FL.

[f] *Metals Handbook* (1961), Vol. 1, *Properties and Selection of Materials*, 8th edition, ASM International, Materials Park, OH.

[g] H. I. McHenry (1983), Chapter 11 in *Materials at Low Temperatures*, eds. R. P. Reed and A. F. Clark, ASM International, Materials Park, OH.

[h] E. W. Collings and S. C. Hart (1979), *Cryogenics* 19, 521–530. (The coefficients given in Table 6 of this reference should be multiplied by 4π to correctly give mass susceptibility in units of m^3/kg.)

[i] I. R. Goldberg, M. R. Mitchell, A. R. Murphy, R. B. Goldfarb, and R. J. Loughran (1990), *Adv. Cryog. Eng. (Mater.)* 36, 755–762.

[j] M. Abrecht, A. Adare, and J. W. Ekin (2006), *Rev. Sci. Inst.*, to be published.

A6.8c FERROMAGNETIC TRACES AT 4.2 K INDUCED BY WELDING AND CYCLIC COOLING OF AUSTENITIC STAINLESS STEELS (SEC. 6.5)

Austenitic stainless steels are paramagnetic, but most of them become unstable below room temperature and partially transform into a martensitic phase, which is ferromagnetic. The transformation depends critically on the exact chemical composition and heat treatment of the alloy, as evidenced by the difference in data below for various samples of the same type of steel, indicated by (a), (b), and (c). Welding can also induce ferromagnetic behavior. Only 316LN and X6CrNi 1811 show no ferromagnetic traces on cooling or welding.

Ferromagnetic traces at 4.2 K in austenitic stainless steels

Stainless-steel alloy	Ferromagnetic traces		
	On first cooling	On welding	On cyclic cooling
303	+	+	Not tested
304 (a)	+	+	Not tested
304 (b)	−	+	Not tested
304 (c)	+	+	Not tested
304 N	+	−	+
310	+	+	+
310 S	+	+	−
316 (a)	−	+	−
316 (b)	−	−	−
316 (c)	−	−	−
316 L	+	+	−
316 LN	−	−	−
316 Ti	+	+	−
X6CrNi 1811	−	−	−
321 (a)	+	+	−
321 (b)	+	+	+

+ ≡ Detected.
− ≡ Not detected.

Source: Data from K. Pieterman, A. Ketting, and J. C. Geerse (1984), *J. Phys.*, 45, C1-625–C1-631.

A6.9 COMPOSITION OF AUSTENITIC STAINLESS STEELS, NICKEL STEELS, AND ALUMINUM ALLOYS (SEC. 6.6)

Composition of austenitic stainless steels

These are Fe–Cr alloys with sufficient Ni and Mn to stabilize the f.c.c. austenitic phase so they retain their strength, ductility, and toughness at cryogenic temperatures.

Temperature-dependent mechanical and physical properties of AISI[a] 304, 310, and 316 are tabulated in Appendix A6.10.

Composition of austenitic stainless steels [wt%]

AISI[a] type no.	Cr	Ni	Mn	*C*, max	*N*	Other
201	16–18	3.5–5.5	5.5–7.5	0.15	0.25, max	1.00 Si max 10.060 P max 0.030 S max
202	17–19	4–6	7.5–10	0.15	0.25, max	1.00 Si max 10.060 P max 0.030 S max
301	16–18	6–8		0.15		
302	17–19	8–10		0.15		
304	18–20	8–12		0.08		
304 L	18–20	8–12		0.03		
304 N	18–20	8–10.5	2.0 max	0.08	0.10–0.16	1.00 Si max 10.060 P max 0.030 S max
304 LN	18–20	8–12	2.0 max	0.03	0.10–0.16	1.00 Si max 10.060 P max 0.030 S max
305	17–19	10.5–13		0.12		
309	22–24	12–15		0.20		
310	24–26	19–22		0.25		1.5 Si max
310 S	24–26	19–22		0.08		1.5 Si max
316	16–18	10–14		0.08		2–3 Mo
316 L	16–18	10–14		0.03		2–3 Mo
316 N	16–18	10–14	2.0 max	0.08	0.10–0.16	1.00 Si max 10.060 P max 0.030 S max
316 LN	16–18	10–14	2.0 max	0.03	0.10–0.16	1.00 Si max 10.060 P max 0.030 S max
321	17–19	9–12		0.08		(5 × %C) Ti, min
347	17–19	9–13		0.08		(10 × %C) Nb + Ta, min
ASTM[b] XM-10	19–21.5	5.5–7.5	8–10	0.08	0.15–0.40	1.00 Si max 10.060 P max 0.030 S max
ASTM XM-11	19–21.5	5.5–7.5	8–10	0.04	0.15–0.40	1.00 Si max 10.060 P max 0.030 S max

(Continued)

Composition of austenitic stainless steels [wt%] (*Continued*)

AISI[a] type no.	Cr	Ni	Mn	*C*, max	*N*	Other
ASTM XM-14	17–19	5–6	14–16	0.12	0.35–0.50	1.00 Si max 10.060 P max 0.030 S max
ASTM XM-19	20.5–23.5	11.5–13.5	4–6	0.06	0.20–0.40	0.10–0.30 Nb, 1.00 Si max 10.060 P max 0.030 S max
ASTM XM-29	17–19	2.25–3.75	11.5–14.5	0.08	0.20–0.40	0.10–0.30 V 1.5–3.0 Mo 1.00 Si max 10.060 P max 0.030 S max

Source: H. I. McHenry (1983), Chapter 11 in *Materials at Low Temperatures*, eds. R. P. Reed and A. F. Clark, ASM International, Materials Park, OH.

[a] AISI: American Iron and Steel Institute, a designation system for steels.

[b] ASTM: Formerly known as the American Society for Testing and Materials, now ASTM International, an organization that provides a global forum for consensus standards for materials, products, systems, and services.

Composition of nickel steels

These Fe–Ni alloys have a predominantly b.c.c. crystal structure that undergoes a ductile-to-brittle transition as temperature is reduced; the transition temperature decreases with increasing nickel content.

Temperature-dependent mechanical and physical properties of 3.5 Ni, 5 Ni, and 9 Ni alloys are tabulated in Appendix A6.10.

Composition of nickel steels [wt%]

ASTM[a] specification	Alloy	Minimum service temp. [K]	C max	Mn	P max	S max	Si	Ni	Mo	Cr
A203 Grade D	3.5 Ni	173	0.17	0.7 max	0.035	0.040	0.15–0.30	3.25–3.75		
A203 Grade E	3.5 Ni	173	0.20	0.7 max	0.035	0.040	0.15–0.30	3.25–3.75		
A645	5 Ni	102	0.13	0.30–0.60	0.025	0.025	0.20–0.35	4.75–5.25	0.20–0.35	
A645	5.5 Ni	77	0.13	0.90–1.50	0.030	0.030	0.15–0.30	5.0–6.0	0.10–0.30	0.10–1.00
A553 Type II	8 Ni	102	0.13	0.90 max	0.035	0.040	0.15–0.30	7.5–8.5		
A553 Type I	9 Ni	77	0.13	0.90 max	0.035	0.040	0.15–0.30	8.5–9.5		

Source: H. I. McHenry (1983), Chapter 11 in *Materials at Low Temperatures*, eds. R. P. Reed and A. F. Clark, ASM International, Materials Park, OH.

[a] ASTM: Formerly known as the American Society for Testing and Materials, now ASTM International, an organization that provides a global forum for consensus standards for materials, products, systems, and services.

Composition of aluminum alloys

Aluminum alloys have an f.c.c. crystal structure and thus retain their strength, ductility, and toughness at cryogenic temperatures. Temperature-dependent mechanical and physical properties of type 1100, 2219, 5083, and 6061 alloys are tabulated in Appendix A6.10.

Composition of aluminum alloys [wt%]

Type	Si max	Fe max	Cu	Mn	Mg	Cr	Zn max	Ti	Other elements
1100	1.0 Si (+Fe)		0.05–0.20	0.05 max	—	—	0.10	—	99.00 Al min
2219	0.2	0.3	5.8–6.8	0.20–0.40	0.02 max	—	0.10	0.02–0.10	0.05–15 V
3003	0.6	0.7	0.05–0.20	1.0–1.5	—	—	0.10	—	0.10–0.25 Zr
5083	0.4	0.4	0.1 max	0.40–1.0	4.0–4.9	0.05–0.25	0.25	0.15 max	
6061	0.4–0.8	0.7	0.15–0.40	0.15 max	0.8–1.2	0.04–0.35	0.25	0.15 max	
7005	0.35	0.40	0.10	0.2–0.7	1.0–1.8	0.06–0.20	4.0–5.0	0.01–0.06	0.08–0.20 Zr

Source: H. I. McHenry (1983), Chapter 11 in *Materials at Low Temperatures*, eds. R. P. Reed and A. F. Clark, ASM International, Materials Park, OH.

A6.10 MECHANICAL PROPERTIES OF STRUCTURAL MATERIALS USED IN CRYOGENIC SYSTEMS (SEC. 6.6)

The following four tables give the mechanical and physical properties of austenitic stainless steels, nickel steels, aluminum alloys, and other selected metal alloys and polymers.

Mechanical and physical properties of austenitic stainless steels

Compositions of these and other stainless-steel alloys are tabulated in Appendix A6.9; a plot of the temperature dependence of the yield strength of AISI 304 with various cold-work conditions is given Fig. 6.17.

Alloy Temperature	Density [a] [g/cm^3]	Young's modulus[a] [GPa]	Shear modulus[a] [GPa]	Poisson's ratio[a]	Fracture toughness[b] [MPa m$^{0.5}$]	Thermal conductivity[b] [W/(m · K)]	Thermal expansion[b] (mean) [K$^{-1}\times10^{-6}$]	Specific heat[b] [J/(kg K)]	Electrical resistivity[c] [μΩ cm]	Magnetic permeability[d] (initial)	0.2% yield strength, annealed[e] [MPa]
AISI[f] 304											
295 K	7.86	200	77.3	0.290		14.7	15.8	480	70.4	1.02	240
77 K		214	83.8	0.278		7.9	13.0	—	51.4	—	—
4 K		210	82.0	0.279		0.28	10.2	1.9	49.6	1.09	—
AISI 310											
295 K	7.85	191	73.0	0.305	150	11.5	15.8	480	87.3	1.003	275
77 K		205	79.3	0.295	220	5.9	13.0	180	72.4	—	—
4 K		207	79.9	0.292	210	0.24	10.2	2.2	68.5	1.10	—
AISI 316											
295 K	7.97	195	75.2	0.294	350	14.7	15.8	480	75.0	1.003	240
77 K		209	81.6	0.283	510	7.9	13.0	190	56.6	—	—
4 K		208	81.0	0.282	430	0.28	10.2	1.9	53.9	1.02	—

Major data source: Compilation by H. I. McHenry (1983), Chapter 11 in *Materials at Low Temperatures*, eds. R. P. Reed and A. F. Clark, ASM International, Materials Park, OH.

[a] H. M. Ledbetter, W. F. Weston, and E. R. Naimon (1975), *J. Appl. Phys.* 46, 3855–3860.

[b] D. B. Mann, ed. (1978), *LNG Materials and Fluids*, National Bureau of Standards, US Government Printing Office, Washington, DC.

[c] A. R. Clark, G. E. Childs, and G. H. Wallace (1970), *Cryogenics* 10, 295–305.

[d] K. R. Efferson and W. J. Leonard (1976), *Magnetic Properties of Some Structural Materials Used in Cryogenic Applications*, ORNL-4150, p. 126, Oak Ridge National Laboratory, Oak Ridge, TN.

[e] *Metals Handbook*, Vol. 1, *Properties and Selection of Materials* (1961), 8th edition, ASM International, Materials Park, OH.

[f] AISI: American Iron and Steel Institute; a designation system for steel alloys.

Mechanical and physical properties of nickel steels

Compositions of these and other nickel-steel alloys are tabulated in Appendix A6.9; a plot of the temperature dependence of the yield strength of quenched and tempered 9% Ni steel is given in Fig. 6.17.

Alloy Temperature	Minimum service temp.[c] [K]	Density[a] [g/cm^3]	Young's modulus[a] [GPa]	Shear modulus[a] [GPa]	Poisson's ratio[a]	Fracture toughness[b] [MPa m$^{0.5}$]	Thermal conductivity[b] [W/(m · K)]	Thermal expansion[b] (mean) [K$^{-1}\times10^{-6}$]	Specific heat[b] [J/(kg K)]
3.5 Ni	173								
295 K		7.86	204	79.1	0.282	190	35	11.9	450
172 K			210	81.9	0.281	210	29	10.2	350
5 Ni	102								
295 K		7.82	198	77.0	0.283	210	32	11.9	450
111 K			208	81.2	0.277	200	20	9.4	250
76 K			209	81.6	0.277	90	16	8.8	150
9 Ni	77								
295 K		7.84	195	73.8	0.286	155	28	11.9	450
111 K			204	77.5	0.281	175	18	9.4	250
76 K			205	77.9	0.280	170	13	8.8	150

Major data source: Compilation by H. I. McHenry (1983), Chapter 11 in *Materials at Low Temperatures*, eds. R. P. Reed and A. F. Clark, ASM International, Materials Park, OH.

[a] W. F. Weston, E. R. Naimon, and H. M. Ledbetter (1975), pp. 397–420 in *Properties of Materials for Liquefied Natural Gas Tankage*. ASTM STP 579, American Society for Testing and Materials, Philadelphia, PA.

[b] D. B. Mann, ed. (1978), *LNG Materials and Fluids*, National Bureau of Standards, US Government Printing Office, Washington, DC.

[c] The minimum service temperature arises because of the ductile-to-brittle-phase transition that occurs at low temperatures in the nickel steels.

Mechanical and physical properties of aluminum alloys

Compositions of these and other aluminum alloys are tabulated in Appendix A6.9; a plot of the temperature dependence of the yield strength of various aluminum alloys is given in Fig. 6.18.

Alloy Temperature	Density [g/cm^3]	Young's modulus [GPa]	Shear modulus [GPa]	Poisson's ratio	0.2% yield strength[g] [MPa]	Thermal conductivity [W/(m · K)]	Thermal expansion (mean) [K^{-1}×10^{-6}]	Specific heat [J/(kg K)]	Electrical resistivity [μΩ cm]
1100-0									
295 K	2.75	69			<35				
Precipitation-hardened 2219-T6									
295 K	2.83	77.4[d]	29.1[d]	0.330[d]	393	120[c]	23[f]	900[f]	5.7[b]
77 K		85.1[d]	32.3[d]	0.319[d]		56[c]	18.1[f]	340[f]	
4 K		85.7[d]	32.5[d]	0.318[d]		3[c]	14.1[f]	0.28[f]	2.9[b]
Annealed 5083									
295 K	2.66	71.5[a]	26.8[a]	0.333[a]	145 (half hard: 228)	120[b]	23[b]	900[b]	5.66[c]
77 K		80.2[a]	30.4[a]	0.320[a]		55[b]	18.1[b]	340[b]	3.32[c]
4 K		80.9[a]	30.7[a]	0.318[a]		3.3[b]	14.1[b]	0.28[b]	3.03[c]
Precipitation-hardened 6061-T87									
295 K	2.70	70.1[b]	26.4[b]	0.338[b]	275		23[b]	900[c]	3.94[c]
77 K		77.2[b]	29.1[b]	0.328[b]			18.1[b]	340[c]	1.66[c]
4 K		77.7[b]	29.2[b]	0.327[b]			14.1[b]	0.28[c]	1.38[c]

Major data source: Compilation by H. I. McHenry (1983), Chapter 11 in *Materials at Low Temperatures*, eds. R. P. Reed and A. F. Clark, ASM International, Materials Park, OH.

[a] E. R. Naimon, H. M. Ledbetter, and W. F. Weston (1975), *J. Mater. Sci.* 10, 1309–1316.

[b] D. B. Mann, ed. (1978), *LNG Materials and Fluids*, National Bureau of Standards, US Government Printing Office, Washington, DC

[c] A. R. Clark, G. E. C hilds, and G. H. Wallace (1970), *Cryogenics* 10, 295–305.

[d] R. P. Read and H. M. Ledbetter (1977), *J. Eng. Mater. Technol.* 99, 181–184.

[e] G. E. Childs, L. J. Ericks, and R. L. Powell (1973), *Thermal Conductivity of Solids at Room Temperature and Below*, NBS Monograph 131, US Government Printing Office, Washington, DC.

[f] Assumed to be the same as that of 5083 and 6061.

[g] Compiled by R. Radebaugh et al. (2001), http://www.cryogenics.nist.gov/ and the references listed therein.

Mechanical properties of metal alloys and polymers commonly used in cryogenic systems

All data are at room temperture, unless noted otherwise by three consecutive values corresponding to 295K/76K/4K.

Mechanical property data for additional materials are available in the literature (Sec. 6.7.1) and on the Internet (Sec. 6.7.2).

Material	Density [g/cm^3]	Young's modulus [GPa]	Yield strength [MPa]
Metal alloys			
Beryllium S-200F[a]	1.86	290	240
Copper, oxygen-free (annealed)[a]	8.95	117	70
Cu–2%Be (UNS C17200-TH 04)[b,c]	8.23	119	1030
Inconel 625[d]	8.44[f]	195/207/207	500/720/810
Inconel 718[a]	8.20	200	1060
Hastelloy C-276[d,e]	8.9	192/209/205	480/700/810
Ni (annealed)[d]	8.9	60/70/91	60/70/80
Ni–13at%Cr[d]	8.7	111/112/119	120/160/190
Ni–5at%W[d]	10.4	118/128/134	180/260/280
Titanium 3A1–2.5V [f] (various shapes)	4.5	100	830
Titanium 6A1–4V [a] (sheet form)	4.4	114	830
Polymers[a]			
G-10 fiberglass epoxy	1.65	28	—
Kapton™ (film)	1.43	3.4	210
Mylar™	1.38	3.8	70
Nylon™	1.14	3.4	—
Teflon™	2.2	0.3	14

[a] R. Radebaugh et al. (2001), http://www.cryogenics.nist.gov/ and the references listed therein.

[b] *Metals Handbook* (1961), Vol. 1, *Properties and Selection of Materials*, ed. T. Lyman, 8th edition, ASM International, Materials Park, OH.

[c] N. J. Simon, E. S. Drexler, and R. P. Reed (1992), *Properties of Copper and Copper Alloys at Cryogenic Temperatures*, NIST Monograph 177, National Institute of Standards and Technology, US Government Printing Office, Washington, DC.

[d] C. C. Clickner, J. W. Ekin, N. Cheggour, C. L. H. Thieme, Y. Qiao, Y.-Y. Xie, and A. Goyal (2006), "Mechanical properties of pure Ni and Ni-alloy substrate materials for Y-Ba-Cu-O coated conductors," *Cryogenics*, to be published.

[e] Values averaged for three different batches of Hastelloy C-276.

[f] http://www.matweb.com/.

A7 (i) Specialized resistivity measurement methods (ref. introduction to Part II)

A7.1 SHEET-RESISTANCE MEASUREMENT OF *UNPATTERNED FILMS*

When film properties are initially screened, it is convenient to measure the sheet resistance of the films without the need for patterning. This can be done by a four-probe contact method, wherein four equally spaced in-line probes (such as pogo pins) are pressed against the film near its middle, as illustrated by the insets in Fig. A7.1 for both circular- and rectangular-shaped samples. The usual four-terminal technique is used (described in detail in Sec. 7.2), wherein a small current I from a constant-current supply is passed through the outer two probes, and the voltage V is measured across the inner two probes. The *sheet resistance* R_s is given by

$$R_s = (V/I)\, C \quad [\Omega/\text{sq}], \tag{A7.1}$$

in units of ohms per square, and C is a factor given by the curves in Fig. A7.1, valid for a thin film having a thickness d that is much less than the sides or diameter of the chip (A or D in the insets of Fig. A7.1). In the limit of small-probe spacing $s \ll D$, $C = \pi/\ln 2 = 4.53$. The *bulk resistivity* of the film is related to the sheet resistance by

$$\rho = R_s d \quad [\Omega\,\text{cm}]. \tag{A7.2}$$

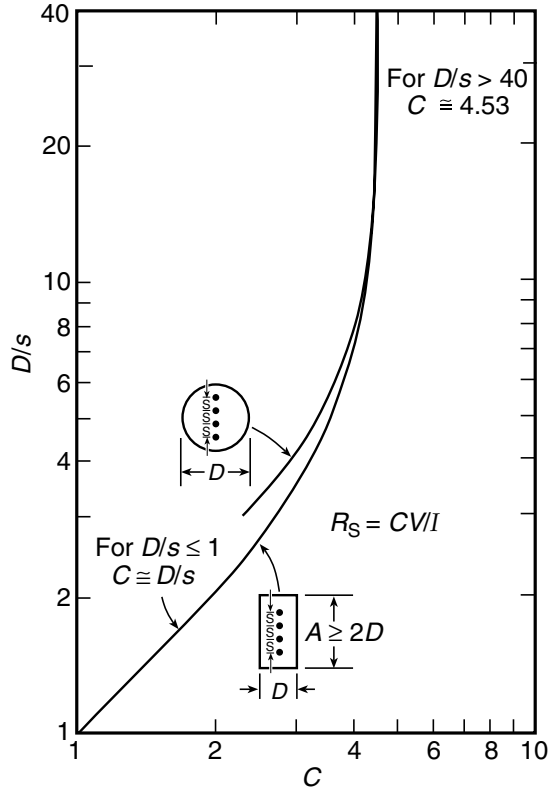

Fig. A7.1 Factor C used in Eq. (A7.1) for determining the sheet resistance of an unpatterned film using four, equally spaced, in-line probes. Adapted from Smits (1958) and Anner (1990).

This in-line probe technique is also insensitive to in-plane anisotropy between the *a*-axis and *b*-axis crystallographic directions, with

$$R_s = (R_{s\,a\text{-axis}}\, R_{s\,b\text{-axis}})^{0.5}.$$

Other probe/sample configurations are treated in Smits (1958) and also in Wasscher (1961).

REFERENCES

Anner, G. E. (1990). *Planar Processing Primer*, p. 585, Van Nostrand Reinhold, New York.
Smits, F. M. (1958), "Measurements of sheet resistivities with four-point probe," *Bell Syst. Tech. J.*, 37, 711–718.
Wasscher, J. D. (1961). "Note on 4-point resistivity measurements on anisotropic conductors", *Philips Res. Rep.* 16, 301–306.

A7.2 VAN DER PAUW METHOD FOR MEASURING THE RESISTIVITY AND HALL MOBILITY IN FLAT ISOTROPIC SAMPLES OF *ARBITRARY SHAPE*

The van der Pauw method (van der Pauw 1958) is particularly useful for measurements of materials that are not easily fabricated into long, uniform, bar shapes: the type of configuration that is usually required for common transport measurements. The method works for electrically isotropic samples of *arbitrary* shape, such as that shown in Fig. A7.2(a). All that is required is that they have a uniform thickness and be *flat*. Thus, this method is well suited to transport measurements of isotropic crystals or brittle materials where it is difficult to cut out bridge-shaped samples without fracturing the narrow arms. (For electrically *an*isotropic materials, use the Montgomery method, described in the next section, Appendix A7.3.) The sample needs to be deposited or grown flat, or to be capable of being polished flat. Also, it cannot have any holes in it (sorry, a slice of Swiss cheese would not work). For Hall-effect measurements, the van der Pauw method also has the advantage that clover-shaped samples [such as that shown in Fig. A7.2(c)] can be used, which give a larger Hall effect for the same amount of heat dissipation compared with the usual bridge-shape samples. This can be a significant advantage for materials with low electron mobility.

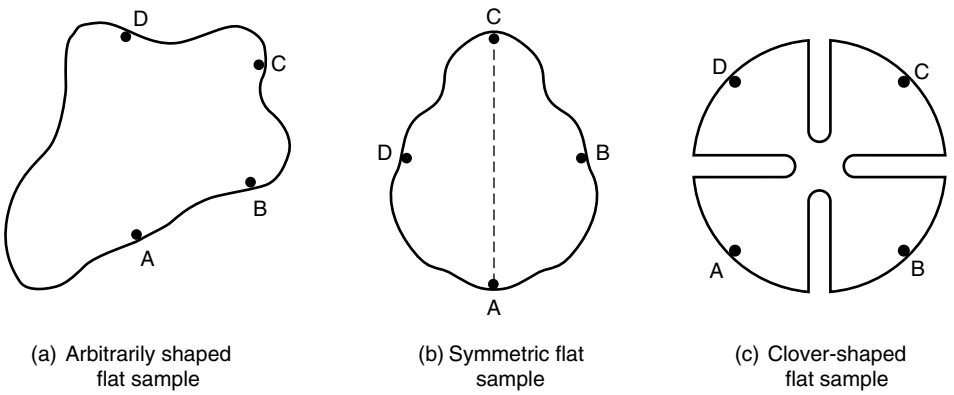

Fig. A7.2 (a) Arbitrarily shaped, flat sample with four small contacts at arbitrary places on the periphery, which can be used to measure the sample's resistivity and Hall effect. (b) The resistivity measurement is simplified to one resistivity measurement if the sample has a line of symmetry; two of the contacts are situated along the symmetry line and the other two symmetrically placed with respect to this line. (c) Clover-shaped sample where the influence of the contact size and placement is significantly reduced. For Hall-effect measurements, the clover shape also gives a larger signal for the same amount of heat dissipation, which can improve the measurement sensitivity for materials with low electron mobility. (Adapted from van der Pauw 1958.)

Here, we present a practical description of how to *use* this method. For details of the derivation, please refer to van der Pauw (1958).

The method consists of attaching small contacts to the sample at its periphery, as illustrated in Fig. A7.2(a–c). The diameter of the contact δ should be small compared with the overall sample size or diameter D. Also, the contacts should be made right at the outer edge of the sample. For disk-shaped samples, the error in resistivity that results from using contacts of size δ or located a distance δ away from the sample's periphery is given approximately by (van der Pauw 1958)

$$\Delta\rho/\rho \approx (\delta/D)^2, \tag{A7.3}$$

whereas the error in the Hall coefficient R_H is given roughly by

$$\Delta R_H/R_H \approx \delta/D. \tag{A7.4}$$

The accuracy of the technique is improved if the contacts are spaced apart around the periphery of the sample, as illustrated in Fig. A7.2(a). Use of a clover-shaped sample shown in Fig. A7.2(c) can help minimize the error due to the finite size and placement of the contacts.

After instrumenting the sample in this way, the resistivity of the sample is then determined by measuring two resistances $R_{AB,CD}$ and $R_{BC,DA}$. Here, $R_{AB,CD}$ is defined as the resistance calculated from the potential difference $V_D - V_C$ measured between contacts D and C in Fig. A7.2(a), divided by the current entering contact A and leaving contact B. The other resistance $R_{BC,DA}$ is correspondingly defined. The sample's resistivity ρ is then given by (van der Pauw 1958)

$$\rho = \pi d\,(2\ln 2)^{-1}\,(R_{AB,CD}+R_{BC,DA})\,f(R_{AB,CD}/R_{BC,DA}), \tag{A7.5}$$

where f is a function only of the ratio $R_{AB,CD}/R_{BC,DA}$. Figure A7.3 gives f as a function of $R_{AB,CD}/R_{BC,DA}$. Notice from Eq. (A7.5) that there are no measurements of the sample's shape that enter into the determination of ρ, only the sample's thickness d.

The measurement is particularly straightforward if the sample has a line of symmetry. In this case, contacts A and C can be placed along this symmetry line, and B and D can be placed symmetrically with respect to this line [Fig. A7.2(b)]. Then, from the reciprocity theorem for passive four poles (interchange

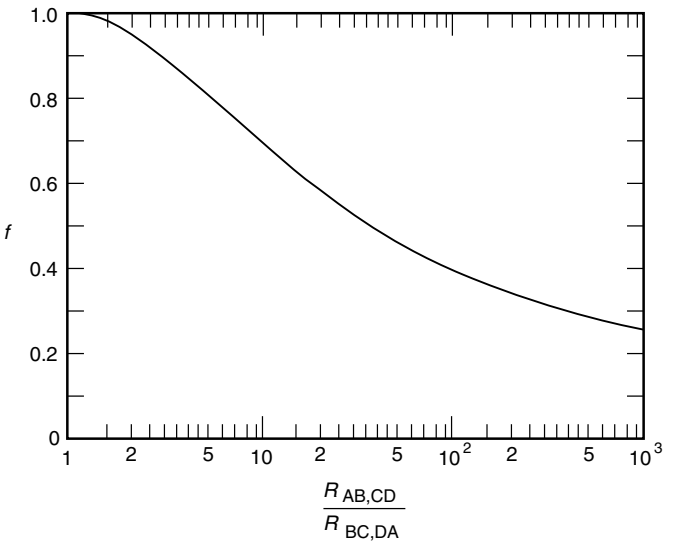

Fig. A7.3 The function $f(R_{AB,CD}/R_{BC,DA})$ in Eq. (A7.5) used to determine the resistivity of an arbitrarily shaped flat sample (from van der Pauw 1958).

of current and voltage contacts), we have, generally, that $R_{AB,CD} = R_{BC,DA}$. Thus, a single measurement of resistance is sufficient.

The van der Pauw method is also well suited for measurements of the Hall coefficient. The Hall coefficient is determined by measuring the *change* of the resistance $R_{AC,BD}$ before and after a uniform magnetic field B is applied perpendicular to the plane of the sample. In this case, current is applied to an arbitrary contact A and removed from contact C (not contact B as with the resistivity measurement described above). The sample's Hall coefficient R_H is then given by (van der Pauw 1958)

$$R_H = (d/B)\,\Delta R_{AC,BD,} \tag{A7.6}$$

where $\Delta R_{AC,BD}$ is the change in the resistance $R_{AC,BD}$ produced by the magnetic field B.

Footnote on reverse-field reciprocity method: For Hall-coefficient or magnetoresistance measurements, the magnetic field is usually reversed and the resistance data averaged to correct for sample inhomogeneities or voltage-terminal misalignment (in the case of a Hall-bar-geometry). The magnetic-field reversal can take a significant amount of time, especially in the case of high magnetic fields, and the extra time can present a problem for some measurements because of temperature drifts, for example.

For such cases, we call attention to the reverse-field reciprocity method by Sample et al. (1987). This method states that the equivalent of the reverse-field resistance measurement can be made by interchanging voltmeter and current sources, without the need to reverse the magnetic field. This is sometimes quite useful since, with computer-controlled data collection and switching, the second resistance measurement can be performed in hundredths of a second, whereas reversing the applied magnetic field can take several minutes.

REFERENCES

Sample, H. H., Bruno, W. J., Sample, S. B., and Sichel, E. K. (1987). "Reverse-field reciprocity for conducting specimens in magnetic fields," *J. Appl. Phys*. 61, 1079–1084.

Van der Pauw, L. J., (1958). "A method of measuring specific resistivity and Hall effect of discs of arbitrary shape," *Philips Res. Rep*. 13, 1–9.

A7.3 MONTGOMERY METHOD FOR MEASURING THE RESISTIVITY OF *ANISOTROPIC* MATERIALS

The Montgomery method facilitates resistivity measurements of *anisotropic* crystals, providing an easier experimental technique of determining the various components of resistivity along their principal axes. (For isotropic materials, the van der Pauw method is better suited; see Appendix A7.2.) The Montgomery method is especially useful for anisotropic materials with two independent components of resistivity. In this two-component case, two samples are usually needed if the conventional four-terminal method is used, with each sample fabricated into long-bar shapes cut along the principal axes. However, with the Montgomery method, both components can be determined from *one* sample. The method is thus extremely useful for the common case where only one sample is available, or if both resistivity components must be measured simultaneously as, for example, when measuring changes in resistivity through a phase transition in a temperature-drift experiment.

Here, my aim is to present a clear, step-by-step description of the procedure for using this method, as well as some practical guidelines on its limitations. The derivation of the method based on the transformation of *anisotropic* sample coordinates into an equivalent *isotropic* space is given in detail in Montgomery (1971), Logan et al. (1971), and the background references cited therein.

Crystalline types appropriate for the application of this method are summarized in Table A7.1 in order of increasing complexity. Here, we denote the various resistivity components of these crystal structures as ρ_1, ρ_2, and ρ_3.

A7.1 **Application notes for Montgomery method**

Crystal structure	Number of independent resistivity components required to characterize the resistivity properties	Application comments
Trigonal Tetragonal Hexagonal	*Two* ρ_2 along the *c*-axis; $\rho_1 = \rho_3$, mutually perpendicular to each other and to ρ_2	ρ_1 and ρ_2 can be obtained from a *single sample face*, which is oriented with one edge along the *c*-axis and the other in any direction perpendicular to the *c*-axis
Orthorhombic	*Three* ρ_1, ρ_2, and ρ_3 orthogonal components along the principal crystal axes	ρ_1, ρ_2, and ρ_3 can be obtained from *two sample faces* with edges along the three principal crystal axes
Monoclinic Triclinic	*Four to six tensor components* Three components are sufficient if specially oriented, but the required orientation cannot be determined from the crystal structure alone	The Montgomery method is usually too cumbersome for these crystal systems

The insets to Fig. A7.4 show the face of a sample with a typical contact arrangement for applying the Montgomery method. If the resistivities $\rho_1$and ρ_2 along sides l_1' and l_2' are expected to be vastly different, it helps to cut the sample face so that $l_2'/l_1' \approx (\rho_1/\rho_2)^{1/2}$. This customized shaping avoids an extreme mismatch in the voltages measured along the two directions, which might otherwise make the smaller voltage difficult to measure.

From a practical standpoint, the Montgomery method is easiest to implement if the sample is relatively *thin*. Thicker samples can be accommodated, but the method becomes more cumbersome, as described under the heading "Thick samples." The simpler thin-sample formulas can be applied to thicker samples, however, if the voltage and current electrodes are extended along the edge of the sample perpendicular to the principal face.

Trigonal, tetragonal, and hexagonal crystal systems

Procedure for determining ρ_1 and ρ_2

1. After connecting instrumentation leads to the sample's principal face (as shown in the insets to Fig. A7.4), measure l_1', l_2', l_3', R_1, and R_2. The quantities R_1 and R_2 are defined in the insets to Fig. A7.4. [Primes are used to indicate the actual physical dimensions l_i' of the *anisotropic* crystal; unprimed quantities denote the transformed sample dimensions in equivalent *isotropic* space. We have used this convention to keep the same notation as in Montgomery's original equations (Montgomery 1971). The figures shown in the first part of Montgomery's article are for the equivalent isotropic case, and then, later in the article, the real sample dimensions are transformed back to the isotropic case, which can be a bit confusing. The reason this works is that the quantities R_1 and R_2 are the same in either real or equivalent space; that is, $R_1 = V_1/I_1 = V_1'/I_1'$ and $R_2 = V_2/I_2 = V_2'/I_2'$. The figure insets shown here have been modified from Montgomery's article to help clarify the practical application of this method.]
2. Determine the ratio l_2/l_1 in the equivalent isotropic space from the experimentally measured ratio R_2/R_1, by using the curves in Fig. A7.4.

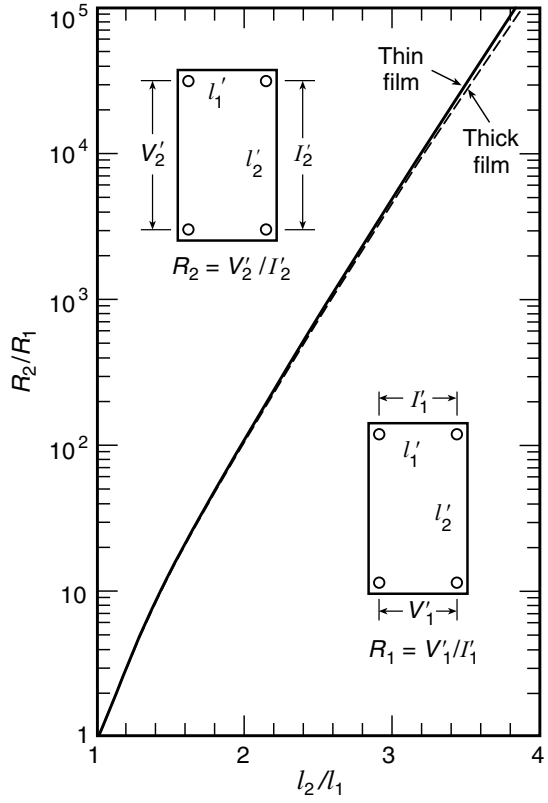

Fig. A7.4 Measured resistance ratio vs. the sample-dimension ratio l_2/l_1. (Unprimed coordinates denote the equivalent isotropic coordinates; see text. The actual physical dimensions of the sample are indicated by primed coordinates l_1' and l_2' as shown in the insets.) (Adapted from Montgomery 1971.)

3. From the value determined for l_1/l_2 (equivalent space) and the value measured for l_1'/l_2' (the actual dimensions of the anisotropic crystal), calculate

$$(\rho_2/\rho_1)^{1/2} = (l_2/l_1) \times (l_1'/l_2'). \tag{A7.7}$$

4. From the ratio l_1/l_2 (equivalent space), determine the dimensionless quantity H from the curve in Fig. A7.5.

Thin samples

5. For thin samples [i.e. $l_3/(l_1 l_2)^{1/2} \lesssim 0.5$, where l_3 is the thickness of the sample in equivalent space determined from Eq. (A7.9) below], calculate

$$(\rho_1\rho_2)^{1/2} = H\, l_3'\, R_1, \tag{A7.8}$$

(where l_3' is the thickness of the sample in real space).

6. Finally, from the quantitative values for $(\rho_2/\rho_1)^{1/2}$ and $(\rho_1\rho_2)^{1/2}$ [Eqs (A7.7) and (A7.8)], calculate ρ_1 and ρ_2.

Thick samples

Steps 1 through 4 are the same as above.

5. For thick samples [$l_3/(l_1 l_2)^{1/2} \gtrsim 0.5$], instead of step 5 above, calculate

$$l_3/(l_1 l_2)^{1/2} = (\rho_1/\rho_2)^{1/4} \times l_3'/(l_1' l_2')^{1/2}, \tag{A7.9}$$

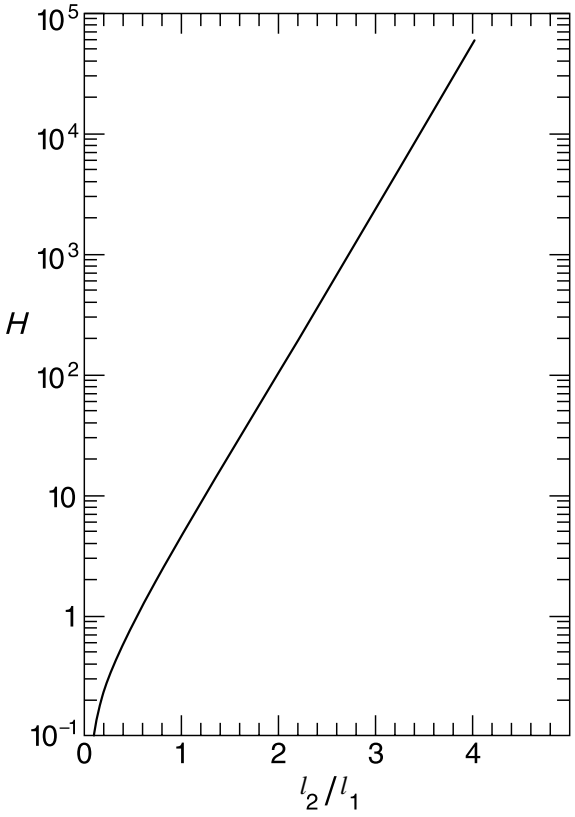

Fig. A7.5 The quantity H [used in Eq. (A7.8)] vs. the sample-dimension ratio (in equivalent isotropic coordinates). (Adapted from Montgomery 1971.)

where the numerical value of $(\rho_1/\rho_2)^{1/4}$ is calculated from the value of $(\rho_2/\rho_1)^{1/2}$ determined in step 3, and $l_3'/(l_1'l_2')^{1/2}$ is calculated from the sample dimensions measured in step 1. [In this step we have taken ρ_3 and ρ_1 to be the equivalent resistivity directions (with ρ_3 defined as the resistivity perpendicular to the sample face); if, on the other hand, $\rho_3 = \rho_2$, interchange subscripts 1 and 2 in Eq. (A7.9) above and in Eq. (A7.10) below.]

6. Use the value of $l_3/(l_1l_2)^{1/2}$ from Eq. (A7.9) to determine $E/(l_1l_2)^{1/2}$ from Fig. A7.6 (where E is defined as the effective sample thickness in equivalent isotropic space).
7. Calculate E' (the effective sample thickness in anisotropic real space) from

$$E'(l_1'l_2')^{1/2} = (\rho_2/\rho_1)^{1/4} \times E/(l_1l_2)^{1/2}, \tag{A7.10}$$

where the value of ρ_2/ρ_1 was determined in step 3.

8. Calculate

$$(\rho_1\rho_2)^{1/2} = HE'R_1, \tag{A7.11}$$

9. Finally, from the quantitative values for $(\rho_2/\rho_1)^{1/2}$ and $(\rho_1\rho_2)^{1/2}$ [Eqs (A7.7) and (A7.11)], calculate ρ_1 and ρ_2.

The numerical limit given in step (5) [i.e. $l_3/(l_1l_2)^{1/2} \gtrsim 0.5$] for the *thin* and *thicker* cases is my subjective estimate for the validity of these two approximations. That is, the thin-sample case requires that $E \approx l_3$, which from Fig. A7.6 would appear to be valid for $l_3/(l_1l_2)^{1/2} \lesssim 0.5$ [or in real space, $(\rho_1/\rho_2)^{1/4} \times l_3'/(l_1'l_2')^{1/2} \lesssim 0.5$ from Eq. (A7.9)].

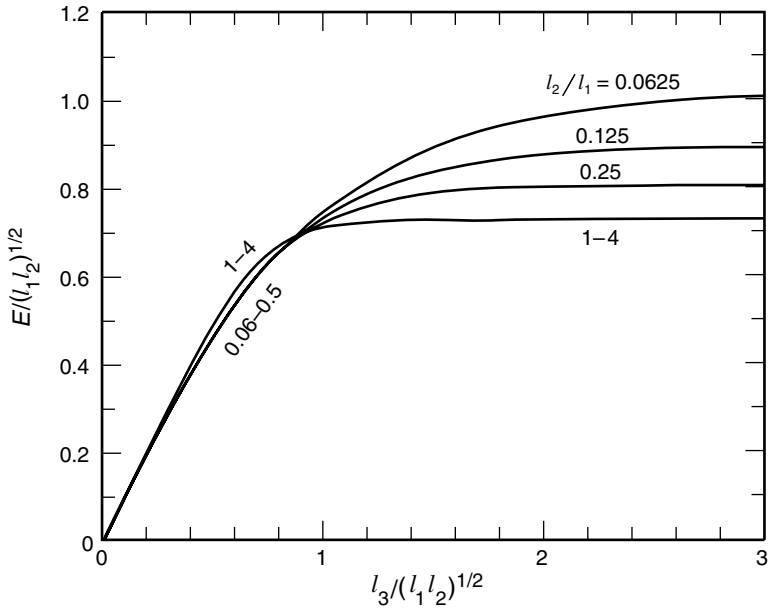

Fig A7.6 Normalized effective thickness E vs. normalized sample thickness l_3 for various ratios of the sample dimensions l_2/l_1 (in equivalent isotropic coordinates). (The ratio $l_2/l_1$was determined from Fig. A7.4 in step 2 above.) (From Montgomery 1971.)

Practical note: To simplify the application of the method when many calculations need to be made for a *single* sample (such as in a temperature-drift experiment), calculate the multiplying factors to convert R_1 to ρ_1 and ρ_2 for several ratios of R_1/R_2, and plot these vs. R_1/R_2 for easier reduction of the data. Nearly straight-line relations are usually obtained on a log–log plot.

Orthorhombic crystal systems

Procedure for determining ρ_1, ρ_2, and ρ_3

With three unknown components of resistivity, the Montgomery method requires measurements on a *second* sample with its face cut normal to that of the first sample and also cut thin enough that the thin-sample condition is met [i.e. $l_3/(l_1 l_2)^{1/2} \lesssim 0.5$ as described above for the two-component case]. Then, the procedure for evaluating the data for the second sample face is the same as that for the *thin*-sample case given above, with corresponding new measured values assigned to l_1', l_2', and l_3'. This works because all the equations are independent of ρ_3 for the *thin*-sample case.

For *thicker* orthorhombic crystals [$l_3/(l_1 l_2)^{1/2} \gtrsim 0.5$], there appears to be no straightforward procedure for applying the Montgomery method unless one assumes a value for ρ_3 and uses an iterative approach (Montgomery 1971). Again, the best procedure in this case would be to mimic the thin-sample case by extending the electrode contacts along the edge of the sample perpendicular to the principal face.

REFERENCES

Logan, B. F., Rice, S. O., and Wick, R. F. (1971). "Series for computing current flow in a rectangular block," *J. Appl. Phys.* 42, 2975–2980.

Montgomery, H. C. (1971). "Method for measuring electrical resistivity of anisotropic materials," *J. Appl. Phys.* 42, 2971–2975.

A7 (ii) Sample-Holder material properties (ref. Chapter 7)

A7.4 SAMPLE-HOLDER MATERIALS: THERMAL CONTRACTION ON COOLING TO LIQUID-HELIUM AND LIQUID-NITROGEN TEMPERATURES (SEC. 7.3.2)

The total linear contraction from room temperature to the indicated temperature T is defined as

$$\Delta L/L_{293\,\mathrm{K}-T} \equiv (L_{293\,\mathrm{K}} - L_T)/L_{293\,\mathrm{K}}.$$

The coefficient of linear expansion at room temperature is defined as

$$\alpha_{293\,\mathrm{K}} \equiv (1/L)\,\mathrm{d}L/\mathrm{d}T.$$

Since the thermal expansion/contraction is approximately linear above room temperature, the total contraction from an upper reference temperature T_u above room temperature (such as soldering temperature) to a low temperature T can be determined approximately from

$$\Delta L/L_{T_u-T} = \Delta L/L_{293\,\mathrm{K}-T} + (\alpha_{293\,\mathrm{K}})\,(T_u - 293\ \mathrm{K}).$$

Tabulated values are generally arranged within each material group by the magnitude of the thermal contraction to facilitate finding sample-holder materials with a thermal contraction which matches that of a given sample.

Additional thermal-expansion data for other materials and temperatures are tabulated in Appendix A6.4.

Thermal contraction of sample-holder materials

Material	$\Delta L/L_{293-4\,\mathrm{K}}$ [%]	$\Delta L/L_{293-77\,\mathrm{K}}$ [%]	$\alpha_{293\,\mathrm{K}}$ [$10^{-6}\,\mathrm{K}^{-1}$]
Metals			
Niobium	0.143[c]	0.130[m]	7.1[r]
Titanium[c]	0.151	0.143[m]	8.5
Iron[c]	0.198	0.190[m]	11.5
Nickel[c]	0.224	0.212[m]	12.5
Copper[b]	0.324	0.302[m]	16.7
Silver[p]	0.412	0.370[c]	18.5
Aluminum[c]	0.415	0.393[m]	22.5
Alloys			
Fe–36Ni[f,m]	~0.037	0.038	3.0
Fe–9Ni[d]	0.195	0.188	11.5
Ti–6%Al–4%V[d]	0.173	0.163[m]	8.0
Ti–5%Al–2.5%Sn[n]	0.20	0.17	8.3
Hastelloy C[s]	0.218	0.216	10.9[t]
Inconel 718[f]	0.24	0.22	13.0
Monel, S (67Ni–30Cu)[d]	0.25	0.24[m]	14.5
SS 304[q]	0.29	0.28[b]	15.1
SS 304L[d]	0.31	0.28	15.5
SS 316[q]	0.30	0.28[b]	15.2
Cu–2%Be (UNS C17200 -TH 04)[c]	0.31	0.30	18.1
Brass 70/30[d]	0.37	0.34[m]	17.5
Bronze (Cu–5wt%Sn)[n]	0.33	0.29	15.0

(Continued)

Thermal contraction of sample-holder materials (*Continued*)

Material	$\Delta L/L_{293-4\,K}$ [%]	$\Delta L/L_{293-77\,K}$ [%]	$\alpha_{293\,K}$ [$10^{-6}\,K^{-1}$]
Bronze (Cu–10wt%Sn)[n]	0.38	0.35	18.2
Bronze (Cu–13.5wt%Sn)[k]	0.40	0.36	18.8
Aluminum 2024-T86 [f]	0.396	0.374	21.5
Aluminum 7045-T73 [f]	0.419	0.394	23.5
Soft-Solder 50/50 [c]	0.514	0.480[m]	25.5
Insulators			
Pyrex™ [j]	0.055	0.054	3.0
G-11 (warp)[a]	0.21	0.19	11
G-11 (normal)[a]	0.62	0.55	37
G-10CR (warp direction)[a]	0.24	0.21[m]	12.5
G-10CR (normal direction)[a]	0.71	0.64[m]	41
Phenolic, Cotton (warp)[f]	0.26	0.24[m]	15
Phenolic, Cotton (normal)[f]	0.73	0.64[m]	42
Stycast 2850 FT™ [r]	0.44	0.40	28
CTFE [c]	1.14	0.97[m]	67
Epoxy [g]	1.16	1.03[m]	66
Plexiglas™ [j]	1.22	1.06[m]	75
Nylon™ [c]	1.39	1.26[m]	80
TFE (Teflon™)[i]	2.14	1.94[m]	250

[a] A. F. Clark, G. Fujii, and M.A. Ranney (1981), *IEEE Trans. Magn.* MAG-17, 2316–2319.

[b] T. A. Hahn (1970), *J. Appl. Phys.* 41, 5096–5101.

[c] R. J. Corruccini and J. J. Gniewek (1961), *Thermal Expansion of Technical Solids at Low Temperatures*. Monograph 29, National Bureau of Standards, US Government Printing Office, Washington, DC

[d] V. Arp, J. H. Wilson, L. Winrich, and P. Sikora, (1962), *Cryogenics* 2, 230–235.

[f] A. F. Clark (1968), *Cryogenics* 8, 282–289.

[g] K. Dahlerup–Peterson and A. Perrot (1979). *Properties of Organic Composite Materials at Cryogenic Temperatures*. ISR-BOM/79-39, CERN, Geneva, Switzerland.

[i] R. K. Kirby (1956), *J. Res. Natl. Bur. Stand.* 57, 91–94.

[j] H. L. Laquer and E. L. Head (1952), *Low Temperature Thermal Expansion of Plastics*. AECU-2161, Technical Information Service Atomic Energy Commission, Oak Ridge, TN.

[k] G. Rupp (1980), in *Multifilamentary 15 Superconductors*, eds. M. Suenaga and A. F. Clark, pp. 155–170, Plenum Press, New York.

[l] D. S. Easton, D. M. Kroeger, W. Specking, and C. C. Koch, (1980), *J. Appl. Phys.* 51, 2748–2757.

[m] A. F. Clark (1983), Chapter 3, in *Materials at Low Temperatures*, pp. 96–97, ASM International, Materials Park, OH.

[n] *Handbook on Materials for Superconducting Machinery* (1977), MCIC-HB-04. Battelle, Columbus, OH.

[o] N. J. Simon, E. S. Drexler, and R.P. Reed (1992), *Properties of Copper and Copper Alloys at Cryogenic Temperatures*, US Government Printing Office, Washington, DC; N. Cheggour and D. P. Hampshire (2000), *Rev. Sci. Instrum.* 71, 4521–4529.

[p] V. J. Johnson, ed. (1961), *Properties of Materials at Low Temperature, Phase 1*, US Air Force.

[q] *Handbook on Materials for Superconducting Machinery* (1974, 1976), National Bureau of Standards, US Government Printing Office, Washington, DC.

[r] C. A. Swenson (1997), *Rev. Sci. Instrum.* 68, 1312–1315.

[s] Y. S. Touloukian (1975), *Thermal Expansion*, 12, 1248.

[t] R. Radebaugh et al. (2001), http://www.cryogenics.nist.gov/ and the references listed therein.

A7.5 SUPERCONDUCTOR MATERIALS: THERMAL CONTRACTION ON COOLING TO LIQUID-HELIUM AND LIQUID-NITROGEN TEMPERATURES (SEC. 7.3.2)

The total linear contraction from room temperature to the indicated temperature T is defined as

$$\Delta L/L_{293\,\mathrm{K}-T} \equiv (L_{293\,\mathrm{K}} - L_T)/L_{293\,\mathrm{K}}.$$

The coefficient of linear expansion at room temperature is defined as

$$\alpha_{293\,\mathrm{K}} \equiv (1/\mathrm{L})\ \mathrm{d}L/\mathrm{d}T.$$

Since the thermal expansion/contraction is approximately linear above room temperature, the total contraction from an upper reference temperature T_u above room temperature (such as soldering temperature) to a low temperature T can be determined approximately from

$$\Delta L/L_{T_u-T} = \Delta L/L_{293\,\mathrm{K}-T} + (\alpha_{293\,\mathrm{K}})\ (T_u - 293\ \mathrm{K}).$$

Tabulated values are generally arranged within each material group by the magnitude of the thermal contraction.

A7.5 Thermal contraction of superconductor materials

Material	$\Delta L/L_{293\text{–}4\,\mathrm{K}}$ [%]	$\Delta L/L_{293\text{–}77\,\mathrm{K}}$ [%]	$\alpha_{293\ \mathrm{K}}$ [$10^{-6}\,\mathrm{K}^{-1}$]
High-T_c superconductors			
YBCO polycrystal[i]	0.23	0.21	11.5
YBCO *a*-axis[i]	0.13	0.12	7.4
YBCO *b*-axis[i]	0.18	0.16	9.6
YBCO *c*-axis[i]	0.38	0.34	17.7
YBCO *a,b*-plane avg.[i]	0.16	0.14	8.5
Bi-2212			
a,b-axes°	0.15	0.14	8.3
c-axis°	0.30	0.27	15.1
Ag[u]	0.41	0.37	18.5
Bi-2223/61%Ag alloy[a,b]		0.24	
Bi-2223 *a,b*-axes[o,p]		0.22	
Ag[q]	0.41	0.37	18.5
Bi-2223/75vol%Ag wire[l]			
1st cool-down	0.22	0.23	16
2nd cool-down (difference due to Ag yielding)	0.29	0.30	13
Low-T_c superconductors			
Nb–67wt%Ti/64vol%Cu wire[c]	0.26	0.25[j]	12.5
Nb–67wt%Ti	0.13[j,h]		5.8[j]
Nb–45wt%Ti	0.19[h]	0.17[j]	8.2[j]
Nb_3Sn wire (10vol%Nb_3Sn)	0.30[g,m]	0.28[g,m]	
Nb_3Sn wire (20vol%Nb_3Sn	0.28[g,m]	0.26[g,m]	
Nb_3Sn	~0.16[j]	0.14[j]	7.6[d]

(Continued)

A7.5 Thermal contraction of superconductor materials (*Continued*)

Material	$\Delta L/L_{293\text{–}4\ \mathrm{K}}$ [%]	$\Delta L/L_{293\text{–}77\ \mathrm{K}}$ [%]	$\alpha_{293\ \mathrm{K}}$ [$10^{-6}\,\mathrm{K}^{-1}$]
Matrix materials			
Bronze (Cu–13.5wt%Sn)[f]	0.40	0.36	18.8
Cu	0.32[k]	0.30[j]	16.7[e,d]
Nb	0.14[e]	0.13[j]	7.3[r]
Ta	0.14[e]	0.13[e]	6.3[e,d]

[a] J. P. Voccio, O. O. Ige, S. J. Young, and C. C. Duchaine (2001), *IEEE Trans. Appl. Supercond*. 11, 3070–3073.
[b] E. Harley (2004), American Superconductor Corp., personal communication.
[c] A. F. Clark (1968), *Cryogenics* 8, 282–289.
[d] D. S. Easton, D. M. Kroeger, W. Specking, and C. C. Koch, (1980), *J. Appl. Phys*. 51, 2748.
[e] R. J. Corruccini, and J. J. Gniewek (1961) *Thermal Expansion of Technical Solids at Low Temperatures*. Monograph 29, National Bureau of Standards, US Government Printing Office, Washington, DC.
[f] G. Rupp (1980), pp. 155–170 in *Multifilamentary 15 Superconductors*, eds. M. Suenaga and A. F. Clark, Plenum Press, New York.
[g] L. F. Goodrich, S. L. Bray, and T. C. Stauffer (1990), *Adv. Cryog. Eng. (Mater.)* 36A, 117–124.
[h] F. J. Jelinek and E. W. Collings (1975), "Low-temperature thermal expansion and specific heat properties of structural materials," in *Materials Research in Support of Superconducting Machinery—IV*, eds. A. F. Clark, R. P. Reed, and E. C. Van Reuth. Fourth Semi-Annual Technical Report, National Bureau of Standards, US Government Printing Office, Washington, DC.
[i] Calculated from data by H. You, J. D. Axe, X. B. Kan, S. Hashimoto, S. C. Moss, J. Z. Liu, G. W. Crabtree, and D. J. Lam (1988), *Phys. Rev*. B38, 9213–9216.
[j] Compilation by A. F. Clark (1983), Chapter 3 in *Materials at Low Temperatures*, ASM International, Materials Park, OH.
[k] T. A. Hahn (1970), *J. Appl. Phys*. 41, 5096–5101.
[l] N. Yamada, K. Nara, M. Okaji, T. Hikata, T. Kaneko, N. Sadakata (1998), *Cryogenics* 38, 397–399.
[m] K. Tachikawa, K. Itoh, H. Wada, D. Gould, H. Jones, C. R. Walters, L. F. Goodrich, J. W. Ekin, and S. L. Bray (1989), *IEEE Trans. Magn*. 25, 2368–2374.
[o] M. Okaji, K. Nara, H. Kato, K. Michishita, and Y. Kubo (1994), *Cryogenics* 34, 163–165.
[p] S. Ochaia, K. Hayashi, and K. Osamura (1991), *Cryogenics* 31, 954–961.
[q] R. J. Corruccini and J. J. Gniewek (1961), *Thermal Expansion of Technical Solids at Low Temperatures*, National Bureau of Standards Monograph 29, US Government Printing Office, Washington, DC.
[r] *CRC Handbook of Chemistry and Physics* (2001), 82nd edition, CRC Press, Boca Raton, FL.

A7.6 THIN-FILM SUBSTRATE MATERIALS: THERMAL CONDUCTIVITY AND THERMAL CONTRACTION (SECS 7.4.1 AND 7.4.2)

Material	Thermal conductivity			Thermal expansion		
	λ (4 K) [W/(m·K)]	λ (77 K) [W/(m·K)]	λ (295 K) [W/(m·K)]	$\Delta L/L$ (293–4 K) [%]	$\Delta L/L$ (293–77 K) [%]	α (293 K) [10^{-6} K^{-1}]
Al N ($\parallel$ *a*-axis)[j]	—	—	—	—	0.032	3.7
($\parallel$ *c*-axis)[j]					0.025	3.0
Sapphire (Al_2O_3)[l] ($\parallel$ *c*-axis)	451[e]	10300[e]		0.079	0.078	5.4[j]
Beryllia	~1[i]	~1000[i]				
C (diamond)				0.024[a]	0.024[a]	1.0[a]
$LaAlO_3$						12.6[b]
MgO	82[d]	507[d]	61[d]	0.139[a]	0.137[a]	10.2[a]
$NdGaO_3$						7.8[b]
Ni			90.7[f]	0.224[c]	0.212[c]	13.4[g]
Quartz ($\parallel$ optic axis)	420	32			0.104[a]	7.5[a]
Si			124[m]	0.022[a]	0.023[a]	2.32[a]
α-SiC (λ: crystal, $\perp$ to *c*-axis) ($\Delta L/L$: polycrystal avg.)	27[k]	4000[k]	510[k]	—	0.030[j]	3.7[j]
$SrTiO_3$			60[f]			11.1[b]
Y-stabilized zirconia (YSZ)						10.3[b]
Cu (OFHC) (for reference)	630[h]	544[h]	397[h]	0.324[c]	0.302[c]	16.7[c]

[a] R. J. Corruccini and J. J. Gniewek (1961), *Thermal Expansion of Technical Solids at Low Temperatures*, National Bureau of Standards Monograph 29, US Government Printing Office, Washington, DC.

[b] Shinkosha Co., Ltd. Tokyo, Japan.

[c] A. F. Clark (1983), Chapter 3 in *Materials At Low Temperatures*, ASM International, Materials Park, OH.

[d] Y.S. Touloukian and E. H. Buyco, (1970), *Specific Heat*, Vols. 1 and 2, Plenum Press, New York.

[e] R. Radebaugh et al. (2003), http://www.cryogenics.nist.gov/ and the references listed therein.

[f] Compiled by M. Paranthaman, Oak Ridge National Laboratory, Oak Ridge, Tennessee; and from J. Evetts, University of Cambridge, UK.

[g] *CRC Handbook of Chemistry and Physics* (2001), 82nd edition, CRC Press, Boca Raton, FL.

[h] Cryogenic Materials Properties Program CD, Release B-01 (June 2001), Cryogenic Information Center, 5445 Conestoga Ct., Ste. 2C, Boulder, CO 80301-2724, Ph. (303) 442-0425, Fax (303) 443-1821.

[i] Lake Shore Cryotronics, Inc. (2002), *Temperature Measurement and Control* , Westerville, OH.

[j] Y. S. Touloukian (1977), *Thermal Expansion: nonmetallic solids*, Vol. 13, IFI/Plenum, New York.

[k] Y. S. Touloukian (1970), *Thermal Conductivity: metallic elements and alloys*, Vol. 2, IFI/Plenum, New York.

[l] For the thermal conductivity data, the heat flow is 60° away from the hexagonal axis; values are thought to be accurate to within 10–15% at temperatures above 60 K, but highly sensitive to small physical and chemical variations below 60 K. Thermal linear-expansion data are parallel to the *c*-axis.

[m] *CRC Handbook of Chemistry and Physics* (2002), 83rd edition, CRC Press, Boca Raton, FL.

A7.7 ULTRASONIC WIRE-BOND MATERIAL COMBINATIONS (SEC. 7.4.3)

Substrate	Metal film	Wire-bond lead	
		Material	Diameter or thickness range [mm]
Glass	Aluminum	Aluminum wire	0.05–0.25
	Aluminum	Gold wire	0.08
	Nickel	Aluminum wire	0.05–0.5
	Nickel	Gold wire	0.05–0.25
	Copper	Aluminum wire	0.05–0.25
	Gold	Aluminum wire	0.05–0.25
	Gold	Gold wire	0.08
	Tantalum	Aluminum wire	0.05–0.5
	Chromel	Aluminum wire	0.05–0.25
	Chromel	Gold wire	0.08
	Nichrome	Aluminum wire	0.06–0.5
	Platinum	Aluminum wire	0.25
	Gold–platinum	Aluminum wire	0.25
	Palladium	Aluminum wire	0.25
	Silver	Aluminum wire	0.25
	Copper on silver	Copper ribbon	0.7
Alumina	Molybdenum	Aluminum ribbon	0.08–0.13
	Gold–platinum	Aluminum wire	0.25
	Gold on molybdenum–lithium	Nickel ribbon	0.05
	Copper	Nickel ribbon	0.05
	Silver on molybdenum–manganese	Nickel ribbon	0.05
Silicon	Aluminum	Aluminum wire	0.25–0.5
	Aluminum	Gold wire	0.05
Quartz	Silver	Aluminum wire	0.25
Ceramic	Silver	Aluminum wire	0.25

Source: *Welding Handbook* (1991), 8th edition, Vol. 2, Chapter 25, pp. 784–812, American Welding Society, Miami, FL; G. G. Harmon (1997), *Wire Bonding in Microelectronics: Materials, Processes, Reliability, and Yield*, p. 7, McGraw-Hill, New York.

A8 **Sample contacts (ref. Chapter 8)**

A8.1 OVERVIEW OF CONTACTS FOR LOW-T_C AND HIGH-T_C SUPERCONDUCTORS (SECS 8.3 AND 8.4)

Contact type	Specific contact resistivity ρ_c^* [$\Omega\,cm^2$]	Common usage/comments
Low-T_c superconductors (copper sheathed)		
Cu / 63%Sn–37%Pb / Cu[a]	4×10^{-9}	Copper-to-copper joint soldered under light pressure
High-T_c Bi–Sr–Ca–Cu–O oxide superconductors		
Silver sheath/BSCCO interface[d]	$\ll 10^{-8}$	Copper connections to the silver sheath can be soldered with standard eutectic Pb–Sn solder and have ρ_c values comparable to those of the copper-to-copper joints listed above
High-T_c Y–Ba–Cu–O oxide superconductors		
Silver or gold deposited on YBCO:		
In situ[c] deposited; no anneal[b]	10^{-9}–10^{-7}	Contacts to oxide superconductor films, typically for electronic applications
Ex situ[c] deposited; oxygen annealed[e]	10^{-9}–10^{-6}	Contacts for high-current applications, including "coated conductors"
Ex situ deposited; no oxygen anneal[f]	10^{-5}–10^{-2}	Applications where oxygen annealing is precluded by other sensitive materials or processing steps. The lowest values of ρ_c are obtained when the superconductor surface is ion milled or sputter etched just prior to contact deposition
Soldered Y–Ba–Cu–O oxide superconductors		
Indium-solder connections to silver or gold pads deposited on YBCO	10^{-1}–10^{-6}	High-current coated-conductor applications. The lowest values of ρ_c are obtained when the gold or silver pad thickness is at least 7–10 μm thick (see the subtopic on soldering in Sec. 8.3.3)
Indium solder applied directly on YBCO[g]	10^{-2}–10^{-1}	Soldered voltage contacts for bulk oxide superconductors

* For low-T_c superconductors, the contact resistivity was measured at 4.2 K. For high-T_c superconductors, the contact resistivity does not appreciably change with temperature below T_c and thus applies to the entire temperature range from liquid-helium to liquid-nitrogen temperatures.

[a] L. F. Goodrich and J. W. Ekin (1981), *IEEE Trans. Magn.* 17, 69–72.

[b] M. Lee, D. Lew, C–B. Eom, T. H. Geballe, and M. R. Beasley (1990), *Appl. Phys. Lett.* 57, 1152–1154.

[c] "Ex-situ" and "in-situ" contacts refer to whether the superconductor surface is exposed to air before the noble-metal contact pad is deposited, as described in Sec. 8.4.2 on superconductor-film contact techniques.

[d] Y. S. Cha, M. T. Lanagan, K. E. Gray, V. Z. Jankus, and Y. Fang (1994), *Appl. Supercond.* 2, 47–59.

[e] J. W. Ekin, T. M. Larson, N. F. Bergren, A. J. Nelson, A. B. Swartzlander, L. L. Kazmerski, A. J. Panson, and B. A. Blankenship, (1988), *Appl. Phys Lett.* 52, 1819–1821.

[f] J. W. Ekin, A. J. Panson, and B. A. Blankenship (1988), *Appl. Phys. Lett.* 52, 331–333.

[g] J. W. Ekin, unpublished data, National Institute of Standards and Technology, Boulder, CO.

A8.2 CONTACT METHODS FOR VOLTAGE AND CURRENT CONNECTIONS TO BARE YBCO SUPERCONDUCTORS (SECS 8.3.1, 8.3.2, 8.3.3, AND 8.4.2)

Contact methods are ordered within each category by the magnitude of contact resistivity ρ_c, with the best (lowest ρ_c) listed first.

Any of the *current* contact methods can also be used for *voltage* contacts, but they are more complex to fabricate than the simple techniques listed for voltage contacts.

Contact materials that do not work well with the oxide superconductors are included at the end of the table for pedagogical reasons (described in Sec. 8.3.3).

Contact type	Procedure	ρ_c[a] [$\Omega\,cm^2$]	Comments
Voltage contacts			
In–3wt.%Ag solder	For these solders to wet YBCO surfaces, lightly scratch the sample surface under the molten solder with the soldering-iron tip, or use an ultrasonic soldering iron; see "Soldered . . ." and "Wetting . . ." in Sec. 8.3.2	$10^{-2}-10^{-1}$	$T_{melt} = 143°C$; eutectic
In–48wt.%Sn solder		$10^{-2}-10^{-1}$	$T_{melt} = 118°C$; eutectic; beware that Sn dissolves thin silver or gold films
Spring contacts	Beryllium copper or other conducting spring stock is used to contact the sample; see "Pressure contacts" in Sec. 8.3.2	—	Silver or gold pads deposited on the test sample lower the contact resistivity
Silver paint		$10^{-1}-10^{0}$	Weak connection, but sometimes needed for delicate samples; ρ_c can be improved by oxygen annealing; solvent carrier in paint can damage thin films
Current contacts			
In situ gold or silver pad deposited on	Descriptions of *in situ* vs. *ex situ* deposition techniques are given in Sec. 8.4.2	$10^{-9}-10^{-7}$	Produces the lowest ρ_c *In situ* contacts are mainly

superconductor, no oxygen annealing			amenable to HTS *film* (not bulk) fabrication techniques Gold is more expensive than silver contact pads, but does not tarnish as readily
Ex situ gold or silver pad deposited on superconductor, with oxygen annealing	See Sec. 8.4.2 and "Fabrication" in Sec. 8.3.3	$10^{-9}-10^{-2}$	
Ex situ gold or silver pad deposited on superconductor, no oxygen annealing	See Sec. 8.4.2 and "Fabrication" in Sec. 8.3.3	$10^{-6}-10^{-2}$	Used for applications where oxygen annealing is not possible, or where very low ρ_c is not needed ρ_c depends on how well the surface is cleaned
Indium-solder connection to silver or gold pad	Make silver or gold pad thickness at least 7–10 μm. See "Soldering to noble-metal contact pads" in Sec. 8.3.3	$10^{-1}-10^{-6}$	Used for connecting high-current bus bars or wires to the sample-contact pads ρ_c depends strongly on the soldering technique used (see text)
Failures			
Copper pad deposited on superconductor	Sputter deposited	10^{-2}	ρ_c no better than indium solder, and a lot more complex to fabricate
Au–Cr pad deposited on superconductor	Sputter deposited	10^{-1}	Contact commonly used for semiconductors, but terrible for superconductors
Pb–Sn solder		no bond	

[a] The contact resistivity does not appreciably change with temperature below T_c, so the same approximate ρ_c values apply at liquid-helium and liquid-nitrogen temperature.

A8.3 OPTIMUM OXYGEN-ANNEALING CONDITIONS FOR SILVER AND GOLD CONTACTS TO Y-, Bi-, AND Tl-BASED HIGH-T_c SUPERCONDUCTORS (SECS 8.3.3 AND 8.4.2)

Annealing times are about 30–60 min (at full temperature) for contacts to bulk superconductors, 30 min or less for thin-film superconductors.

Optimum oxygen-annealing conditions for silver and gold contacts

Contact type	Annealing temperature in O_2 [°C]
Bulk high-T_c superconductors	
Ag/YBCO[a]	500
Au/YBCO[a]	600
Ag/BiPbSrCaCuO	~400
Ag/TlCaBaCuO	500
Film YBCO superconductors	
Ag(<1 μm)/YBCO film[b]	400
Au(<1 μm)/YBCO film[c]	450–500

Annealing is carried out in oxygen at atmospheric pressure, flowing at a rate of about 2×10^{-6} m^3/s (~0.3 scfh, standard cubic feet per hour) by using a furnace such as that shown in Fig. 8.9.

For YBCO, the contacts were cooled in oxygen by ramping the furnace temperature down at a slow rate, ~2.5°C/min for the bulk sintered superconductors used in these tests; rates for thin films should be kept below 50°C/min to allow time for the crystal structure to take up oxygen as it cools and to minimize oxygen disorder. [Further information is given in B. H. Moeckly, D. K. Lathrop, and R. A. Buhrman, (1993), *Phys. Rev*. B47, 400–417.]

For silver-contact pads on films, the silver pad will "ball up" at oxygen-annealing-temperatures higher than about 400°C if the pad is thin (<1 μm); see Fig. 8.13. For thick silver-contact pads ($\gg 1$ μm), the optimum annealing temperature can be slightly higher [A. Roshko, R. H. Ono, J. Beall, J. A. Moreland, A. J. Nelson, and S. E. Asher. (1991), *IEEE Trans. Magn*. 27, 1616–1618].

[a] J. W. Ekin, T. M. Larson, N. F. Bergren, A. J. Nelson, A. B. Swartzlander, L. L. Kazmerski, A. J. Panson, and B. A. Blankenship (1988), *Appl. Phys Lett*. 52, 1819–1821.

[b] J. W. Ekin, C. C. Clickner, S. E. Russek, and S. C. Sanders (1995), *IEEE Trans. Appl. Supercond*. 5, 2400–2403.

[c] Y. Xu, J. W. Ekin, C. C. Clickner, and R. L. Fiske (1998), *Adv. Cryog. Eng. (Mater.)* 44, 381–388.

A8.4 BULK RESISTIVITY OF COMMON SOLDERS, CONTACT-PAD MATERIALS, AND MATRIX MATERIALS (SEC. 8.5.2)

The bulk resistivity values listed below are useful for estimating the effective contact resistivity in conjunction with Eq. (8.5).

Additional properties of solders are tabulated in Appendix A3.7.

Bulk resistivity of common solders, contact-pad materials, and matrix materials

Material	$\rho_{4\,K}$ [$\mu\Omega$ cm]	$\rho_{77\,K}$ [$\mu\Omega$ cm]	$\rho_{295\,K}$ [$\mu\Omega$ cm]
Solder (compositions in wt%)			
52In–48Sn[a] (eutectic) ($T_{melt} = 118°C$)	SC		18.8
97In–3Ag[a] (eutectic) ($T_{melt} = 143°C$)	0.02	1.8	9.7
90In–10Ag[a]	0.03	1.8	9.1
Indium[a] ($T_{melt} = 157°C$)	0.002	1.6	8.8
63Sn–37Pb[a] (standard eutectic soft-solder) ($T_{melt} = 183°C$)	SC	3.0	15
91Sn–9Zn[a] ($T_{melt} = 199°C$)	0.07	2.3	12.2
Contact-pad material			
Silver (pure: evaporated, sputtered, or plasma-sprayed)	Variable	0.27	1.6
Gold (pure: evaporated or sputtered)	Variable	0.43	2.2
Low-T_c superconductor matrix materials			
Copper	Variable (~0.017 typical)	~0.2	1.7
Bronze (Cu–13wt%Sn)	~2	~2	
High-T_c superconductor matrix materials			
Silver	Variable	0.27	1.6
Silver dispersion strengthened with 1at%Mn[b]	2.2	2.7	4.0
Silver dispersion strengthened with 2at%Mn[b]	~4.1	~4.6	~6.0

SC ≡ Superconducting (see Appendix A3.9).

[a] C. Clickner (1999), unpublished data, National Institute of Standards and Technology, Boulder, CO.

[b] M. Putti, C. Ferdeghini, G. Grasso, A. Manca, and W. Goldacker (2000), *Physica C* 341–348, 2585–2586.

A8.5a ARGON ION MILLING RATES OF *ELEMENTS* (SEC. 8.4.2)

Values of argon ion milling rates of elements are tabulated in nm/min, at a current density of 1 mA/cm^2, and incident argon ion energies of 200 eV and 500 eV.

Rates at other energies can be estimated from Fig. 8.11. An example is given in Sec. 8.4.2 under Cleaning etch.

Argon ion milling rates of *elements*

Element	200 eV [nm/min]	500 eV [nm/min]
Ag	100	220
Al	29	73
Au	71	170
Be	5.2	17
C	1.3	4.4
Co	26	55
Cr	33	58
Cu	53	110
Dy	58.0	110
Er	—	98
Fe	26	53
Gd	55.0	110
Ge	49	100
Hf	31	66
Ir	26	60
Mo	24	54
Nb	18	44
Ni	31	66
Os	20	51
Pd	60	130
Pt	39	88
Re	23	52
Rh	31	74
Ru	24	61
Si	16	38
Sm	51.0	110
Sn	85.0	180
Ta	20	42
Th	41	82
Ti	16	38
U	34	74
V	17	37
W	18	38
Y	45	96
Zr	27	62

Source: From a compilation by H. R. Kaufman and R. S. Robinson (1987), *Operation of Broad-Beam Sources*. Commonwealth Scientific Corp., Alexandria, Virginia, from data by G. K. Wehner et al. (1962), General Mills Report **2309**, General Mills Electronic Division, Minneapolis, MN, published by P. R. Puckett, S. L. Michel, and W. E. Hughes, (1991), p. 760 in *Thin Film Processes II*, eds. J. O. Vossen and W. Kern, Academic Press, Boston.

A8.5b ARGON ION MILLING RATES OF *COMPOUNDS* (SEC. 8.4.2)

Values of argon ion milling rates of compounds are tabulated in nm/min, at a current density of 1 mA/cm^2, and incident argon ion energies of 200 eV and 500 eV.

Rates at other energies can be estimated from Fig. 8.11. An example is given in Sec. 8.4.2 under Cleaning etch.

Argon ion milling rates of *compounds*

Compound	200 eV [nm/min]	500 eV [nm/min]
CdS[a]	110	230
GaAs (110)[a]	78	160
GaP (111)[a]	69	160
GaSb (111)[b]	90	190
InSb[a]	76	150
$LiNbO_3$ (Y-cut)[c]	—	40
MgO[e]	—	16
Mo_2C[a]	—	29
PbTe[a]	160	380
SiC (0001)[a]	—	35
SiO_2[c]	—	40
$YBa_2Cu_3O_7$[d]	—	45

Source: From a compilation by H. R. Kaufman and R. S. Robinson (1987), *Operation of Broad-Beam Sources*, Commonwealth Scientific Corp., Alexandria, VA, published by P. R. Puckett, S. L. Michel, and W. E. Hughes (1991), p. 760 in *Thin Film Processes II*, eds. J. O. Vossen and W. Kern, Academic Press, Boston; and from J. W. Ekin (1992), unpublished data, National Institute of Standards and Technology, Boulder, CO.

[a] J. Comas, J. and C. B. Cooper (1966), *J. Appl. Phys*. 37, 2820–2822.

[b] S. P. Wolsky, D. Shooter, and E. J. Zdanuk (1962), pp. 164–168 in *Transactions of the 9th National Vacuum Symposium*, Pergamon Press, New York.

[c] H. L. Garvin (1971), *Bull. Am. Phys. Soc., Ser. II* 16, 836.

[d] J. W. Ekin (1990), unpublished data, National Institute of Standards and Technology, Boulder, CO.

A10 Critical-current analysis parameters (ref. Chapter 10)

A10.1 EFFECTIVE CRITICAL TEMPERATURE $T_c^*(B)$ (SEC. 10.4.4)

Values of the effective critical temperature $T_c^\star$ as a function of magnetic field B are tabulated below. They were determined by linearly extrapolating the $I_c(T,B)$ curves of Figs 10.17, 10.18, 10.19, and 10.21 to zero current.

The value of $T_c^\star(B)$ at a given magnetic field B is useful when the critical current $I_c(T_1)$ is known at one temperature T_1 and we wish to determine its approximate value $I_c(T)$ at an arbitrary temperature T. For this purpose, a linear approximation of the $I_c(T)$ characteristic works fairly well for a number of conductors [Eq. (10.14) in Sec. 10.4.4]:

$$I_c(T)/I_c(T_1) = [T_c^\star - T]/[T_c^\star - T_1].$$

This linear relationship between the critical current and temperature usually breaks down at high temperatures (within about 10% of $T_c^\star$) because of inhomogeneities in the superconductor, but the relationship is useful over most of the practical temperature range leading up to $T_c^\star$ (ref. Figs 10.17, 10.18, 10.19, and 10.21).

For materials that cannot be modeled with a linear relationship, the temperature-transformation method described in Sec. 10.6.3 is much more general in nature and quite accurate for nearby transformations. A summary of the method is also given in Appendix A10.2b under the subsection entitled Temperature dependence of the critical current.

Values of $T_c^*(B)$ at various magnetic fields for selected superconductors

Magnetic field B	Nb–Ti [a] First number valid near T_c^*; the second for the range 4.0–4.5 K		Nb_3Sn[b]	V_3Ga[d]	YBCO[e]
[T]	[K]	[K]	[K]	[K]	[K]
0	9.2	12.4			87
0.3	9.0	11.0			
1	8.66	9.78			
2	8.25	9.31	15.0		
3	7.89	8.77			
4	7.40	8.20	13.7	11.8	
5	7.07	7.54	13.1	11.4	
6	6.52	6.85	12.6		
7	6.14	6.16			
8	5.53	5.53	11.5	10.8	
9	5.16	5.01			
10	4.63	4.63	10.4	10.3	
12			9.5		

[a] For Nb–Ti, the first value of T_c^* is for use over the high-temperature regime where T approaches T_c^*. It is extrapolated from the slope of the data where I_c approaches zero. The second value of T is for use over the liquid-helium temperature range. It is extrapolated from data only between 4.0 K and 4.5 K. Note that because of curvature in the I_c vs. T plot *at low magnetic fields*, the second value of T_c^* (for use in the liquid-helium temperature range) can be significantly greater than the first (nominal) value. Data are from L. F. Goodrich and T. C. Stauffer (2004), *Adv. in Cryog. Eng. (Mater.)* 50B, 338–345 (the source data are plotted in Fig. 10.17 of this textbook).

[b] Extrapolated from data by L. F. Goodrich, L. T. Medina, and T. C. Stauffer (1998), *Adv. Cryog. Eng. (Mater.)* 44, 873–880 (straight-line extrapolations are shown in Fig. 10.18 of this textbook).

[c] Extrapolated from data by S. A. Keys, N. Koizumi, and D. P. Hampshire (2002), *Supercond. Sci. Technol.* 15, 991–1010.

[d] Extrapolated from data by Y. Iwasa and B. Montgomery (1975), pp. 387–487 in *Applied Superconductivity*, Vol. 2, ed. V. L. Newhouse, Academic Press, (straight-line extrapolations are shown in Fig. 10.19).

[e] Extrapolated from data by R. Feenstra and D. T. Verebelyi (1999), unpublished, Oak Ridge National Laboratory, TN (the source data are plotted in Fig. 10.21).

A10.2a SCALING PARAMETERS FOR THE MAGNETIC-FIELD, STRAIN, AND TEMPERATURE DEPENDENCE OF THE CRITICAL CURRENT OF LOW-T_C SUPERCONDUCTORS (SECS 10.3, 10.5, 10.6, AND 10.7)

The scaling-parameter values listed below can be used for technological purposes to analytically model and transform the critical current of multifilamentary low-T_c superconductors as a function of magnetic field, strain, and temperature. These parameters are used in conjunction with the scaling relations summarized in Appendix A10.2b. The scaling relations are listed in Appendix A10.2b in order of increasing complexity, starting with the simplest scaling laws (appropriate for fixed strain or temperature) and working to the most complete (the unified scaling law suitable for variable magnetic field, temperature, and strain). The relations are mutually consistent and build on each other, so it is worth utilizing the simplest relation for the task at hand.

Values of the scaling parameters tabulated here were determined from data correlations for specific classes of superconductors. They show good consistency ($\pm$10–20%) within each class, where sufficient data exist for meaningful statistical correlations to be made (e.g. binary Nb_3Sn, V_3Ga, and, to some extent, Nb_3Al; see, for example, Figs 10.30 and 10.31). These values will no doubt be refined and updated as more data are obtained for given classes of superconductors, such as specific types of ternary Nb_3Sn. To that end, these standard values and the accompanying scaling relations provide a basic *framework* for systematizing additional data as they become available.

This ongoing task is aided by the *separability* of this parameter set into magnetic field, strain, and temperature parameters. Defined in this way, the parameter values show good consistency and are easily updated. A significant advantage of the separable parameter set used here is the independence of strain and temperature parameters, which enables their values to be determined from separate strain and temperature experiments. This offers flexibility and considerable time savings. Also, since the parameters are not commingled, the entire set does not have to be redetermined every time additional new strain or temperature data become available for a particular conductor. (Further information on the practical use of this parameter set is given in Sec. 10.7.1 under the subheading Separable form, and in Sec. 10.7.4.)

If strain and/or temperature data are available for a specific conductor, scaling parameters tailored to that conductor can be determined with the robust methods given in Sec. 10.7.4 and substituted for the standard parameters given in the following table entitled Scaling Parameters. In this case, the values below are needed only to fill in missing gaps in the scaling-parameter set (see Sec. 10.7.4 for more details). These standard values also have predictive utility in the initial design stage of superconducting magnets.

Limitations

1. These parameter values are valid specifically for conductors with *solid filaments* (not tubular filaments, or bundles of filaments that fuse into a tubular structure after reaction).
2. They also depend on *additive content* and *fabrication process* (e.g. bronze process vs. internal tin). The tabulated additive concentrations are not the starting weight percent of additive in the conductor before reaction; rather, they are the atomic percent actually measured in the Nb_3Sn reaction layer *after* fabrication, which can vary depending on the fabrication process. As more data become available, it is expected that consistent correlations of parameter values will be obtained for additional classes of conductors.
3. The tabulated scaling parameters are for technological use over the *moderate intrinsic-strain range* ($-0.5\% < \varepsilon_0 < +0.4\%$), which is the range where most magnets are designed. For high compressive strains ($\varepsilon_0 < -0.5\%$), four more parameters are needed, as described in Secs. 10.5.6 and 10.7.3 and summarized below in Eqs (A10.9)–(A10.11) and (A10.30)–(A10.32); these high-compression parameters may not be so consistent.

Examples

Practical examples for utilizing these parameters with the scaling relations are given in the following sections:

- Magnetic-field modeling — Sec. 10.3.3
- Strain and magnetic-field modeling — Sec. 10.5.7
- Simplified strain transformations — Sec. 10.6.2
- Simplified strain-and-temperature transformations — Sec. 10.7.5

Temperature-scaling parameters

Values of the temperature-scaling parameters {for use with the temperature scaling law [Sec. 10.6.3 and Eq. (A10.12) below] and the unified strain-and-temperature scaling law [Sec. 10.7 and Eq. (A10.18)]} are available mainly for Nb_3Sn and not listed in the table below. The (dimensionless) temperature-scaling parameters v and w appear to be consistent constants for the technological Nb_3Sn conductors evaluated thus far, including binary and ternary Nb_3Sn at both moderate and high intrinsic strains:

$v = 1.5$ for Nb_3Sn, as shown by Figs 10.37 and 10.38

$w \simeq 3$ for Nb_3Sn, as shown by Fig. 10.36.

Although not so nearly consistent, the (dimensionless) temperature exponent η and the critical temperature at zero intrinsic strain $T_c^\star(0)$ can be effectively approximated for nearby temperature transformations by

$\eta \approx 3$ for Nb_3Sn

$T_c^*(\varepsilon_0{=}0) \approx 17.5$ K for Nb_3Sn.

With additional temperature correlations, values of these latter two parameters may become more standardized for individual classes of superconductors.

For Nb_3Sn, the scaling parameter $B_{c2}^\star$ ($T = 0, \varepsilon_0 = 0$) can be estimated by using Eq. (10.57) with the approximate values of $B_{c2}^\star$ (4.2 K, $\varepsilon_0 = 0$) given in the table below; that is,

$$B_{c2}^\star\,(0{,}0) \approx B_{c2}^\star\,(4.2\text{ K}{,}0) \times [1-(4.2\text{ K}/17.5\text{ K})^v]^{-1} \approx 1.13\,B_{c2}^\star\,(4.2\text{ K}{,}0).$$

A10.2a Scaling parameters [dimensionless, except for B^*_{c2}]

Superconductor	Crystal structure	Magnetic-field dependence of I_c			Strain dependence of I_c[‡*] ($-0.5\% < \varepsilon_0 < +0.4\%$)			
		p[†]	q[†]	B^*_{c2} at 4.2 K, $\varepsilon_0 = 0$ [T]	$a^-(\varepsilon_0<0)$	$a^+(\varepsilon_0>0)$	s	Ref.
Strain-dependent superconductors								
Nb_3Al (RHQT)	A15	0.5	2.0	26	370	—	0.1	a
V_3Ga	”	0.4	1.0	21	450	650	1.4	b
Nb_3Ge	”	0.6	1.9	25	500	—	~2	c
Nb_3Sn*	”	0.5	2.0	21	900	1250	1	d
Nb_3Sn +0.6at%Ti*	”	0.6	1.7	23	900	1250	1.1	e
Nb_3Sn +1.85at%Ti*	”	0.5	1.5	25	1100	1450	1.2	e,f
Nb_3Sn +0.6at%Ta*	”	0.5	1.4	24	900	1250	1.0	e
Nb_3Sn +2.2at%Ta*	”	0.5	1.4	24	1350	1800	~1	e,g
V_3Si	”	0.5	1.7	16	3500	—	~1	a
$PbMo_6S_8$	Chevrel	0.3	6	63	—	1900	~2	h
Strain-independent superconductors								
NbN	B1	1.2	2.4	24	0	0	—	i
NbCN	”	1.4	2.5	17	—	0	—	j
V_2(Hf,Zr)	C15	0.7	0.6	20	—	0	—	k

[†] Values of p and q are effectively independent of temperature and strain (Sec. 10.7.1).

[‡] The strain-parameter values listed are valid only for the moderate intrinsic-strain range ($-0.5\% < \varepsilon_0 < +0.4\%$). To model I_c at high-compressive strains ($\varepsilon_0 < -0.5\%$), additional parameters are needed, as described in Sec. 10.5.6 for the strain-scaling law and Sec. 10.7.3 for the unified strain-and-temperature scaling law.

* The strain parameters a^-, a^+, and s are applicable to *solid-filament* superconductors (not superconductors with tabular filaments, nor clusters of filaments fused into tubular shapes). The strain-sensitivity parameter a is defined by Eq. (10.21) of Sec. 10.5.5 for a power-law exponent $u = 1.7$. [This value of u is found to hold experimentally for all the A15 and Chevrel-phase superconductors listed in the above table (see Sec. 10.5.5). It is also given by the model of Markiewicz with no adjustable parameters (see Fig. 10.32).] The values of a^- and a^+ are dependent on the type and amount of *additives*, as shown for the various ternary Nb_3Sn materials listed in the table. Atomic percentages given are those measured in the Nb_3Sn layer *after* reaction. For example, 2.2at%Ta in the reaction layer was obtained with a starting filament alloy of Nb–7.5wt%Ta, but it can vary depending on conductor processing.

[a] N. Banno, D. Uglietti, B. Seeber, T. Takeuchi, and R. Flükiger (2005), *Supercond. Sci. and Technol.* 18, S338–S343. RHQT ≡ rapid heating, quenching and transformation process.

[b] J. W. Ekin (1981), *IEEE Trans. Magn.* MAG-17, 658–661; D. G. Howe, T. L. Francavilla and D. U. Gubser (1977), *IEEE Trans. Magn.* MAG-13, 815–817; Furukawa Corp. (1984), personal communication.

[c] J. W. Ekin (1981), *IEEE Trans. Magn.* MAG-17, 658–661.

[d] J. W. Ekin (1980), *Cryogenics* 20, 611–624.

[e] J. W. Ekin (1985), pp. 267–271 in *Proc. International Symposium of Flux Pinning and Electromagnetic Properties of Superconductors*, eds. K. Yamafuji and F. Irie, Matsukuma Press, Japan.

[f] Sample from G. Ozeryansky (1984), Intermagnetics General Corp.

[g] Sample from W. McDonald (1984), Teledyne Wah-Chang Corp.

[h] J. W. Ekin, T. Yamashita, and K. Hamasaki (1985), *IEEE Trans. Magn.*, MAG-21, 474–477.

[i] J. W. Ekin, J. R. Gavaler, and J. Greggi (1982), *Appl. Phys. Lett.* 41, 996–998.

[j] J. W. Ekin, unpublished data, National Institute of Standards and Technology, Boulder, CO; sample from M. Dietrich (1984), Kernforschungszentrum Karlsruhe, Karlsruhe, Germany.

[k] H. Wada, K. Inoue, K. Tachikawa, and J. W. Ekin (1982), *Appl. Phys. Lett.* 40, 844–846.

A10.2b SUMMARY OF SCALING RELATIONS FOR UTILIZING THE SCALING PARAMETERS IN APPENDIX A10.2a

The relations summarized here are based on consistent scaling data of the critical current as a function of magnetic field, strain, and temperature. Used in conjunction with the scaling parameters tabulated in Appendix A10.2a, they provide analytic expressions for modeling, interpolating, and predicting the critical current of most practical low-T_c superconductors as a function of magnetic field, strain, and temperature for technological applications. Further discussion and examples of the application of these scaling relations are given in the main text sections referred to in parentheses with each summary heading. The scaling relations are mutually consistent and listed progressively from the simplest to the most general. Again, use the simplest relation for the task at hand.

Because the parameter set used here is separable into temperature and strain parameters (see Sec. 10.7.1), the relations, when assembled, become the general unified scaling law described at the end of the list below. The separable nature of this parameter set also has the benefit that limited numbers of scaling parameters determined from early limited data (i.e. an incomplete set of values) are not a wasted effort. Rather, they build on each other and generally do not need to be refit later as more data become available. As refined parameter values are measured for an individual conductor, they can be substituted for the "standard" values listed in the Scaling Parameters table in Appendix A10.2a. This building process also parallels the way data are usually obtained for a given conductor (Sec. 10.7.4).

MAGNETIC-FIELD INTERPOLATIONS (SECS 10.3.2 AND 10.3.3)

The dependence of the critical current I_c on magnetic field B is given by [ref. Eqs. (10.9)–(10.11)]

$$I_c(B) = k\,B^{-1}\,[B/B^{\star}_{c2}]^{p}\,[1-(B/B^{\star}_{c2})]^{q}, \tag{A10.1}$$

where k is a proportionality constant and $B^{\star}_{c2}$ is the effective upper critical field. This is an empirical expression based on the general form of most pinning theories. Typical values of $B^{\star}_{c2}$ and the exponential constants p and q for most of the common high-field low-T_c superconductors are given in columns 3–5 of the Scaling Parameters table in A10.2a. Values of the parameters p and q tailored to a specific conductor can be obtained from a single $I_c(B)$ measurement at a fixed temperature and strain [preferably obtained at a temperature $T \ll T^{\star}_c(0)$ to minimize the effects of B_{c2} inhomogeneity (Sec. 10.3.4), and at a strain not too far from $\varepsilon_0 \approx 0$ to avoid B_{c2} inhomogeneity effects as well as filament breakage at high tensile strains (Sec. 10.5.1)].

STRAIN DEPENDENCE OF THE CRITICAL CURRENT (VALID FOR FIXED TEMPERATURE $T \ll T_c$; E.G. AT 4.2 K IN Nb_3Sn) (SECS 10.5.4–10.5.7)

The magnetic-field and strain dependence of the critical current of most low-T_c superconductors can be modeled at low temperatures with the strain scaling law [Eq. (10.18)]. The simplest parameterization of this law applies to the moderate intrinsic-strain range ($-0.5\% < \varepsilon_0 < +0.4\%$, assuming $\varepsilon_{irr} \geq +0.4\%$), which is also the strain range where most (but not all) magnets are designed, mainly because the critical currents are highest in this regime. [Extended-strain parameters covering the high-compressive-strain range ($\varepsilon_0 \ll -0.5\%$) are given in Secs 10.5.6 and 10.7.3, and are summarized below in Eqs. (A10.9)–(A10.11) and (A10.30–A10.32).] This empirical scaling law is based on extensive correlations of strain data at 4.2 K in low-T_c superconductors, which show strain invariance of the shape of the pinning-force vs. magnetic-field characteristic (Sec. 10.5.4).

For the moderate strain range, the simplest and most consistent parameterization of the strain scaling law for technological purposes gives the following expression for the magnetic-field and strain dependence of the critical current $I_c(B,\varepsilon_0)$ [ref. Eqs. (10.20)–(10.22)]

$$I_c(B,\varepsilon_0)=g(0)\,[1-a|\varepsilon_0|^{1.7}]^s\,B^{-1}\,[B/B^{\star}_{c2}(\varepsilon_0)]^p\,\{1-[B/B^{\star}_{c2}(\varepsilon_0)]\}^q, \tag{A10.2}$$

valid for fixed temperature $T \ll T_c$ (e.g. at 4.2 K in Nb_3Sn). Here, $g(0)$ is a proportionality constant and the scaling parameters p, q, a^- (for $\varepsilon_0 < 0$), a^+ (for $\varepsilon_0 > 0$), and s are tabulated in columns 3, 4, 6, 7, and 8, respectively, of the Scaling Parameters table in A10.2a. (The strain-sensitivity parameters a^- and a^+ are described more fully below.) The scaling parameter $B^{\star}_{c2}(\varepsilon_0)$ is the strain-dependent effective upper critical field; values at 4.2 K are tabulated in column 5 of Table A10.2a.

The variable ε_0 is the *intrinsic* strain, defined as

$$\varepsilon_0 \equiv \varepsilon-\varepsilon_m, \tag{A10.3}$$

where ε is the axial strain applied to the superconductor and ε_m is the axial strain at which I_c is maximum (e.g. Fig. 10.26). Negative values of ε_0 represent the compressive intrinsic strain in the superconductor, and positive values represent tensile intrinsic strain (Sec. 10.5.1). The upper strain limit for the validity of this strain scaling law is given by the irreversible strain limit ε_{0irr}, where the conductor is permanently damaged by axial strain. A typical value of ε_{0irr} in Nb_3Sn is about $\varepsilon_{0irr} \approx +0.4\%$, but it can be more or less than this amount (Sec. 10.5.1). (Lower values of ε_{0irr} usually occur in conductors with larger filament diameters or fused filament clusters, whereas higher values of ε_{0irr} usually occur in conductors with small filament diameters, such as Nb_3Al or fine-filament Nb_3Sn conductors.)

Over the moderate intrinsic strain range ($-0.5\% < \varepsilon_0 < \varepsilon_{0irr}$), the effective upper critical field is well represented by a power law

$$\frac{B^{\star}_{c2}(\varepsilon_0)}{B^{\star}_{c2}(0)} = 1-a|\varepsilon_0|^{1.7}, \tag{A10.4}$$

where $B^{\star}_{c2}(\varepsilon_0 = 0)$ is evaluated at the designated temperature T. This is an empirical parameterization that accurately and consistently represents the fundamental results of anharmonic strain theory over the moderate strain range (Sec. 10.5.5). Values of $B^{\star}_{c2}(\varepsilon_0 = 0)$ at 4.2 K are listed in column 5 of Table A10.2a. For Nb_3Sn, values of $B^{\star}_{c2}(\varepsilon_0 = 0)$ at other temperatures can be estimated from the 4.2 K values by using Eq. (10.57) [i.e. Eq. (A10.19) below] and the temperature-scaling parameter values listed just before Table A10.2a.

The parameter a in Eq. (A10.4) is the *intrinsic strain sensitivity* and is a simple quantitative index of the sensitivity of a given class of superconductors to axial strain. For compressive strains ($\varepsilon_0 < 0$), the strain sensitivity is denoted as a^-, with values listed in column 6 of Table A10.2a. For tensile strains ($\varepsilon_0 > 0$), the strain sensitivity is denoted a^+, with somewhat greater values listed in column 7 of Table A10.2a. (Sec. 10.5.5 gives a discussion of the fundamental origin of this difference.) The compressive parameter a^- (column 6) is usually the more important parameter from a technological standpoint, since it characterizes the strain sensitivity of a conductor over the moderate compressive strain range where most magnets are designed ($-0.5\% < \varepsilon_0 < 0\%$). Again, the tensile parameter a^+ is valid only up to the irreversible strain limit ε_{0irr} where damage occurs in the superconducting filaments.

Limitations

1. It bears reiterating that the strain-scaling parameters a^-, a^+, and s in Table A10.2a apply to the most common types of conductors, *solid-filament* multifilamentary wires, not to other filament shapes such as wires with tubular filaments or fused-tubular clusters, where the strain sensitivity is enhanced by three-dimensional strain effects.

2. Occasionally, particular conductors need to be characterized by unsymmetrical values of the parameter s in Eq. (A10.2) [s^- for compressive intrinsic strain ($\varepsilon_0 < 0$) and s^+ for the tensile side ($\varepsilon_0 > 0$)]. Further data correlations are needed to see if such unsymmetrical values of s are "standard" for certain types of superconductors.
3. For high-compressive strains ($\varepsilon_0 < -0.5\%$), a more general relationship must be used, given by Eqs (10.23) and (10.24) in Sec. 10.5.6. This entails additional parameters that appear to be extrinsic in nature and, therefore, must be fitted on a conductor-by-conductor basis (Sec. 10.5.6).

Strain *transformation* method (Sec. 10.6.1)

The strain *transformation* method is a powerful technique for utilizing the strain scaling law to transform a single $I_c(B, \varepsilon_{01})$ curve obtained at a strain ε_{01} to a curve $I_c(B', \varepsilon_{02})$ valid at a different strain ε_{02}, without the need to know the parameters $p, q, B^*_{c2}(0)$, or $g(0)$ in Eq. (A10.2). The derivation of this transformation method is given in Sec. 10.6.1.

The transformation is independent of the parameterization scheme; it is illustrated here with the separable parameter set employed above because of its practical utility, but it can be used with any of the alternative parameterization schemes that have been proposed for the prefactor term $g(\varepsilon)$ in the strain-scaling law [Eq. (10.18)]. Again, the strain-transformation method is limited to transformations carried out at fixed temperatures $T \ll T_c$, such as 4.2 K in Nb_3Sn. (For combined strain and temperature transformations, see the unified-scaling transformation method summarized in the last subsection of this appendix.)

The application of the transformation consists of two steps. First, to obtain $I_c(B', \varepsilon_{02})$ when ε_{01} and ε_{02} fall within the moderate strain range ($-0.5\% < \varepsilon_0 < \varepsilon_{0irr}$), multiply the magnetic-field data of the $I_c(B, \varepsilon_{01})$ data set by the constant β to obtain a new set of magnetic-field values B' [ref. Eq. (10.32)]

$$B' = \beta B. \tag{A10.5}$$

Second, multiply the critical current data of the $I_c(B, \varepsilon_{01})$ set by β^{s-1} to obtain new critical current values corresponding to the new magnetic-field data; that is [ref. Eq. (10.33)],

$$I_c(B', \varepsilon_{02}) = \beta^{s-1} I_c(B, \varepsilon_{01}). \tag{A10.6}$$

The constant β in these two equations is given by [ref. Eq. (10.34)]

$$\beta \equiv \frac{B^*_{c2}(\varepsilon_{02})}{B^*_{c2}(\varepsilon_{01})} = \frac{1 - a|\varepsilon_{02}|^{1.7}}{1 - a|\varepsilon_{01}|^{1.7}}. \tag{A10.7}$$

(For an immediate clarification of this simple data-transformation procedure, please refer to the example given in Table 10.3 in Sec. 10.6.2.) Thus, all that is needed to carry out the transformation are the scaling parameters a and s. Again, values of s are listed in column 8 of Table A10.2a, and values of the strain-sensitivity parameter a are given in columns 6 and 7 of Table A10.2a (a^- for $\varepsilon_0 < 0$, and a^+ for $\varepsilon_0 > 0$).

For nearby transformations, this method is quite accurate. For example, when transforming from $\varepsilon_0 = -0.3\%$ to 0% in Nb_3Sn conductors, an error of 10% in the value of a results in an error of less than 0.5% in the transformed B values and effectively no error in the I_c values.

High-compressive strains: For transformations involving high-compressive strains ($\varepsilon_0 < -0.5\%$), the magnetic-field transformation remains that given by Eq. (A10.5), but we use the more general transformation for the critical current [Eq. (10.30)]

$$I_c(B', \varepsilon_{02}) = \beta^{-1} \frac{g(\varepsilon_{02})}{g(\varepsilon_{01})} I_c(B, \varepsilon_1), \tag{A10.8}$$

where

$$\beta \equiv \frac{B^{\star}_{c2}(\varepsilon_{02})}{B^{\star}_{c2}(\varepsilon_{01})}.$$

The functions $B^{\star}_{c2}(\varepsilon_0)$ and $g(\varepsilon_0)$ can be parameterized at high-compressive strains by

$$\frac{B^{\star}_{c2}(\varepsilon_0)}{B^{\star}_{c2}(0)} = 1 - a|\varepsilon_0|^{1.7} + a_1|\varepsilon_0 - \varepsilon_0'|^{a_2} I(\varepsilon_0 < \varepsilon_0') \tag{A10.9}$$

and

$$\pounds\frac{g(\varepsilon_0)}{g(0)} = [1 - a|\varepsilon_0|^{1.7}]^{s} + g_1|\varepsilon_0 - 0.005|^{g_2} I(\varepsilon_0 < \varepsilon_0') \tag{A10.10}$$

with

$$I(\varepsilon_0 < \varepsilon_0') \equiv \begin{cases} 1 & \text{if } \varepsilon_0 < \varepsilon_0' \\ 0 & \text{if } \varepsilon_0 > \varepsilon_0'. \end{cases} \tag{A10.11}$$

Here, $I(\varepsilon_0 < \varepsilon_0')$ is an *indicator function*, which is zero except at high-compressive strains: $\varepsilon_0 < \varepsilon_0'$, with $\varepsilon_0' \approx -0.005$ for Nb_3Sn. Unlike transformations carried out over the intrinsic peak strain range, the extra parameters characterizing the extended strain range (a_1, a_2, g_1, and g_2) are probably extrinsic in nature and need to be determined on a conductor-to-conductor basis. The advantage of the parameterization given by Eqs (A10.9)–A(10.10) is that the scaling parameters a and s characterizing the intrinsic peak region remain consistent and unaffected by those characterizing the extrinsic high-compressive regime.

TEMPERATURE DEPENDENCE OF THE CRITICAL CURRENT (VALID FOR FIXED STRAIN) (SEC. 10.6.3)

The magnetic-field and temperature dependence of the critical current of most low-T_c superconductors can be modeled (at a fixed strain) with the temperature scaling law [Eq. (10.36)]. This empirical relation is based on correlations of temperature data at fixed strain, which show temperature invariance of the shape of the pinning-force vs. magnetic-field characteristic (Sec. 10.6.3).

The simplest parameterization of the temperature scaling law for technological purposes is given by [ref. Eqs (10.38)–(10.43)]

$$I_c(B,T) = h(0)\,[(1-t^{\nu})]^{\eta}\,B^{-1}\,[B/B^{\star}_{c2}(t)]^{p}\,\{1-[B/B^{\star}_{c2}(t)]\}^{q}, \tag{A10.12}$$

valid for fixed strain. Here, $h(0)$ is a proportionality constant, p and q are the scaling constants given in columns 3 and 4 of Table A10.2a, and ν and η are temperature-scaling constants listed for Nb_3Sn just before Table A10.2a.

The variable t is the *reduced* temperature, defined as

$$t \equiv T/T^{\star}_c(\varepsilon_0), \tag{A10.13}$$

where T is the temperature of the superconductor and $T^{\star}_c(\varepsilon_0)$ is its effective critical temperature (at a fixed strain ε_0). When $t \ll 1$ and $|\varepsilon_0| \equiv |\varepsilon - \varepsilon_m| < \sim 0.4\%$, the better known *strain-free* value of $T^{\star}_c$ at $\varepsilon_0 = 0$ can be used (since the strain dependence of $T^{\star}_c$ is relatively gradual, as described for the unified-scaling relation below). For Nb_3Sn, the strain-free $T^{\star}_c$ is about 17.5 K, also listed with the temperature-scaling parameter values just before Table A10.2a.

The effective upper critical field in Eq. (A10.12) can be parameterized most simply by

$$B^{\star}_{c2}(t)=B^{\star}_{c2}(0)(1-t^{\nu}), \tag{A10.14}$$

where $B^{\star}_{c2}(t=0)$ is evaluated at the designated strain ε_0. For Nb_3Sn, the strain-free value of $B^{\star}_{c2}(t=0)$ (i.e. at 0 K and at $\varepsilon_0 \equiv \varepsilon - \varepsilon_m = 0$) can be estimated from the values of $B^{\star}_{c2}(4.2\text{ K},\varepsilon_0=0)$ listed in column 5 of Table 10.2a by using the relation $B^{\star}_{c2}(t=0,\varepsilon_0=0) \approx B^{\star}{}_{c2}(4.2\text{ K},\varepsilon_0=0)\ [1-(4.2\text{ K}/17.5\text{ K})^{\nu}]^{-1} \approx 1.13\, B^{\star}_{c2}\ (4.2\text{ K},\varepsilon_0=0)$. (Here we have used the nearly universal value $\nu = 1.5$, which is appropriate for Nb_3Sn.) The strain-free $B^{\star}_{c2}$ also works for small values of intrinsic strain, since the strain dependence of $B^{\star}_{c2}$ is relatively gradual compared with its temperature dependence.

The temperature-scaling parameters are the least well characterized at present. As indicated in the material just before the Scaling Parameters table in Appendix A10.2a, the value $\nu = 1.5$ is fairly well established for Nb_3Sn conductors, but the temperature-scaling parameter η is not yet, with values reported typically in the range 2.5–3.5 for different types of Nb_3Sn superconductors. More standard values of η are expected to be determined as data correlations become available for specific classes of superconductors. In the meantime, a nominal value of $\eta = 3$ can be used at least for estimation purposes. This nominal value of η also serves well for temperature *transformations*, particularly if they are nearby transformations, as described next.

Temperature *transformation* method (Sec. 10.6.3)

Similar to the strain transformation summarized earlier, the temperature transformation method is a greatly simplified technique for utilizing the temperature scaling law to transform a single $I_c(B,t_1)$ curve, obtained at a temperature t_1, to a curve $I_c(B',t_2)$ valid at a different temperature t_2, without the need to know the parameters p, q, $B^{\star}_{c2}$ $(t=0)$, or $h(0)$ in Eq. (A10.12).

The transformation is independent of the parameterization scheme. Again, it is illustrated here with the separable parameter set employed above because of its practical utility, but it can be used with any of the alternative parameterization schemes that have been proposed for the prefactor term $h(T)$ in the temperature scaling law [Eq. (10.36)] The temperature-transformation technique is limited to transformations carried out at a fixed strain; for combined strain and temperature transformations, see the unified scaling law summarized in the next subsection.

As for strain transformations, the application of the temperature transformation method consists of two steps. First, to obtain $I_c(B',t_2)$, multiply the magnetic-field data of the $I_c(B,t_1)$ data set by the constant β to obtain a new set of magnetic-field values B' [ref. Eq. (10.39)]

$$B'=\beta\, B. \tag{A10.15}$$

Second, multiply the critical-current data of the $I_c(B,t_1)$ set by $\beta^{\eta-1}$ to obtain values of the critical current corresponding to the new magnetic-field values; that is [ref. Eq. (10.41)]

$$I_c(B',\ t_2)=\beta^{\eta-1}\, I_c(B,\, t_1). \tag{A10.16}$$

The constant β is given by [ref. Eqs (10.42) and (10.43)]

$$\beta \equiv \frac{B^{\star}_{c2}(T_2)}{B^{\star}_{c2}(T_1)} = \frac{1-(T_2/T^{\star}_{c2})^{\nu}}{1-(T_1/T^{\star}_{c2})^{\nu}}\ . \tag{A10.17}$$

(Again, for a clarification of this simple data-transformation procedure, please refer to the example given for strain in Table 10.3 in Sec. 10.6.2.) All that is needed to carry out the transformation are the scaling parameters $T^{\star}_c$, ν, and η.

As noted above, data correlations of the temperature-scaling parameters have not yet been made for many of the different classes of technological superconductors. The value $\nu = 1.5$ is fairly well

established for Nb_3Sn conductors and the strain-free T_c^* at $\varepsilon_0 = 0$ is about 17.5 K for Nb_3Sn, but the scaling parameter η is not so nearly universal, with values reported over the range 2.5–3.5 for a variety of Nb_3Sn conductors. A nominal value of $\eta = 3$ can be used for estimation purposes with most Nb_3Sn superconductors.

Nevertheless, this method is quite accurate if the transformations are nearby. For example, when making the very useful data transformation from 4.2 K to, say, 5.5 K in Nb_3Sn conductors, even a large error of $\pm 20\%$ in the value of η (which covers the range $2.5 < \eta < 3.5$) results in a difference of only about $\pm 3.5\%$ in the transformed I_c (and no error in B). For the same example, an error of 5% in the parameter T_c^* results in a difference of only 1.2% in the transformed I_c, and only 0.6% in the transformed B.

UNIFIED STRAIN-AND-TEMPERATURE DEPENDENCE OF THE CRITICAL CURRENT (SEC. 10.7)

The combined magnetic-field, temperature, and strain dependence of the critical current of most low-T_c superconductors can be modeled with the unified scaling law [Eq. (10.45)]. The simplest parameterization of this scaling law applies to the moderate intrinsic-strain range ($-0.5\% < \varepsilon_0 < +0.4\%$, assuming $\varepsilon_{irr} \geq +0.4\%$), which is where most superconductor applications are designed (again, because in this regime the conductors are under the least stress and their critical currents are maximized). [Extended-strain parameters covering the high-compressive-strain range ($\varepsilon_0 < -0.5\%$) are discussed below with the unified-transformation method.] The unified scaling law is based on data in low-T_c superconductors showing shape invariance of the pinning-force vs. magnetic-field characteristic with respect to both strain and temperature simultaneously.

For the moderate intrinsic-strain range, the unified scaling law can be parameterized with the separable parameter set, giving the combined magnetic-field, temperature, and strain dependence of the critical current $I_c(B,T,\varepsilon_0)$ [ref. Eqs (10.56)–(10.58)]

$$I_c(B,T,\varepsilon_0) = C\, B^{-1} (1 - a|\varepsilon_0|^{1.7})^s (1 - t^\nu)^\eta b^p (1-b)^q \tag{A10.18}$$

where

$$B_{c2}^*(t,\varepsilon_0) = B_{c2}^*(0,0)(1 - a|\varepsilon_0|^{1.7})(1 - t^\nu) \tag{A10.19}$$

and

$$\frac{T_c^*(\varepsilon_0)}{T_c^*(0)} = (1 - a|\varepsilon_0|^{1.7})^{1/w}. \tag{A10.20}$$

Here, C is a proportionality constant and the variables are defined by:

$\varepsilon_0 \equiv \varepsilon - \varepsilon_m$ Intrinsic strain (where ε is the applied strain and ε_m is the applied strain at the peak of the critical current, all in absolute units, not percent)

$b \equiv \dfrac{B}{B_{c2}^*(t,\varepsilon_0)}$ Reduced magnetic field

$t \equiv \dfrac{T}{T_c^*(\varepsilon_0)}.$ Reduced temperature

Equations (A10.18) through (A10.20) utilize the separable parameter set, mentioned in the introduction to this section of the appendix, wherein the scaling parameters are separated into magnetic-field, strain, and temperature-scaling parameters with consistent, independent values that are easily updated as additional strain or temperature data become available for a given conductor. With this set, parameter

values can also be determined from independent strain or temperature data [rather than from a lengthy, full matrix of combined $I_c(B,t,\varepsilon_0)$ data], which can save a month or more of data acquisition per sample. Robust methods for determining values of the separable parameter set are described in detail in Sec. 10.7.4. Because this parameterization results in such consistent values, standard values of the parameters work for many purposes when values tailored to a particular conductor are not available. These parameters are discussed in the following paragraphs.

Magnetic-field scaling parameters: Standard values of the magnetic-field parameters $B^*_{c2}(T{=}4.2\text{ K},\varepsilon_0{=}0)$, p, and q are tabulated for most of the common low-T_c superconductors in columns 3 to 5 of the Scaling Parameters table of A10.2a. For Nb_3Sn, the parameter $B^*_{c2}(0,0)$ can be estimated from the measured values of $B^*_{c2}(4.2\text{ K},0)$ by using Eq. (A10.19); that is, $B^*_{c2}(0,0) \approx B^*_{c2}(4.2\text{ K},0)\,[1 - (4.2\text{ K}/17.5\text{ K})^{\nu}]^{-1} \approx 1.13\,B^*_{c2}(4.2\text{ K},0)$. Here, we have used $\nu = 1.5$ and $T^*_c(0) \approx 17.5$ K for technical Nb_3Sn conductors, as listed just before Table A10.2a.

Strain scaling parameters: Standard values of the *strain* parameters $a^-(\varepsilon_0{<}0)$, $a^+(\varepsilon_0{>}0)$, and s are tabulated in columns 6, 7, and 8, respectively, of Table A10.2a. The strain-sensitivity parameters a^- and a^+ are described more fully with the strain-scaling relation summarized above. The limitations of the validity of these standard strain-scaling parameter values are also summarized above (solid filaments, additive concentration dependence, and strain range). Note especially that they are limited to the moderate intrinsic strain range ($-0.5\% < \varepsilon_0 < +0.4\%$). The more general parameterization of the unified strain-and-temperature scaling law, valid for strains extending to high compression ($\varepsilon_0 < -0.5\%$), is given in Secs. 10.5.6 and 10.7.3, and is summarized in Eqs (A10.30–A10.32) below. As described in Sec. 10.5.6, this entails additional parameters that appear to be extrinsic in nature, and thus consistent parameter values cannot be tabulated; instead they must be fitted on a conductor-by-conductor basis.

Temperature scaling parameters: The temperature parameters ν and w have nearly universal values, at least for technical Nb_3Sn superconductors; values are listed for these two parameters just before Table A10.2a. The temperature parameters $T^*_c(0)$ and η are not yet well established. As noted for the temperature-scaling law above, a value for $T^*_c(0)$ of about 17.5 K can be used for Nb_3Sn, but this would benefit from further data correlations for given classes of superconductors. Likewise, values of η have been reported anywhere from 2.5–3.5 for different types of Nb_3Sn superconductors, but a nominal value of $\eta = 3$ can at least be used for estimation purposes and serves well for the transformation technique to nearby strains and temperatures (described just below).

Extrinsic parameters: This leaves the parameters ε_m and C, which are highly variable extrinsic parameters that mainly depend, respectively, on conductor geometry and heat-treatment conditions. Therefore, they must be determined on a conductor-by-conductor basis. Often ε_m can be approximated from measurements on similar conductors, or determined for a specific conductor from a single $I_c(\varepsilon)$ measurement at any fixed magnetic field. The proportionality constant C can be determined from a single I_c measurement on the conductor in question (at any fixed magnetic field, temperature, and strain).

Unified strain-and-temperature *transformation* method (Sec. 10.7.5)

Similar to the transformations described above, the transformation method is a powerful technique for utilizing the unified scaling law to transform a single $I_c(B)$ curve measured at strain ε_{01} and temperature T_1, to another combination of strain ε_{02} and temperature T_2 without the need to know the parameters $p, q, B^*_{c2}(0)$, and C. The method is especially effective for nearby transformations, achieving high accuracy even with standard parameter values (see below). The transformation is independent of the parameterization scheme, but it is illustrated here with the separable parameter set because of its practical utility.

As shown in the example at the end of Sec. 10.7.5, the transformation is carried out in a spreadsheet program simply by multiplying a column of magnetic-field values and a column of corresponding

critical-current values by two constant prefactors. That is, to transform a data set $I_c(B,T_1,\varepsilon_{01})$, which was obtained at temperature T_1 and strain ε_{01}, to a corresponding data set $I_c(B',T_2,\varepsilon_{02})$ valid at T_2 and ε_{02}, multiply the *magnetic-field* values in the first set by the constant β

$$B' = \{\beta\}\, B, \tag{A10.21}$$

and the *critical-current* values in the first set by the constant shown in brackets { }

$$I_c(B',\, T_2, \varepsilon_{02}) = \left\{\beta^{-1}\frac{K(T_2, \varepsilon_{02})}{K(T_1, \varepsilon_{01})}\right\} I_c(B,\, T_1, \varepsilon_{01}), \tag{A10.22}$$

where

$$\beta \equiv \frac{B^*_{c2}(T_2, \varepsilon_{02})}{B^*_{c2}(T_1, \varepsilon_{01})}. \tag{A10.23}$$

For the common case where ε_{01} and ε_{02} fall within the moderate strain range ($-0.5\% < \varepsilon_0 < +0.4\%$), these two transformation constants {the terms in curly brackets in Eqs (A10.21) and (A10.22)} can be evaluated with the separable parameter set as

$$\beta = \left(\frac{1 - a|\varepsilon_{02}|^{1.7}}{1 - a|\varepsilon_{01}|^{1.7}}\right)\left(\frac{1 - t_2^{\nu}}{1 - t_1^{\nu}}\right) \tag{A10.24}$$

and

$$\beta^{-1}\frac{K(T_2, \varepsilon_{02})}{K(T_1, \varepsilon_{01})} = \left(\frac{1 - a|\varepsilon_{02}|^{1.7}}{1 - a|\varepsilon_{01}|^{1.7}}\right)^{s-1}\left(\frac{1 - t_2^{\nu}}{1 - t_1^{\nu}}\right)^{\eta-1}. \tag{A10.25}$$

Again, the variables are defined by:

$\varepsilon_0 \equiv \varepsilon - \varepsilon_m$ Intrinsic strain (where ε is the applied strain and ε_m is the applied strain at the peak, all in absolute units, not percent)

$t \equiv \dfrac{T}{T_c^*(\varepsilon_0)}$ Reduced temperature

with

$$\frac{T_c^*(\varepsilon_0)}{T_c^*(0)} = (1 - a|\varepsilon_0|^{1.7}) \tag{A10.26}$$

Thus, for the moderate strain range ($-0.5\% < \varepsilon_0 < +0.4\%$), the task of transforming both strain and temperature with Eqs (10.21) and (10.22) is reduced to evaluating these two transformation constants from the scaling parameters: $\nu, w, \eta, s, a^-, a^+, T_c^*(0)$, and ε_m. Again, the strain parameters are given in Table A10.2a, and the temperature parameters are listed for Nb_3Sn just above the table. This leaves ε_m as the one extrinsic parameter that must be determined on a conductor-by-conductor basis from a single $I_c(\varepsilon)$ measurement at any fixed magnetic field and temperature, or it can be estimated from a single $I_c(\varepsilon)$ measurement on a similar conductor.

For transformations where either ε_{01} or ε_{02} fall in the high-compressive-strain range ($\varepsilon_0 < -0.5\%$), a more general form must be used for the two transformation constants because of the extrinsic nature of their strain dependence in this regime. The more general parameterization [which replaces Eq. (A10.24)] for the transformation constant β is

$$\beta = \frac{B^*_{c2}(0,\varepsilon_{02})}{B^*_{c2}(0,\varepsilon_{01})}\left(\frac{1-t_2^{\nu}}{1-t_1^{\nu}}\right), \tag{A10.27}$$

and the more general parameterization [which replaces Eq. (A10.25)] for the critical-current transformation factor is

$$\beta^{-1}\frac{K(T_2,\varepsilon_{02})}{K(T_1,\varepsilon_{01})} = \frac{g(\varepsilon_{02})}{g(\varepsilon_{01})}\left[\frac{B^*_{c2}(0,\varepsilon_{02})}{B^*_{c2}(0,\varepsilon_{01})}\right]^{-1}\left(\frac{1-t_2^{\nu}}{1-t_1^{\nu}}\right)^{\eta-1}, \tag{A10.28}$$

with

$$\frac{T^*_c(\varepsilon_0)}{T^*_c(0)} = \left[\frac{B^*_{c2}(0,\varepsilon_0)}{B^*_{c2}(0,0)}\right]^{1/w}. \tag{A10.29}$$

Any parameterization of $B^*_{c2}(0,\varepsilon_0)$ and $g(\varepsilon_0)$ will work with the general transformation factors given by Eqs (A10.27)–(A10.29). The extended-range parameterizations discussed in Secs 10.5.6 and 10.7.3 are suggested as a practical scheme that is easy to use because they preserve the consistency of the intrinsic parameter values a and s for the moderate strain range; that is,

$$\frac{B^*_{c2}(0,\varepsilon_0)}{B^*_{c2}(0,0)} = 1 - a|\varepsilon_0|^{1.7} + a_1|\varepsilon_0 - \varepsilon_0'|^{a_2} I(\varepsilon_0 < \varepsilon_0'), \tag{A10.30}$$

$$\frac{g(\varepsilon_0)}{C} = [1 - a|\varepsilon_0|^{1.7}]^s + g_1|\varepsilon_0 - \varepsilon_0'|^{g_2} I(\varepsilon_0 < \varepsilon_0'). \tag{A10.31}$$

Here, C is the same proportionality constant as in Eq. (A10.18), and the indicator function is defined as

$$I(\varepsilon_0 < \varepsilon_0') \equiv \begin{cases} 1 & \text{if } \varepsilon_0 < \varepsilon_0' \\ 0 & \text{if } \varepsilon_0 > \varepsilon_0' \end{cases}, \tag{A10.32}$$

with $\varepsilon_0' = -0.005$ for Nb_3Sn. [This function is readily programmed in spreadsheet programs with a conditional clause of the form: IF($\varepsilon_0 < -0.5\%$, 1 if true, 0 if false).] Again, for the many applications at moderate intrinsic-strain levels, the high-compression term is not needed. This happens seamlessly with Eqs (A10.30) and (A10.31) because the indicator function automatically drops the extra term for moderate strains, reducing these relations to the simpler power-law expressions.

The simplicity of this transformation procedure becomes readily clear by referring to the example given in Table 10.4 at the end of Sec. 10.7.5. The entire process can be carried out in a few minutes with a spreadsheet program. It is also quite accurate. For example, a relatively large error of 20% in the temperature parameter η would result in an error in the I_c values of only about 3.5% when transforming from the canonical temperature of 4.2 K to a difficult-to-measure temperature, such as 5.5 K. Likewise, when transforming from, say, $\varepsilon_0 = -0.3\%$ to 0% in Nb_3Sn conductors, a relatively large error of 10% in the value of the strain sensitivity parameter a would result in an error of less than 0.5% in the transformed B values and negligible error in the transformed I_c values. Again, with this method there is no need to determine the shape of the I_c–B curve, and it is independent of the extrapolation method used to determine B^*_{c2}. The method, given in general form by Eqs (A10.21) through (A10.23), *relies only on the unified scaling law,* not on the separable parameter set used to illustrate it here. *Thus, it would readily work with any other parameterization of the prefactor $K(T,\varepsilon_0)$ in the unified scaling law, Eq. (10.45).*

Index

The suffix *f* following a page number indicates a figure and *t* indicates a table.